

**NIST Special Publication 1018-3**  
**Sixth Edition**

**Fire Dynamics Simulator  
Technical Reference Guide  
Volume 3: Validation**

Kevin McGrattan  
Simo Hostikka  
Randall McDermott  
Jason Floyd  
Craig Weinschenk  
Kristopher Overholt

<http://dx.doi.org/10.6028/NIST.SP.1018-3>



VTT Technical Research Centre of Finland





**NIST Special Publication 1018-3**  
**Sixth Edition**

**Fire Dynamics Simulator**  
**Technical Reference Guide**  
**Volume 3: Validation**

Kevin McGrattan  
Randall McDermott  
*Fire Research Division*  
*Engineering Laboratory*  
*Gaithersburg, Maryland, USA*

Simo Hostikka  
*Aalto University*  
*Espoo, Finland*

Jason Floyd  
*JENSEN HUGHES*  
*Baltimore, Maryland, USA*

Craig Weinschenk  
*UL Firefighter Safety Research Institute*  
*Columbia, Maryland, USA*

Kristopher Overholt  
*Continuum Analytics*  
*Austin, Texas, USA*

<http://dx.doi.org/10.6028/NIST.SP.1018-3>

February 7, 2017  
FDS Version 6.5.3  
Revision: FDS6.5.3-739-g9e39475



U.S. Department of Commerce  
*Penny Pritzker, Secretary*

National Institute of Standards and Technology  
*Willie May, Under Secretary of Commerce for Standards and Technology and Director*

Certain commercial entities, equipment, or materials may be identified in this document in order to describe an experimental procedure or concept adequately. Such identification is not intended to imply recommendation or endorsement by the National Institute of Standards and Technology, nor is it intended to imply that the entities, materials, or equipment are necessarily the best available for the purpose.

**National Institute of Standards and Technology Special Publication 1018-3**  
**Natl. Inst. Stand. Technol. Spec. Publ. 1018-3, 706 pages (October 2013)**  
**CODEN: NSPUE2**

# FDS Developers

The Fire Dynamics Simulator and Smokeview are the products of an international collaborative effort led by the National Institute of Standards and Technology (NIST) and VTT Technical Research Centre of Finland. Its developers and contributors are listed below.

## Principal Developers of FDS

Kevin McGrattan, NIST  
Simo Hostikka, Aalto University  
Randall McDermott, NIST  
Jason Floyd, JENSEN HUGHES, Baltimore, Maryland, USA  
Craig Weinschenk, UL Firefighter Safety Research Institute, Columbia, Maryland, USA  
Kristopher Overholt, Continuum Analytics, Austin, Texas, USA

## Principal Developer of Smokeview

Glenn Forney, NIST

## Principal Developer of FDS+Evac

Timo Korhonen, VTT

## Contributors

Daniel Haarhoff, Jülich Supercomputing Centre, Germany  
Susan Kilian, hhpberlin, Germany  
Vivien Lecoustre, University of Maryland, USA  
Anna Matala, VTT  
William Mell, U.S. Forest Service, Seattle, Washington, USA  
Topi Sikanen, VTT  
Ben Trettel, The University of Texas at Austin, USA  
Julio Cesar Silva, National Council for Scientific and Technological Development, Brazil  
Benjamin Ralph, University of Edinburgh, UK



# About the Developers

**Kevin McGrattan** is a mathematician in the Fire Research Division of NIST. He received a bachelor of science degree from the School of Engineering and Applied Science of Columbia University in 1987 and a doctorate at the Courant Institute of New York University in 1991. He joined the NIST staff in 1992 and has since worked on the development of fire models, most notably the Fire Dynamics Simulator.

**Simo Hostikka** is an associate professor of fire safety engineering at Aalto University School of Engineering, since January 2014. Before joining Aalto, he worked as a Principal Scientist and Team Leader at VTT Technical Research Centre of Finland. He received a master of science (technology) degree in 1997 and a doctorate in 2008 from the Department of Engineering Physics and Mathematics of the Helsinki University of Technology. He is the principal developer of the radiation and solid phase sub-models within FDS.

**Randall McDermott** joined the Fire Research Division at NIST in 2008. He received a B.S. from the University of Tulsa in Chemical Engineering in 1994 and a Ph.D. from the University of Utah in 2005. His research interests include subgrid-scale models and numerical methods for large-eddy simulation, turbulent combustion, immersed boundary methods, and Lagrangian particle methods.

**Jason Floyd** is a Senior Engineer at JENSEN HUGHES, in Baltimore, Maryland. He received a bachelor of science and a doctorate in the Nuclear Engineering Program of the University of Maryland. After graduating, he was awarded a National Research Council Post-Doctoral Fellowship at the Building and Fire Research Laboratory of NIST. He is a principal developer of the combustion, control logic, and HVAC sub-models within FDS.

**Craig Weinschenk** is an engineer at Underwriters Laboratories Firefighter Safety Research Institute, in Columbia, Maryland. He worked in the Fire Research Division at NIST as a National Research Council Postdoctoral Research Associate in 2011. He received a B.S. from Rowan University in 2006 in Mechanical Engineering. He received an M.S. in 2007 and a doctorate in 2011 from The University of Texas at Austin in Mechanical Engineering. His research interests include numerical combustion, fire-structure interaction, and human factors research of fire-fighting tactics.

**Kristopher Overholt** is a software engineer at Continuum Analytics, developers of the Anaconda Python distribution. He received a B.S. in Fire Protection Engineering Technology from the University of Houston-Downtown in 2008, an M.S. in Fire Protection Engineering from Worcester Polytechnic Institute in 2010, and a Ph.D. in Civil Engineering from The University of Texas at Austin in 2013. He worked in the Fire Research Division at NIST from 2013 to 2015, where he was central to the development of the FDS continuous integration framework, Firebot. He also worked on aspects of FDS related to verification and validation and quality metrics. His research interests include inverse fire modeling problems, soot deposition in fires, and the use of fire models in forensic applications.

**Glenn Forney** is a computer scientist in the Fire Research Division of NIST. He received a bachelor of science degree in mathematics from Salisbury State College and a master of science and a doctorate in mathematics from Clemson University. He joined NIST in 1986 (then the National Bureau of Standards) and has since worked on developing tools that provide a better understanding of fire phenomena, most notably Smokeview, an advanced scientific software tool for visualizing Fire Dynamics Simulation data.

**Timo Korhonen** is a Senior Scientist at VTT Technical Research Centre of Finland. He received a master of science (technology) degree in 1992 and a doctorate in 1996 from the Department of Engineering Physics and Mathematics of the Helsinki University of Technology. He is the principal developer of the evacuation sub-model within FDS.

**Daniel Haarhoff** did his masters work at the Jülich Supercomputing Centre in Germany, graduating in 2015. His thesis is on providing and analyzing a hybrid parallelization of FDS. For this, he implemented OpenMP into FDS 6.

**Susan Kilian** is a mathematician with numerics and scientific computing expertise. She received her diploma from the University of Heidelberg and received her doctorate from the Technical University of Dortmund in 2002. Since 2007 she has been a research scientist for hhpberlin, a fire safety engineering firm located in Berlin, Germany. Her research interests include high performance computing and the development of efficient parallel solvers for the pressure Poisson equation.

**Vivien Lecoustre** is a Research Associate at the University of Maryland. He received a master of science in Aerospace Engineering from ENSMA (France) in 2005 and a doctorate in Mechanical Engineering from the University of Maryland in 2009. His research interests include radiation properties of fuels and numerical turbulent combustion.

**Anna Matala** is a Research Scientist at VTT Technical Research Centre of Finland and a Ph.D. candidate at Aalto University School of Science. She received her M.Sc. degree in Systems and Operations Research from Helsinki University of Technology in 2008. Her research concentrates on pyrolysis modelling and parameter estimation in fire simulations

**William (Ruddy) Mell** is an applied mathematician currently at the U.S. Forest Service in Seattle, Washington. He holds a B.S. degree from the University of Minnesota (1981) and doctorate from the University of Washington (1994). His research interests include the development of large-eddy simulation methods and sub-models applicable to the physics of large fires in buildings, vegetation, and the wildland-urban interface.

**Topi Sikanen** is a Research Scientist at VTT Technical Research Centre of Finland and a graduate student at Aalto University School of Science. He received his M.Sc. degree in Systems and Operations Research from Helsinki University of Technology in 2008. He works on the Lagrangian particle and liquid evaporation models.

**Ben Trettel** is a graduate student at The University of Texas at Austin. He received a B.S. in Mechanical Engineering in 2011 and an M.S. in Fire Protection Engineering in 2013, both from the University of Maryland. He develops models for the transport of Lagrangian particles for the Fire Dynamics Simulator.

**Julio Cesar Silva** is a Guest Researcher in the Fire Research Division of NIST from National Council for Scientific and Technological Development, Brazil. He received a M.Sc. in 2010 and a doctorate in 2014 from Federal University of Rio de Janeiro in Civil Engineering. His research interests include fire-structure interaction and he develops coupling strategies between FDS and finite-element codes.

**Benjamin Ralph** is a fire safety engineer and Ph.D. student at the BRE Centre for Fire Safety Engineering at University of Edinburgh, UK. He received his M.Eng. in Civil Engineering from the University of Southampton, UK in 2008 and his P.G.Dip. in Fire Safety Engineering from the University of Ulster, UK in 2014. He was a Guest Researcher in the Engineered Fire Safety Group at NIST in 2016. His research interests include coupled hybrid modeling and performance-based design in fire safety engineering. He is a developer of the HVAC sub-model - specifically the transient mass and energy transport solver.



# Preface

This is Volume 3 of the FDS Technical Reference Guide. Volume 1 describes the mathematical model and numerical method. Volume 2 documents past and present model verification work. Instructions for using FDS are contained in a separate User’s Guide [1].

The FDS Technical Reference Guide is based in part on the “Standard Guide for Evaluating the Predictive Capability of Deterministic Fire Models,” ASTM E 1355 [2]. ASTM E 1355 defines *model evaluation* as “the process of quantifying the accuracy of chosen results from a model when applied for a specific use.” The model evaluation process consists of two main components: verification and validation. *Verification* is a process to check the correctness of the solution of the governing equations. Verification does not imply that the governing equations are appropriate; only that the equations are being solved correctly. *Validation* is a process to determine the appropriateness of the governing equations as a mathematical model of the physical phenomena of interest. Typically, validation involves comparing model results with experimental measurement. Differences that cannot be explained in terms of numerical errors in the model or uncertainty in the measurements are attributed to the assumptions and simplifications of the physical model.

Evaluation is critical to establishing both the acceptable uses and limitations of a model. Throughout its development, FDS has undergone various forms of evaluation, both at NIST and beyond. This volume provides a survey of validation work conducted to date to evaluate FDS.



# **Disclaimer**

The US Department of Commerce makes no warranty, expressed or implied, to users of the Fire Dynamics Simulator (FDS), and accepts no responsibility for its use. Users of FDS assume sole responsibility under Federal law for determining the appropriateness of its use in any particular application; for any conclusions drawn from the results of its use; and for any actions taken or not taken as a result of analysis performed using these tools.

Users are warned that FDS is intended for use only by those competent in the fields of fluid dynamics, thermodynamics, heat transfer, combustion, and fire science, and is intended only to supplement the informed judgment of the qualified user. The software package is a computer model that may or may not have predictive capability when applied to a specific set of factual circumstances. Lack of accurate predictions by the model could lead to erroneous conclusions with regard to fire safety. All results should be evaluated by an informed user.

Throughout this document, the mention of computer hardware or commercial software does not constitute endorsement by NIST, nor does it indicate that the products are necessarily those best suited for the intended purpose.



# Acknowledgments

The following individuals and organizations played a role in the validation process of FDS.

- The US Nuclear Regulatory Commission Office of Research has funded key validation experiments, the preparation of the FDS manuals, and the development of various sub-models that are of importance in the area of nuclear power plant safety. Special thanks to Mark Salley, David Stroup, and Jason Dreisbach for their efforts and support.
- Anthony Hamins of NIST directed the NIST/NRC and WTC experiments, conducted smaller methane burner measurements, and quantified the experimental uncertainty of these and other experiments used in this study. Alex Maranghides was the Director of the Large Fire Laboratory at NIST at the time these tests were conducted, and he helped to design the experiments. Therese McAllister oversaw the instrumentation of the structural steel during the WTC experiments.
- Anthony Hamins of NIST developed the technique of evaluating experimental uncertainty that is used throughout this Guide. Blaza Toman of the Statistical Engineering Division of NIST developed the method of quantifying the model uncertainty.
- Rick Peacock of NIST assisted in the interpretation of results from the “NBS Multi-Room Test Series,” a set of three room fire experiments conducted at the National Bureau of Standards (now NIST) in the mid-1980’s.
- Bryan Klein, currently employed at Thunderhead Engineering, Inc., assisted in the development of techniques to automatically generate the plots that are found throughout this Guide.
- Bill Pitts, Nelson Bryner, and Erik Johnsson of NIST contributed and interpreted test data for the “NIST Reduced Scale Enclosure Experiments.” Matthew Bundy, Erik Johnsson, Paul Fuss, David Lenhart, Sung Chan Kim, and Andrew Lock of NIST contributed similar data collected within a full-scale standard compartment in 2010.
- Rodney Bryant of NIST contributed velocity profile data for the “Bryant Doorway” series.
- Tony Putorti and Scott Bareham of NIST contributed temperature measurements from plate thermometer experiments in a cone calorimeter.
- David Sheppard, currently of the Bureau of Alcohol, Tobacco and Firearms (ATF), conducted the experiments referred to as the “UL/NFPRF Test Series” on behalf of the Fire Protection Research Foundation (then known as the National Fire Protection Research Foundation) while working at Underwriters Labs in Northbrook, Illinois. Sheppard, along with Bryan Klein, currently employed at Thunderhead Engineering, Inc., conducted the experiments referred to as the “ATF Corridors” series in 2008.

- Jerry Back, Craig Beyler and Phil DiNenno of Hughes Associates and Pat Tatem of the Naval Research Laboratory contributed experimental data for the “HAI/NRL Wall Fire” series. Thanks also to Craig Beyler for assistance with the data for the “Beyler Hood Experiments.”
- Ken Steckler provided details about the “Steckler Compartment Experiments” of 1979.
- Jianping Zhang at the University of Ulster contributed heat flux measurements from the SBI apparatus.
- At the University of Maryland, Professor Fred Mowrer and Phil Friday were the first to apply FDS to the NRC-sponsored experiments referred to in this document as the “FM/SNL Test Series” (Factory Mutual and Sandia National Laboratories conducted these experiments).
- Jukka Vaari of VTT, Finland, contributed the Cup Burner test cases.
- Steve Nowlen of Sandia National Laboratory provided valuable information about the FM/SNL series, and he also conducted the CAROLFIRE experiments.
- Ulf Wickström of SP, Sweden, contributed experimental data from a series of experiments (SP AST) that were designed to evaluate the feasibility of using plate thermometer measurements as boundary conditions for a heat conduction calculation within several types of steel beams. The adiabatic surface temperature concept was tested in both the experiments and model.
- Jeremy Thornock at the University of Utah provided data on the Sandia helium plume.
- Sheldon Teiszen at Sandia National Laboratories, Albuquerque, provided detailed statistics for the helium plume and pool fire experiments conducted in the Sandia FLAME facility.
- Taylor Myers, a student at the University of Maryland and a Summer Undergraduate Research Fellow (SURF) at NIST, analyzed the Vettori Flat and Sloped Ceiling sprinkler experiments. Thanks also to Bob Vettori of the U.S. Nuclear Regulatory Commission and formerly of NIST for his help in locating the original test data and laboratory notebooks.
- Hans la Cour-Harbo, a masters degree student at the Technical University of Denmark, provided guidance and insight on the NRCC Facade experiments. Scott Bareham of NIST provided the technical drawing of the test enclosure.
- Prof. Stanislav Stolarov and graduate students Mark McKinnon and Jing Li of the University of Maryland provided the properties of several polymers for the FAA Polymers example.
- Michael Spearpoint and masters degree students Roger Harrison and Rob Fleury of the University of Canterbury, New Zealand, supplied measurements of mass entrainment rates into spill plumes (Harrison Spill Plumes) and heat flux measurements from propane burner fires (Fleury Heat Flux).
- Ezti Oztekin of the Federal Aviation Administration (FAA) developed the FAA Cargo Compartments cases based on experiments sponsored by the FAA.
- Topi Sikanen of VTT, Finland, and Jonathan Wahlqvist of Lund University, Sweden, contributed FDS input files for the PRISME DOOR series.
- Paul Tyson, a student at the University of Ulster, Northern Ireland, contributed the input files and supporting documents for the NRCC Smoke Tower experiments.
- James White, a student at the University of Maryland, provided documentation and input files for the UMD Line Burner cases.

# Contents

<b>FDS Developers</b>	i
<b>About the Developers</b>	iii
<b>Preface</b>	vii
<b>Disclaimer</b>	ix
<b>Acknowledgments</b>	xi
<b>Contents</b>	xiii
<b>List of Figures</b>	xxi
<b>List of Tables</b>	xxxiii
<b>List of Acronyms</b>	xxxv
<b>1 What is Model Validation?</b>	1
1.1 Blind, Specified, and Open Validation Experiments . . . . .	1
1.2 How to Use this Guide . . . . .	2
<b>2 Survey of Past Validation Work</b>	5
2.1 Validation Work with Pre-Release Versions of FDS . . . . .	6
2.2 Validation of FDS since 2000 . . . . .	7
2.2.1 Fire Plumes . . . . .	7
2.2.2 Pool Fires . . . . .	8
2.2.3 Air and Gas Movement in the Absence of Fire . . . . .	8
2.2.4 Wind Engineering . . . . .	9
2.2.5 Atmospheric Dispersion . . . . .	9
2.2.6 Growing Fires . . . . .	10
2.2.7 Flame Spread . . . . .	10
2.2.8 Compartment Fires . . . . .	11
2.2.9 Sprinklers, Mist System, and Suppression by Water . . . . .	12
2.2.10 Airflows in Fire Compartments . . . . .	13
2.2.11 Tunnel Fires . . . . .	13
2.2.12 Smoke Detection . . . . .	13
2.2.13 Combustion Model . . . . .	14
2.2.14 Soot Deposition . . . . .	14
2.3 Reconstructions of Actual Fires . . . . .	15

<b>3 Description of Experiments</b>	<b>17</b>
3.1 ArupFire Tunnel Fire Experiments . . . . .	17
3.2 ATF Corridors Experiments . . . . .	17
3.3 Backward Facing Step . . . . .	19
3.4 Beyler Hood Experiments . . . . .	19
3.5 Bouchair Solar Chimney . . . . .	20
3.6 BRE Spray Test for Radiation Attenuation . . . . .	21
3.7 Bryant Doorway Velocity Measurements . . . . .	21
3.8 Cable Response to Live Fire – CAROLFIRE . . . . .	21
3.9 CSIRO Grassland Fires . . . . .	23
3.10 Cup Burner Experiments . . . . .	23
3.11 DelCo Trainer Experiments . . . . .	23
3.12 FAA Cargo Compartments . . . . .	23
3.13 FAA Polymers . . . . .	24
3.14 Fleury Heat Flux Measurements . . . . .	24
3.15 FM/FPRF Datacenter Experiments . . . . .	26
3.16 FM Parallel Panel Experiments . . . . .	26
3.17 FM/SNL Experiments . . . . .	26
3.18 Hamins Gas Burner Experiments . . . . .	30
3.19 Harrison Spill Plumes . . . . .	30
3.20 Heskestad Flame Height Correlation . . . . .	30
3.21 LEMTA Spray Test for Radiation Attenuation . . . . .	30
3.22 LLNL Enclosure Experiments . . . . .	32
3.23 LNG Dispersion Experiments . . . . .	32
3.24 McCaffrey Plume Experiments . . . . .	32
3.25 NBS Multi-Room Experiments . . . . .	32
3.26 NIST Douglas Firs . . . . .	35
3.27 NIST Enclosure Experiments . . . . .	35
3.27.1 NIST Reduced Scale Enclosure Experiments, 1994 . . . . .	35
3.27.2 NIST Reduced Scale Enclosure Experiments, 2007 . . . . .	35
3.27.3 NIST Full-Scale Enclosure Experiments, 2008 . . . . .	37
3.28 NIST Helium Experiments . . . . .	37
3.29 NIST/NRC Compartment Experiments . . . . .	40
3.30 NIST Smoke Alarm Experiments . . . . .	42
3.31 NRCC Facade Heat Flux Measurements . . . . .	44
3.32 NRCC Smoke Tower Experiments . . . . .	44
3.33 NRL/HAI Wall Heat Flux Measurements . . . . .	47
3.34 PRISME Project . . . . .	47
3.35 Purdue Flames . . . . .	48
3.36 Restivo Compartment Air Flow Experiment . . . . .	48
3.37 Sandia Plume Experiments . . . . .	48
3.38 Sippola Aerosol Deposition Experiments . . . . .	48
3.39 Smyth Slot Burner Experiment . . . . .	49
3.40 SP Adiabatic Surface Temperature Experiments . . . . .	49
3.41 Steckler Compartment Experiments . . . . .	51
3.42 UL/NIST Vent Experiments . . . . .	51
3.43 UL/NFPRF Sprinkler, Vent, and Draft Curtain Study . . . . .	53
3.44 Ulster SBI Corner Heat Flux Measurements . . . . .	60

3.45 UMD Polymers . . . . .	60
3.46 UMD Line Burner . . . . .	61
3.47 USCG/HAI Water Mist Suppression Tests . . . . .	62
3.48 USN High Bay Hangar Experiments . . . . .	63
3.49 Vettori Flat Ceiling Experiments . . . . .	63
3.50 Vettori Sloped Ceiling Experiments . . . . .	66
3.51 VTT Large Hall Tests . . . . .	66
3.52 VTT Water Spray Experiments . . . . .	67
3.53 WTC Spray Burner Experiments . . . . .	67
3.54 Summary of Experiments . . . . .	70
<b>4 Quantifying Model Uncertainty</b>	<b>75</b>
4.1 Introduction . . . . .	75
4.2 Sources of Model Uncertainty . . . . .	77
4.3 Experimental Uncertainty . . . . .	78
4.3.1 Uncertainty of Common Fire Measurements . . . . .	79
4.3.2 Propagation of Input Parameter Uncertainty . . . . .	81
4.3.3 Summary of Experimental Uncertainty Estimates . . . . .	85
4.4 Calculating Model Uncertainty . . . . .	85
4.5 Example . . . . .	88
4.6 Additional Considerations . . . . .	89
<b>5 HGL Temperature and Depth</b>	<b>91</b>
5.1 HGL Reduction Method . . . . .	91
5.2 ATF Corridors . . . . .	92
5.3 DeCo Trainers . . . . .	96
5.4 FM/SNL Test Series . . . . .	100
5.5 LLNL Enclosure Series . . . . .	105
5.6 NBS Multi-Room Test Series . . . . .	114
5.7 NIST Full-Scale Enclosure (FSE), 2008 . . . . .	118
5.8 NIST/NRC Test Series . . . . .	125
5.9 NRCC Smoke Tower . . . . .	130
5.10 PRISME DOOR Experiments . . . . .	132
5.11 PRISME SOURCE Experiments . . . . .	136
5.12 Steckler Compartment Experiments . . . . .	139
5.13 UL/NIST Vent Experiments . . . . .	147
5.14 VTT Test Series . . . . .	149
5.15 WTC Test Series . . . . .	150
5.16 Summary of Hot Gas Layer Temperature and Height . . . . .	153
<b>6 Fire Plumes</b>	<b>157</b>
6.1 Plume Temperatures . . . . .	157
6.1.1 FM/SNL Experiments . . . . .	158
6.1.2 McCaffrey's Plume Correlation . . . . .	161
6.1.3 NRCC Smoke Tower Experiments, Stairwell Plumes . . . . .	162
6.1.4 SP Adiabatic Surface Temperature Experiments . . . . .	164
6.1.5 USN High Bay Hangar Experiments . . . . .	166
6.1.6 VTT Large Hall Experiments . . . . .	170

6.1.7	Summary of Plume Temperature Predictions . . . . .	171
6.2	Heskestad's Flame Height Correlation . . . . .	172
6.3	Harrison Spill Plumes/Entrainment Experiments . . . . .	176
6.4	Sandia Plume Experiments . . . . .	177
6.4.1	Sandia 1 m Helium Plume . . . . .	177
6.4.2	Sandia 1 m Methane Pool Fire . . . . .	182
6.4.3	Sandia 1 m Hydrogen Pool Fire . . . . .	188
6.5	Purdue 7.1 cm Methane Flame . . . . .	191
6.6	UMD Line Burner . . . . .	195
<b>7</b>	<b>Ceiling Jets and Device Activation</b>	<b>197</b>
7.1	Ceiling Jet Temperatures . . . . .	197
7.1.1	ATF Corridors Experiment . . . . .	198
7.1.2	Arup Tunnel Experiments . . . . .	204
7.1.3	DelCo Trainers . . . . .	205
7.1.4	FAA Cargo Compartments . . . . .	208
7.1.5	FM/SNL Experiments . . . . .	213
7.1.6	NIST Smoke Alarm Experiments . . . . .	216
7.1.7	NIST/NRC Experiments . . . . .	218
7.1.8	NRCC Smoke Tower . . . . .	221
7.1.9	PRISME DOOR Experiments . . . . .	223
7.1.10	PRISME SOURCE Experiments . . . . .	225
7.1.11	SP Adiabatic Surface Temperature Experiments . . . . .	227
7.1.12	UL/NFPRF Series I Experiments . . . . .	229
7.1.13	UL/NIST Vent Experiments . . . . .	232
7.1.14	Vettori Flat Ceiling Experiments . . . . .	234
7.1.15	Vettori Sloped Ceiling Experiments . . . . .	241
7.1.16	WTC Experiments . . . . .	251
7.1.17	Summary of Ceiling Jet Temperature Predictions . . . . .	252
7.2	Sprinkler Activation Times . . . . .	253
7.2.1	Time to First Sprinkler Activation . . . . .	253
7.2.2	Number of Sprinkler Activations . . . . .	254
7.3	Smoke Detector Activation Times . . . . .	262
<b>8</b>	<b>Gas Velocity</b>	<b>265</b>
8.1	ATF Corridor Experiments . . . . .	265
8.2	Backward Facing Step . . . . .	270
8.3	Bryant Doorway Experiments . . . . .	273
8.4	FM/FPRF Datacenter Experiments . . . . .	275
8.5	McCaffrey's Plume Correlation . . . . .	277
8.6	PRISME DOOR Experiments . . . . .	278
8.7	Restivo Experiment . . . . .	279
8.8	Steckler Compartment Experiments . . . . .	280
8.9	WTC Experiments . . . . .	288
8.10	Summary of Velocity Predictions . . . . .	293

<b>9 Gas Species and Smoke</b>	<b>295</b>
9.1 Major Combustion Products, O <sub>2</sub> and CO <sub>2</sub>	295
9.1.1 DelCo Trainers	296
9.1.2 FAA Cargo Compartments	299
9.1.3 NIST/NRC Experiments	300
9.1.4 NRCC Smoke Tower	304
9.1.5 PRISME DOOR Experiments	306
9.1.6 PRISME SOURCE Experiments	310
9.1.7 WTC Experiments	313
9.1.8 UMD Line Burner	315
9.1.9 Summary of Major Combustion Products Predictions	317
9.2 Smoke and Aerosols	318
9.2.1 FM/FPRF Datacenter Experiments	318
9.2.2 NIST/NRC Experiments	319
9.2.3 FAA Cargo Compartments	323
9.2.4 Sippola Aerosol Deposition Experiments	325
9.3 Products of Incomplete Combustion	328
9.3.1 Smyth Slot Burner Experiment	328
9.3.2 Beyler Hood Experiments	332
9.3.3 NIST Reduced Scale Enclosure (RSE) Experiments, 1994	334
9.3.4 NIST Reduced-Scale Enclosure (RSE) Experiments, 2007	336
9.3.5 NIST Full-Scale Enclosure (FSE) Experiments, 2008	349
9.3.6 Summary, Products of Incomplete Combustion	377
9.4 Helium Release in a Reduced Scale Garage Geometry	378
<b>10 Pressure</b>	<b>383</b>
10.1 FM/FPRF Datacenter Experiments	383
10.2 NIST/NRC Experiments	383
10.3 LLNL Enclosure Experiments	386
10.4 PRISME DOOR Experiments	392
10.5 PRISME SOURCE Experiments	397
10.6 Summary of Pressure Predictions	400
<b>11 Surface Temperature</b>	<b>401</b>
11.1 Wall, Ceiling and Floor Temperatures	402
11.1.1 FAA Cargo Compartments	402
11.1.2 NIST Full-Scale Enclosure (FSE), 2008	403
11.1.3 NIST/NRC Experiments	411
11.1.4 PRISME DOOR Experiments	424
11.1.5 PRISME SOURCE Experiments	428
11.1.6 WTC Experiments	431
11.1.7 Summary of Wall, Ceiling, and Floor Temperature Predictions	445
11.2 Target Temperature	446
11.2.1 NIST/NRC Experiments	446
11.2.2 SP Adiabatic Surface Temperature Experiments	461
11.2.3 WTC Experiments	489
11.2.4 CAROLFIRE Experiments	501
11.2.5 PRISME Experiments	507

11.2.6	Summary of Target Temperature Predictions . . . . .	515
11.2.7	Time to Failure . . . . .	516
<b>12 Heat Flux</b>		<b>517</b>
12.1	Heat Flux to Walls, Ceiling, and Floor . . . . .	518
12.1.1	FAA Cargo Compartments . . . . .	518
12.1.2	FM Parallel Panel Experiments . . . . .	519
12.1.3	NIST/NRC Experiments . . . . .	520
12.1.4	NRCC Facade Experiments . . . . .	533
12.1.5	NRL/HAI Experiments . . . . .	537
12.1.6	PRISME DOOR Experiments . . . . .	540
12.1.7	PRISME SOURCE Experiments . . . . .	546
12.1.8	Ulster SBI Experiments . . . . .	550
12.1.9	WTC Experiments . . . . .	551
12.1.10	Summary of Wall, Ceiling and Floor Heat Flux Predictions . . . . .	555
12.2	Heat Flux to Targets . . . . .	556
12.2.1	Fleury Experiments . . . . .	556
12.2.2	Hamins Gas Burner Experiments . . . . .	562
12.2.3	NIST/NRC Experiments . . . . .	587
12.2.4	WTC Experiments . . . . .	596
12.2.5	Summary of Target Heat Flux Predictions . . . . .	600
12.3	Attenuation of Thermal Radiation in Water Spray . . . . .	601
12.3.1	BRE Spray Experiments . . . . .	601
12.3.2	LEMTA Spray Experiments . . . . .	601
12.4	Convective Heat Flux . . . . .	603
12.4.1	Bouchair Solar Chimney . . . . .	603
<b>13 Suppression</b>		<b>611</b>
13.1	Cup Burner Experiments . . . . .	611
13.2	USCG/HAI Water Mist Suppression Tests . . . . .	614
13.3	VTT Water Spray Experiments . . . . .	621
<b>14 Burning Rate and Fire Spread</b>		<b>623</b>
14.1	FAA Polymers . . . . .	623
14.1.1	Glossary of Terms . . . . .	623
14.1.2	Non-Charring Polymers, HDPE, HIPS, and PMMA . . . . .	625
14.1.3	Complex Non-Charring Polymers: PP, PA66, POM, and PET . . . . .	627
14.1.4	Polycarbonate (PC) . . . . .	629
14.1.5	Poly(vinyl chloride) (PVC) . . . . .	631
14.1.6	Poly(aryl ether ether ketone)) (PEEK) . . . . .	633
14.1.7	Poly(butylene terephthalate) (PBT) . . . . .	636
14.1.8	PBT with Glass Fibers (PBT-GF) . . . . .	638
14.2	UMD Polymers . . . . .	640
14.2.1	One-Step Degradation: ABS, HIPS, and PMMA . . . . .	640
14.2.2	Two-Step Degradation: Kydex . . . . .	643
14.2.3	Three-Step Degradation: PEI, PET, and POM . . . . .	645
14.3	Corrugated Cardboard . . . . .	648

14.4 Electrical Cables (CHRISTIFIRE) . . . . .	652
14.4.1 Estimation of Pyrolysis Kinetics . . . . .	652
14.4.2 Estimation of Thermal Parameters and Validation . . . . .	653
14.5 Liquid Pool Fires . . . . .	658
14.6 Wildland Fire Spread (CSIRO Grassland Fires) . . . . .	660
14.7 Burning Trees (NIST Douglas Firs) . . . . .	662
14.8 Summary of Burning Rates . . . . .	665
<b>15 Wind Engineering and Atmospheric Dispersion</b>	<b>667</b>
15.1 LNG Dispersion Experiments . . . . .	667
<b>16 Conclusion</b>	<b>679</b>
16.1 Summary of FDS Model Uncertainty Statistics . . . . .	679
16.2 Normality Tests . . . . .	680
16.3 Summary of FDS Validation Git Statistics . . . . .	684
<b>Bibliography</b>	<b>687</b>



# List of Figures

3.1	Geometry of the ATF Corridors Experiments . . . . .	18
3.2	Geometry of the Backward Facing Step experiments . . . . .	19
3.3	Geometry of the Bouchair Solar Chimney experiment . . . . .	20
3.4	Geometry of Bryant's compartment . . . . .	22
3.5	Instrumentation of the single level DelCo training structure . . . . .	24
3.6	Instrumentation of the two level DelCo training structure . . . . .	25
3.7	Geometry of the FM/SNL Experiments . . . . .	28
3.8	Geometry of the Harrison Spill Plumes Experiments. . . . .	31
3.9	Geometry of the LLNL Enclosure Experiments . . . . .	34
3.10	Geometry of the NBS Multi-Room Experiments . . . . .	36
3.11	Geometry of the compartment used in the NIST Full-Scale Enclosure experiments . . . . .	38
3.12	Geometry of the NIST/NRC Experiments . . . . .	41
3.13	Geometry of the manufactured home from the NIST Smoke Alarm Experiments . . . . .	43
3.14	Geometry of the NRCC Facade Experiments . . . . .	45
3.15	Geometry of the NRCC Smoke Tower Experiments . . . . .	46
3.16	Geometry of Restivo's compartment . . . . .	49
3.17	Geometry of the SP/AST compartment for Test 2. . . . .	50
3.18	Geometry of the Steckler Compartment Experiments. . . . .	52
3.19	Geometry of the UL/NIST Experiments. . . . .	54
3.20	Plan view of the UL/NFPRF heptane spray experiments, Series I. . . . .	55
3.21	Plan view of the UL/NFPRF heptane spray experiments, Series II . . . . .	56
3.22	Plan view of the UL/NFPRF plastic commodity Test P-3. . . . .	57
3.23	UMD Line Burner isometric view of burner and oxidizer assembly. . . . .	62
3.24	Geometry of the Vettori Flat Ceiling compartment . . . . .	64
3.25	Geometry of the VTT Large Fire Test Hall . . . . .	68
3.26	Geometry of the WTC Experiments . . . . .	69
4.1	Demonstration of model uncertainty. . . . .	76
4.2	Sample scatter plot. . . . .	78
4.3	Sample time history plots. . . . .	86
5.1	ATF Corridors, HGL temperature and height, first floor, 50 kW, 100 kW, 240 kW . . . . .	92
5.2	ATF Corridors, HGL temperature and height, first floor, 250 kW, 500 kW, mixed . . . . .	93
5.3	ATF Corridors, HGL temperature and height, second floor, 50 kW, 100 kW, 240 kW . . . . .	94
5.4	ATF Corridors, HGL temperature and height, second floor, 250 kW, 500 kW, mixed . . . . .	95
5.5	DelCo Trainers, HGL Temperature, Test 2 . . . . .	96
5.6	DelCo Trainers, HGL Temperature, Tests 3 and 4 . . . . .	97
5.7	DelCo Trainers, HGL Temperature, Tests 5 and 6 . . . . .	98
5.8	DelCo Trainers, HGL Temperature, Tests 22-25 . . . . .	99

5.9	FM/SNL experiments, HGL temperature and height, Tests 1, 2, 3 . . . . .	100
5.10	FM/SNL experiments, HGL temperature and height, Tests 4, 5, 6, 7 . . . . .	101
5.11	FM/SNL experiments, HGL temperature and height, Tests 8, 9, 10, 11 . . . . .	102
5.12	FM/SNL experiments, HGL temperature and height, Tests 12, 13, 14, 15 . . . . .	103
5.13	FM/SNL experiments, HGL temperature and height, Tests 16, 17, 21, 22 . . . . .	104
5.14	LLNL Enclosure experiments, HGL temperature, Tests 1-8 . . . . .	106
5.15	LLNL Enclosure experiments, HGL temperature, Tests 9-16 . . . . .	107
5.16	LLNL Enclosure experiments, HGL temperature, Tests 17-24 . . . . .	108
5.17	LLNL Enclosure experiments, HGL temperature, Tests 25-32 . . . . .	109
5.18	LLNL Enclosure experiments, HGL temperature, Tests 33-40 . . . . .	110
5.19	LLNL Enclosure experiments, HGL temperature, Tests 41-48 . . . . .	111
5.20	LLNL Enclosure experiments, HGL temperature, Tests 49-56 . . . . .	112
5.21	LLNL Enclosure experiments, HGL temperature, Tests 57-64 . . . . .	113
5.22	NBS Multi-Room experiments, HGL temperature and height, Test 100A . . . . .	115
5.23	NBS Multi-Room experiments, HGL temperature and height, Test 100O . . . . .	116
5.24	NBS Multi-Room experiments, HGL temperature and height, Test 100Z . . . . .	117
5.25	NIST FSE, HGL temperature and height, Tests 8-11 . . . . .	119
5.26	NIST FSE, HGL temperature and height, Tests 12-15 . . . . .	120
5.27	NIST FSE, HGL temperature and height, Tests 16-19 . . . . .	121
5.28	NIST FSE, HGL temperature and height, Tests 20-23 . . . . .	122
5.29	NIST FSE, HGL temperature and height, Tests 24-27 . . . . .	123
5.30	NIST FSE, HGL temperature and height, Tests 28-30, 32 . . . . .	124
5.31	NIST/NRC experiments, HGL temperature and height, Tests 1-2, 7-8 . . . . .	126
5.32	NIST/NRC experiments, HGL temperature and height, Tests 4, 10, 13, 16 . . . . .	127
5.33	NIST/NRC experiments, HGL temperature and height, Tests 3, 9, 17 . . . . .	128
5.34	NIST/NRC experiments, HGL temperature and height, Tests 5, 14, 15, 18 . . . . .	129
5.35	NRCC Smoke Tower experiments, HGL temperature in the fire room and stair vestibule . . . . .	131
5.36	PRISME DOOR experiments, HGL temperature and height, Room 1, Tests 1-3 . . . . .	132
5.37	PRISME DOOR experiments, HGL temperature and height, Room 1, Tests 4-6 . . . . .	133
5.38	PRISME DOOR experiments, HGL temperature and height, Room 2, Tests 1-3 . . . . .	134
5.39	PRISME DOOR experiments, HGL temperature and height, Room 2, Tests 4-6 . . . . .	135
5.40	PRISME SOURCE experiments, HGL temperature and height, Room 2, Tests 1-4 . . . . .	137
5.41	PRISME SOURCE experiments, HGL temperature and height, Room 2, Tests 5-6 . . . . .	138
5.42	Steckler experiments, HGL temperature, Tests 10, 11, 12, 13, 14, 18, 612, 710 . . . . .	140
5.43	Steckler experiments, HGL temperature, Tests 16, 17, 19, 22, 23, 30, 41, 810 . . . . .	141
5.44	Steckler experiments, HGL temperature, Tests 20, 21, 114, 144, 210, 212, 242, 410 . . . . .	142
5.45	Steckler experiments, HGL temperature, Tests 116, 122, 220, 221, 224, 240, 310, 324 . . . . .	143
5.46	Steckler experiments, HGL temperature, Tests 510, 512, 514, 517, 540, 542, 544, 610 . . . . .	144
5.47	Steckler experiments, HGL temperature, Tests 160, 513, 520, 521, 522, 524, 541, 622 . . . . .	145
5.48	Steckler experiments, HGL temperature, Tests 161, 162, 163, 164, 165, 166, 167 . . . . .	146
5.49	UL/NIST experiments, HGL temperature and height, Tests 1-4 . . . . .	148
5.50	VTT experiments, HGL temperature and height, Tests 1-3 . . . . .	149
5.51	WTC experiments, HGL temperature and height, Tests 1-3 . . . . .	150
5.52	WTC experiments, HGL temperature and height, Tests 4-6 . . . . .	151
5.53	Summary of HGL temperature predictions for natural and forced ventilation . . . . .	153
5.54	Summary of HGL temperature for unventilated compartments . . . . .	154
5.55	Summary of HGL Depth predictions . . . . .	155

6.1	FM/SNL experiments, plume temperature, Tests 1-4 . . . . .	158
6.2	FM/SNL experiments, plume temperature, Tests 5-12 . . . . .	159
6.3	FM/SNL experiments, plume temperature, Tests 13-17, 21-22 . . . . .	160
6.4	McCaffrey experiments, plume temperature . . . . .	161
6.5	NRCC Smoke Tower, stairwell temperatures . . . . .	163
6.6	SP AST experiments, plume temperature, 1.1 m diesel fire . . . . .	164
6.7	SP AST experiments, plume temperature, 1.9 m diesel and 1.1 m heptane fires . . . . .	165
6.8	USN Hangar experiments, Iceland, plume temperature, Tests 1-6 . . . . .	166
6.9	USN Hangar experiments, Iceland, plume temperature, Tests 7, 9-13 . . . . .	167
6.10	USN Hangar experiments, Iceland, plume temperature, Tests 14-15, 17-20 . . . . .	168
6.11	USN Hangar experiments, Hawaii, plume temperature, Tests 1-7, 11 . . . . .	169
6.12	VTT experiments, plume temperature . . . . .	170
6.13	Summary of plume temperature predictions . . . . .	171
6.14	Verification of the heat release rate for Heskestad Flame Height cases . . . . .	173
6.15	Summary of flame height predictions, Heskestad correlation . . . . .	174
6.16	Flame height uncertainty, multiple correlations and flame height definitions . . . . .	174
6.17	Predicted HRR as a function of height above the burner . . . . .	175
6.18	Summary of plume entrainment predictions . . . . .	176
6.19	Sandia 1 m helium plume image . . . . .	178
6.20	Sandia 1 m helium plume vertical velocity profiles . . . . .	179
6.21	Sandia 1 m helium plume radial velocity profiles. . . . .	180
6.22	Sandia 1 m helium plume mean and RMS mass fraction profiles. . . . .	181
6.23	Sandia 1 m methane pool fire instantaneous temperature contours. . . . .	182
6.24	Sandia 1 m methane pool fire (Test 14) mean velocity profiles . . . . .	183
6.25	Sandia 1 m methane pool fire (Test 24) mean velocity profiles . . . . .	184
6.26	Sandia 1 m methane pool fire (Test 24) turbulent kinetic energy . . . . .	185
6.27	Sandia 1 m methane pool fire (Test 17) mean velocity profiles . . . . .	186
6.28	Sandia 1 m methane pool fire velocity signal and power spectrum . . . . .	187
6.29	Sandia 1 m hydrogen pool fire instantaneous temperature contours . . . . .	188
6.30	Sandia 1 m hydrogen pool fire (Test 35) mean velocity profiles . . . . .	189
6.31	Sandia 1 m hydrogen pool fire (Test 25) turbulent kinetic energy . . . . .	190
6.32	Purdue 7.1 cm methane flame mean mixture fraction profiles . . . . .	191
6.33	Purdue 7.1 cm methane flame mean temperature profiles . . . . .	192
6.34	Purdue 7.1 cm methane flame mean velocity profiles . . . . .	193
6.35	Purdue 7.1 cm methane flame rms velocity profiles . . . . .	194
6.36	UMD_Line_Burner temperature profiles . . . . .	195
6.37	UMD_Line_Burner temperature contours . . . . .	196
7.1	ATF Corridors experiments, ceiling jet, 50 kW . . . . .	199
7.2	ATF Corridors experiments, ceiling jet, 100 kW . . . . .	200
7.3	ATF Corridors experiments, ceiling jet, 250 kW . . . . .	201
7.4	ATF Corridors experiments, ceiling jet, 500 kW . . . . .	202
7.5	ATF Corridors experiments, ceiling jet, mixed HRR . . . . .	203
7.6	Arup Tunnel experiments, ceiling jet . . . . .	204
7.7	DelCo Trainers, ceiling jet temperature, Tests 2-4 . . . . .	205
7.8	DelCo Trainers, ceiling jet temperature, Tests 5 and 6 . . . . .	206
7.9	DelCo Trainers, ceiling jet temperature, Tests 22-25 . . . . .	207
7.10	Layout of ceiling TCs, FAA Cargo Compartments . . . . .	208

7.11	FAA Cargo Compartment experiments, ceiling jet, Test 1 . . . . .	209
7.12	FAA Cargo Compartment experiments, ceiling jet, Test 1 and 2 . . . . .	210
7.13	FAA Cargo Compartment experiments, ceiling jet, Test 2 and 3 . . . . .	211
7.14	FAA Cargo Compartment experiments, ceiling jet, Test 3 . . . . .	212
7.15	FM/SNL experiments, ceiling jet, Tests 1-6 . . . . .	213
7.16	FM/SNL experiments, ceiling jet, Tests 7-14 . . . . .	214
7.17	FM/SNL experiments, ceiling jet, Tests 15-17, 21-22 . . . . .	215
7.18	NIST Smoke Alarm experiments, ceiling jet . . . . .	217
7.19	NIST/NRC experiments, ceiling jet, Tests 1, 2, 4, 7, 8, 10, 13, 16 . . . . .	219
7.20	NIST/NRC experiments, ceiling jet, Tests 3, 5, 9, 14, 15, 17, 18 . . . . .	220
7.21	NRCC Smoke Tower experiments, ceiling jet. . . . .	221
7.22	NRCC Smoke Tower, upper floor temperatures . . . . .	222
7.23	PRISME DOOR experiments, ceiling jet, Room 1. . . . .	223
7.24	PRISME DOOR experiments, ceiling jet, Room 2. . . . .	224
7.25	PRISME SOURCE experiments, ceiling jet, Room 2. . . . .	226
7.26	SP AST experiments, ceiling jet, Test 1. . . . .	227
7.27	SP AST experiments, ceiling jet, Tests 2 and 3. . . . .	228
7.28	UL/NFPPRF experiments, ceiling jet, Series I, Tests 1-6. . . . .	229
7.29	UL/NFPPRF experiments, ceiling jet, Series I, Tests 7-14. . . . .	230
7.30	UL/NFPPRF experiments, ceiling jet, Series I, Tests 15-22. . . . .	231
7.31	UL/NIST Vents experiments, ceiling jet. . . . .	233
7.32	Vettori Flat Ceiling experiments, ceiling jet, Tests 1-8. . . . .	235
7.33	Vettori Flat Ceiling experiments, ceiling jet, Tests 9-16. . . . .	236
7.34	Vettori Flat Ceiling experiments, ceiling jet, Tests 17-24. . . . .	237
7.35	Vettori Flat Ceiling experiments, ceiling jet, Tests 25-32. . . . .	238
7.36	Vettori Flat Ceiling experiments, ceiling jet, Tests 33-40. . . . .	239
7.37	Vettori Flat Ceiling experiments, ceiling jet, Tests 41-45. . . . .	240
7.38	Vettori Sloped Ceiling experiments, ceiling jet, Tests 1-8. . . . .	242
7.39	Vettori Sloped Ceiling experiments, ceiling jet, Tests 9-16. . . . .	243
7.40	Vettori Sloped Ceiling experiments, ceiling jet, Tests 17-24. . . . .	244
7.41	Vettori Sloped Ceiling experiments, ceiling jet, Tests 25-32. . . . .	245
7.42	Vettori Sloped Ceiling experiments, ceiling jet, Tests 33-40. . . . .	246
7.43	Vettori Sloped Ceiling experiments, ceiling jet, Tests 41-48. . . . .	247
7.44	Vettori Sloped Ceiling experiments, ceiling jet, Tests 49-56. . . . .	248
7.45	Vettori Sloped Ceiling experiments, ceiling jet, Tests 57-64. . . . .	249
7.46	Vettori Sloped Ceiling experiments, ceiling jet, Tests 65-72. . . . .	250
7.47	WTC experiments, ceiling jet, Tests 1-6. . . . .	251
7.48	Summary of ceiling jet temperature predictions . . . . .	252
7.49	Comparison of measured and predicted sprinkler actuation times . . . . .	253
7.50	UL/NFPPRF experiments, number of sprinkler activations, Series I, Tests 1-8. . . . .	255
7.51	UL/NFPPRF experiments, number of sprinkler activations, Series I, Tests 9-16. . . . .	256
7.52	UL/NFPPRF experiments, number of sprinkler activations, Series I, Tests 17-22. . . . .	257
7.53	UL/NFPPRF experiments, number of sprinkler activations, Series II, Tests 1-6. . . . .	258
7.54	UL/NFPPRF experiments, number of sprinkler activations, Series II, Tests 7-12. . . . .	259
7.55	UL/NFPPRF experiments, number of sprinkler activations, Group A Commodity, Tests 1-5. . . . .	260
7.56	Comparison of the number of predicted and measured sprinkler activations . . . . .	261
7.57	Summary of smoke detector activation times (temperature rise), NIST Smoke Alarms. . . . .	262

7.58	Summary of smoke detector activation times (smoke detector model), NIST Smoke Alarms.	263
8.1	ATF Corridors, gas velocity, first level, Location H.	266
8.2	ATF Corridors, gas velocity, first level, Location I.	267
8.3	ATF Corridors, gas velocity, second level, Location J.	268
8.4	ATF Corridors, gas velocity, second level, Location K.	269
8.5	Instantaneous contours of velocity magnitude	270
8.6	Friction coefficient and pressure coefficient	271
8.7	Flow profiles	272
8.8	Bryant Doorway experiments, gas velocity profiles.	274
8.9	FM/FPRF experiments, gas velocity, low fan rate.	275
8.10	FM/FPRF experiments, gas velocity, high fan rate.	276
8.11	McCafrey experiments, centerline plume velocity.	277
8.12	PRISME DOOR experiments, gas velocity.	278
8.13	Restivo experiment, gas velocity.	279
8.14	Steckler experiments, velocity profiles, Tests 10, 11, 12, 13, 14, 18, 612, 710.	281
8.15	Steckler experiments, velocity profiles, Tests 16, 17, 19, 22, 23, 30, 41, 810.	282
8.16	Steckler experiments, velocity profiles, Tests 20, 21, 114, 144, 210, 212, 242, 410.	283
8.17	Steckler experiments, velocity profiles, Tests 116, 122, 220, 221, 224, 240, 310, 324.	284
8.18	Steckler experiments, velocity profiles, Tests 510, 512, 514, 517, 540, 542, 544, 610.	285
8.19	Steckler experiments, velocity profiles, Tests 160, 513, 520, 521, 522, 524, 541, 622.	286
8.20	Steckler experiments, velocity profiles, Tests 161, 162, 163, 164, 165, 166, 167.	287
8.21	Layout of velocity probes, WTC Experiments	288
8.22	WTC experiments, inlet velocity, Points 1-3.	289
8.23	WTC experiments, inlet velocity, Points 6-8.	290
8.24	WTC experiments, outlet velocity, Points 1-5.	291
8.25	WTC experiments, outlet velocity, Points 6-10.	292
8.26	Summary of velocity predictions	293
9.1	DelCo Trainers, CO <sub>2</sub> and O <sub>2</sub> concentration, Tests 2-4.	296
9.2	DelCo Trainers, CO <sub>2</sub> and O <sub>2</sub> concentration, Tests 5-6.	297
9.3	DelCo Trainers, CO <sub>2</sub> and O <sub>2</sub> concentration, Tests 22-25.	298
9.4	FAA Cargo Compartment experiments, CO <sub>2</sub> and O <sub>2</sub> concentration.	299
9.5	NIST/NRC experiments, CO <sub>2</sub> and O <sub>2</sub> concentration, Tests 3, 9, 17.	300
9.6	NIST/NRC experiments, CO <sub>2</sub> and O <sub>2</sub> concentration, Tests 5, 14, 15, 18.	301
9.7	NIST/NRC experiments, CO <sub>2</sub> and O <sub>2</sub> concentration, Tests 1, 2, 7, 8.	302
9.8	NIST/NRC experiments, CO <sub>2</sub> and O <sub>2</sub> concentration, Tests 4, 10, 13, 16.	303
9.9	NRCC Smoke Tower, CO <sub>2</sub> and O <sub>2</sub> concentration, Tests BK-R and COMP-R.	304
9.10	NRCC Smoke Tower, CO <sub>2</sub> and O <sub>2</sub> concentration, Tests CLC-I-R and CLC-II-R.	305
9.11	PRISME DOOR experiments, CO <sub>2</sub> and O <sub>2</sub> concentration, Room 1, Tests 1-3.	306
9.12	PRISME DOOR experiments, CO <sub>2</sub> and O <sub>2</sub> concentration, Room 1, Tests 4-6.	307
9.13	PRISME DOOR experiments, CO <sub>2</sub> and O <sub>2</sub> concentration, Room 2, Tests 1-3.	308
9.14	PRISME DOOR experiments, CO <sub>2</sub> and O <sub>2</sub> concentration, Room 2, Tests 4-6.	309
9.15	PRISME SOURCE experiments, CO <sub>2</sub> and O <sub>2</sub> concentration, Room 2, Tests 1-4.	311
9.16	PRISME SOURCE experiments, CO <sub>2</sub> and O <sub>2</sub> concentration, Room 2, Tests 5-6.	312
9.17	WTC experiments, CO <sub>2</sub> and O <sub>2</sub> concentration, Tests 1-3.	313
9.18	WTC experiments, CO <sub>2</sub> and O <sub>2</sub> concentration, Tests 4-6.	314
9.19	UMD_Line_Burner oxygen concentration profiles	315

9.20	Summary of major gas species predictions . . . . .	317
9.21	Summary of smoke concentration predictions for the FM/FPRF Datacenter Tests . . . . .	318
9.22	NIST/NRC experiments, smoke concentration, Tests 1, 2, 4, 7, 8, 10, 13, 16. . . . .	320
9.23	NIST/NRC experiments, smoke concentration, Tests 3, 5, 9, 14, 15, 17, 18. . . . .	321
9.24	Summary of smoke concentration predictions . . . . .	322
9.25	FAA Cargo Compartments experiments, smoke obscuration. . . . .	323
9.26	Summary of smoke obscuration predictions . . . . .	324
9.27	Predicted and measured aerosol deposition velocities, Sippola experiments . . . . .	326
9.28	Summary of aerosol deposition velocity predictions . . . . .	327
9.29	Species predictions at 7 mm, 9 mm, and 11 mm above burner, Smyth experiment . . . . .	329
9.30	Species predictions at 7 mm, 9 mm, and 11 mm above burner, Smyth experiment . . . . .	330
9.31	Temperature predictions at 7 mm, 9 mm, and 11 mm above burner, Smyth experiment . . . . .	331
9.32	Summary of gas species predictions, Beyler hood experiments . . . . .	333
9.33	Summary of species concentrations in NIST RSE experiments . . . . .	334
9.34	Summary of species concentrations in NIST RSE experiments . . . . .	335
9.35	Summary of thermocouple values in NIST RSE experiments . . . . .	335
9.36	Summary of Test 1, NIST RSE 2007 . . . . .	337
9.37	Summary of Test 2, NIST RSE 2007 . . . . .	338
9.38	Summary of Test 3, NIST RSE 2007 . . . . .	339
9.39	Summary of Test 4, NIST RSE 2007 . . . . .	340
9.40	Summary of Test 5, NIST RSE 2007 . . . . .	341
9.41	Summary of Test 6, NIST RSE 2007 . . . . .	342
9.42	Summary of Test 7, NIST RSE 2007 . . . . .	343
9.43	Summary of Test 10, NIST RSE 2007 . . . . .	344
9.44	Summary of Test 11, NIST RSE 2007 . . . . .	345
9.45	Summary of Test 12, NIST RSE 2007 . . . . .	346
9.46	Summary of Test 15, NIST RSE 2007 . . . . .	347
9.47	Summary of Test 16, NIST RSE 2007 . . . . .	348
9.48	Summary of ISONG3, NIST FSE 2008 . . . . .	350
9.49	Summary of ISOHept4, NIST FSE 2008 . . . . .	351
9.50	Summary of ISOHept5, NIST FSE 2008 . . . . .	352
9.51	Summary of ISOHept8, NIST FSE 2008 . . . . .	353
9.52	Summary of ISOHept9, NIST FSE 2008 . . . . .	354
9.53	Summary of ISONylon10, NIST FSE 2008 . . . . .	355
9.54	Summary of ISOPP11, NIST FSE 2008 . . . . .	356
9.55	Summary of ISOHeptD12, NIST FSE 2008 . . . . .	357
9.56	Summary of ISOHeptD13, NIST FSE 2008 . . . . .	358
9.57	Summary of ISOPropD14, NIST FSE 2008 . . . . .	359
9.58	Summary of ISOProp15, NIST FSE 2008 . . . . .	360
9.59	Summary of ISOStyrene16, NIST FSE 2008 . . . . .	361
9.60	Summary of ISOStyrene17, NIST FSE 2008 . . . . .	362
9.61	Summary of ISOPP18, NIST FSE 2008 . . . . .	363
9.62	Summary of ISOHept19, NIST FSE 2008 . . . . .	364
9.63	Summary of ISOToluene20, NIST FSE 2008 . . . . .	365
9.64	Summary of ISOStyrene21, NIST FSE 2008 . . . . .	366
9.65	Summary of ISOHept22, NIST FSE 2008 . . . . .	367
9.66	Summary of ISOHept23, NIST FSE 2008 . . . . .	368
9.67	Summary of ISOHept24, NIST FSE 2008 . . . . .	369

9.68	Summary of ISOHept25, NIST FSE 2008 . . . . .	370
9.69	Summary of ISOHept26, NIST FSE 2008 . . . . .	371
9.70	Summary of ISOHept27, NIST FSE 2008 . . . . .	372
9.71	Summary of ISOHept28, NIST FSE 2008 . . . . .	373
9.72	Summary of ISOToluene29, NIST FSE 2008 . . . . .	374
9.73	Summary of ISOPropanol30, NIST FSE 2008 . . . . .	375
9.74	Summary of ISONG32, NIST FSE 2008 . . . . .	376
9.75	Summary of carbon monoxide predictions . . . . .	377
9.76	Results of the NIST_He_2009 experiments . . . . .	379
9.77	Results of the NIST_He_2009 experiments . . . . .	380
9.78	Results of the NIST_He_2009 experiments . . . . .	381
9.79	Summary of species concentration predictions . . . . .	382
10.1	NIST/NRC experiments, compartment pressure, Tests 1, 2, 4, 7, 8, 10, 13, 16. . . . .	384
10.2	NIST/NRC experiments, compartment pressure, Tests 3, 5, 9, 14, 15, 17, 18. . . . .	385
10.3	LLNL Enclosure experiments, compartment pressure, Tests 9, 11-17. . . . .	387
10.4	LLNL Enclosure experiments, compartment pressure, Tests 18-20, 23, 26, 29-31. . . . .	388
10.5	LLNL Enclosure experiments, compartment pressure, Tests 32-36, 38, 40, 42. . . . .	389
10.6	LLNL Enclosure experiments, compartment pressure, Tests 44, 50-52, 54-55, 57-58. . . . .	390
10.7	LLNL Enclosure experiments, compartment pressure, Tests 59-64. . . . .	391
10.8	PRISME DOOR, compartment pressure and supply/exhaust, Room 1, Tests 1-3. . . . .	393
10.9	PRISME DOOR, compartment pressure and supply/exhaust, Room 1, Tests 4-6. . . . .	394
10.10	PRISME DOOR, compartment pressure and supply/exhaust, Room 2, Tests 1-3. . . . .	395
10.11	PRISME DOOR, compartment pressure and supply/exhaust, Room 2, Tests 4-6. . . . .	396
10.12	PRISME SOURCE, pressure and supply/exhaust flow rates, Tests 1, 2, 3 and 4. . . . .	398
10.13	PRISME SOURCE, pressure and supply/exhaust flow rates, Tests 5, 5a, 6 and 6a. . . . .	399
10.14	Summary of pressure predictions . . . . .	400
11.1	FAA Cargo Compartment experiments, ceiling surface temperatures. . . . .	402
11.2	NIST FSE experiments, floor and ceiling temperatures, Tests 3-4, 8. . . . .	404
11.3	NIST FSE experiments, floor and ceiling temperatures, Tests 9-12. . . . .	405
11.4	NIST FSE experiments, floor and ceiling temperatures, Tests 13-16. . . . .	406
11.5	NIST FSE experiments, floor and ceiling temperatures, Tests 17-20. . . . .	407
11.6	NIST FSE experiments, floor and ceiling temperatures, Tests 21-24. . . . .	408
11.7	NIST FSE experiments, floor and ceiling temperatures, Tests 25-28. . . . .	409
11.8	NIST FSE experiments, floor and ceiling temperatures, Tests 29, 30, 32. . . . .	410
11.9	NIST/NRC experiments, north wall temperatures, Tests 1, 2, 4, 7, 8, 10, 13, 16. . . . .	412
11.10	NIST/NRC experiments, north wall temperatures, Tests 3, 5, 9, 14, 15, 18. . . . .	413
11.11	NIST/NRC experiments, south wall temperatures, Tests 1, 2, 4, 7, 8, 10, 13, 16. . . . .	414
11.12	NIST/NRC experiments, south wall temperatures, Tests 3, 5, 9, 14, 15, 18. . . . .	415
11.13	NIST/NRC experiments, east wall temperatures, Tests 1, 2, 4, 7, 8, 10, 13, 16. . . . .	416
11.14	NIST/NRC experiments, east wall temperatures, Tests 3, 5, 9, 14, 15, 18. . . . .	417
11.15	NIST/NRC experiments, west wall temperatures, Tests 1, 2, 4, 7, 8, 10, 13, 16. . . . .	418
11.16	NIST/NRC experiments, west wall temperatures, Tests 3, 5, 9, 14, 15, 18. . . . .	419
11.17	NIST/NRC experiments, ceiling temperatures, Tests 1, 2, 4, 7, 8, 10, 13, 16. . . . .	420
11.18	NIST/NRC experiments, ceiling temperatures, Tests 3, 5, 9, 14, 15, 18. . . . .	421
11.19	NIST/NRC experiments, floor wall temperatures, Tests 1, 2, 4, 7, 8, 10, 13, 16. . . . .	422
11.20	NIST/NRC experiments, floor temperatures, Tests 3, 5, 9, 14, 15, 18. . . . .	423

11.21	PRISME DOOR experiments, wall temperatures, vertical array, Room 1 . . . . .	424
11.22	PRISME DOOR experiments, wall temperatures, four sides, Room 1 . . . . .	425
11.23	PRISME DOOR experiments, wall temperatures, vertical array, Room 2 . . . . .	426
11.24	PRISME DOOR experiments, wall temperatures, four sides, Room 2 . . . . .	427
11.25	PRISME SOURCE experiments, wall temperatures, vertical array, Room 2 . . . . .	429
11.26	PRISME SOURCE experiments, wall temperatures, four sides, Room 2 . . . . .	430
11.27	WTC experiments, ceiling temperatures, north array. . . . .	432
11.28	WTC experiments, ceiling temperatures, south array. . . . .	433
11.29	WTC experiments, ceiling temperatures, east array, Points 1-4. . . . .	434
11.30	WTC experiments, ceiling temperatures, east array, Points 5-7. . . . .	435
11.31	WTC experiments, ceiling temperatures, west array, Points 1-4. . . . .	436
11.32	WTC experiments, ceiling temperatures, west array, Points 5-8. . . . .	437
11.33	WTC experiments, ceiling temperatures, diagonal array. . . . .	438
11.34	WTC experiments, wall temperatures, Points 98, 100, 102. . . . .	439
11.35	WTC experiments, wall temperatures, Points 103, 105, 106. . . . .	440
11.36	WTC experiments, wall temperatures, Points 107, 109, 110. . . . .	441
11.37	WTC experiments, inner ceiling temperatures, north-south axis. . . . .	442
11.38	WTC experiments, inner ceiling temperatures, east-west axis. . . . .	443
11.39	WTC experiments, inner wall temperatures. . . . .	444
11.40	Summary of compartment surface temperature predictions . . . . .	445
11.41	NIST/NRC experiments, Cable A temperatures, Tests 1, 2, 4, 7, 8, 10, 13, 16. . . . .	447
11.42	NIST/NRC experiments, Cable A temperatures, Tests 3, 5, 9, 14, 15, 18. . . . .	448
11.43	NIST/NRC experiments, Cable B temperatures, Tests 1, 2, 4, 7, 8, 10, 13, 16. . . . .	449
11.44	NIST/NRC experiments, Cable B temperatures, Tests 3, 5, 9, 14, 15, 18. . . . .	450
11.45	NIST/NRC experiments, Cable Ca temperatures, Tests 1, 2, 4, 7, 8, 10, 13, 16. . . . .	451
11.46	NIST/NRC experiments, Cable Ca temperatures, Tests 3, 5, 9, 14, 15, 18. . . . .	452
11.47	NIST/NRC experiments, Cable Cb temperatures, Tests 1, 2, 4, 7, 8, 10, 13, 16. . . . .	453
11.48	NIST/NRC experiments, Cable Cb temperatures, Tests 3, 5, 9, 14, 15, 18. . . . .	454
11.49	NIST/NRC experiments, Cable D temperatures, Tests 1, 2, 4, 7, 8, 10, 13, 16. . . . .	455
11.50	NIST/NRC experiments, Cable D temperatures, Tests 3, 5, 9, 14, 15, 18. . . . .	456
11.51	NIST/NRC experiments, Cable F temperatures, Tests 1, 2, 4, 7, 8, 10, 13, 16. . . . .	457
11.52	NIST/NRC experiments, Cable F temperatures, Tests 3, 5, 9, 14, 15, 18. . . . .	458
11.53	NIST/NRC experiments, Cable G temperatures, Tests 1, 2, 4, 7, 8, 10, 13, 16. . . . .	459
11.54	NIST/NRC experiments, Cable G temperatures, Tests 3, 5, 9, 14, 15, 18. . . . .	460
11.55	SP AST experiments, Station A plate, adiabatic surface, and steel temperatures, Test 1. . .	462
11.56	SP AST experiments, Station B plate, adiabatic surface, and steel temperatures, Test 1. .	463
11.57	SP AST experiments, Station C plate, adiabatic surface, and steel temperatures, Test 1. .	464
11.58	SP AST experiments, Station A plate, adiabatic surface, and steel temperatures, Test 2. .	465
11.59	SP AST experiments, Station B plate, adiabatic surface, and steel temperatures, Test 2. .	466
11.60	SP AST experiments, Station C plate, adiabatic surface, and steel temperatures, Test 2. .	467
11.61	SP AST experiments, Station A plate, adiabatic surface, and steel temperatures, Test 3. .	468
11.62	SP AST experiments, Station B plate, adiabatic surface, and steel temperatures, Test 3. .	469
11.63	SP AST experiments, Station C plate, adiabatic surface, and steel temperatures, Test 3. .	470
11.64	SP AST experiments, steel temperatures, 1.1 m diesel fire. . . . .	472
11.65	SP AST experiments, steel temperatures, 1.1 m and 1.9 m diesel, 1.1 m heptane fires. . .	473
11.66	SP AST experiments, steel temperatures, 1.1 m heptane fire. . . . .	474
11.67	SP AST experiments, Insulated Room, Test A1. . . . .	476
11.68	SP AST experiments, Insulated Room, Test A2. . . . .	477

11.69	SP AST experiments, Insulated Room, Test A3. . . . .	478
11.70	SP AST experiments, Insulated Room, Test A4. . . . .	479
11.71	SP AST experiments, Insulated Room, Test A5. . . . .	480
11.72	SP AST experiments, Insulated Room, Test B1. . . . .	481
11.73	SP AST experiments, Insulated Room, Test B2. . . . .	482
11.74	SP AST experiments, Insulated Room, Test C1. . . . .	483
11.75	SP AST experiments, Insulated Room, Test C2. . . . .	484
11.76	SP AST experiments, Insulated Room, Test C3. . . . .	485
11.77	SP AST experiments, Insulated Room, Test D1. . . . .	486
11.78	SP AST experiments, Insulated Room, Test D2. . . . .	487
11.79	Predictions of plate thermometer temperatures in a cone calorimeter . . . . .	488
11.80	WTC experiments, steel temperatures, upper column. . . . .	490
11.81	WTC experiments, steel temperatures, middle column. . . . .	491
11.82	WTC experiments, steel temperatures, lower column. . . . .	492
11.83	WTC experiments, steel temperatures, upper Truss A. . . . .	493
11.84	WTC experiments, steel temperatures, middle Truss A. . . . .	494
11.85	WTC experiments, steel temperatures, lower Truss A. . . . .	495
11.86	WTC experiments, steel temperatures, upper Truss B. . . . .	496
11.87	WTC experiments, steel temperatures, middle Truss B. . . . .	497
11.88	WTC experiments, steel temperatures, lower Truss B. . . . .	498
11.89	WTC experiments, steel temperatures, Bar 1. . . . .	499
11.90	WTC experiments, slug temperatures. . . . .	500
11.91	CAROLFIRE, electrical cable temperatures, Penlight Tests 1, 2, 3, 7, 9, 11-13. . . . .	502
11.92	CAROLFIRE, electrical cable temperatures, Penlight Tests 17, 19-20, 22-24, 27-28. . . . .	503
11.93	CAROLFIRE, electrical cable temperatures, Penlight Tests 4-6, 8, 10, 14-16. . . . .	504
11.94	CAROLFIRE, electrical cable temperatures, Penlight Tests 21, 25-26, 29-30, 63, 65. . . . .	505
11.95	CAROLFIRE, electrical cable temperatures, Penlight Tests 18, 31, 62, 64. . . . .	506
11.96	PRISME LEAK experiments, cable temperature, Tests 1 and 2. . . . .	508
11.97	PRISME LEAK experiments, cable temperature, Tests 3 and 4. . . . .	509
11.98	PRISME DOOR experiments, cable temperature, Room 1, Cable BW. . . . .	510
11.99	PRISME DOOR experiments, cable temperature, Room 1, Cable HW. . . . .	511
11.100	PRISME DOOR experiments, cable temperature, Room 2, Cable BE. . . . .	512
11.101	PRISME DOOR experiments, cable temperature, Room 2, Cable HE. . . . .	513
11.102	PRISME DOOR experiments, cable temperature, Room 2, Cable HW. . . . .	514
11.103	Summary of target temperature predictions . . . . .	515
11.104	Summary of time to failure predictions for electrical cables . . . . .	516
12.1	FAA Cargo Compartment experiments, heat flux to ceiling. . . . .	518
12.2	FM Parallel Panel experiments, side wall heat flux . . . . .	519
12.3	NIST/NRC experiments, heat flux to north wall, Tests 1, 2, 4, 7, 8, 10. . . . .	521
12.4	NIST/NRC experiments, heat flux to north wall, Tests 3, 5, 9, 14, 15, 18. . . . .	522
12.5	NIST/NRC experiments, heat flux to south wall, Tests 1, 2, 4, 7, 8, 10. . . . .	523
12.6	NIST/NRC experiments, heat flux to south wall, Tests 3, 5, 9, 14, 15, 18. . . . .	524
12.7	NIST/NRC experiments, heat flux to east wall, Tests 1, 2, 4, 7, 8, 10. . . . .	525
12.8	NIST/NRC experiments, heat flux to east wall, Tests 3, 5, 9, 14, 15, 18. . . . .	526
12.9	NIST/NRC experiments, heat flux to west wall, Tests 1, 2, 4, 7, 8, 10. . . . .	527
12.10	NIST/NRC experiments, heat flux to west wall, Tests 3, 5, 9, 14, 15, 18. . . . .	528
12.11	NIST/NRC experiments, heat flux to the floor, Tests 1, 2, 4, 7, 8, 10. . . . .	529

12.12	NIST/NRC experiments, heat flux to the floor, Tests 3, 5, 9, 14, 15, 18. . . . .	530
12.13	NIST/NRC experiments, heat flux to the ceiling, Tests 1, 2, 4, 7, 8, 10. . . . .	531
12.14	NIST/NRC experiments, heat flux to the ceiling, Tests 3, 5, 9, 14, 15, 18. . . . .	532
12.15	Smokeview rendering of NRCC Facade experiment . . . . .	533
12.16	NRCC Facade experiments, heat flux, window configuration 1 and 2. . . . .	534
12.17	NRCC Facade experiments, heat flux, window configuration 3 and 4. . . . .	535
12.18	NRCC Facade experiments, heat flux, window configuration 5. . . . .	536
12.19	NRL/HAI experiments, heat flux to the wall, Tests 1-5. . . . .	538
12.20	NRL/HAI experiments, heat flux to the wall, Tests 6-9. . . . .	539
12.21	PRISME DOOR experiments, total heat flux, vertical array, Room 1. . . . .	540
12.22	PRISME DOOR experiments, radiative heat flux, vertical array, Room 1. . . . .	541
12.23	PRISME DOOR experiments, total heat flux, four walls, Room 1. . . . .	542
12.24	PRISME DOOR experiments, total heat flux, vertical array, Room 2. . . . .	543
12.25	PRISME DOOR experiments, radiative heat flux, vertical array, Room 2. . . . .	544
12.26	PRISME DOOR experiments, total heat flux, four walls, Room 2. . . . .	545
12.27	PRISME SOURCE experiments, total heat flux, vertical array, Room 2. . . . .	547
12.28	PRISME SOURCE experiments, radiative heat flux, vertical array, Room 2. . . . .	548
12.29	PRISME SOURCE experiments, total heat flux, four walls, Room 2. . . . .	549
12.30	Ulster SBI experiments, corner fire heat flux . . . . .	550
12.31	WTC experiments, heat flux to the floor. . . . .	552
12.32	WTC experiments, heat flux to the ceiling. . . . .	553
12.33	WTC experiments, heat flux to the ceiling. . . . .	554
12.34	Summary of compartment surface heat flux predictions . . . . .	555
12.35	Fleury Heat Flux, 100 kW fires. . . . .	557
12.36	Fleury Heat Flux, 150 kW fires. . . . .	558
12.37	Fleury Heat Flux, 200 kW fires. . . . .	559
12.38	Fleury Heat Flux, 250 kW fires. . . . .	560
12.39	Fleury Heat Flux, 300 kW fires. . . . .	561
12.40	Heat flux predictions, Hamins methane burner Tests 1-4 . . . . .	564
12.41	Heat flux predictions, Hamins methane burner Tests 5-8 . . . . .	565
12.42	Heat flux predictions, Hamins methane burner Tests 9-12 . . . . .	566
12.43	Heat flux predictions, Hamins methane burner Tests 13-16 . . . . .	567
12.44	Heat flux predictions, Hamins methane burner Tests 17-20 . . . . .	568
12.45	Heat flux predictions, Hamins methane burner Tests 21-24 . . . . .	569
12.46	Heat flux predictions, Hamins methane burner Tests 25-28 . . . . .	570
12.47	Heat flux predictions, Hamins methane burner Tests 29-30 . . . . .	571
12.48	Heat flux predictions, Hamins propane burner Tests 1-4 . . . . .	573
12.49	Heat flux predictions, Hamins propane burner Tests 5-8 . . . . .	574
12.50	Heat flux predictions, Hamins propane burner Tests 9-12 . . . . .	575
12.51	Heat flux predictions, Hamins propane burner Tests 13-16 . . . . .	576
12.52	Heat flux predictions, Hamins propane burner Tests 17-20 . . . . .	577
12.53	Heat flux predictions, Hamins propane burner Tests 21-24 . . . . .	578
12.54	Heat flux predictions, Hamins propane burner Tests 25-28 . . . . .	579
12.55	Heat flux predictions, Hamins propane burner Tests 29-32 . . . . .	580
12.56	Heat flux predictions, Hamins propane burner Tests 33-34 . . . . .	581
12.57	Heat flux predictions, Hamins acetylene burner Tests 1-4 . . . . .	583
12.58	Heat flux predictions, Hamins acetylene burner Tests 5-8 . . . . .	584
12.59	Heat flux predictions, Hamins acetylene burner Tests 9-12 . . . . .	585

12.60	Heat flux predictions, Hamins acetylene burner Tests 13-16 . . . . .	586
12.61	NIST/NRC experiments, heat flux to Cable B, Tests 1, 2, 4, 7, 8, 10, 13, 16. . . . .	588
12.62	NIST/NRC experiments, heat flux to Cable B, Tests 3, 5, 9, 14, 15, 18. . . . .	589
12.63	NIST/NRC experiments, heat flux to Cable D, Tests 1, 2, 4, 7, 8, 10, 13, 16. . . . .	590
12.64	NIST/NRC experiments, heat flux to Cable D, Tests 5, 9, 14. . . . .	591
12.65	NIST/NRC experiments, heat flux to Cable F, Tests 1, 2, 4, 7, 8, 10, 13, 16. . . . .	592
12.66	NIST/NRC experiments, heat flux to Cable F, Tests 3, 5, 9, 14, 15, 18. . . . .	593
12.67	NIST/NRC experiments, heat flux to Cable G, Tests 1, 2, 4, 7, 8, 10, 13, 16. . . . .	594
12.68	NIST/NRC experiments, heat flux to Cable G, Tests 3, 5, 9, 14, 15, 18. . . . .	595
12.69	WTC experiments, heat flux at Station 2, high position. . . . .	596
12.70	WTC experiments, heat flux at Station 2, low position. . . . .	597
12.71	WTC experiments, heat flux to upper column. . . . .	598
12.72	WTC experiments, heat flux to lower column. . . . .	599
12.73	Summary of target heat flux predictions . . . . .	600
12.74	Droplet speeds and mean diameters for the three nozzles . . . . .	601
12.75	Comparison of radiation attenuation, BRE and LEMTA Spray experiments . . . . .	602
12.76	Bouchair Solar Chimney, 0.1 m thermal cavity. . . . .	604
12.77	Bouchair Solar Chimney, 0.2 m thermal cavity. . . . .	605
12.78	Bouchair Solar Chimney, 0.3 m thermal cavity. . . . .	606
12.79	Bouchair Solar Chimney, 0.5 m thermal cavity. . . . .	607
12.80	Bouchair Solar Chimney, 1.0 m thermal cavity. . . . .	608
12.81	Summary of Bouchair Solar Chimney results. . . . .	609
13.1	Results of Cup Burner experiments with methane and heptane . . . . .	612
13.2	Results of Cup Burner experiments with methane and heptane . . . . .	613
13.3	Extinguishment times for the USCG/HAI water mist suppression tests . . . . .	620
13.4	Droplet speed, flux, and mean diameter profiles of the LN-2 nozzle . . . . .	622
14.1	Results of FAA Polymers, non-charring, comparison. . . . .	626
14.2	Results of FAA Polymers, complex, non-charring, comparison. . . . .	628
14.3	Heat release rate of polycarbonate (PC). . . . .	630
14.4	Heat release rate of poly(vinyl chloride) (PVC). . . . .	632
14.5	Heat release rate of poly(aryl ether ether ketone) (PEEK). . . . .	635
14.6	Mass loss rate of poly(butylene terephthalate) (PBT). . . . .	637
14.7	Mass loss rate of poly(butylene terephthalate) with glass fibers (PBT-GF). . . . .	639
14.8	Mass loss rate of ABS and HIPS . . . . .	641
14.9	Mass loss rate of PMMA . . . . .	642
14.10	Mass loss rate of Kydex . . . . .	644
14.11	Mass loss rate of PEI and PET . . . . .	646
14.12	Mass loss rate of POM . . . . .	647
14.13	Mass loss rate of corrugated cardboard . . . . .	651
14.14	Small scale results of the CHRISTIFIRE cable 701 sheath and insulation. . . . .	655
14.15	Cone calorimeter fitting of CHRISTIFIRE cable 701 at 50 kW/m <sup>2</sup> heat flux. . . . .	656
14.16	Cone calorimeter validation of CHRISTIFIRE cable 701 at 25 and 75 kW/m <sup>2</sup> heat fluxes. . . . .	657
14.17	Comparison of burning rates for various liquid pool fires. . . . .	659
14.18	Snapshot of the simulation of CSIRO Grassland Fire F19 . . . . .	660
14.19	Comparison measured and predicted fire front position for the CSIRO Grassland Fires . . . . .	661
14.20	Snapshots of a 2 m Douglas fir fire simulation . . . . .	662

14.21	Comparison measured and predicted mass loss rate for the Douglas fir tree experiments . . . . .	664
14.22	Summary of burning rate predictions . . . . .	665
15.1	LNG Dispersion experiments, Burro velocity and temperature profiles . . . . .	671
15.2	LNG Dispersion experiments, Coyote velocity and temperature profiles . . . . .	672
15.3	LNG Dispersion experiments, Falcon velocity and temperature profiles . . . . .	673
15.4	LNG Dispersion experiments, Maplin Sands velocity and temperature profiles . . . . .	674
15.5	LNG Dispersion experiments, Burro and Coyote . . . . .	675
15.6	LNG Dispersion experiments, Falson and Maplin Sands . . . . .	676
15.7	Summary of LNG Dispersion predictions . . . . .	677

# List of Tables

3.1	Summary of FM/SNL Experiments . . . . .	29
3.2	Summary of LLNL Enclosure Experiments . . . . .	33
3.3	Summary of NIST Reduced-Scale Experiments, 2007. . . . .	37
3.4	Summary of NIST FSE Experiments selected for model validation. . . . .	39
3.5	Summary of NIST Smoke Alarm Experiments selected for model validation. . . . .	44
3.6	Summary of Steckler compartment experiments. . . . .	53
3.7	Summary of UL/NIST Vent experiments . . . . .	58
3.8	Results of the UL/NFPRF heptane spray experiments, Series I . . . . .	59
3.9	Results of the UL/NFPRF heptane spray experiments, Series II . . . . .	60
3.10	Heat release rate profiles for the Vettori experiments . . . . .	65
3.11	Summary of important experimental parameters. . . . .	71
3.12	Summary of important experimental parameters (continued). . . . .	72
3.13	Summary of important numerical parameters. . . . .	74
4.1	Summary of uncertainty estimates . . . . .	85
6.1	Summary of parameters for the flame height predictions . . . . .	173
9.1	Summary of Sippola aerosol deposition experiments selected for model validation. . . . .	325
9.2	Test parameters of the NIST_He_2009 experiments . . . . .	378
11.1	Wall measurement positions for the NIST/NRC series . . . . .	411
11.2	Ceiling surface measurement locations for the WTC series . . . . .	431
12.1	Summary of the NRL/HAI Wall Heat Flux Measurements. . . . .	537
12.2	Heat flux gauge positions relative to the center of the fire pan in the WTC series. . . . .	551
12.3	Parameters of the Hamins methane burner experiments . . . . .	563
12.4	Parameters of the Hamins propane burner experiments . . . . .	572
12.5	Parameters of the Hamins acetylene burner experiments . . . . .	582
13.1	USCG/HAI water mist suppression extinguishment times . . . . .	614
14.1	FAA non-charring polymer properties. . . . .	625
14.2	FAA complex non-charring polymer properties . . . . .	627
14.3	Properties of polycarbonate (PC). . . . .	629
14.4	Properties of poly(vinyl chloride) (PVC). . . . .	631
14.5	Properties of poly(aryl ether ether ketone) (PEEK). . . . .	634
14.6	Properties of poly(butylene terephthalate) (PBT). . . . .	636
14.7	Properties of poly(butylene terephthalate) with glass fibers (PBT-GF). . . . .	638
14.8	Properties of ABS, HIPS, and PMMA . . . . .	640

14.9	Properties of Kydex . . . . .	643
14.10	Properties of PEI, PET, and POM . . . . .	645
14.11	Properties of corrugated cardboard. . . . .	648
14.12	Cardboard composition and dimensions . . . . .	650
14.13	Kinetic parameters for CHRISTIFIRE cable 701 v1. . . . .	652
14.14	Kinetic parameters for CHRISTIFIRE cable 701 v2. . . . .	653
14.15	Thermal parameters for CHRISTIFIRE cable 701 v1. . . . .	654
14.16	Thermal parameters for CHRISTIFIRE cable 701 v2. . . . .	654
14.17	Liquid fuel properties. . . . .	658
14.18	Measured properties for the CSIRO Grassland Fire cases . . . . .	661
14.19	Assumed properties for dry grass and soil . . . . .	661
14.20	Measured properties for the NIST Douglas fir trees . . . . .	663
14.21	Assumed properties for the vegetation . . . . .	663
15.1	Summary of LNG Dispersion Experiments. . . . .	670
16.1	Summary statistics . . . . .	679
16.2	Validation Git Statistics . . . . .	684

# List of Acronyms

ALOFT	A Large Outdoor Fire plume Trajectory model
AST	Adiabatic Surface Temperature
ASTM	American Society for Testing and Materials
ATF	Bureau of Alcohol, Tobacco, Firearms, and Explosives
BRE	British Research Establishment
CAROLFIRE	Cable Response to Live Fire Test Program
CFAST	Consolidated Model of Fire Growth and Smoke Transport
CHRISTIFIRE	Cable Heat Release, Ignition, and Spread in Fire Test Program
DNS	Direct Numerical Simulation
FAA	Federal Aviation Administration
FDS	Fire Dynamics Simulator
FLAME	Fire Laboratory for Accreditation of Models by Experimentation
FM	Factory Mutual Global
HAI	Hughes Associates, Inc.
HDPE	high density polyethylene
HGL	Hot Gas Layer
HIPS	high-impact polystyrene
HRR	Heat Release Rate
ISO	International Standards Organization
LEMTA	Laboratoire d'Energétique et de Méchanique Théorique et Appliquée
LES	Large Eddy Simulation
LLNL	Lawrence Livermore National Laboratory
NBS	National Bureau of Standards (former name of NIST)
NFPRF	National Fire Protection Research Foundation
NIST	National Institute of Standards and Technology
NRC	Nuclear Regulatory Commission
NRCC	National Research Council of Canada
NRL	Naval Research Laboratory
PDPA	Phase Doppler Particle Analyzer
PIV	Particle Image Velocimetry
PMMA	poly(methyl methacrylate)
PRISME	Propagation d'un incendie pour des scénarios multi-locaux élémentaires
PVC	Polyvinyl chloride
RANS	Reynolds Averaged Navier-Stokes
SBI	Single Burning Item
SNL	Sandia National Laboratory
SP	Statens Provningsanstalt (Technical Research Institute of Sweden)

TGA	Thermal Gravimetric Analysis
THIEF	Thermally-Induced Electrical Failure
UL	Underwriters Laboratories
USN	United States Navy
VTFRL	Virginia Tech Fire Research Laboratory
VTT	Valtion Teknillinen Tutkimuskeskus (Technical Research Centre of Finland)
WTC	World Trade Center

# Chapter 1

## What is Model Validation?

Although there are various definitions of model validation, for example the one contained in ASTM E 1355 [2], most define it as the process of determining how well the mathematical model predicts the actual physical phenomena of interest. Validation typically involves (1) comparing model predictions with experimental measurements, (2) quantifying the differences in light of uncertainties in both the measurements and the model inputs, and (3) deciding if the model is appropriate for the given application. This guide only does (1) and (2). Number (3) is the responsibility of the end user. To say that FDS is “validated” means that the end user has quantified the model uncertainty for a given application and decided that the model is appropriate. Although the FDS developers spend a considerable amount of time comparing model predictions with experimental measurements, it is ultimately the end user who decides if the model is adequate for the job at hand.

This Guide is merely a collection of calculation results. As FDS develops, it will expand to include new experimental measurements of newly modeled physical phenomena. With each minor release of FDS (version 5.2 to 5.3, for example), the plots and graphs are all regenerated to ensure that changes to the model have not decreased the accuracy of a previous version.

The following sections discuss key issues that must be considered when deciding whether or not FDS is appropriate for a given application. It depends on (a) the scenarios of interest, (b) the predicted quantities, and (c) the desired level of accuracy. FDS can be used to model most any fire scenario and predict almost any quantity of interest, but the prediction may not be accurate because of limitations in the description of the fire physics, and also because of limited information about the fuels, geometry, and so on.

### 1.1 Blind, Specified, and Open Validation Experiments

ASTM E 1355 [2] describes three basic types of validation calculations – *Blind*, *Specified*, and *Open*.

**Blind Calculation:** The model user is provided with a basic description of the scenario to be modeled.

For this application, the problem description is not exact; the model user is responsible for developing appropriate model inputs from the problem description, including additional details of the geometry, material properties, and fire description, as appropriate. Additional details necessary to simulate the scenario with a specific model are left to the judgement of the model user. In addition to illustrating the comparability of models in actual end-use conditions, this will test the ability of those who use the model to develop appropriate input data for the models.

**Specified Calculation:** The model user is provided with a complete detailed description of model inputs, including geometry, material properties, and fire description. As a follow-on to the blind calculation, this

test provides a more careful comparison of the underlying physics in the models with a more completely specified scenario.

**Open Calculation:** The model user is provided with the most complete information about the scenario, including geometry, material properties, fire description, and the results of experimental tests or benchmark model runs which were used in the evaluation of the blind or specified calculations of the scenario. Deficiencies in available input (used for the blind calculation) should become most apparent with comparison of the open and blind calculation.

The calculations presented in this Guide all fall into the *Open* category. There are several reasons for this, the first being the most practical:

- All of the calculations presented in this Guide are re-run with each minor release of FDS (i.e., 5.3 to 5.4). The fact that the experiments have already been performed and the results are known qualify these calculations as *Open*.
- Some of the calculations described in this Guide did originally fall into the *Specified* category because they were first performed before the experiments were conducted. However, in almost every case, the experiment was not conducted exactly as specified, and the pre-calculated results were not particularly useful in determining the accuracy of the model.
- None of the calculations were truly *Blind*, even those performed prior to the experiments. The purpose of a *Blind* calculation is to assess the degree to which the choice of input parameters affects the outcome. However, in such cases it is impossible to discern the uncertainty associated from the choice of input parameters from that associated with the model itself. The primary purpose of this Guide is to quantify the uncertainty of the model itself, in which case *Blind* calculations are of little value.

## 1.2 How to Use this Guide

When considering whether to use FDS for a given application, do the following:

1. Survey Chapter 2 to learn about past efforts by others to validate the model for similar applications. Keep in mind that most of the referenced validation exercises have been performed with older versions of FDS, and you may want to obtain the experimental data and the old FDS input files and redo the simulations with the version of FDS that you plan to use.
2. Identify in Chapter 3 the experimental data sets appropriate for your application. In particular, the summary of the experiments found in Section 3.54 contains a table listing various non-dimensional quantities that characterize the parameters of the experiments. For example, the equivalence ratio of a compartment fire experiment indicates the degree to which the fire was over or under-ventilated. To say that the results of a given experiment are relevant to your scenario, you need to demonstrate that its parameters “fit” within the parameter space outlined in Table 3.11.
3. Search the Table of Contents to find comparisons of FDS simulations with the relevant experiments. For a given experiment, there may be numerous measurements of quantities like the gas temperature, heat flux, and so on. It is a challenge to sort out all the plots and graphs of all the different quantities and come to some general conclusion. For this reason, this Guide is organized by output quantity, not by individual experiment or fire scenario. In this way, it is possible to assess, over a range of different experiments and scenarios, the performance of the model in predicting a given quantity. Overall trends and biases become much more clear when the data is organized this way.

4. Determine the accuracy of the model for given output quantities of interest listed in Table 16.1. An explanation of the accuracy metrics is given in Chapter 4.

The experimental data sets and FDS input/output files described in this Guide are all managed via the on-line project archiving system. You might want to re-run examples of interest to better understand how the calculations were designed, and how changes in the various parameters might affect the results. This is known as a *sensitivity study*, and it is difficult to document all the parameter variations of the calculations described in this report. Thus, it is a good idea to determine which of the input parameters are particularly important.



## Chapter 2

# Survey of Past Validation Work

In this chapter, a survey of FDS validation work is presented. Some of the work has been performed at NIST, some by its grantees and some by engineering firms using the model. Because each organization has its own reasons for validating the model, the referenced papers and reports do not follow any particular guidelines. Some of the works only provide a qualitative assessment of the model, concluding that the model agreement with a particular experiment is “good” or “reasonable.” Sometimes, the conclusion is that the model works well in certain cases, not as well in others. These studies are included in the survey because the references are useful to other model users who may have a similar application and are interested in even qualitative assessment. It is important to note that some of the papers point out flaws in early releases of FDS that have been corrected or improved in more recent releases. Some of the issues raised, however, are still subjects of active research. The research agenda for FDS is greatly influenced by the feedback provided by users, often through publication of validation efforts.

It is useful to divide the various validation exercises described in this chapter into two classes – those for which the heat release rate (HRR) of the fire is *specified* as an input to the model and those for which the HRR is *predicted* by the model. The former is often the case for a design application, the latter for a forensic reconstruction.

Design applications typically involve an existing building or a building under design. A so-called “design fire” is specified either by a regulatory authority or by the engineers performing the analysis. Because the fire’s heat release rate is specified, the role of the model is to predict the transport of heat and combustion products throughout the room or rooms of interest. Ventilation equipment is often included in the simulation, like fans, blowers, exhaust hoods, HVAC ducts, smoke management systems, etc. Sprinkler and heat and smoke detector activation are also of interest. The effect of the sprinkler spray on the fire is usually less of interest since the heat release rate of the fire is specified rather than predicted. Detailed descriptions of the contents of the building are usually not necessary because these items are assumed to not contribute to the fire, and even if they are, the burning rate will be specified, not predicted. Sometimes, it is necessary to predict the heat flux from the fire to a nearby “target,” and even though the target may heat up to some specified ignition temperature, the subsequent spread of the fire usually goes beyond the scope of the analysis because of the uncertainty inherent in object to object fire spread.

Forensic reconstructions require the model to simulate an actual fire based on information that is collected after the event, such as eye witness accounts, unburned materials, burn signatures, etc. The purpose of the simulation is to connect a sequence of discrete observations with a continuous description of the fire dynamics. Usually, reconstructions involve more gas/solid phase interaction because virtually all objects in a given room are potentially ignitable, especially when flashover occurs. Thus, there is much more emphasis on such phenomena as heat transfer to surfaces, pyrolysis, flame spread, and suppression. In general, forensic reconstructions are more challenging simulations to perform because they require more detailed

information about the room contents, and there is much greater uncertainty in the total heat release rate as the fire spreads from object to object.

Validation studies of FDS to date have focused more on design applications than reconstructions. The reason is that design applications usually involve specified fires and demand a minimum of thermo-physical properties of real materials. Transport of smoke and heat is the primary focus, and measurements can be limited to well-placed thermocouples, a few heat flux gauges, gas samplers, etc. Phenomena of importance in forensic reconstructions, like second item ignition, flame spread, vitiation effects and extinction, are more difficult to model and more difficult to study with well-controlled experiments. Uncertainties in material properties and measurements, as well as simplifying assumptions in the model, often force the comparison between model and measurement to be qualitative at best. Nevertheless, current validation efforts are moving in the direction of these more difficult issues.

## 2.1 Validation Work with Pre-Release Versions of FDS

FDS was officially released in 2000. However, for two decades various CFD codes using the basic FDS hydrodynamic framework were developed at NIST for different applications and for research. In the mid 1990s, many of these different codes were consolidated into what eventually became FDS. Before FDS, the various models were referred to as LES, NIST-LES, LES3D, IFS (Industrial Fire Simulator), and ALOFT (A Large Outdoor Fire Plume Trajectory).

The NIST LES model describes the transport of smoke and hot gases during a fire in an enclosure using the Boussinesq approximation, where it is assumed that the density and temperature variations in the flow are relatively small [3, 4, 5, 6]. Such an approximation can be applied to a fire plume away from the fire itself. Much of the early work with this form of the model was devoted to the formulation of the low Mach number form of the Navier-Stokes equations and the development of the basic numerical algorithm. Early validation efforts compared the model with salt water experiments [7, 8, 9], and fire plumes [10, 11, 12, 13]. Clement validated the hydrodynamic model in FDS by measuring salt water flows using Laser Induced dye Fluorescence (LIF) [14]. An interesting finding of this work was that the transition from a laminar to a turbulent plume is very difficult to predict with any technique other than DNS.

Eventually, the Boussinesq approximation was dropped and simulations began to include more fire-specific phenomena. Simulations of enclosure fires were compared to experiments performed by Steckler [15]. Mell et al. [16] studied small helium plumes, with particular attention to the relative roles of baroclinic torque and buoyancy as sources of vorticity. Cleary et al. [17] used the LES model to simulate the environment seen by multi-sensor fire detectors and performed some simple validation work to check the model before using it. Large fire experiments were performed by NIST at the FRI test facility in Japan, and at US Naval aircraft hangars in Hawaii and Iceland [18]. Room airflow applications were considered by Emmerich and McGrattan [19, 20].

These early validation efforts were encouraging, but highlighted the need to improve the hydrodynamic model by introducing the Smagorinsky form of large eddy simulation. This addition improved the stability of the model because of the relatively simple relation between the local strain rate and the turbulent viscosity. There is both a physical and numerical benefit to the Smagorinsky model. Physically, the viscous term used in the model has the right functional form to describe sub-grid mixing processes. Numerically, local oscillations in the computed flow quantities are damped if they become large enough to threaten the stability of the entire calculation.

## 2.2 Validation of FDS since 2000

There is an on-going effort at NIST and elsewhere to evaluate FDS as new capabilities are added. To date, most of this work has focused on the model's ability to predict the transport of heat and exhaust products from a fire through an enclosure. In these studies, the heat release rate is usually prescribed, along with the production rates of various products of combustion. More recently, validation efforts have moved beyond just transport issues to consider fire growth, flame spread, suppression, sprinkler/detector activation, and other fire-specific phenomena.

The validation work discussed below can be organized into several categories: Comparisons with full-scale tests conducted especially for the chosen evaluation, comparisons with previously published full-scale test data, comparisons with standard tests, comparisons with documented fire experience, and comparisons with engineering correlations. There is no single method by which the predictions and measurements are compared. Formal, rigorous validation exercises are time-consuming and expensive. Most validation exercises are done simply to assess if the model can be used for a very specific purpose. While not comprehensive on their own, these studies collectively constitute a valuable assessment of the model.

### 2.2.1 Fire Plumes

There are several examples of fire flows that have been extensively studied, so much so that a set of engineering correlations combining the results of many experiments have been developed. These correlations are useful to modelers because of their simplicity. The most studied phenomena include fire plumes, ceiling jets, and flame heights.

Although much of the early validation work before FDS was released involved fire plumes, it remains an active area of interest. One study by Chow and Yin [21] surveys the performance of various models in predicting plume temperatures and entrainment for a 470 kW fire with a diameter of 1 m and an unbounded ceiling. They compare the FDS results with various correlations and a RANS (Reynolds-Averaged Navier-Stokes) model.

Battaglia et al. [22] used FDS to simulate fire whirls. First, the model was shown to reproduce the McCaffrey correlation of a fire plume, then it was shown to reproduce qualitatively certain features of fire whirls. At the time, FDS used Lagrangian elements to introduce heat from the fire (no longer used), and this combustion model could not replicate the extreme stretching of the core of the flame zone.

Quintiere and Ma [23, 24] compared predicted flame heights and plume centerline temperatures to empirical correlations. For plume temperature, the Heskestad correlation [25] was chosen. Favorable agreement was found in the plume region, but the results near the flame region were found to be grid-dependent, especially for low  $Q^*$  fires. At this same time, researchers at NIST were reaching similar conclusions, and it was noticed by both teams that a critical parameter for the model is  $D^*/\delta x$ , where  $D^*$  is the characteristic fire diameter and  $\delta x$  is the grid cell size. If this parameter is sufficiently large, the fire can be considered well-resolved and agreement with various flame height correlations was found. If the parameter is not large enough, the fire is not well-resolved and adjustments must be made to the combustion routine to account for it.

Gutiérrez-Montes et al. [26] simulated 1.3 MW and 2.3 MW fires in a 20 m cubic atrium using FDS version 4. Similar experiments were conducted at VTT, Finland, in a 19 m tall test hall with similar sized fires. These results are included in Section 6.1.6.

Hurley and Munguia [27, 28] compared FDS (version 4) simulations with plume and ceiling jet measurements from a series of full-scale tests conducted by Underwriters Laboratories. The tests were conducted in a 36.6 m by 36.6 m compartment with ceiling heights ranging from 3 m to 12.2 m. Heat release rates followed a modified t-squared growth profile. Thermocouples attached to brass disks were used to simulate thermal detectors.

## 2.2.2 Pool Fires

Xin et al. [29] used FDS to model a 1 m diameter methane pool fire. The computational domain was 2 m by 2 m by 4 m with a uniform grid size of 2.5 cm. The predicted results were compared to experimental data and found to qualitatively and quantitatively reproduce the velocity field. The same authors performed a similar study of a 7.1 cm methane burner [30] and a helium plume [31].

The 7.1 cm diameter buoyant diffusion flame has been extensively studied both experimentally and computationally. Zhou and Gore [32] reported radial profiles of mixture fraction and vertical velocity for estimation of thermal expansion for natural gas buoyant diffusion flames stabilized on a 7.1 cm diameter diffuser burner. Xin et al. [33] used a Lagrangian thermal element based combustion model to simulate this flame. The authors noted that the simulations were sensitive to the burnout time utilized by the combustion model. To gain further insight into the species distribution inside the fire, Xin et al. [30] performed fire dynamics simulations using a mixture fraction based combustion model. Xin and Gore [34] used laser-induced incandescence to determine soot distributions in vertical and horizontal planes for methane and ethane turbulent buoyant flames. Biswas et al. [35] utilized a novel time series model to simulate the scalar concentrations and temperature fields for these flames.

Hostikka et al. [36] modeled small pool fires of methane, natural gas and methanol to test the FDS radiation solver for low-sooting fires. They conclude that the predicted radiative fluxes are higher than measured values, especially at small heat release rates, due to an over-prediction of the gas temperature. These tests are also included in the Heat Flux section of this report.

Hietaniemi, Hostikka and Vaari [37] considered heptane pool fires of various diameters. Predictions of the burning rate as a function of diameter follow the trend observed in a number of experimental studies. Their results show an improvement in the model over the earlier work with methanol fires, due to improvements in the radiation routine and the fact that heptane is more sooty than methanol, simplifying the treatment of radiation. The authors point out that reliable predictions of the burning rate of liquid fuels require roughly twice as fine a grid spanning the burner than would be necessary to predict plume velocities and temperatures. The reason for this is the prediction of the heat feedback to the burning surface necessary to *predict* rather than to *specify* the burning rate.

## 2.2.3 Air and Gas Movement in the Absence of Fire

The low Mach number assumption in FDS is appropriate not only to fire, but to most building ventilation scenarios. An example of how the model can be used to assess indoor air quality is presented by Musser et al. [38]. The test compartment was a displacement ventilation test room that contained computers, furniture, and lighting fixtures as well as heated rectangular boxes intended to represent occupants. A detailed description of the test configuration is given by Yuan et al. [39]. The room is ventilated with cool supply air introduced via a diffuser that is mounted on a side wall near the floor. The air rises as it is warmed by heat sources and exits through a return duct located in the upper portion of the room. The flow pattern is intended to remove contaminants by sweeping them upward at the source and removing them from the room. Sulphur hexafluoride, SF<sub>6</sub>, was introduced into the compartment during the experiment as a tracer gas near the breathing zone of the occupants. Temperature, tracer concentration, and velocity were measured during the experiments.

In another study, Musser and Tan [40] used FDS to assess the design of ventilation systems for facilities in which train locomotives operate. Although there is only a limited amount of validation, the study is useful in demonstrating a practical use of FDS for a non-fire scenario.

Mniszewski [41] used FDS to model the release of flammable gases in simple enclosures and open areas. In this work, the gases were not ignited.

Kerber and Walton [42] provided a comparison between FDS version 1 and experiments on positive

pressure ventilation in a full-scale enclosure without a fire.

## 2.2.4 Wind Engineering

Most applications of FDS involve fires within buildings. However, it can be used to model thermal plumes in the open and wind impinging on the exterior of a building. Rehm, McGrattan, Baum and Simiu [43] used the LES solver to estimate surface pressures on simple rectangular blocks in a crosswind, and compared these estimates to experimental measurements. In a subsequent paper [44], they considered the qualitative effects of multiple buildings and trees on a wind field.

A different approach to wind was taken by Wang and Joulain [45]. They considered a small fire in a wind tunnel 0.4 m wide and 0.7 m tall with flow speeds of 0.5 m/s to 2.5 m/s. Much of the comparison with experiment is qualitative, including flame shape, lean, length. They also use the model to determine the predominant modes of heat transfer for different operating conditions. To assess the combustion, they implemented an “eddy break-up” combustion model [46] and compared it to the mixture fraction approach used by FDS. The two models performed better or worse, depending on the operating conditions. Some of the weaknesses of the mixture fraction model as implemented in FDS version 2 were addressed in subsequent versions.

Chang and Meroney [47] compared the results of FDS with the commercial CFD package FLUENT in simulating the transport of pollutants from steady point sources in an idealized urban environment. FLUENT employs a variety of RANS (Reynolds Averaged Navier-Stokes) closure methods, whereas FDS employs large eddy simulation (LES). The results of the numerical models were compared with wind tunnel measurements within a 1:50 scale physical model of an urban street “canyon.”

FDS has recently been applied to urban canopy modeling [48] and wind engineering. Le et al. [49] modeled flow over a backward facing step using DNS with a Reynolds number of 5,100. To verify the results, Jovic and Driver [50] supplemented the DNS simulation with an identically proportioned wind tunnel experiment. Together, the data sets from these two studies have provided the baseline for analysis of recent simulations of flow over a backward facing step that are documented in this guide.

Sarwar et al. [51] used FDS to compare SGS eddy viscosity models. The constant Smagorinsky model performed the best, although the dynamic Smagorinsky and Deardorff models, nearly equivalent in accuracy, were found to perform better than the Vreman model. To avoid explicit specification of inlet turbulence conditions, the authors created an extremely long inlet section to allow turbulence to develop.

## 2.2.5 Atmospheric Dispersion

During the 1980s and 1990s, the Building and Fire Research Laboratory at NIST studied the burning of crude oil under the sponsorship of the US Minerals Management Service. The aim of the work was to assess the feasibility of using burning as a means to remove spilled oil from the sea surface. As part of the effort, Rehm and Baum developed a special application of the LES model called ALOFT. The model was a spin-off of the two-dimensional LES enclosure model, in which a three-dimensional steady-state plume was computed as a two-dimensional evolution of the lateral wind field generated by a large fire blown in a steady wind. The ALOFT model is based on large eddy simulation in that it attempts to resolve the relevant scales of a large, bent-over plume. Validation work was performed by simulating the plumes from several large experimental burns of crude oil in which aerial and ground sampling of smoke particulate was performed [52]. Yamada [53] performed a validation of the ALOFT model for 10 m oil tank fire. The results indicate that the prediction of the plume cross section 500 m from the fire agree well with the experimental observations.

Mouilleau and Champassith [54] performed a validation study to assess the ability of FDS (version 4) to model atmospheric dispersion. They concluded that the best results were obtained for simulations done with

explicitly-modeled wind fluctuations. Specific atmospheric flow characteristics were evaluated for passive releases in open and flat fields.

## 2.2.6 Growing Fires

Floyd [55, 56] compared FDS predictions with measurements from fire tests at the Heiss-Dampf Reaktor (HDR) facility in Germany. The structure was originally the containment building for a nuclear power reactor. The cylindrical structure was 20 m in diameter and 50 m in height topped by a hemispherical dome 10 m in radius. The building was divided into eight levels. The total volume of the building was approximately 11,000 m<sup>3</sup>. From 1984 to 1991, four fire test series were performed within the HDR facility. The T51 test series consisted of eleven propane gas tests and three wood crib tests.

FDS predictions of fire growth and smoke movement in large spaces were performed by Kashef [57]. The experiments were conducted at the National Research Council Canada. The tests were performed in a compartment with dimensions of 9 m by 6 m by 5.5 m with 32 exhaust inlets and a single supply fan. A burner generated fires ranging in size from 15 kW to 1000 kW.

## 2.2.7 Flame Spread

Although FDS simulations have been compared to actual and experimental large-scale fires, it is difficult to quantify the accuracy because of the uncertainty associated with material properties. Most quantified validation work associated with flame spread have been for small, laminar flames with length scales ranging from millimeters to a few centimeters.

For example, FDS (or its core algorithms) have been used at a grid resolution of roughly 1 mm to look at flames spreading over paper in a micro-gravity environment [58, 59, 60, 61, 62, 63], as well as “g-jitter” effects aboard spacecraft [64]. Simulations have been compared to experiments performed aboard the Space Shuttle. The flames are laminar and relatively simple in structure, and the materials are relatively well-characterized.

FDS flame spread predictions were compared to experiments over a 5 m slab of PMMA performed by Factory Mutual Research Corporation (FMRC) [23, 24].

A charring model was implemented in FDS by Hostikka and McGrattan [65]. The model was a simplification of work done at NIST by Ritchie et al. [66]. The charring model was first used to predict the burning rate of a small wooden sample in the cone calorimeter. Full-scale room tests with wood paneling were modeled, but the results were grid-dependent. This was likely a consequence of the gas phase spatial resolution, rather than the solid phase.

Kwon et al. [67] performed three simulations to evaluate the capability of FDS, version 4, in predicting upward flame spread. The FDS predictions were compared with empirical correlations and experimental data for upward flame spread on a 5 m PMMA panel. A simplified flame spread model was also applied to assess the simulation results.

An extensive amount of flame spread validation work with FDS version 4 has been performed by Hi- etaniemi, Hostikka, and Vaari at VTT, Finland [37]. The case studies are comprised of fire experiments ranging in scale from the cone calorimeter (ISO 5660-1, 2002) to full-scale fire tests such as the room corner test (ISO 9705, 1993). Comparisons are also made between FDS 4 results and data obtained in the SBI (Single Burning Item) Euro-classification test apparatus (EN 13823, 2002) as well as data obtained in two ad hoc experimental configurations: one is similar to the room corner test but has only partial linings and the other is a space to study fires in building cavities. In the study of upholstered furniture, the experimental configurations are the cone and furniture calorimeters, and the ISO room. For liquid pool fires, comparison is made to data obtained by numerous researchers. The burning materials include spruce timber, MDF (Medium Density Fiber) board, PVC wall carpet, upholstered furniture, cables with plastic sheathing, and

heptane. The scope of the VTT work is considerable. Assessing the accuracy of the model must be done on a case by case basis. In some cases, predictions of the burning rate of the material were based solely on its fundamental properties, as in the heptane pool fire simulations. In other cases, some properties of the material are unknown, as in the spruce timber simulations. Thus, some of the simulations are true predictions, some are calibrations. The intent of the authors was to provide guidance to engineers using the model as to appropriate grid sizes and material properties. In many cases, the numerical grid was made fairly coarse to account for the fact that in practice, FDS is used to model large spaces of which the fuel may only comprise a small fraction.

Mangs and Hostikka [68] carried out experiments and simulations (FDS 5.4.3) of the vertical flame spread on the surface of thin birch wood cylinders at different ambient temperatures. The parameters for the pyrolysis model were estimated from TGA and cone calorimeter experiments. The gas phase flow was calculated in the DNS mode with 1.0 mm grid cells in axi-symmetric geometry. The simulation model was able to predict the flame spread rates within the uncertainties associated with the experiments and postsimulation analysis of the spread rate.

## 2.2.8 Compartment Fires

As part of the NIST investigation of the World Trade Center fires and collapse, a series of large scale fire experiments were performed specifically to validate FDS [69]. The tests were performed in a rectangular compartment 7.2 m long by 3.6 m wide by 3.8 m tall. The fires were fueled by heptane for some tests and a heptane/toluene mixture for the others. The results of the experiments and simulations are included in detail in this Guide.

A second set of experiments to validate FDS for use in the World Trade Center investigation is documented in Ref. [70]. The experiments are not described as part of this Guide. The intent of these tests was to evaluate the ability of the model to simulate the growth of a fire burning three office workstations within a compartment of dimensions 11 m by 7 m by 4 m, open at one end to mimic the ventilation of windows similar to those in the WTC towers. Six tests were performed with various initial conditions exploring the effect of jet fuel spray and ceiling tiles covering the surface of the desks and carpet. Measurements were made of the heat release rate and compartment gas temperatures at four locations using vertical thermocouple arrays. Six different material samples were tested in the NIST cone calorimeter: desk, chair, paper, computer case, privacy panel, and carpet. Data for the carpet, desk and privacy panel were input directly into FDS, with the other three materials lumped together to form an idealized fuel type. Open burns of single workstations were used to calibrate the simplified fuel package. Details of the modeling are contained in Ref. [71].

The BRE Centre for Fire Safety Engineering at the University of Edinburgh conducted a series of large-scale fire tests in a real high rise building in Dalmarnock, Glasgow, Scotland [72, 73]. The experiments took place in July, 2006, with the close collaboration of the Strathclyde Fire Brigade and other partners. These experiments attempted to create realistic scenario in which a wide range of modern fire safety engineering tools could be put to a test. Jahn, Rein and Torero assessed the sensitivity of FDS when applied to these experiments [74]. Fire size and location, convection, radiation and combustion parameters were varied in order to determine the associated degree of sensitivity. Emphasis was put in the prediction of secondary ignition and time to flashover. In this context and while keeping the HRR constant, simulations of fire growth were significantly sensitive to location of the heat release rate, fire area, flame radiative fraction, and material thermal and ignition properties.

Students at Stord/Haugesund University College in Norway simulated full-scale experiments of temperature and smoke spread in a realistic multi-room setting using both CFAST and FDS [75]. Data from the top 0.5 m of the compartments was compared with measurements. The simulations were found to provide satisfying results in CFAST, as an alternative to FDS.

## 2.2.9 Sprinklers, Mist System, and Suppression by Water

Vettori [76] modeled sprinkler activation patterns in a room with an obstructed ceiling. In a follow-up report, Vettori [77] extended his study to include sloped ceilings, with and without obstructions. Both of these experimental series are included within the current validation guide and are referred to as the Vettori Flat and Sloped Ceiling Experiments.

A significant validation effort for sprinkler activation and suppression was a project entitled the International Fire Sprinkler, Smoke and Heat Vent, Draft Curtain Fire Test Project organized by the National Fire Protection Research Foundation [78]. Thirty-nine large scale fire tests were conducted at Underwriters Laboratories in Northbrook, IL. The tests were aimed at evaluating the performance of various fire protection systems in large buildings with flat ceilings, like warehouses and “big box” retail stores. All the tests were conducted under a 30 m by 30 m adjustable-height platform in a 37 m by 37 m by 15 m high test bay. At the time, FDS had not been publicly released and was referred to as the Industrial Fire Simulator (IFS), but it was essentially the same as FDS version 1. The first and second series of heptane spray burner fires are included in this guide under the heading “UL/NFPRF Sprinkler, Vent, and Draft Curtain Study.” Most of the full-scale experiments performed during the project used a heptane spray burner to generate controlled fires of 1 MW to 10 MW. However, five experiments were performed with 6 m high racks containing the Factory Mutual Standard Plastic Commodity, or Group A Plastic. To model these fires, bench scale experiments were performed to characterize the burning behavior of the commodity, and larger test fires provided validation data with which to test the model predictions of the burning rate and flame spread behavior [79, 80]. Two to four tier configurations were evaluated.

High rack storage fires of pool chemicals were modeled by Olenick et al. [81] to determine the validity of sprinkler activation predictions of FDS. The model was compared to full-scale fires conducted in January, 2000 at Southwest Research Institute in San Antonio, Texas.

FDS has been used to study the behavior of a fire undergoing suppression by a water mist system. Kim and Ryou [82, 83] compared FDS predictions to results of compartment fire tests with and without the application of a water mist. The cooling and oxygen dilution were predicted to within about 10 % of the measurements, but the simulations failed to predict the complete extinguishment of a hexane pool fire. The authors suggest that this is a result of the combustion model rather than the spray or droplet model.

Another study of water mist suppression using FDS was conducted by Hume at the University of Canterbury, Christchurch, New Zealand [84]. Full-scale experiments were performed in which a fine water mist was combined with a displacement ventilation system to protect occupants and electrical equipment in the event of a fire. Simulations of these experiments with FDS showed qualitative agreement, but the version of the model used in the study (version 3) was not able to predict accurately the decrease in heat release rate of the fire.

Hostikka and McGrattan [85] evaluated the absorption of thermal radiation by water sprays. They considered two sets of experimental data and concluded that FDS has the ability to predict the attenuation of thermal radiation “when the hydrodynamic interaction between the droplets is weak.” However, modeling interacting sprays would require a more costly coalescence model. They also note that the results of the model were sensitive to grid size, angular discretization, and droplet sampling.

O’Grady and Novozhilov [86] compared the predictions of FDS version 4 against full-scale fire tests performed at SP Sweden involving a 1.5 MW steady-state fire with two different sprinkler flow rates [87]. The authors reported results for gas temperatures and the tangential flow velocity in the ceiling jet. Sensitivity of the model to a range of input parameters was investigated. The model demonstrated moderate sensitivity to the spray parameters, such as spray cone configuration, initial droplet velocities, and droplet sizes. On the other hand, the sensitivity to other parameters such as sprinkler atomization length and rms of droplet size distribution was low.

Xiao [88] compared FDS simulations with real scale compartment measurements for unsprinklered and

sprinklered experiments. Numerical results for doorway mass flow rate and temperature are compared with the experimental data for three fire sizes.

### 2.2.10 Airflows in Fire Compartments

Friday studied the use of FDS in large scale mechanically ventilated spaces. The ventilated enclosure was provided with air injection rates of 1 to 12 air changes per hour and a fire with heat release rates ranging from 0.5 MW to 2 MW. The test measurements and model output were compared to assess the accuracy of FDS [89]. These simulations have been repeated with the latest version of FDS and reported in this guide under the heading “FM/SNL Test Series.”

Zhang et al. [90] utilized the FDS model to predict turbulence characteristics of the flow and temperature fields due to fire in a compartment. The experimental data was acquired through tests that replicated a half-scale ISO Room Fire Test. Two cases were explored – the heat source in the center of the room and the heat source adjacent to a wall. In both cases, the heat source was a heating element with an output of  $12 \text{ kW/m}^2$ .

### 2.2.11 Tunnel Fires

Cochard [91] used FDS to study the ventilation within a tunnel. He compared the model results with a full-scale tunnel fire experiment conducted as part of the Massachusetts Highway Department Memorial Tunnel Fire Ventilation Test Program. The test consisted of a single point supply of fresh air through a  $28 \text{ m}^2$  opening in a  $135 \text{ m}$  tunnel.

McGrattan and Hamins [92] also applied FDS to simulate two of the Memorial Tunnel Fire Tests as validation for the use of the model in studying an actual fire in the Howard Street Tunnel, Baltimore, Maryland, July 2001. The experiments chosen for the comparison were unventilated. One experiment was a 20 MW fire; the other a 50 MW fire.

Piergoirgio et al. [93] provided a qualitative analysis of FDS applied to a truck fire within a tunnel. The goal of their analysis was to describe the spread of the toxic gases within the tunnels, to determine the places not involved in the spreading of combustion products and to quantify the oxygen, carbon monoxide and hydrochloric acid concentrations during the fire.

Edwards et al. [94, 95] used FDS to determine the critical air velocity for smoke reversal in a tunnel as a function of the fire intensity, and his results compared favorably with experimental results. In a further study, Edwards and Hwang [96] applied FDS to study fire spread along combustibles in a ventilated mine entry. Analyses such as these are intended for planning and implementation of ventilation changes during mine fire fighting and rescue operations.

Bilson et al. [97] used FDS to evaluate the interaction of a deluge system with a tunnel ventilation and smoke exhaust system.

Harris [98] used FDS to determine the heat flux from a tunnel fire under varying water application rates. These results were qualitatively consistent with experimental results of Arvidson [99], who conducted burn tests for shielded and unshielded standard plastic commodities under a variety of spray conditions.

Trelles and Mawhinney [100, 101] simulated with FDS 4 a series of full-scale fire suppression experiments conducted at the San Pedro de Anes test tunnel near Gijon, Asturias, Spain in February, 2006. The fuel consisted of wooden and polyethylene pallets, and the suppression system consisted of different configurations of water mist nozzles.

### 2.2.12 Smoke Detection

The ability of version 1 of FDS to accurately predict smoke detector activation was studied by D’Souza [102]. The smoke transport model within FDS was tested and compared with UL 217 test data. The second step

in this research was to further validate the model with full-scale multi-compartment fire tests. The results indicated that FDS is capable of predicting smoke detector activation when used with smoke detector lag correlations that correct for the time delay associated with smoke having to penetrate the detector housing. A follow-up report by Roby et al. [103] and paper by Zhang et al. [104] describes the implementation and validation of the smoke detector algorithm currently incorporated in FDS.

Another study of smoke detector activation was carried out by Brammer at the University of Canterbury, New Zealand [105]. Two fire tests from a series performed in a two-story residence were simulated, and smoke detector activation times were predicted using three different methods. The methods consisted of either a temperature correlation, a time-lagged function of the optical density, or a thermal device much like a heat detector. The purpose was to identify ways to reliably predict smoke detector activation using typical model output like temperature and smoke concentration. It was remarked that simulating the early stage of the fire is critical to reliable prediction.

Cleary [106] also provided a comparison between FDS computed gas velocity, temperature and concentrations at various detector locations. The research concluded that multi-room fire simulations with the FDS model can accurately predict the conditions that a sensor might experience during a real fire event.

### 2.2.13 Combustion Model

A few studies have been performed comparing direct numerical simulations (DNS) of a simple burner flame to laboratory experiments [107]. Another study compared DNS calculations of a counterflow diffusion flames to experimental measurements and the results of a one-dimensional multi-step kinetics model [108].

Bundy, Dillon and Hamins [109, 110] studied the use of FDS in providing data and correlations for fire investigators to support their investigations. A paraffin wax candle was placed within a small plexi-glass enclosure. The heat flux from the candle flame was modeled with FDS.

Floyd et al. [111, 56] compared the radiation model of FDS version 2 with full-scale data from the Virginia Tech Fire Research Laboratory (VTFRL). The test compartment was outfitted with equipment capable of taking temperature, air velocity, gas concentrations, unburned hydrocarbon and heat flux measurements. The test facility consisted of a single compartment geometrically similar to the ISO 9705 standard compartment with dimensions of 1.2 m by 1.8 m by 1.2 m in height. The ceiling and walls were constructed of fiberboard over a steel shell with a floor of concrete. Three baseline experiments were completed with fires ranging in size from 90 kW to 440 kW.

Xin and Gore [112] compared FDS predictions and measurements of the spectral radiation intensities of small fires. The fuel flow rates for methane and ethylene burners were selected so that the Froude numbers matched that of liquid toluene pool fires. The heat release rate was 4.2 kW for the methane flame and 3.4 kW for the ethylene flame. Line of sight spectral radiation intensities were measured at six downstream locations. The spectral radiation intensity calculations were performed by post-processing the transient scalar distributions provided by FDS.

Zhang et al. [113] compared the experimental results of a circular methane gas burner to predictions computed by FDS. The compartment was 2.8 m by 2.8 m by 2.2 m high with natural ventilation from a standard door.

### 2.2.14 Soot Deposition

Several studies have been conducted that indicate soot deposition is an important factor in compartment fires for the accurate prediction of smoke concentrations, smoke detector activations, and visibility. Gottuk et al. [114] reported that smoke concentrations predicted by FDS near smoke alarms in a corridor were two to five times greater than measured smoke concentrations. Hamins et al. [115] conducted full-scale compartment fire experiments for use in validation studies of various fire models, including FDS. The results

indicated that smoke concentrations predicted by FDS were up to five times greater than measured smoke concentrations. Floyd and McDermott [116] implemented thermophoretic and turbulent diffusion soot deposition mechanisms in FDS and compared predicted soot densities and concentrations to measurements from small- and large-scale experiments. Riahi [117] conducted bench-scale experiments to measure soot densities and soot deposition patterns on walls for various fuels. Riahi identified thermophoretic deposition as an important soot deposition mechanism in the hot gas layer. Cohan [118] used FDS to simulate select cases from the Gottuk [114] corridor tests, Hamins et al. [115] NRC experiments, and Riahi [117] hood experiments with thermophoretic and turbulent diffusion soot deposition mechanisms. Overholt and Ezekoye [119] implemented gravitational settling of soot in the gas-phase in FDS and quantified the effects of gravitational settling/deposition compared to thermophoretic and turbulent diffusion deposition for small- and large-scale validation cases.

## 2.3 Reconstructions of Actual Fires

ASTM E 1355 states that a model may be evaluated by comparing it with “Documented Fire Experience” which includes:

- eyewitness accounts of real fires,
- known behavior of materials in fires (for example, melting temperatures of materials), and
- observed post-fire conditions, such as the extent of fire spread.

Often the term “reconstruction” is applied to this type of simulation, because the model is used to reconstruct events based on evidence collected during and after the fire. Some of the more notable studies performed at NIST include:

- McGrattan, Bouldin, and Forney simulated the fires within the World Trade Center towers and Building 7 on September 11, 2001 [71].
- Grosshandler et al. investigated the fire that occurred at the Station Nightclub in Rhode Island in February, 2003 [120].
- Madrzykowski and Vettori examined a fire in a townhouse in Washington, D.C., where two fire fighters were killed and one severely injured in 1999 [121].
- Vettori, Madrzykowski, and Walton simulated a fire in a Houston restaurant that killed two fire fighters in 2000 [122].
- Madrzykowski, Forney and Walton simulated a fire that killed three children and three fire fighters in a two story duplex house in Iowa in 1999 [123].
- Madrzykowski and Walton investigated the fire in the Cook County (Chicago) Administration Building in October, 2003, that killed six people trapped in a stairwell [124].
- Bryner et al. simulated a fire in a large furniture store that occurred in June, 2007, killing nine fire fighters [125].

Outside of NIST, FDS has been used to investigate many actual fires, but very few of these studies are documented in the literature. Exceptions include:

- A large fire in a “cash & carry” warehouse in the UK was studied by Camp and Townsend using both hand calculations and FDS (version 1) [126].

- A study by Rein et al. [127] looked at several fire events using an analytical fire growth model, the NIST zone model CFAST, and FDS.
- A similar study was performed several years earlier by Spearpoint et al. [128] as a class exercise at the University of Maryland.
- During the SFPE Professional Development Week in the fall of 2001, a workshop was held in which several engineers related their experiences using FDS as a forensic tool [129].
- The role of carbon monoxide in the deaths of three fire fighters was studied by Christensen and Icove [130].

# **Chapter 3**

## **Description of Experiments**

This chapter contains a brief description of the experiments that were used for model validation. Only enough detail is included here to provide a general understanding of the model simulations. Anyone wishing to use the experimental measurements for validation ought to consult the cited test reports or other publications for a comprehensive description.

### **3.1 ArupFire Tunnel Fire Experiments**

Gabriele Vigne and Jimmy Jönsson of ArupFire conducted a series of fire experiments within a tunnel with a  $50\text{ m}^2$  cross section. The tunnel is located in La Ribera del Folgoso, Spain. It is approximately 6.5 m high, 8 m wide and 300 m long. Five replicate tests were conducted using a 1 m by 2 m steel pan filled with heptane on water. Near-ceiling temperatures were measured 2 m, 4 m, 6 m and 8 m from the plume centerline. The peak heat release rate was approximately 5.3 MW.

### **3.2 ATF Corridors Experiments**

A series of eighteen experiments were conducted in a two-story structure with long hallways and a connecting stairway in the large burn room of the ATF Fire Research Laboratory in Ammendale, Maryland, in 2008 [131]. The test enclosure consisted of two 17.0 m long hallways connected by a stairway consisting of two staircases and an intermediary landing. There was a door at the opposite end of the first floor hallway, which was closed during all tests. The end of the second floor hallway was open with a soffit near the ceiling.

The walls and ceilings of the test structure were constructed of 1.2 cm gypsum wallboard. The flooring throughout the structure, including the stairwell landing floor, consisted of one layer of 1.3 cm thick cement board on one layer of 1.9 cm thick plywood supported by wood joists. The first set of stairs, which had eight risers, led from the first floor up to the landing area. The second set of stairs, which had nine risers, led from the landing area up to the second floor. The stairs were constructed of 2.5 cm thick clear pine lumber. The two set of stairs were separated by an approximately 0.42 m wide gap in the middle of the stairwell. This gap was separated from the stairs by a 0.91 m tall barrier constructed of a single piece of gypsum board. The flue space was open to the first floor. The flue space was separated from the second floor by a 0.9 m tall barrier constructed of gypsum board. There was a metal exterior type door at the end of the first floor near the burner. The door was closed during all experiments.

The fire source was a natural gas diffusion burner. The burner surface was horizontal, square and 0.45 m on each side, its surface was 0.37 m above the floor, and it was filled with gravel. The burner was located near the end of the first floor away from the stairs. A diagram of the test structure is displayed in Figure 3.1.

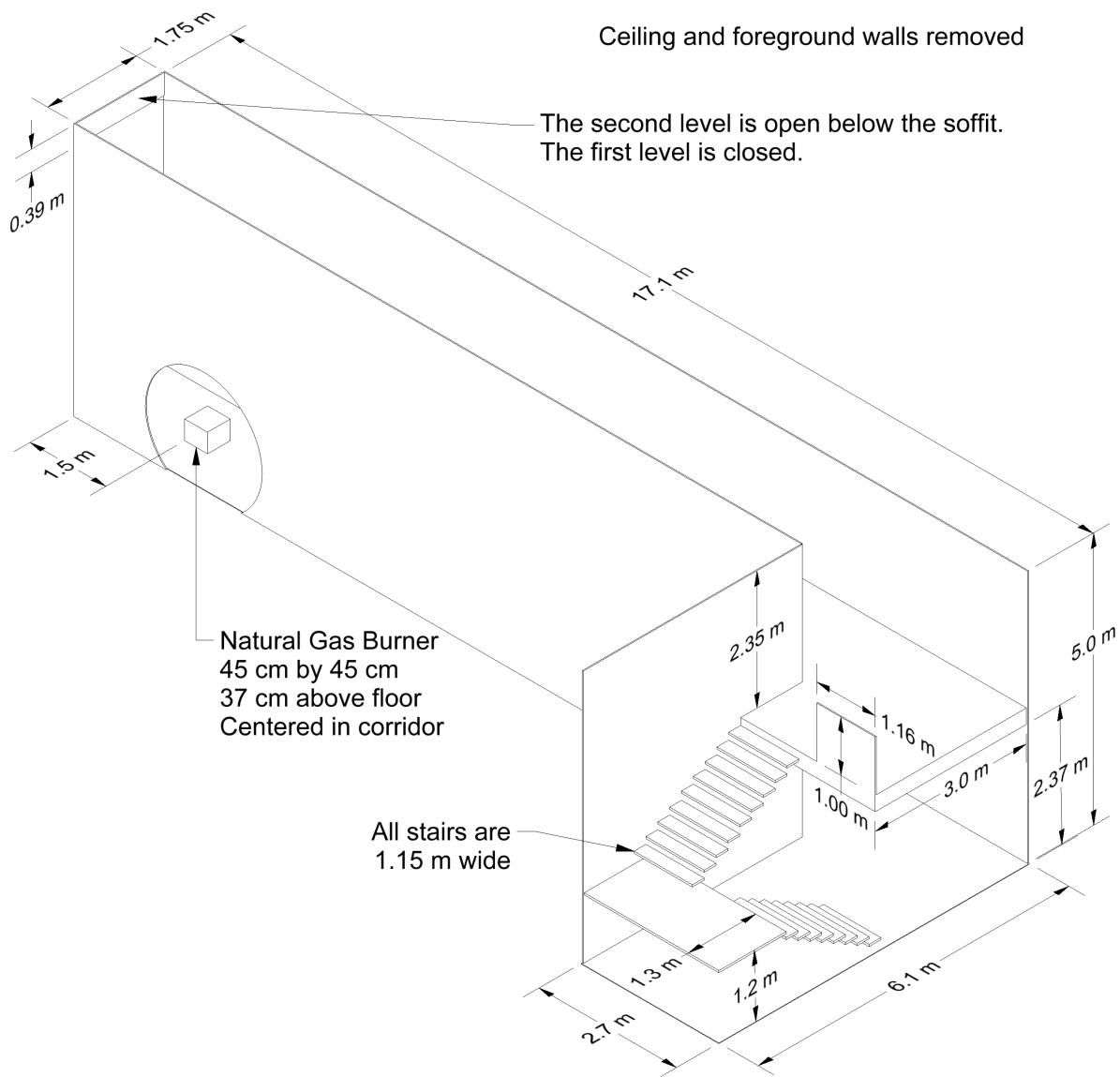


Figure 3.1: Geometry of the ATF Corridors Experiments.

### 3.3 Backward Facing Step

A common validation experiment for CFD codes involves flow through a channel with a backward facing step. These experiments are designed to test the influence of grid resolution, inlet turbulence, wall boundary treatments, and eddy viscosity models. One set of experiments has been conducted by Jovic and Driver [50]. A schematic view of the experiment is shown in Fig. 3.2. The dimensions of the channel are based on step height  $h = 0.0098$  m. The length of the channel is  $24h$ . The width of the channel is  $4h$ . The height of the inlet section is  $5h$ , and the height of the channel downstream of the step is  $6h$ . The expansion ratio is thus 1.2. The inlet is split into three sub-inlets to permit localized variation of inlet turbulence. The Reynolds number of the flow is 5100, based on the free-stream velocity (7.2 m/s) and the step height.

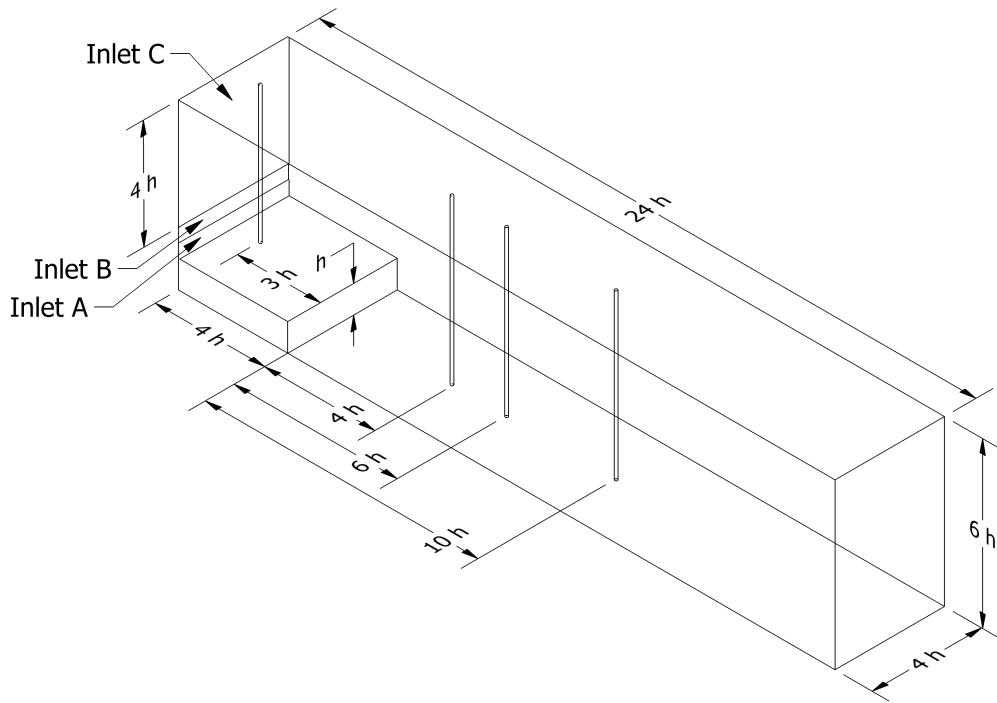


Figure 3.2: Geometry of the Backward Facing Step experiments.

### 3.4 Beyler Hood Experiments

Craig Beyler performed a large number of experiments involving a variety of fuels, fire sizes, burner diameters, and burner distances beneath a hood [132]. The hood consisted of concentric cylinders separated by an air gap. The inner cylinder was shorter than the outer and this allowed combustion products to be removed uniformly from the hood perimeter. The exhaust gases were then analyzed to determine species concentrations. The burner could be raised and lowered with respect to the bottom edge of the hood. Based on the published measurement uncertainties, species errors are estimated at 6 %. 148 tests were performed with measurements made in the exhaust duct. The fuels in those tests were as follows: 16 acetone, 11 ethanol, 13 isopropanol, 18 methanol, 51 propane, 28 propylene, and 11 toluene. Hood equivalence ratios varied from 0.2 to 1.7. A subset of 47 tests spanning the equivalence ratio range for each fuel was simulated for

validation (5, 5, 5, 5, 15, 7, and 5 respectively for the fuels mentioned above).

### 3.5 Bouchair Solar Chimney

To evaluate solar-induced ventilation systems in desert climates, Bouchair [133] constructed a simple test apparatus shown in Fig. 3.3. A compartment with interior dimensions of approximately 1.6 m long, 1.8 m, and 2.0 m high had a window on one side and an air inlet slot on the other, leading into a 1.5 m wide cavity with two heating panels spanning the long dimension. The panels were heated to 10 °C, 20 °C, 30 °C, or 40 °C above ambient, drawing air through the compartment and into the thermal cavity. The mass flow rate of air through the cavity was measured. The inlet slot was either 0.1 m or 0.4 m high, and 1.4 m wide. The thermal cavity was 1.5 m wide, and the hot panels were separated by 0.1 m, 0.2 m, 0.3 m, 0.5 m, or 1.0 m. In all, there were 40 different sets of test parameters.

In addition to the results presented in this guide, simulations of this experiment were performed by Shi and Zhang [134]. The objective of the simulations is to predict the mass flow rate by accurately modeling the convective heat transfer between the air and hot panels.

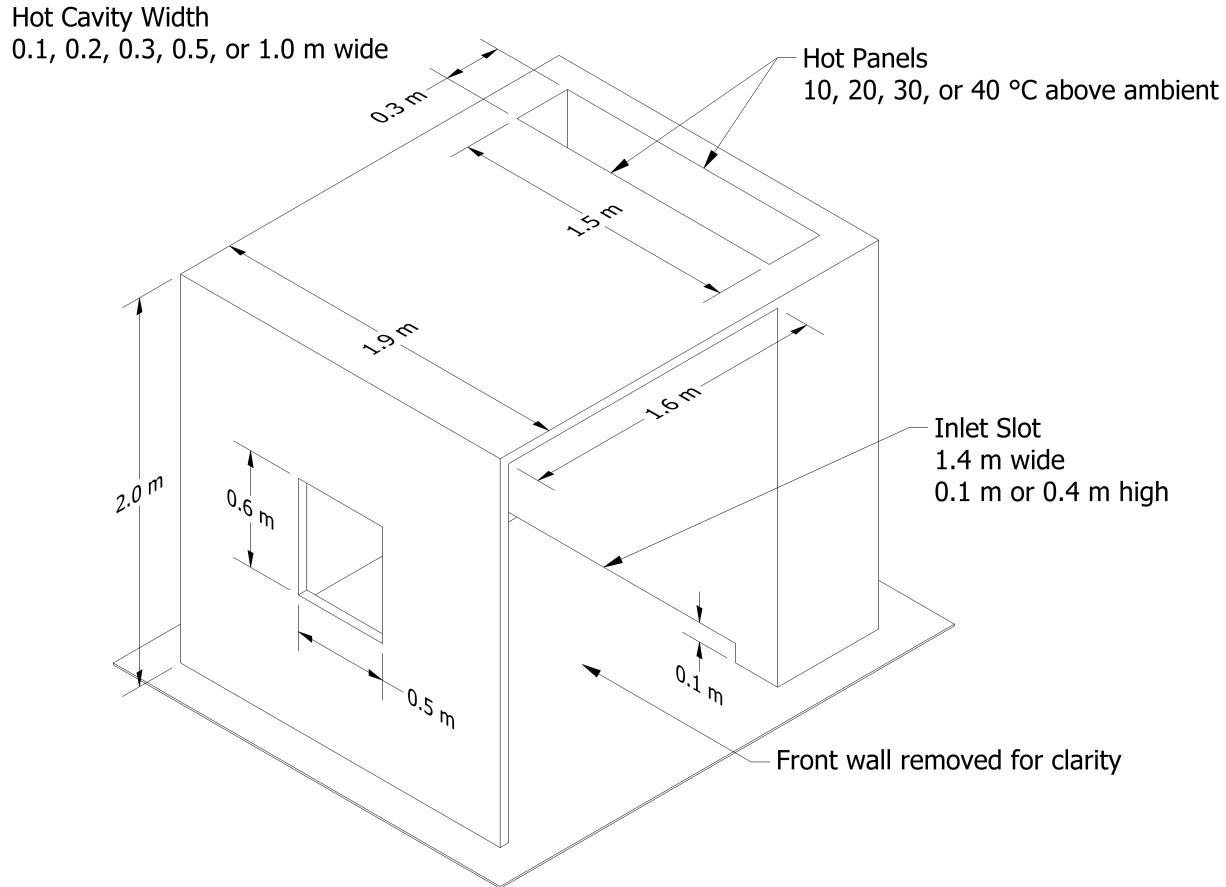


Figure 3.3: Geometry of the Bouchair Solar Chimney experiment.

## 3.6 BRE Spray Test for Radiation Attenuation

Murrel et al. [135] measured the attenuation of thermal radiation passing through a water spray using a heat flux gauge. The radiation was produced by a heat panel, one meter square, at 900 °C. The horizontal distance from the radiation panel to the spray nozzle was 2 m and to the measurement point 4 m. The nozzles were positioned at a height 0.24 m above the panel upper edge. The heat flux gauge was positioned at the line passing through the center of the panel. The attenuation of radiation was defined as  $(q_0 - q_s)/q_0$ , where  $q_0$  is the initial radiative heat flux, measured without a spray, and  $q_s$  is the heat flux measured during the spray operation.

Experimental results are used from three full-cone type nozzles, labeled A, B and D. The opening angles of the nozzles were between 90 and 108 degrees. The purpose of the simulation is to compare the measured and simulated attenuation of radiation at different flow conditions. The nozzles were specified in terms of median droplet size and mean vertical velocity using PDPA measurement in a single position, 0.7 m below the nozzle. The droplet boundary conditions were determined by assuming  $d_m \propto p^{-1/3}$  and  $v \propto p^{1/2}$  type of dependences between the droplet size, speed and pressure.

## 3.7 Bryant Doorway Velocity Measurements

Rodney Bryant of the Fire Research Division at NIST performed a series of velocity measurements of the gas velocity within the doorway of a standard ISO 9705 compartment for fires ranging from 34 kW to 511 kW [136, 137, 138]. A doorway served as the only vent for the enclosure. It included a jamb of 37 cm extending outward to facilitate the laser measurements. The entire compartment was elevated 0.3 m off the floor of the laboratory (see Fig. 3.4). The measurements were made using both bi-directional probes and PIV (Particle Image Velocimetry). The PIV measurements only cover the lower two-thirds of the doorway because of difficulties in seeding the hot outflow gases. The bi-directional probe measurements span the entire height of the doorway, but Bryant reports that these measurements were up to 20 % greater than the PIV measurements in certain regions of the flow. Consequently, only the PIV data was used for comparison to the model.

## 3.8 Cable Response to Live Fire – CAROLFIRE

CAROLFIRE was a project sponsored by the U.S. Nuclear Regulatory Commission to study the thermal response and functional behavior of electrical cables [139]. The primary objective of CAROLFIRE was to characterize the various modes of electrical failure (e.g., hot shorts, shorts to ground) within bundles of power, control and instrument cables. A secondary objective of the project was to develop a simple model to predict thermally-induced electrical failure (THIEF). The measurements used for these purposes were conducted at Sandia National Laboratories and are described in Volume II of the CAROLFIRE test report. In brief, there were two series of experiments. The first were conducted within a heated cylindrical enclosure. Single and bundled cables were exposed to various heat fluxes and the electrical failure modes recorded. The second series of experiments involved cables within trays in a semi-enclosed space under which a gas-fueled burner created a hot layer to force cable failure. Only results from the first series are used here.

Petra Andersson and Patrick Van Hees of the Swedish National Testing and Research Institute (SP) proposed that a cable's thermally-induced electrical failure can be predicted via a one-dimensional heat transfer calculation, under the assumption that the cable can be treated as a homogenous cylinder [140]. Their results

Note: All values refer to inner dimension.

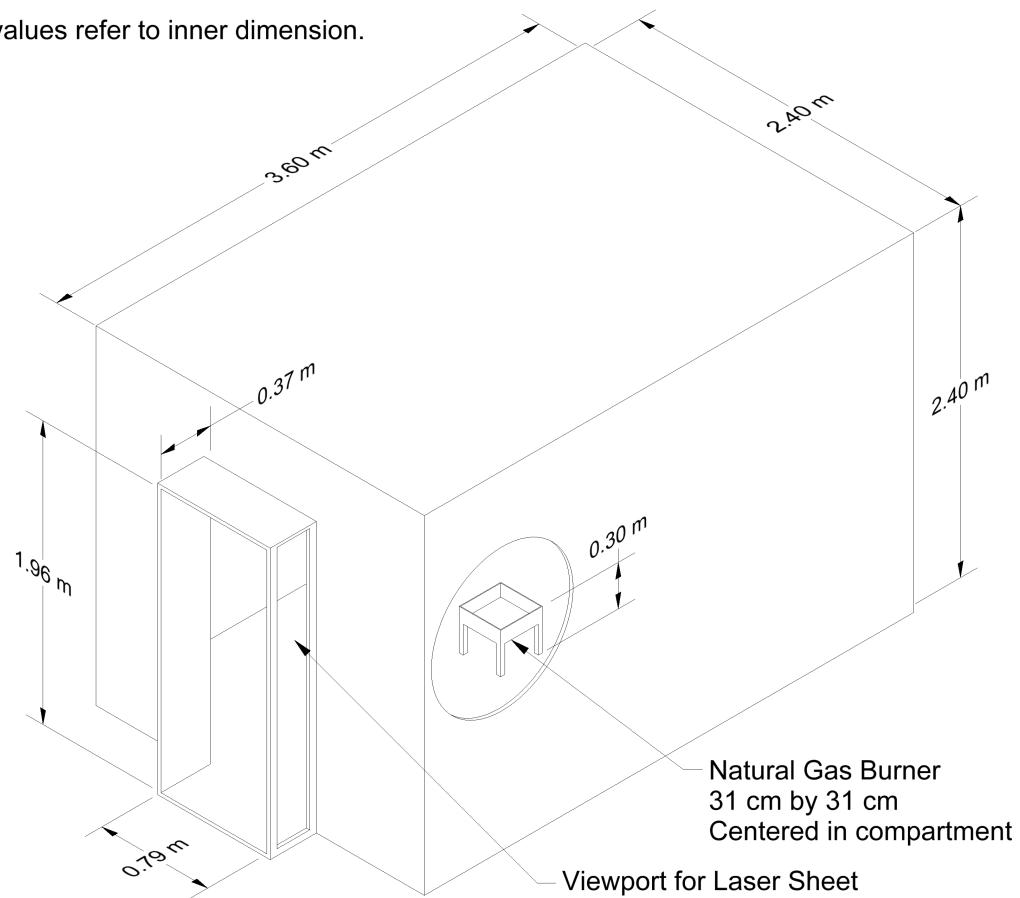


Figure 3.4: Geometry of Bryant's compartment.

for PVC cables were encouraging and suggested that the simplification of the analysis is reasonable and that it should extend to other types of cables. The assumptions underlying the THIEF model are as follows:

1. The heat penetration into a cable of circular cross section is primarily in the radial direction.
2. The cable is homogenous in composition. In reality, a cable is constructed of several different types of polymeric materials, cellulosic fillers, and a conducting metal, most often copper.
3. The thermal conductivity, specific heat, and density of the assumed homogenous cable are independent of temperature. In reality, both the thermal conductivity and specific heat of polymers are temperature-dependent, but this information is not easily obtained from manufacturers.
4. It is assumed that no decomposition reactions occur within the cable during its heating, and ignition and burning are not considered in the model. In fact, thermoplastic cables melt, thermosets form a char layer, and both release volatile gases up to and beyond the point of electrical failure.
5. Electrical failure occurs when the temperature just inside the cable jacket reaches an experimentally determined value.

## 3.9 CSIRO Grassland Fires

In July and August of 1986, the Commonwealth Scientific and Industrial Research Organisation (CSIRO) of Australia conducted controlled grassland fire experiments near Darwin, Northern Territory [141]. July and August are in the middle of the dry season when the grasses are fully cured (dried) and the weather is warm and dry. The experiments were conducted on flat plots measuring 100 m by 100 m, 200 m by 200 m, or 200 m by 300 m. Two of these experiments were simulated with FDS by Mell et al. [142] and are included in this guide. Case C064 was conducted on a 100 m by 100 m plot of kerosene grass (*Eriachne burkittii*); Case F19 was conducted on a 200 m by 200 m plot of kangaroo grass (*Themeda australis*).

## 3.10 Cup Burner Experiments

The cup-burner is a widely used experimental apparatus for studying the effectiveness of flame extinguishing agents. The test is designed to determine the effectiveness of various extinguishing agents. Typically, these experiments feature a steady fuel-air coflow diffusion flame that is established above the cup. The extinguishing agent is gradually introduced into the air stream to determine the minimum concentration of the agent that leads to lift off. Two experimental data sets are examined: methane ( $\text{CH}_4$ ) - air coflow [143] and n-heptane ( $\text{C}_7\text{H}_{16}$ ) - air coflow [144]. The extinguishing agents of interest are argon (Ar), carbon dioxide ( $\text{CO}_2$ ), helium (He), and nitrogen ( $\text{N}_2$ ).

## 3.11 DelCo Trainer Experiments

The NIST Fire Fighting Technology Group conducted a series of experiments in two structures of similar design located at the Delaware County (“DelCo”) Emergency Services Training Center in Sharon Hill, Pennsylvania [145]. Three propane burners were used to provide the fire source for all experiments, and various sensors were used to collect gas temperature, gas velocity, heat flux, and gas concentration measurements throughout the structure.

The single level structure was instrumented with five bare-bead thermocouple arrays and two gas sample inlet pipes at the locations shown in Fig. 3.5. Both floors of the two level structure were instrumented with three bare-bead thermocouple arrays and one gas sample inlet pipe at the locations shown in Fig. 3.6.

## 3.12 FAA Cargo Compartments

The U.S. Federal Aviation Administration (FAA) has sponsored experiments and modeling of smoke transport within aircraft storage compartments [146, 147]. Two types of compartments were used; one from a Boeing 707 and one from a McDonnell Douglas DC-10. The 707 compartment was 6.7 m in length, 3.2 m in width, and 1.4 m in height. The DC-10 compartment was 14 m in length, 4.4 m in width, and 1.7 m in height. The fire for all experiments was fueled by a 0.1 m by 0.1 m tray of plastic resin producing a peak HRR of 5 kW [148]. The long walls of the compartments were barrel-shaped to conform to the shape of the aircraft fuselage. The fire was placed in different locations, and measurements of gas and ceiling temperature, heat flux, gas concentration, and smoke obscuration were made at a variety of locations, mostly near the ceiling.

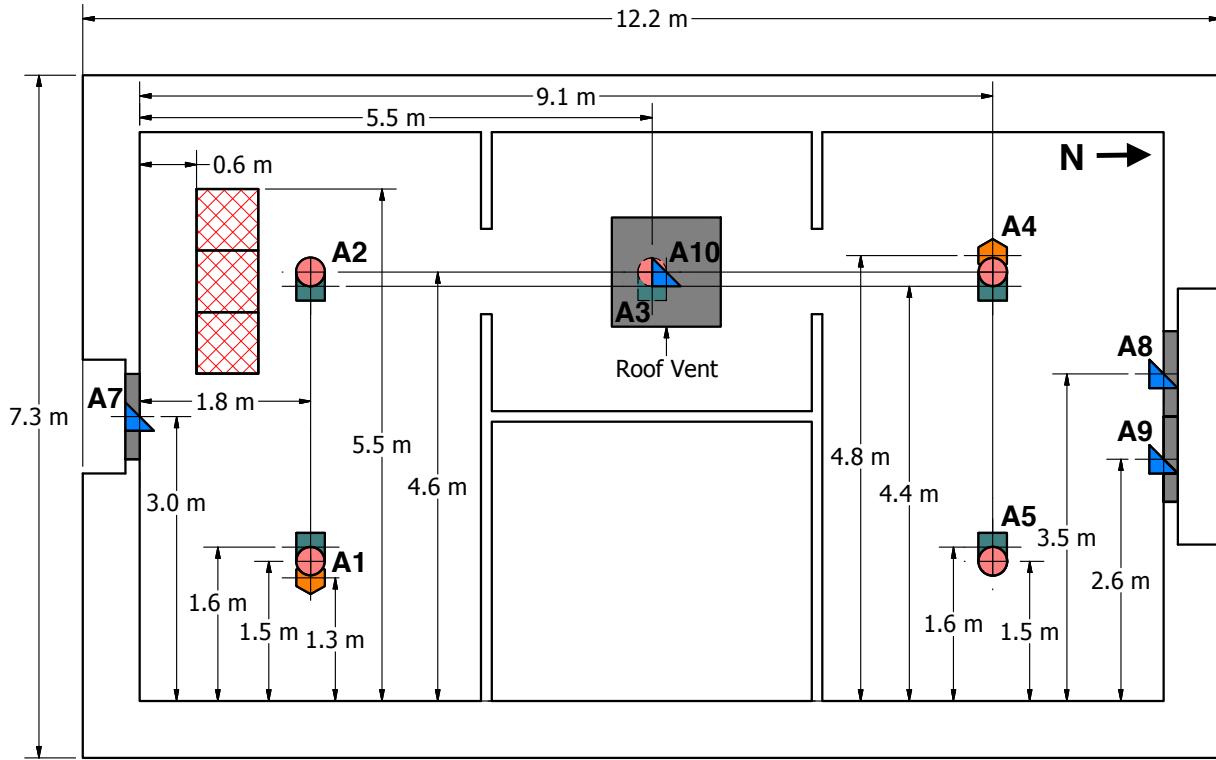


Figure 3.5: Instrumentation of the single level DelCo training structure. The thermocouple arrays are denoted by crossed circles and the gas sampling measurement locations are denoted by hexagons at locations A1 and A4. The burner is denoted by three cross-hatched squares.

### 3.13 FAA Polymers

As part of their efforts to characterize the burning behavior of commonly used plastics, the U.S. Federal Aviation Administration (FAA) conducted measurements of the thermal properties of charring and non-charring polymers with the specific purpose of providing input data for numerical pyrolysis models [149, 150]. The study aimed to determine whether a one-dimensional conduction/reaction model could be used as a practical tool for prediction and/or extrapolation of the results of fire calorimetry tests. The non-charring polymers included poly(methyl methacrylate) (PMMA), high-impact polystyrene (HIPS), and high density polyethylene (HDPE). The charring polymers included polycarbonate (PC) and polyvinyl chloride (PVC).

### 3.14 Fleury Heat Flux Measurements

Rob Fleury, a masters degree student at the University of Canterbury in Christchurch, New Zealand, measured the heat flux from a variety of propane fires [151]. The objective of the work was to evaluate a variety of empirical heat flux calculation methods. For the measurements, heat flux gauges were mounted on moveable dollies that were placed in front of, and to the side of, burners with dimensions of 0.3 m by 0.3 m (1:1 burner), 0.6 m by 0.3 m (2:1 burner), and 0.9 m by 0.3 m (3:1 burner). The heat release rates were set to 100 kW, 150 kW, 200 kW, 250 kW, and 300 kW. The gauges were mounted at heights of 0 m, 0.5 m, 1.0 m, and 1.5 m relative to the top edge of the burner.

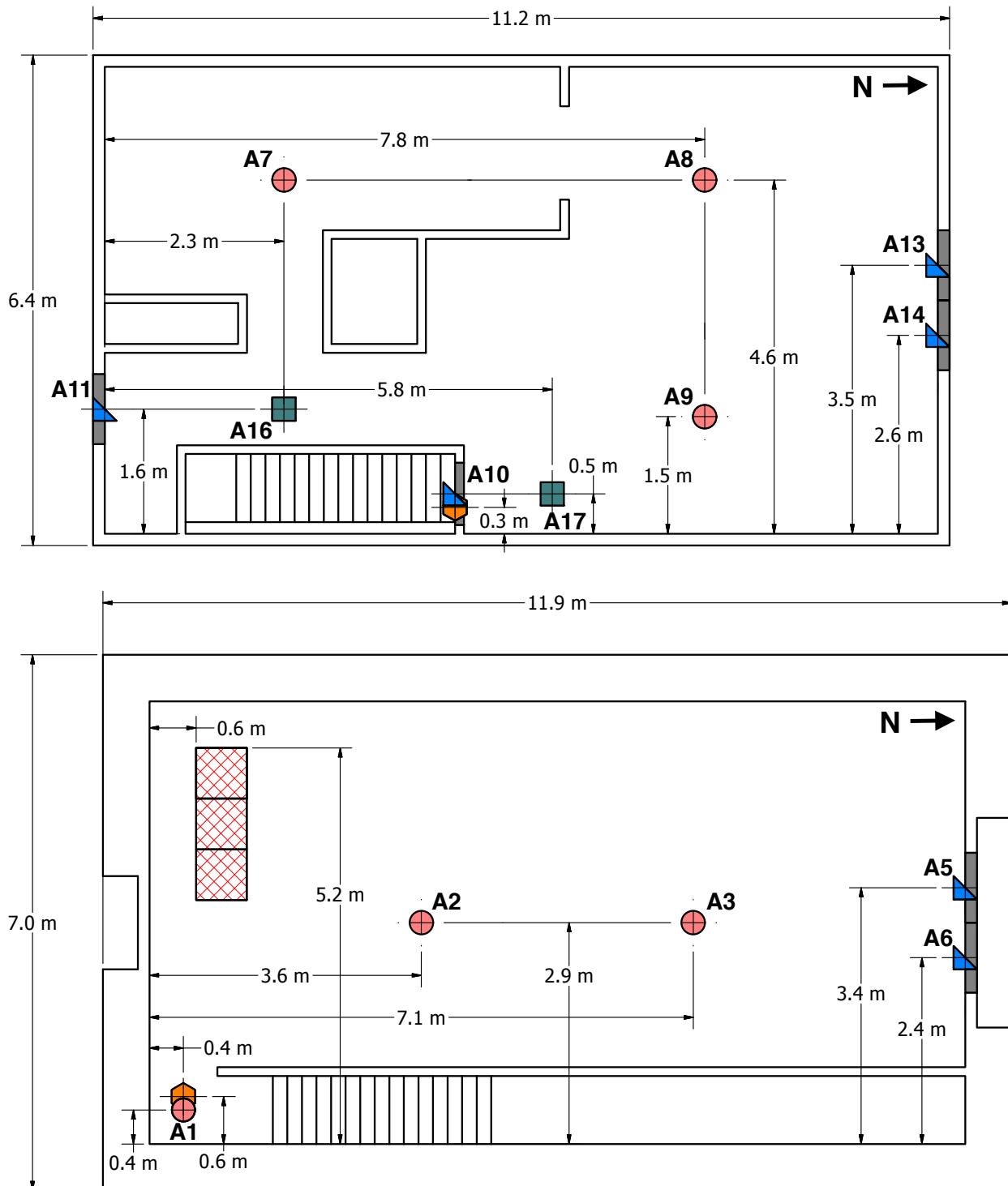


Figure 3.6: Instrumentation of the second floor (top) and first floor (bottom) of the two level DelCo training structure. The thermocouple arrays are denoted by crossed circles and the gas sampling measurement locations are denoted by hexagons at locations A1 and A10. The burner is denoted by three cross-hatched squares.

## 3.15 FM/FPRF Datacenter Experiments

The Fire Protection Research Foundation funded a series of large scale tests of smoke detection in high airflow datacenters as part of a research project on behalf of the NFPA 75 and NFPA 76 Technical Committees [152]. The tests consisted of a datacenter mockup that was 4.9 m high, 4.9 m wide, and 7.3 m deep. The mockup was divided into a 0.9 m tall subfloor with air supplied via a natural vent opening on one short wall, a 0.9 m tall ceiling plenum with air removed via a mechanical vent opening on one short wall, two 2 m tall by 0.6 m wide by 5.3 m long enclosed cold aisles located along the outer walls, and a 3.1 m tall hot aisle. Flow from the subfloor to the cold aisles occurred through grated floor tiles, flow from the cold aisles to the hot aisle was through two rows of empty equipment cabinets with perforated metal doors, and flow from the hot aisle to the ceiling plenum was through perforated metal ceiling tiles.

Two groups of tests were performed. The first group of tests used a sonic anemometer to map the flowfield in the facility for a flow of 78 air changes per hour (ACH) and 265 ACH. Additional measurements were made of the pressure drops through the floor and ceiling tiles. The second group of tests measured smoke detection response to a variety of detectors from a range of typical smoke sources plus propylene (used for its ease of characterization and repeatability).

The FDS model of the facility makes use of the screen drag model for Lagrangian particles to model the pressure losses through the various metal meshes and grates present in the mockup. The FDS model also uses the specified leakage location model to model leakage through the seams of floor and ceiling tiles. The actual leakage area was not measured during the test. Instead the area was estimated using the reduction in the FM measured pressure drop from to the manufacture's reported pressure drop to compute a leakage flow. A description of the process used to create the FDS model and the test uncertainties can be found in a companion report documenting modeling of the tests with FDS 6.0.0 [153].

## 3.16 FM Parallel Panel Experiments

Patricia Beaulieu of Worcester Polytechnic Institute made heat flux measurements within a set of vertical parallel panels as part of a cooperative research program between Worcester Polytechnic Institute and FM Global (Factory Mutual) [154]. The experimental apparatus consisted of two vertical parallel panels, 2.4 m high and 0.6 m wide, with a sand burner at the base. The objective of the project was to measure the flame spread rate over various composite wall lining materials, but there were also experiments conducted with inert walls for the purpose of measuring the heat flux from fires fueled by propane and propylene at heat release rates of 30 kW, 60 kW, and 100 kW.

## 3.17 FM/SNL Experiments

The Factory Mutual and Sandia National Laboratories (FM/SNL) test series consists of 25 compartment fire experiments conducted in 1985 for the U.S. Nuclear Regulatory Commission (NRC) by Factory Mutual Research Corporation (FMRC), under the direction of Sandia National Laboratories (SNL) [155, 156]. The primary purpose of these experiments was to provide data with which to validate computer models for various types of compartments typical of nuclear power plants. The experiments were conducted in an enclosure measuring approximately 18 m long by 12 m wide by 6 m high, constructed at the FMRC fire test facility in Rhode Island. A drawing is included in Fig. 3.7. All of the experiments included forced ventilation to simulate typical power plant conditions. Six of the experiments were conducted with a full-scale control room mock-up in place. Parameters varied during the experiments included fire intensity, enclosure ventilation rate, and fire location. Only data from nineteen experiments (Tests 1-17, 21, and 22) is used in the current study. In these experiments, the fires were fueled by a propylene gas burner, and heptane

and methanol liquid pools. In the experiments not selected, the heat release was not reported and could not be estimated with confidence. Table 3.1 lists the test parameters.

The following information was provided by the test director, Steve Nowlen of Sandia National Laboratory. In particular, Tests 4, 5, and 21 were given extra attention.

**Heat Release Rate:** The HRR was determined using oxygen consumption calorimetry in the exhaust stack with a correction applied for the carbon dioxide in the upper layer of the compartment. The uncertainty of the fuel mass flow was not documented. Several tests selected for this study had the same target peak heat release rate of 516 kW following a 4 min “t-squared” growth profile. The test report contains time histories of the measured HRR, for which the average, sustained HRR following the ramp up for Tests 4, 5, and 21 have been estimated as 510 kW, 480 kW, and 470 kW, respectively. Once reached, the peak HRR was maintained essentially constant during a steady-burn period of 6 min in Tests 4 and 5, and 16 min in Test 21. Note that in Test 21, Nowlen reports a “significant” loss of effluent from the exhaust hood that could lead to an under-estimate of the HRR towards the end of the experiment.

**Radiative Fraction:** The radiative fraction was not measured during the experiment, but in this study it is assumed to equal 0.35, which is typical for a smoky hydrocarbons. It was further assumed that the radiative fraction was about the same in Test 21 as the other tests, as fuel burning must have occurred outside of the electrical cabinet in which the burner was placed.

**Measurements:** Four types of measurements were conducted during the FM/SNL test series that are used in the current model evaluation study, including the HGL temperature and depth, and the ceiling jet and plume temperatures. Aspirated thermocouples (TCs) were used to make all of the temperature measurements. Generally, aspirated TC measurements are preferable to bare-bead TC measurements, as systematic radiative exchange measurement error is reduced.

**HGL Depth and Temperature:** Data from all of the vertical TC trees were used when reducing the HGL height and temperature. For the majority of the tests, Sectors 1, 2, and 3 were used, all weighted evenly. For Tests 21 and 22, Sectors 1 and 3 were used, evenly weighted. Sector 2 was partially within the fire plume.

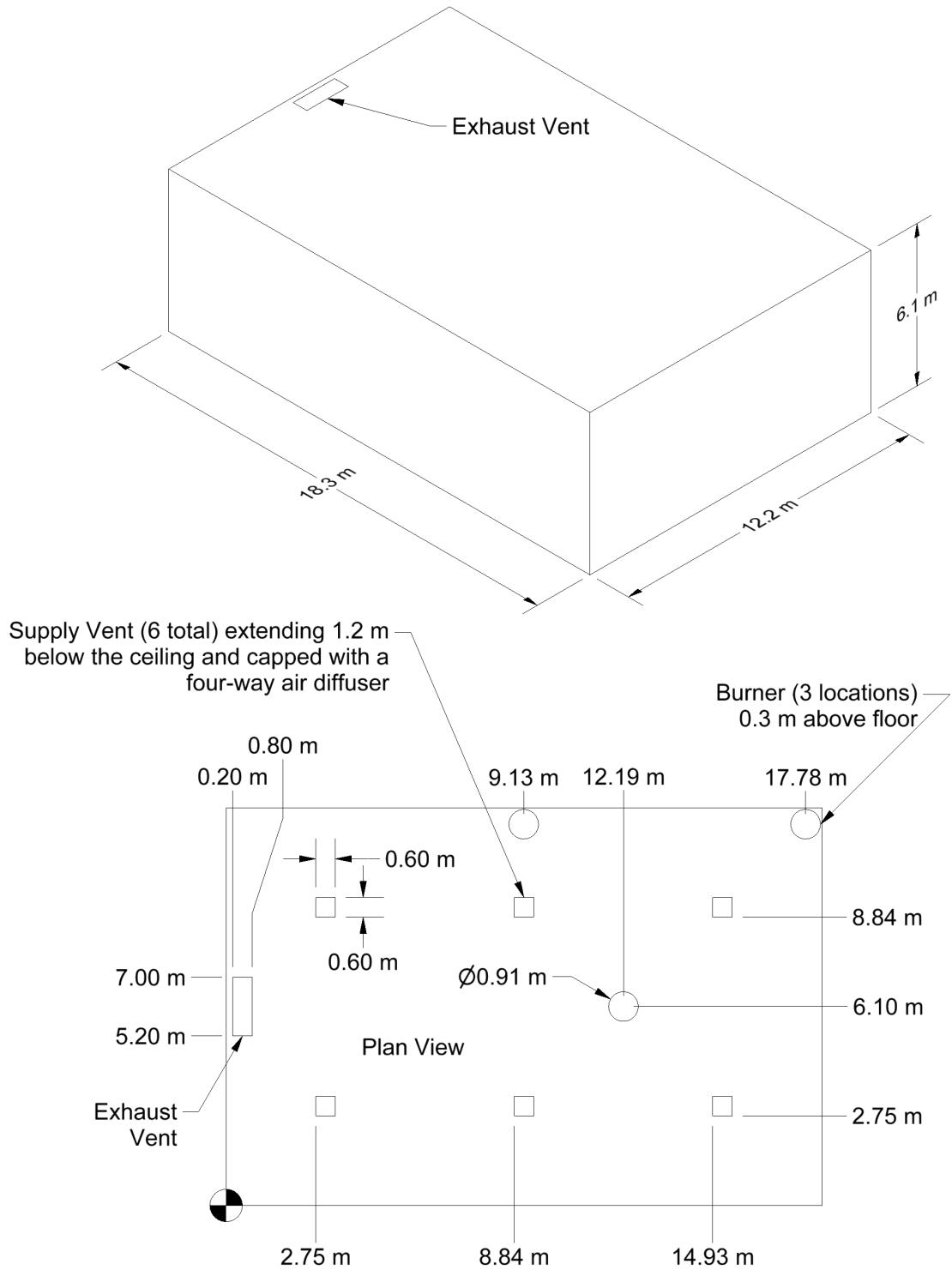


Table 3.1: Summary of FM/SNL Experiments. ACH stands for Air Changes per Hour.

Test No.	Fuel Type	Nominal Peak HRR (kW)	Fire Position	Ventilation Rate (ACH)	Room Configuration
1	Propylene Burner	516	Center	10	Empty
2	Propylene Burner	516	Center	10	Empty
3	Propylene Burner	2000	Center	10	Empty
4	Propylene Burner	516	Center	1	Empty
5	Propylene Burner	516	Center	10	Empty
6	Heptane Pool	500	Wall	1	Empty
7	Propylene Burner	516	Center	1	Empty
8	Propylene Burner	1000	Center	1	Empty
9	Propylene Burner	1000	Center	8	Empty
10	Heptane Pool	1000	Wall	4.4	Empty
11	Methanol Pool	500	Wall	4.4	Empty
12	Heptane Pool	2000	Wall	4.4	Empty
13	Heptane Pool	2000	Wall	8	Empty
14	Methanol Pool	500	Wall	1	Empty
15	Heptane Pool	1000	Wall	1	Empty
16	Heptane Pool	500	Corner	1	Empty
17	Heptane Pool	500	Corner	10	Empty
21	Propylene Burner	500	Cabinet	1	Furnished
22	Propylene Burner	1000	Cabinet	1	Furnished

## 3.18 Hamins Gas Burner Experiments

Anthony Hamins of NIST measured the heat flux at various points around gas burner fires [36]. Three different sized circular burners were used, with diameters of 0.10 m, 0.38 m, and 1.0 m. Three different gases were used, acetylene, methane, and propane. The heat release rates ranged from 2 kW to 200 kW, and values of  $\dot{Q}^*$  ranged from 0.04 to 10.6.

## 3.19 Harrison Spill Plumes

Roger Harrison, a student at the University of Canterbury, New Zealand, performed a series of one-tenth scale experiments to characterize thermal spill plume entrainment [157, 158, 159, 160]. The dimensions of the fire compartment were 1 m by 1 m by 0.5 m high. The height of the compartment opening was equal to the height of the compartment. The width of the opening was varied from 0.2 m to 1 m. A 0.3 m balcony was attached to the top of the compartment opening. The balcony extended 0.5 m beyond each side of the fire compartment. The heat release rate of the fire varied from 5 kW to 15 kW. The plume entrainment rate was measured at different heights by varying the exhaust rate of gases from a hood above the compartment. Two different test configurations were used to model both detached and adhered spill plumes. A diagram of the test structure is displayed in Figure 3.8.

## 3.20 Heskestad Flame Height Correlation

A widely used experimental correlation for flame height is given by the expression [161, 25]:

$$\frac{L_f}{D} = 3.7 (\dot{Q}^*)^{2/5} - 1.02 \quad ; \quad \dot{Q}^* = \frac{\dot{Q}}{\rho_\infty c_p T_\infty \sqrt{g} D^{5/2}} \quad (3.1)$$

where  $\rho_\infty$ ,  $c_p$ , and  $T_\infty$  are the ambient density, specific heat, and temperature.  $\dot{Q}^*$  is a non-dimensional quantity that relates the fire's heat release rate,  $\dot{Q}$ , with the diameter of its base,  $D$ . The greater the value of  $\dot{Q}^*$ , the higher the flame height relative to its base diameter.

## 3.21 LEMTA Spray Test for Radiation Attenuation

Lechene et al. [162] measured the attenuation of thermal radiation passing through a water spray using a heat flux gauge. The radiation was produced by a 30 cm by 35 cm heat panel whose emission was close to a black body at 500 °C. The horizontal distance from the radiation panel to the spray nozzle was 1.5 m and to the measurement point 3 m. The heat flux gauge was positioned at the line passing through the center of the panel. Seven nozzles were arranged in a row, 10 cm apart. They were positioned 1.5 m high. The heat panel was translated vertically during the experiment, the distance between the panel upper edge and the nozzle row varying between 20 cm and 100 cm. The attenuation of radiation is defined as previously described for the BRE Spray experiments. The purpose of the simulations is to compare the measured and simulated attenuation of radiation at different heights. The water mist nozzle has been characterized by Lechene by measuring the spray angles and the water flow rate. The droplet size is set by using a PDPA measurement in a single position, 20 cm below the injection point.

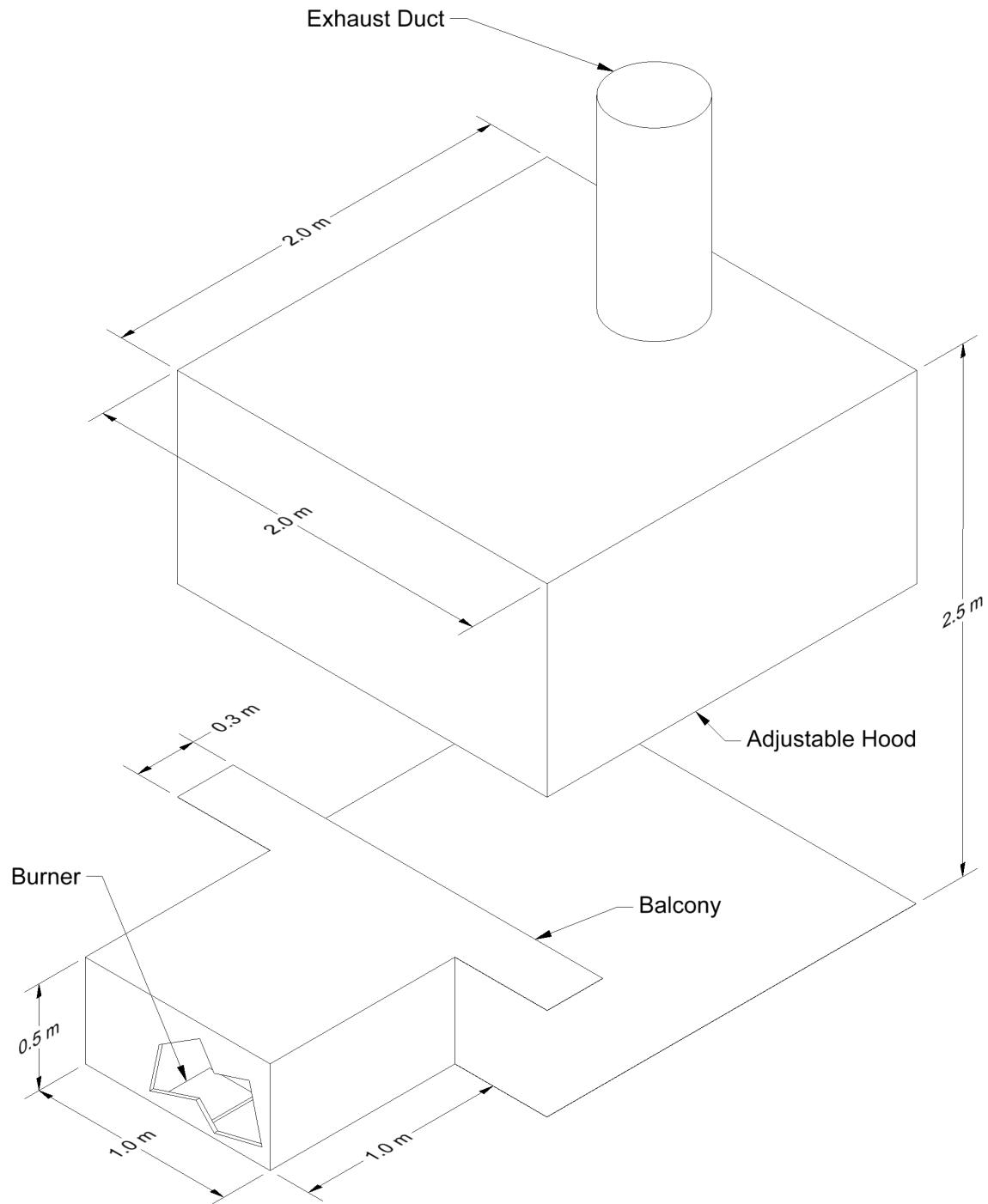


Figure 3.8: Geometry of the Harrison Spill Plumes Experiments.

## 3.22 LLNL Enclosure Experiments

Sixty-four tests were conducted by Lawrence Livermore National Laboratory (LLNL) in 1986 to study the effects of ventilation on enclosure fires [163]. The test enclosure was 6 m long, 4 m wide, and 4.5 m high (Fig. 3.9). It contained a methane rock burner which was placed in the center of the space. For most of the tests the burner was placed on the floor. The fires varied in size from 50 kW to 400 kW. The burner was 0.57 m in diameter and 0.23 m height. The door was closed and sealed for most tests, and air was pulled through the space at rates varying from 100 g/s to 500 g/s. In some tests the enclosure included a plenum space, where make-up air could be injected from above or below. The test matrix is listed in Table 3.2.

## 3.23 LNG Dispersion Experiments

In 2006, the Fire Protection Research Foundation (FPRF) undertook a research project for the National Fire Protection Association (NFPA) Liquefied Natural Gas (LNG) Technical Committee to develop tools for evaluating LNG dispersion models. The work was carried out by the Health and Safety Laboratory (HSL), a directorate of the UK Health and Safety Executive (HSE). HSL developed the LNG Model Evaluation Protocol (MEP), which contained a structure for complete evaluation of LNG dispersion models [164]. The experiments are described in Ref. [165].

## 3.24 McCaffrey Plume Experiments

In 1979, at the National Bureau of Standards (now NIST), Bernard McCaffrey measured centerline temperature and velocity profiles above a porous, refractory burner. There were five distinct heat release rates, ranging from 14 kW to 57 kW. The fuel was natural gas. The burner was square, 0.3 m on each side. The results of the experiments are reported in Reference [166].

## 3.25 NBS Multi-Room Experiments

The National Bureau of Standards (NBS, which is now called the National Institute of Standards and Technology, NIST) Multi-Room Experiments consisted of 45 fire tests representing 9 different sets of conditions were conducted in a three-room suite (see Fig. 3.10). The experiments were conducted in 1985 and are described in detail in Ref. [167]. The suite consisted of two relatively small rooms, connected via a relatively long corridor. The fire source, a gas burner, was located against the rear wall of one of the small compartments. Fire tests of 100 kW, 300 kW and 500 kW were conducted. For the current study, only three 100 kW fire experiments have been used, including Test 100A from Set 1, Test 100O from Set 2, and Test 100Z from Set 4. These tests were selected because they had been used in prior validation studies, and because these tests had the steadiest values of measured heat release rate during the steady-burn period.

Following is additional information provided by the test director, Richard Peacock of NIST:

**Heat Release Rate:** In the two tests for which the door was open, the HRR during the steady-burn period measured via oxygen consumption calorimetry was 110 kW with an uncertainty of about 15 %, consistent with the replicate measurements made during the experimental series and the uncertainty typical of oxygen consumption calorimetry. It was assumed that the closed door test (Test 100O) had the same HRR as the open door tests.

Table 3.2: Summary of LLNL Enclosure Experiments.

Test No.	Room Config.	$h_0$ m	$\dot{Q}$ kW	$\dot{m}$ g/s	$T_\infty$ °C	Test No.	Room Config.	$h_0$ m	$\dot{Q}$ kW	$\dot{m}$ g/s	$T_\infty$ °C
1	TL	0	200	0	23	33	PH	0	100	200	23
2	TL	0	200	0	27	34	PH	0	100	300	34
3	TL	0	400	0	27	35	PH	0	100	400	22
4	TL	0	300	0	24	36	PH	0	100	500	29
5	TL	0	50	0	28	37	PH	0	200	100	20
6	TL	0	100	0	29	38	PH	0	200	300	29
7	TL	0	100	0	35	39	PH	0	250	100	18
8	TL	0	200	0	35	40	PH	0	200	400	28
9	TL	0	200	500	33	41	PH	0	150	100	20
10	TL	0	200	100	28	42	PHE	2	200	180	30
11	TL	0	200	200	18	43	PHE	2	200	0	32
12	TL	0	200	300	21	44	PHE	1	200	180	19
13	TL	0	200	400	28	45	PHE	1	200	0	30
14	TL	0	200	400	28	46	PHE	0.6	200	180	19
15	TL	0	100	300	24	47	PHE	0.6	200	0	19
16	TL	0	200	300	21	48	PHE	0.3	200	0	21
17	PL	0	200	500	26	49	PHE	0.3	200	180	26
18	PL	0	200	400	21	50	PHE	1	200	180	21
19	PL	0	200	300	18	51	PNE	1	200	NAT	33
20	PL	0	200	200	16	52	PN	0	200	NAT	23
21	PL	0	200	100	23	53	PHGS	0	200	185	33
22	PH	0	200	190	30	54	PHGS	0	200	215	21
23	PH	0	200	215	28	55	PN	0	100	NAT	31
24	PH	0	200	205	26	56	PHGW	0	200	190	20
25	PH	0	200	205	25	57	PHGW	0	200	215	29
26	PH	0	200	500	24	58	PHX	0	200	190	18
27	PH	0	200	100	23	59	PHXE	1	200	190	24
28	PH	0	150	150	31	60	PN	0	400	NAT	22
29	PH	0	250	250	28	61	TN	0	200	NAT	31
30	PH	0	250	300	34	62	TN	0	400	NAT	22
31	PH	0	250	500	36	63	TN	0	50	NAT	28
32	PH	0	100	100	33	64	TN	0	100	NAT	17

T full compartment  
 P plenum configuration  
 L low inlet duct  
 H high inlet duct  
 E elevated fire,  $h_0$

N natural ventilation (door open)  
 X 3 ft extension on inlet opening  
 GS grate on inlet, north/south configuration  
 GW grate on inlet, east/west configuration

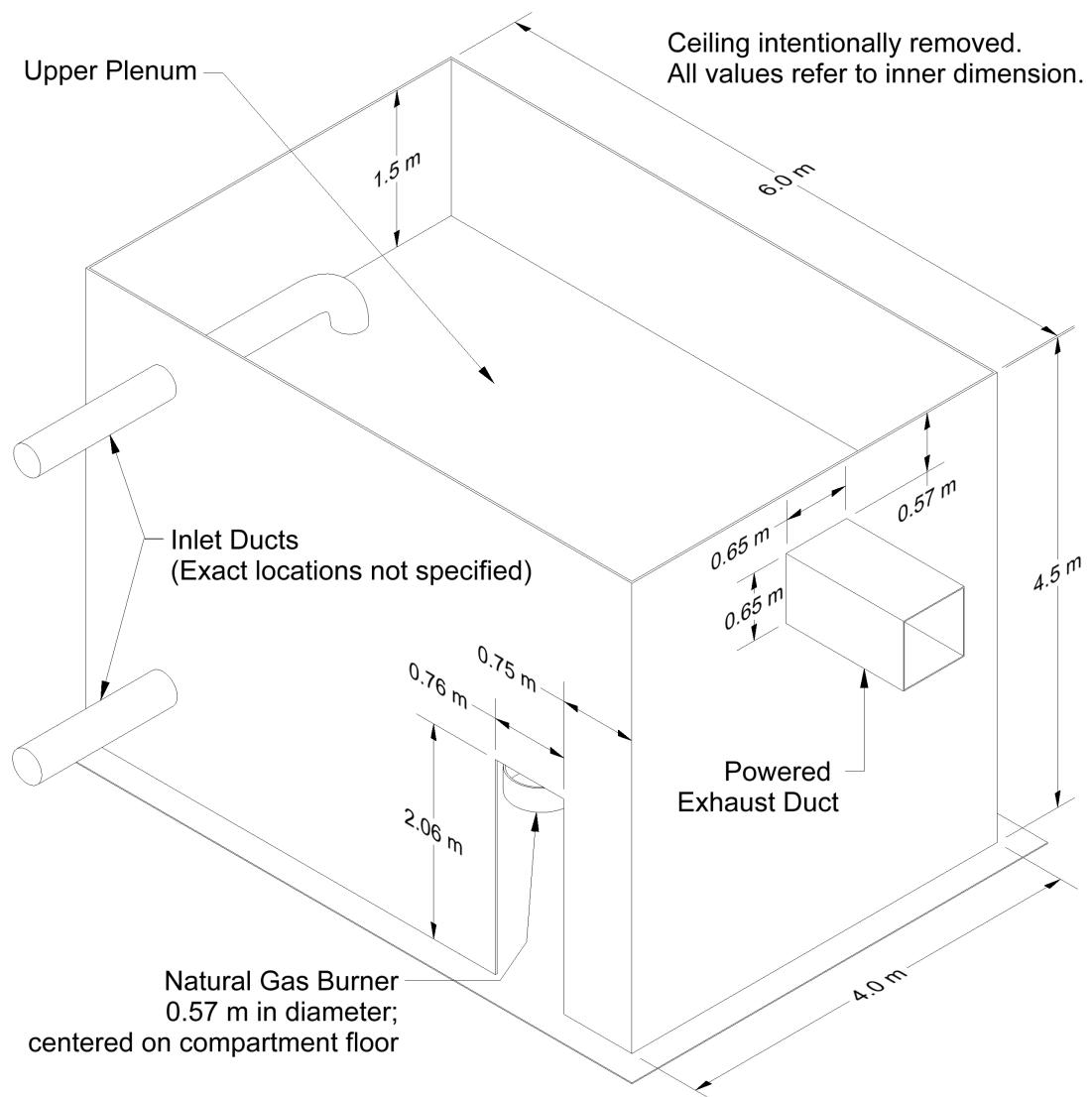


Figure 3.9: Geometry of the LLNL Enclosure Experiments.

**Radiative Fraction:** Natural gas was used as the fuel in Test 100A. In Tests 100O and 100Z, acetylene was added to the natural gas to increase the smoke yield, and as a consequence, the radiative fraction increased. The radiative fraction of natural gas has been studied previously, whereas the radiative fraction of the acetylene/natural gas mixture has not been studied. The radiative fraction for the natural gas fire was assigned a value of 0.20, whereas a value of 0.30 was assigned for the natural gas/acetylene fires.

**Measurements:** Only two types of measurements conducted during the NBS test series were used in the evaluation considered here, because there was less confidence in the other measurements. The measurements considered here were the HGL temperature and depth, in which bare bead TCs were used to make these measurements. Single point measurements of temperature within the burn room were not used in the evaluation of plume or ceiling jet algorithms. This is because the geometry was not consistent in either case with the assumptions used in the model algorithms of plumes or jets. Specifically, the burner was mounted against a wall, and the room width-to-height ratio was less than that assumed by the various ceiling jet correlations.

## 3.26 NIST Douglas Firs

In 2009, Mell et al. measured the burning rate of individual Douglas fir trees of various sizes and moisture contents [168]. Nine of the trees were approximately 2 m tall, and three were approximately 5 m tall. The results were presented as averages: the three 5 m trees had an average moisture content of 26 %, three of the 2 m trees had an average moisture content of 49 %, and the remaining six 2 m trees had a moisture content of 14 %. The 2 m trees were ignited with a natural gas ring burner with a diameter of 80 cm and a heat release rate of 30 kW. The trees with a moisture content of 14 % were exposed to the burner for 10 s and the 49 % trees were exposed for 30 s. The 5 m trees were exposed to a hexagonal burner with a span of 122 cm and HRR of 130 kW for 30 s.

## 3.27 NIST Enclosure Experiments

A variety of reduced-scale and full-scale compartment fire experiments have been performed at NIST over the past few decades. The main objective of each series is to measure the concentrations of oxygen, carbon dioxide, carbon monoxide, soot, and unburned hydrocarbons in an under-ventilated compartment. These data sets also provide extreme temperature and heat flux measurements.

### 3.27.1 NIST Reduced Scale Enclosure Experiments, 1994

The NIST Reduced Scale Enclosure (RSE) is a 40 % scale version of the ISO 9705 compartment [169]. It measures 0.98 m wide by 1.46 m deep by 0.98 m tall. The compartment contains a door centered on the smaller wall that measures 0.48 m wide by 0.81 m tall. A 15 cm diameter natural gas burner was positioned in the center of the compartment. The burner was on a stand so that its top was 15 cm above the floor. The fires ranged from 50 kW to 600 kW. Species measurements, including CO concentration, were made near the ceiling in the front and back of the compartment.

### 3.27.2 NIST Reduced Scale Enclosure Experiments, 2007

Another set of reduced-scale compartment experiments was conducted in 2007 at NIST [170]. The compartment was similar in dimension: 0.95 m wide by 1.42 m deep by 0.98 m tall with the exact same door

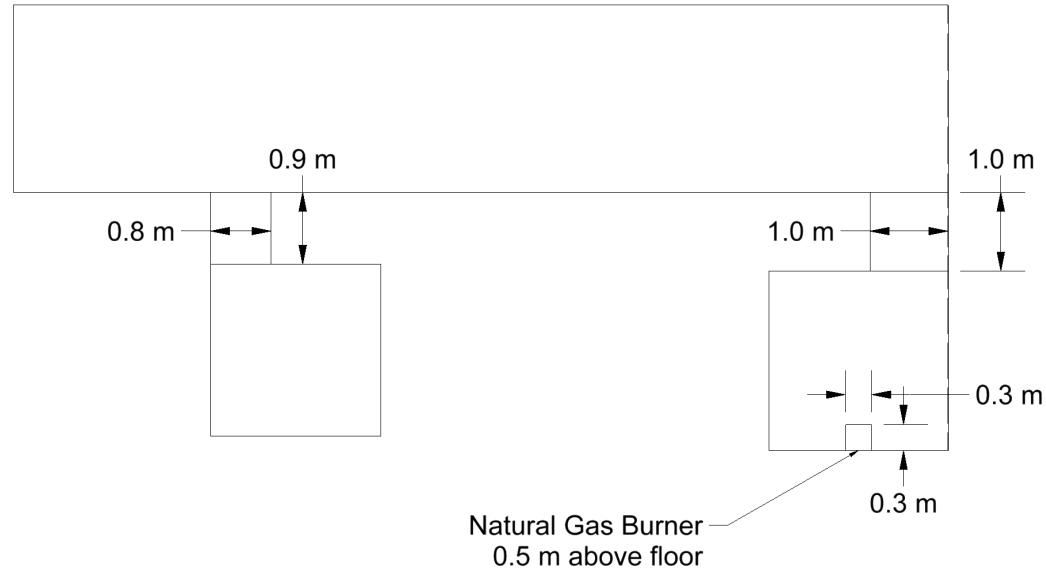
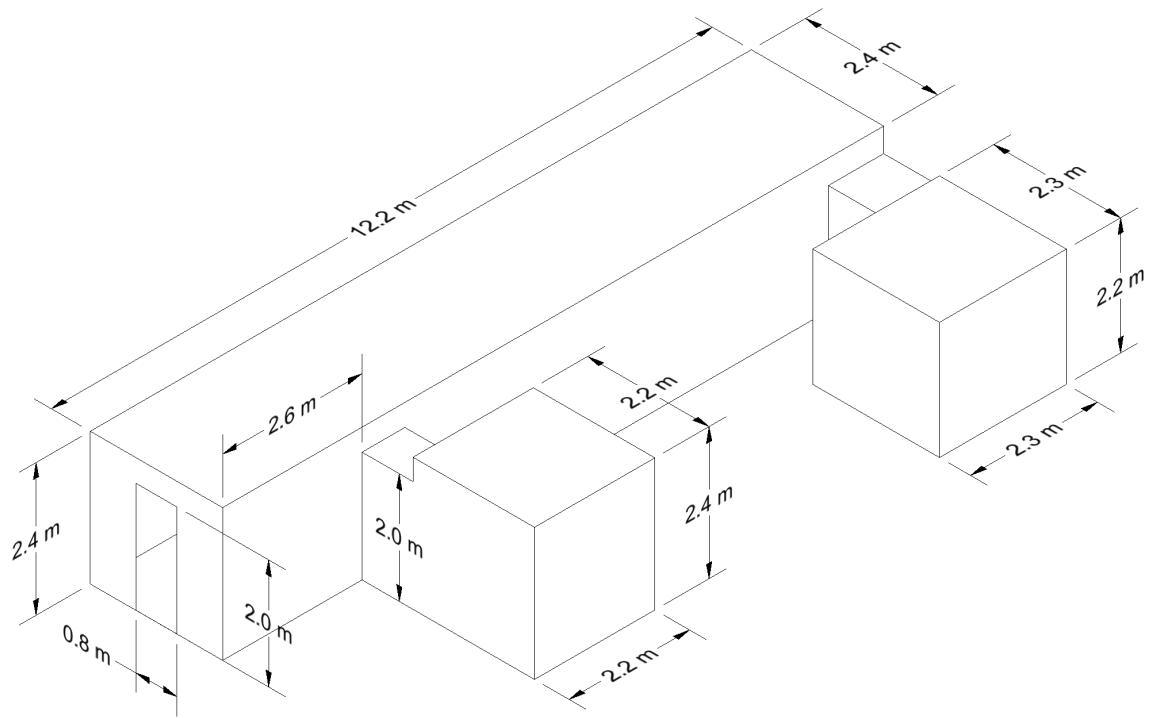


Figure 3.10: Geometry of the NBS Multi-Room Experiments.

dimensions. Four different burner types were used: a 13 cm square sand burner, a 25 cm square liquid fuel burner, a spray nozzle into 0.4 m diameter circular pan, and a 60 cm diameter circular pan. Six different fuels were used: natural gas; heptane, methanol, ethanol and toluene liquids; and solid polystyrene beads. The fires ranged from 15 kW to 425 kW, but only fires greater than 190 kW were used for comparison because the smaller fires produced no significant CO. Measurements of O<sub>2</sub>, CO<sub>2</sub>, CO, soot, and unburned hydrocarbon concentration were made near the ceiling in the front and back of the compartment.

Table 3.3: Summary of NIST Reduced-Scale Experiments, 2007.

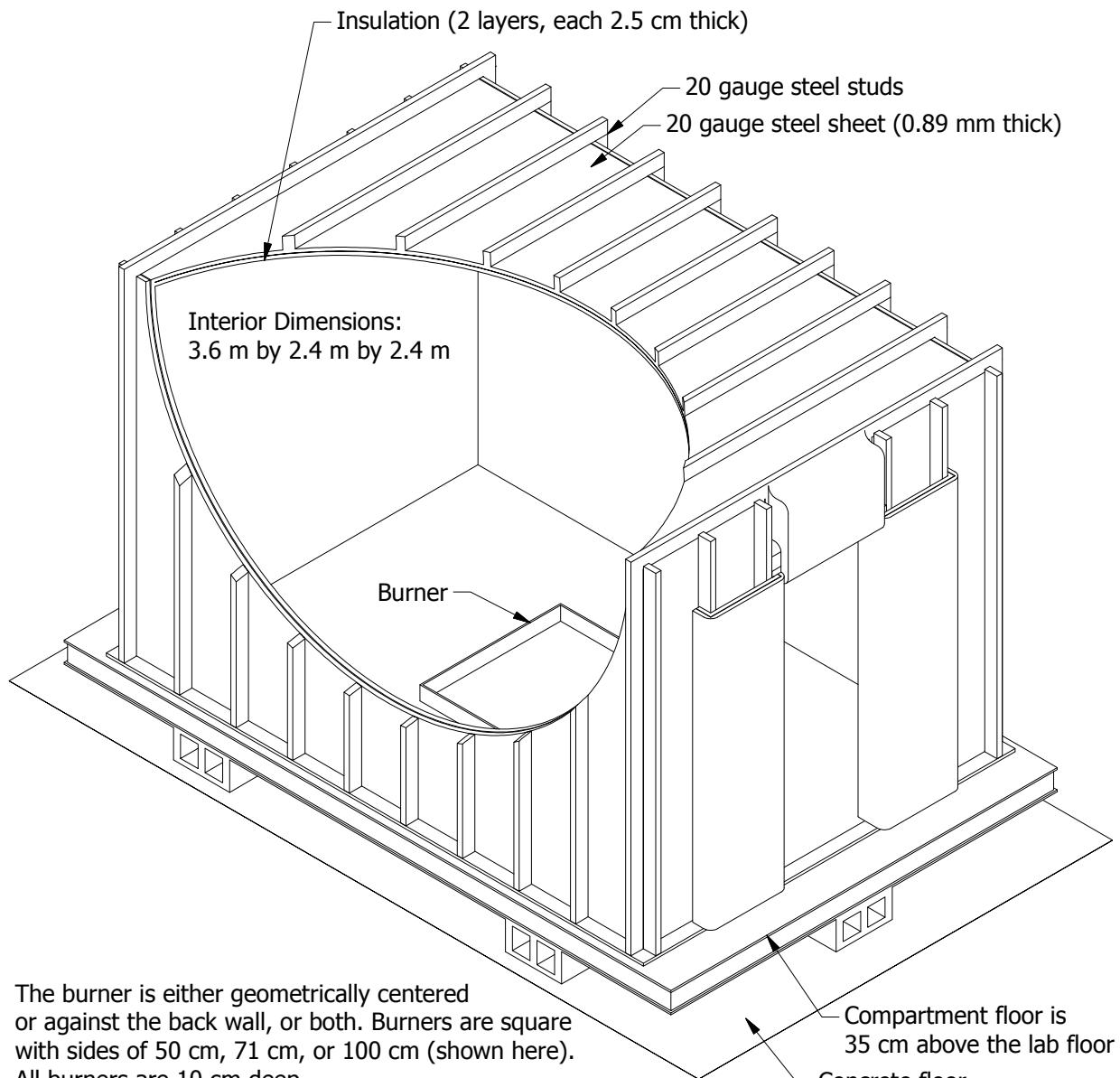
Test Number	Fuel Type	Peak HRR (kW)	Burner Size (m <sup>2</sup> )	Doorway Opening (cm)
1	Natural Gas	190	0.017	48
2	Natural Gas	395	0.017	48
3	Natural Gas	410	0.017	48
4	Heptane	375	0.063	48
5	Heptane	220	0.063	24
6	Natural Gas	420	0.063	24
7	Heptane	340	0.063	48
10	Toluene	340	0.063	48
11	Ethanol	335	0.126	48
12	Methanol	305	0.126	48
15	Heptane	375	0.126	48
16	Polystyrene	360	0.283	48

### 3.27.3 NIST Full-Scale Enclosure Experiments, 2008

The NIST FSE (2008) Experiments were conducted in an ISO 9705 compartment [171]. The compartment was 2.4 m wide by 3.6 m long by 2.4 m high with a 2 m high door at one end (Fig. 3.11). The door width varied between 0.1 m and 0.8 m. The experiments were designed to study the effects of fuel type, fuel distribution, and vent size on under-ventilated compartment fires. Thirty experiments were conducted, which included 7 different fuels, 3 fuel sources, and 4 ventilation openings. Table 3.4 provides a summary of the experiments. Species concentrations and temperature measurements were made at the front and rear of the compartment.

## 3.28 NIST Helium Experiments

Eighteen experiments were conducted at NIST in which helium was released over a lengthy time period inside of a 1.5 m by 1.5 m by 0.75 m plexiglass box with one or two small leakage holes [172]. The experiments were intended to represent the release of hydrogen from passenger vehicle fuel cell inside of a residential garage. Test parameters included the release rate and length, the location of the release, and the size and location of the leakage. Measurements were made of the helium concentration in a rake at seven locations over the height of the compartment during the release and for a period of up to 11 hours post-release.



The door is 2 m tall, with widths of 80 cm (shown), 40 cm, 20 cm, or 10 cm.

Figure 3.11: Geometry of the compartment used in the NIST Full-Scale Enclosure (FSE) experiments.

Table 3.4: Summary of NIST FSE Experiments selected for model validation.

Test Name	Fuel Type	Fuel Mass (kg)	No. of Burners	Burner Size (m <sup>2</sup> )	Doorway Opening (cm)
ISONG3	Natural Gas		1	1.0	80
ISOHept4	Heptane	Pool Fed	1	1.0	80
ISOHept5	Heptane	Pool Fed	1	1.0	40
ISOHept8	Heptane	10	1	0.5	20
ISOHept9	Heptane	20	1	0.5	20
ISONylon10	Nylon	10	1	0.5	20
ISOPP11	Propylene	10	1	0.5	20
ISOHeptD12	Heptane	20	2	0.25	20
ISOHeptD13	Heptane	20	2	0.25	20
ISOPropD14	Propanol	24	2	0.25	20
ISOProp15	Propanol	24	1	0.5	20
ISOStyrene16	Styrene	10	1	0.5	20
ISOStyrene17	Styrene	30	1	1.0	20
ISOPP18	Propylene	20	2	0.5	20
ISOHept19	Heptane	20	1	0.5	20
ISOToluene20	Toluene	17	1	0.5	20
ISOStyrene21	Styrene	15	1	0.5	20
ISOHept22	Heptane	Spray	1	0.5	20
ISOHept23	Heptane	Spray	1	0.5	10
ISOHept24	Heptane	Spray	1	0.5	10
ISOHept25	Heptane	Spray	1	0.5	40
ISOHept26	Heptane	Spray	1	0.5	40
ISOHept27	Heptane	Spray	1	0.5	10
ISOHept28	Heptane	Spray	1	0.5	20
ISOToluene29	Toluene	Spray	1	0.5	20
ISOPropanol30	Propanol	Spray	1	0.5	20
ISONG32	Natural Gas		1	0.28	20

Test variables included all permutations of the leak rate and time (14.8 L/min over 3600 s or 3.71 L/min over 14400 s), leak location (on the floor at the center of the compartment, on the floor at the center of the rear wall, and 2.5 cm below the ceiling at the center of the compartment), and the leak area (2.4 cm by 2.4 cm at the center of the front wall, 3.05 cm by 3.05 cm at the center of the front wall, and a pair of 2.15 cm by 2.15 cm centered on the front wall 2.5 cm from the floor and ceiling).

Leakage areas were square holes under 10 cm<sup>2</sup> in area. Attempting to resolve flows through these holes would have required very small grid cells in the vicinity of the holes. Instead, the FDS HVAC model was used. For each leakage hole a pair of HVAC ducts was defined over a height of two grid cells (one grid cell height for each vent). Each duct was assigned one-half the leakage area and the experimentally determined orifice flow coefficient. This approach enabled bi-directional flow to occur at the leakage vent as occurred during each test following the termination of the helium release.

### 3.29 NIST/NRC Compartment Experiments

These experiments, sponsored by the US NRC and conducted at NIST, consisted of 15 large-scale experiments performed in June 2003. All 15 tests were included in the validation study. The experiments are documented in Ref. [115]. The fire sizes ranged from 350 kW to 2.2 MW in a compartment with dimensions 21.7 m by 7.1 m by 3.8 m high, designed to represent a compartment in a nuclear power plant containing power and control cables. A diagram of the test structure is displayed in Figure 3.12.

The walls and ceiling were covered with two layers of marinate boards, each layer 0.0125 m thick. The floor was covered with one layer of gypsum board on top of a layer of plywood. Thermo-physical and optical properties of the marinate and other materials used in the compartment are given in Ref. [115]. The room had one door and a mechanical air injection and extraction system. Ventilation conditions, the fire size, and fire location were varied. Numerous measurements (approximately 350 per test) were made including gas and surface temperatures, heat fluxes and gas velocities.

Following are some notes provided by Anthony Hamins, who conducted the experiments:

**Natural Ventilation:** The compartment had a 2 m by 2 m door in the middle of the west wall. Some of the tests had a closed door and no mechanical ventilation (Tests 2, 7, 8, 13, and 17), and in those tests the measured compartment leakage was an important consideration. The test report lists leakage areas based on measurements performed prior to Tests 1, 2, 7, 8, and 13. For the closed door tests, the leakage area used in the simulations was based on the last available measurement. The chronological order of the tests differed from the numerical order. For Test 4, the leakage area measured before Test 2 was used. For Tests 10 and 16, the leakage area measured before Test 7 was used.

**Mechanical Ventilation:** The mechanical ventilation and exhaust was used during Tests 4, 5, 10, and 16, providing about 5 air changes per hour. The door was closed during Test 4 and open during Tests 5, 10, and 16. The supply duct was positioned on the south wall, about 2 m off the floor. An exhaust duct of equal area to the supply duct was positioned on the opposite wall at a comparable location. The flow rates through the supply and exhaust ducts were measured in detail during breaks in the testing, in the absence of a fire. During the tests, the flows were monitored with single bi-directional probes during the tests themselves.

**Heat Release Rate:** A single nozzle was used to spray liquid hydrocarbon fuels onto a 1 m by 2 m fire pan that was about 0.1 m deep. The test plan originally called for the use of two nozzles to provide the fuel spray. Experimental observation suggested that the fire was less unsteady with the use of a single nozzle. In addition, it was observed that the actual extent of the liquid pool was well-approximated by a 1 m circle in the center of the pan. For safety reasons, the fuel flow was terminated when the lower-layer

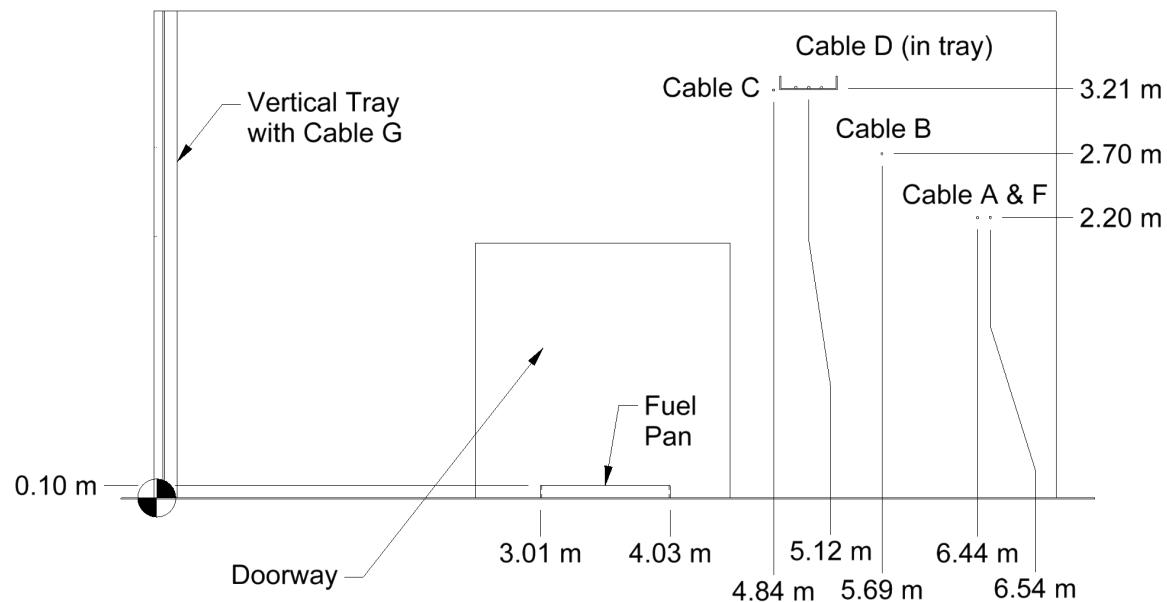
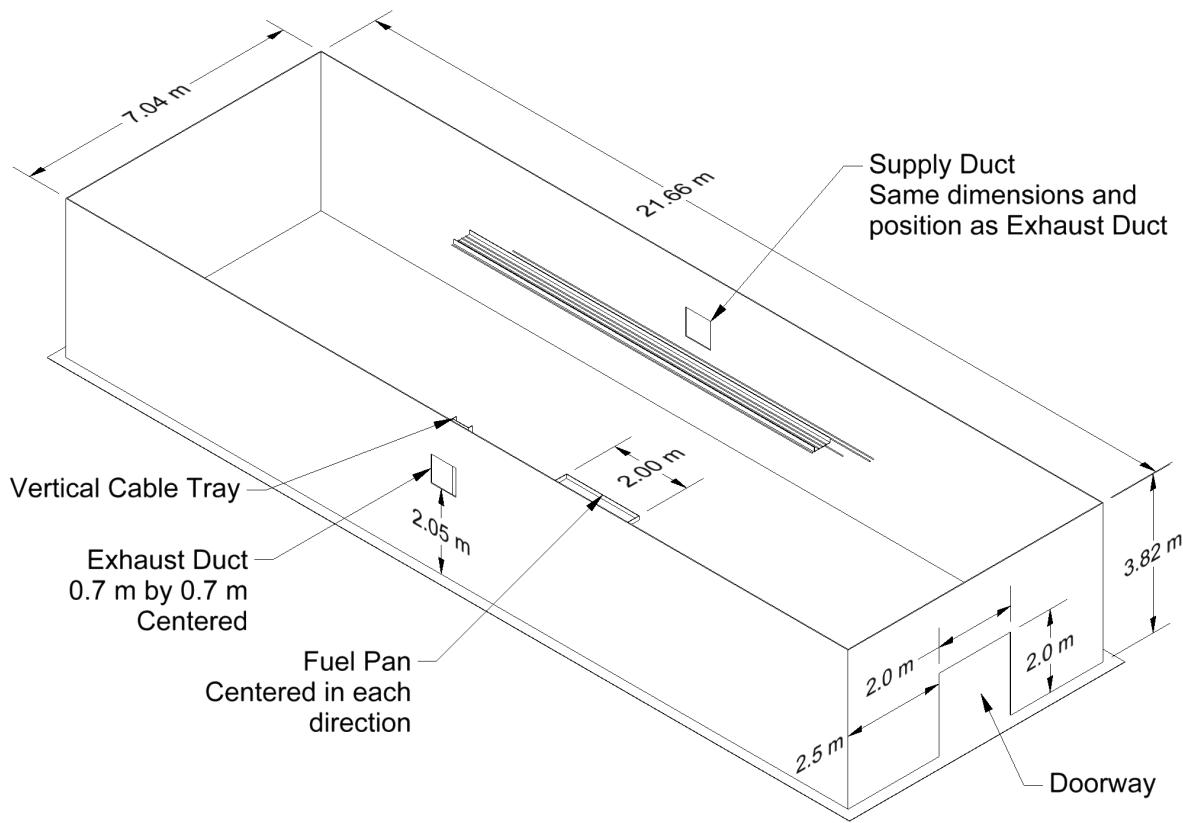


Figure 3.12: Geometry of the NIST/NRC Experiments.

oxygen concentration dropped to approximately 15 % by volume. The fuel used in 14 of the tests was heptane, while toluene was used for one test. The HRR was determined using oxygen consumption calorimetry. The recommended uncertainty values were 17 % for all of the tests.

**Radiative Fraction:** The values of radiative fraction and its uncertainty were reported as  $0.44 \pm 0.07$  and  $0.40 \pm 0.09$  for heptane and toluene, respectively.

**Soot Yield:** The values of the soot yield and its uncertainty were reported as  $0.0149 \text{ kg/kg} \pm 0.0033 \text{ kg/kg}$  and  $0.195 \text{ kg/kg} \pm 0.052 \text{ kg/kg}$  for heptane and toluene, respectively.

### 3.30 NIST Smoke Alarm Experiments

A series of experiments was conducted by NIST to measure the activation time of ionization and photoelectric smoke alarms in a residential setting [173]. Tests were conducted in actual homes with representative sizes and floor plans, utilized actual furnishings and household items for fire sources, and tested actual smoke alarms sold in retail stores at that time. Thirty-six tests were conducted in two homes; 27 in a single-story manufactured home, and 8 in a two-story home. Eight experiments that were conducted in the single-story manufactured home were selected for model validation. Only tests that used a flaming ignition source with a couch or mattress fuel package were considered; the cooking oil fires and tests that used a smoldering ignition source were not considered. The flaming ignition tests used a moderate flame source to quickly ignite the fuel package.

The primary partitioning of the single-story floor plan consisted of three bedrooms, one full bathroom, one kitchen/dining area, one living room, and two hallways (see Fig. 3.13). For testing, the doors to Bedroom 3 and the bathroom were always closed. The ceiling was peaked on the long axis, reaching a height of 2.4 m. The outside walls were approximately 2.1 m in height. The slope of the ceiling was approximately  $8.4^\circ$ . Groups of smoke alarms were located in the room of fire origin, at least one bedroom, and in a central location. Five stations (Station A through Station E) containing smoke alarm<sup>1</sup> arrays were mounted parallel to the ceiling.

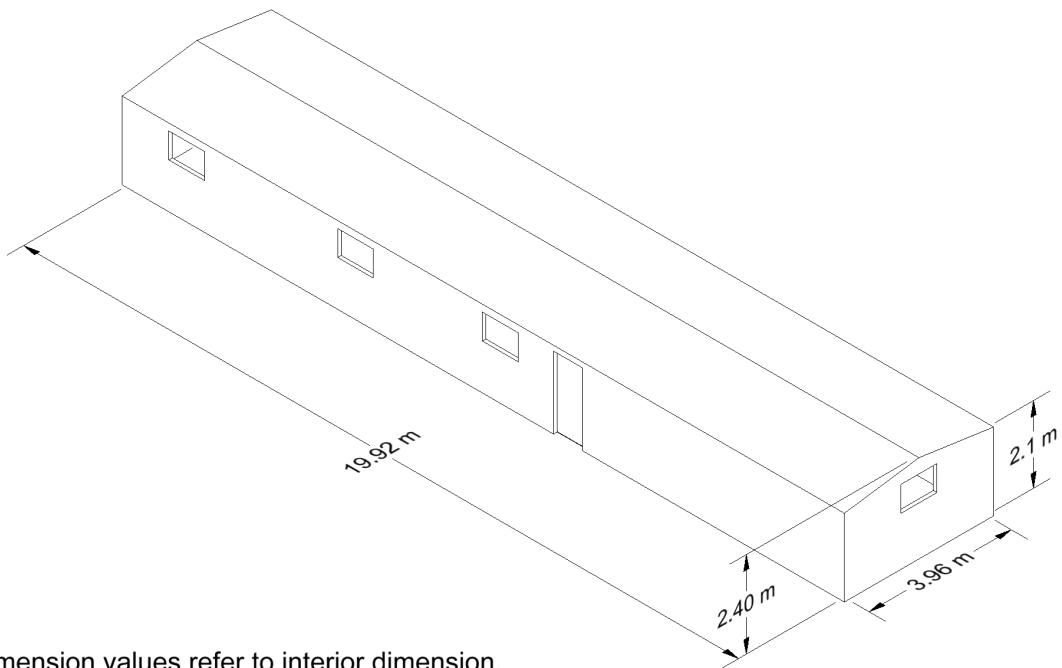
Although a load cell was used in the experiments to measure the mass loss rate of the fuel package, the mass loss data were not reliable enough to reconstruct the HRR curves for each test. Instead, the HRR curves were determined by approximating the fire growth using a  $t$ -squared ramp, as in Eq. (3.2). The parameters for the  $t$ -squared ramp were calibrated in FDS by using the temperature measured at the highest thermocouple in the tree (2 cm below the ceiling) in the fire room.

$$\dot{Q} = \dot{Q}_0 \left( \frac{t}{\tau} \right)^2 \quad (3.2)$$

A time offset was used to align the predicted ceiling thermocouple temperatures with the measured temperatures. This offset is reported as the time at which the  $t$ -squared ramp begins. The  $t$ -squared calibration parameters and time offsets for the HRR ramps are shown in Table 3.5. Additionally, the ignition source had a small effect on the measured ceiling thermocouple temperatures. Therefore, the size of the ignition source was approximated as either 3 kW or 7 kW, and the time offset of the ignition source was also calibrated by using the measured ceiling thermocouple temperatures. The resulting HRR curve was input into FDS as a fire ramp. A summary of the eight tests selected for model validation is shown in Table 3.5.

---

<sup>1</sup>Note that, in the FDS Guides, smoke detectors and smoke alarms are collectively referred to as smoke detectors because the same smoke detection algorithm is used to predict activation of either type of device.



**Notes:**

1. All dimension values refer to interior dimension.
2. The letters A-E refer to detector locations.
3. All walls are 10 cm thick.
4. All exterior doors and windows were closed during testing.
5. Doors to Bath and Bedroom #3 closed during testing.

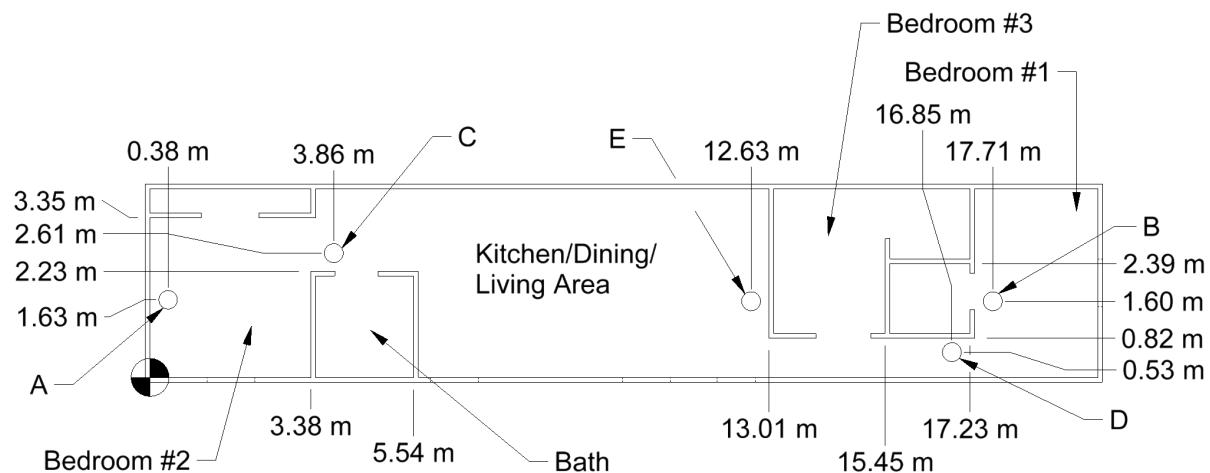


Figure 3.13: Geometry of the manufactured home from the NIST Smoke Alarm Experiments.

Table 3.5: Summary of NIST Smoke Alarm Experiments selected for model validation.

Test No.	Fire Source	Fire Location	$\dot{Q}_0$ (kW)	$\tau$ (s)	Time Offset (s)
SDC02	Chair	Living Room	150	180	20
SDC05	Mattress	Bedroom	200	180	20
SDC07	Mattress	Bedroom	350	180	50
SDC10	Chair	Living Room	150	180	40
SDC33	Chair	Living Room	100	180	10
SDC35	Chair	Living Room	100	180	10
SDC38	Mattress	Bedroom	120	180	25
SDC39	Mattress	Bedroom	200	180	25

### 3.31 NRCC Facade Heat Flux Measurements

A series of experiments was conducted by the Fire Research Section of the Institute for Research in Construction, National Research Council of Canada (NRCC), to measure the heat flux to a mock exterior building facade due to a fire within a compartment [174, 175]. The experiments selected for model validation were conducted using a series of propane line burners within a compartment whose interior dimensions were 5.95 m wide, 4.4 m deep, and 2.75 m high (see Fig. 3.14). There were five different door/window sizes:

1. 0.94 m by 2.00 m high
2. 0.94 m by 2.70 m high (door)
3. 2.60 m by 1.37 m high (shown in Fig. 3.14)
4. 2.60 m by 2.00 m high
5. 2.60 m by 2.70 m high (door)

There were four fire sizes: 5.5 MW, 6.9 MW, 8.6 MW, and 10.3 MW. In all, 19 experiments were conducted, with the exception of the 10.3 MW fire with Window 1. In each experiment, heat flux measurements were made 0.5 m, 1.5 m, 2.5 m, and 3.5 m above the top of the door/window.

### 3.32 NRCC Smoke Tower Experiments

In 2006 and 2007, the National Research Council of Canada (NRCC) conducted 10 fire experiments in a 10 story experimental facility in Almonte, Ontario to study smoke movement through the stair shaft to the upper floors of the building. Four of these experiments utilized actual commodities as fuel, and six utilized a propane burner. Four of the six propane fires were intended to reproduce the heat release of the commodity fires, and these experiments (BK-R, CMP-R, CLC-I-R, and CLC-II-R) have been chosen for this guide. Details of the experiments are included in a masters thesis and paper by Yan Wang [176, 177]. A description of FDS simulations of the propane experiments not included in this guide is given by Hadjisophocleous and Jia [178]. The analysis of the propane burner experiments discussed in this guide are based on the work of Paul Tyson at Ulster University as part of his masters thesis [179].

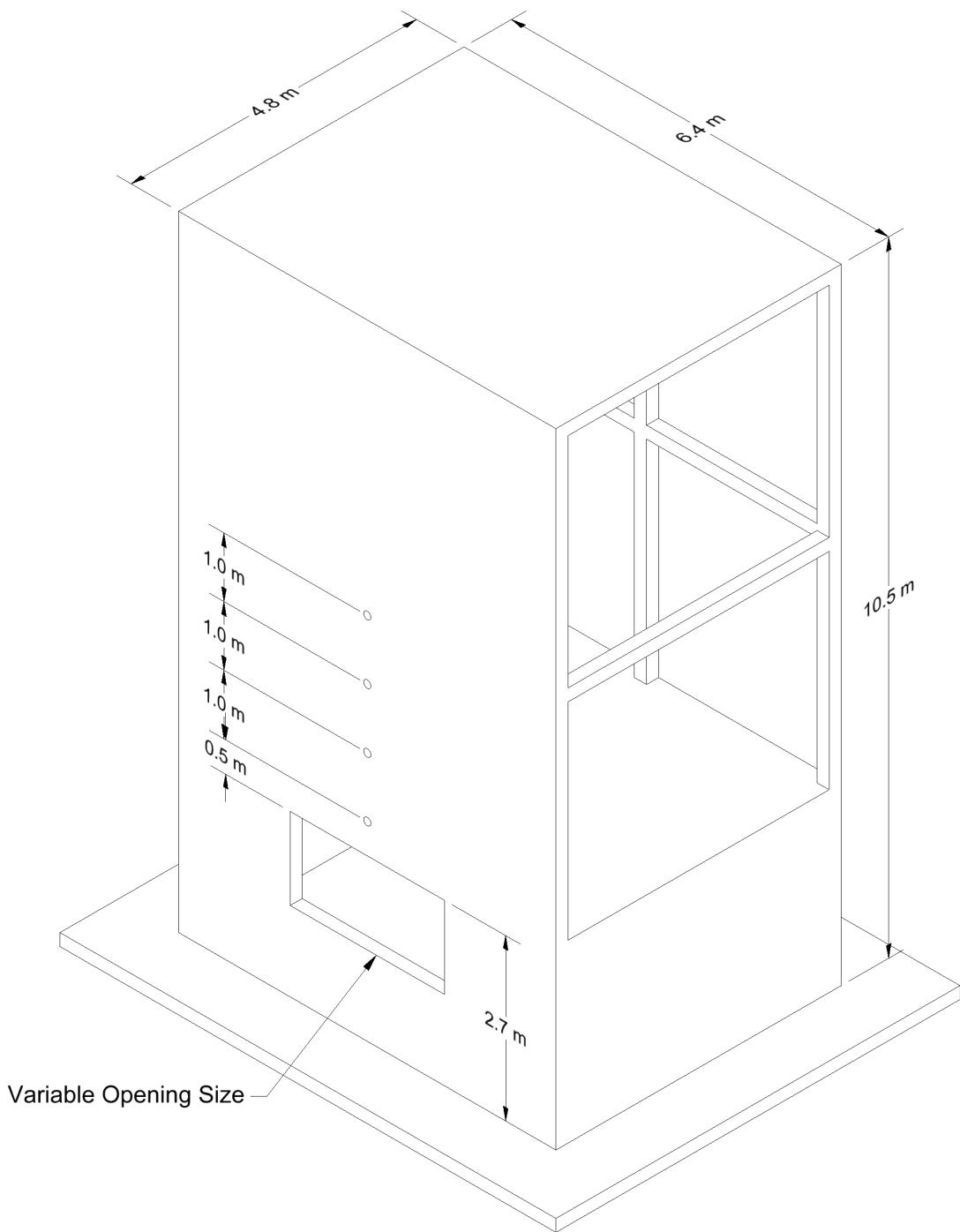


Figure 3.14: Geometry of the NRCC Facade Experiments.

1. Building Supply Shaft
2. Building Return/Exhaust Shaft
3. Smoke Shaft
4. Elevator/Stair Vestibule Supply Shaft
5. Stair Supply Shaft
6. Stair Exhaust Shaft
7. Service Shaft
8. Elevator Shaft
9. Elevator Vestibule

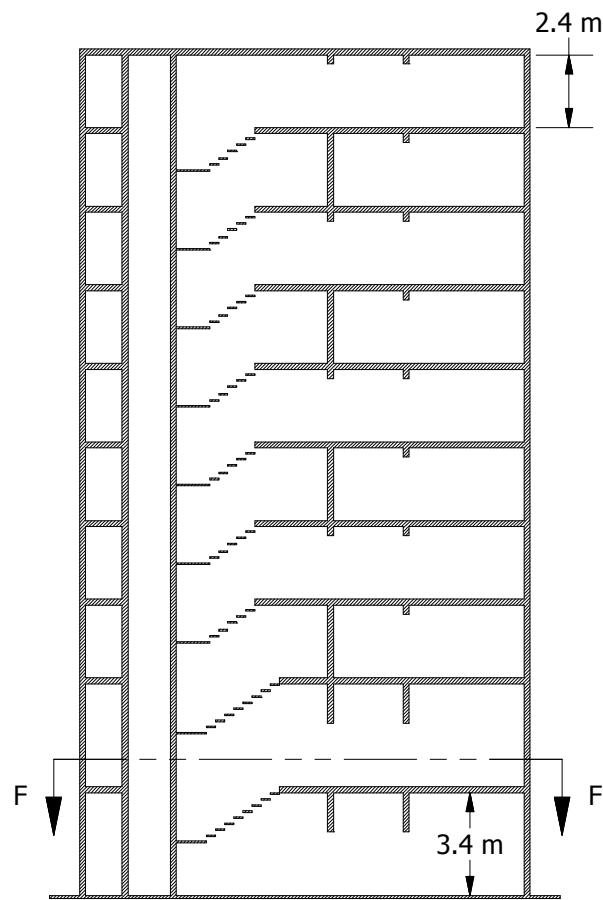
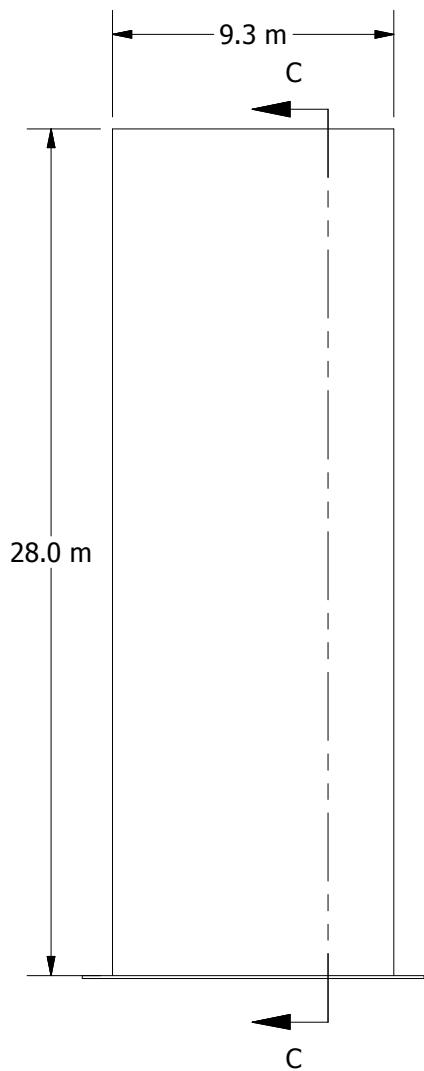
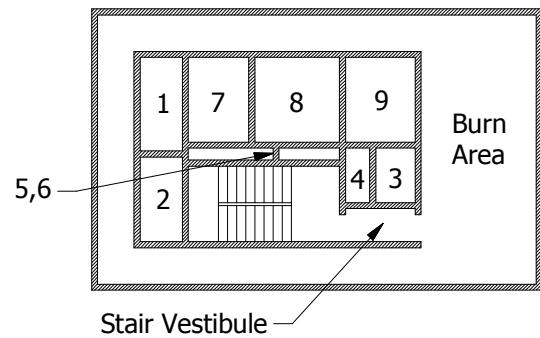


Figure 3.15: Geometry of the NRCC Smoke Tower Experiments.

The tower was designed as a test bed for the center core of a high-rise building. It includes a compartment and corridor on each floor, a stair shaft, elevator shaft and service shafts [180]. Figure 3.15 displays the geometry of the building as modeled in FDS. All walls and floor slabs are taken to be 0.2 m thick. The first two floors are 3.4 m high, slab to slab. The upper eight floors are 2.4 m, slab to slab. The propane burner was located on the second floor and the smoke flowed through open doors to the stair vestibule and stair shaft itself. In the four experiments considered in this guide, the stair shaft was open on the fourth, sixth, eighth, and tenth floors. The other floors were closed off to the stair shaft. The ventilation system was turned off. A single door was opened on the first floor, and there were no other openings to the outside save natural building leakage. The referenced documents do not explicitly include estimates of leakage areas, but for the sake of modeling, the leakage for each floor was concentrated at a single 1.5 m by 1.5 m exterior window. The leakage area was specified based on an estimate of a “loose” building exterior in NFPA 92 [181]. This is a very important consideration in modeling because it determines the extent to which the smoke rising up the stair shaft encounters an opposing downward flow.

Thermocouples and gas analyzers were placed at various locations to measure temperature and O<sub>2</sub>, CO<sub>2</sub> and CO concentrations. A vertical array of TCs was located in the fire compartment and the doorway leading into the stair shaft on the second floor. TCs were also placed at each floor in the stair shaft. The gas analyzers were located in the stair shaft at the second floor, just outside the door to the fire compartment.

### 3.33 NRL/HAI Wall Heat Flux Measurements

Back, Beyler, DiNenno and Tatem [182] measured the heat flux from 9 different sized propane fires set up against a wall composed of gypsum board. The experiments were sponsored by the Naval Research Laboratory and conducted by Hughes Associates, Inc., of Baltimore, Maryland. The square sand burner ranged in size from 0.28 m to 0.70 m, and the fires ranged in size from 50 kW to 520 kW.

### 3.34 PRISME Project

PRISME is the name of a fire test program conducted under the auspices of the Organization for Economic Cooperation and Development, Nuclear Energy Agency (OECD/NEA). The experiments were conducted at the French Institut de radioprotection et de sûreté nucléaire (IRSN) at Cadarache. A variety of experiments were conducted to study ventilation effects, electrical cable failure, and leakage. The test reports are not publicly available, but an entire edition of *Fire Safety Journal* documented various experimental and modeling studies [183].

The PRISME DOOR series consisted of six experiments, five of which involving two compartments connected by an open door (Tests 1-5) and one involving a third compartment (Test 6). The compartments were 5 m by 6 m by 4 m high. A well-instrumented ventilation system supplied air and exhausted combustion products at specified rates, but the thermal expansion of the gases caused these rates to change, a phenomenon that was intended to test the ventilation capabilities of the models. Wahlqvist and van Hees [184] modeled these experiments using FDS and contributed the input files for the cases documented in this guide.

The PRISME LEAK series consisted of experiments where smoke and heat flowed through various types of leaks between the test compartments. Instrumented cables were placed at various locations, and gas and solid phase temperatures were measured. FDS was used to simulate the heating up of the cables using the measured gas temperature several centimeters from the cables [185].

### 3.35 Purdue Flames

A turbulent buoyant diffusion flame is established on a diffuser burner with an exit diameter of 7.1 cm. The diverging angle of the burner is  $7^\circ$  such that the gaseous fuel (methane) is decelerated and forms a uniform velocity distribution at the burner exit [30]. The methane ( $\text{CH}_4$ ) mass flow rate (84.3 mg/s) The buoyant diffusion flame burns in a quiescent atmospheric pressure environment. The flame is surrounded by a screened enclosure to minimize flame disturbance. The Froude number of the flame is 0.109 and matches that of a 7.1 cm diameter liquid toluene pool fire [30, 32]. The total heat release rate of the methane flame is 4.2 kW under the assumption of complete combustion, and the visible flame height is approximately 36 cm [30]. Measured and computed vertical and horizontal velocity, mixture fraction, and temperature values for this flame have been reported by Xin et al. [30, 186] and Zhou et al. [32, 187]. The mean temperatures have been inferred from the measured species concentrations [30] by assuming an adiabatic flame. The interdependencies between species concentrations, temperature and specific heat have been ignored for determining the mean temperature.

### 3.36 Restivo Compartment Air Flow Experiment

Velocity measurements for forced airflow within a 9 m by 3 m by 3 m high compartment (Fig. 3.16) were made by Restivo [188]. These measurements have been widely used to validate CFD models designed for indoor air quality applications. It was also used to assess early versions of FDS [19, 20, 38]. In the experiment, air was forced into the compartment through a 16.8 cm vertical slot along the ceiling running the width of the compartment with a velocity of 0.455 m/s. A passive exhaust was located near the floor on the opposite wall, with conditions specified such that there was no buildup of pressure in the enclosure. The component of velocity in the lengthwise direction was measured in four arrays: two vertical arrays located 3 m and 6 m from the inlet along the centerline of the room, and two horizontal arrays located 8.4 cm above the floor and below the ceiling, respectively. These measurements were taken using hot-wire anemometers. While data on the specific instrumentation used are not readily available, hot-wire systems tend to have limitations at low velocities, with typical thresholds of approximately 0.1 m/s.

### 3.37 Sandia Plume Experiments

The Fire Laboratory for Accreditation of Models by Experimentation (FLAME) facility [189, 190] at Sandia National Laboratories in Albuquerque, New Mexico, is designed specifically for validating models of buoyant fire plumes. The plume source is 1 m in diameter surrounded by a 0.5 m steel ‘ground plane’. PIV/PLIF techniques are used to obtain instantaneous joint scalar and velocity fields. O’Hern et al. [189] studied a turbulent buoyant helium plume in the FLAME facility. Earlier work to model this experiment has been performed by DesJardin et al. [191]. Tieszen et al. [192, 193] studied methane and hydrogen pool fires.

### 3.38 Sippola Aerosol Deposition Experiments

Mark Sippola, a doctoral student at the University of California, Berkeley, measured aerosol deposition velocities for various sizes of monodisperse fluorescent particles and various air velocities in a duct [194, 195]. For the experiments considered here, the straight steel duct with smooth walls was square with dimensions of 15 cm by 15 cm. The particle diameters were 1  $\mu\text{m}$ , 3  $\mu\text{m}$ , 5  $\mu\text{m}$ , 9  $\mu\text{m}$ , and 16  $\mu\text{m}$ . The air velocities in the duct were 2.2 m/s, 5.3 m/s, and 9.0 m/s. A total of twelve panels (20 cm by 10 cm) were cut from the duct section to measure the amount of particles deposited to the duct surfaces; four panels each from

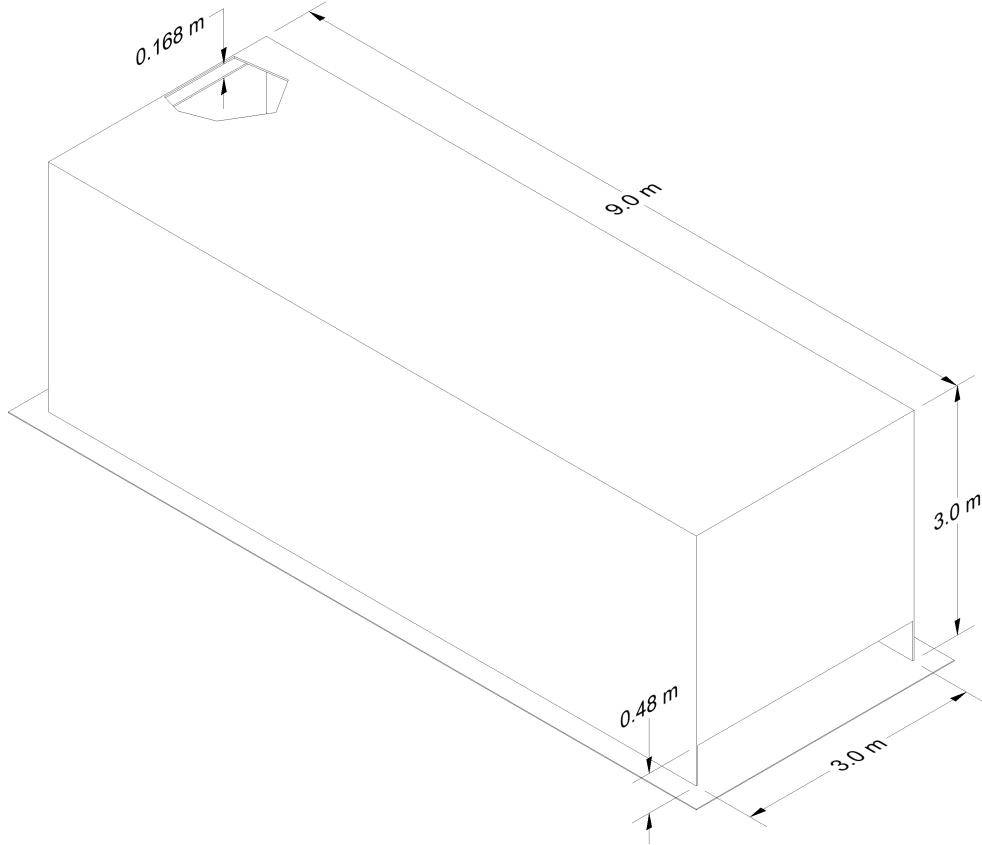


Figure 3.16: Geometry of Restivo’s compartment.

the duct ceiling, wall, and floor surfaces. Fluorescent measurement techniques and aerosol concentration measurements were used to calculate the deposition velocities of the particles to duct surfaces (ceiling, wall, and floor) at two straight duct sections where the turbulent flow profile was fully developed.

### 3.39 Smyth Slot Burner Experiment

Kermit Smyth et al. conducted diffusion flame experiments at NIST using a methane/air Wolfhard-Parker slot burner. The experiments are described in detail in Refs. [196, 197]. The Wolfhard-Parker slot burner consists of an 8 mm wide central slot flowing fuel surrounded by two 16 mm wide slots flowing dry air with 1 mm separations between the slots. The slots are 41 mm in length. Measurements were made of all major species and a number of minor species along with temperature and velocity. Experimental uncertainties have been reported as 5 % for temperature and 10 % to 20 % for the major species.

### 3.40 SP Adiabatic Surface Temperature Experiments

In 2008, three compartment experiments were performed at SP Technical Research Institute of Sweden under the sponsorship of Brandforsk, the Swedish Fire Research Board [198]. The objective of the experiments was to demonstrate how plate thermometer measurements in the vicinity of a simple steel beam can be used to supply the boundary conditions for a multi-dimensional heat conduction calculation for the beam. The adiabatic surface temperature was derived from the plate temperatures.

The experiments were performed inside a standard compartment designed for corner fire testing (ISO 9705). The compartment is 3.6 m deep, 2.4 m wide and 2.4 m high and includes a door opening 0.8 m by 2.0 m (Fig. 3.17). The room was constructed of 20 cm thick light weight concrete blocks with a density of  $600 \text{ kg/m}^3 \pm 100 \text{ kg/m}^3$ . The heat source was a gas burner run at a constant power of 450 kW. The top of the burner, with a square opening 30 cm by 30 cm, was placed 65 cm above the floor, 2.5 cm from the walls. A single steel beam was suspended 20 cm below the ceiling along the centerline of the compartment. There were three measurement stations along the beam at lengths of 0.9 m (Position A), 1.8 m (Position B), and 2.7 m (Position C) from the far wall where the fire was either positioned in the corner (Tests 1 and 2), or the center (Test 3). The beam in Test 1 was a rectangular steel tube filled with an insulation material. The beam in Tests 2 and 3 was an I-beam. A diagram of the room used in Test 2 is displayed in Figure 3.17.

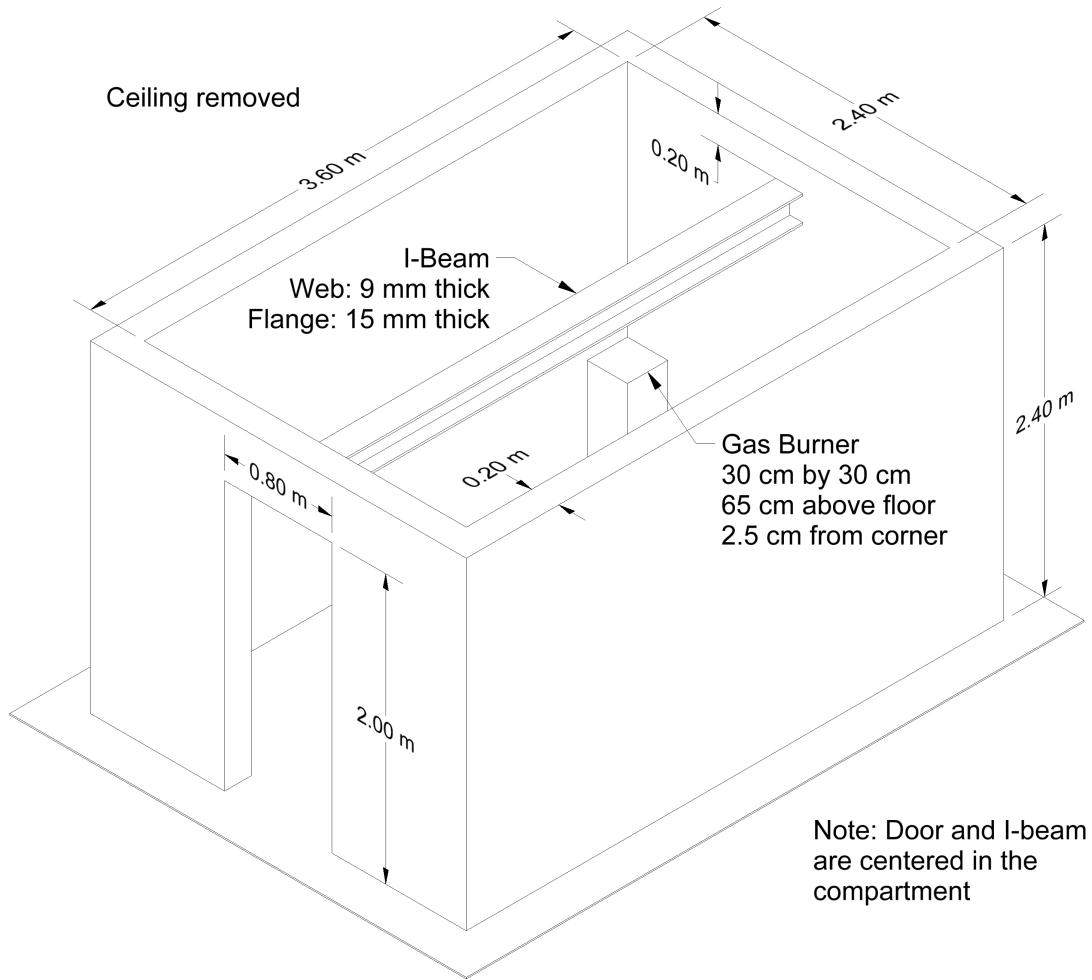


Figure 3.17: Geometry of the SP/AST compartment for Test 2.

A second series of experiments involving plate thermometers was carried out in 2011 [199]. A 6 m long, 20 cm diameter vertical steel column was positioned in the center of 1.1 m and 1.9 m diesel fuel and 1.1 m heptane pool fires. Gas, plate thermometer, and surface temperatures were measured at heights of 1 m, 2 m, 3 m, 4 m, and 5 m above the pool surface. These experiments are notable because the column is partially

engulfed in flames.

A third series of experiments involving plate thermometers was conducted in 2015 [200]. A simple compartment with a single door was constructed and instrumented primarily with plate thermometers. The compartment was 2.7 m long, 1.8 m wide, and 1.8 m tall, with a 0.6 m by 1.5 m door centered on one of the short walls. The PTs were affixed to the walls. The 12 experiments were conducted with four different wall linings. In Series A, the compartment was lined with a 10 cm thick light concrete block. In Series B, the compartment was lined with a 5 cm thick layer of insulation backed by a 3 mm thick plate of steel. In Series C, the compartment was lined with an uninsulated 3 mm thick steel plate. In Series D, the compartment was lined with a 3 mm thick steel plate backed by a 5 cm thick layer of insulation (the opposite of Series B). The fires were fueled by a 0.3 m by 0.3 m propane burner located in the center of the room except for Test A3, where it was centered on the back wall. For most of the experiments, the heat release rate was 1000 kW, except for A2 and C1, which were 500 kW, and A4 and C3, which employed linear ramp-ups to 1250 kW.

### 3.41 Steckler Compartment Experiments

Steckler, Quintiere and Rinkinen performed a set of 55 compartment fire tests at NBS in 1979. The compartment was 2.8 m by 2.8 m by 2.13 m high<sup>2</sup>, with a single door of various widths, or alternatively a single window with various heights. A 30 cm diameter methane burner was used to generate fires with heat release rates of 31.6 kW, 62.9 kW, 105.3 kW and 158 kW. Vertical profiles of velocity and temperature were measured in the doorway, along with a single vertical profile of temperature within the compartment. A full description and results are reported in Reference [201]. The basic test matrix is listed in Table 3.6. Note that the test report does not include a detailed description of the compartment. However, an internal report<sup>3</sup> by the test sponsor, Armstrong Cork Company, reports that the compartment floor was composed of 19 mm calcium silicate board on top of 12.7 mm plywood on wood joists. The walls and ceiling consisted of 12.7 mm ceramic fiber insulation board over 0.66 mm aluminum sheet attached to wood studs. A diagram of the compartment is displayed in Fig. 3.18.

### 3.42 UL/NIST Vent Experiments

In 2012, the Fire Fighting Technology Group at NIST conducted experiments at Underwriters Laboratories (UL) in Northbrook, Illinois, to assess the change in compartment temperature due to the opening of one or two 1.2 m square ceiling vents [202]. Four experiments were conducted using a natural gas burner in a 6.1 m by 4.3 m by 2.4 m compartment with a single door opening. The fires ranged in size from 500 kW to 2 MW, and the vents were opened and closed such that during the four experiments there were 31 discrete time intervals in which model predictions could be compared to quasi-steady conditions. The compartment contained two vertical arrays of thermocouples, and the door and vents were instrumented with thermocouples and bi-directional velocity probes. Only the thermocouple data has been used in the validation study. A diagram of the compartment is displayed in Figure 3.19. The major test parameters are listed in Table 3.7.

<sup>2</sup>The test report gives the height of the compartment as 2.18 m. This is a misprint. The compartment was 2.13 m high.

<sup>3</sup> *Technical Research Report, Fire Induced Flows Through Room Openings - Flow Coefficients*, Project 203005-003, Armstrong Cork Company, Lancaster, Pennsylvania, May, 1981.

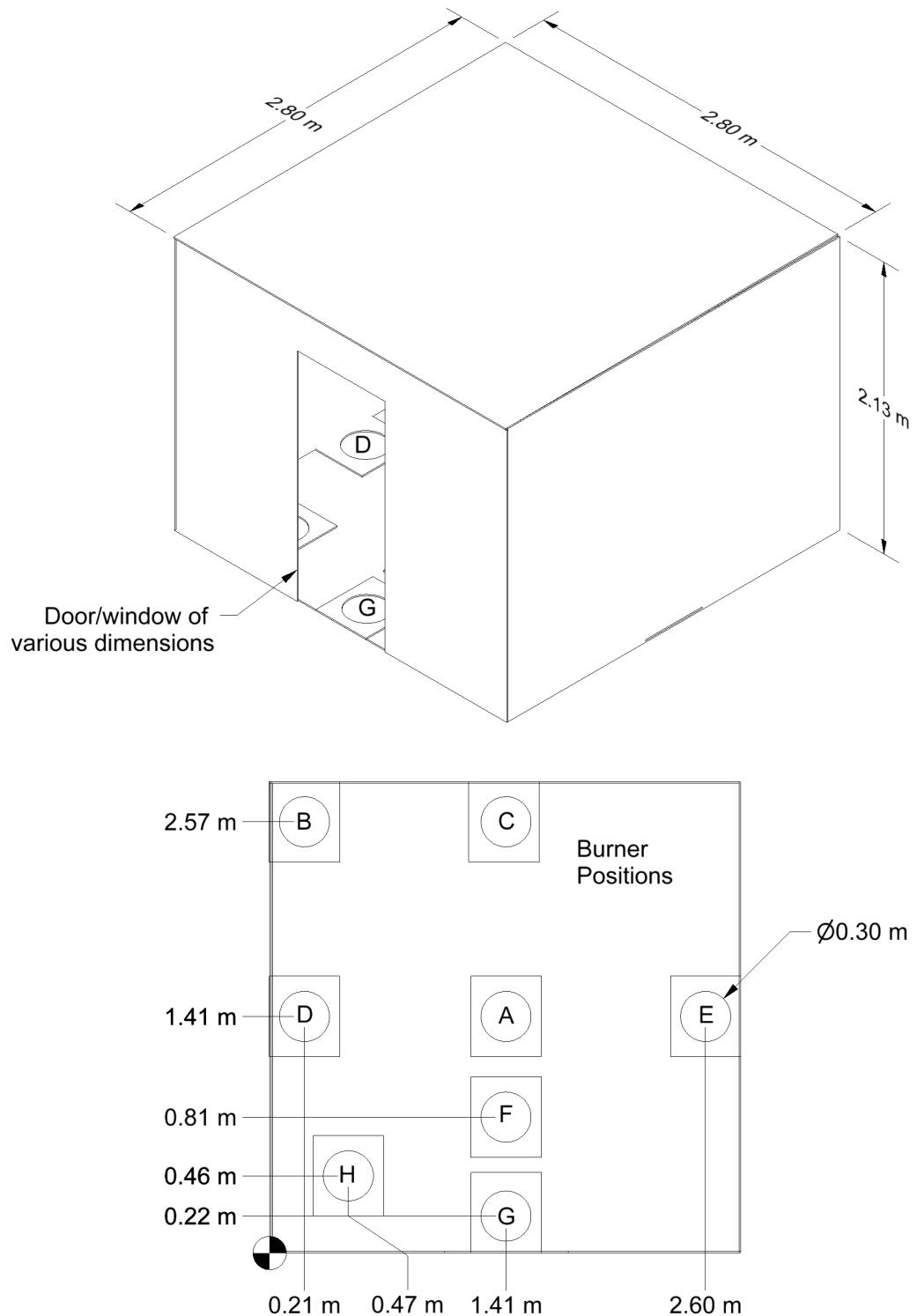


Figure 3.18: Geometry of the Steckler Compartment Experiments.

Table 3.6: Summary of Steckler compartment experiments.

Test	Door Width (m)	Door Height (m)	HRR $\dot{Q}$ (kW)	Burner Location	Test	Door Width (m)	Door Height (m)	HRR $\dot{Q}$ (kW)	Burner Location
10	0.24	1.83	62.9	Center	224	0.74	0.92	62.9	Back Corner
11	0.36	1.83	62.9	Center	324	0.74	0.92	62.9	Back Corner
12	0.49	1.83	62.9	Center	220	0.74	1.83	31.6	Back Corner
612	0.49	1.83	62.9	Center	221	0.74	1.83	105.3	Back Corner
13	0.62	1.83	62.9	Center	514	0.24	1.83	62.9	Back Wall
14	0.74	1.83	62.9	Center	544	0.36	1.83	62.9	Back Wall
18	0.74	1.83	62.9	Center	512	0.49	1.83	62.9	Back Wall
710	0.74	1.83	62.9	Center	542	0.62	1.83	62.9	Back Wall
810	0.74	1.83	62.9	Center	610	0.74	1.83	62.9	Back Wall
16	0.86	1.83	62.9	Center	510	0.74	1.83	62.9	Back Wall
17	0.99	1.83	62.9	Center	540	0.86	1.83	62.9	Back Wall
22	0.74	1.38	62.9	Center	517	0.99	1.83	62.9	Back Wall
23	0.74	0.92	62.9	Center	622	0.74	1.38	62.9	Back Wall
30	0.74	0.92	62.9	Center	522	0.74	1.38	62.9	Back Wall
41	0.74	0.46	62.9	Center	524	0.74	0.92	62.9	Back Wall
19	0.74	1.83	31.6	Center	541	0.74	0.46	62.9	Back Wall
20	0.74	1.83	105.3	Center	520	0.74	1.83	31.6	Back Wall
21	0.74	1.83	158.0	Center	521	0.74	1.83	105.3	Back Wall
114	0.24	1.83	62.9	Back Corner	513	0.74	1.83	158.0	Back Wall
144	0.36	1.83	62.9	Back Corner	160	0.74	1.83	62.9	Center*
212	0.49	1.83	62.9	Back Corner	163	0.74	1.83	62.9	Back Corner*
242	0.62	1.83	62.9	Back Corner	164	0.74	1.83	62.9	Back Wall*
410	0.74	1.83	62.9	Back Corner	165	0.74	1.83	62.9	Left Wall*
210	0.74	1.83	62.9	Back Corner	162	0.74	1.83	62.9	Right Wall*
310	0.74	1.83	62.9	Back Corner	167	0.74	1.83	62.9	Front Center*
240	0.86	1.83	62.9	Back Corner	161	0.74	1.83	62.9	Doorway*
116	0.99	1.83	62.9	Back Corner	166	0.74	1.83	62.9	Front Corner*
122	0.74	1.38	62.9	Back Corner					* Raised burner

### 3.43 UL/NFPRF Sprinkler, Vent, and Draft Curtain Study

In 1997, thirty-four heptane spray burner and five racked commodity experiments were conducted at the Large Scale Fire Test Facility at Underwriters Laboratories (UL) in Northbrook, Illinois [203, 78]. The spray burner experiments were divided into two test series. Series I consisted of 22 4.4 MW experiments. Series II consisted of 12 10 MW experiments. The objective of the spray burner experiments was to characterize the temperature and flow field for fire scenarios with a controlled heat release rate in the presence of sprinklers, draft curtains, and smoke & heat vents.

The Large Scale Fire Test Facility at UL contains a 37 m by 37 m (120 ft by 120 ft) main fire test cell, equipped with a 30.5 m by 30.5 m (100 ft by 100 ft) adjustable height ceiling. The UL/NFPRF test results (Series I) are summarized in Table 3.8. The UL/NFPRF test results (Series II) are summarized in Table 3.9.

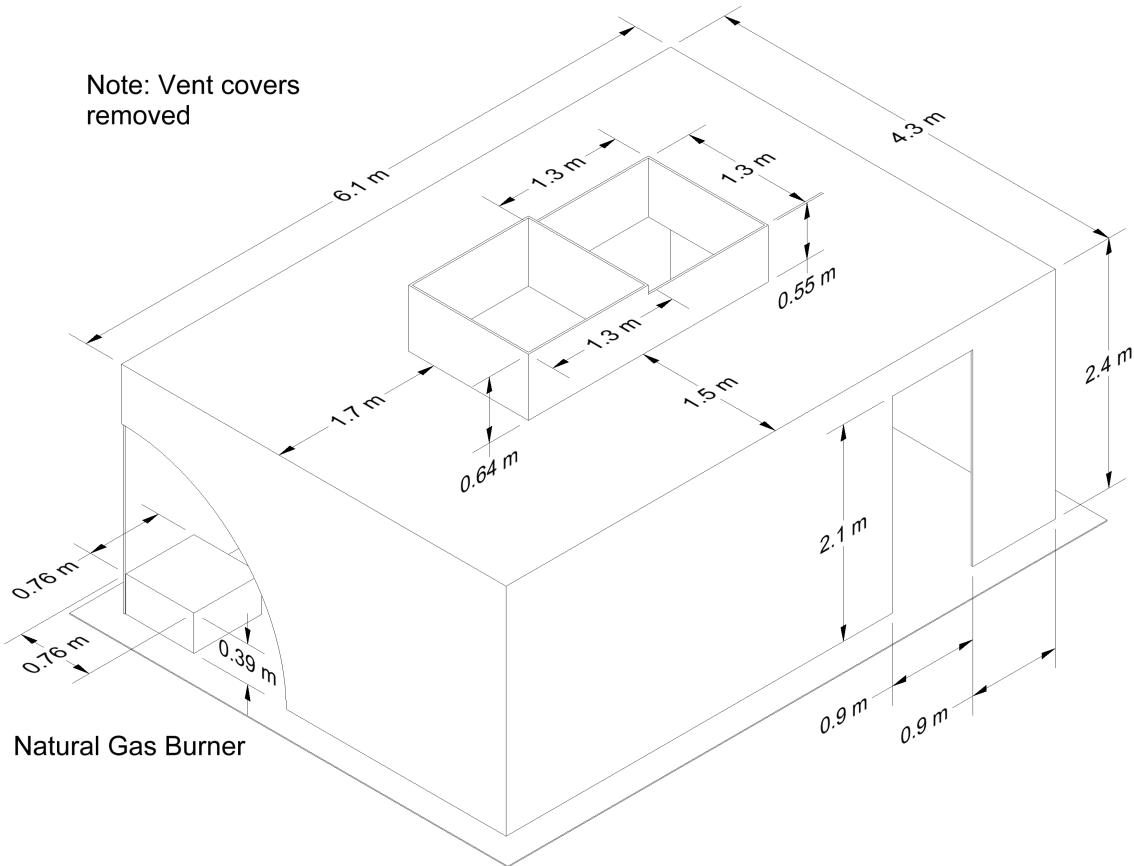


Figure 3.19: Geometry of the UL/NIST Experiments.

The layout of the experiments is shown in Figs. 3.20, 3.21, and 3.22.

**Ceiling:** The ceiling was raised to a height of 7.6 m and instrumented with thermocouples and other measurement devices. The ceiling was constructed of 0.6 m by 1.2 m by 1.6 cm UL fire-rated Armstrong Ceramaguard (Item 602B) ceiling tiles. The manufacturer reported the thermal properties of the material to be: specific heat 753 J/(kg·K), thermal conductivity 0.0611 W/(m·K), and density 313 kg/m<sup>3</sup>.

**Draft Curtains:** Sheet metal, 1.2 mm thick and 1.8 m deep, was suspended from the ceiling for 16 of the 22 Series I tests, enclosing an area of about 450 m<sup>2</sup> and 49 sprinklers. The curtains were in place for all of the Series II tests.

**Sprinklers:** Central ELO-231 (Extra Large Orifice) uprights were used for all the tests. The orifice diameter of this sprinkler is reported by the manufacturer to be nominally 1.6 cm (0.64 in), the reference actuation temperature is reported by the manufacturer to be 74°C (165°F). The RTI (Response Time Index) and C-factor (Conductivity factor) were reported by UL to be 148 (m·s)<sup>½</sup> and 0.7 (m/s)<sup>½</sup>, respectively [203].

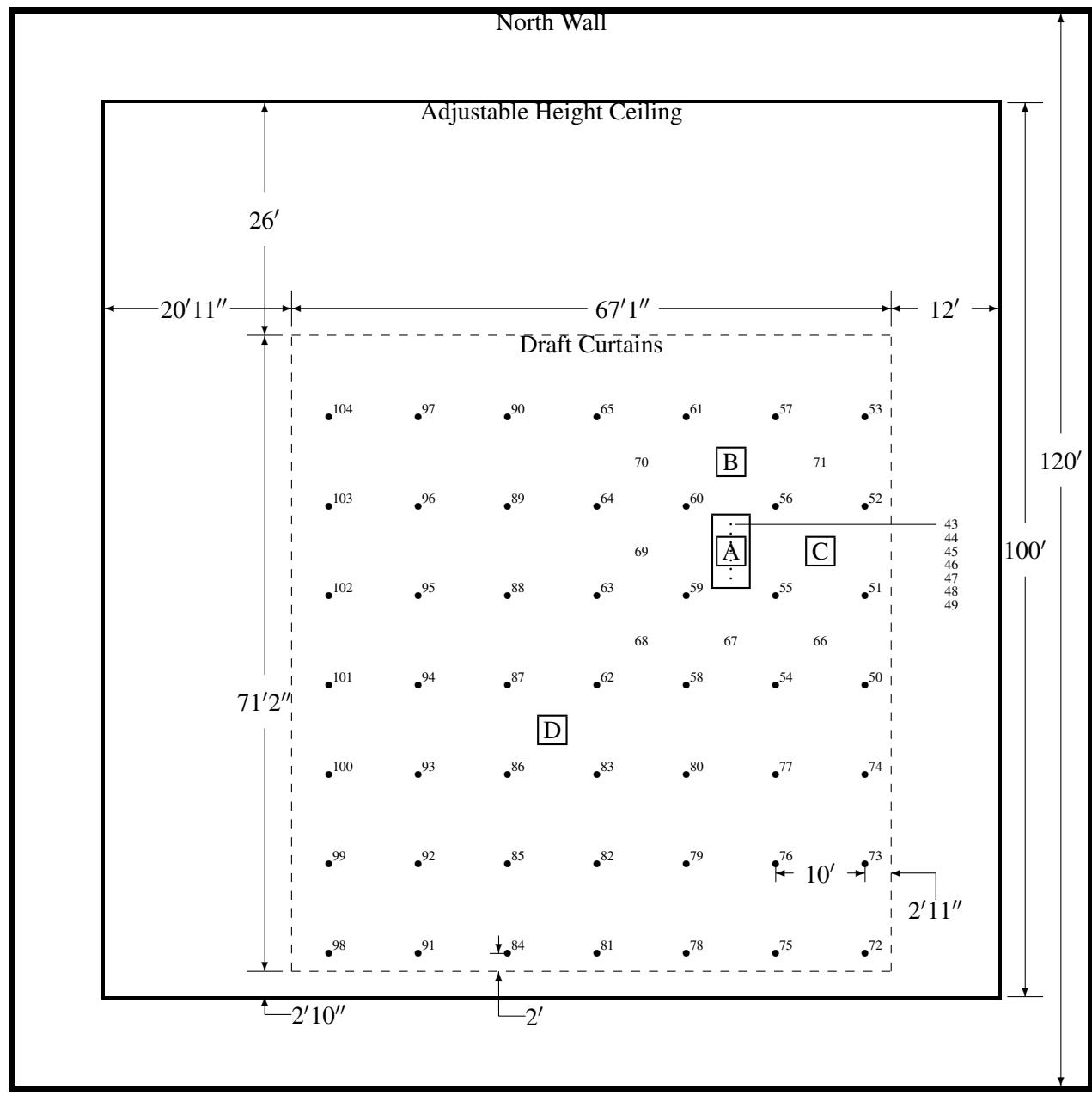


Figure 3.20: Plan view of the UL/NFPRF heptane spray experiments, Series I. The sprinklers are indicated by the solid circles and are spaced exactly 10 ft apart. The number beside each sprinkler location indicates the channel number of the nearest thermocouple. The vent dimensions are 4 ft by 8 ft. The boxed letters A, B, C and D indicate burner positions. Corresponding to each burner position is a vertical array of thermocouples. Thermocouples 1–9 hang 7, 22, 36, 50, 64, 78, 92, 106 and 120 in from the ceiling, respectively, above Position A. Thermocouples 10 and 11 are positioned above and below the ceiling tile directly above Position B, followed by 12–20 that hang at the same levels below the ceiling as 1–9. The same pattern is followed at Positions C and D, with thermocouples 21–31 at C and 32–42 at D.

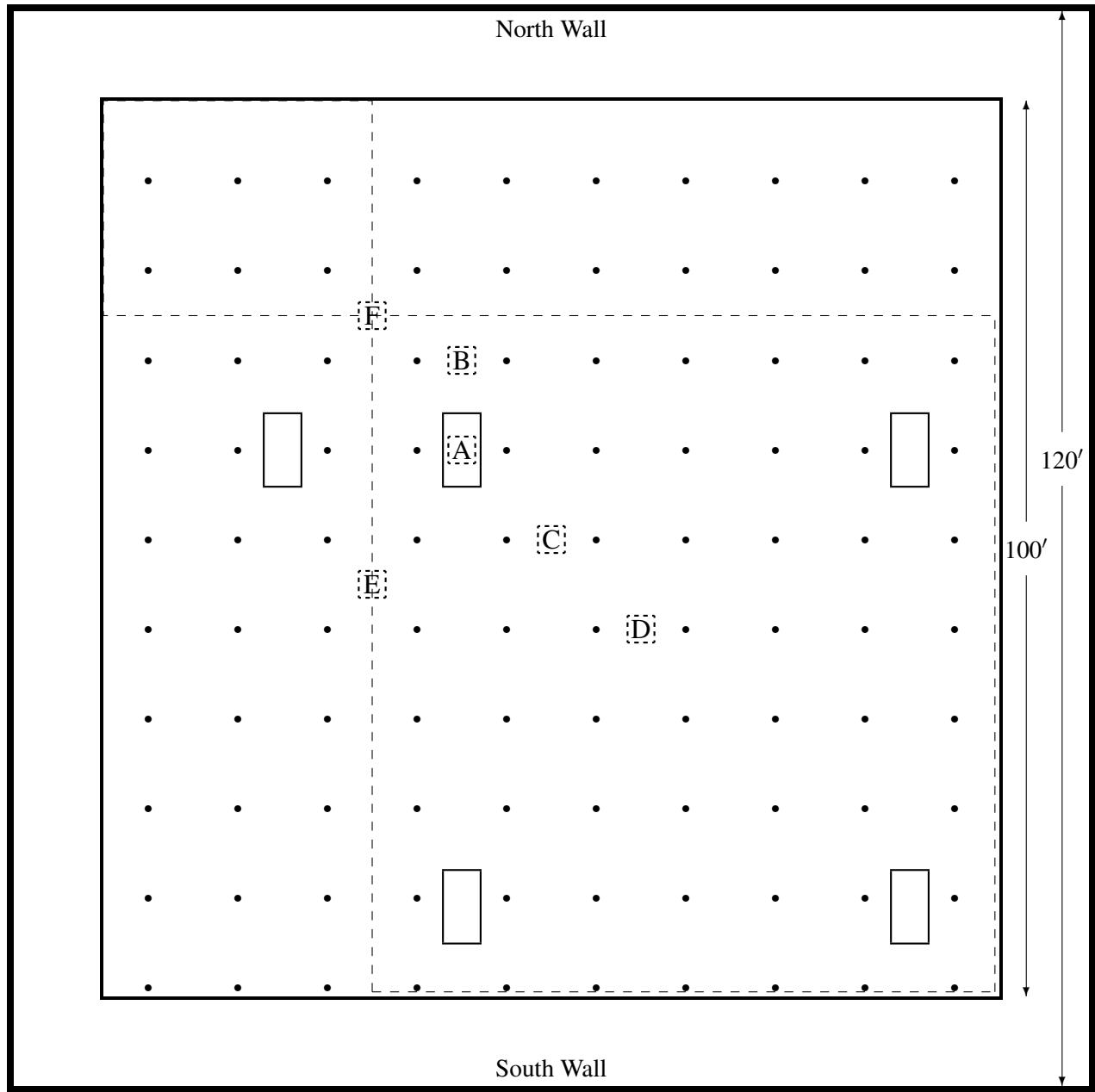


Figure 3.21: Plan view of the UL/NFPRF heptane spray experiments, Series II. The boxed letters A, B, C, D, E and F indicate burner positions. The sprinklers are indicated by the solid circles and are spaced exactly 10 ft apart. The vents are 4 ft by 8 ft.

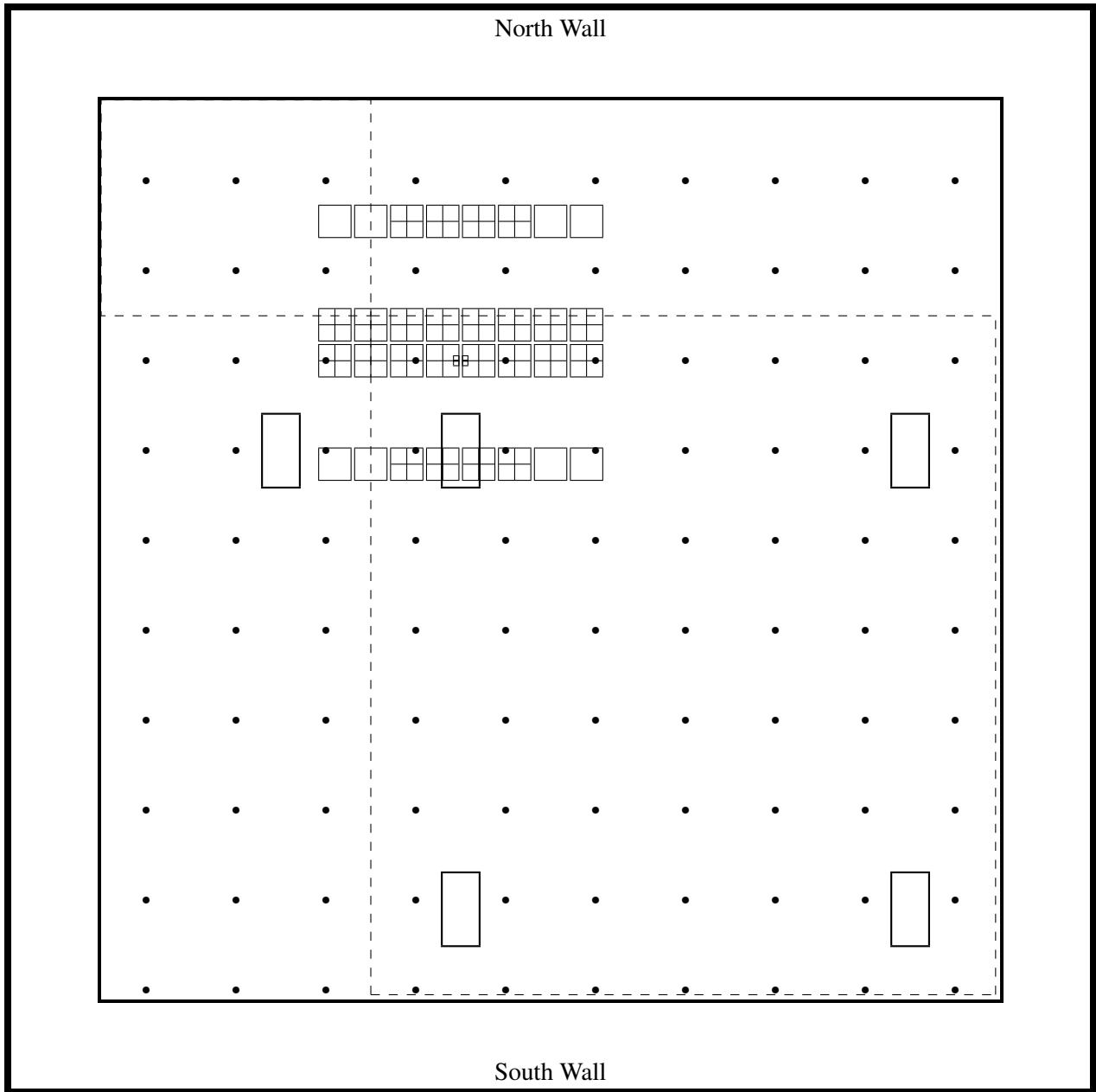


Figure 3.22: Plan view of the UL Large Scale Fire Test Facility with the layout of plastic commodity Test P-3. Tests P-1 and P-2 did not include the draft curtains (dashed lines). The sprinklers (dots) were separated by exactly 10 ft. The racks were located 30 ft south and 20 ft east of the position shown in Tests P-1, P-4, and P-5. The racks were located 10 ft south of the position shown in Test P-2. Each pallet load of boxed plastic commodity is represented by a square subdivided into four smaller squares to depict the individual boxes. Pallets containing empty boxes are represented by empty squares. Roof vents are represented by rectangles.

Table 3.7: Summary of UL/NIST Vent experiments. Note that the 31 “experiments” are actually discrete time intervals during the course of four separate fires.

Exp. No.	End Time (s)	HRR (kW)	No. of Vents	Exp. No.	End Time (s)	HRR (kW)	No. of Vents
Fire 1				Fire 3			
1	1215	430	0	14	453	476	0
2	1840	430	1	15	816	476	1
3	2168	430	2	16	1153	476	2
4	2474	430	0	17	1640	1002	0
5	2955	1011	0	18	1936	1002	1
6	3170	1011	1	19	2233	1002	2
7	3604	1011	2	Fire 4			
8	3840	1011	0	20	519	1011	0
9	4153	2188	0	21	967	1011	1
10	4284	2188	1	22	1325	1011	2
Fire 2				23	1559	470	2
11	565	2144	0	24	1653	470	1
12	833	2144	1	25	2013	470	0
13	931	2144	2	26	2411	470	1
				27	2910	470	2
				28	3399	2188	2
				29	3586	2188	0
				30	3803	2188	1
				31	4035	2188	2

When installed, the sprinkler deflector was located 8 cm below the ceiling. The thermal element of the sprinkler was located 11 cm below the ceiling. The sprinklers were installed with nominal 3 m by 3 m (exact 10 ft by 10 ft) spacing in a system designed to deliver a constant  $0.34 \text{ L}/(\text{s} \cdot \text{m}^2)$  ( $0.50 \text{ gpm}/\text{ft}^2$ ) discharge density when supplied by a 131 kPa (19 psi) discharge pressure

**Vent:** UL-listed double leaf fire vents with steel covers and steel curb were installed in the adjustable height ceiling in the position shown in Figs. 3.20 and 3.21. The vent is designed to open manually or automatically. The vent doors were recessed into the ceiling about 0.3 m (1 ft).

**Heptane Spray Burner:** The heptane spray burner consisted of a 1 m by 1 m square of 1.3 cm pipe supported by four cement blocks 0.6 m off the floor. Four atomizing spray nozzles were used to provide a free spray of heptane that was then ignited. For all but one of the Series I tests, the total heat release rate from the fire was manually ramped up following a “t-squared” curve to a steady-state in 75 s (150 s was used in Test I-16). The fire was ramped to 10 MW in 75 s for the Series II tests. The fire growth curve was followed until a specified fire size was reached or the first sprinkler activated. After either of these events, the fire size was maintained at that level until conditions reached roughly a steady state, i.e., the temperatures recorded near the ceilings remained steady and no more sprinkler activations occurred. The heat release rate from the burner was confirmed by placing it under the large product calorimeter at UL, ramping up the flow of heptane in the same manner as in the tests, and measuring the total and convective heat release rates. It was found that the convective heat release rate was  $0.65 \pm 0.02$  of the

Heptane Spray Burner Test Series I						
Test No.	Burner Pos.	Vent Operation	First Actuation (s)	Total Actuations	Draft Curtains	Heat Release Rate MW @ s
I-1	B	Closed	65	11	Yes	4.4 @ 50
I-2	B	Manual (0:40)	66	12	Yes	4.4 @ 50
I-3	B	Manual (1:30)	64	12	Yes	4.4 @ 50
I-4	C	Closed	60	10	Yes	4.4 @ 50
I-5	C	Manual (0:40)	72	9	Yes	4.4 @ 50
I-6	C	Manual (1:30)	62	8	Yes	4.4 @ 50
I-7	C	74°C link (DNO)	70	10	Yes	4.4 @ 50
I-8	B	74°C link (9:26)	60	11	Yes	4.4 @ 50
I-9	D	74°C link (DNO)	70	12	Yes	4.4 @ 50
I-10	D	Manual (0:40)	72	13	Yes	4.4 @ 50
I-11	D	74°C link (4:48)	N/A	N/A	Yes	4.4 @ 50
I-12	A	Closed	68	14	Yes	4.4 @ 50
I-13	A	74°C link (1:04)	69	5	Yes	6.0 @ 60
I-14	A	Manual (0:40)	74	7	Yes	5.8 @ 60
I-15	A	Manual (1:30)	64	5	Yes	5.8 @ 60
I-16	A	74°C link (1:46)	106	4	Yes	5.0 @ 110
I-17	B	100°C link (DNO)	58	4	No	4.6 @ 50
I-18	C	100°C link (DNO)	58	4	No	3.7 @ 50
I-19	A	100°C link (10:00)	56	10	No	4.6 @ 50
I-20	A	74°C link (1:20)	54	4	No	4.2 @ 50
I-21	C	74°C link (7:00)	58	10	No	4.6 @ 50
I-22	D	100°C link (DNO)	60	6	No	4.6 @ 50

Table 3.8: Results of Series I of the UL/NFPRF heptane spray experiments. Note that DNO means “Did Not Open”. Also note, the fires grew at a rate proportional to the square of the time until a certain flow rate of fuel was achieved at which time the flow rate was held steady. Thus, the “Heat Release Rate” was the size of the fire at the time when the fuel supply was leveled off.

total.

**Plastic Commodity:** The Factory Mutual Research Corporation (FMRC) standard “Group A Plastic” test commodity served as the fuel for the rack storage experiments [204]. The cartoned plastic commodity consists of rigid crystalline polystyrene cups packaged in compartmented, single-wall, corrugated paper cartons. Each carton is a cube 0.53 m (21 in) on a side. Eight boxes comprise a pallet load. Two-way, slatted deck hardwood pallets support the loads. A pallet load weighs approximately 80 kg (170 lb), of which about 36 % is plastic, 35 % is wood, and 29 % is corrugated paper [204]. Each storage array consisted of a main (ignition) double-row rack at the center, flanked on two sides by single row target racks. The rows were separated by 8 ft wide aisles. Each of the two rows of the main array consisted of four 2.4 m (8 ft) long bays; a 0.15 m (6 in) flue separated the rows. Longitudinal flues of 0.2 m (7.5 in) were used to separate the pallets within a row. The overall loaded area of the double-row rack measured approximately 2.3 m (7.5 ft) wide by 10 m (33 ft) long. The racks were divided vertically into 4 tiers; the overall loaded height was 5.8 m (19 ft). The fire was ignited with 2 standard igniters which consisted of 8 cm (3 in) long by 8 cm diameter cylinders of rolled cotton material, each soaked in 120 mL (4 oz)

Heptane Spray Burner Test Series II (10 MW Fires)							
Test No.	Burner Position	Vent Operation	Sprinklers Opened	First Activation	Last Activation	Avg. Peak Temp.	
						°C	°F
II-1	D	74°C link (DNO)	27	1:15	6:13	129.4	264.9
II-2	D	All Open at Start	28	1:05	5:53	128.8	263.8
II-3	A	74°C link (1:15)	12	1:08	4:00	101.8	215.2
II-4	B	74°C link (1:48)	16	1:03	5:54	108.8	227.8
II-5	D	74°C link (DNO)	28	1:10	7:07	130.0	266.0
II-6	D	All Open at Start	27	1:10	5:21	127.5	261.5
II-7	A	Closed	18	1:09	4:11	117.2	243.0
II-8	B	74°C link (1:12)	13	1:10	3:34	107.7	225.9
II-9	E	74°C link (DNO)	23	1:07	3:28	115.8	240.4
II-10	F	74°C link (3:20)	19	1:14	3:01	108.4	227.1
II-11	C	74°C link (DNO)	23	1:02	3:56	123.4	254.1
II-12	C	All Open at Start	23	0:58	4:55	119.0	246.2

Table 3.9: Results of the UL/NFPRF heptane spray experiments, Series II. Note that all fires were ramped up to 10 MW in 75 s following a  $t$ -squared curve.

of gasoline and enclosed in a polyethylene bag. The rolls were placed against the carton surfaces in the first tier, just above the pallet. The igniters were lit with a flaming propane torch at the start of each test.

**Instrumentation:** The instrumentation for the tests consisted of thermocouples, gas analysis equipment, and pressure transducers. The locations of the instrumentation are referenced in the plan view of the facility (Fig. 3.20). Temperature measurements were recorded at 104 locations. Type K 0.0625 in diameter Inconel sheathed thermocouples were positioned to measure (i) temperatures near the ceiling, (ii) temperatures of the ceiling jet, and (iii) temperatures near the vent.

### 3.44 Ulster SBI Corner Heat Flux Measurements

Zhang et al. [205] measured the heat flux and flame heights from fires in the single burning item (SBI) enclosure at the University of Ulster, Northern Ireland. Thin steel plate probes were used to measure the surface heat flux, and flame heights were determined by analyzing the instantaneous images extracted from the videos of the experiments by a CCD camera. Three heat release rates were used – 30 kW, 45 kW, and 60 kW.

### 3.45 UMD Polymers

Stoliarov et al. conducted measurements of the thermal properties of charring and non-charring polymers with the specific purpose of providing input data for numerical pyrolysis models [206, 207, 208, 209]. The study aimed to determine whether a one-dimensional conduction/reaction model could be used as a practical tool for prediction and/or extrapolation of the results of fire calorimetry tests. The non-charring polymers included poly(methyl methacrylate) (PMMA), high-impact polystyrene (HIPS), and polyoxymethylene (POM). The charring polymers included acrylonitrile butadiene styrene (ABS), polyethylene terephthalate (PET), Kydex, and polyethylenimine (PEI).

### 3.46 UMD Line Burner

James P. White, University of Maryland, College Park

The University of Maryland (UMD) Line Burner experimental facility provides for the study of a low-strain, buoyancy-driven, fully-turbulent diffusion flame in a canonical line-fire configuration. This facility provides well-controlled inlet and boundary conditions while introducing the complicating effects of buoyancy and turbulence characteristic of large-scale accidental fires. A variety of non-intrusive diagnostics are employed to measure local and integral flame characteristics. The facility comprises a slot burner centrally located within a surrounding, uniform co-flowing oxidizer. Controlled suppression of the flame is achieved via the introduction of either excess nitrogen gas or a fine water mist into the oxidizer stream. A detailed description of this facility is presented in White et al. [210].

A plan view illustration of the burner and oxidizer assembly is presented in Fig. 3.23. The burner features a sand-filled, stainless-steel fuel port, measuring 5 cm wide by 50 cm long, with 1.5 mm thick side walls. Methane gas (99.5 % purity) or propane gas (99.5 % purity) are the primary burner fuels. A methane flow rate of  $1.00 \pm 0.02$  g/s (nominal 5.4 cm/s) or a propane flow rate of  $1.08 \pm 0.02$  g/s (nominal 2.1 cm/s) is utilized, measured using a mass flow controller. Assuming complete combustion, the total heat-release rate is roughly 50 kW for either fuel.

The burner is centrally located at the mouth of a surrounding oxidizer port, measuring 50 cm wide by 75 cm long, with 10 cm thick side walls. Flow conditioning elements ensure that the oxidizer is well-mixed and exits the oxidizer port with a uniform, flat velocity profile. The co-flowing oxidizer is provided at a fixed flow rate of  $75 \pm 5$  g/s (total, including variable suppressant flow, nominal 22 cm/s), measured using a calibrated pitot-static probe.

Sitting on top of the oxidizer port and surrounding the fuel port is a thin, 5 mm tall, 5 cm wide annulus of ceramic fiberboard, positioned so the top of the board is 10 mm below the lip of the fuel port (and 5 mm above the oxidizer port). This board serves as a flow blockage to reduce the oxidizer velocity near the flame base, forcing the onset of buoyancy-generated turbulence upstream toward the fuel port and reducing the tendency to form laminar structures at the base of the flame.

For nitrogen-dilution suppression experiments, the flame is suppressed via the introduction of a variable flow of gaseous nitrogen into the oxidizer. Suppression potential is characterized by the oxygen mole-fraction in the oxidizer,  $X_{O_2}$ . Quantity  $X_{O_2}$  is measured using a paramagnetic oxygen analyzer via a probe located in the oxidizer port. The analyzer provides a measurement accuracy of  $\pm 0.125$  mol % O<sub>2</sub> and a response time of 5 s. An additional transport delay averaging around 20 s, is compensated to provide synchronous data collection with other measurements.

For water-mist suppression experiments, the flame is suppressed via the introduction of a fine water mist into the oxidizer.

Visible flame height is measured using a video camera, defined based on the 50 % intermittent flame height [210]. These image-based measurements rely on visible flame emissions, including the incandescence of soot particles, and do not strictly locate the stoichiometric flame sheet. The uncertainty in each flame height measurement is less than  $\pm 1.5$  cm.

Infrared radiative emissions are measured using a water-cooled Schmidt-Boelter heat-flux transducer. The sensor is positioned 100 cm radially outward from the burner centroid, 18 cm above the fuel port, facing perpendicular to the long axis of the burner. This device has a hemispherical absorptance of 0.94 for a spectral range between 0.6-15.0  $\mu\text{m}$ , a maximum viewing angle of 90°, and a response time of 0.25 s. Measurement accuracy is  $\pm 3$  %. The convective portion of the measured heat flux is neglected and sans-flame measurements are applied to correct for background irradiation.

Heat flux data are converted to radiative loss fraction,  $\chi_r$ , using a weighted multipoint radiation source model, whereby the measured heat flux is assumed to be received from an array of isotropic point sources

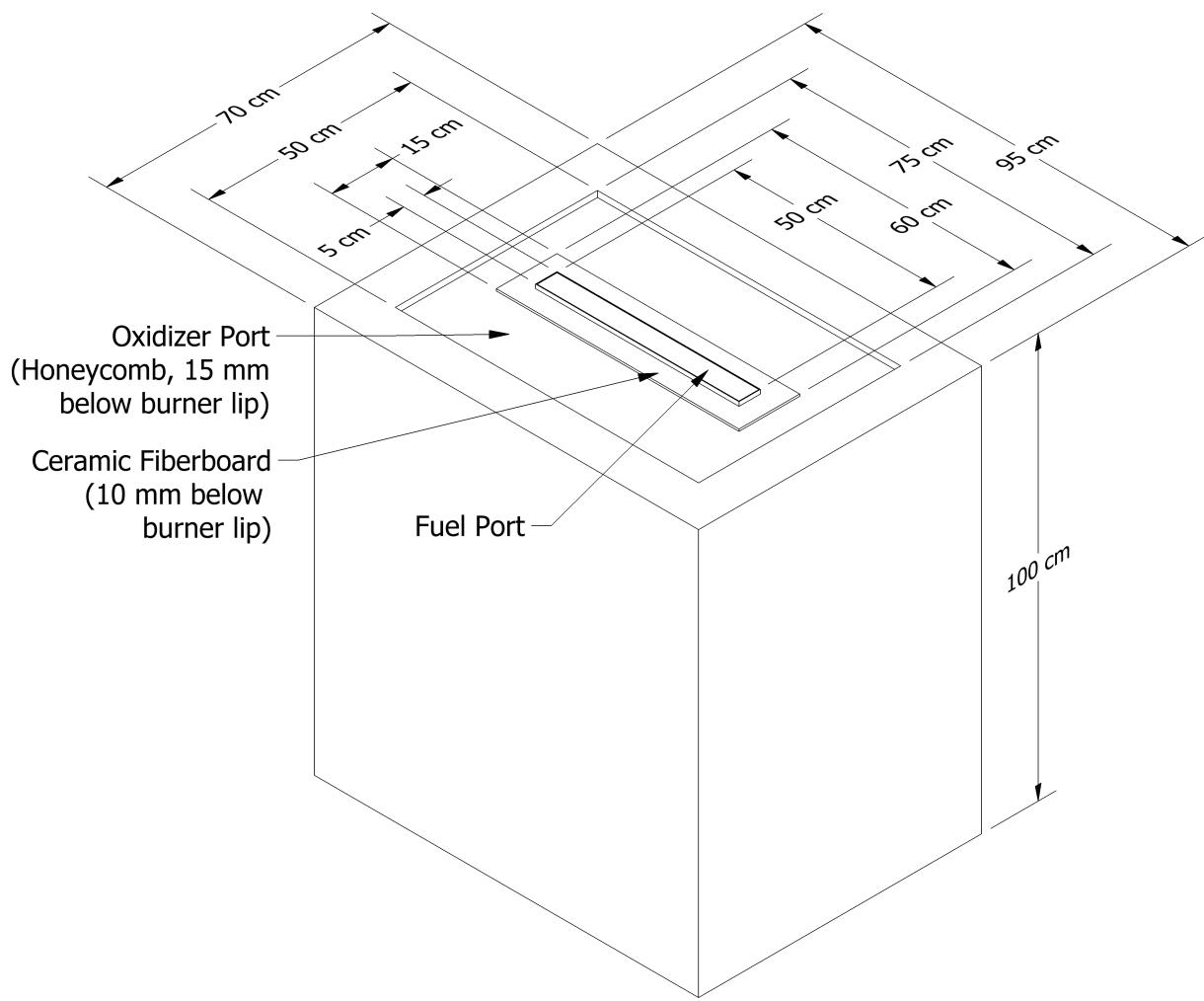


Figure 3.23: UMD Line Burner isometric view of burner and oxidizer assembly.

uniformly distributed over a two-dimensional plane oriented across the visible flame surface [1]. The uncertainty in each  $\chi_r$  measurement is less than  $\pm 4.5\%$ .

Mean and rms temperature data are recorded using an array of R-Type thermocouple probes positioned at selected locations along the centerline of the flame. These probes are constructed using 50  $\mu\text{m}$  diameter wires with exposed, bead-welded junctions. Combustion products are collected in an exhaust evacuation system, wherein a gas sampling system provides measurement of the molar concentrations of oxygen ( $\pm 0.25$  mol % O<sub>2</sub>), carbon dioxide ( $\pm 1000$  ppm CO<sub>2</sub>), carbon monoxide ( $\pm 100$  ppm CO), water vapor ( $\pm 3\%$  RH), and total hydrocarbons ( $\pm 10$  ppm THC) in the exhaust stream. From these measurements, integral heat release rate and combustion efficiency measurements are derived using species-based calorimetry techniques.

### 3.47 USCG/HAI Water Mist Suppression Tests

The U.S. Coast Guard sponsored a series of experiments to assess the fire suppression capabilities of a variety of water mist systems in a variety of ship board configurations. The experiments were conducted in

1999 by Hughes Associates, Inc., in a simulated machinery space aboard the test vessel *State of Maine* at the USCG Fire and Safety Test Detachment, Mobile, Alabama [211]. The space had nominal dimensions of 7 m by 5 m by 3 m, containing two steel engine mock-ups each measuring 3 m by 1 m by 1.5 m. The space was equipped with a door for natural ventilation and a forced ventilation system providing approximately 15 air changes per hour. Five commercially available water mist systems were evaluated. The obstructed heptane spray fires ranged in size from approximately 250 kW to 1 MW.

### 3.48 USN High Bay Hangar Experiments

The U.S. Navy sponsored a series of 33 tests within two hangars examining fire detection and sprinkler activation in response to spill fires in large enclosures. Experiments were conducted using JP-5 and JP-8 fuels in two Navy high bay aircraft hangars located in Naval Air Stations in Barber's Point, Hawaii and Keflavik, Iceland [212].

The Hawaii tests were conducted in a 15 m high hangar measuring 97.8 m in length and 73.8 m in width. Of the 13 tests conducted in the facility 11 were conducted in pans ranging from .09 m<sup>2</sup> to 4.9 m<sup>2</sup> in area with heat release rates varying from 100 kW to 7.7 MW. The burner was placed in the center of the room on a scale that continuously recorded the pans weight. The facility was equipped with a number of detection devices including thermocouples, electronic smoke and spot heat detectors, projected beam smoke detectors, combination UV/IR optical flame detectors, line-type heat detectors, as well as sprinklers. Measurements were recorded at a large number of locations allowing for a thorough profile of compartment behavior.

It was suspected that fire plume behavior and response of detection devices in a cold building may not have been well replicated by the experiments held in the warm hangar in Hawaii. The Iceland tests were conducted under a 22 m barrel vaulted ceiling in a hangar measuring 45.7 m by 73.8 m. 22 tests in total were conducted. The majority of these tests fires burned JP-5 fuel with the remainder burning JP-8. The jet fuel fires ranged in size from .06 m<sup>2</sup> to 20.9 m<sup>2</sup> and in heat release rate from 100 kW to approximately 33 MW. The facility was equipped similarly to the Hawaii hangar.

### 3.49 Vettori Flat Ceiling Experiments

Vettori [76] analyzed a series of 45 experiments conducted at NIST that were intended to compare the effects of different ceiling configurations on the activation times of quick response residential pendent sprinklers. The two ceiling configurations used consisted of an obstructed ceiling, with parallel beams 0.038 m wide by 0.24 m deep placed 0.41 m on center, and a smooth ceiling configuration, in which the beams were covered by a sheet of gypsum board. In addition to the two ceiling configurations, there were also three fire growth rates and three burner locations used – a total of 18 test configurations. The fire growth rate was provided by a computer controlled methane gas burner to mimic a standard t-squared<sup>4</sup> fire growth rate with either a slow, medium, or fast ramp up. The burner was placed in a corner of the room, then against an adjacent wall, and then in a location removed from any wall. Measurements were taken to record sprinkler activation time, temperatures at varying heights and locations within the room, and the ceiling jet velocities at several other locations. A diagram of the test structure is displayed in Figure 3.24.

---

<sup>4</sup>The actual heat release rate are presented in Table 3.10.

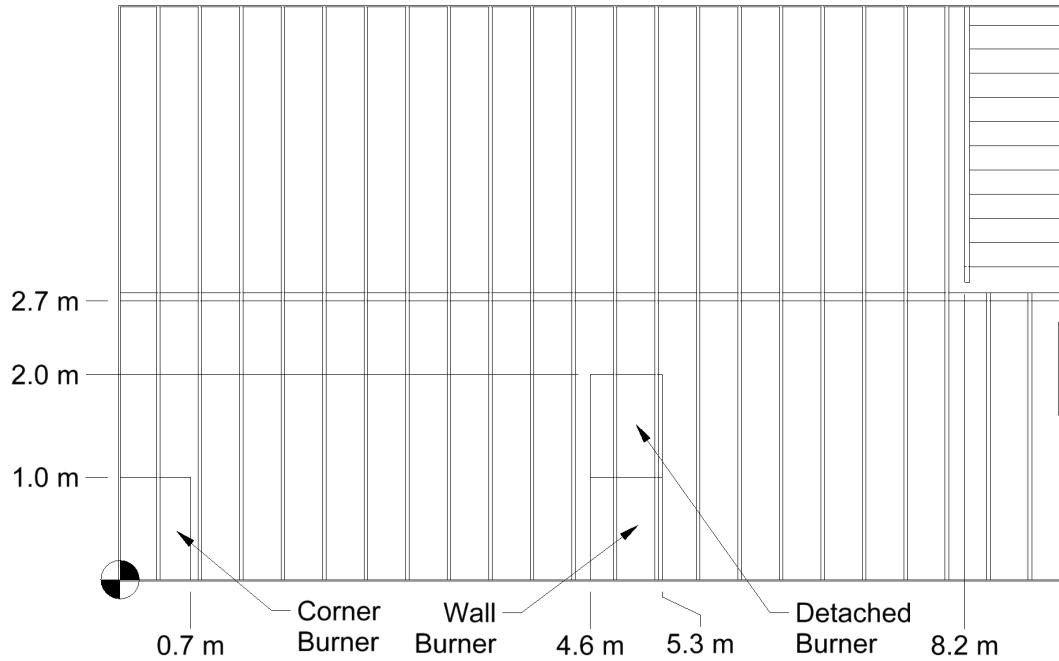
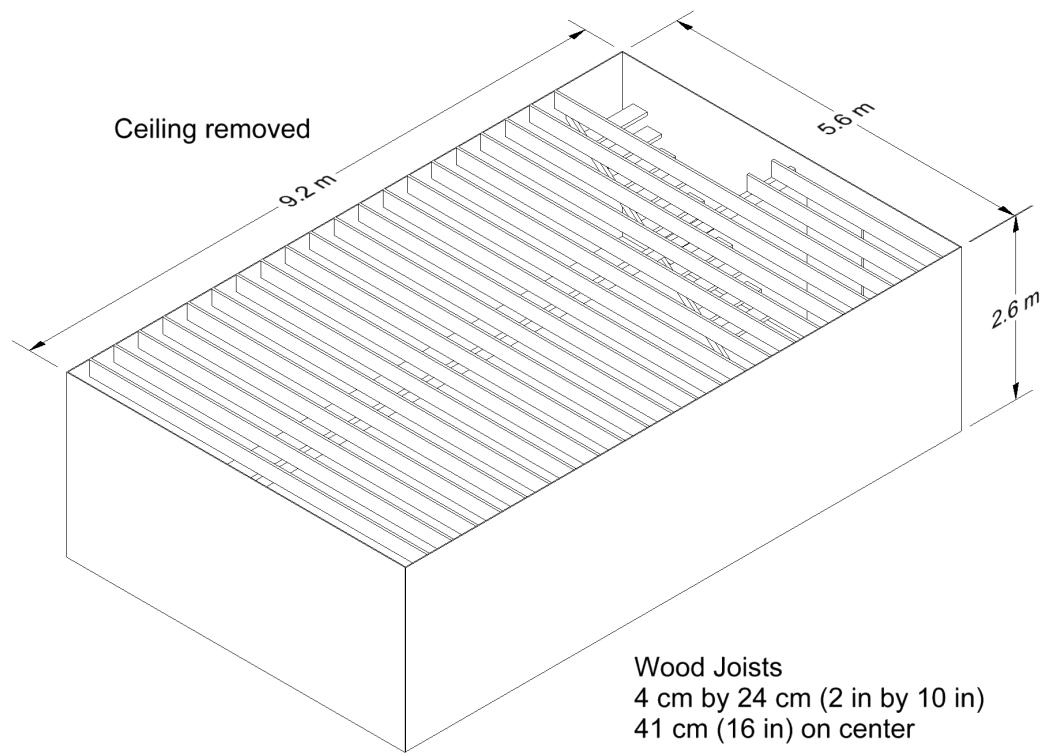


Figure 3.24: Geometry of the Vettori Flat Ceiling compartment.

Table 3.10: Heat release rate profiles for the Vettori experiments.

Time (s)	Slow (kW)	Medium (kW)	Fast (kW)
0	0	0	0
10	9	20	75
20	16	34	127
30	23	51	173
40	30	67	196
50	35	83	271
60	42	104	379
70	52	125	515
80	62	143	673
90	68	162	852
100	78	174	1053
110	85	192	
120	94	239	
130	100	279	
140	109	325	
150	115	373	
160	125	424	
170	137	479	
180	148	537	
190	163	599	
200	179	663	
210	195		
220	213		
230	231		
240	250		
250	269		
260	290		
270	311		
280	333		
290	354		
300	378		
310	402		
320	427		
330	453		
340	479		
350	506		
360	534		
370	562		

## 3.50 Vettori Sloped Ceiling Experiments

Vettori [77] performed a series of 72 compartment experiments to measure the activation times of quick-response residential pendent sprinklers mounted under a ceiling with an adjustable slope. There were 36 unique configurations (2 replicates of each) combining the following parameters:

- Flat, 13°, or 24° Ceiling Slope
- Smooth or Obstructed Ceiling Surface
- Fast or Slow Growth Fire
- Corner, Wall, or Detached Burner Location

Note that the Slow and Fast fire growth profiles were the same as those reported in Table 3.10.

## 3.51 VTT Large Hall Tests

The experiments are described in Ref. [213]. The series consisted of 8 experiments, but because of replicates only three unique fire scenarios. The experiments were undertaken to study the movement of smoke in a large hall with a sloped ceiling. The tests were conducted inside the VTT Fire Test Hall, with dimensions of 19 m high by 27 m long by 14 m wide. Each test involved a single heptane pool fire, ranging from 2 MW to 4 MW. Four types of predicted output were used in the present evaluation – the HGL temperature and depth, average flame height and the plume temperature. Three vertical arrays of thermocouples (TC), plus two thermocouples in the plume, were compared to FDS predictions. The HGL temperature and height were reduced from an average of the three TC arrays using the standard algorithm described in Chapter 5. The ceiling jet temperature was not considered, because the ceiling in the test hall is not flat, and the standard model algorithm is not appropriate for this geometry.

The VTT test report lacks some information needed to model the experiments, which is why some information was based on private communications with the principal investigator, Simo Hostikka.

**Surface Materials:** The walls and ceiling of the test hall consist of a 1 mm thick layer of sheet metal on top of a 5 cm layer of mineral wool. The floor was constructed of concrete. The report does not provide thermal properties of these materials.

**Natural Ventilation:** In Cases 1 and 2, all doors were closed, and ventilation was restricted to infiltration through the building envelope. Precise information on air infiltration during these tests is not available. The scientists who conducted the experiments recommend a leakage area of about  $2 \text{ m}^2$ , distributed uniformly throughout the enclosure. By contrast, in Case 3, the doors located in each end wall (Doors 1 and 2, respectively) were open to the external ambient environment. These doors are each 0.8 m wide by 4 m high, and are located such that their centers are 9.3 m from the south wall.

**Mechanical Ventilation:** The test hall has a single mechanical exhaust duct, located in the roof space, running along the center of the building. This duct had a circular section with a diameter of 1 m, and opened horizontally to the hall at a distance of 12 m from the floor and 10.5 m from the west wall. Mechanical exhaust ventilation was operational for Case 3, with a constant volume flow rate of  $11 \text{ m}^3/\text{s}$  drawn through the exhaust duct.

**Heat Release Rate:** Each test used a single liquid fuel pan with its center located 16 m from the west wall and 7.4 m from the south wall. For all tests, the fuel was heptane in a circular steel pan that was partially filled with water. The pan had a diameter of 1.17 m for Case 1 and 1.6 m for Cases 2 and 3. In

each case, the fuel surface was 1 m above the floor. The trays were placed on load cells, and the HRR was calculated from the mass loss rate. For the three cases, the fuel mass loss rate was averaged from individual replicate tests. In the HRR estimation, the heat of combustion (taken as 44,600 kJ/kg) and the combustion efficiency for n-heptane was used. Hostikka suggests a value of 0.8 for the combustion efficiency. Tewarson reports a value of 0.93 for a 10 cm pool fire [214]. For the calculations reported in the current study, a combustion efficiency of 0.85 is assumed. In general, an uncertainty of 15 % has been assumed for the reported HRR of most of the large scale fire experiments used.

**Radiative Fraction:** The radiative fraction was assumed to be 0.35, similar to many smoky hydrocarbons.

A diagram of the test structure is displayed in Figure 3.25.

## 3.52 VTT Water Spray Experiments

The spray from a single water mist nozzle was measured at Tampere University of Technology using a direct imaging technique [215]. The model number of the nozzle is LN-2, manufactured by the Spraying Systems Company. It is a fine spray hydraulic atomizing nozzle of the standard spray, small capacity type. Measurements were made 40 cm and 62 cm below the nozzle. Measured quantities include the average droplet velocity, droplet flux, and median diameter.

## 3.53 WTC Spray Burner Experiments

As part of its investigation of the World Trade Center disaster, the Building and Fire Research Laboratory at NIST conducted several series of fire experiments to both gain insight into the observed fire behavior and also to validate FDS for use in reconstructing the fires. The first series of experiments involved a relatively simple compartment with a liquid spray burner and various structural elements with varying amounts of sprayed fire-resistive materials (SFRM). A diagram of the compartment is shown in Fig. 3.26. A complete description of the experiments can be found in the NIST WTC report NCSTAR 1-5B [69]. The overall enclosure was rectangular, as were the vents and most of the obstructions. The compartment walls and ceiling were made of 2.54 cm thick marinite. The manufacturer provided the thermal properties of the material used in the calculation. The density was 737 kg/m<sup>3</sup>, conductivity 0.12 W/m/K. The specific heat ranged from 1.17 kJ/kg/K at 93 °C to 1.42 kJ/kg/K at 425 °C. This value was assumed for higher temperatures. The steel used to construct the column and truss flanges was 0.64 cm thick. The density of the steel was assumed to be 7,860 kg/m<sup>3</sup>; its specific heat 0.45 kJ/kg/K.

Two fuels were used in the tests. The properties of the fuels were obtained from measurements made on a series of unconfined burns that are referenced in the test report. The first fuel was a blend of heptane isomers, C<sub>7</sub>H<sub>16</sub>. Its soot yield was set at a constant 1.5 %. The second fuel was a mixture (40 % - 60 % by mass) of toluene, C<sub>7</sub>H<sub>8</sub>, and heptane. Because FDS only considers the burning of a single hydrocarbon fuel, the mixture was taken to be C<sub>7</sub>H<sub>12</sub> with a soot yield of 11.4 %. The radiative fraction for the heptane blend was 0.44; for the heptane/toluene mixture it was 0.39. The heat release rate of the simulated burner was set to that which was measured in the experiments. The spray burner was modeled using reported properties of the nozzle and liquid fuel droplets.

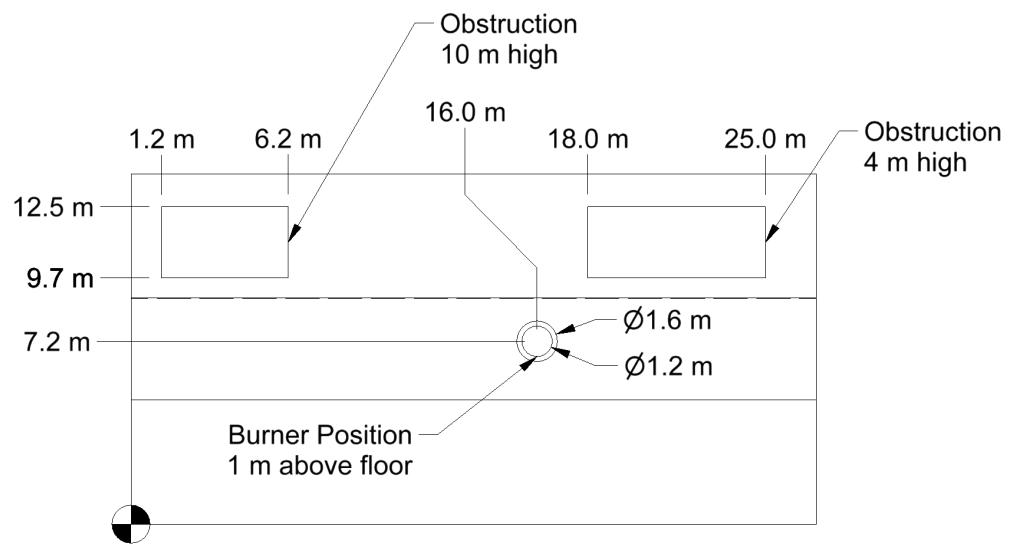
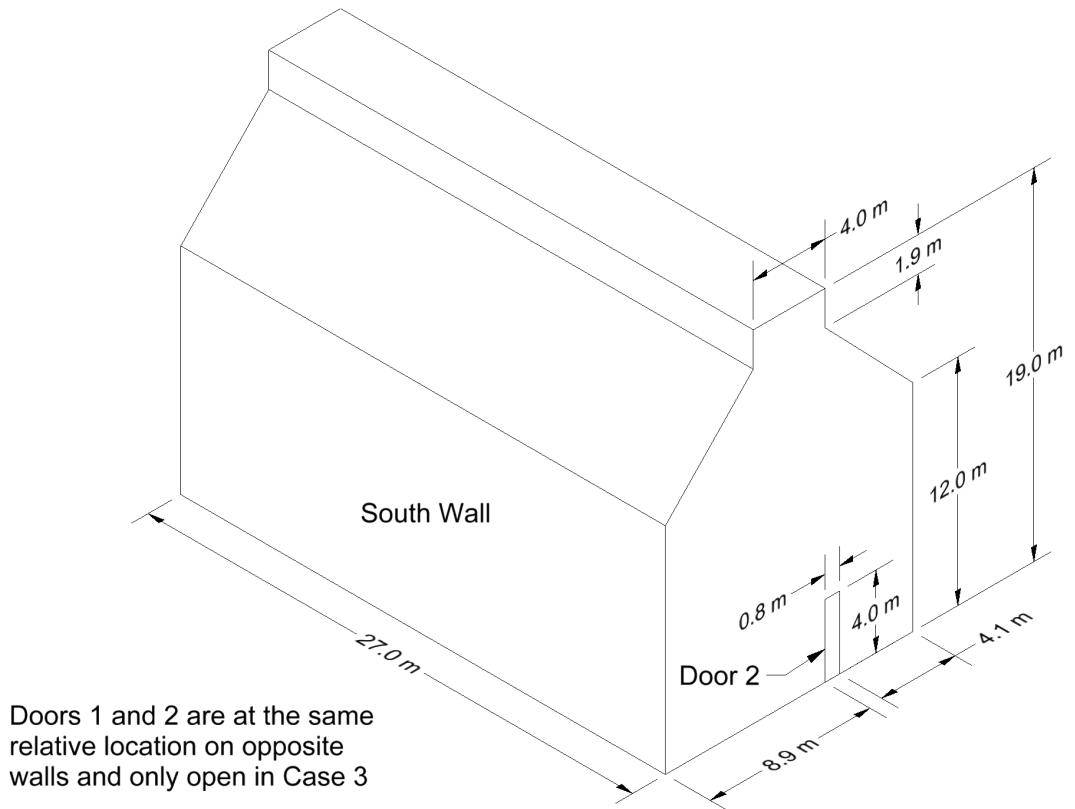


Figure 3.25: Geometry of the VTT Large Fire Test Hall.

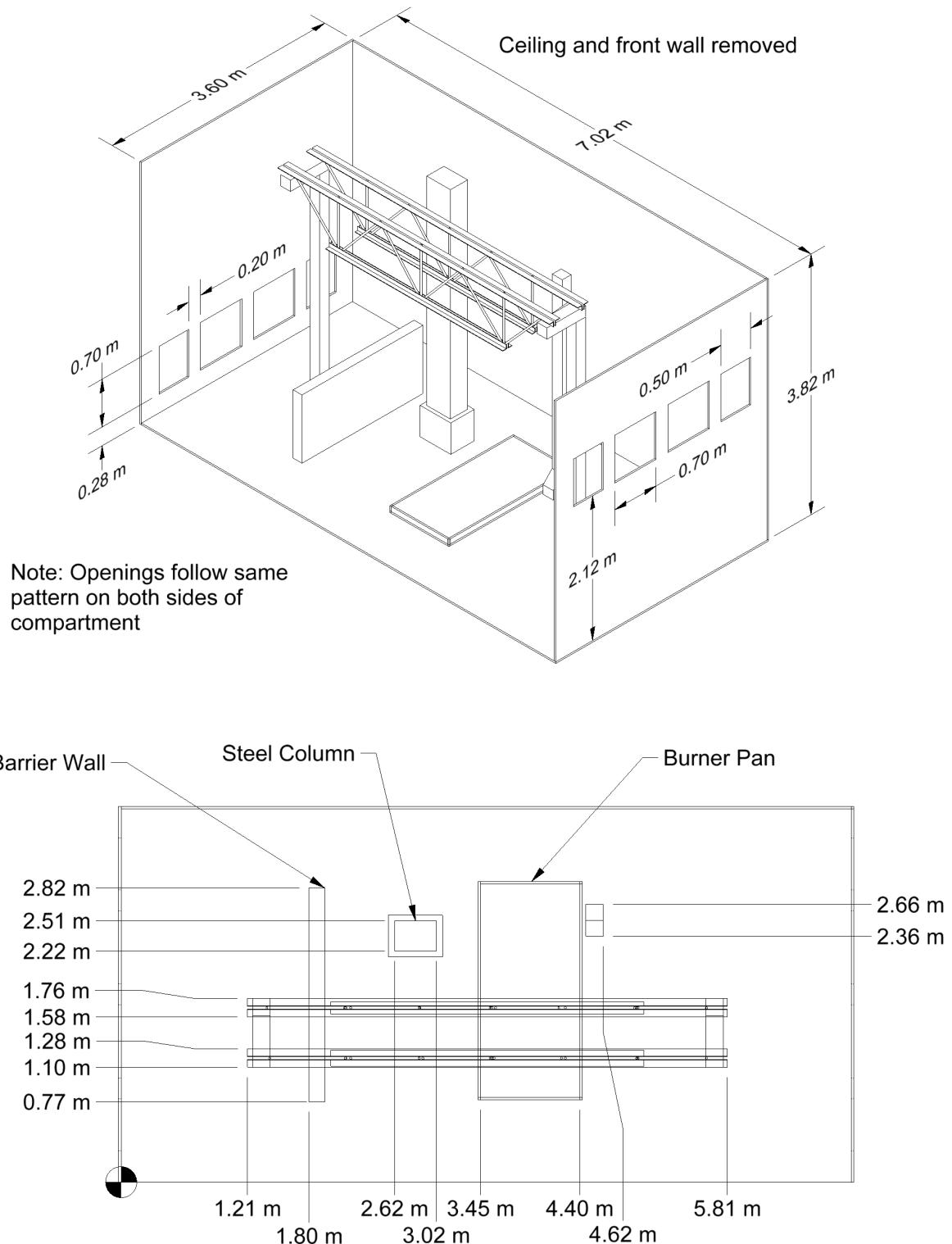


Figure 3.26: Geometry of the compartment used for the WTC Experiments.

## 3.54 Summary of Experiments

Table 3.11 presents a summary of all the experiments described in this chapter in terms of parameters commonly used in fire protection engineering. This “parameter space” outlines the range of applicability of the validation studies performed to date. In other words, if this guide is to be cited as justification for using FDS to simulate a given fire scenario, that scenario must be similar to these experiments in the sense of having comparable physical parameters. These parameters are explained below:

**Heat Release Rate,  $\dot{Q}$ ,** is the range of peak heat release rates of the fires in the test series.

**Fire Diameter,  $D$ ,** is the equivalent diameter of the base of the fire, calculated  $D = \sqrt{4A/\pi}$ , where  $A$  is the area of the base.

**Ceiling Height,  $H$ ,** is the distance from floor to ceiling.

**Fire Froude Number,  $\dot{Q}^*$ ,** is a useful non-dimensional quantity for plume correlations and flame height estimates.

$$\dot{Q}^* = \frac{\dot{Q}}{\rho_\infty c_p T_\infty \sqrt{g D D^2}} \quad (3.3)$$

It is essentially the ratio of the fuel gas exit velocity and the buoyancy-induced plume velocity. Jet fires are characterized by large Froude numbers. Typical accidental fires have a Froude number near unity.

**Flame Height relative to Ceiling Height,  $L_f/H$ ,** is a convenient way to express the physical size of the fire relative to the size of the room. The height of the visible flame, based on Heskestad's correlation, is estimated by:

$$L_f = D \left( 3.7 (\dot{Q}^*)^{2/5} - 1.02 \right) \quad (3.4)$$

**Global Equivalence Ratio,  $\phi$ ,** is the ratio of the mass flux of fuel to the mass flux of oxygen into the compartment, divided by the stoichiometric ratio.

$$\phi = \frac{\dot{m}_f}{r \dot{m}_{O_2}} \equiv \frac{\dot{Q} \text{ (kW)}}{13,100 \text{ (kJ/kg)} \dot{m}_{O_2}} ; \quad \dot{m}_{O_2} = \begin{cases} \frac{1}{2} 0.23 A_0 \sqrt{H_0} & : \text{Natural Ventilation} \\ 0.23 \rho \dot{V} & : \text{Mechanical Ventilation} \end{cases} \quad (3.5)$$

Here,  $r$  is the stoichiometric ratio,  $A_0$  is the area of the compartment opening,  $H_0$  is the height of the opening,  $\rho$  is the density of air, and  $\dot{V}$  is the volume flow of air into the compartment. If  $\phi < 1$ , the compartment is considered “well-ventilated” and if  $\phi > 1$ , the compartment is considered “under-ventilated.”

**Compartment Aspect Ratios,  $W/H$  and  $L/H$ ,** indicate if the compartment is shaped like a hallway, typical room, or vertical shaft.

**Relative Distance along the Ceiling,  $r_{cj}/H$ ,** indicates the distance from the fire plume of a sprinkler, smoke detector, etc., relative to the compartment height,  $H$ .

**Relative Distance from the Fire,  $r_{rad}/D$ ,** indicates whether a “target” is near or far from the fire.

Table 3.11: Summary of important experimental parameters.

Test Series	$\dot{Q}$ (kW)	$D$ (m)	$H$ (m)	$\dot{Q}^*$	$L_f/H$	$\phi$	$W/H$	$L/H$	$r_{ej}/H$	$r_{rad}/D$
Arup Tunnel	5344	1.6	7	1.5	0.8	0.0	1.1	43	0.0 – 1.1	N/A
ATF Corridors	50 – 500	0.5	2.4	0.3 – 3.3	0.3 – 0.9	0.0 – 0.1	0.8	7.1	0.8 – 6.0	N/A
Beyler Hood	8 – 30	0.2	0.5	0.5 – 1.1	0.7 – 1.3	0.2 – 1.7	2.0	2.0	N/A	N/A
Bryant Doorway	34 – 511	0.3	2.4	0.5 – 6.9	0.2 – 1.0	0.0 – 0.2	1.0	2.1	0.6 – 0.8	N/A
Cup Burner	0.3	0.028	Open	2.1	Open	Varying	Open	Open	Open	N/A
FAA Cargo	5	0.1	1.4	1.4	0.2	0.2	2.3	4.8	0.1 – 4.8	N/A
Fleury Heat Flux	100 – 300	0.3 – 0.6	Open	0.3 – 5.5	Open	Open	Open	Open	Open	1.7 – 3.3
FM Panels	30 – 100	0.5	Open	0.2 – 0.5	Open	Open	Open	Open	Open	0
FM/SNL	470 – 516	0.9	6.1	0.6 – 2.4	0.3 – 0.6	0.0 – 0.2	2.0	3.0	0.2 – 0.3	N/A
Hamins CH <sub>4</sub>	0.4 – 162	0.1 – 1.0	Open	0.1	Open	Open	Open	Open	Open	0.1 – 12
Harrison Plumes	5 – 15	0.16	0.5	0.5 – 1.4	0.5 – 1.0	Open	Open	Open	N/A	N/A
Heskestad	10 <sup>2</sup> – 10 <sup>7</sup>	1.1	Open	10 <sup>-1</sup> – 10 <sup>4</sup>	Open	Open	Open	Open	N/A	N/A
LLNL Enclosure	50 – 400	0.6	4.5	0.2 – 1.5	0.1 – 0.4	0.1 – 0.4	0.9	1.3	0.3 – 1.0	N/A
McCaffrey Plume	14 – 57	0.3	Open	0.2 – 0.8	Open	Open	Open	Open	N/A	N/A
NBS Multi-Room	110	0.3	2.4	1.5	0.5	0.0	1.0	5.1	N/A	N/A
NIST FSE	100 – 2500	0.6 – 1.1	2.4	0.5 – 1.8	0.4 – 1.7	0.2 – 5.9	1.0	1.5	0.4 – 0.8	N/A
NIST/NRC	350 – 2200	1.0	3.8	0.3 – 2.0	0.3 – 1.0	0.0 – 0.3	1.9	5.7	0.3 – 2.1	2.0 – 4.0
NIST RSE	50 – 600	0.15	1.0	5.2 – 63	0.9 – 2.8	0.1 – 1.1	1.0	1.5	N/A	N/A
NIST Smoke Alarms	100 – 350	1.0	2.4	0.2 – 0.3	0.2 – 0.5	N/A	1.7	8.3	1.3 – 8.3	N/A
NRCC Facade	5000 – 10300	4.3	2.8	0.1 – 0.2	0.9 – 1.7	0.6 – 1.2	1.6	2.2	N/A	0
NRCC Smoke Tower	3000	2.2	3.4	0.4	1.0	0.7	0.1	0.2	1.2	N/A
NRL/HAI	50 – 520	0.3 – 0.7	Open	1.1 – 1.2	Open	Open	Open	Open	N/A	0
PRISME	480 – 1600	0.7 – 1.1	4.0	1.1	0.5 – 0.8	0.5	1.3	1.5	0.0 – 0.5	2.3 – 5.7
Sandia Plume	2025 – 5450	1.0	Open	1.8 – 5.0	Open	Open	Open	Open	N/A	N/A
SP AST	450	0.3	2.4	6.1	1.1	0.1	1.0	1.5	N/A	N/A
Steckler	31.6 – 158	0.3	2.1	0.8 – 3.8	0.3 – 0.7	0.0 – 0.6	1.3	1.3	N/A	N/A
UL/NFPRF	4400 – 10000	1.0	7.6	4.0 – 9.1	0.7 – 1.0	Open	4.9	4.9	0.6 – 3.9	N/A
UL/NIST Vents	500 – 2000	0.9	2.4	0.7 – 2.6	0.8 – 1.6	0.2 – 0.6	1.8	2.5	1.0 – 2.3	N/A
Ulster SBI	30 – 60	0.2	Open	1.5 – 3.0	Open	Open	Open	N/A	0	N/A
USCG/HAI	250 – 1000	0.3	3.0	6.0 – 24	0.6 – 1.1	0.3 – 1.0	1.7	2.3	N/A	N/A

Table 3.12: Summary of important experimental parameters (continued).

Test Series	$\dot{Q}$ (kW)	D (m)	H (m)	$\dot{Q}^*$	$L_f/H$	$\phi$	$W/H$	$L/H$	$r_{ci}/H$	$r_{rad}/D$
USN Hawaii	100 – 7700	0.3 – 2.5	15	0.7 – 1.3	0.1 – 0.4	Open	4.9	6.5	0 – 1.2	N/A
USN Iceland	100 – 15700	0.3 – 3.4	22	0.7 – 1.3	0.0 – 0.3	Open	2.1	3.4	0 – 1.0	N/A
Vettori Flat	1055	0.7	2.6	2.5	1.1	0.3	2.1	3.5	0.8 – 2.9	N/A
Vettori Sloped	1055	0.7	2.5	2.5	1.2	0.3	2.2	2.9	N/A	N/A
VTT Large Hall	1860 – 3640	1.4 – 1.8	19	0.7	0.2	0	1.0	1.4	0 – 0.6	N/A
WTC	1970 – 3240	1.6	3.8	0.6 – 0.9	0.8 – 1.1	0.3 – 0.5	0.9	1.8	0.0 – 0.8	0.3 – 1.3

Table 3.13 lists a few important parameters related to the numerical resolution of the calculation.

**Characteristic Fire Diameter,  $D^*$ ,** is a useful length scale that incorporates the heat release rate of the fire.

$$D^* = \left( \frac{\dot{Q}}{\rho_\infty c_p T_\infty \sqrt{g}} \right)^{2/5} \quad (3.6)$$

**Plume Resolution Index,  $D^*/\delta x$ ,** is the number of grid cells of length  $\delta x$  that span the characteristic diameter of the fire. The greater its value, the more “resolved” are the fire dynamics.

**Ceiling Height relative to Fire Diameter,  $H/D^*$ ,** is the non-dimensional height of the smoke plume.

Note that the calculations performed for the various validation studies described in this Guide use a wide range of values of the Plume Resolution Index,  $D^*/\delta x$ . There are several reasons for this. First, typical applications of FDS often involve relatively small fires in relatively large spaces, and it is impractical to use a very fine grid that captures the detailed fire dynamics. Second, for some applications the accuracy of calculation is highly dependent on resolving the plume well, but for others, it is less important. For those citing the validation studies in this Guide, it is important that both the physical and numerical parameters are comparable to the given application.

Table 3.13: Summary of important numerical parameters.

Test Series	$D^*$ (m)	$D^*/\delta x$	$H/D^*$
Arup Tunnel	1.8	9	3.8
ATF Corridors	0.3 – 0.7	3 – 7	3.4 – 8.5
Beyler Hood	0.1 – 0.2	5 – 8	2.1 – 3.5
Bryant Doorway	0.2 – 0.7	5 – 14	3.4 – 9.9
Cup Burner	0.04	36	Open
FAA Cargo	0.1	5.6	12
Fleury Heat Flux	0.4 – 0.6	8 – 12	Open
FM Panels	0.2 – 0.4	12 – 19	Open
FM/SNL	0.7	7	8.5 – 8.8
Hamins Burner	0.04 – 0.5	6	Open
Harrison Plumes	0.1 – 0.2	5 – 7	2.8 – 4.4
Heskestad	0.4 – 44	5 – 20	Open
LLNL Enclosure	0.3 – 0.6	1 – 3	6.9 – 15.9
McCaffrey Plume	0.2 – 0.3	5 – 20	Open
NBS Multi-Room	0.4	4	6.2
NIST FSE	0.4 – 1.4	3.8 – 14	1.7 – 6.3
NIST/NRC	0.6 – 1.3	5 – 11	3.1 – 6.5
NIST RSE	0.3 – 0.8	12 – 32	1.3 – 3.5
NIST Smoke Alarms	0.4 – 0.6	3.8 – 6.3	3.8 – 6.3
NRCC Facade	1.8 – 2.4	18 – 24	1.2 – 1.5
NRCC Smoke Tower	1.5	15	18.6
NRL/HAI	0.3 – 0.7	9 – 10	Open
PRISME	0.7 – 1.2	7 – 12	3.4 – 5.6
Sandia Plume	1.2 – 1.8	20 – 118	Open
SP AST	0.7	14	3.5
Steckler	0.2 – 0.4	5 – 9	4.8 – 9.1
UL/NFPRF	1.7 – 2.4	8 – 12	3.2 – 4.5
UL/NIST	0.7 – 1.2	7 – 12	1.9 – 3.4
Ulster SBI	0.2 – 0.3	12 – 15	Open
USCG/HAI	0.5 – 0.9	5 – 9	3.2 – 5.6
USN Hawaii	0.4 – 2.1	2 – 11	7.1 – 40.3
USN Iceland	0.4 – 2.8	2 – 14	7.8 – 59
Vettori Flat	1.0	12	2.8
Vettori Sloped	1.0	10	2.6
VTT Large Hall	1.2 – 1.6	5 – 6	12.1 – 15.8
WTC	0.9 – 1.1	9 – 11	3.5 – 4.1

## Chapter 4

# Quantifying Model Uncertainty

This chapter describes a method to estimate the model uncertainty using comparisons of model predictions with experimental measurements whose uncertainty has been quantified. The method is ideal for complex numerical models like FDS for which a systematic analysis of sub-components is impractical, but for which there exists a relatively large amount of experimental data with which to evaluate the accuracy of the model predictions. If the uncertainty in the experiments can be quantified, the uncertainty in the model can then be expressed in the form of a normal distribution whose mean and standard deviation are estimated from the relative difference between the predicted and measured values.

This method only addresses model uncertainty. It does not account for the uncertainty associated with the model input parameters. How the *parameter uncertainty* is treated depends greatly on the type of application. Regardless of how the parameter uncertainty is calculated, the model uncertainty needs to be addressed independently. In fact, it is incumbent on the model developers to express the uncertainty of the model in as simple a form as possible to enable the end user to assess the impact of parameter uncertainty and then combine the two forms of uncertainty into a final result.

### 4.1 Introduction

The most effective way of introducing the subject of uncertainty in fire modeling is by way of an example. Suppose that a fire model is used to estimate the likelihood that an electrical control cable could be damaged by a fire. It is assumed that the cable loses functionality when its surface temperature reaches 200 °C, and the model predicts that the cable temperature could reach as high as 175 °C. Does this mean that there is no chance of damage? The answer is no, because the input parameters, like the heat release rate of the fire, and the model assumptions, like the way the cables are modeled, are uncertain. The combination of the two – the *parameter uncertainty* and the *model uncertainty* – leave open the possibility that the cable temperature could exceed 200 °C.

This chapter addresses *model uncertainty* only and suggests a simple method to quantify it. While parameter uncertainty is certainly an important consideration in fire modeling, its treatment varies considerably depending on the particular application. For example, in what is often referred to as a “bounding analysis,” the model input parameters are chosen so as to simulate a “maximum credible” or “worst case” fire. In other cases, mean values of the input parameters constitute a “50th percentile” design scenario. Sometimes entire statistical distributions, rather than individual values, of the input parameters are “propagated” through the model in a variety of ways, leading to a statistical distribution of the model output. Notarianni and Parry survey these techniques in the SFPE Handbook [216]. Regardless of the method that is chosen for assessing the impact of the input parameters on the model prediction, there needs to be a way of quantifying the uncertainty of the model itself. In other words, how good is the prediction for a given set of input parameters?

The issue of model uncertainty has been around as long as the models themselves. The scenario above, for example, was considered by Siu and Apostolakis in the early 1980s [217] as part of their development of risk models for nuclear power plants. The fire models at the time were relatively simple. In fact, many were engineering correlations in the form of simple formulae. This made the methods for quantifying their uncertainty reasonably tractable because each formula consisted of only a handful of physical parameters. Over the past thirty years, however, both fire modeling and the corresponding methods of uncertainty analysis have become far more complex. The current generation of computational fluid dynamics fire models require such a large number of physical and numerical parameters that it is considered too cumbersome to estimate model uncertainty by systematically assessing their combined effect on the final prediction. The more practical approach is to compare model predictions with actual fire experiments in a validation study, the conclusions of which typically come in the form of statements like: “The model generally over-predicts the measured temperatures by about 10 %,” or “The model predictions are within about 20 % of the measured heat fluxes.” This information is helpful, at the very least to demonstrate that the model is appropriate for the given application. However, even the statement that the model over-predicts measured temperatures by 10 % is useful not only to gain acceptance of the model but also to provide a better sense of the model’s accuracy, and a greater level of assurance in answering the question posed above. Knowing that the model not only predicted a temperature of 175 °C, but also that the model tends to over-predict temperatures by a certain amount, increases the confidence that the postulated fire would not cause the cable to fail. The probability of cable failure could be quantified further via a statistical distribution like the one shown in Fig. 4.1. The area indicated by the shaded region is the probability that the temperature will exceed 200 °C, even though the model has predicted a peak temperature of only 175 °C.

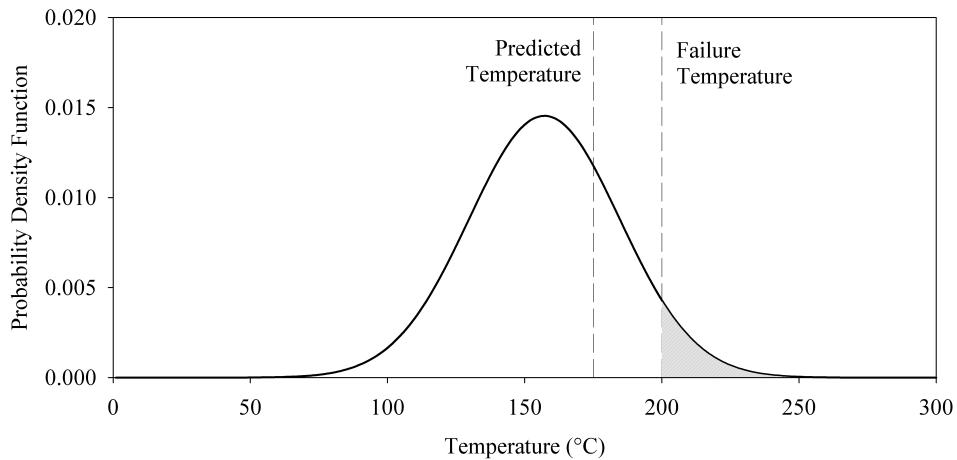


Figure 4.1: Plot showing a possible way of expressing the uncertainty of the model prediction.

This chapter describes a method for expressing *model uncertainty* by way of a distribution like the one shown in Fig. 4.1. The procedure is not a dramatic departure from the current practice of fire model validation in that it relies entirely on comparisons of model predictions and experimental measurements. The advantage of the approach is that it does not demand advanced knowledge of statistics or details of the numerical model. The parameters of the distribution shown in Fig. 4.1, namely the mean and standard deviation, are not generated by the model user. Rather, they are reported as the results of the validation study. The calculation of the probability of exceeding some critical threshold (i.e., the area under the curve) is a simple table look-up or function call in data analysis software like Microsoft Excel®.

## 4.2 Sources of Model Uncertainty

A deterministic fire model is based on fundamental conservation laws of mass, momentum and energy, applied either to entire compartments or smaller control volumes that make up the compartments. A CFD model may use millions of control volumes to compute the solution of the Navier-Stokes equations. However, it does not actually solve the Navier-Stokes equations, but rather an approximate form of these equations. The approximation involves simplifying physical assumptions, like the various techniques for treating subgrid-scale turbulence. One critical approximation is the discretization of the governing equations. For example, the partial derivative of the density,  $\rho$ , with respect to the spatial coordinate,  $x$ , can be written in approximate form as:

$$\frac{\partial \rho}{\partial x} = \frac{\rho_{i+1} - \rho_{i-1}}{2 \delta x} + \mathcal{O}(\delta x^2) \quad (4.1)$$

where  $\rho_i$  is the average value of the density in the  $i$ th grid cell and  $\delta x$  is the spacing between cells. The second term on the right represents all of the terms of order  $\delta x^2$  and higher in the Taylor series expansion and are known collectively as the *discretization error*. These extra terms are simply dropped from the equation set, the argument being that they become smaller and smaller with decreasing grid cell size,  $\delta x$ . The effect of these neglected terms is captured, to some extent, by the subgrid-scale turbulence model, but that is yet another approximation of the true physics. What effect do these approximations have on the predicted results? It is very difficult to determine based on an analysis of the discretized equations. One possibility for estimating the magnitude of the discretization error is to perform a detailed convergence analysis, but this still does not answer a question like, “What is the uncertainty of the model prediction of the gas temperature at a particular location in the room at a particular point in time?”

To make matters worse, there are literally dozens of subroutines that make up a CFD fire model, from its transport equations, radiation solver, solid phase heat transfer routines, pyrolysis model, empirical mass, momentum and energy transfer routines at the wall, and so on. It has been suggested by some that a means to quantify the model uncertainty is to combine the uncertainties of all the model components. However, such an exercise is very difficult, especially for a computational fluid dynamics (CFD) model, for a number of reasons. First, fire involves a complicated interaction of gas and solid phase phenomena that are closely coupled. Second, grid sensitivity in a CFD model or the error associated with a two-layer assumption in a zone model are dependent on the particular fire scenario. Third, fire is an inherently transient phenomenon in which relatively small changes in events, like a door opening or sprinkler actuation, can lead to significant changes in outcome.

Rather than attempt to decompose the model into its constituent parts and assess the uncertainty of each, the strategy adopted here is to compare model predictions to as many experiments as possible. This has been the traditional approach for quantifying model uncertainty in fire protection engineering because of the relative abundance of test data. Consider, for example, the plot shown in Fig. 4.2. This is the typical outcome of a validation study, where in this case a series of heat flux measurements are compared with model predictions. The diagonal line indicates where the prediction and measurement agree. But because there is uncertainty associated with each, it cannot be said that the model is perfect if its predictions agree exactly with measurements. There needs to be a way of quantifying the uncertainties of each before any conclusions can be drawn. Such an exercise would result in the uncertainty bars<sup>1</sup> shown in the figure. The horizontal bar associated with each point represents the uncertainty in the measurement itself. For example, the heat flux gauge is subject to uncertainty due to its design and fabrication. Because the horizontal bar represents the experimental uncertainty, it is assumed that the vertical bar represents the model uncertainty. This is only partially true. In fact the vertical bar represents the total uncertainty of the prediction, which is a combination of the *model* and *parameter* uncertainties. The physical input parameters, like the heat

---

<sup>1</sup>The data in Fig. 4.2 was extracted from Ref. [218]. The uncertainty bars are for demonstration only.

release rate and material properties, are based on measurements that are reported in the documentation of the experiment. The total *experimental uncertainty* is represented by all of the horizontal bar and part of the vertical. If the *experimental uncertainty* can be quantified, then the *model uncertainty* can be obtained as a result.

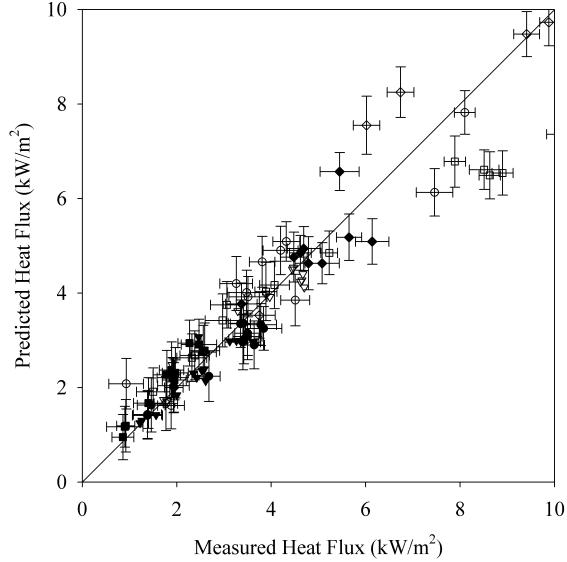


Figure 4.2: Example of a typical scatter plot of model predictions and experimental measurements.

### 4.3 Experimental Uncertainty

The difference between a model prediction and an experimental measurement is a combination of three components: (1) uncertainty in the measurement of the predicted quantity, (2) uncertainty in the model input parameters, and (3) uncertainty in the model physics and numerics. The first two components are related to uncertainty in the measured input and output quantities. For example, consider the hot gas layer (HGL) temperature. First, the thermocouple measurements used to calculate the HGL temperature have uncertainty. Second, the measurement of the heat release rate of the fire has uncertainty, and this uncertainty affects the predicted HGL temperature. Third, the model itself, including its physical assumptions and numerical approximations, has uncertainty. The objective of the validation study is to quantify this third component, the model uncertainty. To do this, the first two components of uncertainty related to the experimental measurements must be quantified. The combination of these two, the experimental uncertainty, is the objective of this section.

For many of the experiments considered in this guide, the uncertainty of the measurements was not documented. Instead, estimates of measurement uncertainty are made based on those few experiments that do include uncertainty estimates, and this information is supplemented by engineering judgment. In the following two subsections, each component of the experimental uncertainty is considered separately. First, the uncertainty in the measurement of the predicted quantity of interest, like the surface temperature of the compartment. Second, the uncertainties of the most important input parameters are propagated through simple models to quantify their effect on the predicted quantity. Then, the uncertainties are combined via simple quadrature to estimate the total experimental uncertainty.

Note that in this guide, all uncertainties are expressed in relative form, as a percentage. The uncertainty of a measurement is a combination of the systematic uncertainty associated with the various underlying measurements and assumptions; and the random uncertainty associated with the conduct of the experiment. Following the recommended guidelines for evaluating and expressing the uncertainty of measurements [219], the systematic and random uncertainty values are combined via quadrature resulting in a combined relative standard uncertainty.

### 4.3.1 Uncertainty of Common Fire Measurements

Because most of the experiments described in this guide have little or no information about the uncertainty of the measurements, much of this section is based on the uncertainty analysis contained in the test report of the NIST/NRC Experiments<sup>2</sup>. The types of measurements described in this report are the ones most commonly used in large scale fire experiments. They include thermocouples for gas and surface temperature measurements, heat flux gauges, smoke and gas analyzers, and pressure sensors.

#### Thermocouples

Thermocouples are used to measure both gas and surface temperatures. They come in a variety of sizes and are constructed of different types of metals. Some are shielded or aspirated to limit the influence of thermal radiation from remote sources. In Ref. [115], Hamins et al. estimate the uncertainty of the various thermocouple measurements. Estimates of the combined relative standard uncertainty fall in a range between 2.5 % and 7.5 %. Because it is not possible to analyze the thousands of thermocouple measurements made in the experiments, the relative standard uncertainty applied to all thermocouple measurements is 5 %.

#### Heat Flux Gauges

For the NIST/NRC experiments, four types of heat flux gauges were used, some of which measured the total heat flux, and some of which measured only the radiation heat flux. The uncertainty associated with a heat flux measurement depends on many factors, including gauge characteristics, the calibration conditions and accuracy, as well as the incident flux modes (convective, radiative, conductive). Typically, the reported relative standard uncertainty of heat flux gauges varies from about 2.5 % to 5 %, with the measurement uncertainty dominated by uncertainty in the calibration and repeatability of the measurement. Repeatability of the various heat flux measurements in the NIST/NRC experiments was determined by examining measurements by the same instruments for different pairs of repeat tests. The difference between the measurements was about 3.5 %, on average, for both the radiative flux measurements and the total flux measurements. For all of the experiments described in this guide, a combined relative standard uncertainty of 5 % is suggested based on the measurement repeatability and calibration uncertainties reported for the NIST/NRC experiments.

#### Gas Analyzers

Gas concentrations were measured in two sets of experiments conducted at NIST, the NIST/NRC and the WTC experiments. The volume fractions of the combustion products, carbon monoxide (CO) and carbon dioxide (CO<sub>2</sub>), were measured using gas sampling in conjunction with non-dispersive infrared analyzers, while the oxygen (O<sub>2</sub>) volume fraction was typically measured using a paramagnetic analyzer. Gases were

---

<sup>2</sup>Note that the uncertainties in Ref. [115] are reported in the form of 95 % confidence intervals, or “2-sigma”. This is referred to as the expanded uncertainty with a coverage factor of 2. To avoid confusion, in this report the uncertainty of all measurements and model predictions shall be reported in terms of a relative standard uncertainty; that is, the estimated standard deviation of the measured or predicted quantity.

extracted through stainless steel or other types of lines and were pumped from the compartment and passed through the analyzers. For several reasons, water in the sample was typically filtered, so the reported results are denoted as “dry”. Analyzers were calibrated through the use of standard gas mixtures, with low relative uncertainties. Problems with the technique may involve instrument drift, analyzer response, incomplete and partial drying of sample gases, or (in the case when drying is not used) undetermined amounts of water vapor in the oxygen cell, which result in inaccurate readings.

For the NIST/NRC experiments, the species were measured in both the upper and lower layers. The relative standard uncertainty in the measured values was about 1.5 % for both the O<sub>2</sub> depletion and the CO<sub>2</sub> measurements. The largest contributors were the uncertainty in the composition of the calibration gas and the possibility of an undetermined amount of water vapor in the sample. The difference between the repeat measurements was about 1 %, on average, for both the O<sub>2</sub> depletion and the CO<sub>2</sub> measurements. Therefore, the combined relative standard uncertainty is estimated to be 2 % for measurements of both the O<sub>2</sub> decrease and the CO<sub>2</sub> increase.

### **Smoke Light Extinction Calculations**

The smoke concentration was measured in the NIST/NRC experiments using laser transmission at 632.8 nm. The reported mass concentration of smoke,  $m_s'''$ , was computed using the following expression:

$$m_s''' = \frac{\ln(I_0/I)}{\phi_s L} \quad (4.2)$$

where  $L$  is the path length,  $I$  and  $I_0$  are the laser signal and reference signal, respectively, and  $\phi_s$  is the specific extinction coefficient, which has a nearly universal value of 8.7 m<sup>2</sup>/g ± 5 % for hydrocarbons [220]. The systematic relative standard uncertainty of this measurement was reported to be 9 % in Ref. [115], with the dominant contribution to the uncertainty coming from drift in the laser measurement. Repeatability of the smoke measurement was investigated for the NIST/NRC experiments. The mean difference between replicate measurements was about 11 %. Therefore, a combined relative standard uncertainty of 14 % is suggested.

### **Pressure Gauges**

The uncertainty in pressure measurements is typically small, but depends on the sensor type and calibration. In the NIST/NRC experiments, the differential pressure gauge used was temperature compensated, highly linear, and very stable. The estimated relative standard uncertainty is 0.5 %.

### **Bi-Directional Probes**

Gas velocity is typically measured in fire experiments using bi-directional probes. These devices work like pitot tubes but have much larger openings. Bryant [136] estimates that the standard relative uncertainty of this measurement, assuming that the probe is aligned well with the flow, is approximately 7 %.

### **Oxygen Consumption Calorimeters**

For all of the experiments described in this guide, the heat release rate (HRR) is determined either via oxygen consumption calorimetry or via the mass loss rate multiplied by the fuel heat of combustion. The accuracy of each method varies roughly between 2.5 %, where the fire is small and the fuel stoichiometry is well understood, and 13 %, where the fire is large or the smoke is not completely captured or the fuel stoichiometry is not well understood. In Ref. [115], the relative standard uncertainty of a 2 MW heptane

spray fire is estimated to be 7.5 %. It is assumed that the uncertainty of the HRR for the other experiments is comparable.

### Device Activation or Failure Time

Fire models are often used to predict the time to activation of devices like sprinklers and smoke detectors, and time to failure of critical equipment like electrical cables. Measuring activation or failure times in experiments is fairly precise, and, thus, the uncertainty of such measurements is essentially zero. Almost all of the uncertainty associated with these times is in the measurement or characterization of the mechanism of activation or failure. For example, the activation of a sprinkler is based on its measured RTI (Response Time Index) and activation temperature. Estimates of the uncertainty of these parameters are discussed in the next section.

### 4.3.2 Propagation of Input Parameter Uncertainty

Empirical correlations for basic fire phenomena provide a convenient way to assess the propagation of the uncertainty of the model input parameters. The more complex fire models may require dozens of physical and numerical input parameters for a given fire scenario. However, only a few of these parameters, when varied over their plausible range of values, significantly impact the results. For example, the thermal conductivity of the compartment walls does not significantly affect a predicted cable surface temperature, but the HRR of the fire does. The relatively simple empirical models identify the key parameters that impact the predicted quantity, and they provide the means to quantify the functional relationship between model inputs and outputs.

### Gas and Surface Temperatures

According to the McCaffrey, Quintiere, and Harkleroad (MQH) correlation, the HGL temperature rise,  $T - T_0$ , in compartment fire is proportional to the HRR,  $\dot{Q}$ , raised to the two-thirds power:

$$T - T_0 = C \dot{Q}^{\frac{2}{3}} \quad (4.3)$$

The constant,  $C$ , involves a number of geometric and thermo-physical parameters that are unique to the given fire scenario. By way of differentials, this empirical relationship can be expressed in the form:

$$\frac{\Delta T}{T - T_0} \approx \frac{2}{3} \frac{\Delta \dot{Q}}{\dot{Q}} \quad (4.4)$$

This is a simple formula with which one can readily estimate the relative change in the temperature rise due to the relative change in the HRR. The uncertainty in the HRR of the validation experiments was estimated to be 7.5 %. Equation (4.4) indicates that a 7.5 % increase in the HRR should lead to a 5 % increase in the HGL temperature.

### HGL Depth

Most of the experiments for which the HGL depth was predicted had at least one open door or window that effectively determined the steady-state HGL depth. Unlike all of the other predicted quantities, the HGL depth is relatively insensitive to the fire's HRR. It is largely determined by the height of the opening, and for this reason there is essentially no uncertainty associated with the model inputs that affect the layer depth.

## Gas and Smoke Concentration

Most fire models assume that combustion product gases and soot, once beyond the flaming region of the fire, are passively transported throughout the compartment. The major products of combustion, like CO<sub>2</sub> and water vapor, plus the major reactant, O<sub>2</sub>, are generated, or consumed, in direct proportion to the burning rate of the fuel, which is directly proportional to the HRR. The mass fraction of any species in the HGL is directly proportional to the product of its yield and the HRR.

For many of the experiments described in this guide, the yields of the major product gases like O<sub>2</sub> and CO<sub>2</sub> from pure fuels like methane gas and heptane liquid are known from the basic stoichiometry to a high level of accuracy. Thus, the relative uncertainty in the concentration of major products gases is the same as that of the HRR, 7.5 %. The uncertainty in the smoke concentration, however, is a combination of the uncertainty of the HRR and the soot yield. The relative standard uncertainty of the soot yield of heptane reported in Ref. [115] is 11 %. The uncertainties for HRR and soot yield are combined via quadrature and the resulting expanded relative uncertainty is 13 %.

## Pressure

In a closed, ventilated compartment, the average pressure,  $p$ , is governed by the following equation:

$$\frac{dp}{dt} = \frac{\gamma - 1}{V} (\dot{Q} - \dot{Q}_{\text{loss}}) + \frac{\gamma p}{V} (\dot{V} - \dot{V}_{\text{leak}}) \quad (4.5)$$

where  $\gamma$  is the ratio of specific heats (about 1.4),  $V$  is the compartment volume,  $\dot{Q}$  is the HRR,  $\dot{Q}_{\text{loss}}$  is the sum of all heat losses to the walls,  $\dot{V}$  is the net ventilation rate into the compartment, and  $\dot{V}_{\text{leak}}$  is the leakage rate out of the compartment. The leakage rate is a function of the compartment over-pressure:

$$\dot{V}_{\text{leak}} = A_{\text{leak}} \sqrt{\frac{2(p - p_{\infty})}{\rho_{\infty}}} \quad (4.6)$$

The maximum compartment pressure is achieved when the pressure rise term in Eq. (4.5) is set to zero. Rearranging terms yields an estimate for the maximum pressure:

$$(p - p_{\infty})_{\max} \approx \frac{\rho_{\infty}}{2} \left( \frac{(\gamma - 1)(\dot{Q} - \dot{Q}_{\text{loss}}) + \gamma p_{\infty} \dot{V}}{\gamma p_{\infty} A_{\text{leak}}} \right)^2 \quad (4.7)$$

The test report for the NIST/NRC experiments contains estimates of the uncertainty in the HRR, ventilation rate and leakage area. To calculate the uncertainty in the maximum pressure rise resulting from the uncertainty in these three parameters, the pressure rise estimate in Eq. (4.7) was calculated using 1000 randomly selected sets of values of the HRR, ventilation rate, and leakage area. These parameters were assumed to be randomly distributed with mean values of 1000 kW, 1 m<sup>3</sup>/s, and 0.06 m<sup>2</sup> and relative standard uncertainties of 75 kW, 0.1 m<sup>3</sup>/s, and 0.0021 m<sup>2</sup>. The mean values of these parameters were typical of the NIST/NRC experiments, and the uncertainties were reported in the test report. The resulting relative standard uncertainty in the pressure of a closed compartment due to the uncertainty in the HRR, ventilation rate, and leakage area is 21 %.

For an open compartment, in which the ventilation rate and leakage area have much less influence, the relative standard uncertainty in the pressure is twice that of the HRR, 15 %.

## Velocity

Fire-induced velocities, as in a plume or ceiling jet, are roughly proportional to the HRR to the 1/3 power [221]. Given that the relative standard uncertainty in the HRR is 7.5 %, the uncertainty in gas velocity due to the propagated effect of the uncertainty in the HRR is 2.5 %.

## Heat Flux

The heat flux to a target or wall is a combination of direct thermal radiation from the fire and convective and thermal radiation from the HGL. If the heat flux is predominantly due to the thermal radiation of the fire, it can be approximated using the point source radiation model:

$$\dot{q}'' = \frac{\chi_r \dot{Q}}{4\pi r^2} \quad (4.8)$$

where  $\chi_r$  is the radiative fraction,  $\dot{Q}$  is the HRR, and  $r$  is the distance from the fire. The relative standard uncertainty of the heat flux is a combination of the uncertainty in the radiative fraction and the HRR:

$$\frac{\delta \dot{q}''}{\dot{q}''} \approx \frac{\delta \dot{Q}}{\dot{Q}} + \frac{\delta \chi_r}{\chi_r} \quad (4.9)$$

Reference [115] estimates the relative standard uncertainty of the radiative fraction of a heptane pool fire to be 8 %. Combined with the 7.5 % uncertainty in the HRR (via quadrature) yields a 11 % relative standard uncertainty in the heat flux directly from a fire.

The heat flux to a cold surface due to the exposure to hot gases and not necessarily the fire itself is the sum of radiative and convective components:

$$\dot{q}'' = \varepsilon \sigma (T_{\text{gas}}^4 - T_{\infty}^4) + h (T_{\text{gas}} - T_{\infty}) \quad (4.10)$$

where  $\varepsilon$  is the surface emissivity,  $\sigma$  is the Stefan-Boltzmann constant,  $T_{\text{gas}}$  is the gas temperature,  $T_{\infty}$  is the ambient temperature, and  $h$  is the convective heat transfer coefficient. From the discussion above, the relative standard uncertainty in the gas temperature rise above ambient is 5 % resulting from an estimated uncertainty in the HRR of 7.5 %. There is also uncertainty in the convective heat transfer coefficient, but this is attributed to the model, not the experimental measurements. Thus, the uncertainty in the heat flux is largely a function of the uncertainty in the gas temperature which is largely a function of the HRR. As was done for the pressure, 1000 randomly selected values of gas temperature with a mean of 300 °C above ambient and an relative uncertainty of 5 % resulted in a corresponding uncertainty of 9 % in the heat flux.

In actual compartment fires, the heat flux to surfaces is a combination of direct thermal radiation from the fire and indirect radiation and convection from the hot gases. Given that the calculation of the former incurs a 11 % relative standard uncertainty and the latter 9 %, to simplify the analyses, a value of 10 % is used for all heat flux predictions.

## Sprinkler Activation Time

The uncertainty in the reported sprinkler activation times is due mainly to uncertainties in the measured HRR, RTI (Response Time Index), and activation temperature. There is a negligible uncertainty in the measured activation time itself, which is typically determined with a pressure transducer. To determine the effect of the uncertainties in the HRR, RTI and activation temperature, consider the ordinary differential equation governing the temperature,  $T_{\text{link}}$ , of a conventional glass bulb of fusible link sprinkler:

$$\frac{dT_{\text{link}}}{dt} = \frac{\sqrt{u}}{\text{RTI}} (T_{\text{gas}} - T_{\text{link}}) \quad (4.11)$$

Here,  $u$  and  $T_{\text{gas}}$  are the velocity and the temperature of the ceiling jet, respectively. According to Alpert's ceiling jet correlation [221], the ceiling jet temperature and velocity are proportional to the HRR raised to the power of 2/3 and 1/3, respectively. Given the relative standard uncertainty in the HRR of 7.5 %, the uncertainty in the ceiling jet temperature and velocity are, thus, 5 % and 2.5 %, respectively. As for the RTI

and activation temperature, these values are measured experimentally and the uncertainties differ depending on the test procedure. Vettori [76] reports that the RTI of the sprinklers used in his experiments is  $56 \text{ (m}\cdot\text{s)}^{1/2}$  with a relative standard uncertainty of 11 %, and that the activation temperature is  $68^\circ\text{C} \pm 2.4^\circ\text{C}$ . This latter uncertainty estimate is assumed to represent one standard deviation. Assuming an ambient temperature of approximately  $20^\circ\text{C}$ , the relative standard uncertainty in the activation temperature is assumed to be 5 %.

To determine how the uncertainties in the measured parameters affect the sprinkler activation time, Eq. (4.11) was integrated 1000 times using random selections of the ceiling jet temperature and velocity, RTI, and activation temperature. The mean ceiling jet temperature was increased linearly at rates varying from  $0.5^\circ\text{C/s}$  to  $2^\circ\text{C/s}$ , consistent with the variety of growth rates measured by Vettori. The mean ceiling jet velocity was assumed to be 1 m/s. This procedure yielded a relative standard uncertainty in the sprinkler activation time of 6 %.

The activation times recorded by Vettori include two or three replicates for each configuration. The standard deviation of the 45 measured activation times, normalized by the mean of each set of replicates, was 6 %, consistent with the result obtained above.

### Number of Activated Sprinklers

Alpert's ceiling jet correlation [221] predicts the temperature rise,  $T - T_\infty$  ( $^\circ\text{C}$ ), as a function of the HRR,  $\dot{Q}$  (kW), and radial distance,  $r$  (m), from the plume centerline:

$$T - T_\infty = 5.38 \frac{\dot{Q}^{2/3}/H^{5/3}}{(r/H)^{2/3}} \quad ; \quad r/H > 0.18 \quad (4.12)$$

For a given ceiling height,  $H$ , the radial extent of the sprinkler activation temperature is directly proportional to  $\dot{Q}$ . The number of activated sprinklers is roughly proportional to the square of this radial distance, assuming the sprinklers are uniformly spaced on a rectangular grid. Thus, the uncertainty in the number of activated sprinklers due to the uncertainty in the HRR is 15 %.

### Electrical Cable Failure Time

The uncertainty in the reported cable failure times is due mainly to uncertainties in the measured exposing temperature, cable diameter, and jacket thickness. The uncertainty in the measured mass per unit length of the cable is assumed to be negligible. To determine the uncertainty in the cable failure time, the heat conduction equation in the THIEF model was solved numerically using 10,000 random selections of the exposing temperature, cable diameter, and jacket thickness. The cable diameter was varied from 16.25 mm to 16.35 mm, and the jacket thickness was varied from 1.45 mm to 1.55 mm. The uncertainty in the exposing temperature of the cylindrical heater was assumed to be 2.5 %, the lower bound of the range of uncertainty estimates for thermocouple measurements. The mass per unit length of the cable was assumed to be 0.529 kg/m, and the ambient temperature was assumed to be  $20^\circ\text{C}$ . This procedure yielded an estimated relative standard uncertainty in the cable failure time of 12 %.

### Smoke Detector Activation Time

There is a single set of experiments with which to evaluate model predictions of smoke detector activation time, the NIST Home Smoke Alarm Experiments. The test report [173] does not include detailed information about the alarm mechanism within the various smoke detectors used in the experiments. Thus, from a modeling standpoint, these devices are “black boxes” and their activation can only be discerned from a variety of empirical techniques, the most popular of which is to assume that the smoke detector behaves like a sprinkler or heat detector whose activation is governed by Eq. (4.11) with a low activation temperature and

RTI, Bukowski and Averill [222] suggest an activation temperature of 5 °C to be typical of many residential smoke alarms. The propagated uncertainty of this estimate is difficult to determine because temperature rise is not particularly well-correlated with smoke concentration within the sensing chamber of the detector. Nevertheless, the relative standard deviation of the normalized activation times for the NIST Home Smoke Alarm Experiments is 34 %. Without more detailed information about the activation criteria, the models cannot predict the activation times more accurately than this value.

### 4.3.3 Summary of Experimental Uncertainty Estimates

Table 4.1 summarizes the estimated uncertainties of the major output quantities. The right-most column in the table represents the total experimental uncertainty, denoted as  $\tilde{\sigma}_E$ , a combination of the uncertainty in the measurement of the output quantity itself, along with the propagated uncertainties of the key measured input quantities. This total experimental uncertainty is obtained by taking the square root of the sum of the squares of the measurement and propagation uncertainties that have been estimated in the previous two sections. It is assumed that the two forms of uncertainty are independent.

Table 4.1: Summary of uncertainty estimates. All values are expressed in the form of a standard relative uncertainty.

Output Quantity	Measurement Uncertainty	Propagated Input Uncertainty	Combined Uncertainty, $\tilde{\sigma}_E$
Gas and Solid Temperatures	0.05	0.05	0.07
HGL Depth	0.05	0.00	0.05
Gas Concentrations	0.02	0.08	0.08
Smoke Concentration	0.14	0.13	0.19
Pressure, Closed Compartment	0.01	0.21	0.21
Pressure, Open Compartment	0.01	0.15	0.15
Velocity	0.07	0.03	0.08
Heat Flux	0.05	0.10	0.11
No. Activated Sprinklers	0.00	0.15	0.15
Sprinkler Activation Time	0.00	0.06	0.06
Cable Failure Time	0.00	0.12	0.12
Smoke Alarm Activation Time	0.00	0.34	0.34

## 4.4 Calculating Model Uncertainty

This section describes a method for calculating the *model uncertainty* [223]. Specifically, this entails developing formulae for the mean and standard deviation of a statistical distribution like the one shown in Fig. 4.1. These formulae are functions solely of the model predictions and the experimental measurements against which the model is compared. The objective is to characterize the performance of the model in predicting a given quantity of interest (e.g., the hot gas layer temperature) with two parameters; one that expresses the tendency for the model to under or over-predict the true value of the quantity and one that expresses the degree of scatter about the true value.

The predicted and measured values of the quantity of interest are obtained from one or more validation studies. Figure 4.3 is a typical example of a comparison of model and measurement. Given that usually dozens of such measurements are made during each experiment, and potentially dozens of experiments are conducted as part of a test series, hundreds of such plots can be produced for any given quantity of interest. Usually, the data is condensed into a more tractable form by way of a single metric with which to compare

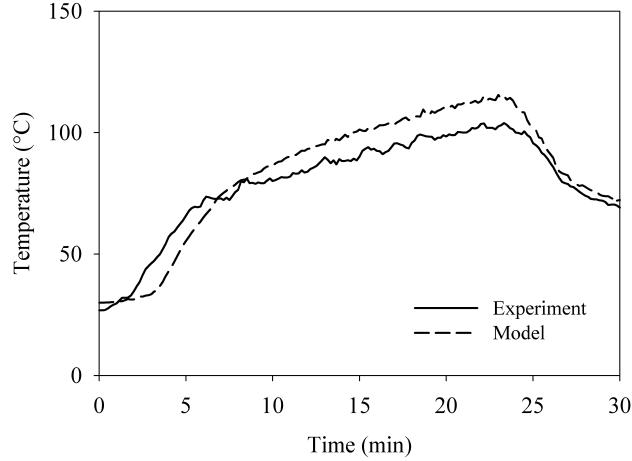


Figure 4.3: Example of a typical time history comparison of model prediction and experimental measurement.

the two curves like the ones shown in Fig. 4.3. Peacock et al. [224] discuss various possible metrics. A commonly used metric is simply to compare the measured and predicted peak values. If the data is spiky, some form of time-averaging can be used. Regardless of the exact form of the metric, what results from this exercise is a pair of numbers for each time history,  $(E_i, M_i)$ , where  $i$  ranges from 1 to  $n$  and both  $M_i$  and  $E_i$  are positive numbers expressing the increase in the value of a quantity above its ambient. As mentioned above, measurements from full-scale fire experiments often lack uncertainty estimates. In cases where the uncertainty is reported, it is usually expressed as either a standard deviation or confidence interval about the measured value. In other words, there is rarely a reported systematic bias in the measurement because if a bias can be quantified, the reported values are adjusted accordingly. For this reason, assume that a given experimental measurement,  $E_i$ , is normally distributed about the “true” value,  $\theta_i$ , and there is no systematic bias:

$$E | \theta \sim N(\theta, \sigma_E^2) \quad (4.13)$$

The notation<sup>3</sup>  $E | \theta$  means that  $E$  is conditional on a particular value of  $\theta$ . This is the usual way of defining a likelihood function. It is convenient to use the so-called delta method<sup>4</sup> to obtain the approximate distribution

$$\ln E | \theta \sim N\left(\ln \theta - \frac{\tilde{\sigma}_E^2}{2}, \tilde{\sigma}_E^2\right) \quad (4.14)$$

The purpose of applying the natural log to the random variable is so that its variance can be expressed in terms of the relative uncertainty,  $\tilde{\sigma}_E = \sigma_E / \theta$ . This is the way that experimental uncertainties are reported.

<sup>3</sup>Note that the subscript,  $i$ , has been dropped merely to reduce the notational clutter.

<sup>4</sup>Given the random variable  $X \sim N(\mu, \sigma^2)$ , the delta method [225] provides a way to estimate the distribution of a function of  $X$ :

$$g(X) \sim N\left(g(\mu) + g''(\mu) \sigma^2 / 2, (g'(\mu) \sigma)^2\right)$$

In addition, the results of past validation exercises, when plotted as shown in Fig. 4.2, form a wedge-shaped pattern that suggests that the difference between predicted and measured values is roughly proportional to the magnitude of the measured value.

It cannot be assumed, as in the case of the experimental measurements, that the model predictions have no systematic bias. Instead, it is assumed that the model predictions are normally distributed about the true values multiplied by a bias factor,  $\delta$ :

$$M | \theta \sim N(\delta \theta, \sigma_M^2) \quad (4.15)$$

The standard deviation,  $\sigma_M$ , and the bias factor,  $\delta$ , represent the model uncertainty. Again, the delta method renders a distribution for  $\ln M$  whose parameters can be expressed in terms of a relative standard deviation:

$$\ln M | \theta \sim N\left(\ln \delta + \ln \theta - \frac{\tilde{\sigma}_M^2}{2}, \tilde{\sigma}_M^2\right) ; \quad \tilde{\sigma}_M = \frac{\sigma_M}{\delta \theta} \quad (4.16)$$

Combining Eq. (4.14) with Eq. (4.16) yields:

$$\ln M - \ln E = \ln(M/E) \sim N\left(\ln \delta - \frac{\tilde{\sigma}_M^2}{2} + \frac{\tilde{\sigma}_E^2}{2}, \tilde{\sigma}_M^2 + \tilde{\sigma}_E^2\right) \quad (4.17)$$

To estimate the mean and standard deviation of the distribution<sup>5</sup>, first define:

$$\overline{\ln(M/E)} = \frac{1}{n} \sum_{i=1}^n \ln(M_i/E_i) \quad (4.18)$$

The least squares estimate of the standard deviation of the combined distribution is defined as:

$$\tilde{\sigma}_M^2 + \tilde{\sigma}_E^2 \approx \frac{1}{n-1} \sum_{i=1}^n \left[ \ln(M_i/E_i) - \overline{\ln(M/E)} \right]^2 \quad (4.19)$$

Recall that  $\tilde{\sigma}_E$  is known and the expression on the right can be evaluated using the pairs of measured and predicted values. Equation (4.19) imposes a constraint on the value of the experimental uncertainty,  $\tilde{\sigma}_E$ . A further constraint is that  $\tilde{\sigma}_M$  cannot be less than  $\tilde{\sigma}_E$  because it is not possible to demonstrate that the model is more accurate than the measurements against which it is compared. Combining the two constraints leads to:

$$\tilde{\sigma}_E^2 < \frac{1}{2} \text{Var}(\ln(M/E)) \quad (4.20)$$

An estimate of  $\delta$  can be found using the mean of the distribution:

$$\delta \approx \exp\left(\overline{\ln(M/E)} + \frac{\tilde{\sigma}_M^2}{2} - \frac{\tilde{\sigma}_E^2}{2}\right) \quad (4.21)$$

Taking the assumed normal distribution of the model prediction,  $M$ , in Eq. (4.15) and using a Bayesian argument<sup>6</sup> with a non-informative prior for  $\theta$ , the posterior distribution can be expressed:

$$\delta \theta | M \sim N(M, \sigma_M^2) \quad (4.22)$$

---

<sup>5</sup>The assumption that  $\ln(M/E)$  is normally distributed has been tested for each quantity of interest discussed in the chapters ahead. The results are shown in Section 16.2.

<sup>6</sup>The form of Bayes theorem used here states that the posterior distribution is the product of the prior distribution and the likelihood function, normalized by their integral:  $f(\theta|M) = p(\theta)f(M|\theta)/\int p(\theta)f(M|\theta)d\theta$ . A constant prior is also known as a Jeffreys prior [226].

The assumption of a non-informative prior implies that there is not sufficient information about the prior distribution (i.e., the true value) of  $\theta$  to assume anything other than a uniform<sup>7</sup> distribution. This is equivalent to saying that the modeler has not biased the model input parameters to compensate for a known bias in the model output. For example, if a particular model has been shown to over-predict compartment temperature, and the modeler has reduced the specified heat release rate to better estimate the true temperature, then it can no longer be assumed that the prior distribution of the true temperature is uniform. Still another way to look at this is by analogy to target shooting. Suppose a particular rifle has a manufacturers defect such that, on average, it shoots 10 cm to the left of the target. It must be assumed that any given shot by a marksman without this knowledge is going to strike 10 cm to the left of the intended target. However, if the marksman knows of the defect, he or she will probably aim 10 cm to the right of the intended target to compensate for the defect. If that is the case, it can no longer be assumed that the intended target was 10 cm to the right of the bullet hole.

The final step in the derivation is to rewrite Eq. (4.22) as:

$$\theta | M \sim N\left(\frac{M}{\delta}, \tilde{\sigma}_M^2 \left(\frac{M}{\delta}\right)^2\right) \quad (4.23)$$

This formula has been obtained<sup>8</sup> by dividing by the bias factor,  $\delta$ , in Eq. (4.22). To summarize, given a model prediction,  $M$ , of a particular quantity of interest (e.g., a cable temperature), the true (but unknown) value of this quantity is normally distributed. The mean value and variance of this normal distribution are based solely on comparisons of model predictions with past experiments that are similar to the particular fire scenario being analyzed. The performance of the model is quantified by the estimators of the parameters,  $\delta$  and  $\tilde{\sigma}_M$ , which have been corrected to account for uncertainties associated with the experimental measurements.

When computing the relative error between measured and predicted values, an additional step is performed to ensure that the bias factor,  $\delta$ , is not skewed by a large number of data points at any particular region in the scatter plot. The approach used for this procedure is called a regressogram, i.e., a bin-smoothed estimator function [227]. This approach accounts for cases in which small measured values are compared to small predicted values, which can result in a large relative error. In these cases, the calculated bias factor might not be representative of the overall model bias, especially for larger measured and predicted values. Alternatively, a regressogram treats the average values throughout the scatter plot equally by subdividing the scatter plot into bins and normalizing each bin by the number of local data points. The regressogram estimator function is implemented as follows. For each scatter plot, the  $x$ -axis is subdivided into 10 equally spaced bins. Each bin is assigned a weight that is inversely proportional to the number of points in the bin; a bin with more points is assigned a smaller weight, and a bin with fewer points is assigned a larger weight. Finally, when the relative error is calculated, each bin is multiplied by its respective bin weight.

## 4.5 Example

This section describes how to make use of Eq. (4.23). Referring to the sample problem given above, suppose a fire model is being used to estimate the likelihood that electrical control cables could be damaged due to a fire in a compartment. Damage is assumed to occur when the surface temperature of any cable reaches 200 °C. What is the likelihood that the cables would be damaged if the model predicts that the maximum surface temperature of the cables is 175 °C. Assuming that the input parameters are not in question, the following procedure is suggested:

---

<sup>7</sup>A uniform distribution means that for any two equally sized intervals of the real line, there is an equal likelihood that the random variable takes a value in one of them.

<sup>8</sup>Note that if  $X \sim N(\mu, \sigma^2)$ , then  $cX \sim N(c\mu, (c\sigma)^2)$ .

1. Assemble a collection of model predictions,  $M_i$ , and experimental measurements,  $E_i$ , from past experiments involving objects with similar thermal characteristics as the cables in question. How “similar” the experiment is to the hypothetical scenario under study can be quantified by way of various parameters, like the thermal inertia of the object, the size of the fire, the size of the compartment, and so on. Obtain estimates of the experimental uncertainty from those who conducted the experiments or follow the procedure outlined by Hamins [218]. Express the experimental uncertainty in relative terms,  $\tilde{\sigma}_E$ .
2. Calculate the bias factor,  $\delta$ , and relative standard deviation,  $\tilde{\sigma}_M$ , from Eqs. (4.21) and (4.19), respectively.

Consider the distribution, Eq. (4.23), of the “true” temperature,  $\theta$ , shown graphically in Fig. 4.1. The vertical lines indicate the “critical” temperature at which damage is assumed to occur ( $T_c = 200^\circ\text{C}$ ), and the temperature predicted by the model ( $175^\circ\text{C}$ ). Given an ambient temperature of  $20^\circ\text{C}$ , the predicted temperature rise,  $M$ , is  $155^\circ\text{C}$ . The mean and standard deviation in Eq. (4.23) are calculated:

$$\mu = 20 + \frac{M}{\delta} = 20 + \frac{155}{1.13} = 157^\circ\text{C} ; \quad \sigma = \tilde{\sigma}_M \frac{M}{\delta} = 0.20 \times \frac{155}{1.13} = 27^\circ\text{C} \quad (4.24)$$

respectively. The shaded area beneath the bell curve is the probability that the “true” temperature can exceed the critical value,  $T_c = 200^\circ\text{C}$ , which can be expressed via the *complimentary error function*:

$$P(T > T_c) = \frac{1}{2} \operatorname{erfc} \left( \frac{T_c - \mu}{\sigma \sqrt{2}} \right) = \frac{1}{2} \operatorname{erfc} \left( \frac{200 - 157}{27 \sqrt{2}} \right) \approx 0.06 \quad (4.25)$$

This means that there is a 6 % chance that the cables could become damaged, assuming that the model’s input parameters are not subject to uncertainty.

## 4.6 Additional Considerations

Keep in mind that for any fire experiment, FDS might predict a particular quantity accurately (within the experimental uncertainty bounds, for example), but another quantity less accurately. For example, in a series of 15 full-scale fire experiments conducted at NIST in 2003, sponsored by the U.S. Nuclear Regulatory Commission, the average hot gas layer (HGL) temperature predictions were nearly within the accuracy of the measurements themselves, yet the smoke concentration predictions differed from the measurements by as much as a factor of 3. Why? Consider the following issues associated with various types of measurements:

- Is the measurement taken at a single point, or averaged over many points? In the example above, the HGL temperature is an average of many thermocouple measurements, whereas the smoke concentration is based on the extinction of laser light over a short length span. Model error tends to be reduced by the averaging process, plus most fire models, including FDS, are based on global mass and energy conservation laws that are expressed as spatial averages.
- Is the measured quantity time-averaged or instantaneous? For example, a surface temperature prediction is less prone to error in comparison to a heat flux prediction because the former is, in some sense, a time-integral of the latter.
- In the case of a point measurement, how close to the fire is it? The terms “near-field” and “far-field” are used throughout this Guide to describe the relative distance from the fire. In general, predictions of near-field phenomena are more prone to error than far-field. There are exceptions, however. For example, a prediction of the temperature directly within the flaming region may be more accurate than that made just a fire diameter away because of the fact that temperatures tend to stabilize at about  $1000^\circ\text{C}$  within the fire itself, but then rapidly decrease away from the flames. Less accurate predictions typically occur in regions of steep gradients (rapid changes, both in space and time).



# Chapter 5

## HGL Temperature and Depth

FDS, like any CFD model, does not perform a direct calculation of the HGL temperature or height. These are constructs unique to two-zone models. Nevertheless, FDS does make predictions of gas temperature at the same locations as the thermocouples in the experiments, and these values can be reduced in the same manner as the experimental measurements to produce an “average” HGL temperature and height. Regardless of the validity of the reduction method, the FDS predictions of the HGL temperature and height ought to be representative of the accuracy of its predictions of the individual thermocouple measurements that are used in the HGL reduction. The temperature measurements from all six test series are used to compute an HGL temperature and height with which to compare to FDS. The same layer reduction method is used for all the data presented in this chapter.

### 5.1 HGL Reduction Method

Fire protection engineers often need to estimate the location of the interface between the hot, smoke-laden upper layer and the cooler lower layer in a burning compartment. Relatively simple fire models, often referred to as *two-zone models*, compute this quantity directly, along with the average temperature of the upper and lower layers. In a computational fluid dynamics (CFD) model like FDS, there are not two distinct zones, but rather a continuous profile of temperature. Nevertheless, there are methods that have been developed to estimate layer height and average temperatures from a continuous vertical profile of temperature. One such method [228] is as follows: Consider a continuous function  $T(z)$  defining temperature  $T$  as a function of height above the floor  $z$ , where  $z = 0$  is the floor and  $z = H$  is the ceiling. Define  $T_u$  as the upper layer temperature,  $T_\ell$  as the lower layer temperature, and  $z_{\text{int}}$  as the interface height. Compute the quantities:

$$\begin{aligned} (H - z_{\text{int}}) T_u + z_{\text{int}} T_\ell &= \int_0^H T(z) dz = I_1 \\ (H - z_{\text{int}}) \frac{1}{T_u} + z_{\text{int}} \frac{1}{T_\ell} &= \int_0^H \frac{1}{T(z)} dz = I_2 \end{aligned}$$

Solve for  $z_{\text{int}}$ :

$$z_{\text{int}} = \frac{T_\ell(I_1 I_2 - H^2)}{I_1 + I_2 T_\ell^2 - 2 T_\ell H} \quad (5.1)$$

Let  $T_\ell$  be the temperature in the lowest mesh cell and, using Simpson’s Rule, perform the numerical integration of  $I_1$  and  $I_2$ .  $T_u$  is defined as the average upper layer temperature via

$$(H - z_{\text{int}}) T_u = \int_{z_{\text{int}}}^H T(z) dz \quad (5.2)$$

Further discussion of similar procedures can be found in Ref. [229].

## 5.2 ATF Corridors

The ATF Corridors experiments consisted of two corridors one on top of the other and connected by a stairwell. HGL temperature and depth reductions were carried out using three arrays of thermocouples in the lower corridor (Trees A, B, and C) and two arrays in the upper corridor (Trees G and H).

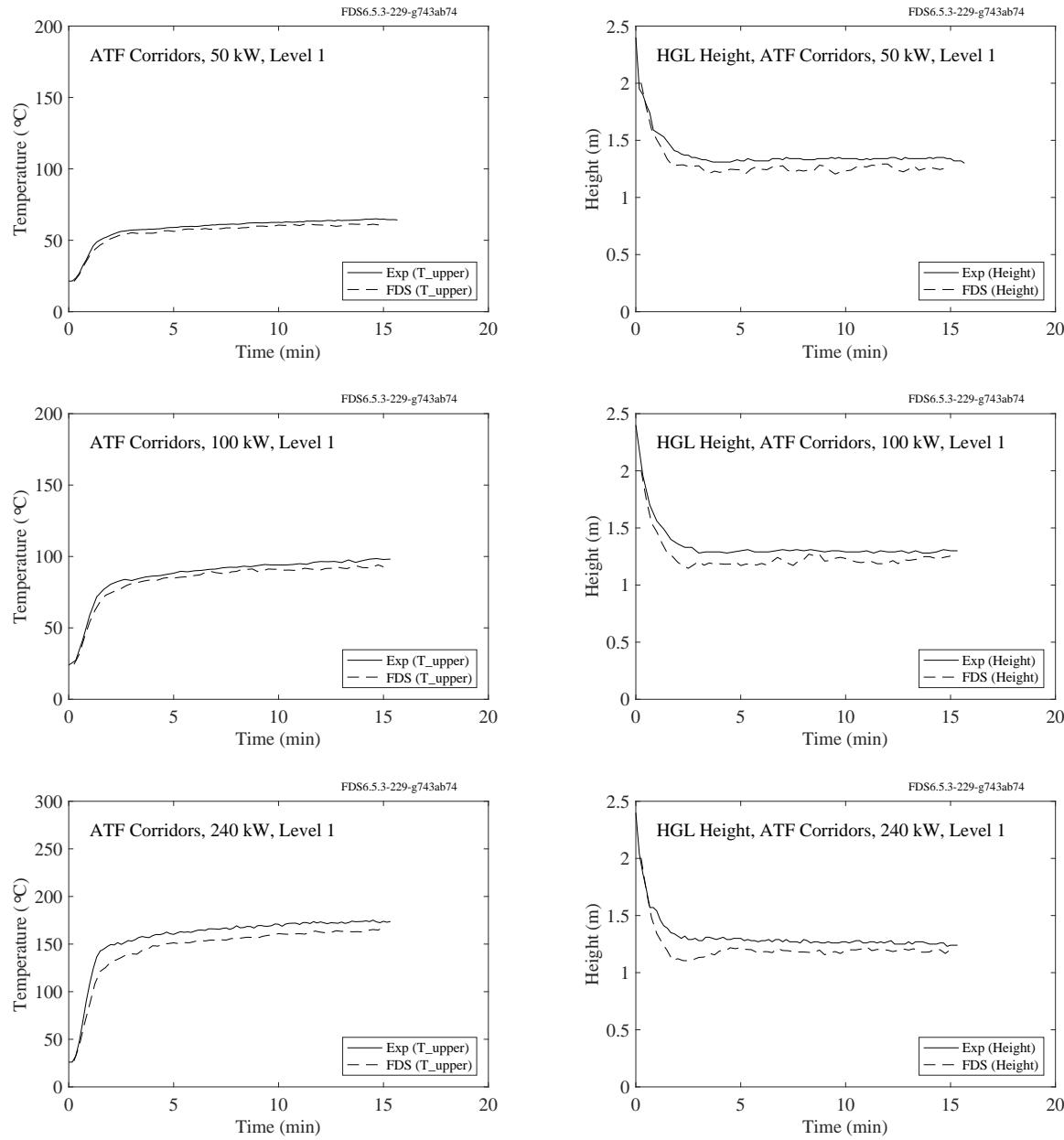


Figure 5.1: ATF Corridors, HGL temperature and height, first floor, 50 kW, 100 kW, 240 kW.

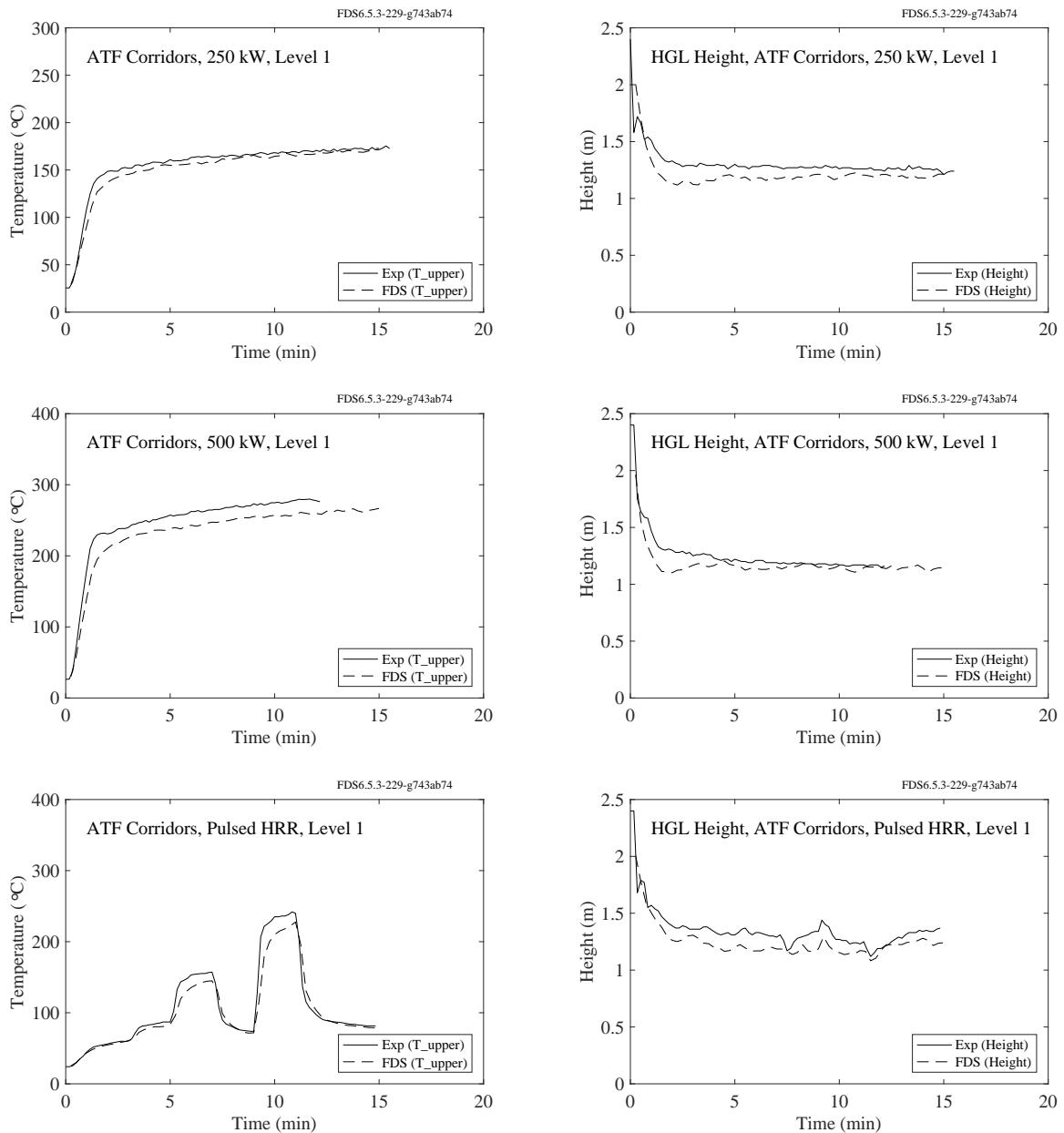


Figure 5.2: ATF Corridors, HGL temperature and height, first floor, 250 kW, 500 kW, mixed.

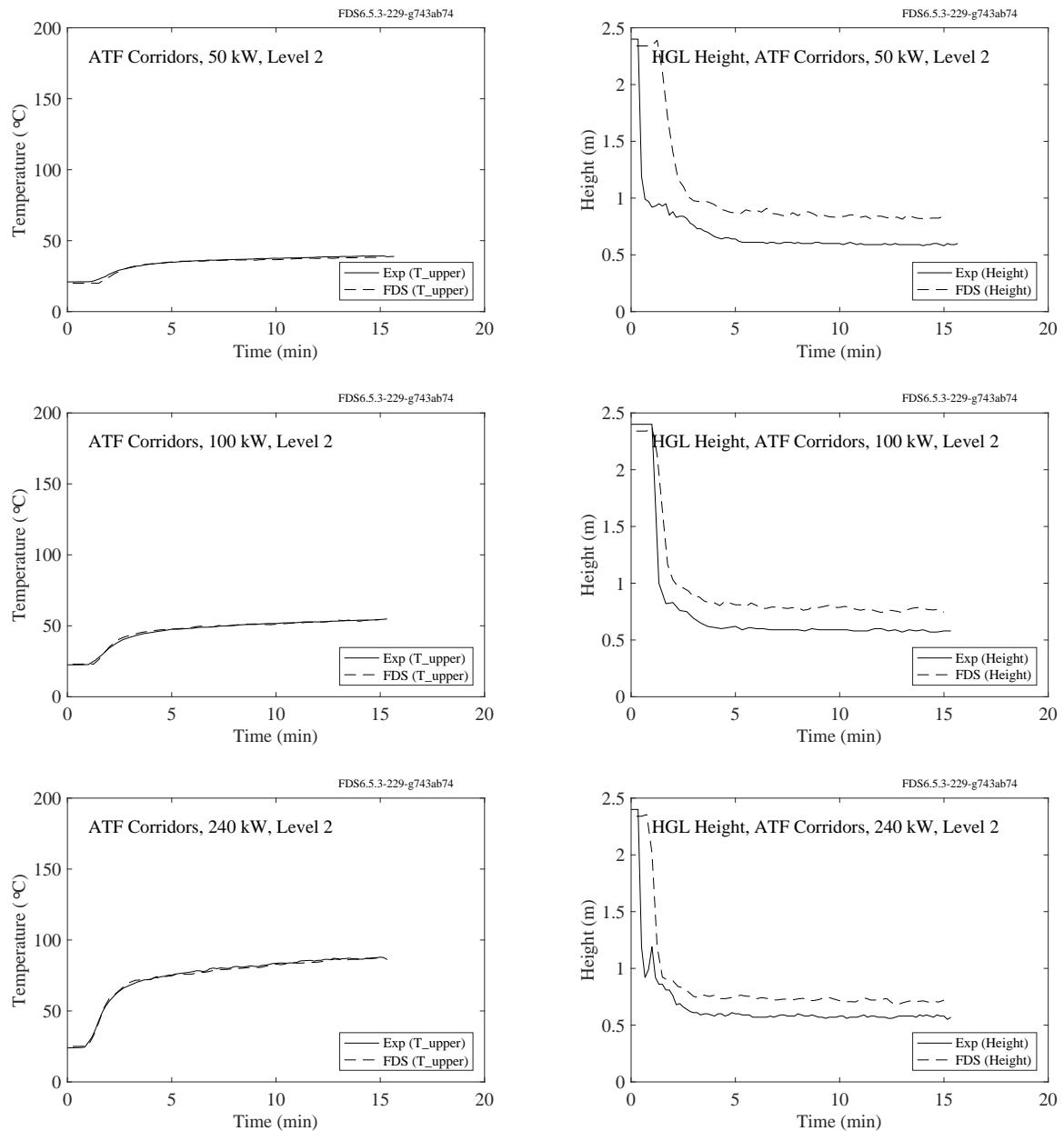


Figure 5.3: ATF Corridors, HGL temperature and height, second floor, 50 kW, 100 kW, 240 kW.

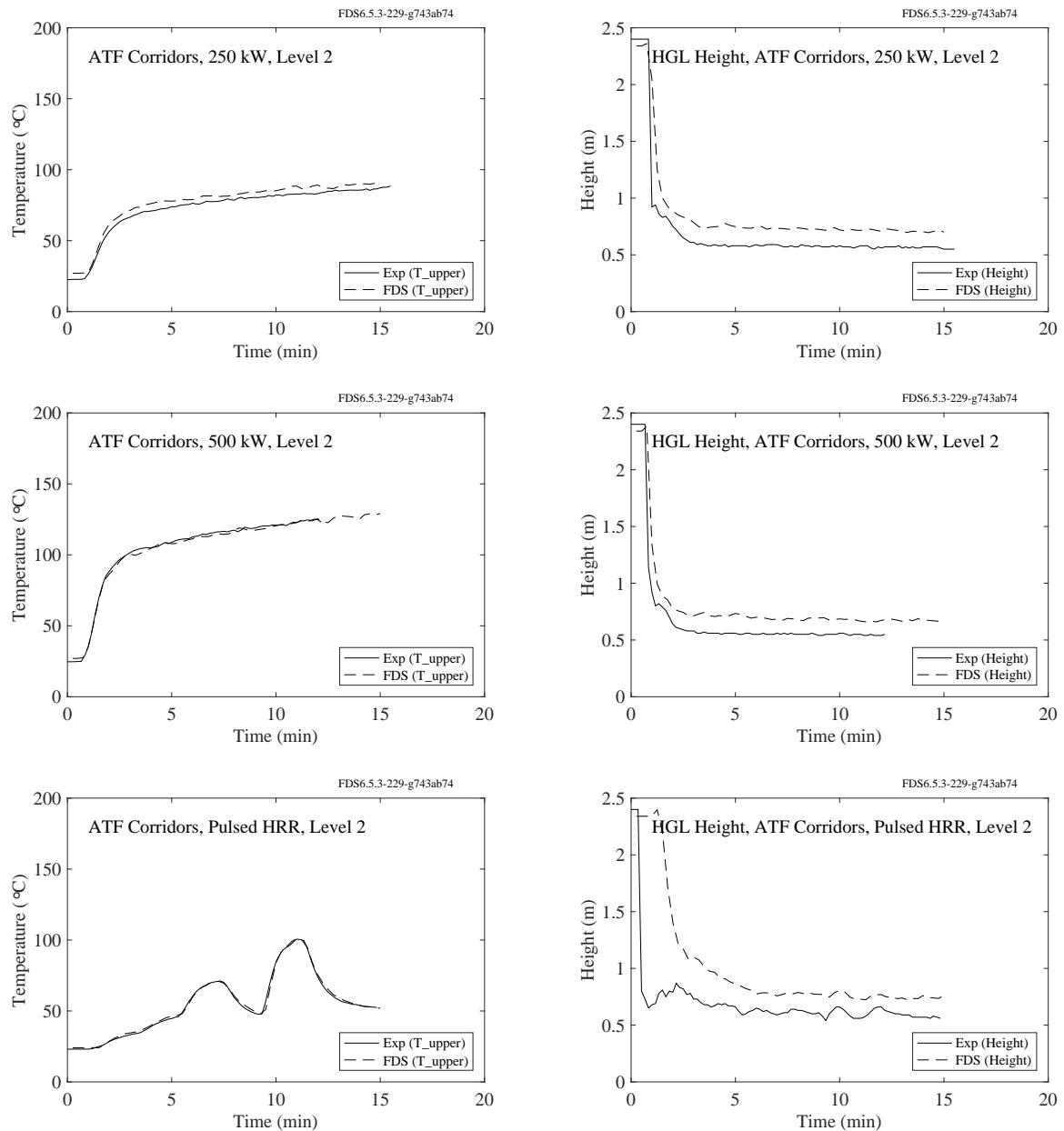


Figure 5.4: ATF Corridors, HGL temperature and height, second floor, 250 kW, 500 kW, mixed.

### 5.3 DelCo Trainers

The DelCo Trainer experiments were conducted in two different structures. Tests 2-6 were conducted in a single level structure consisting of three rooms. Rooms 1 and 3 had two thermocouple trees and Room 2 had one. Tests 22-25 were conducted in a two level structure. Floors 1 and 2 each had three thermocouple arrays. See Section 3.11 for their exact locations.

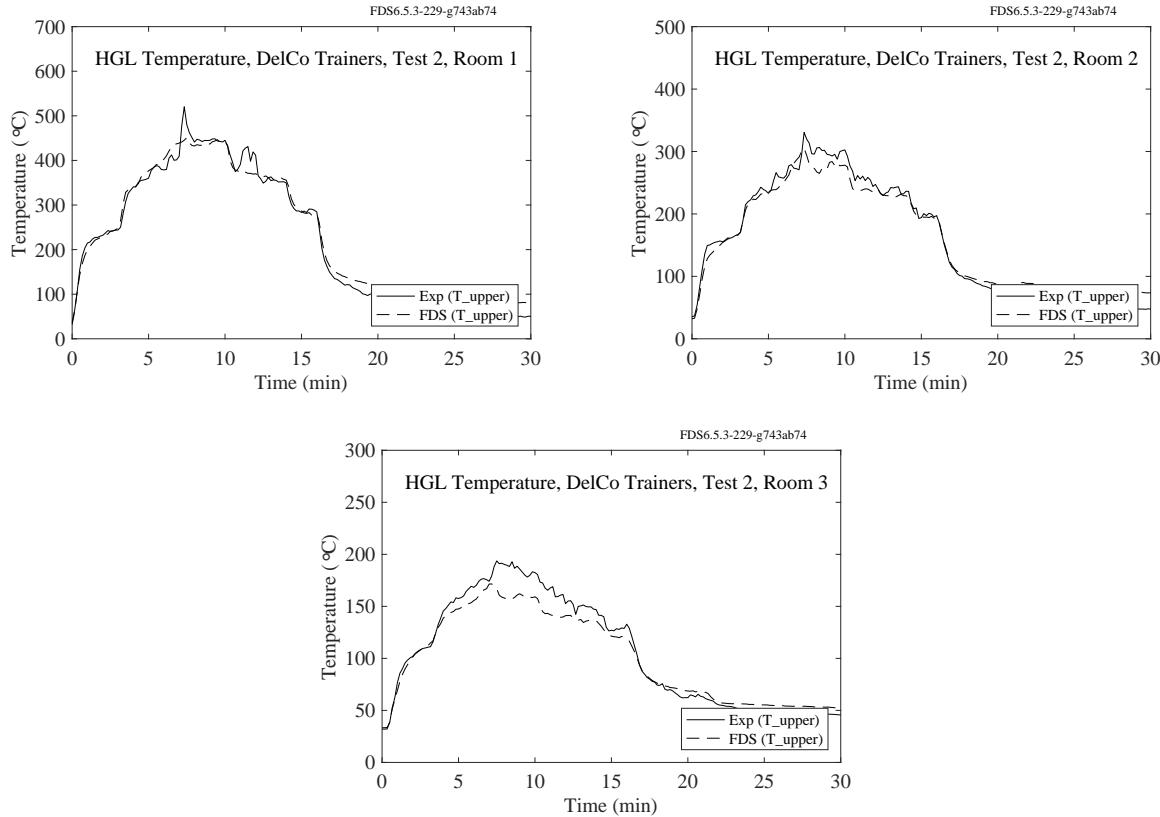


Figure 5.5: DelCo Trainers, HGL Temperature, Test 2.

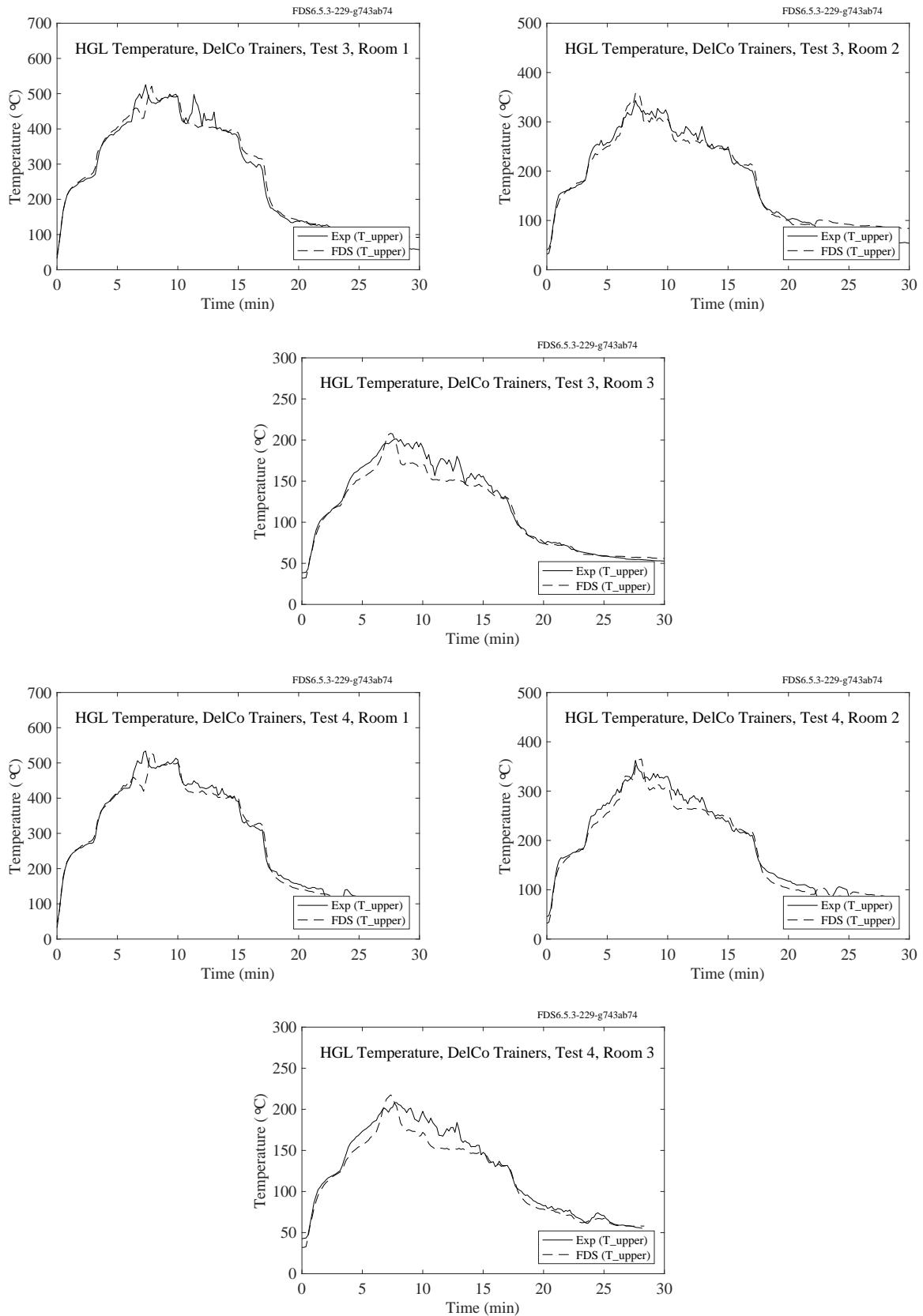


Figure 5.6: DelCo Trainers, HGL Temperature, Tests 3 and 4.

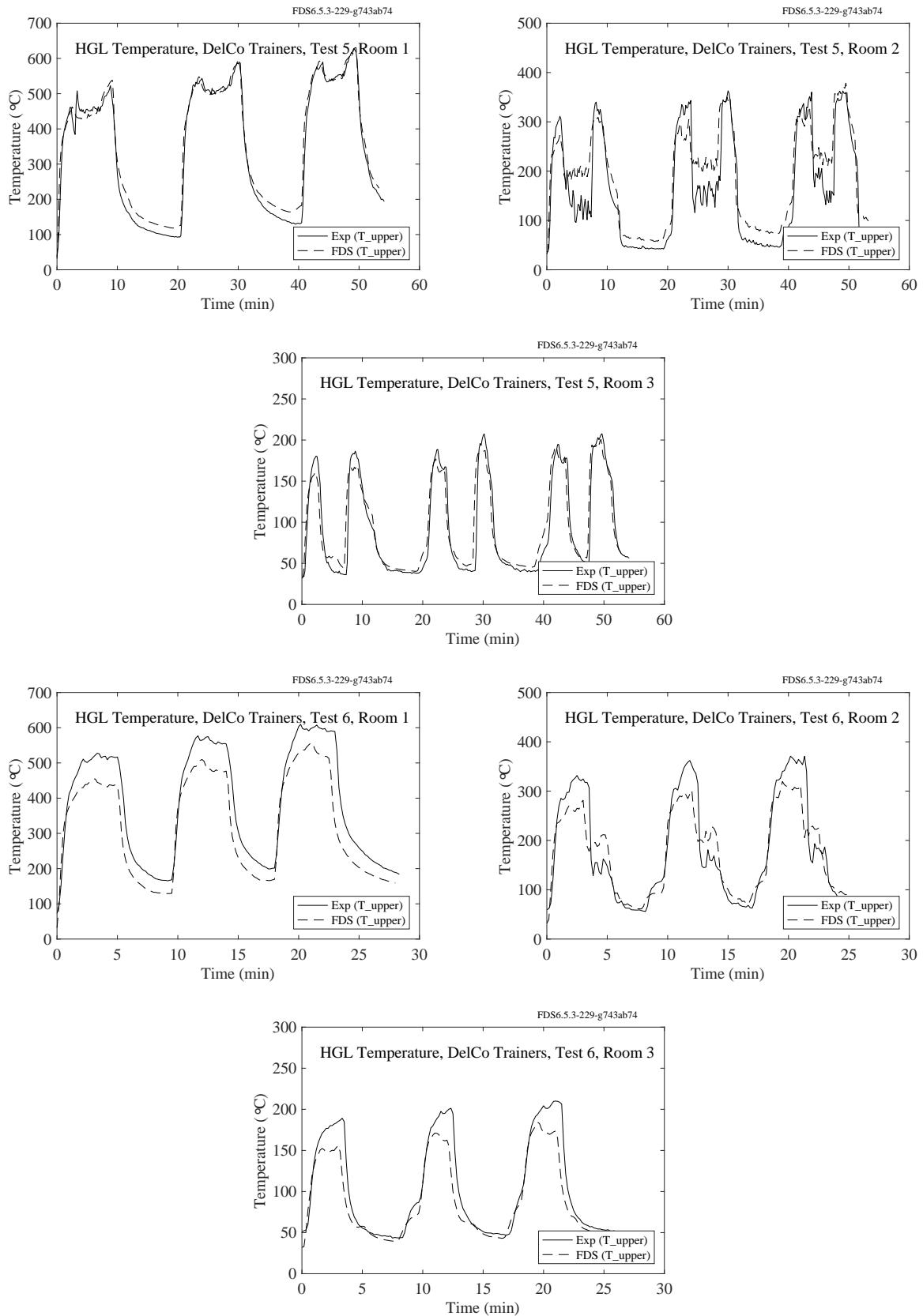


Figure 5.7: DelCo Trainers, HGL Temperature, Tests 5 and 6.

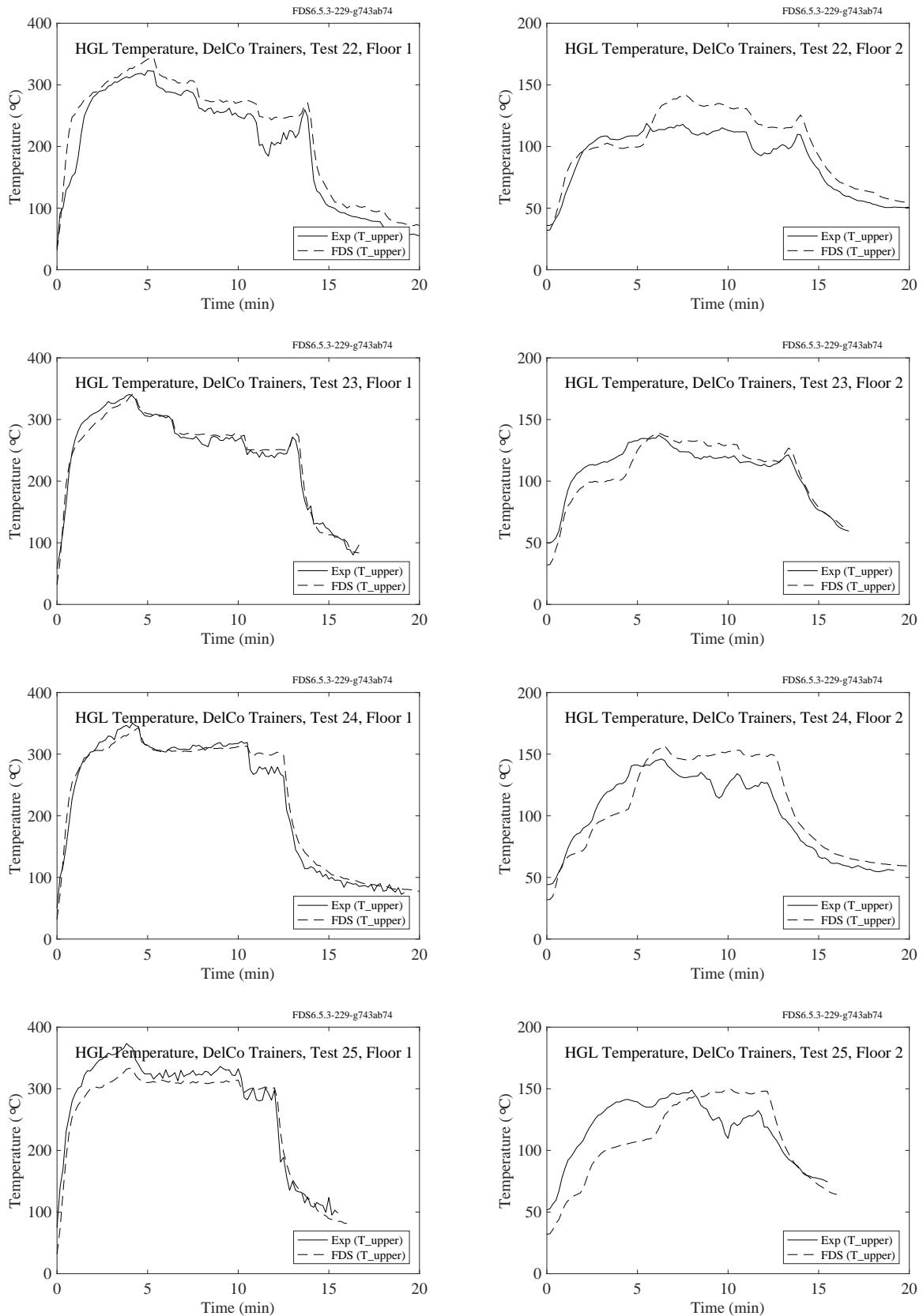


Figure 5.8: DelCo Trainers, HGL Temperature, Tests 22-25.

## 5.4 FM/SNL Test Series

Nineteen tests from the FM/SNL test series were selected for comparison. The HGL temperature and height are calculated using the standard method. The thermocouple arrays that were located in Sectors 1, 2 and 3 are averaged (with an equal weighting for each) for all tests except Tests 21 and 22. For these tests, only Sectors 1 and 3 are used, as Sector 2 falls within the smoke plume. Also, for all but the gas burner experiments, the time history of the HRR is estimated. Only the peak HRR is reported.

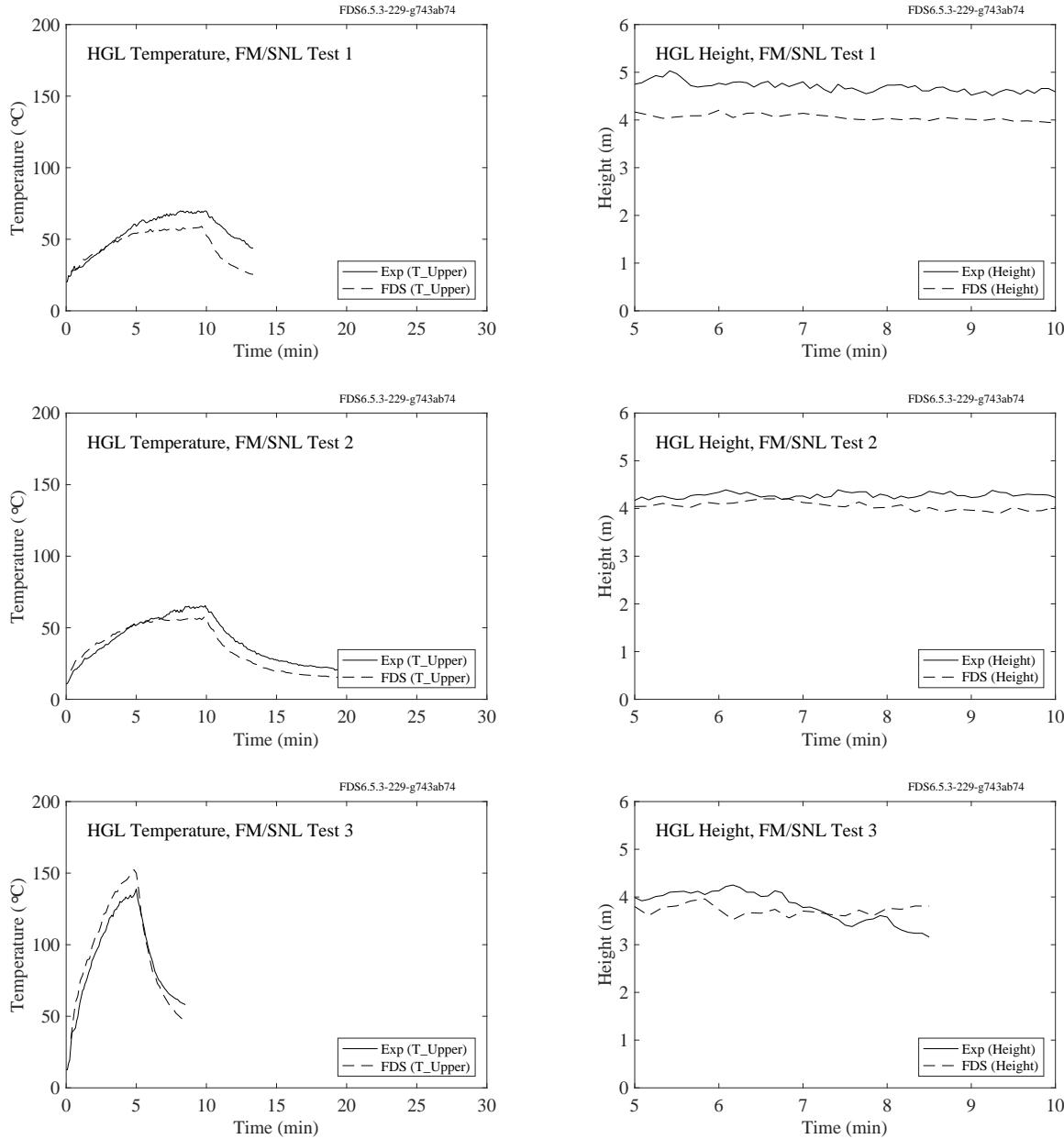


Figure 5.9: FM/SNL experiments, HGL temperature and height, Tests 1, 2, 3.

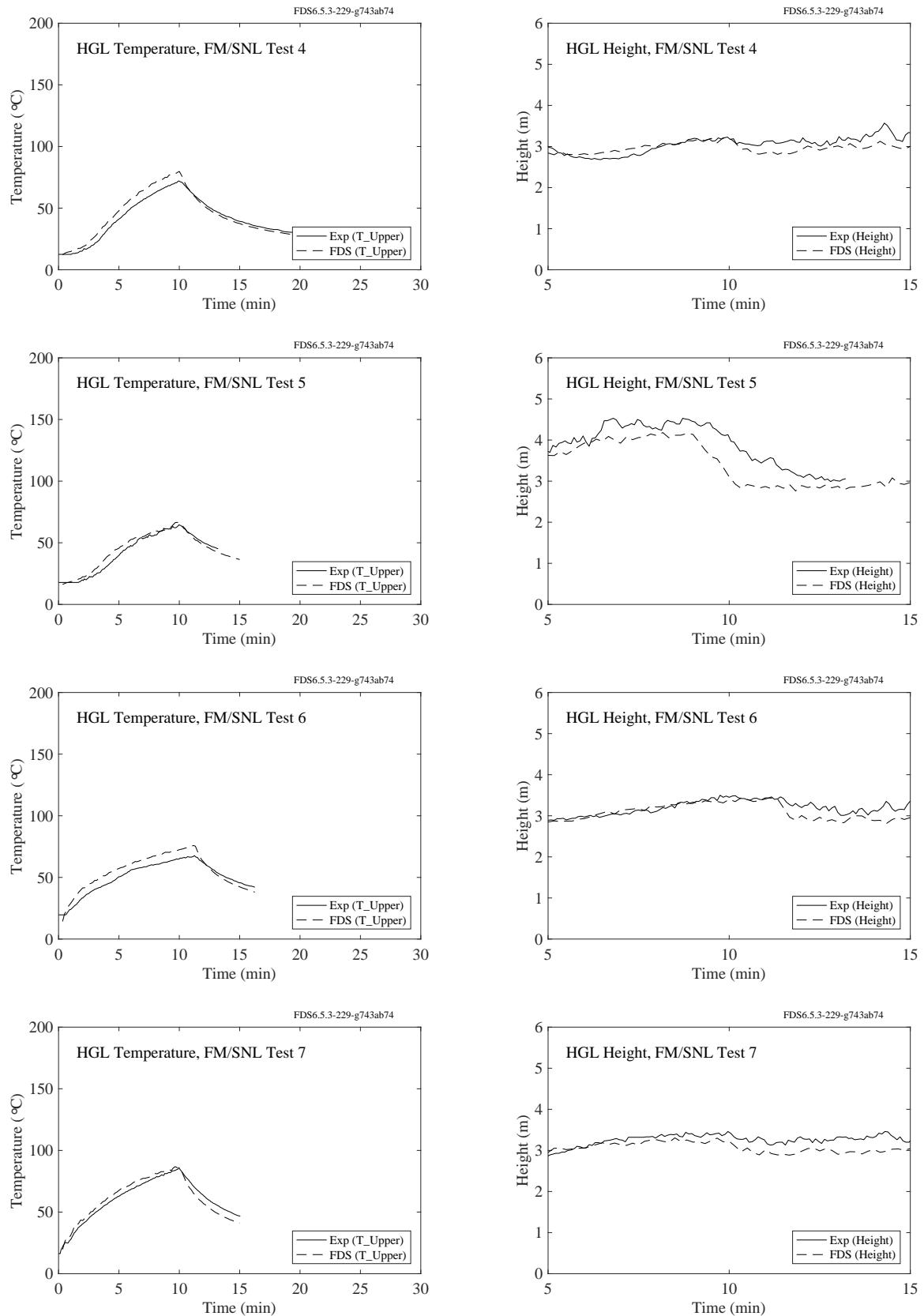


Figure 5.10: FM/SNL experiments, HGL temperature and height, Tests 4, 5, 6, 7.

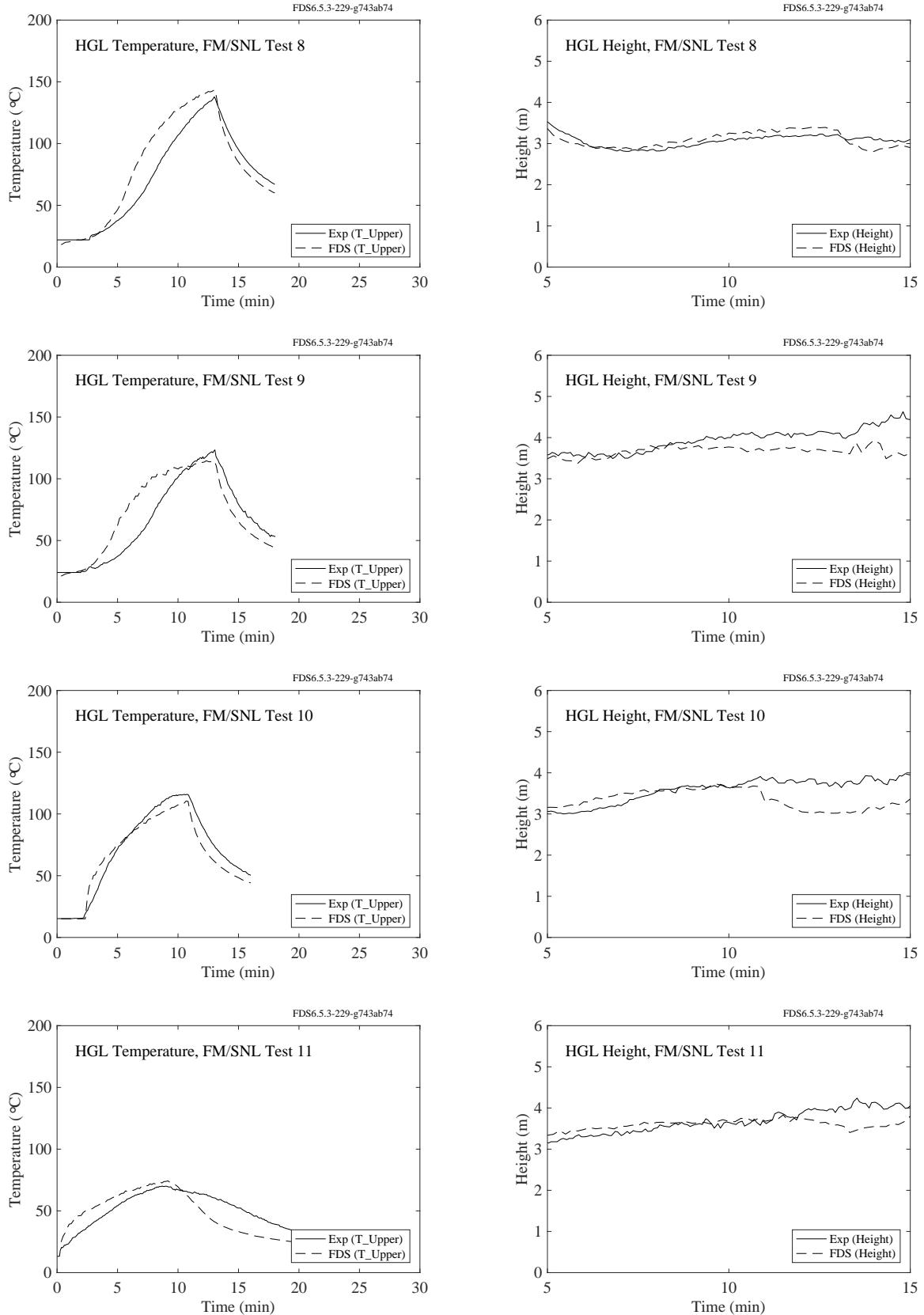


Figure 5.11: FM/SNL experiments, HGL temperature and height, Tests 8, 9, 10, 11.

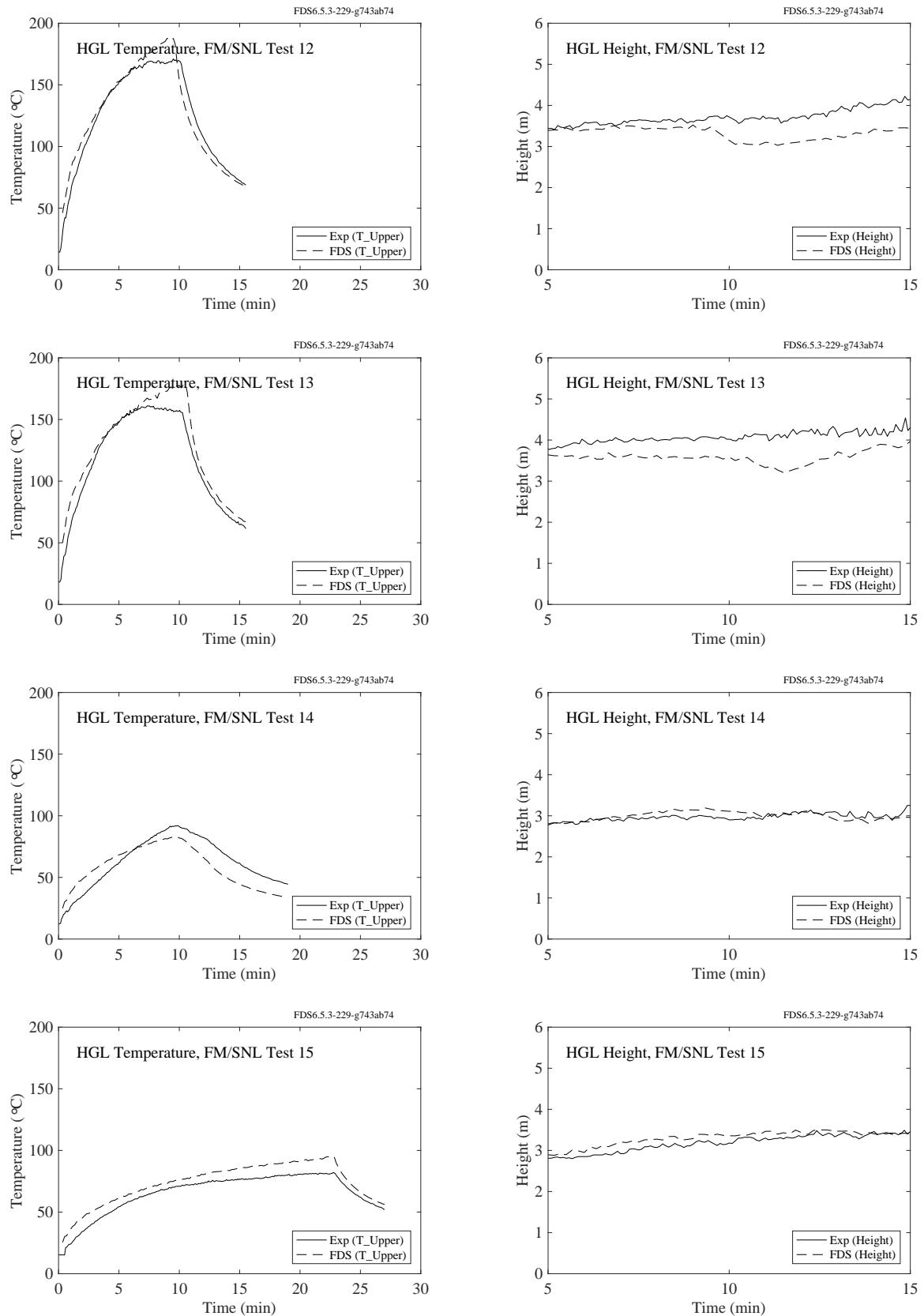


Figure 5.12: FM/SNL experiments, HGL temperature and height, Tests 12, 13, 14, 15.

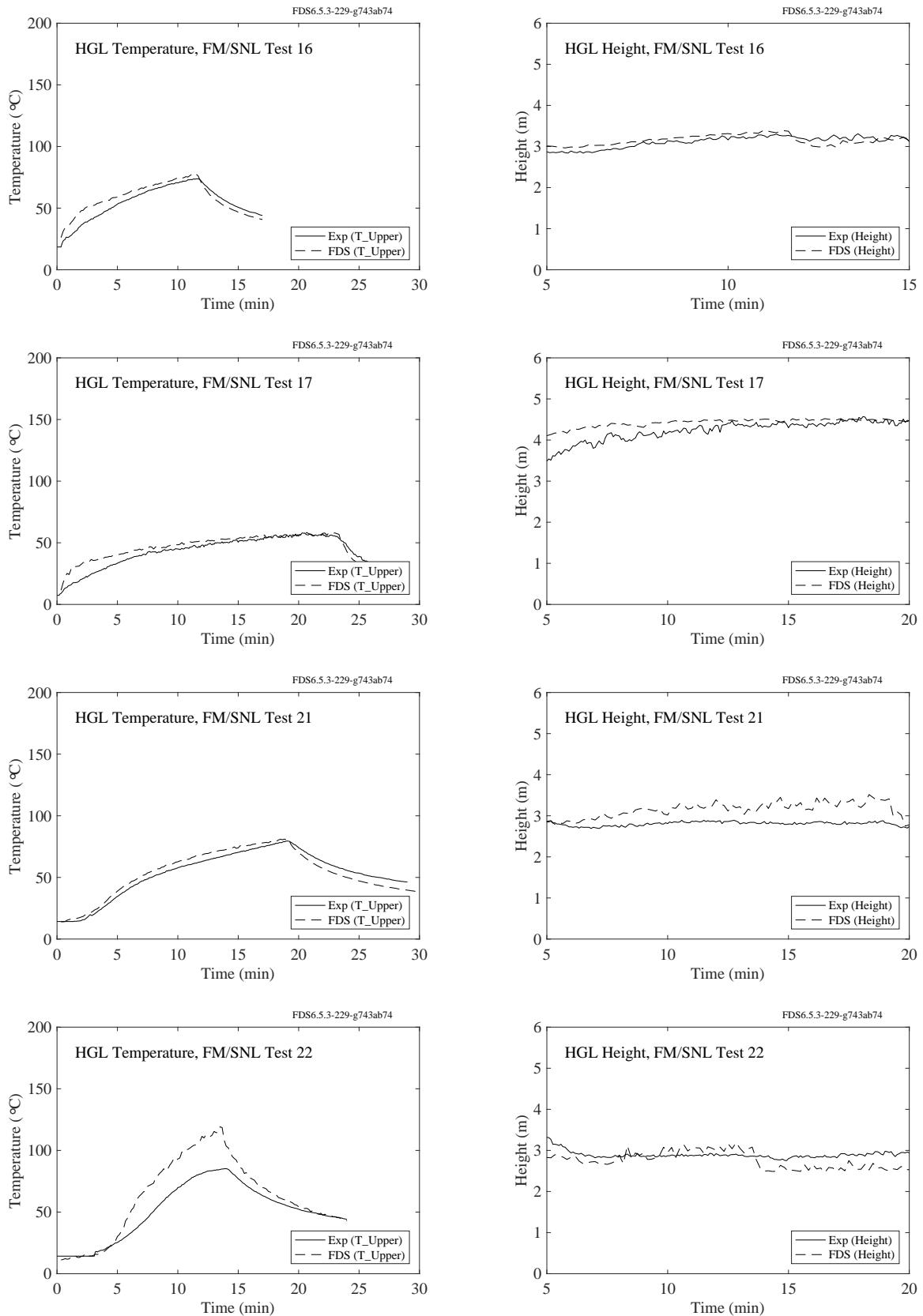


Figure 5.13: FM/SNL experiments, HGL temperature and height, Tests 16, 17, 21, 22.

## 5.5 LLNL Enclosure Series

The plots on the following pages compare predicted and measured layer temperatures from the LLNL Enclosure test series. In the experiments, fifteen thermocouples were evenly spaced from floor to ceiling on either side of the burner. The measured temperatures were reported as averages of the lower, middle, and upper five TCs. Some of the experiments were conducted with a separated plenum space in the top one-third of the overall compartment (Tests 17-60). In these cases, the upper five TCs are a measure of the average plenum temperature.

In the figures on the following pages, the black circles represent the average of the five upper-most TC measurements. The lines represent the simulation. The red circles represent the average of the middle five TC measurements. For the plenum tests, these TCs are located immediately beneath the plenum and their average temperature is typically greater than that of the plenum. Note that in a number of tests, the fuel flow was stopped or the fire self-extinguished. The simulations last only as long as the reported measurements.

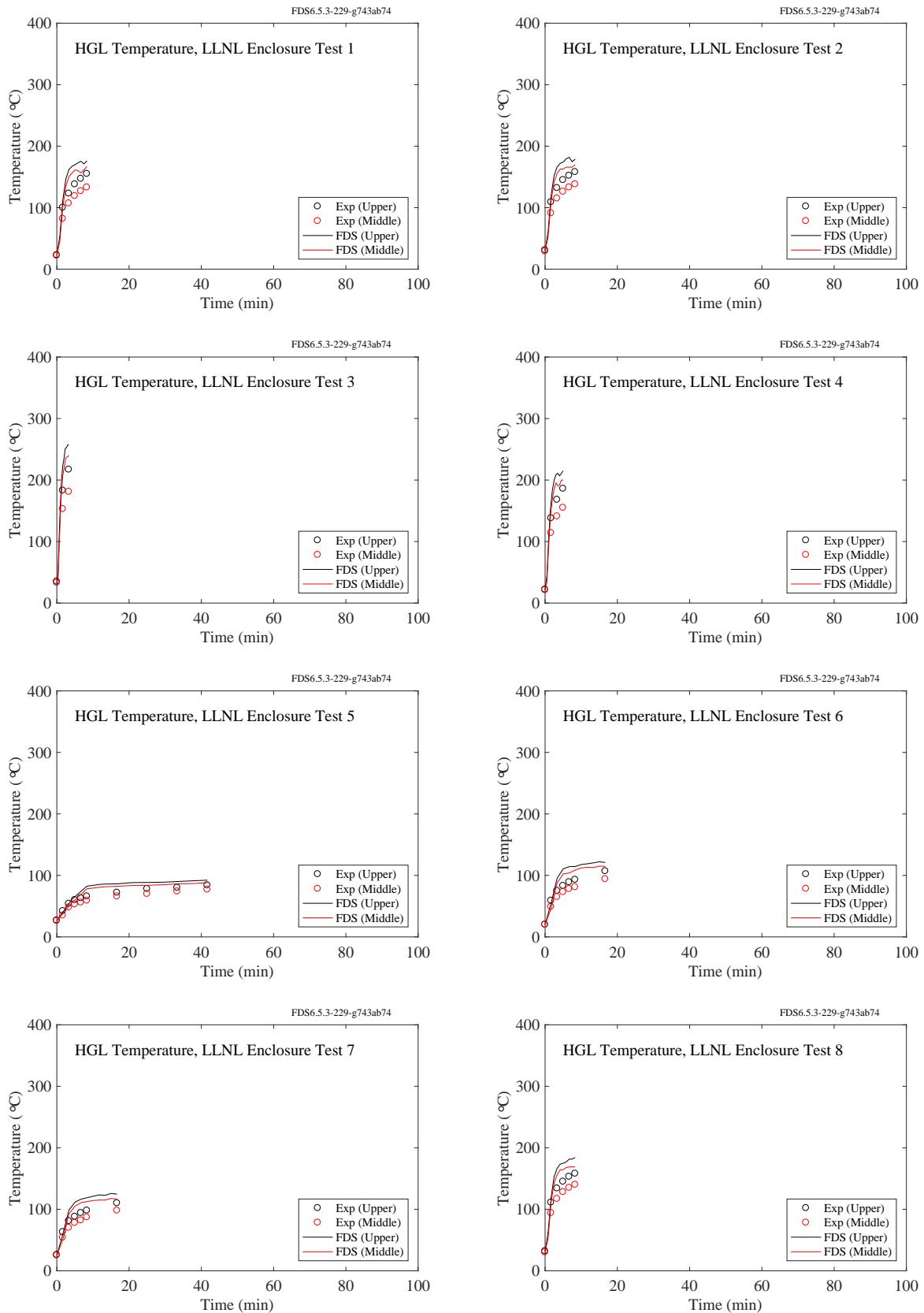


Figure 5.14: LLNL Enclosure experiments, HGL temperature, Tests 1-8.

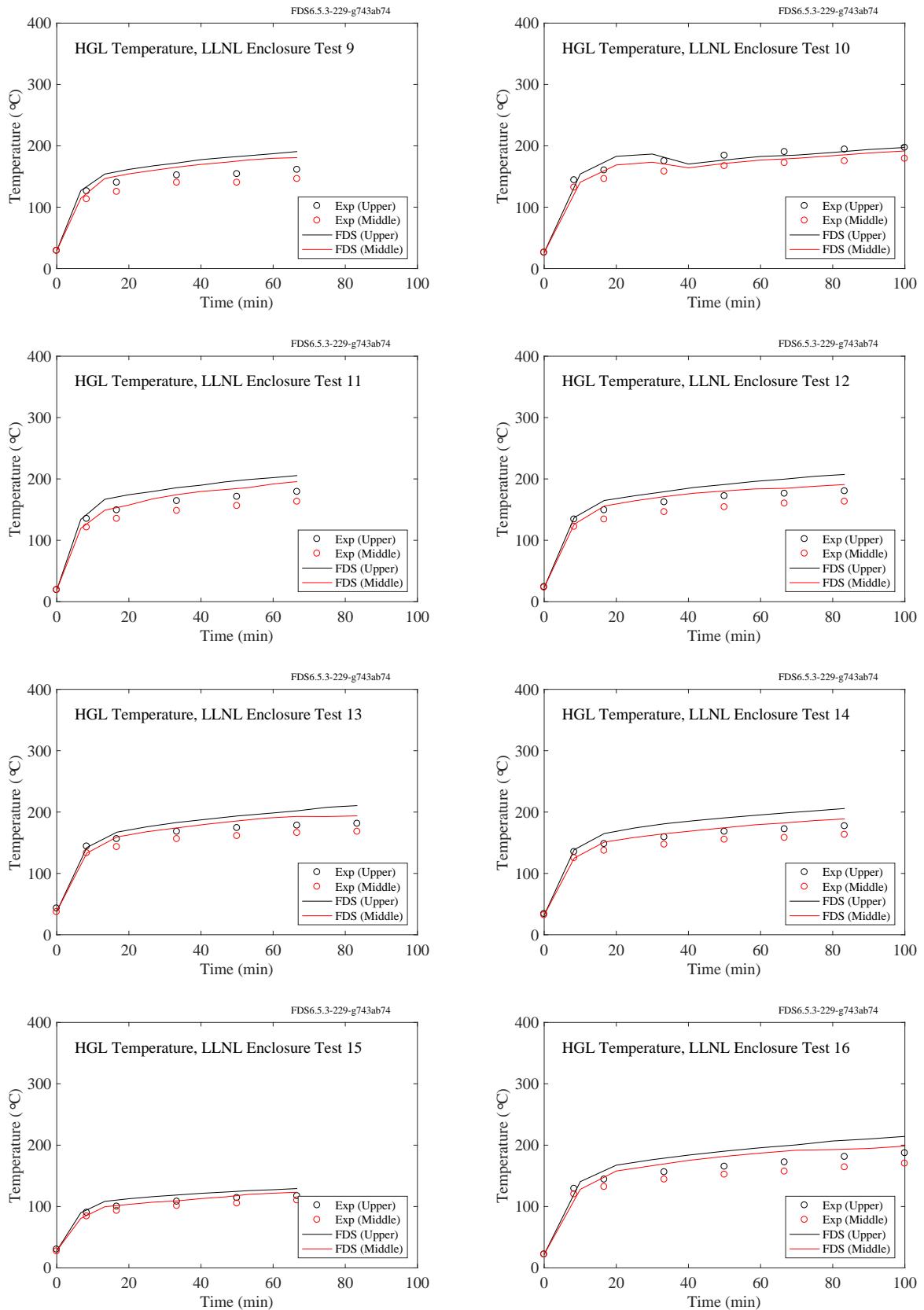


Figure 5.15: LLNL Enclosure experiments, HGL temperature, Tests 9-16.

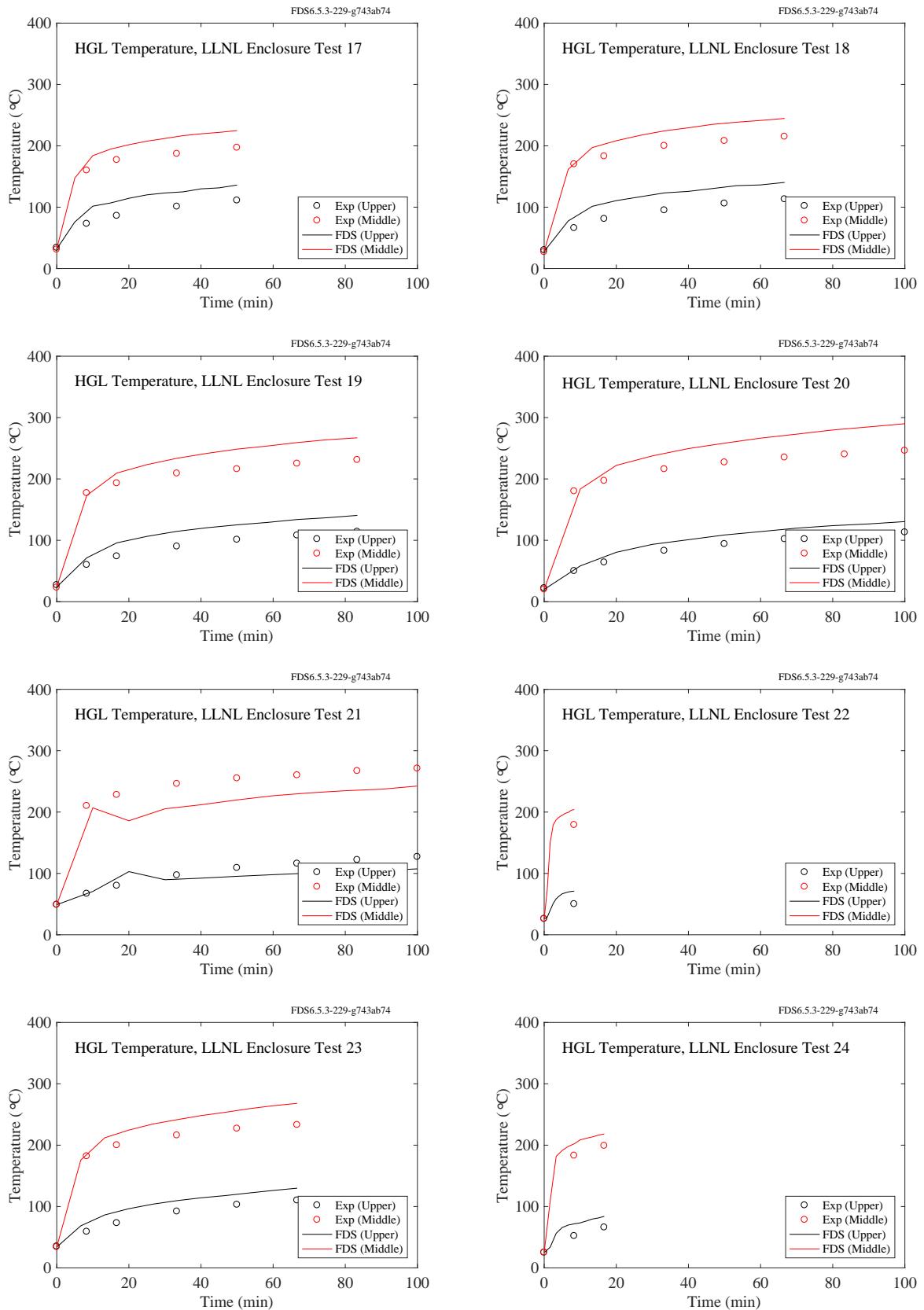


Figure 5.16: LLNL Enclosure experiments, HGL temperature, Tests 17-24.

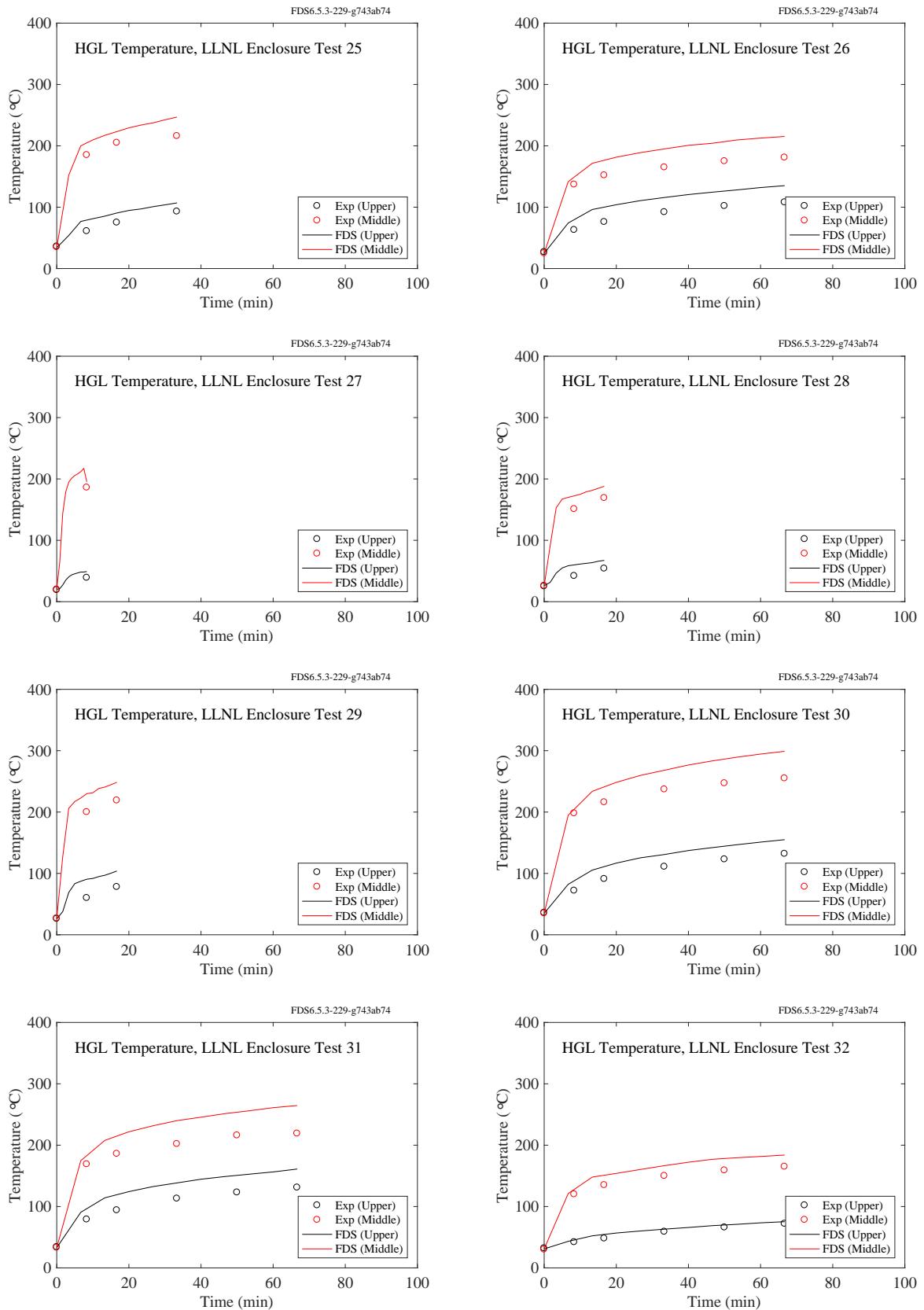


Figure 5.17: LLNL Enclosure experiments, HGL temperature, Tests 25-32.

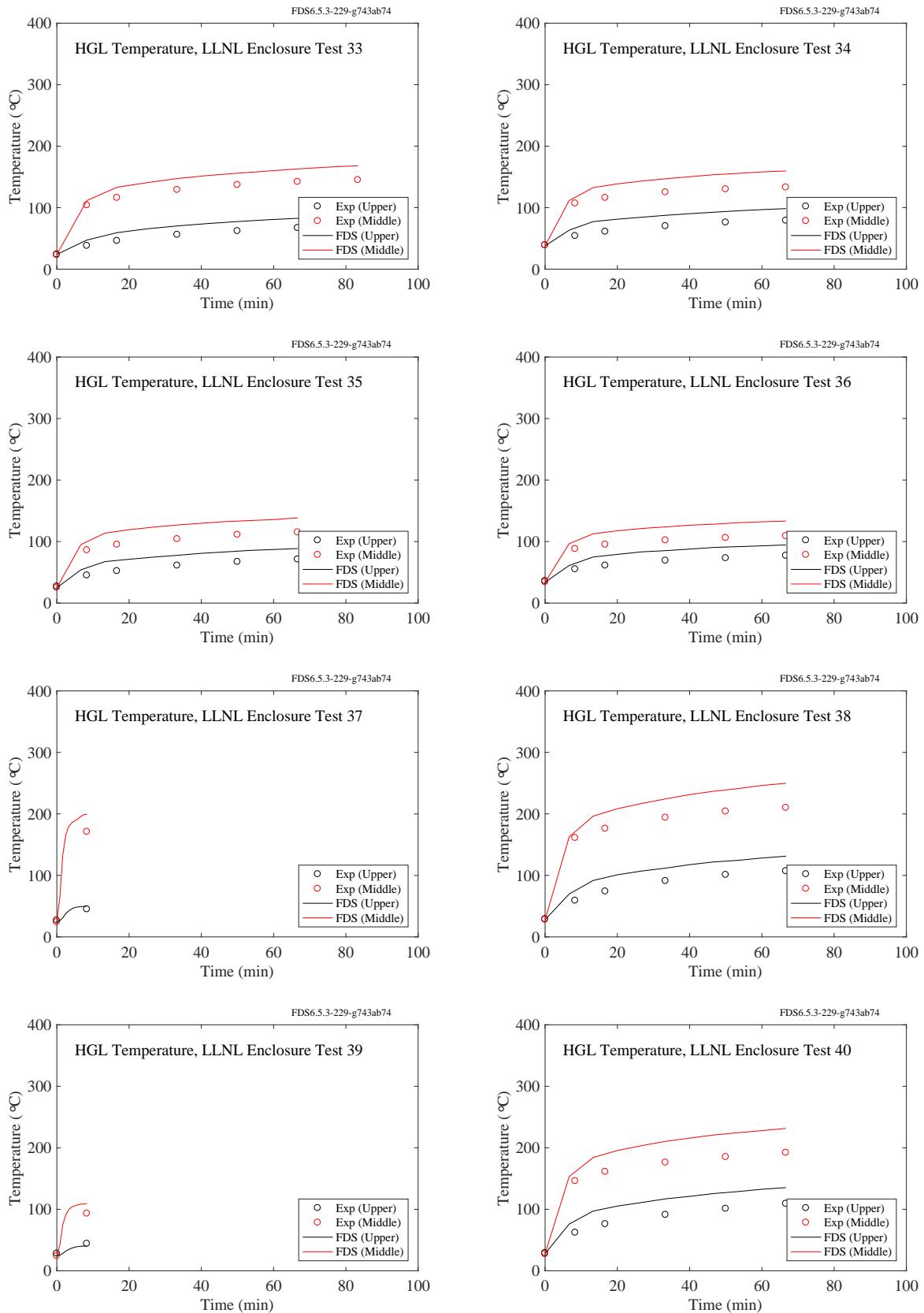


Figure 5.18: LLNL Enclosure experiments, HGL temperature, Tests 33-40.

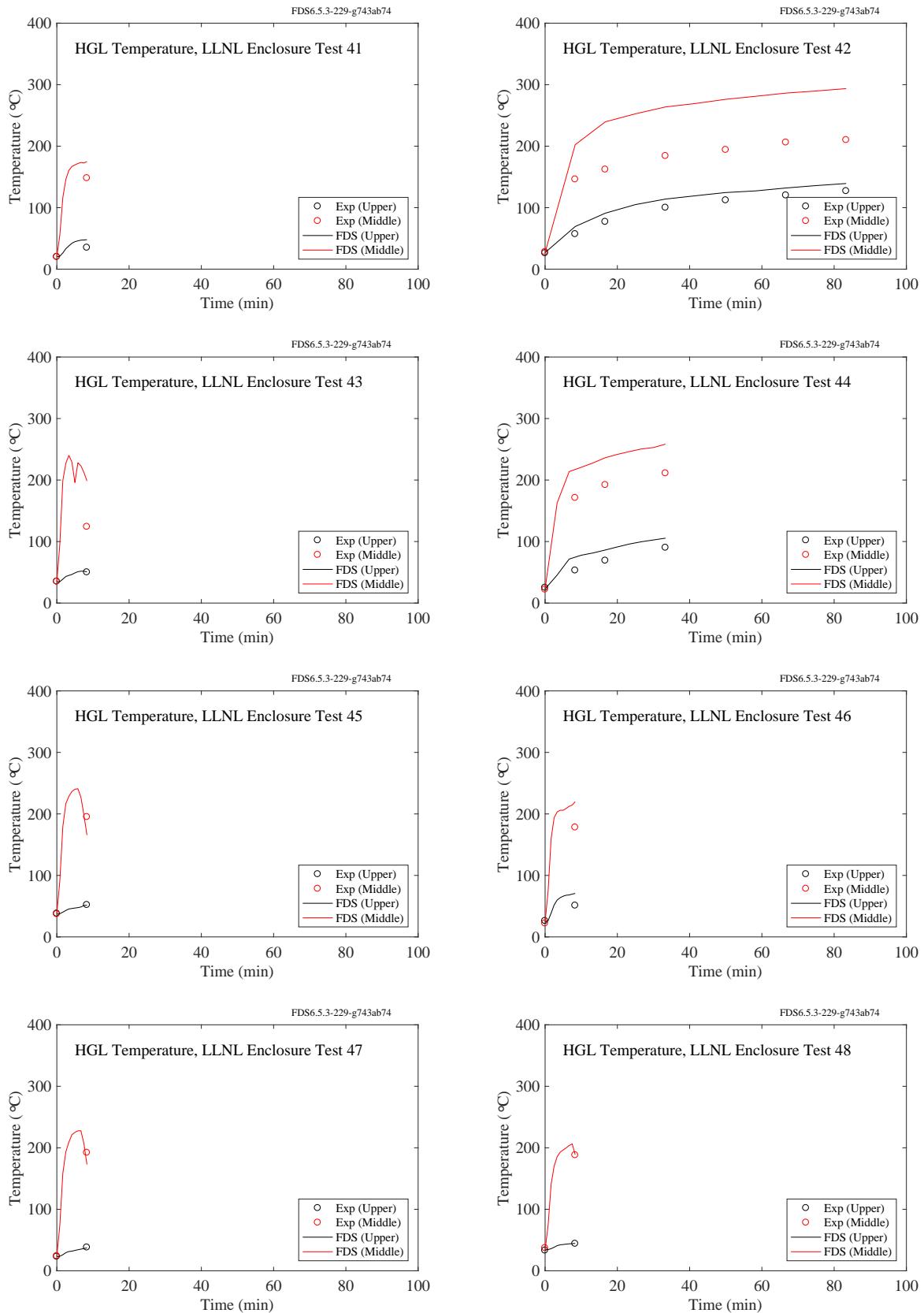


Figure 5.19: LLNL Enclosure experiments, HGL temperature, Tests 41-48.

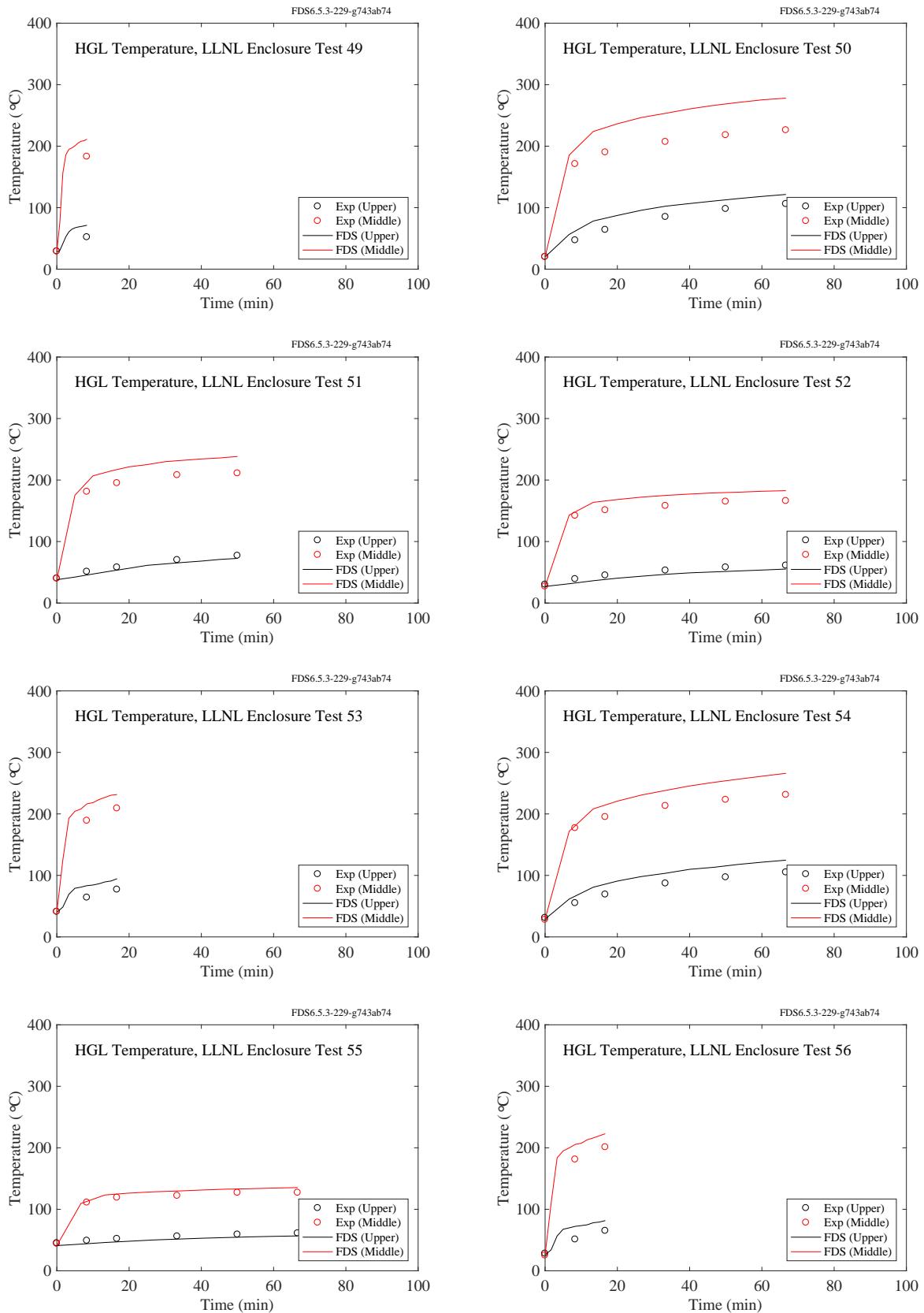


Figure 5.20: LLNL Enclosure experiments, HGL temperature, Tests 49-56.

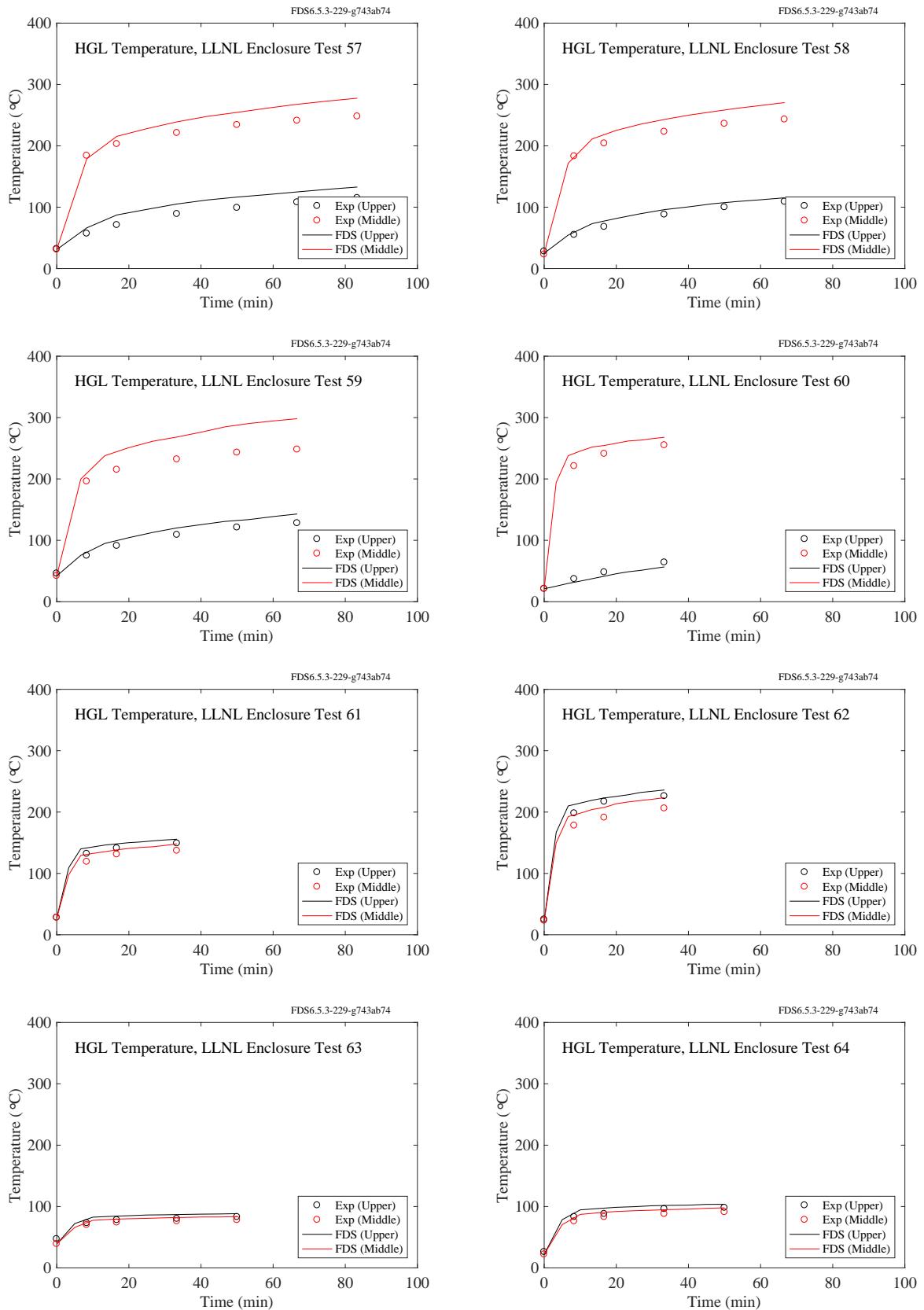


Figure 5.21: LLNL Enclosure experiments, HGL temperature, Tests 57-64.

## 5.6 NBS Multi-Room Test Series

This series of experiments was performed in two relatively small rooms connected by a long corridor. The fire was located in one of the rooms. Eight vertical arrays of thermocouples were positioned throughout the test space: Tree 1 in the burn room, Tree 2 in the doorway of the burn room, Trees 3, 4, and 5 in the corridor, Tree 6 in the exit doorway to the outside at the far end of the corridor, Tree 7 in the doorway of the “target” room, and Tree 8 inside the target room. Four trees have been selected for comparison with model prediction: Tree 1 in the burn room, the trees in the corridor, and Tree 8 in the target room in Test 100Z. In Tests 100A and 100O, the target room was closed. The test director reduced the layer information individually for the eight thermocouple arrays using an alternative method. These results were included in the original data sets. However, in this report the selected TC trees were reduced using the method described in Section 5.1.

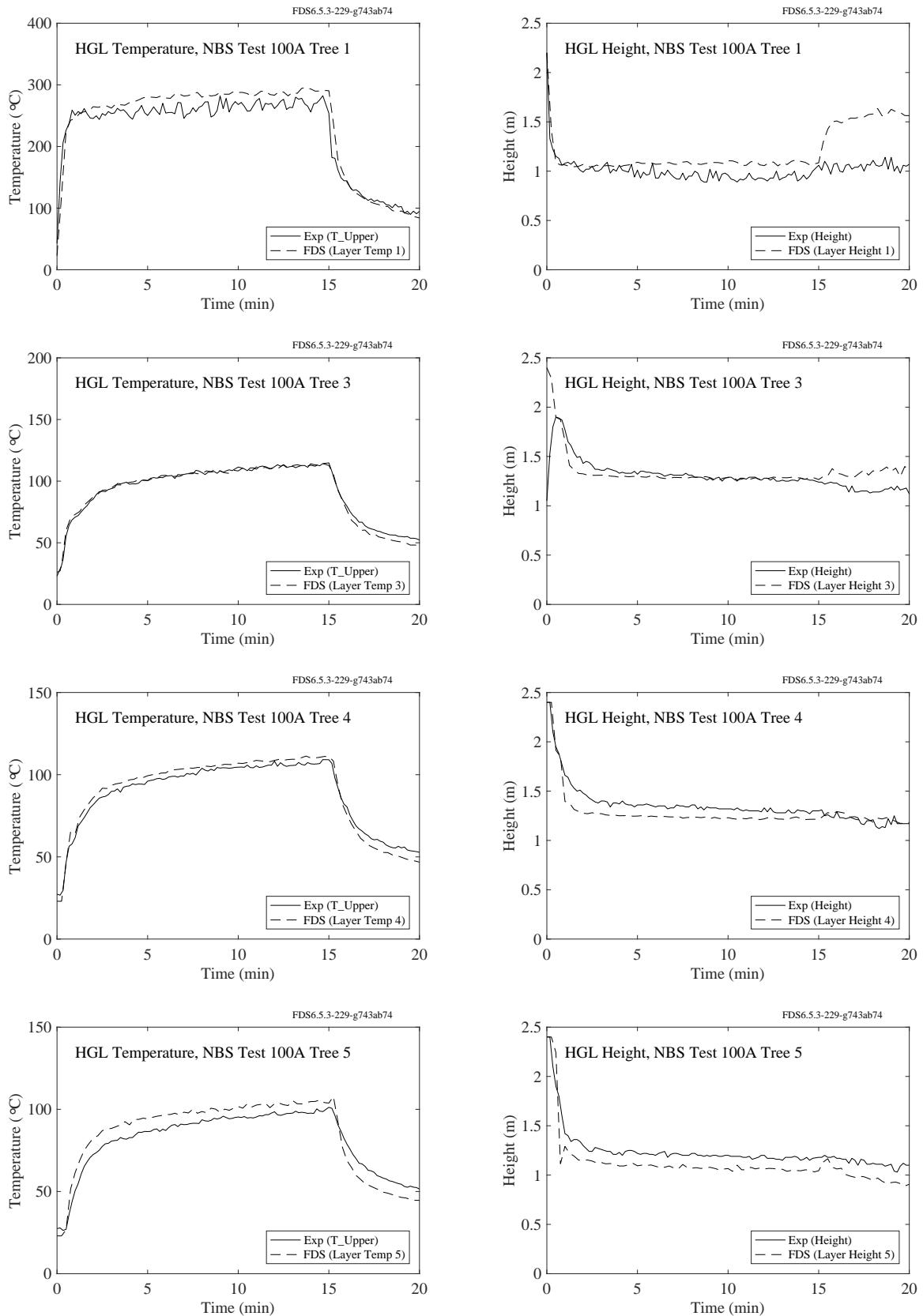


Figure 5.22: NBS Multi-Room experiments, HGL temperature and height, Test 100A.

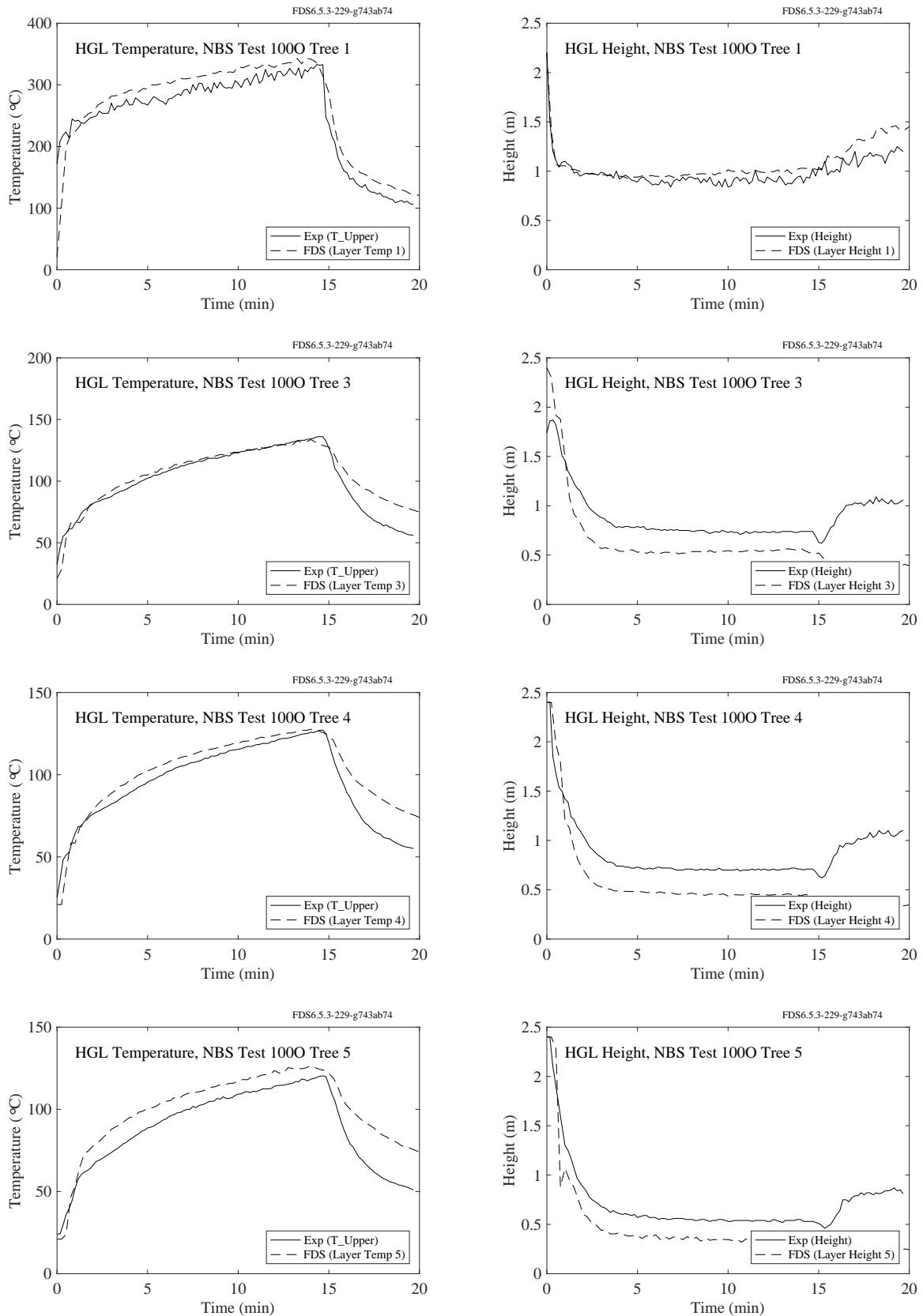


Figure 5.23: NBS Multi-Room experiments, HGL temperature and height, Test 100O.

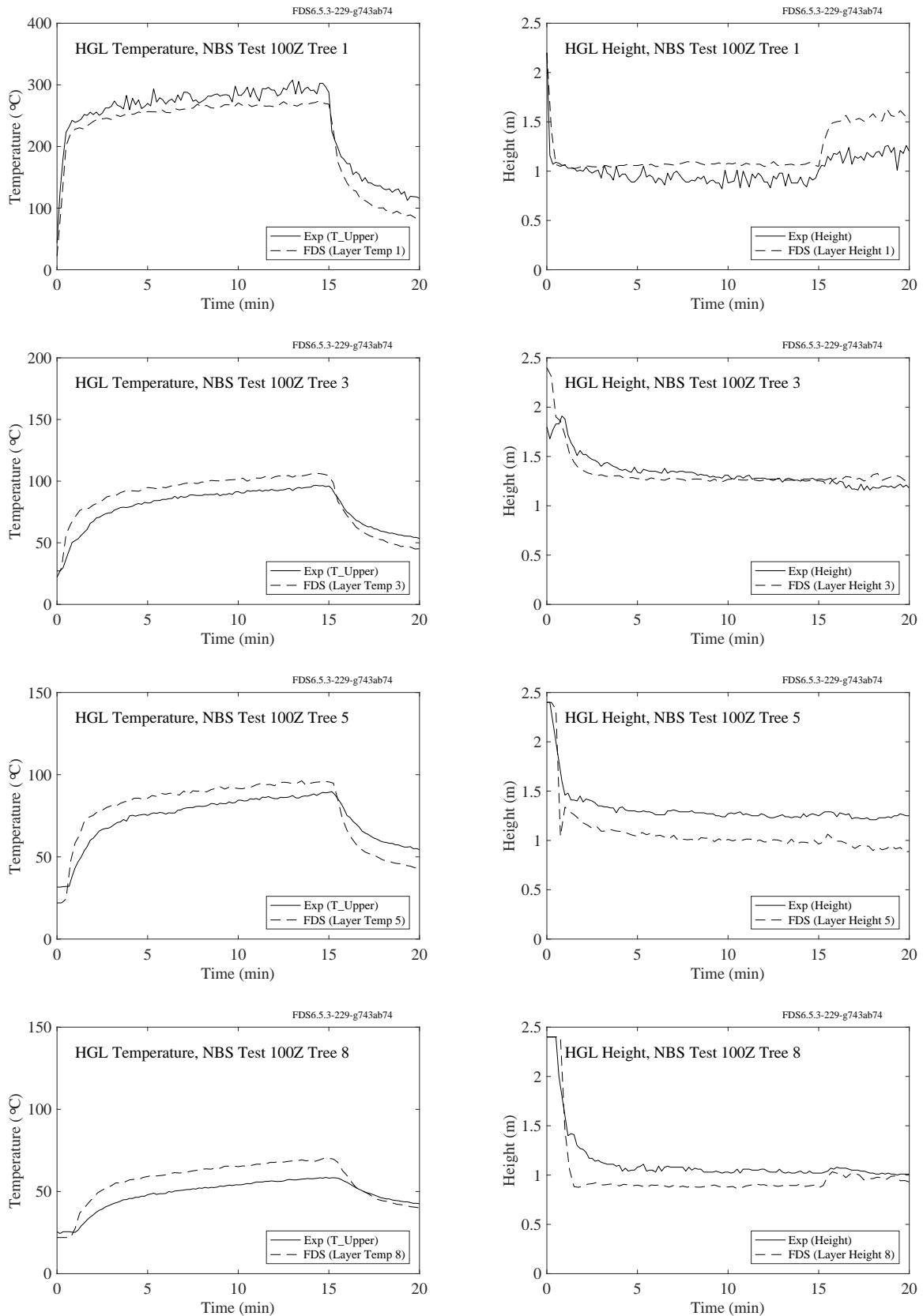


Figure 5.24: NBS Multi-Room experiments, HGL temperature and height, Test 100Z.

## **5.7 NIST Full-Scale Enclosure (FSE), 2008**

Thermocouple arrays were suspended from the ceiling at two points along the centerline of the ISO 9705 compartment. The array in the front of the compartment was located 72 cm inside the door, and the array in the rear was 72 cm from the back wall. Each array consisted of 11 TCs positioned at heights of 3 cm, 30 cm, 60 cm, 90 cm, 105 cm, 120 cm, 135 cm, 150 cm, 180 cm, 210 cm, and 2.38 cm. The height of the compartment was 2.4 m. In the plots on the following pages, the average HGL temperature and layer height are shown for experiments 8 through 32. The thermocouple arrays were not installed for experiments labelled ISONG3, ISOHept4, or ISOHept5.

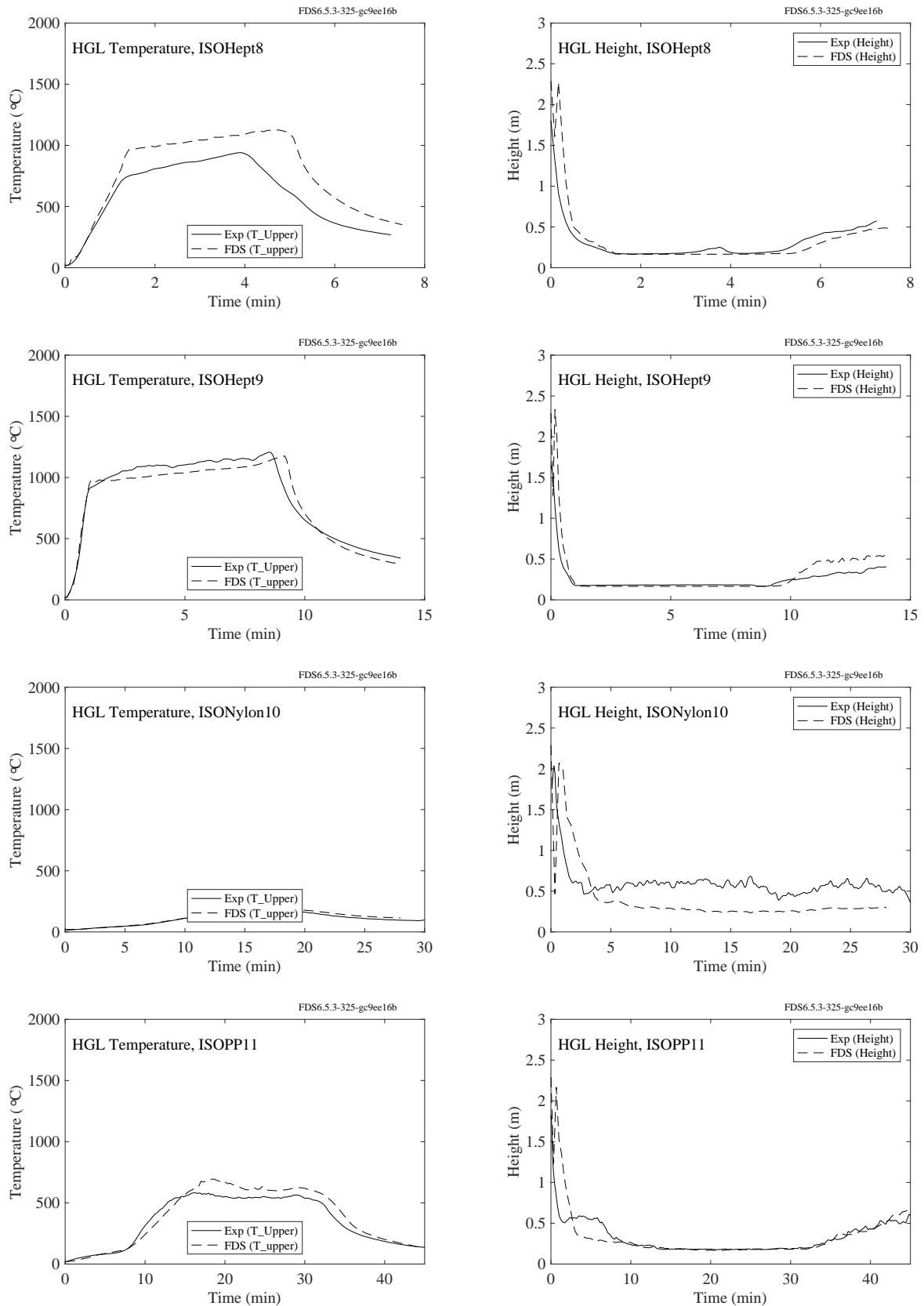


Figure 5.25: NIST FSE, HGL temperature and height, Tests 8-11.

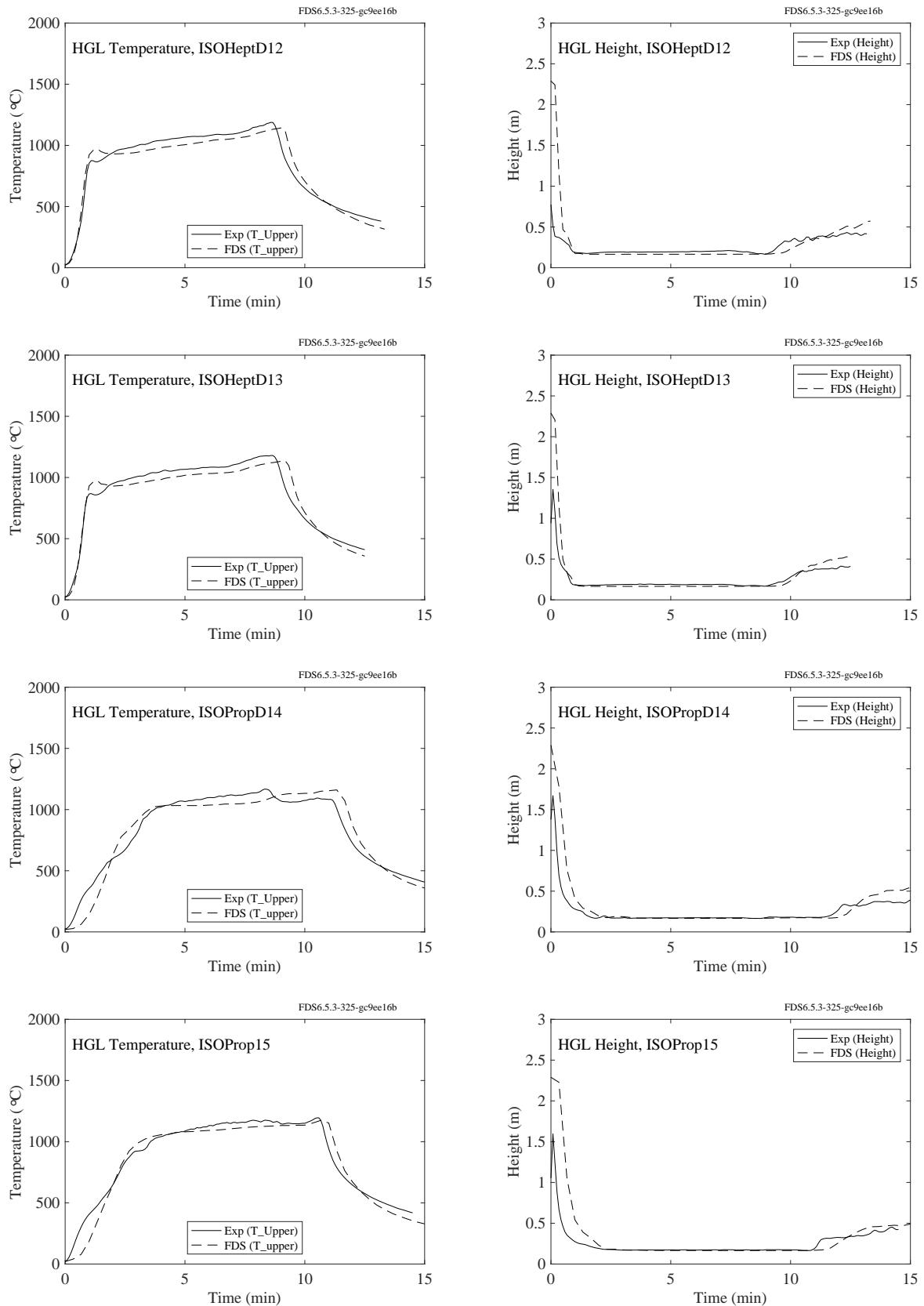


Figure 5.26: NIST FSE, HGL temperature and height, Tests 12-15.

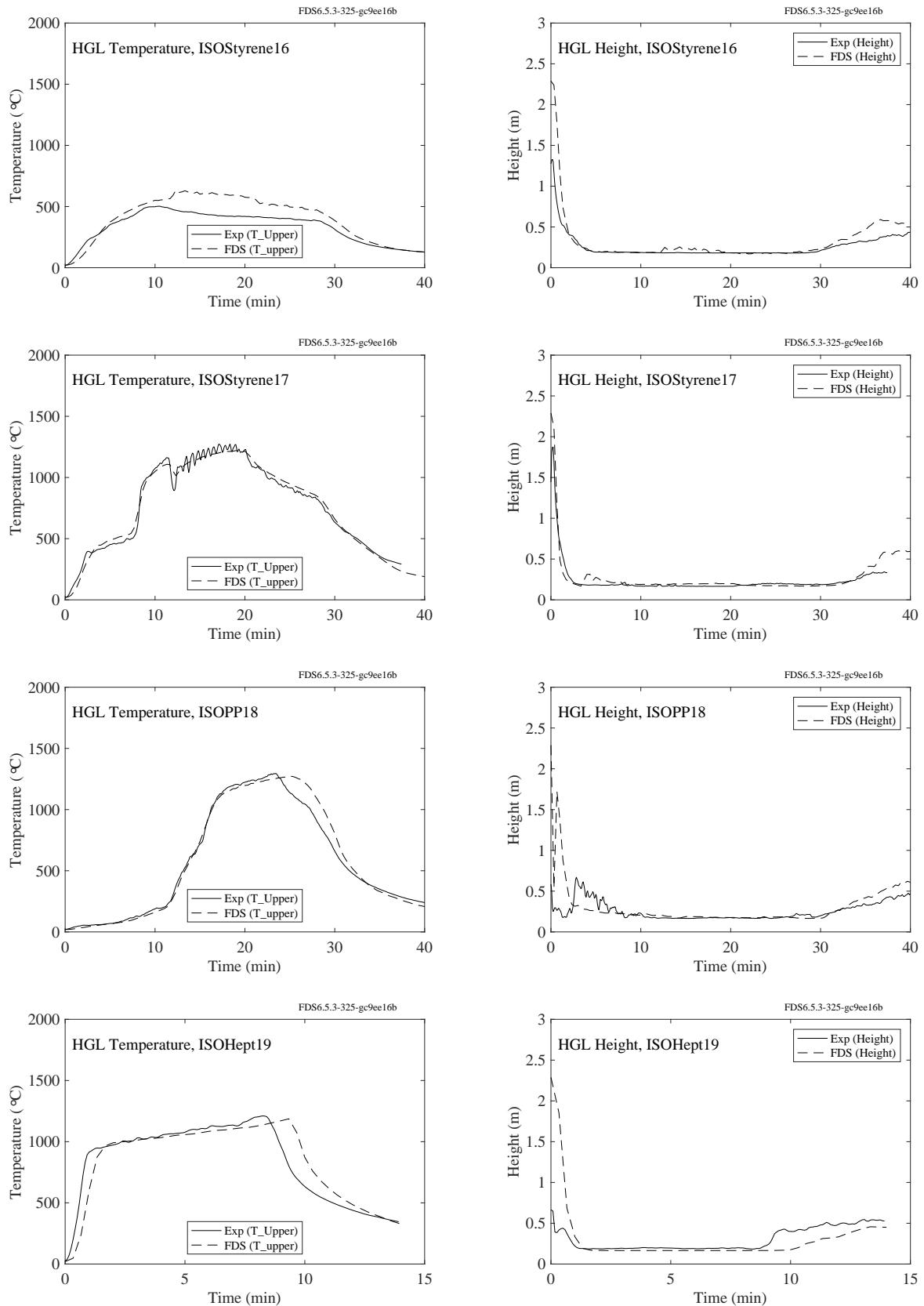


Figure 5.27: NIST FSE, HGL temperature and height, Tests 16-19.

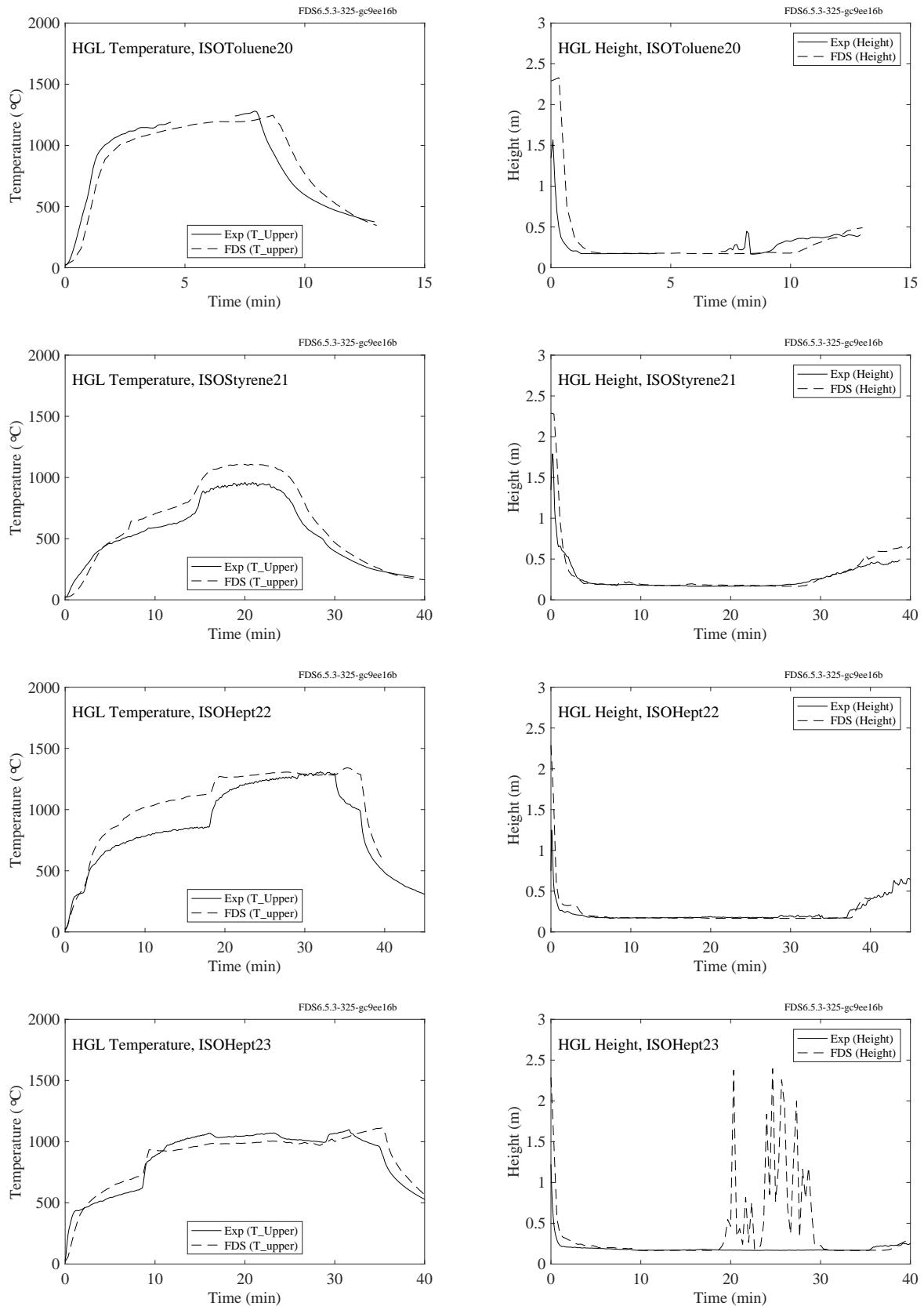


Figure 5.28: NIST FSE, HGL temperature and height, Tests 20-23.

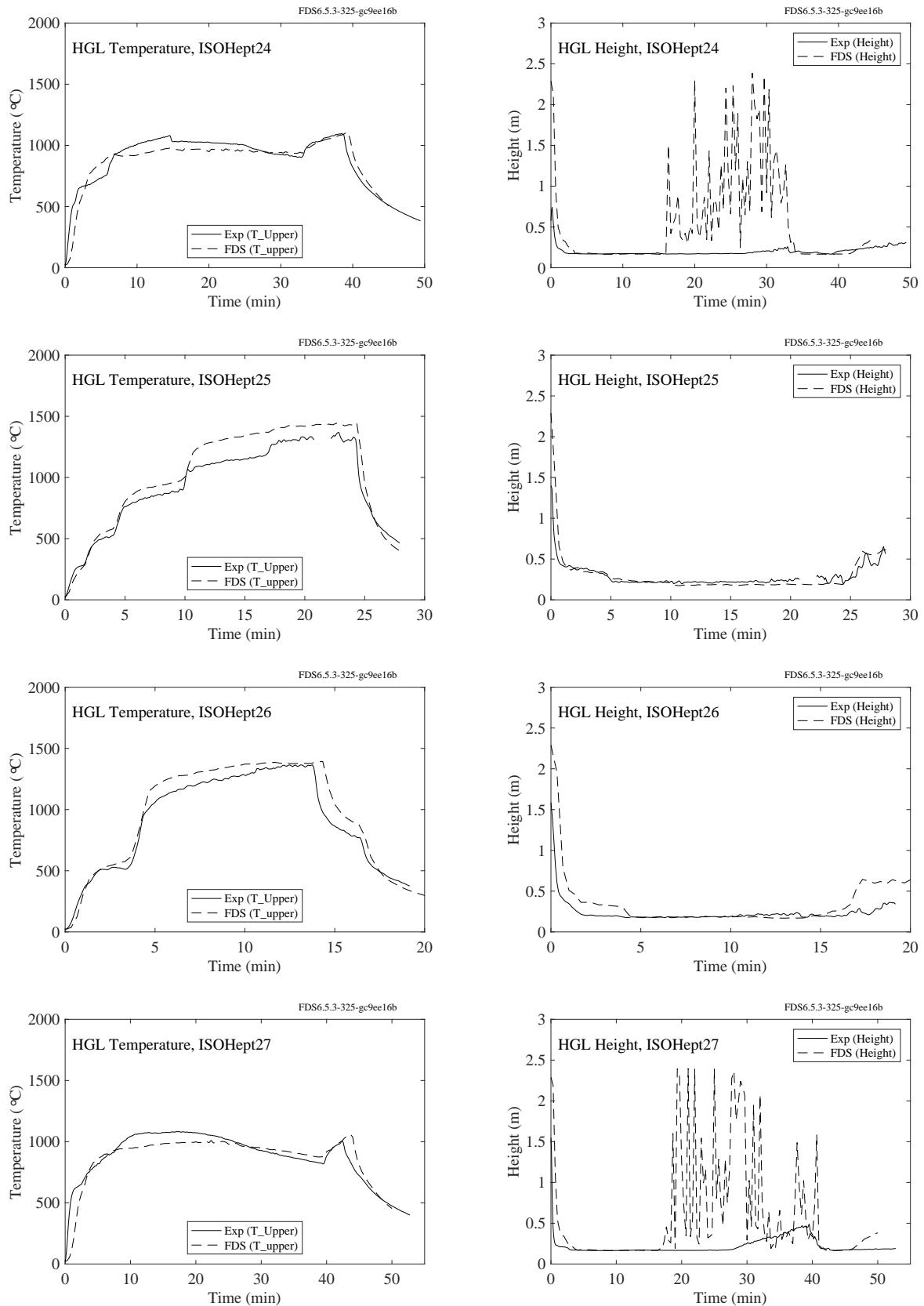


Figure 5.29: NIST FSE, HGL temperature and height, Tests 24-27.

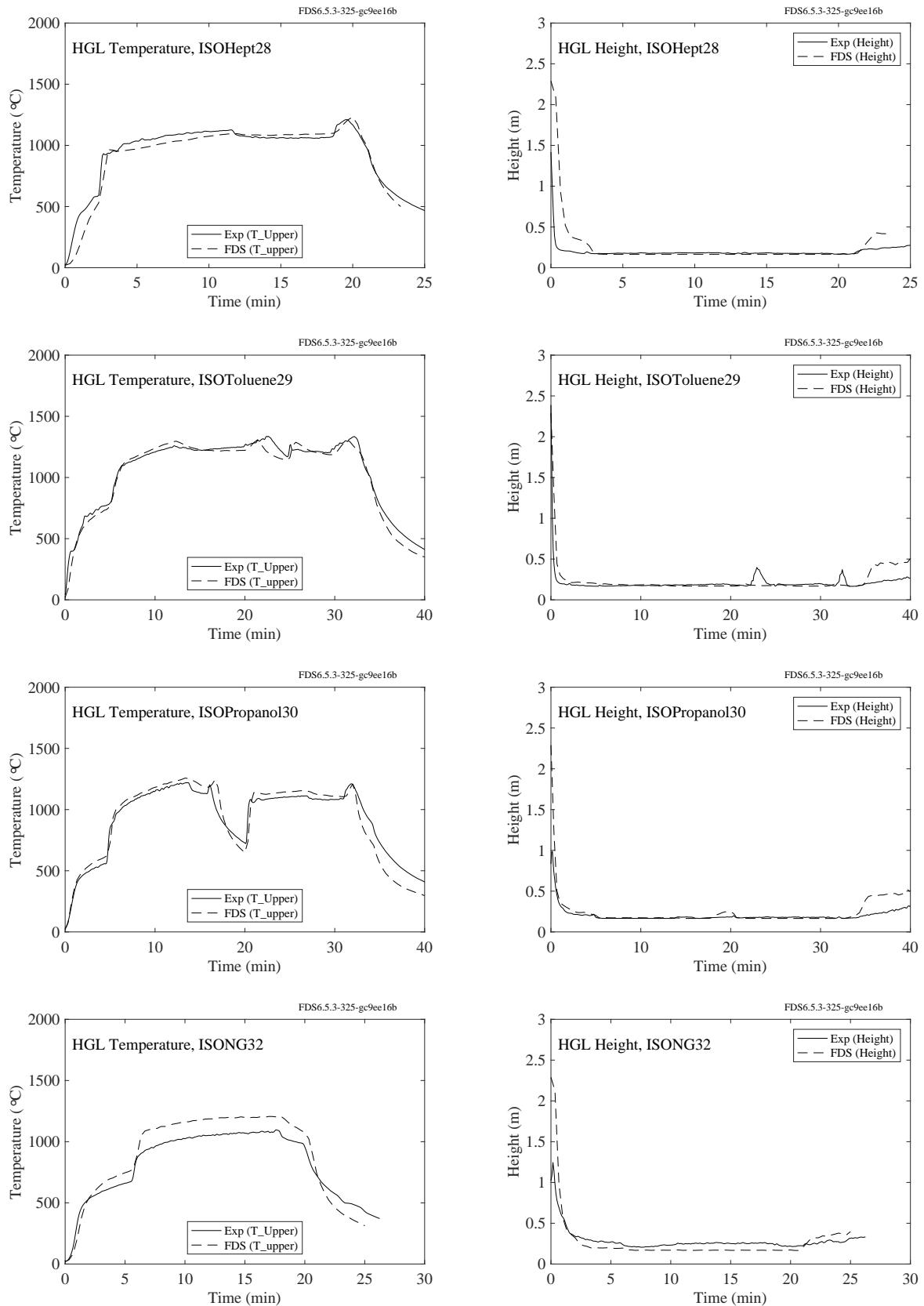


Figure 5.30: NIST FSE, HGL temperature and height, Tests 28-30,, 32.

## 5.8 NIST/NRC Test Series

The NIST/NRC series consisted of 15 heptane spray fire experiments with varying heat release rates, pan locations, and ventilation conditions. Gas temperatures were measured using seven floor-to-ceiling thermocouple arrays (or “trees”) distributed throughout the compartment. The average hot gas layer temperature and height are calculated using thermocouple Trees 1, 2, 3, 5, 6 and 7. Tree 4 was not used because one of its thermocouples (TC 4-9) malfunctioned during most of the experiments. A few observations about the simulations:

- During Tests 4, 5, 10 and 16 a fan blew air into the compartment through a vent in the south wall. The measured velocity profile of the fan was not uniform, with the bulk of the air blowing from the lower third of the duct towards the ceiling at a roughly 45° angle. The exact flow pattern is difficult to replicate in the model, thus, the results for Tests 4, 5, 10 and 16 should be evaluated with this in mind. The effect of the fan on the hot gas layer is small, but it does have a some effect on target temperatures near the vent.
- For all of the tests involving a fan, the predicted HGL height increased after the fire was extinguished, while the measured HGL decreased. This appears to be a curious artifact of the layer reduction algorithm. It is not included in the calculation of the relative difference.
- In the closed door tests, the hot gas layer descended all the way to the floor. However, the reduction method, used on both the measured and predicted temperatures, does not account for the formation of a single layer, and therefore does not indicate that the layer drops all the way to the floor. This is neither a flaw in the measurements nor in FDS, but rather in the layer reduction method.
- The HGL reduction method produces spurious results in the first few minutes of each test because no clear layer has yet formed. These early times are not included in the relative difference calculation.

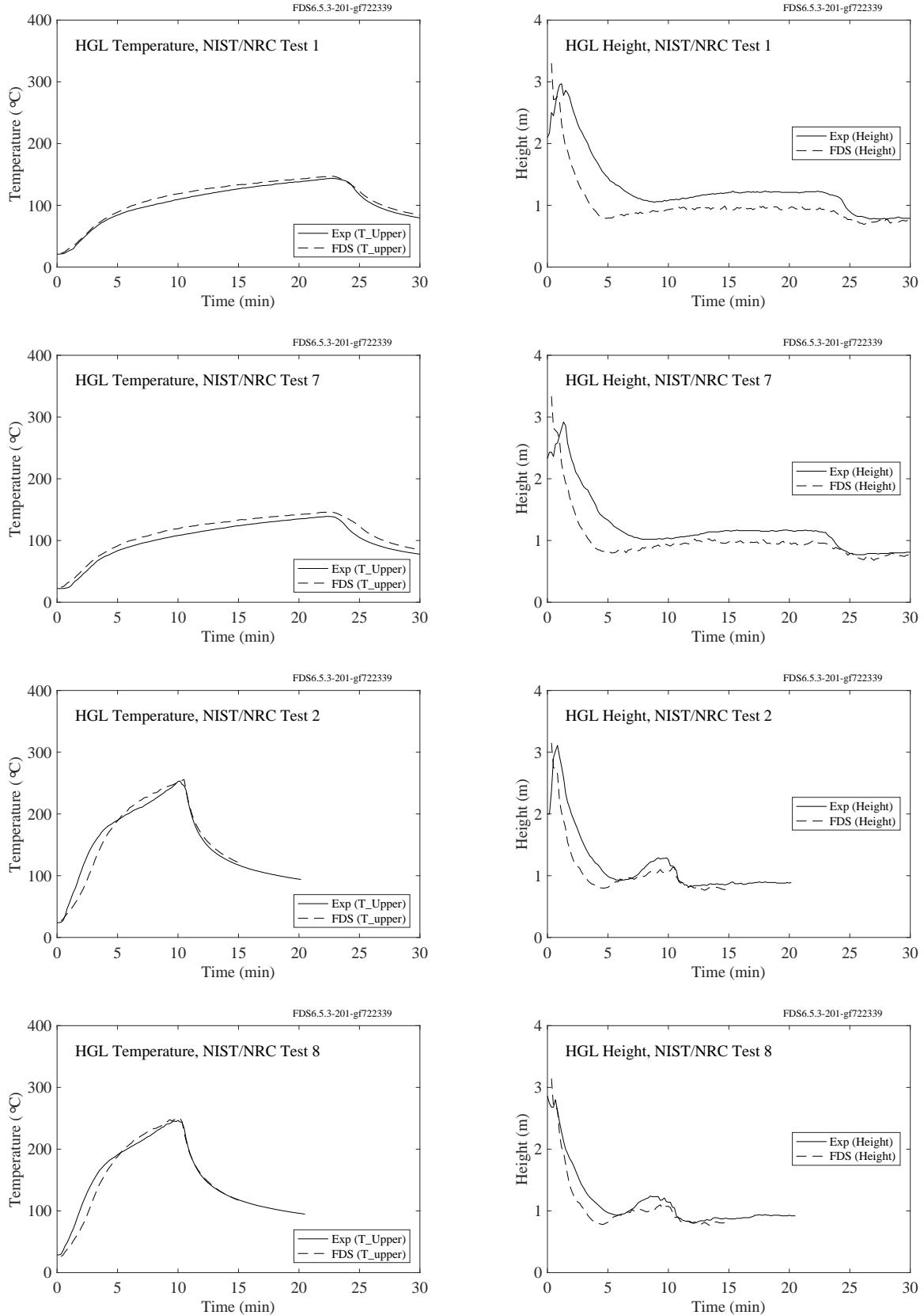


Figure 5.31: NIST/NRC experiments, HGL temperature and height, Tests 1-2, 7-8.

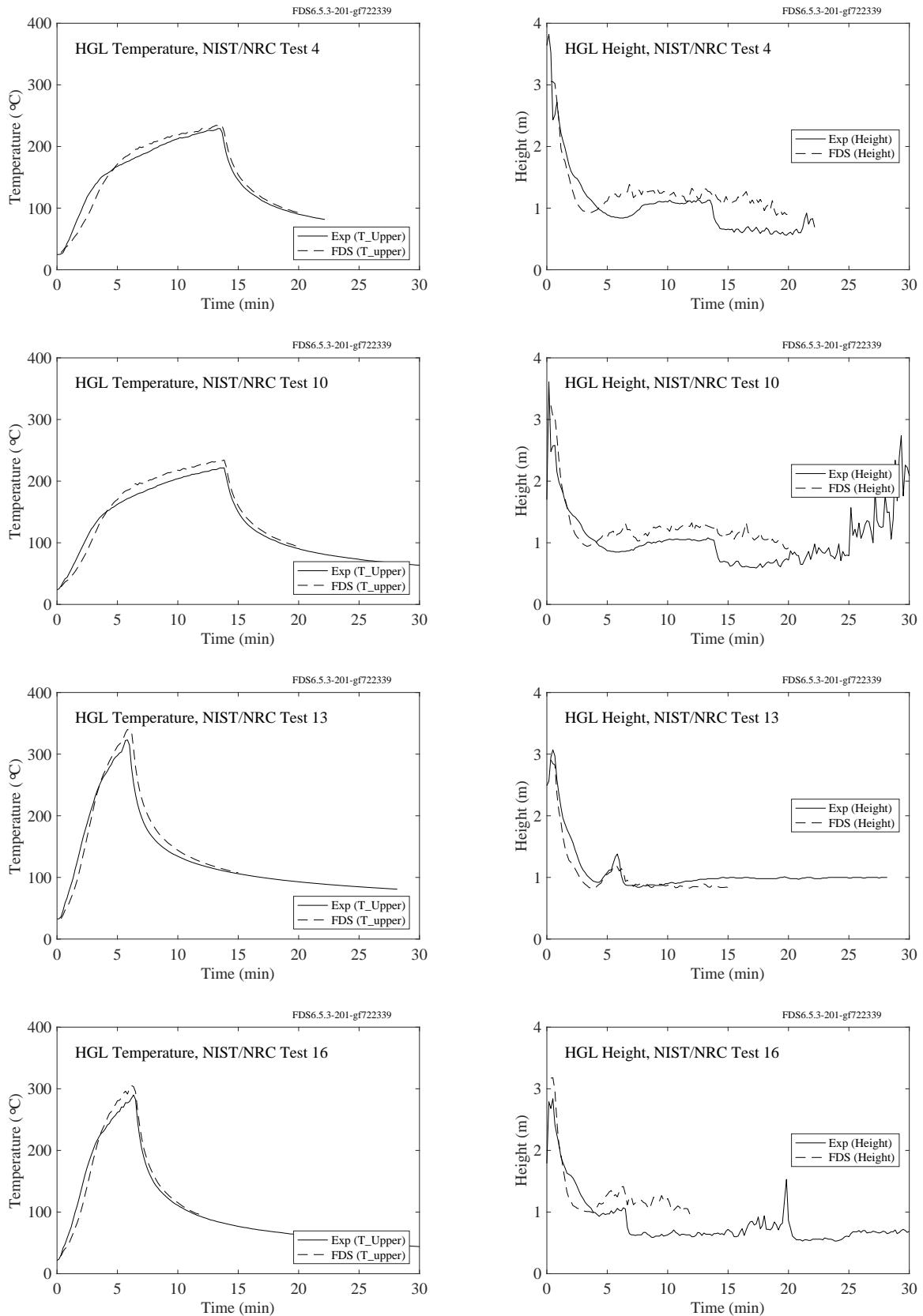
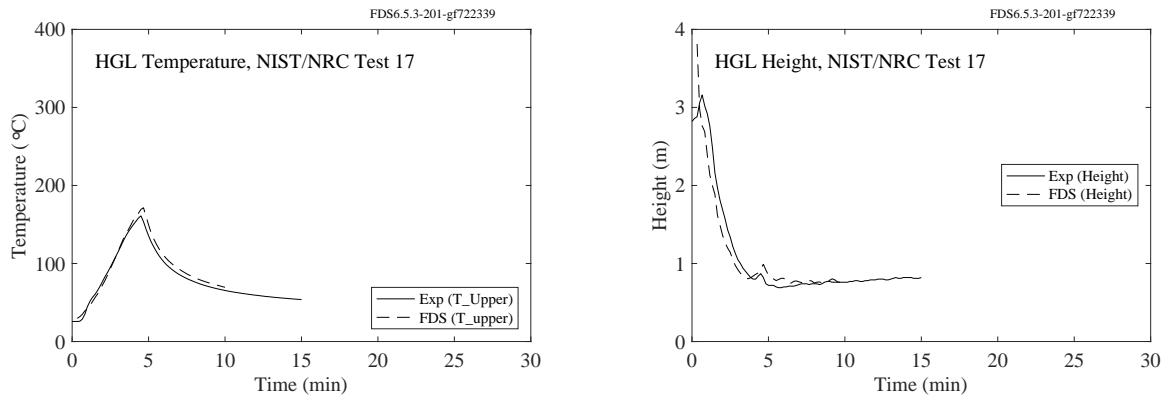


Figure 5.32: NIST/NRC experiments, HGL temperature and height, Tests 4, 10, 13, 16.



Open door tests to follow

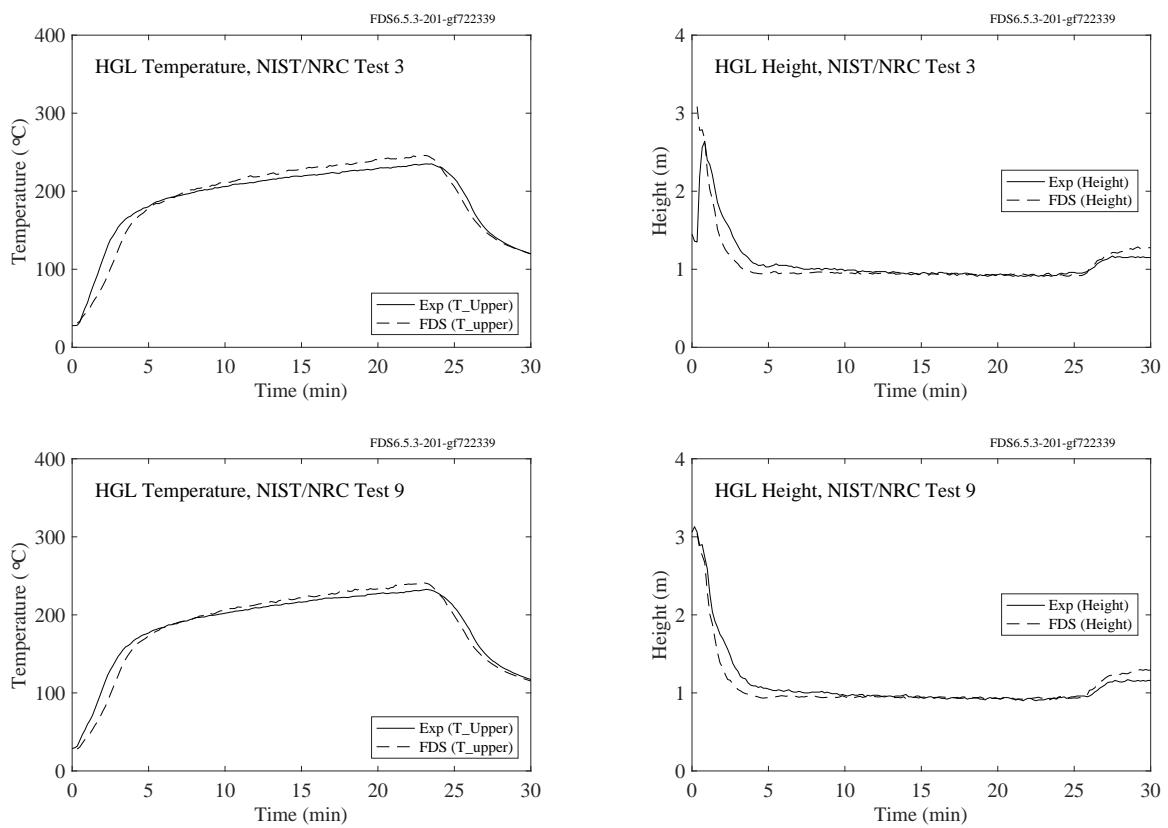


Figure 5.33: NIST/NRC experiments, HGL temperature and height, Tests 3, 9, 17.

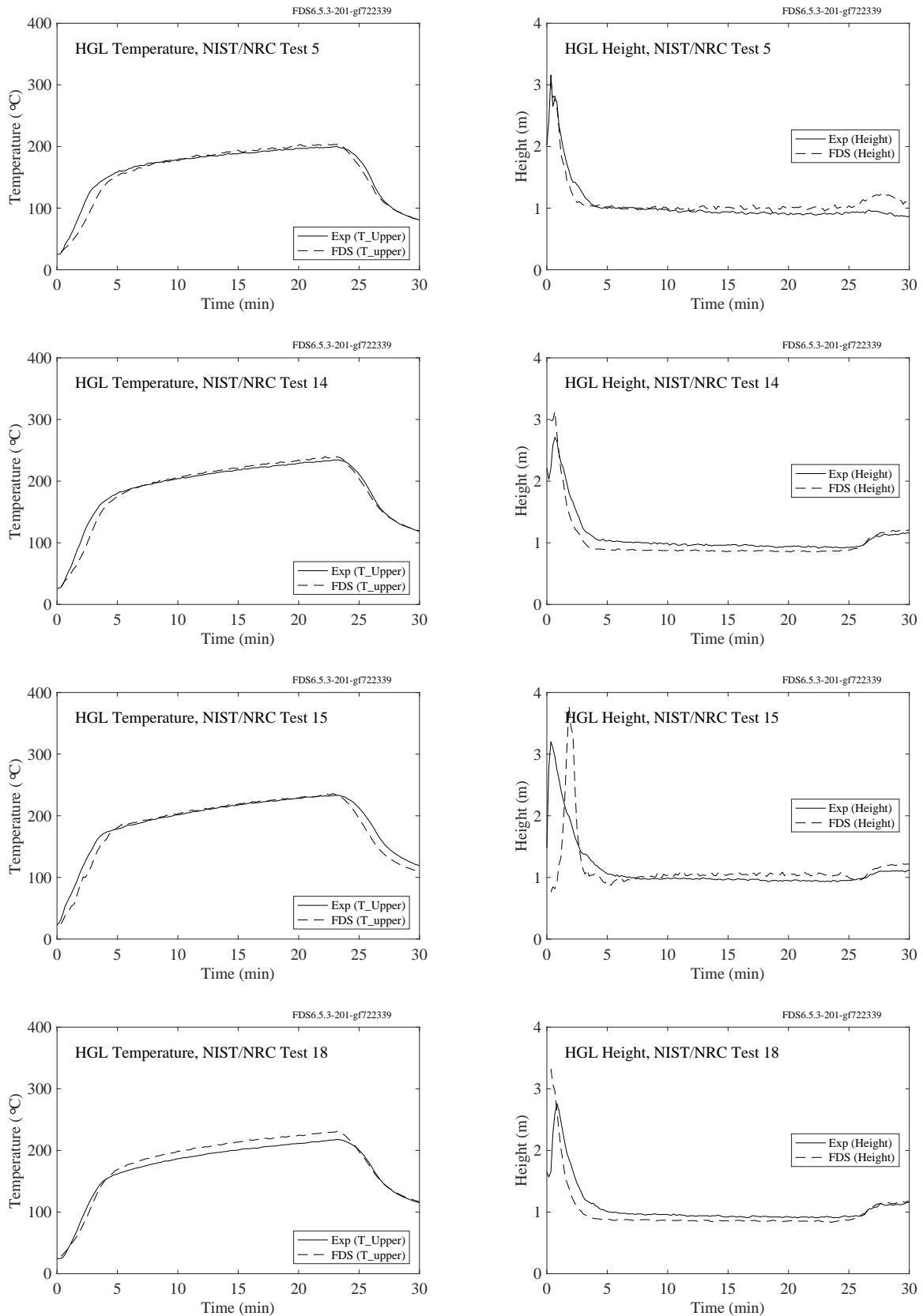


Figure 5.34: NIST/NRC experiments, HGL temperature and height, Tests 5, 14, 15, 18.

## 5.9 NRCC Smoke Tower

In the NRCC Smoke Tower experiments, there was a vertical array consisting of thirteen TCs that were installed in the fire compartment on the second floor at the following heights: 0.62 m, 0.92 m, 1.22 m, 1.37 m, 1.52 m, 1.67 m, 1.82 m, 1.97 m, 2.12 m, 2.27 m, 2.42 m, 2.57 m and 2.95 m. Also, five TCs were installed in the doorway between the stair vestibule and stair shaft on the second floor. Figure 5.35 shows the predicted and measured HGL temperature for both vertical arrays.

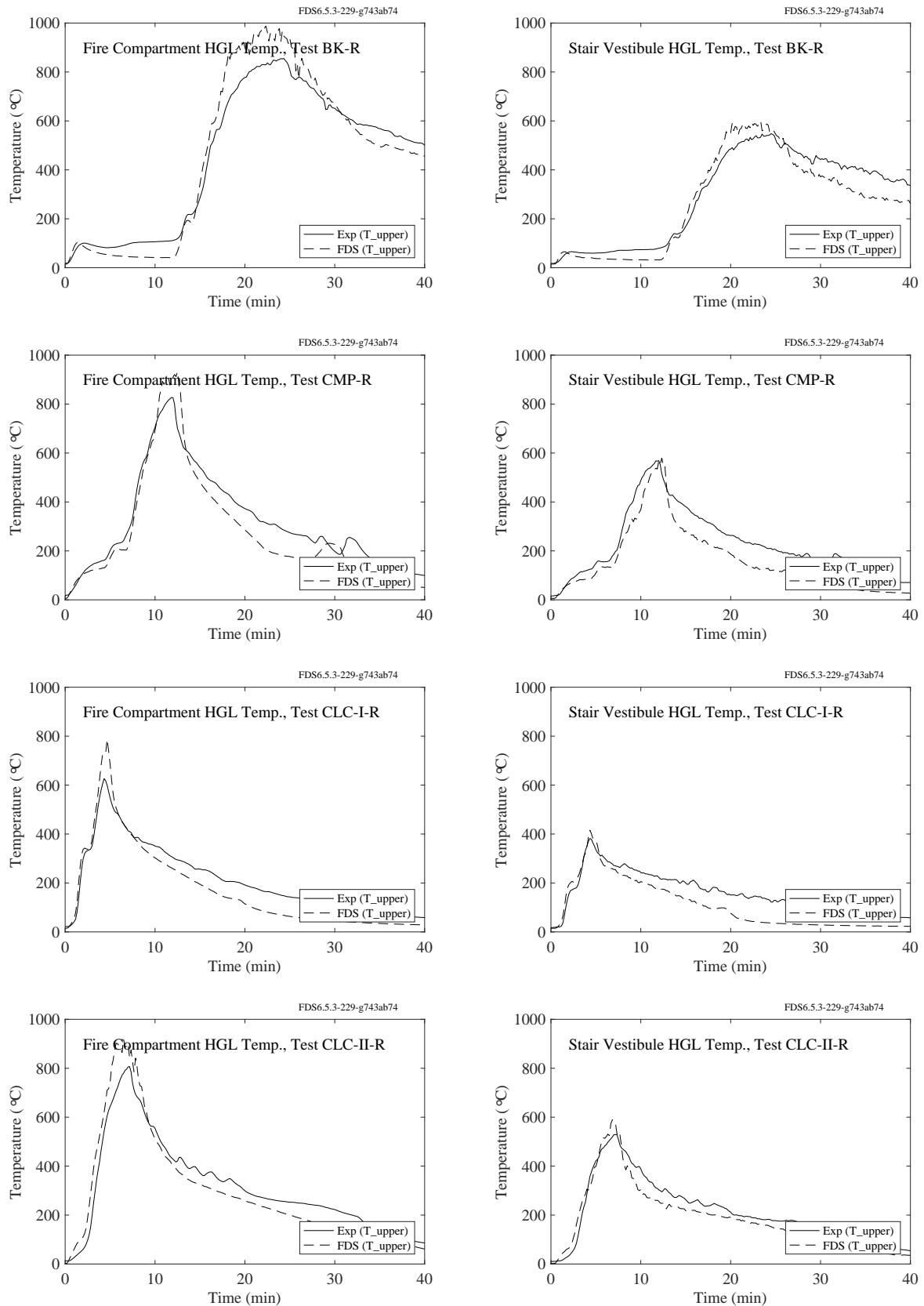


Figure 5.35: NRCC Smoke Tower experiments, HGL temperature in the fire room and stair vestibule.

## 5.10 PRISME DOOR Experiments

The compartments in the PRISME DOOR experiments contained vertical arrays of thermocouples to measure the HGL temperature and depth. Each array contained 18 TCs and each compartment included three arrays. The array above the fire was excluded from the calculation of the HGL temperature and depth.

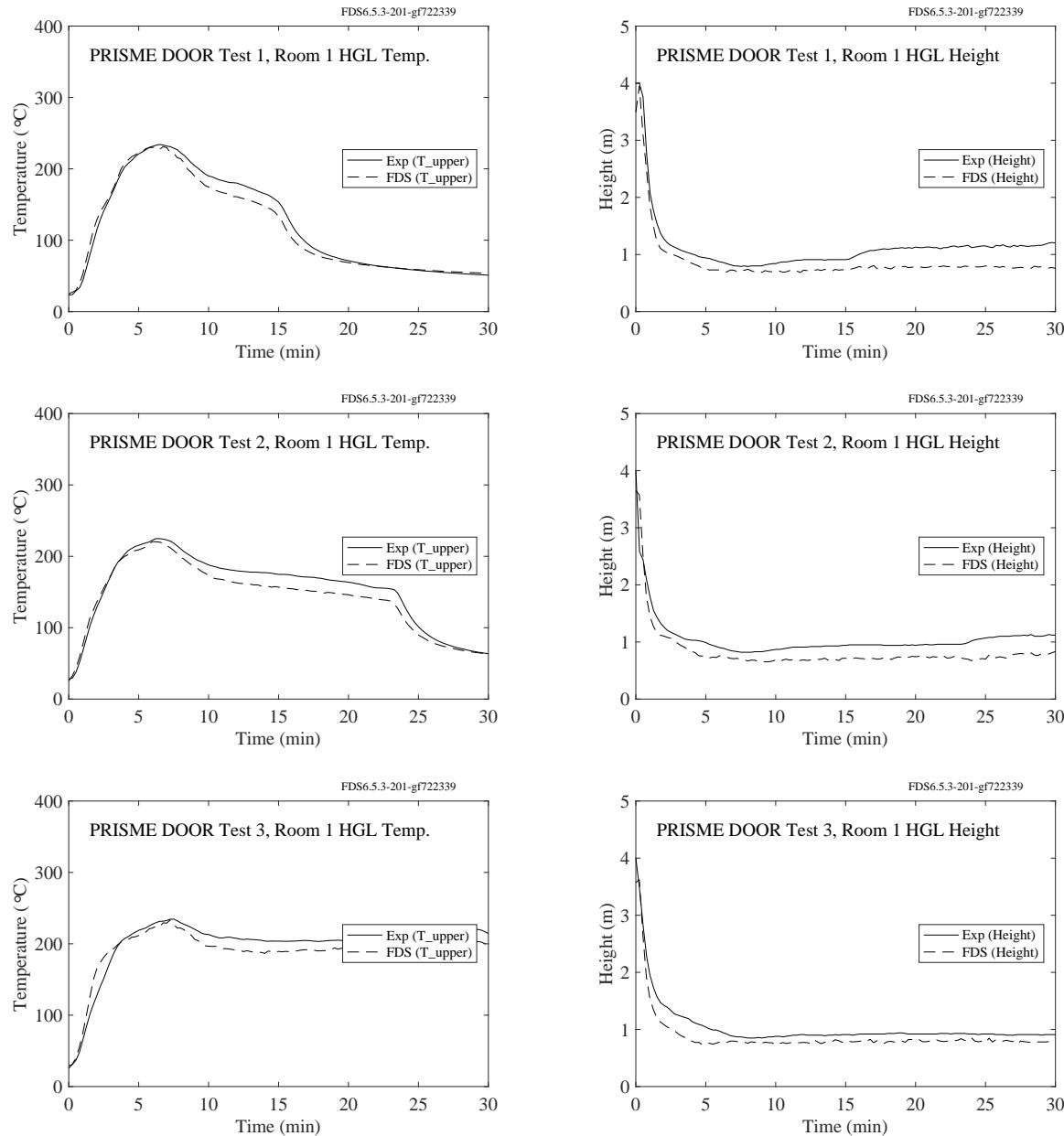


Figure 5.36: PRISME DOOR experiments, HGL temperature and height, Room 1, Tests 1-3.

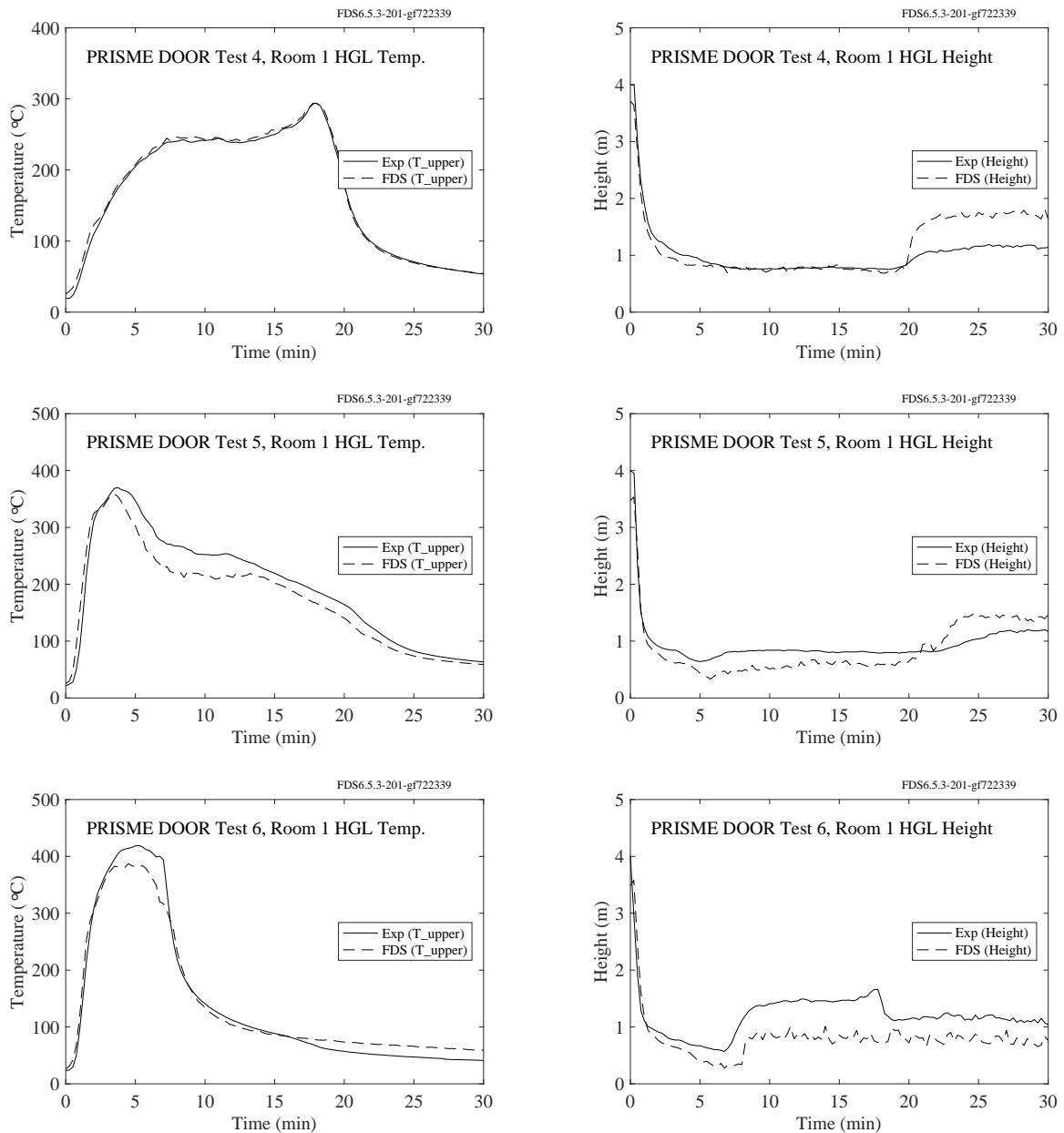


Figure 5.37: PRISME DOOR experiments, HGL temperature and height, Room 1, Tests 4-6.

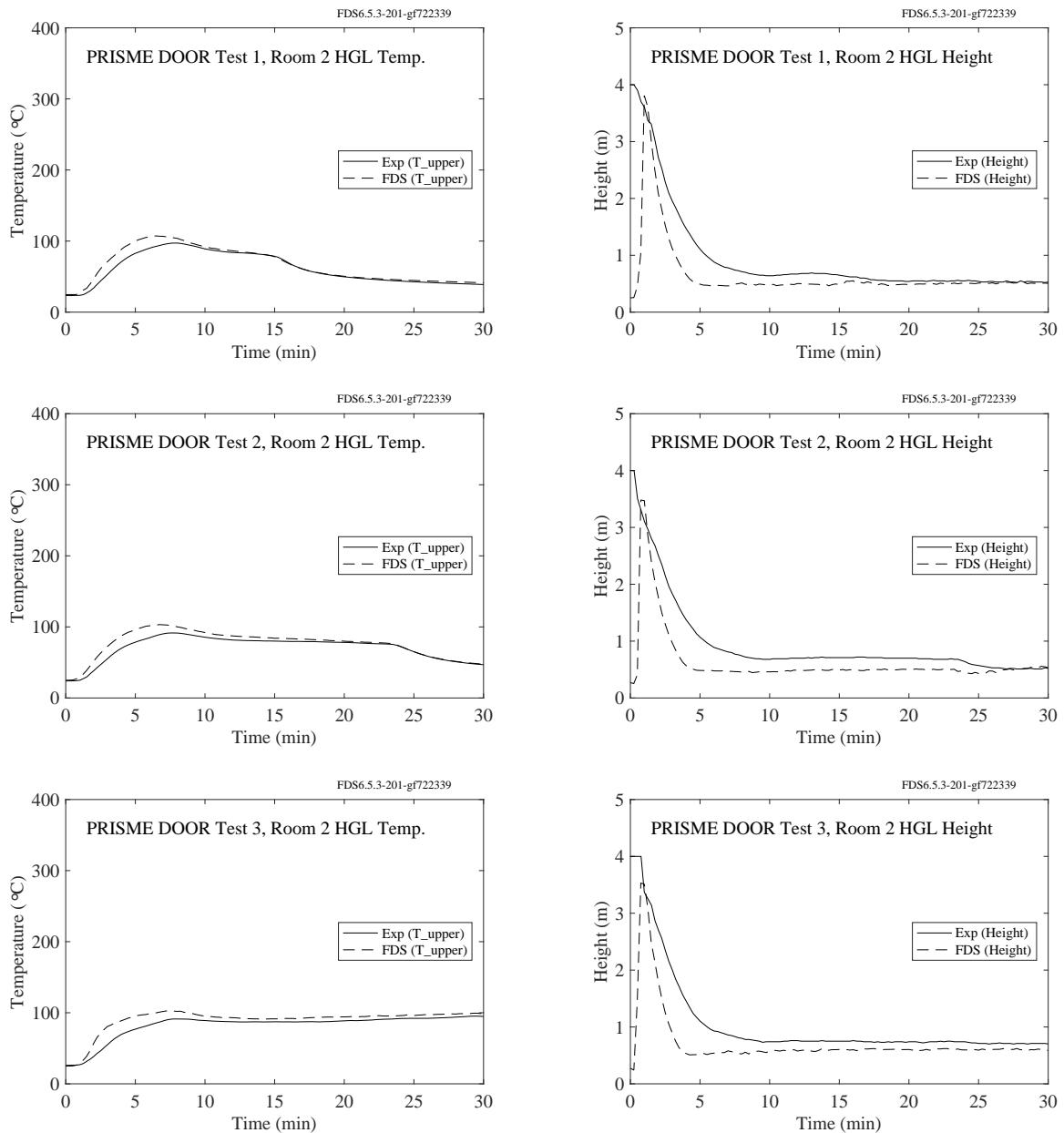


Figure 5.38: PRISME DOOR experiments, HGL temperature and height, Room 2, Tests 1-3.

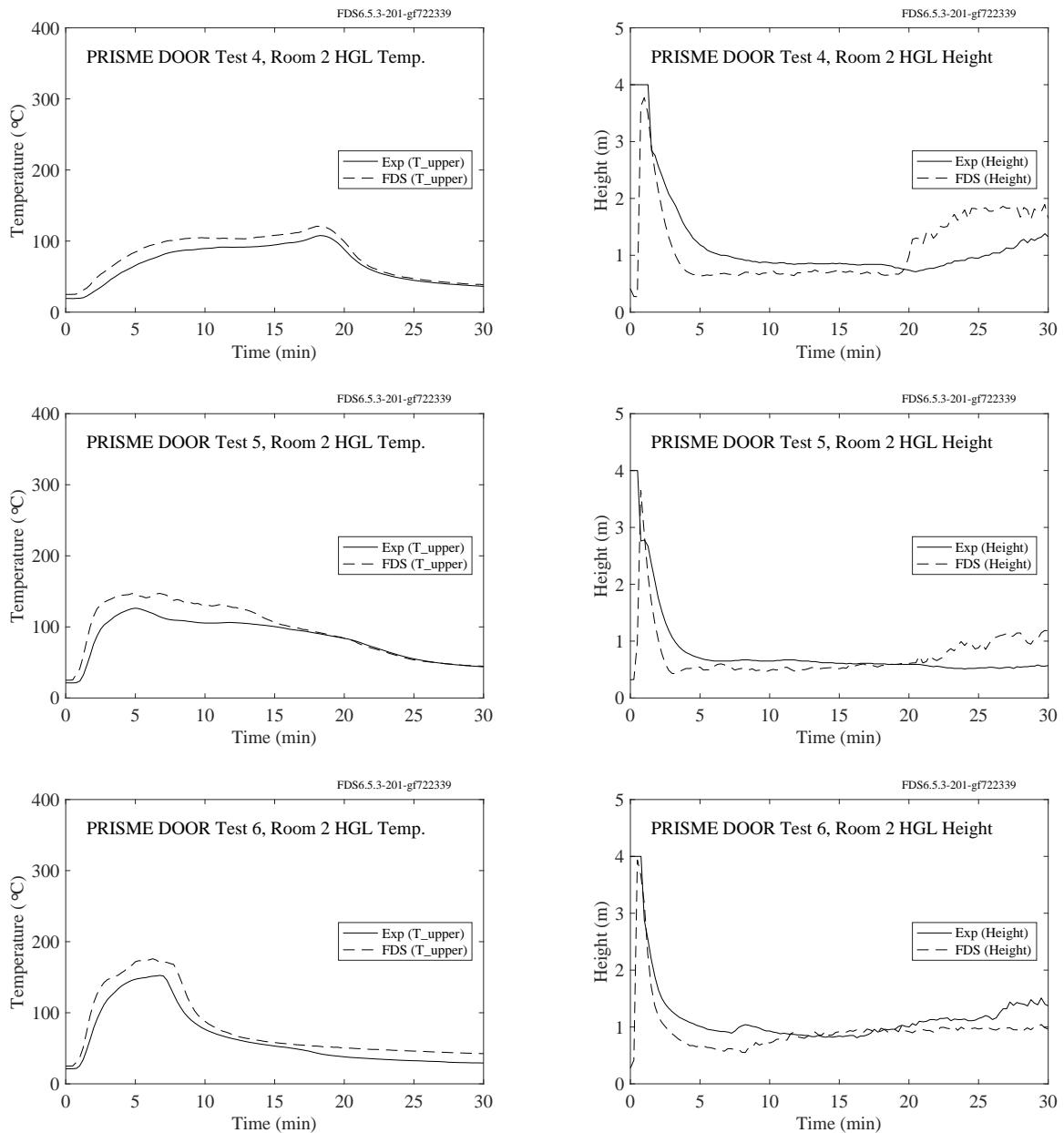


Figure 5.39: PRISME DOOR experiments, HGL temperature and height, Room 1, Tests 4-6.

## **5.11 PRISME SOURCE Experiments**

The PRISME SOURCE experiments were conducted in a single compartment connected to an HVAC network. The compartment was 5 m by 6 m by 4 m high. The HGL temperature was computed from a single vertical thermocouple array located in the northeast quadrant of the compartment. The array contained 18 TCs; the highest one 0.1 m below the ceiling.

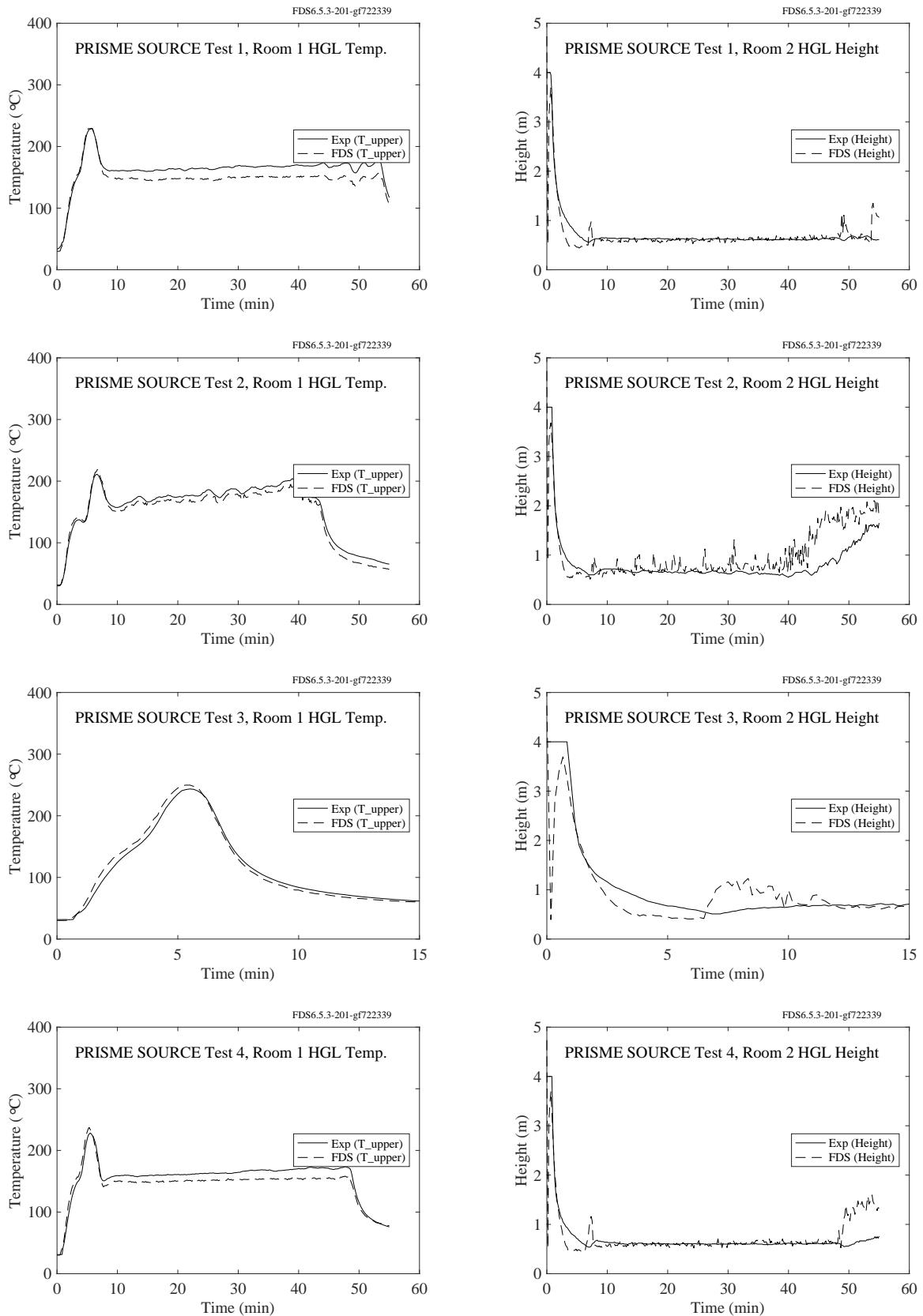


Figure 5.40: PRISME SOURCE experiments, HGL temperature and height, Room 2, Tests 1-4.

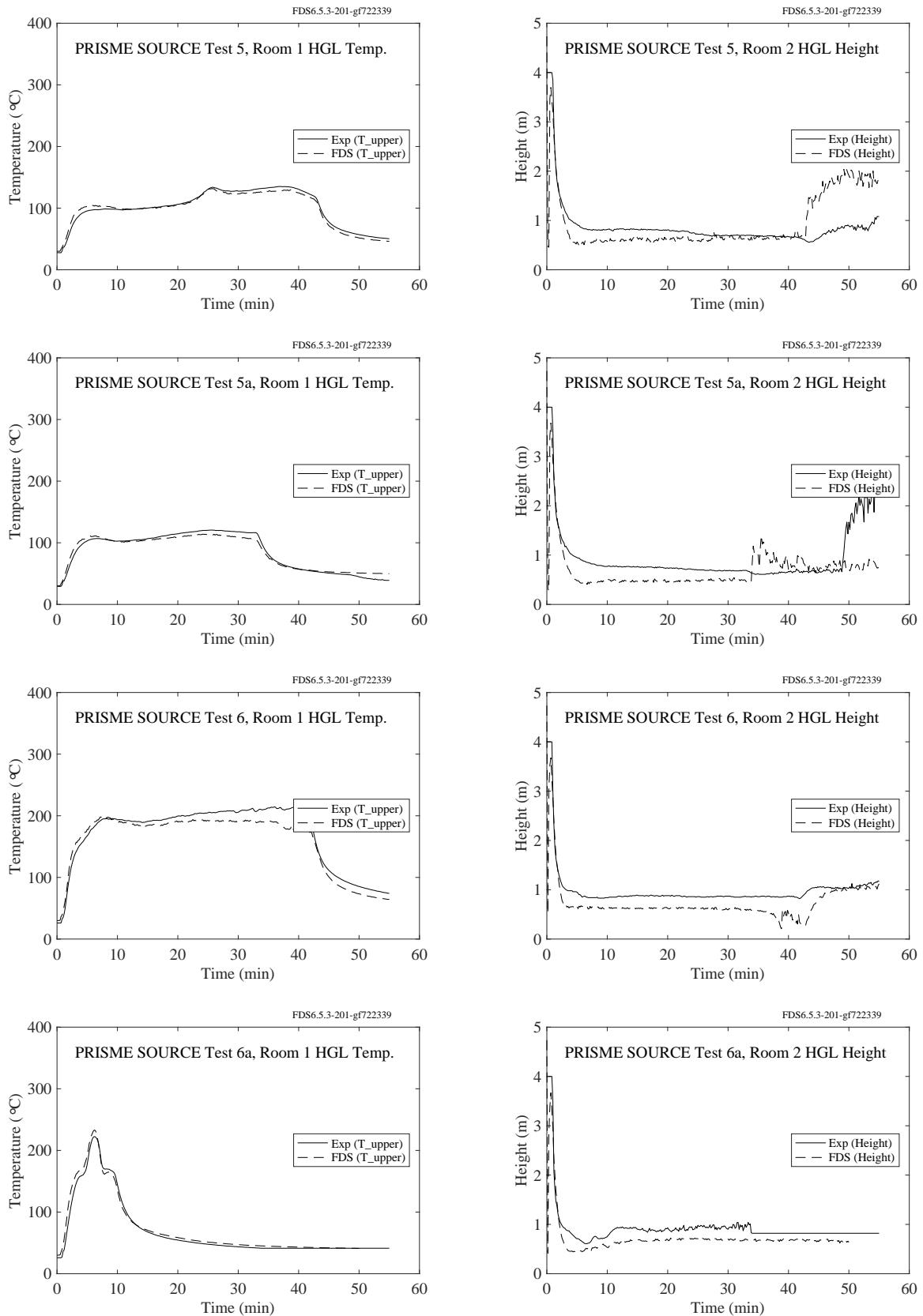


Figure 5.41: PRISME SOURCE experiments, HGL temperature and height, Room 2, Tests 5-6.

## 5.12 Steckler Compartment Experiments

Steckler et al. [201] mapped the doorway/window flows in 55 compartment fire experiments. The test matrix is presented in Table 3.6. Shown on the following pages are the temperature profiles inside the compartment compared with model predictions. To quantify the difference between prediction and measurement, the maximum temperatures were compared.

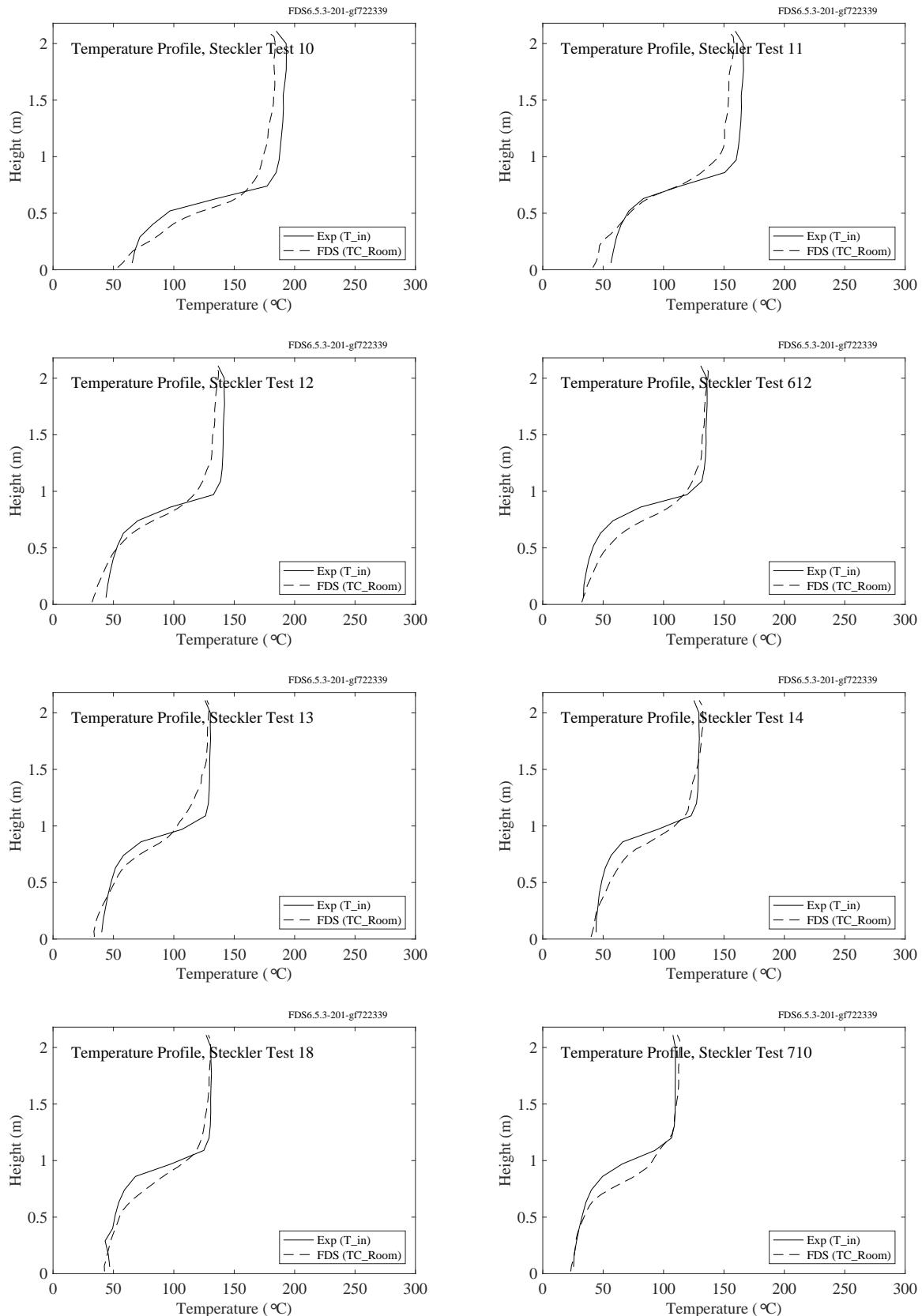


Figure 5.42: Steckler experiments, HGL temperature, Tests 10, 11, 12, 13, 14, 18, 612, 710.

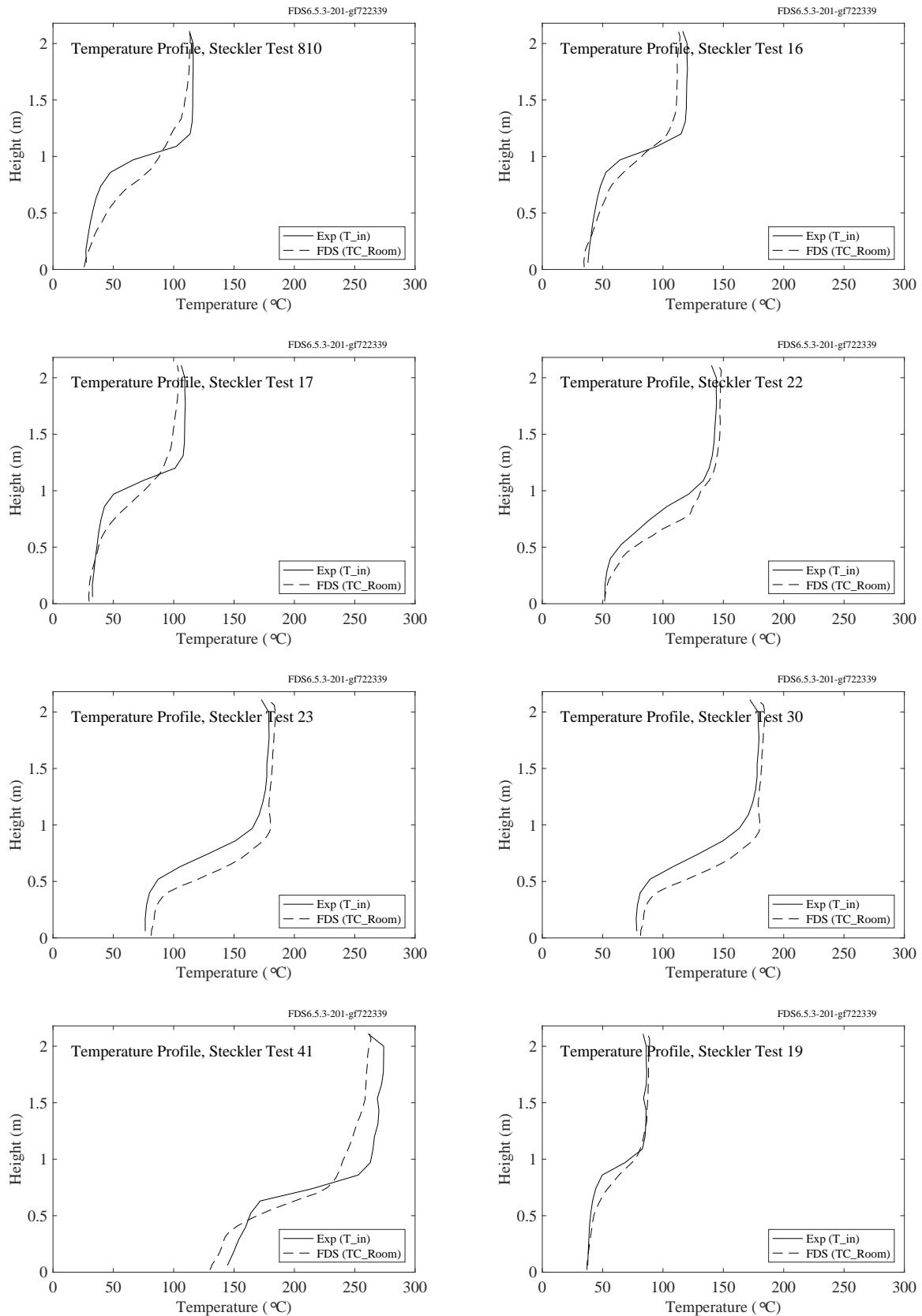


Figure 5.43: Steckler experiments, HGL temperature, Tests 16, 17, 19, 22, 23, 30, 41, 810.

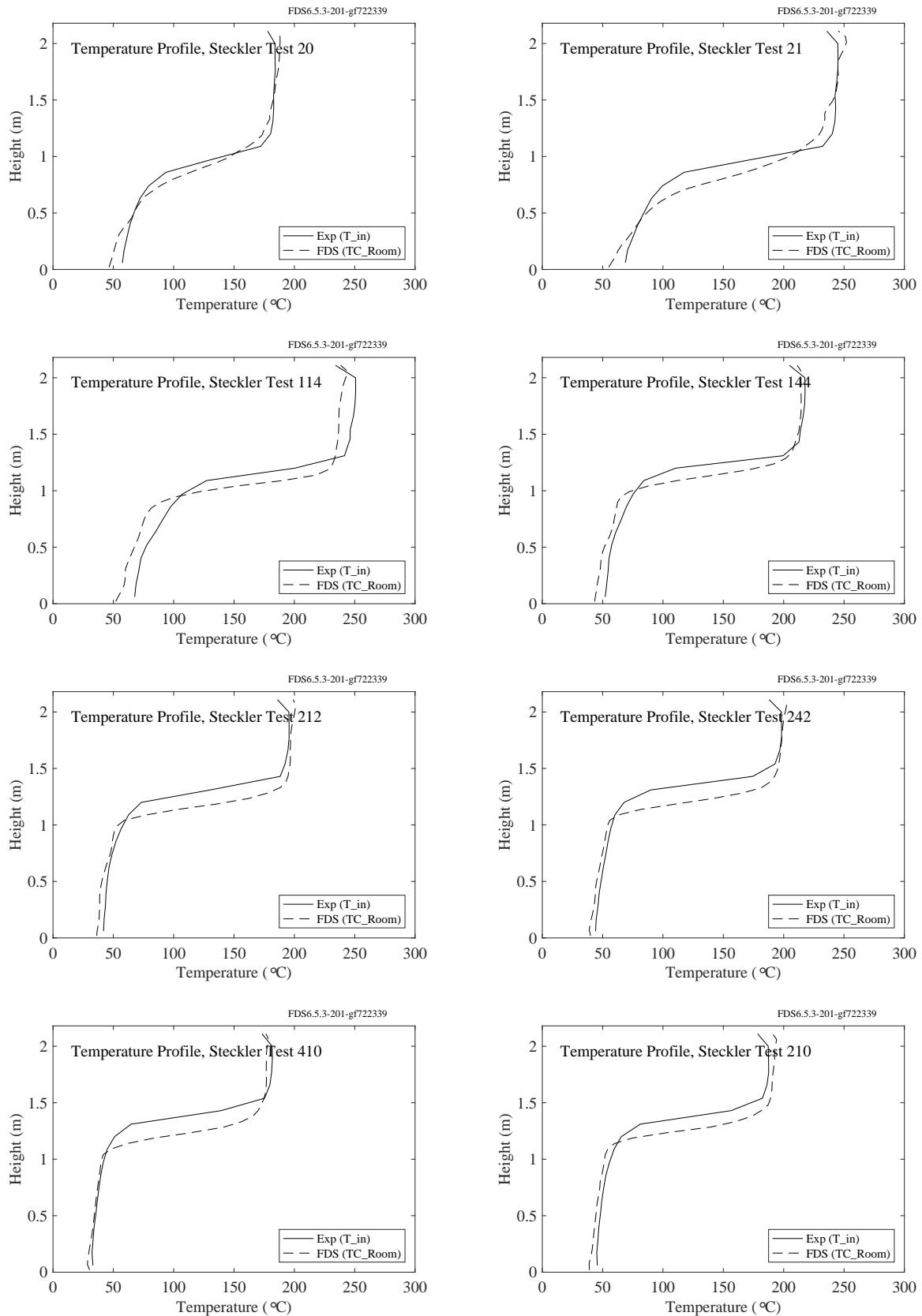


Figure 5.44: Steckler experiments, HGL temperature, Tests 20, 21, 114, 144, 210, 212, 242, 410.

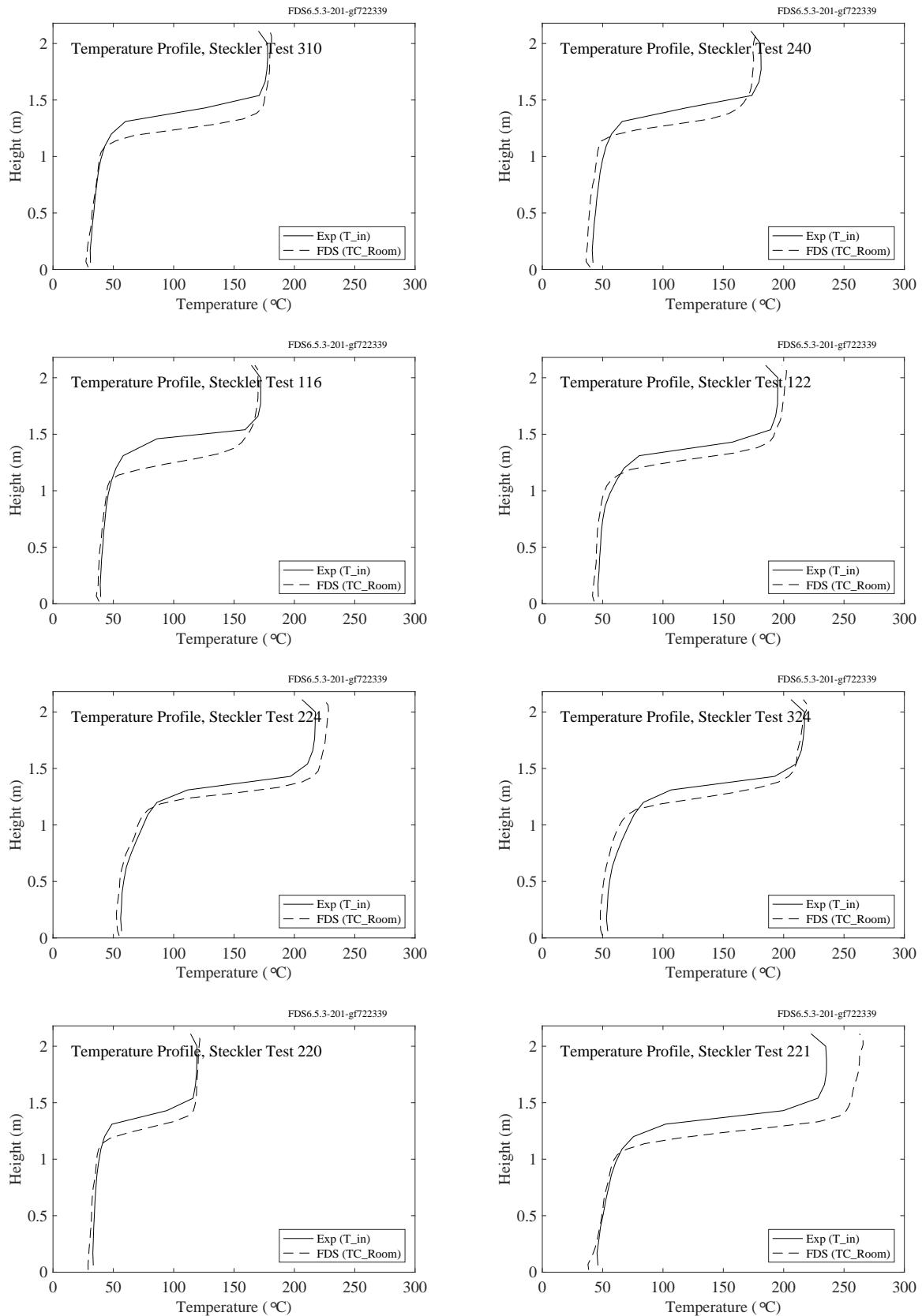


Figure 5.45: Steckler experiments, HGL temperature, Tests 116, 122, 220, 221, 224, 240, 310, 324.

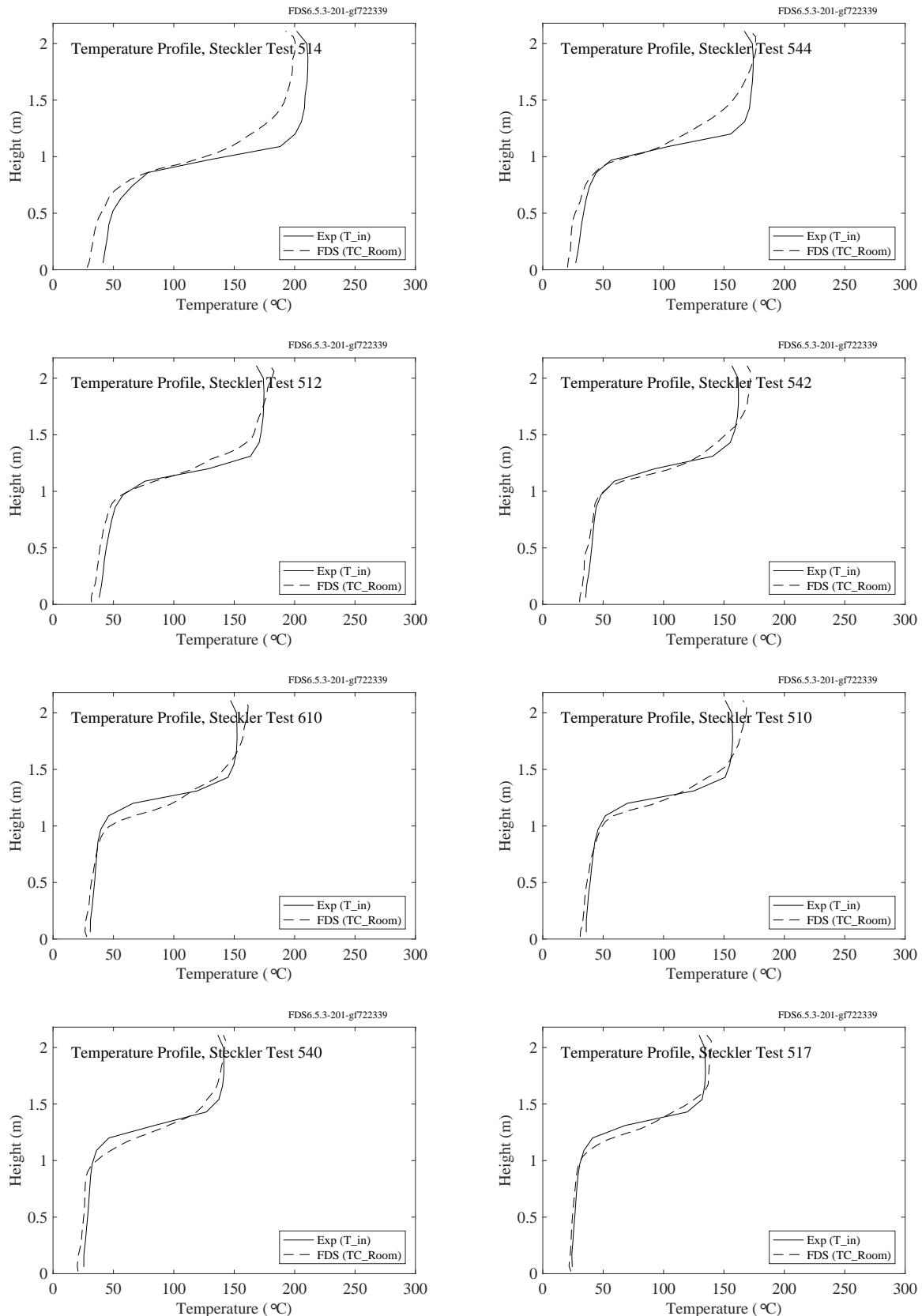


Figure 5.46: Steckler experiments, HGL temperature, Tests 510, 512, 514, 517, 540, 542, 544, 610.

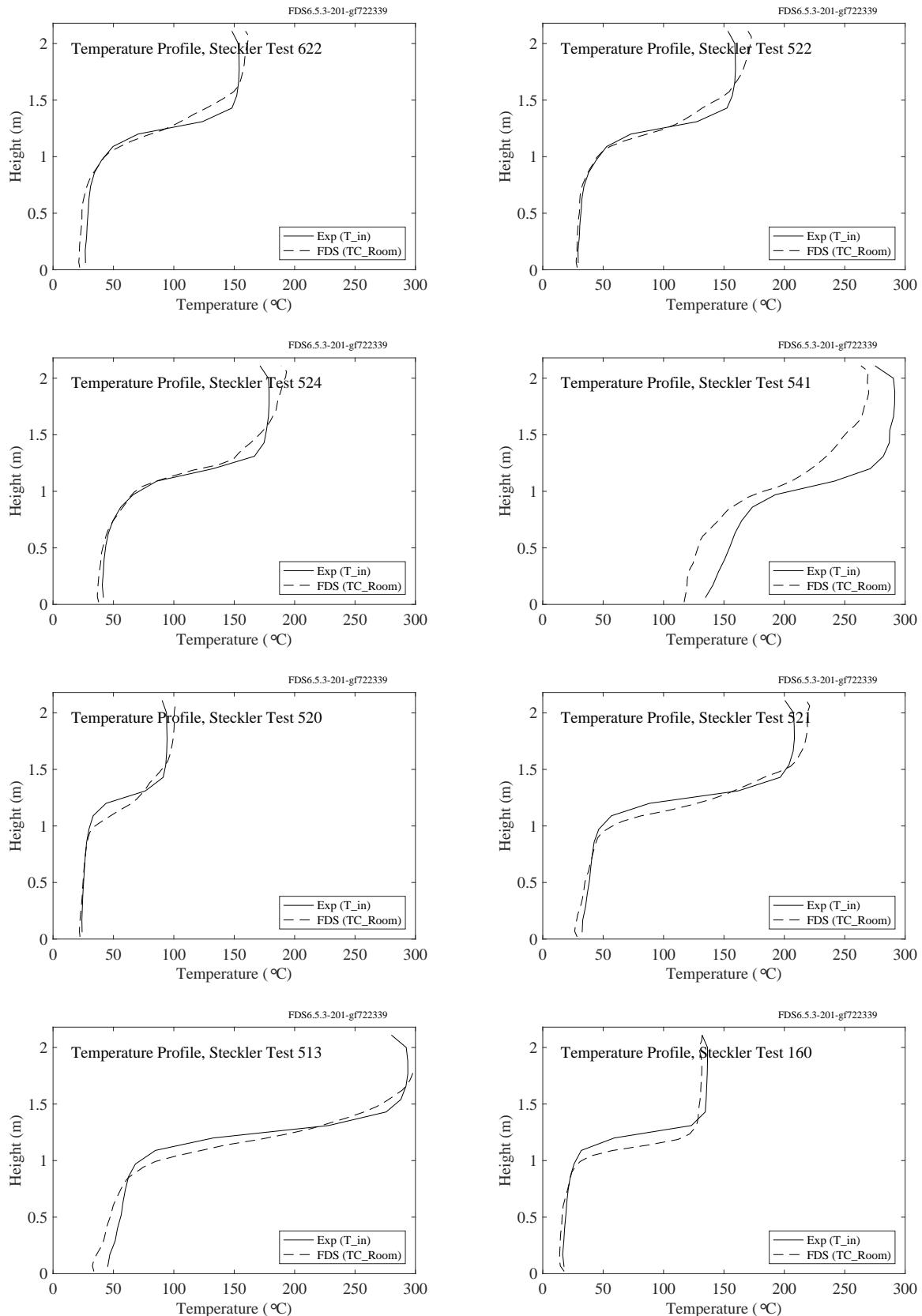


Figure 5.47: Steckler experiments, HGL temperature, Tests 160, 513, 520, 521, 522, 524, 541, 622.

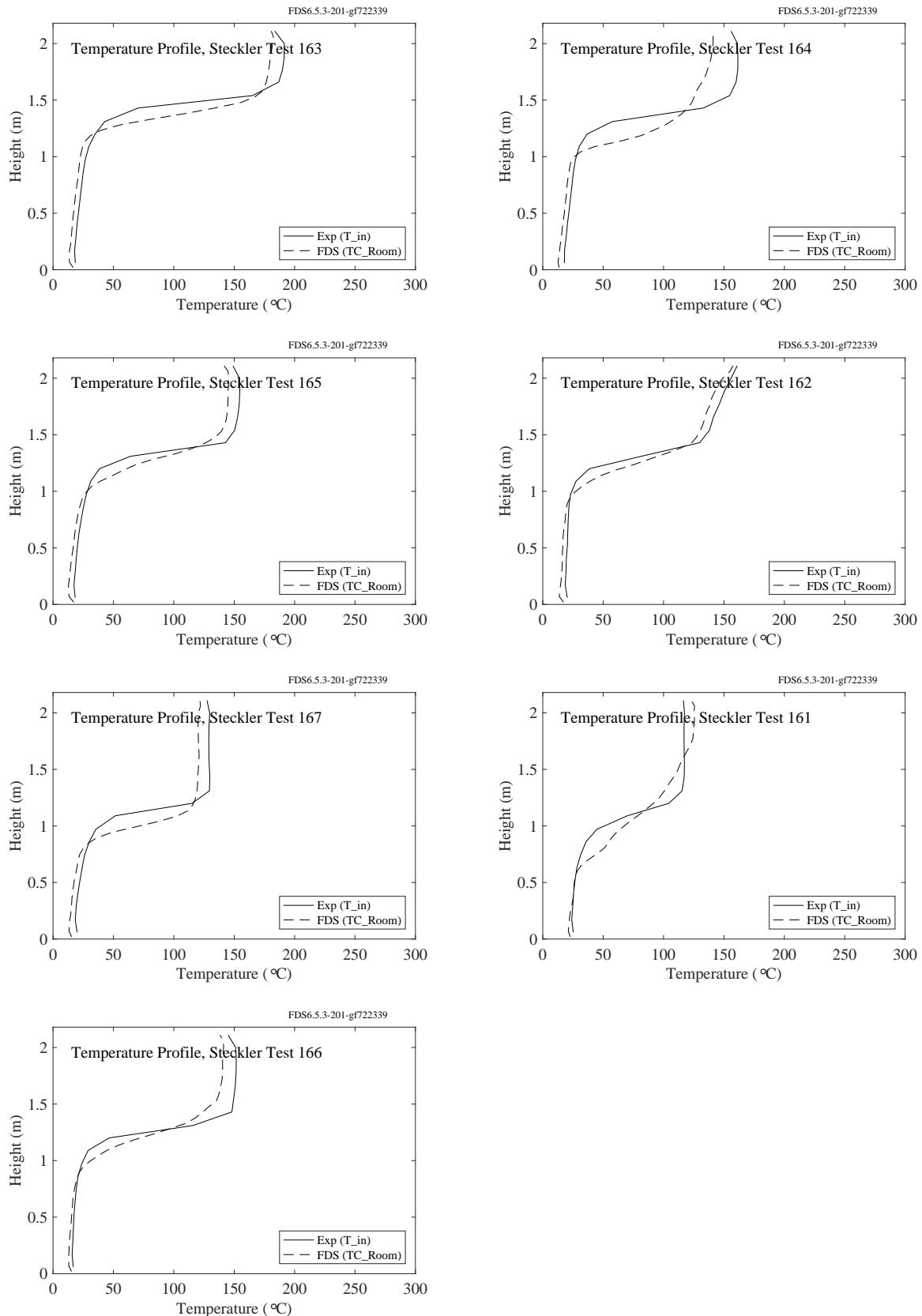


Figure 5.48: Steckler experiments, HGL temperature, Tests 161, 162, 163, 164, 165, 166, 167.

## **5.13 UL/NIST Vent Experiments**

The HGL temperature and height for the four experiments was calculated from two vertical arrays of eight thermocouples each. The arrays were centered on the long central axis of the compartment and 90 cm from each short size wall. The 2.4 m by 1.2 m double vent was 90 cm from each array. The uppermost TC was 2.5 cm below the ceiling. The second TC was 30 cm (1 ft) below the ceiling, and the rest were spaced evenly by 1 ft.

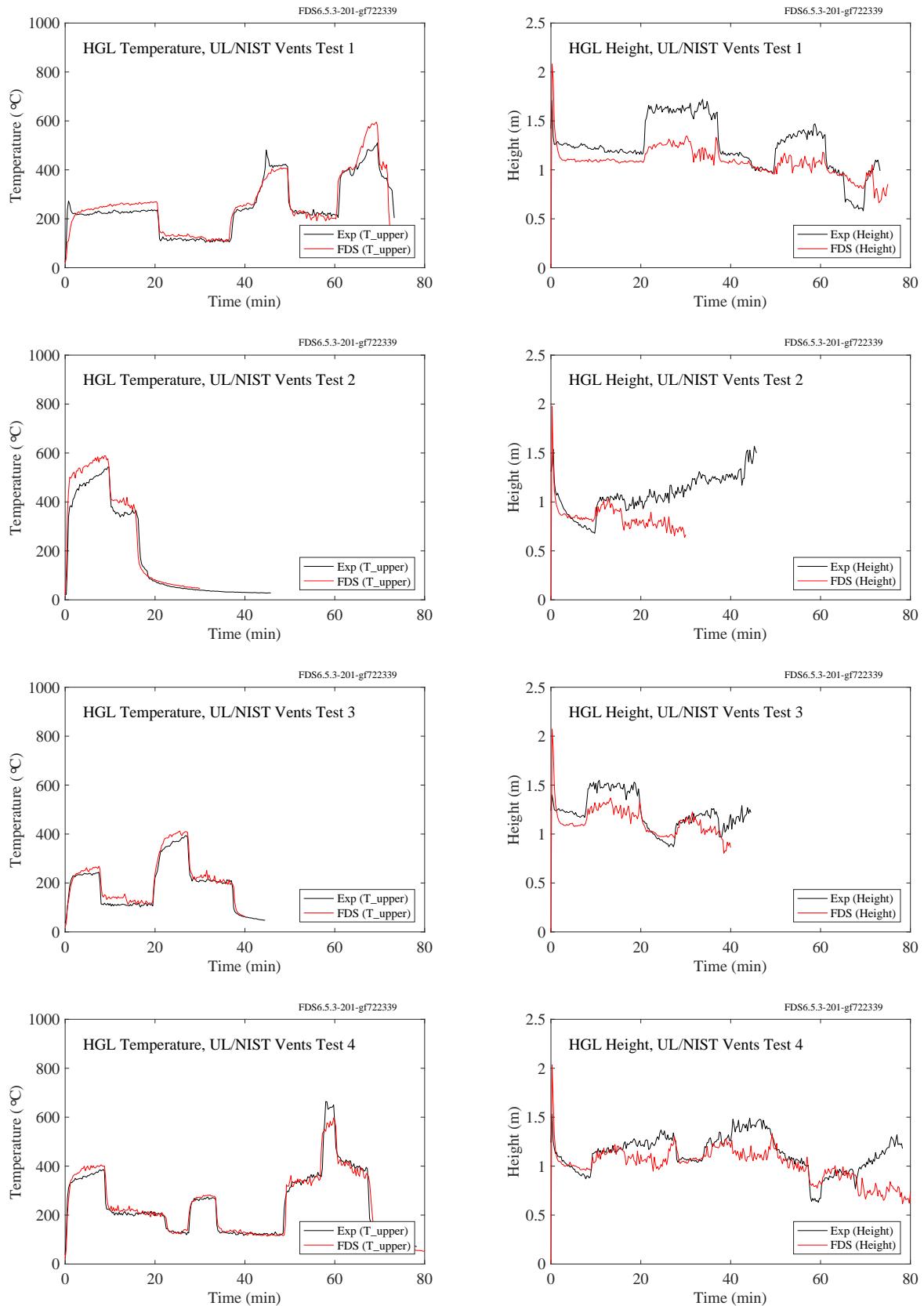


Figure 5.49: UL/NIST experiments, HGL temperature and height, Tests 1-4.

## 5.14 VTT Test Series

The HGL temperature and height are calculated from the (1 min) averaged gas temperatures from three vertical thermocouple arrays using the standard reduction method. There are 10 thermocouples in each vertical array, spaced 2 m apart in the lower two-thirds of the hall, and 1 m apart near the ceiling.

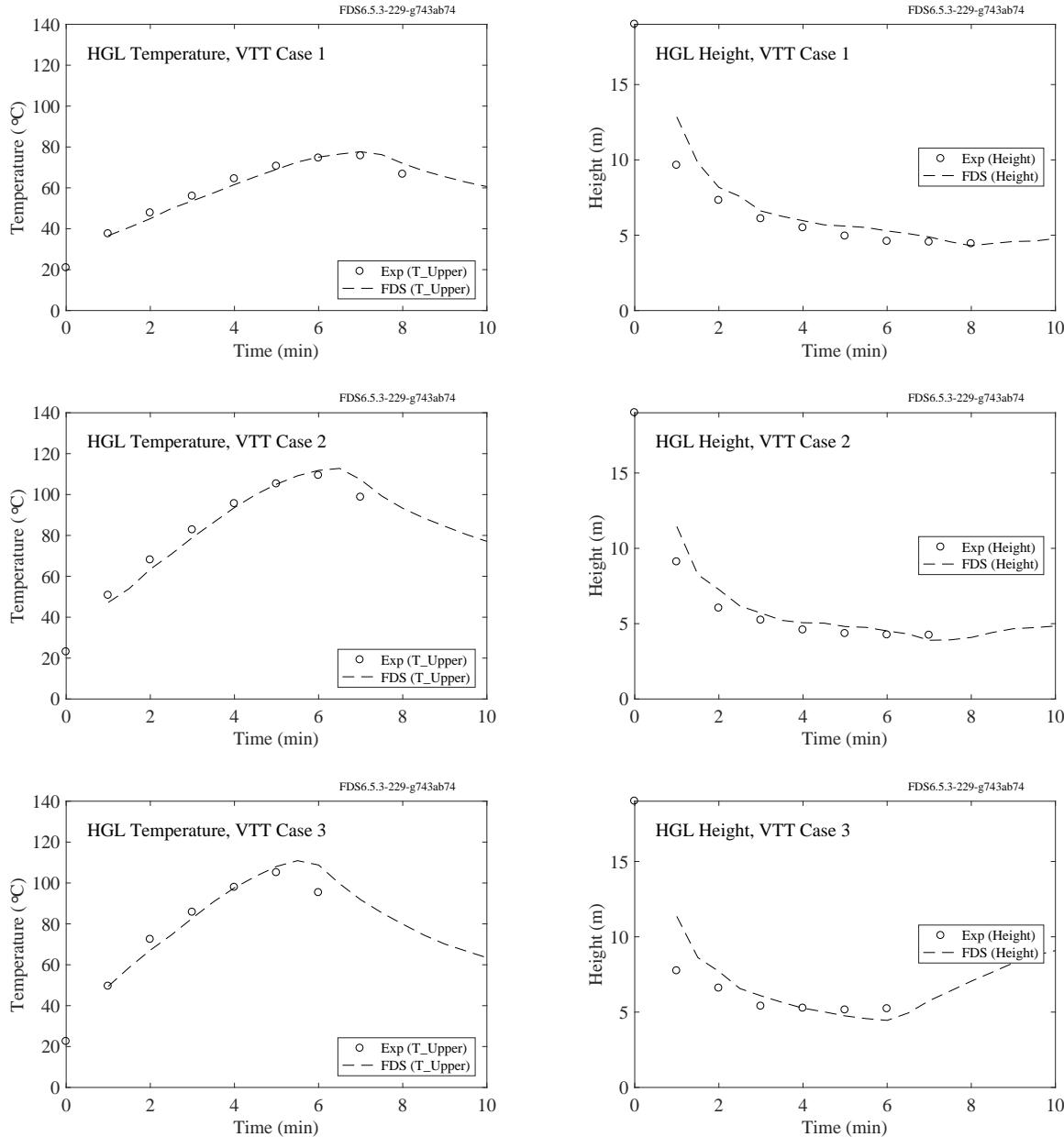


Figure 5.50: VTT experiments, HGL temperature and height, Tests 1-3.

## 5.15 WTC Test Series

The HGL temperature and height for the WTC experiments were calculated from two TC trees, one that was approximately 3 m to the west and one 2 m to the east of the fire pan (see Fig. 3.26). Each tree consisted of 15 thermocouples, the highest point being 5 cm below the ceiling.

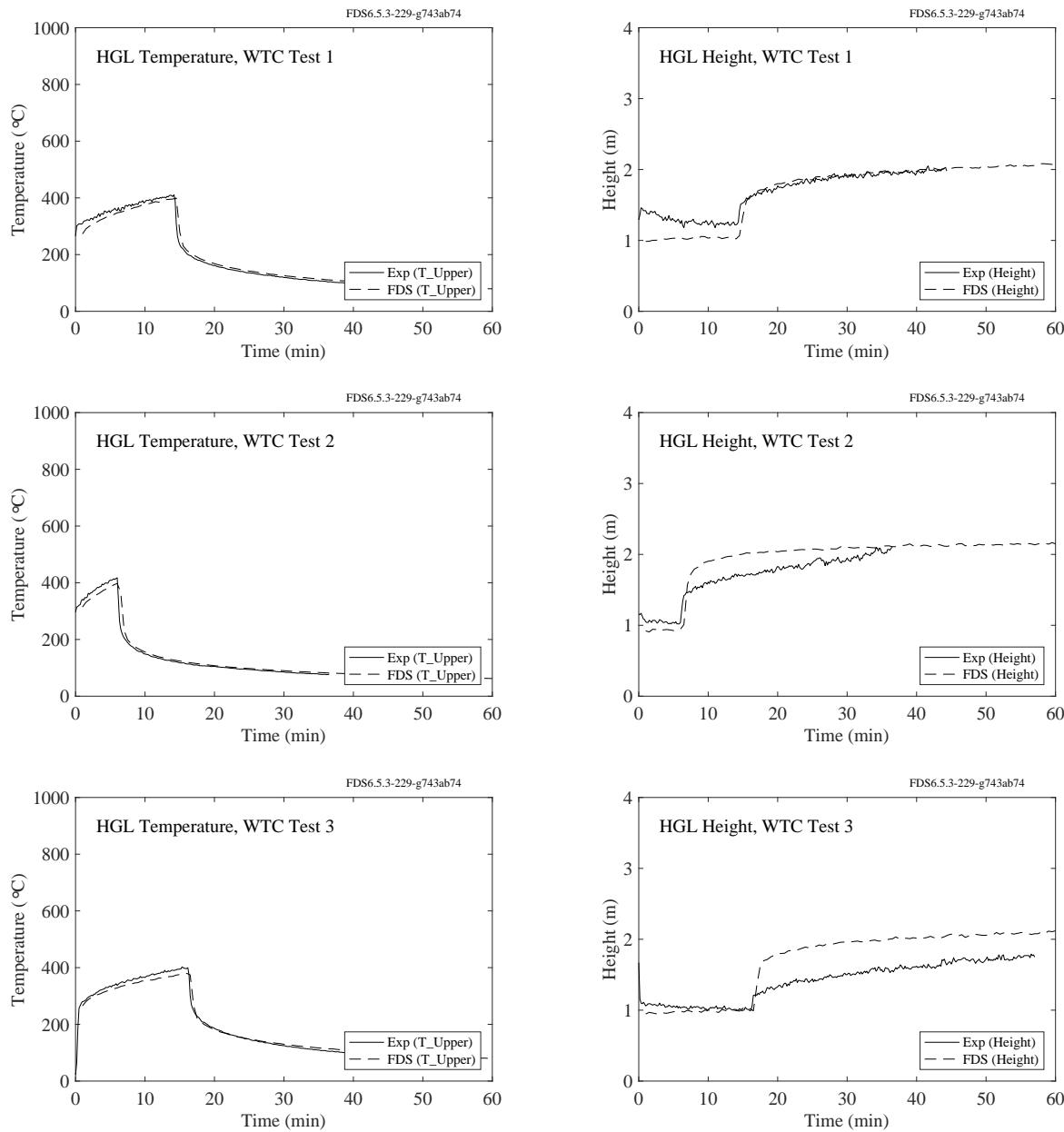


Figure 5.51: WTC experiments, HGL temperature and height, Tests 1-3.

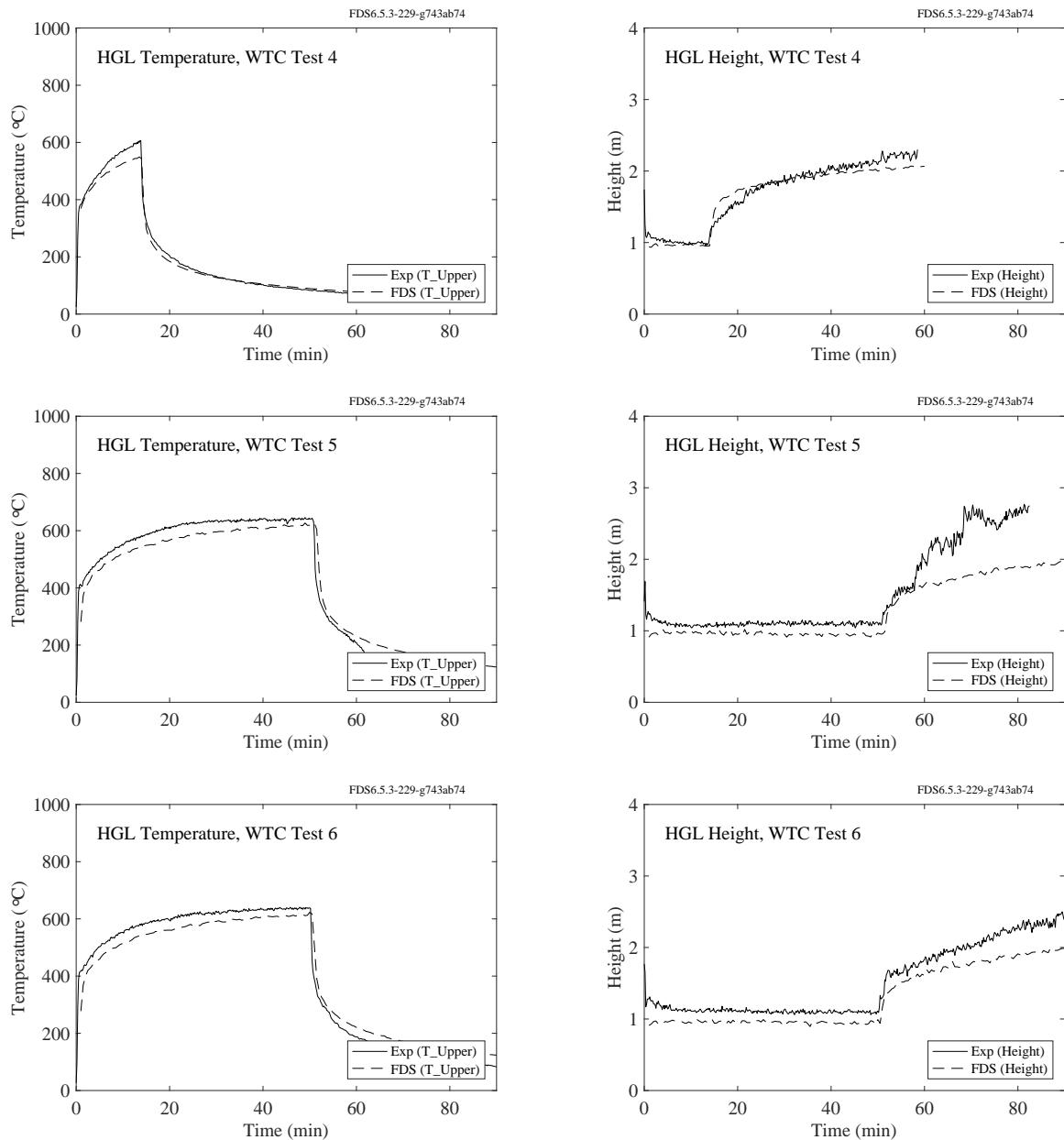


Figure 5.52: WTC experiments, HGL temperature and height, Tests 4-6.



## 5.16 Summary of Hot Gas Layer Temperature and Height

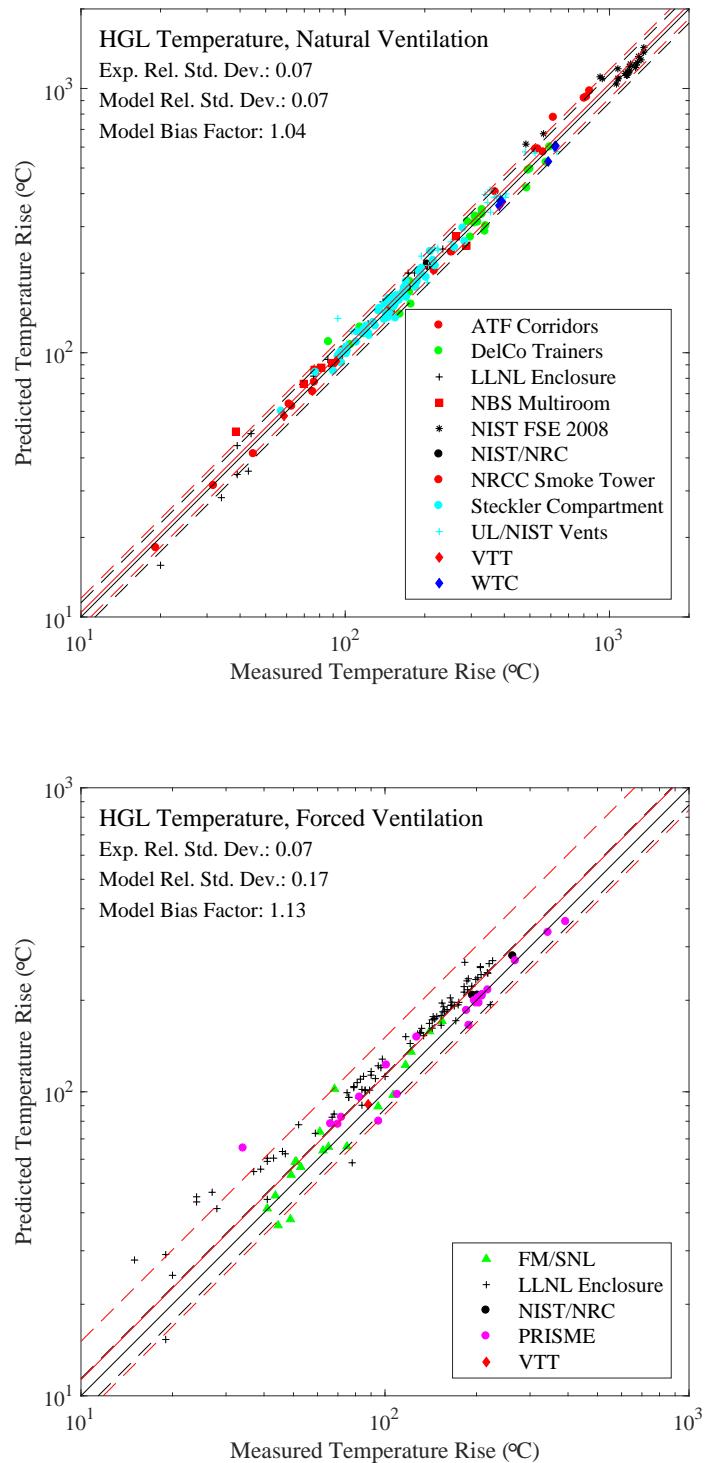


Figure 5.53: Summary of the HGL temperature predictions for natural and forced ventilation.

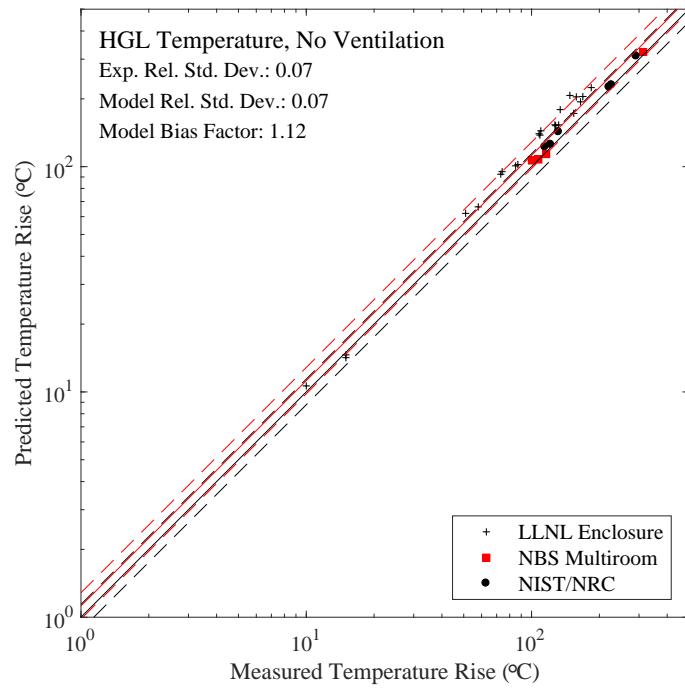


Figure 5.54: Summary of HGL temperature predictions for unventilated compartments.

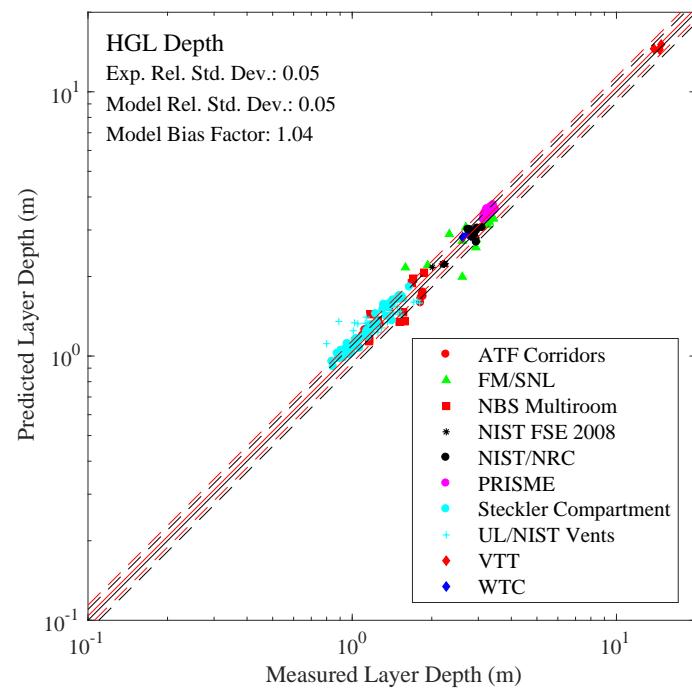


Figure 5.55: Summary of HGL Depth predictions.



# Chapter 6

## Fire Plumes

### 6.1 Plume Temperatures

For fire plumes, a measure of how well the flow field is resolved is given by the non-dimensional expression  $D^*/\delta x$ , where  $D^*$  is a characteristic fire diameter

$$D^* = \left( \frac{\dot{Q}}{\rho_\infty c_p T_\infty \sqrt{g}} \right)^{\frac{2}{5}} \quad (6.1)$$

and  $\delta x$  is the nominal size of a mesh cell<sup>1</sup>. The quantity  $D^*/\delta x$  can be thought of as the number of computational cells spanning the characteristic (not necessarily the physical) diameter of the fire. The more cells spanning the fire, the better the resolution of the calculation. It is better to assess the quality of the mesh in terms of this non-dimensional parameter, rather than an absolute mesh cell size. For example, a cell size of 10 cm may be “adequate,” in some sense, for evaluating the spread of smoke and heat through a building from a sizable fire, but may not be appropriate to study a very small, smoldering source. The resolution of all the numerical simulations included in this chapter is given in Table 3.13.

---

<sup>1</sup>The characteristic fire diameter is related to the characteristic fire size via the relation  $Q^* = (D^*/D)^{5/2}$ , where  $D$  is the physical diameter of the fire.

### 6.1.1 FM/SNL Experiments

The FM/SNL tests consisted of propylene gas burners, heptane pools, methanol pools, PMMA solids, as well as qualified and unqualified cables, burned in a large room which, for the first 18 tests, was free of obstructions. Plume Temperatures shown here were measured at approximately 6 m from the floor, or 0.98 times the total ceiling height. For Tests 1-5 and 7-9, the thermocouple station (Station 13) was centered above the fire pan. Tests 6 and 10-15 used an alternate fire location, centered along the south wall. Station 9 was not centered above these fires, but fell within the plume. Tests 16 and 17 had fires located in the south-west corner of the room, too remote from any stations to allow for plume measurements.

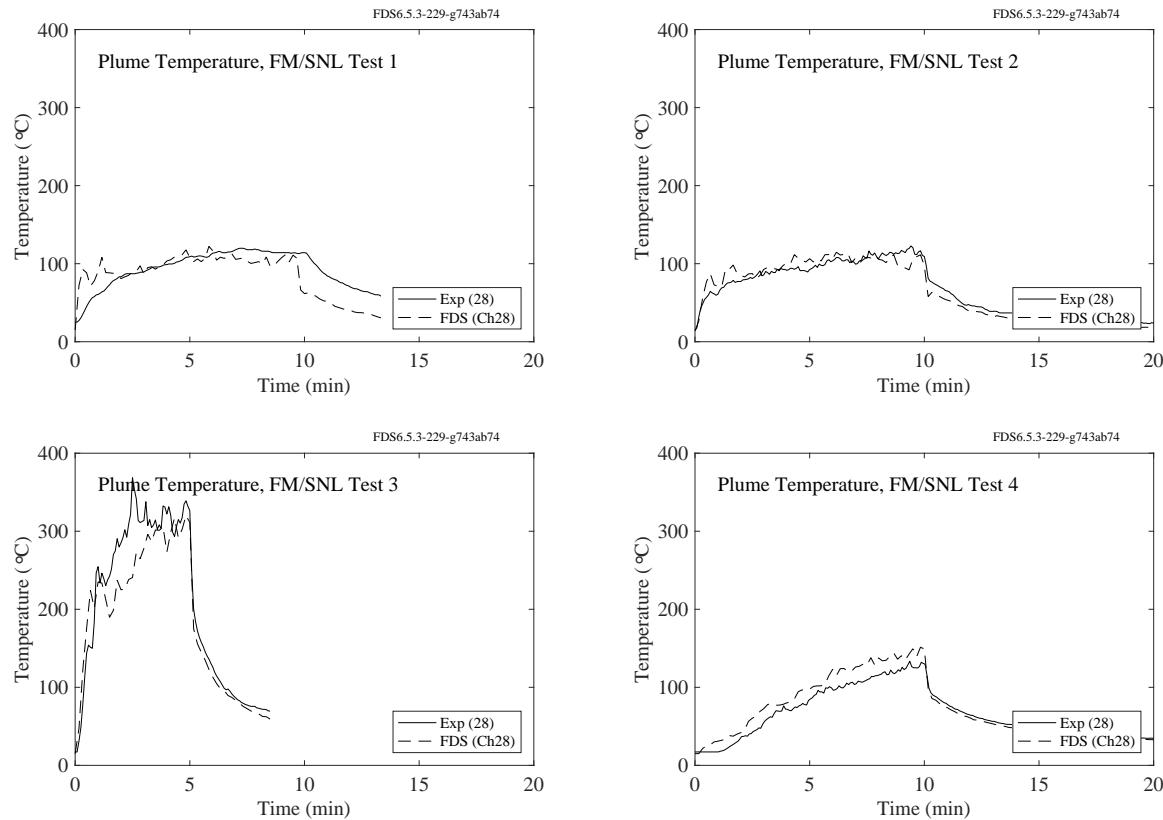


Figure 6.1: FM/SNL experiments, plume temperature, Tests 1-4.

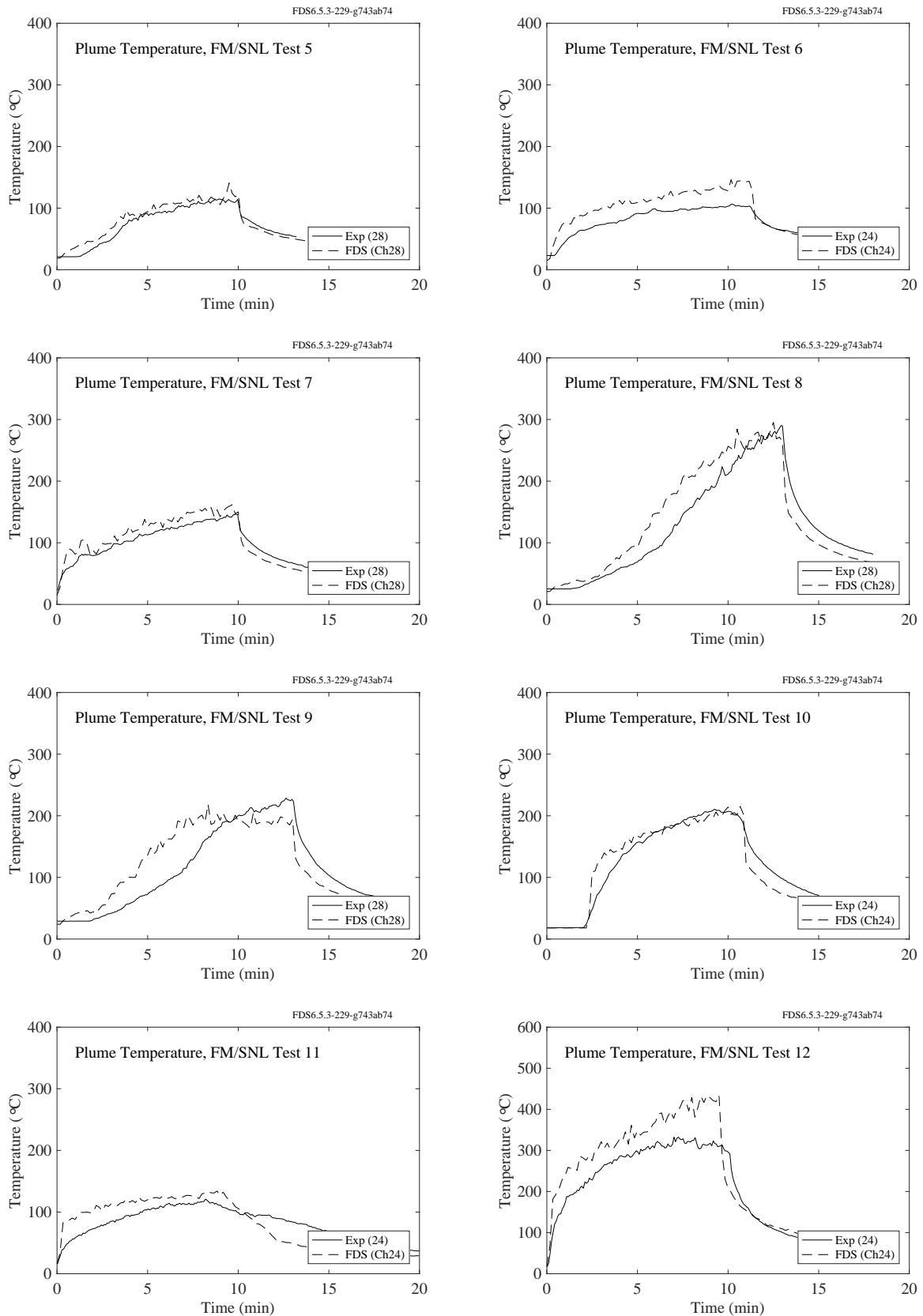


Figure 6.2: FM/SNL experiments, plume temperature, Tests 5-12.

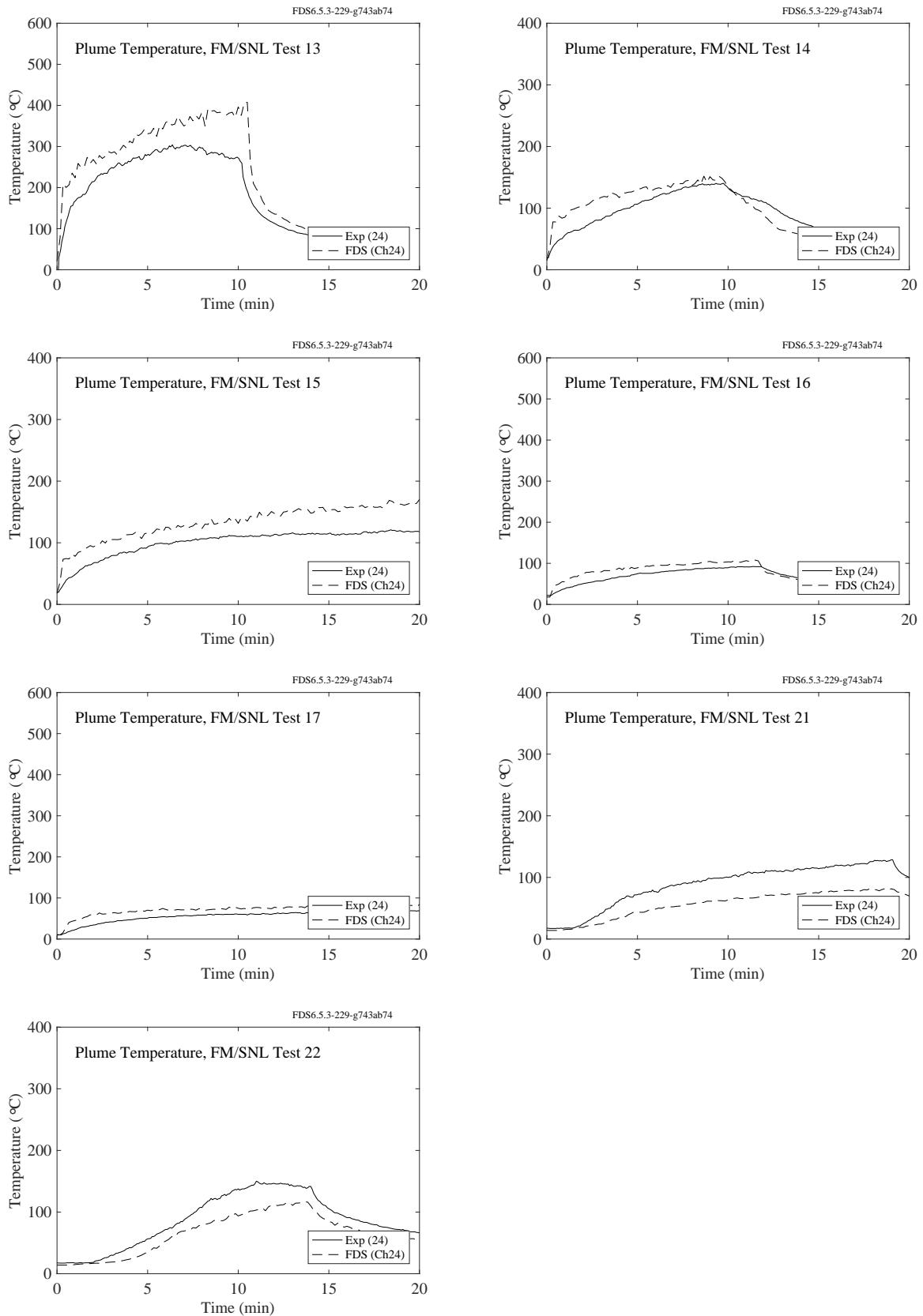


Figure 6.3: FM/SNL experiments, plume temperature, Tests 13-17, 21-22.

### 6.1.2 McCaffrey's Plume Correlation

The following plots show the results of simulations of McCaffrey's five fires at three grid resolutions,  $D^*/\delta x = [5, 10, 20]$  (note this resolution index is used to label the legend entries). The mesh cells are cubic and the spacing is uniform (no stretching).

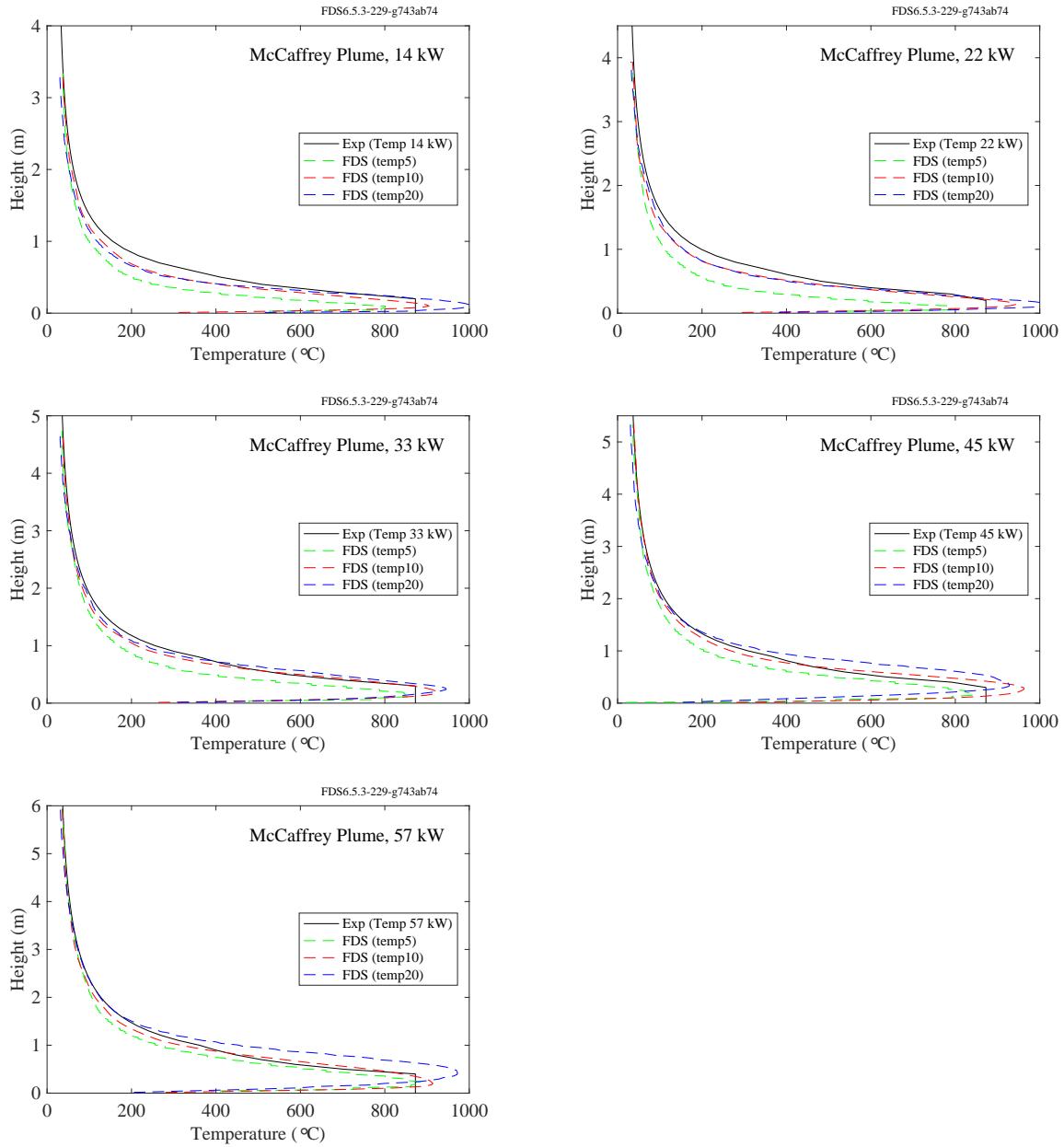


Figure 6.4: McCaffrey experiments, plume temperature.

### **6.1.3 NRCC Smoke Tower Experiments, Stairwell Plumes**

The NRCC Smoke Tower experiments include measurements of the temperature of smoke ascending a 10 story stairwell. This data is included here in the chapter on Fire Plumes because smoke movement in a vertical shaft with stairs can be considered an obstructed plume. Shown in Fig. 6.5 are predictions of gas temperature measurements made in the center of the stairwell approximately 1.8 m above the slab at floors 2-10. Note that the plot labels “Slot” refer to the data acquisition system in the experiments only and have no meaning in the present context. It should be clear from the plot title how the various curves ought to be interpreted.

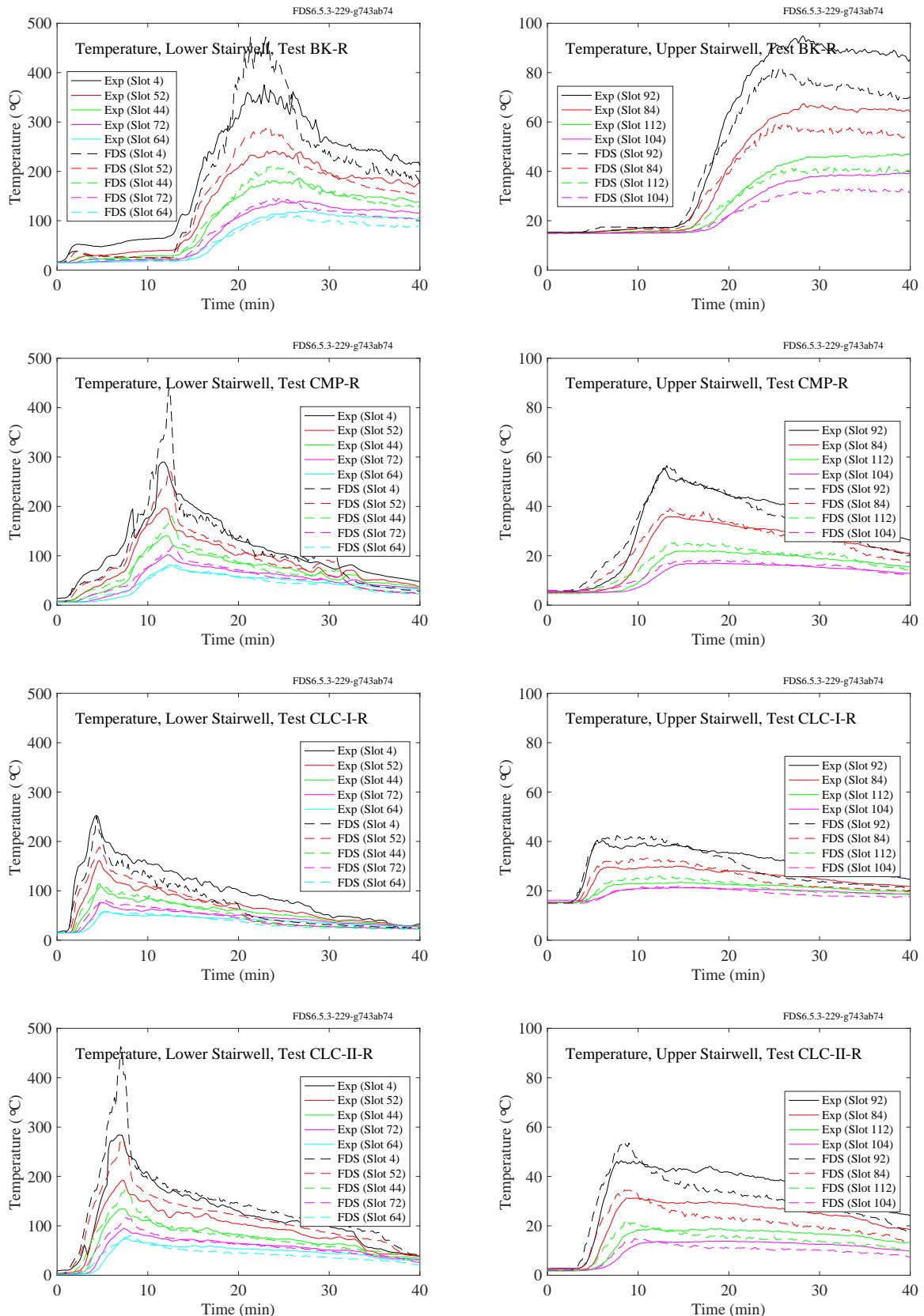


Figure 6.5: NRCC Smoke Tower, stairwell temperatures.

### 6.1.4 SP Adiabatic Surface Temperature Experiments

Three experiments were conducted at SP, Sweden, in 2011, in which a 6 m long, 20 cm diameter vertical column was positioned in the middle of 1.1 m and 1.9 m diesel fuel and 1.1 m heptane pool fires [199]. Gas, plate, and steel surface temperature measurements were made at heights of 1 m, 2 m, 3 m, 4 m, and 5 m above the pool surface. Gas temperatures were measured with 0.25 mm and 0.50 mm bead thermocouples. The results are very similar and only the 0.25 mm values are used. In the experiments, the fire was reported to lean. The lean was significant for the 1.9 m diesel fuel fire. In that case, only data from 1 m and 2 m above the pool are used. The average temperature between 10 min and 15 min is the basic of comparison.

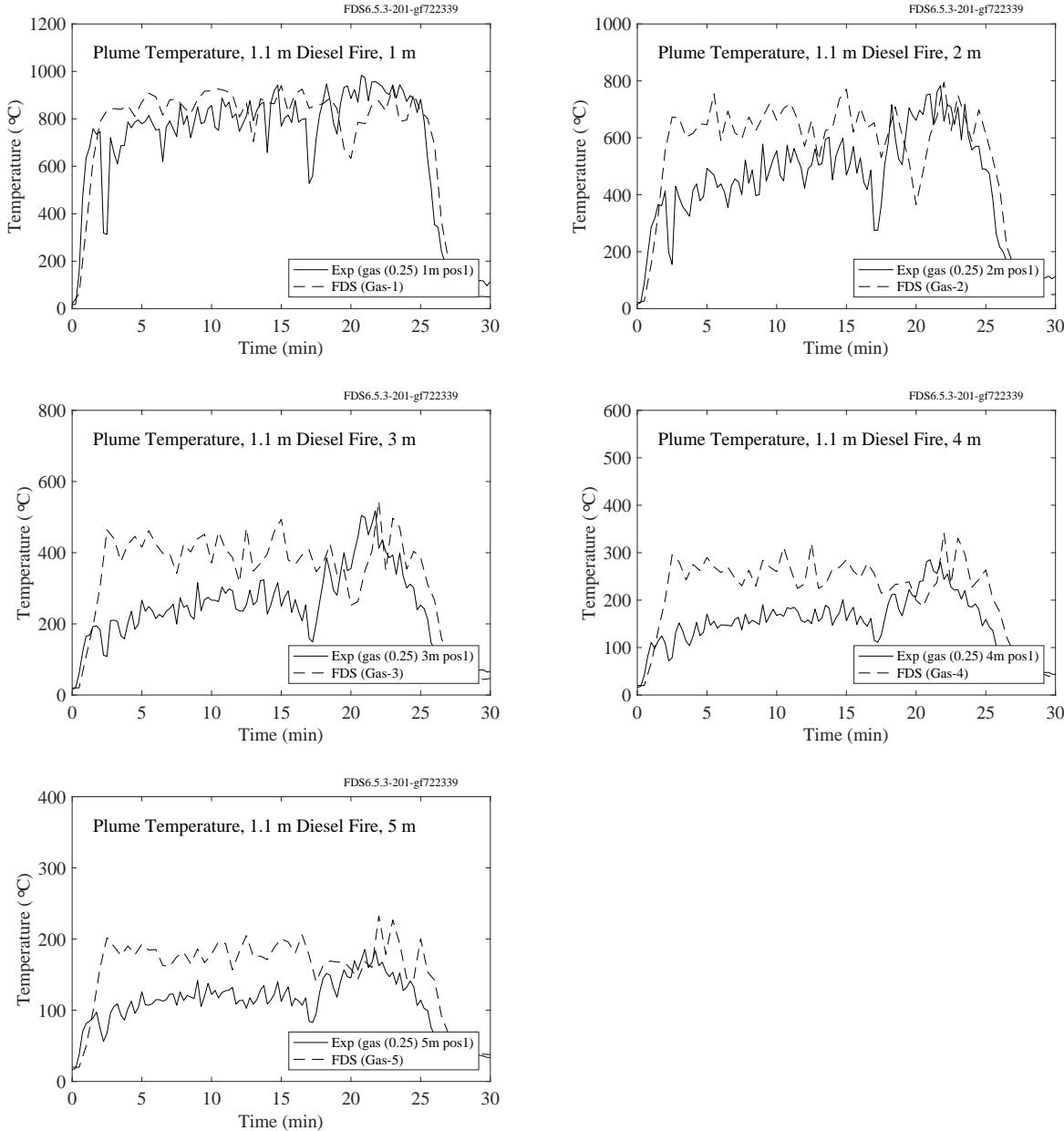


Figure 6.6: SP AST experiments, plume temperature, 1.1 m diesel fire.

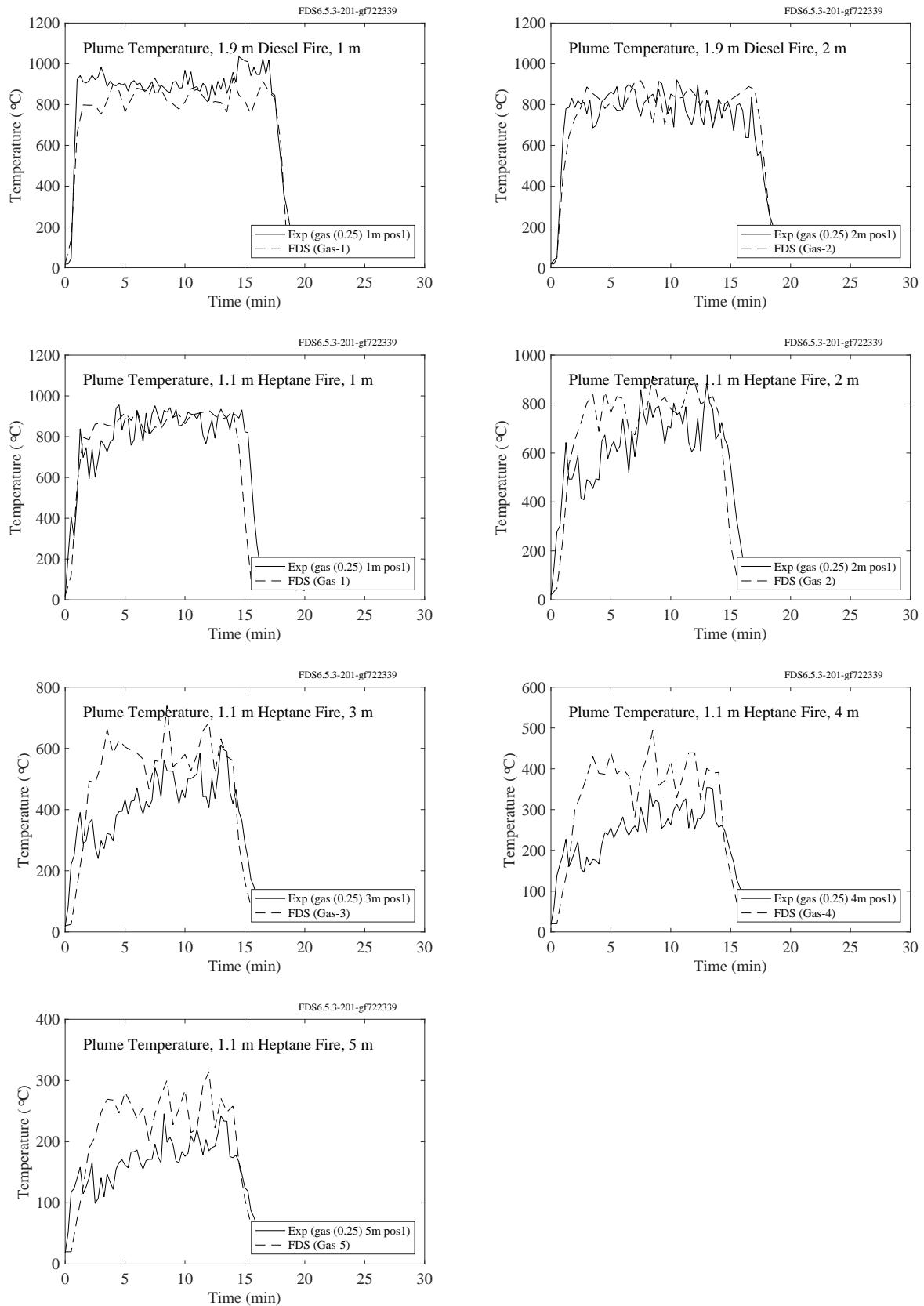


Figure 6.7: SP AST experiments, plume temperature, 1.9 m diesel and 1.9 m heptane fires.

### 6.1.5 USN High Bay Hangar Experiments

A large number of plume temperature measurements are available from the US Navy experiments conducted at Keflavik, Iceland, and Barber's Point, Hawaii. The hangars were very large in size (22 m high in Iceland and 15 m high in Hawaii) and the heat release rates varied from 100 kW to 33 MW. All experiments made use of a fuel pan filled with either JP-5 or JP-8 jet fuel, positioned in the center of the hangar.

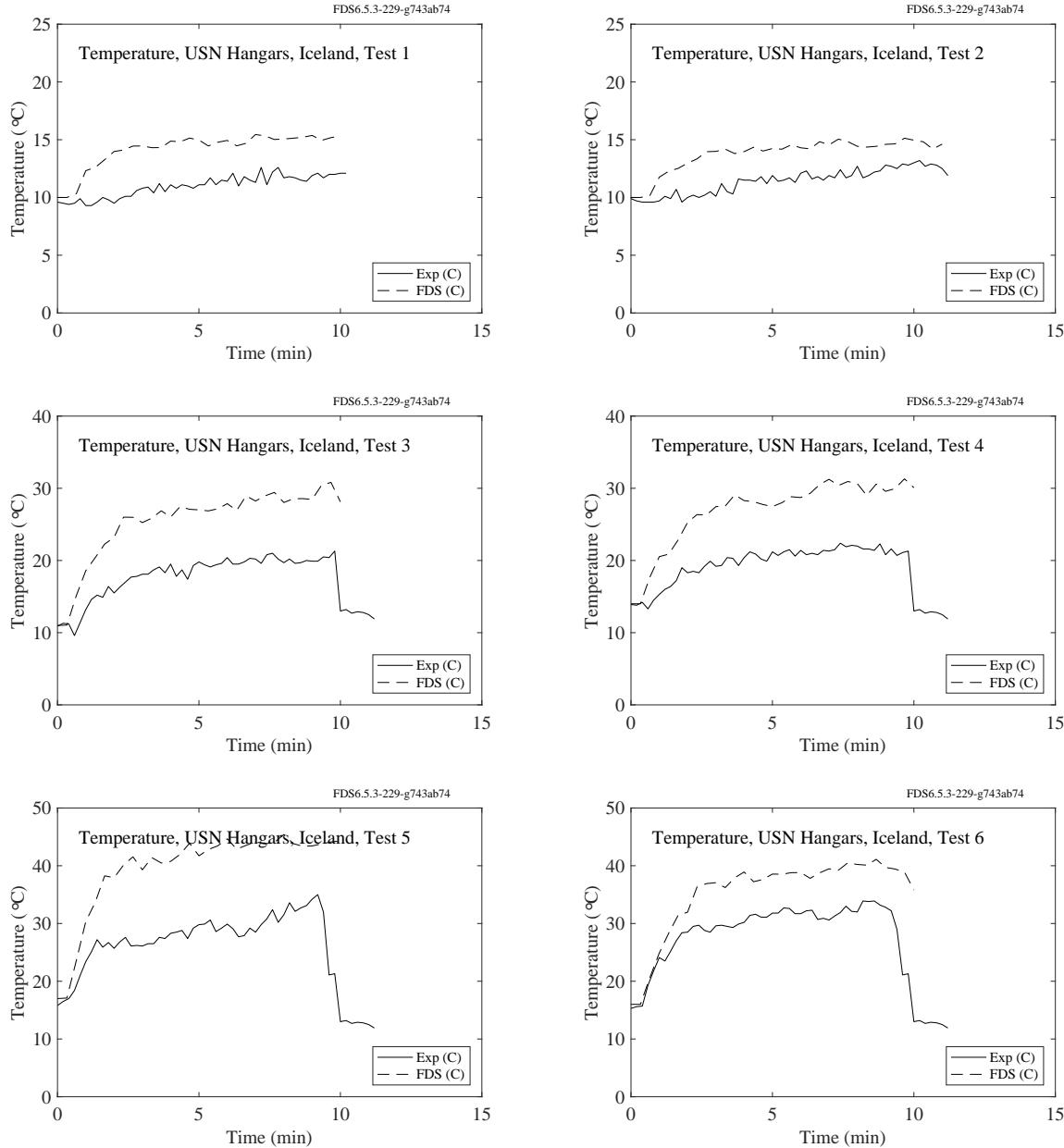


Figure 6.8: USN Hangar experiments, Iceland, plume temperature, Tests 1-6.

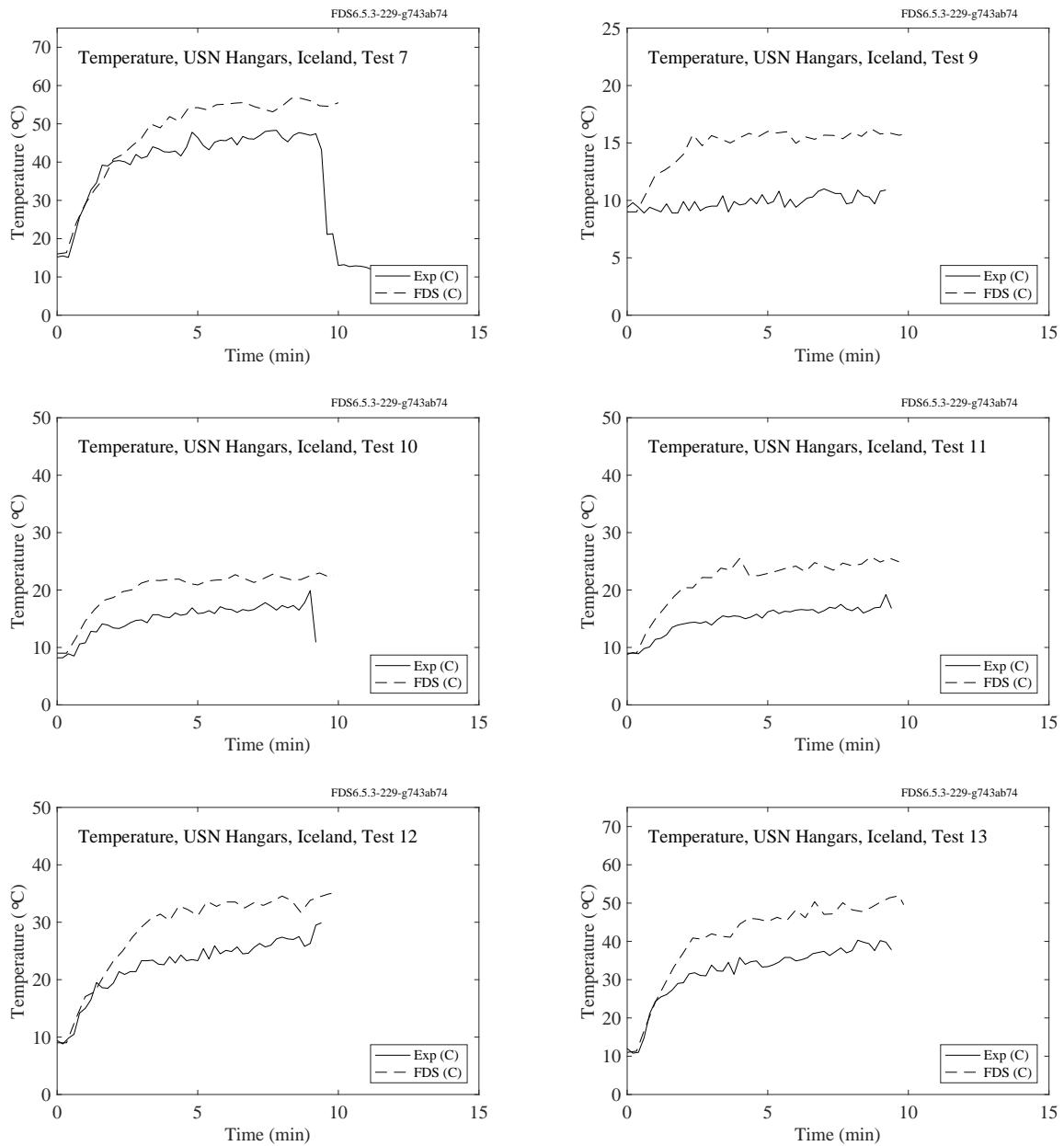


Figure 6.9: USN Hangar experiments, Iceland, plume temperature, Tests 7, 9-13.

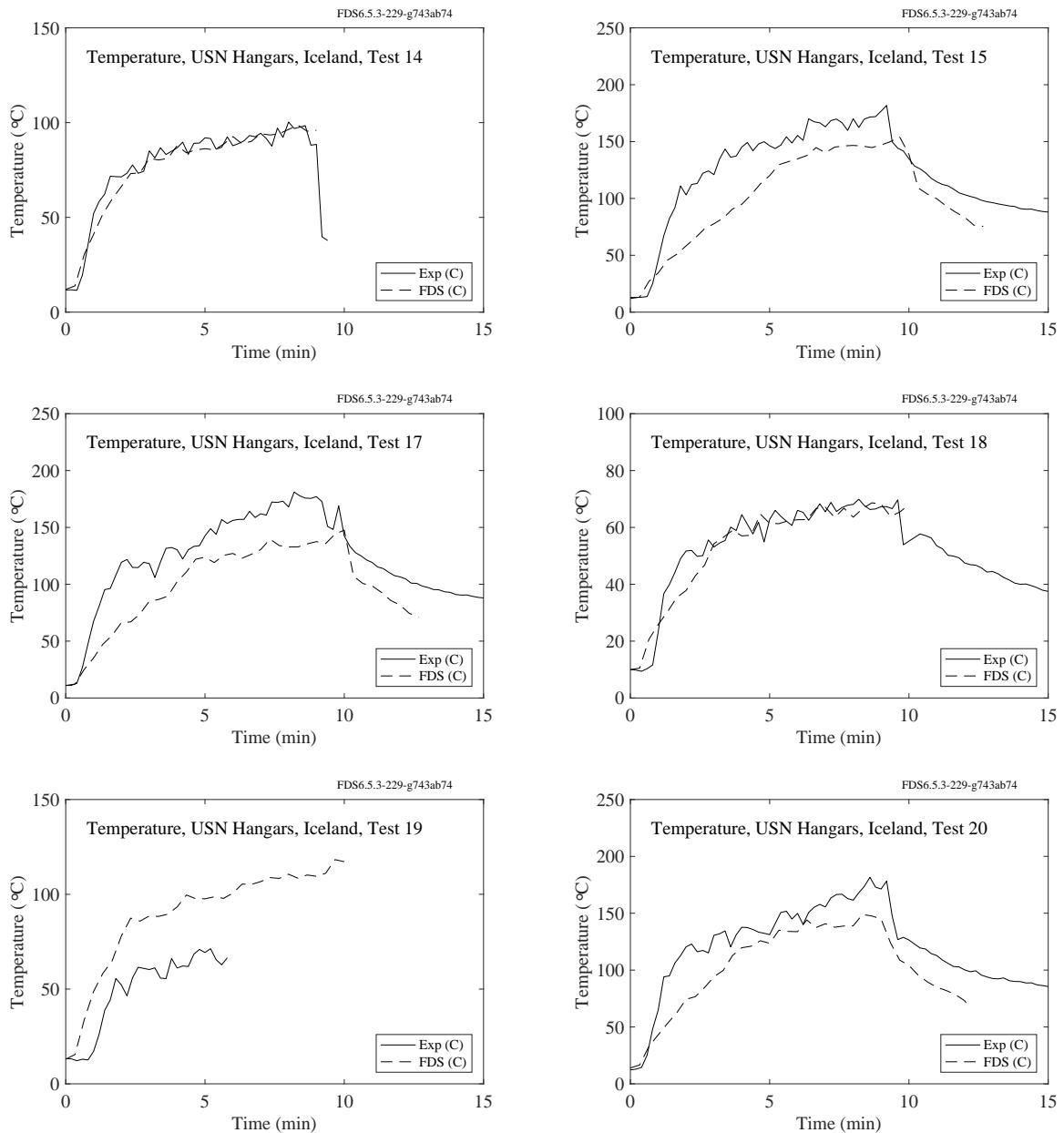


Figure 6.10: USN Hangar experiments, Iceland, plume temperature, Tests 14-15, 17-20.

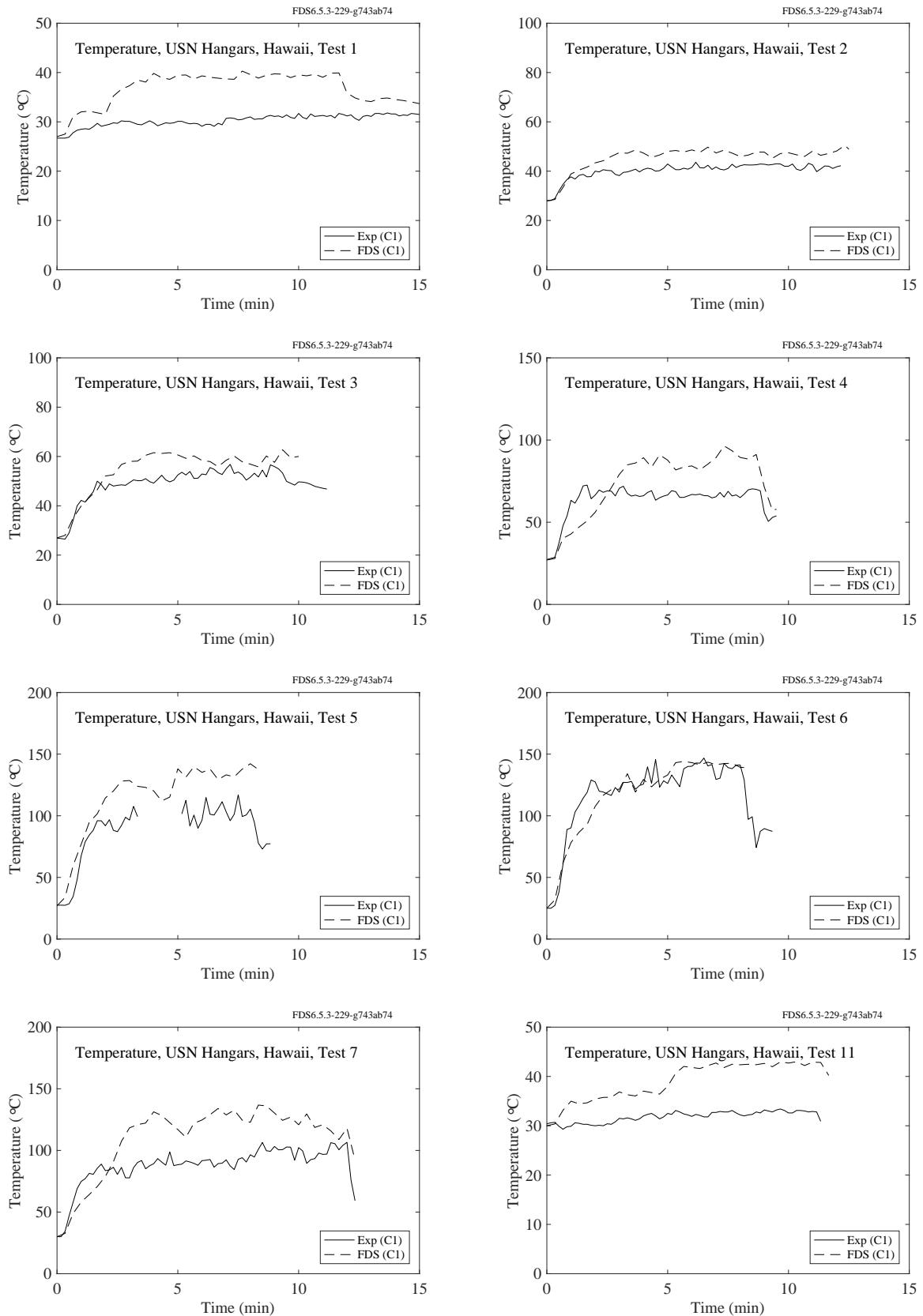


Figure 6.11: USN Hangar experiments, Hawaii, plume temperature, Tests 1-7, 11.

### 6.1.6 VTT Large Hall Experiments

The VTT experiments consisted of liquid fuel pan fires positioned in the middle of a large fire test hall. Plume temperatures were measured at two heights above the fire, 6 m (T G.1) and 12 m (T G.2). The flames were observed to extend to about 4 m above the fire pan.

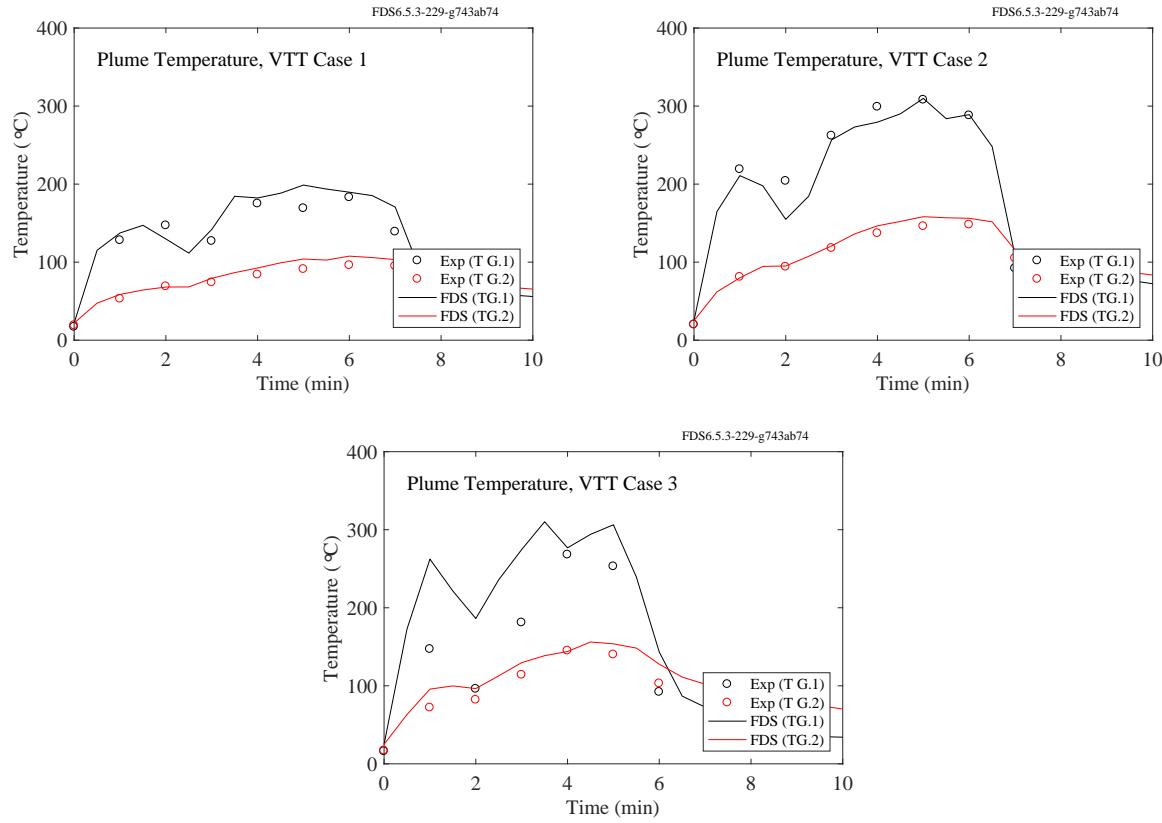


Figure 6.12: VTT experiments, plume temperature.

### 6.1.7 Summary of Plume Temperature Predictions

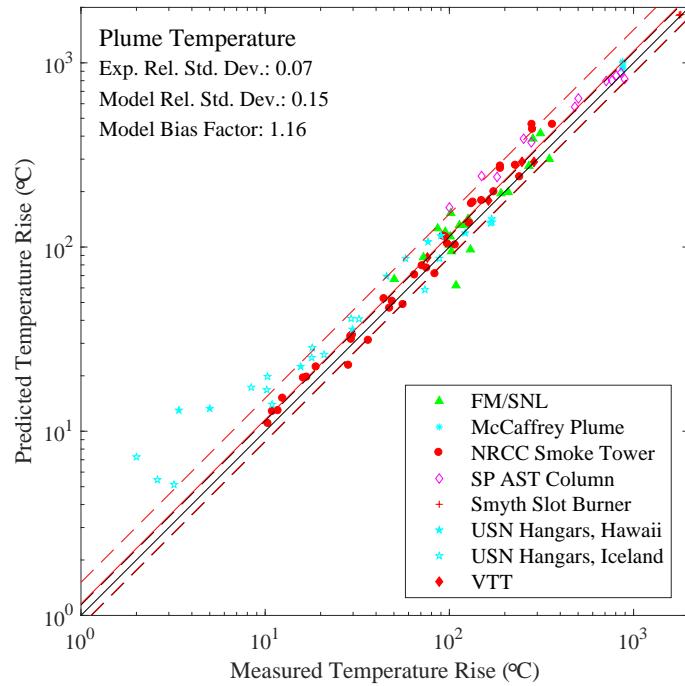


Figure 6.13: Summary of plume temperature predictions.

## 6.2 Heskestad's Flame Height Correlation

Table 6.1 lists the parameters for FDS simulations of fires in a 1 m by 1 m square pan<sup>2</sup>. Figure 6.14 shows a verification of the heat release rate for each case, and Fig. 6.15 compares the FDS predictions with Heskestad's empirical correlation. Note that the flame height for the FDS simulations is defined as the distance above the pan, on average, at which 99 % of the fuel has been consumed. Note also that the simulations were run at three different grid resolutions. A convenient length scale is given by

$$D^* = (Q^*)^{2/5} D \quad (6.2)$$

Given a grid cell size,  $\delta x$ , the three resolutions can be characterized by the non-dimensional quantity,  $D^*/\delta x$ , whose values in these cases are 5, 10 and 20.

The flame height definition used in Fig. 6.15 (99 % fuel consumption) is admittedly arbitrary and is often questioned when FDS predictions of flame height are compared with experimental values, which are usually based on luminosity (effectively measuring radiation emission from soot). Further, Heskestad's flame height correlation is one among many such correlations [25, 230, 231, 232, 233, 234, 235], and the reported variation is significant, especially at low values of  $Q^*$  where the details of the burner configuration (shape of the burner, etc.) become important. To illustrate the uncertainty one can expect from FDS calculations and to test the sensitivity of the reported FDS results to the flame height definition, Fig. 6.16 shows two different FDS flame height predictions, one at 99 % fuel consumption (as in Fig. 6.15)—the red curve—and one using 95 % fuel consumption—the blue curve. Three different grid resolutions were run for each flame height definition. For 99 % fuel consumption, the red dashed line is the maximum flame height from the three resolutions. For 95 % fuel consumption, the blue dashed line is the minimum flame height from the three resolutions. We also overlay several different flame height correlations (colored solid lines).

Figure 6.17 includes comparisons of the predicted HRR as a function of the height of the burner for three different values of  $Q^*$ . The experimental measurements were performed by Tamanini at Factory Mutual [236]. Both the HRR and height above the burner have been non-dimensionalized by the total HRR and the flame height, respectively. These results demonstrate that the predicted spatial distribution of the energy release improves as the numerical grid is refined.

---

<sup>2</sup>The effective diameter,  $D$ , of a 1 m square pan is 1.13 m, obtained by equating the area of a square and circle.

Table 6.1: Summary of parameters for the flame height predictions. The grid cell size,  $\delta x_{10}$ , refers to the case where  $D^*/\delta x=10$ .

$Q^*$	$\dot{Q}$ (kW)	$D^*$ (m)	$\delta x_5$ (m)	$\delta x_{10}$	$\delta x_{20}$
0.1	151	0.45	0.090	0.045	0.022
0.2	303	0.59	0.119	0.059	0.030
0.5	756	0.86	0.171	0.086	0.043
1	1513	1.13	0.226	0.113	0.057
2	3025	1.49	0.298	0.149	0.075
5	7564	2.15	0.430	0.215	0.108
10	15127	2.84	0.568	0.284	0.142
20	30255	3.75	0.749	0.375	0.187
50	75636	5.40	1.081	0.540	0.270
100	151273	7.13	1.426	0.713	0.356
200	302545	9.41	1.882	0.941	0.470
500	756363	13.6	2.715	1.357	0.679
1000	1512725	17.9	3.582	1.791	0.895
2000	3025450	23.6	4.726	2.363	1.182
5000	7563625	34.1	6.819	3.409	1.705
10000	15127250	45.0	8.997	4.499	2.249

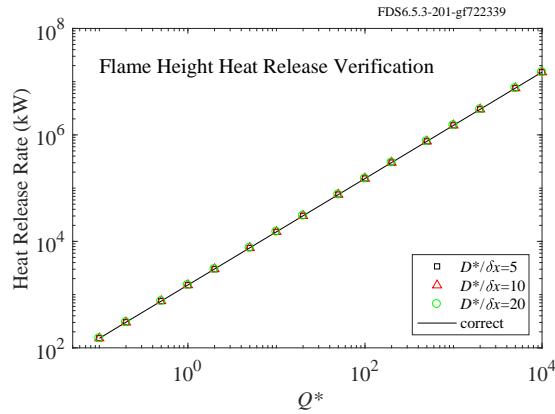


Figure 6.14: Verification of the heat release rate for Heskestad Flame Height cases.

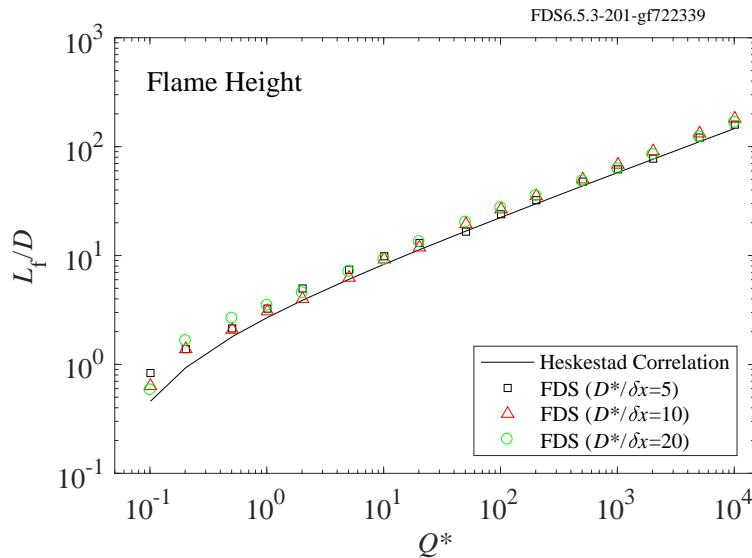


Figure 6.15: Comparison of FDS predictions of flame height from a 1 m square pan fire for  $Q^*$  values ranging from 0.1 to 10000.

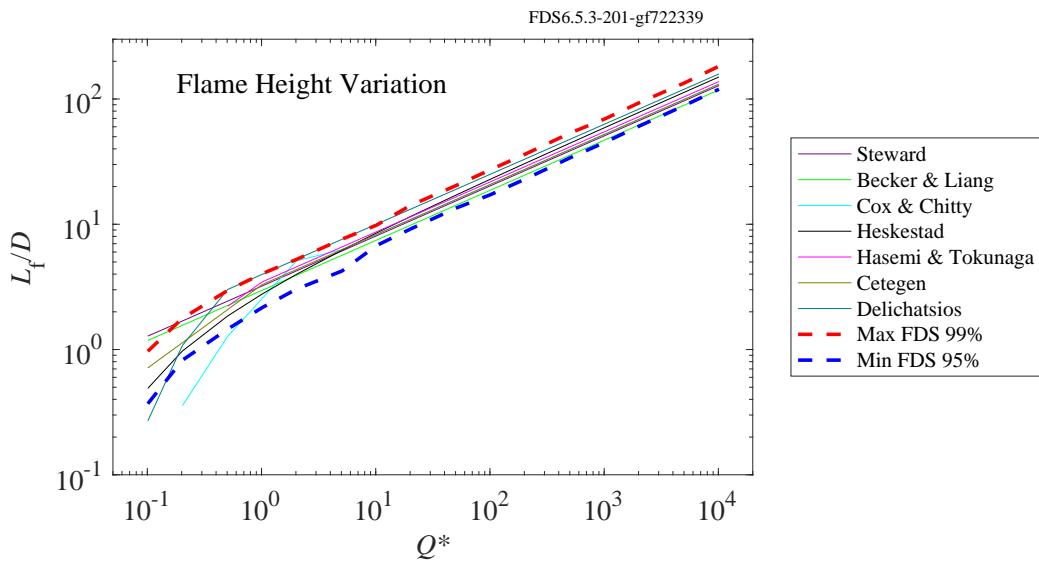


Figure 6.16: Flame height predictions from various correlations compared with FDS predictions using two different flame height definitions. Uncertainty (maximum variation) at  $Q^* > 1$  is  $\pm 15\%$ . At  $Q^* = 0.1$ , the uncertainty is approximately  $\pm 65\%$ . Correlation references: Steward [230], Becker and Liang [231], Cox and Chitty [232], Heskestad [25], Hasemi and Tokunaga [233], Cetegen [234], Delichatsios [235].

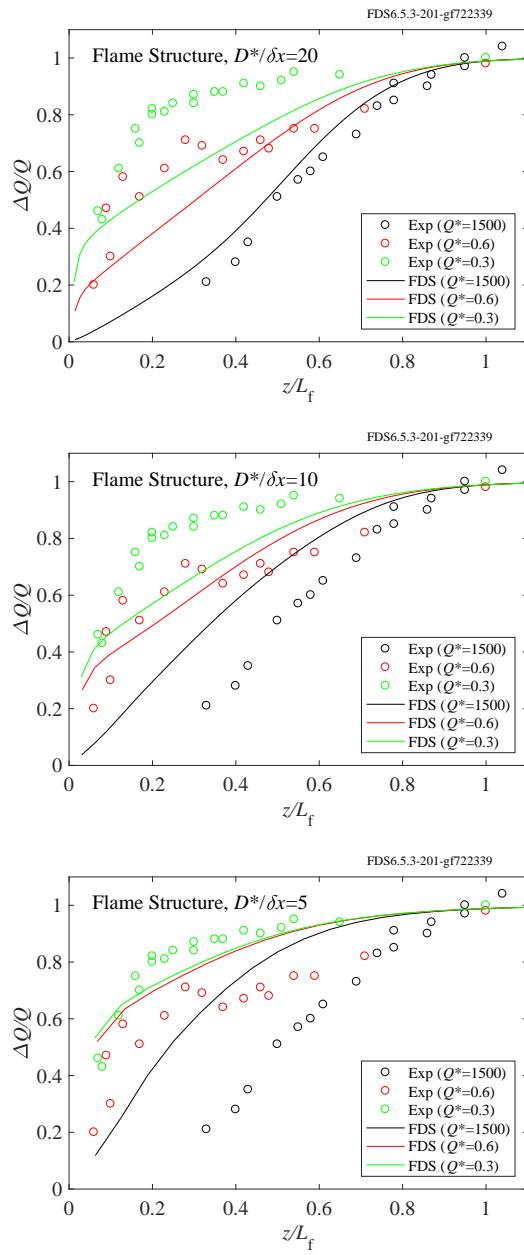


Figure 6.17: Predicted HRR as a function of height above the burner compared to measurements.

### 6.3 Harrison Spill Plumes/Entrainment Experiments

In each of these reduced-scale spill plume experiments, the entrained mass flow rate into the plume was measured at a series of heights by varying the flow through an exhaust hood to maintain a constant smoke layer depth. Figure 6.18 compares measured and predicted entrainment rates at five different elevations for the fire scenarios labelled SE4 through SE21 in Ref. [157]. Two general configurations are considered – one that is intended to mimic a balcony spill plume and one in which the plume adheres to a vertical wall above the compartment opening.

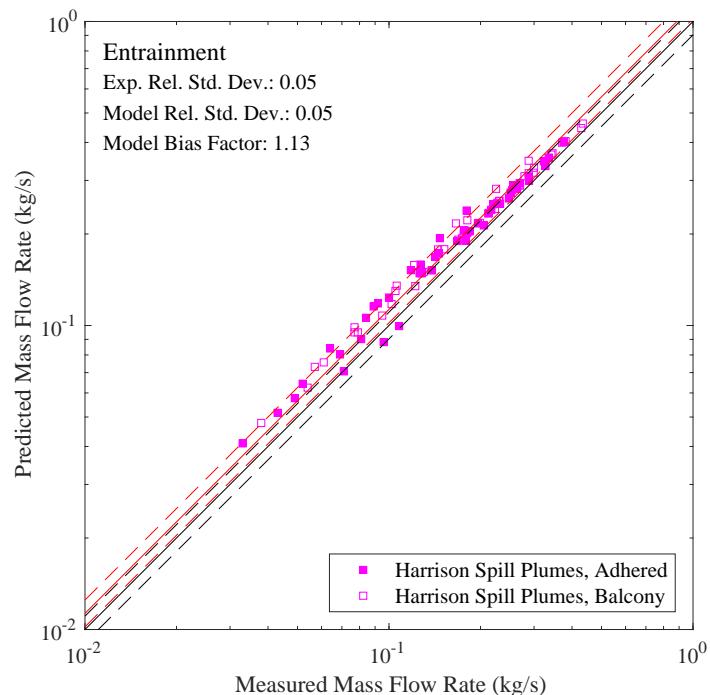


Figure 6.18: A comparison of predicted and measured mass flow rates at various heights for the Harrison Spill Plume experiments.

## 6.4 Sandia Plume Experiments

The Fire Laboratory for Accreditation of Models by Experimentation (FLAME) facility [189, 190] at Sandia National Laboratories in Albuquerque, New Mexico, is designed specifically for validating models of buoyant fire plumes. The plume source is 1 m in diameter surrounded by a 0.5 m steel “ground plane”. Particle Image Velocimetry (PIV) and Planar Laser-Induced Fluorescence (PLIF) techniques were used to obtain instantaneous joint scalar and velocity fields.

### 6.4.1 Sandia 1 m Helium Plume

Calculations of the Sandia 1 m helium plume are run at three grid resolutions: 6 cm, 3 cm, and 1.5 cm. To give the reader with a qualitative feel for the results, Fig. 6.19 provides a snapshot of density contours from the simulation. The calculations are run in parallel on 16 processors; the outlined blocks indicate the domain decomposition. Data for vertical velocity, radial velocity, and helium mass fraction are recorded at three levels downstream from the base of the plume,  $z = [0.2, 0.4, 0.6]$  m, corresponding to the experimental measurements of O’Hern et al. [189]. Results for the mean and root mean square (RMS) profiles are given in Figs. 6.20 - 6.22. The means are taken between  $t = 10$  and  $t = 20$  seconds in the simulation.

The domain is 3 m by 3 m by 4 m. The boundary conditions are open on all sides with a smooth solid surface surrounding the 1 m diameter helium pool. The ambient and helium mixture temperature is set to 12 °C and the background pressure is set to 80900 Pa to correspond to the experimental conditions. The helium/acetone/oxygen mixture molecular weight is set to 5.45 kg/kmol. The turbulent Schmidt and Prandtl numbers are left at the FDS default value of 0.5. The helium mixture mass flux is specified as 0.0605 kg/s/m<sup>2</sup>. This case was studied previously by DesJardin et al. [191].

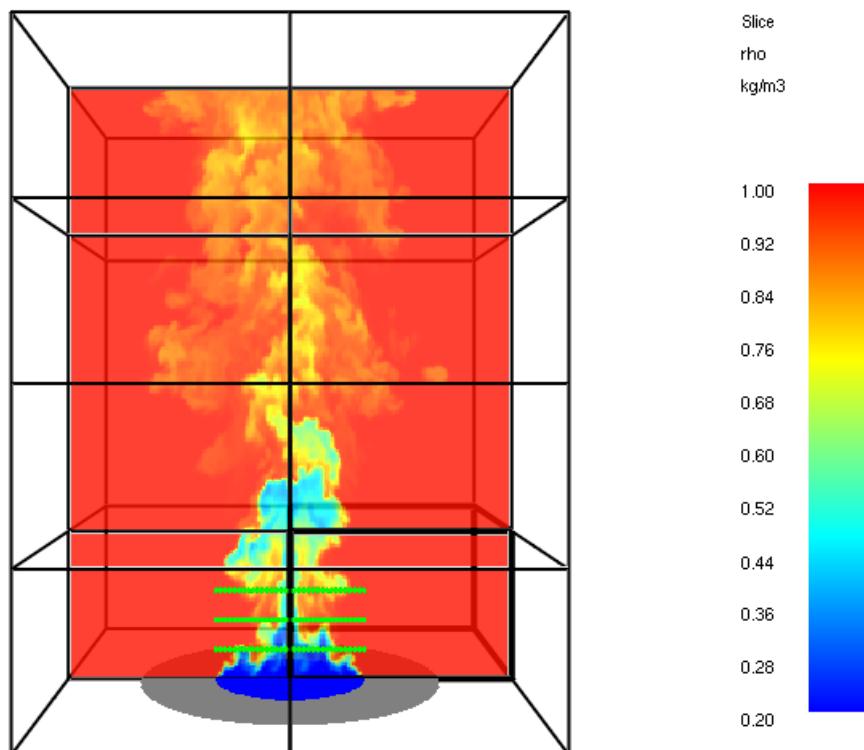


Figure 6.19: A snapshot of FDS results at 1.5 cm resolution for the Sandia 1 m helium plume showing density contours. The rows of measurement devices are visible near the base. The calculations are run in parallel on 16 processors; the outlined blocks indicate the domain decomposition.

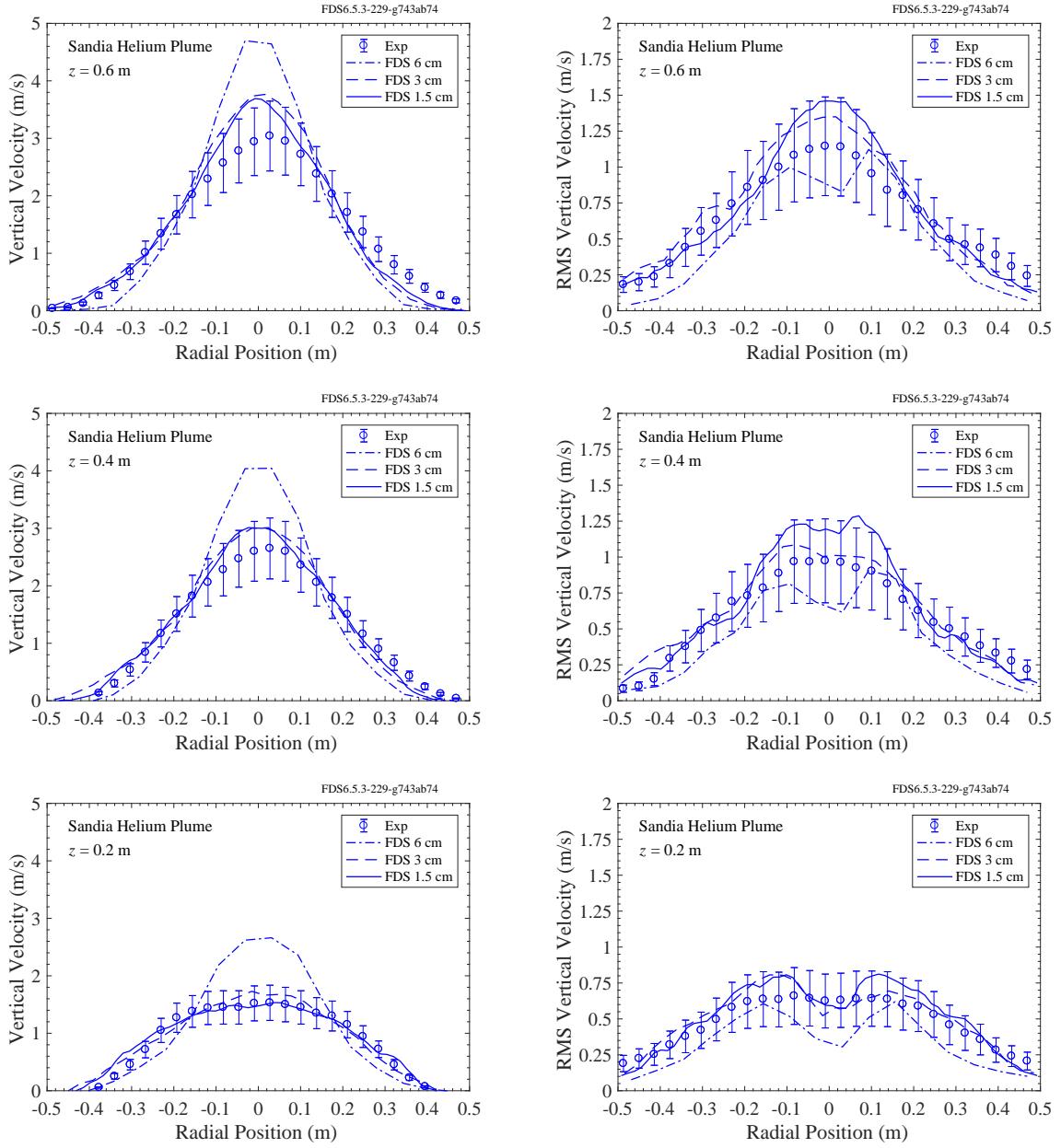


Figure 6.20: FDS predictions of mean and root mean square (RMS) vertical velocity profiles for the Sandia 1 m helium plume experiment. Results are shown for 6 cm, 3 cm, and 1.5 cm grid resolutions. With  $z$  being the streamwise coordinate, the bottom row is at  $z = 0.2$  m, the middle row is at  $z = 0.4$  m, and the top row is at  $z = 0.6$  m.

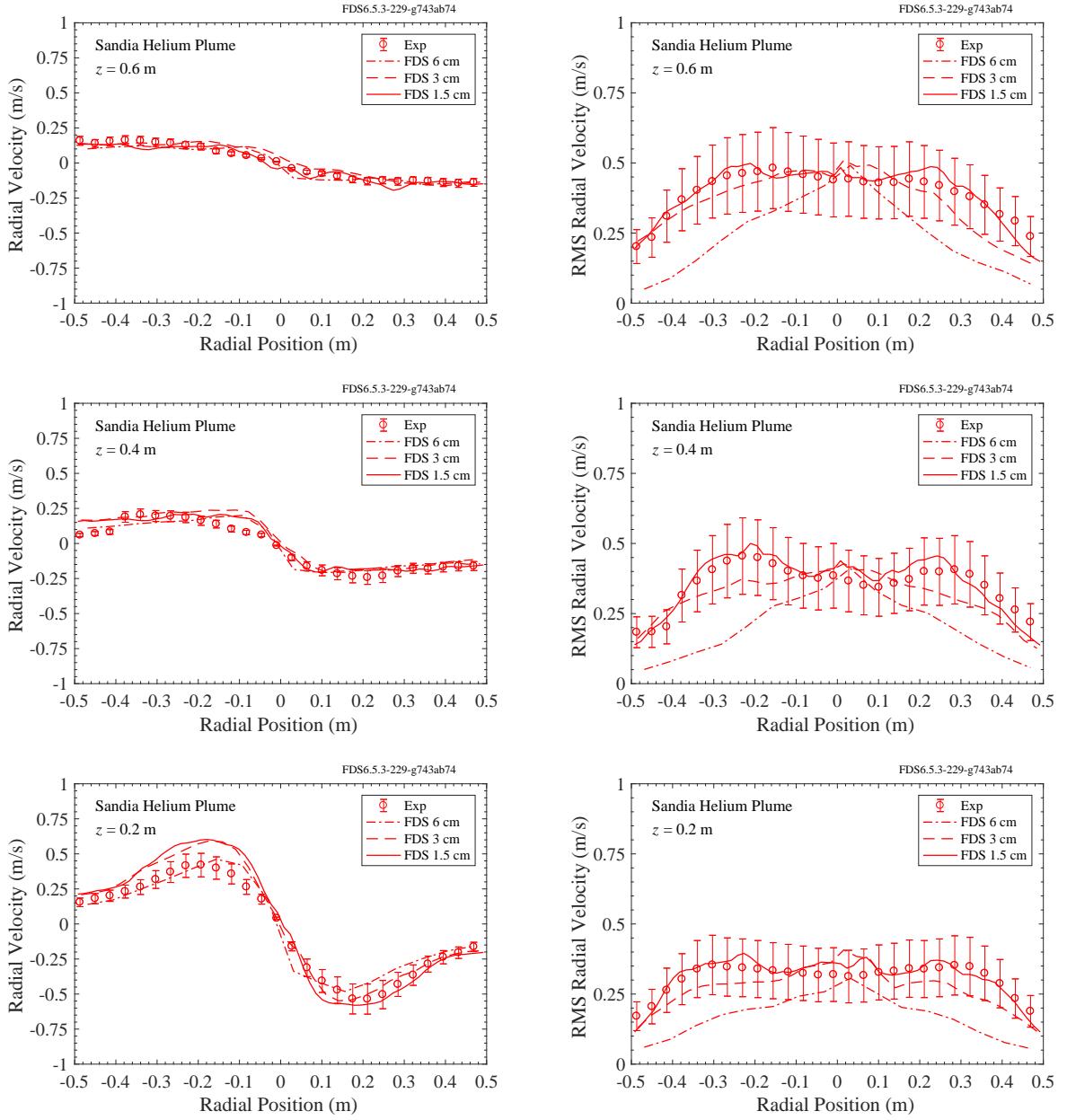


Figure 6.21: FDS predictions of mean and root mean square (RMS) radial velocity profiles for the Sandia 1 m helium plume experiment. Results are shown for 6 cm, 3 cm, and 1.5 cm grid resolutions. With  $z$  being the streamwise coordinate, the bottom row is at  $z = 0.2$  m, the middle row is at  $z = 0.4$  m, and the top row is at  $z = 0.6$  m.

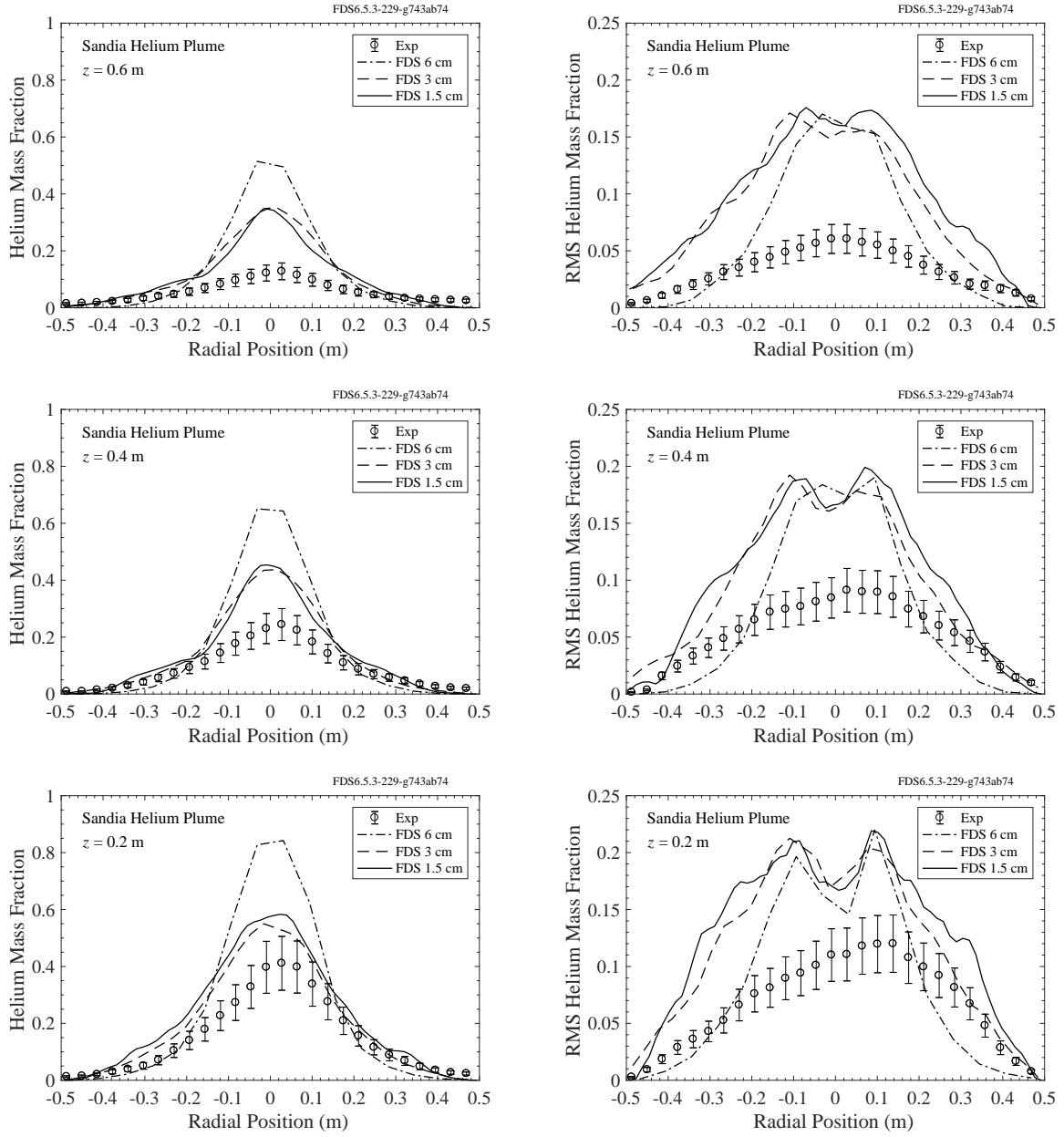


Figure 6.22: FDS predictions of mean and root mean square (RMS) helium mass fraction profiles for the Sandia 1 m helium plume experiment. Results are shown for 6 cm, 3 cm, and 1.5 cm grid resolutions. With  $z$  being the streamwise coordinate, the bottom row shows data at  $z = 0.2$  m, the middle row shows data at  $z = 0.4$  m, and the top row shows data at  $z = 0.6$  m.

### 6.4.2 Sandia 1 m Methane Pool Fire

The Sandia 1 m methane pool fire series provides data for three methane flow rates: Test 14 (low flow rate), Test 24 (medium flow rate), and Test 17 (high flow rate) [192]. The experiments are simulated using three grid resolutions: 6 cm, 3 cm, and 1.5 cm. Fig. 6.23 provides a snapshot of temperature contours from the 1.5 cm Test 17 simulation. The calculations are run in parallel on 16 processors—a similar computational set up as the helium case (the experiments were run in the same facility at Sandia). Data for vertical velocity and radial velocity are recorded at three levels downstream from the base of the plume,  $z = [0.3, 0.5, 0.9]$  m. Results for the mean profiles (and turbulent kinetic energy for Test 24) are given in Figs. 6.24 - 6.27. The means are taken between  $t = 10$  and  $t = 20$  seconds in the simulation.

For Test 17, we recorded the vertical velocity as a time series in four locations in the plume—at two positions along the centerline and at two positions on the edge. The time series from our 1.5 cm simulation at  $x = 0$  m and  $z = 0.5$  m, corresponding to Fig. 6 in [193], is shown in Fig. 6.28 along with the power spectrum from the average of the four time series locations. The FDS results compare well with the experimentally obtained puffing frequency of 1.65 Hz [193].

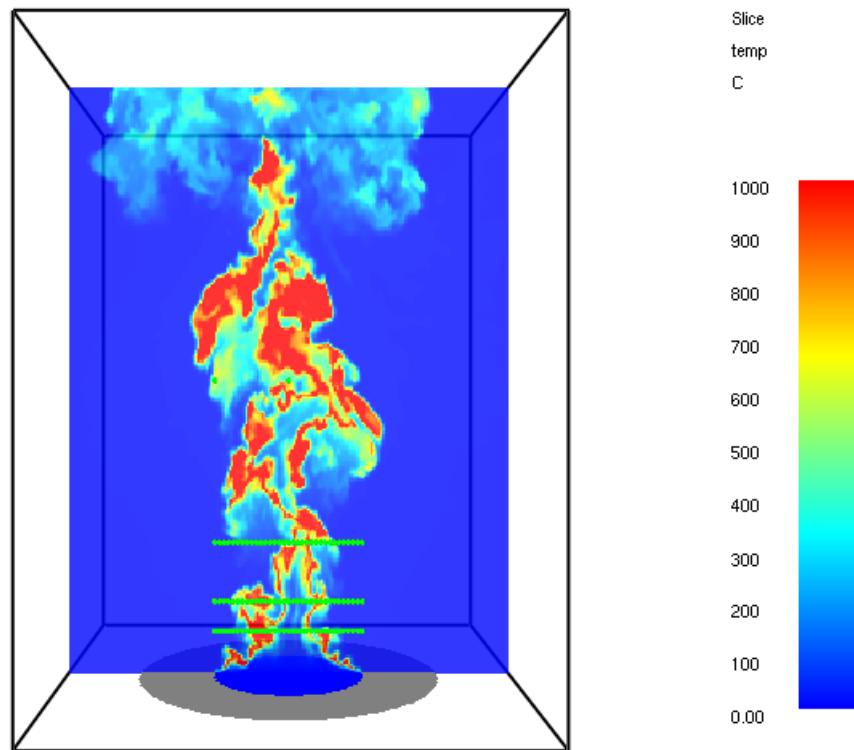


Figure 6.23: A snapshot of FDS results at 1.5 cm resolution for the Sandia 1 m methane pool fire (Test 17 – high flow rate) showing instantaneous contours of temperature. The rows of measurement devices (green) are visible near the base.

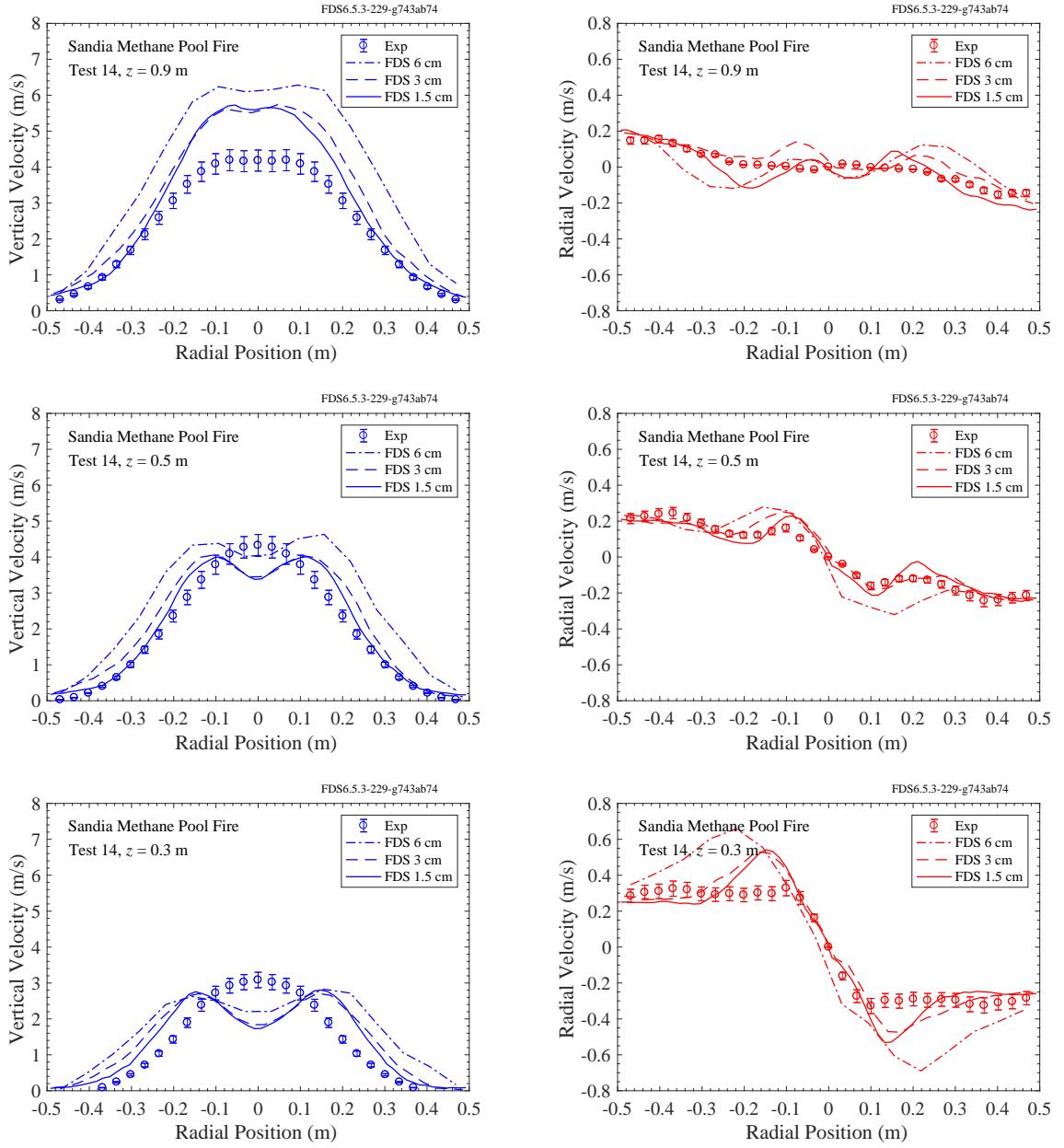


Figure 6.24: FDS predictions of mean velocity profiles for the Sandia 1 m methane pool fire experiment (Test 14 – low flow rate). Results are shown for 6 cm, 3 cm, and 1.5 cm grid resolutions. The  $z$  coordinate represents height above the methane pool; bottom row:  $z = 0.3\text{ m}$ , middle row:  $z = 0.5\text{ m}$ , and top row:  $z = 0.9\text{ m}$ .

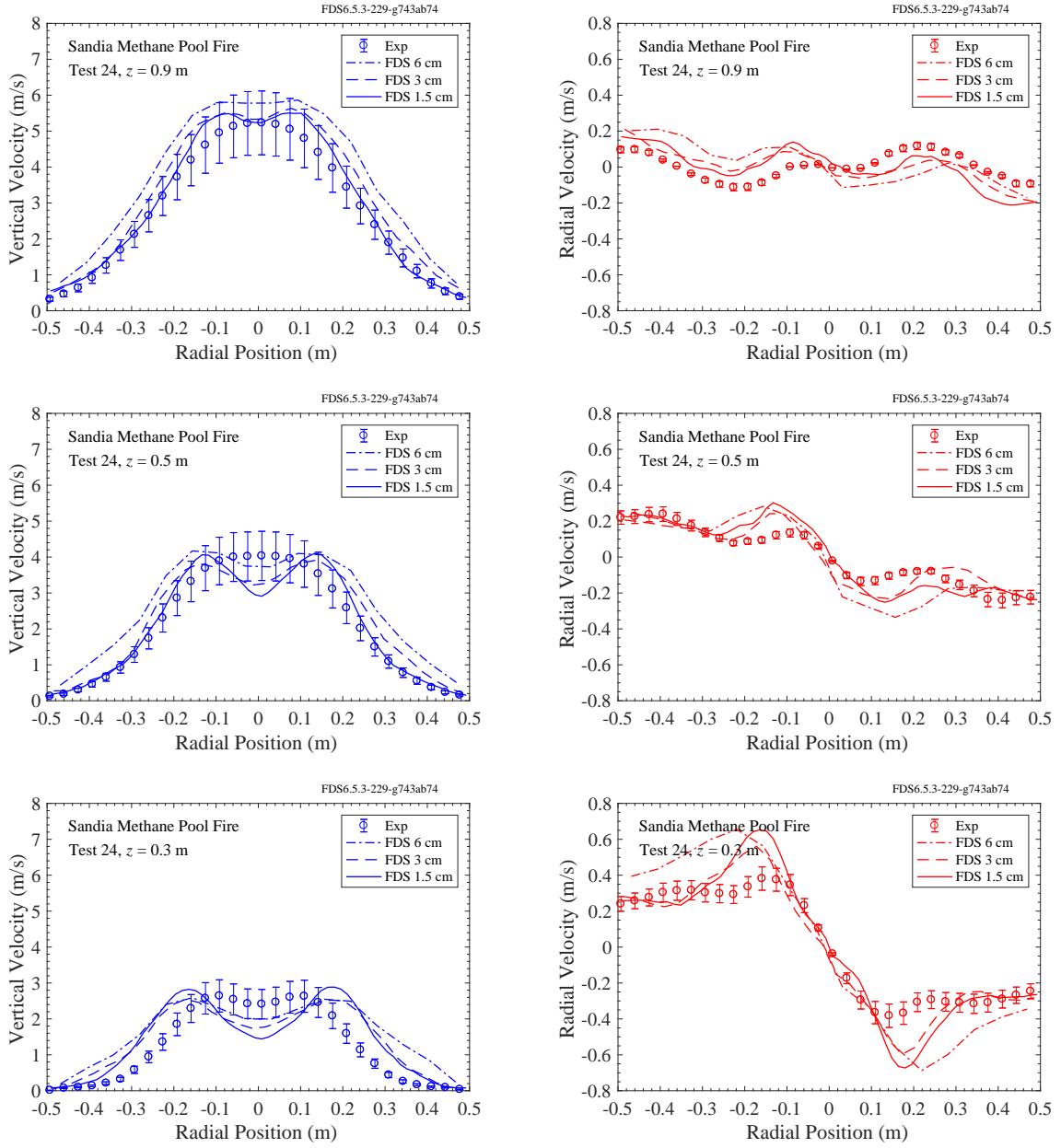


Figure 6.25: FDS predictions of mean velocity profiles for the Sandia 1 m methane pool fire experiment (Test 24 – medium flow rate). Results are shown for 6 cm, 3 cm, and 1.5 cm grid resolutions. The  $z$  coordinate represents height above the methane pool; bottom row:  $z = 0.3\text{ m}$ , middle row:  $z = 0.5\text{ m}$ , and top row:  $z = 0.9\text{ m}$ .

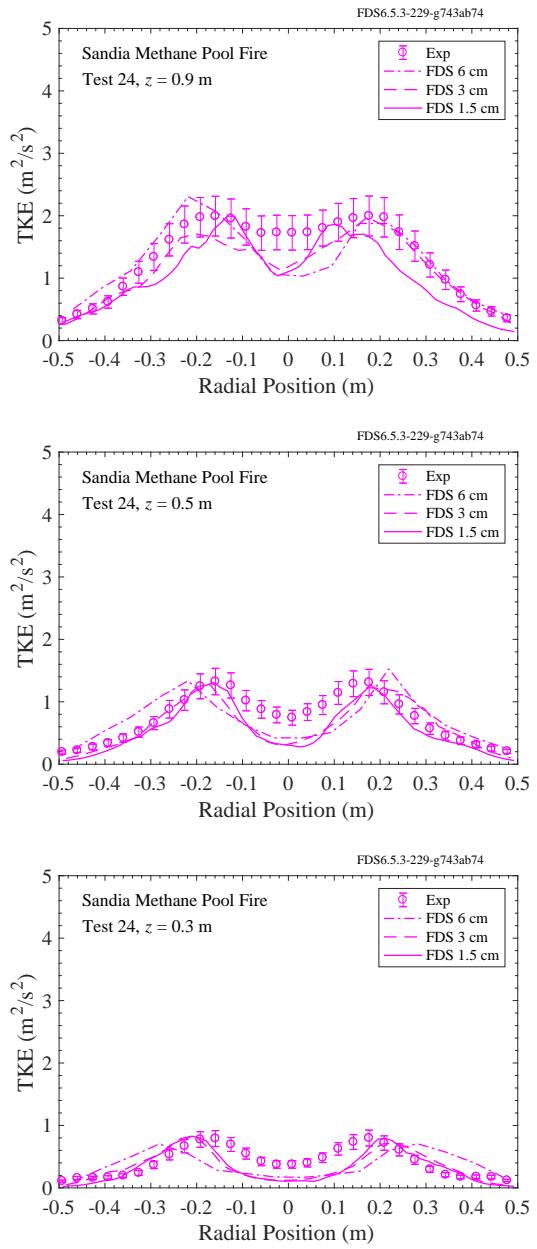


Figure 6.26: FDS predictions of turbulent kinetic energy (TKE) profiles for the Sandia 1 m methane pool fire experiment (Test 24 – medium flow rate). Results are shown for 6 cm, 3 cm, and 1.5 cm grid resolutions. The  $z$  coordinate represents height above the methane pool; bottom row:  $z = 0.3$  m, middle row:  $z = 0.5$  m, and top row:  $z = 0.9$  m.

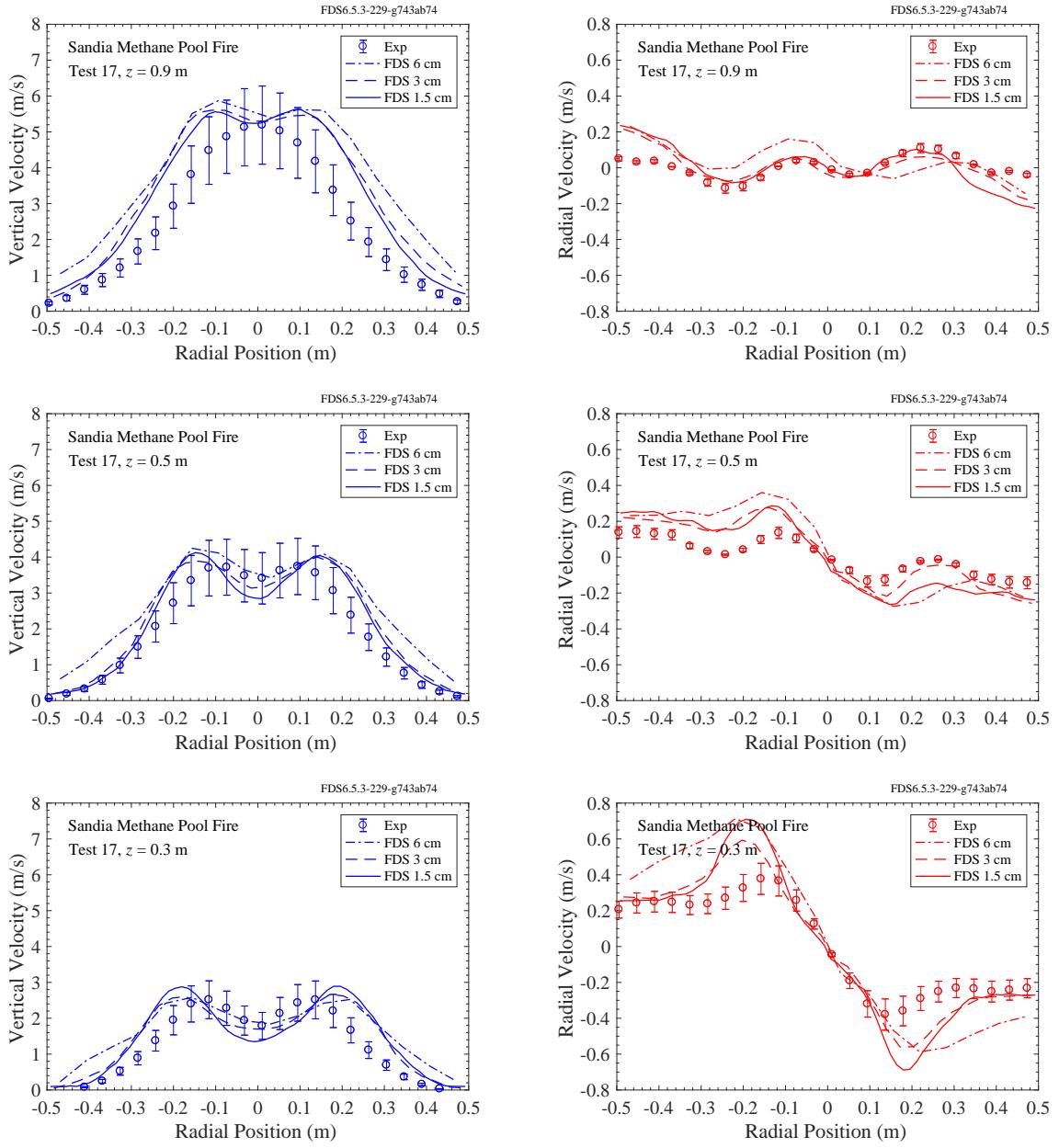


Figure 6.27: FDS predictions of mean velocity profiles for the Sandia 1 m methane pool fire experiment (Test 17). Results are shown for 3 cm and 1.5 cm grid resolutions. The  $z$  coordinate represents height above the methane pool; bottom row:  $z = 0.3\text{ m}$ , middle row:  $z = 0.5\text{ m}$ , and top row:  $z = 0.9\text{ m}$ .

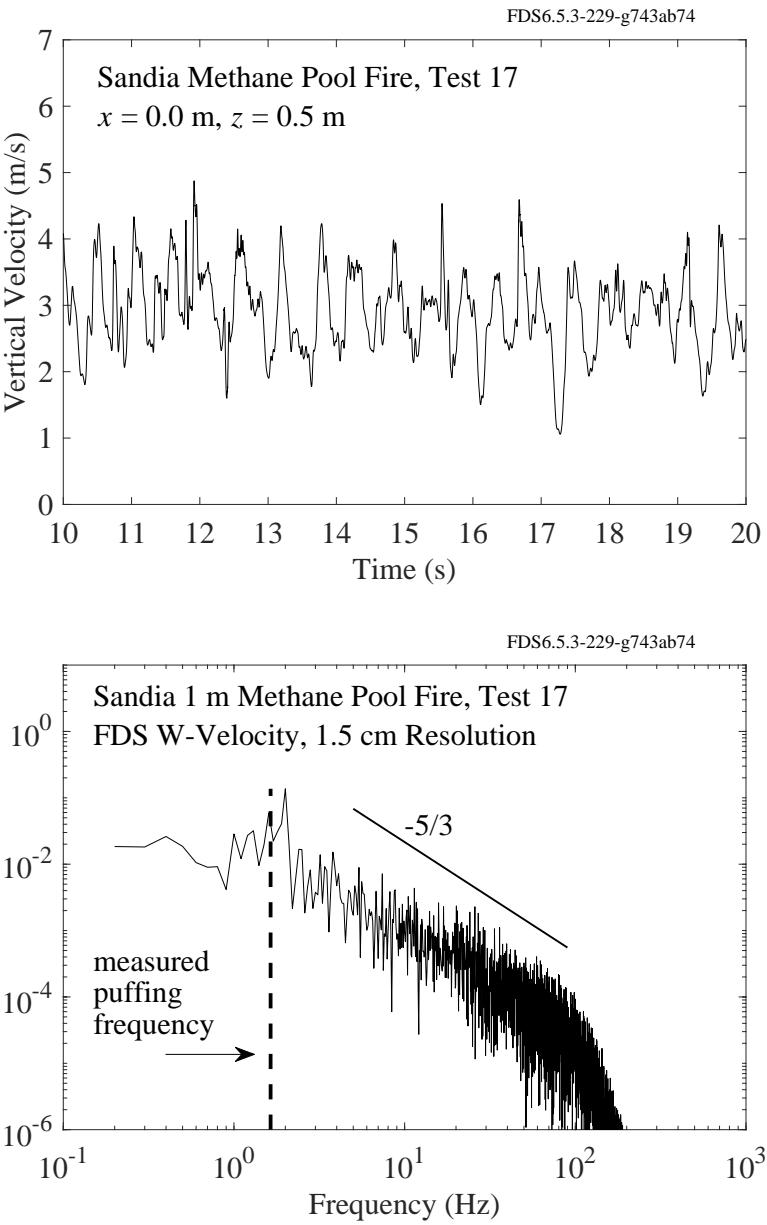


Figure 6.28: FDS velocity signal and power spectrum for the Sandia 1 m methane pool fire experiment (Test 17). The vertical velocity signal (top plot) is output from FDS on the centerline at  $z = 0.5$  m downstream of the fuel source. The power spectrum of vertical velocity is measured at four locations and averaged. Two of the measurement locations are along the centerline, at  $z = [0.5, 2.0]$  m, and two are along the edge of the plume,  $x = 0.5$  m and  $z = [0.5, 2.0]$  m. The measured puffing frequency of the plume is 1.65 Hz [193]. The temporal Nyquist limit of the simulation (the highest resolvable frequency due to the discrete time increment) is  $1/(2\delta t) \approx 1000$  Hz ( $\delta t \approx 0.0005$ ).

### 6.4.3 Sandia 1 m Hydrogen Pool Fire

Sandia Test 35 [192] is simulated at three grid resolutions: 6 cm, 3 cm, and 1.5 cm. The computational set up is nearly identical to the methane cases. Results for mean vertical and radial velocity are given in Figs. 6.30. Results for turbulent kinetic energy are presented in Fig. 6.31. Means are taken from a time average between  $t = 10$  and  $t = 20$  seconds in the simulation.

By examining movies of the simulation results we can see a qualitative difference between the methane and hydrogen cases. The dynamics of the hydrogen case tend to dominated by near total consumption events which create blowback on the pool followed by streaks of accelerating buoyant flow which increase the mean vertical velocity. An example of the consumption event is seen near the end of the case shown in Fig. 6.29. It is possible that we have not run the simulation long enough for accurate statistics and that streaking events early in the time window (between 10-20 seconds) are biasing the mean vertical velocity to be too high, as is clear from the top-left plot in Fig. 6.30.

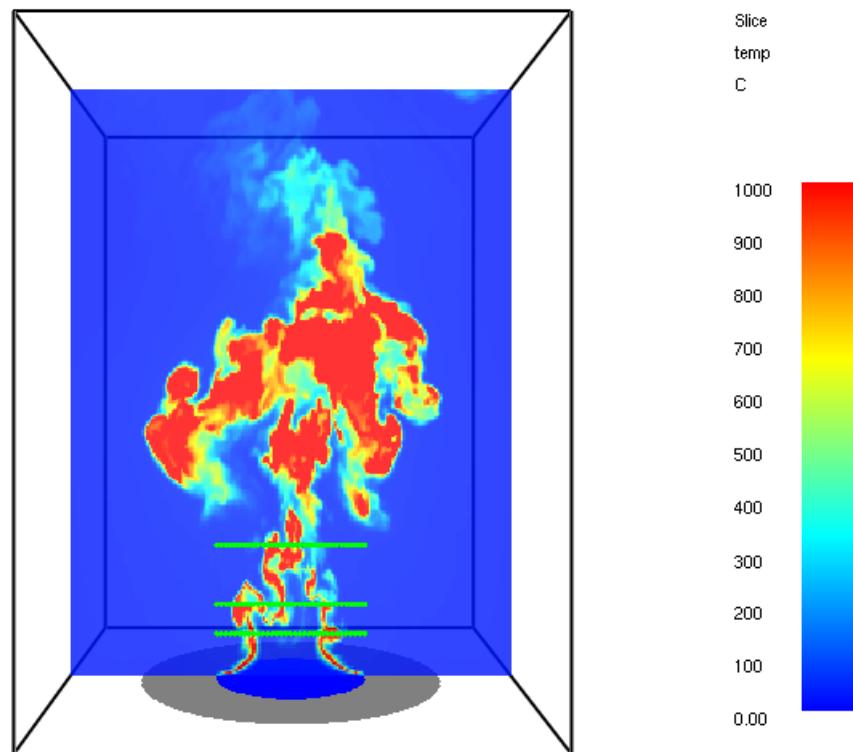


Figure 6.29: A snapshot of FDS results at 1.5 cm resolution for the Sandia 1 m hydrogen pool fire (Test 35) showing instantaneous contours of temperature. The rows of measurement devices (green) are visible near the base.

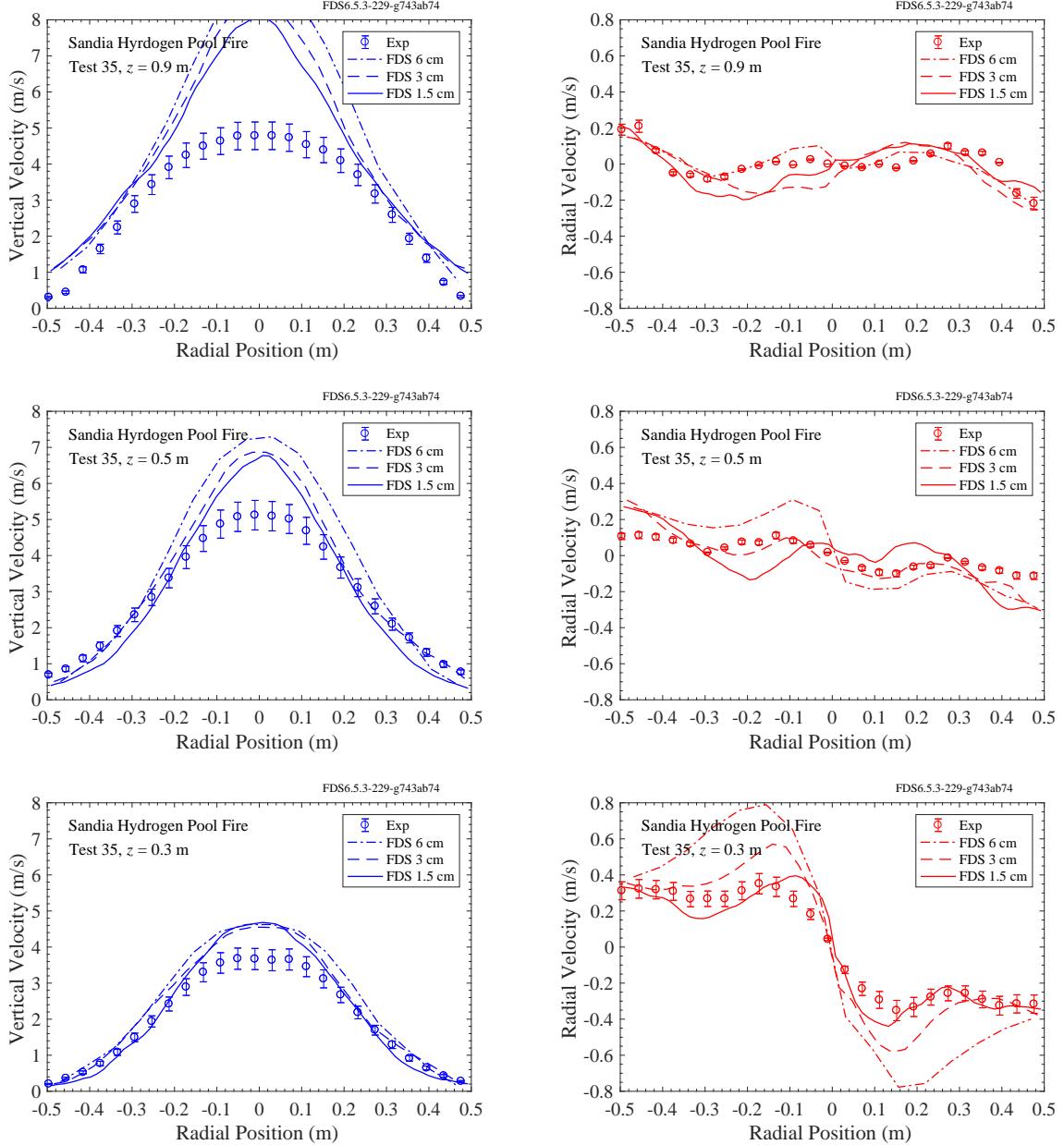


Figure 6.30: FDS predictions of mean velocity profiles for the Sandia 1 m hydrogen pool fire experiment (Test 35). Results are shown for 6 cm, 3 cm, and 1.5 cm grid resolutions. The  $z$  coordinate represents height above the pool; bottom row:  $z = 0.3$  m, middle row:  $z = 0.5$  m, and top row:  $z = 0.9$  m.

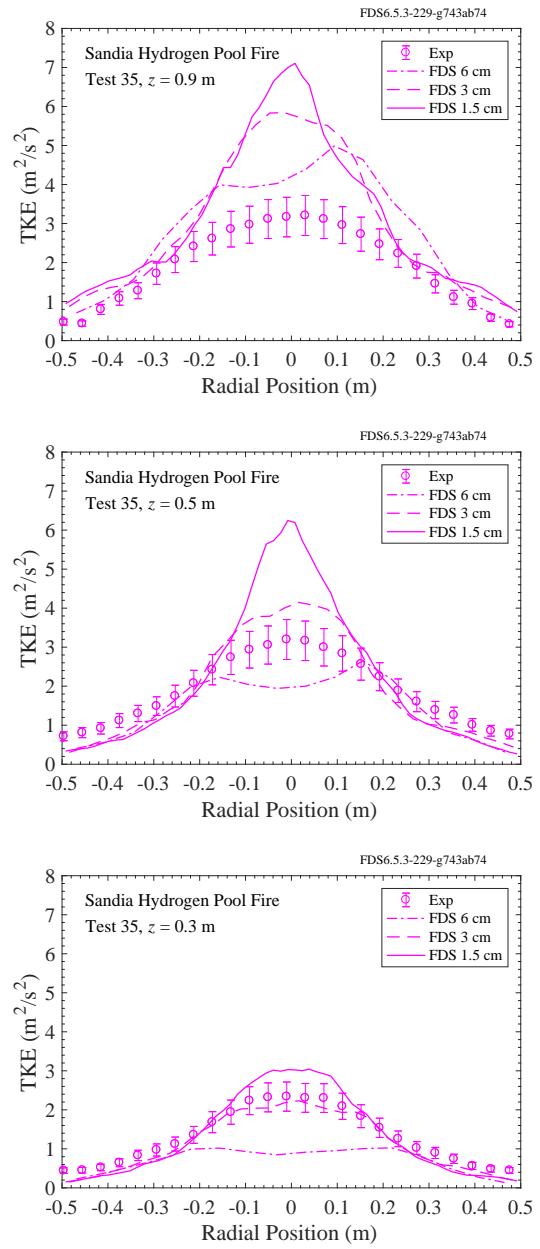


Figure 6.31: FDS predictions of turbulent kinetic energy (TKE) profiles for the Sandia 1 m hydrogen pool fire experiment (Test 35). Results are shown for 6 cm, 3 cm, and 1.5 cm grid resolutions. The  $z$  coordinate represents height above the methane pool; bottom row:  $z = 0.3$  m, middle row:  $z = 0.5$  m, and top row:  $z = 0.9$  m.

## 6.5 Purdue 7.1 cm Methane Flame

Figures 6.32-6.35 show results for the Purdue 7.1 cm methane flame [30]. Three sets of results are presented: two coarse (4 mm) cases and one fine (2 mm) case. The fine mesh case is run with MPI on 16 meshes. The coarse cases are run two ways: a single mesh case (dashed lines) and a 16 mesh case (dotted lines). As should be the case, the single- and multi-mesh cases yield the same results. This gives confidence in the domain decomposition strategy for open plume flows with FDS.

The discrepancy at the centerline for mixture fraction and vertical velocity may be attributed to our not accounting for (1) the slight divergence of the flow at the burner exit ( $7^\circ$  [30]) and (2) the asymmetries and fluctuations in the burner exit and ambient environment. Examination of the FDS output shows the solution remains very symmetric, preventing large gulps of air from penetrating the centerline of the plume, which would tend to smooth out the profiles near the center reducing the bimodal vertical velocity profile and centerline mixture fraction.

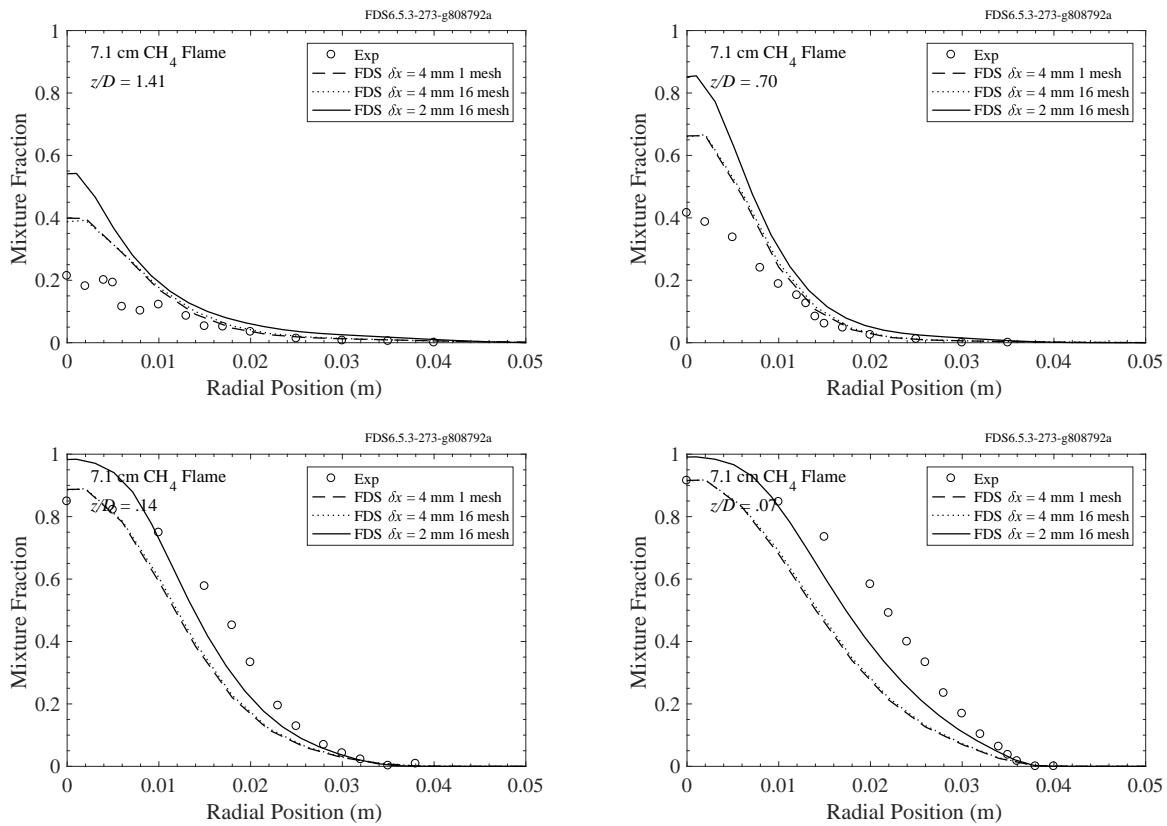


Figure 6.32: Measured [32] and computed radial profiles of the mean mixture fraction at select heights above the burner exit simulated using grids with different spatial resolutions.

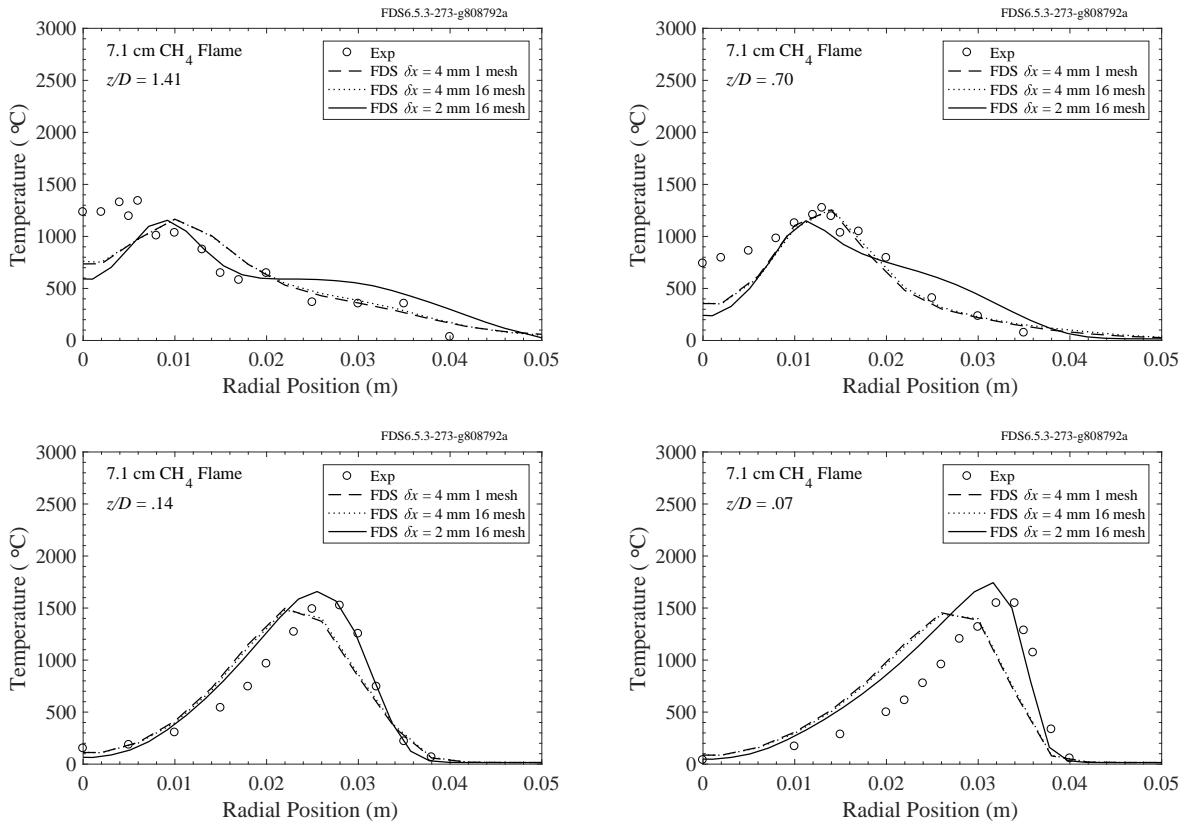


Figure 6.33: Inferred [30] and computed radial profiles of the mean temperature at select heights above the burner exit simulated using grids with different spatial resolutions.

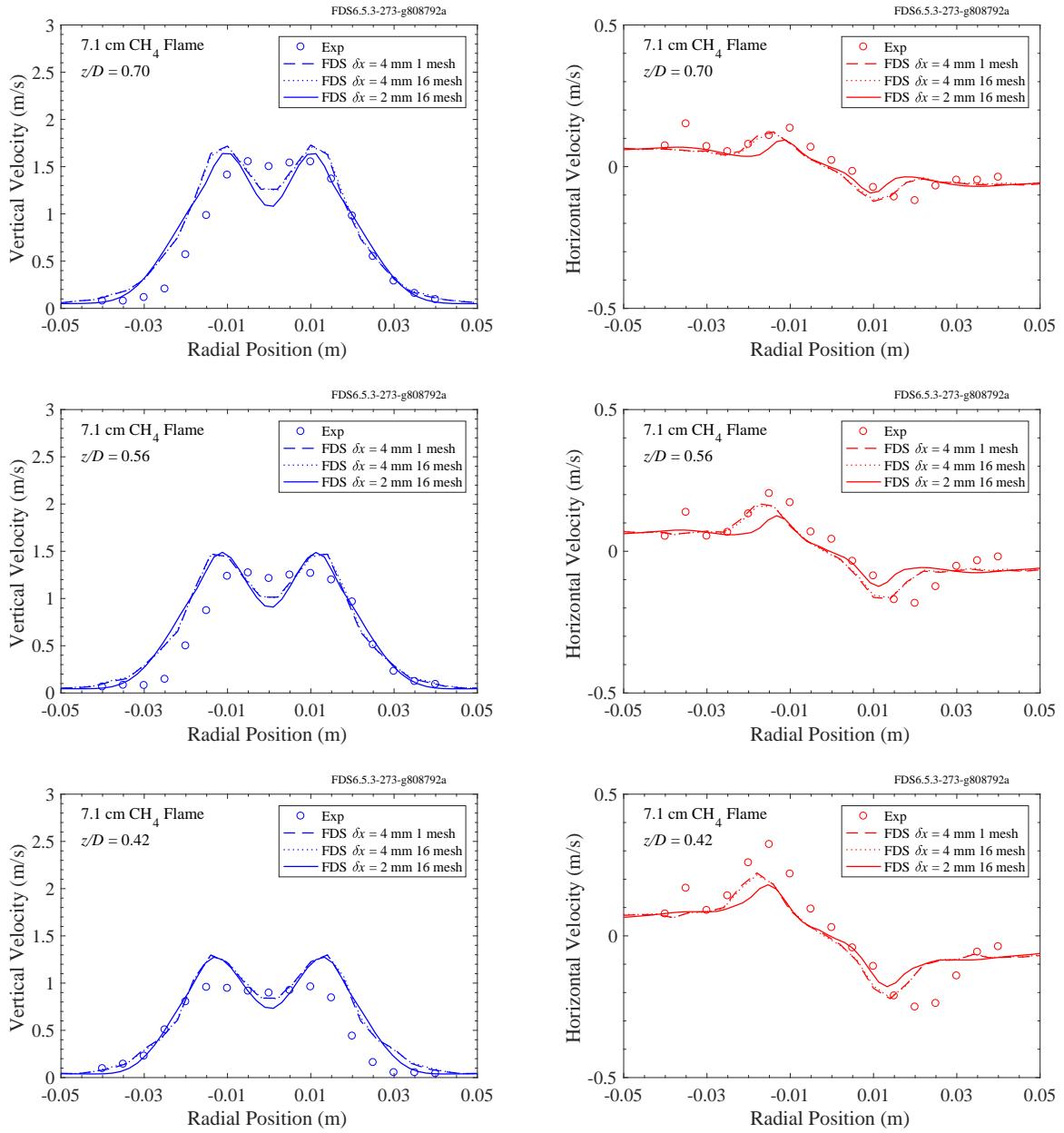


Figure 6.34: Measured [32] and computed radial profiles of the mean vertical and horizontal velocities at select heights above the burner exit simulated using grids with different spatial resolutions.

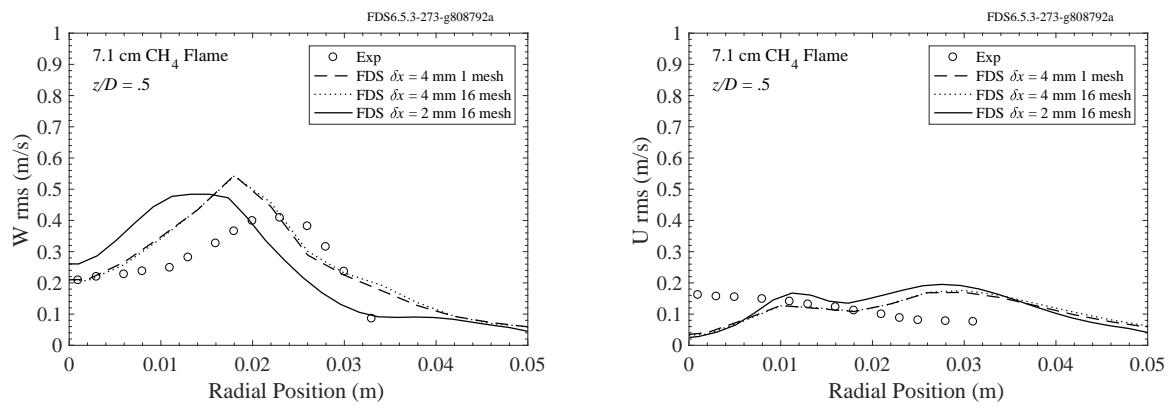


Figure 6.35: Measured and computed profiles of rms vertical (left) and radial (right) velocity profiles at  $z/D = 0.5$ .

## 6.6 UMD Line Burner

In this section, we present thermocouple temperature measurements and computational results for the UMD Line Burner. Experimental details may be found in White et al. [210]. FDS simulations are performed at three grid resolutions corresponding to  $W/\delta x = 4, 8, 16$ , where  $W = 5 \text{ cm}$  is the width of the fuel slot in the line burner. The radiant fraction is measured to be  $\chi_r = 0.18$  for the 18 vol. %  $\text{O}_2$  coflow. We use this value in the simulations.

Fig. 6.36 shows measured and computational results for mean thermocouple temperature across the width of the burner at two heights,  $z$ , above the burner surface. Fig. 6.37 shows a slice of gas temperature for the case with methane fuel and 18 vol. %  $\text{O}_2$  in the coflow stream (nitrogen dilution). The purpose of the image is to provide a qualitative result for the flame.

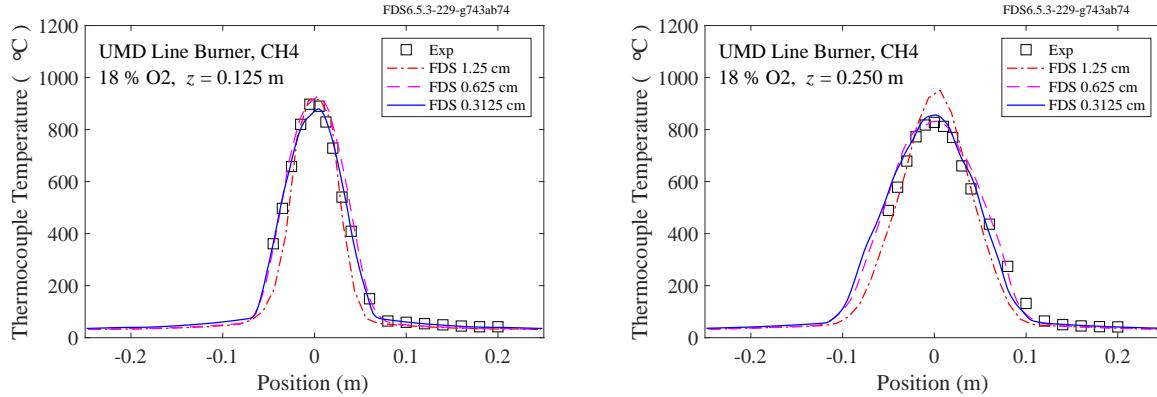


Figure 6.36: Measured and computed mean thermocouple temperature profiles at 18 vol %  $\text{O}_2$ .

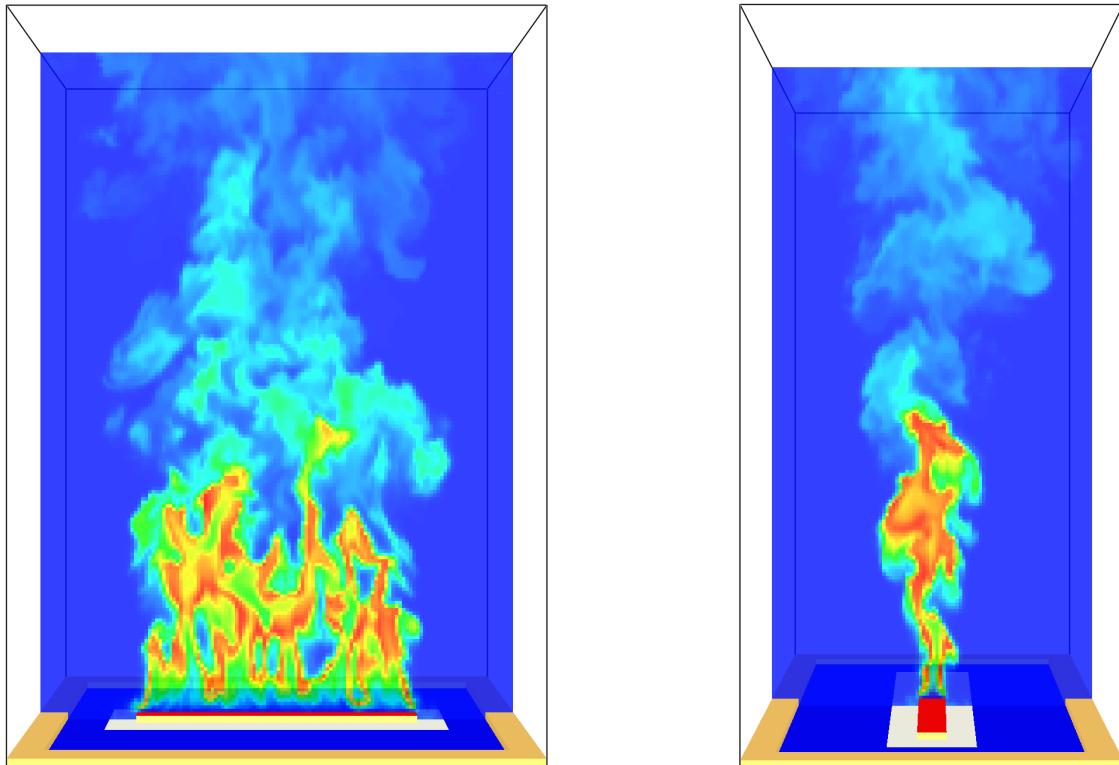


Figure 6.37: UMD Line Burner temperature contours, front (left) and side (right) views for the  $\delta x = 0.625$  cm case. Fuel (natural gas in this case) enters through the red surface. The air with nitrogen dilution (to 18 vol. % O<sub>2</sub> in this case) enters through the blue surface. The white ceramic flame holder is seen surrounding the red burner surface. The right side view corresponds to the profiles shown in Fig. 6.36 through the center of the burner at different heights  $z$  from the red burner surface. Within the slice plane blue represents 20 °C, red 1500 °C.

## Chapter 7

# Ceiling Jets and Device Activation

FDS is a computational fluid dynamics (CFD) model and has no specific ceiling jet algorithm. Rather, temperatures throughout the fire compartment are computed directly from the governing conservation equations. Nevertheless, temperature measurements near the ceiling are useful in evaluating the model's ability to predict the activation times of sprinklers, smoke detectors, and other fire protection devices. The term "ceiling jet" is used loosely here – it distinguishes a point temperature measurement near the ceiling from an average "hot gas layer" (HGL) temperature.

This chapter first presents comparisons of model predictions and temperature measurements near to the ceiling. Next, predicted sprinkler activation times and the total number of activations are compared with measurements. Finally, predicted smoke detector activation times are compared with measurements.

### 7.1 Ceiling Jet Temperatures

The ceiling jet temperature measurements presented in this section were made for a variety of reasons. Most often, these measurements were simply the upper most thermocouple temperature in a vertical array. Sometimes, these measurements were designed to detect the activation time of a sprinkler. In any case, these measurements are used to evaluate the model's ability to predict the gas temperature at a single point, as opposed to the hot gas layer average.

### **7.1.1 ATF Corridors Experiment**

This series of experiments involved two fairly long corridors connected by a staircase. The fire, a natural gas sand burner, was located on the first level at the end of the corridor away from the stairwell. The corridor was closed at this end, and open at the same position on the second level. Two-way flow occurred on both levels because make-up air flowed from the opening on the second level down the stairs to the first. The only opening to the enclosure was the open end of the second-level corridor.

Temperatures were measured with seven thermocouple trees. Tree A was located fairly close to the fire on the first level. Tree B was located halfway down the first-level corridor. Tree C was close to the stairwell entrance on the first level. Tree D was located in the doorway of the stairwell on the first level. Tree E was located roughly along the vertical centerline of the stairwell. Tree F was located near the stairwell opening on the second level. Tree G was located near the exit at the other end of the second-level corridor. The graphs on the following pages show the top and bottom TC from each tree for the given fire sizes of 50 kW, 100 kW, 250 kW, 500 kW, and a mixed HRR “pulsed” fire.

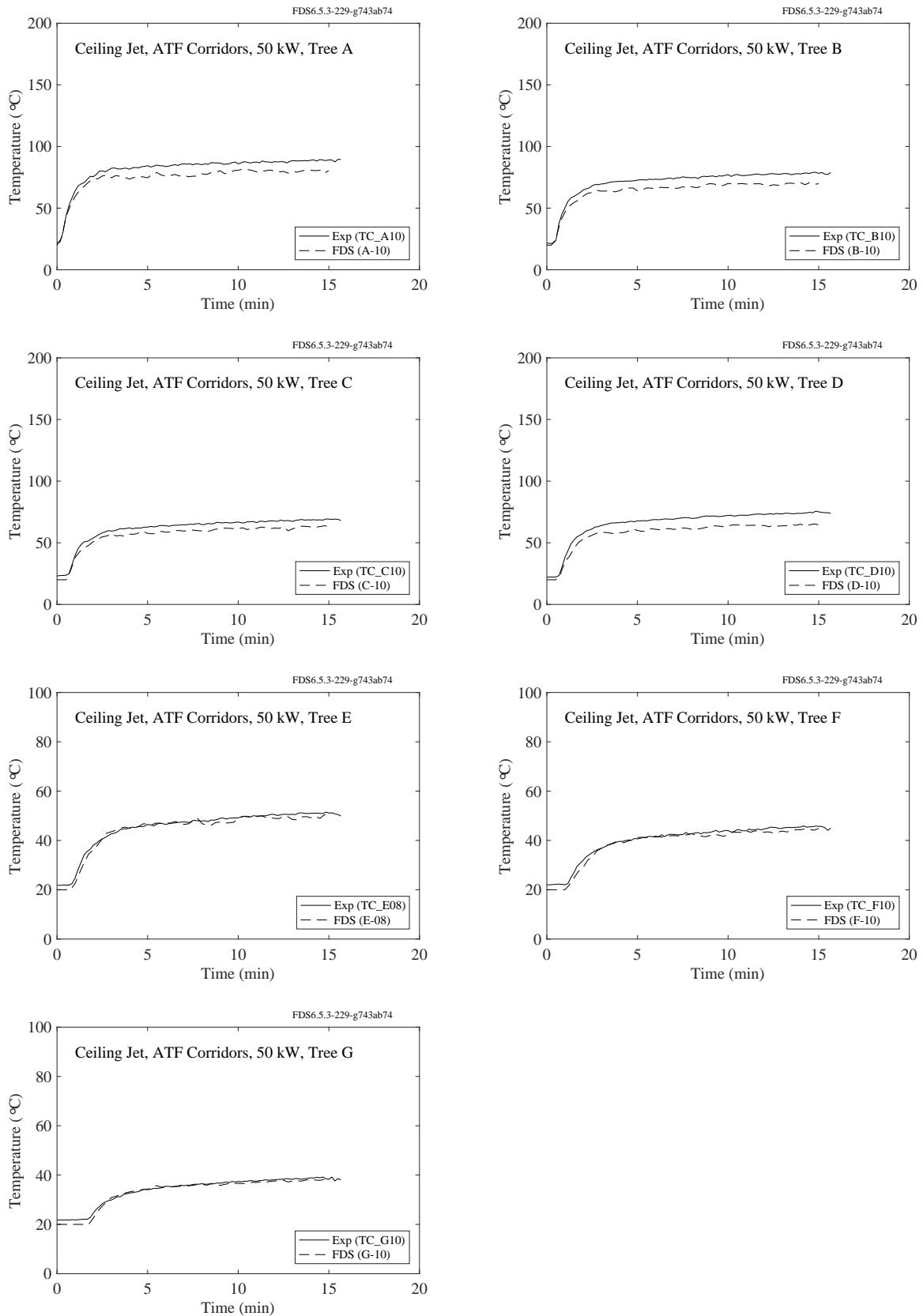


Figure 7.1: ATF Corridors experiments, ceiling jet, 50 kW.

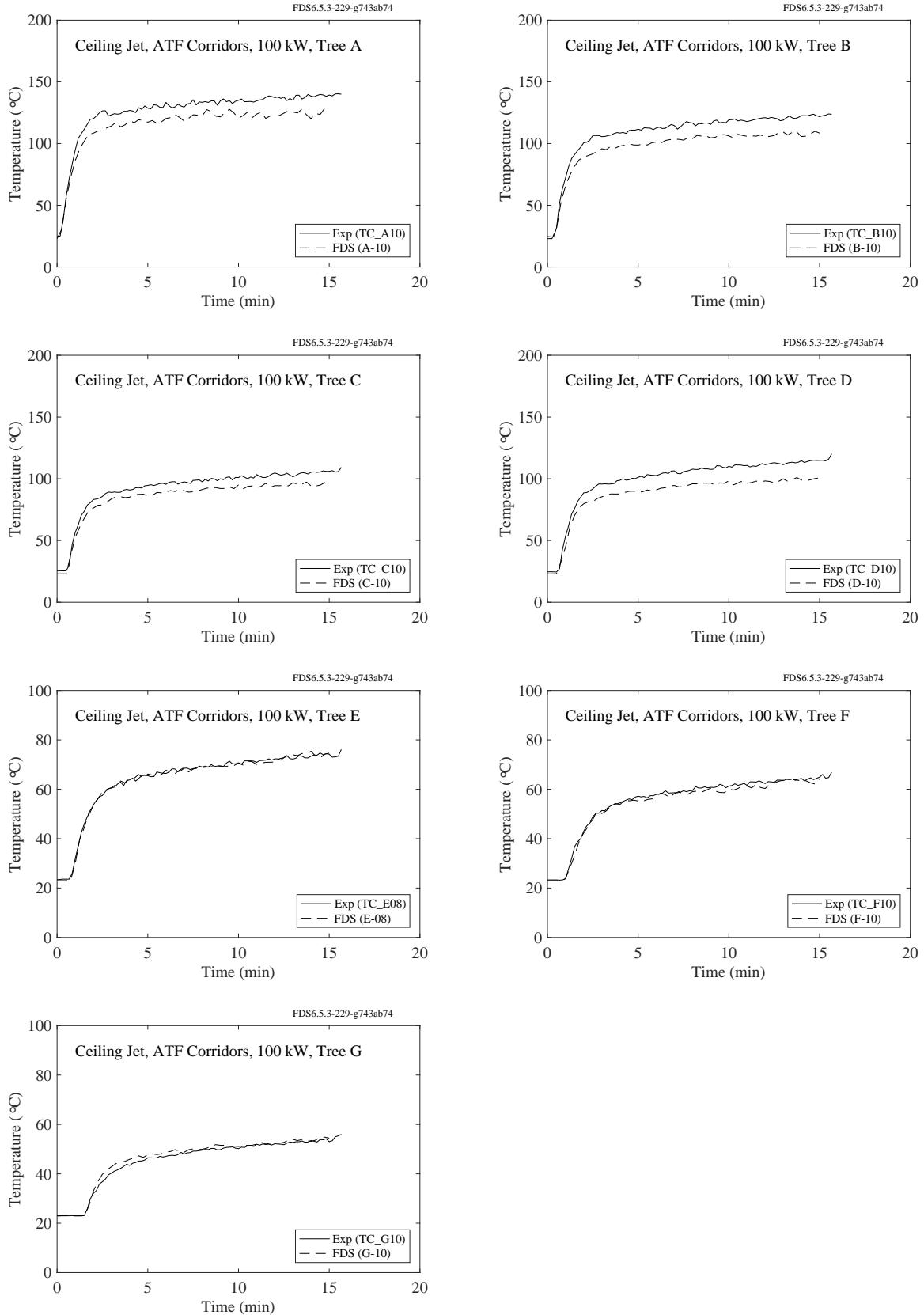


Figure 7.2: ATF Corridors experiments, ceiling jet, 100 kW.

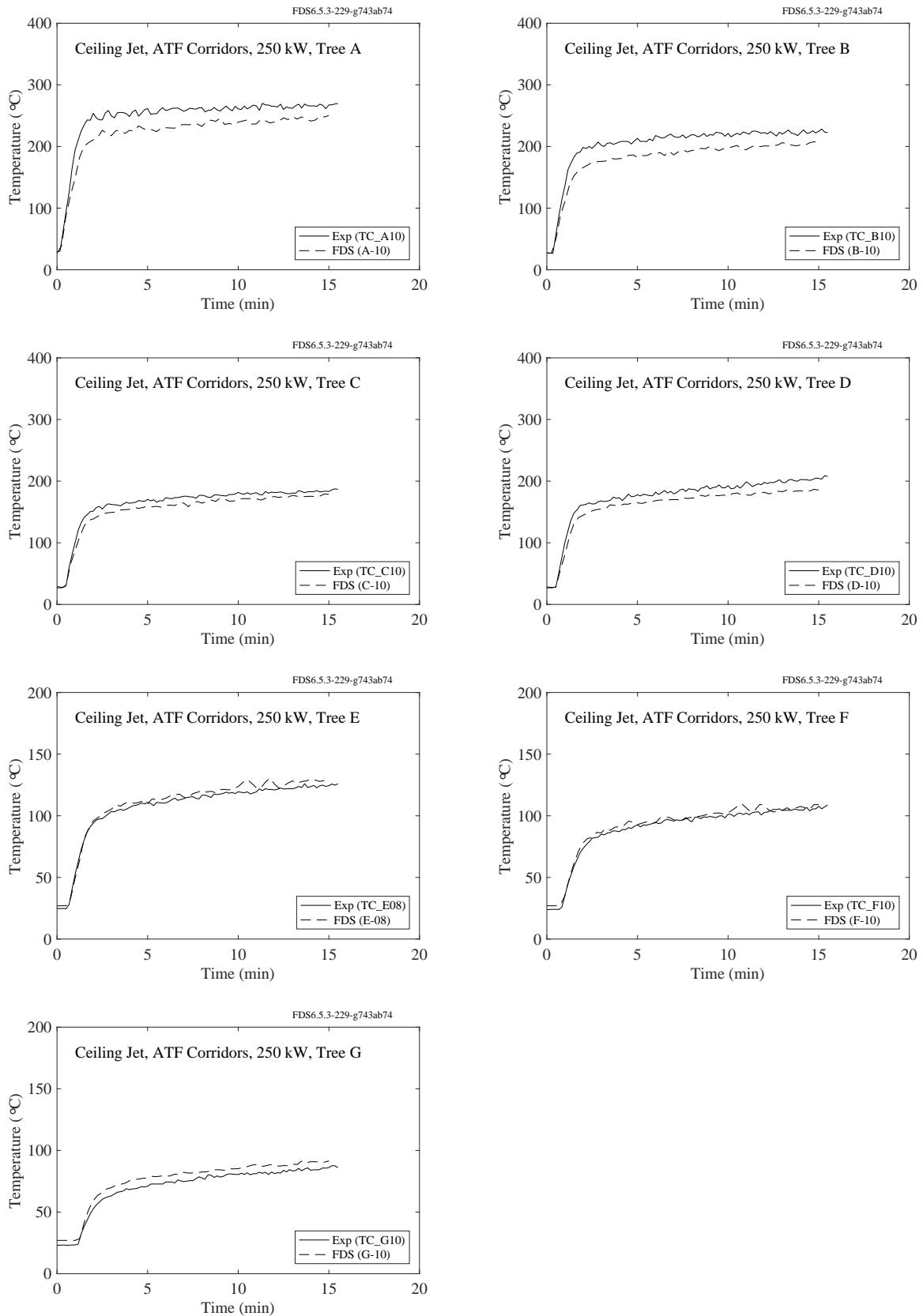


Figure 7.3: ATF Corridors experiments, ceiling jet, 250 kW.

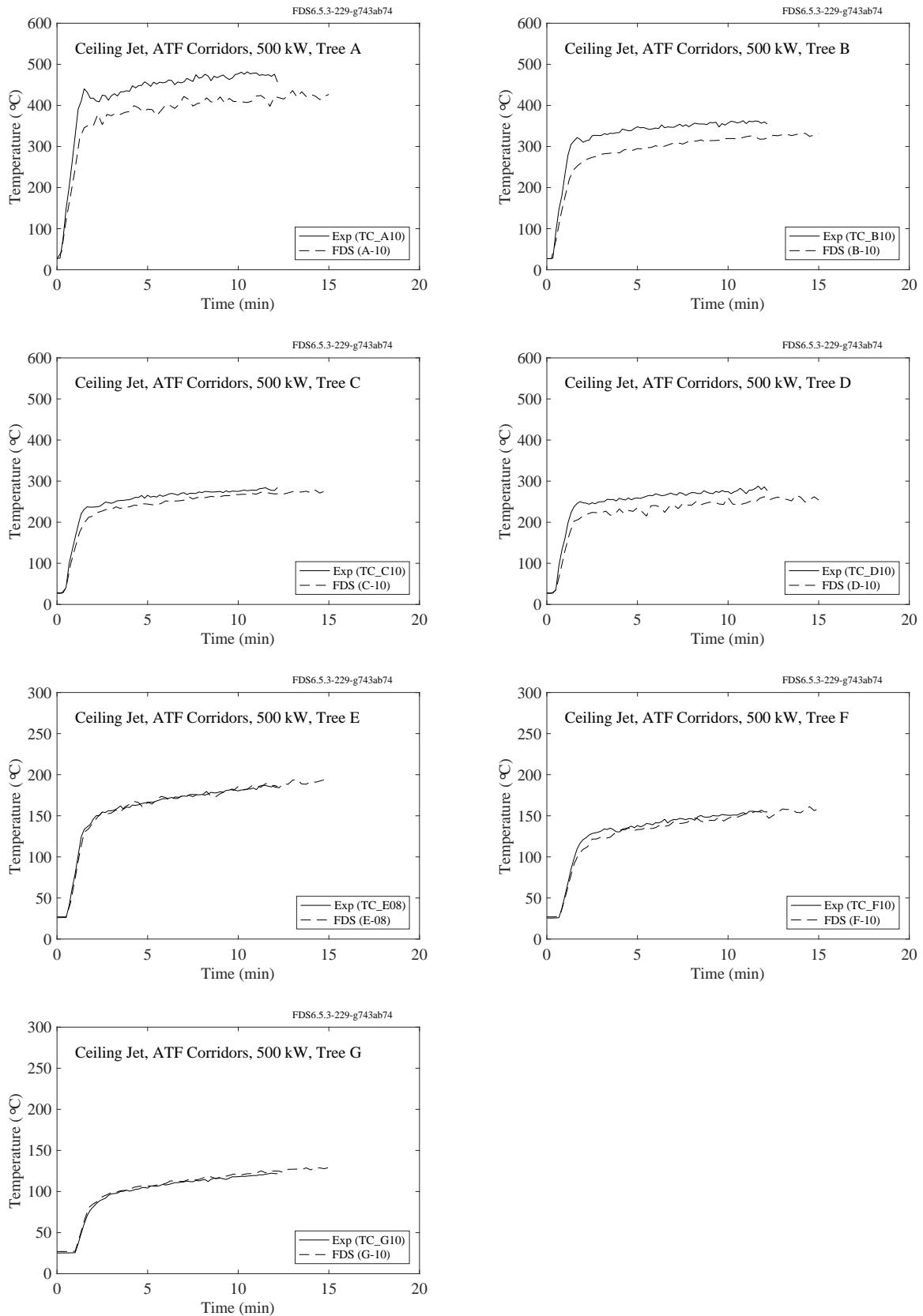


Figure 7.4: ATF Corridors experiments, ceiling jet, 500 kW.

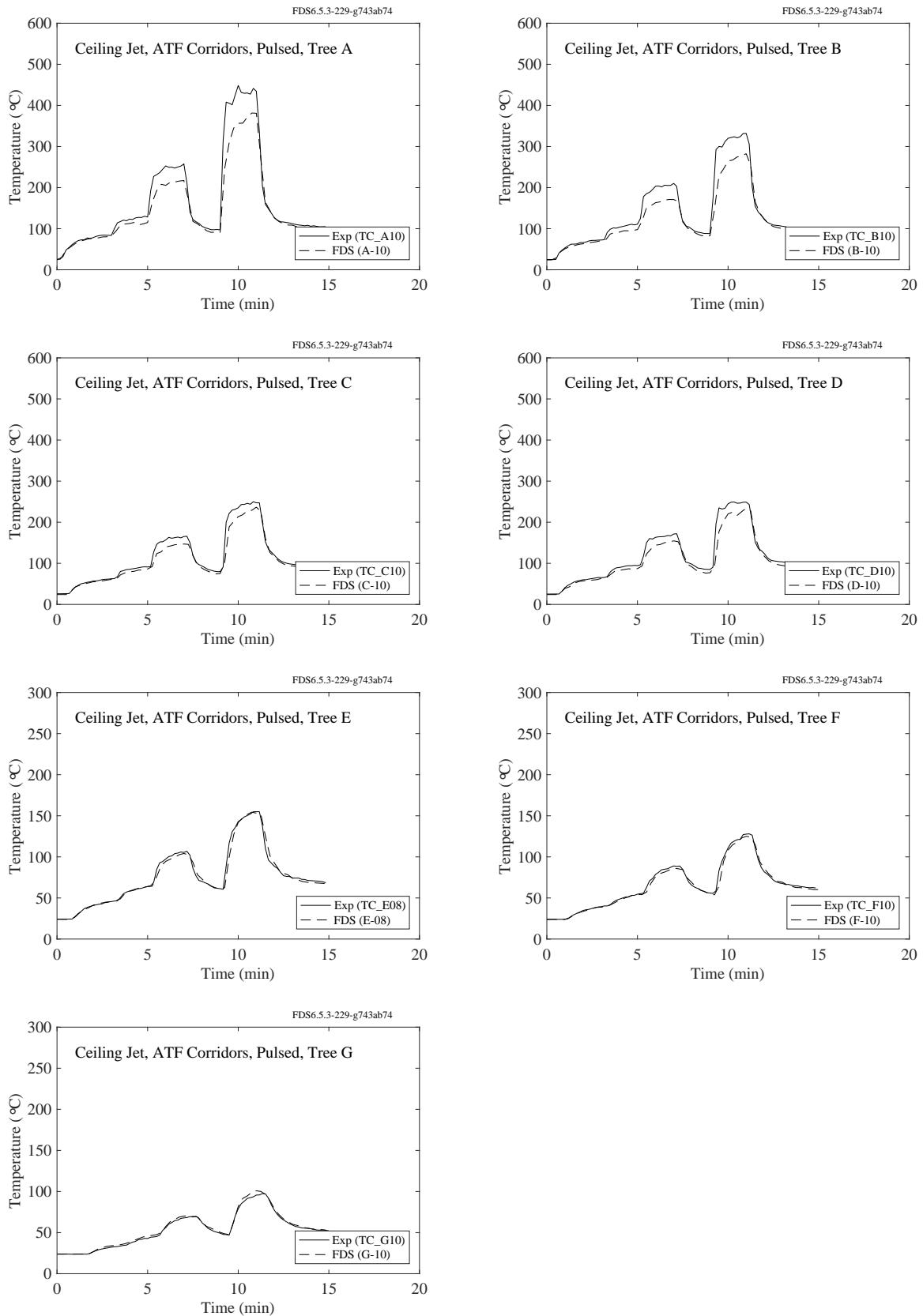


Figure 7.5: ATF Corridors experiments, ceiling jet, mixed HRR.

### 7.1.2 Arup Tunnel Experiments

The plots below show the predicted and measured temperatures from a fire experiment conducted in a tunnel. Near-ceiling temperatures were measured at distances of 2 m, 4 m, 6 m and 8 m from the fire along the centerline of tunnel.

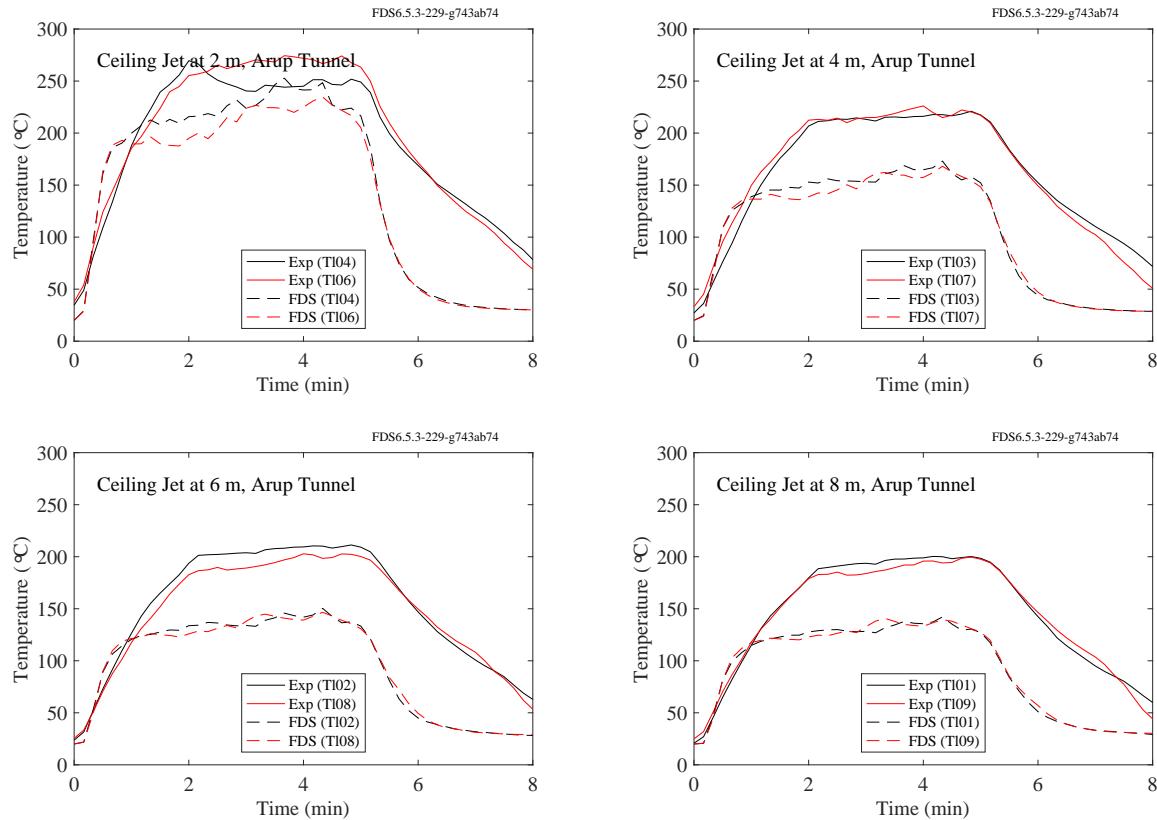


Figure 7.6: Arup Tunnel experiments, ceiling jet.

### 7.1.3 DelCo Trainers

The plots below and on the following pages display comparisons of ceiling jet temperatures for the DelCo Trainer experiments. Tests 2-6 were conducted in a single level house mock-up with three rooms adjacent to one another. Locations A1 and A2 were in the fire room, A3 was in an adjacent room, and A4 and A5 were in a room next to the adjacent room. Tests 22-25 were conducted in a two level house mock-up. Locations A1, A2, and A3 were 2 cm below the ceiling of the first level, and A7, A8, and A9 were 2 cm below the ceiling of the second level. See Section 3.11 for their exact locations.

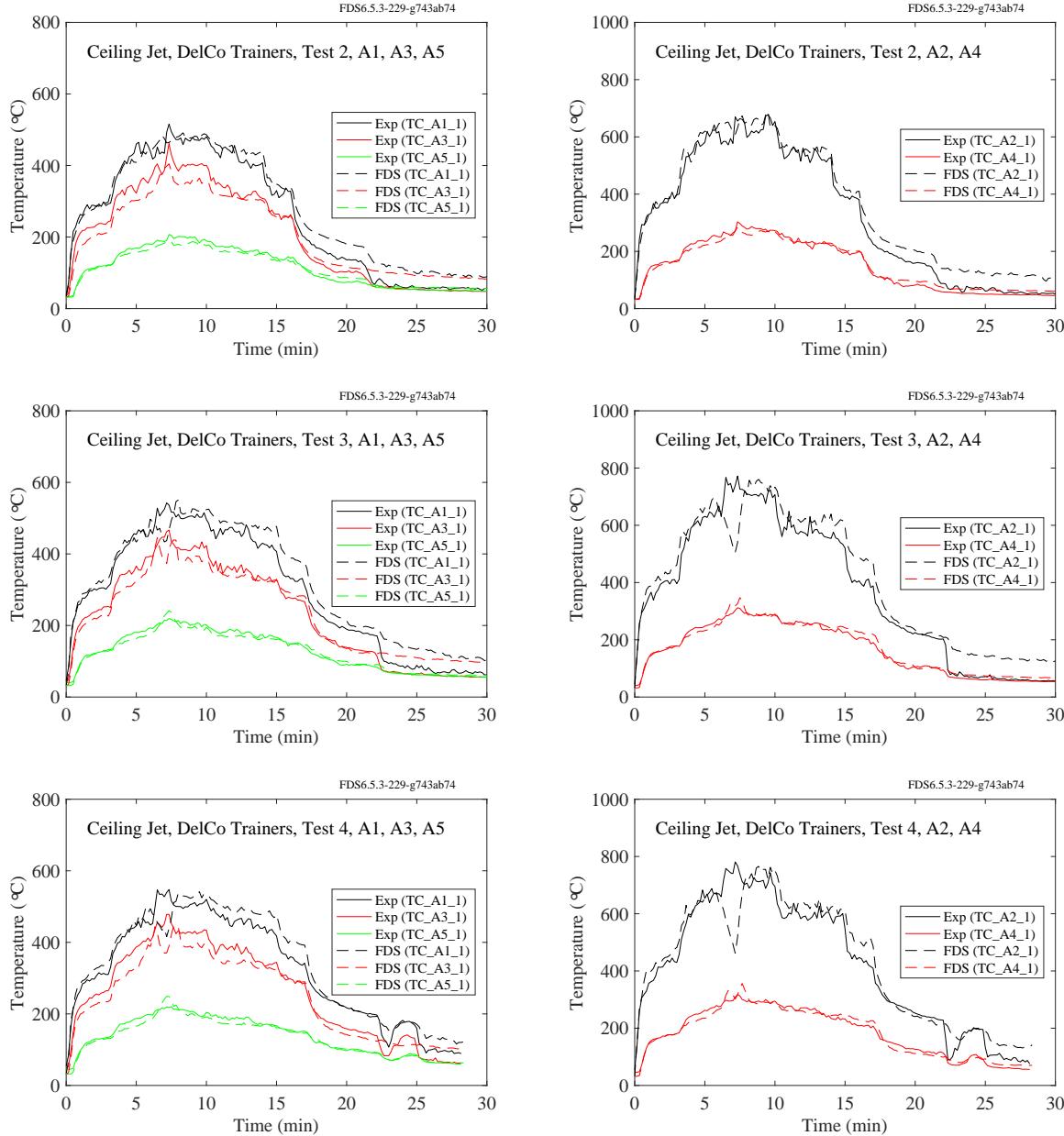


Figure 7.7: DelCo Trainers, ceiling jet temperature, Tests 2-4.

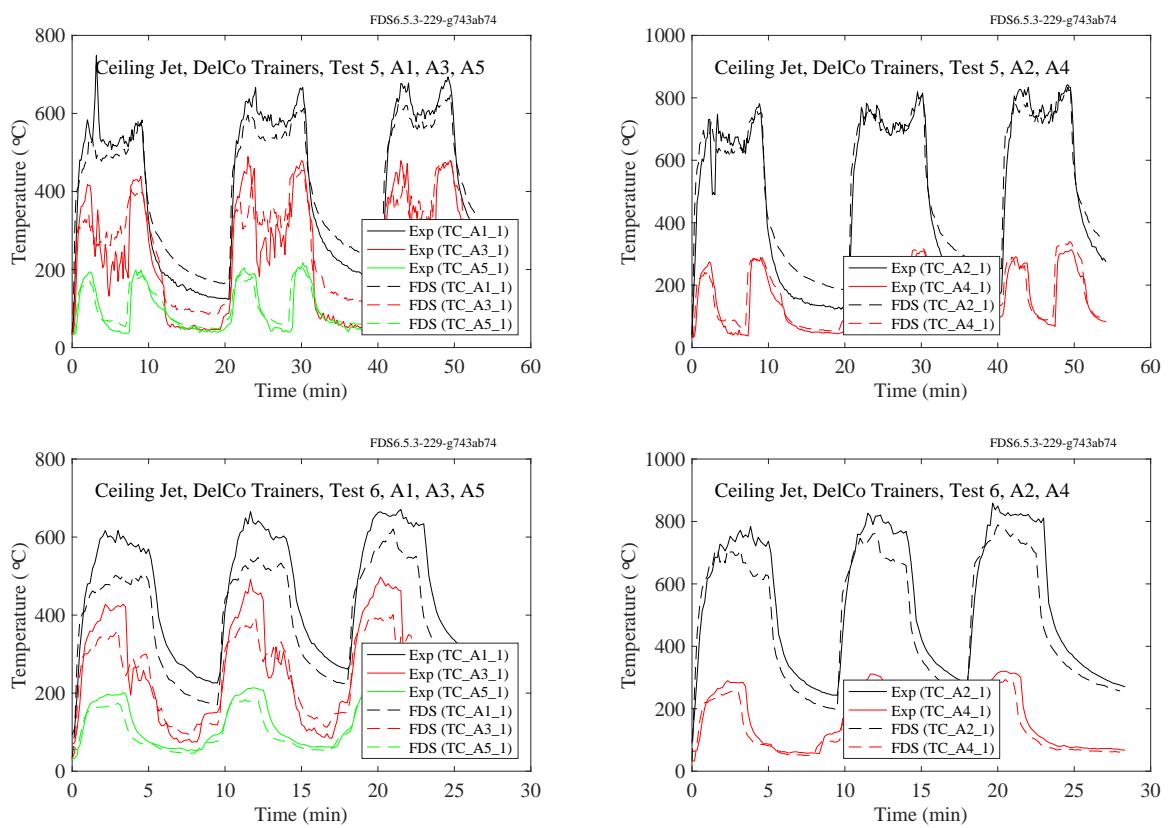


Figure 7.8: DelCo Trainers, ceiling jet temperature, Tests 5 and 6.

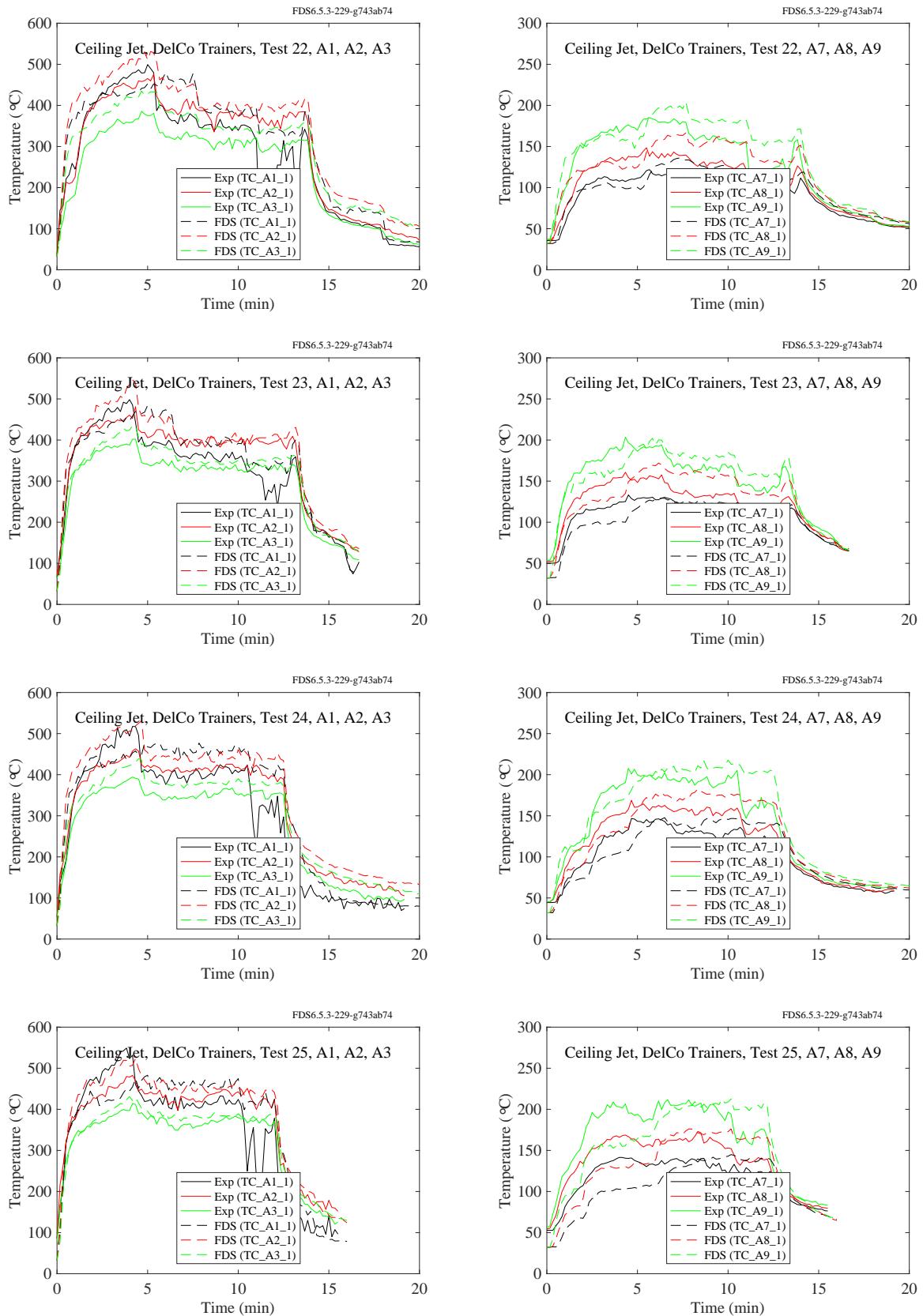


Figure 7.9: DelCo Trainers, ceiling jet temperature, Tests 22-25.

### 7.1.4 FAA Cargo Compartments

Figure 7.10 displays the locations of the near-ceiling thermocouples in the Boeing 707 compartment. The TCs were positioned approximately 4 cm below the ceiling. The small numbered squares indicate the fire locations for Tests 1, 2 and 3.

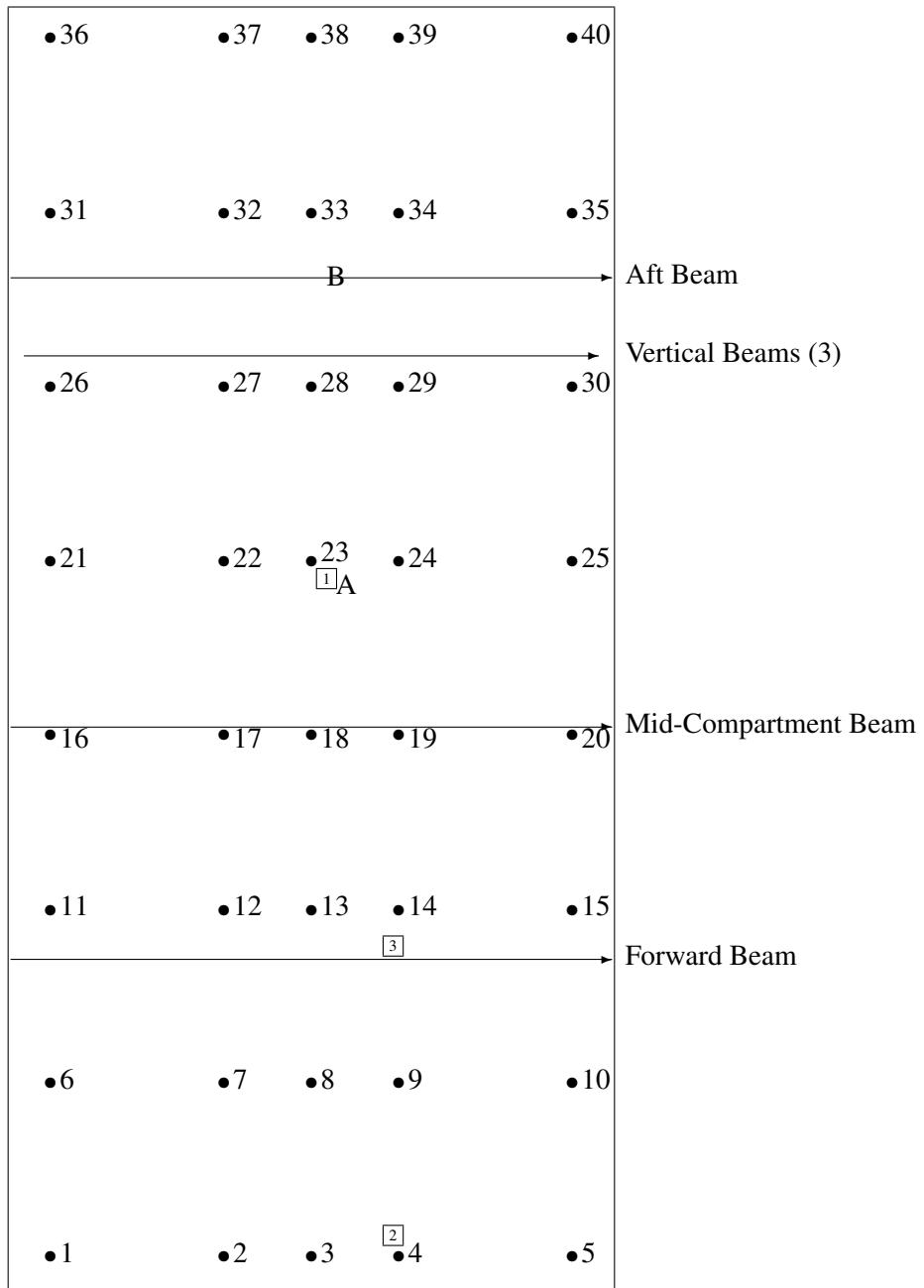


Figure 7.10: Layout of the near-ceiling thermocouples and other instruments, FAA Cargo Compartment Experiments.

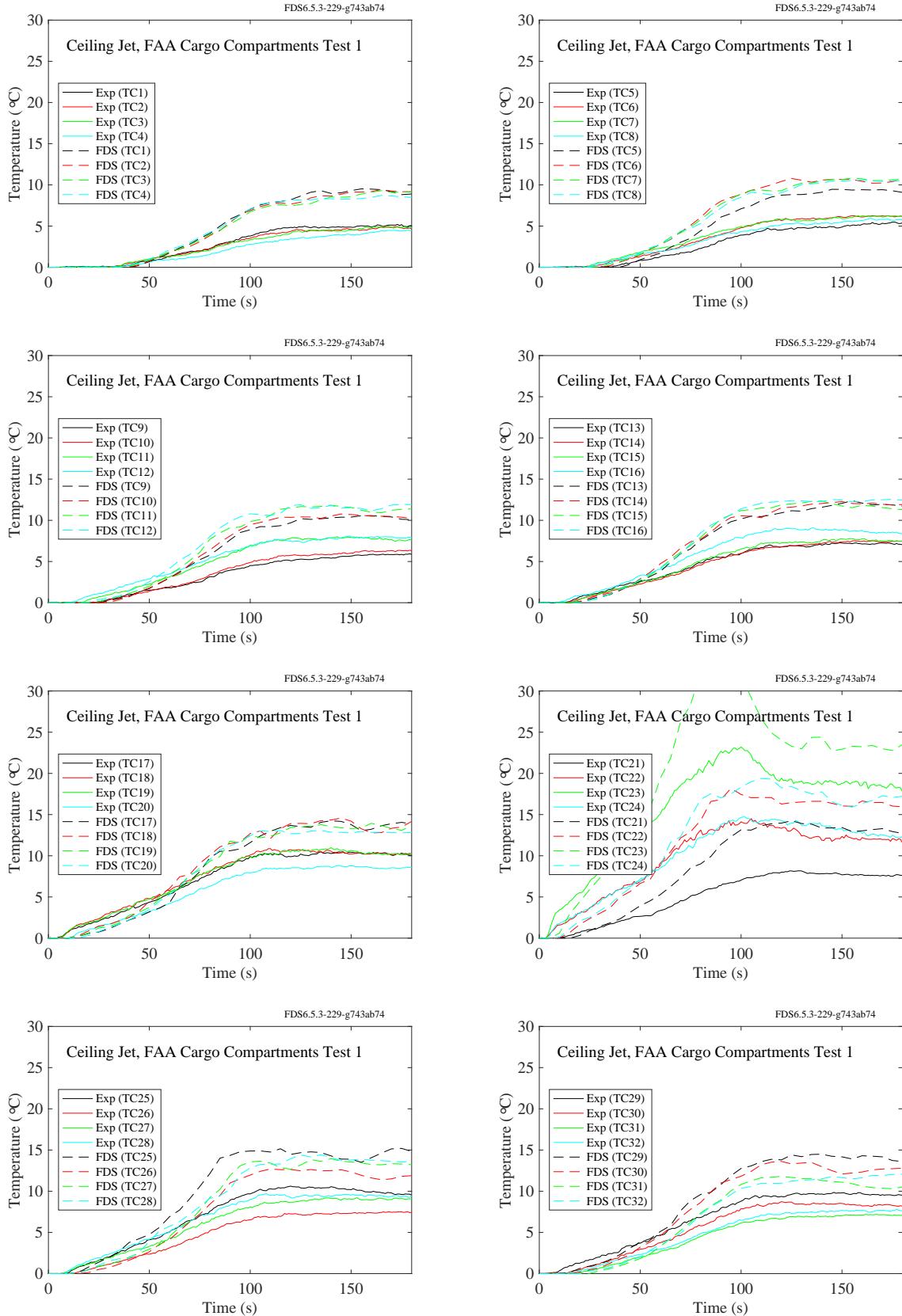


Figure 7.11: FAA Cargo Compartment experiments, ceiling jet, Test 1.

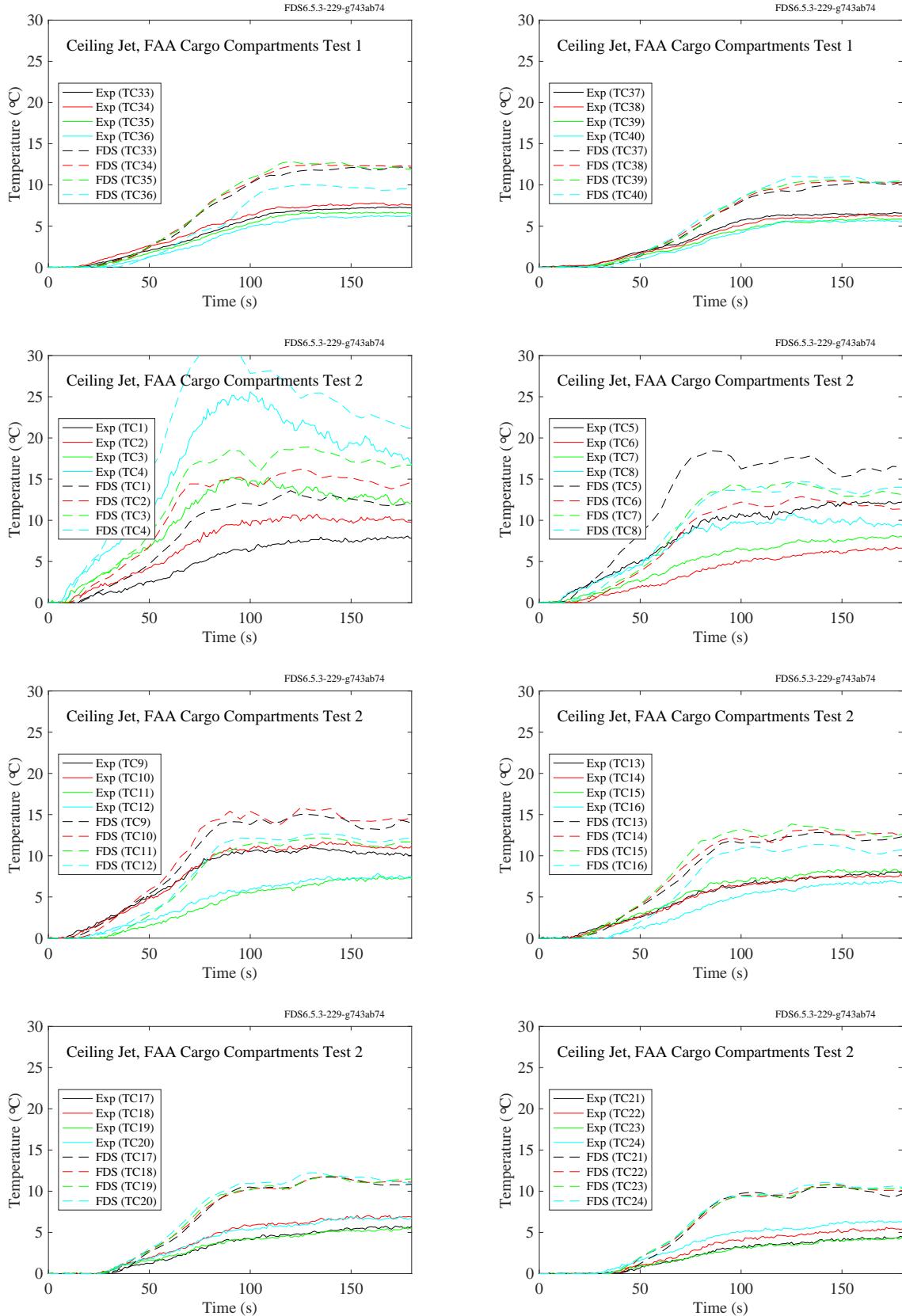


Figure 7.12: FAA Cargo Compartment experiments, ceiling jet, Test 1 and 2.

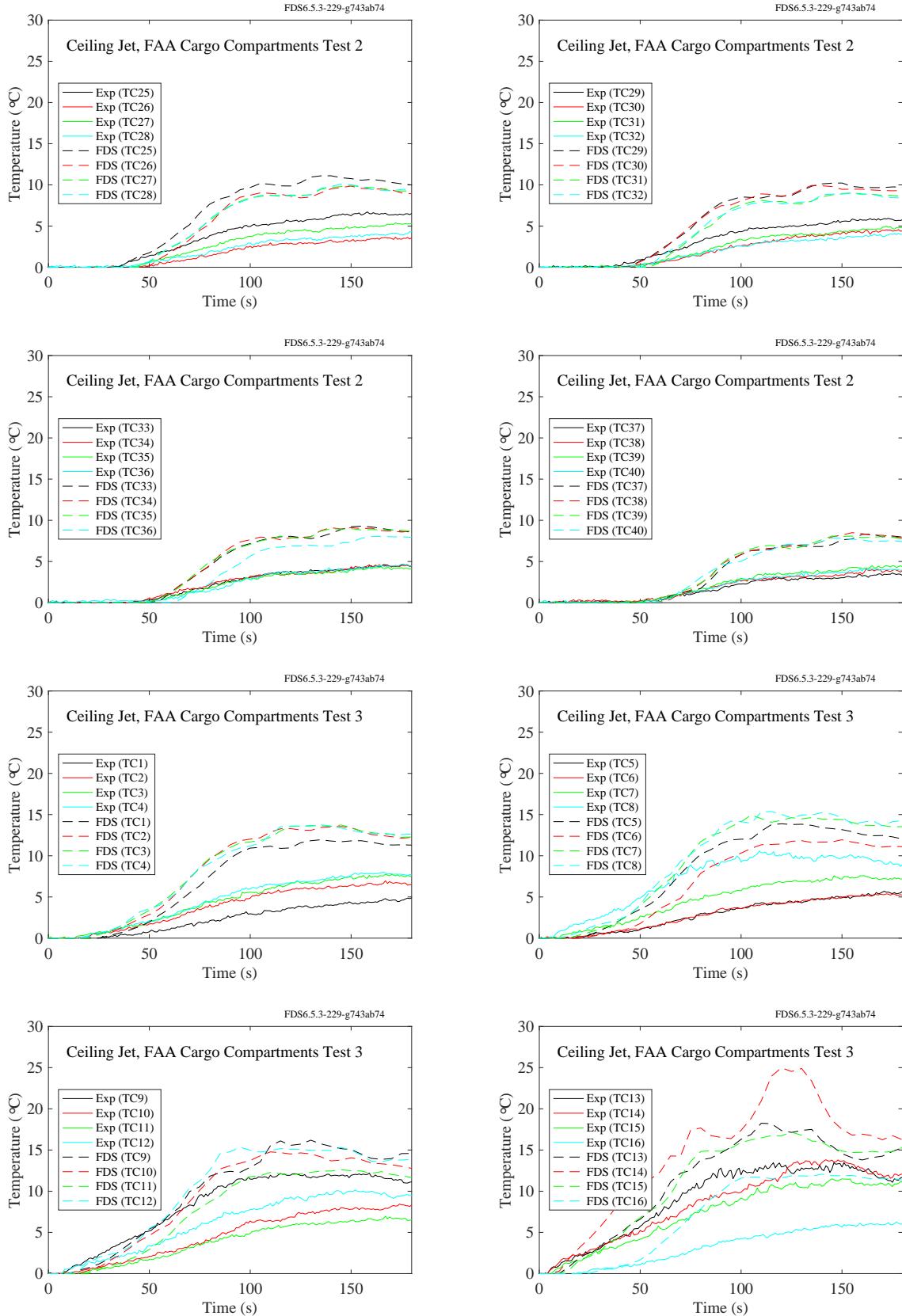


Figure 7.13: FAA Cargo Compartment experiments, ceiling jet, Test 2 and 3.

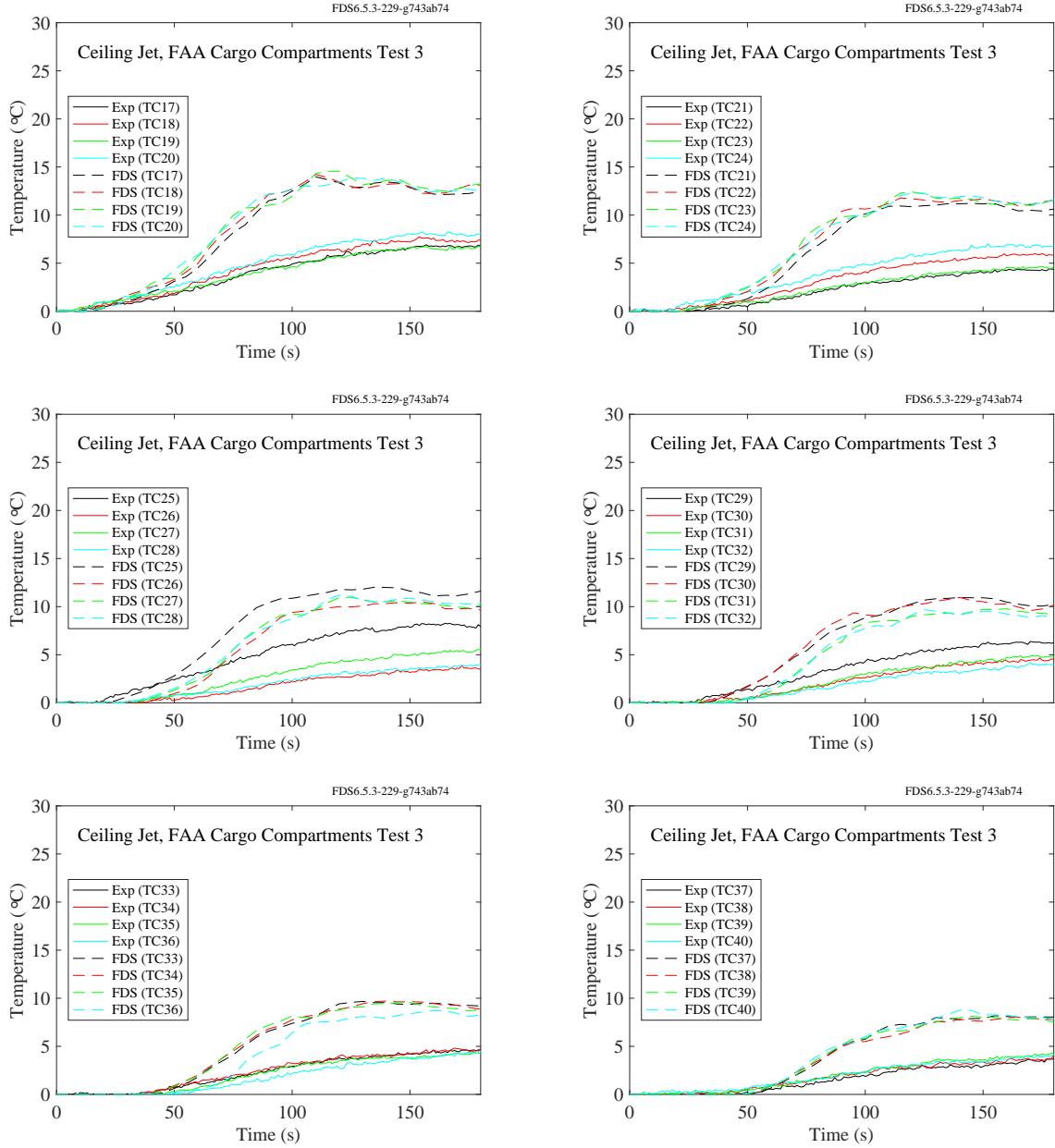


Figure 7.14: FAA Cargo Compartment experiments, ceiling jet, Test 3.

### 7.1.5 FM/SNL Experiments

The near-ceiling thermocouples in Sectors 1 and 3 have been chosen to evaluate the ceiling jet temperature prediction.

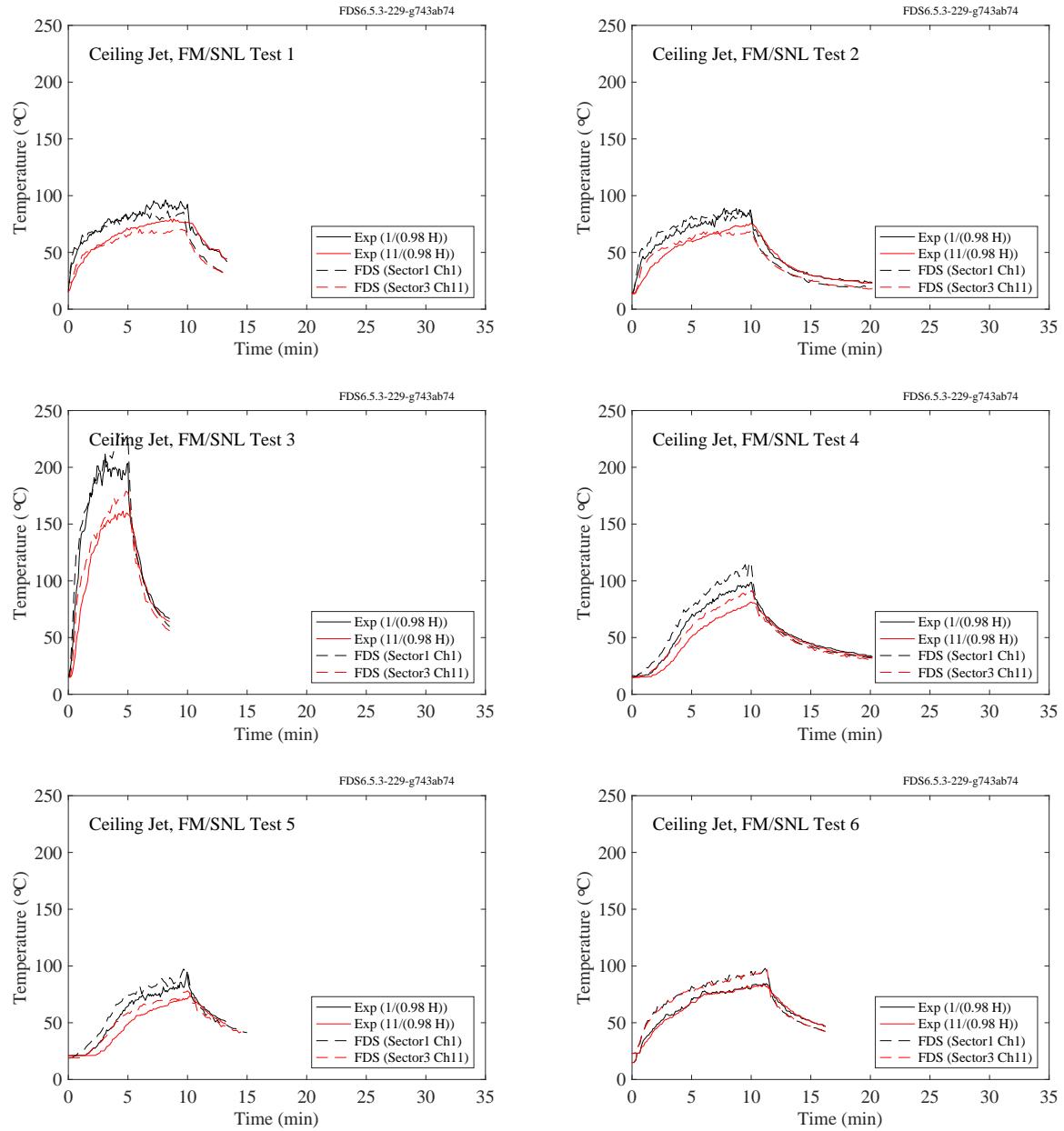


Figure 7.15: FM/SNL experiments, ceiling jet, Tests 1-6.

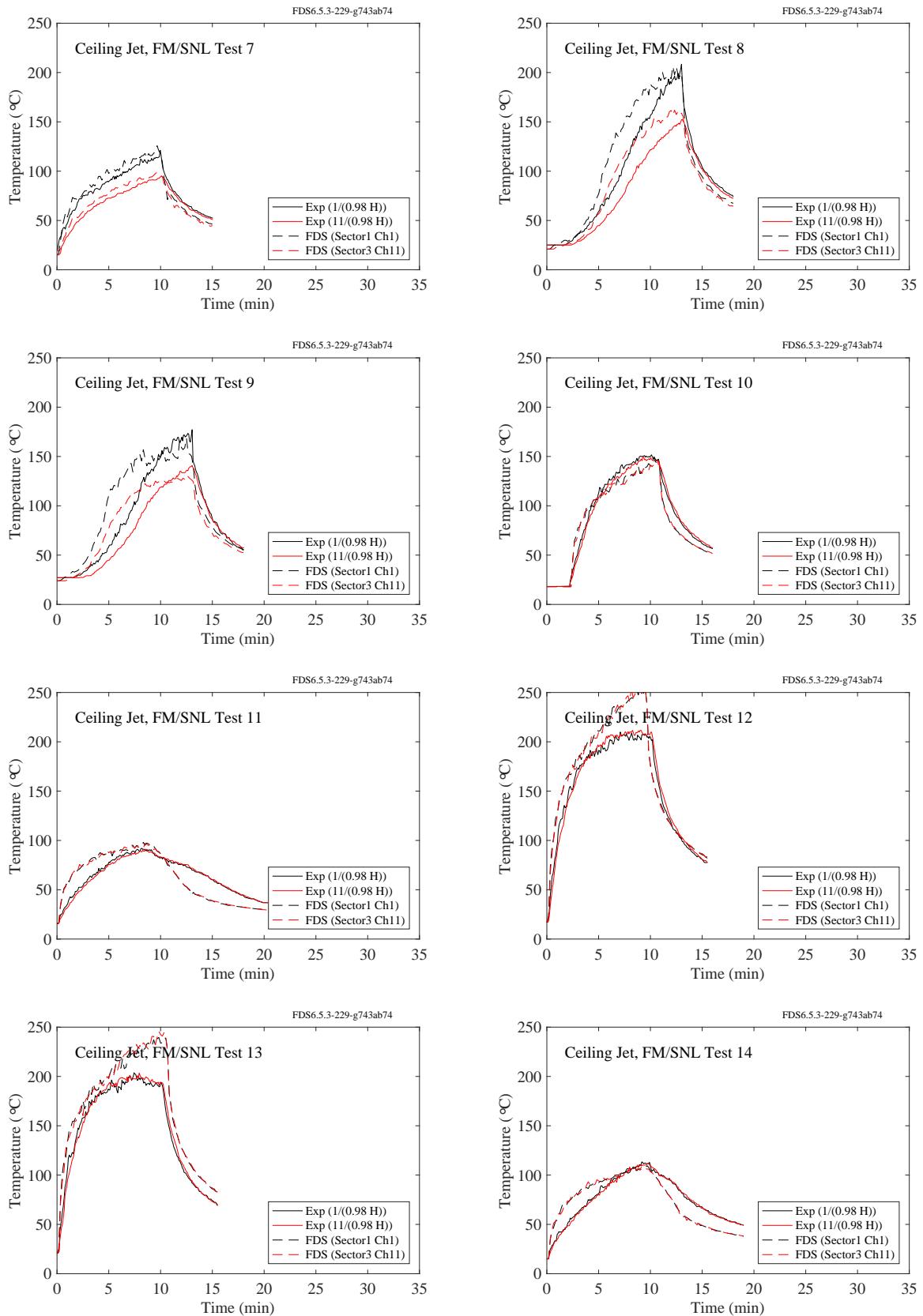


Figure 7.16: FM/SNL experiments, ceiling jet, Tests 7-14.

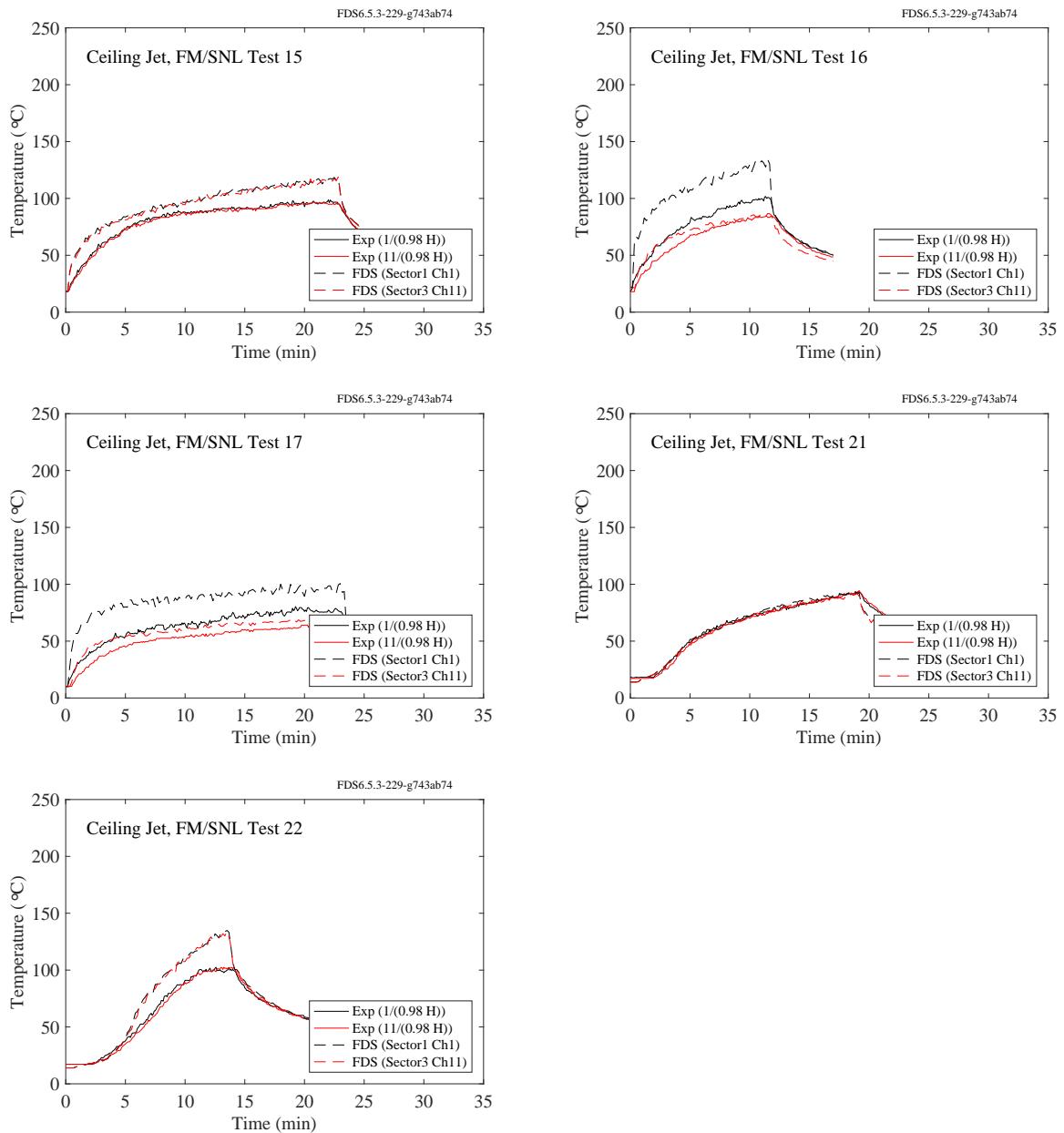


Figure 7.17: FM/SNL experiments, ceiling jet, Tests 15-17, 21-22.

### **7.1.6 NIST Smoke Alarm Experiments**

The primary purpose of the NIST Smoke Alarm Experiments was to measure smoke detector activation times in residential settings. In the single-story manufactured home tests that were selected for validation, five smoke detector measurement stations (Station A through Station E) were located in different areas of the manufactured home. Thermocouple trees were also located at each measurement station. The highest thermocouple in the tree can be compared to ceiling jet temperature predictions. The plots on the following page show the measured and predicted ceiling jet temperatures for the five measurement stations in each test.

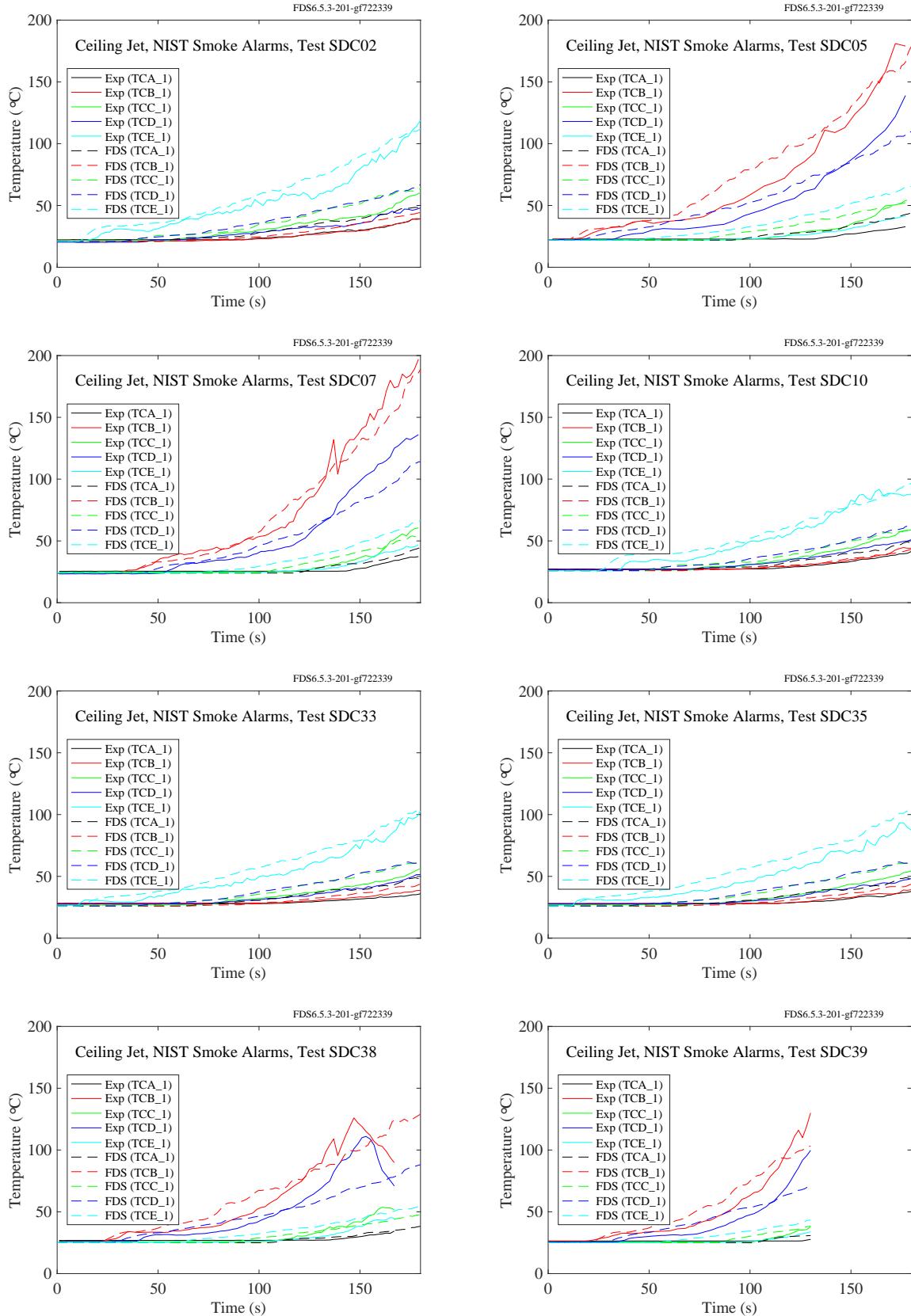


Figure 7.18: NIST Smoke Alarm experiments, ceiling jet.

### **7.1.7 NIST/NRC Experiments**

In the NIST/NRC experiments, seven vertical arrays of thermocouples were positioned throughout the compartment. The thermocouple nearest the ceiling in Tree 7, located towards the back of the compartment away from the door, has been chosen to evaluate the ceiling jet temperature prediction.

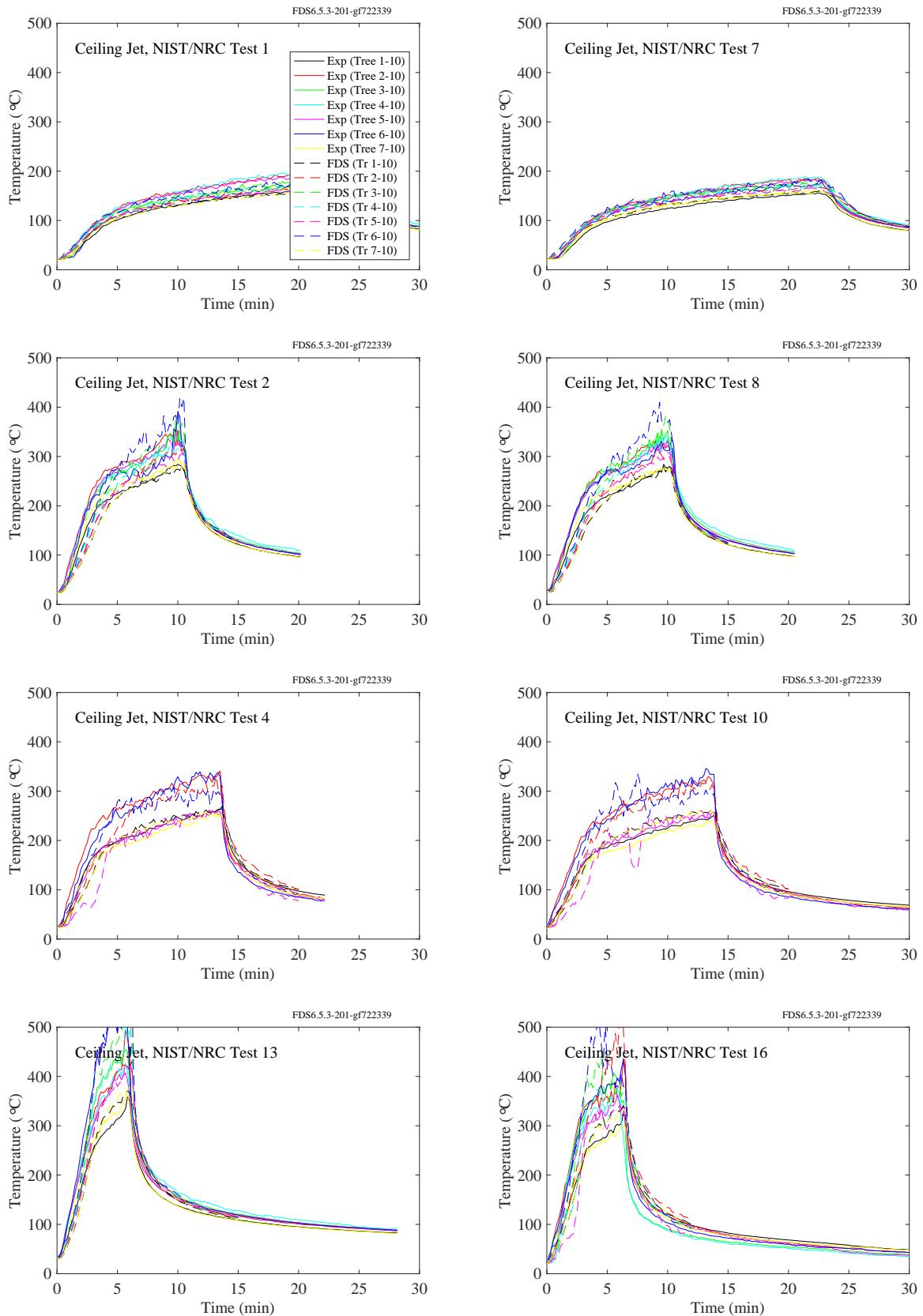


Figure 7.19: NIST/NRC experiments, ceiling jet, Tests 1, 2, 4, 7, 8, 10, 13, 16.

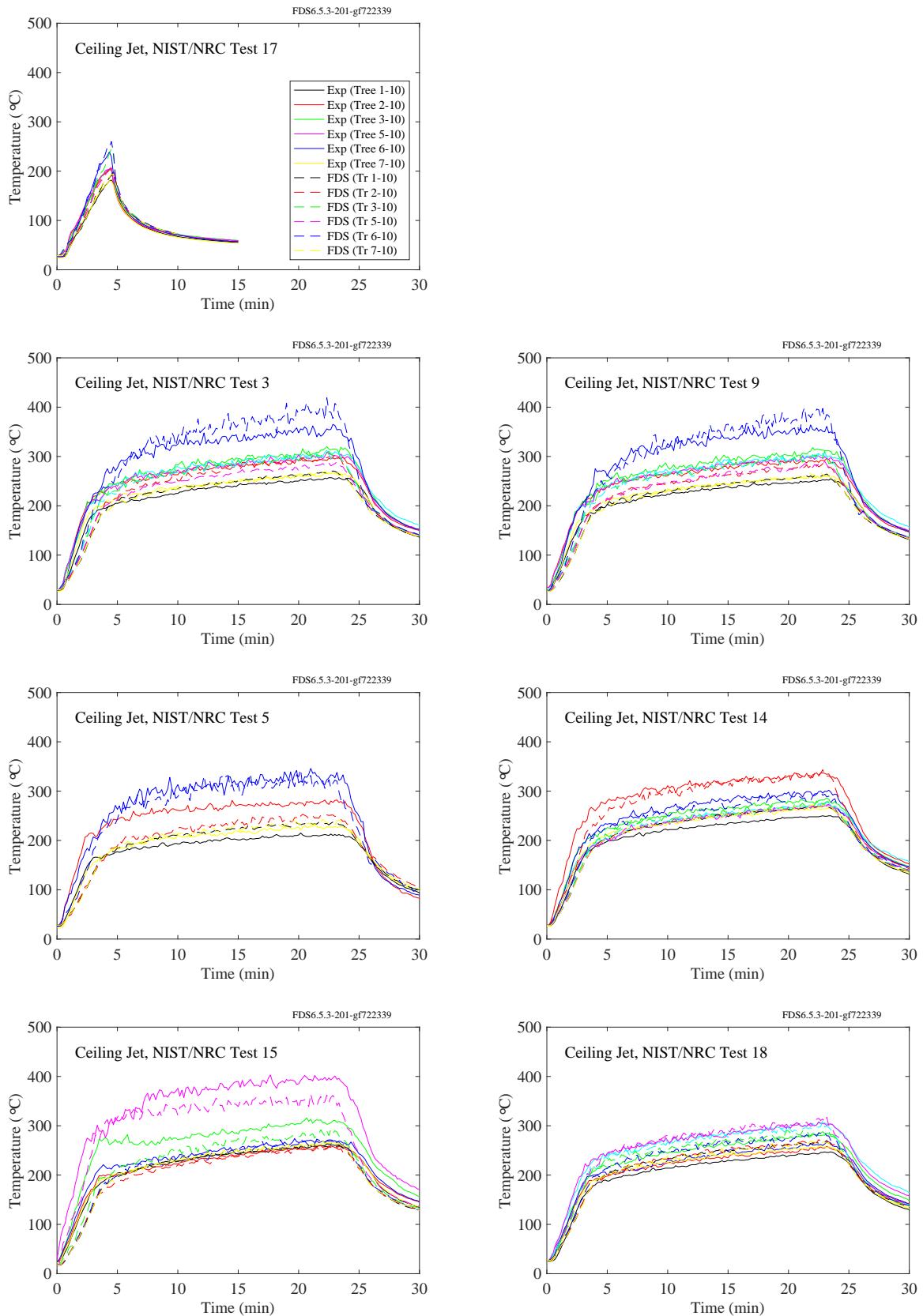


Figure 7.20: NIST/NRC experiments, ceiling jet, Tests 3, 5, 9, 14, 15, 17, 18.

### 7.1.8 NRCC Smoke Tower

In the NRCC Smoke Tower experiments, there was a vertical array of 13 TCs and a single near-ceiling TC on the opposite side of the fire compartment. Shown in Fig. 7.21 are the predicted and measured temperatures of the single TC and the uppermost TC of the vertical array in the fire compartment. Shown in Fig. 7.22 are predictions of gas temperature measurements made in the stair vestibule of floors 4, 6, 8, and 10, along with inner compartment temperature measurements made on floors 4, 8, and 10. Note that the plot labels “Slot” refer to the data acquisition system in the experiments only and have no meaning in the present context. It should be clear from the plot title how the various curves ought to be interpreted.

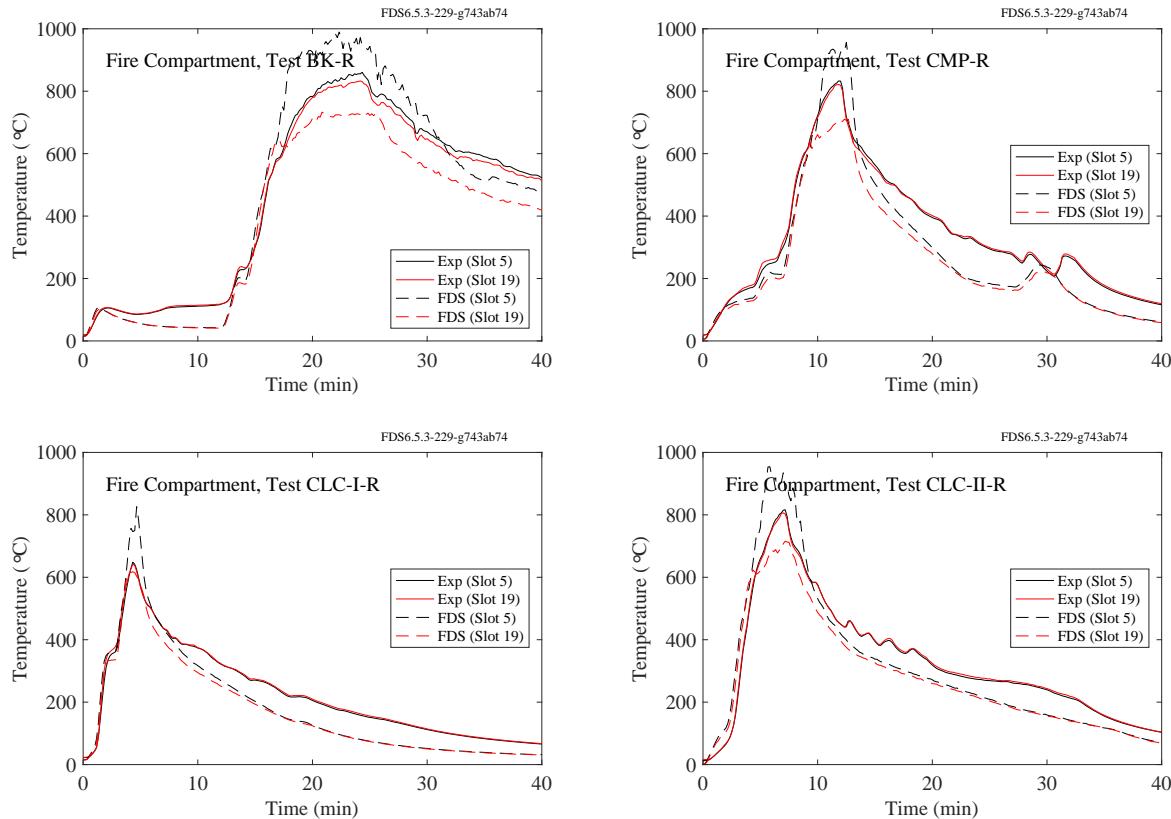


Figure 7.21: NRCC Smoke Tower experiments, ceiling jet.

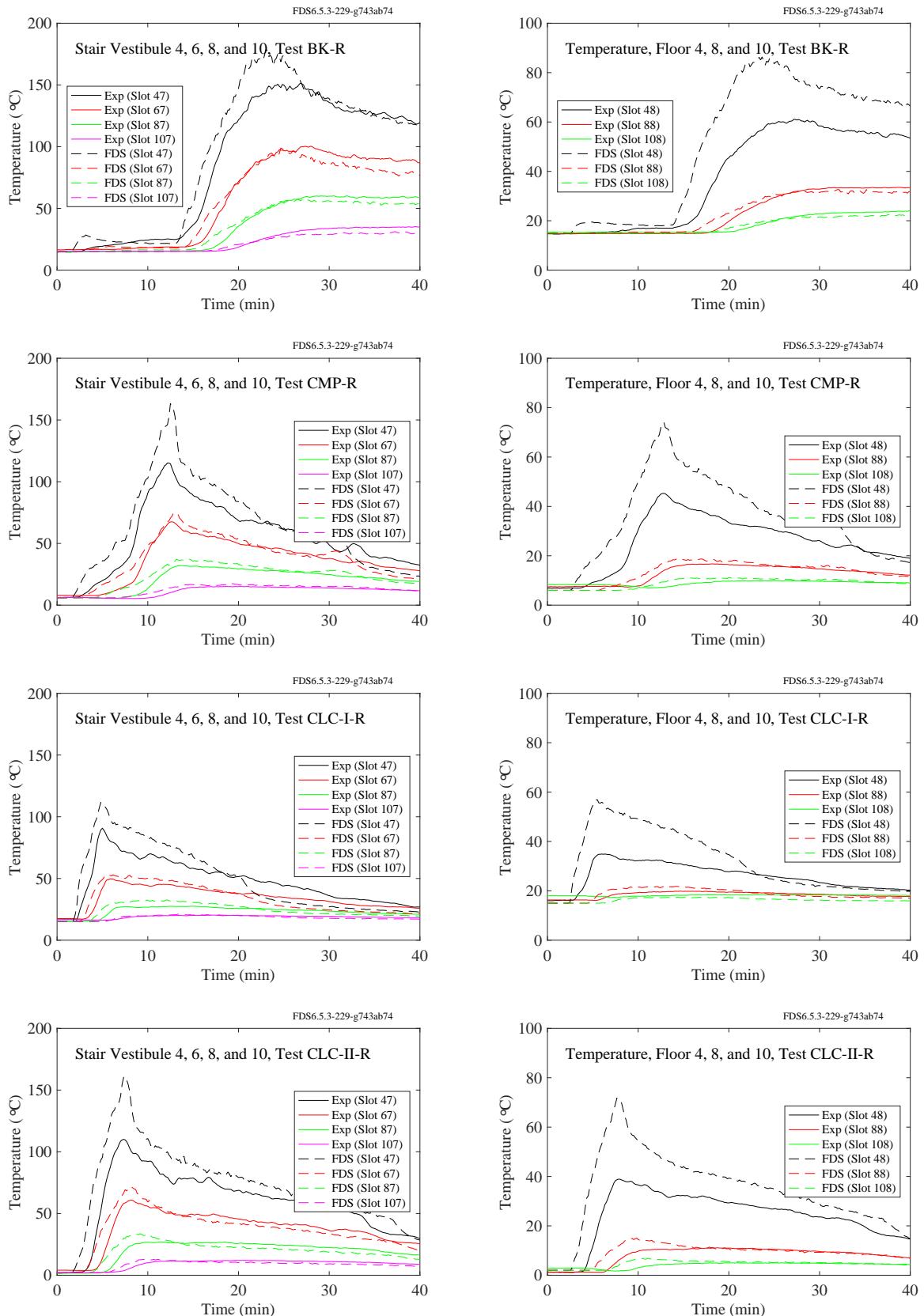


Figure 7.22: NRCC Smoke Tower, upper floor temperatures.

### 7.1.9 PRISME DOOR Experiments

In the PRISME DOOR experiments, the uppermost TC in the vertical arrays were used to measure the ceiling jet temperature. These TCs were approximately 10 cm below the ceiling.

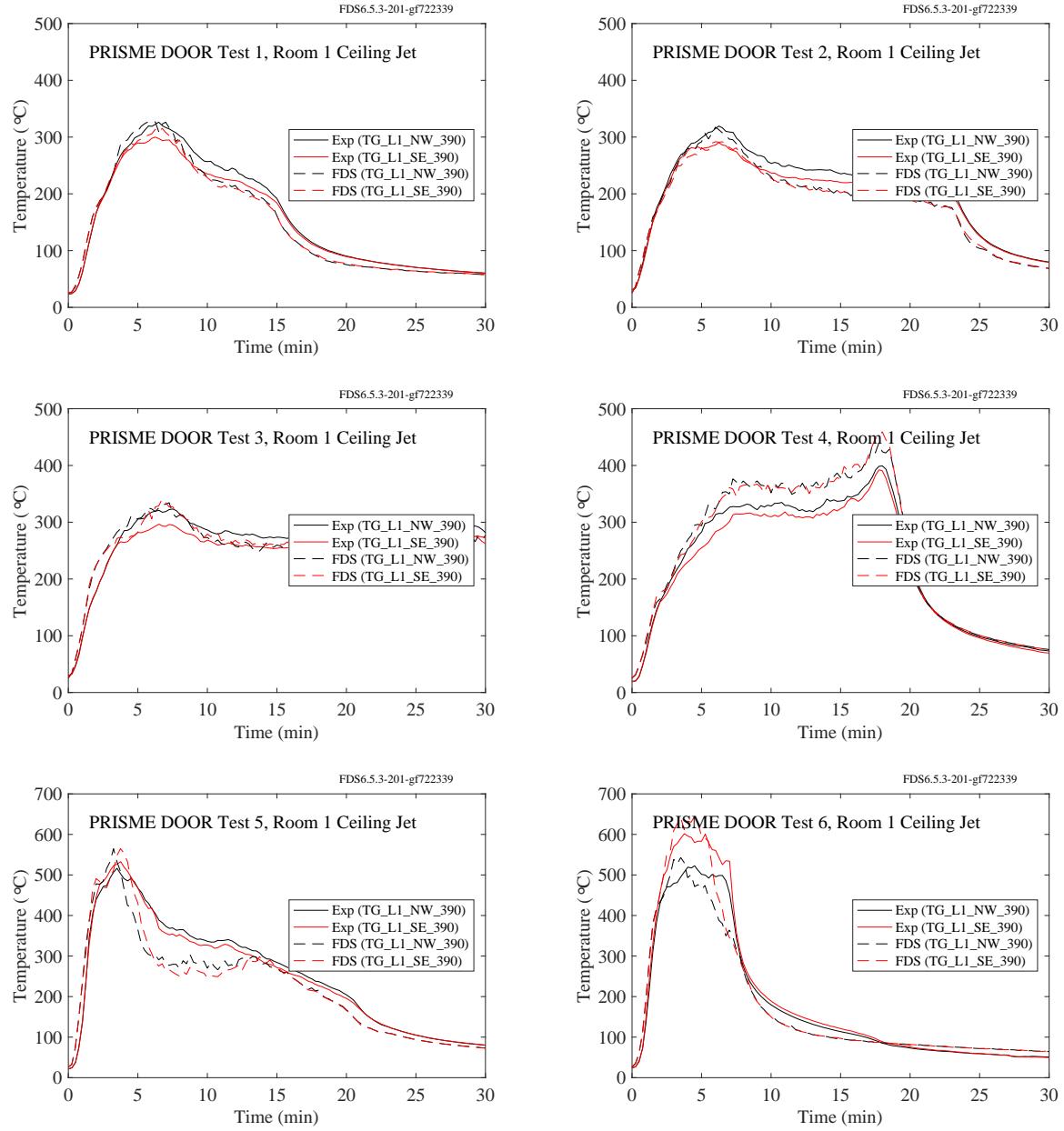


Figure 7.23: PRISME DOOR experiments, ceiling jet, Room 1.

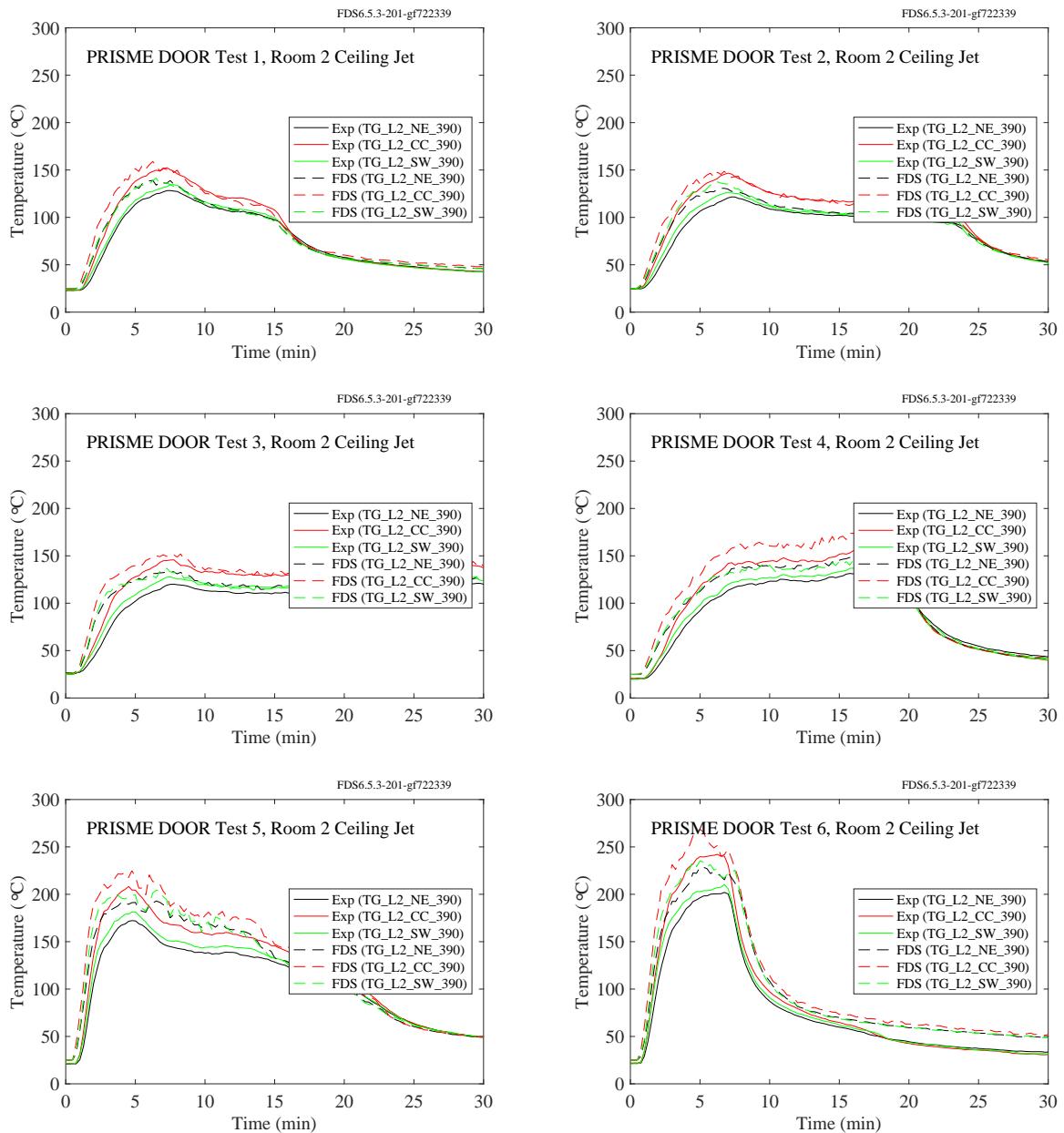


Figure 7.24: PRISME DOOR experiments, ceiling jet, Room 2.

### **7.1.10 PRISME SOURCE Experiments**

In the PRISME SOURCE experiments, the uppermost TC in the vertical array was used to measure the ceiling jet temperature. The thermocouple array was located in the northeast corner of the room. This TC was approximately 10 cm below the ceiling.

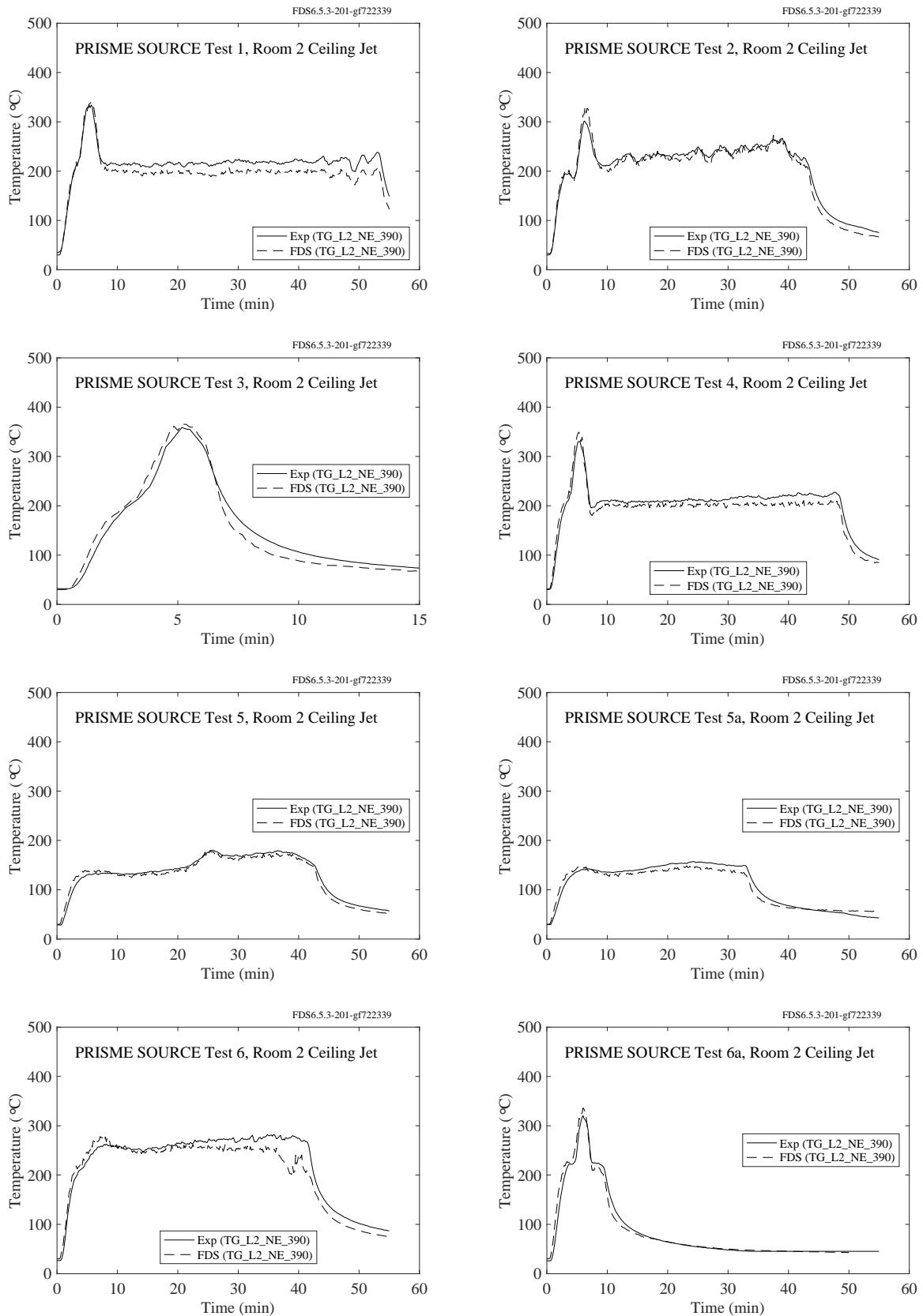


Figure 7.25: PRISME SOURCE experiments, ceiling jet, Room 2.

### 7.1.11 SP Adiabatic Surface Temperature Experiments

Three experiments were conducted in a standard compartment, 3.6 m long by 2.4 m wide by 2.4 m high, with a 0.8 m wide by 2.0 m high door centered on the narrow wall. A single beam was suspended 20 cm below the ceiling lengthwise along the centerline of the compartment. There were three measurement stations along the beam at distances of 0.9 m (Station A), 1.8 m (Station B), and 2.7 m (Station C) from the far wall where the fire was either positioned in the corner (Tests 1 and 2), or the center (Test 3). The gas temperatures reported here were measured 10 cm away from all four sides of the beam at Station A, and 10 cm away from the two lateral sides at Stations B and C. In the figure legends, the measurement station is denoted A, B, or C, and the position is denoted 1, 2, 3, or 4. Position 1 is 10 cm above the beam. Position 2 is 10 cm from the side of the beam facing away from the fire, Position 3 is 10 cm below the beam, and Position 4 is 10 cm away from the side of the beam facing the fire.

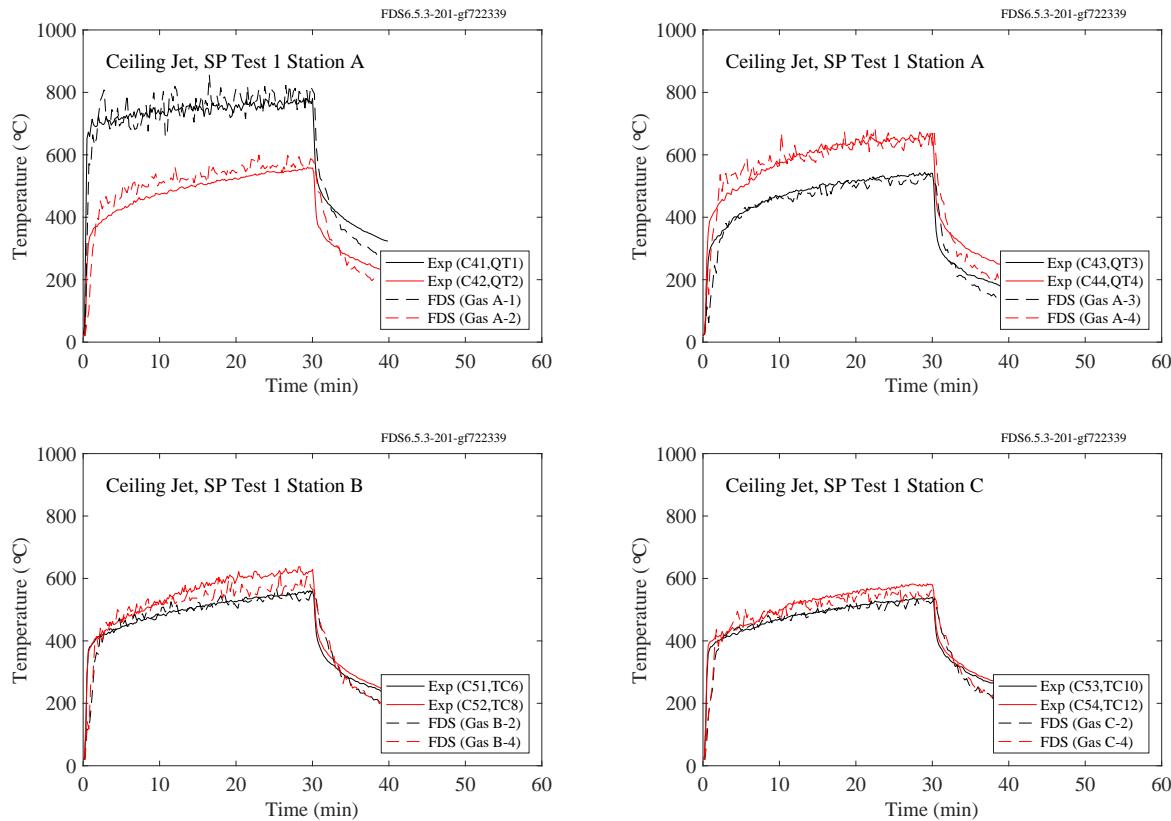


Figure 7.26: SP AST experiments, ceiling jet, Test 1.

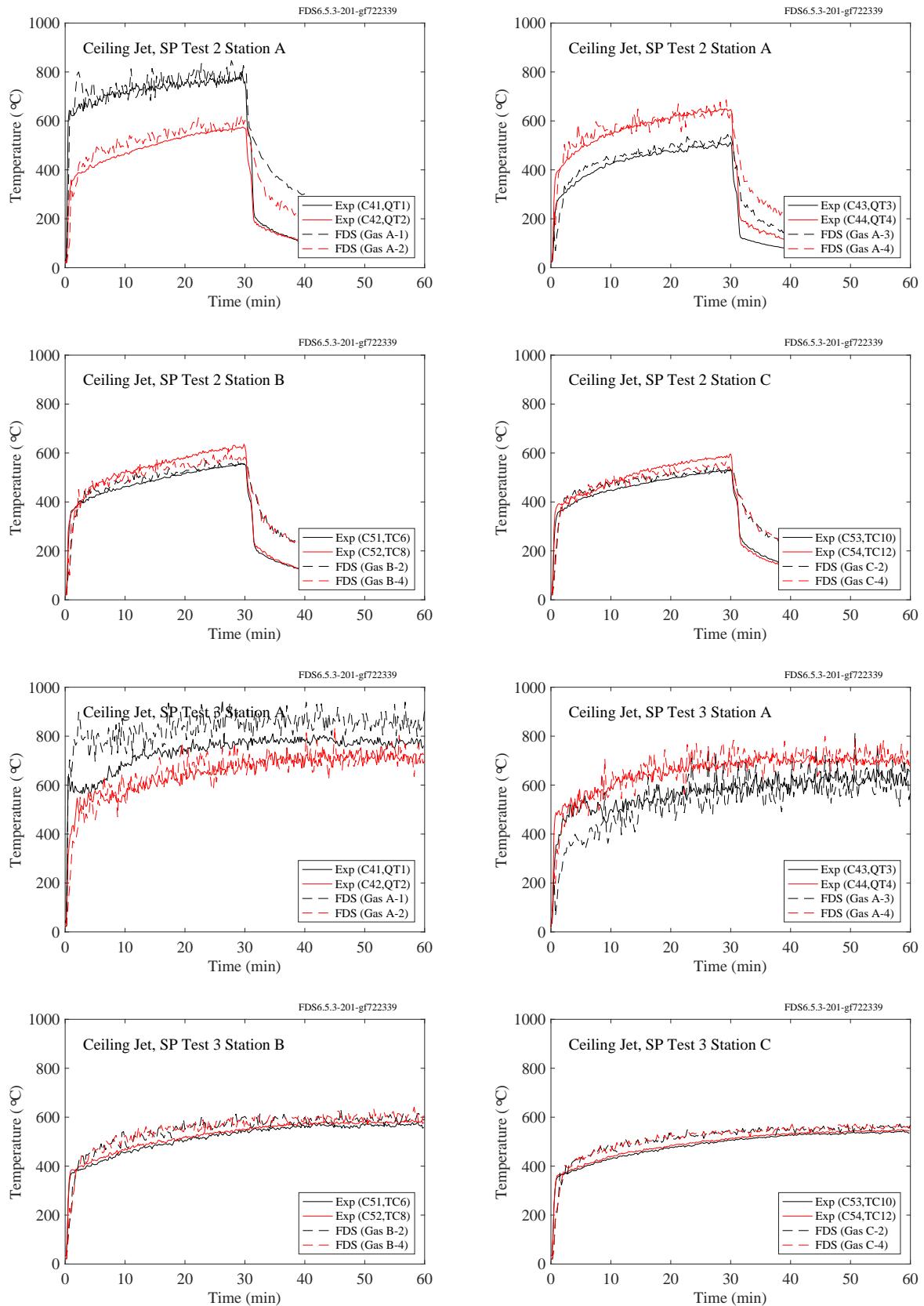


Figure 7.27: SP AST experiments, ceiling jet, Tests 2 and 3.

### 7.1.12 UL/NFPRF Series I Experiments

The primary purpose of the UL/NFPRF experiments was to measure sprinkler activation times for a series of heptane spray burner fires. To determine activation times, thermocouples were affixed to each sprinkler, and a sudden drop in temperature indicated activation. These same thermocouple temperatures can be compared to ceiling jet temperature predictions. Referring to Fig. 3.20, the chosen measurement locations are 56, 68, 86, and 98, providing comparisons as close to, and as far away from, the fire as possible.

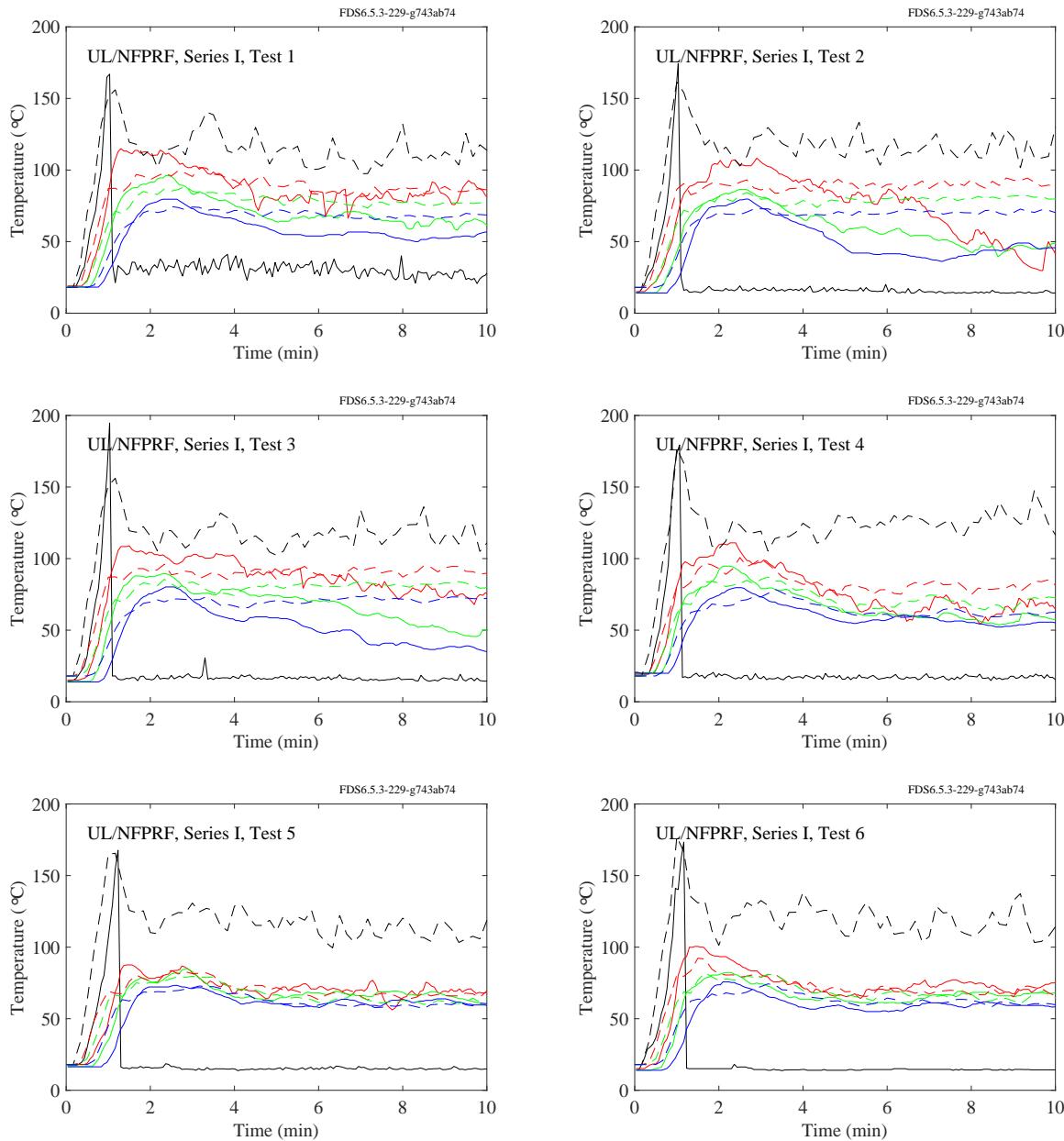


Figure 7.28: UL/NFPPRF experiments, ceiling jet, Series I, Tests 1-6.

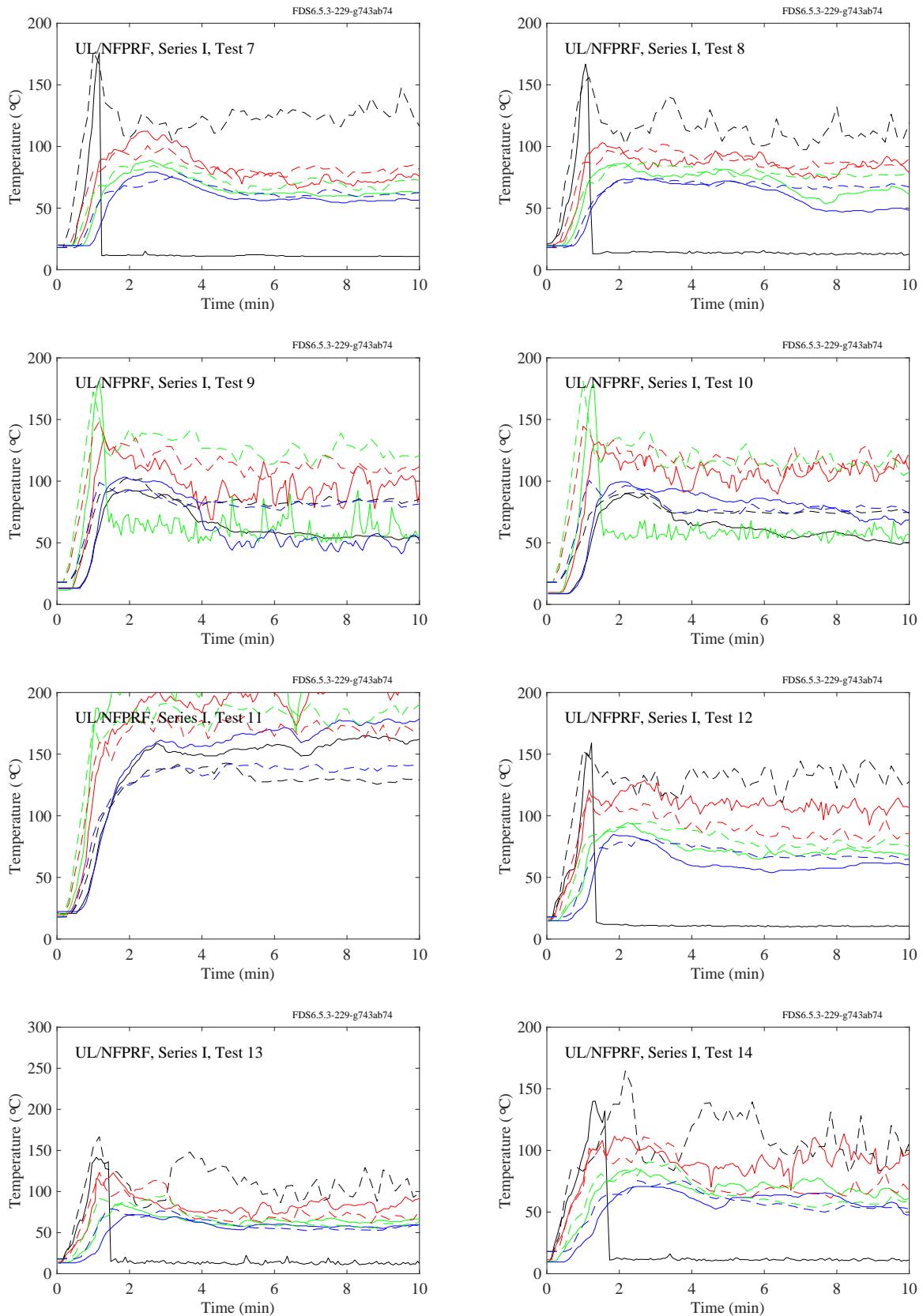


Figure 7.29: UL/NFPPRF experiments, ceiling jet, Series I, Tests 7-14.

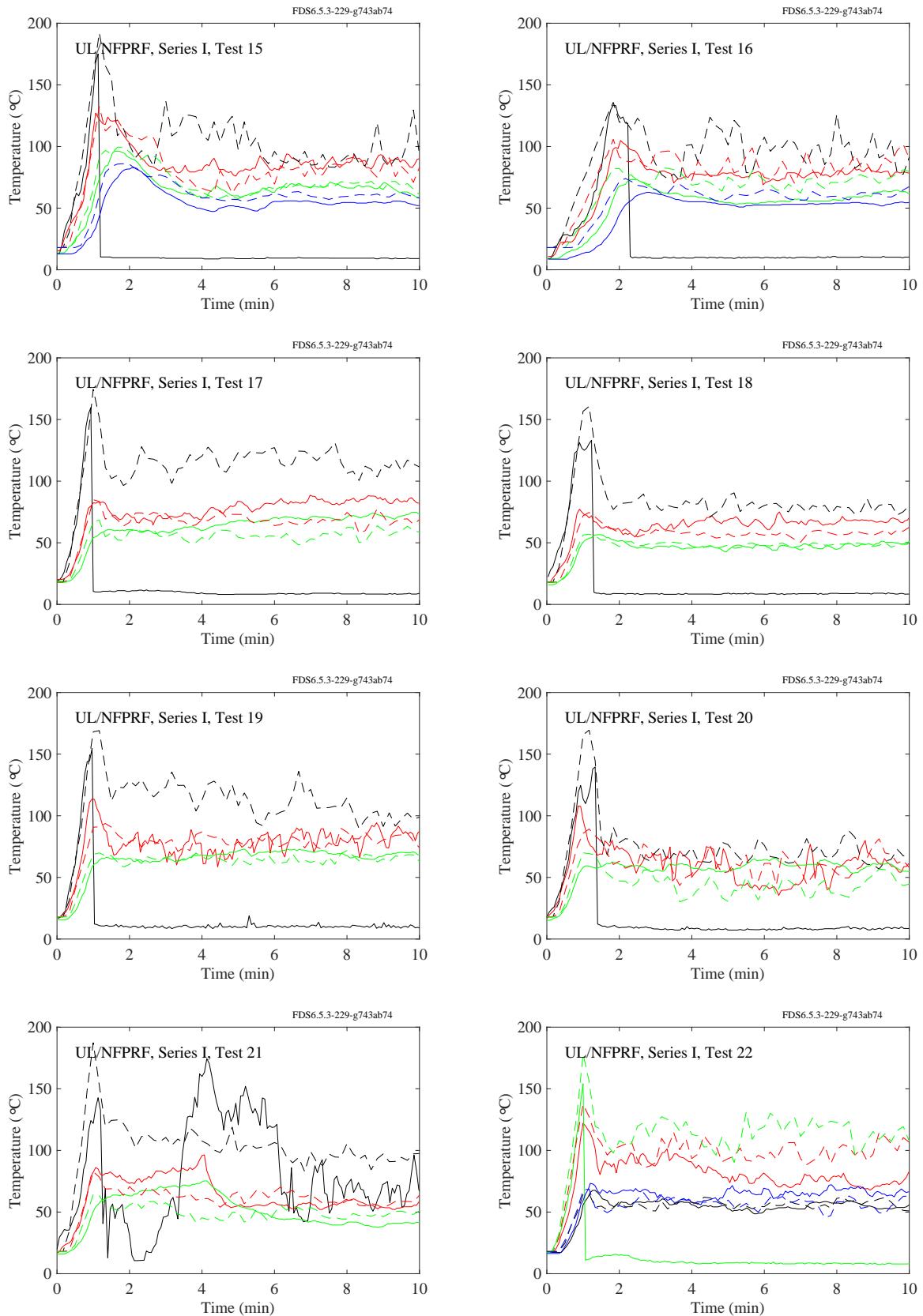


Figure 7.30: UL/NFPPRF experiments, ceiling jet, Series I, Tests 15-22.

### **7.1.13 UL/NIST Vent Experiments**

The ceiling jet temperatures were measured at two locations, 90 cm from the short ends of the 2.4 m by 1.2 m double vent.

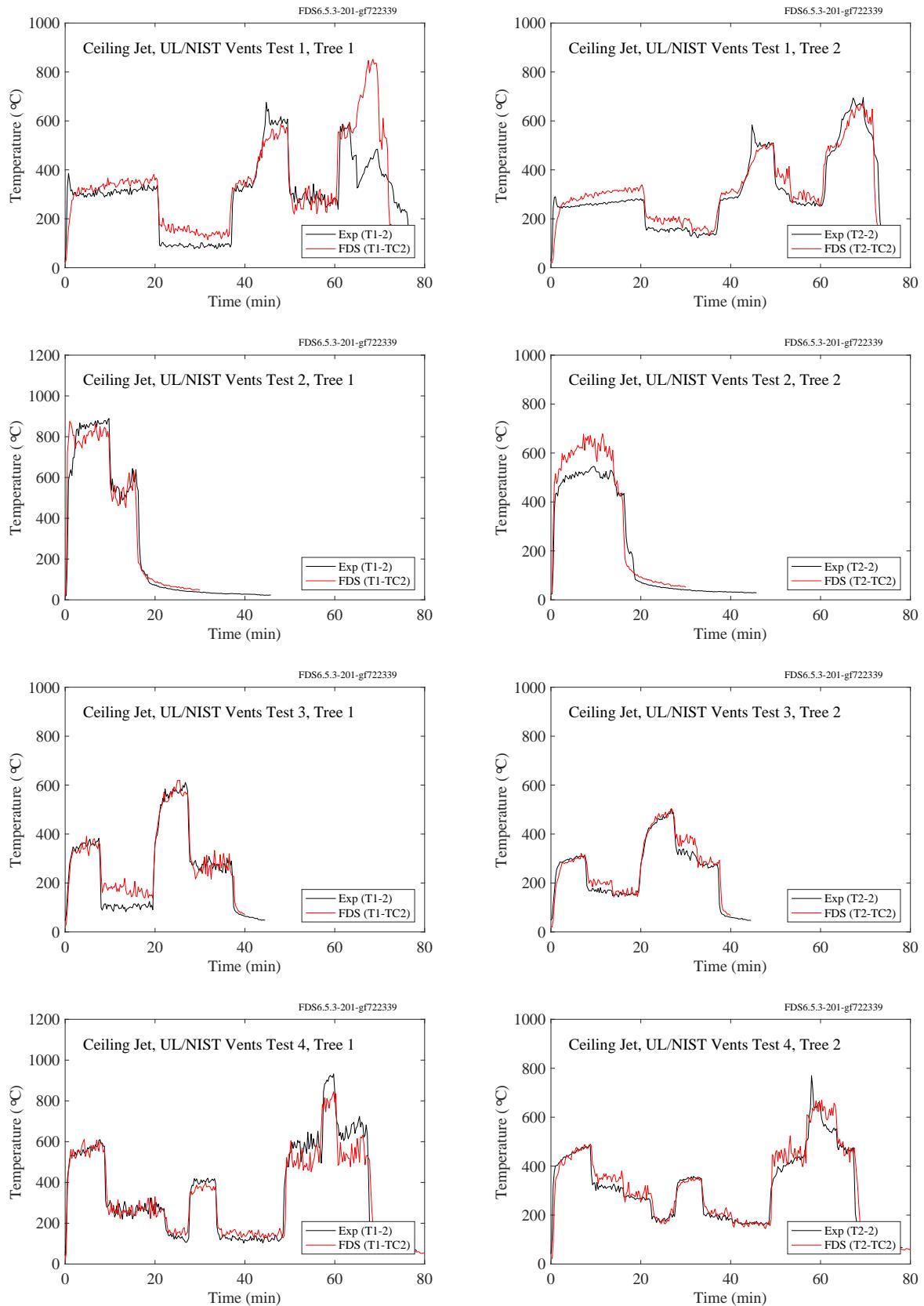


Figure 7.31: UL/NIST Vents experiments, ceiling jet.

### **7.1.14 Vettori Flat Ceiling Experiments**

For these experiments, the measured and predicted thermocouple temperature at the location of the first two activating sprinklers are compared. The experiments consisted of either Smooth or Obstructed ceilings; Slow, Medium or Fast fires; and a burner in the Open, at the Wall, or in the Corner. The experiments included three replicates of each of the smooth ceiling configurations and two replicates of each of the obstructed ceiling configurations.

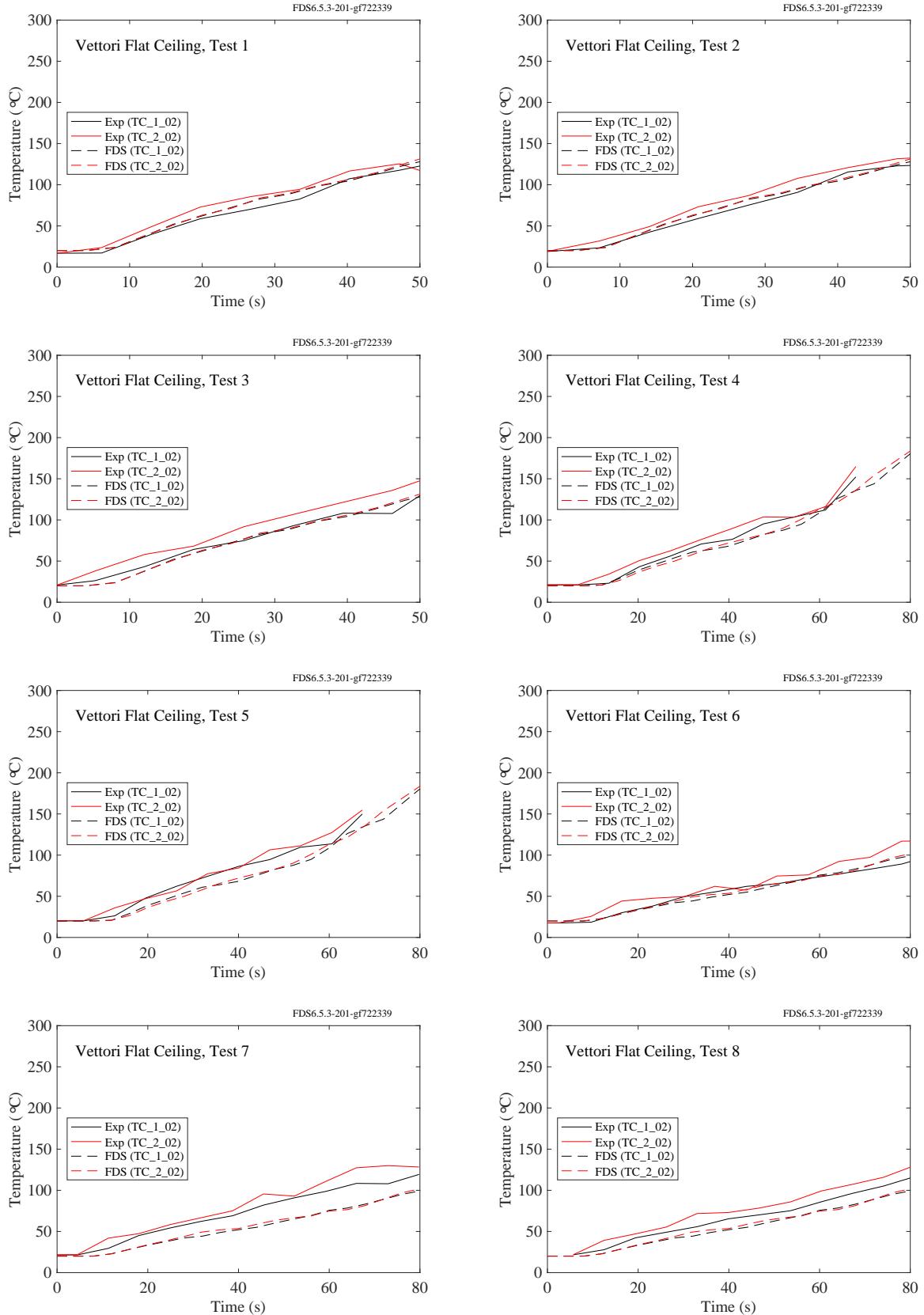


Figure 7.32: Vettori Flat Ceiling experiments, ceiling jet, Tests 1-8.

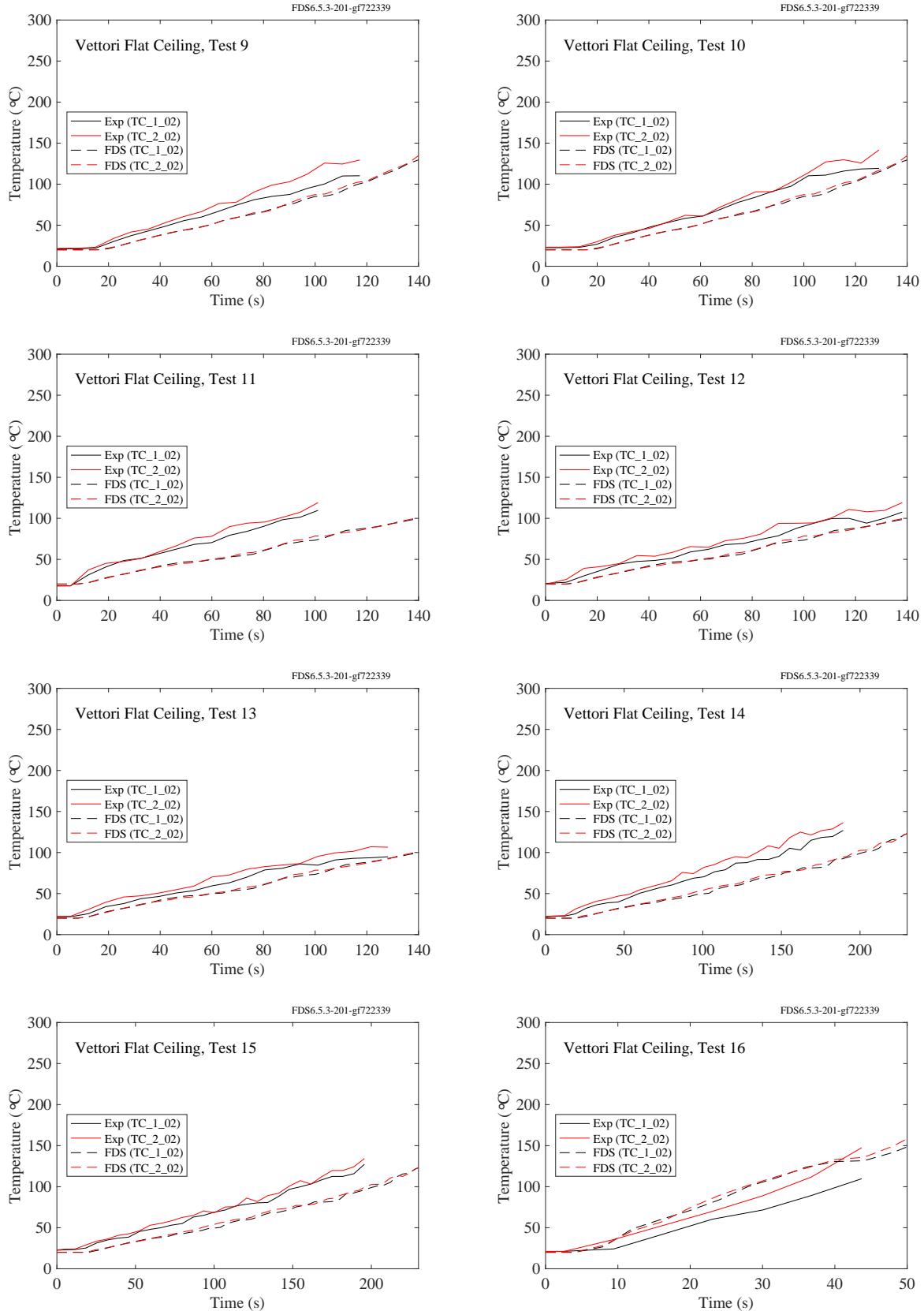


Figure 7.33: Vettori Flat Ceiling experiments, ceiling jet, Tests 9-16.

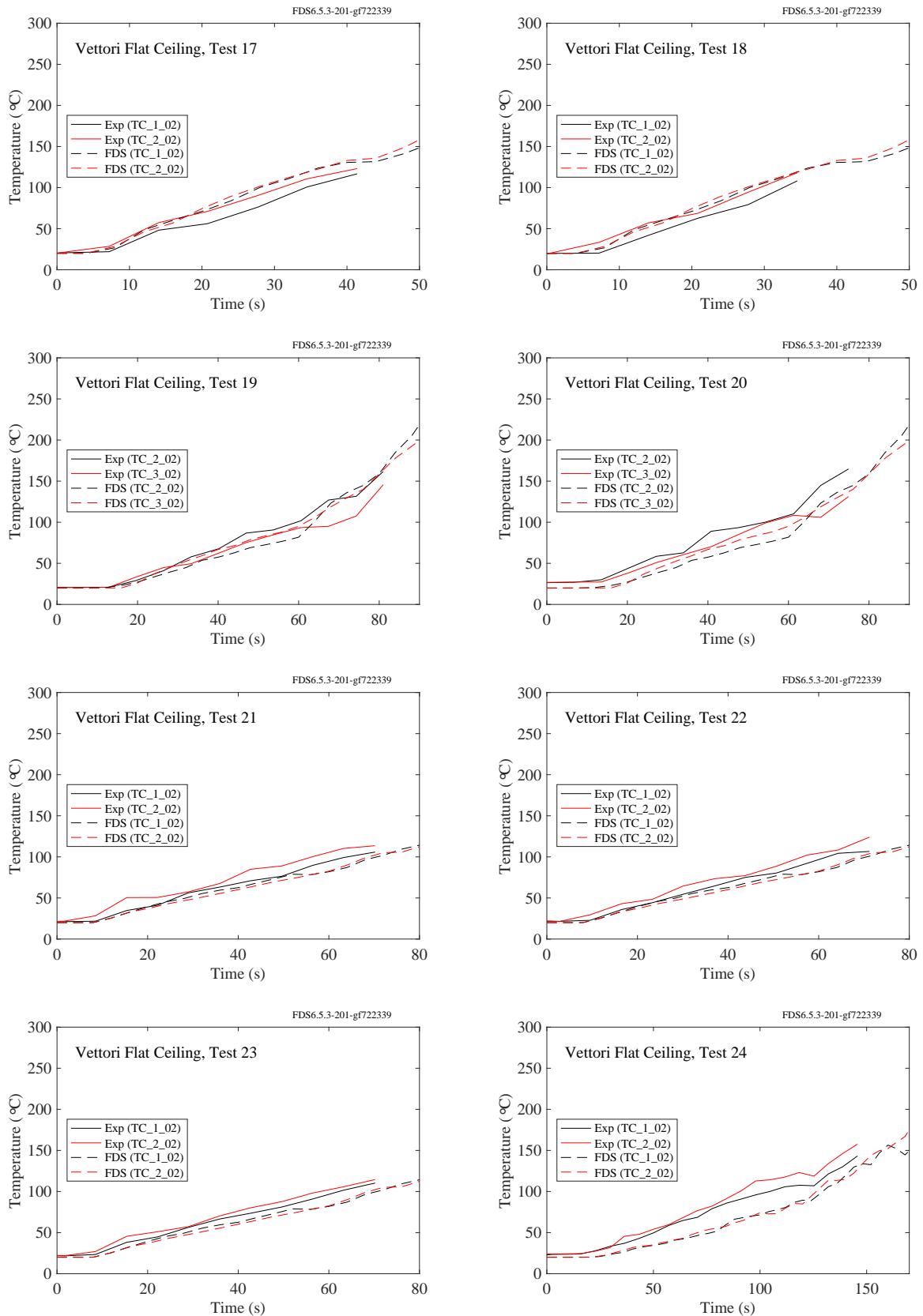


Figure 7.34: Vettori Flat Ceiling experiments, ceiling jet, Tests 17-24.

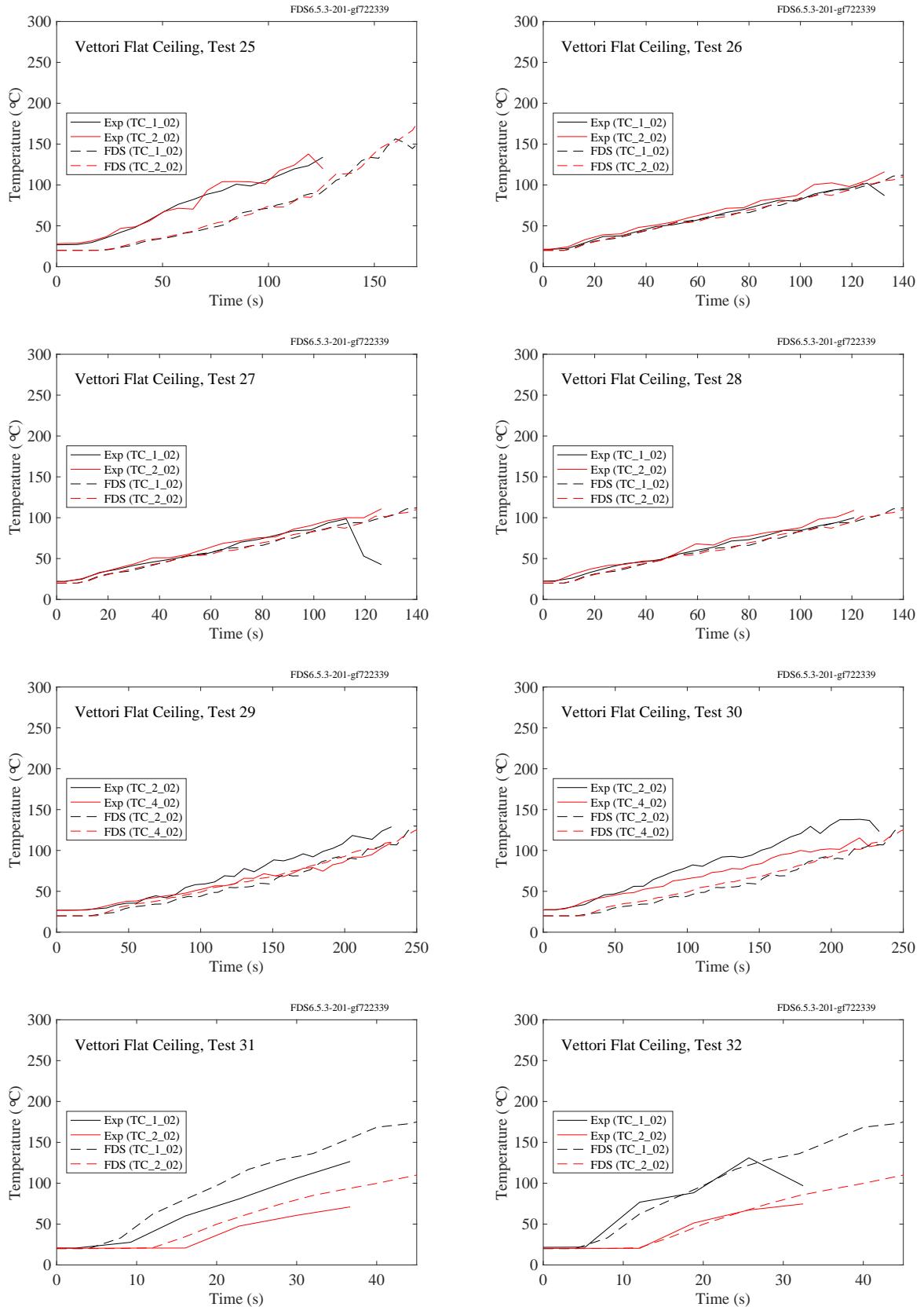


Figure 7.35: Vettori Flat Ceiling experiments, ceiling jet, Tests 25-32.

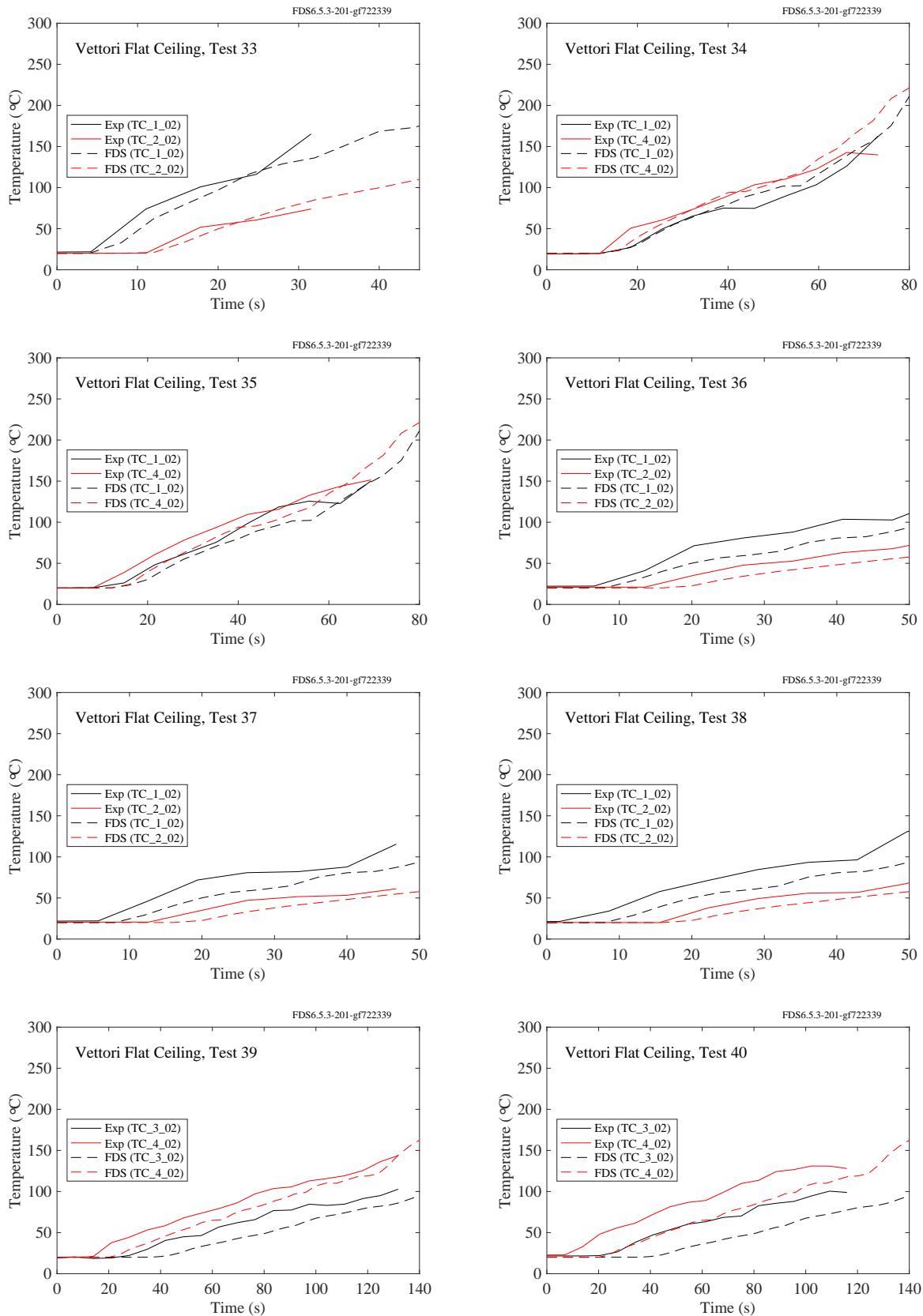


Figure 7.36: Vettori Flat Ceiling experiments, ceiling jet, Tests 33-40.

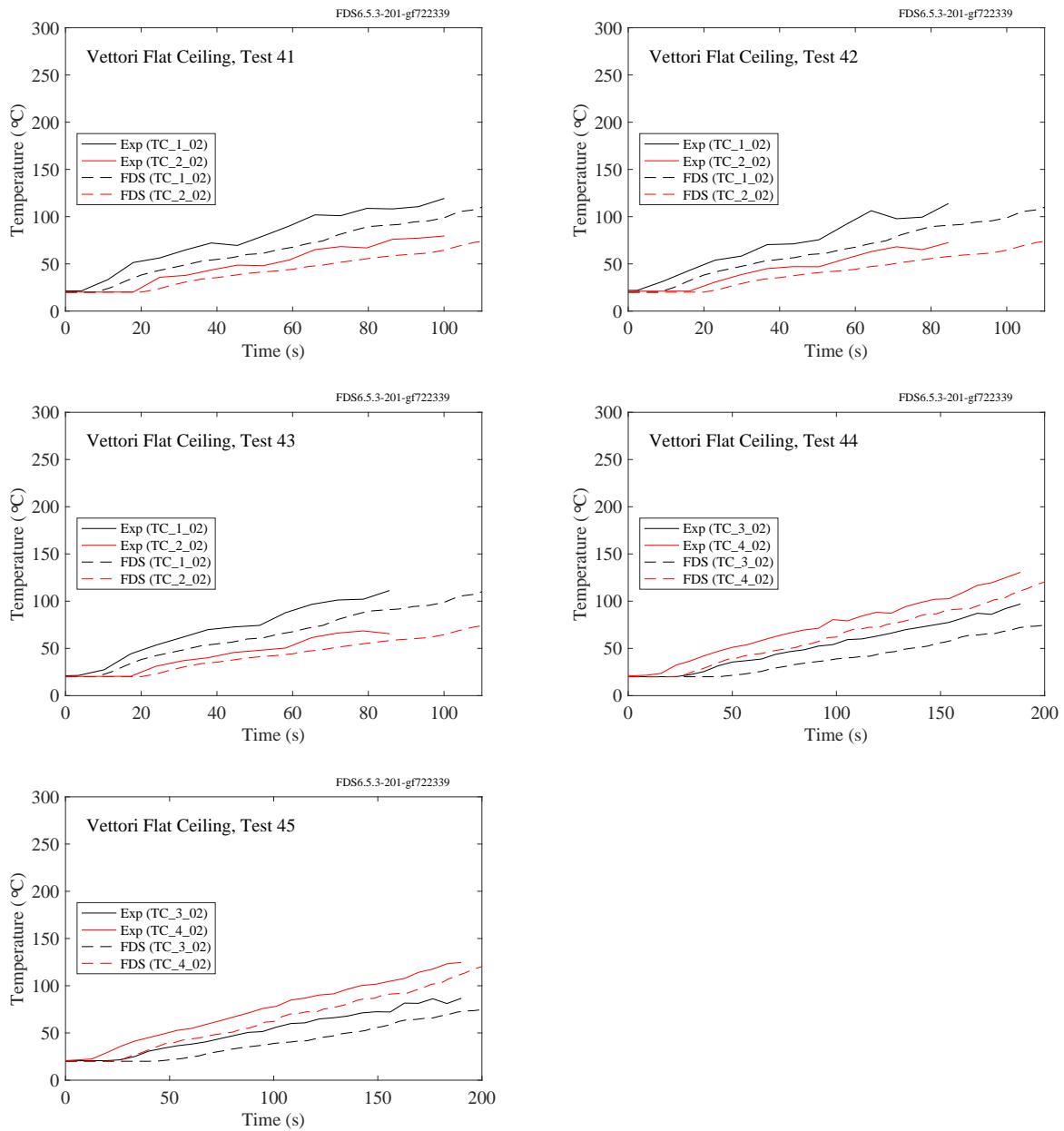


Figure 7.37: Vettori Flat Ceiling experiments, ceiling jet, Tests 41-45.

### 7.1.15 Vettori Sloped Ceiling Experiments

For these experiments, the measured and predicted thermocouple temperature at the locations of the first two activating sprinklers are compared. The thermocouples were located 15 cm below the ceiling. Replicate results are shown side by side, i.e. Test 2 is a replicate of Test 1; Test 4 is a replicate of Test 3, and so on. There were 36 unique configurations (2 replicates of each) combining the following parameters:

- Flat, 13°, or 24° Ceiling Slope
- Smooth or Obstructed Ceiling Surface
- Fast or Slow Growth Fire
- Corner, Wall, or Detached Burner Location

The plots are labelled using this convention. For example, “13SFC” means that the ceiling is sloped 13° from horizontal, the ceiling is Smooth (no beams), the fire growth rate is Fast, and the burner is in the Corner of the room.

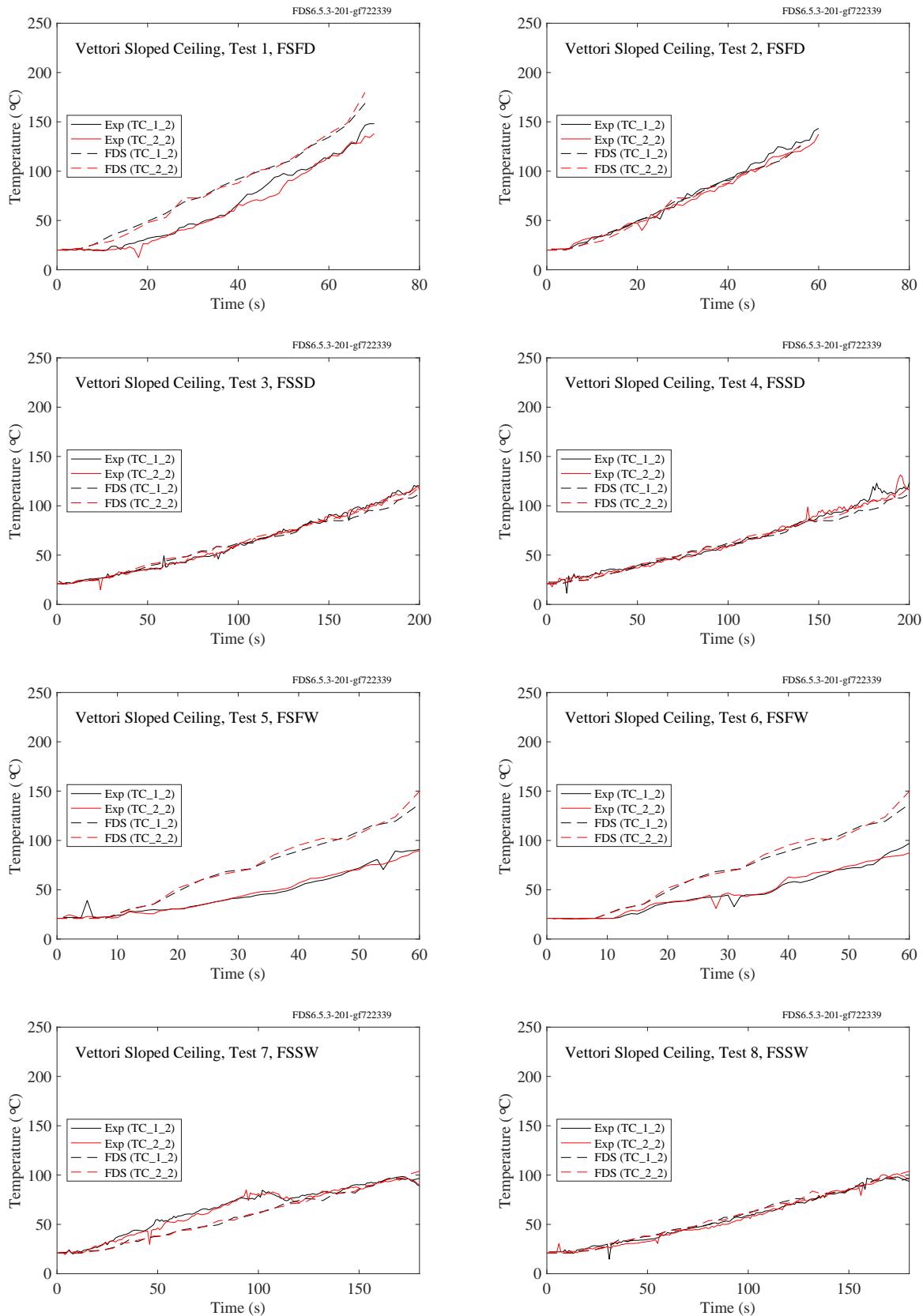


Figure 7.38: Vettori Sloped Ceiling experiments, ceiling jet, Tests 1-8.

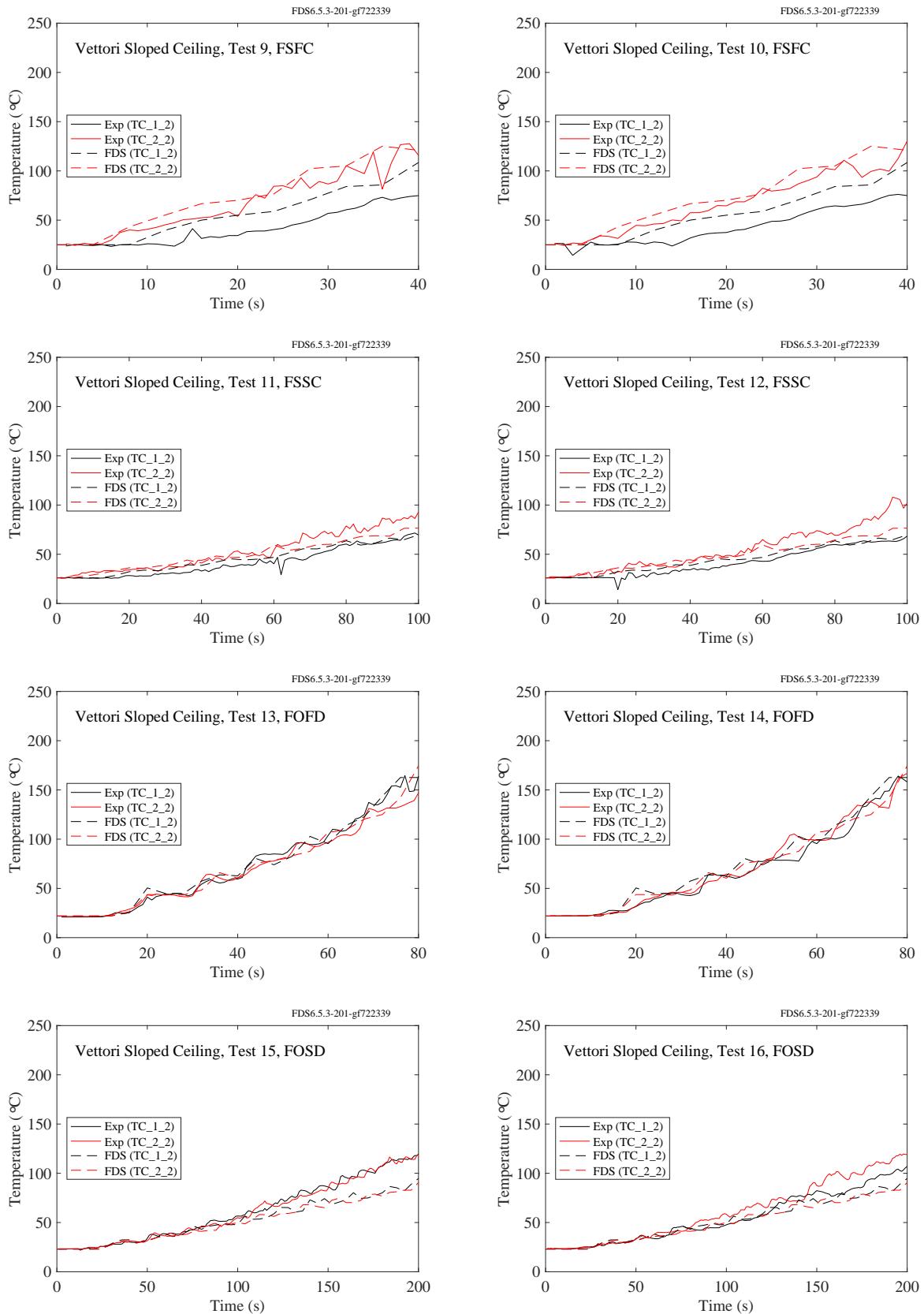


Figure 7.39: Vettori Sloped Ceiling experiments, ceiling jet, Tests 9-16.

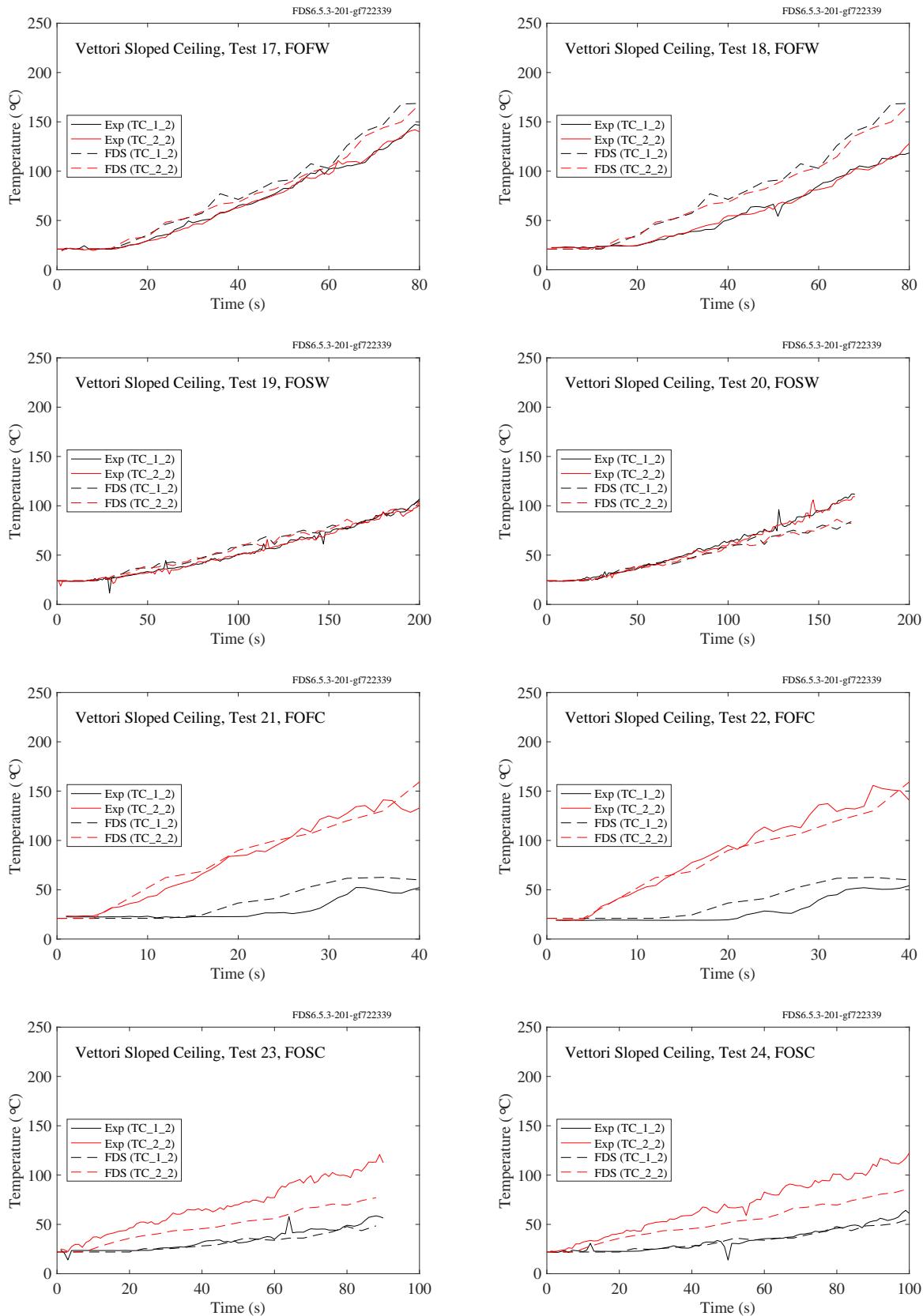


Figure 7.40: Vettori Sloped Ceiling experiments, ceiling jet, Tests 17-24.

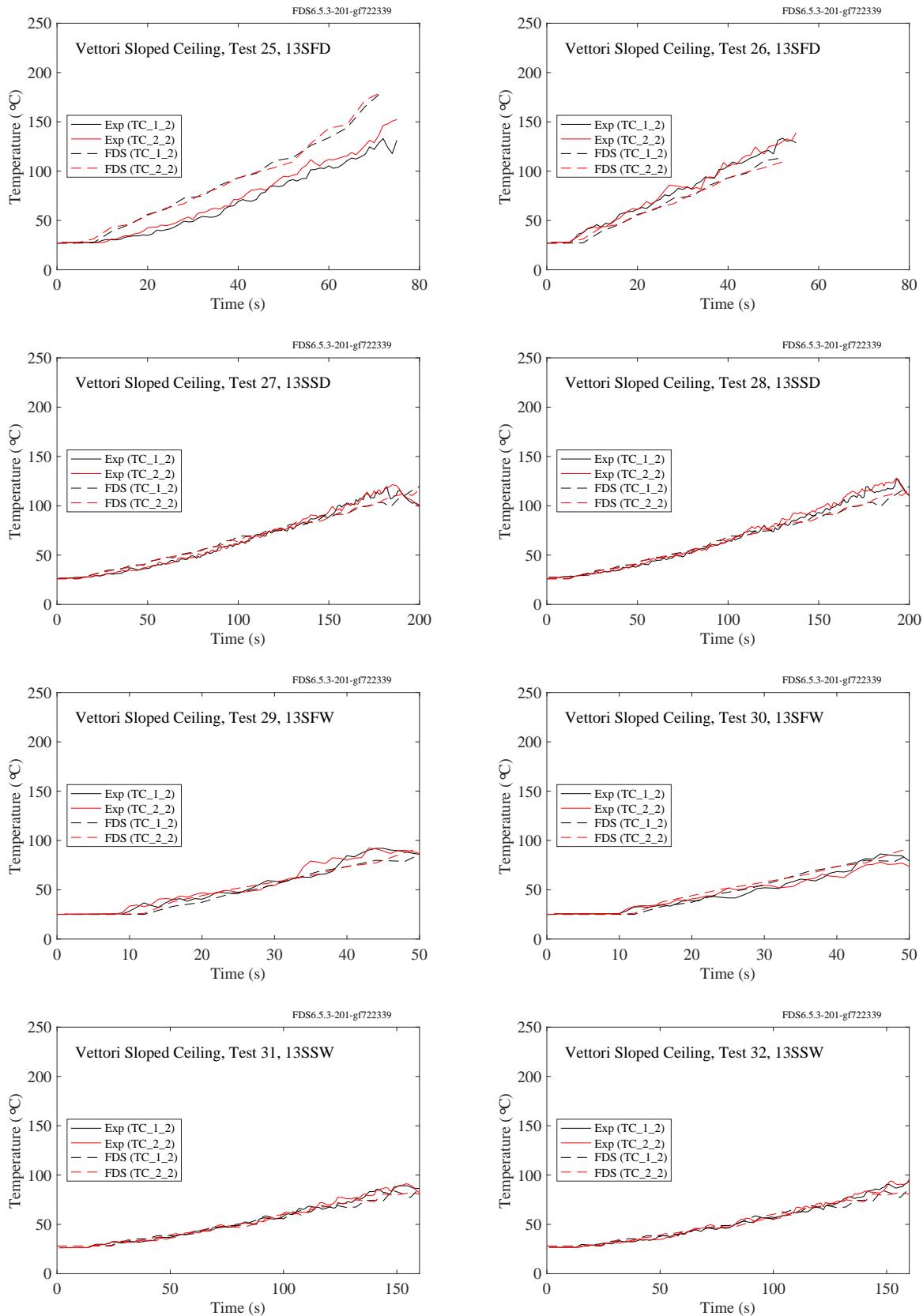


Figure 7.41: Vettori Sloped Ceiling experiments, ceiling jet, Tests 25-32.

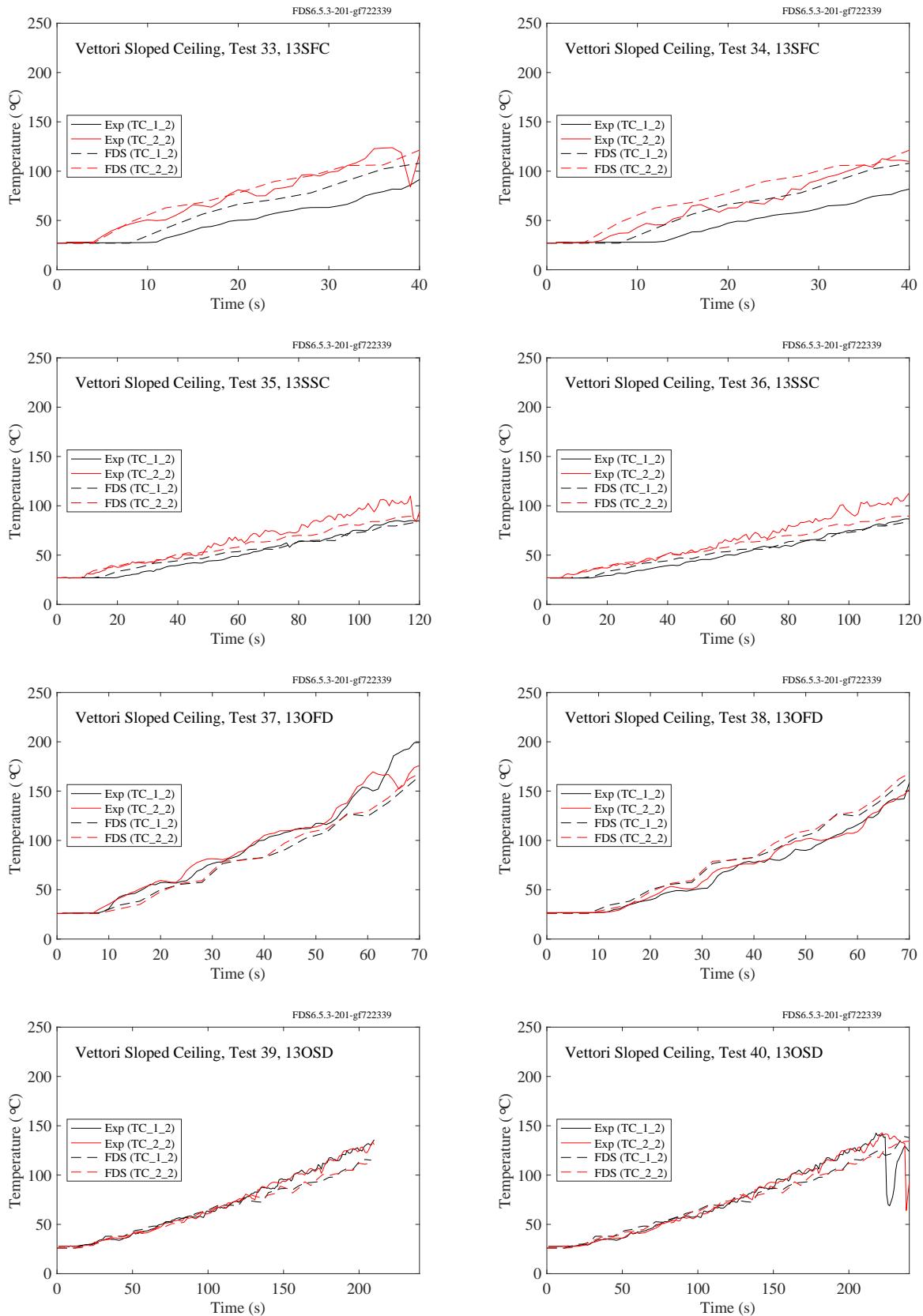


Figure 7.42: Vettori Sloped Ceiling experiments, ceiling jet, Tests 33-40.

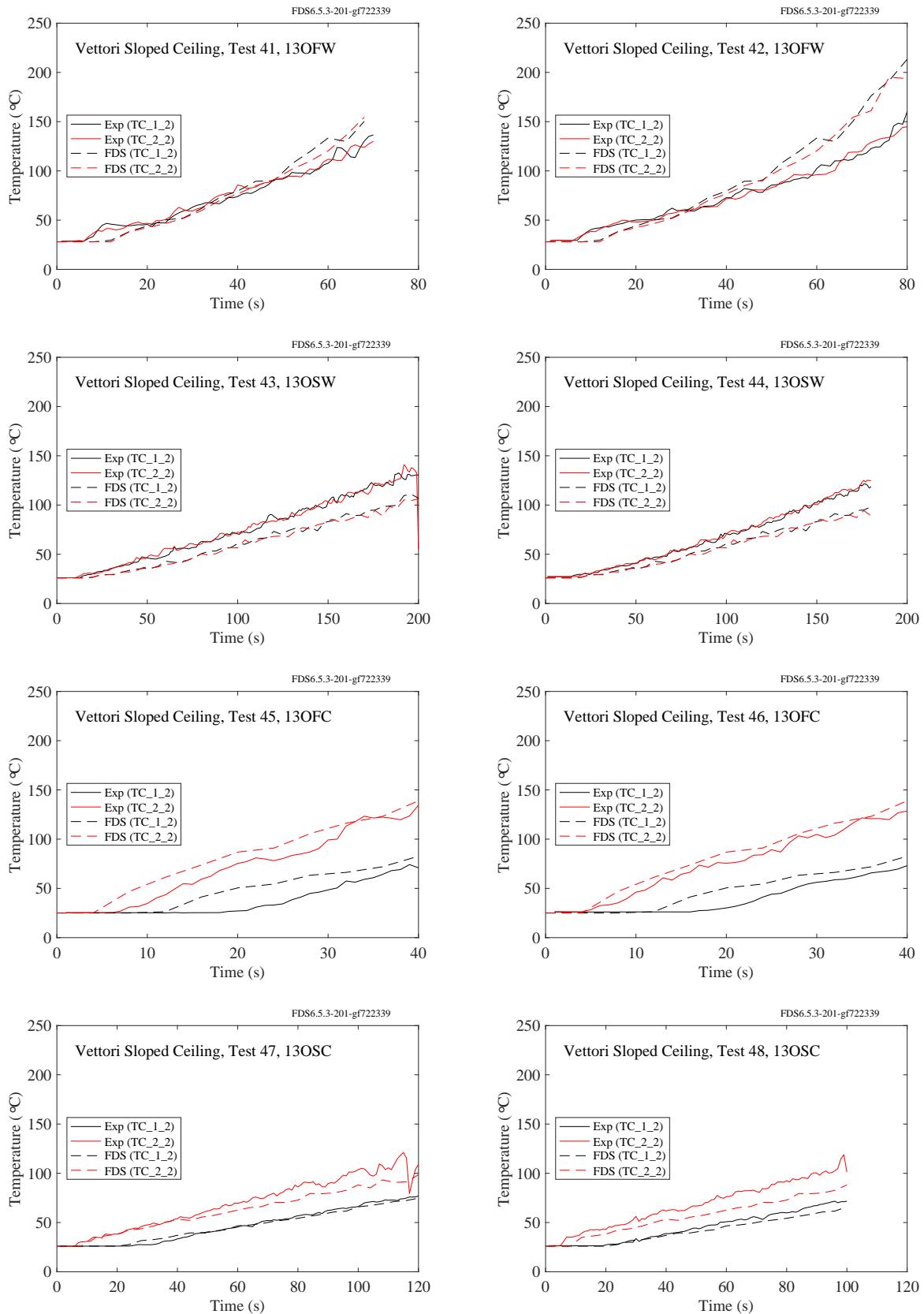


Figure 7.43: Vettori Sloped Ceiling experiments, ceiling jet, Tests 41-48.

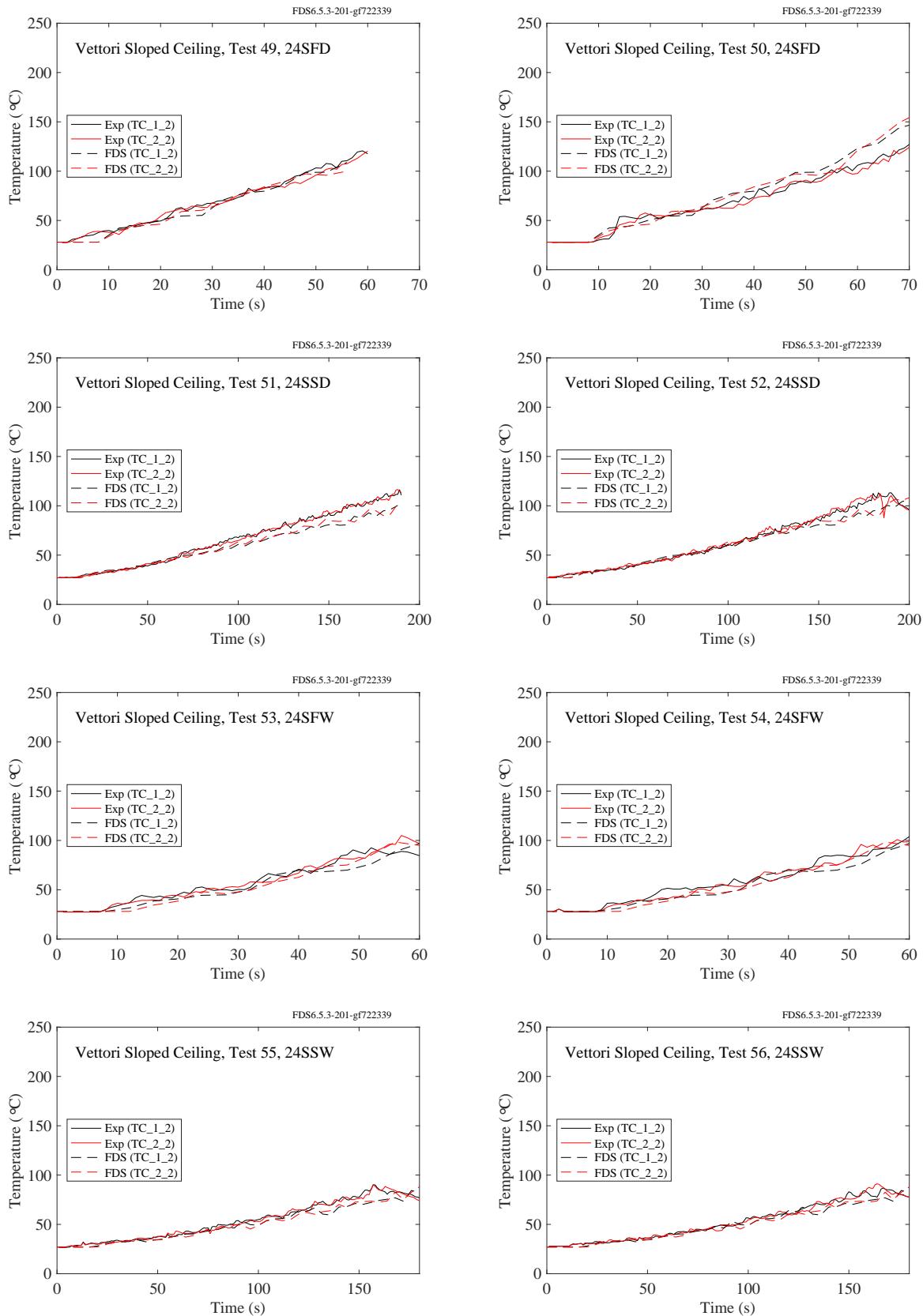


Figure 7.44: Vettori Sloped Ceiling experiments, ceiling jet, Tests 49-56.

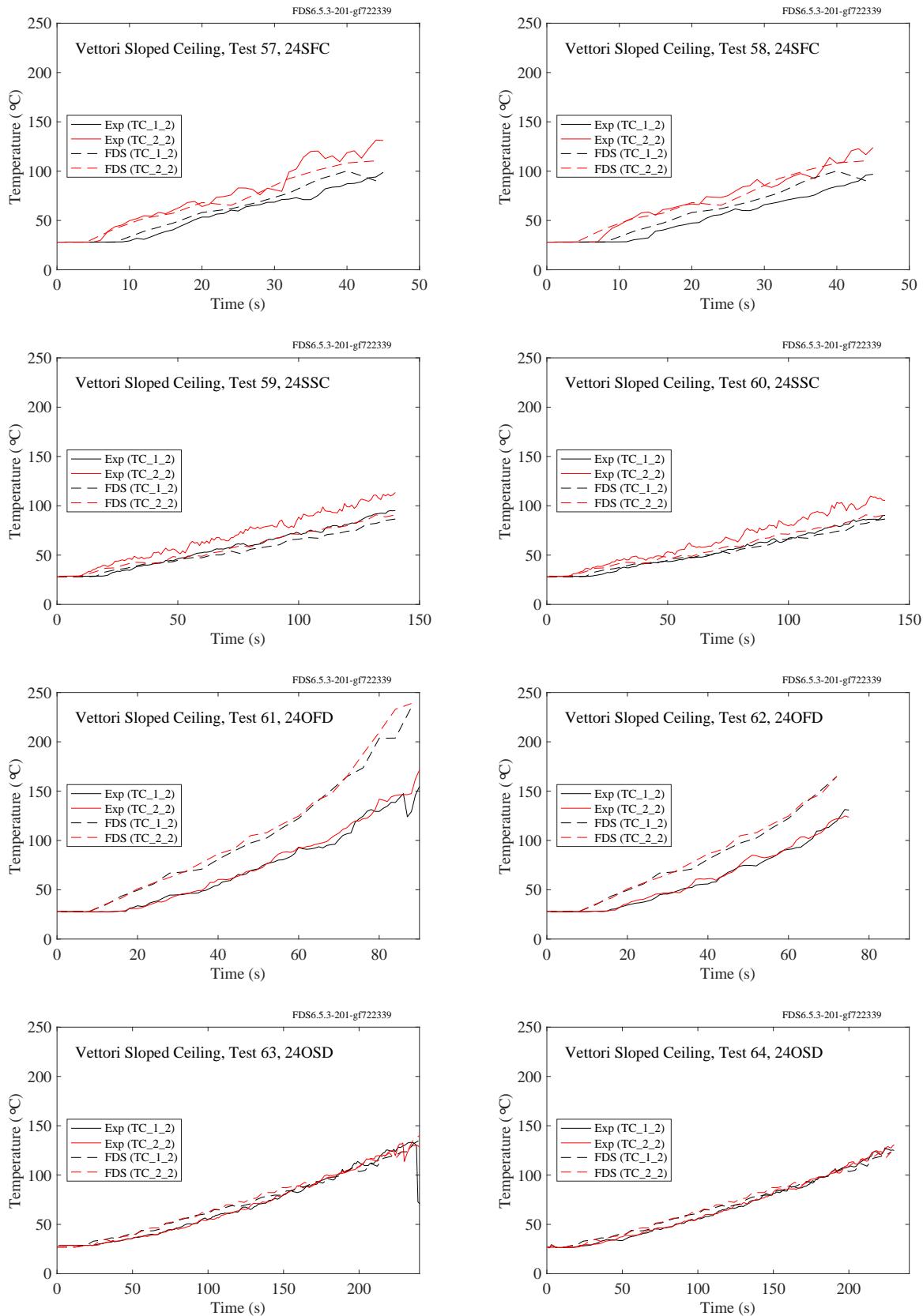


Figure 7.45: Vettori Sloped Ceiling experiments, ceiling jet, Tests 57-64.

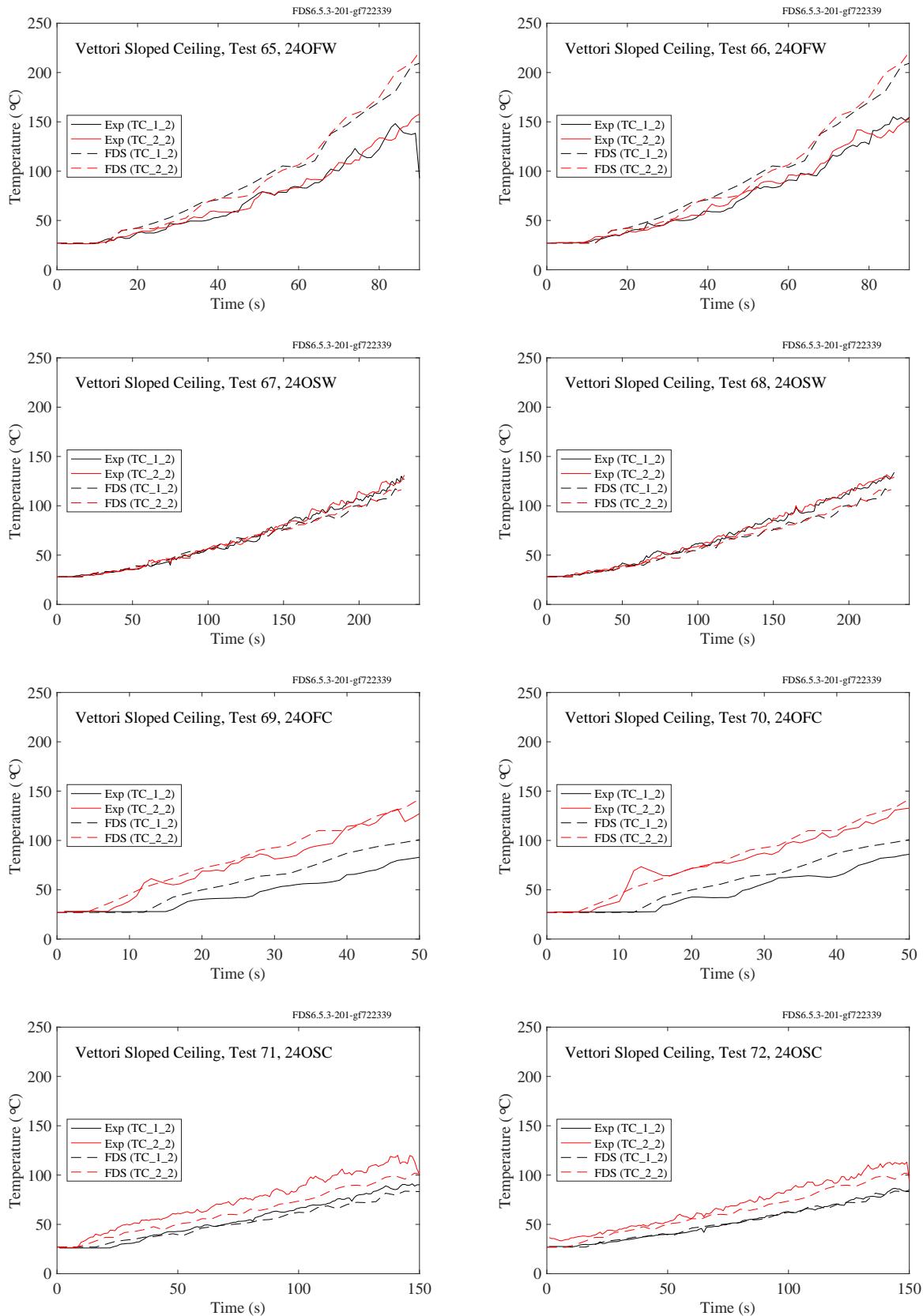


Figure 7.46: Vettori Sloped Ceiling experiments, ceiling jet, Tests 65-72.

### 7.1.16 WTC Experiments

In the WTC experiments, the compartment was 7 m long, 3.6 m wide and 3.8 m high. A 1 m by 2 m pan was positioned close to the center of the compartment. Aspirated thermocouples were positioned 3 m to the west (TTRW1) and 2 m to the east (TTRE1) of the fire pan, 18 cm below the ceiling.

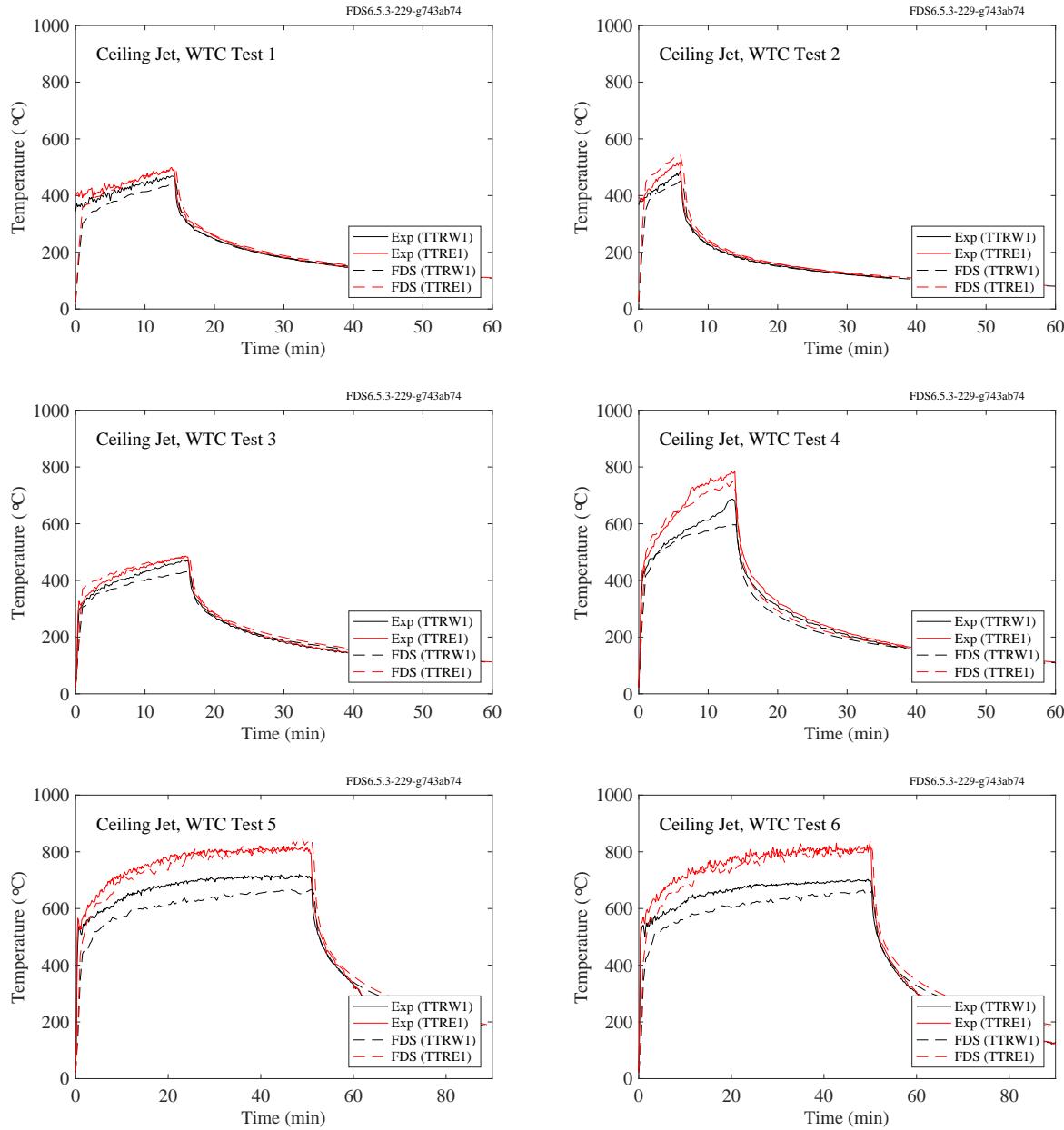


Figure 7.47: WTC experiments, ceiling jet, Tests 1-6.

### 7.1.17 Summary of Ceiling Jet Temperature Predictions

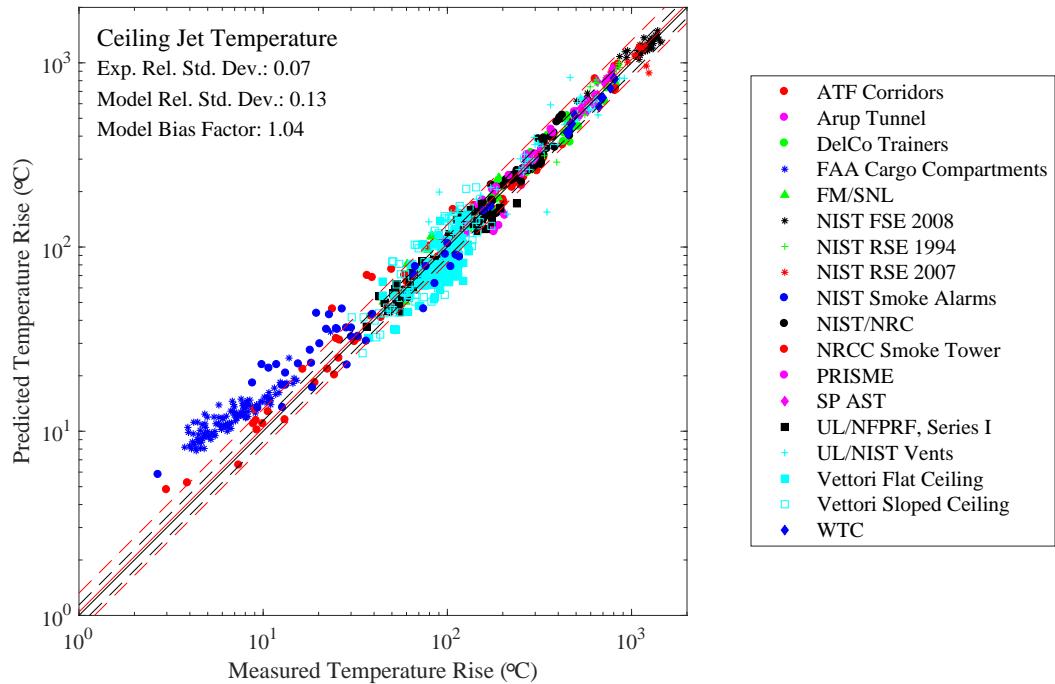


Figure 7.48: Summary of ceiling jet temperature predictions.

## 7.2 Sprinkler Activation Times

There are two ways to evaluate the model's ability to predict sprinkler activation. The first is to simply compare the total number of predicted versus observed activations. The second is to compare the time to first activation. Comparing the total number of activations indirectly indicates if the model accurately predicts the cooling of the hot gases by the water spray. Comparing time to first activation indirectly indicates if the model accurately predicts the velocity and temperature of the ceiling jet.

### 7.2.1 Time to First Sprinkler Activation

Figure 7.49 compares measured and predicted sprinkler activation times. For the UL/NFPRF experiments, only the time to first activation is compared because the resulting water spray sometimes delays the second activation substantially. While the model accounts for the cooling effect of the spray, the disruption of the activation sequence is somewhat random. A better way to check the accuracy of the model is to compare the predicted and measured total number of activation, which is discussed in the next section. For the Vettori experiments, the sprinklers did not flow water; thus, it is possible to consider the activation times of up to four sprinklers.

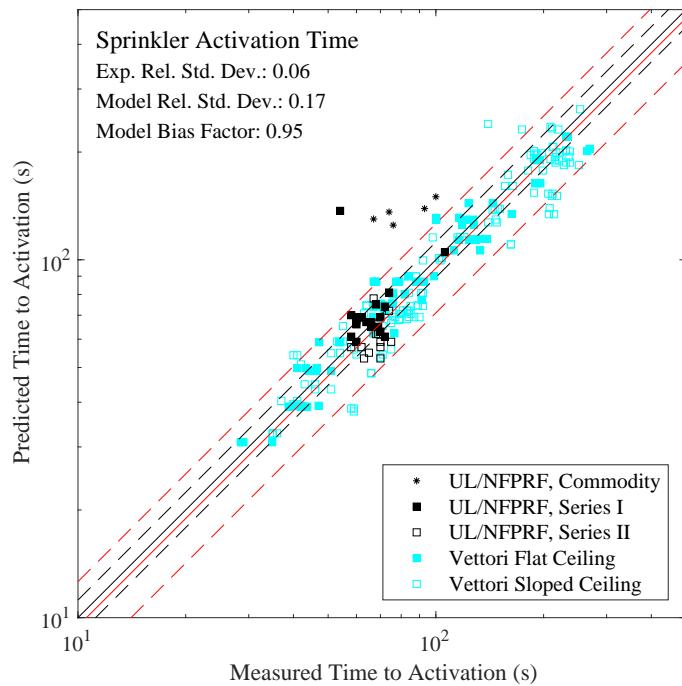


Figure 7.49: Comparison of measured and predicted sprinkler actuation times.

## 7.2.2 Number of Sprinkler Activations

The figures on the following pages display the number of sprinklers actuated as a function of time. The results are summarized in Fig. 7.56. The discussion of the uncertainty for this quantity can be found in Section 4.3.2.

Note that no sprinklers were installed for Test 11, Series I.

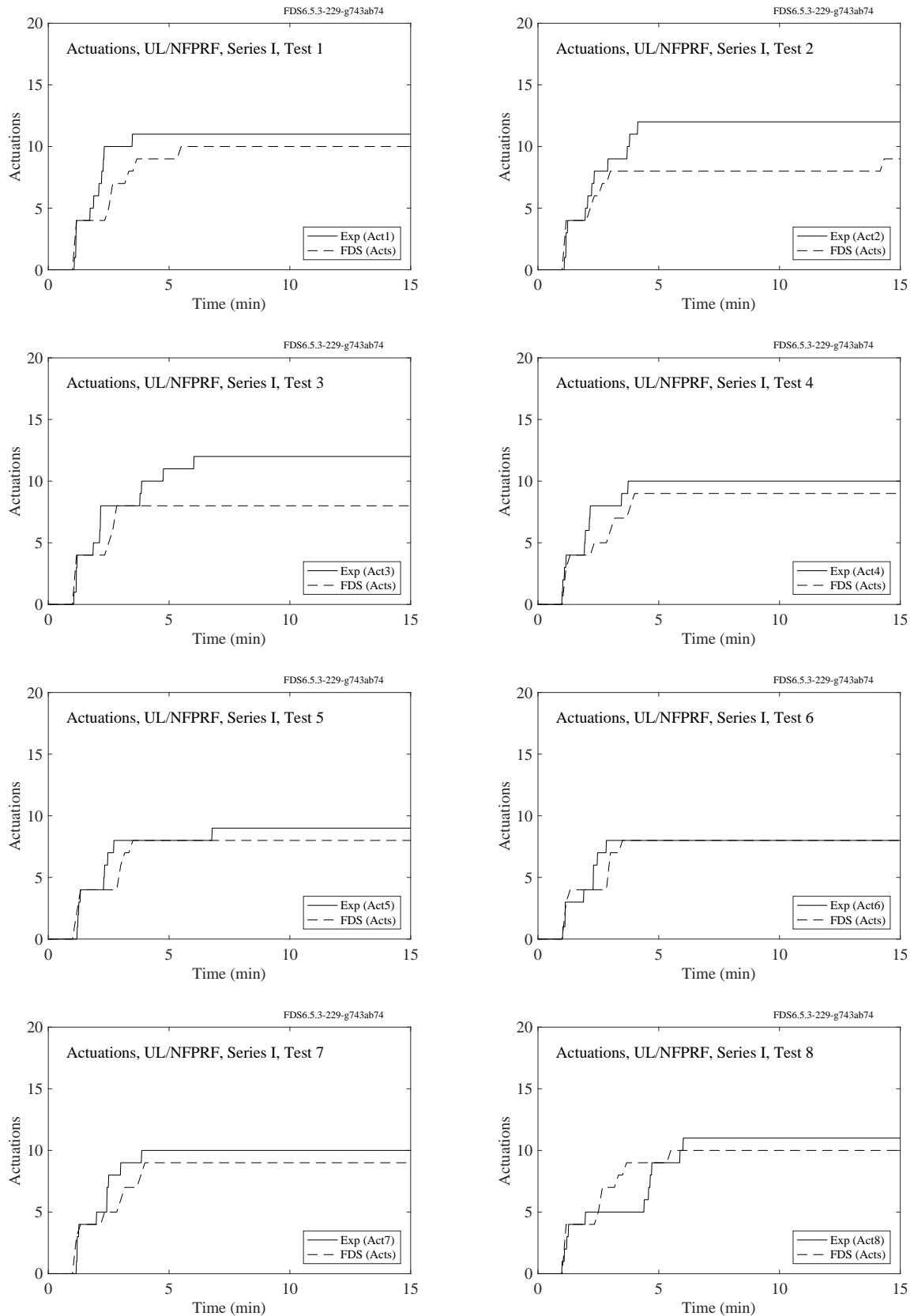


Figure 7.50: UL/NFPRF experiments, number of sprinkler activations, Series I, Tests 1-8.

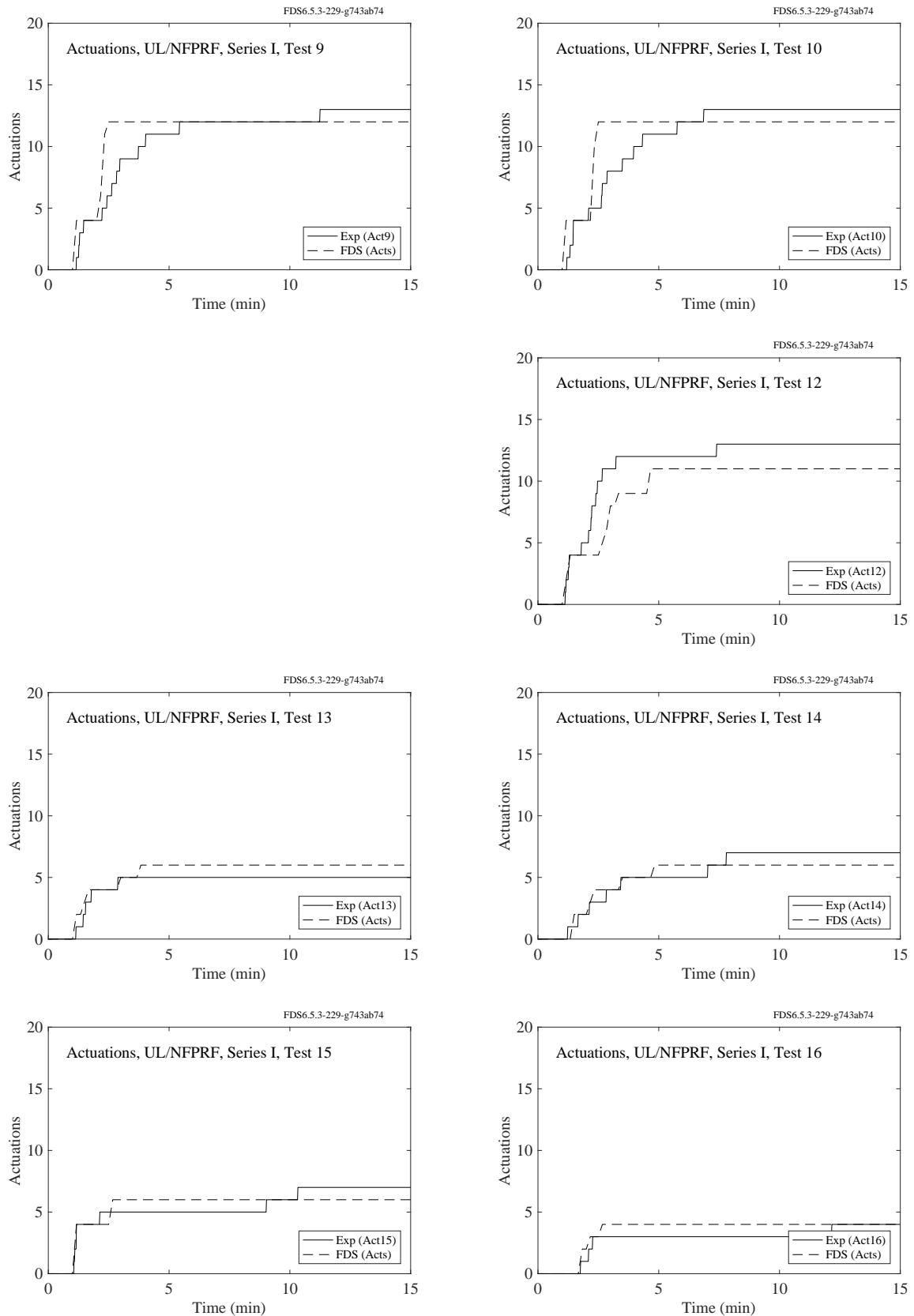


Figure 7.51: UL/NFPRF experiments, number of sprinkler activations, Series I, Tests 9-16.

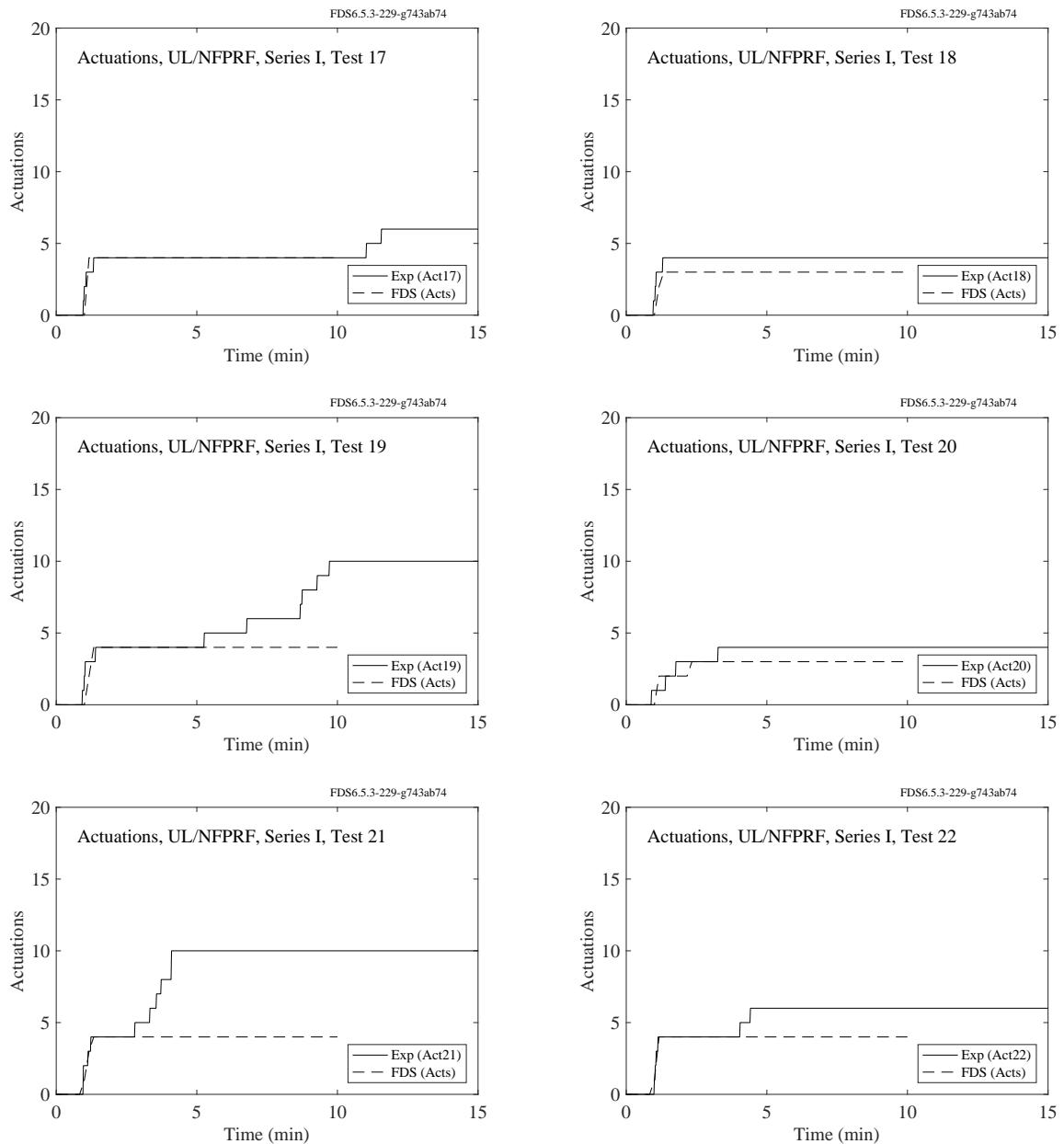


Figure 7.52: UL/NFPRF experiments, number of sprinkler activations, Series I, Tests 17-22.

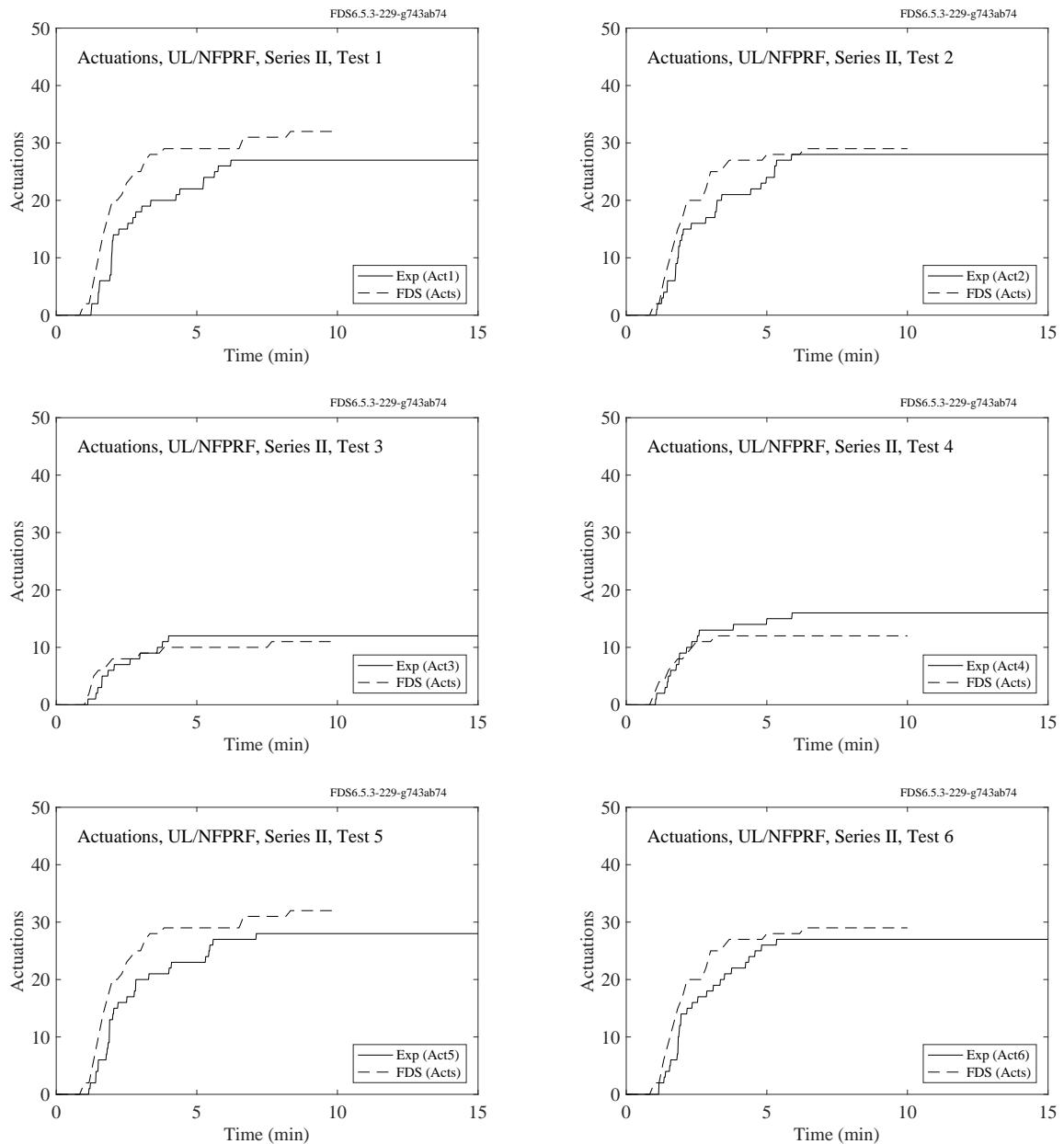


Figure 7.53: UL/NFPRF experiments, number of sprinkler activations, Series II, Tests 1-6.

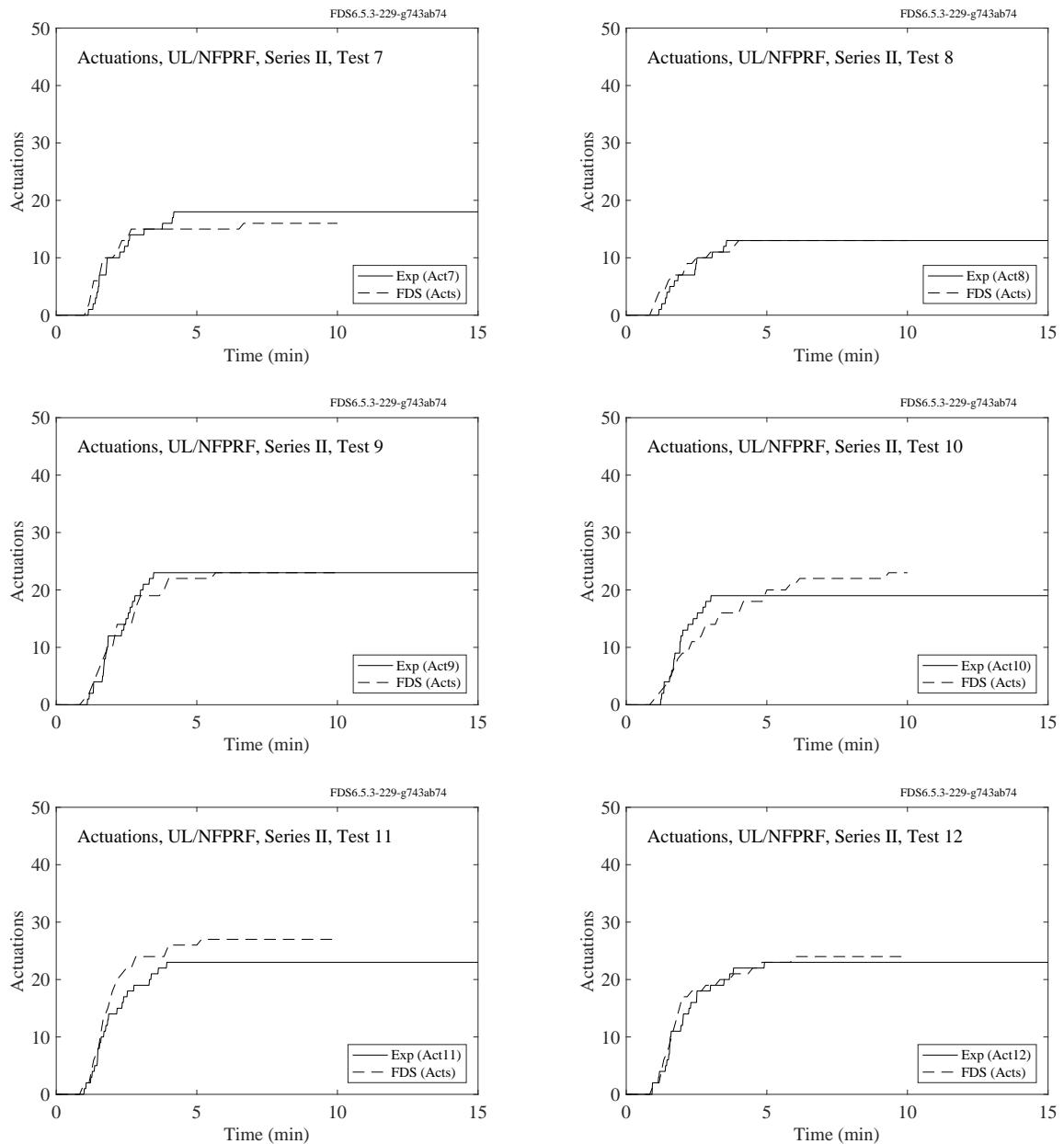


Figure 7.54: UL/NFPRF experiments, number of sprinkler activations, Series II, Tests 7-12.

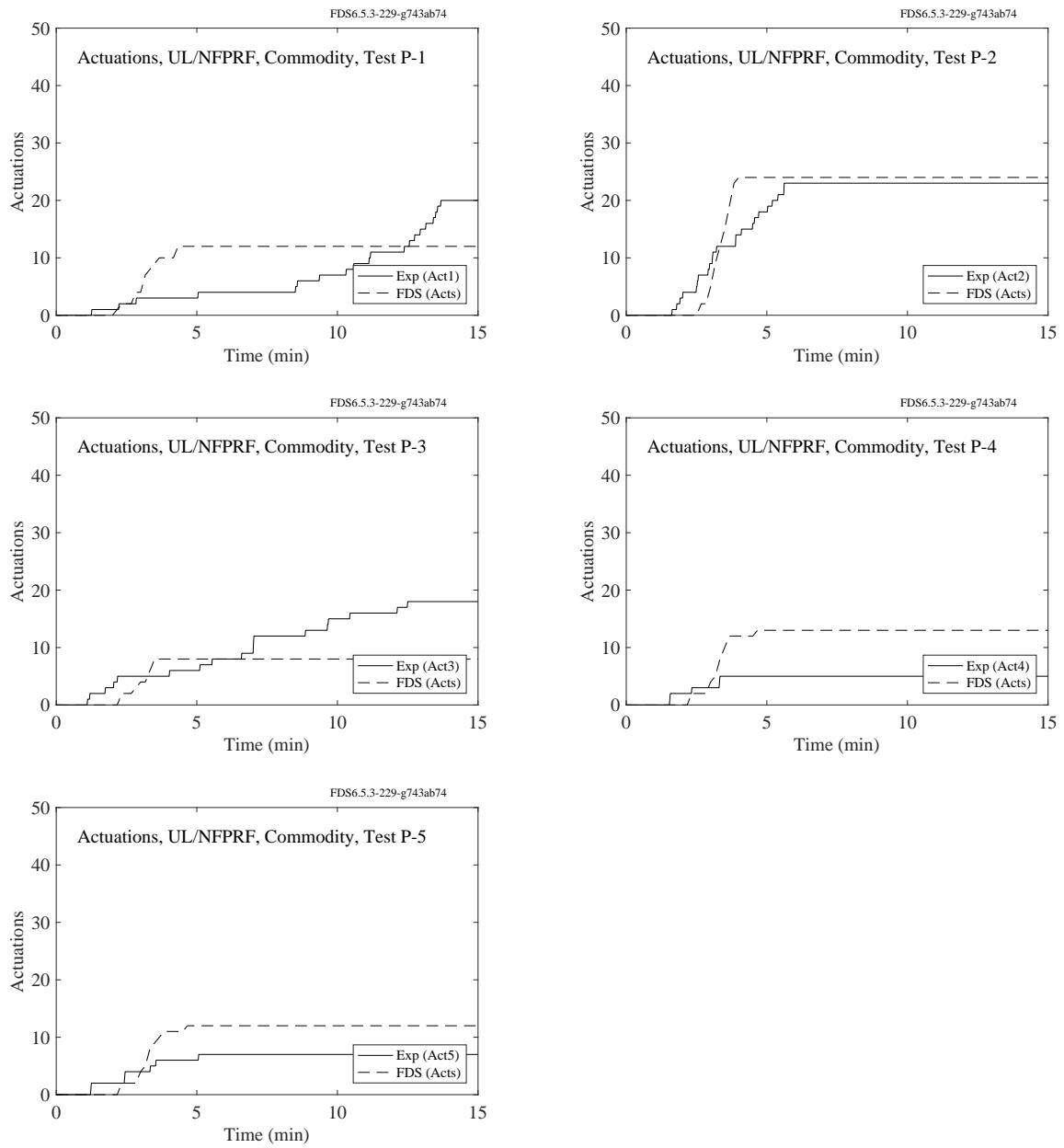


Figure 7.55: UL/NFPRF experiments, number of sprinkler activations, Group A Commodity, Tests 1-5.

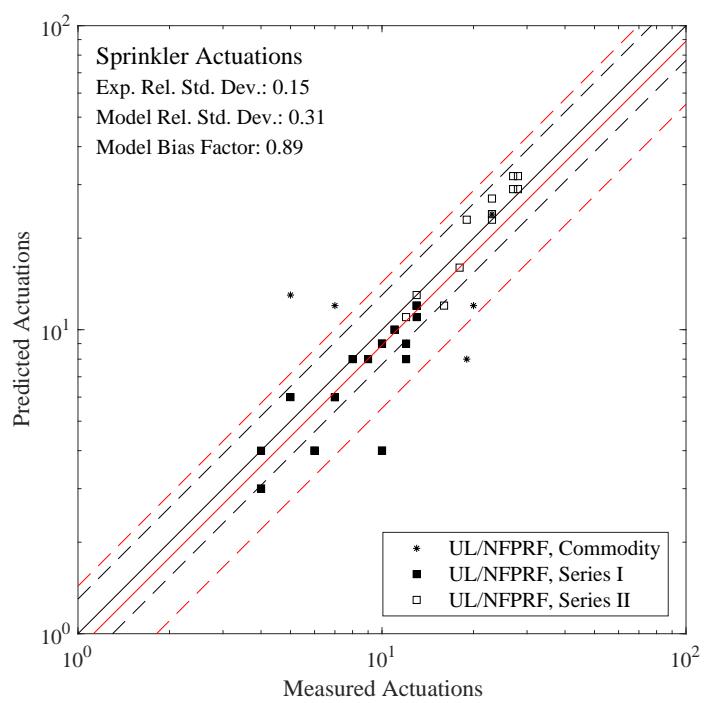


Figure 7.56: Comparison of the number of predicted and measured sprinkler activations.

### 7.3 Smoke Detector Activation Times

FDS can model smoke detector activation in two ways. The first method is based on the assumption that activation occurs when the gas temperature near the detector rises above a given threshold. Essentially this method treats the smoke detector exactly like a heat detector with a relatively low RTI value. Figure 7.57 compares the measured versus predicted smoke detector activation times using a heat detector/temperature rise approach. The heat detectors were set with an RTI of  $5 \sqrt{\text{m} \cdot \text{s}}$  and an activation temperature of  $5^\circ\text{C}$  above ambient, based on the suggestion of Bukowski and Averill [222].

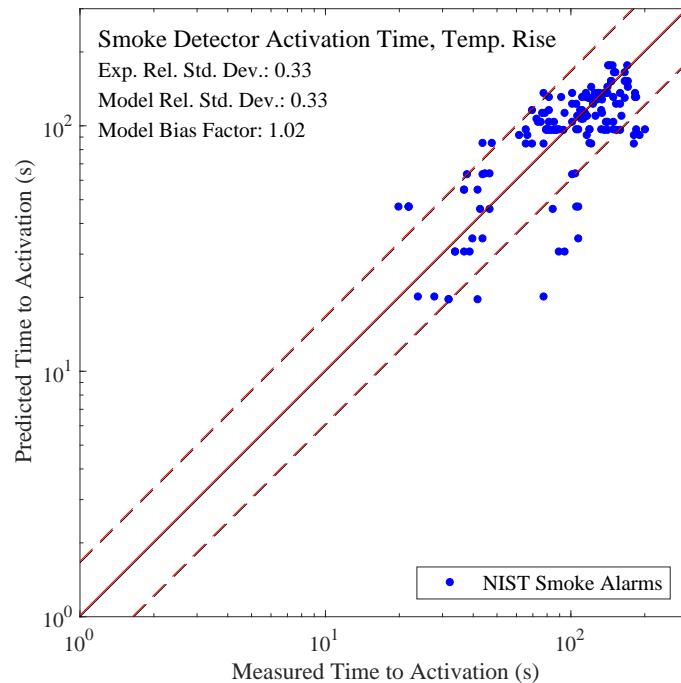


Figure 7.57: Summary of smoke detector activation times (using temperature rise), NIST Smoke Alarms.

The second method of predicting smoke detector activation is to use an empirical model of the smoke transit time within the device to estimate when the smoke concentration will rise above a particular threshold value set by the manufacturer. Figure 7.58 compares the measured versus predicted smoke detector activation times using the smoke detector model. Note that the test report [173] does not provide the parameters that characterize the smoke transit time within the detector. Instead, generic values are used.

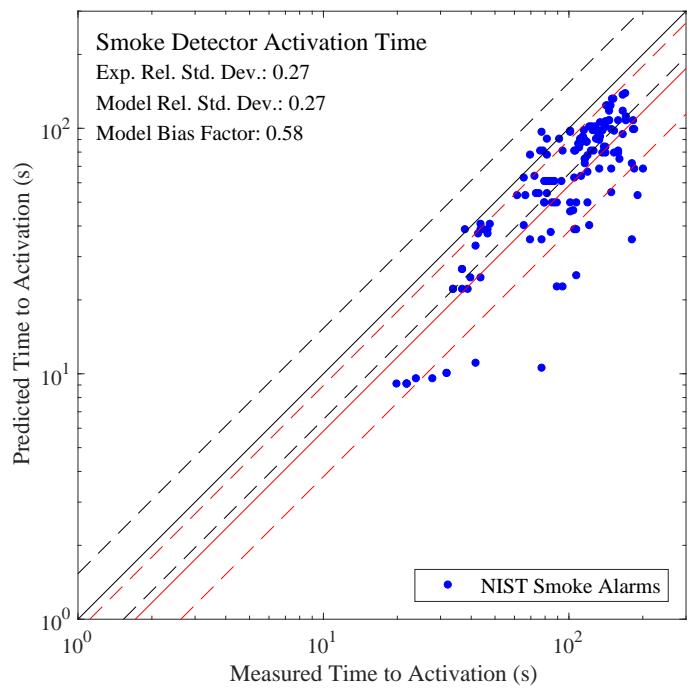


Figure 7.58: Summary of smoke detector activation times (using smoke detector model), NIST Smoke Alarms.



# **Chapter 8**

## **Gas Velocity**

Gas velocity is often measured at compartment inlets and outlets as part of a global assessment of mass and energy conservation. This chapter contains measurements of gas velocity and related quantities.

### **8.1 ATF Corridor Experiments**

Comparisons of bi-directional velocity measurements with FDS predictions for the ATF Corridor experiments are presented on the following pages. Velocity measurements were made at four locations, two on the first level (Trees H and I) and two on the second level (Trees J and K). Shown are the upper-most and lower-most probe for each vertical array. Typically there were four probes per tree, with the number 1 indicating the upper-most probe.

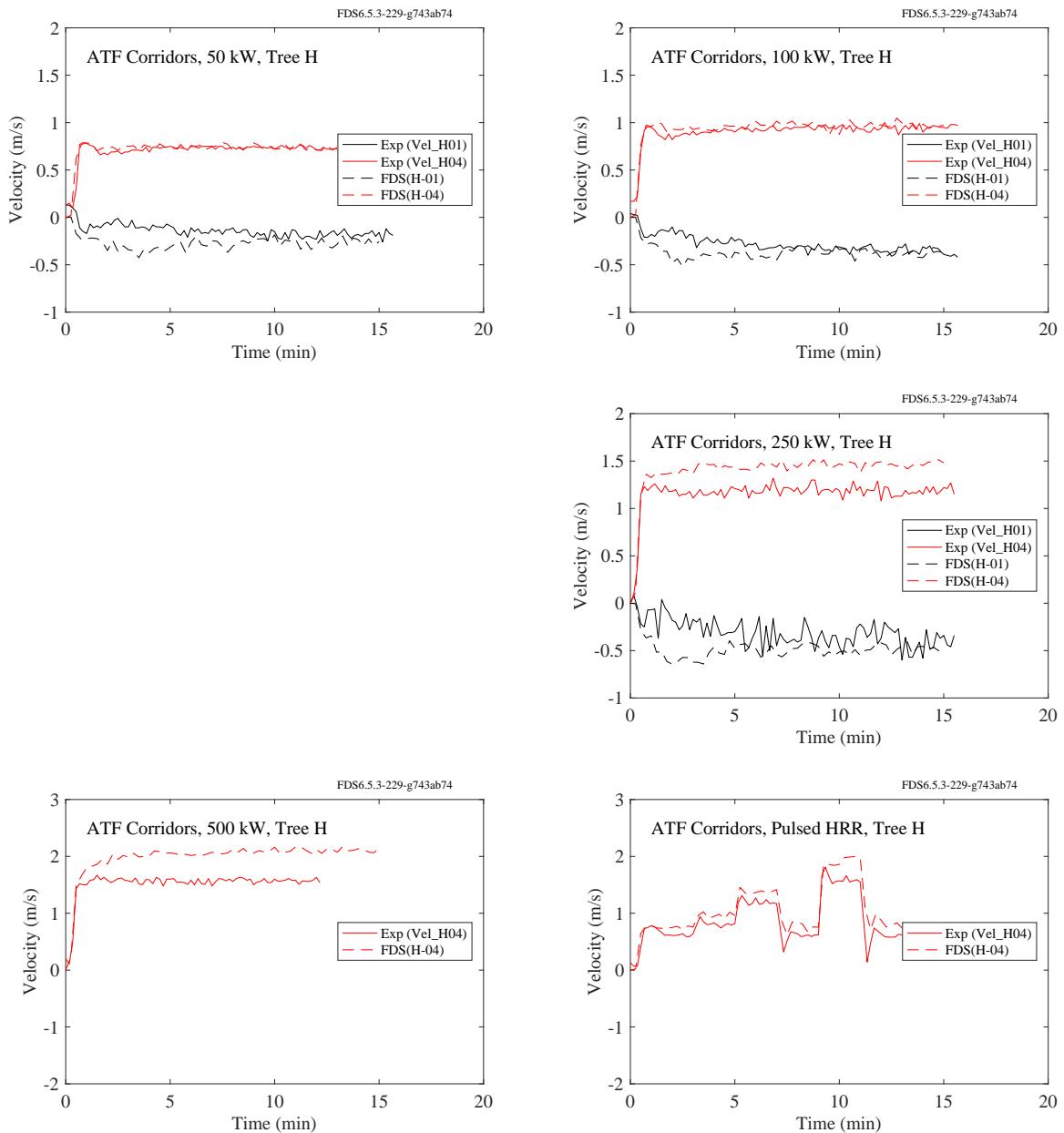


Figure 8.1: ATF Corridors, gas velocity, first level, Location H.

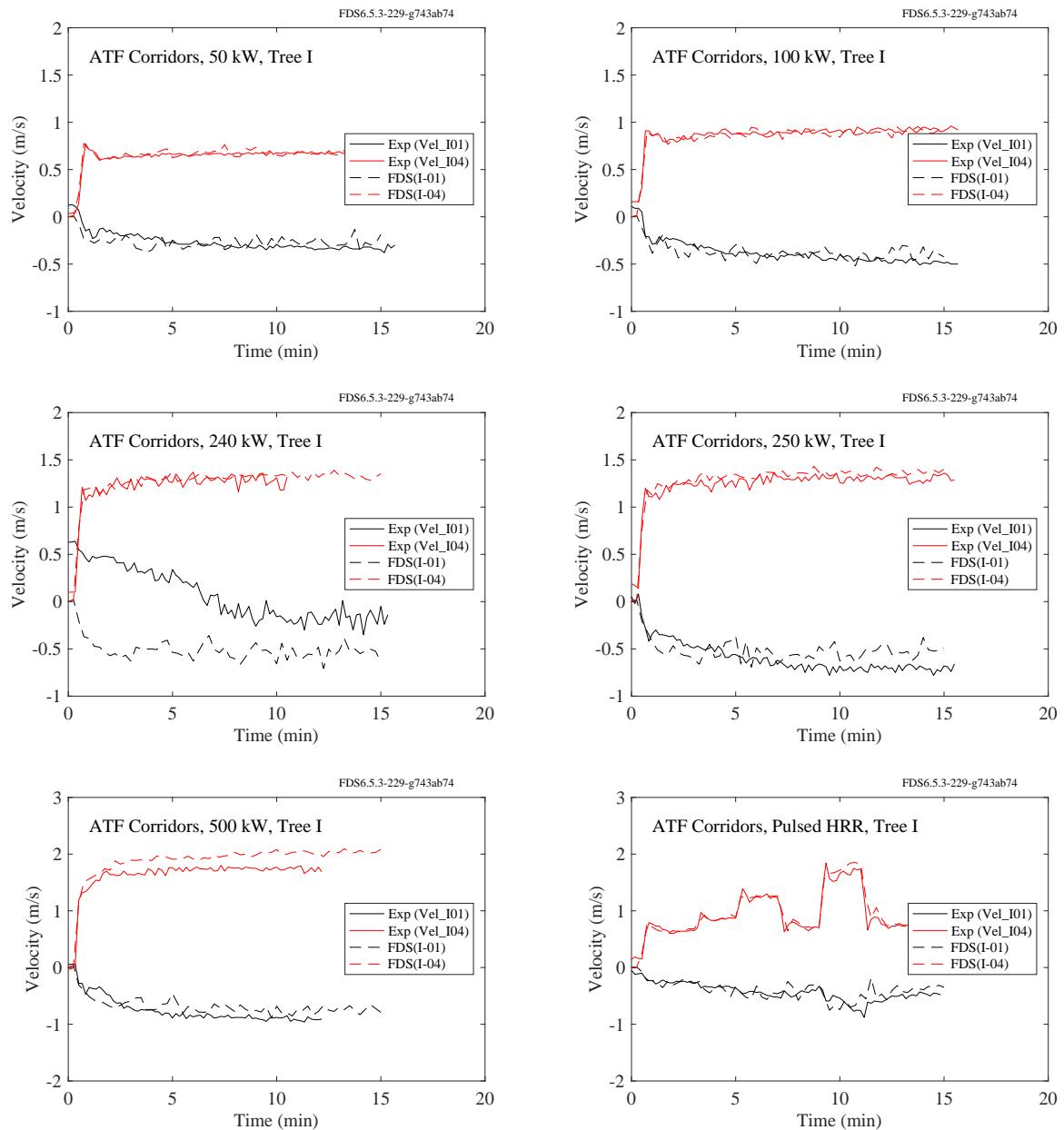


Figure 8.2: ATF Corridors, gas velocity, first level, Location I.

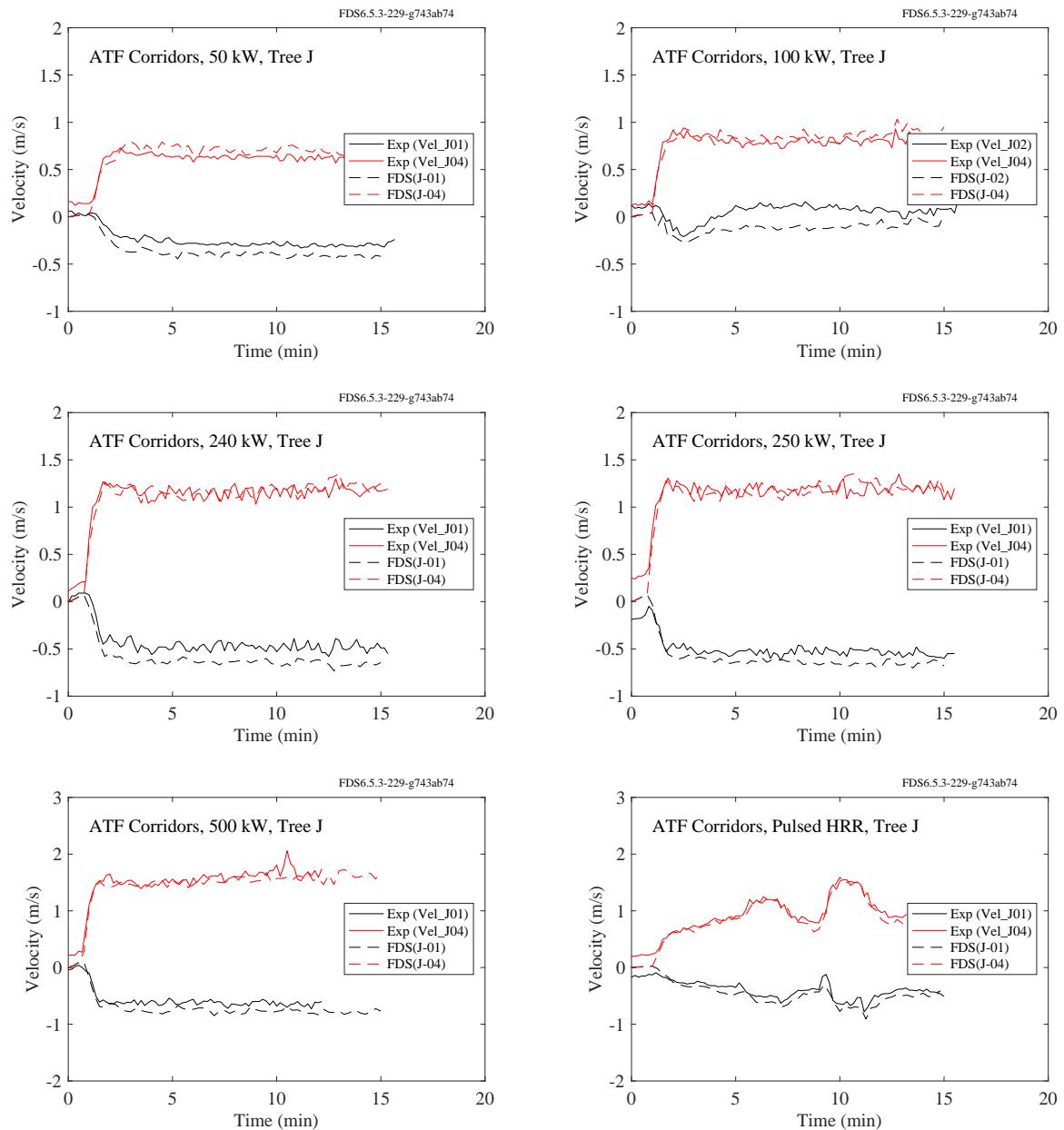


Figure 8.3: ATF Corridors, gas velocity, second level, Location J.

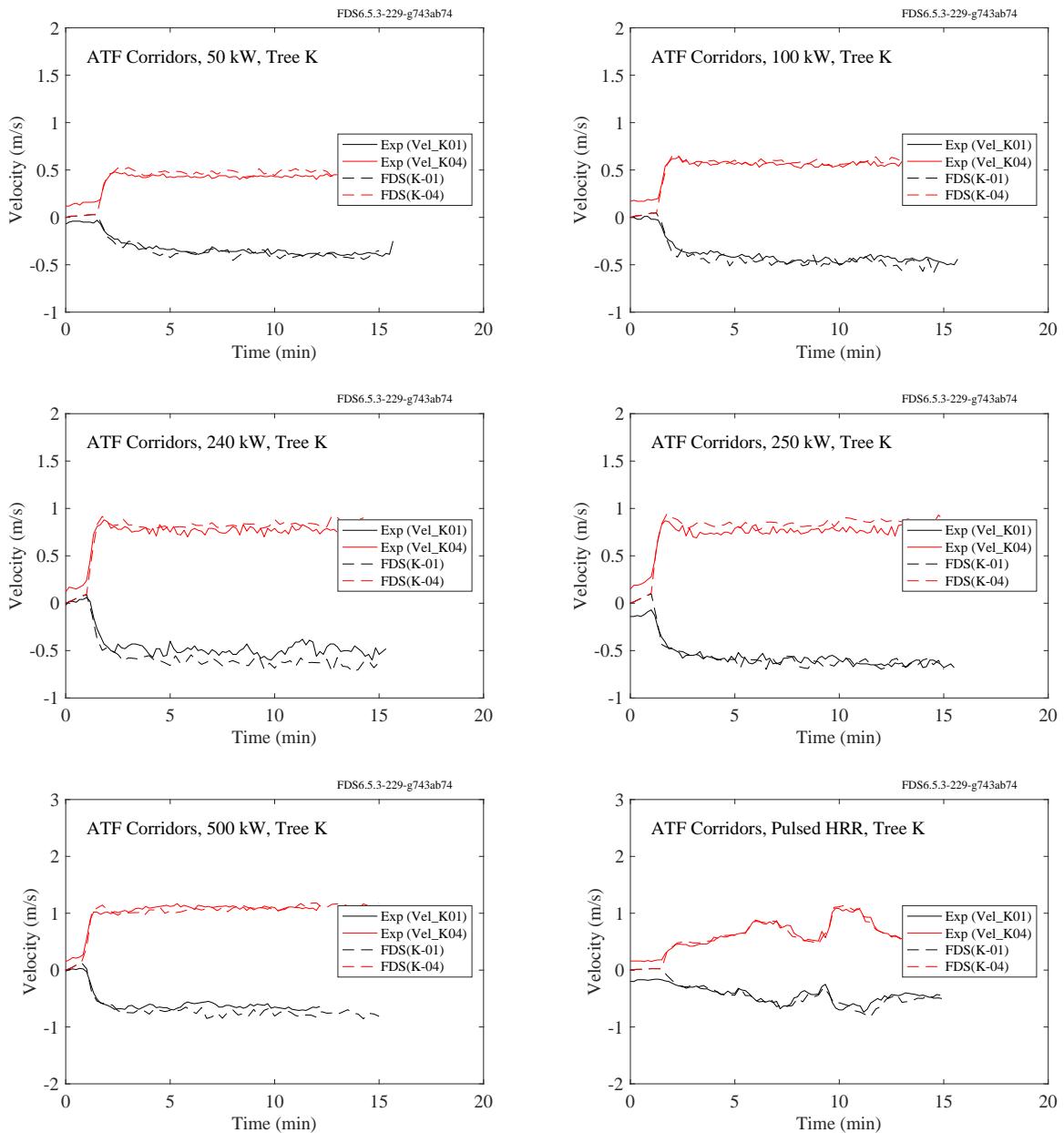


Figure 8.4: ATF Corridors, gas velocity, second level, Location K.

## 8.2 Backward Facing Step

A snapshot the instantaneous velocity contours of the flow over a backward facing step is shown in Fig. 8.5. The dimensions of the tunnel are given in Fig. 3.2. Virtual measurement devices are placed throughout the channel to collect data relating to flow characteristics such as velocity, turbulence RMS velocity, and friction velocity. These virtual measurement devices are placed into lines, four vertical and one horizontal, with a device in the volumetric center of each grid cell. A vertical line device is placed within the inlet region at a location of  $x = -3h$ , and three line devices are placed in the post-step region at locations of  $4h$ ,  $6h$ , and  $10h$ . The post-step vertical line devices are placed accordingly to sample the recirculation, reattachment, and recovery regions. A horizontal line device is used to sample data directly adjacent to the bottom wall of the channel in the post-step region ( $0h$  to  $20h$ ).

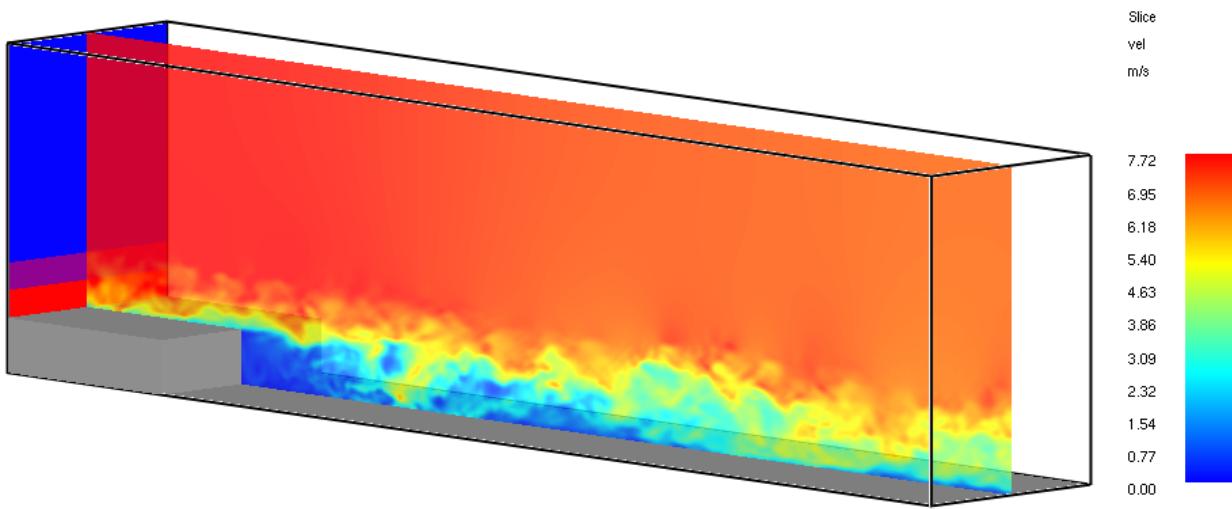


Figure 8.5: Instantaneous contours of velocity magnitude.

The profile of the inlet streamwise velocity component,  $\bar{u}(z)$ , is specified using experimental data provided by Jovic and Driver [50], while the transverse components,  $\bar{v}(z)$  and  $\bar{w}(z)$ , are set to zero. Turbulent eddies are injected using the Synthetic Eddy Method of Jarrin [237]. Eddies are injected at random locations in the bottom two inlets, advected with the flow over a distance equal to the maximum eddy length scale and recycled at the inlet. The inlet maximum eddy length scale is 0.03 m, the number of eddies is 100, and the RMS velocity is set to 0.5 m/s for the middle inlet and 1.0 m/s for the bottom inlet to match the measured inlet data at  $x/h = -3$  as closely as possible.

The boundary conditions for velocity and pressure on the top of the domain are “mirror”, that is, zero gradient. The spanwise boundaries are periodic. The outlet boundary is “open”.

Figure 8.6 shows the longitudinal profiles of the friction coefficient (left) and the pressure coefficient (right). The  $x/h$  location where  $C_f$  crosses zero is the reattachment length, a key validation metric for this flow. The measured value is approximately 6. Figure 8.7 shows the inlet ( $x/h = -3$ ) and downstream mean and covariance profiles.

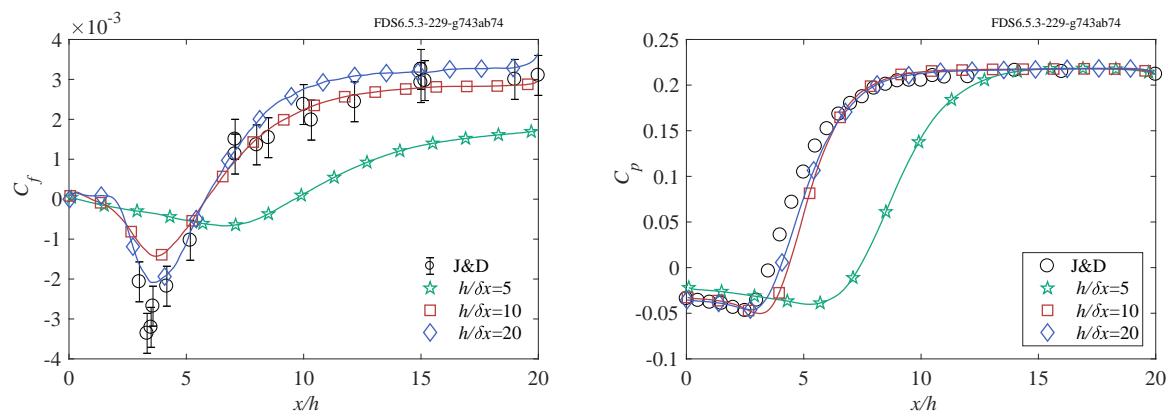


Figure 8.6: Longitudinal profiles of (left) friction coefficient and (right) pressure coefficient.

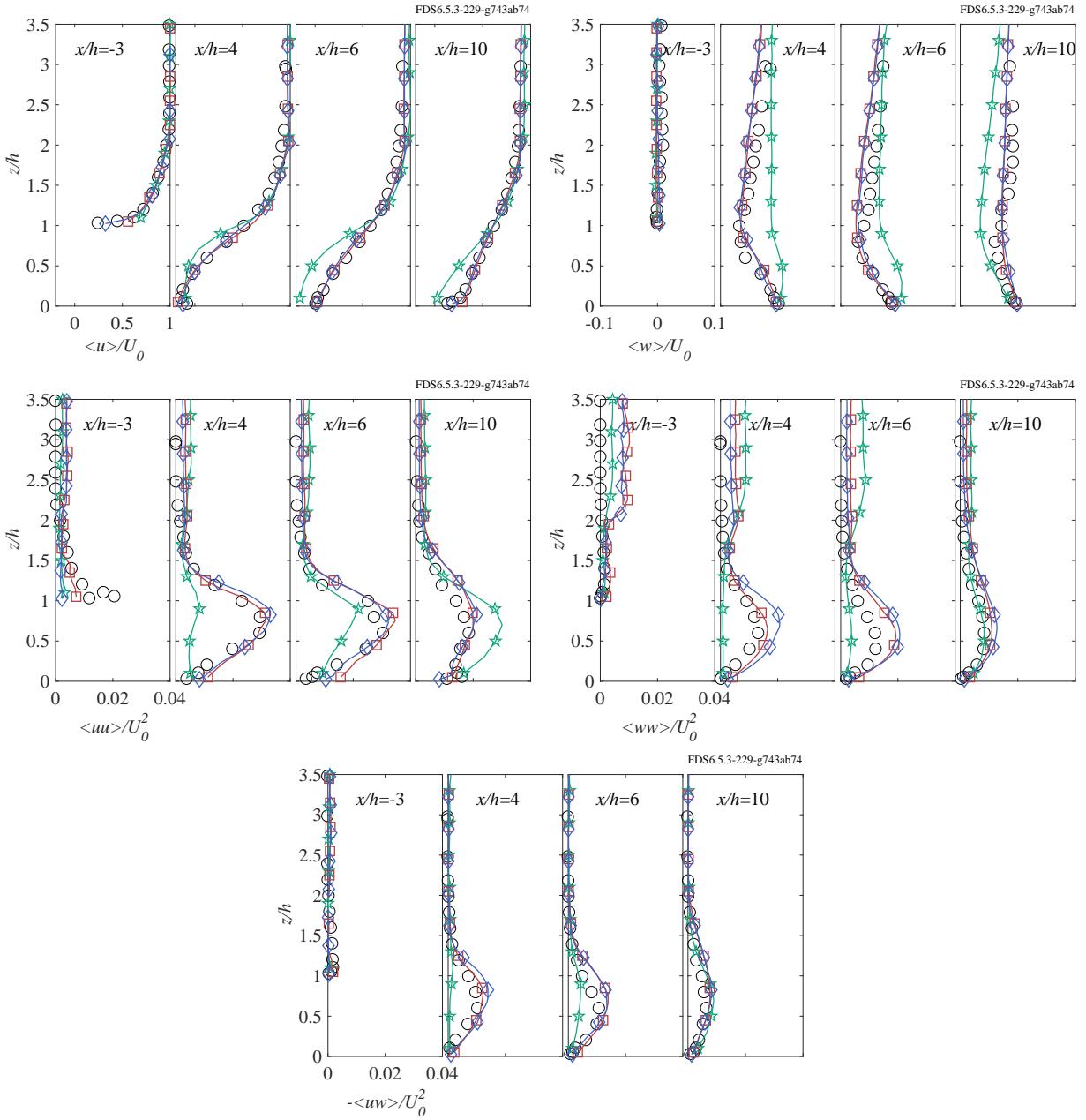


Figure 8.7: Flow profiles for various grid resolutions. Symbols:  $\star$ ,  $h/\delta z = 5$ ;  $\square$ ,  $h/\delta z = 10$ ;  $\diamond$ ,  $h/\delta z = 20$ ;  $\circ$ , J&D experimental data.

### 8.3 Bryant Doorway Experiments

On the following page there are seven plots comparing the predicted and measured centerline velocity<sup>1</sup> profiles in a doorway of a standard ISO 9705 compartment. The measurements shown are based on PIV (Particle Image Velocimetry). Note that some of the measurements do not extend to the top of the doorway (1.96 m above the compartment floor) because the heat from the fire prevented adequate laser resolution of the particles. Velocity measurements were also made using bi-directional probes [136], but these measurements were shown to be up to 20 % greater in magnitude than the comparable PIV measurement.

---

<sup>1</sup>Note that the quantity that is being compared is the total velocity multiplied by the sign of its normal component.

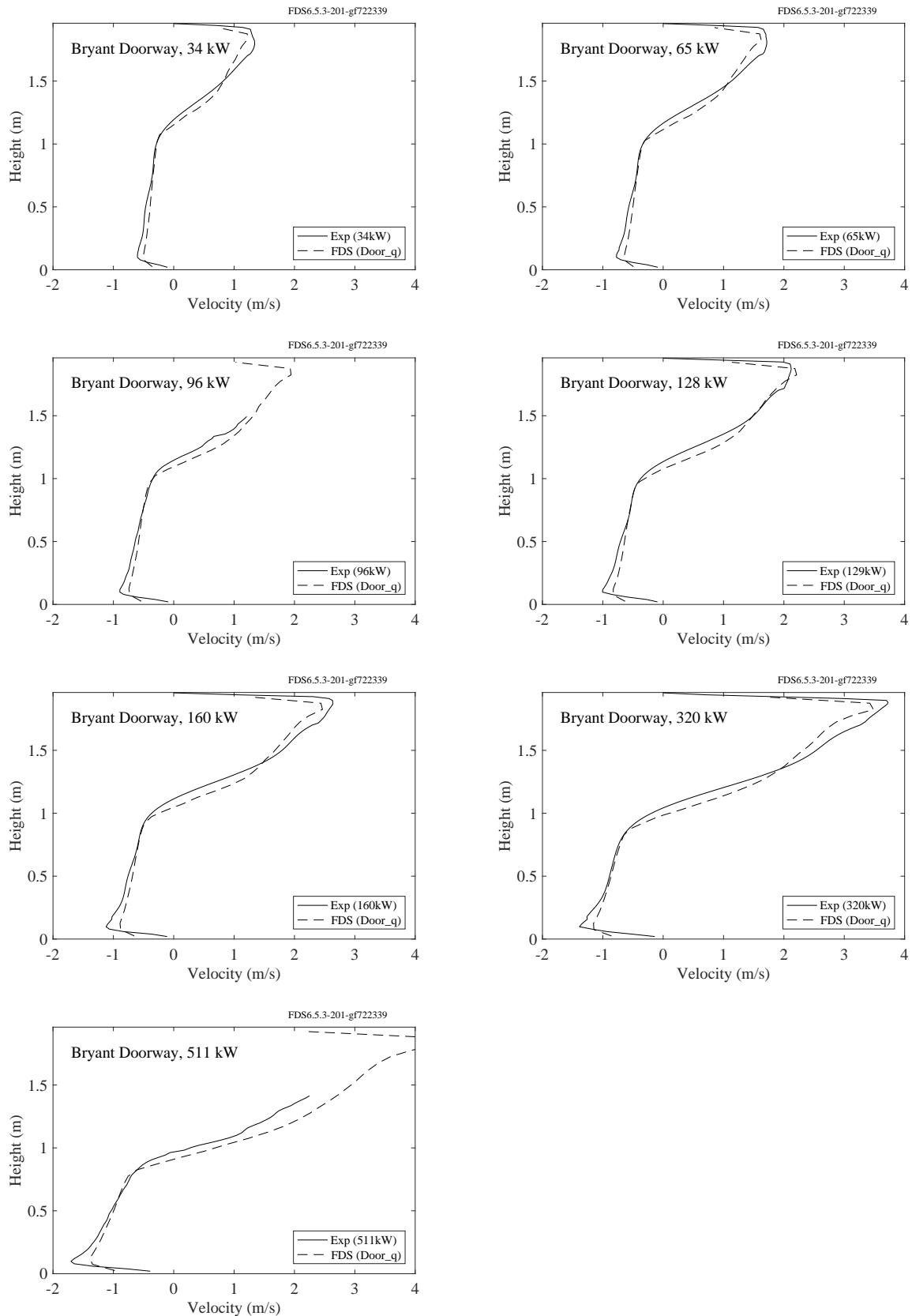


Figure 8.8: Bryant Doorway experiments, gas velocity profiles.

## 8.4 FM/FPRF Datacenter Experiments

On the following page there are eight plots comparing the predicted and measured velocities for the high and low fan speed flow mapping tests in the FM/FPRF datacenter mockup. For each test there are plots for u-velocity, v-velocity, w-velocity and total velocity. Error bars are the measured and predicted RMS values. The dotted lines represent the measurement error. Measurement error was not a simple percentage of the measured value but rather was a propagation of fan flow error (the primary FDS input), sonic anemometer intrinsic error, and an estimate of the error based on the accuracy of placing the anemometer (determined from attempts to make repeat measurements after removing and replacing the probe).

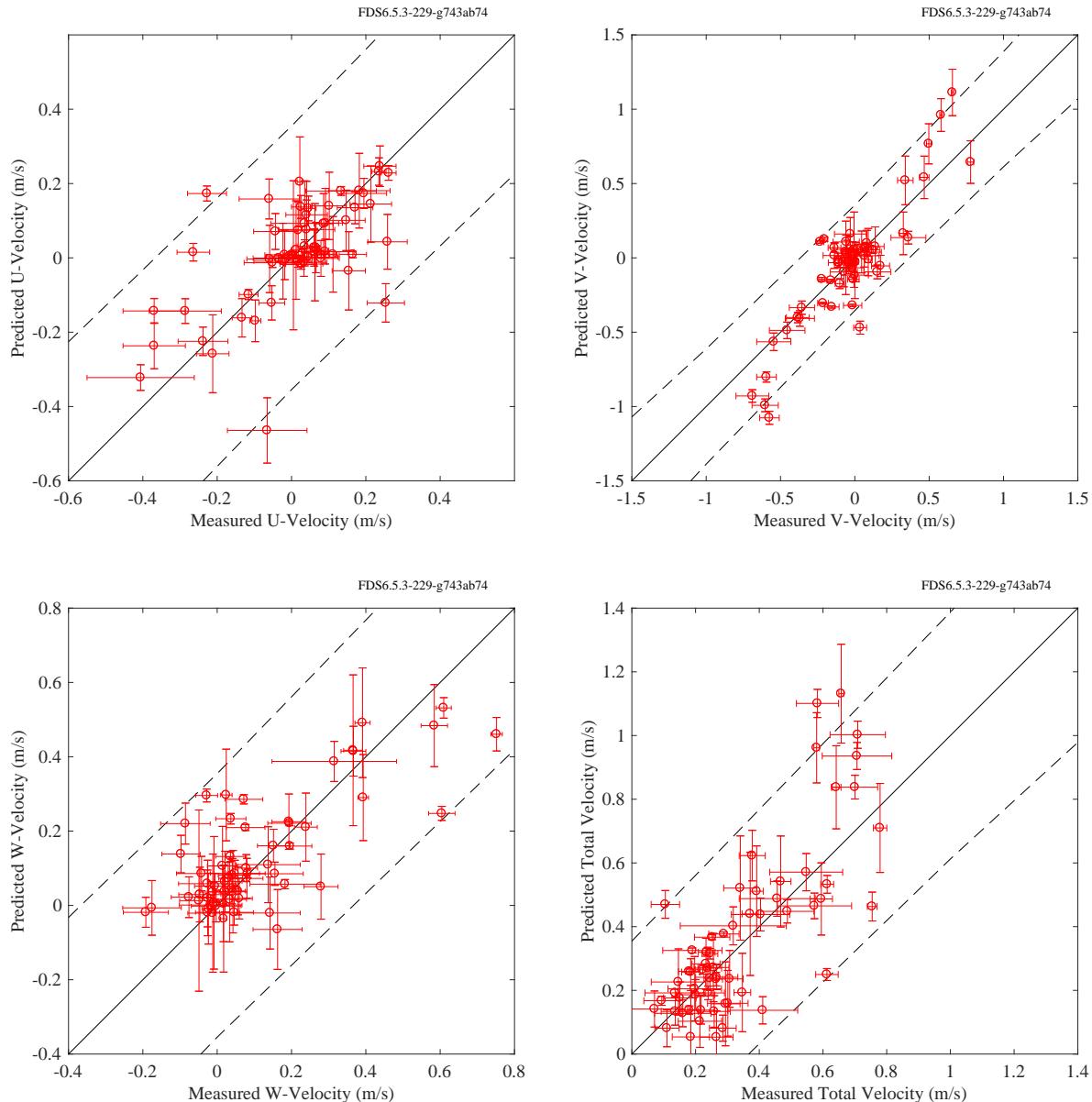


Figure 8.9: FM/FPRF experiments, gas velocity, low fan rate.

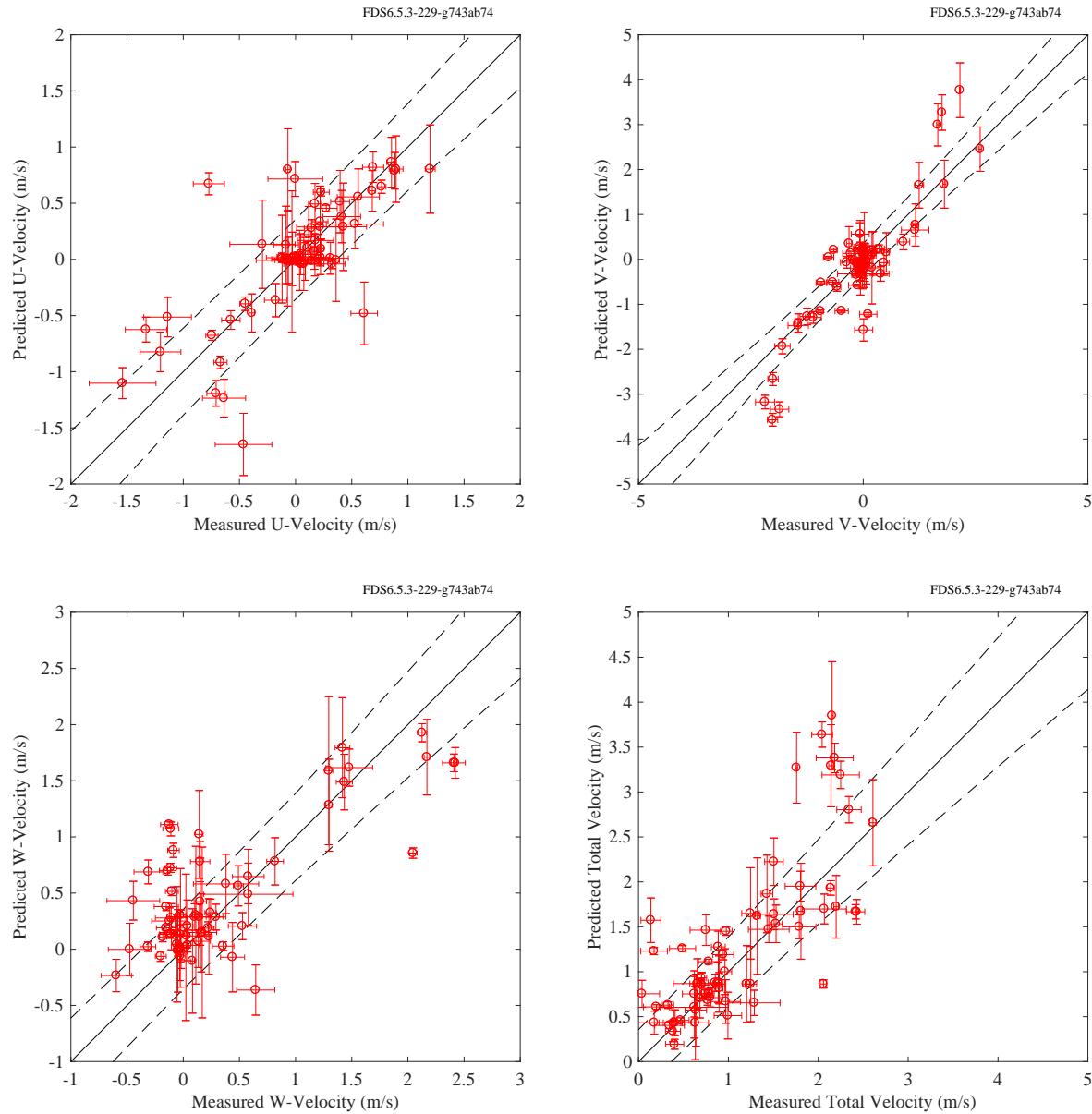


Figure 8.10: FM/FPRF experiments, gas velocity, high fan rate.

## 8.5 McCaffrey's Plume Correlation

The following plots show the results of simulations of McCaffrey's five fires at three grid resolutions,  $D^*/\delta x = [5, 10, 20]$  (note this resolution index is used to label the legend entries). The mesh cells are cubic and the spacing is uniform (no stretching).

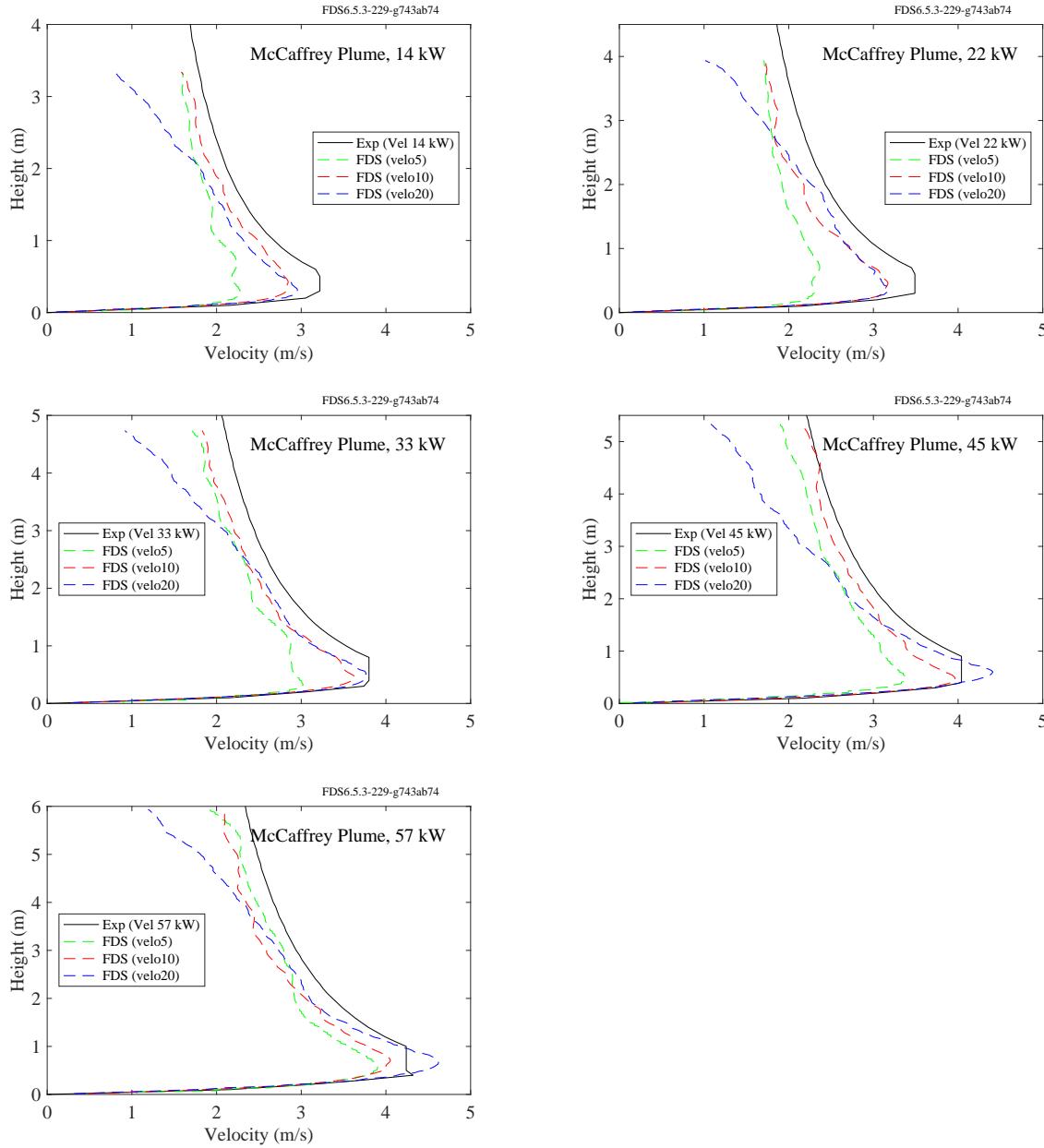


Figure 8.11: McCaffrey experiments, centerline plume velocity.

## 8.6 PRISME DOOR Experiments

Bi-directional probes were placed in the doorway separating the two compartments of the PRISME DOOR experiments. Shown on the plots below are the uppermost and lowest measurement points.

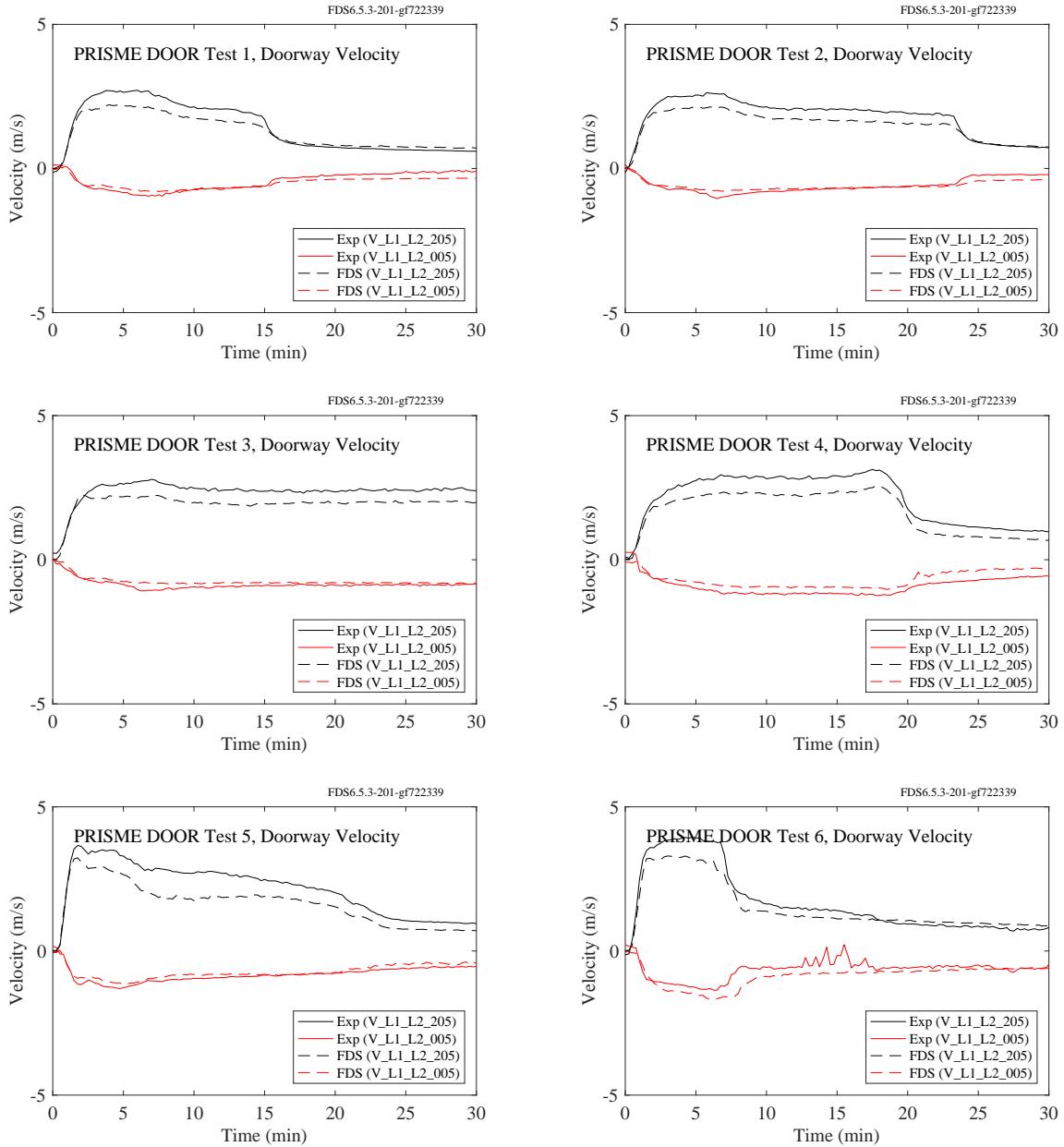


Figure 8.12: PRISME DOOR experiments, gas velocity.

## 8.7 Restivo Experiment

The results of a simulation of Restivo's room ventilation experiment are presented below. To capture the forced inlet flow, the volume near the supply slot needs a fairly fine grid to capture the mixing of air at the shear layer. For the results shown here, the height of the inlet was spanned with 6 grid cells, roughly 3 cm in the vertical dimension, 6 cm in the other two. Finer grids were used in the Musser study [38], but with no appreciable change in results. The component of velocity in the lengthwise direction was measured in four arrays: two vertical arrays located 3 m and 6 m from the inlet along the centerline of the room, and two horizontal arrays located 8.4 cm above the floor and below the ceiling, respectively. These measurements were taken using hot-wire anemometers. While data on the specific instrumentation used are not readily available, hot-wire systems tend to have limitations at low velocities, with typical thresholds of approximately 0.1 m/s.

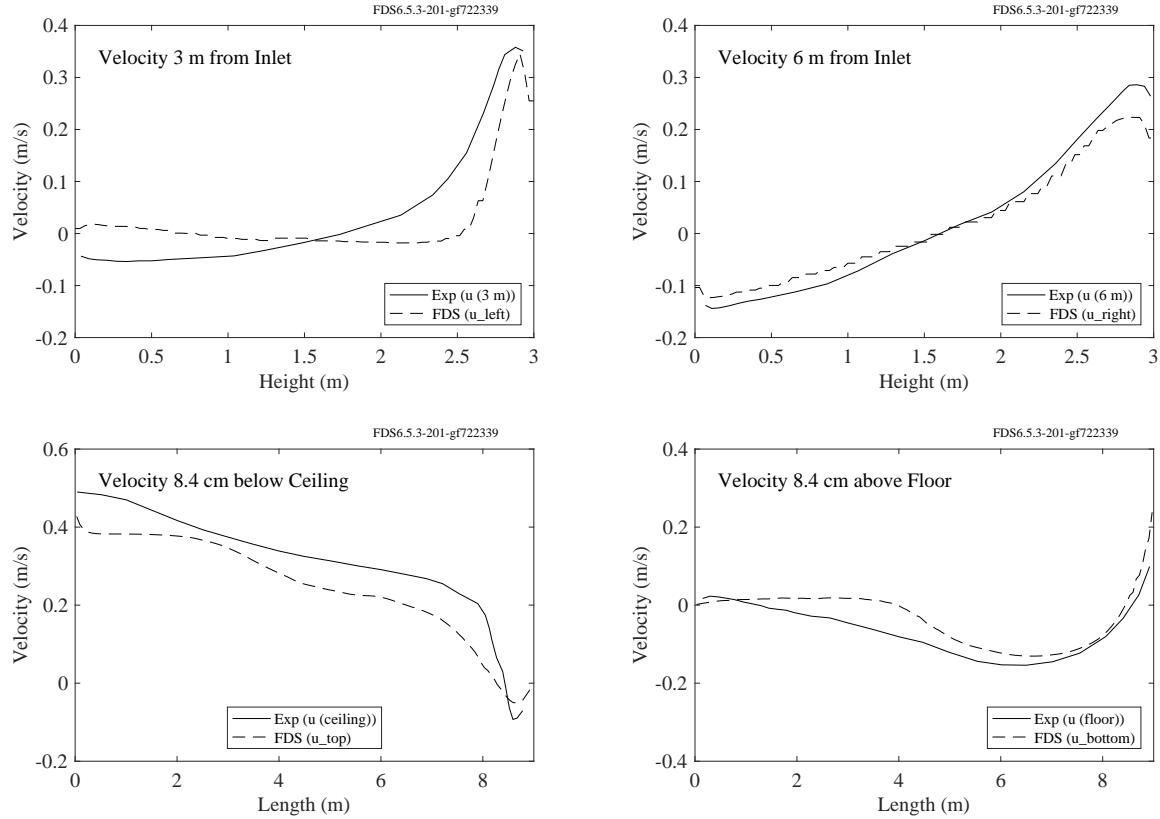


Figure 8.13: Restivo experiment, gas velocity.

## 8.8 Steckler Compartment Experiments

Steckler et al. [201] mapped the doorway/window flows in 55 compartment fire experiments. The test matrix is presented in Table 3.6. Shown on the following pages are the centerline velocity profiles, compared with model predictions. Off-center profiles are not considered. The vertical spacing of the measurements was approximately 11 cm, with the uppermost velocity probe centered 5.7 cm below the 10 cm thick soffit. The FDS simulations were uniformly gridded with cells of 5 cm on each side. To quantify the difference between prediction and measurement, the maximum outward velocities, which always occurred at the uppermost measurement location, were compared. It has been found that relatively minor changes in the velocity boundary conditions at the edges and bottom of the door soffit can have a noticeable impact on these results.

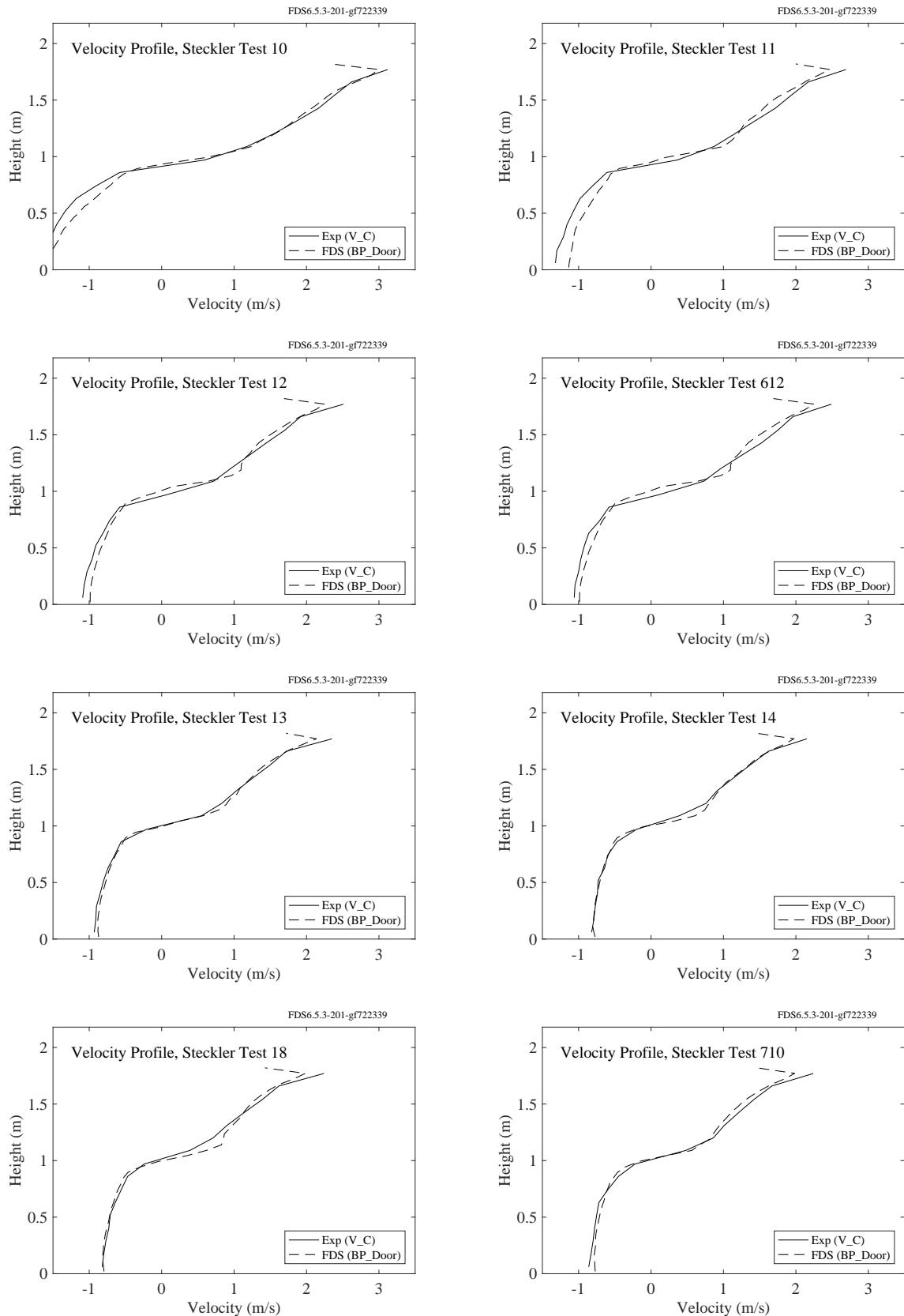


Figure 8.14: Steckler experiments, velocity profiles, Tests 10, 11, 12, 13, 14, 18, 612, 710.

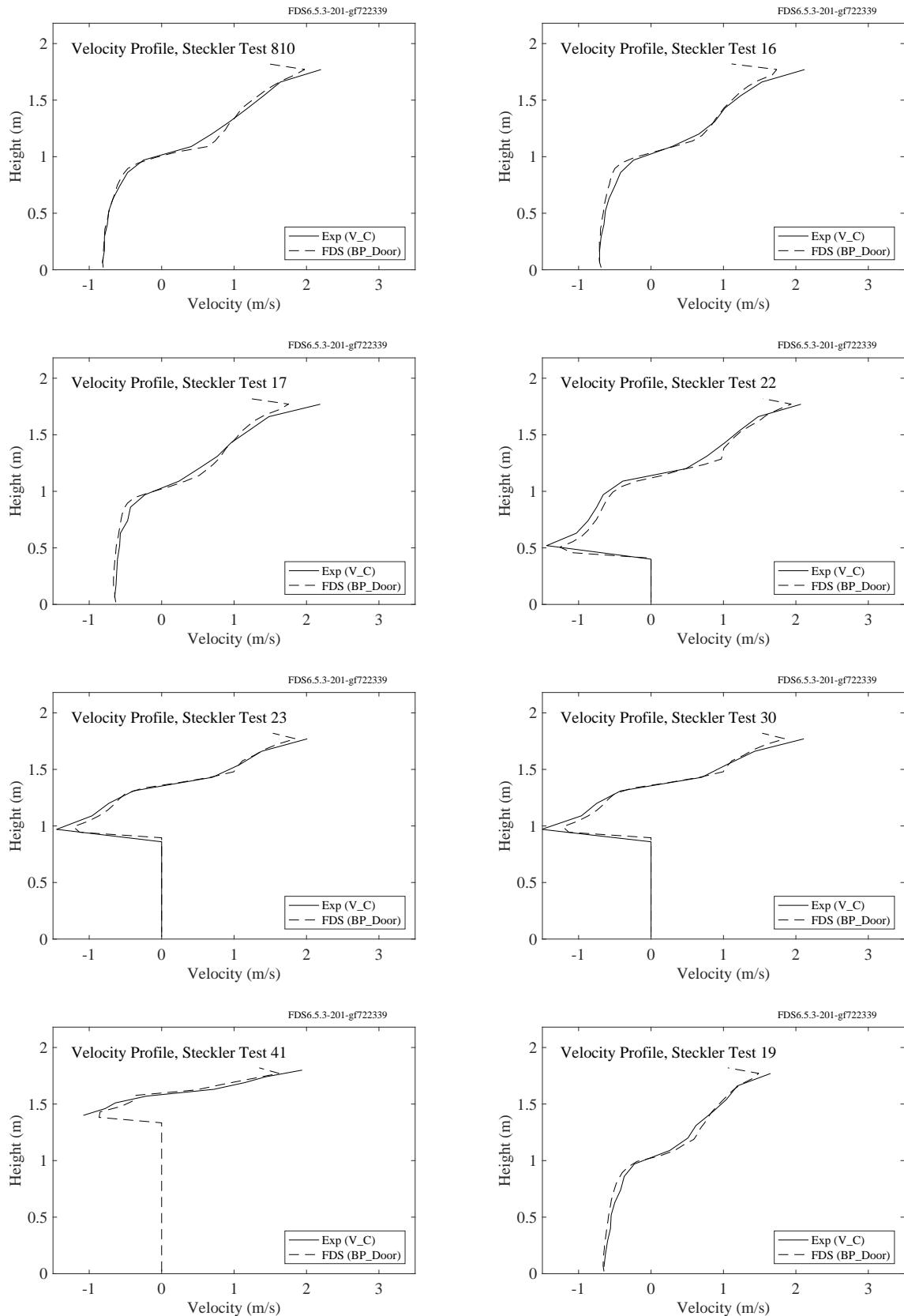


Figure 8.15: Steckler experiments, velocity profiles, Tests 16, 17, 19, 22, 23, 30, 41, 810.

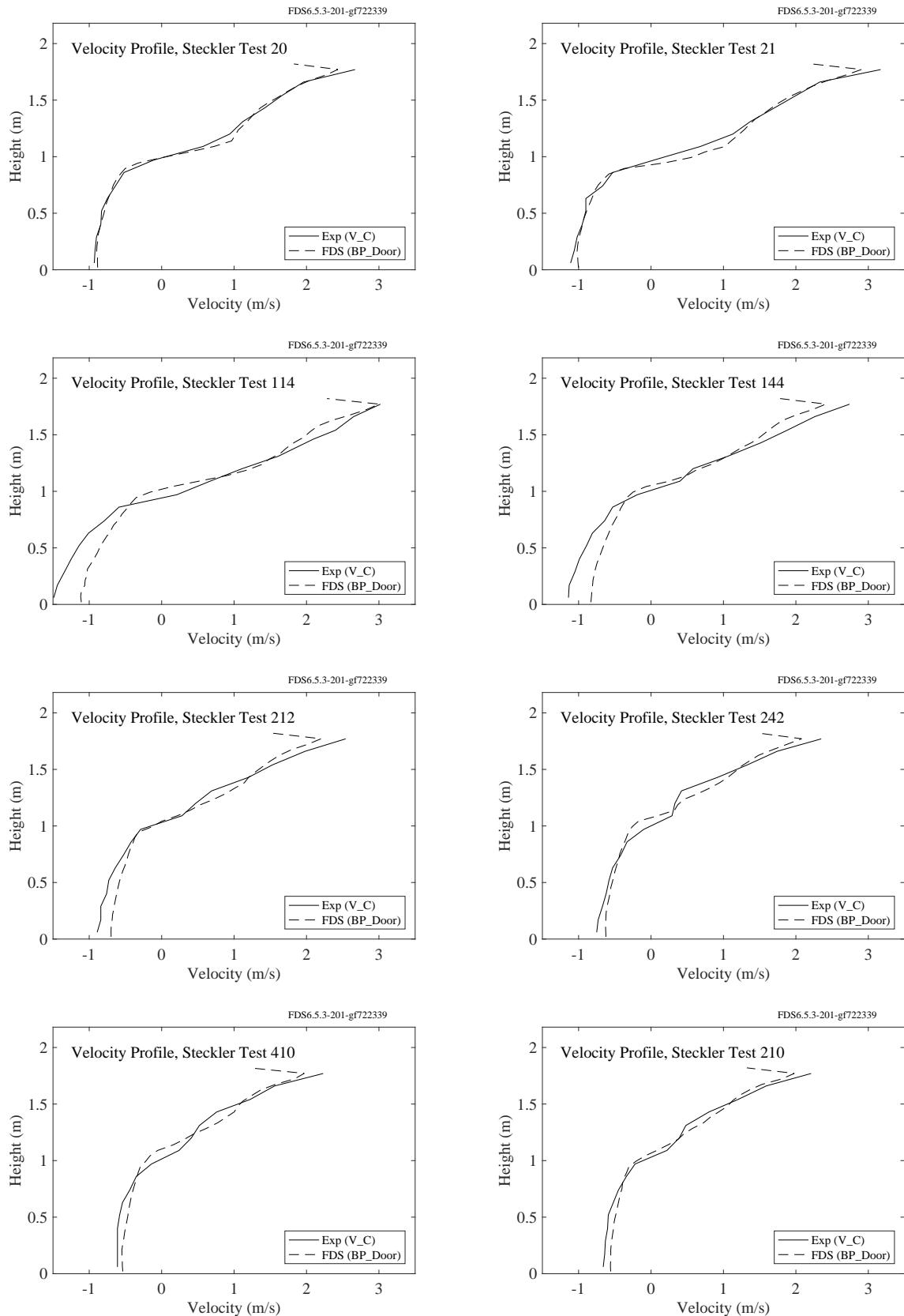


Figure 8.16: Steckler experiments, velocity profiles, Tests 20, 21, 114, 144, 210, 212, 242, 410.

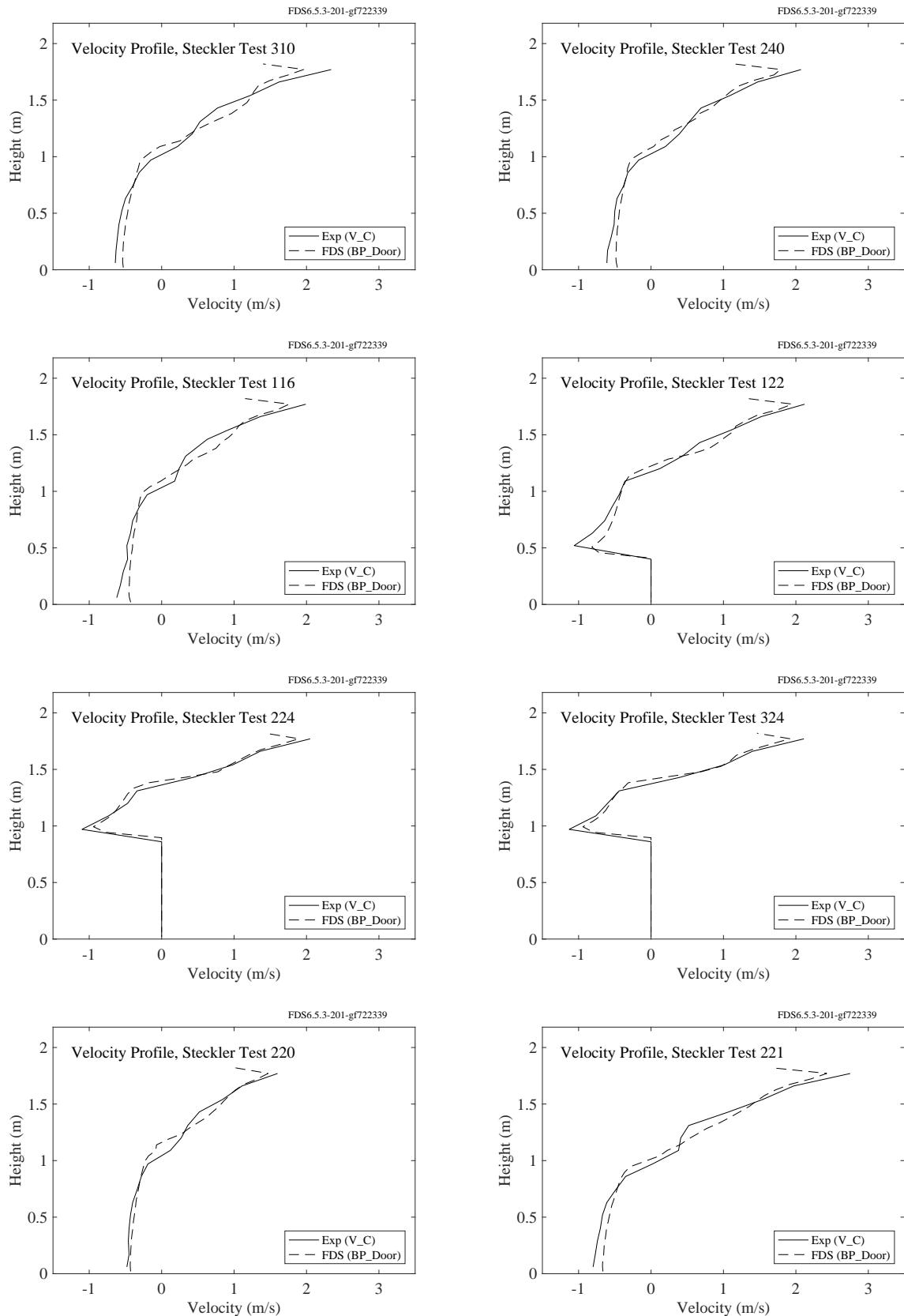


Figure 8.17: Steckler experiments, velocity profiles, Tests 116, 122, 220, 221, 224, 240, 310, 324.

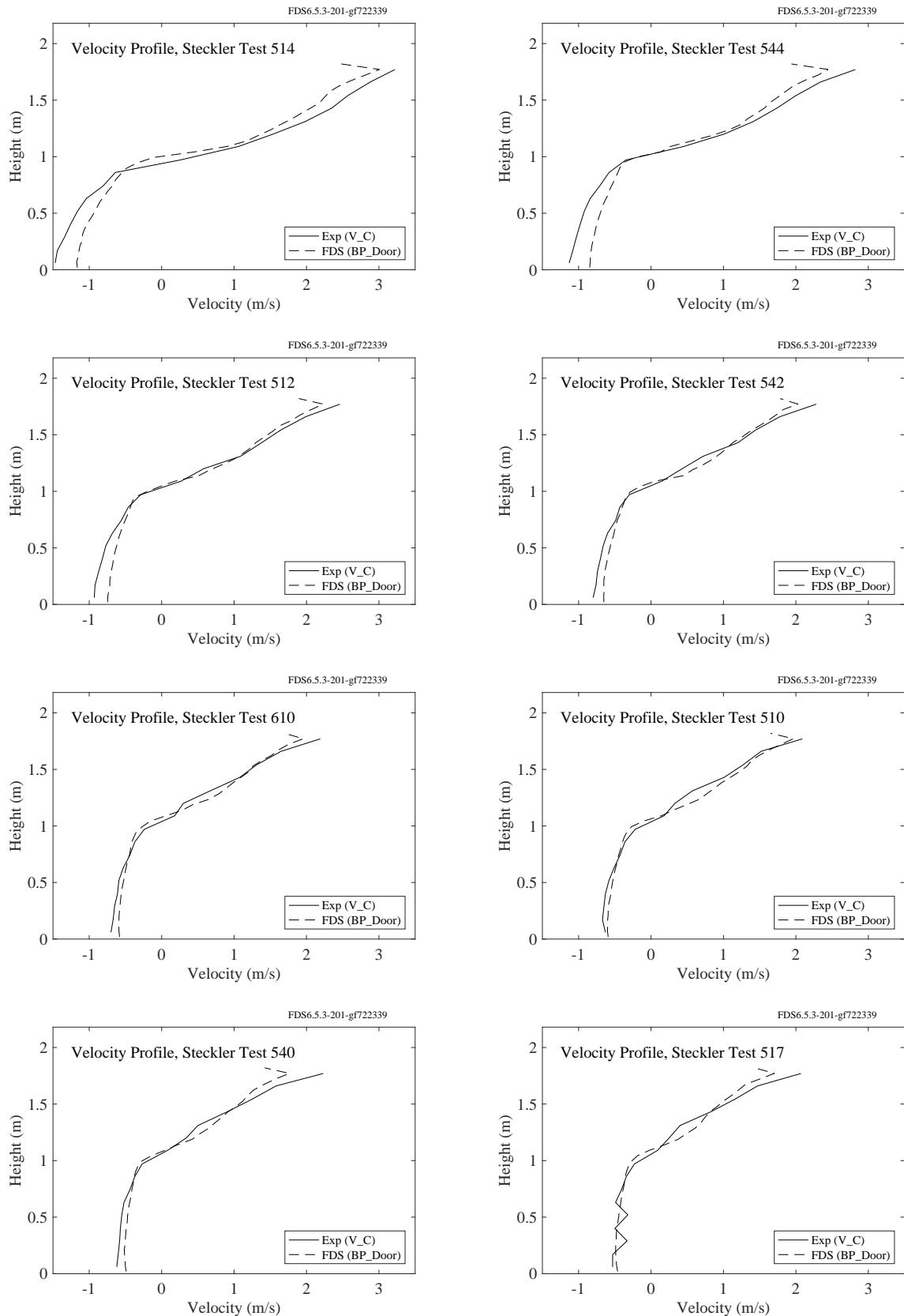


Figure 8.18: Steckler experiments, velocity profiles, Tests 510, 512, 514, 517, 540, 542, 544, 610.

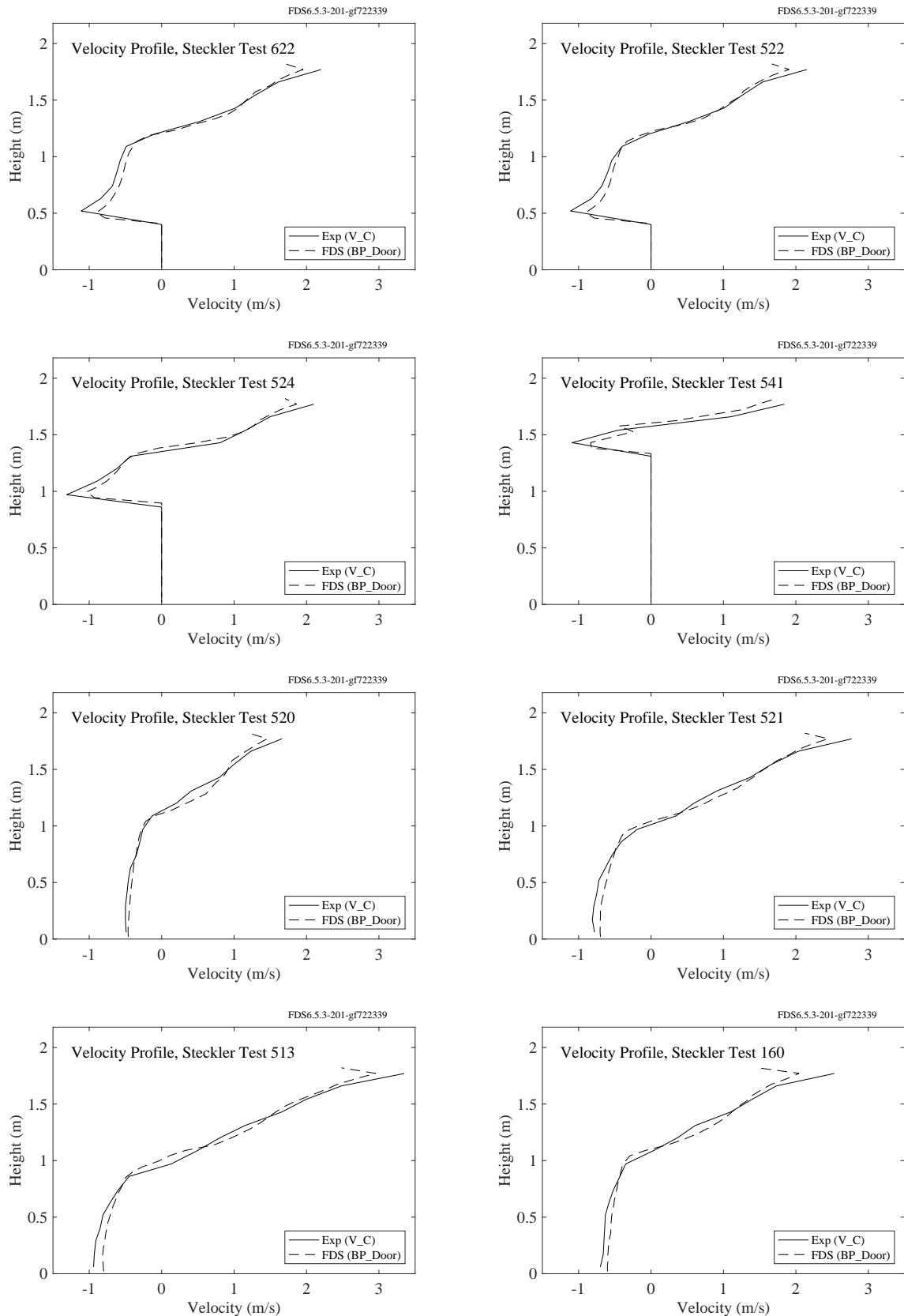


Figure 8.19: Steckler experiments, velocity profiles, Tests 160, 513, 520, 521, 522, 524, 541, 622.

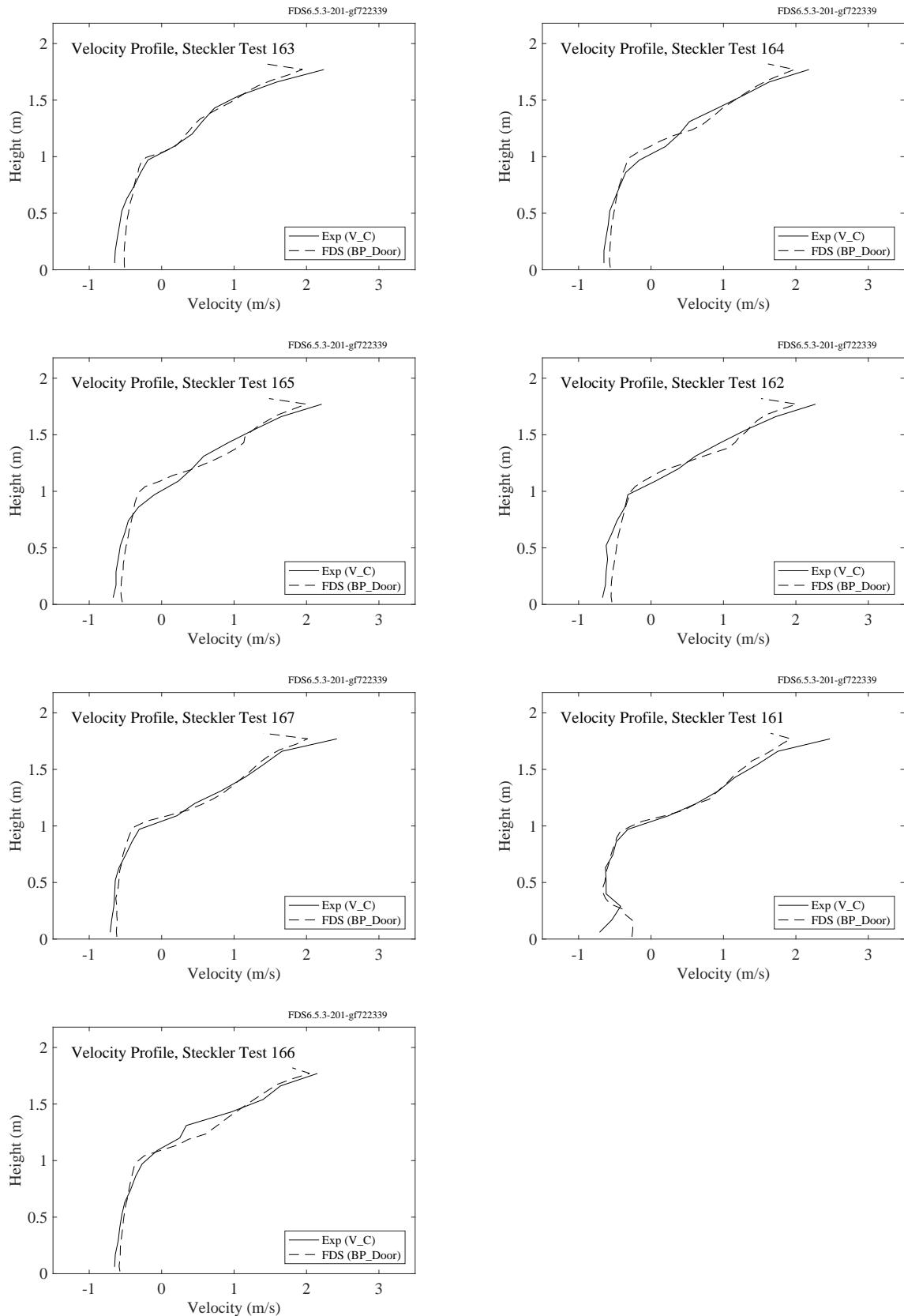


Figure 8.20: Steckler experiments, velocity profiles, Tests 161, 162, 163, 164, 165, 166, 167.

## 8.9 WTC Experiments

Bi-directional probes were positioned inside two of the four inlet openings and three of the four outlet openings. The locations are shown in Fig. 8.21. Exact dimensions are given in Ref. [69].

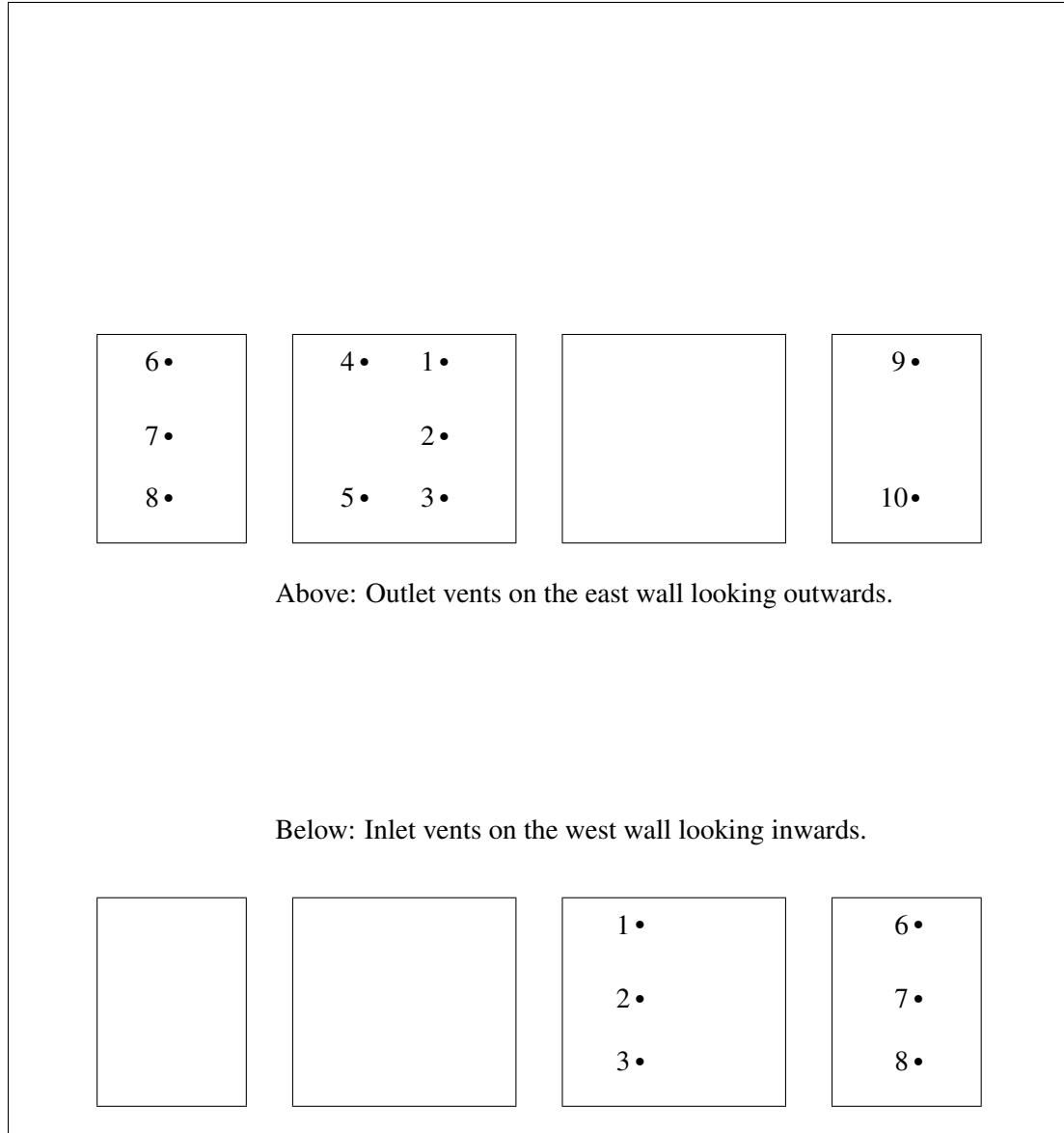


Figure 8.21: Layout of the bi-directional probes in the inlet (west wall) and outlet (east wall) vents, WTC Experiments.

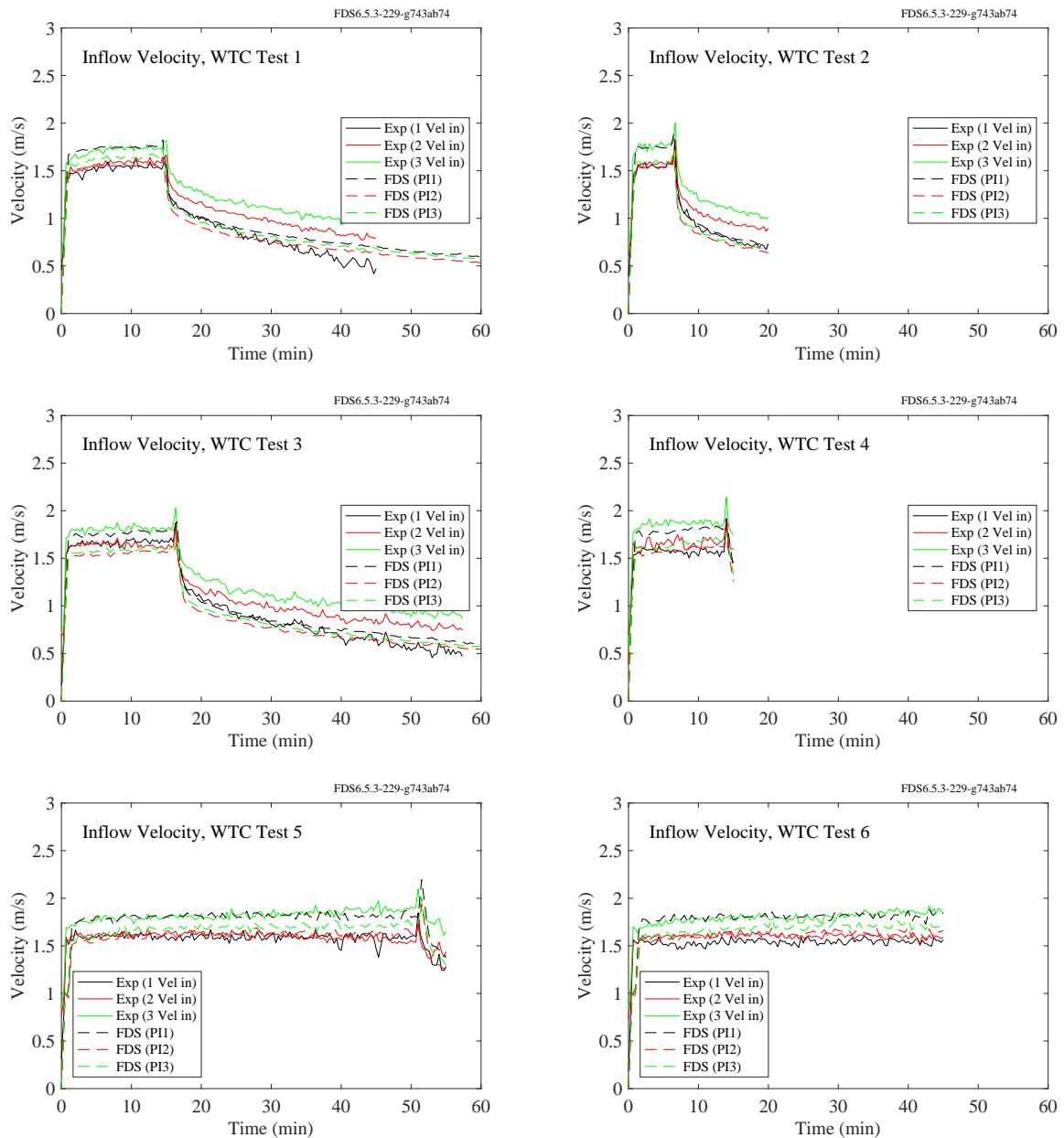


Figure 8.22: WTC experiments, inlet velocity, Points 1-3.

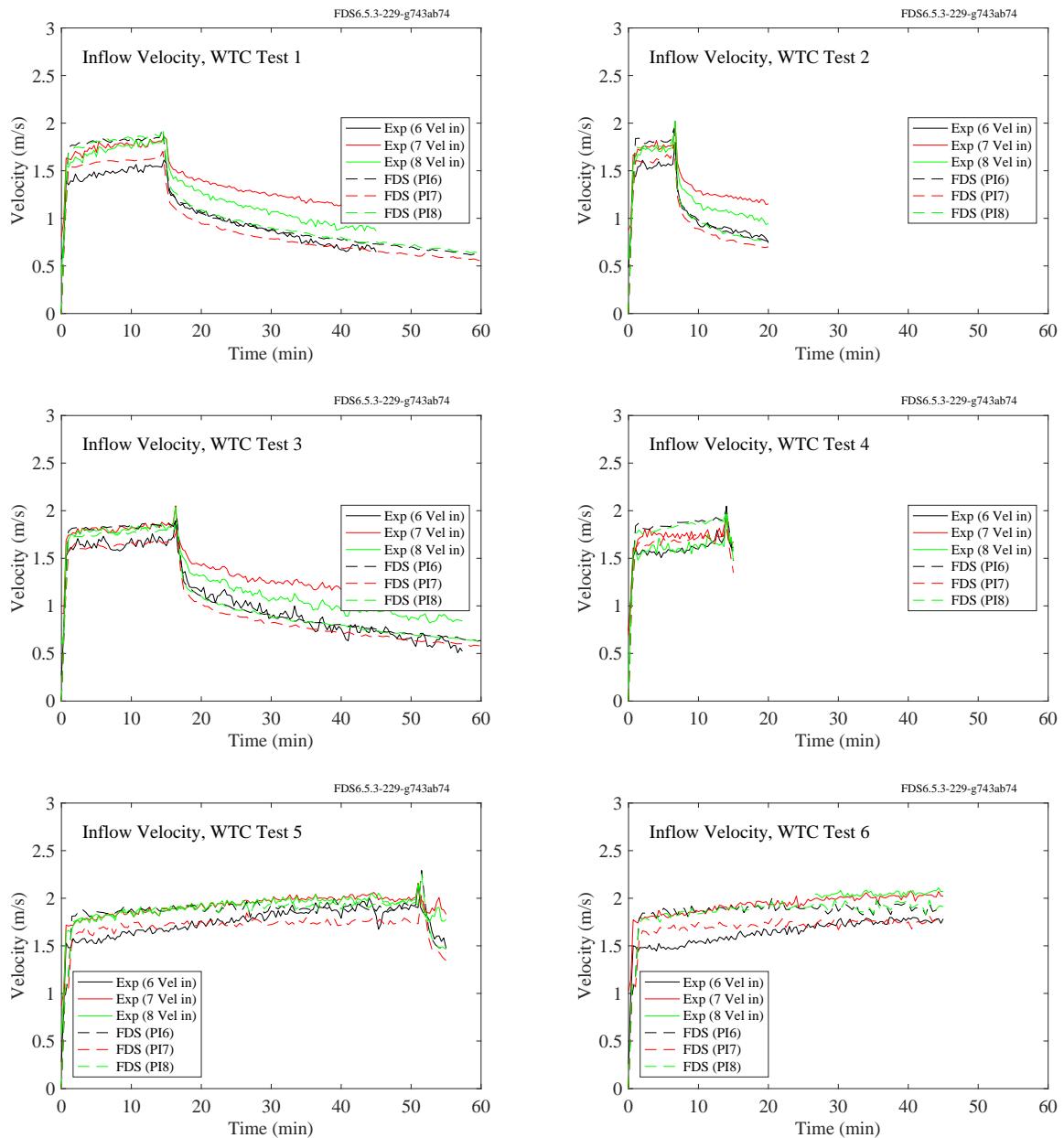


Figure 8.23: WTC experiments, inlet velocity, Points 6-8.

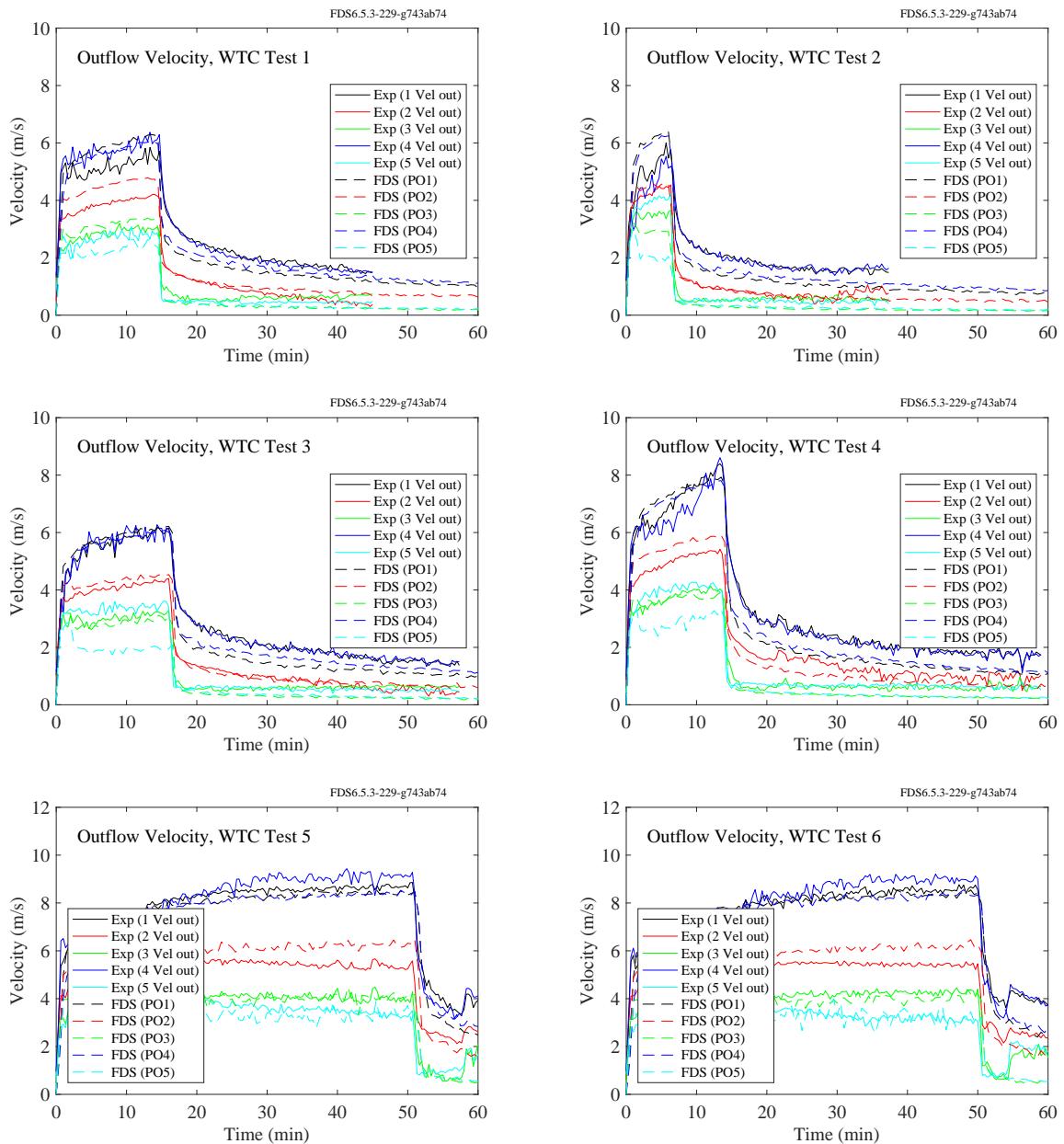


Figure 8.24: WTC experiments, outlet velocity, Points 1-5.

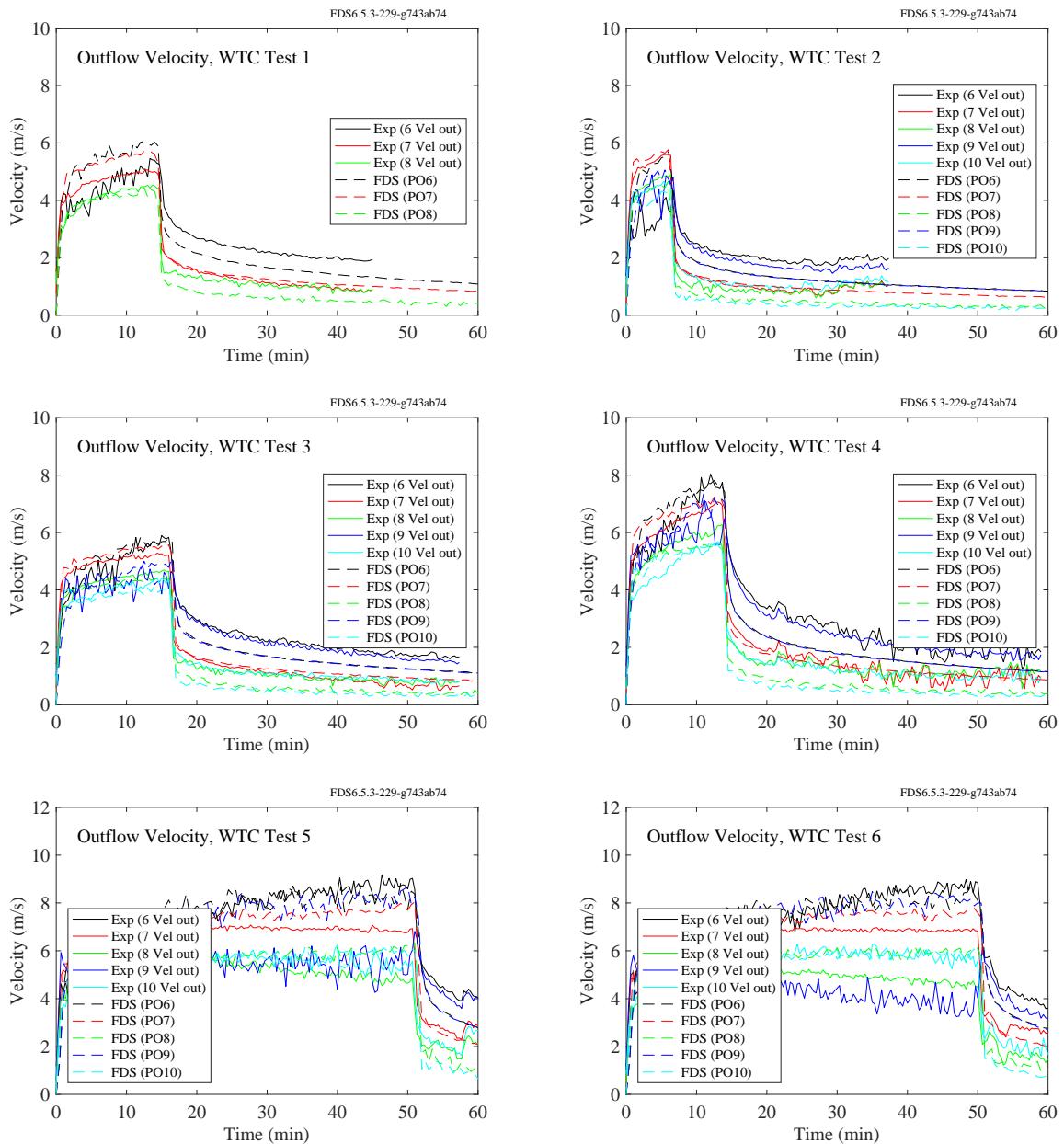


Figure 8.25: WTC experiments, outlet velocity, Points 6-10.

## 8.10 Summary of Velocity Predictions

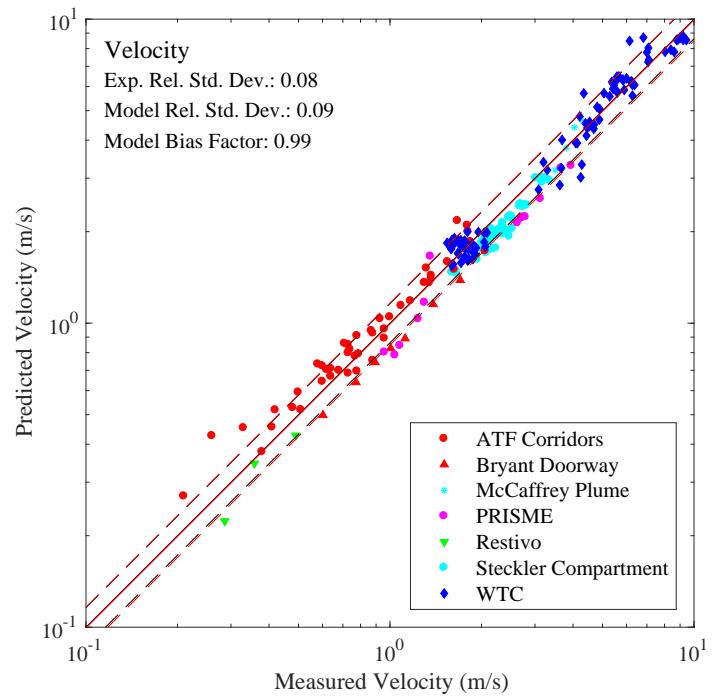


Figure 8.26: Summary of comparisons of predicted and measured maximum velocities.



## **Chapter 9**

# **Gas Species and Smoke**

For most applications, FDS uses a single step, mixing-controlled combustion model. The products of combustion are “lumped” together and tracked as a single gas mixture. These products include CO<sub>2</sub>, H<sub>2</sub>O, CO, and soot. However, in some cases, the combustion is incomplete due to a lack of oxygen. In others, a multiple-step reaction scheme is used to predict the production of CO.

### **9.1 Major Combustion Products, O<sub>2</sub> and CO<sub>2</sub>**

For any hydrocarbon fuel, the major combustion products are oxygen and carbon dioxide. Accurate predictions of these gases requires knowledge of the chemical composition of the fuel and an accurate transport algorithm for the combustion products.

### 9.1.1 DelCo Trainers

Oxygen and carbon dioxide measurements were made at several locations in the one and two level DelCo training structures. See Section 3.11 for their exact locations.

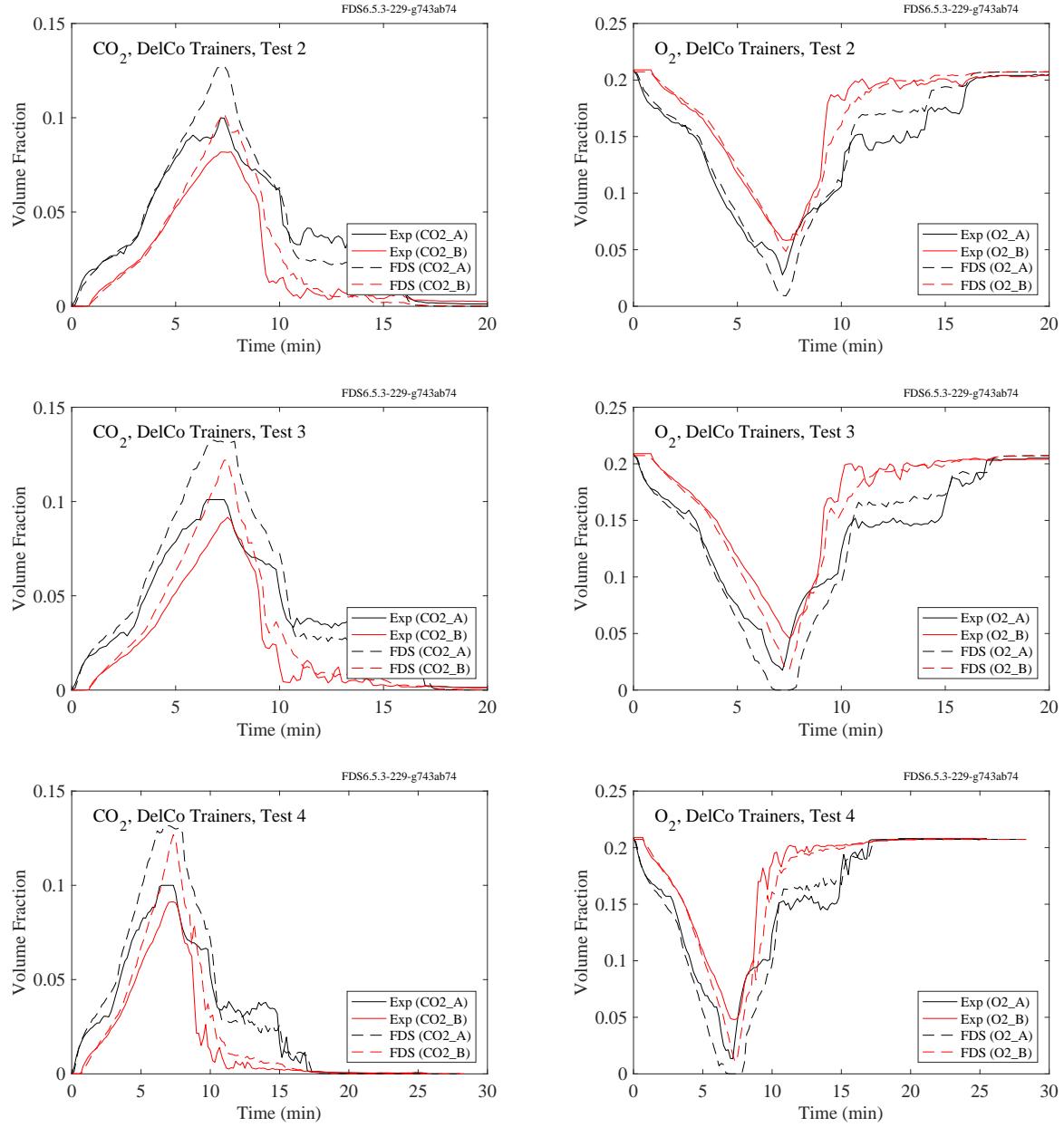


Figure 9.1: DelCo Trainers,  $\text{CO}_2$  and  $\text{O}_2$  concentration, Tests 2-4.

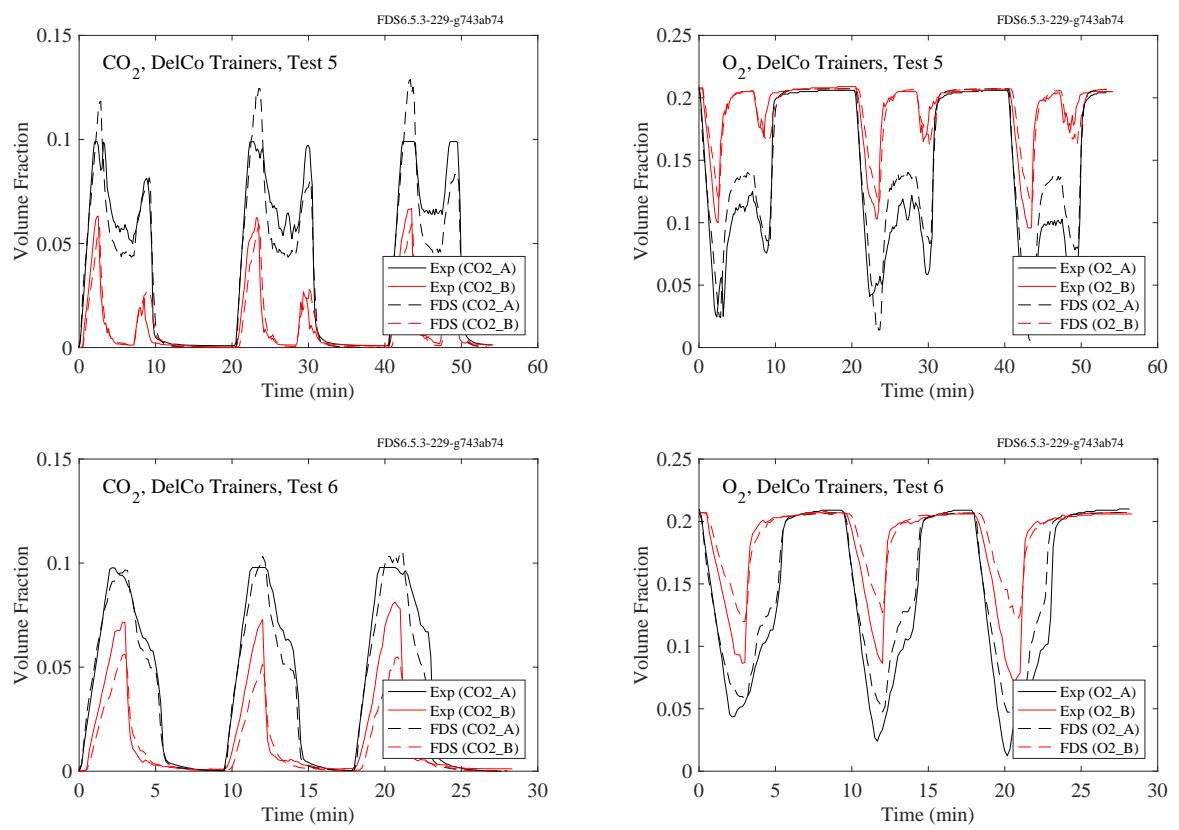


Figure 9.2: DelCo Trainers,  $\text{CO}_2$  and  $\text{O}_2$  concentration, Tests 5-6.

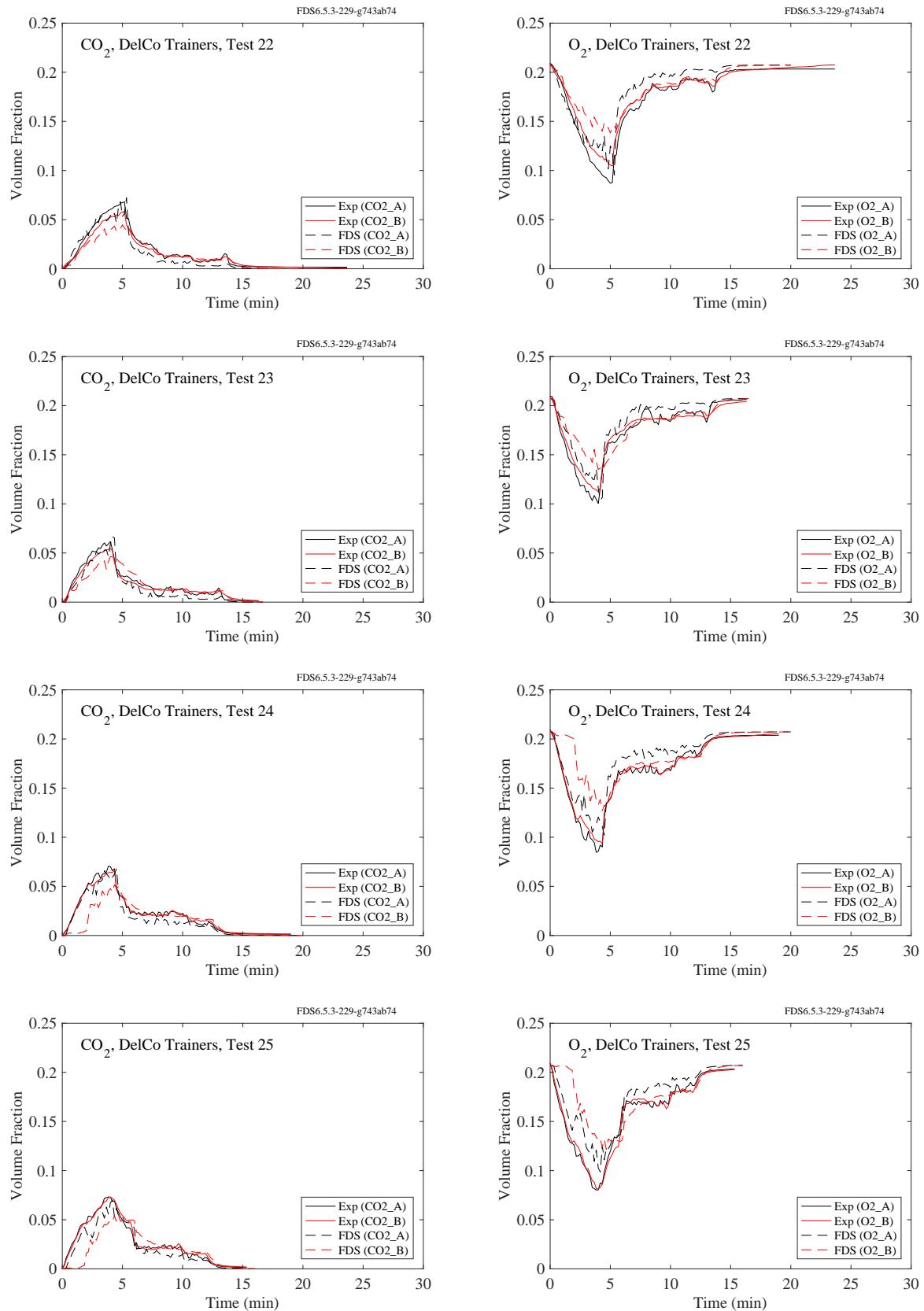


Figure 9.3: DelCo Trainers,  $\text{CO}_2$  and  $\text{O}_2$  concentration, Tests 22-25.

### 9.1.2 FAA Cargo Compartments

Carbon dioxide and carbon monoxide were measured near the ceiling in the forward, middle, and aft sections of the compartment. Note that all but the middle compartment concentrations were measured in Tests 2 and 3.

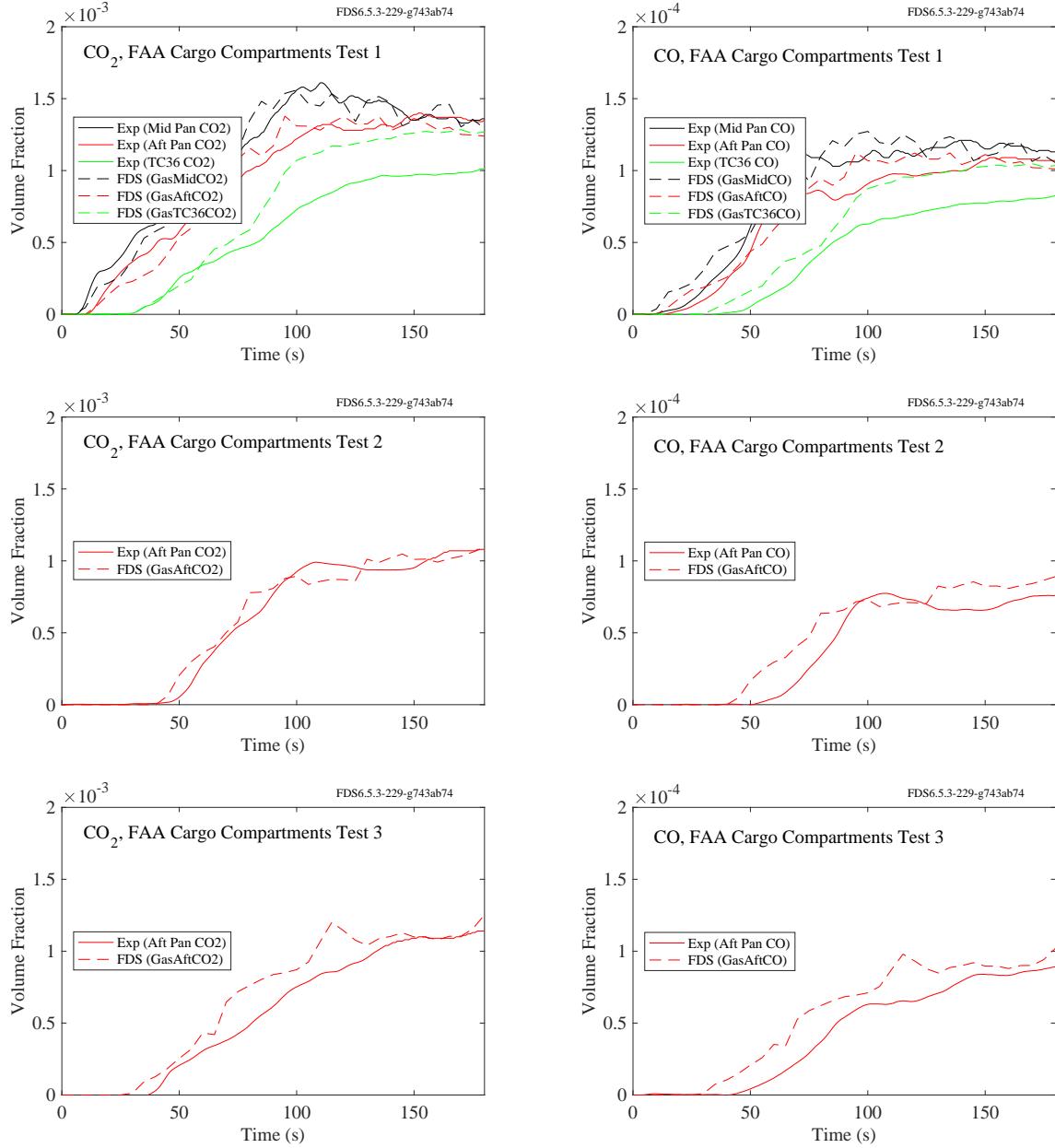


Figure 9.4: FAA Cargo Compartment experiments,  $\text{CO}_2$  and  $\text{O}_2$  concentration.

### 9.1.3 NIST/NRC Experiments

The following pages present comparisons of oxygen and carbon dioxide concentration predictions and measurements for the NIST/NRC series. There were two oxygen measurements, one in the upper layer, one in the lower. There was only one carbon dioxide measurement in the upper layer.

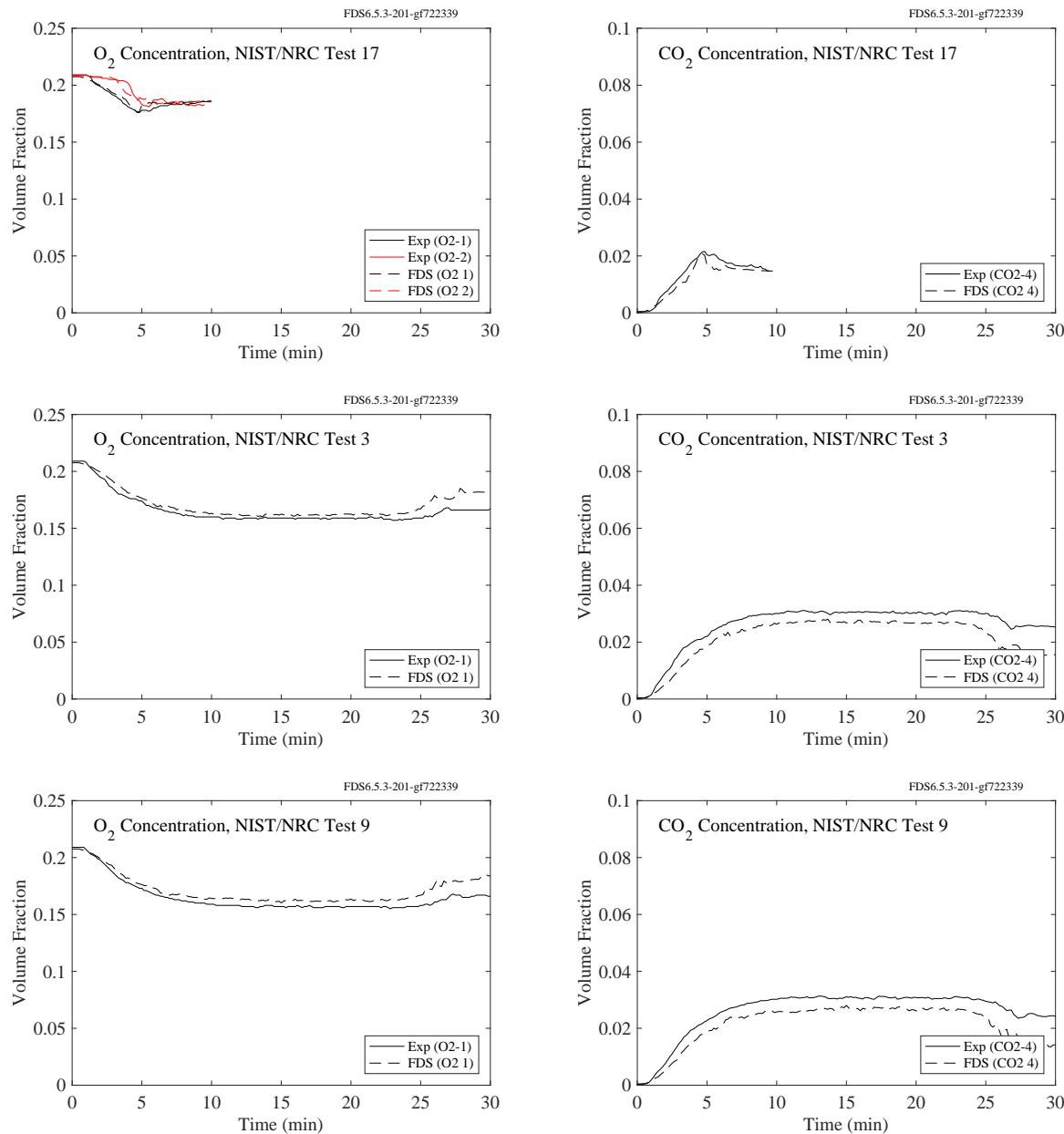


Figure 9.5: NIST/NRC experiments,  $CO_2$  and  $O_2$  concentration, Tests 3, 9, 17.

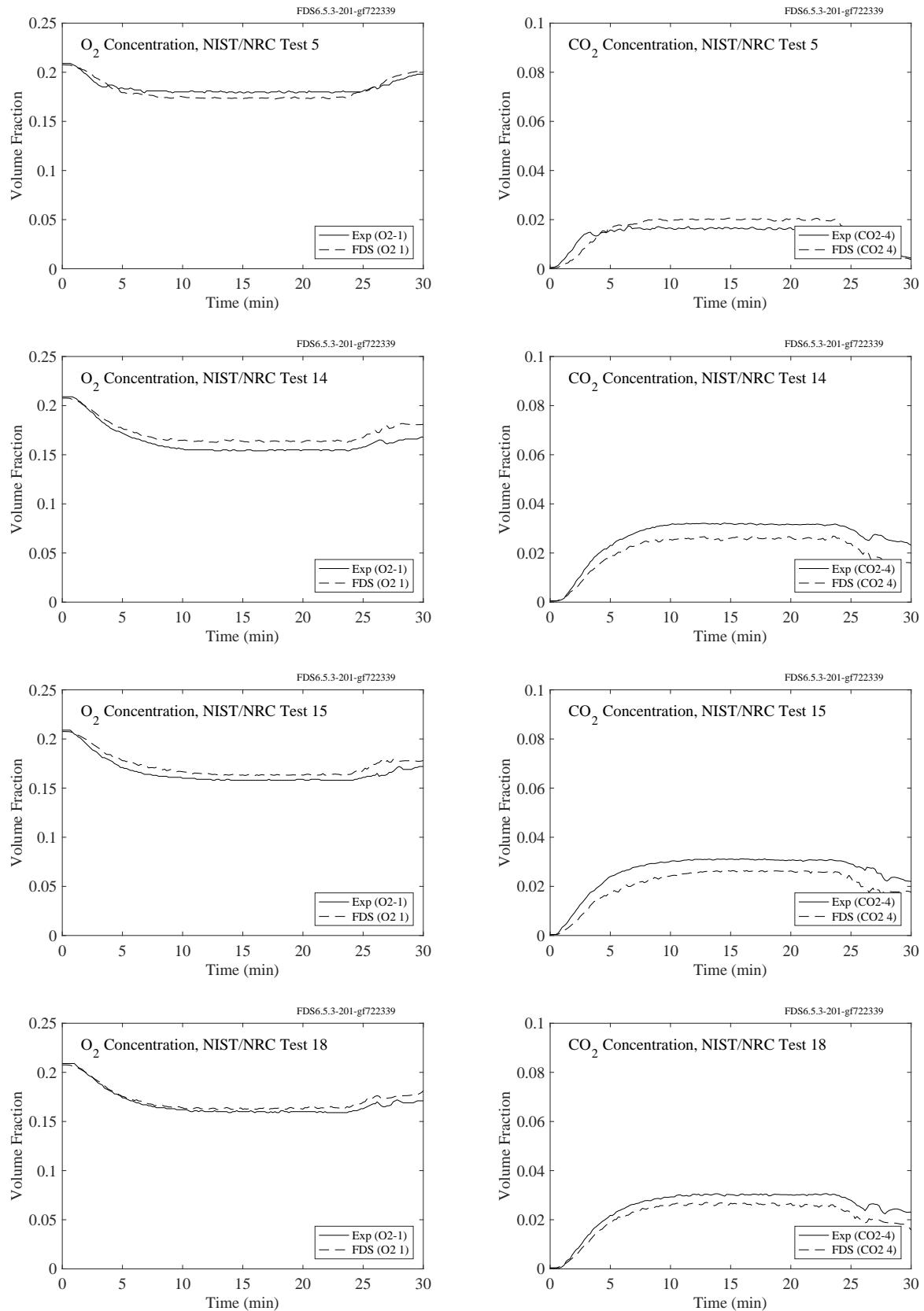


Figure 9.6: NIST/NRC experiments,  $CO_2$  and  $O_2$  concentration, Tests 5, 14, 15, 18.

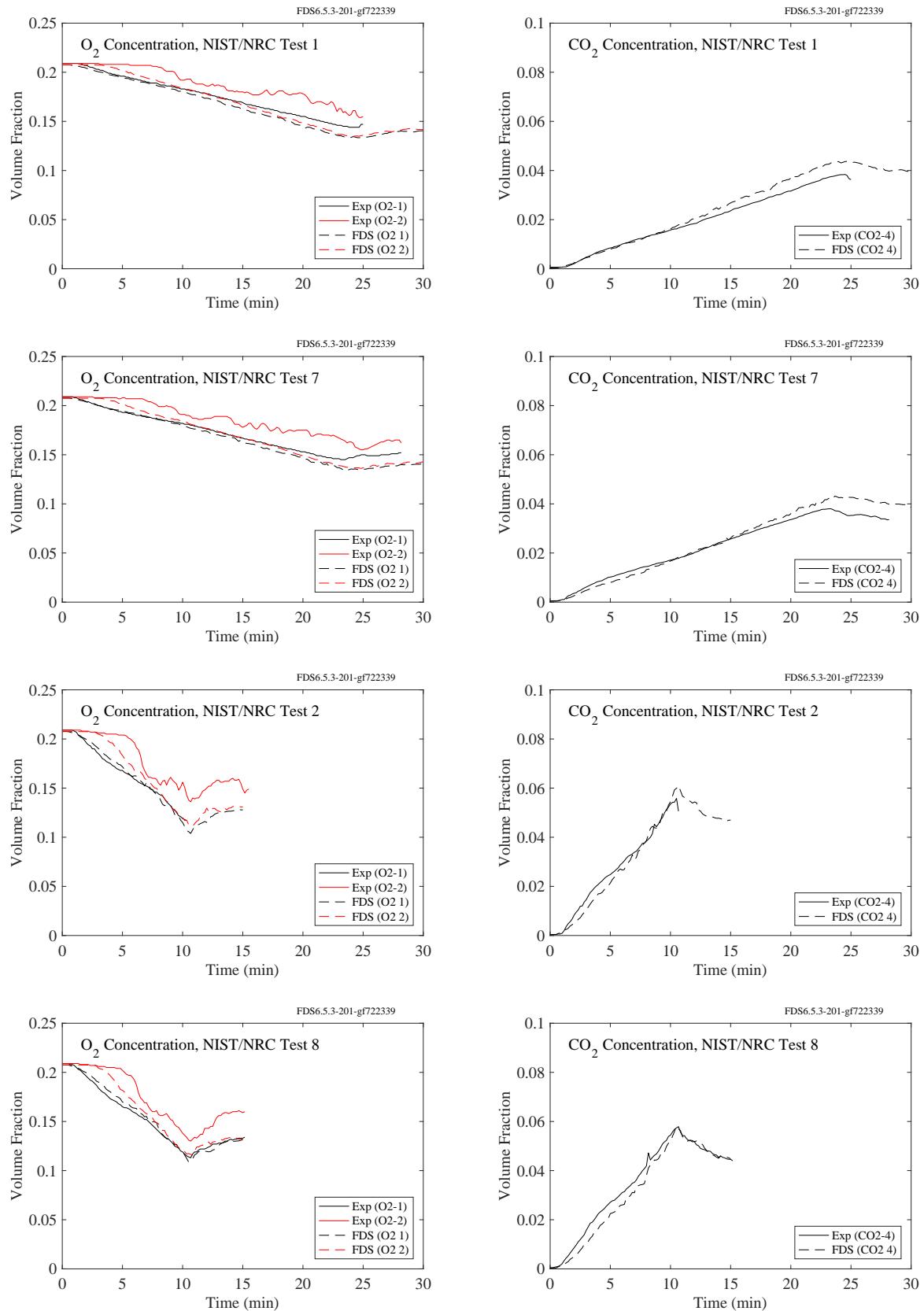


Figure 9.7: NIST/NRC experiments,  $CO_2$  and  $O_2$  concentration, Tests 1, 2, 7, 8.

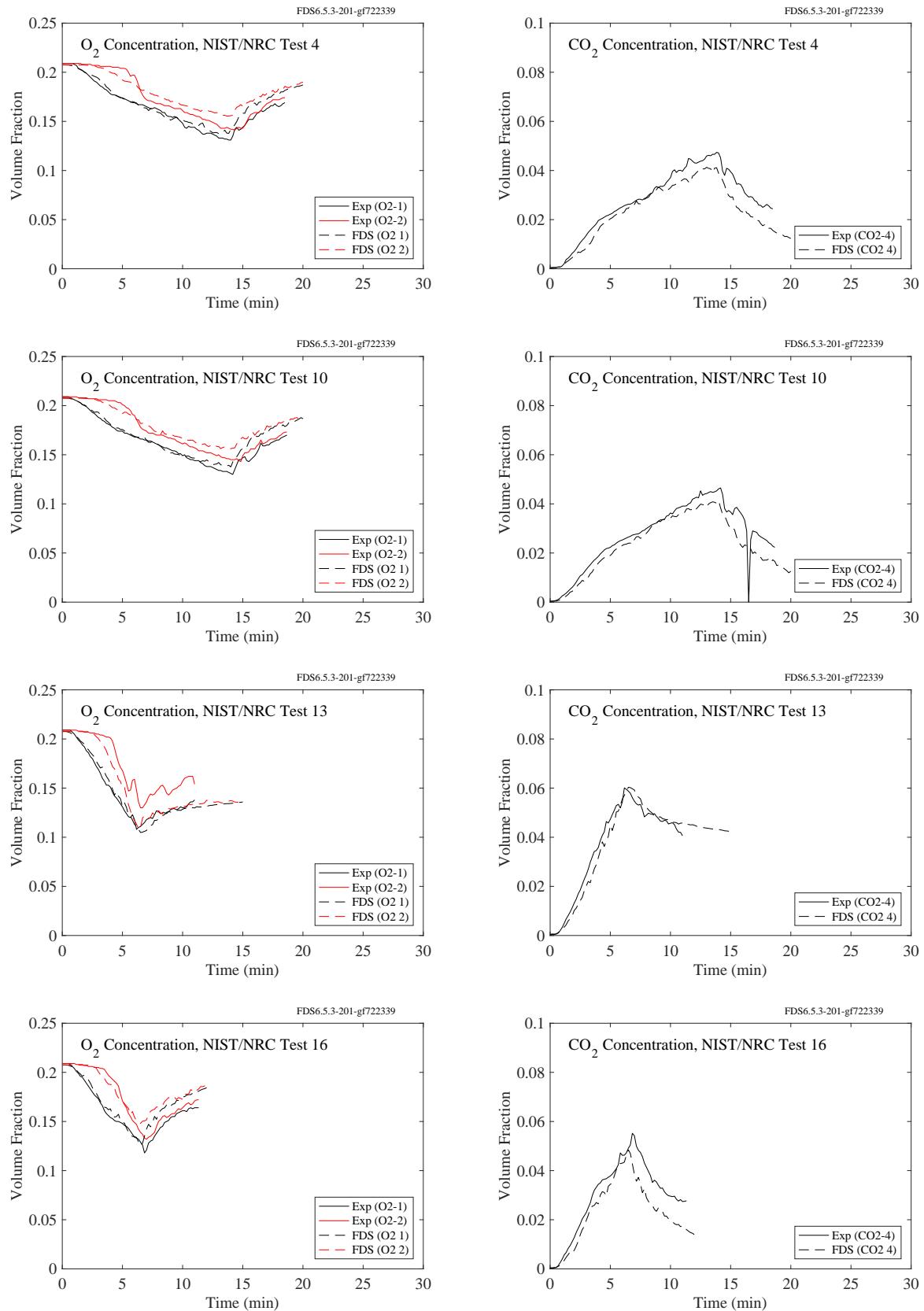


Figure 9.8: NIST/NRC experiments,  $\text{CO}_2$  and  $\text{O}_2$  concentration, Tests 4, 10, 13, 16.

### 9.1.4 NRCC Smoke Tower

In the NRCC Smoke Tower experiments, there were oxygen and carbon dioxide analysers in the stair shaft on the second floor just outside the door of the fire compartment.

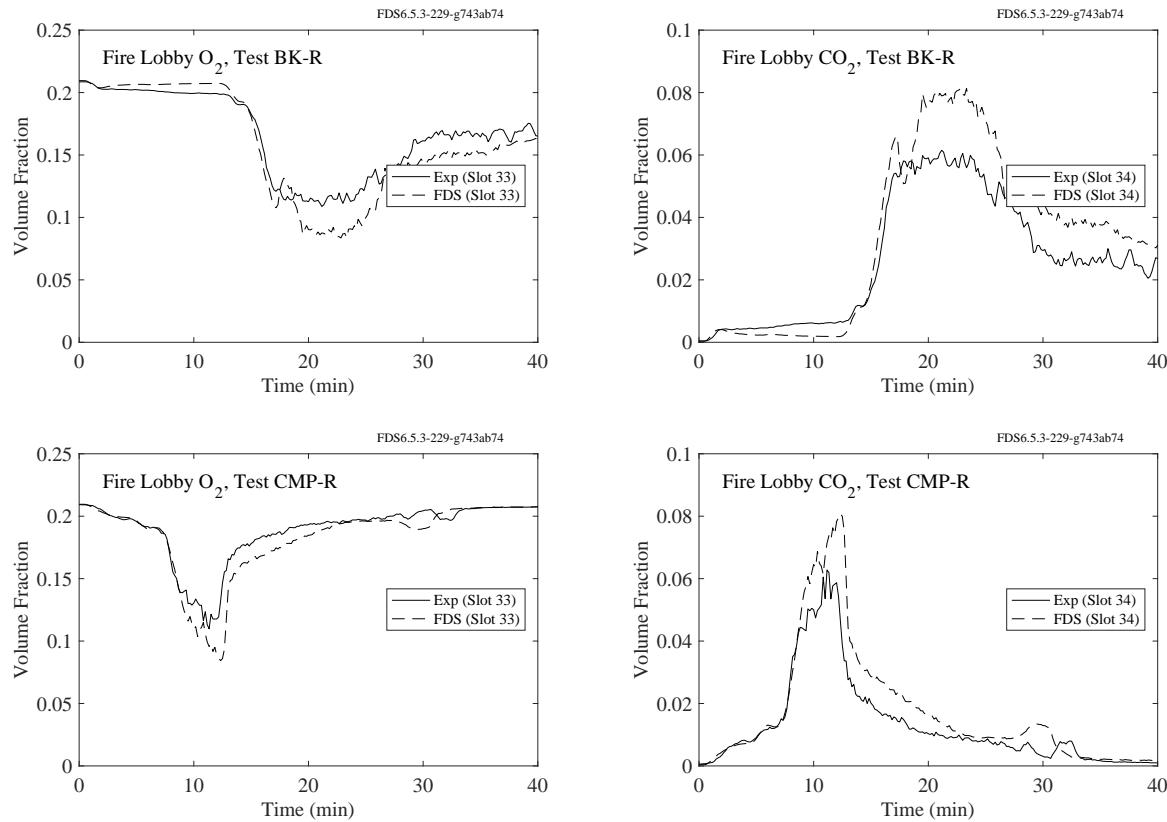


Figure 9.9: NRCC Smoke Tower,  $CO_2$  and  $O_2$  concentration, Tests BK-R and COMP-R.

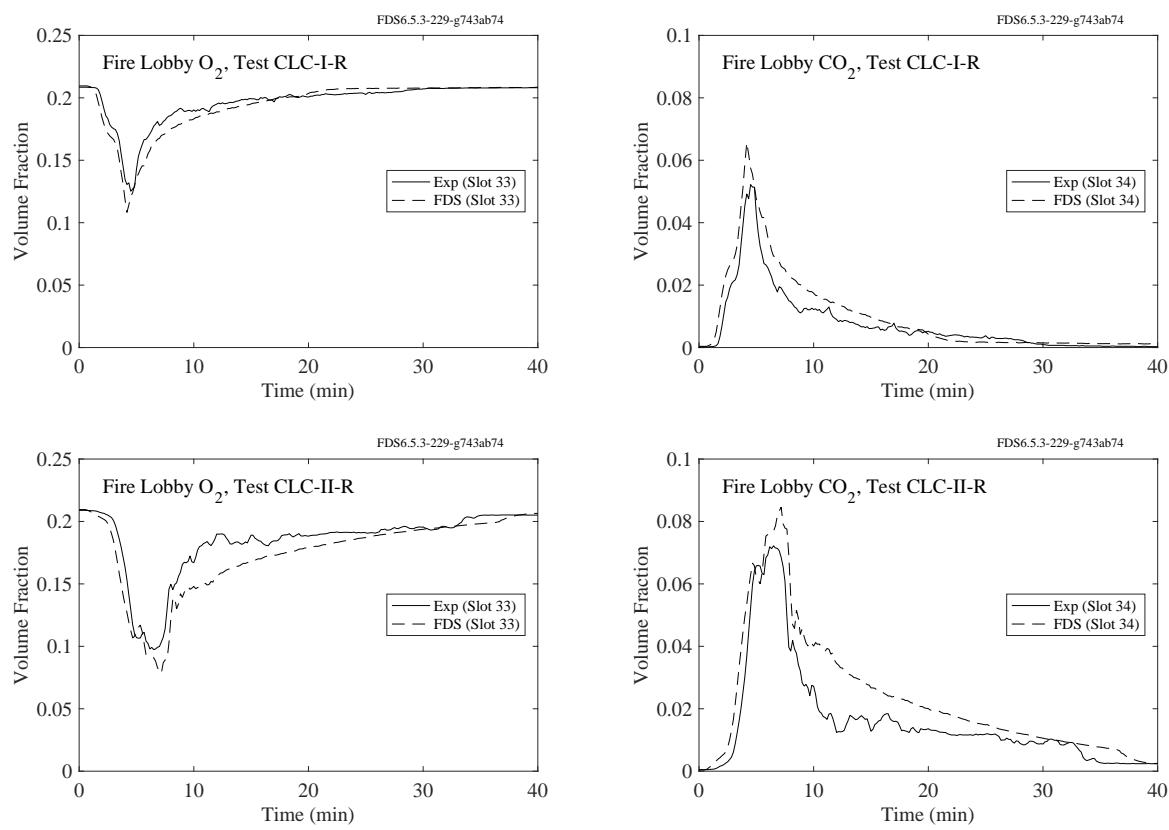


Figure 9.10: NRCC Smoke Tower,  $CO_2$  and  $O_2$  concentration, Tests CLC-I-R and CLC-II-R.

### 9.1.5 PRISME DOOR Experiments

Each compartment in the PRISME DOOR experiments contained an oxygen and carbon dioxide measurement in the upper (haut) and lower (bas) layers.

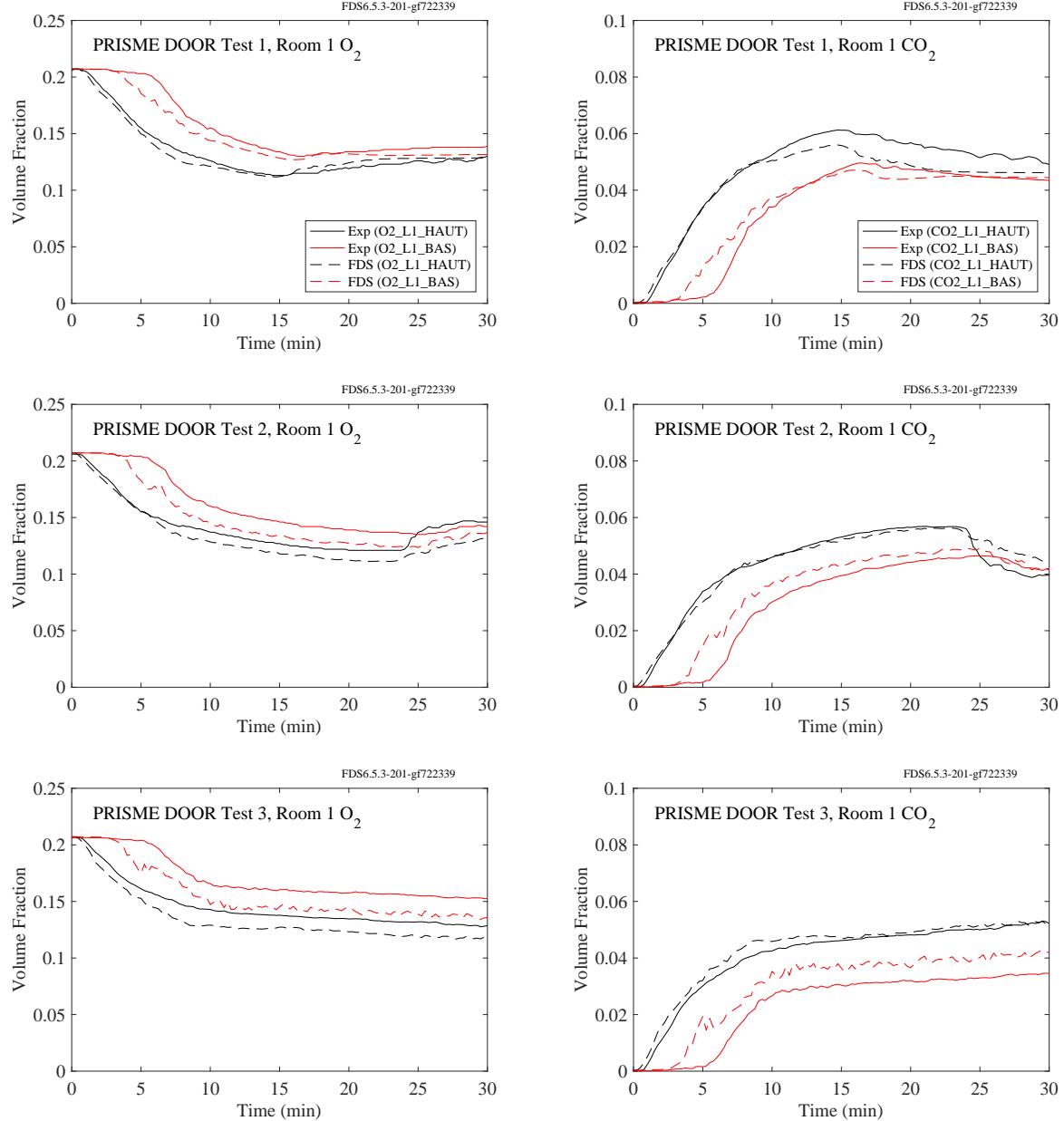


Figure 9.11: PRISME DOOR experiments,  $CO_2$  and  $O_2$  concentration, Room 1, Tests 1-3.

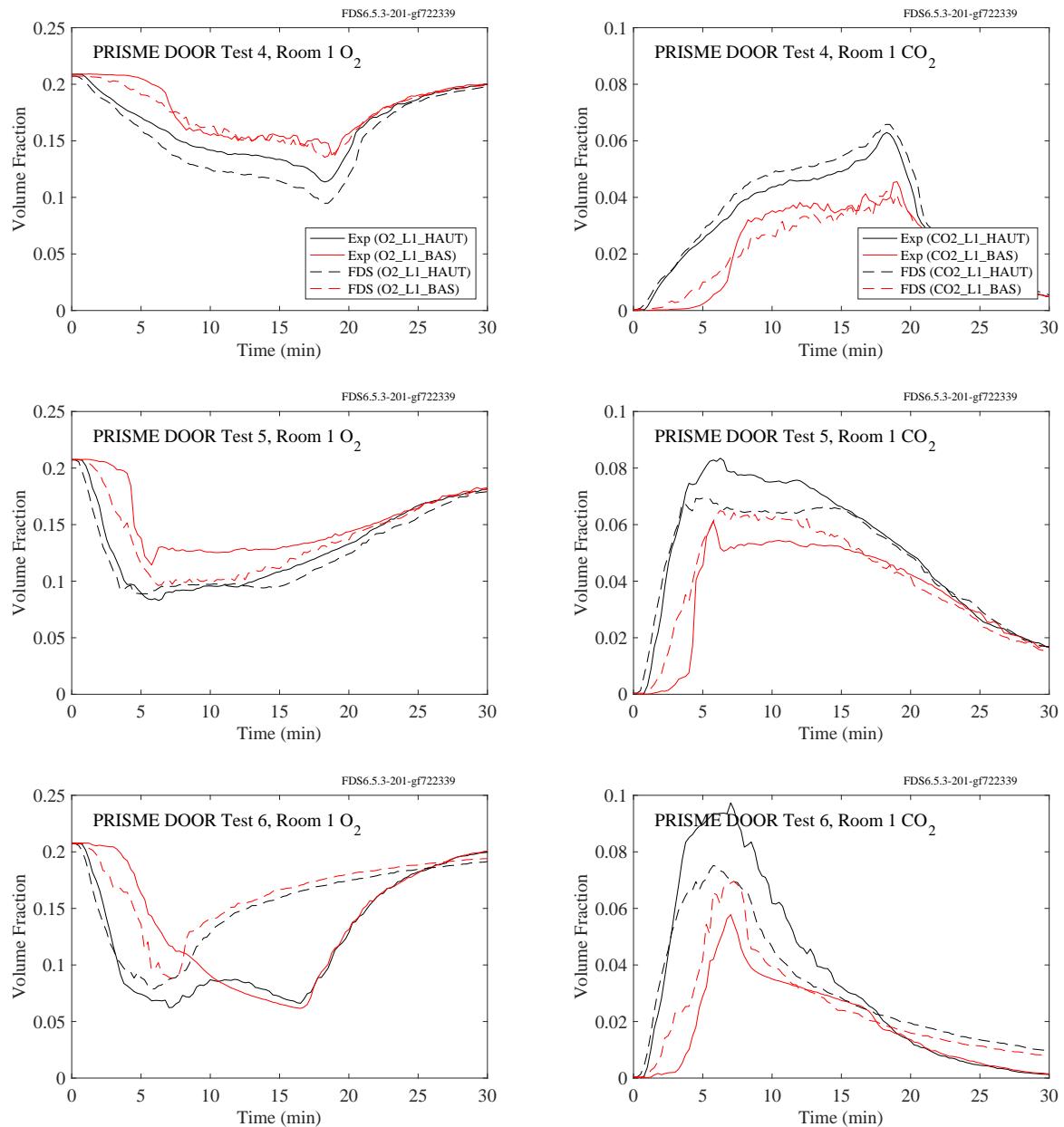


Figure 9.12: PRISME DOOR experiments,  $CO_2$  and  $O_2$  concentration, Room 1, Tests 4-6.

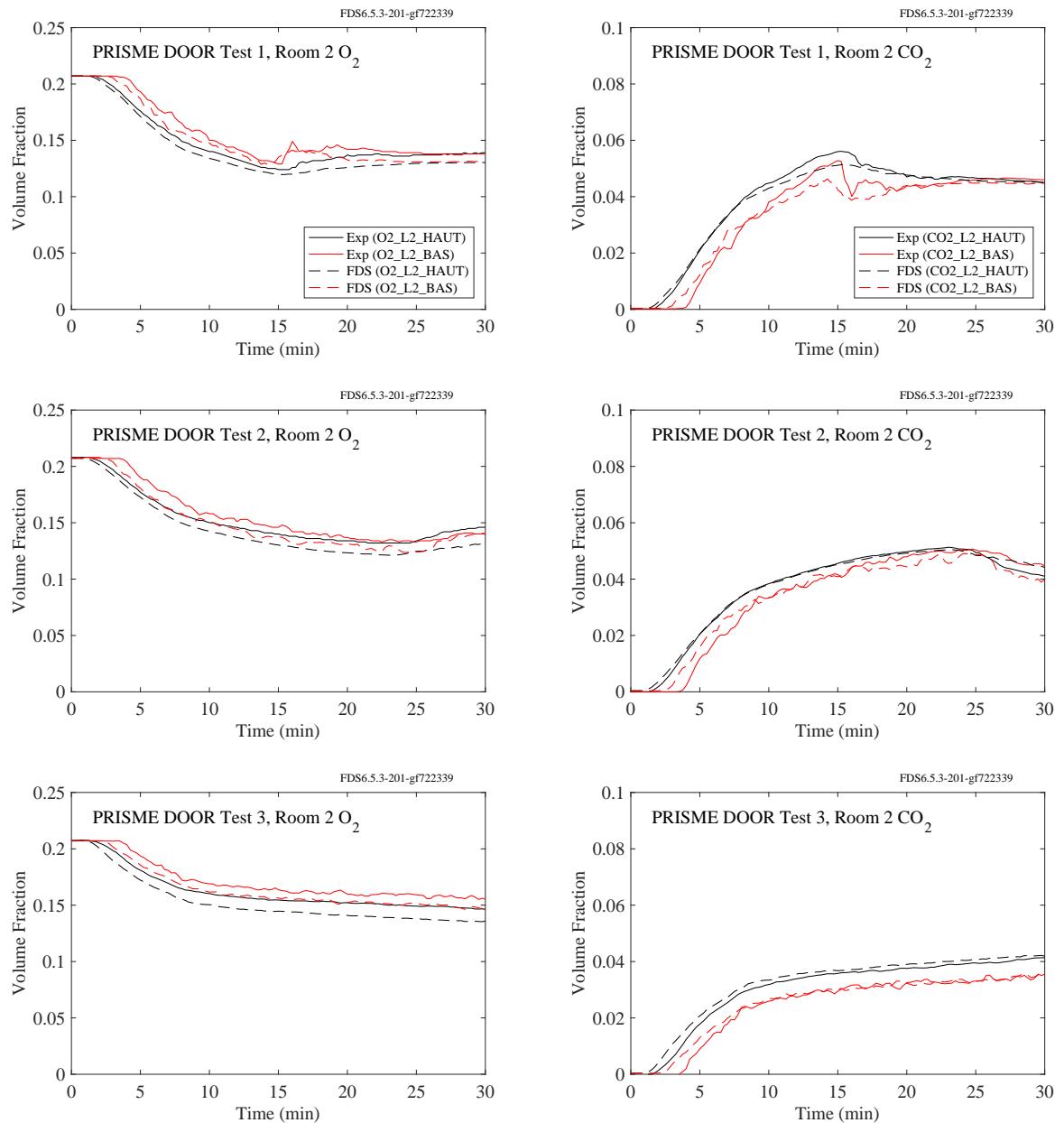


Figure 9.13: PRISME DOOR experiments,  $CO_2$  and  $O_2$  concentration, Room 2, Tests 1-3.

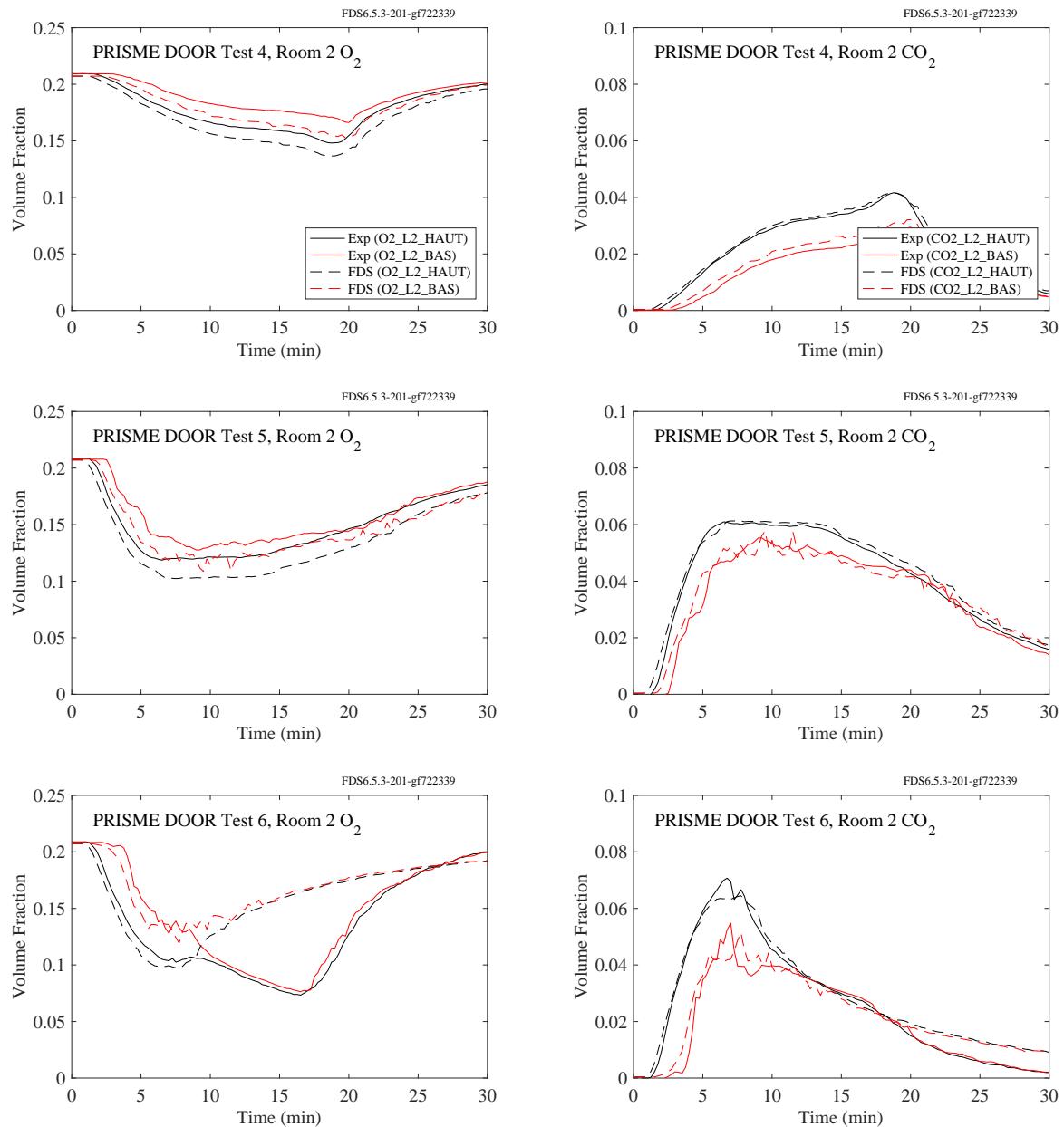


Figure 9.14: PRISME DOOR experiments,  $\text{CO}_2$  and  $\text{O}_2$  concentration, Room 2, Tests 4-6.

### **9.1.6 PRISME SOURCE Experiments**

The compartment in the PRISME SOURCE experiments contained an oxygen and carbon dioxide measurement in the upper (haut) and lower (bas) layers.

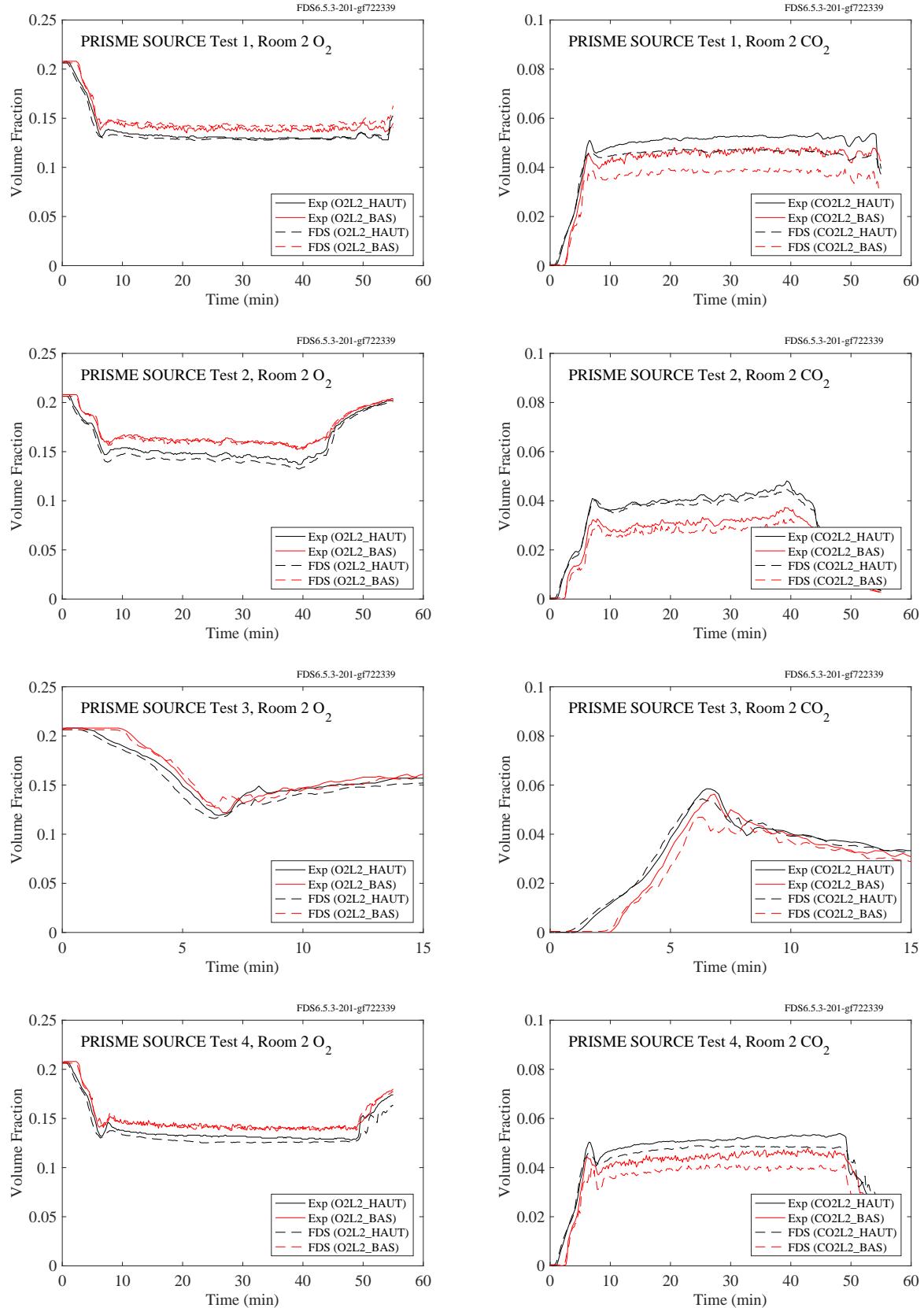


Figure 9.15: PRISME SOURCE experiments,  $\text{CO}_2$  and  $\text{O}_2$  concentration, Room 2, Tests 1-4.

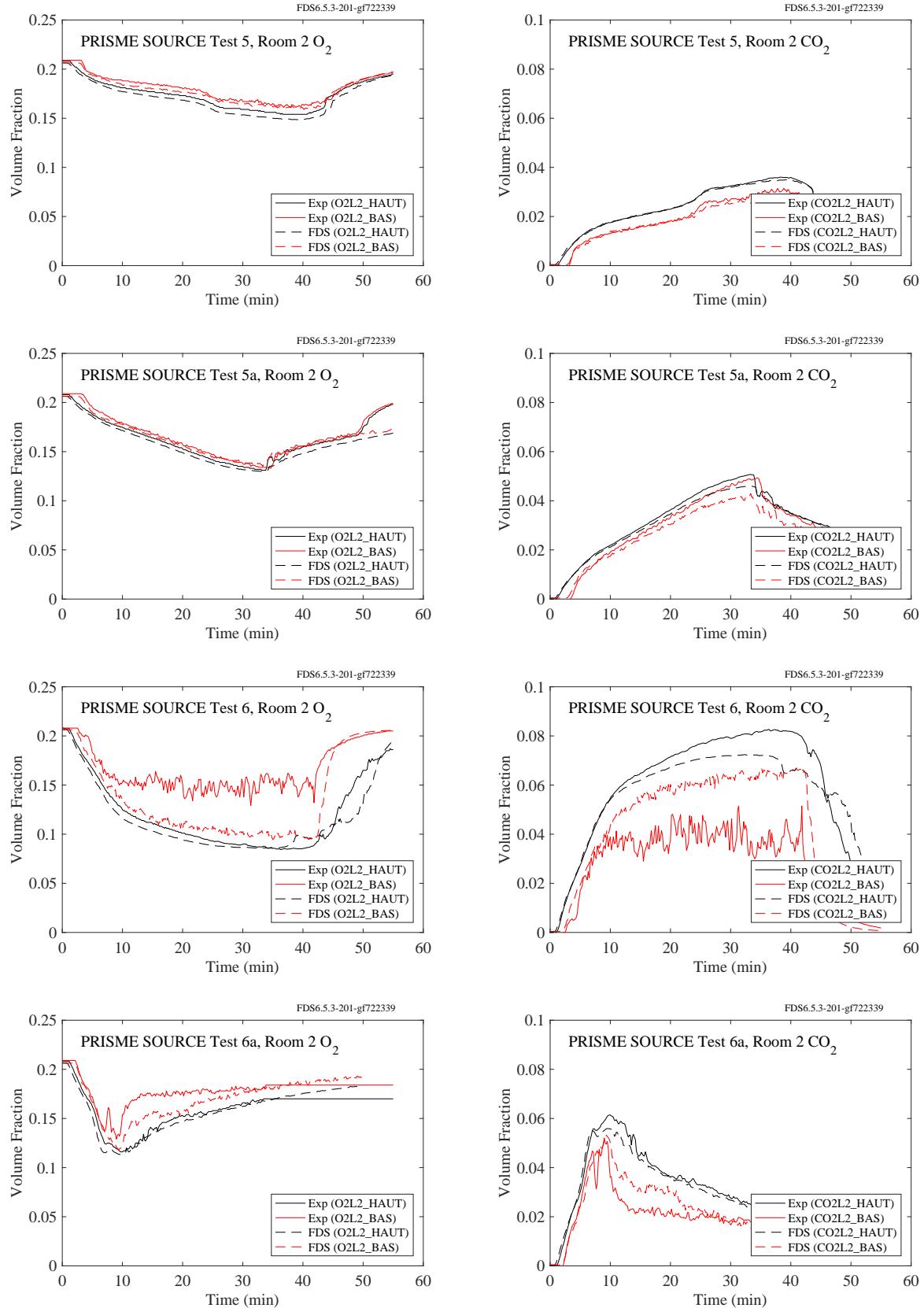


Figure 9.16: PRISME SOURCE experiments,  $\text{CO}_2$  and  $\text{O}_2$  concentration, Room 2, Tests 5-6.

### 9.1.7 WTC Experiments

The following pages present comparisons of oxygen and carbon dioxide concentration predictions and measurements for the WTC experiments. There was only one measurement of each made near the ceiling of the compartment roughly 2 m from the fire.

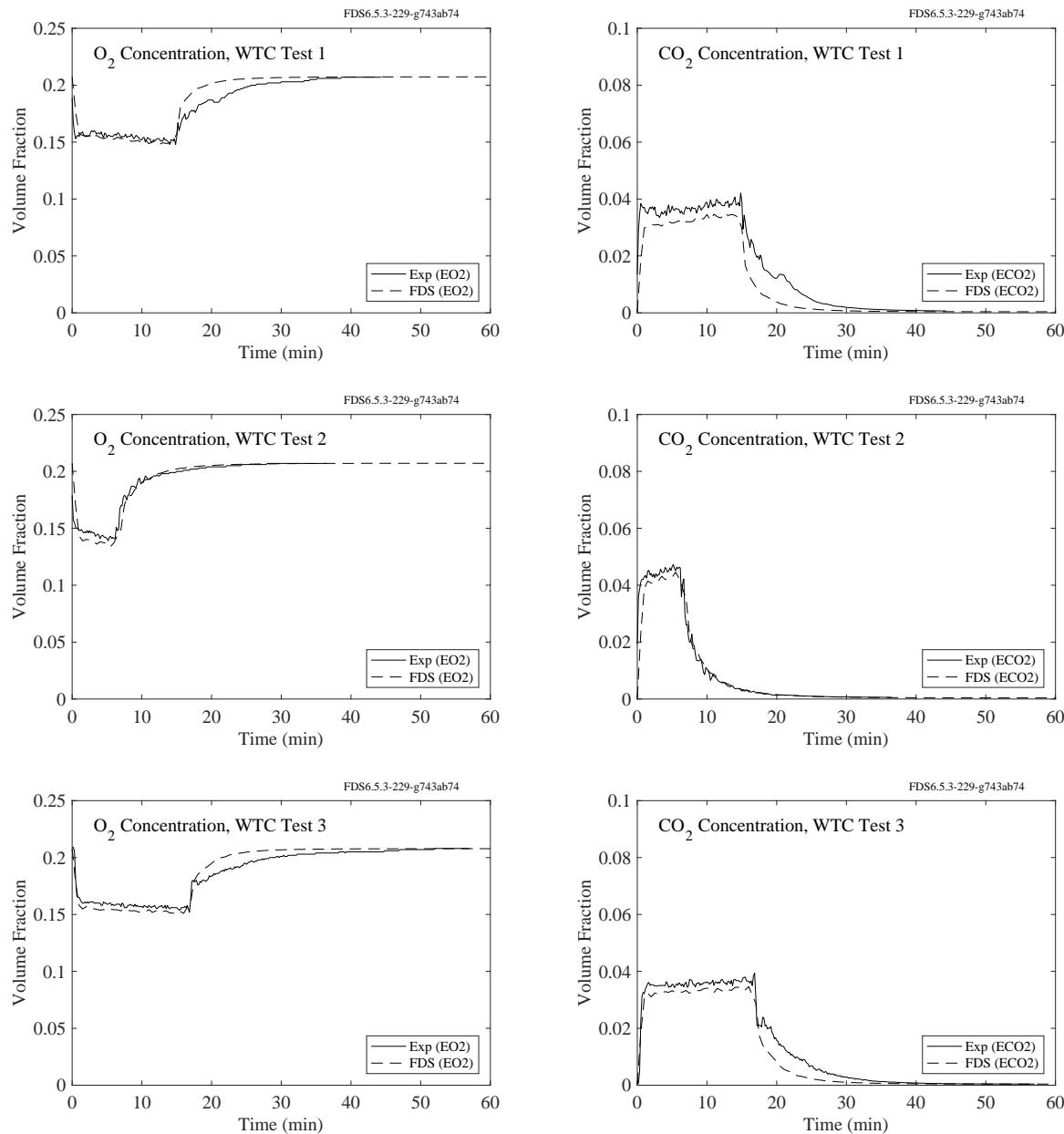


Figure 9.17: WTC experiments,  $CO_2$  and  $O_2$  concentration, Tests 1-3.

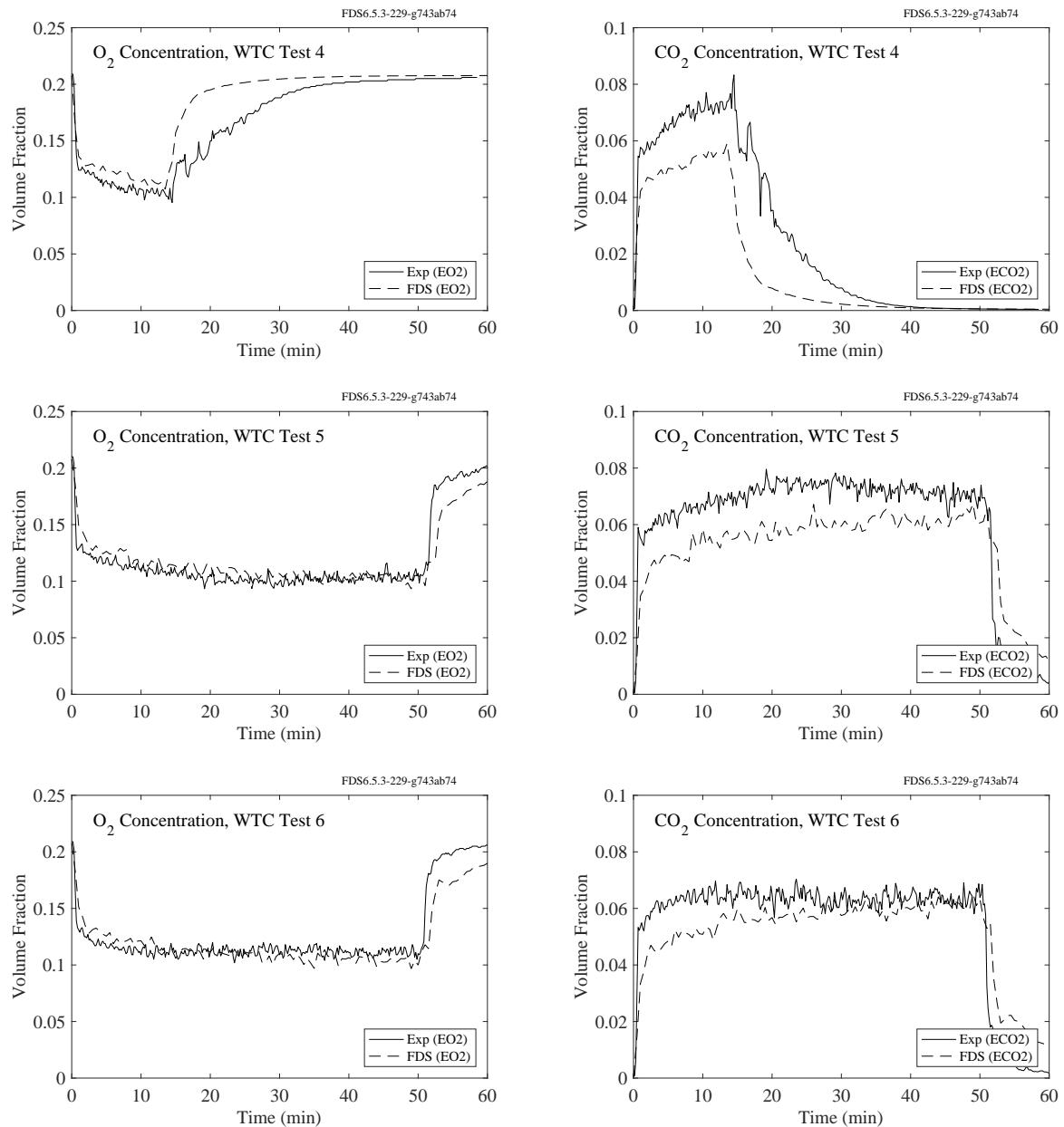


Figure 9.18: WTC experiments,  $CO_2$  and  $O_2$  concentration, Tests 4-6.

### 9.1.8 UMD Line Burner

Oxygen concentration measurements were made across the coflow section of the burner. Fig. 9.19 shows mean volume fraction O<sub>2</sub> profiles for two heights,  $z$ , above the burner surface for the experiment with nitrogen dilution of the coflowing air to 18 vol. % O<sub>2</sub> with methane as fuel. Notice that the O<sub>2</sub> level at the outer edge of the burner is the ambient value of 21 vol. %. Further experimental details may be found in White et al. [210].

FDS simulations are performed at three grid resolutions corresponding to  $W/\delta x = 4, 8, 16$ , where  $W = 5$  cm is the width of the line burner (see Fig. 3.23). Note that White et al. [210] report measured global radiant fraction of  $\chi_r = 0.18$  for 18 vol. % O<sub>2</sub> level with methane fuel. We use this value in the simulations. Also, because these simulations are well-resolved and we are interested in convergence of the numerical solution, we employ the CHARM flux limiter for scalar transport. Second-order interpolated boundaries are used at mesh interfaces. The domain decompositions, in order of increasing grid resolution, use 8, 16, and 128 meshes, respectively.

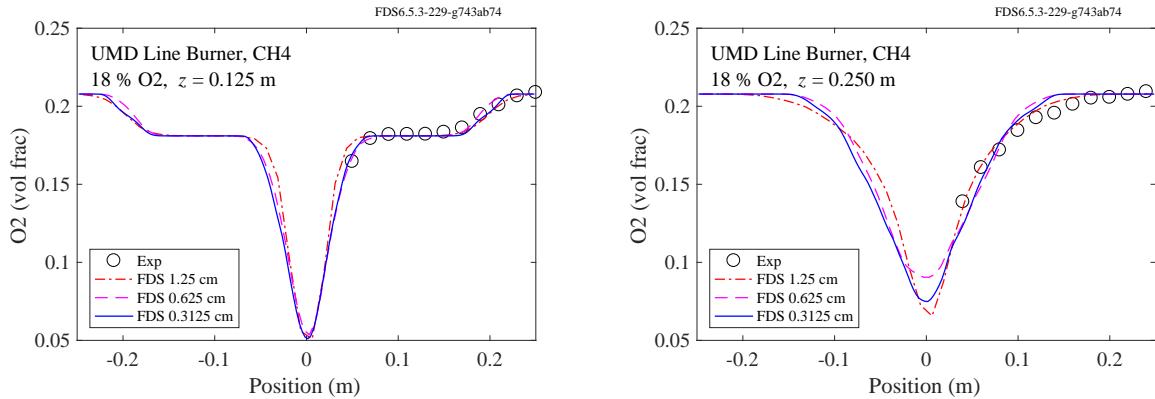


Figure 9.19: Measured and computed mean oxygen concentration profiles at 18 vol % O<sub>2</sub>.



### 9.1.9 Summary of Major Combustion Products Predictions

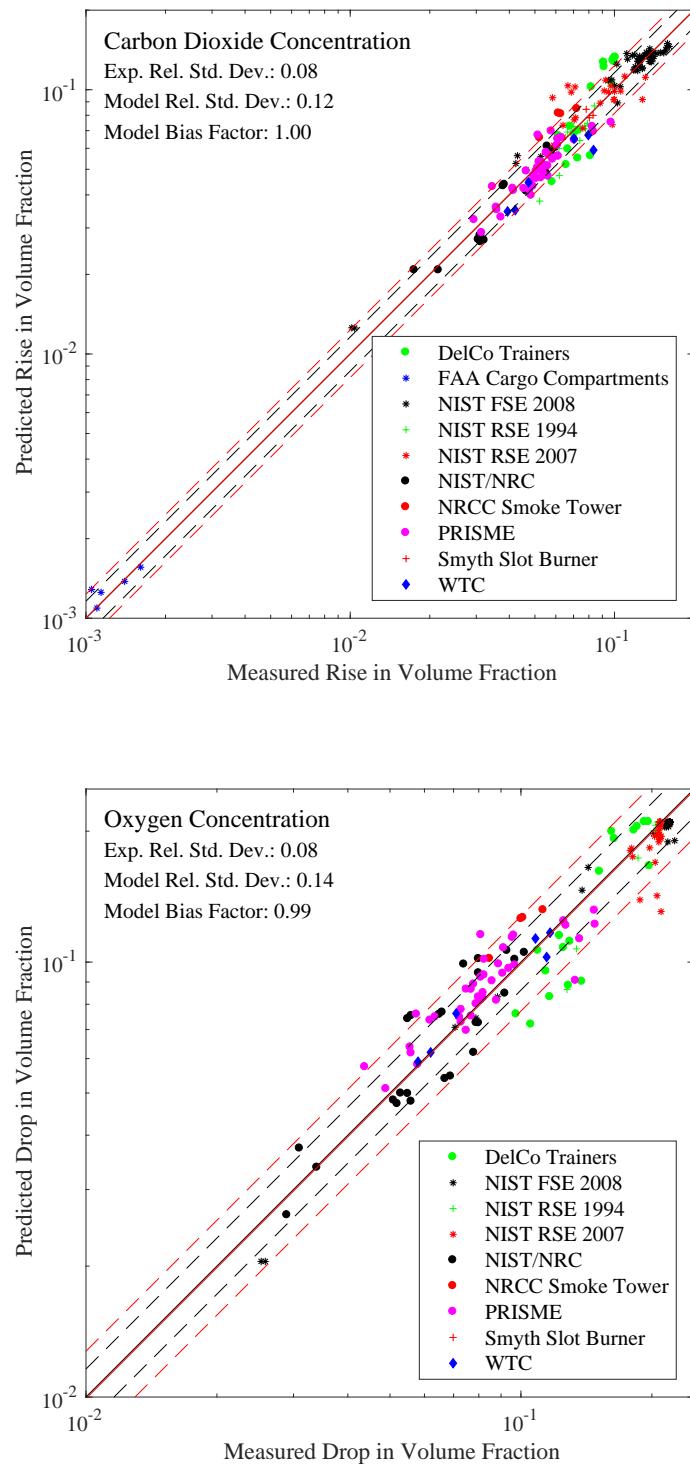


Figure 9.20: Summary of major gas species predictions.

## 9.2 Smoke and Aerosols

### 9.2.1 FM/FPRF Datacenter Experiments

Results of the low speed (78 ACH) and high speed (265 ACH) tests for propylene and cables is shown in the figure below. The error is a propagation of the non-linear error in the FM laser aspiration device combined with the fan flow error. Each test had three measurement locations (subfloor, ceiling, and ceiling plenum); however, not all locations for all tests had a measurement above background noise in the laser signal.

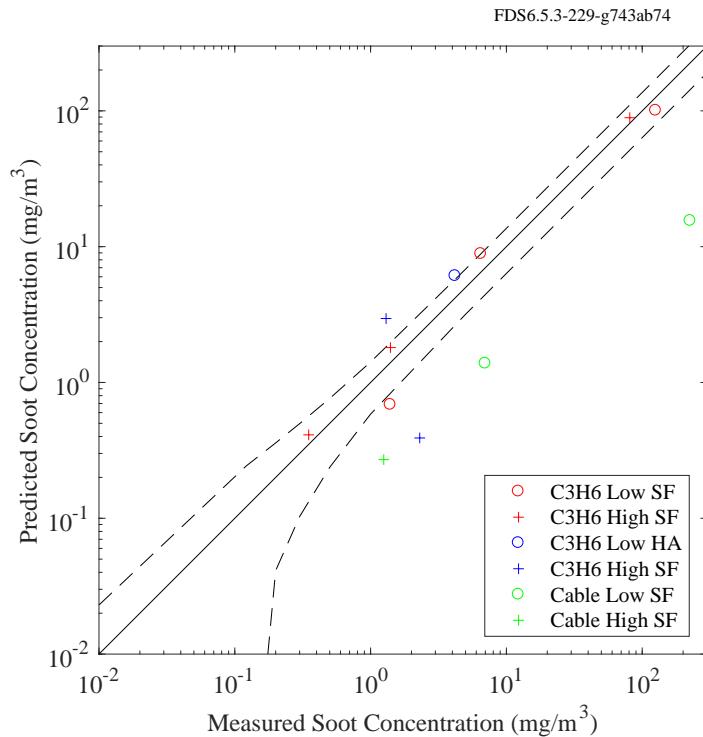


Figure 9.21: Summary of smoke concentration predictions for the FM/FPRF Datacenter Tests.

## **9.2.2 NIST/NRC Experiments**

For the simulations of the NIST/NRC tests, the smoke yield is specified as one of the test parameters. The figures on the following pages contain comparisons of measured and predicted smoke concentration at one measuring station in the upper layer.

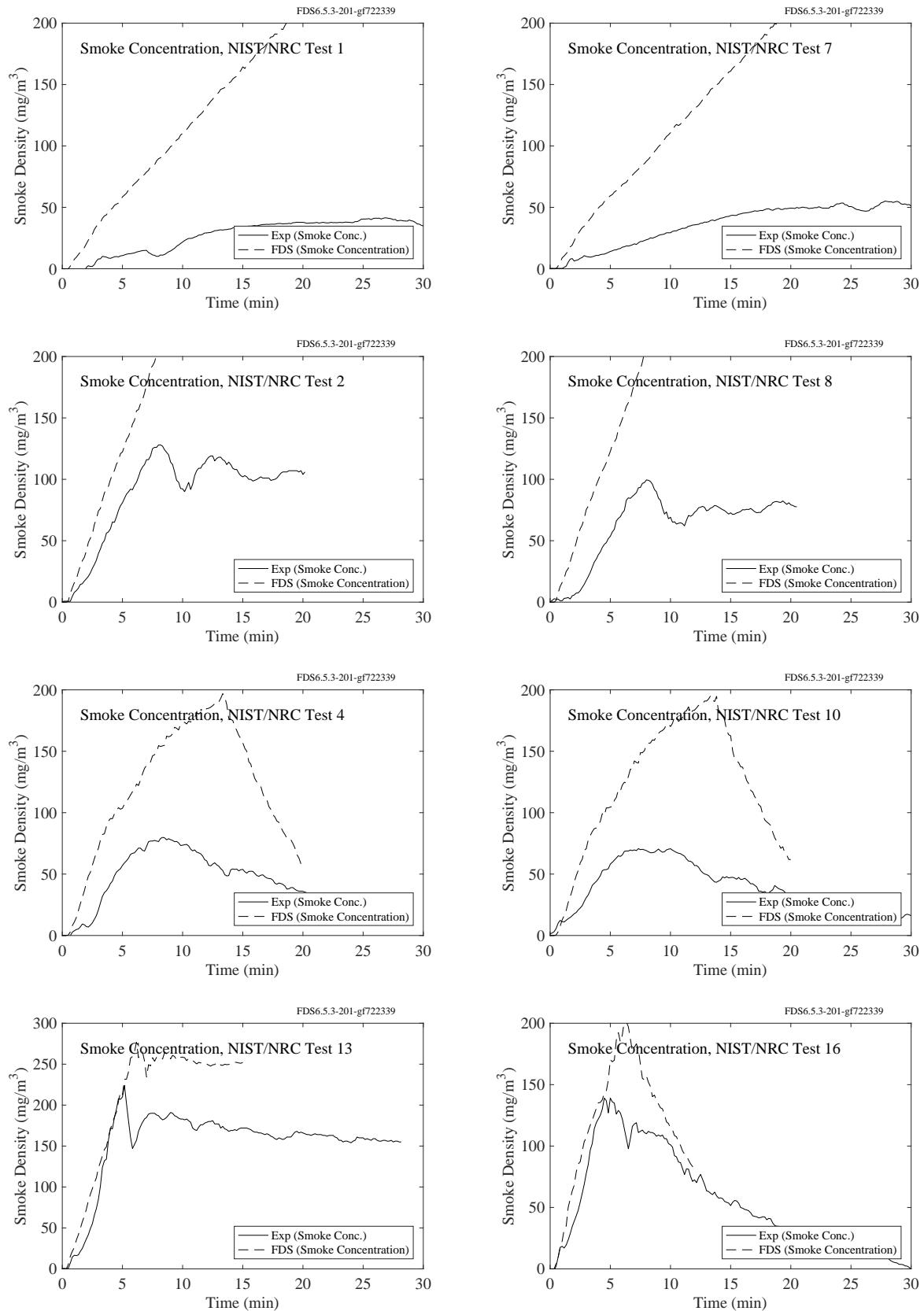


Figure 9.22: NIST/NRC experiments, smoke concentration, Tests 1, 2, 4, 7, 8, 10, 13, 16.

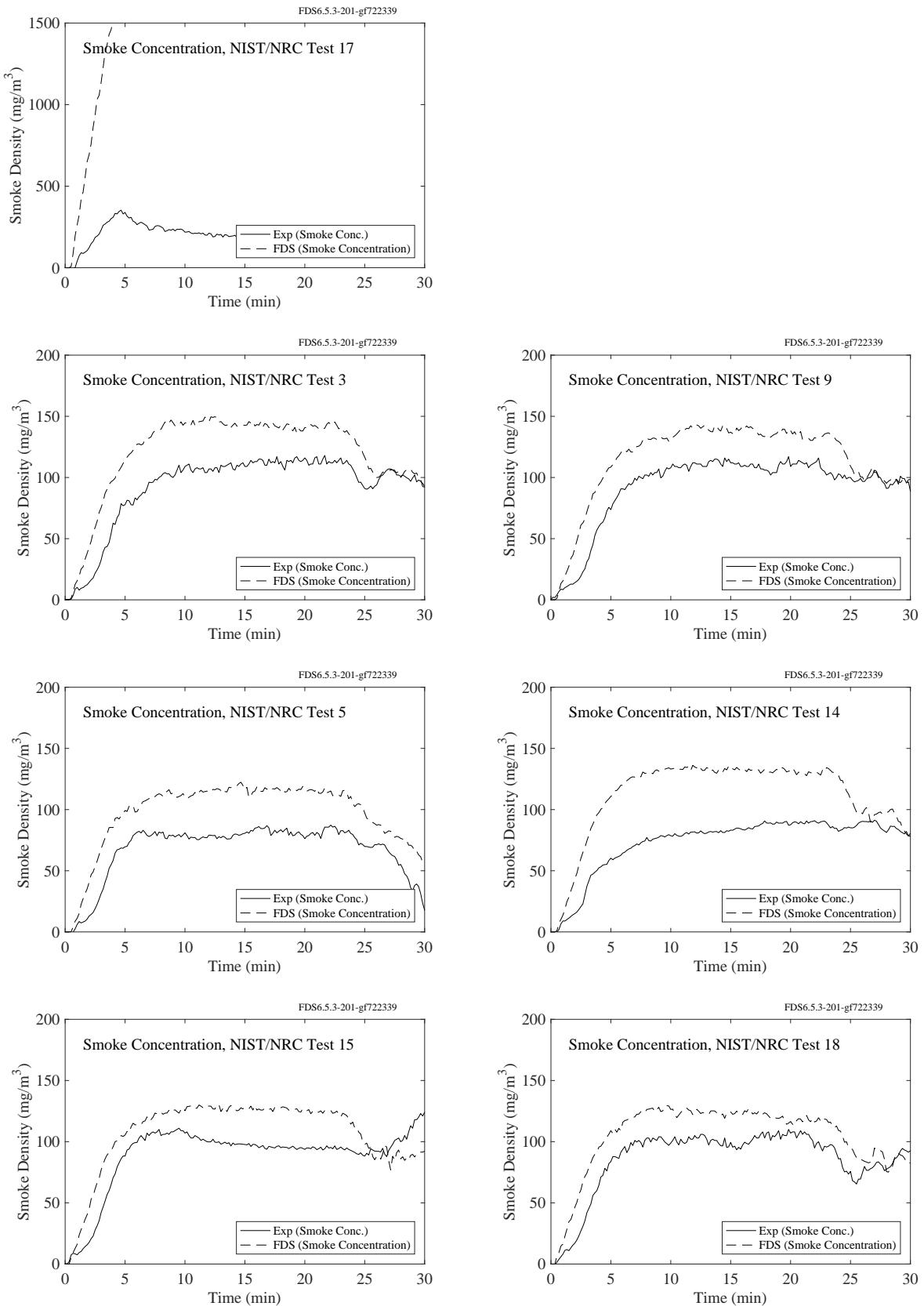


Figure 9.23: NIST/NRC experiments, smoke concentration, Tests 3, 5, 9, 14, 15, 17, 18.

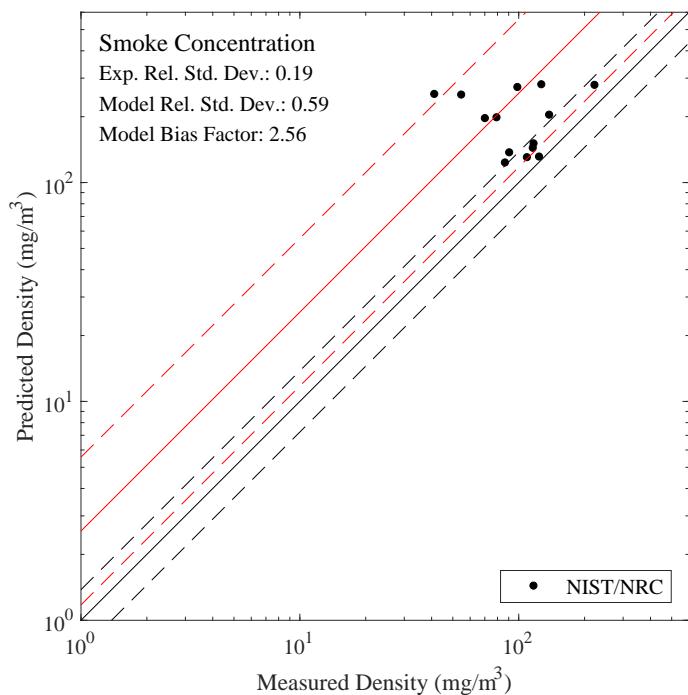


Figure 9.24: Summary of smoke concentration predictions.

### 9.2.3 FAA Cargo Compartments

Beam obscuration measurements were made at different locations within the compartment (see Fig. 7.10). The data is presented below in terms of percent transmission per meter,  $100(I/I_0)^{1/L}$ , where  $I$  is the light intensity and  $L$  is the beam pathlength in units of meters.

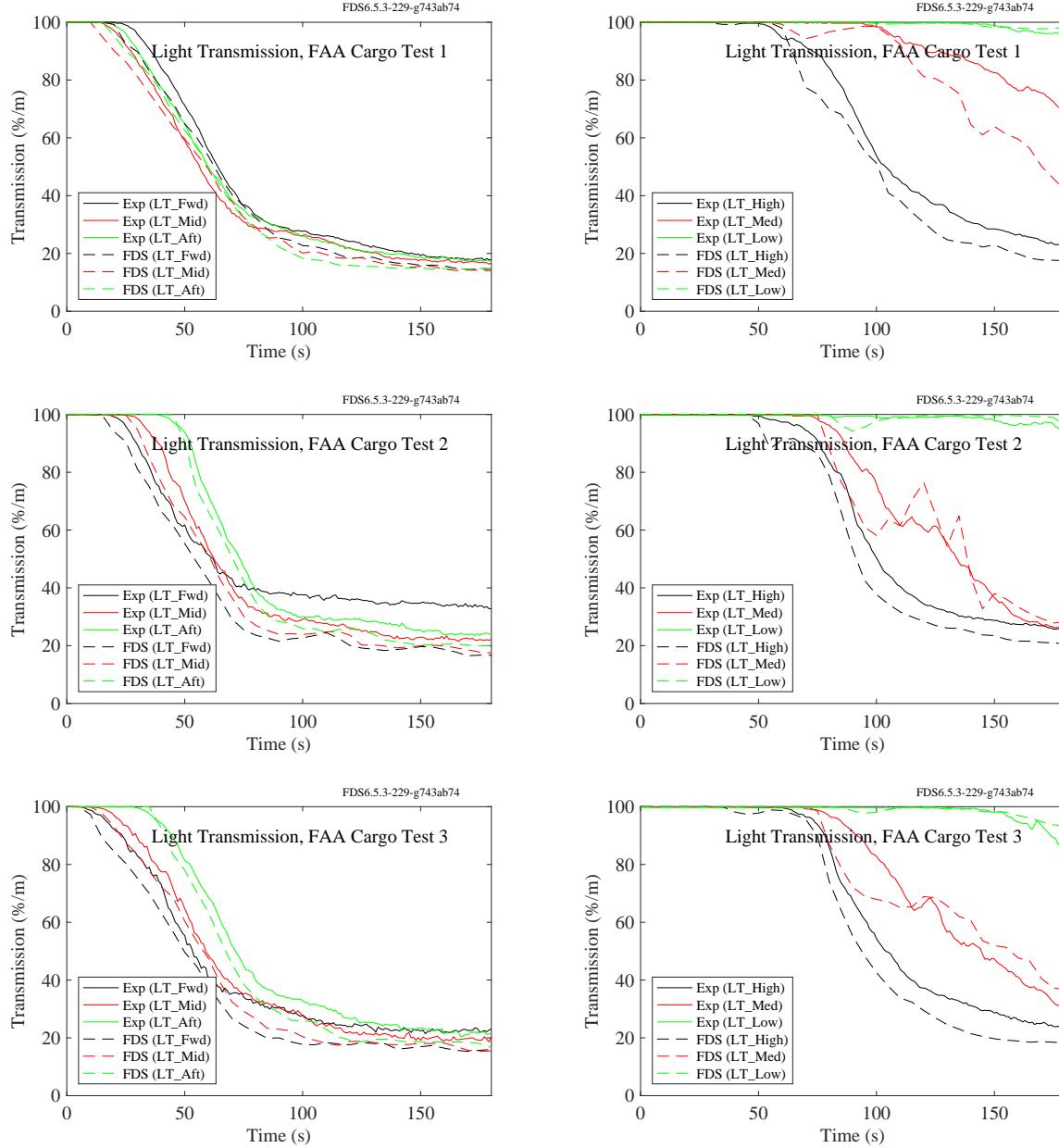


Figure 9.25: FAA Cargo Compartments experiments, smoke obscuration.

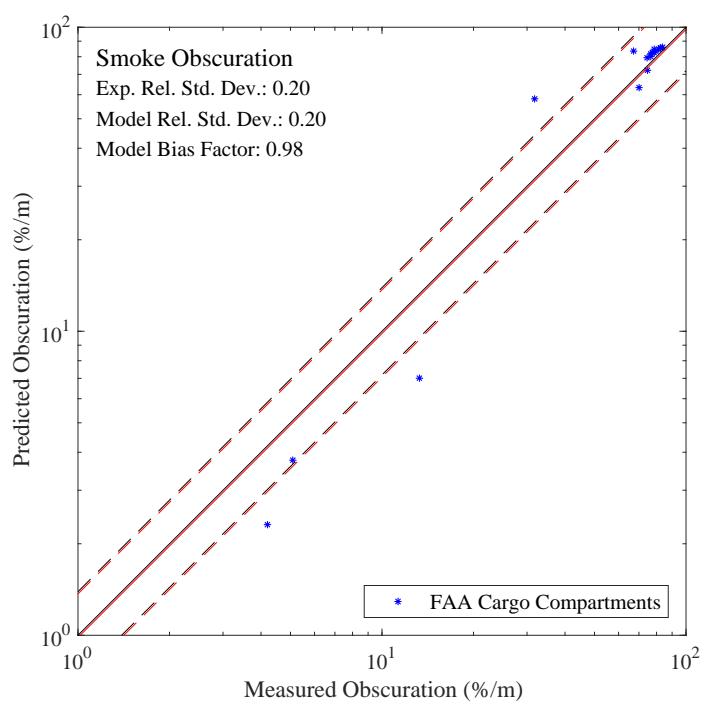


Figure 9.26: Summary of smoke obscuration predictions.

## 9.2.4 Sippola Aerosol Deposition Experiments

FDS treats smoke particulate and aerosols in a similar way to other gaseous combustion products, basically a tracer gas whose production rate is a fixed fraction of the fuel consumption rate. However, there is an option in the model to allow smoke or aerosols to deposit on solid surfaces, thus reducing its concentration in the product stream. A total of 16 aerosol deposition experiments were conducted in a straight steel duct with smooth walls for 5 different particle diameters ( $1\text{ }\mu\text{m}$ ,  $3\text{ }\mu\text{m}$ ,  $5\text{ }\mu\text{m}$ ,  $9\text{ }\mu\text{m}$ , and  $16\text{ }\mu\text{m}$ ) and 3 different air velocities (2.2 m/s, 5.3 m/s, and 9.0 m/s). In the simulations, the aerosol is tracked explicitly, and the aerosol deposition routines are enabled (refer to the Aerosol Deposition section in the FDS User Guide [1] and FDS Technical Reference Guide [238] for more details). A summary of the 16 experiments is shown in Table 9.1.

Table 9.1: Summary of Sippola aerosol deposition experiments selected for model validation.

Test No.	Air Speed (m/s)	Particle Diameter ( $\mu\text{m}$ )	Particle Density ( $\text{kg}/\text{m}^3$ )
1	2.2	1.0	1350
2	2.2	2.8	1170
3	2.1	5.2	1210
4	2.2	9.1	1030
5	2.2	16	950
6	5.3	1.0	1350
7	5.2	1.0	1350
8	5.2	3.1	1170
9	5.4	5.2	1210
10	5.3	9.8	1030
11	5.3	16	950
12	9.0	1.0	1350
13	9.0	3.1	1170
14	8.8	5.4	1210
15	9.2	8.7	1030
16	9.1	15	950

The particle deposition velocity,  $u_{\text{dep}}$ , is calculated by

$$u_{\text{dep}} = \frac{J_1 + J_2 + J_3 + J_4}{4 C_{\text{avg}}} \quad (9.1)$$

where  $J_1$  through  $J_4$  are the deposition fluxes ( $\text{kg}/(\text{m}^2 \cdot \text{s})$ ) for duct panels 1 through 4 given by

$$J = \frac{m_d}{A_d \Delta t} \quad (9.2)$$

where  $m_d$  is the mass of particles on the duct panel (kg),  $A_d$  is the area of the duct panel ( $\text{m}^2$ ), and  $\Delta t$  is the duration over which the aerosol deposits onto the panel (s).  $C_{\text{avg}}$  is the average aerosol concentration in the duct test section ( $\text{kg}/\text{m}^3$ ) and is given by

$$C_{\text{avg}} = \frac{C_{\text{upstream}} + C_{\text{downstream}}}{2} \quad (9.3)$$

Figure 9.27 compares the measured and predicted aerosol deposition velocities, and Figure 9.28 shows a summary of the results.

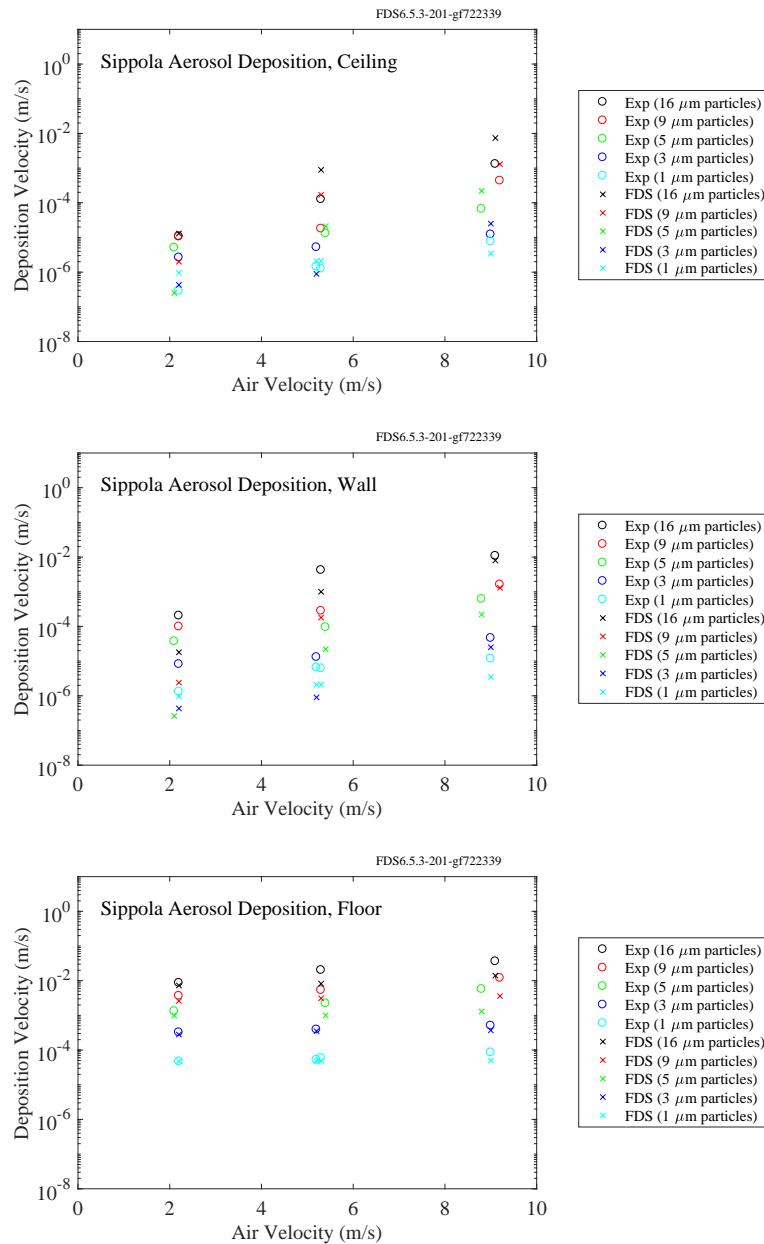


Figure 9.27: Predicted and measured aerosol deposition velocities, Sippola experiments.

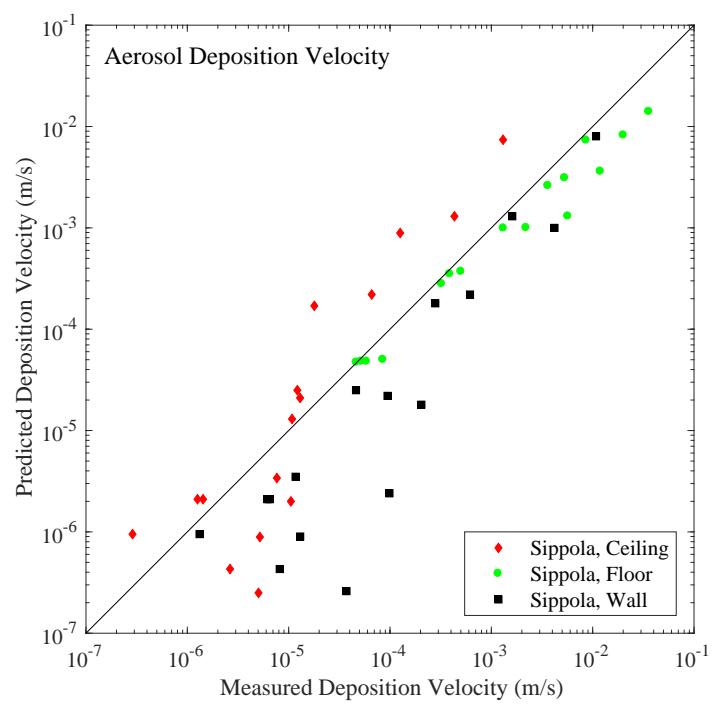


Figure 9.28: Summary of aerosol deposition velocity predictions.

## 9.3 Products of Incomplete Combustion

Predicting the concentration of products of incomplete combustion is challenging because it requires information about the chemical composition of the fuel and the multiple reactions that convert fuel to products. FDS contains a fairly general framework by which users can specify the reaction mechanism, and the examples in the following subsections highlight some of the more commonly used schemes.

### 9.3.1 Smyth Slot Burner Experiment

A two-step CO production model (a modified version of the mechanism by Andersen et al. [239]) is used to simulate a methane/air slot burner diffusion flame. A 2D DNS calculation is run at two different grid resolutions:  $\delta x = 0.250$  mm and  $\delta x = 0.125$  mm. In our modified mechanism the hydrocarbon/oxygen reaction to CO is assumed to be infinitely fast (mixed is burnt) to avoid complications of modeling ignition. The reversible CO to  $\text{CO}_2$  reaction is modeled with Arrhenius kinetics. As discussed by Westbrook and Dryer [240], the kinetics constants for the reduced CO mechanisms may be model dependent. Here, the Arrhenius constant for the forward CO to  $\text{CO}_2$  reaction is tuned to match the Smyth experimental data. These same model parameters are then also used in the NIST Reduced Scale Enclosure LES without modification (see Section 9.3.3). Figures 9.29 through 9.30 show predicted and measured concentrations of  $\text{CH}_4$ ,  $\text{O}_2$ , CO, and  $\text{CO}_2$  at three elevations above the burner. Figure 9.31 shows predicted and measured temperatures at these same elevations. The reported uncertainty in the species concentration measurements ranges from 10 % to 20 %.

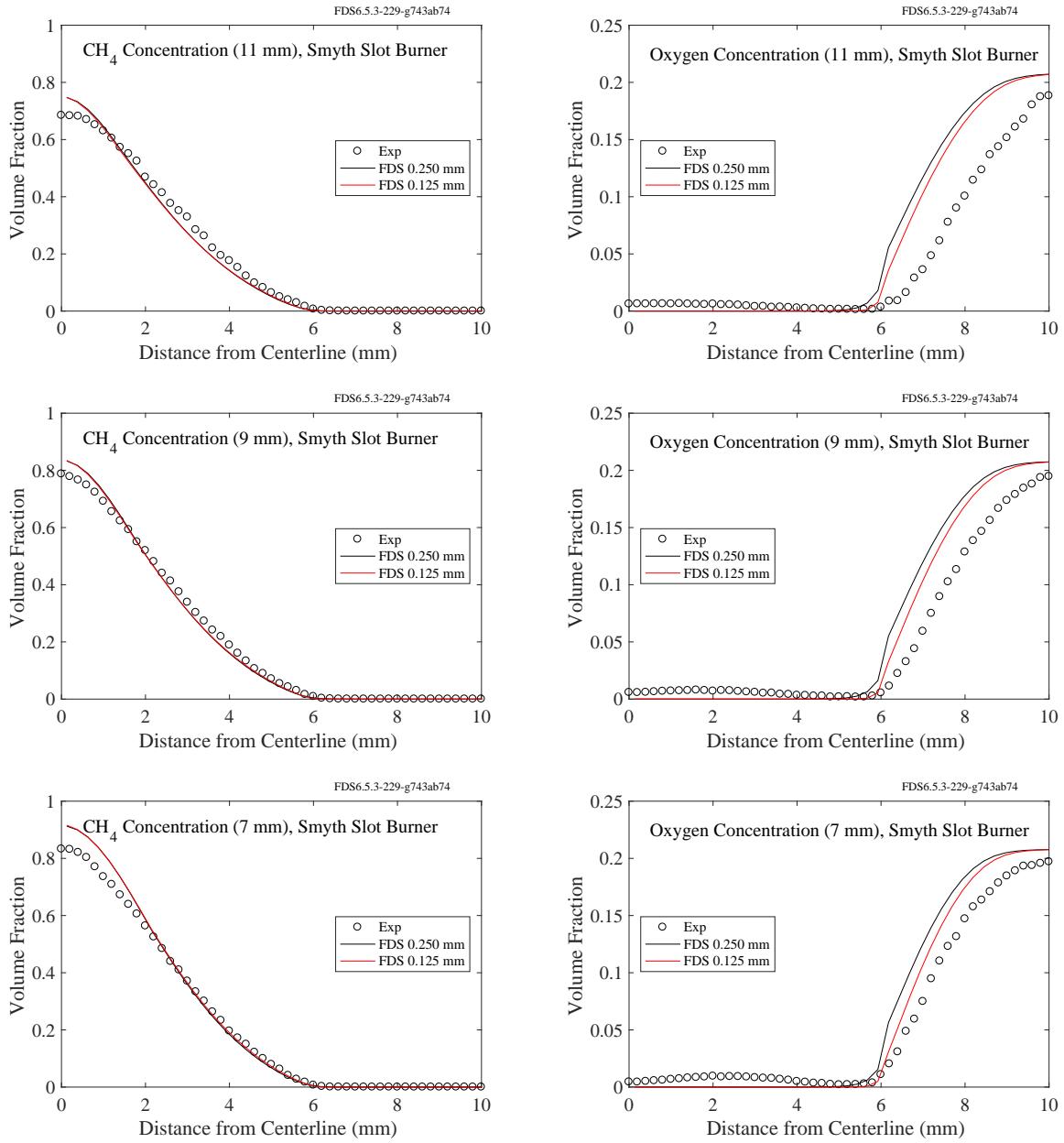


Figure 9.29: Predicted and measured fuel and oxygen species at 7 mm, 9 mm, and 11 mm above a methane-air slot burner.

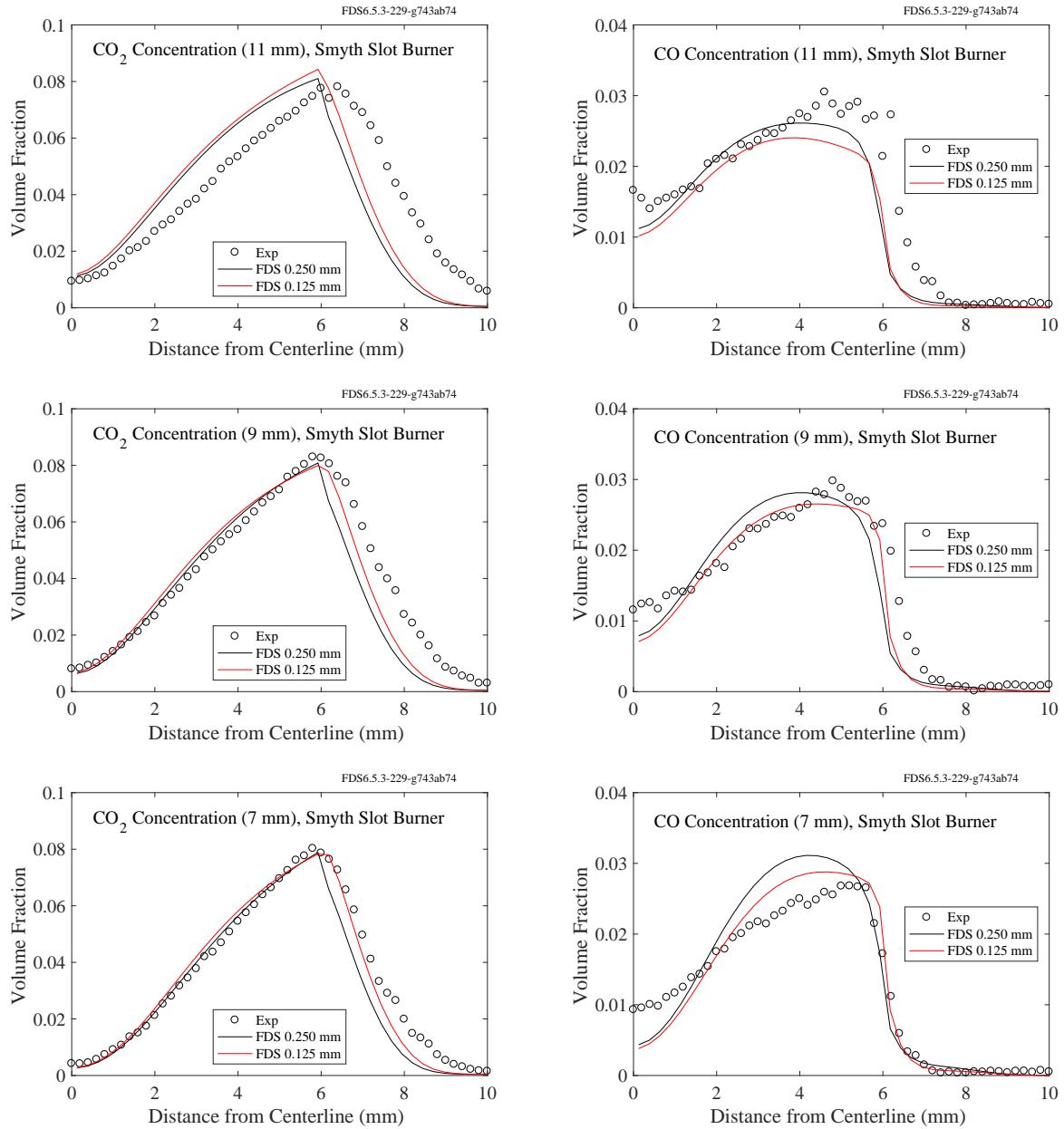


Figure 9.30: Predicted and measured carbon dioxide and carbon monoxide species at 7 mm, 9 mm, and 11 mm above a methane-air slot burner.

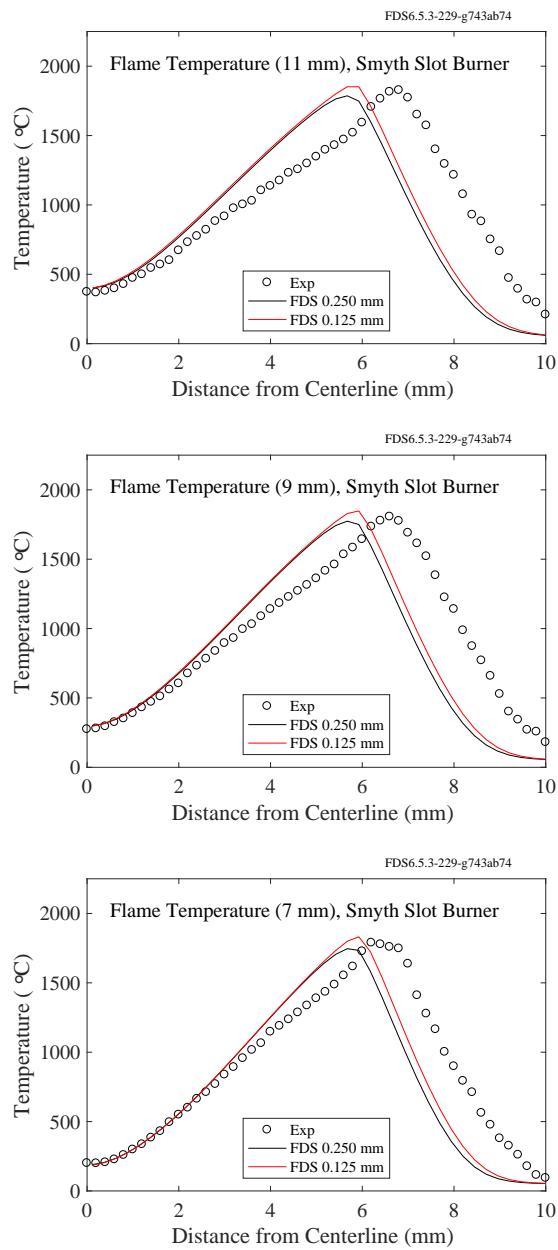


Figure 9.31: Predicted and measured temperature at 7 mm, 9 mm, and 11 mm above a methane-air slot burner.

### **9.3.2 Beyler Hood Experiments**

Fig. 9.32 shows species predictions made by the two-step model compared with measured data for a range of fire sizes and burner positions. The model outputs are the time-averaged species concentration at the hood exhaust vent whereas the experiment is the time-averaged species concentration downstream in the exhaust duct.

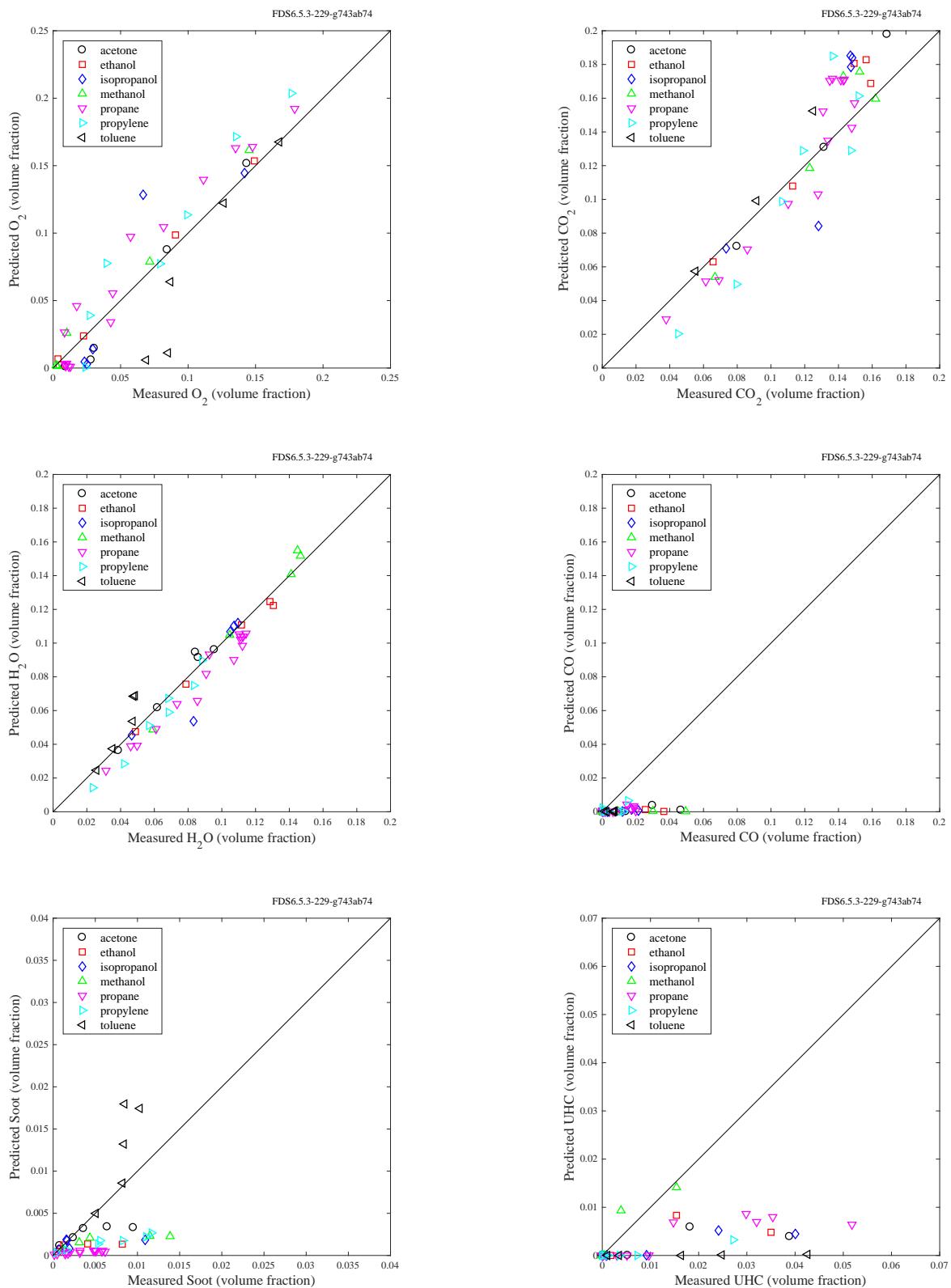


Figure 9.32: Comparison of measured and predicted species concentrations in the Beyler hood experiments

### 9.3.3 NIST Reduced Scale Enclosure (RSE) Experiments, 1994

The RSE natural gas experiments were selected to assess the CO production capability rather than soot production. Nine fire sizes were simulated: 50 kW, 75 kW, 100 kW, 150 kW, 200 kW, 300 kW, 400 kW, 500 kW, and 600 kW. The experiments were modeled using properties of the natural gas supplied to the test facility. The model geometry included the compartment interior along with a 0.6 m deep region outside the door. Figures 9.33 and 9.33 show the measured and predicted CO, CO<sub>2</sub> and O<sub>2</sub>, and H<sub>2</sub>O concentrations. Figure 9.35 shows the measured and predicted thermocouple temperatures in the front and rear of the compartment. The measured values are from the test series performed by Bryner, Johnsson, and Pitts [169].

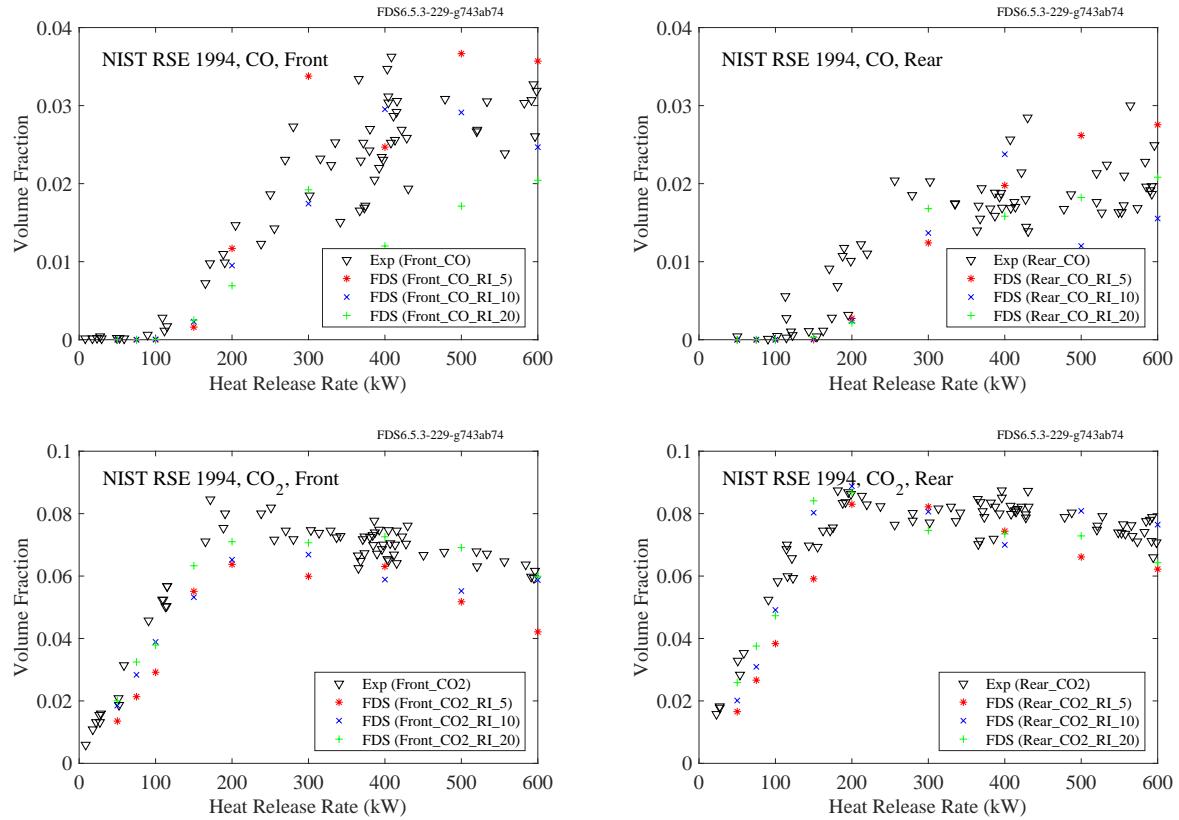


Figure 9.33: Summary of species concentrations in NIST Reduced Scale Enclosure experiments.

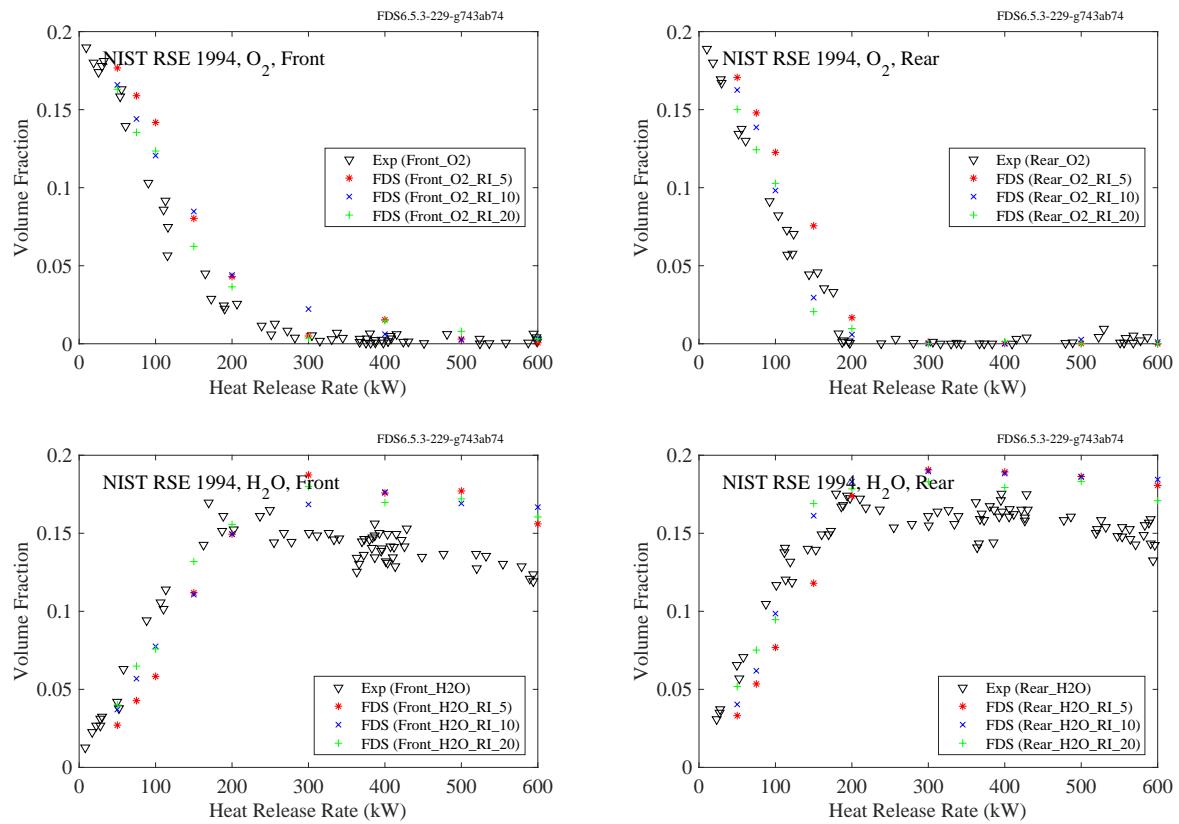


Figure 9.34: Summary of species concentrations in NIST Reduced Scale Enclosure experiments.

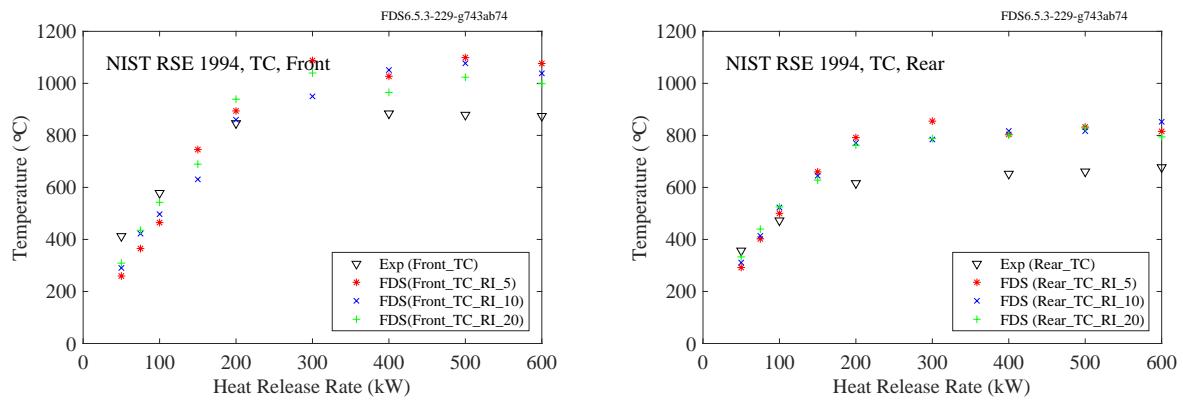
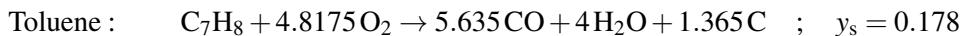
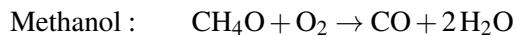
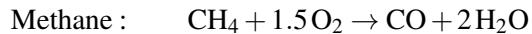


Figure 9.35: Summary of thermocouple values in NIST Reduced Scale Enclosure experiments.

### 9.3.4 NIST Reduced-Scale Enclosure (RSE) Experiments, 2007

In the simulations of the NIST RSE Experiments, it is assumed that the combustion can be simplified to two fast reactions, the first converting fuel to CO and soot, and the second converting CO to CO<sub>2</sub>. The stoichiometry for the first reaction is given here:



A single carbon atom serves as a surrogate for soot. Its stoichiometric coefficient is based on measured soot yields,  $y_s$ , provided by Tewarson [214]. The heats of combustion for the reactions are calculated directly from the heats of formation of the individual molecules.

In the experiments, the heat release rate was measured via oxygen consumption calorimetry. In the simulations, the mass loss rate of fuel was specified by taking the measured HRR and dividing by the heats of combustion listed in Ref. [214].

Species and temperature measurements were made in the front and rear of the compartment, 10 cm below the ceiling, 29 cm from the right wall (looking into the compartment), and 10 cm from the front wall or 29 cm from the rear wall.

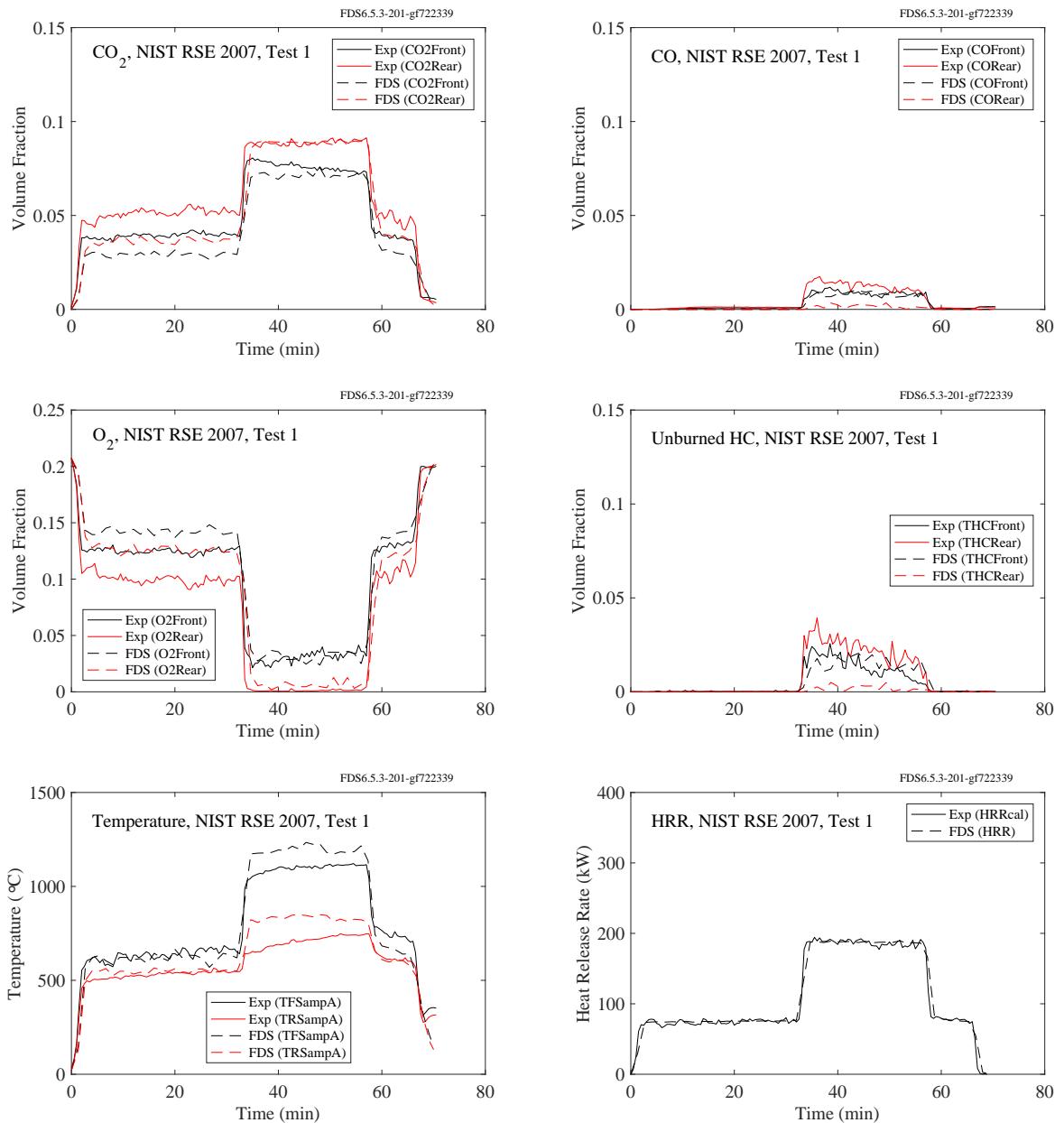


Figure 9.36: Summary of Test 1, NIST RSE 2007.

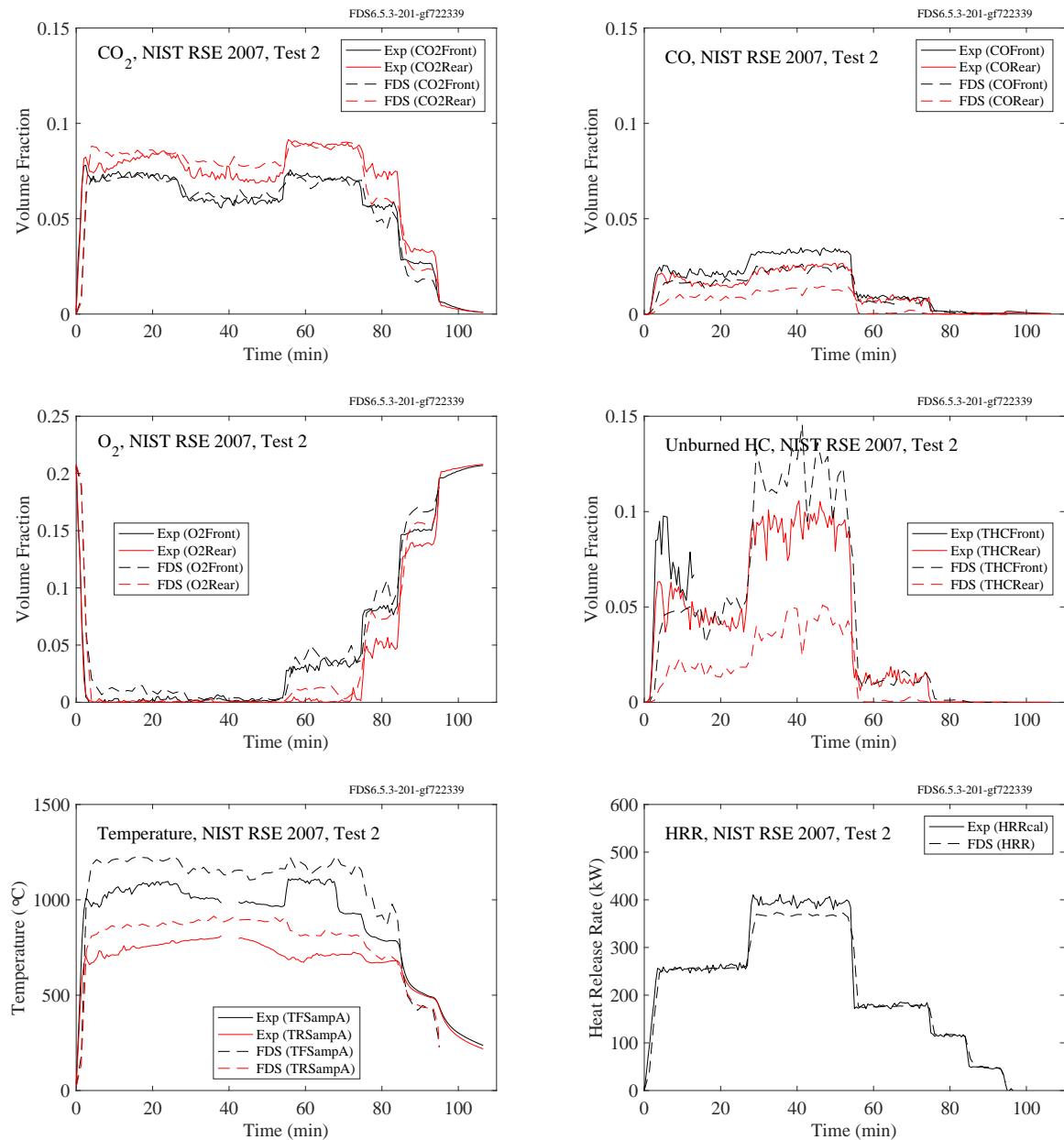


Figure 9.37: Summary of Test 2, NIST RSE 2007.

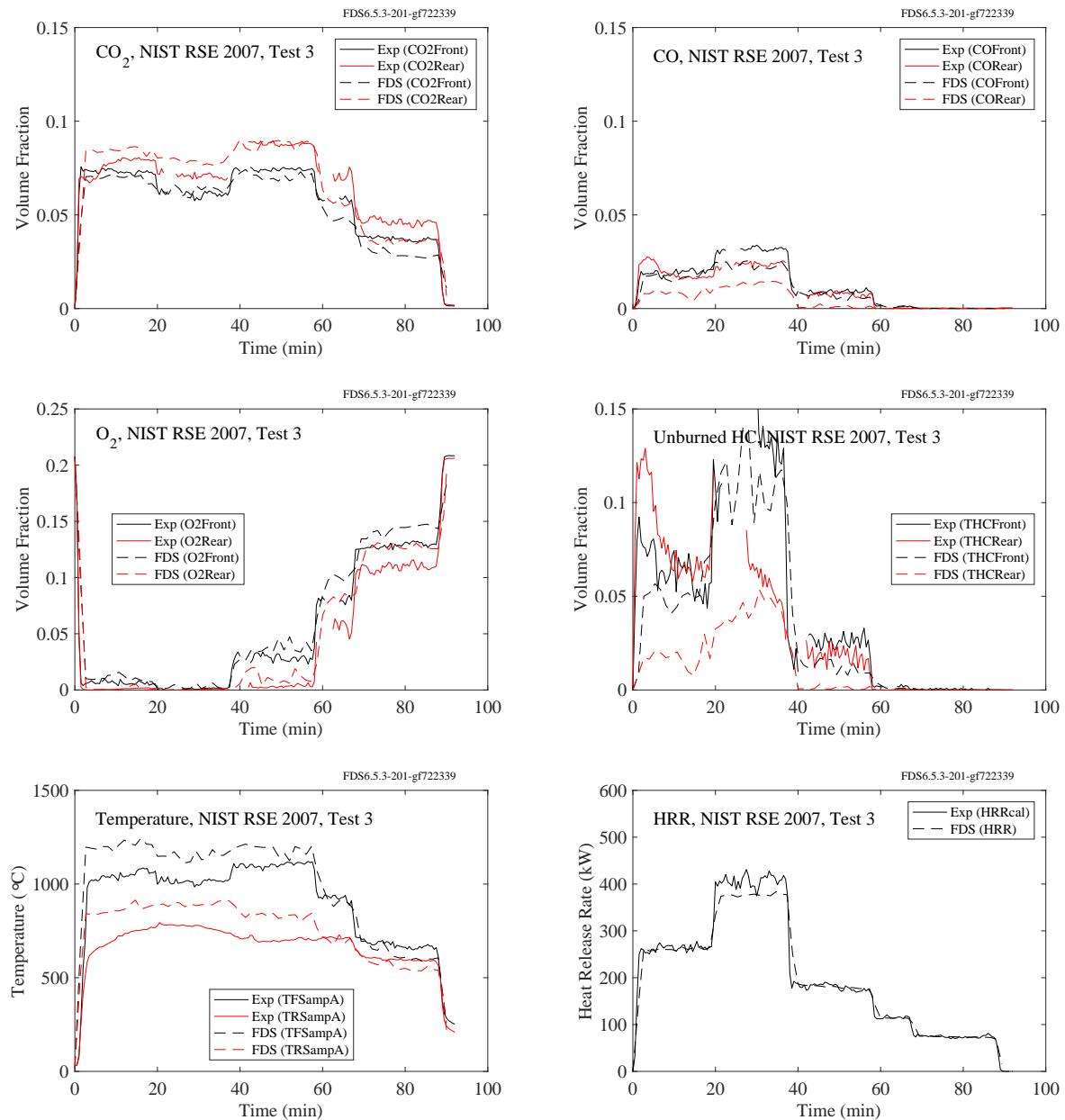


Figure 9.38: Summary of Test 3, NIST RSE 2007.

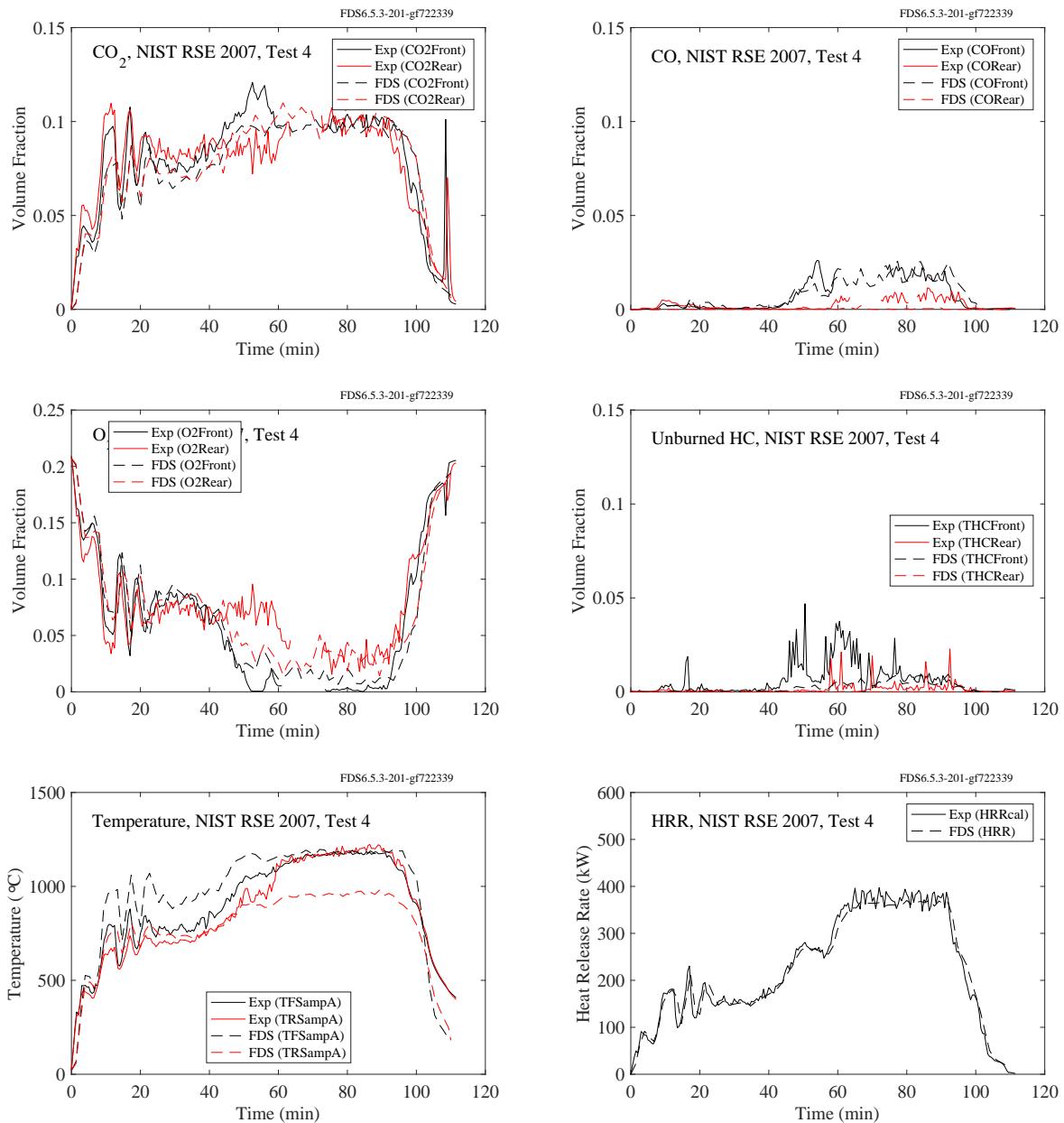


Figure 9.39: Summary of Test 4, NIST RSE 2007.

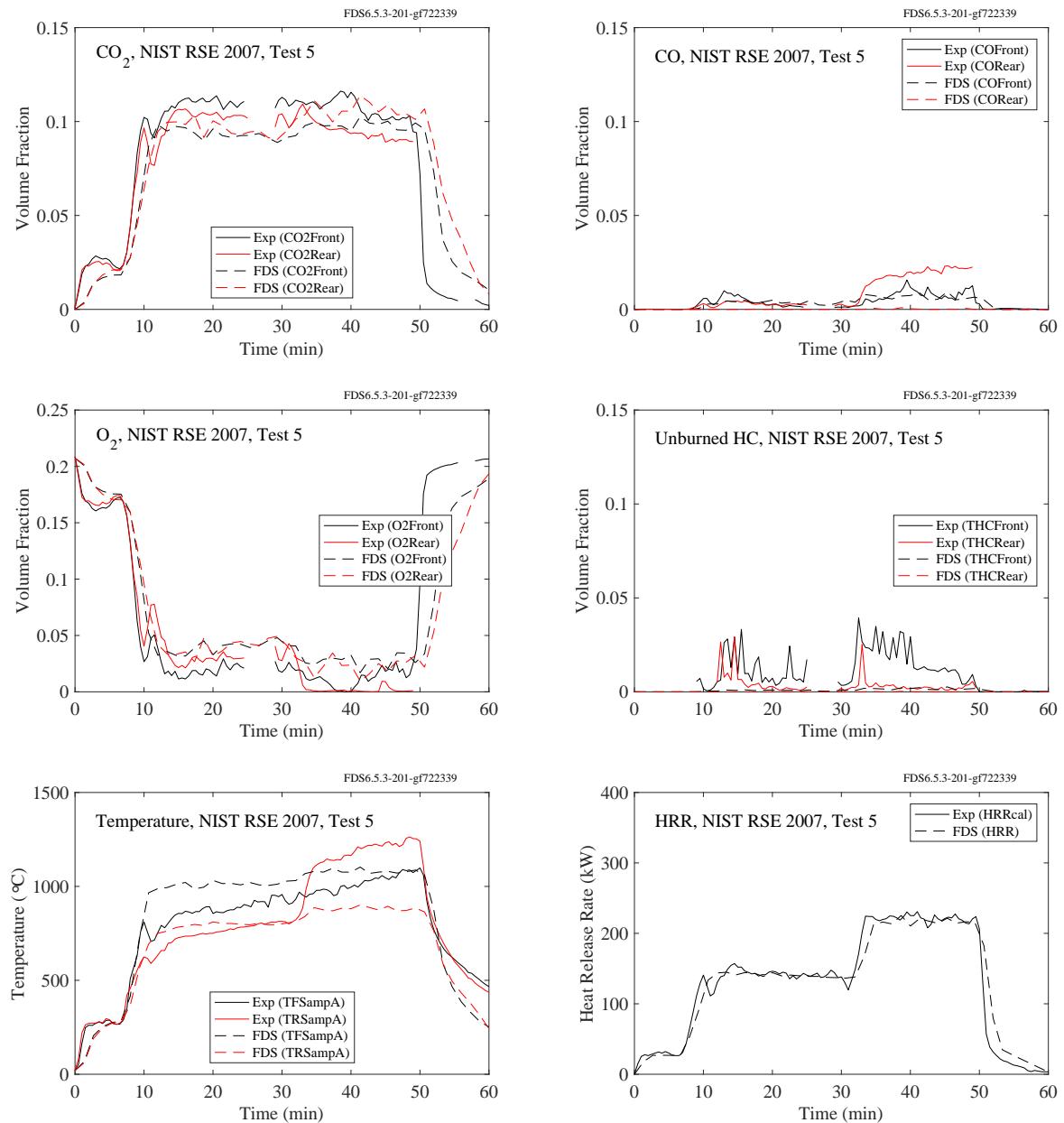


Figure 9.40: Summary of Test 5, NIST RSE 2007.

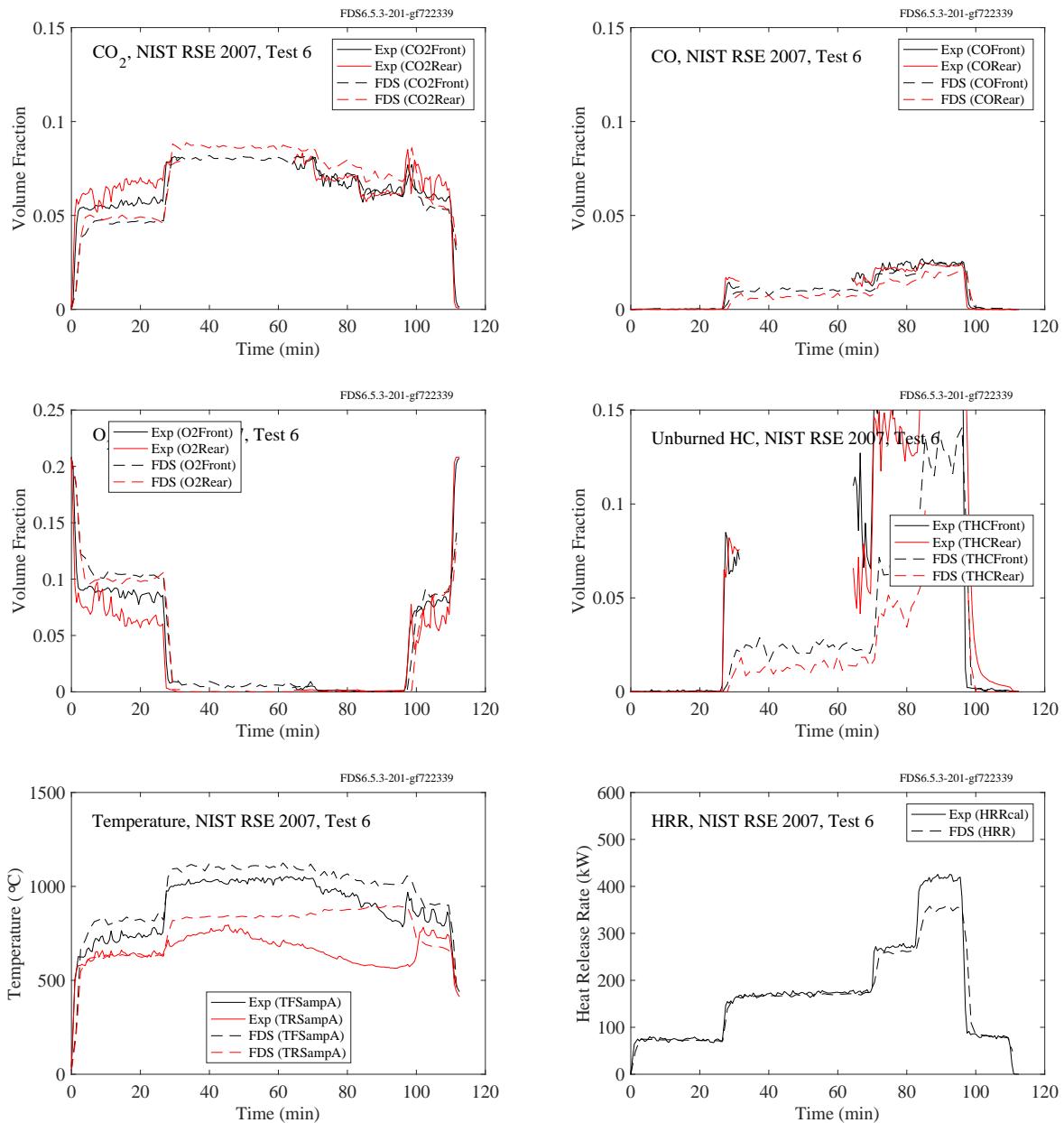


Figure 9.41: Summary of Test 6, NIST RSE 2007.

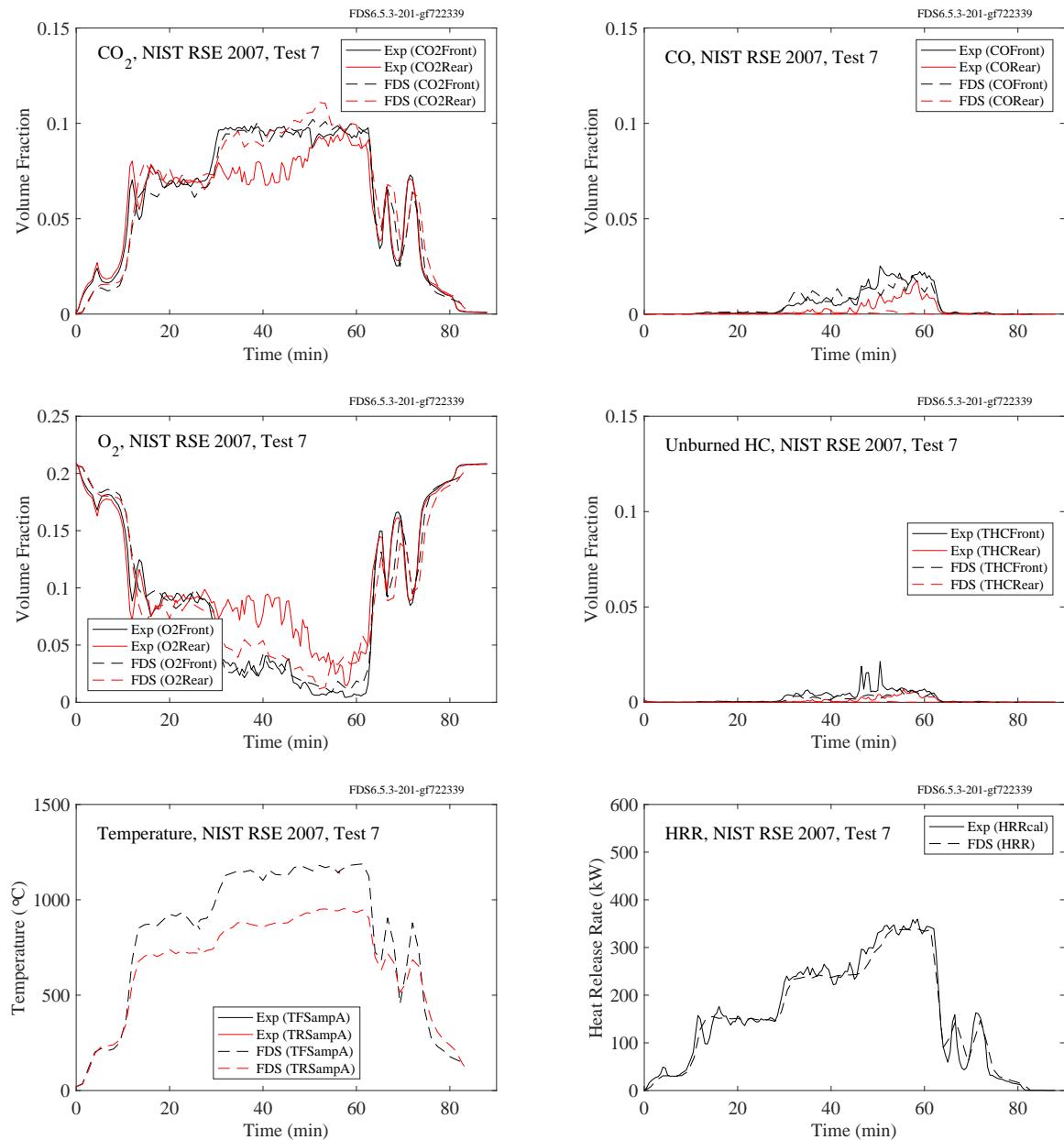


Figure 9.42: Summary of Test 7, NIST RSE 2007.

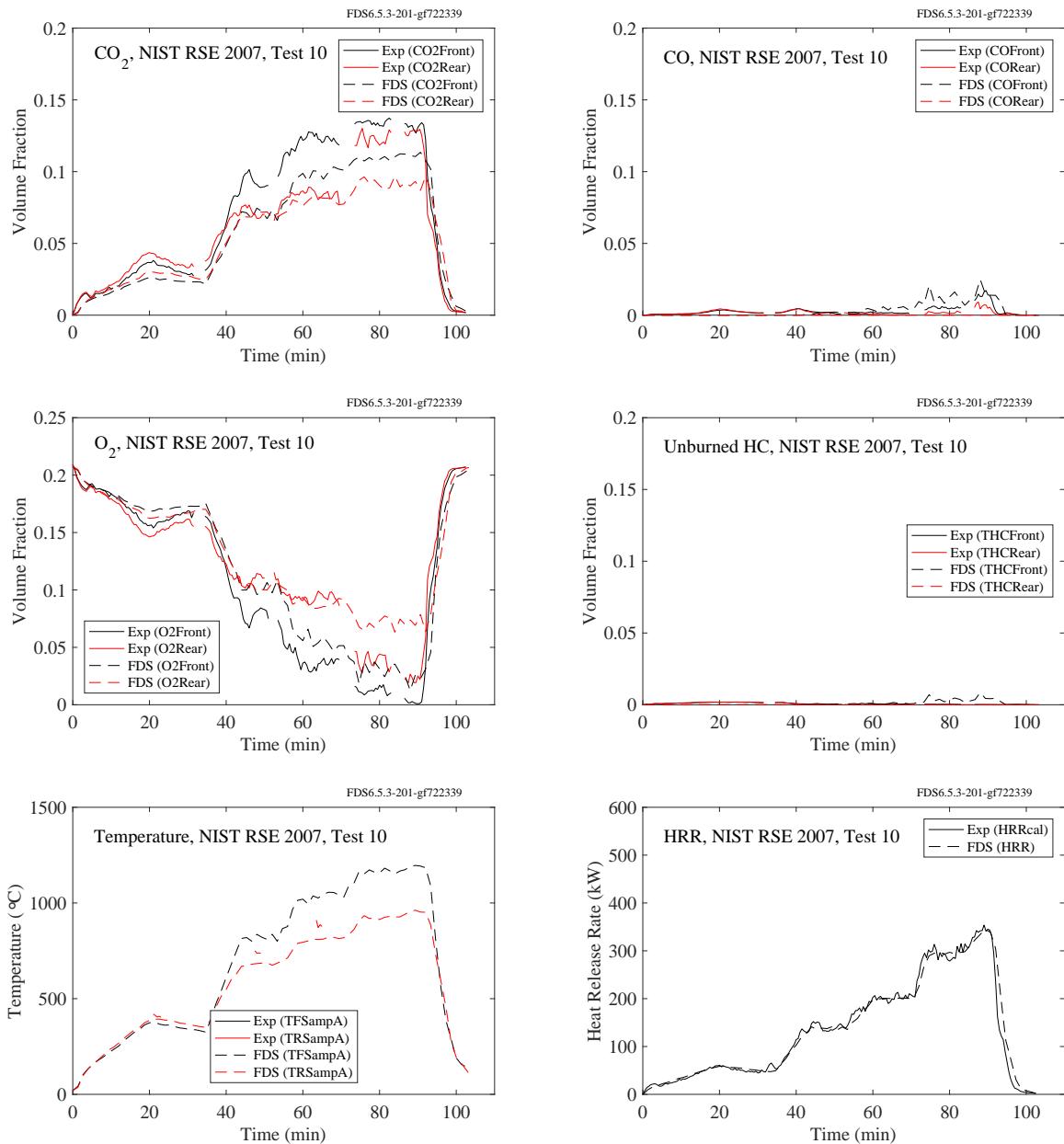


Figure 9.43: Summary of Test 10, NIST RSE 2007.

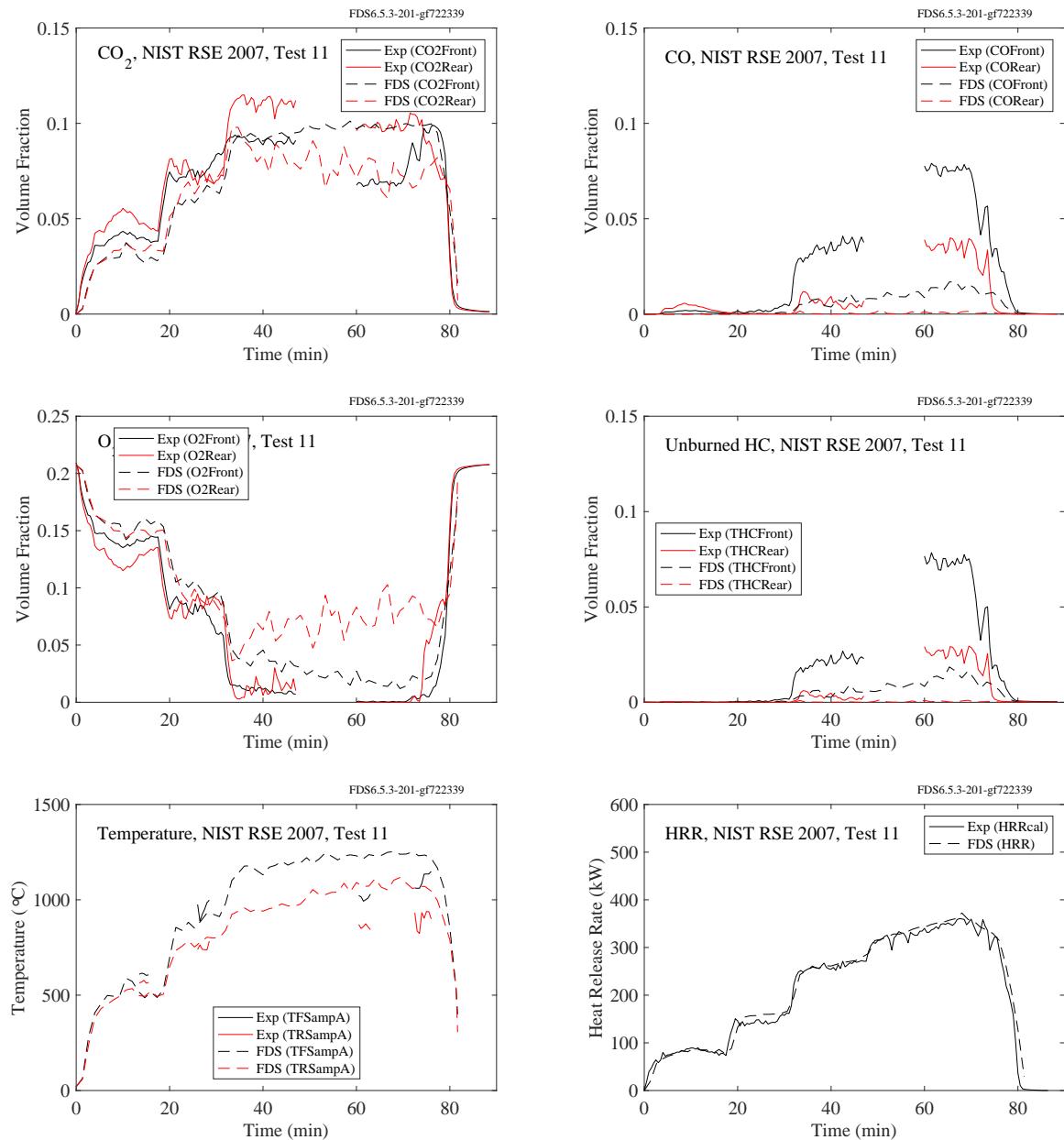


Figure 9.44: Summary of Test 11, NIST RSE 2007.

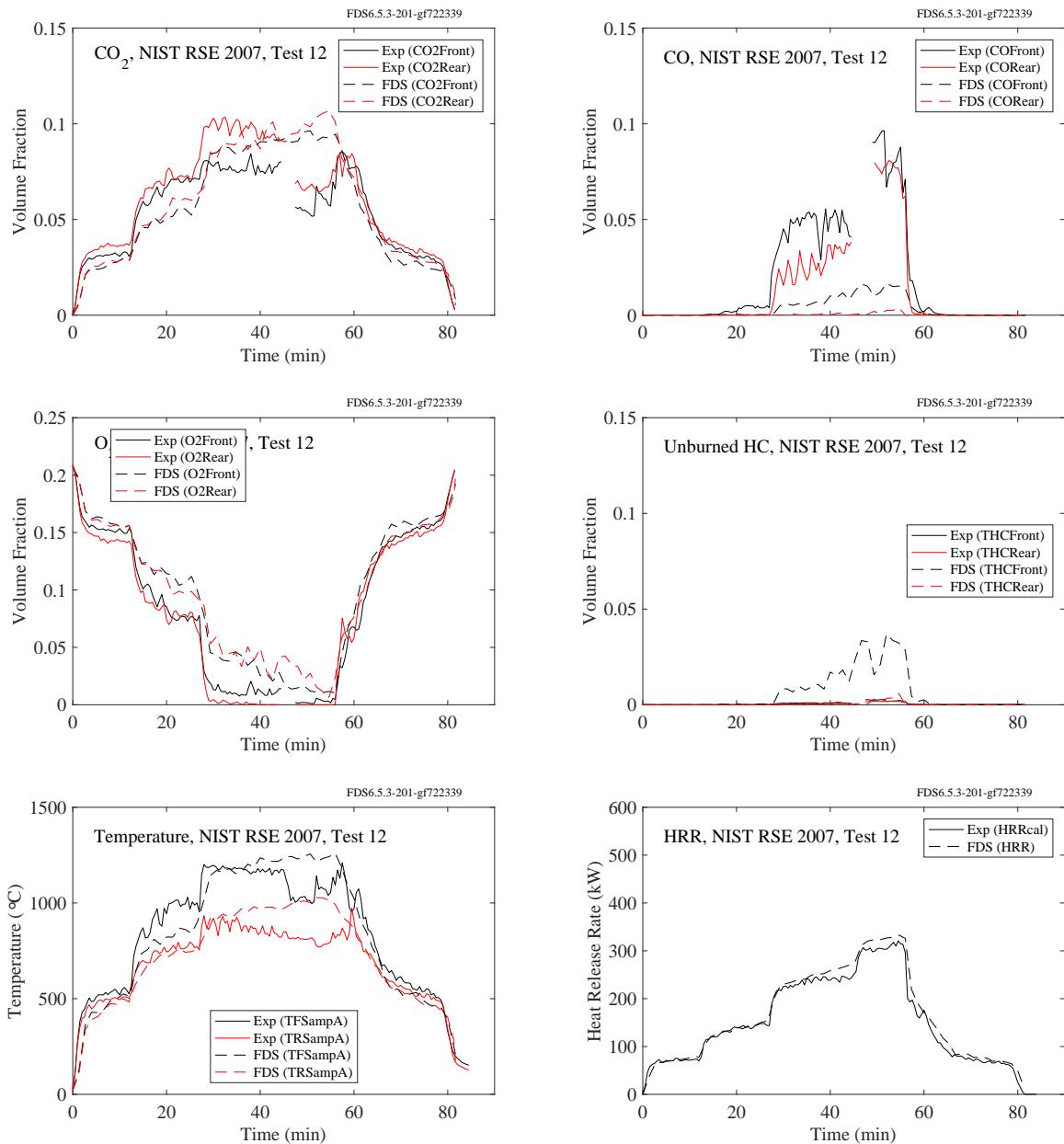


Figure 9.45: Summary of Test 12, NIST RSE 2007.

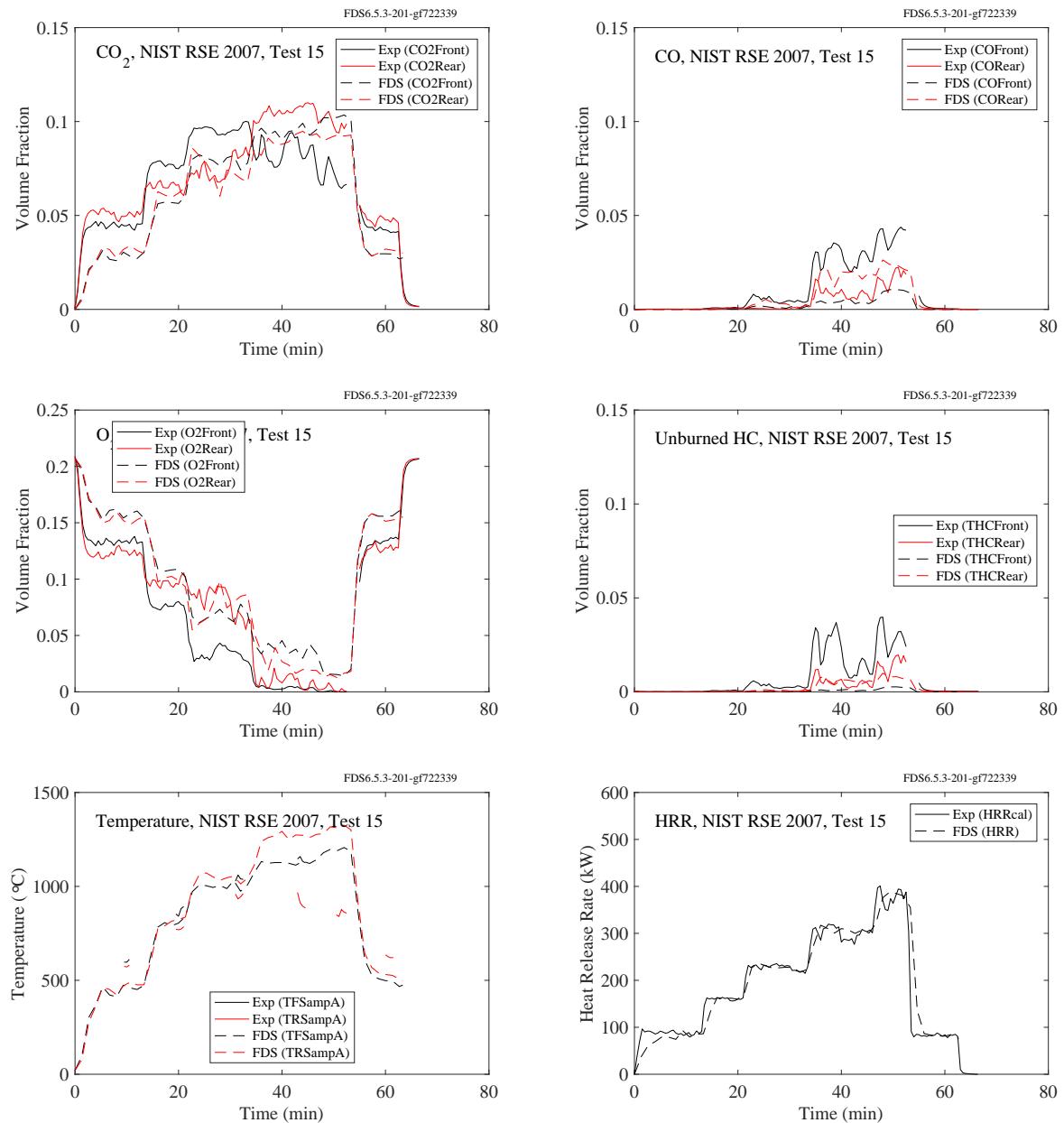


Figure 9.46: Summary of Test 15, NIST RSE 2007.

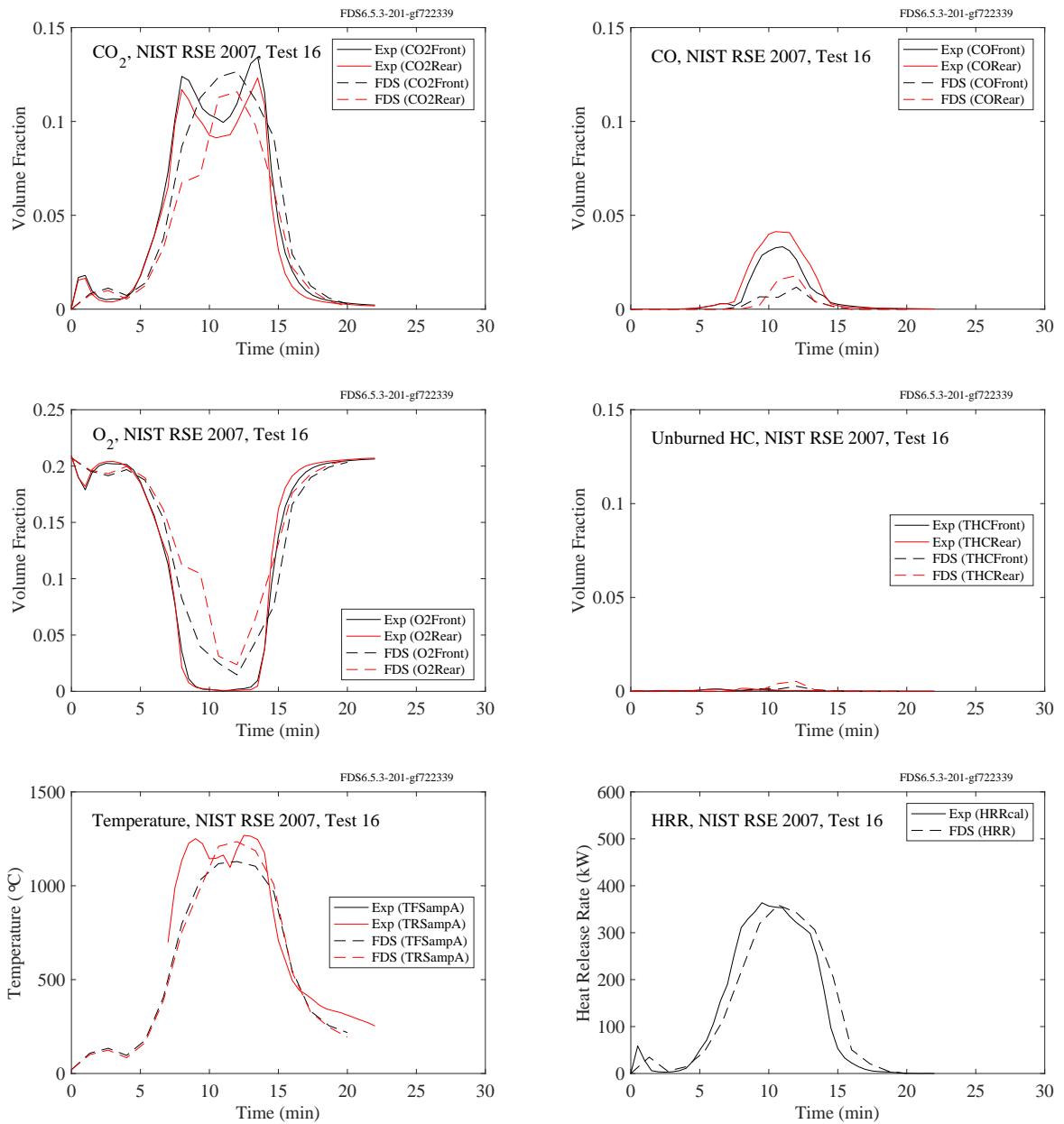


Figure 9.47: Summary of Test 16, NIST RSE 2007.

### 9.3.5 NIST Full-Scale Enclosure (FSE) Experiments, 2008

The FSE experiments [171] were selected to assess CO production capability in under-ventilated compartment fires over a range of fuels types and fire sizes in a full-scale ISO 9705 enclosure. The 30 experiments (of which 27 were selected) featured 7 different fuels: heptane, natural gas, nylon, propylene, isopropanol, styrene, and toluene. Peak heat release rates ranged from approximately 100 kW to 2.5 MW. Compartment ventilation was varied from a full 80 cm door opening to 40 cm, 20 cm, and 10 cm openings. The fuel sources in the experiments were either pool fires or spray burners, both of which were modeled. The fuel flow rates were specified in the experiments even though the fuel did not always burn.

In the simulations, there are fuels which are not pre-defined in FDS (e.g., styrene, nylon). In these cases, the fuel's enthalpy of formation is specified instead of the heat of combustion. Typically, the heat of combustion is reported for complete combustion. For the reaction mechanism used to model these experiments, however, the oxidation of fuel produces only carbon monoxide (i.e., incomplete combustion). Thus, typical literature values are not appropriate. An alternative to specifying the heat of combustion is to use the enthalpy of formation of the fuel. If that value cannot be found from literature or if a fuel mixture has been created, FDS can be used to determine an approximate value. Consider the following REAC line:

```
&REAC ID='NG', FUEL='NATURAL_GAS', FORMULA='C1.06084H4.076451N0.01552900.014848' /
```

FDS will compute a balanced reaction assuming complete combustion and the heat of combustion will be determined based on oxygen consumption (see the FDS User's Guide discussion of the parameter EPUMO2). A benefit of this process is that the enthalpy of formation of the fuel is automatically computed and is written to the CHID.out file. Enthalpy of formation is a fundamental fuel property and not a reaction property like heat of combustion. As a result, this value can be used to define the fuel for the reaction mechanism with incomplete combustion.

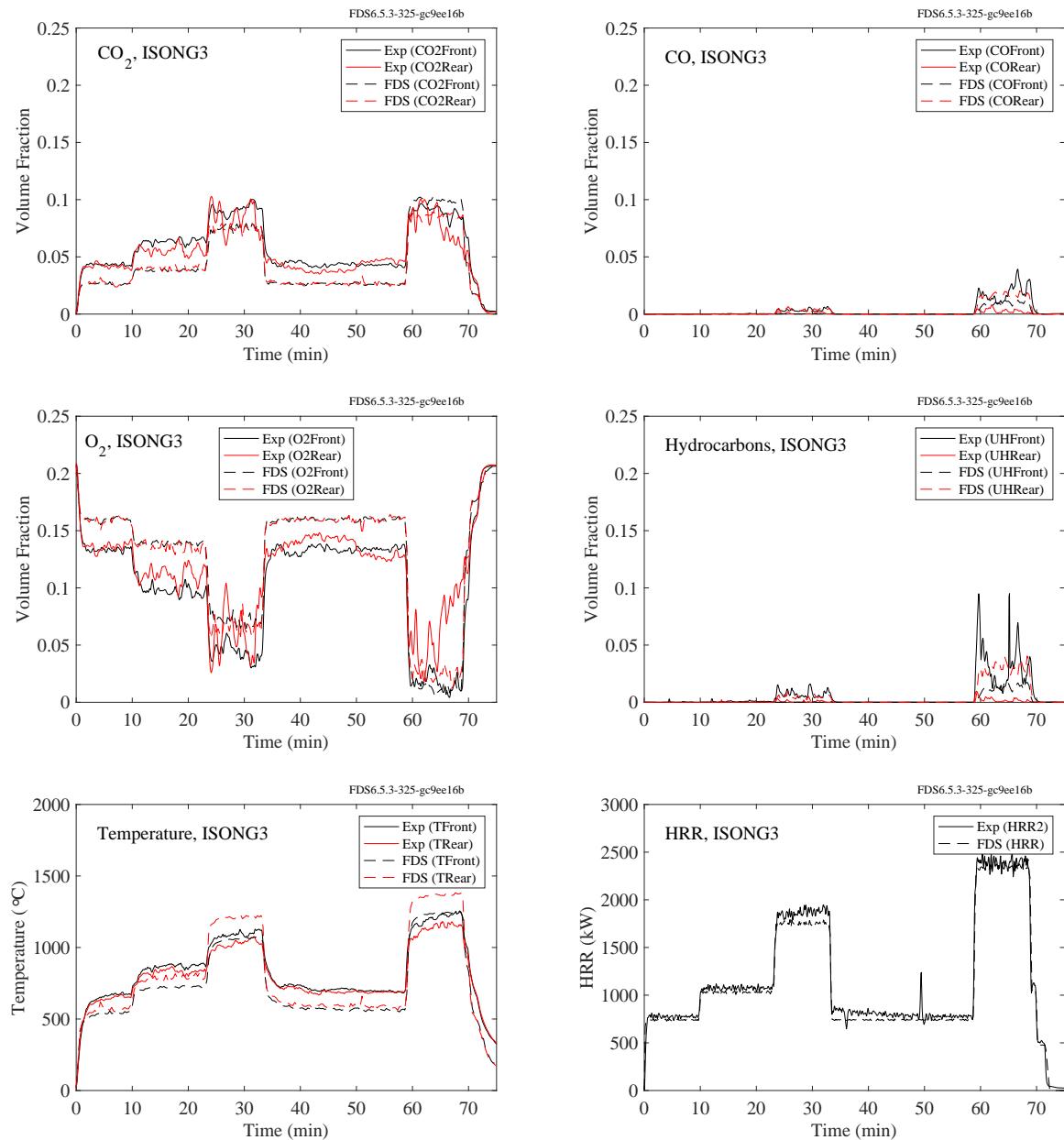


Figure 9.48: Summary of ISONG3, NIST FSE 2008.

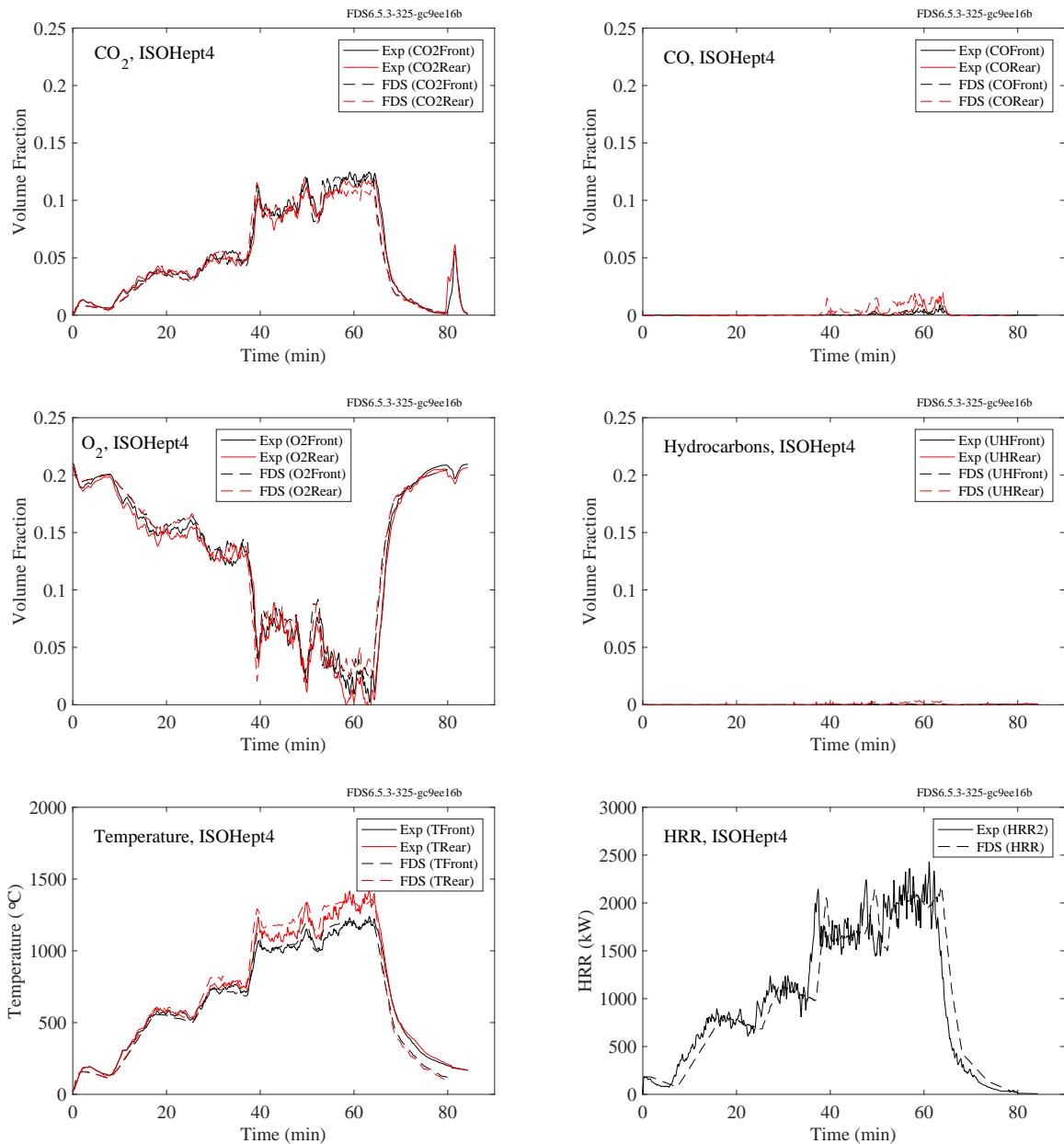


Figure 9.49: Summary of ISOHept4, NIST FSE 2008.

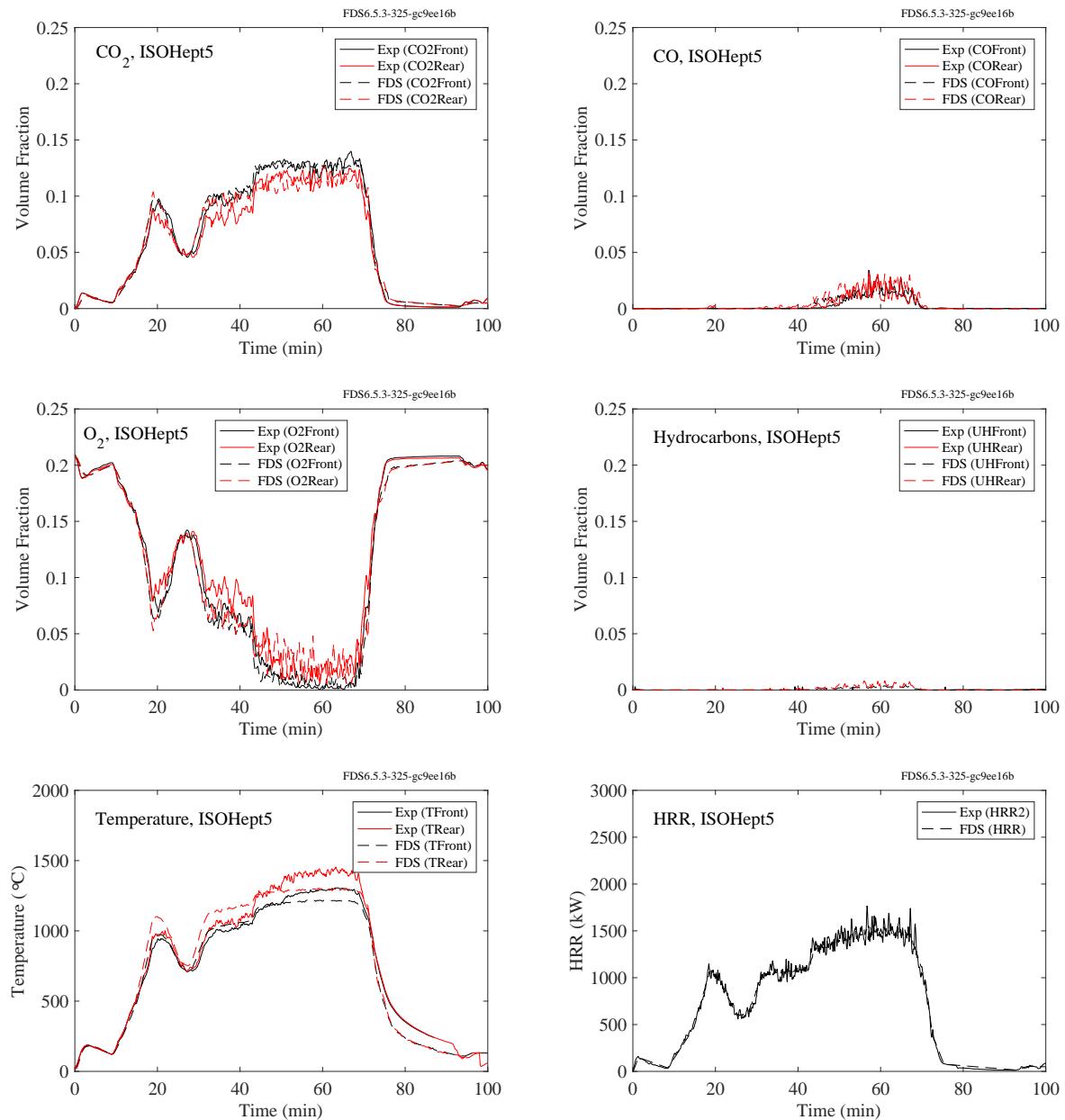


Figure 9.50: Summary of ISOHept5, NIST FSE 2008.

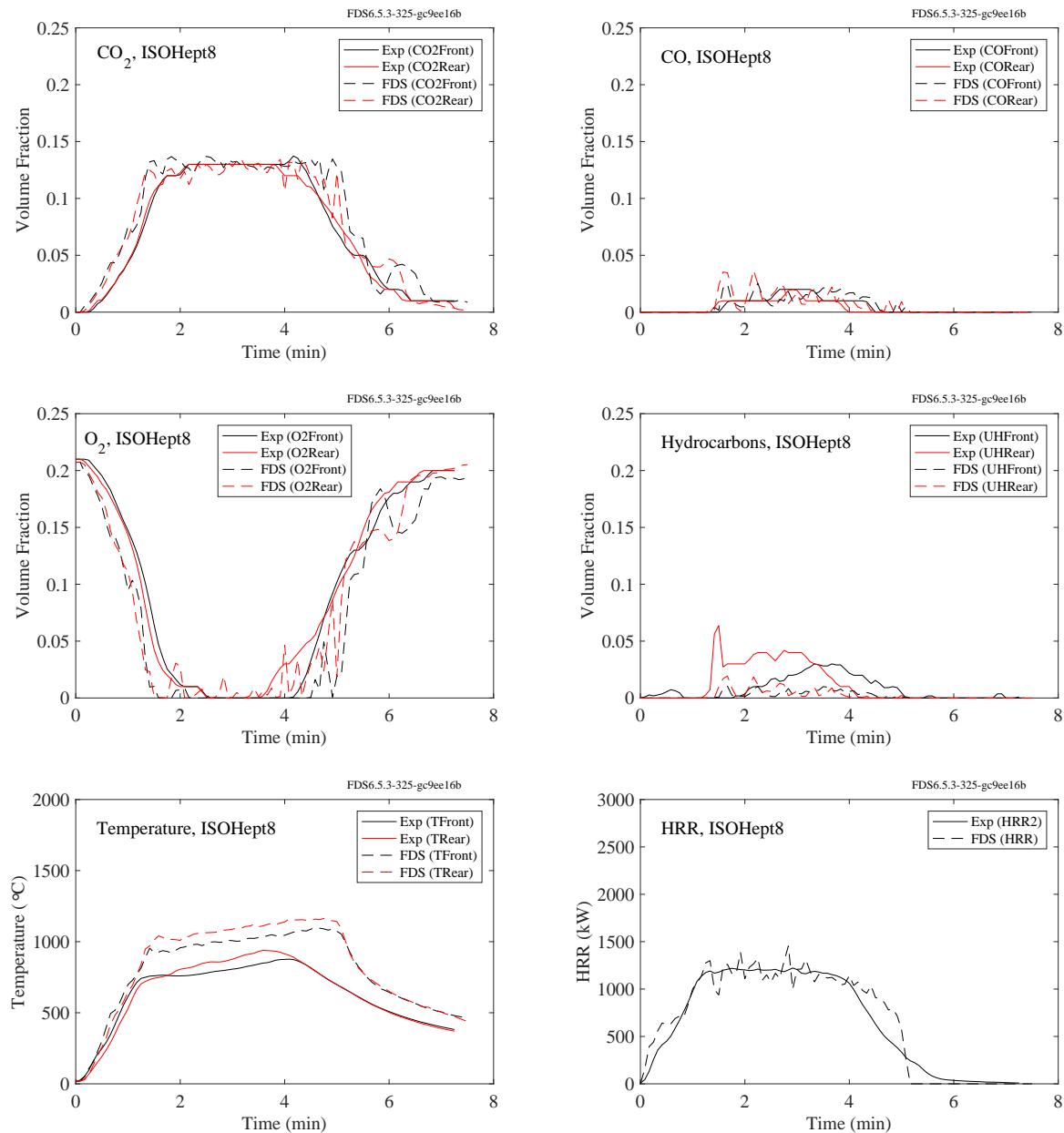


Figure 9.51: Summary of ISOHept8, NIST FSE 2008.

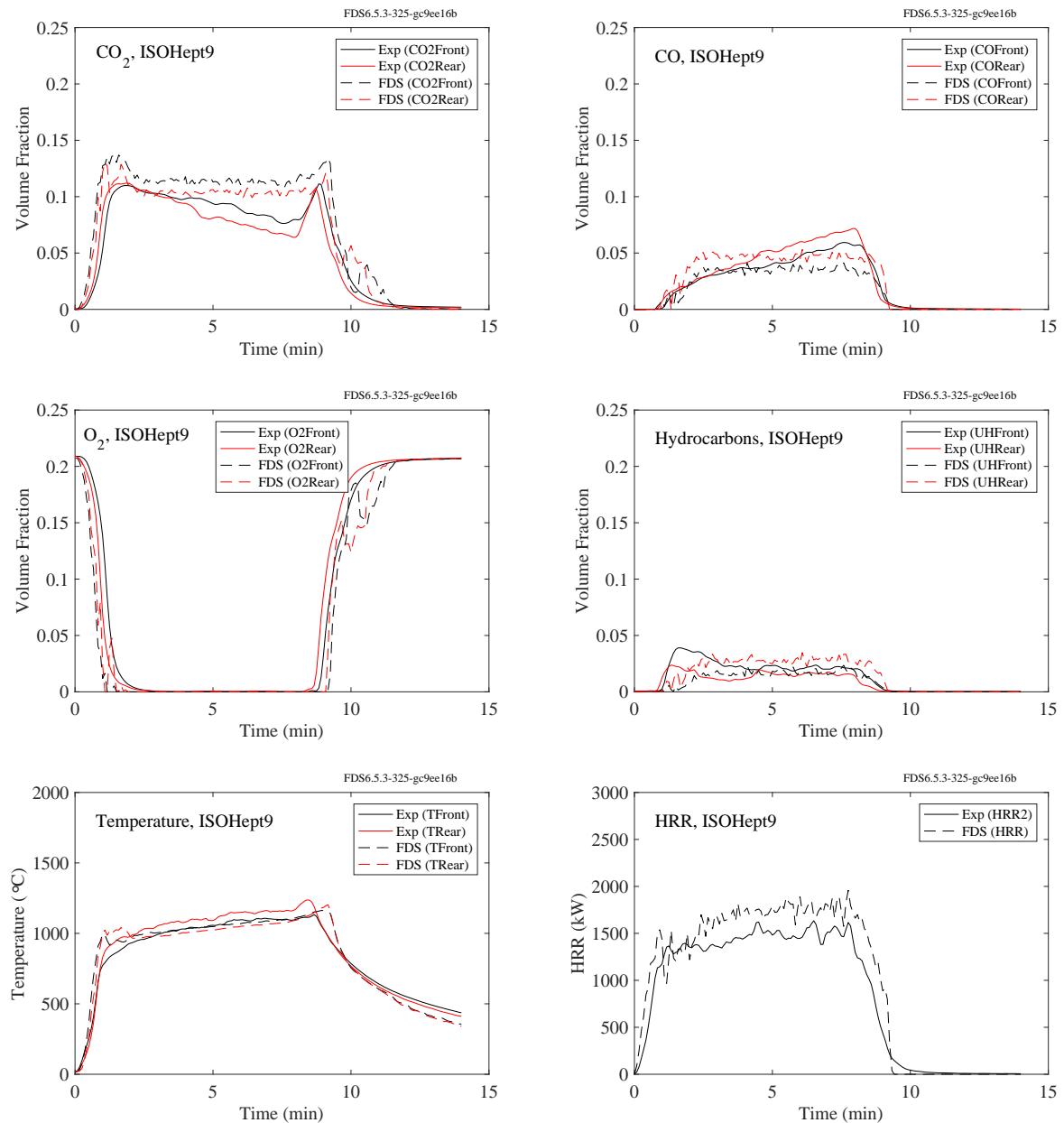


Figure 9.52: Summary of ISOHept9, NIST FSE 2008.

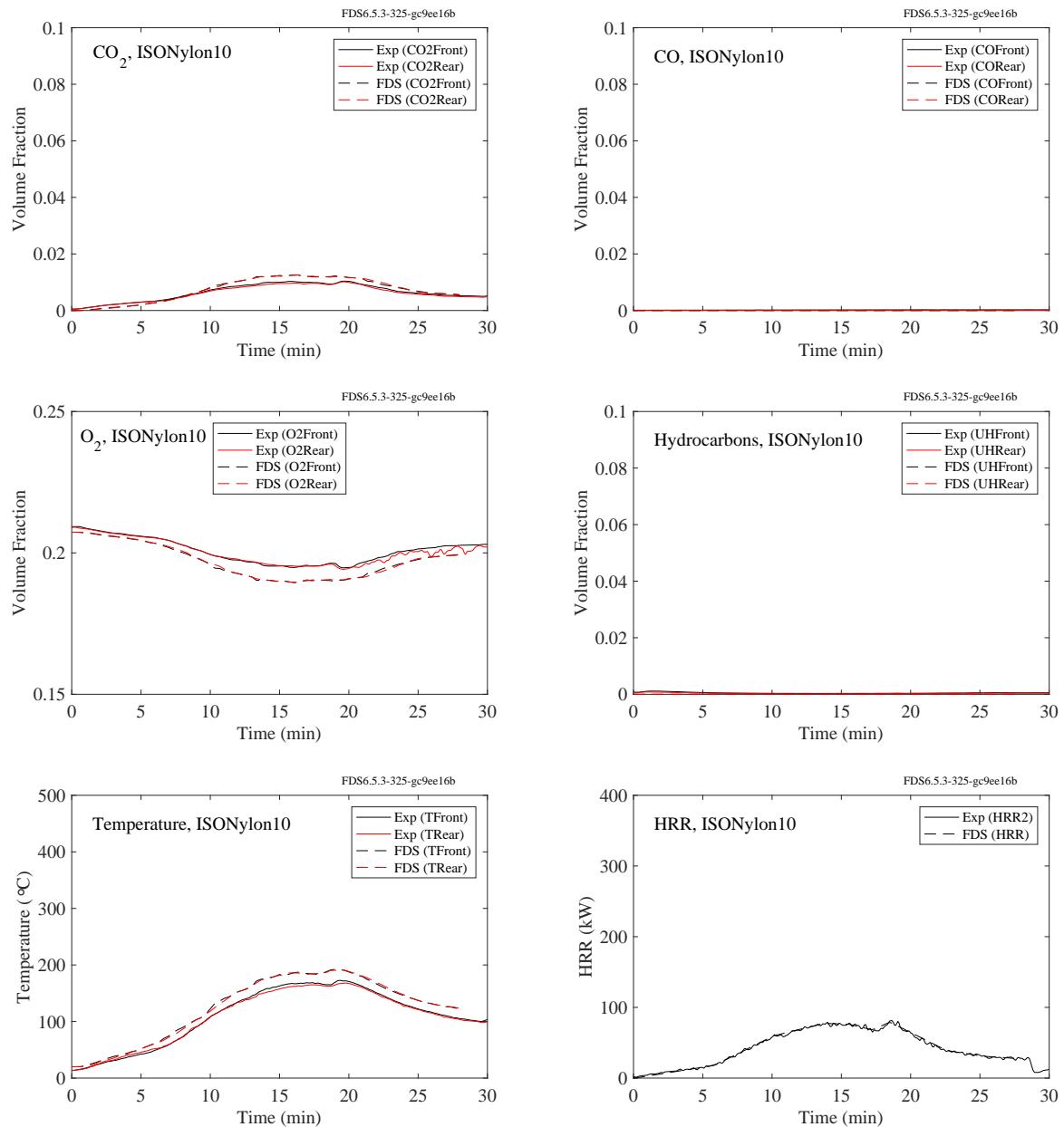


Figure 9.53: Summary of ISONylon10, NIST FSE 2008.

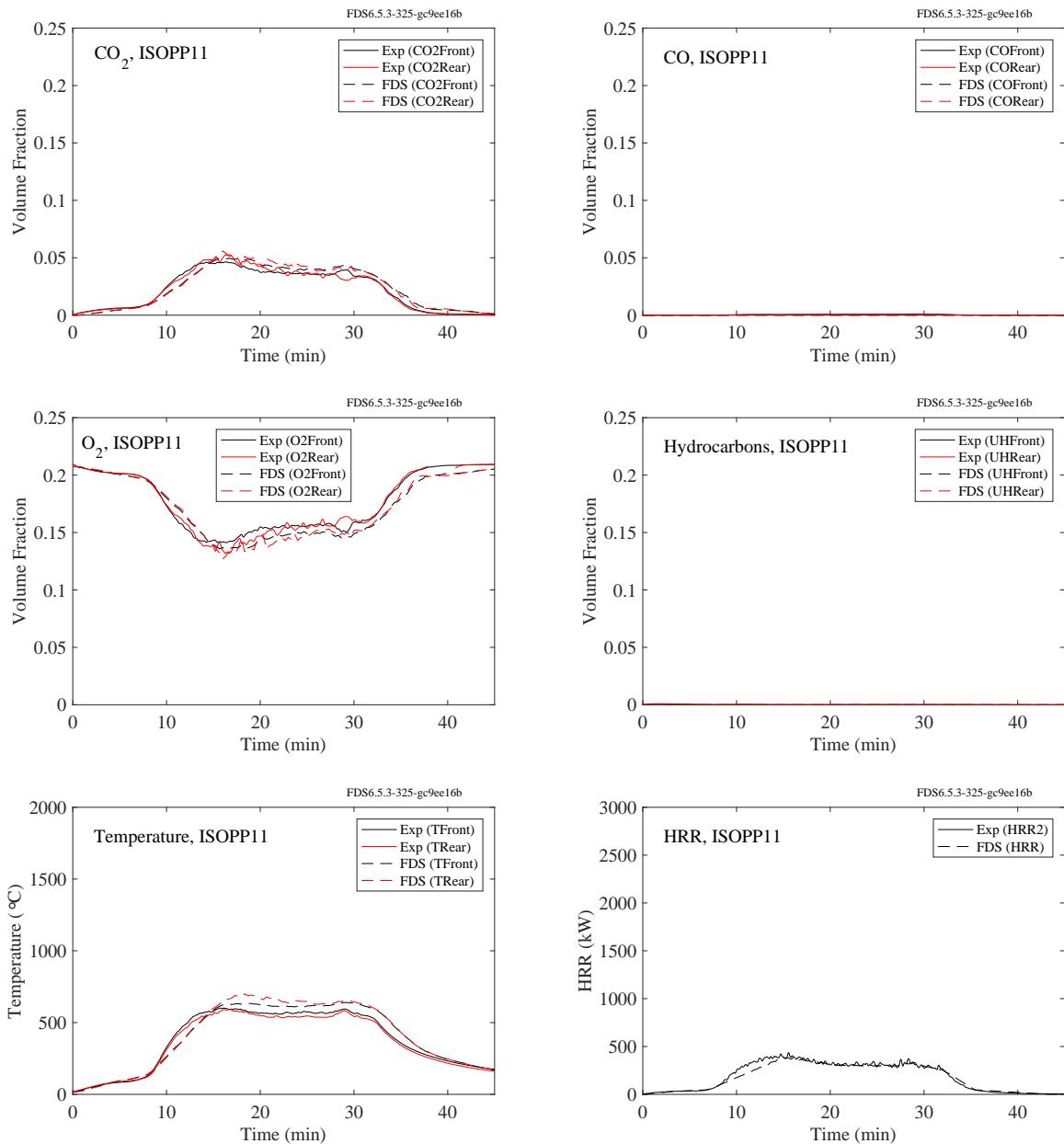


Figure 9.54: Summary of ISOPP11, NIST FSE 2008.

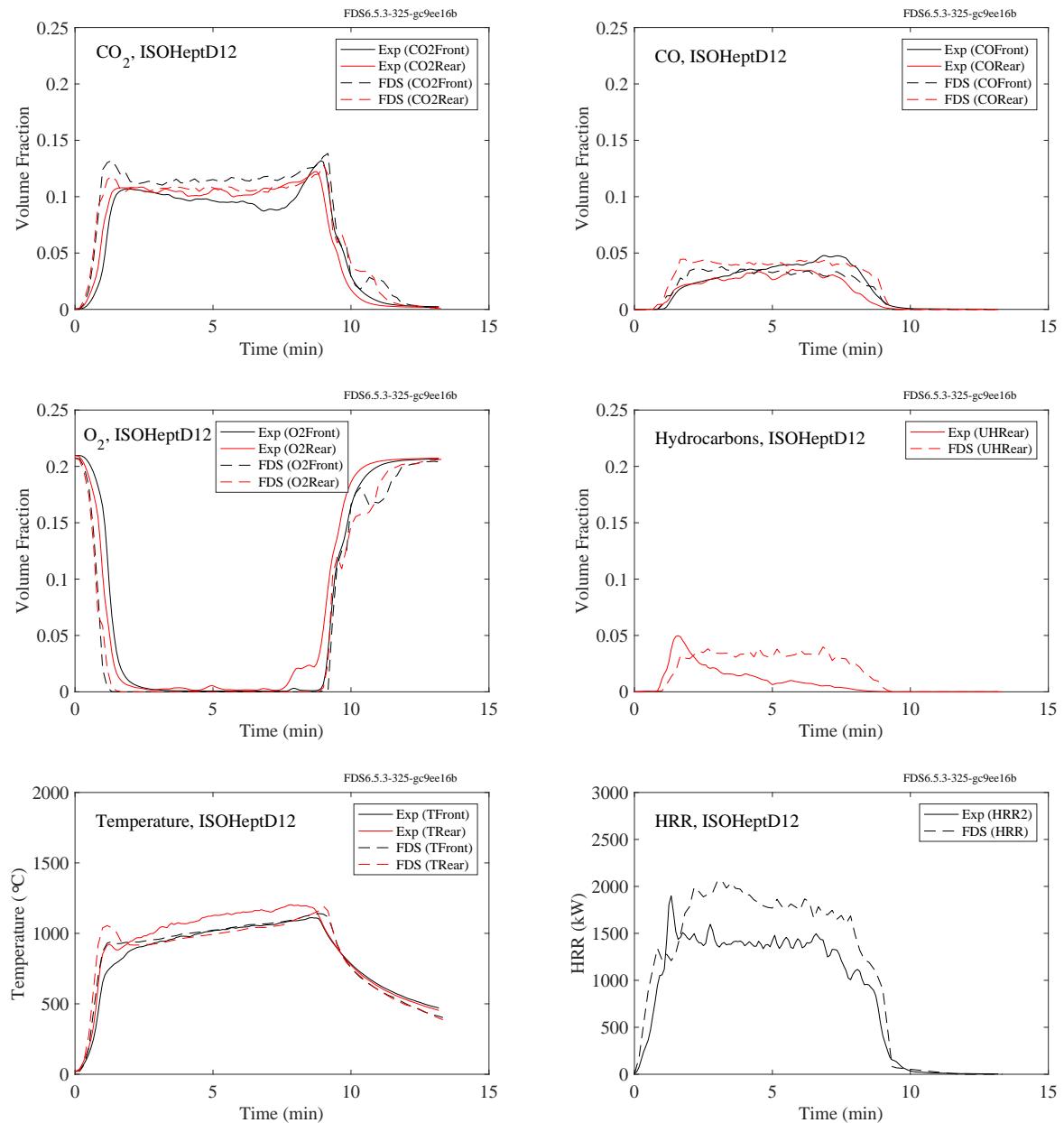


Figure 9.55: Summary of ISOHeptD12, NIST FSE 2008.

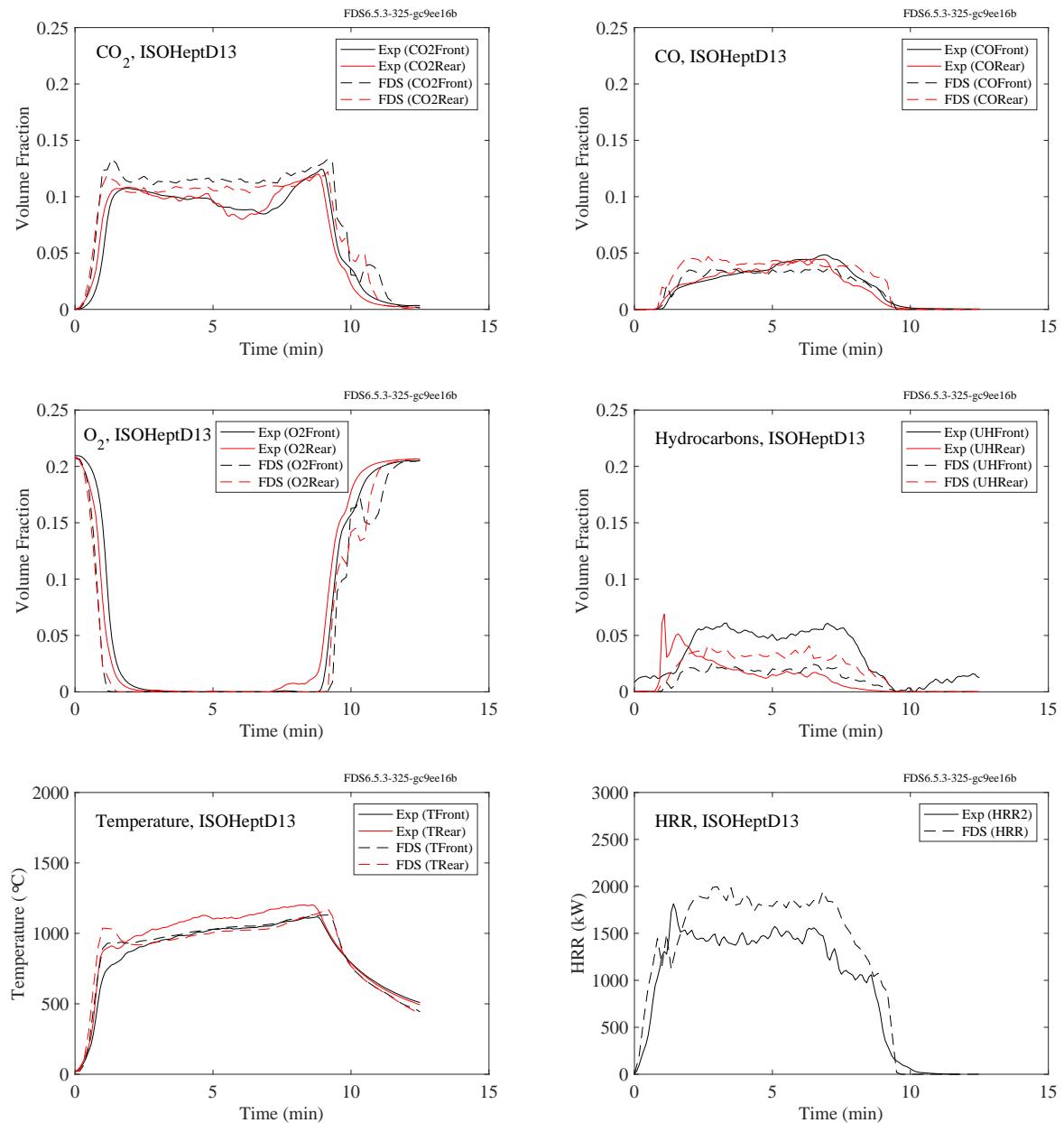


Figure 9.56: Summary of ISOHeptD13, NIST FSE 2008.

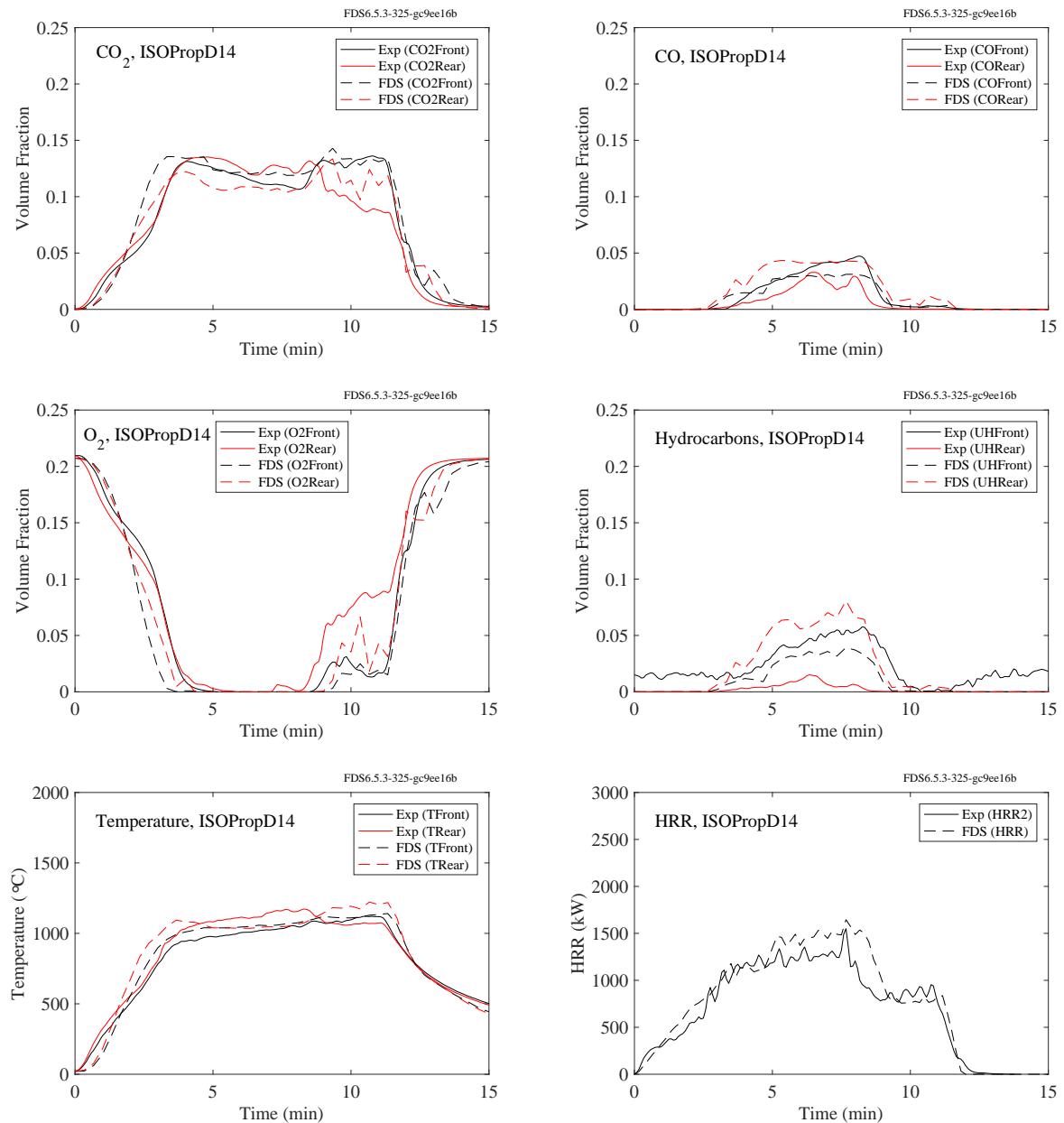


Figure 9.57: Summary of ISOPropD14, NIST FSE 2008.

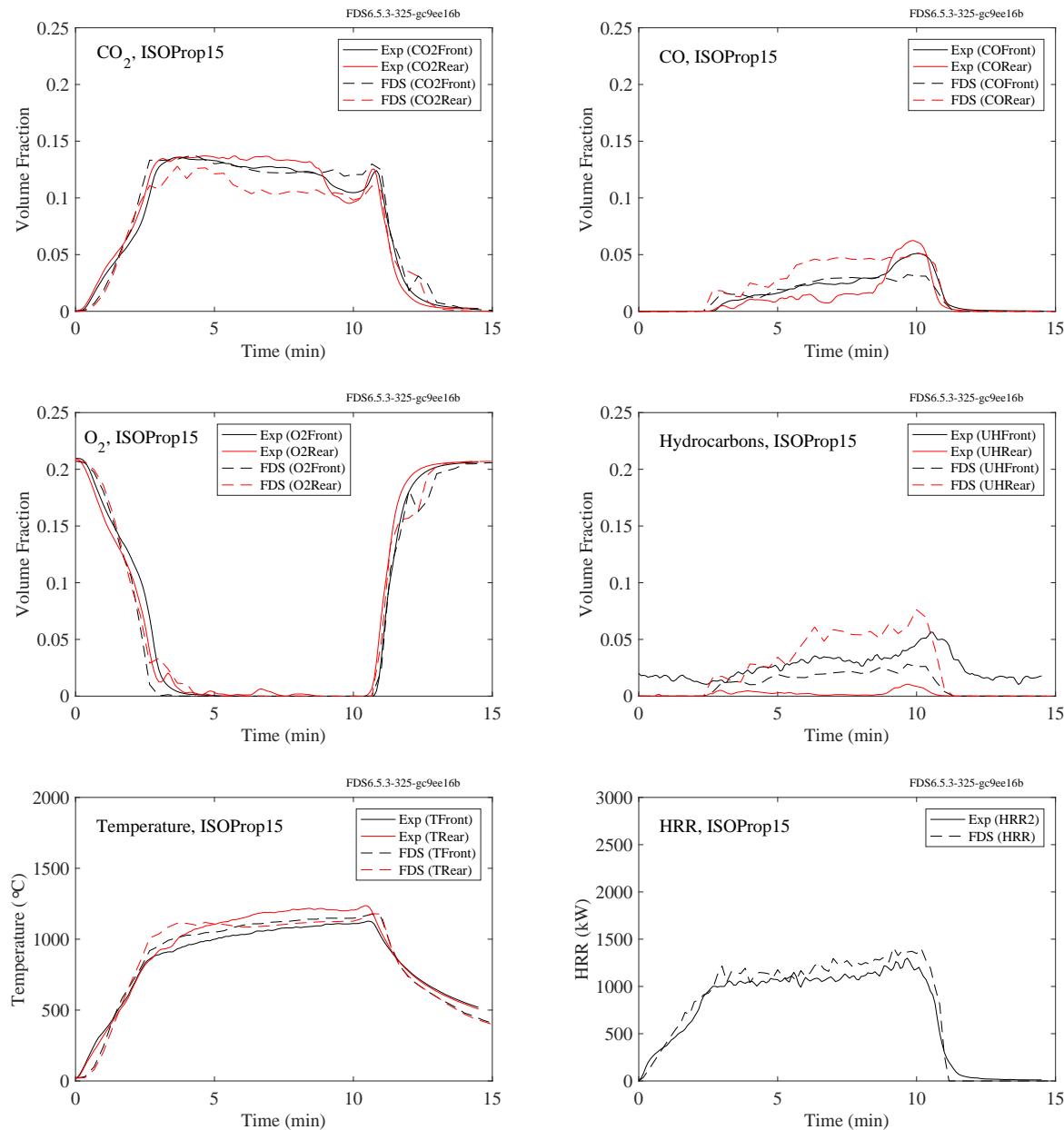


Figure 9.58: Summary of ISOProp15, NIST FSE 2008.

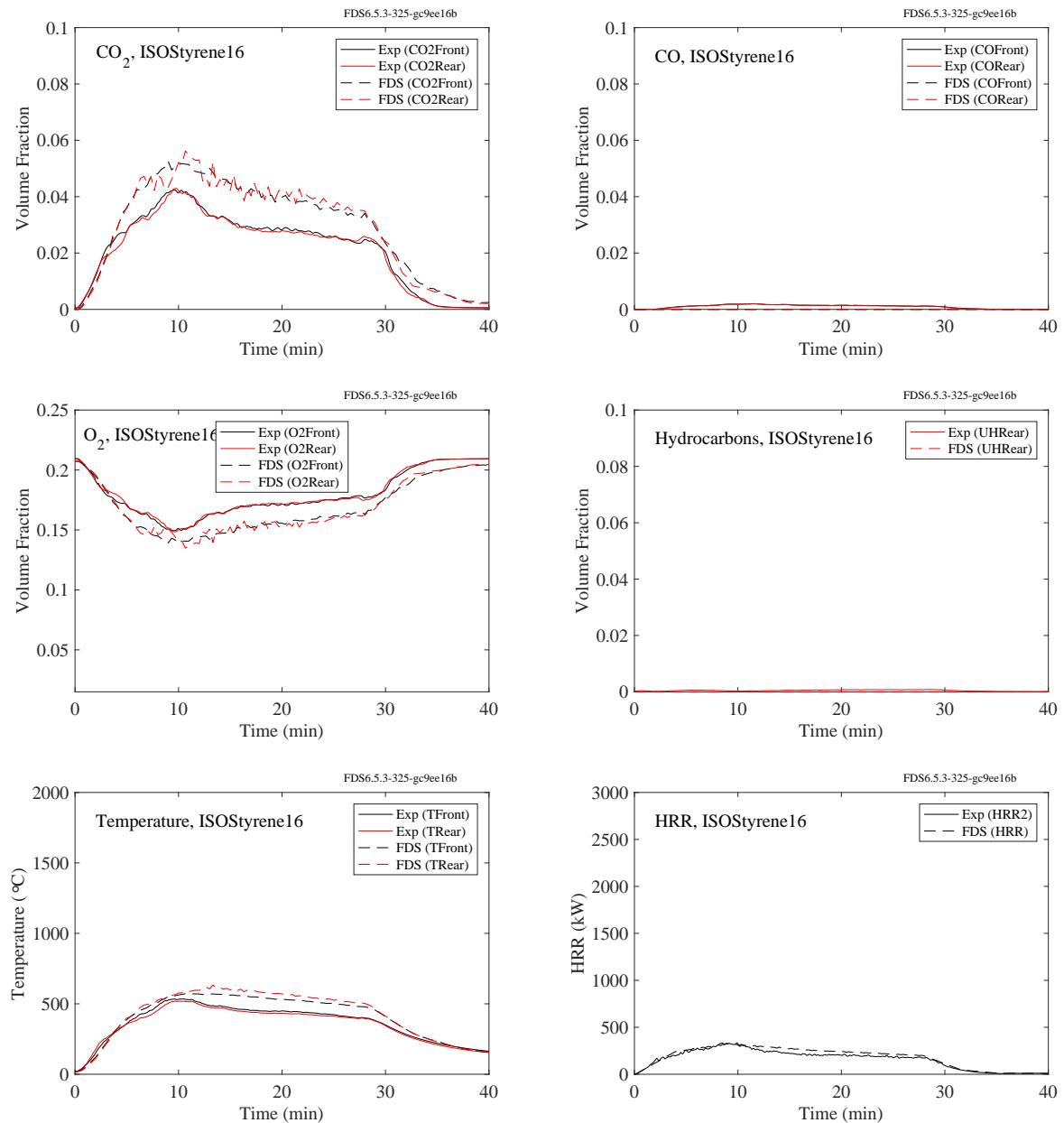


Figure 9.59: Summary of ISOStyrene16, NIST FSE 2008.

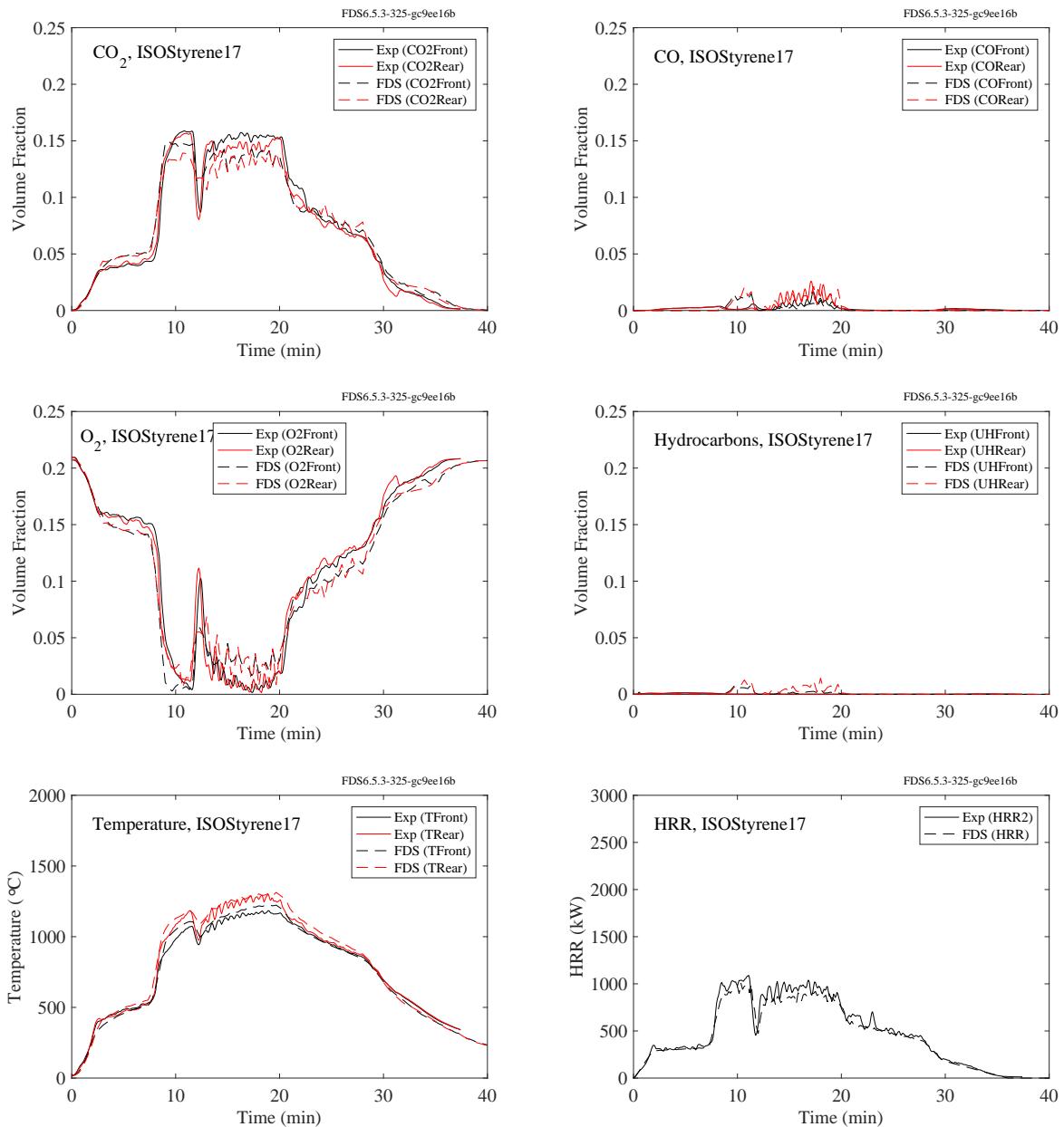


Figure 9.60: Summary of ISOStyrene17, NIST FSE 2008.

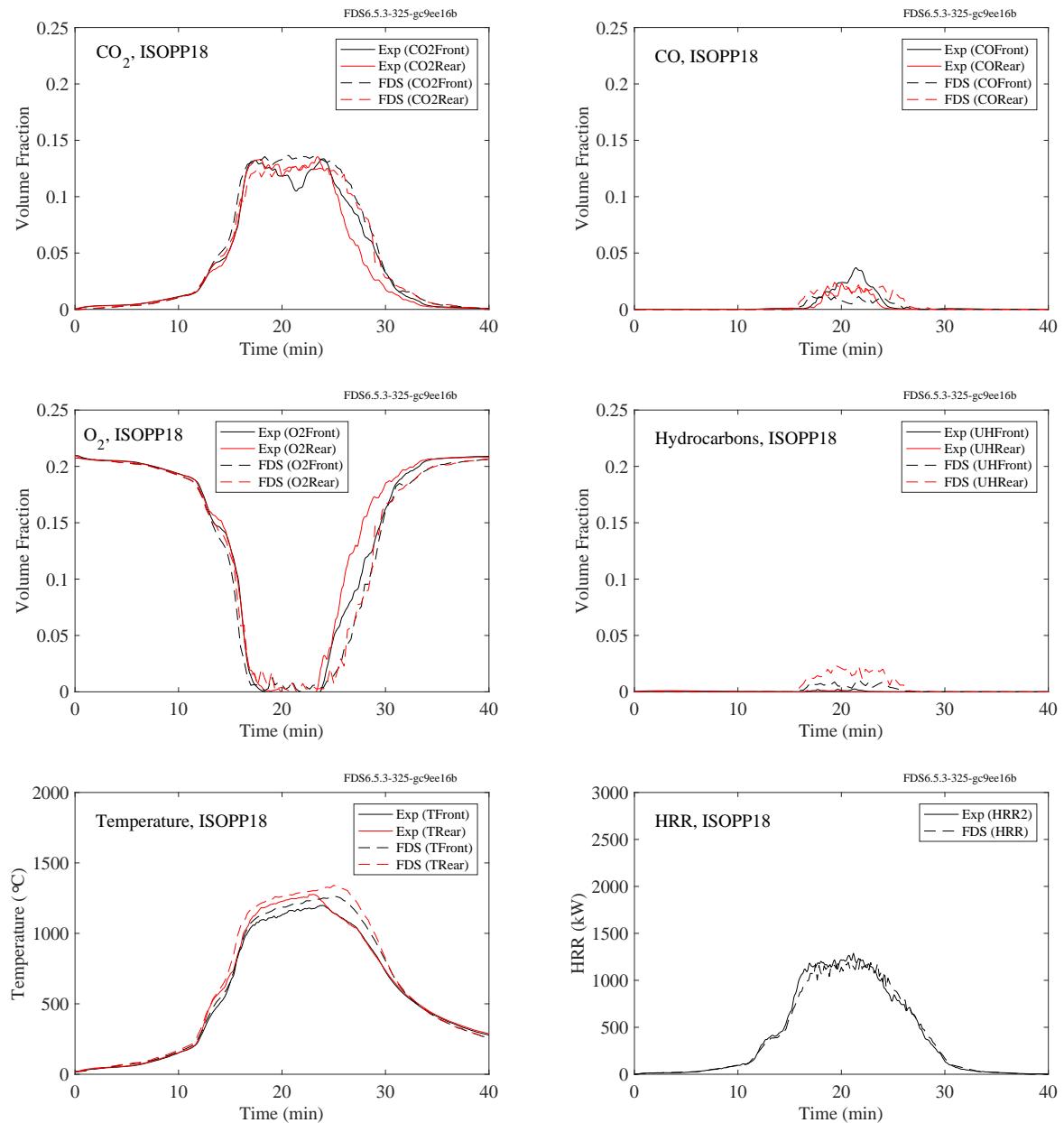


Figure 9.61: Summary of ISOPP18, NIST FSE 2008.

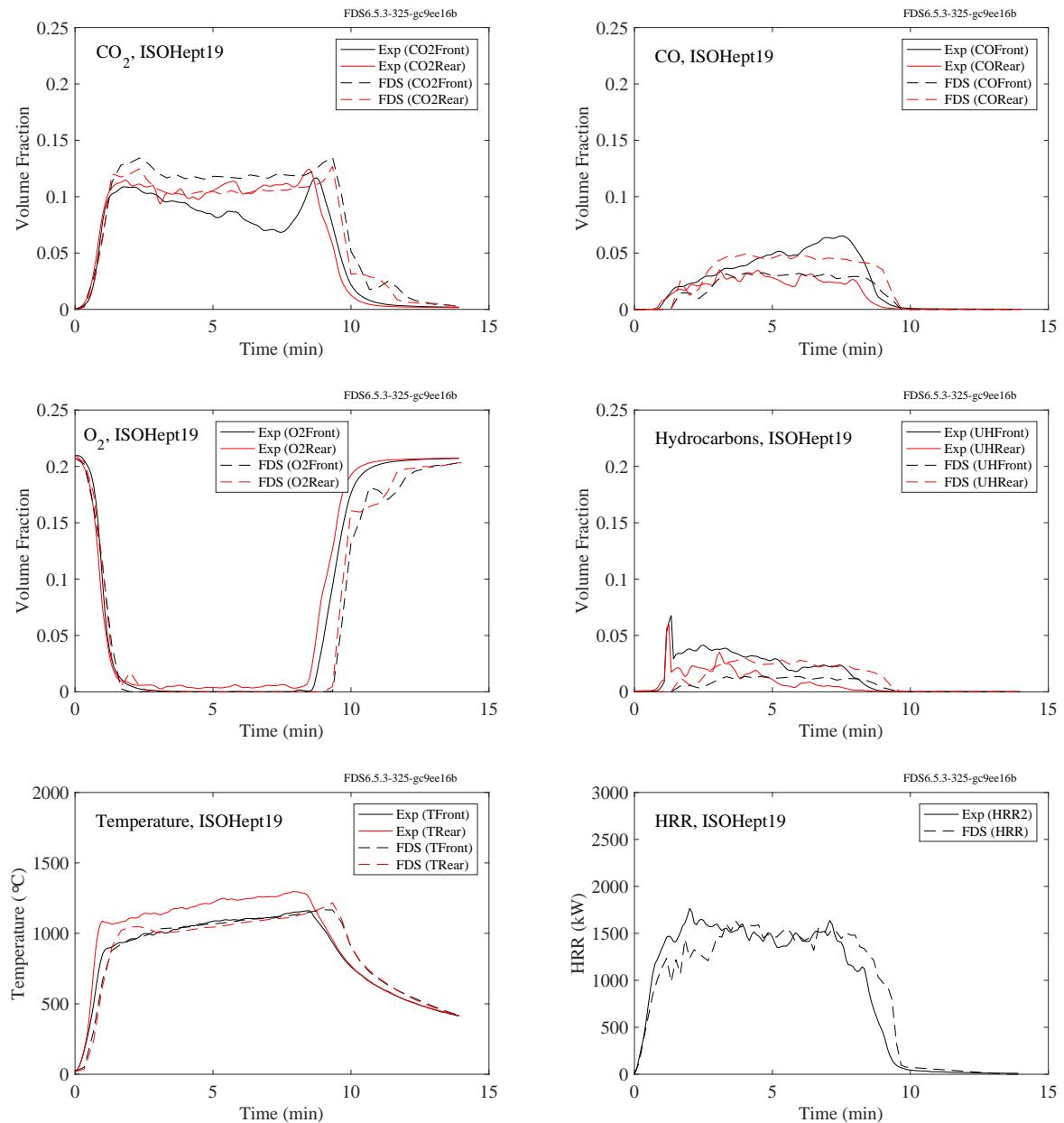


Figure 9.62: Summary of ISOHept19, NIST FSE 2008.

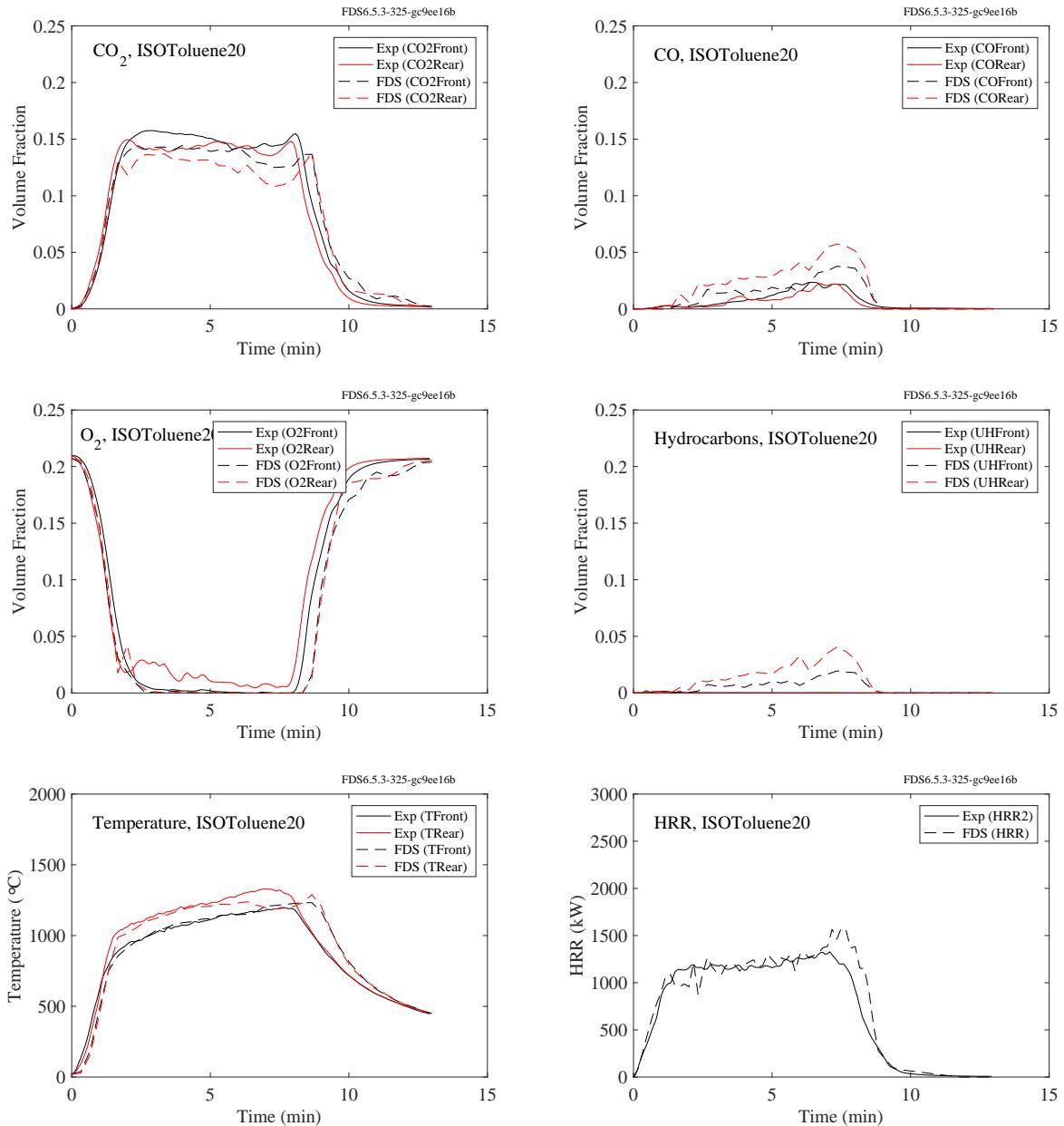


Figure 9.63: Summary of ISOToluene20, NIST FSE 2008.

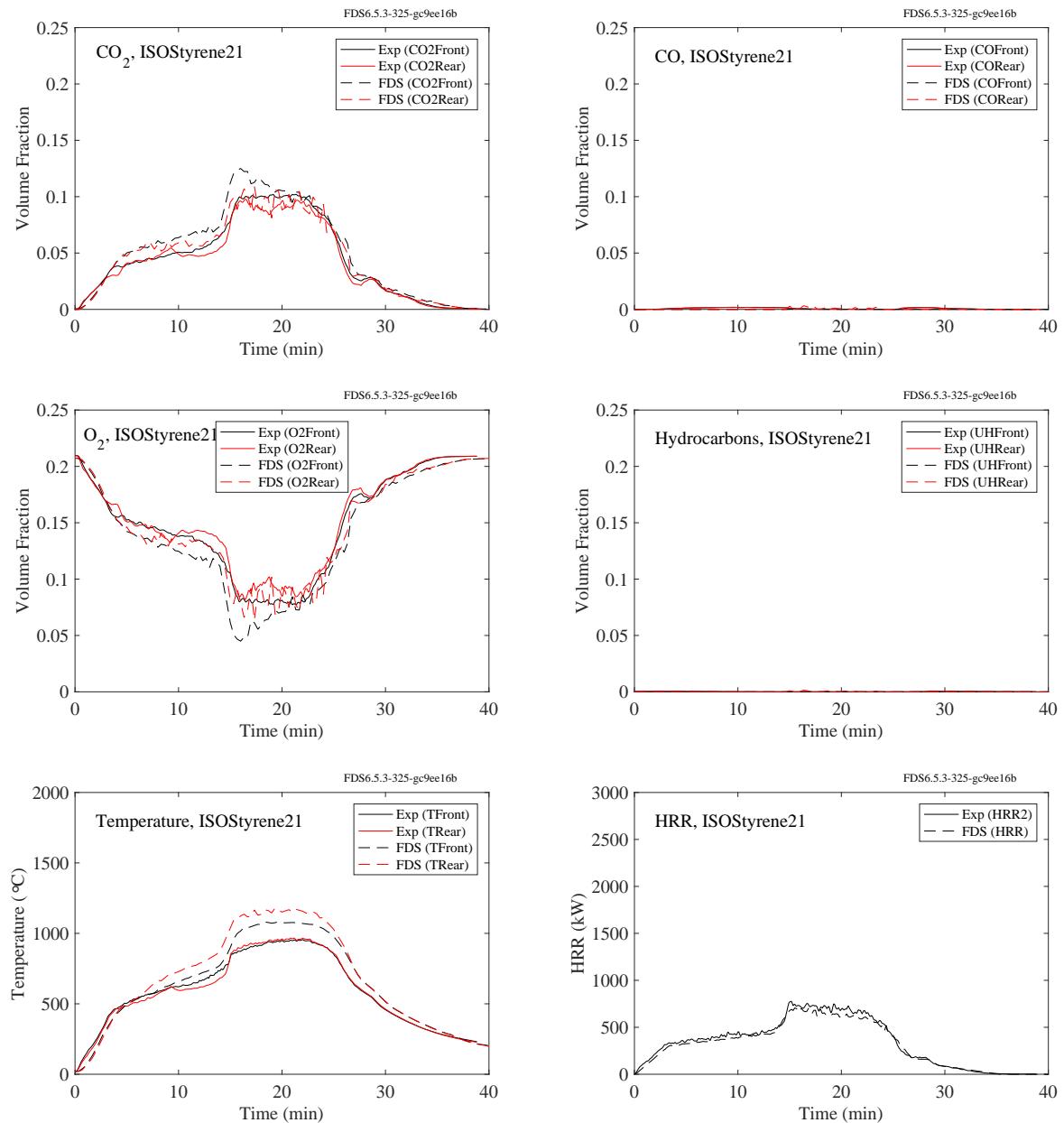


Figure 9.64: Summary of ISOStyrene21, NIST FSE 2008.

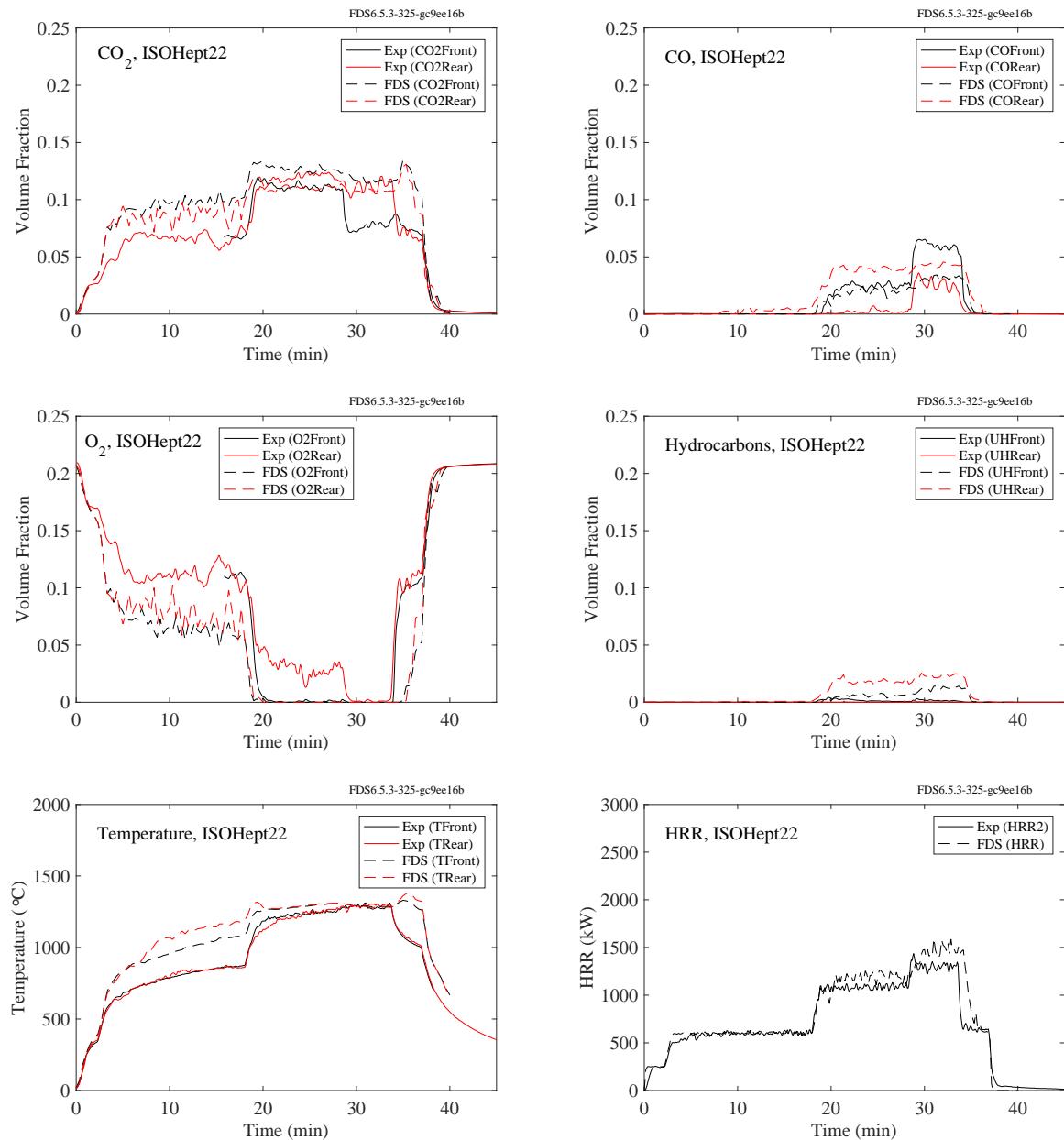


Figure 9.65: Summary of ISOHept22, NIST FSE 2008.

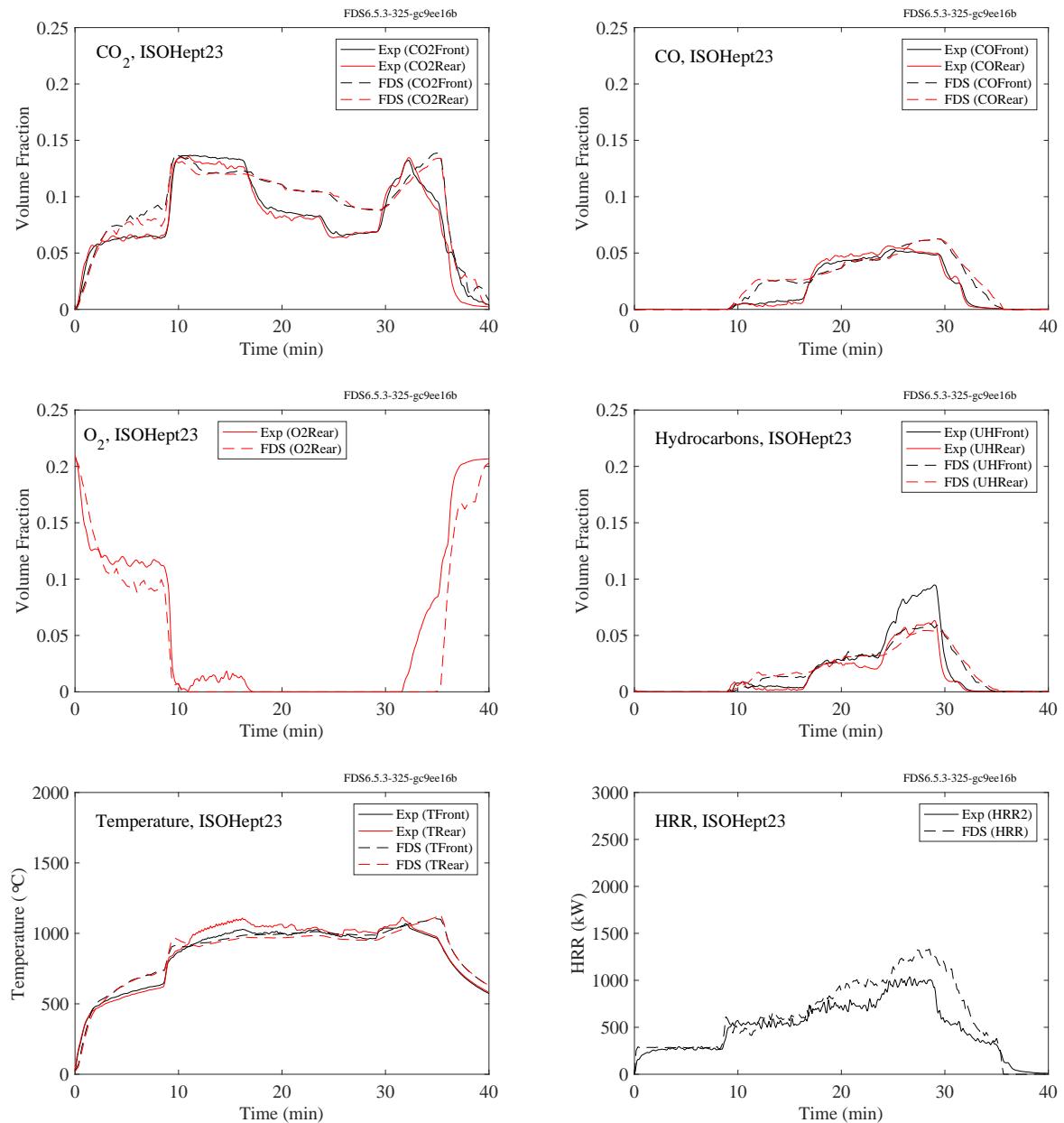


Figure 9.66: Summary of ISOHept23, NIST FSE 2008.

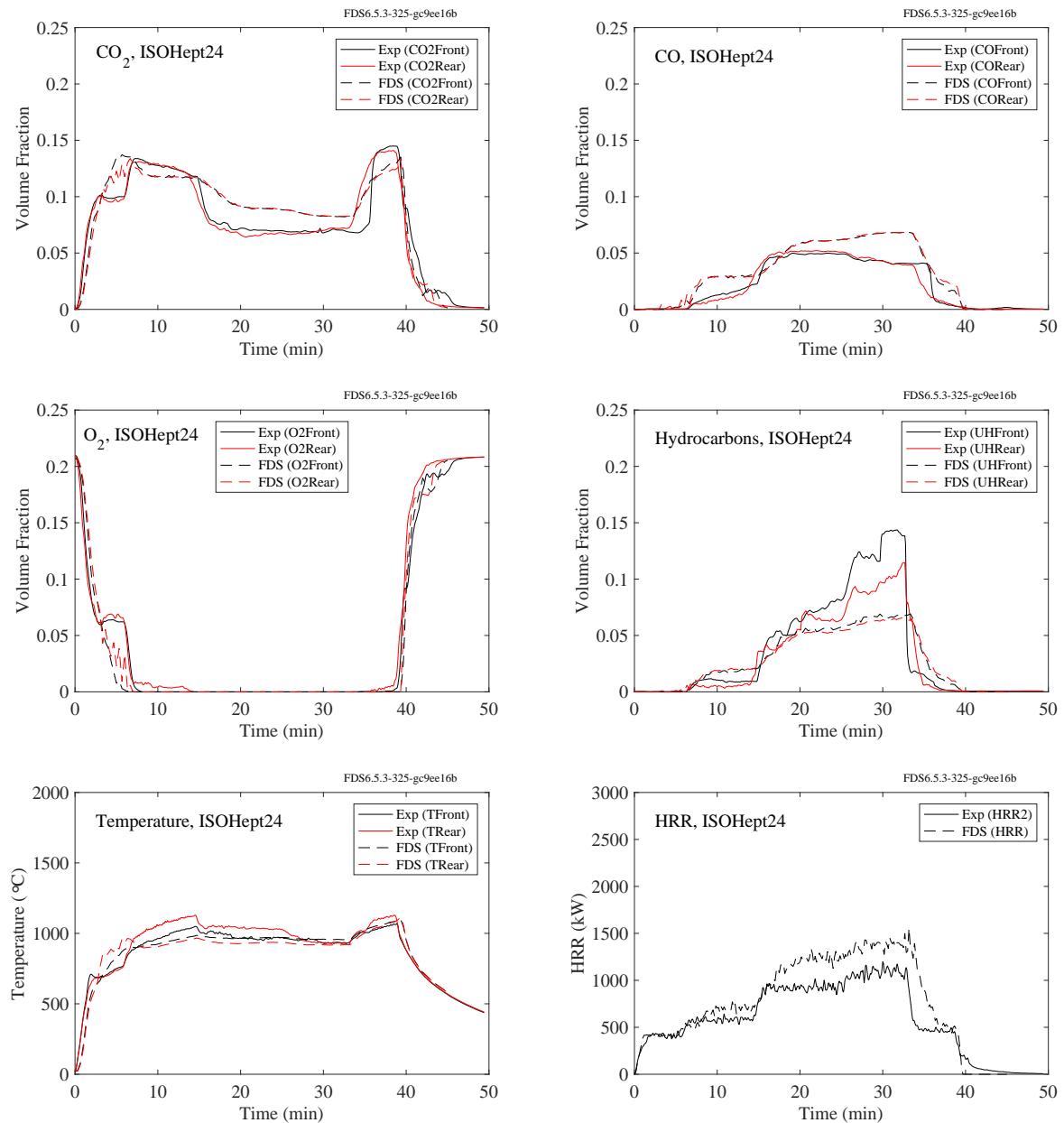


Figure 9.67: Summary of ISOHept24, NIST FSE 2008.

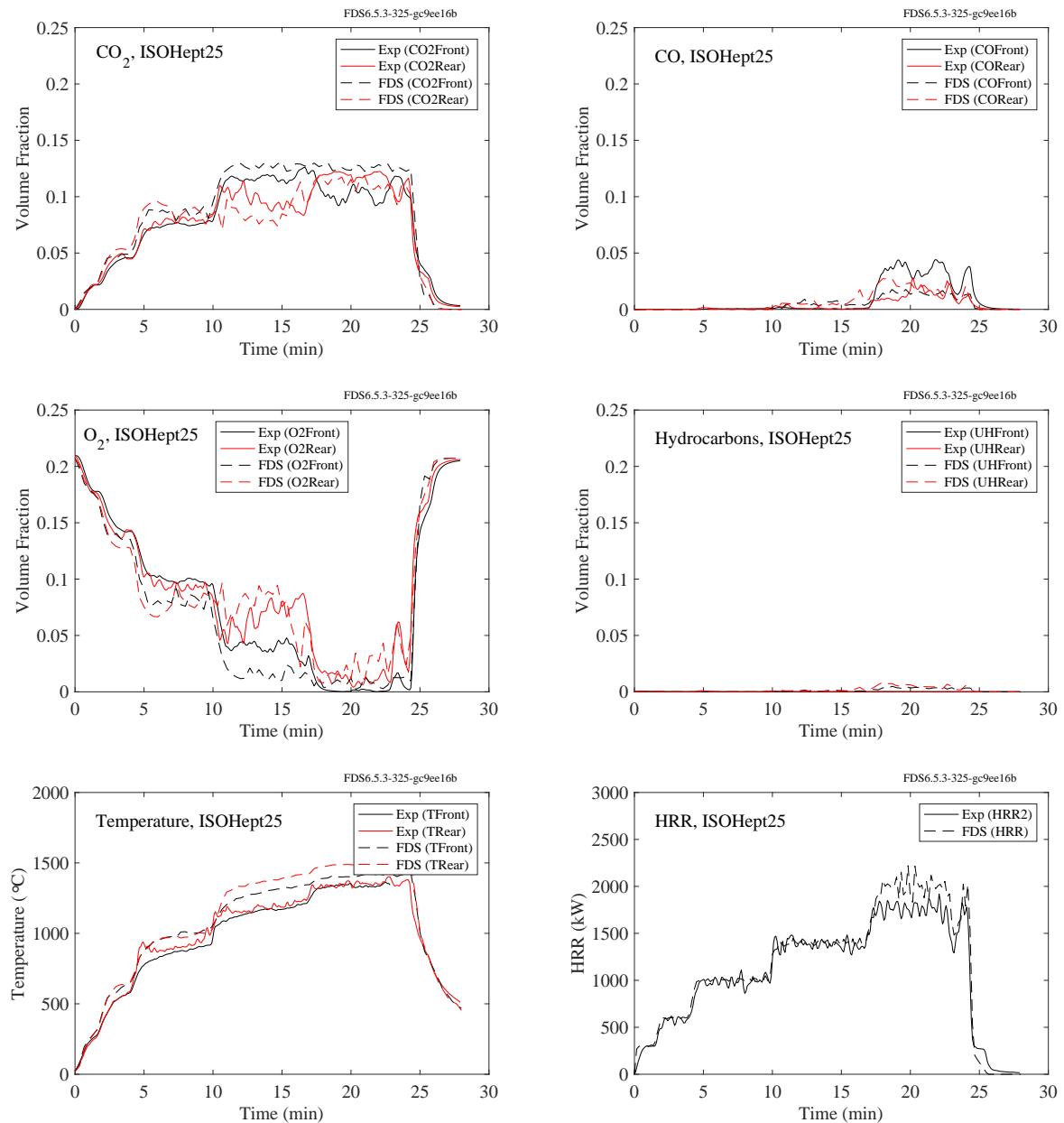


Figure 9.68: Summary of ISOHept25, NIST FSE 2008.

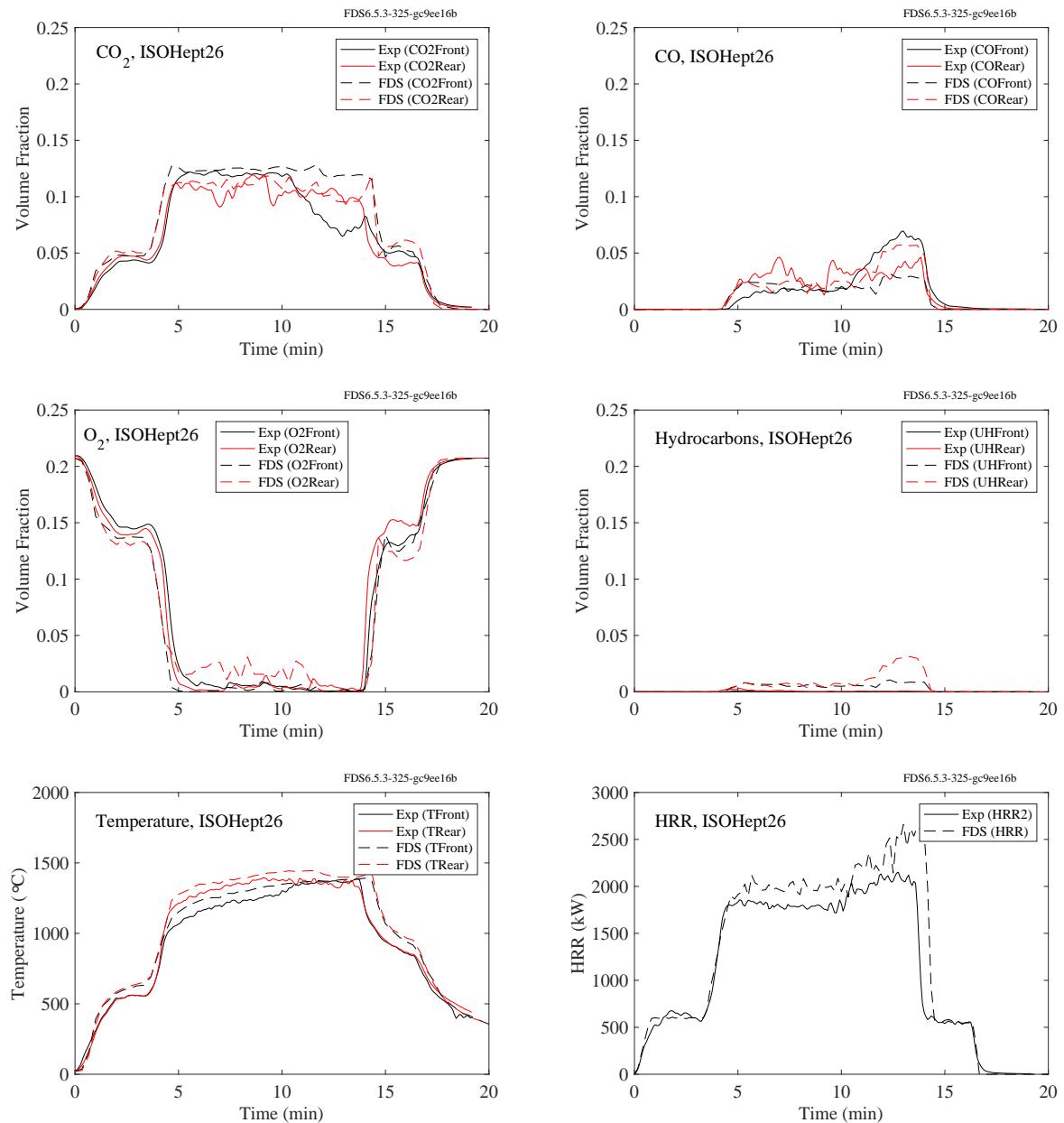


Figure 9.69: Summary of ISOHept26, NIST FSE 2008.

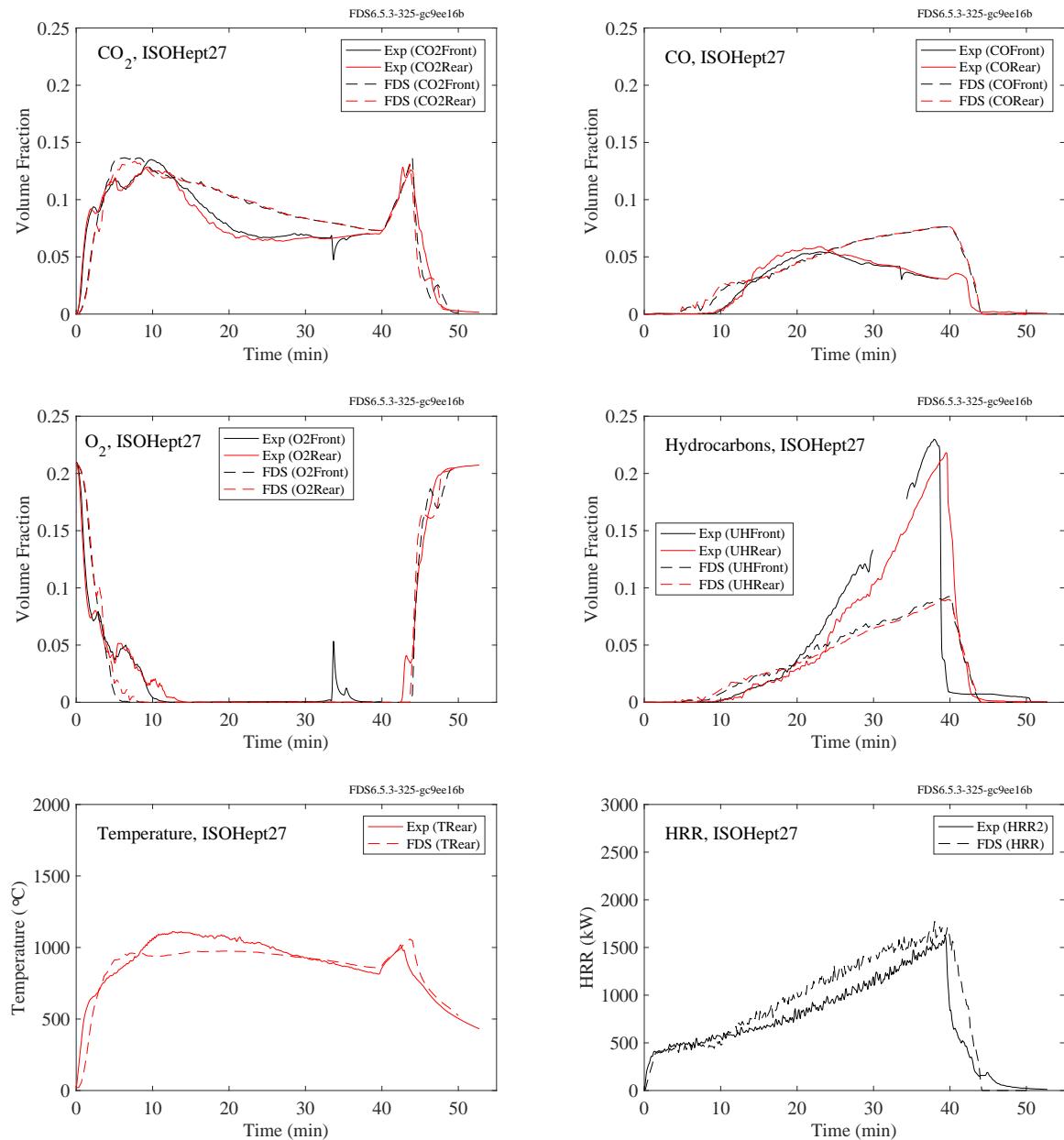


Figure 9.70: Summary of ISOHept27, NIST FSE 2008.

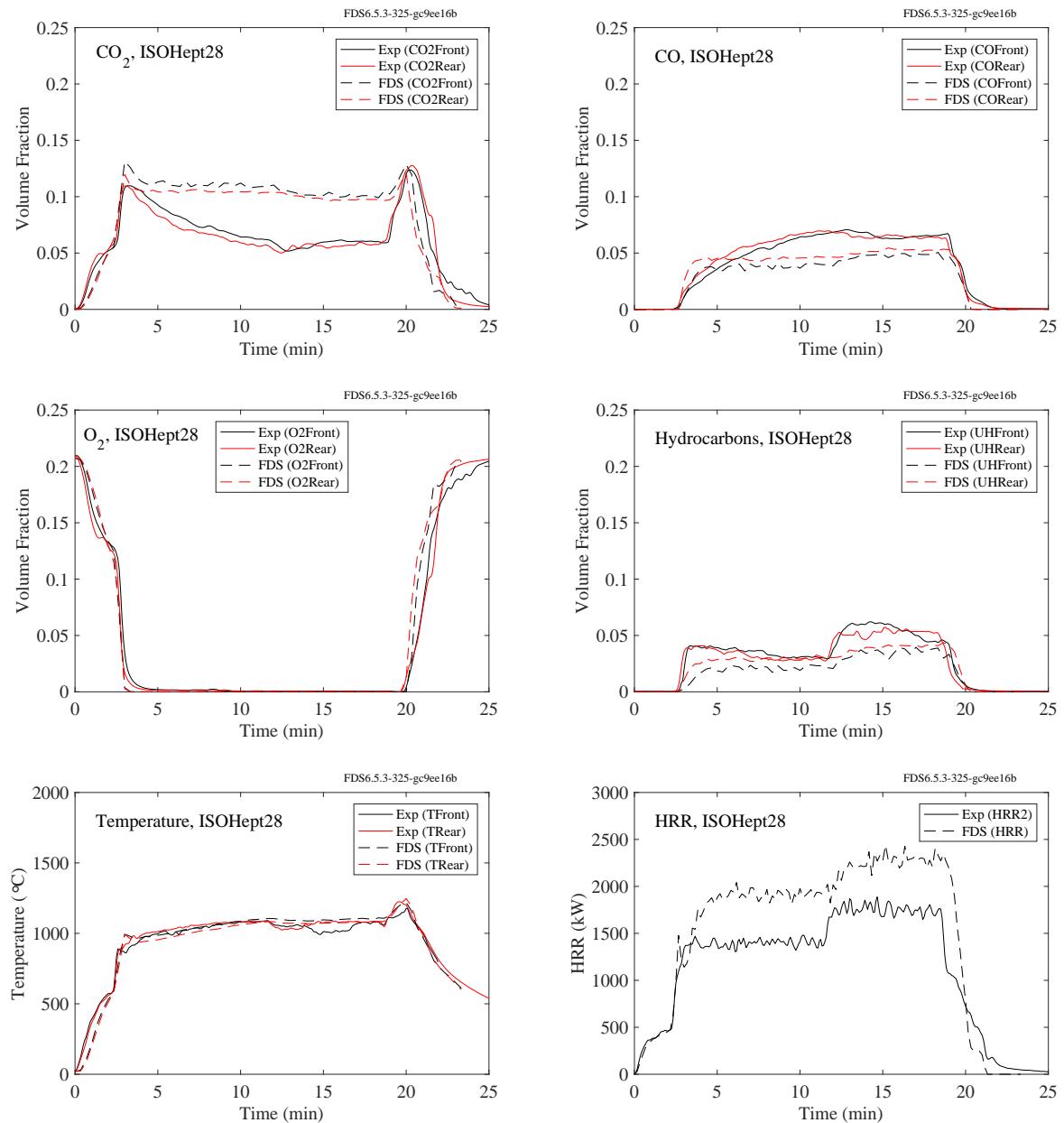


Figure 9.71: Summary of ISOHept28, NIST FSE 2008.

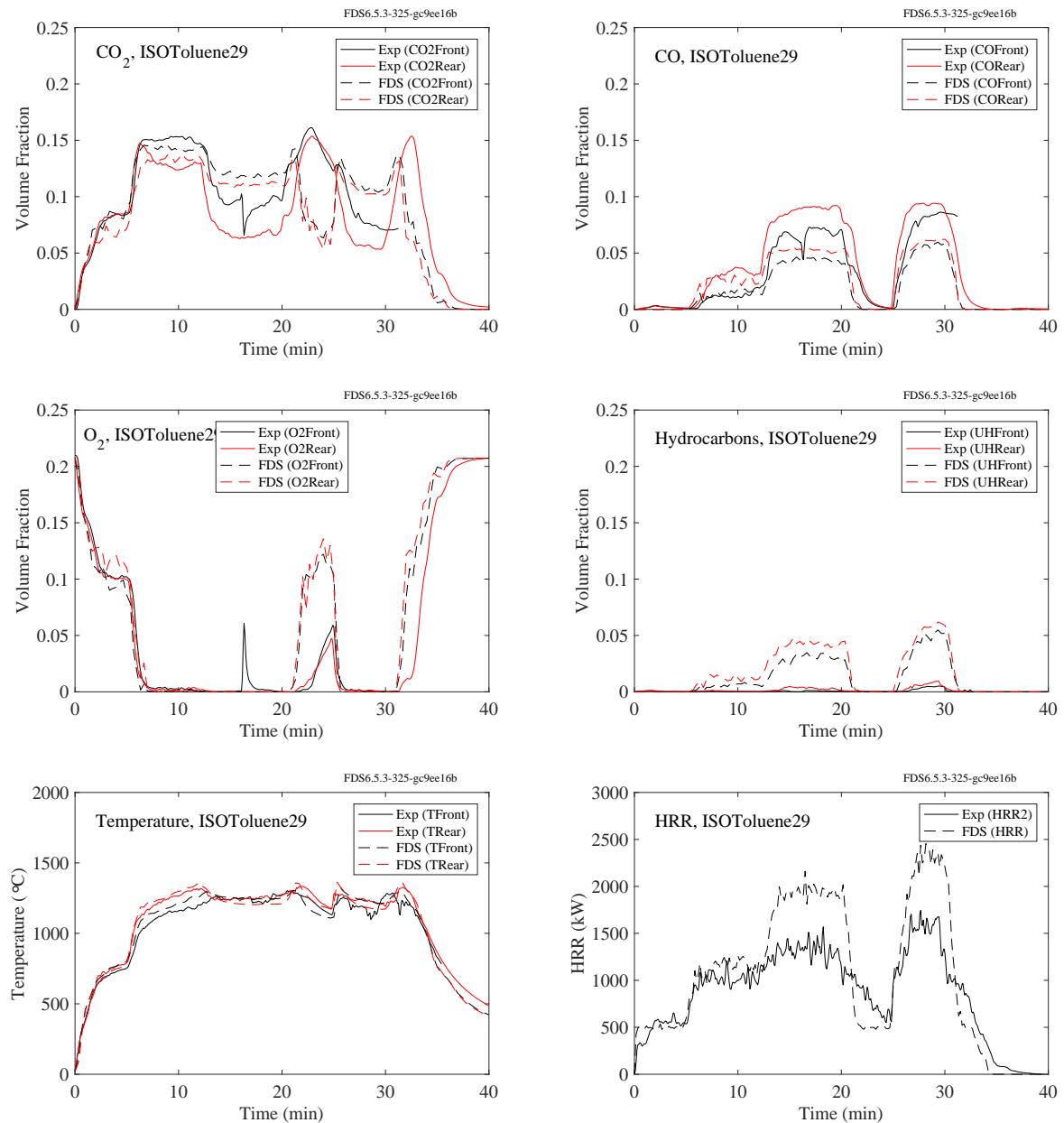


Figure 9.72: Summary of ISOToluene29, NIST FSE 2008.

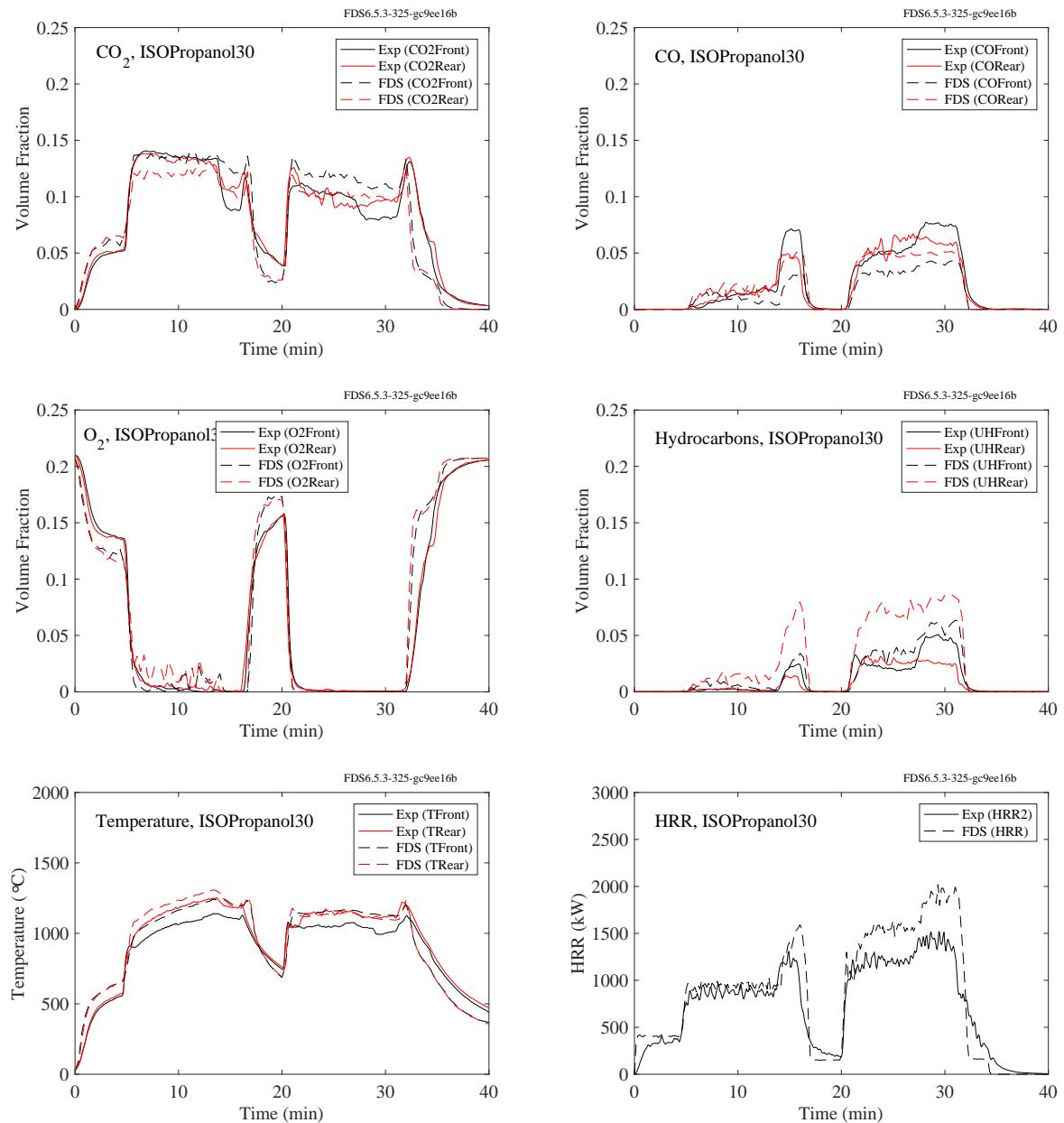


Figure 9.73: Summary of ISOPropanol30, NIST FSE 2008.

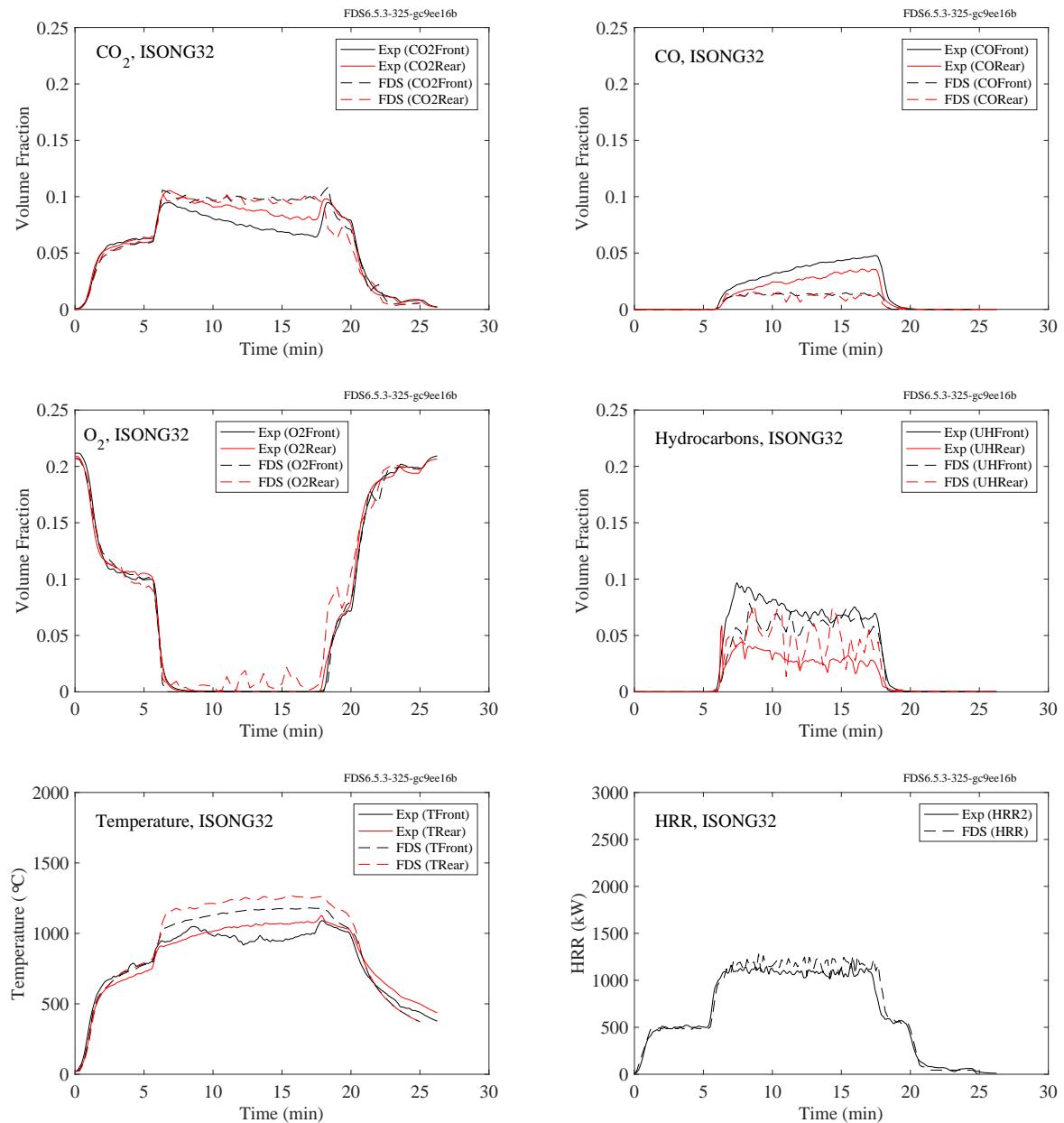


Figure 9.74: Summary of ISONG32, NIST FSE 2008.

### 9.3.6 Summary, Products of Incomplete Combustion

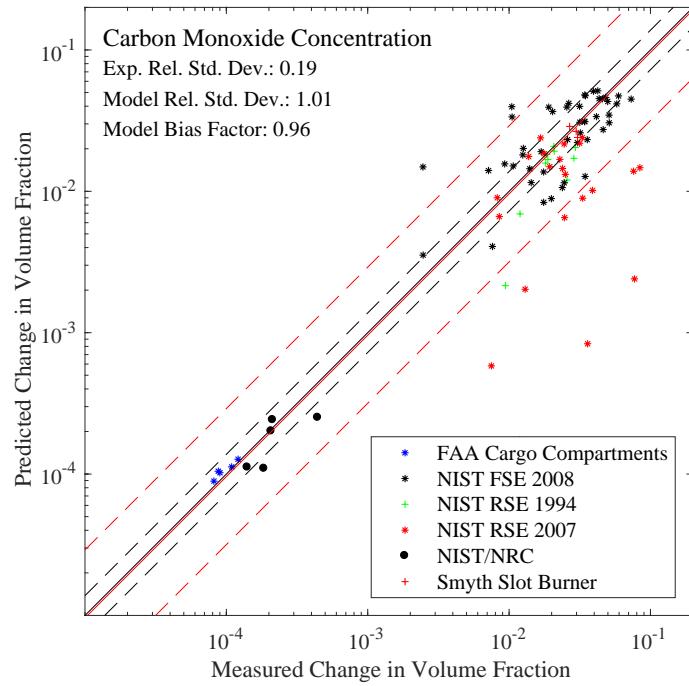


Figure 9.75: Summary of carbon monoxide predictions.

## 9.4 Helium Release in a Reduced Scale Garage Geometry

FDS simulations were performed to predict the helium release and dispersion in a reduced scale garage geometry. The figures on the following pages show the comparison between the FDS predictions and the measured values for the eighteen experiments. Table 9.2 lists the experimental parameters, including the release duration, release location (21 cm off the floor at the center of the compartment, 21 cm off the floor and 5 cm from the center of the rear wall, and 2.5 cm below the ceiling at the center of the compartment), and the leak area (single small vent, 2.4 cm by 2.4 cm, at the center of the front wall, single large vent, 3.05 cm by 3.05 cm, at the center of the front wall, and a pair of vents, 2.15 cm by 2.15 cm, centered on the front wall, 2.5 cm from the floor and ceiling, respectively). The seven sensors were located 37.5 cm from the front and side walls, at heights of 9 cm, 19 cm, 28 cm, 37 cm, 47 cm, 56 cm, and 65 cm off the floor. In the figures on the following pages, the highest concentrations correspond to the highest measurement locations.

Table 9.2: Test parameters of the NIST\_He\_2009 experiments.

Test Label	Release Duration (h)	Release Location	Leak Configuration
3600-LC-SSV	1	Lower Center	Single Small Vent
3600-LC-SLV	1	Lower Center	Single Large Vent
3600-LC-ULV	1	Lower Center	Dual Vents
3600-LR-SSV	1	Lower Rear	Single Small Vent
3600-LR-SLV	1	Lower Rear	Single Large Vent
3600-LR-ULV	1	Lower Rear	Dual Vents
3600-UC-SSV	1	Upper Center	Single Small Vent
3600-UC-SLV	1	Upper Center	Single Large Vent
3600-UC-ULV	1	Upper Center	Dual Vents
14400-LC-SSV	4	Lower Center	Single Small Vent
14400-LC-SLV	4	Lower Center	Single Large Vent
14400-LC-ULV	4	Lower Center	Dual Vents
14400-LR-SSV	4	Lower Rear	Single Small Vent
14400-LR-SLV	4	Lower Rear	Single Large Vent
14400-LR-ULV	4	Lower Rear	Dual Vents
14400-UC-SSV	4	Upper Center	Single Small Vent
14400-UC-SLV	4	Upper Center	Single Large Vent
14400-UC-ULV	4	Upper Center	Dual Vents

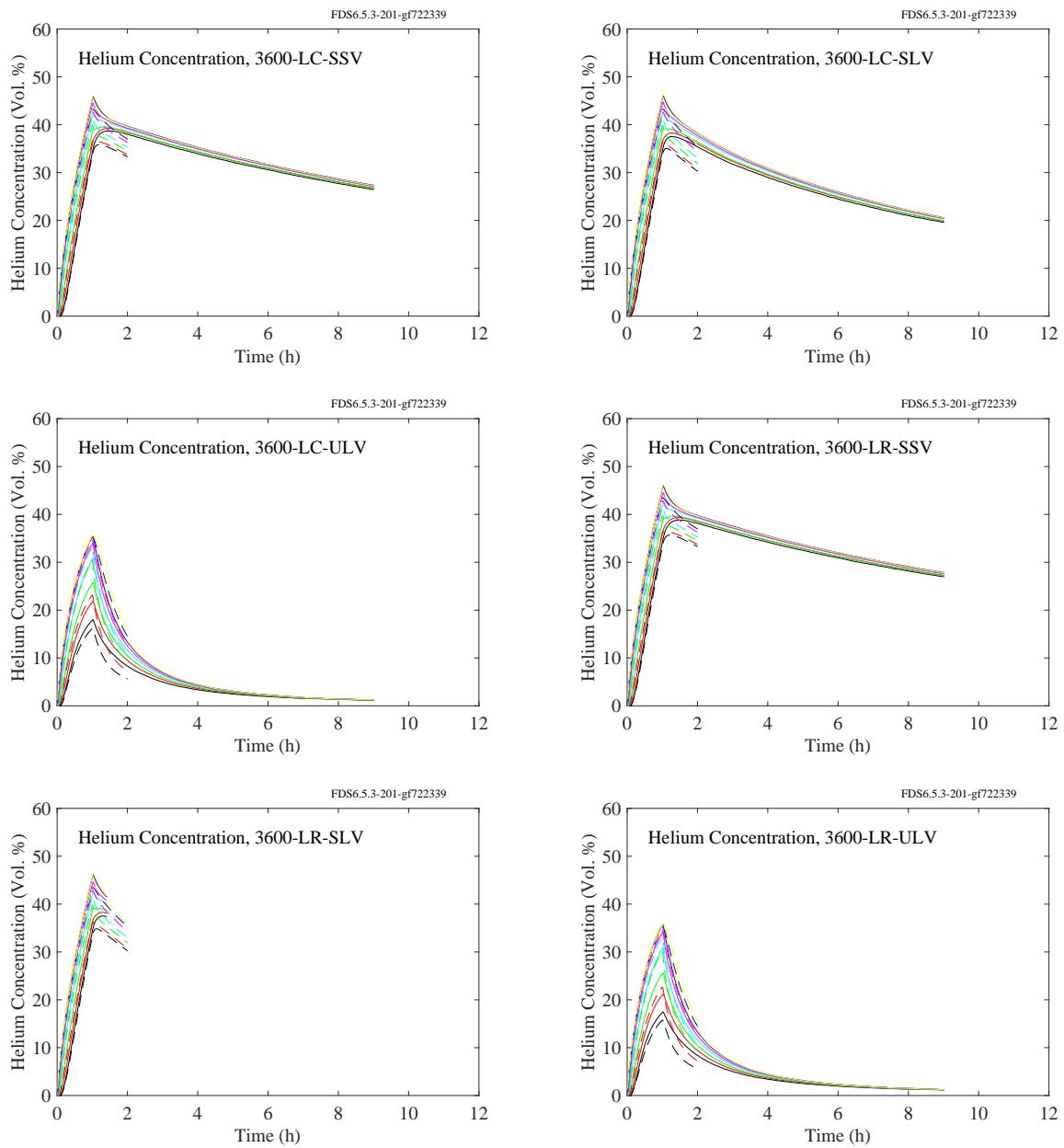


Figure 9.76: Comparison of measured (solid lines) and predicted (dashed lines) helium concentrations in the NIST\_He\_2009 experiments.

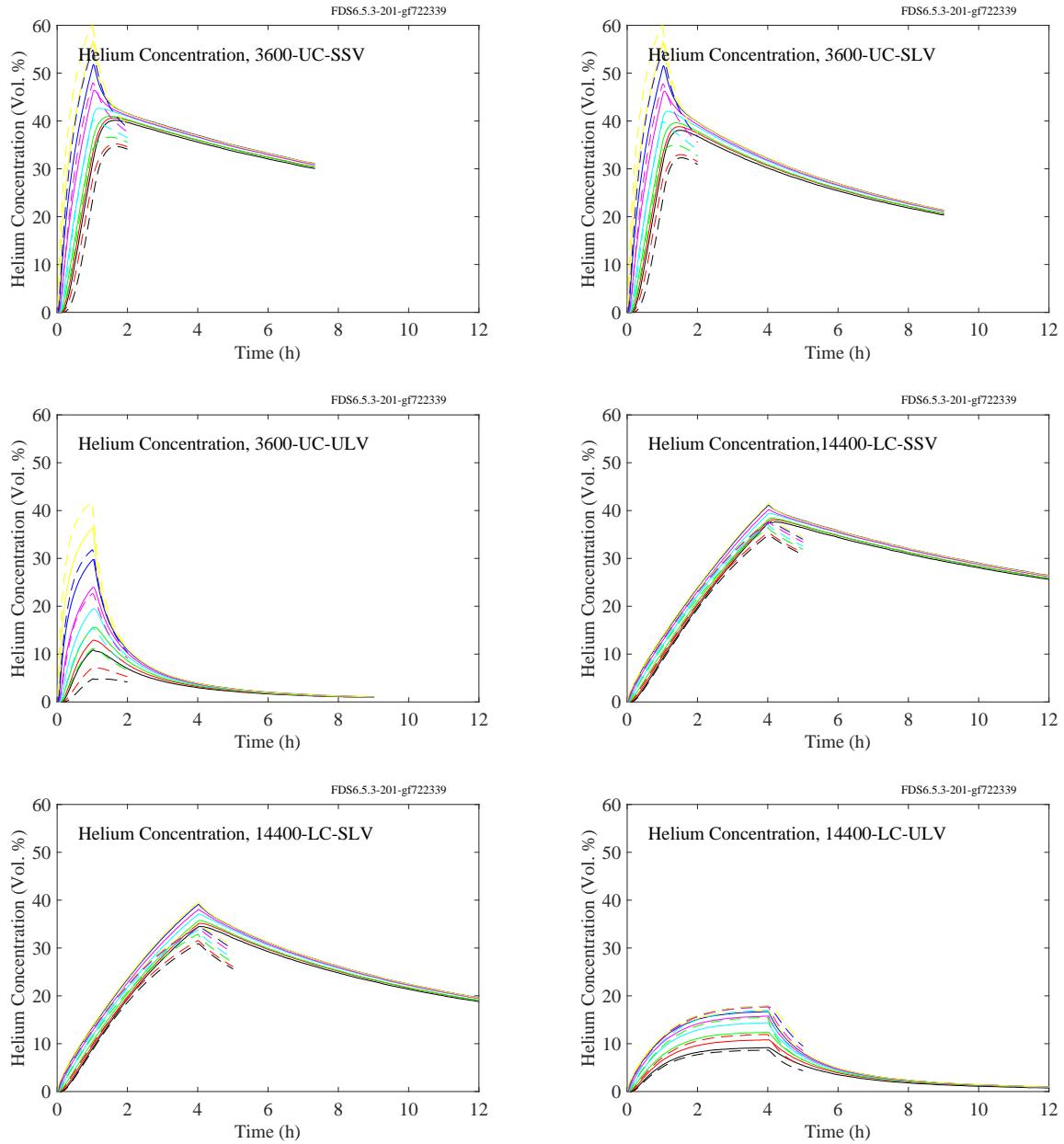


Figure 9.77: Comparison of measured (solid lines) and predicted (dashed lines) helium concentrations in the NIST\_He\_2009 experiments.

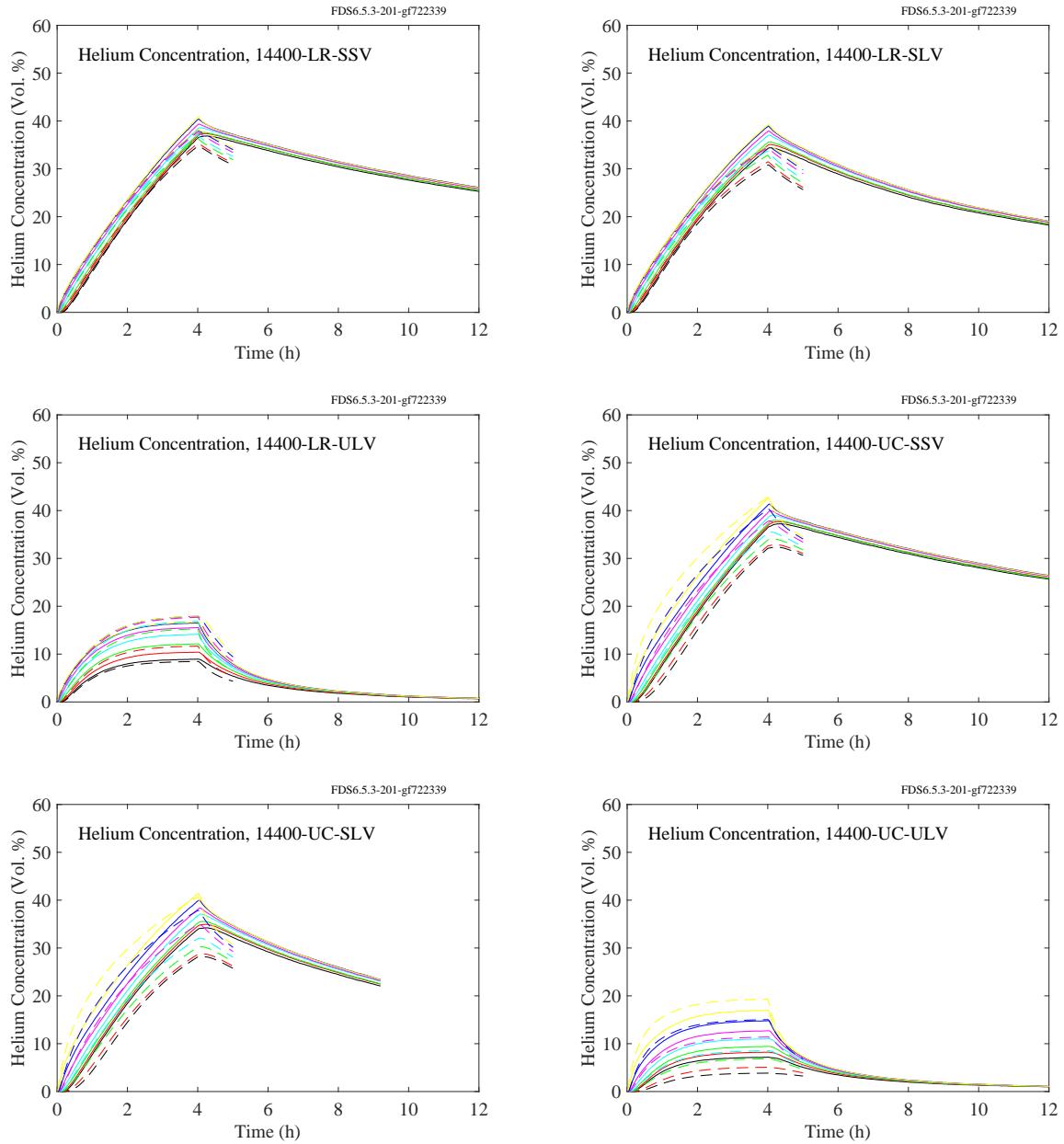


Figure 9.78: Comparison of measured (solid lines) and predicted (dashed lines) helium concentrations in the NIST\_He\_2009 experiments.

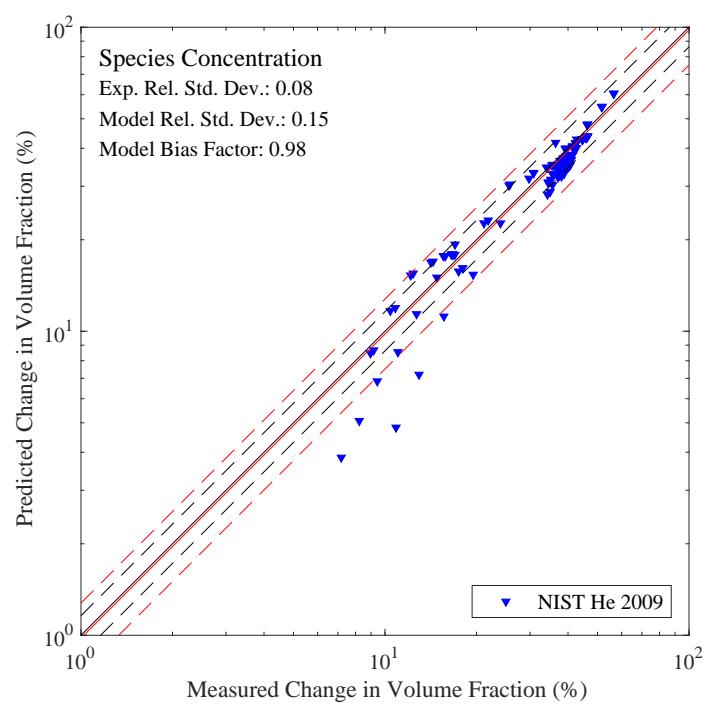


Figure 9.79: Summary of species concentration predictions.

# Chapter 10

## Pressure

In FDS, the pressure is decomposed into a temporally-varying background pressure plus a temporally and spatially-varying perturbation that drives the flow. The former can be thought of as the “over-pressure” which increases if heat is introduced into a closed compartment. In real buildings, leakage and ventilation affect the compartment “over-pressure” along with the fire.

### 10.1 FM/FPRF Datacenter Experiments

Measurements made during flow mapping in the FM datacenter mockup included two pairs of differential pressure transmitters. One pair measured the pressure difference between the subfloor (SF) and the cold aisle (CA). The other pair measured the pressure difference between the hot aisle (HA) and the ceiling plenum (CP). A comparison of measured and predicted pressures is shown in the table below.

Fan Speed	FDS SF to CA (Pa)	Exp SF to CA (Pa)	FDS HA to CP (Pa)	Exp HA to CP (Pa)
78 ACH	1.6	$1.7 \pm 0.3$	1.8	$2.2 \pm 0.4$
265 ACH	18.1	$20.9 \pm 2.1$	20.6	$17.3 \pm 1.7$

### 10.2 NIST/NRC Experiments

Comparisons between measured and predicted pressures for the NIST/NRC series are shown on the following pages. For those tests in which the door to the compartment was open, the over-pressures were only a few Pascals, whereas when the door was closed, the over-pressures were several hundred Pascals. The pressure within the compartment was measured at a single point, near the floor. For the simulations of the closed door tests, the compartment is assumed to leak via a small uniform flow distributed over the walls and ceiling. The flow rate is calculated based on the assumption that the leakage rate is proportional to the measured leakage area times the square root of compartment over-pressure.

Note that for the closed door tests, there is often a dramatic drop in the predicted compartment pressure. This is the result of the assumption in FDS that the heat release rate is decreased to zero in one second at the time in the experiment when the fuel flow was stopped for safety reasons. In reality, the fire did not extinguish immediately because there was an excess of fuel in the pan following the flow stoppage. For the purpose of model comparison, the peak over-pressures are compared in the closed door tests, and the peak (albeit small) under-pressures are compared in the open door tests.

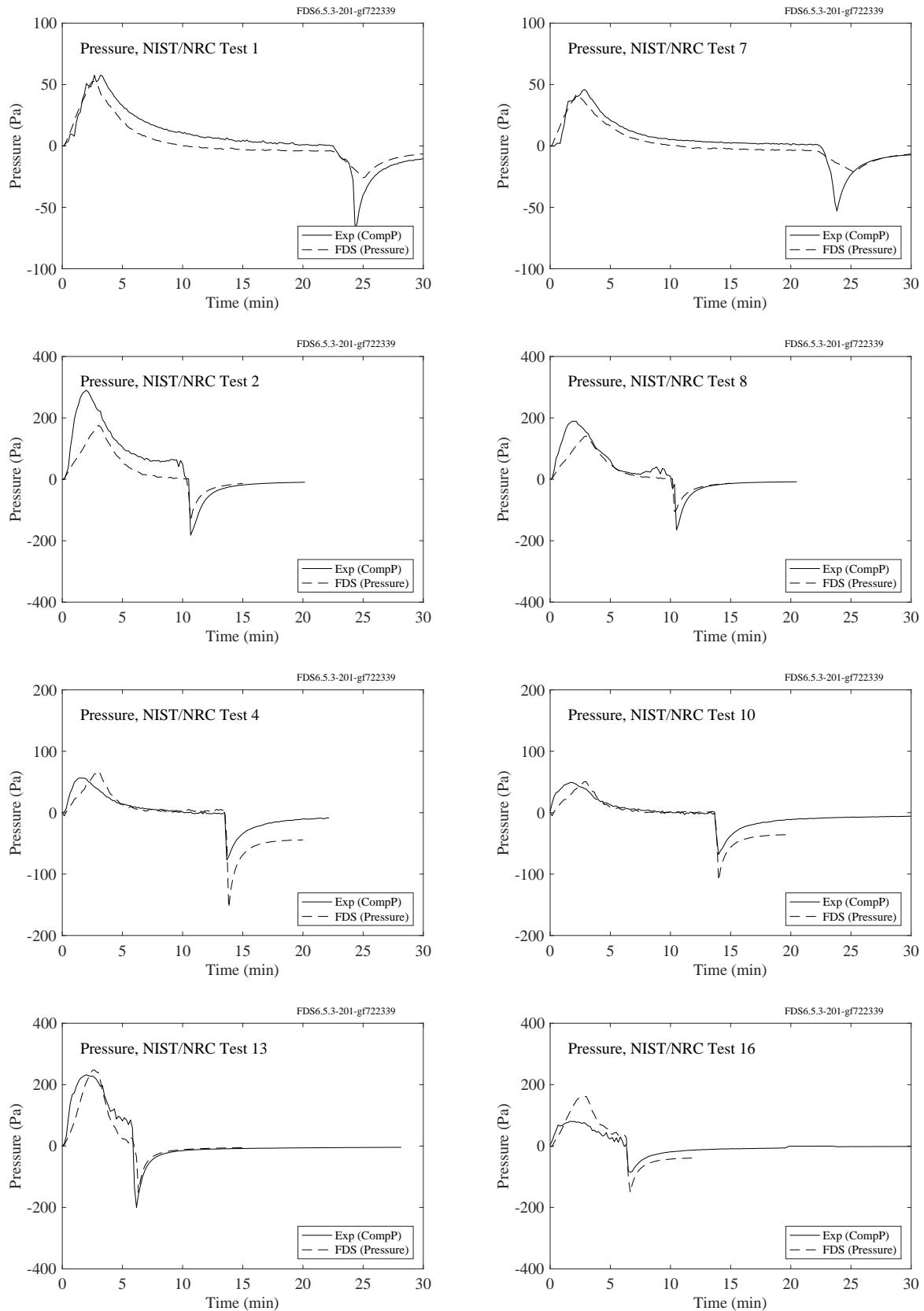


Figure 10.1: NIST/NRC experiments, compartment pressure, Tests 1, 2, 4, 7, 8, 10, 13, 16.

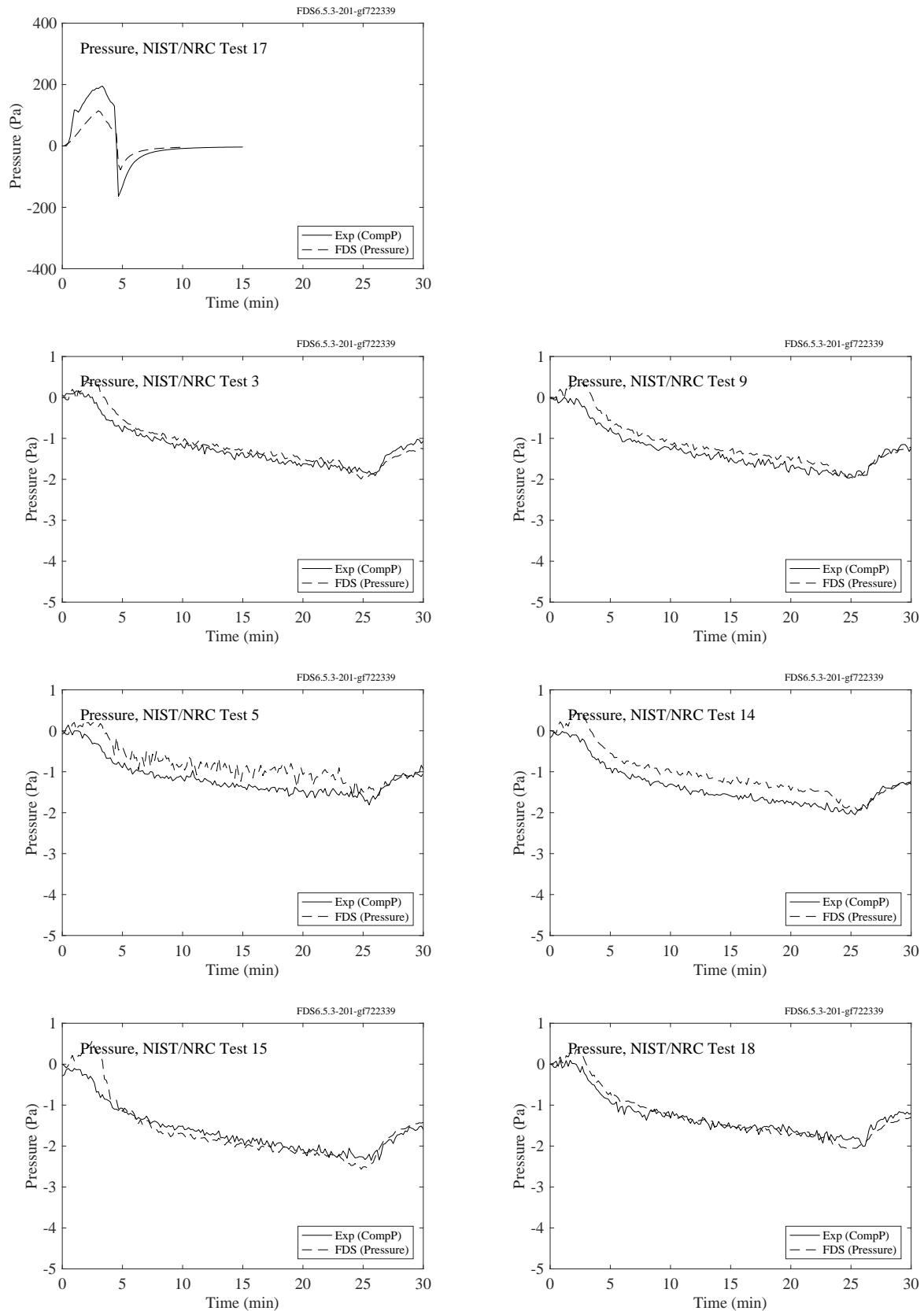


Figure 10.2: NIST/NRC experiments, compartment pressure, Tests 3, 5, 9, 14, 15, 17, 18.

### 10.3 LLNL Enclosure Experiments

The test report of the LLNL Enclosure experiments lists the mass flow rate,  $\dot{m}$ , through the exhaust duct at different times during the tests. It also lists the compartment pressures,  $\Delta p$ , at these same times. From the simple leak formula:

$$\frac{\dot{m}}{\rho_0} = A \sqrt{\frac{2\Delta p}{\rho_0}} \quad (10.1)$$

the leakage area,  $A$ , is estimated to be  $0.018 \text{ m}^2$ , based on the initial exhaust rate and pressure. For modeling purposes, the “leakage area” is assumed to be the sum of the inlet duct area plus any actual compartment leakage area. The mass flow rate through the exhaust duct is specified explicitly in the model. The test report does not provide enough information about the ventilation system to model the fan and filtration system within the exhaust duct.

In the figures on the following pages, the open circles represent the measured pressure; the line represents the predicted pressure. The predicted pressures are time-averaged over a time interval that is one-tenth the total simulation time. In general, the short-duration pressure spike that is typical of fires within relatively tight compartments has been smoothed over in the reported test data. Depending on the simulation, it often appears in the simulation data. The comparison of measurement and prediction is based on the final few pressure points, not the initial spike.

Only some of the 64 experiments are included. In some cases, the fan was turned off and there is not enough information in the test report to determine the pressure losses through the duct. In other cases, there are only two pressure measurements reported; one at the start of the test, the other either before or after extinction. In various other cases, either there is not enough data or the data is inconsistent with the reported conditions. For cases where the door to the compartment was open, the measured gauge pressures at the start of the experiment ranged from 0 Pa to 10 Pa. There is not enough information in the test report to explain why the starting pressures were not 0 Pa; thus, the measured pressures were adjusted so that the starting pressure is 0 Pa.

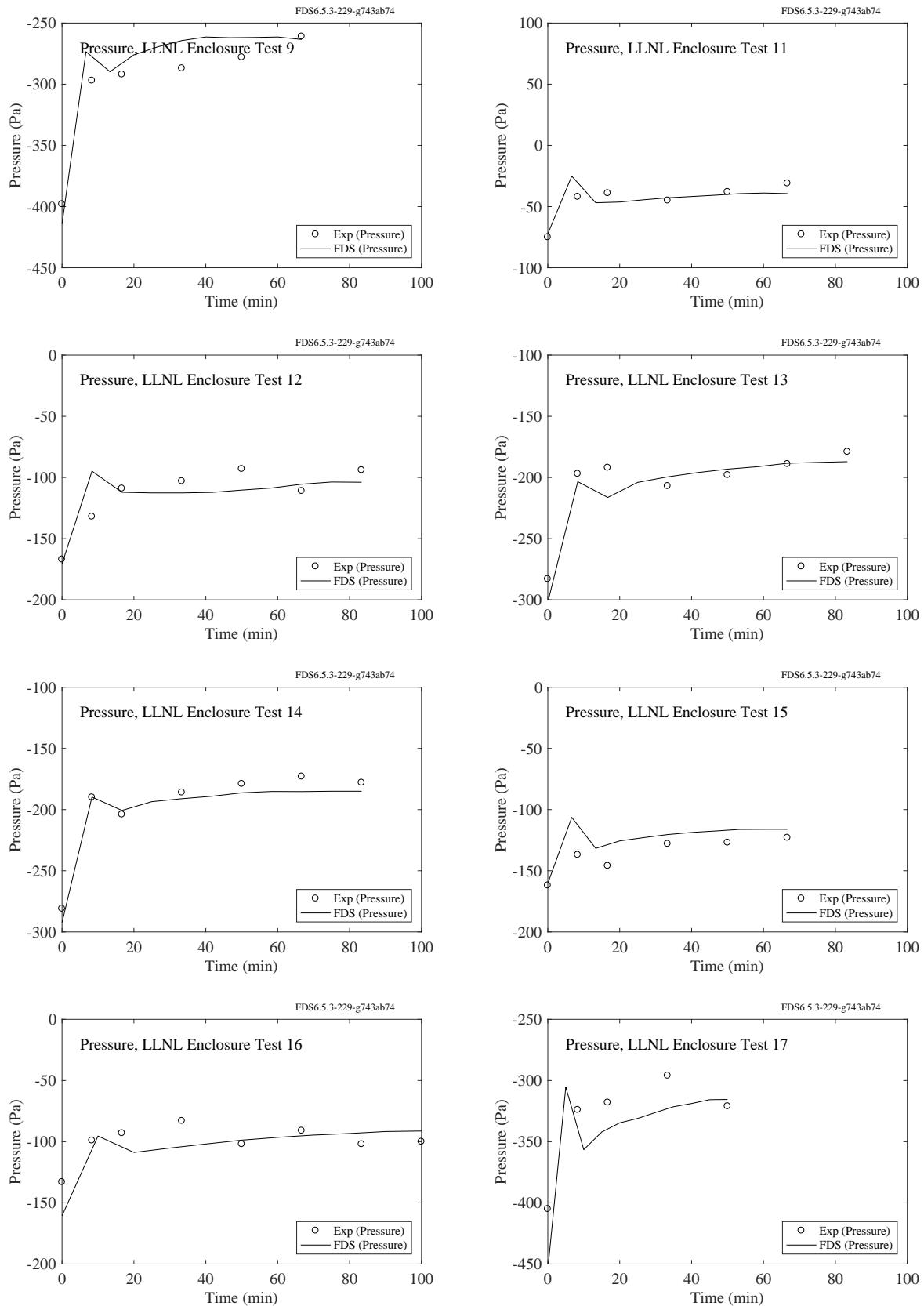


Figure 10.3: LLNL Enclosure experiments, compartment pressure, Tests 9, 11-17.

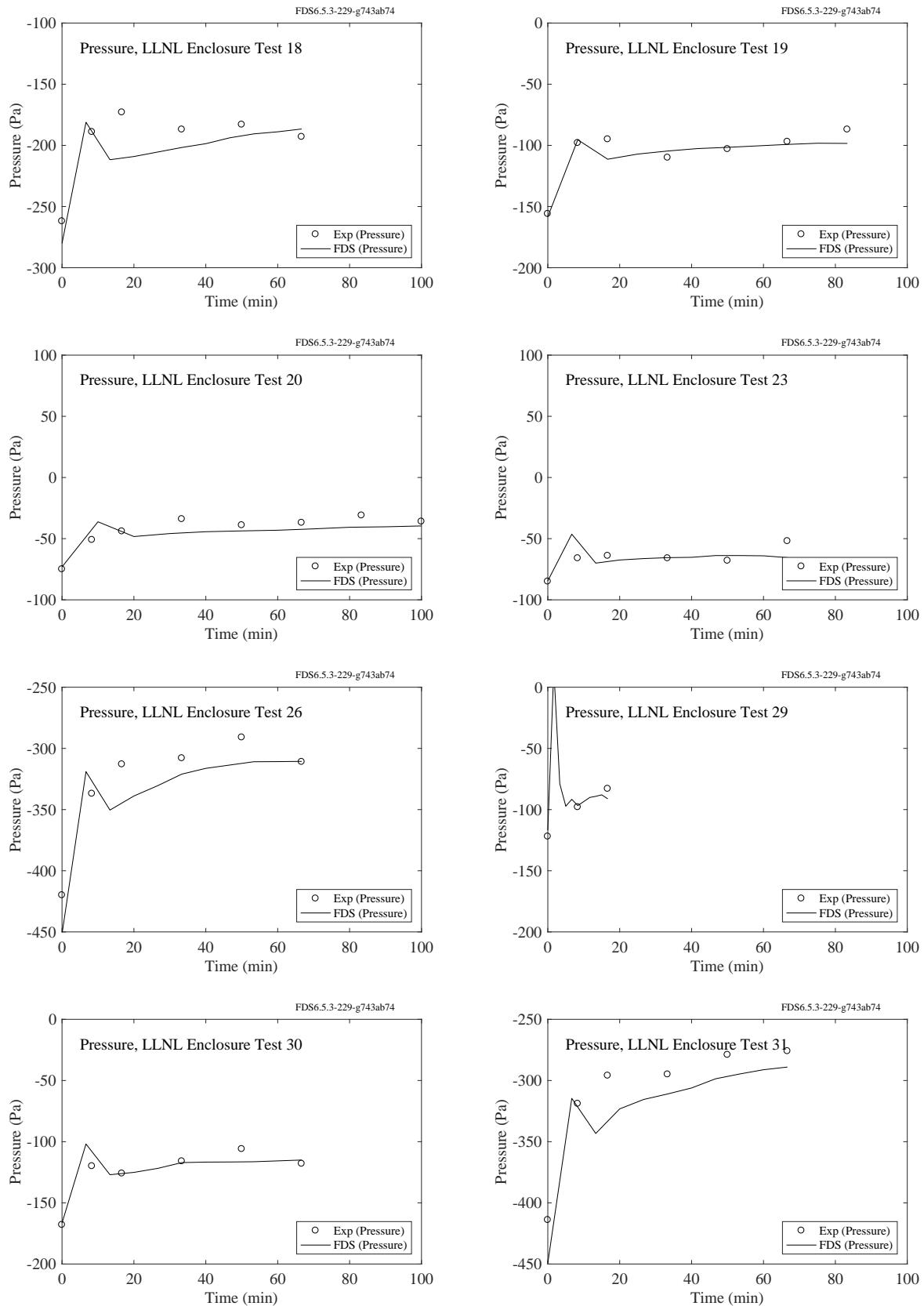


Figure 10.4: LLNL Enclosure experiments, compartment pressure, Tests 18-20, 23, 26, 29-31.

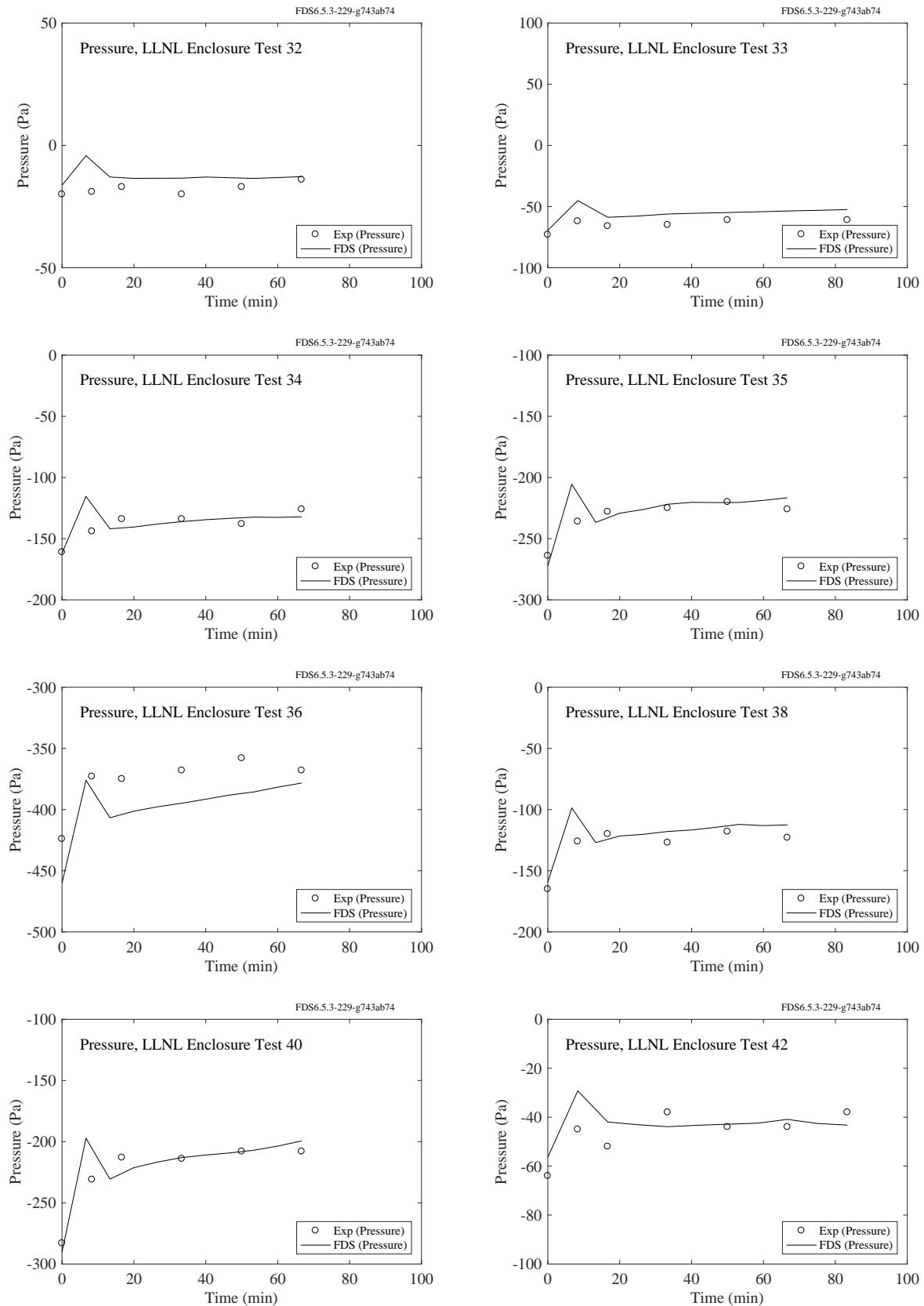


Figure 10.5: LLNL Enclosure experiments, compartment pressure, Tests 32-36, 38, 40, 42.

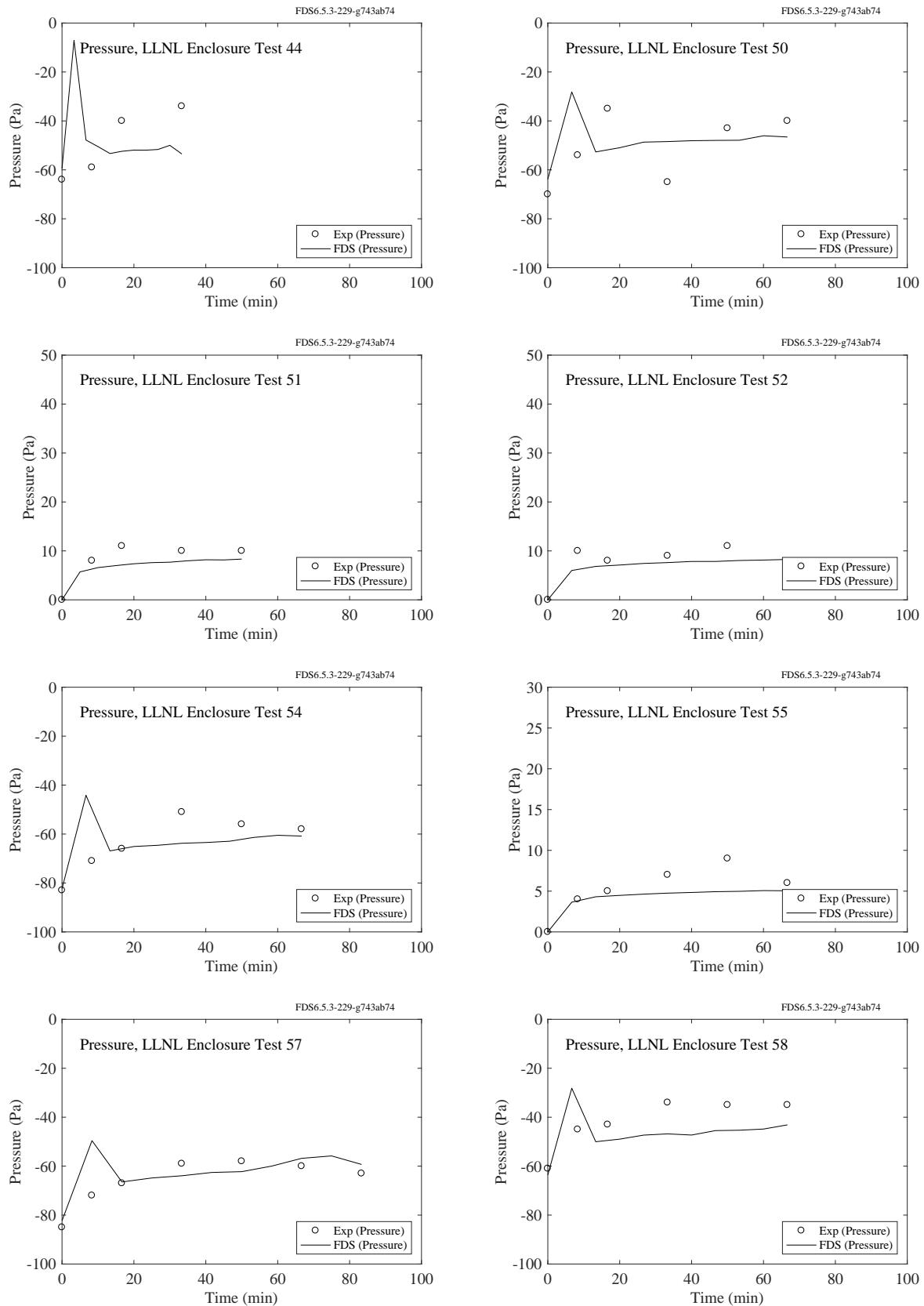


Figure 10.6: LLNL Enclosure experiments, compartment pressure, Tests 44, 50-52, 54-55, 57-58.

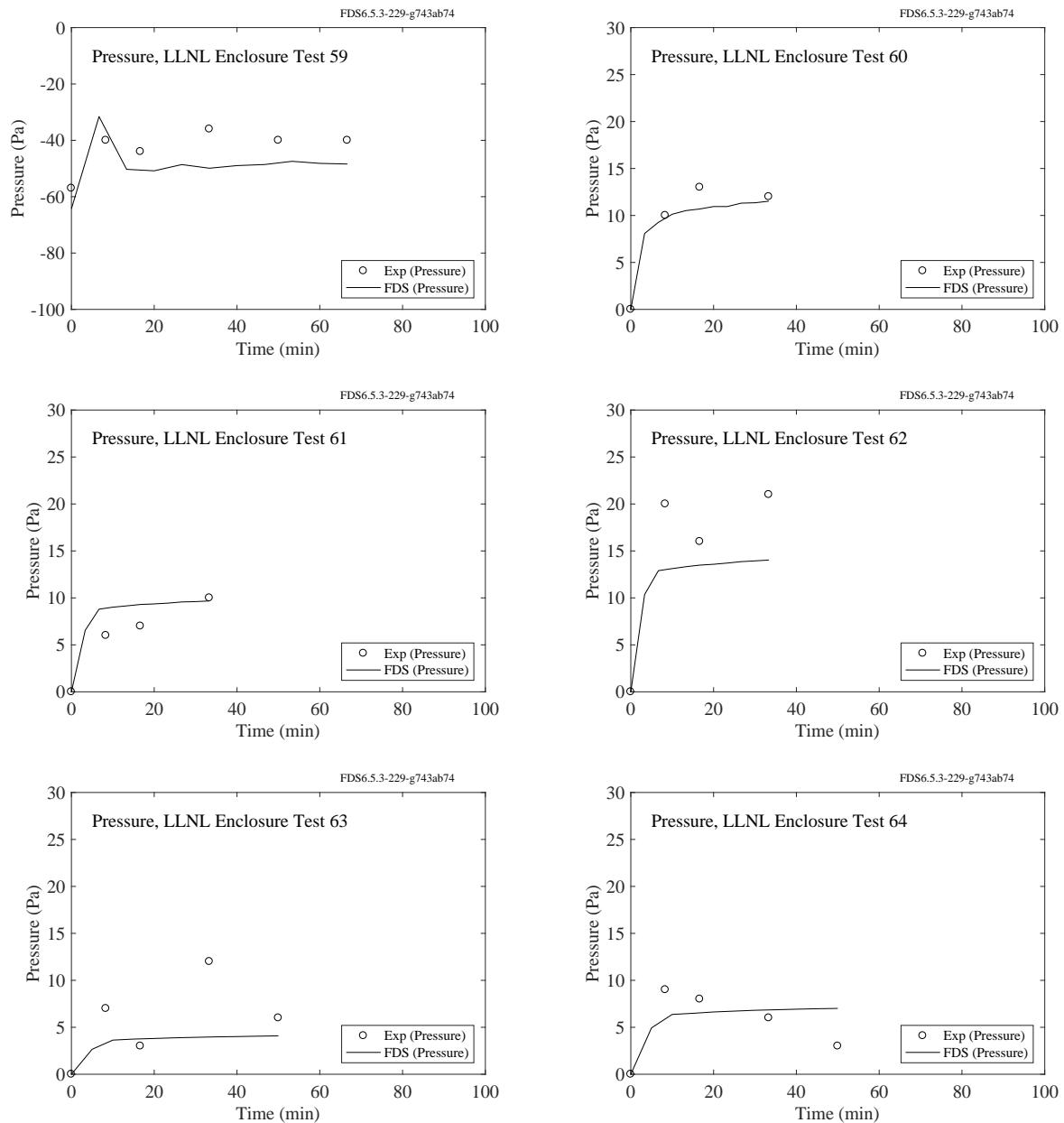


Figure 10.7: LLNL Enclosure experiments, compartment pressure, Tests 59-64.

## **10.4 PRISME DOOR Experiments**

The PRISME experiments were conducted in a relatively well-sealed set of compartments with a well-controlled ventilation system. Supply air was forced into and exhaust products extracted from the test compartments via two fans and a fairly extensive ventilation network. The air flow rates and nodal pressures were measured throughout the system. The FDS simulations included the ventilation system, and for each segment of the network a loss coefficient was calculated so as to match the initial conditions of the experiments. The plots to follow show the predicted and measured compartment pressures and supply and exhaust flows. These air flows were predicted by the model, based on the initial specification of the ventilation system.

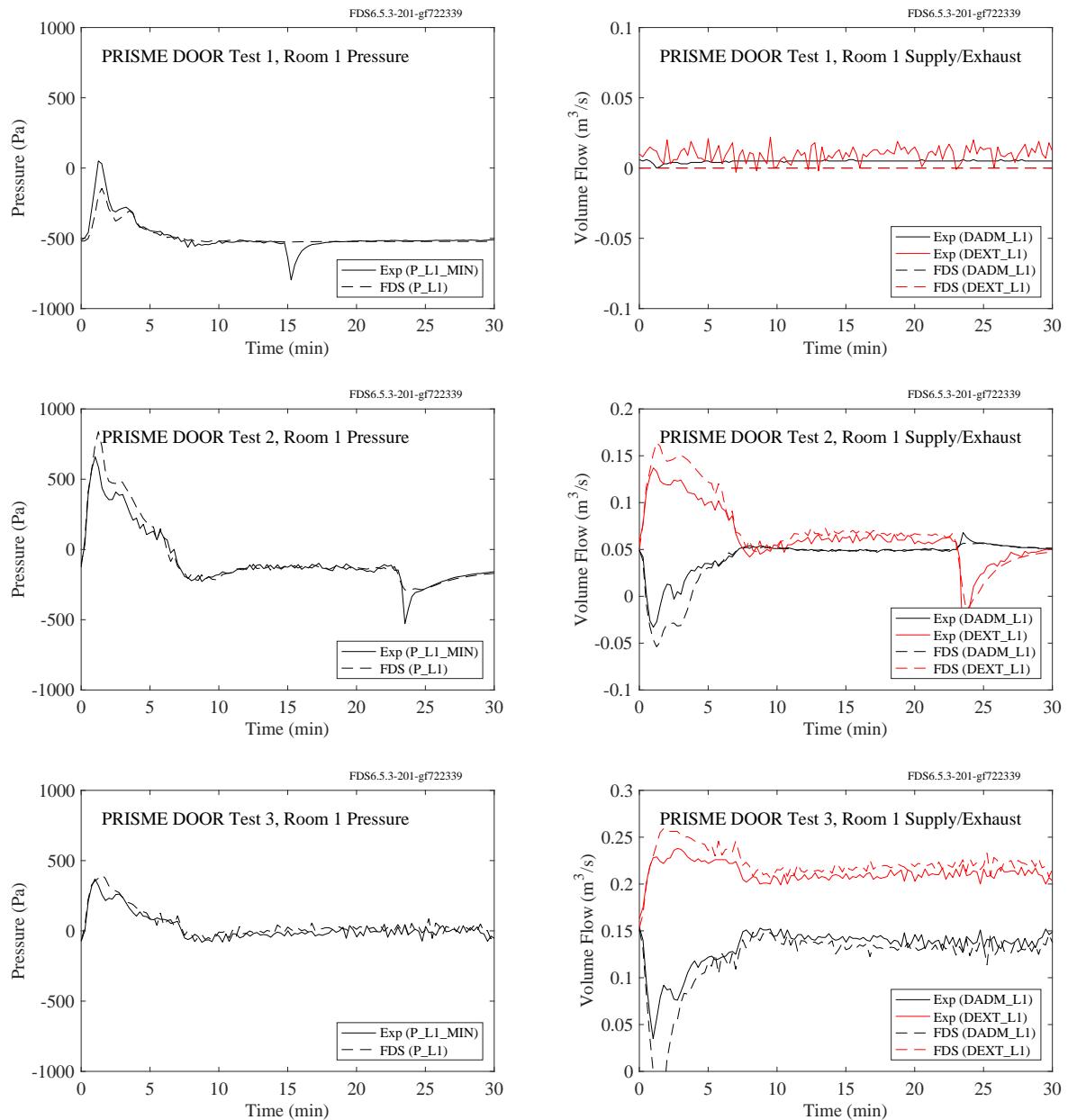


Figure 10.8: PRISME DOOR, compartment pressure and supply/exhaust, Room 1, Tests 1-3.

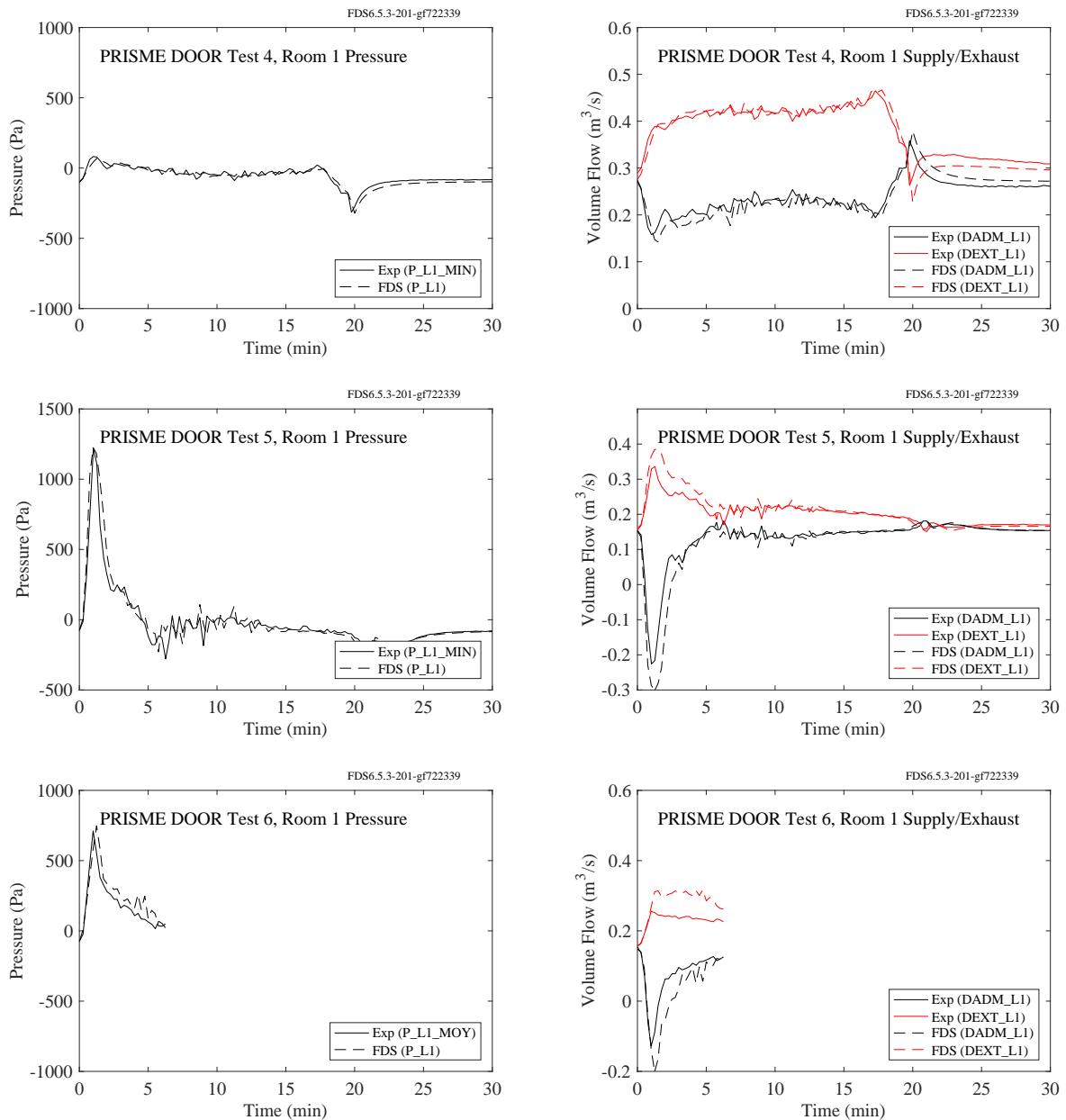


Figure 10.9: PRISME DOOR, compartment pressure and supply/exhaust, Room 1, Tests 4-6.

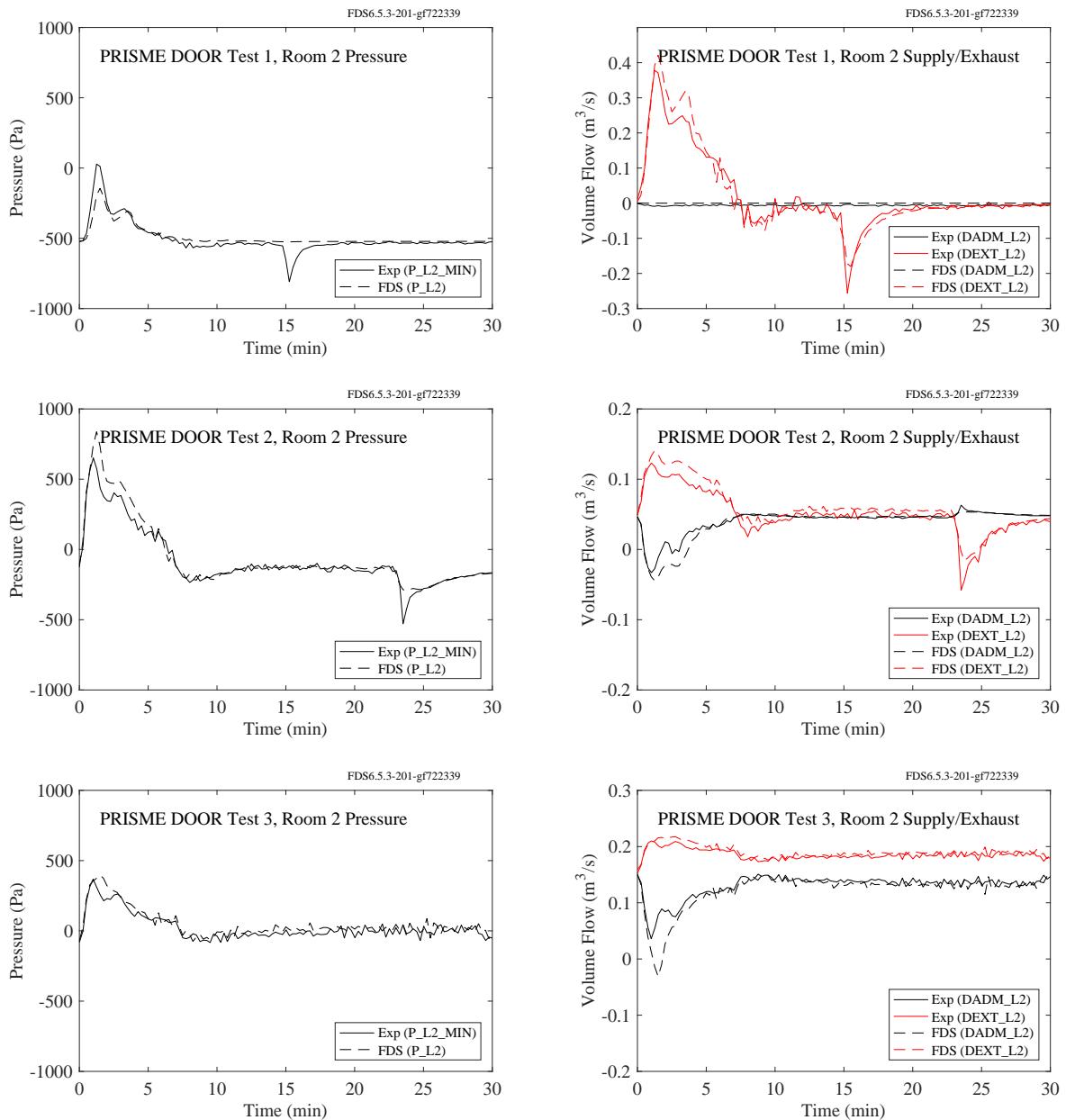


Figure 10.10: PRISME DOOR, compartment pressure and supply/exhaust, Room 2, Tests 1-3.

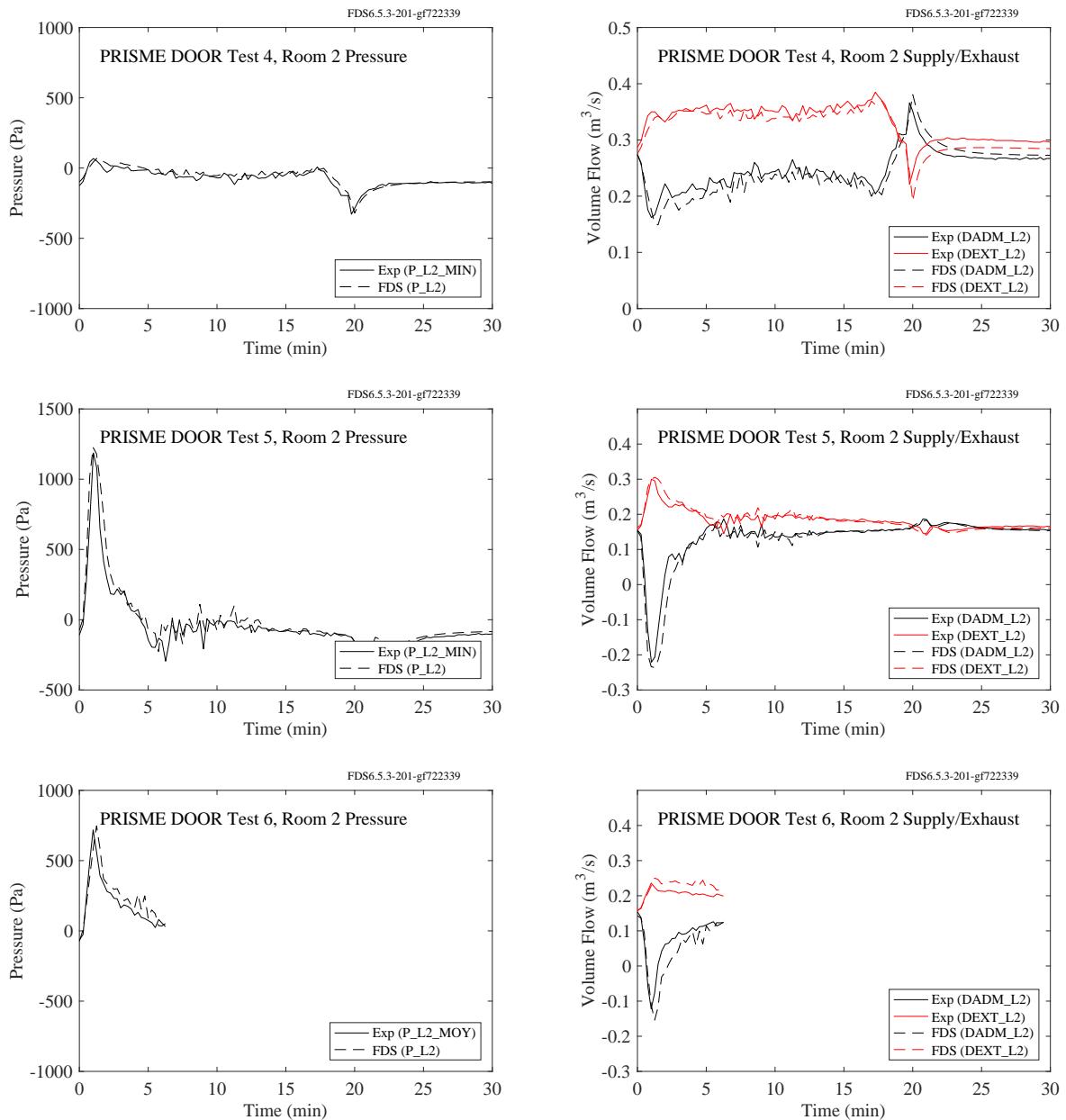


Figure 10.11: PRISME DOOR, compartment pressure and supply/exhaust, Room 2, Tests 4-6.

## **10.5 PRISME SOURCE Experiments**

The PRISME SOURCE experiments were conducted in a single compartment with a well-controlled ventilation system. Supply air was forced into and exhaust products extracted from the test compartment via two fans and a fairly extensive ventilation network. The air flow rates and nodal pressures were measured throughout the system. The FDS simulations included the ventilation system, and for each segment of the network a loss coefficient was calculated so as to match the initial conditions of the experiments. The plots to follow show the predicted and measured compartment pressures and supply and exhaust flows. These air flows were predicted by the model, based on the initial specification of the ventilation system.

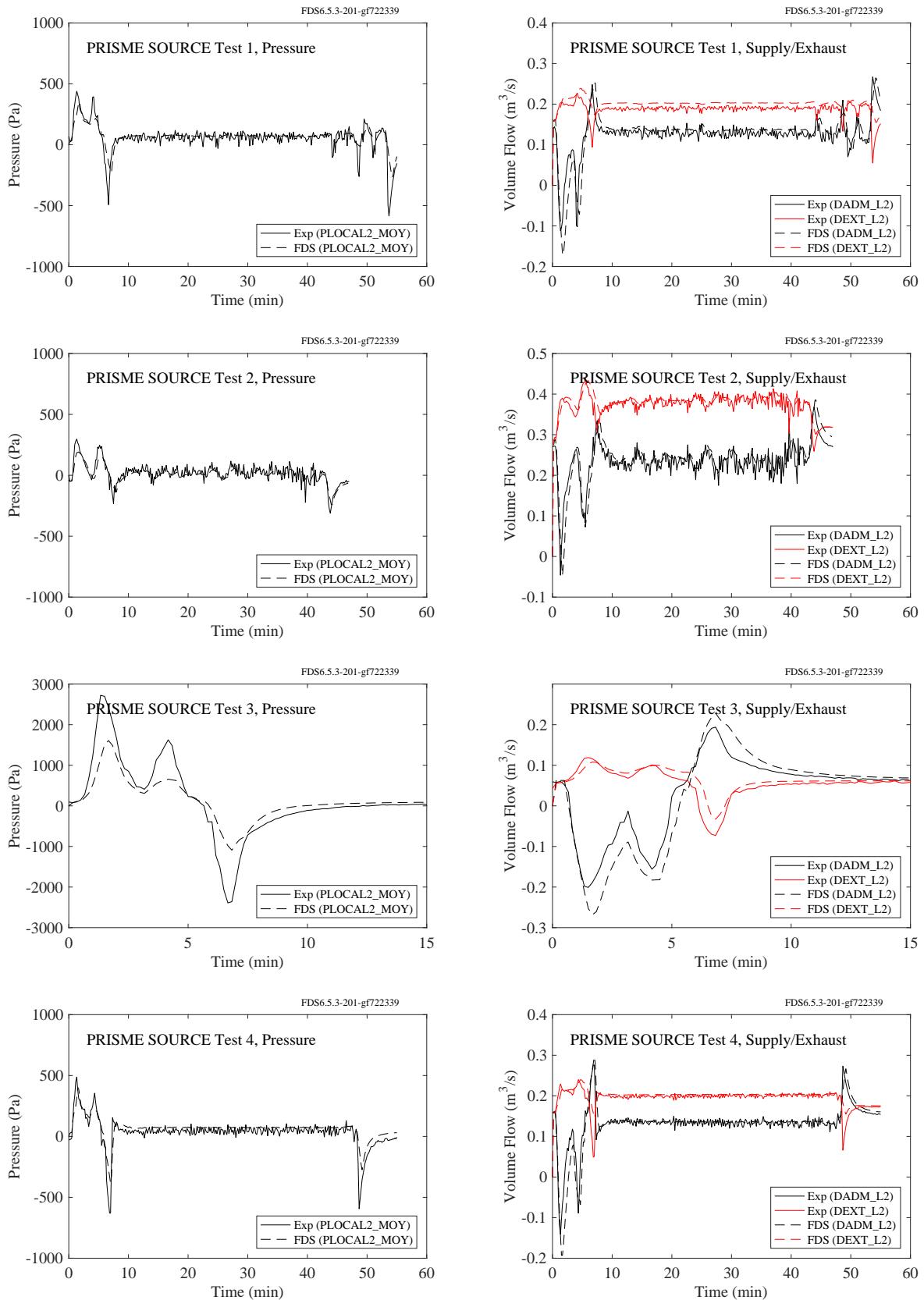


Figure 10.12: PRISME SOURCE, pressure and supply/exhaust flow rates, Tests 1, 2, 3 and 4.

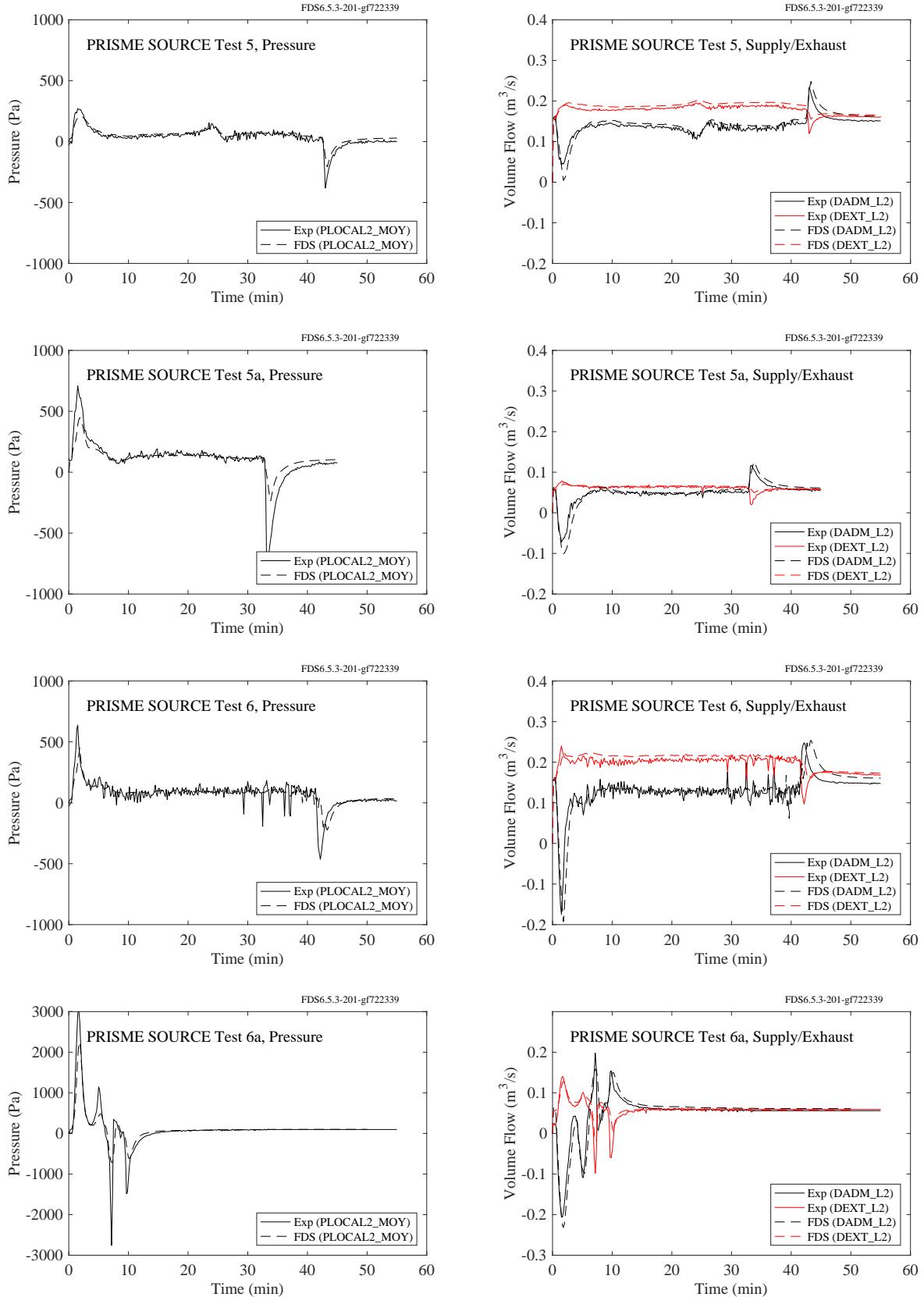


Figure 10.13: PRISME SOURCE, pressure and supply/exhaust flow rates, Tests 5, 5a, 6 and 6a.

## 10.6 Summary of Pressure Predictions

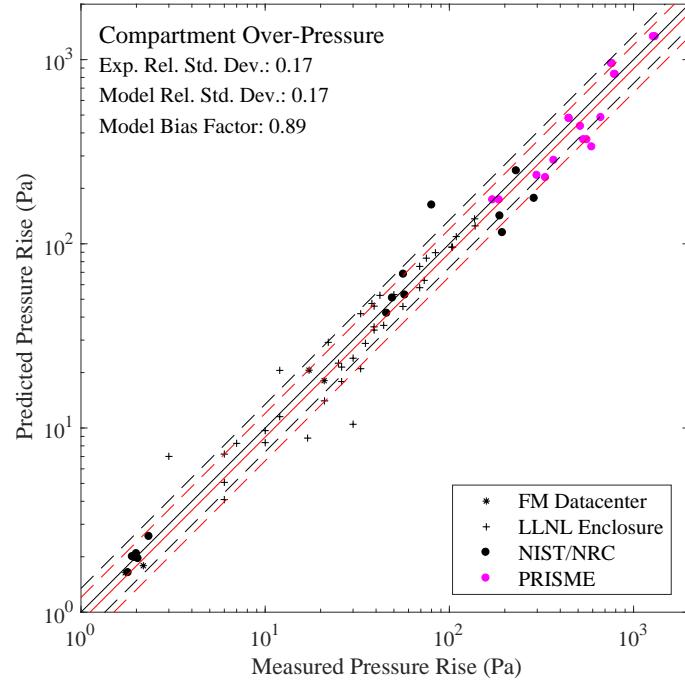


Figure 10.14: Summary of pressure predictions for open and closed compartments.

## Chapter 11

# Surface Temperature

All solid surfaces in an FDS model are assigned thermal boundary conditions. Heat and mass transfer to and from surfaces is usually handled with empirical correlations, although it is possible to compute directly the heat and mass transfer when performing a Direct Numerical Simulation (DNS). Heat conduction into a solid surface is calculated via a one-dimensional solution of the heat equation in cartesian, cylindrical, or spherical coordinates. The latter two are useful for predicting the thermal response of so-called “targets,” which include structural steel, electrical cables, sensitive equipment, or any type of intervening combustible.

This chapter divides solid surfaces into two major categories – compartment linings (i.e., walls, ceiling, floor) and targets (i.e., anything that is not a wall, ceiling, or floor). The reason for this distinction is that some models treat the two categories differently. In general, FDS does not.

## 11.1 Wall, Ceiling and Floor Temperatures

### 11.1.1 FAA Cargo Compartments

Measurements of surface temperature were made at two ceiling locations (denoted A and B in Fig. 7.10). The surface temperature measurements are shown below.

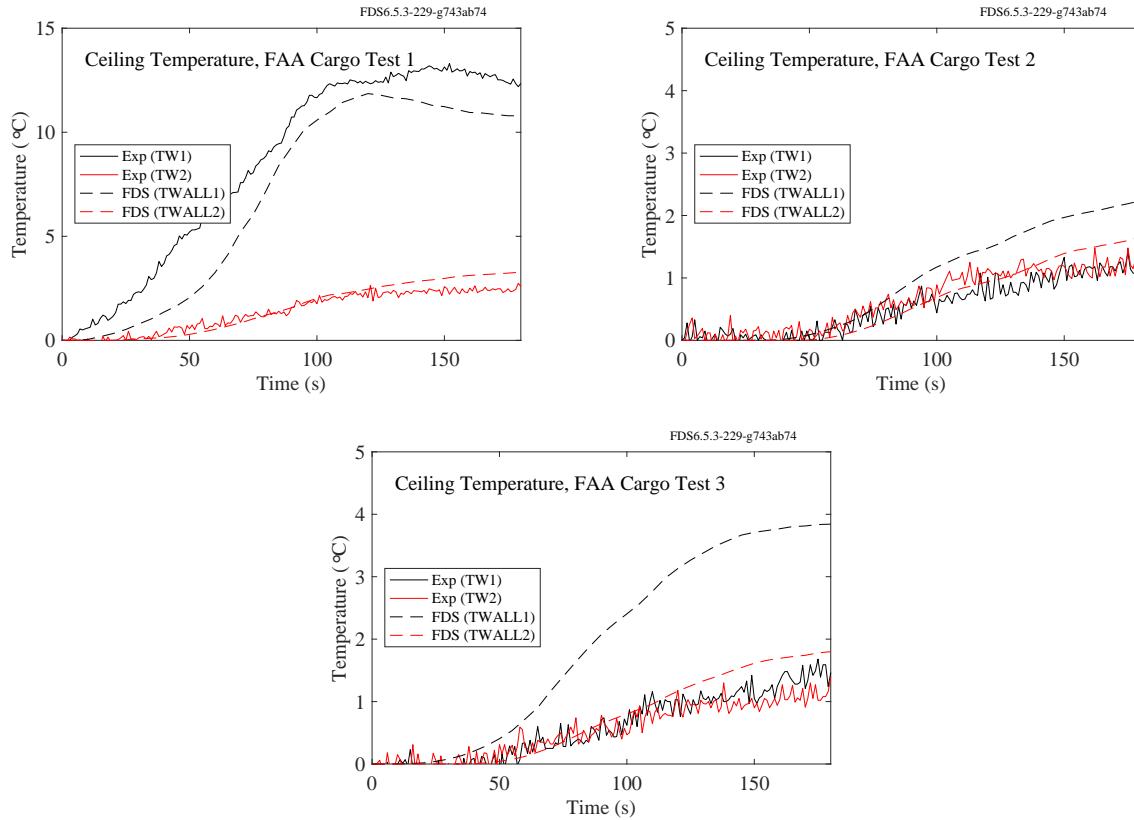


Figure 11.1: FAA Cargo Compartment experiments, ceiling surface temperatures.

### **11.1.2 NIST Full-Scale Enclosure (FSE), 2008**

Measurements of surface temperature were made at three ceiling and three floor locations in a standard ISO 9705 compartment. In the plots on the following the pages, the ceiling measurements at the rear, center and front of the compartment are denoted by TSHFRCE, TSHFCCE, and TSHFFCE, respectively (Temperature Surface Heat Flux Rear CEiling, etc.). The floor measurements at the rear and front are denoted TSHFRFL and TSHFFFL. The surface temperatures measurements that were made just outside the door were faulty and are not used. All of the floor measurements for the experiment labelled ISOHept8 were faulty.

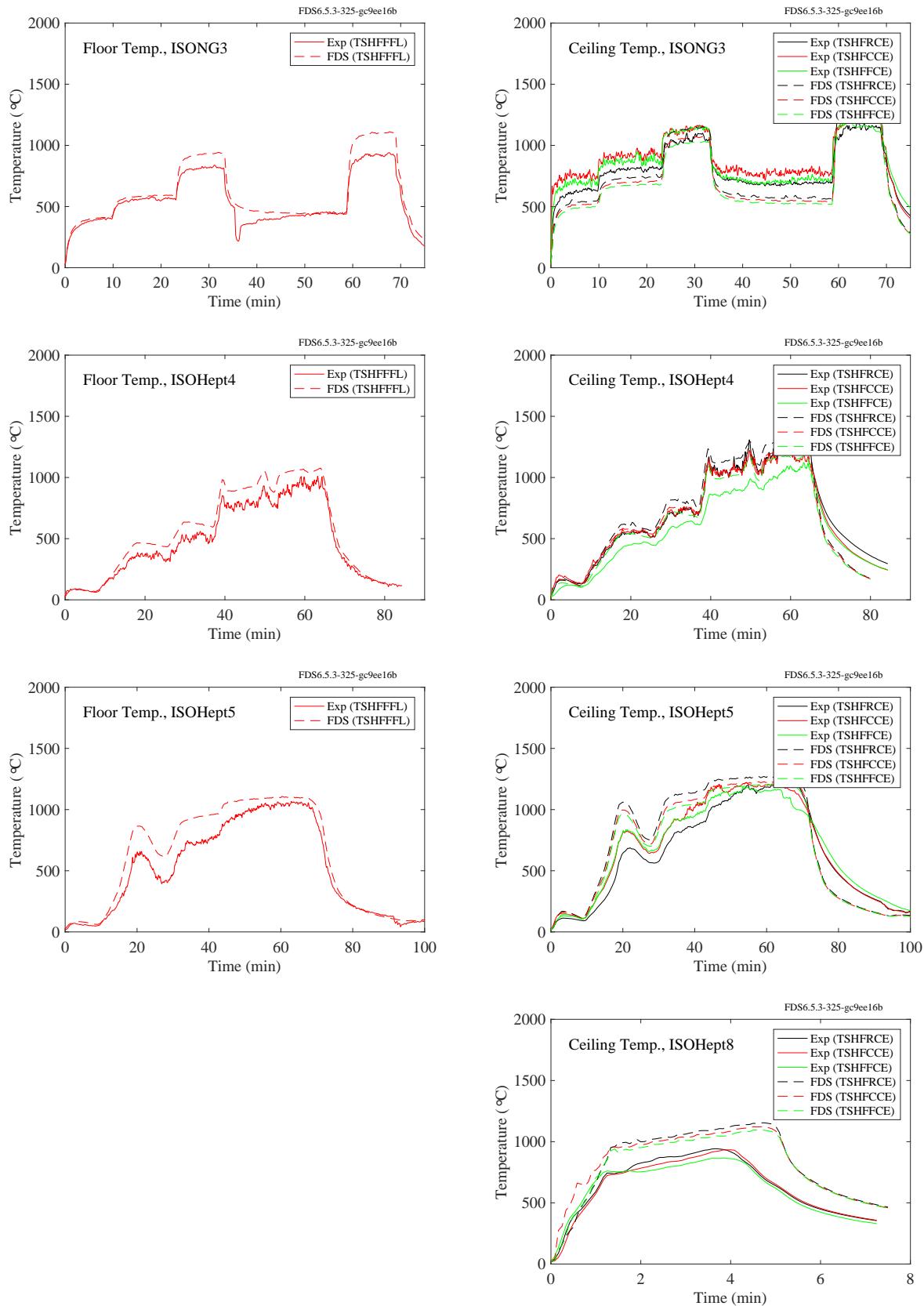


Figure 11.2: NIST FSE experiments, floor and ceiling temperatures, Tests 3-4, 8.

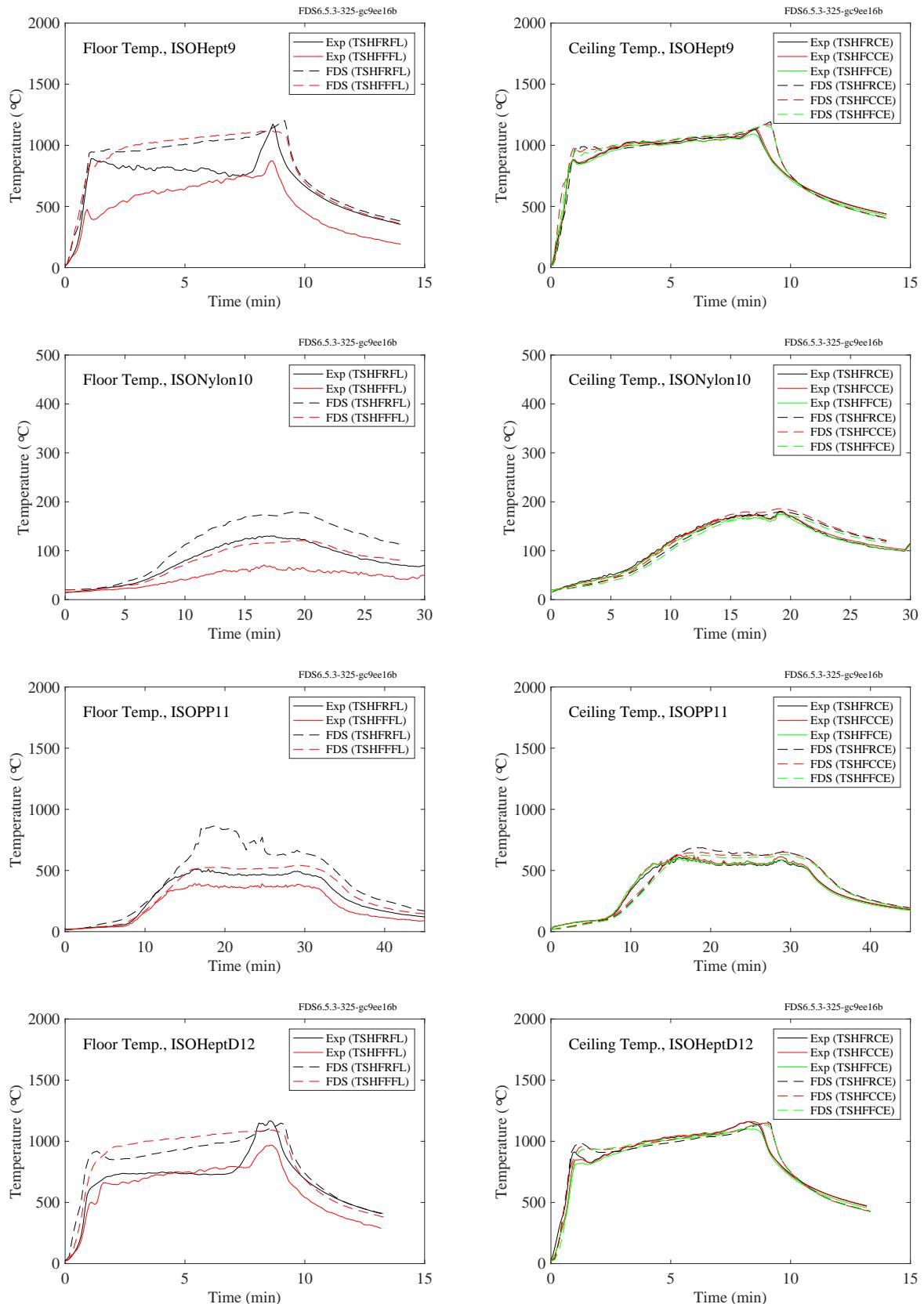


Figure 11.3: NIST FSE experiments, floor and ceiling temperatures, Tests 9-12.

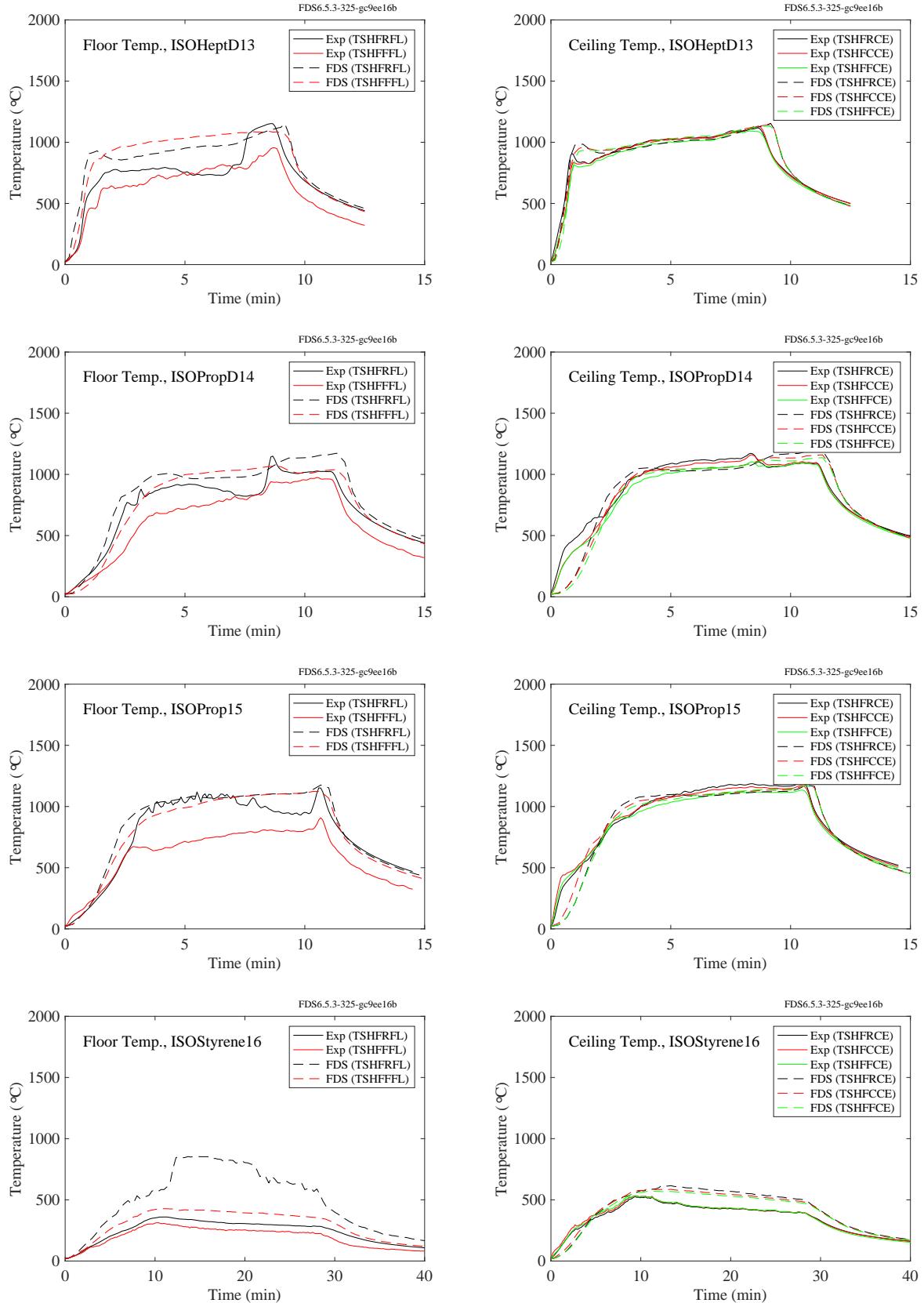


Figure 11.4: NIST FSE experiments, floor and ceiling temperatures, Tests 13-16.

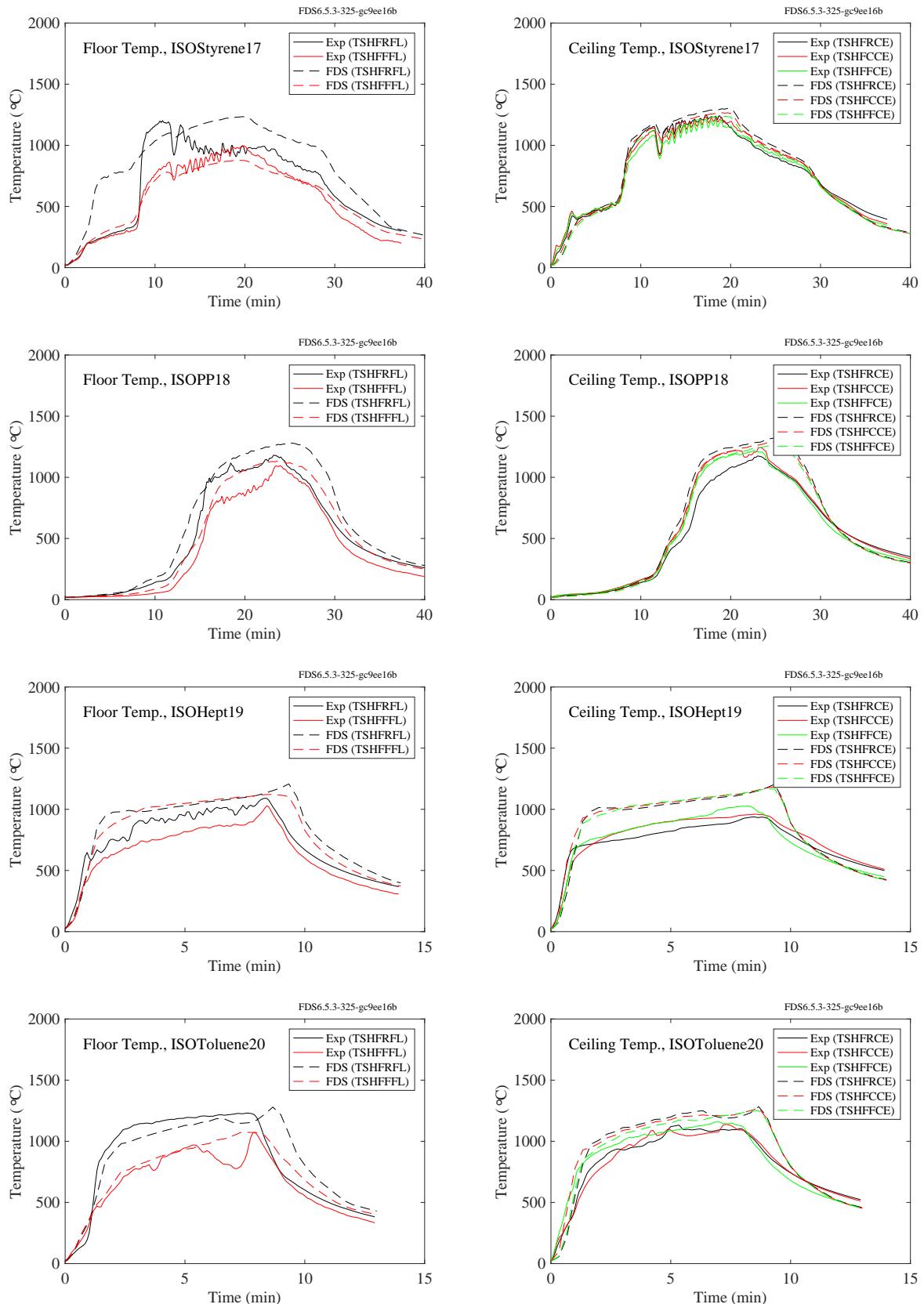


Figure 11.5: NIST FSE experiments, floor and ceiling temperatures, Tests 17-20.

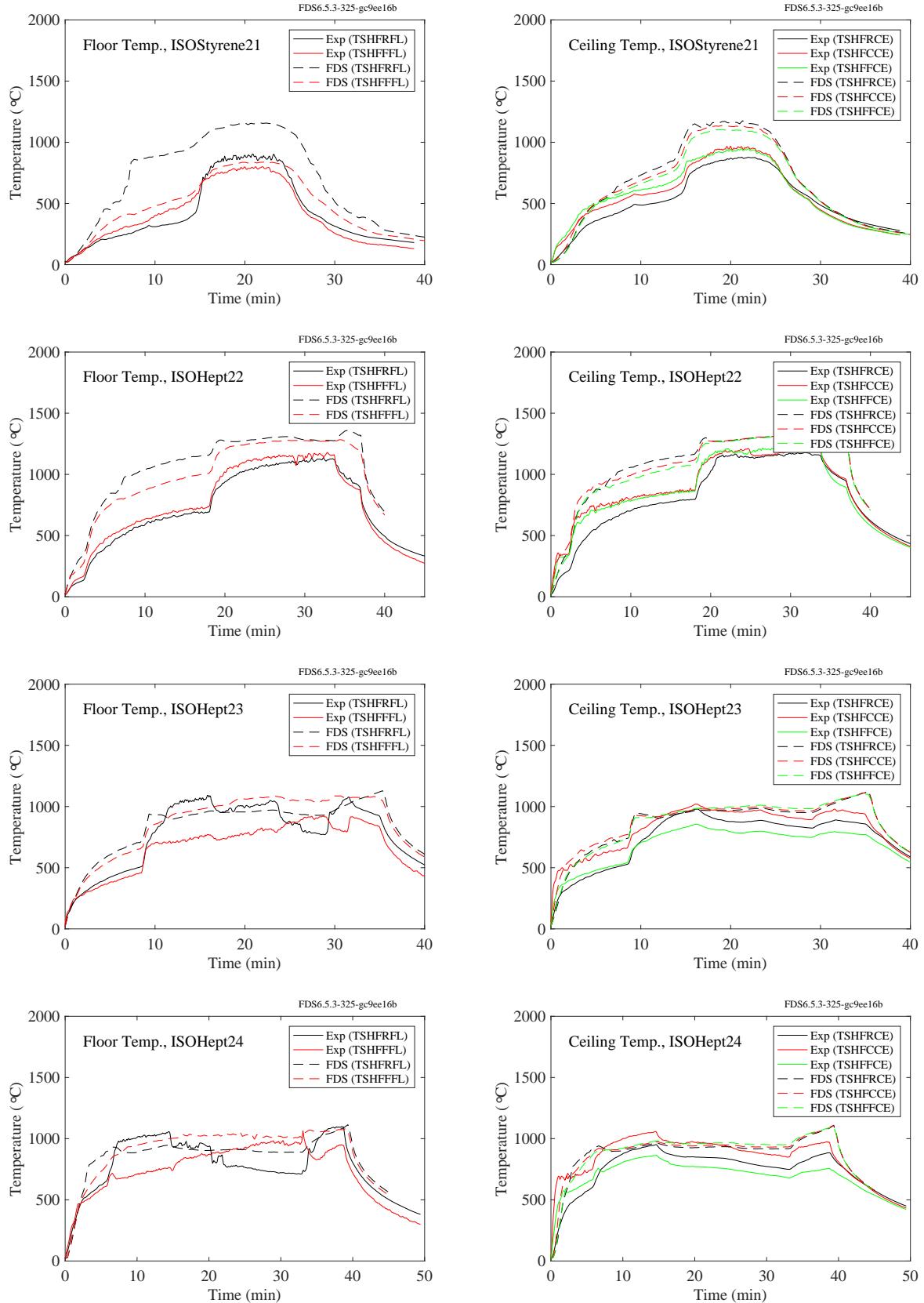


Figure 11.6: NIST FSE experiments, floor and ceiling temperatures, Tests 21-24.

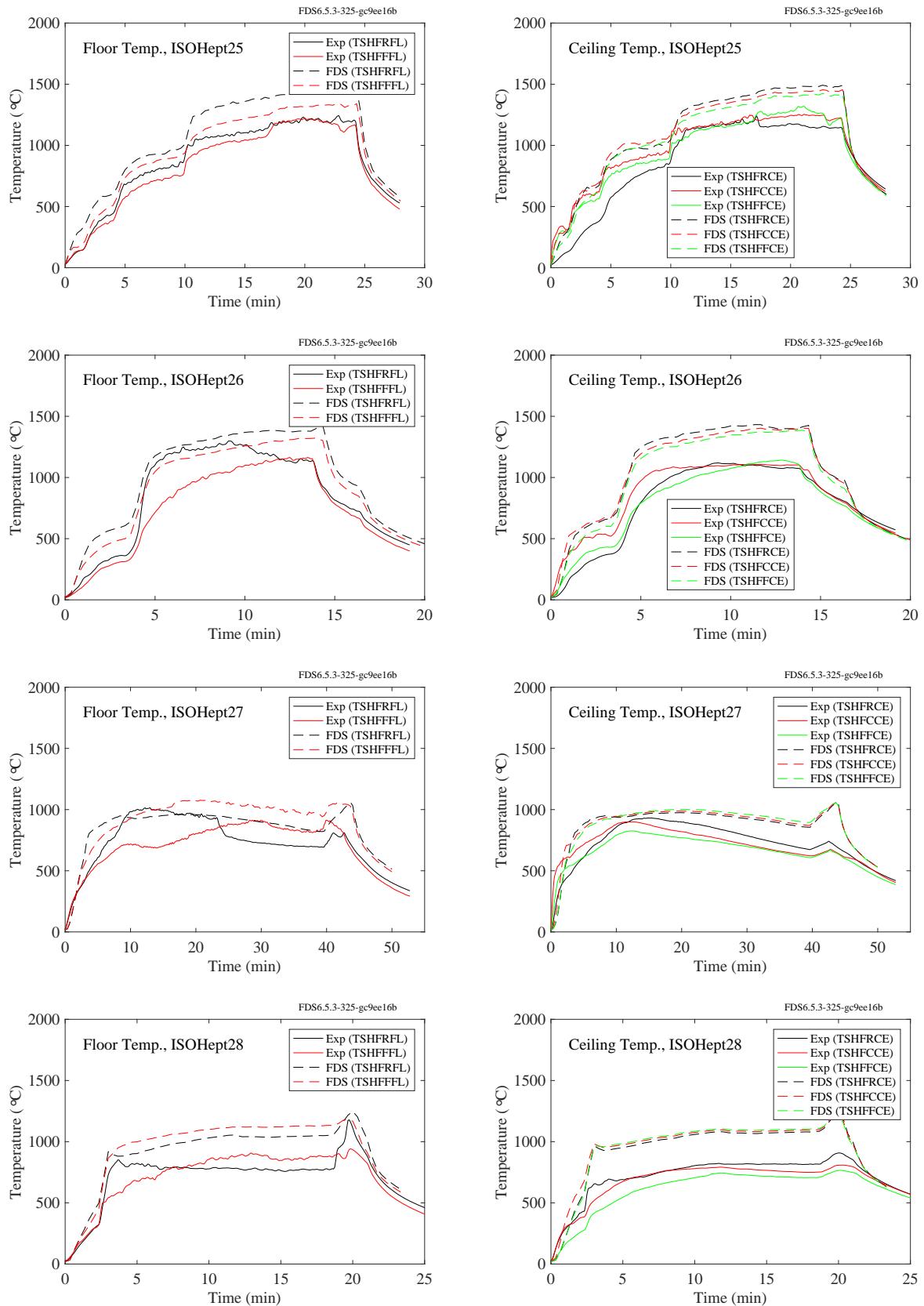


Figure 11.7: NIST FSE experiments, floor and ceiling temperatures, Tests 25-28.

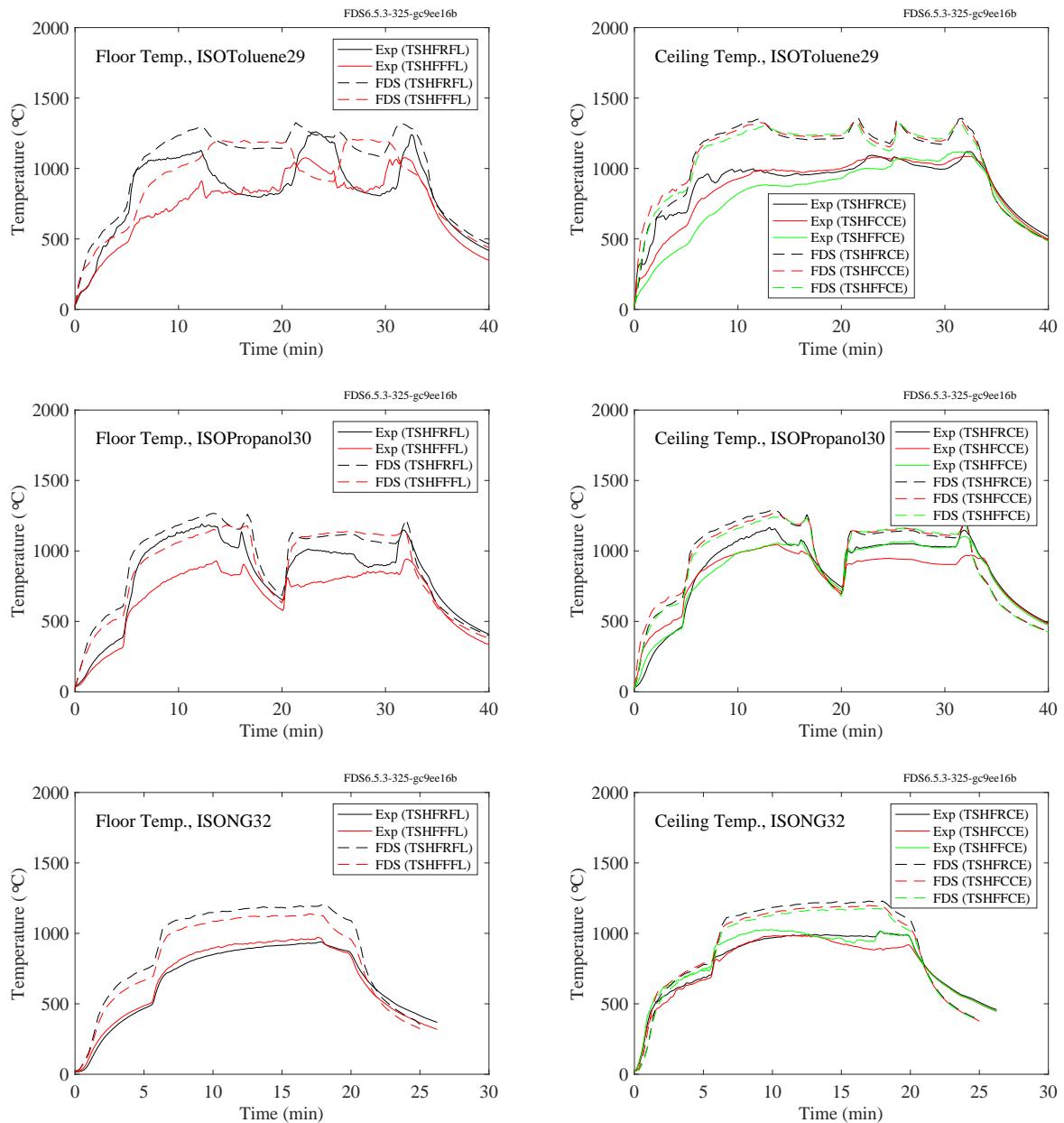


Figure 11.8: NIST FSE experiments, floor and ceiling temperatures, Tests 29, 30, 32.

### 11.1.3 NIST/NRC Experiments

Thermocouples and heat flux gauges were positioned at various locations on all four walls of the test compartment, plus the ceiling and floor. Comparisons between measured and predicted surface temperatures are shown on the following pages. Over the course of 15 experiments, a number of the thermocouples and gauges failed, but because over half of the measurement points were in roughly the same relative location to the fire, the faulty data was discarded based on examining replicate experiments or locations on the opposite wall. Note that Position 8 for the floor and ceiling is not used, simply because the plotting routine is limited to 7 distinct colors and Position 8 is on the opposite side of the compartment to Position 1. Table 11.1 lists the locations for each test.

Table 11.1: Wall thermocouple and heat flux gauge positions for the NIST/NRC series. The origin of the coordinate system lies on the floor in the southwest corner of the compartment. The designation “U” and “C” is irrelevant, and the last digit “2” indicates that the thermocouple is measuring the wall temperature rather than the heat flux gauge temperature.

Name	<i>x</i>	<i>y</i>	<i>z</i>	Name	<i>x</i>	<i>y</i>	<i>z</i>
TC North U-1-2	3.85	7.04	1.49	TC South U-1-2	3.86	0	1.49
TC North U-2-2	3.86	7.04	3.71	TC South U-2-2	3.86	0	3.82
TC North U-3-2	9.48	7.04	1.86	TC South U-3-2	9.54	0	1.86
TC North U-4-2	12.07	7.04	1.88	TC South U-4-2	12.08	0	1.86
TC North U-5-2	17.69	7.04	1.49	TC South U-5-2	17.69	0	1.50
TC North U-6-2	17.69	7.04	3.69	TC South U-6-2	17.74	0	3.70
TC East U-1-2	21.66	1.52	1.12	TC West U-1-2	0	1.59	1.12
TC East U-2-2	21.66	1.52	2.40	TC West U-2-2	0	1.59	2.42
TC East U-3-2	21.66	5.68	1.13	TC West U-3-2	0	5.70	1.12
TC East U-4-2	21.66	5.70	2.42	TC West U-4-2	0	5.70	2.42
TC Floor U-1-2	3.08	3.51	0	TC Ceiling U-1-2	3.04	3.60	3.82
TC Floor U-2-2	9.08	1.94	0	TC Ceiling C-2-2	8.99	2.00	3.82
TC Floor U-3-2	9.06	5.97	0	TC Ceiling C-3-2	9.03	5.97	3.82
TC Floor U-4-2	10.86	2.38	0	TC Ceiling C-4-2	10.79	2.38	3.82
TC Floor C-5-2	10.93	5.20	0	TC Ceiling C-5-2	10.79	5.20	3.82
TC Floor U-6-2	13.13	1.99	0	TC Ceiling C-6-2	13.00	2.07	3.82
TC Floor U-7-2	13.00	5.92	0	TC Ceiling C-7-2	12.84	5.98	3.82
TC Floor U-8-2	18.63	3.54	0	TC Ceiling U-8-2	18.71	3.54	3.82

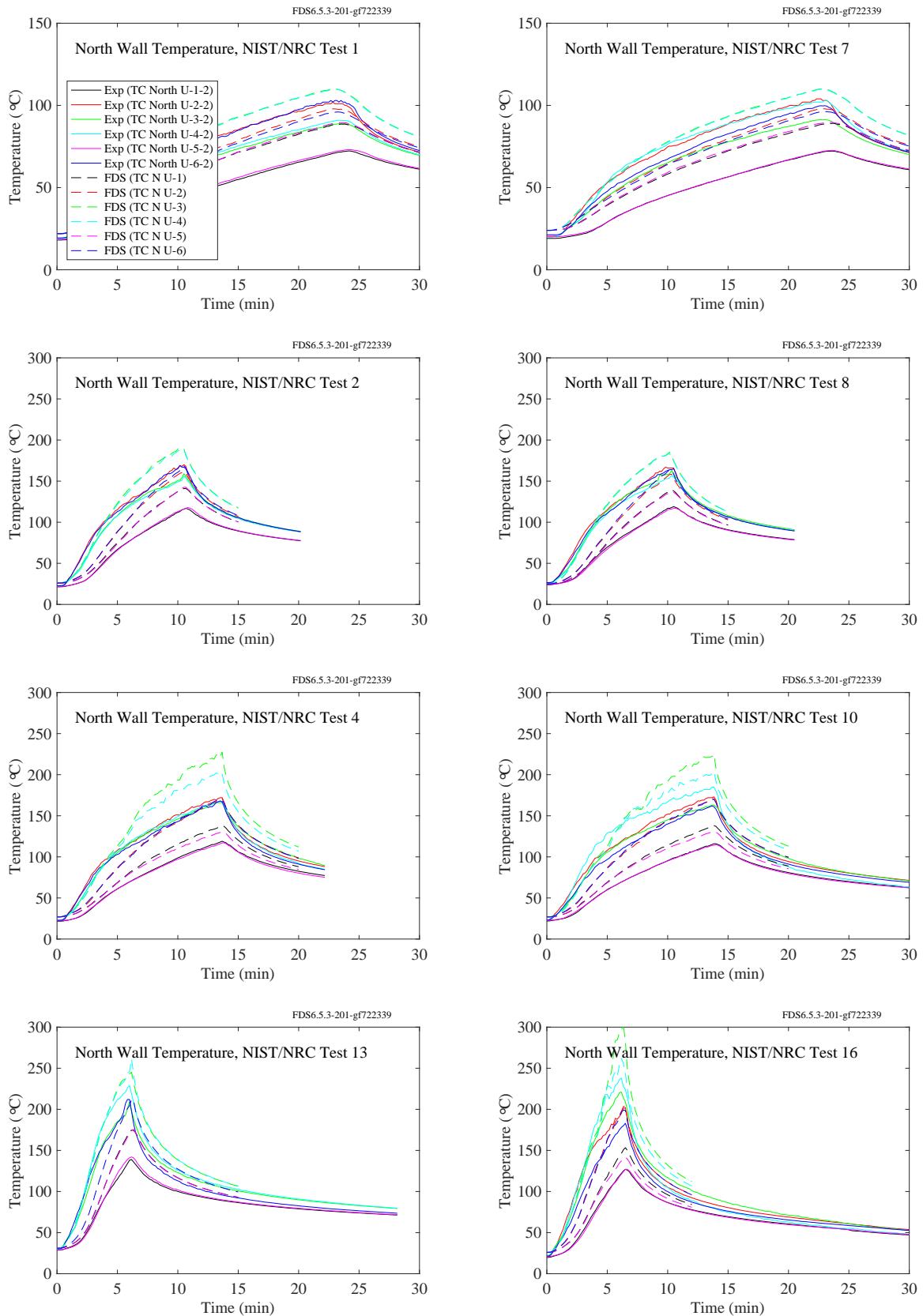


Figure 11.9: NIST/NRC experiments, north wall temperatures, Tests 1, 2, 4, 7, 8, 10, 13, 16.

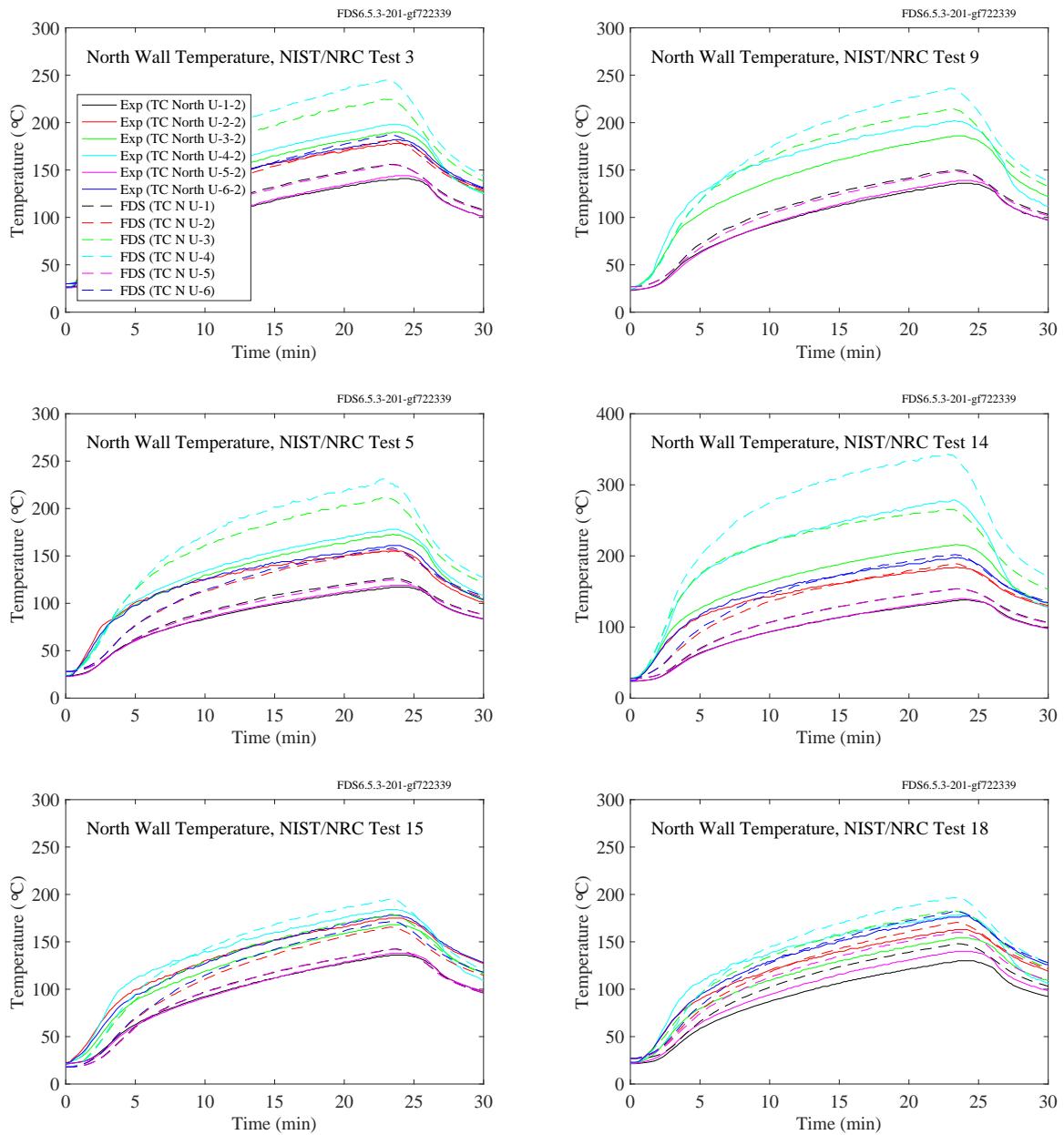


Figure 11.10: NIST/NRC experiments, north wall temperatures, Tests 3, 5, 9, 14, 15, 18.

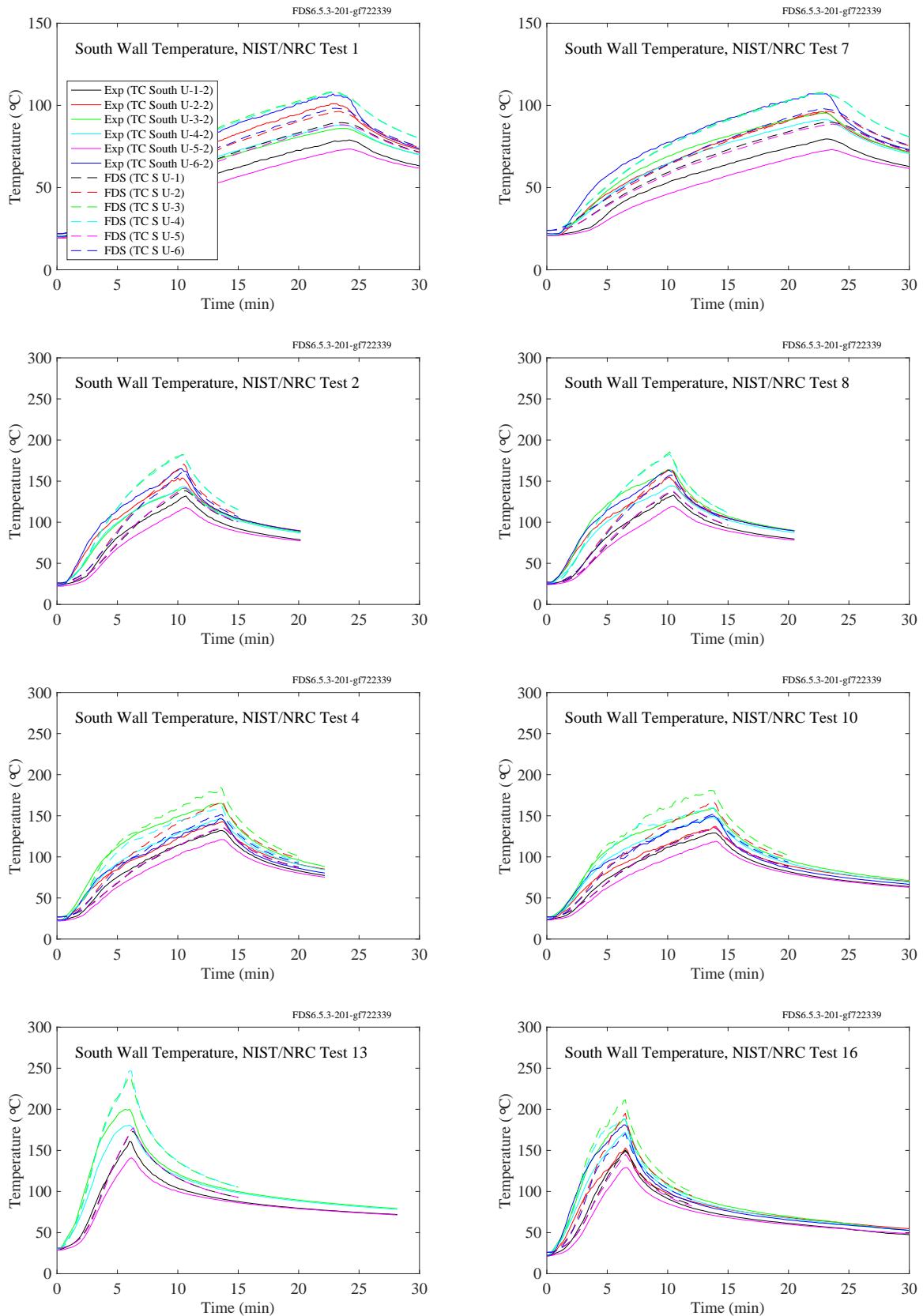


Figure 11.11: NIST/NRC experiments, south wall temperatures, Tests 1, 2, 4, 7, 8, 10, 13, 16.

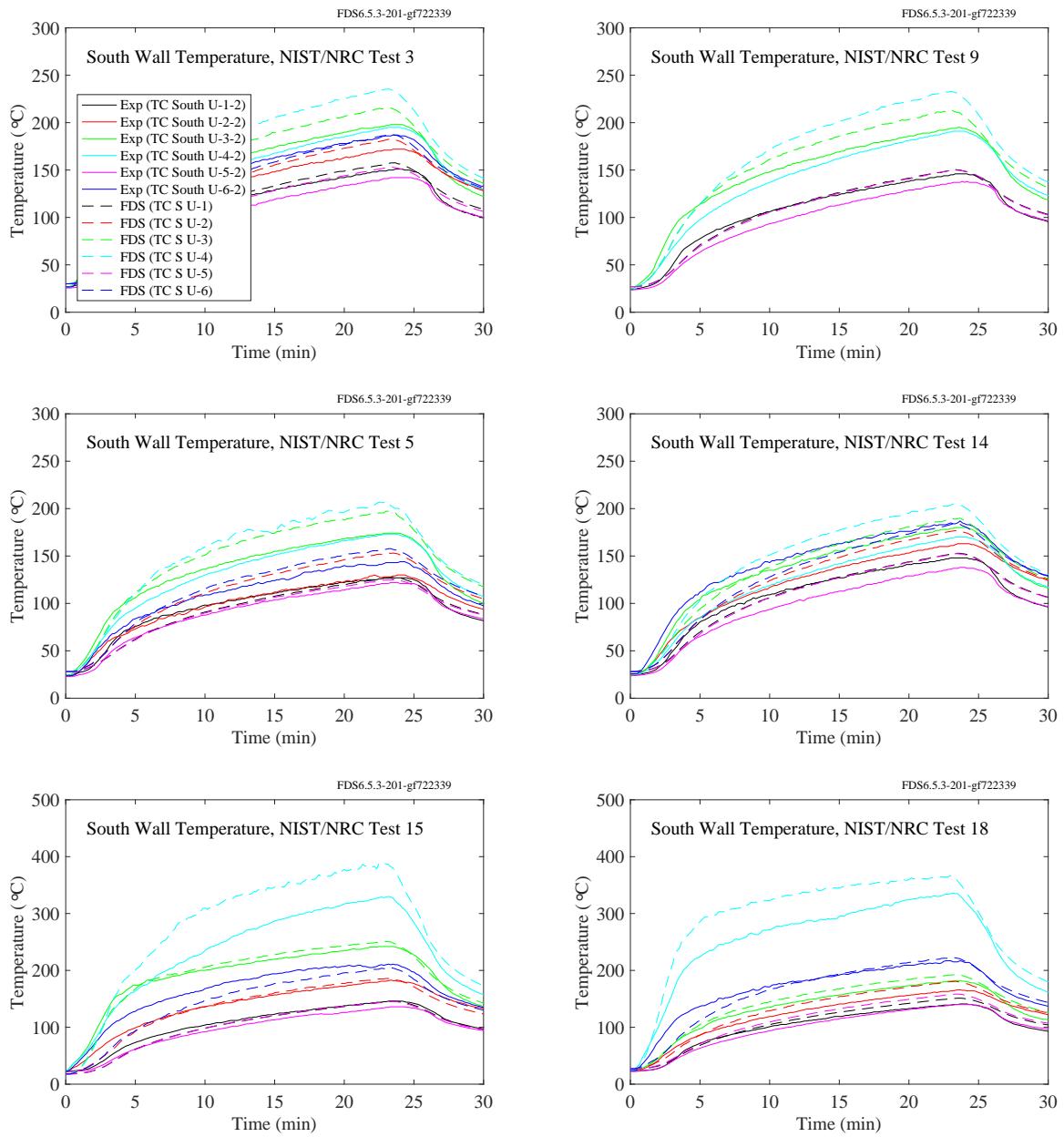


Figure 11.12: NIST/NRC experiments, south wall temperatures, Tests 3, 5, 9, 14, 15, 18.

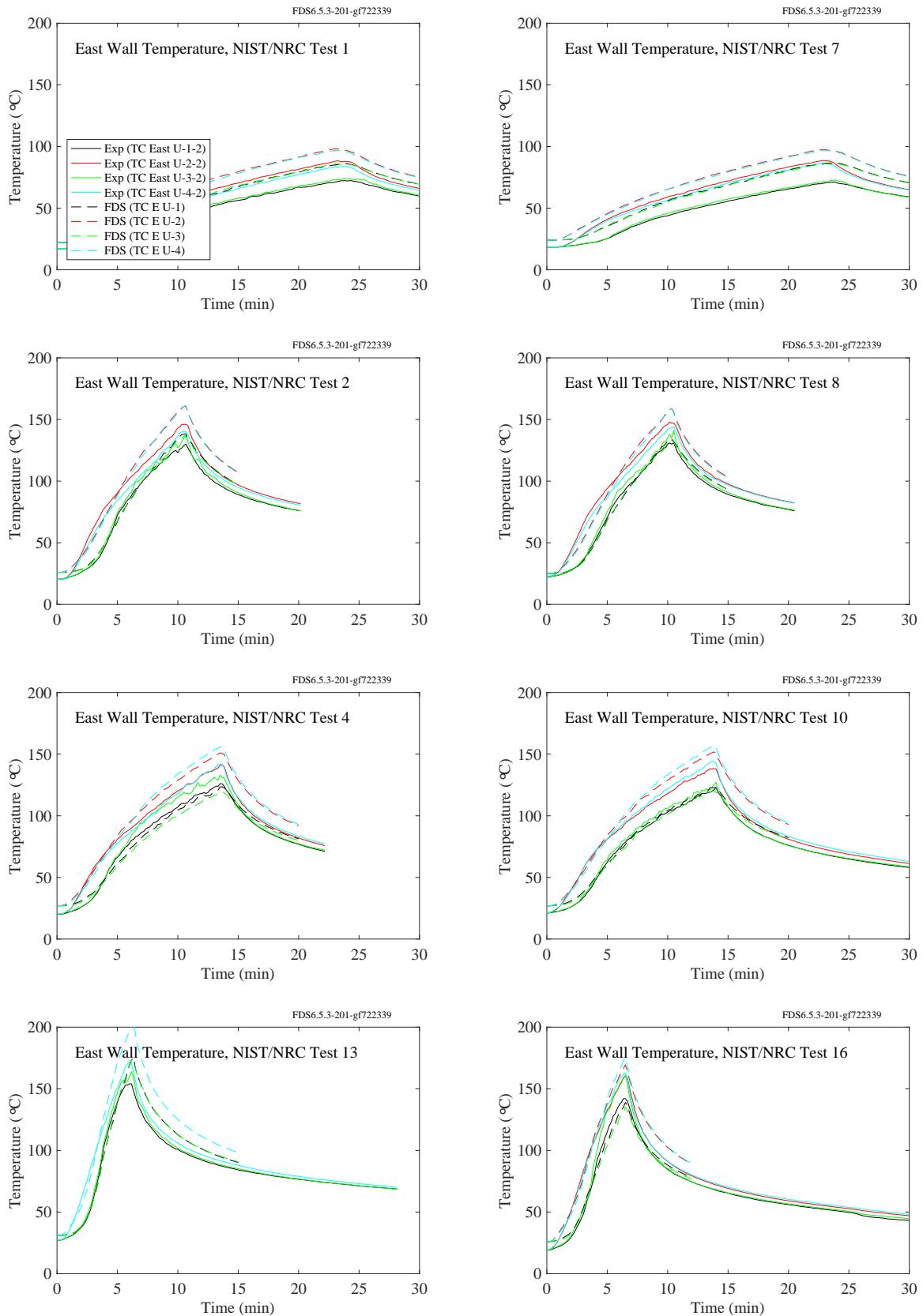


Figure 11.13: NIST/NRC experiments, east wall temperatures, Tests 1, 2, 4, 7, 8, 10, 13, 16.

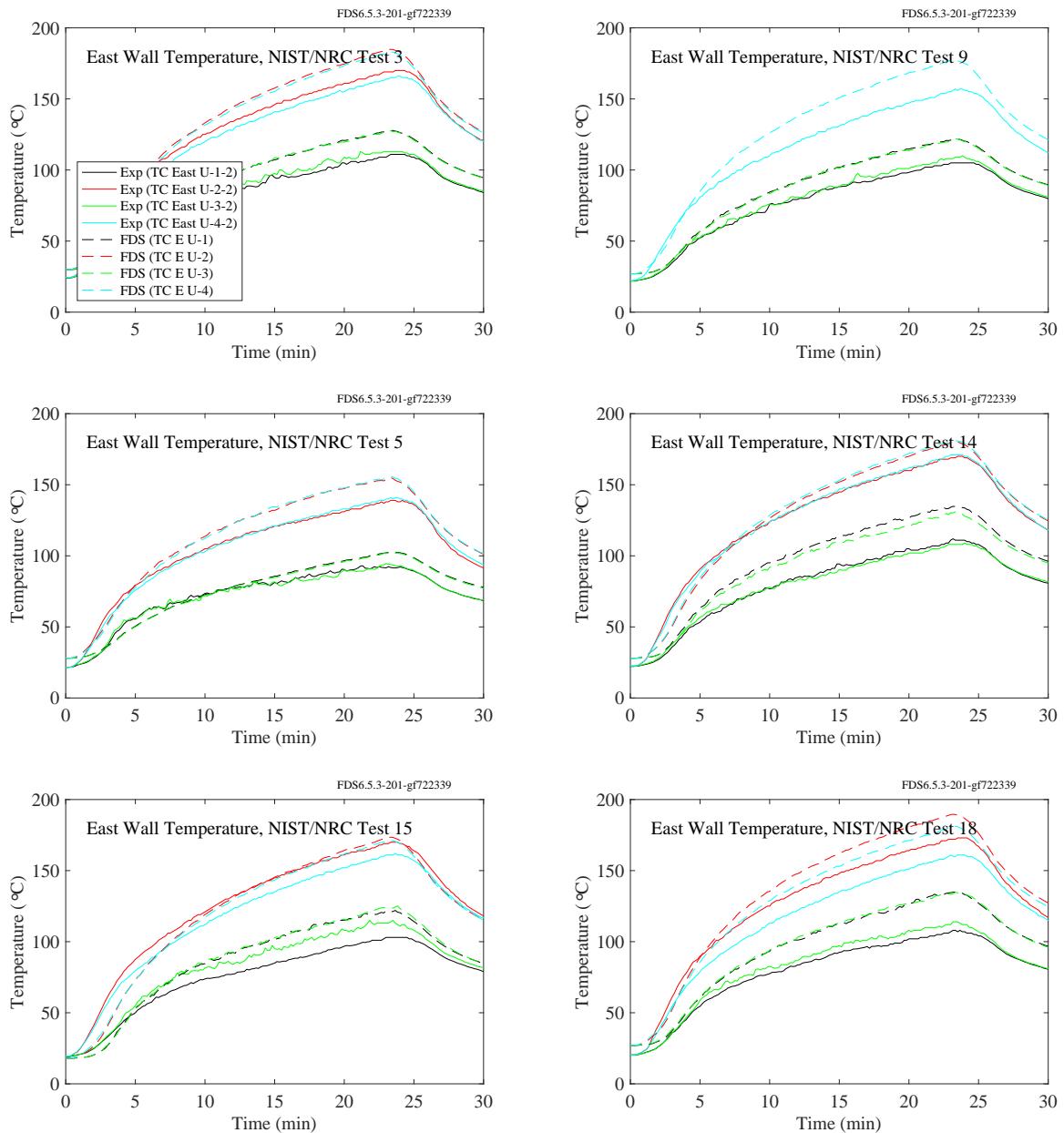


Figure 11.14: NIST/NRC experiments, east wall temperatures, Tests 3, 5, 9, 14, 15, 18.

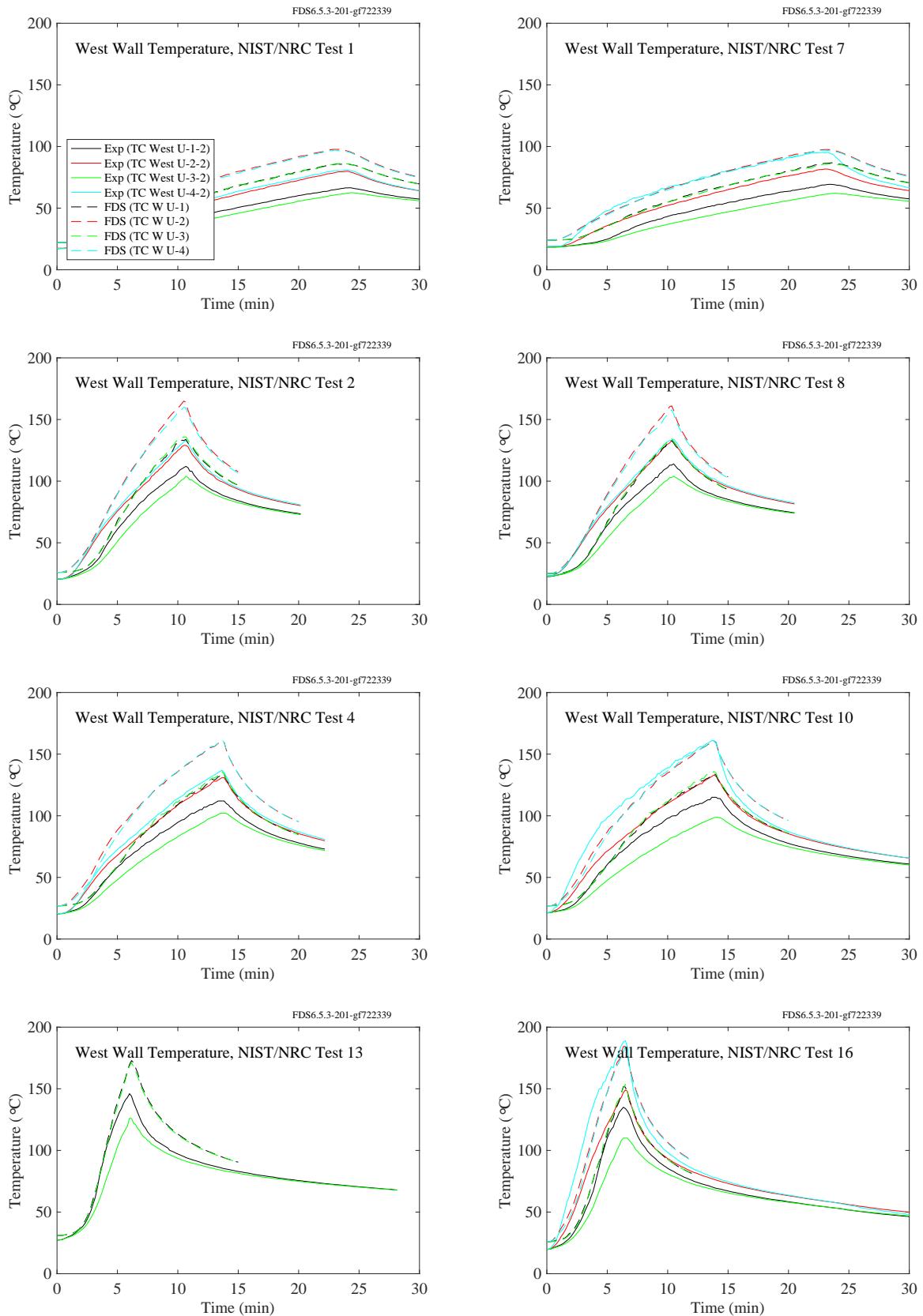


Figure 11.15: NIST/NRC experiments, west wall temperatures, Tests 1, 2, 4, 7, 8, 10, 13, 16.

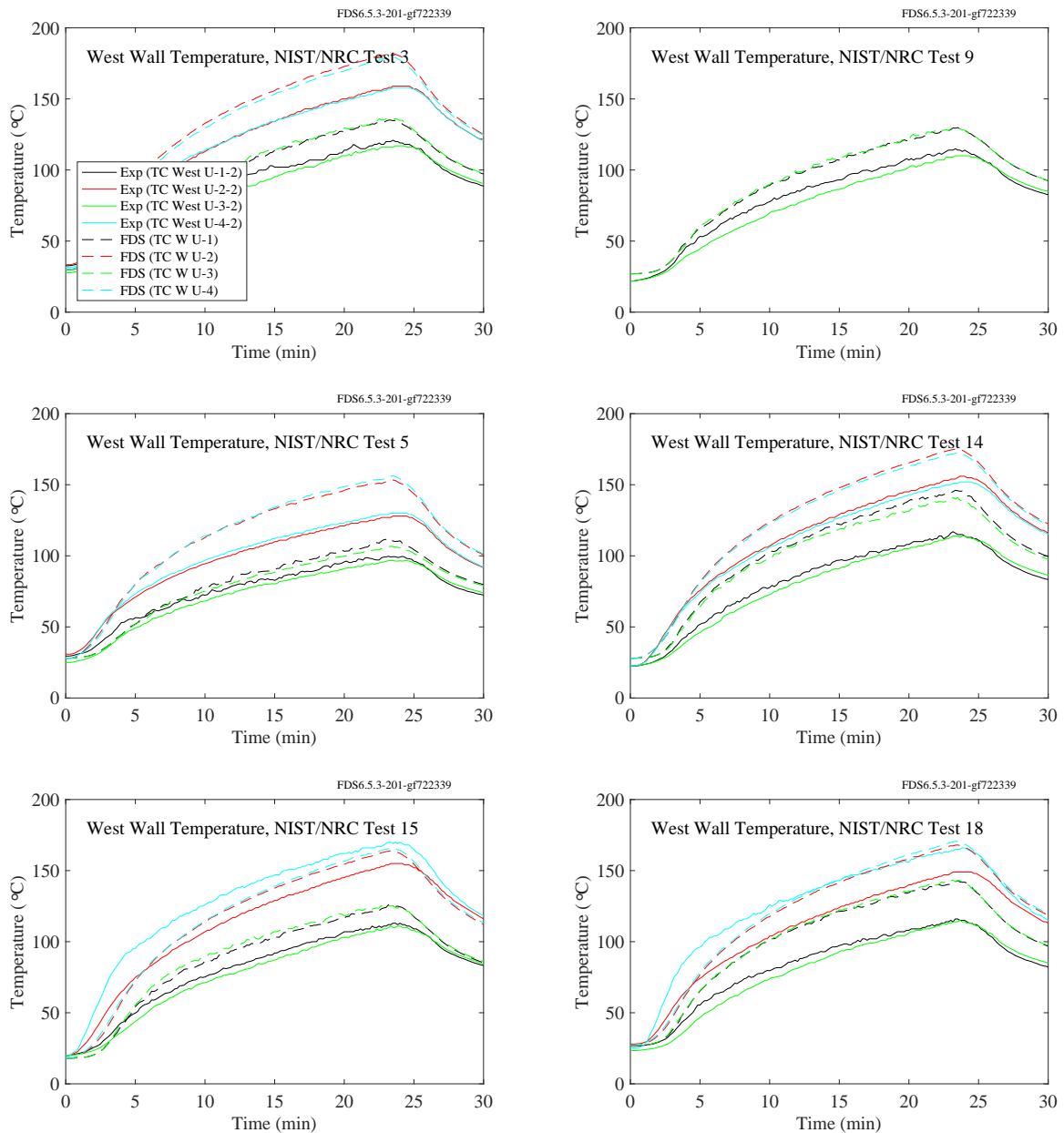


Figure 11.16: NIST/NRC experiments, west wall temperatures, Tests 3, 5, 9, 14, 15, 18.

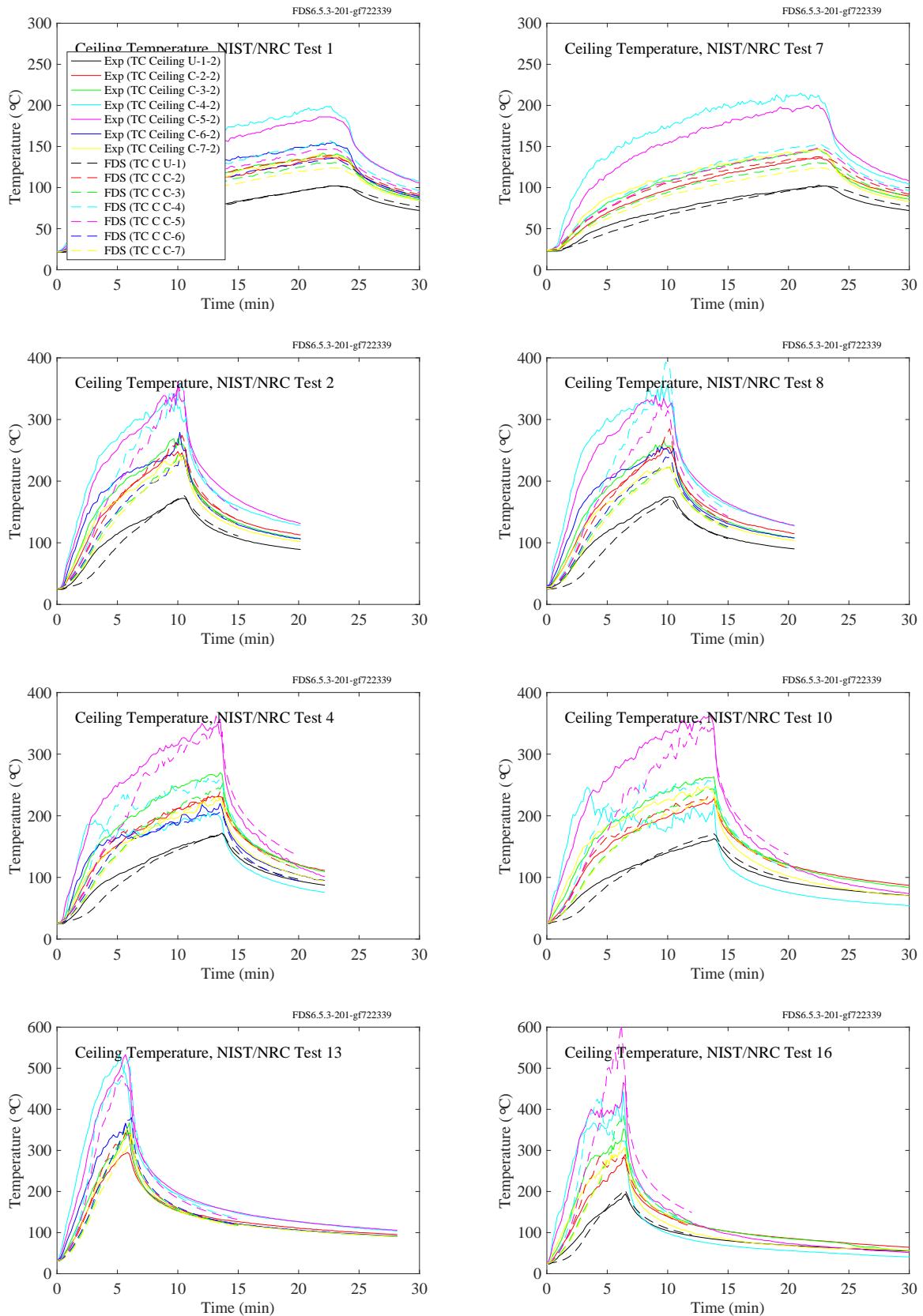


Figure 11.17: NIST/NRC experiments, ceiling temperatures, Tests 1, 2, 4, 7, 8, 10, 13, 16.

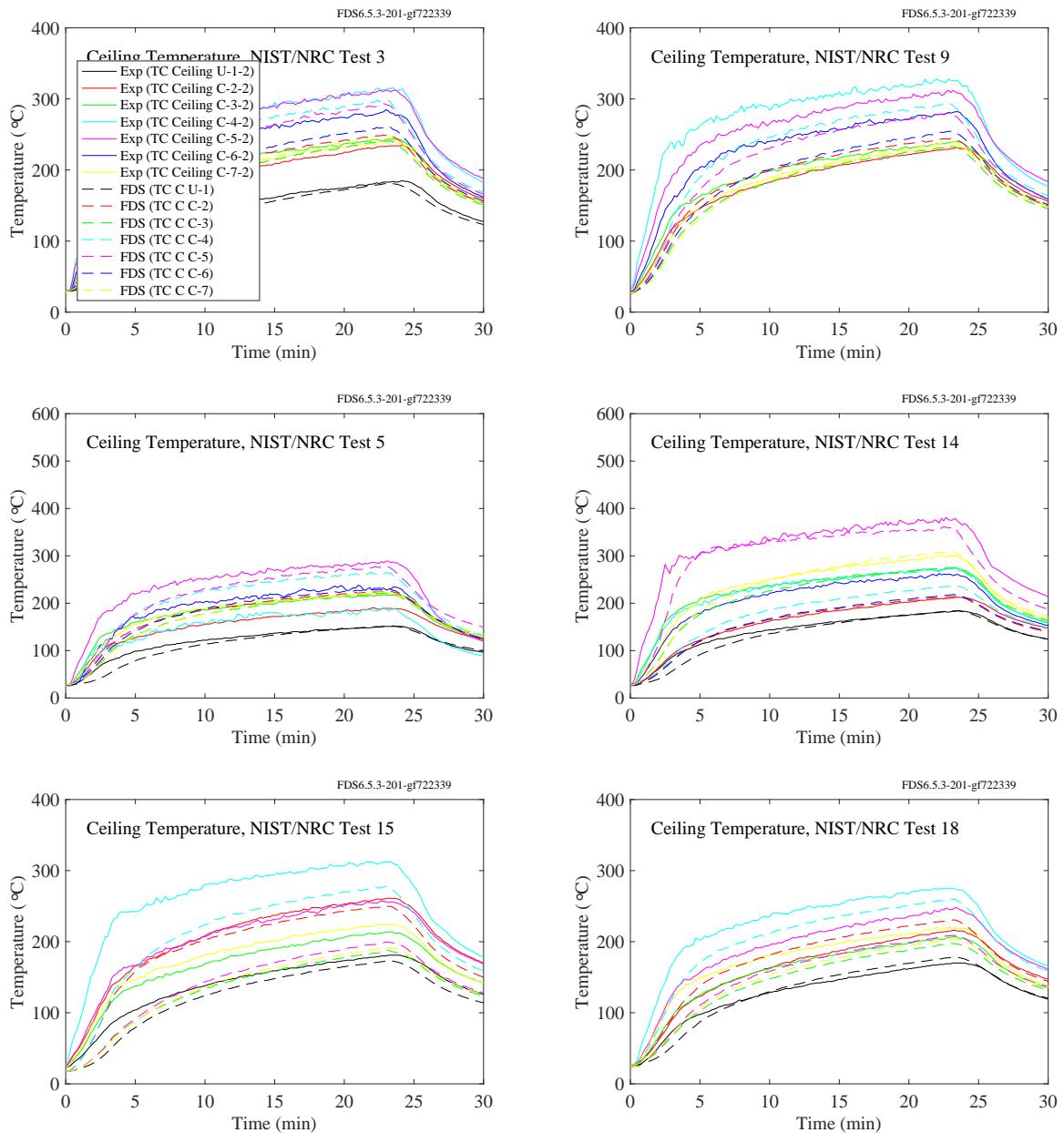


Figure 11.18: NIST/NRC experiments, ceiling temperatures, Tests 3, 5, 9, 14, 15, 18.

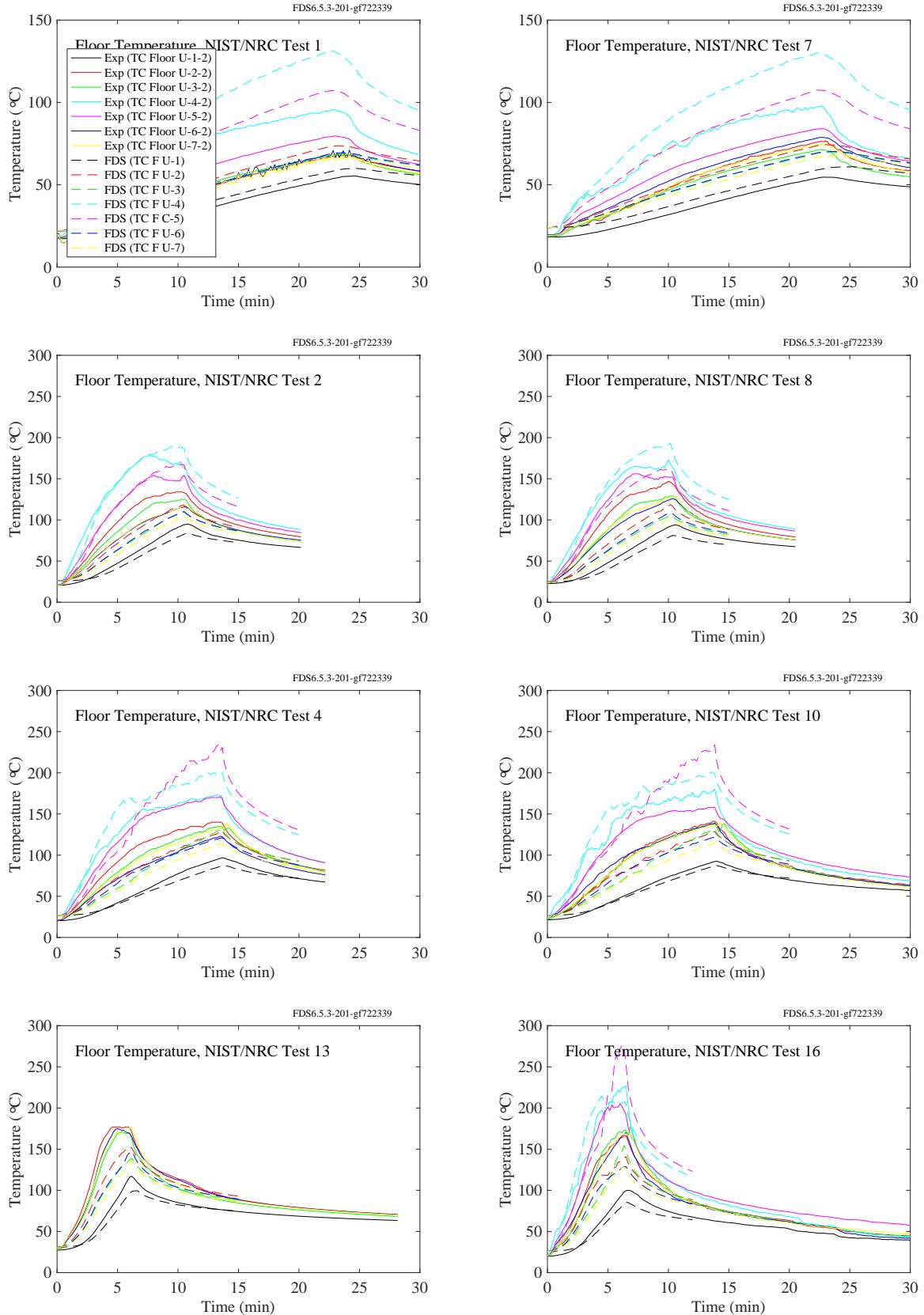


Figure 11.19: NIST/NRC experiments, floor wall temperatures, Tests 1, 2, 4, 7, 8, 10, 13, 16.

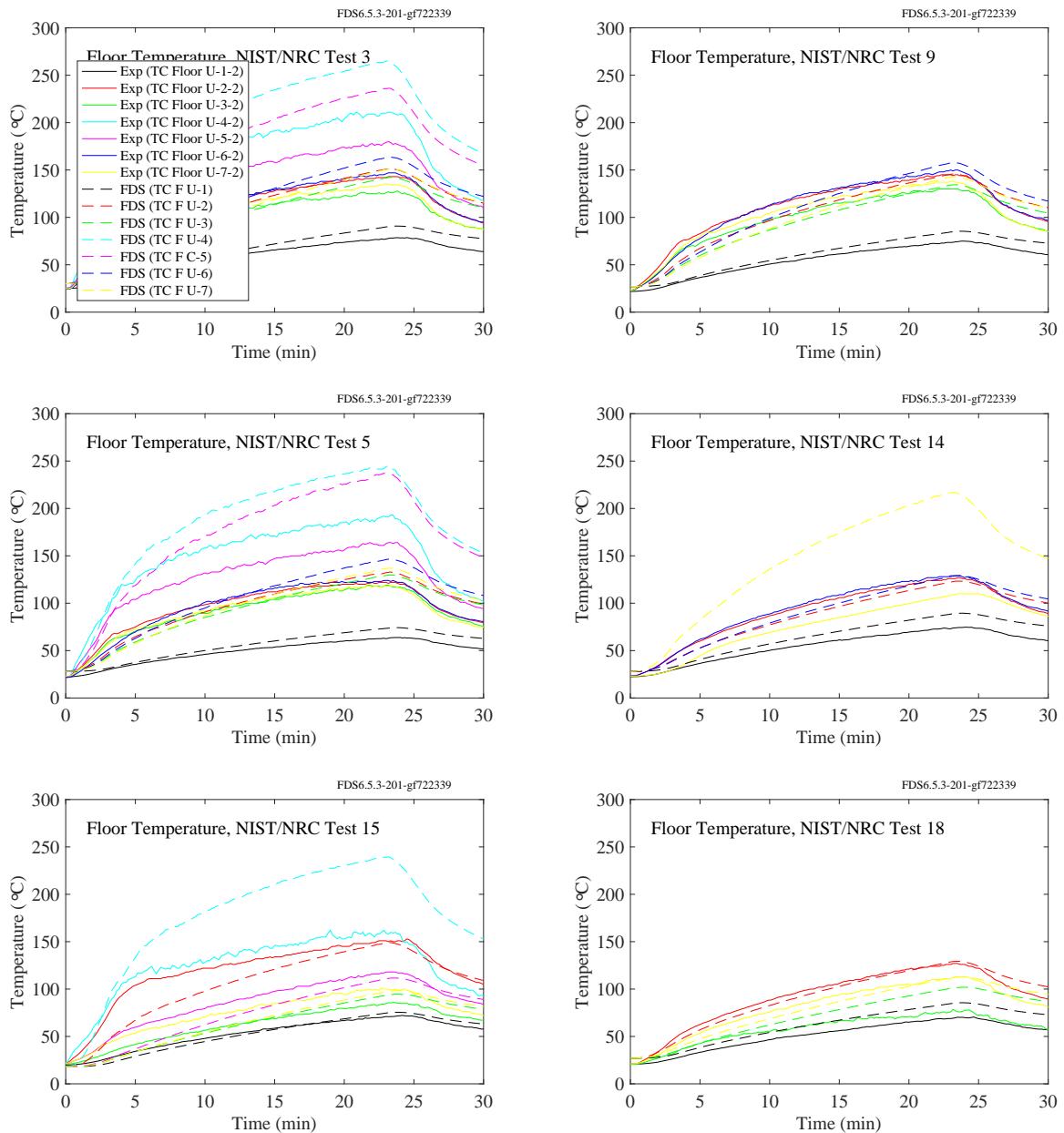


Figure 11.20: NIST/NRC experiments, floor temperatures, Tests 3, 5, 9, 14, 15, 18.

### 11.1.4 PRISME DOOR Experiments

Thermocouples were positioned at various points on the walls. Each room contained a vertical array labelled, for example, TP\_L1\_NE265. The TP indicates a surface temperature measurement, L1 indicates compartment 1, which is where the fire was located, NE indicates northeast corner of the room, and 265 indicates the number of centimeters above the floor. In addition, each room contained four measurement points centered on each wall at a height of approximately 260 cm. These points are labelled, for example, TP\_L2\_SC265, compartment 2, center of south wall, 265 cm high.

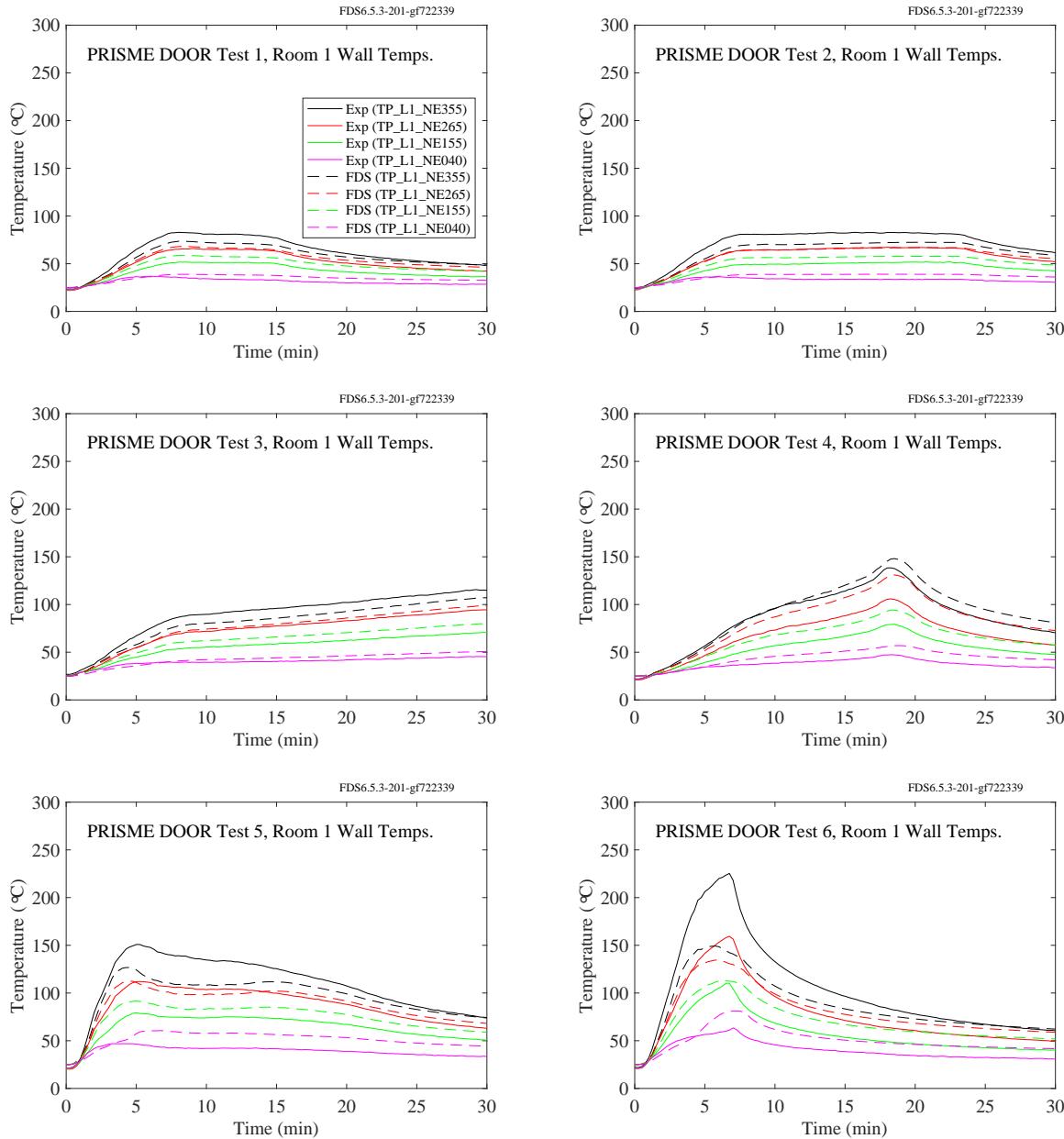


Figure 11.21: PRISME DOOR experiments, wall temperatures, vertical array, Room 1.

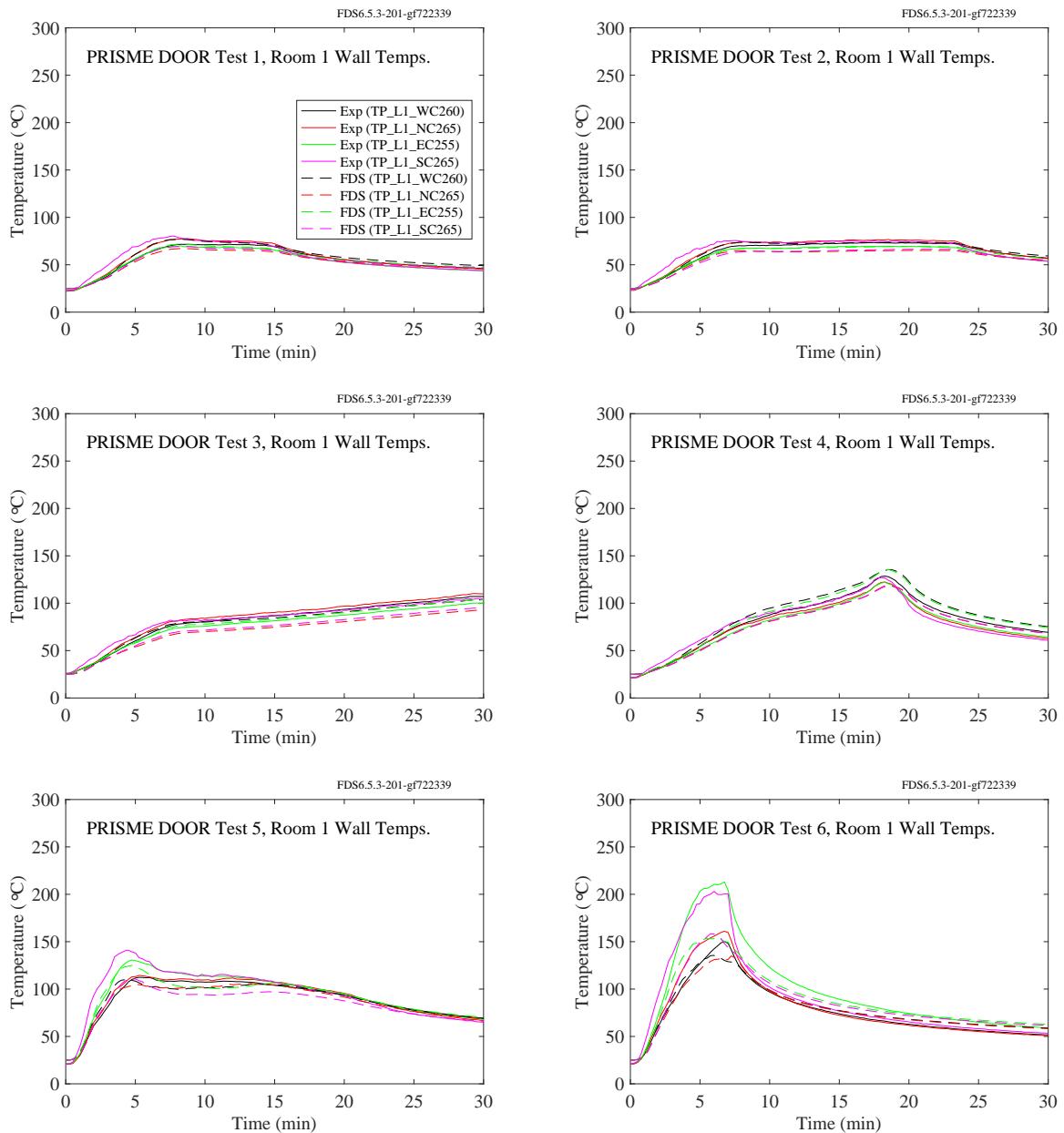


Figure 11.22: PRISME DOOR experiments, wall temperatures, four sides, Room 1.

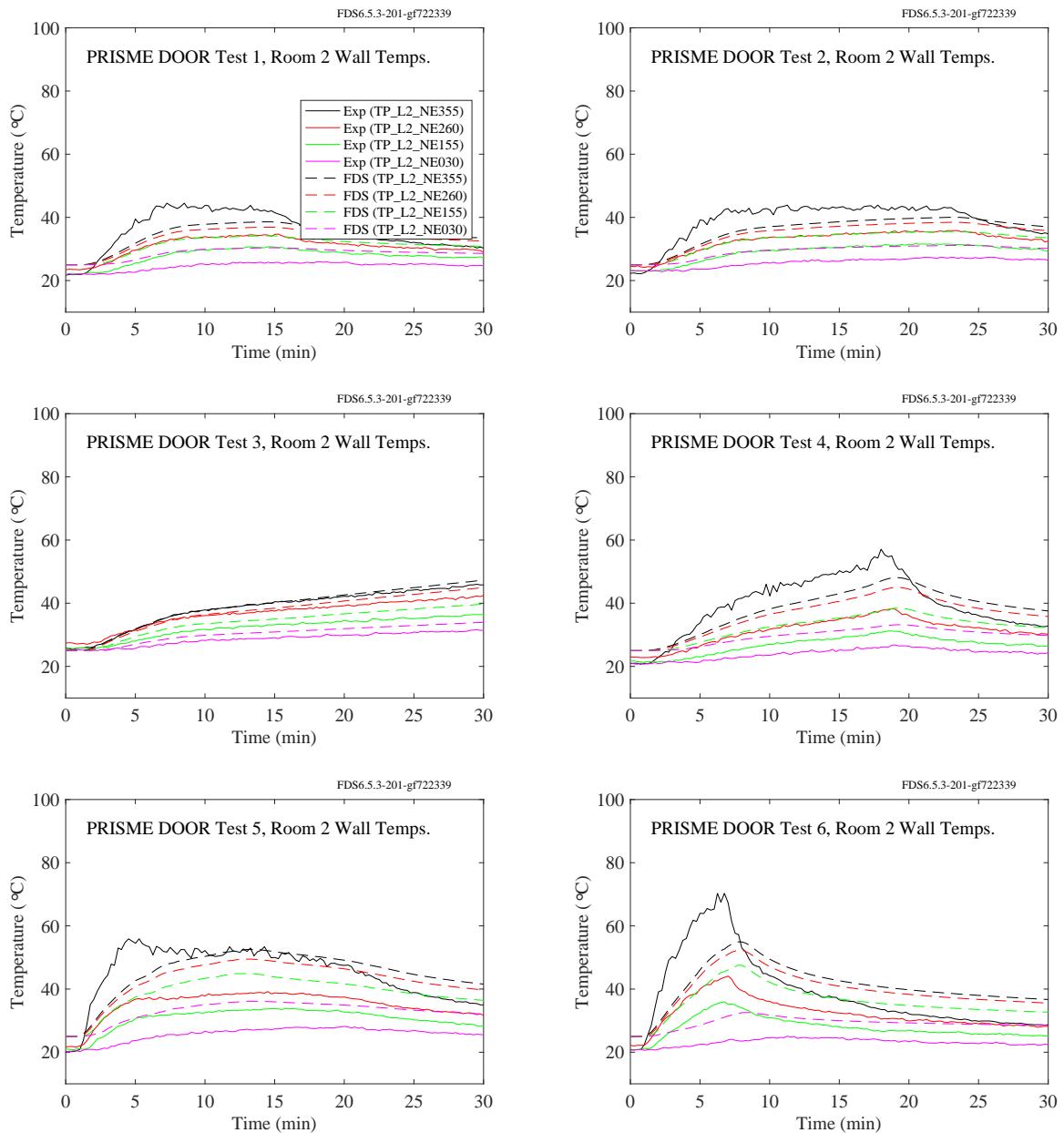


Figure 11.23: PRISME DOOR experiments, wall temperatures, vertical array, Room 2.

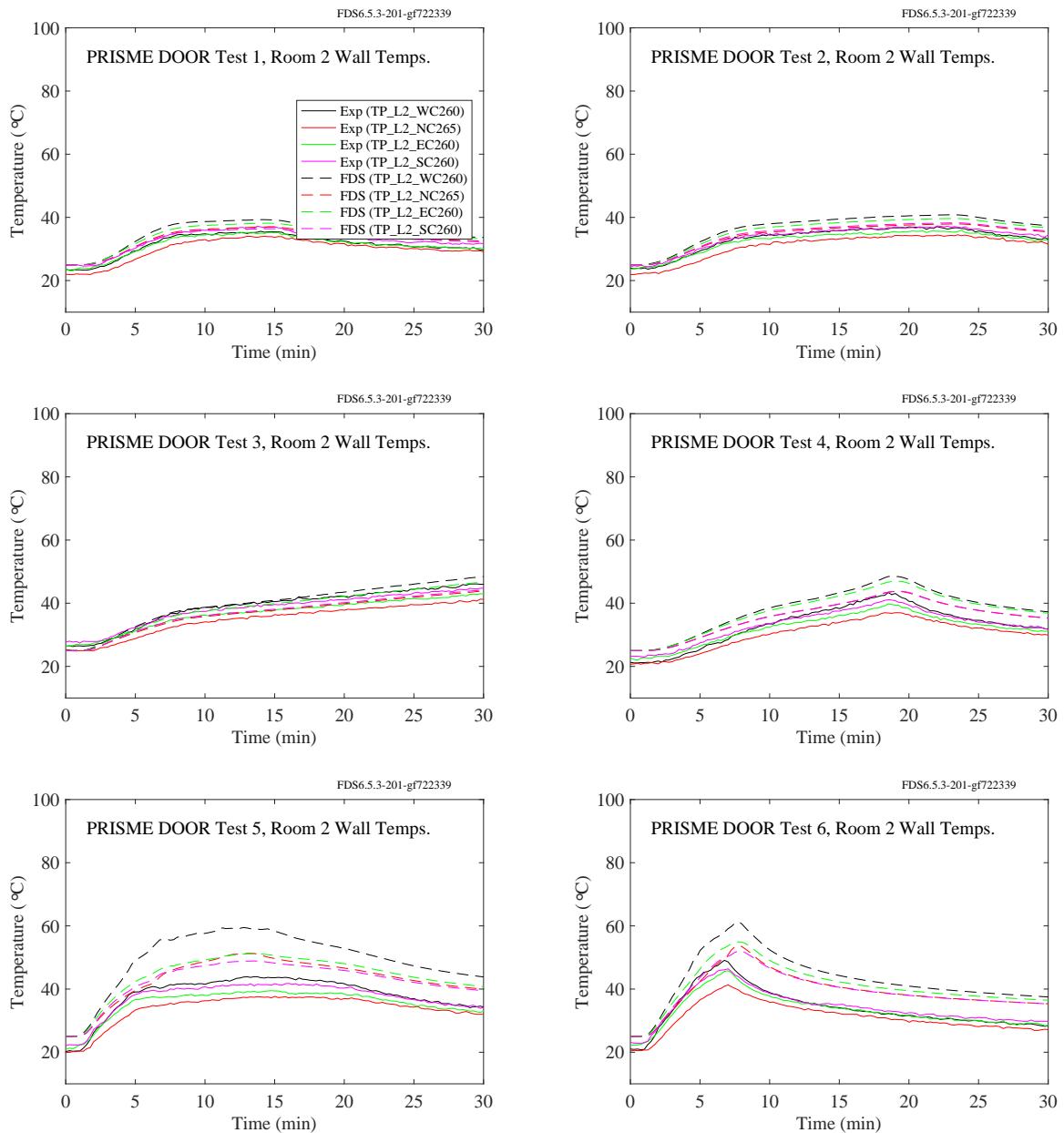


Figure 11.24: PRISME DOOR experiments, wall temperatures, four sides, Room 2.

### **11.1.5 PRISME SOURCE Experiments**

Thermocouples were positioned at various points on the walls. The room contained a vertical array labelled, for example, TP\_L2\_NE265. The TP indicates a surface temperature measurement, L2 indicates compartment 2, which is where the fire was located, NE indicates northeast corner of the room, and 265 indicates the number of centimeters above the floor. In addition, each room contained four measurement points centered on each wall at a height of approximately 260 cm.

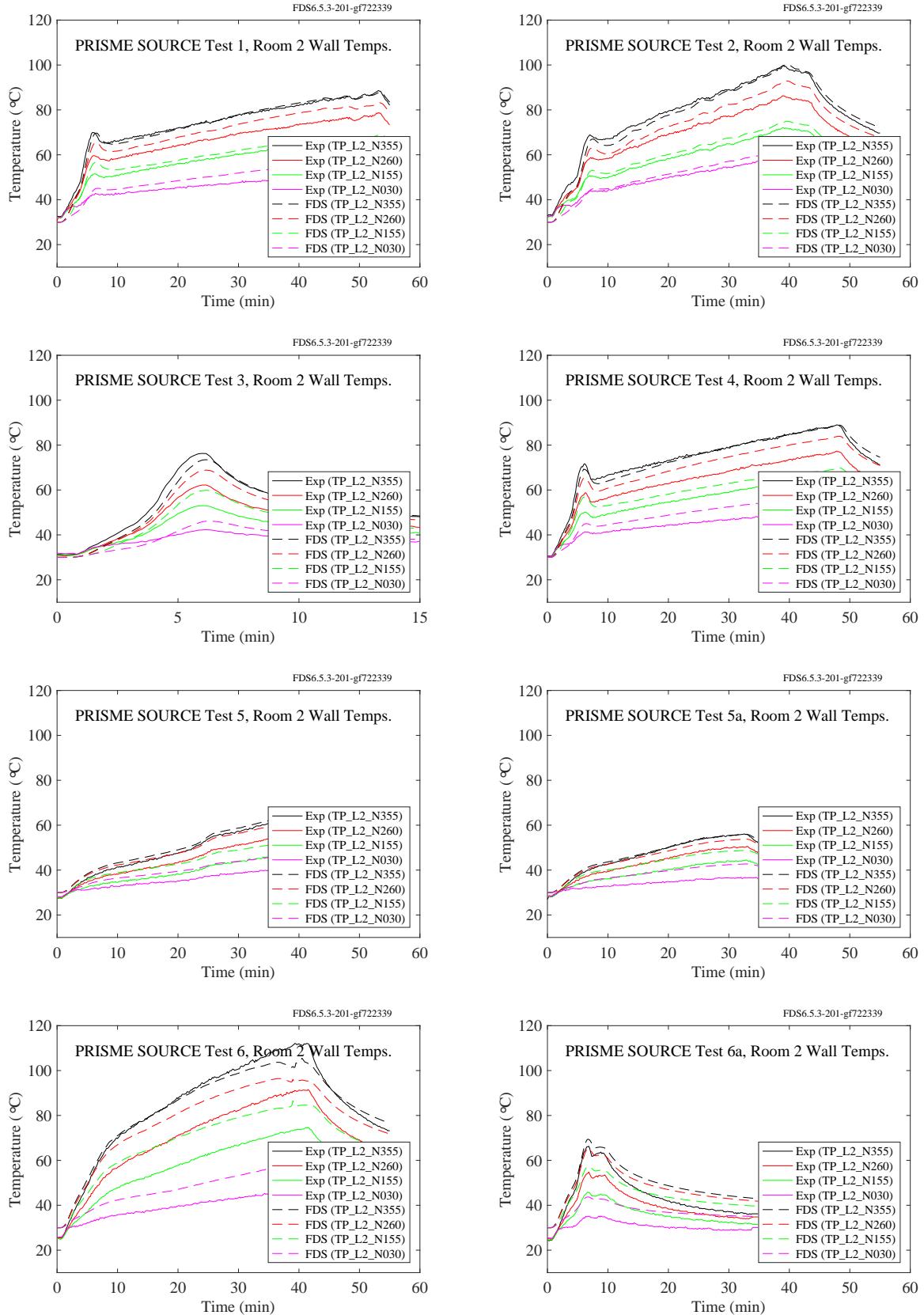


Figure 11.25: PRISME SOURCE experiments, wall temperatures, vertical array, Room 2.

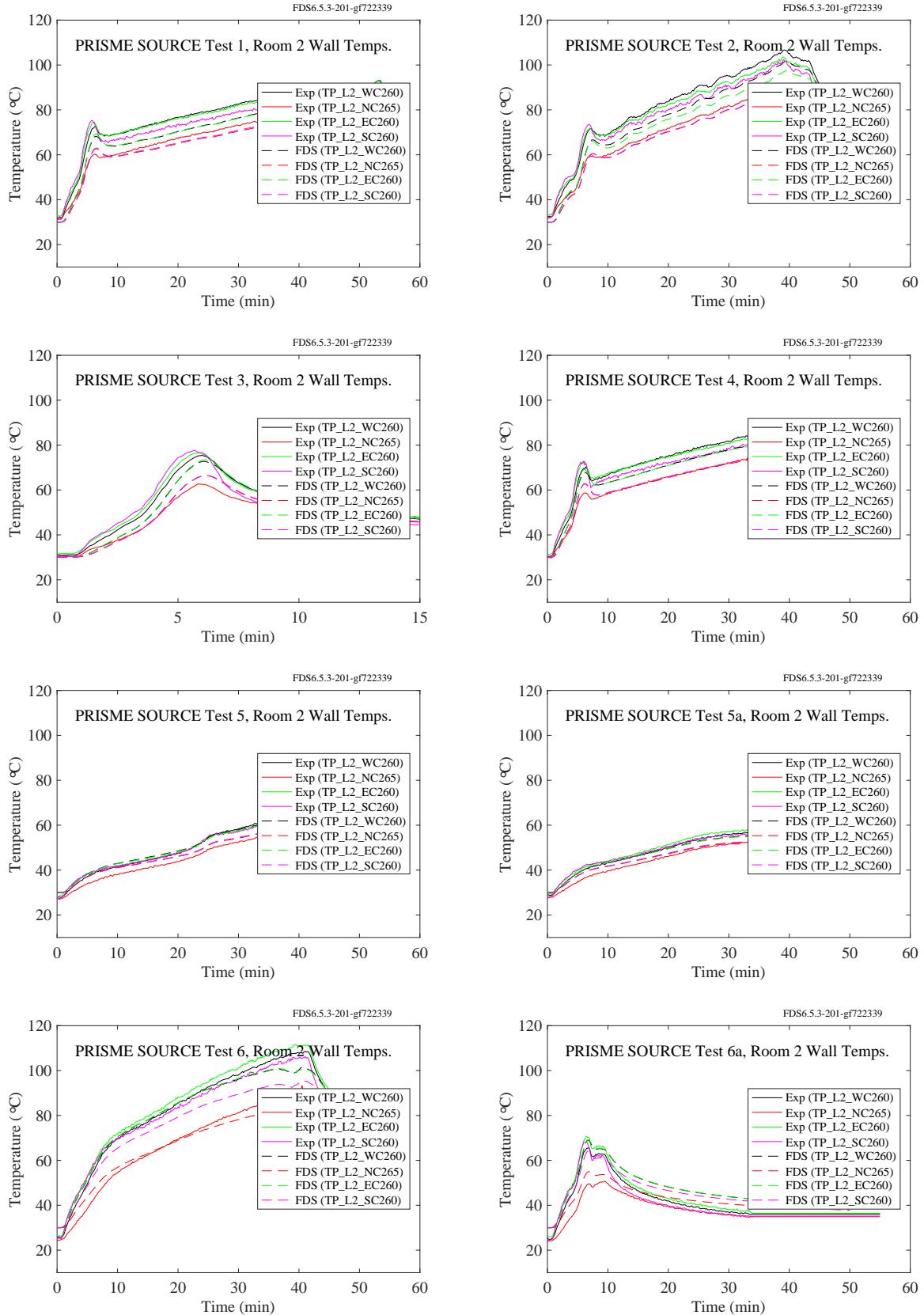


Figure 11.26: PRISME SOURCE experiments, wall temperatures, four sides, Room 2.

### 11.1.6 WTC Experiments

The following pages contain comparisons of predicted and measured ceiling temperatures, both at the surface and beneath a layer of marinite board. Table 11.2 below lists the coordinates of the measurement locations relative to the center of the fire pan. Names with “IN” appended are measurements made under the marinite board.

Table 11.2: Locations of ceiling surface temperature measurements relative to the fire pan in the WTC series.

Name	x (m)	y (m)	z (m)
TCC	0.62	0.07	3.82
TCN3	0.62	0.67	3.82
TCS3	0.62	-0.53	3.82
TCE7	2.18	0.07	3.82
TCW7	-1.15	0.07	3.82
TCCIN	0.62	0.07	3.83
TCN3IN	0.62	0.67	3.83
TCS3IN	0.62	-0.53	3.83
TCE4IN	1.28	0.07	3.83
TCW4IN	0.05	0.07	3.83

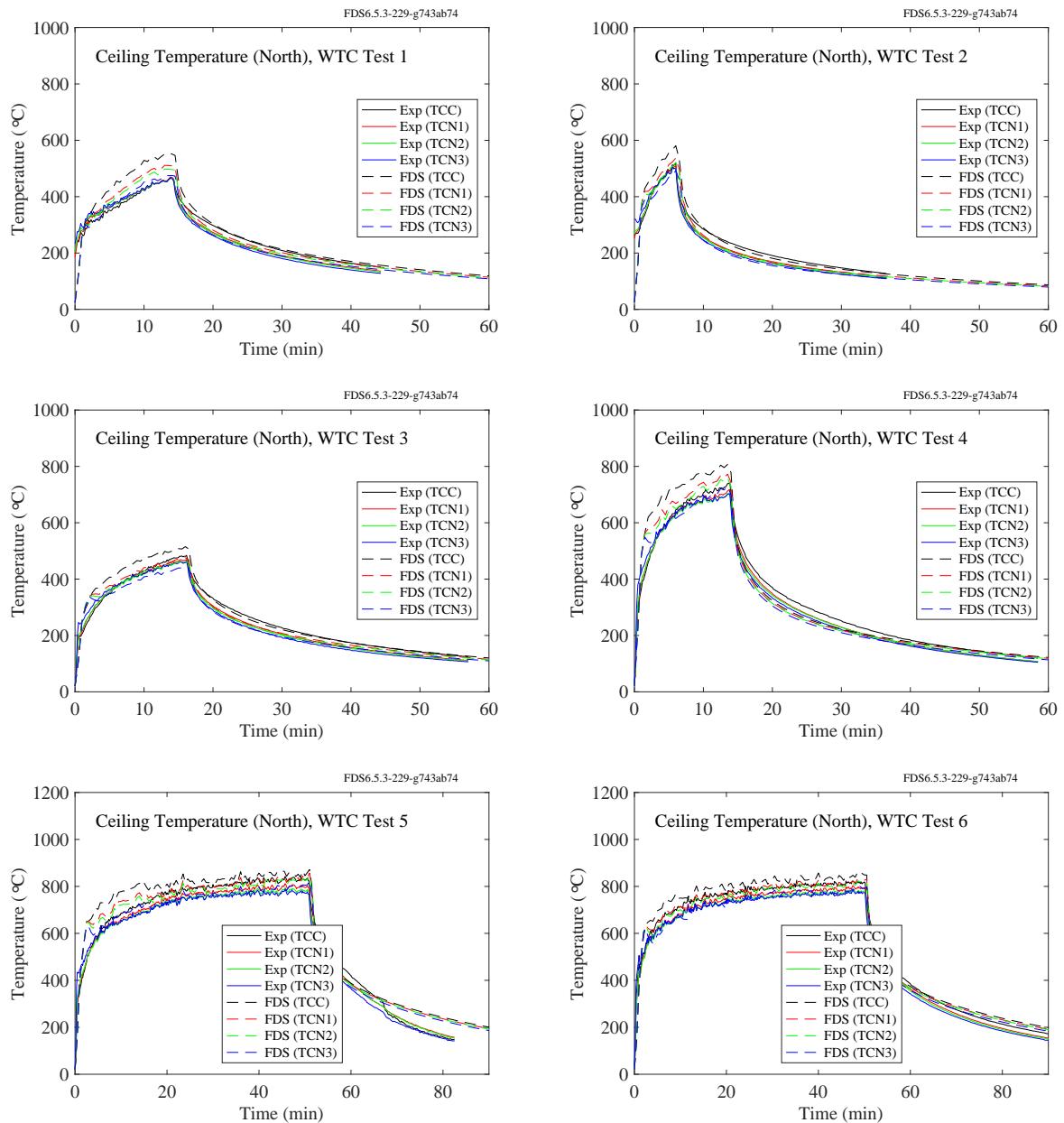


Figure 11.27: WTC experiments, ceiling temperatures, north array.

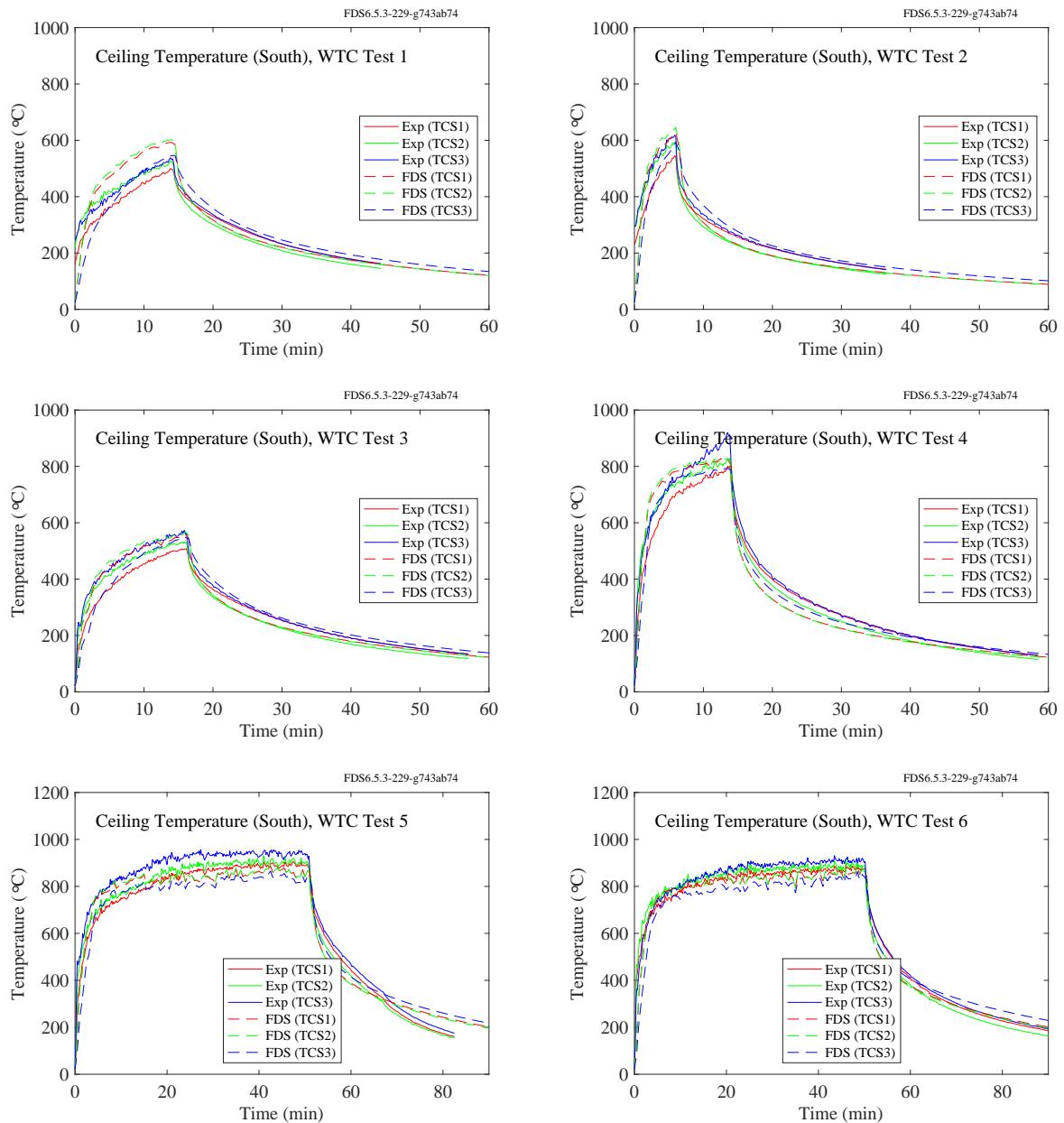


Figure 11.28: WTC experiments, ceiling temperatures, south array.

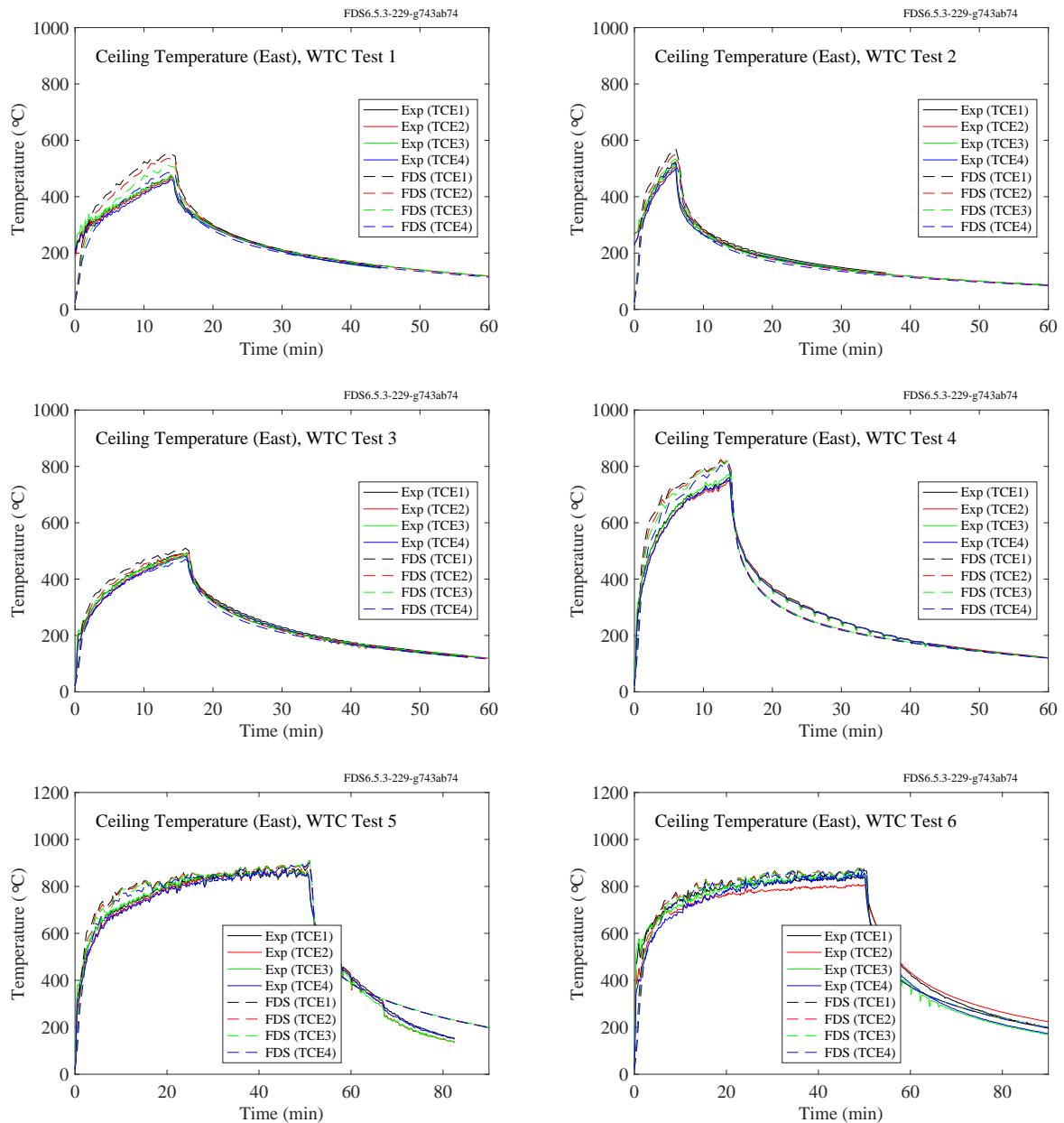


Figure 11.29: WTC experiments, ceiling temperatures, east array, Points 1-4.

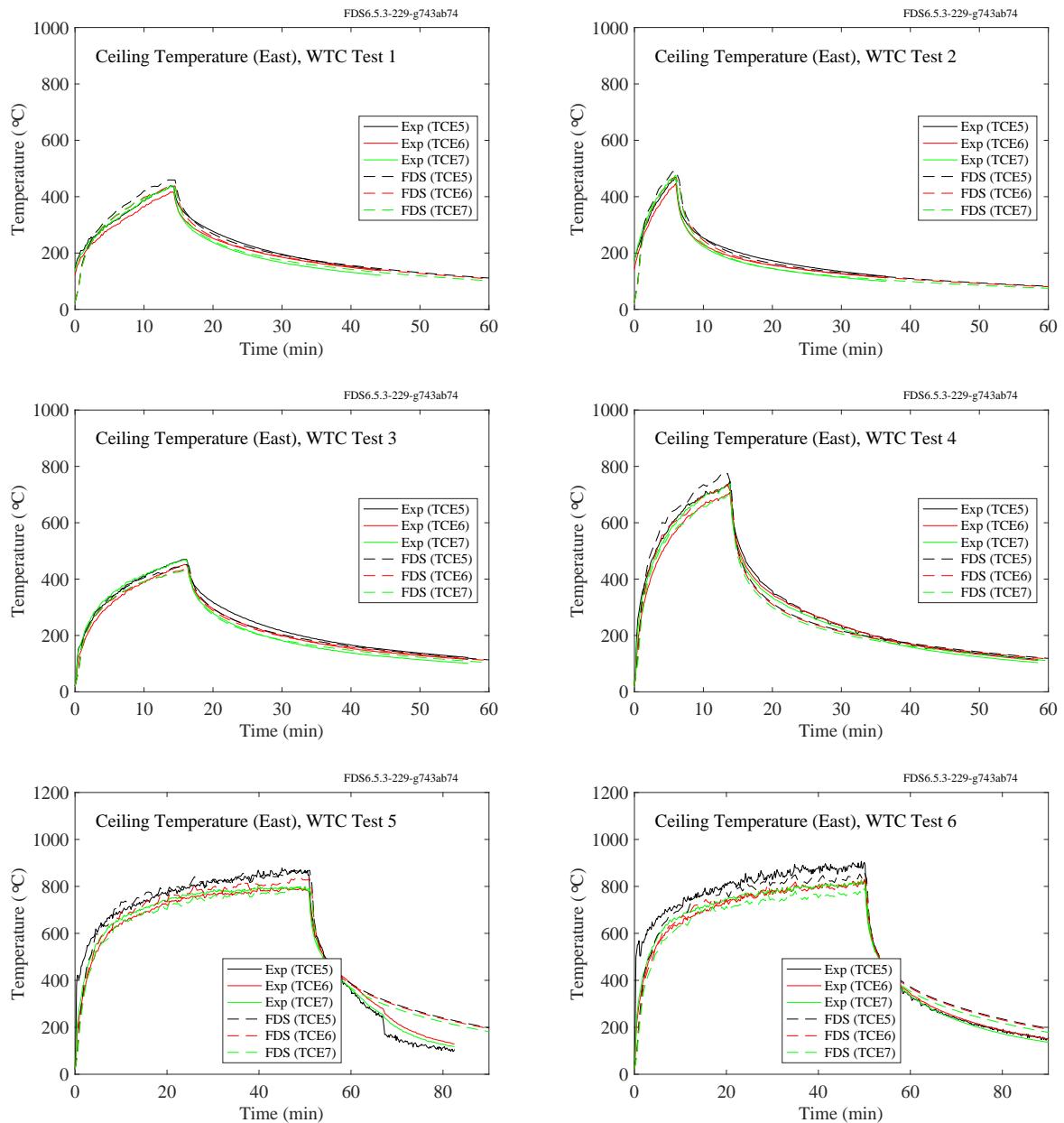


Figure 11.30: WTC experiments, ceiling temperatures, east array, Points 5-7.

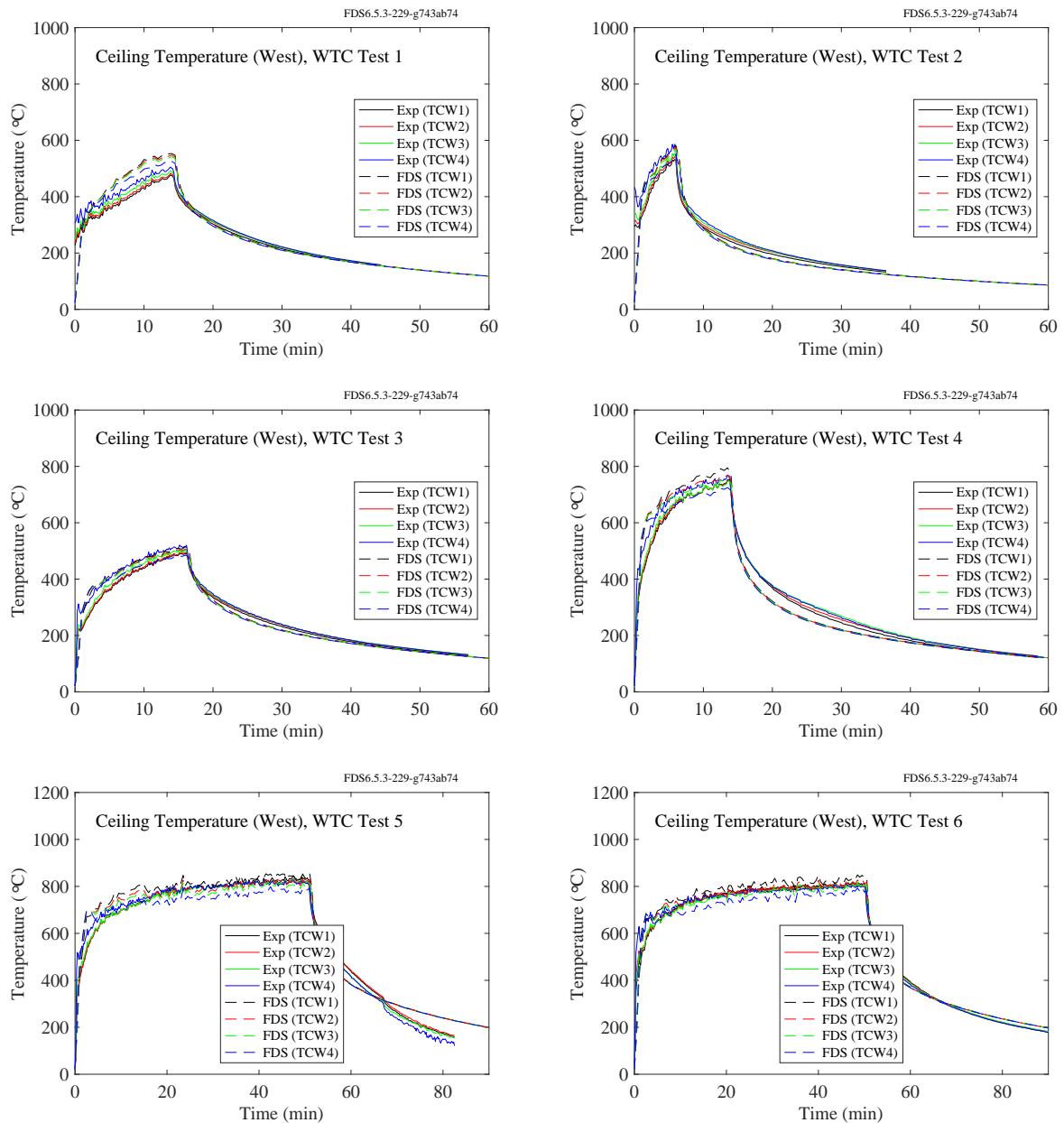


Figure 11.31: WTC experiments, ceiling temperatures, west array, Points 1-4.

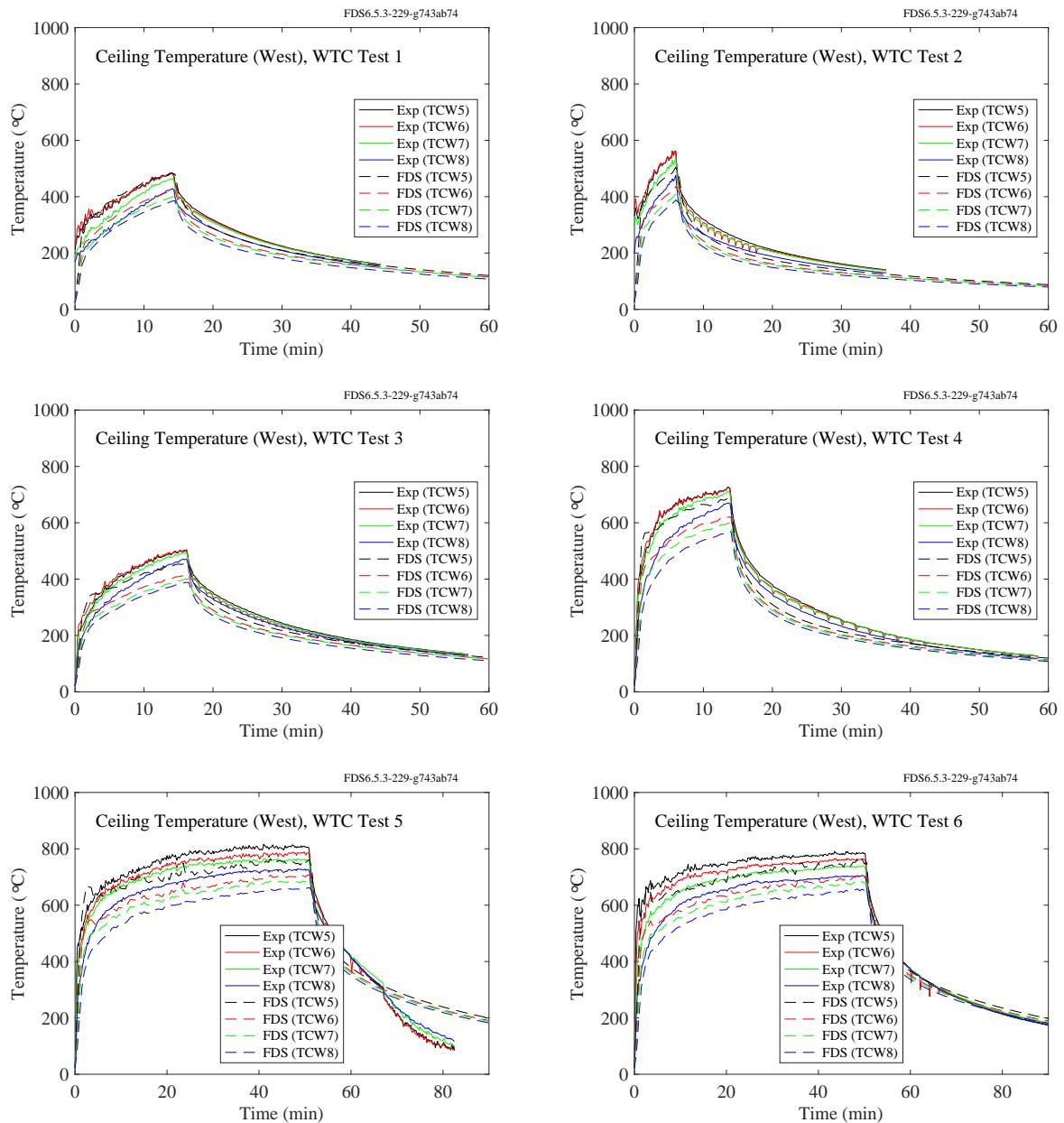


Figure 11.32: WTC experiments, ceiling temperatures, west array, Points 5-8.

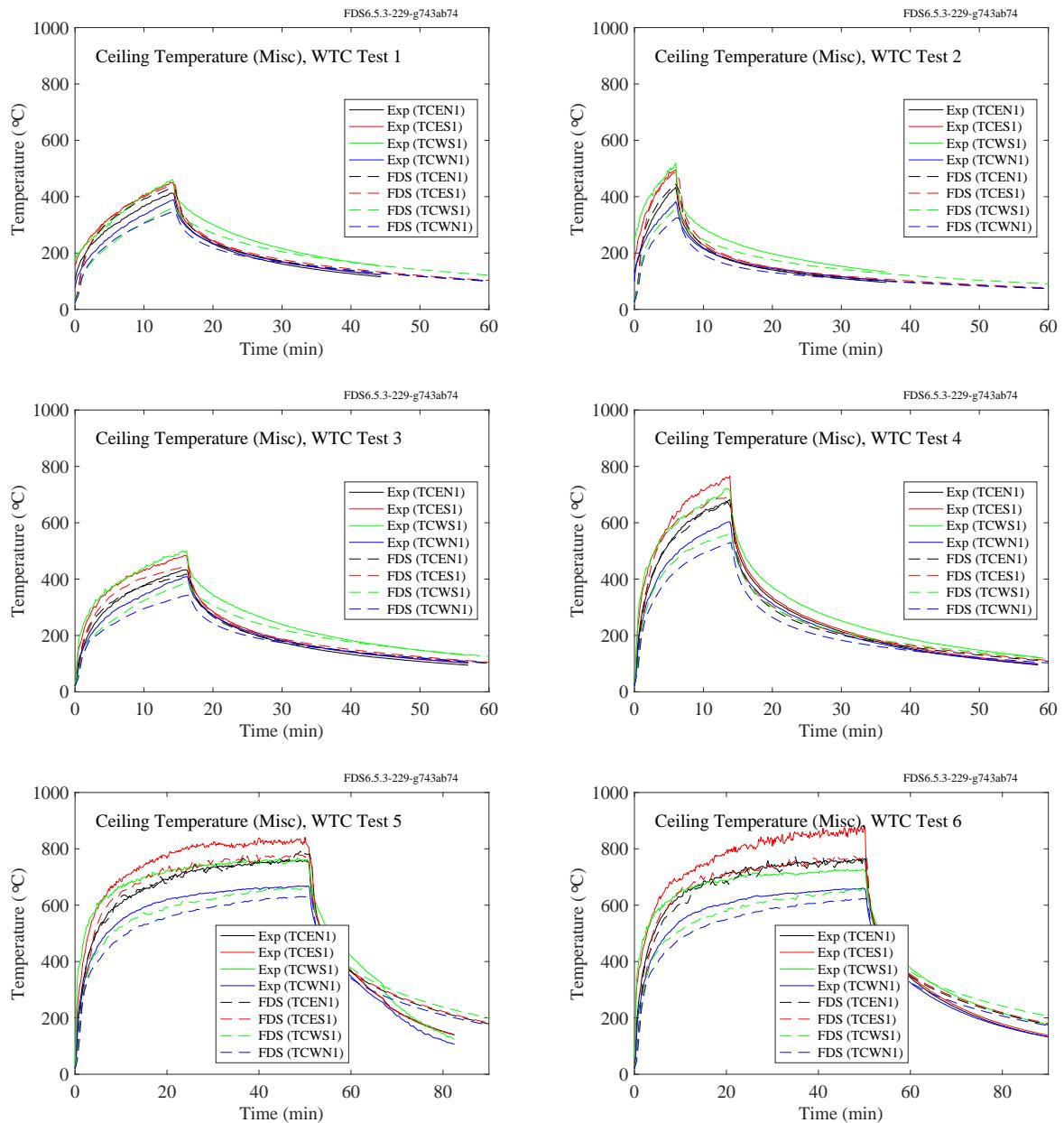


Figure 11.33: WTC experiments, ceiling temperatures, diagonal array.

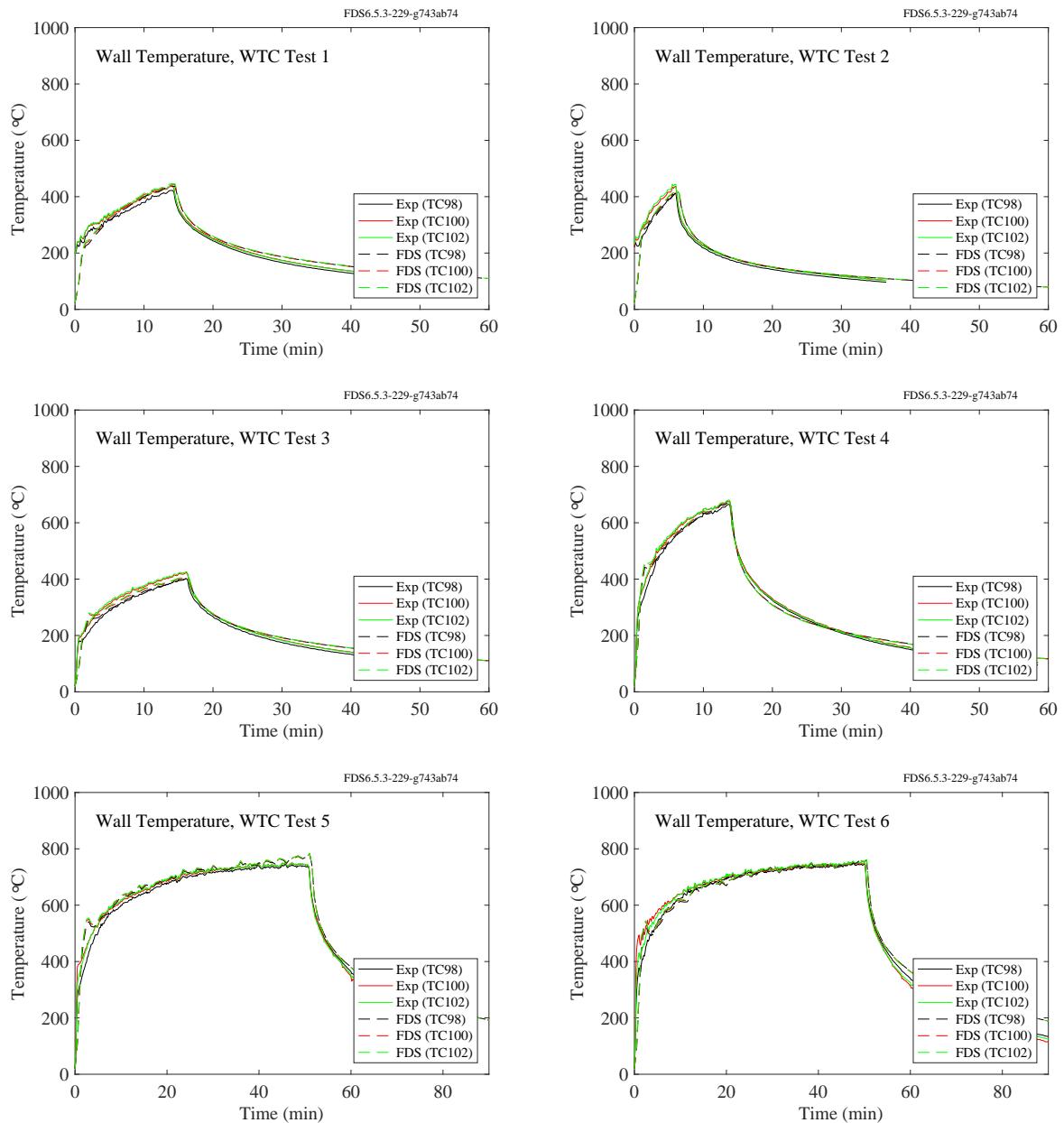


Figure 11.34: WTC experiments, wall temperatures, Points 98, 100, 102.

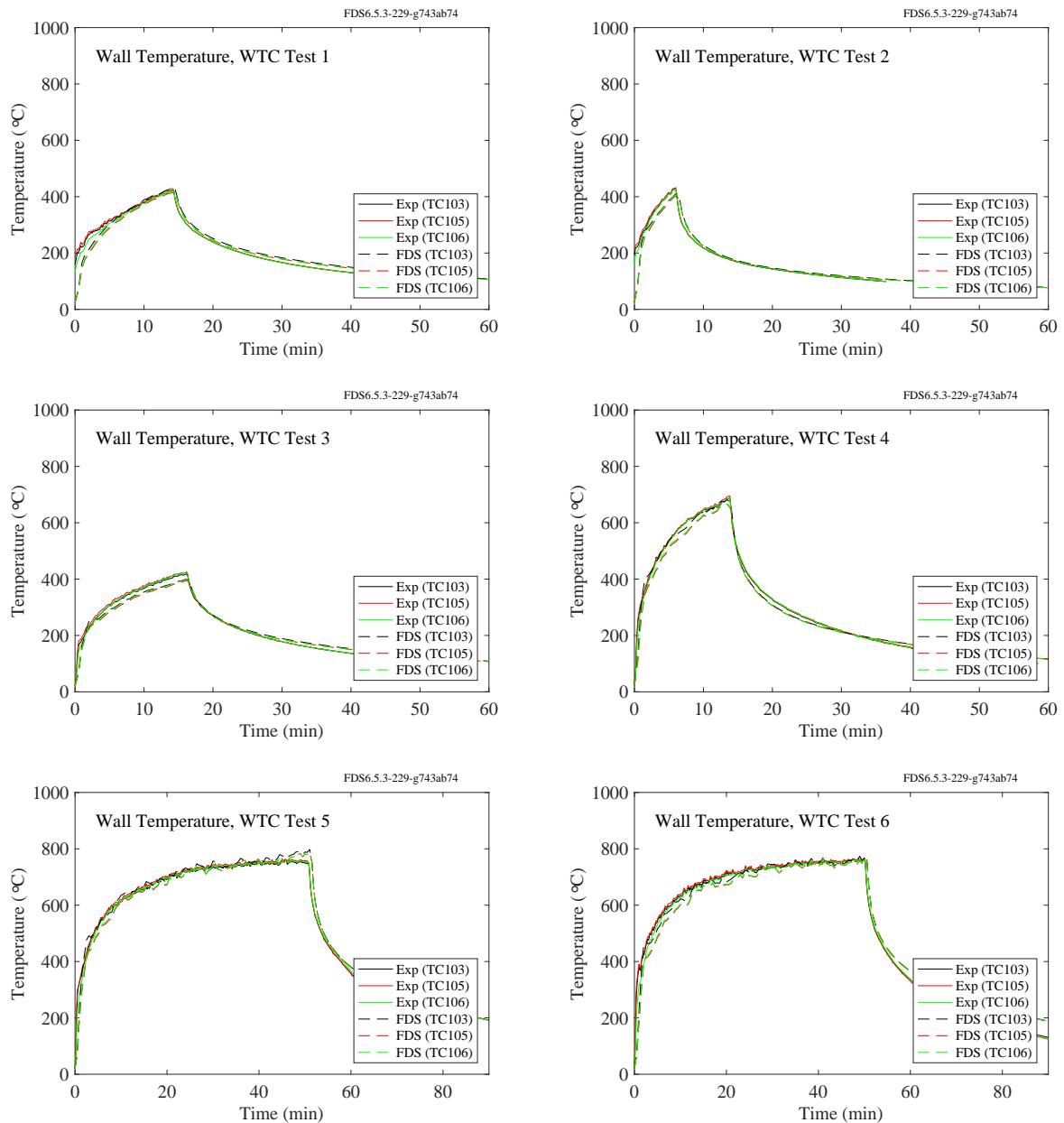


Figure 11.35: WTC experiments, wall temperatures, Points 103, 105, 106.

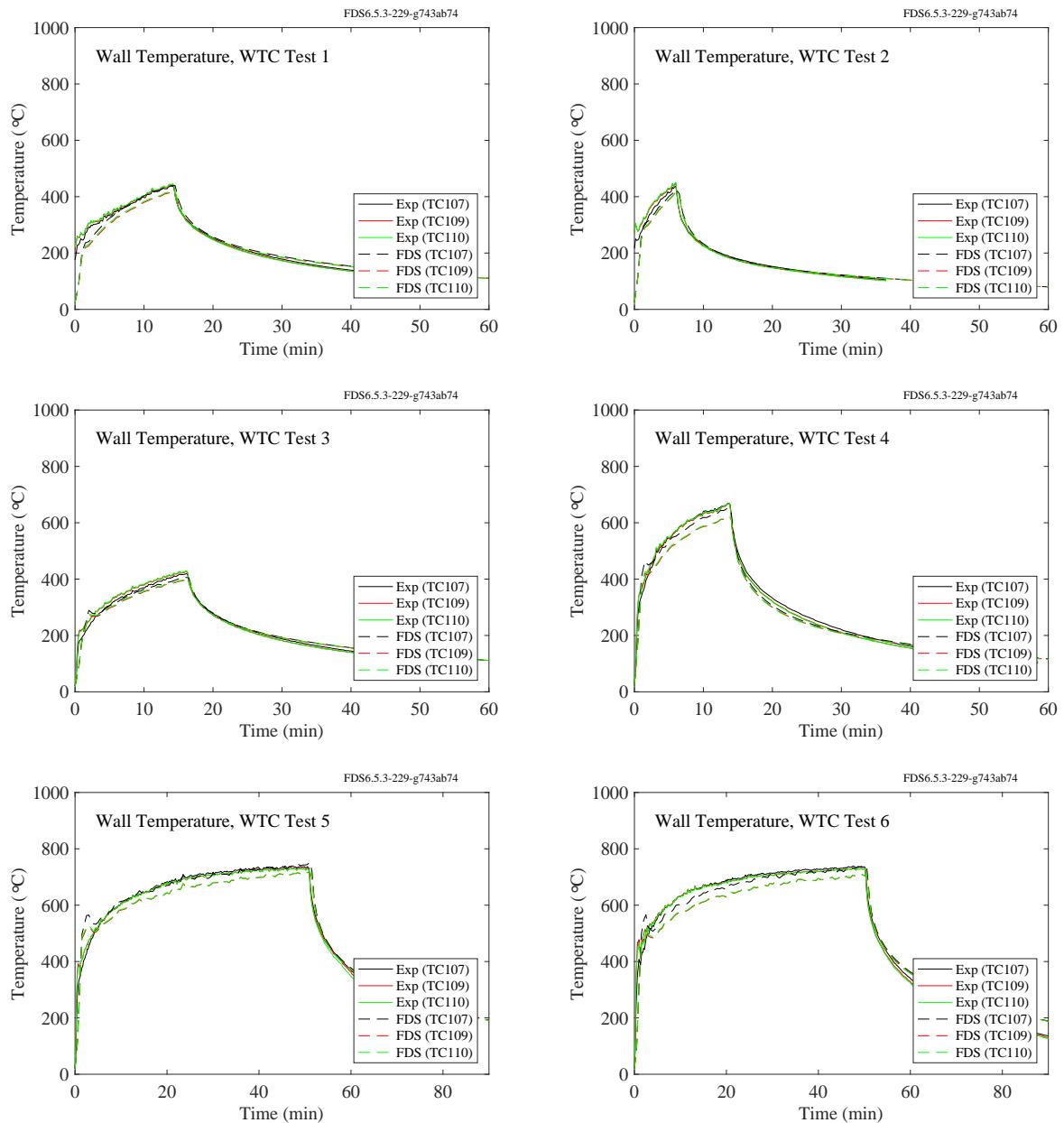


Figure 11.36: WTC experiments, wall temperatures, Points 107, 109, 110.

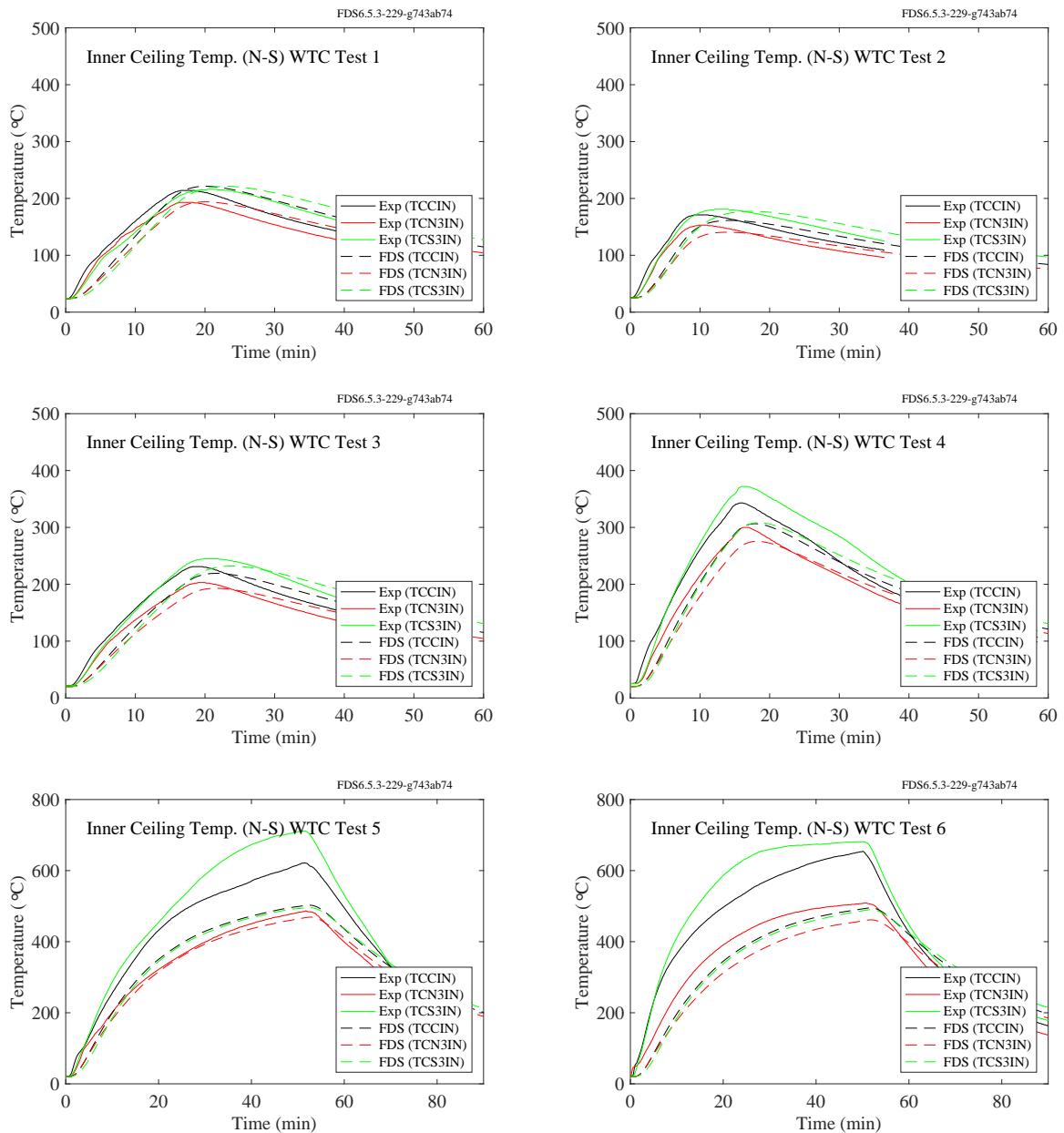


Figure 11.37: WTC experiments, inner ceiling temperatures, north-south axis.

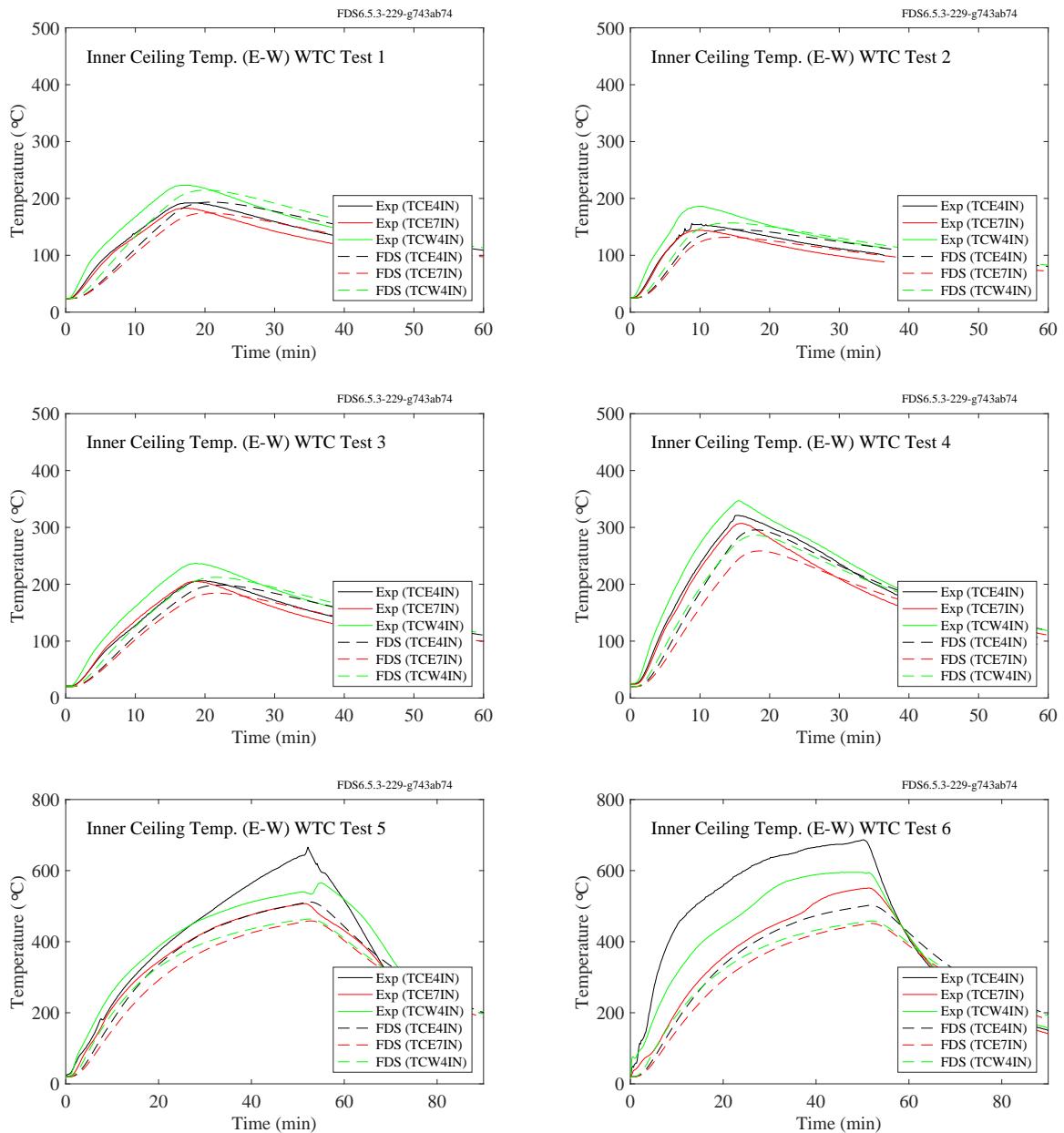


Figure 11.38: WTC experiments, inner ceiling temperatures, east-west axis.

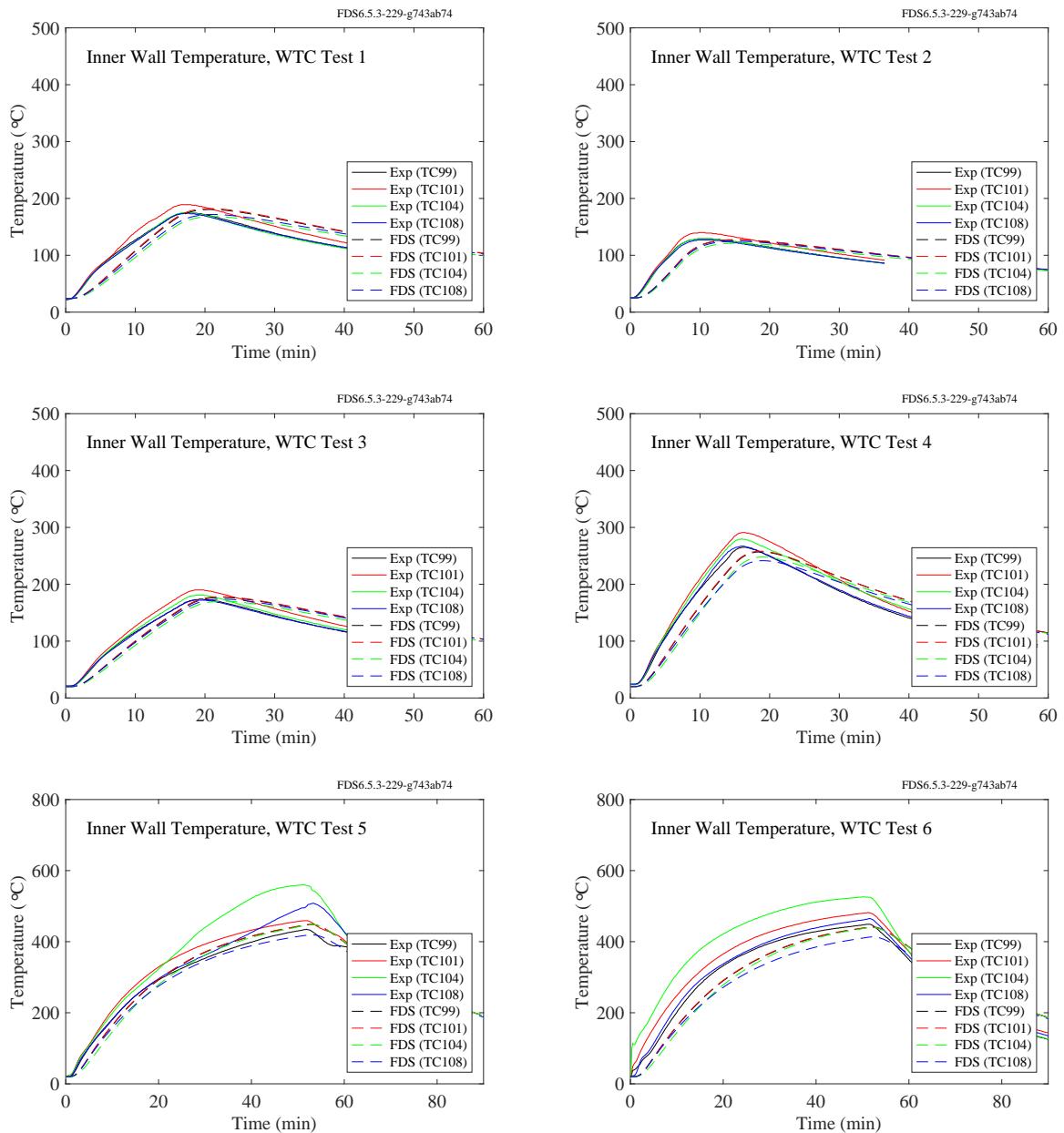


Figure 11.39: WTC experiments, inner wall temperatures.

### 11.1.7 Summary of Wall, Ceiling, and Floor Temperature Predictions

Figure 11.40 summarizes the temperature predictions for walls, ceilings, and floors.

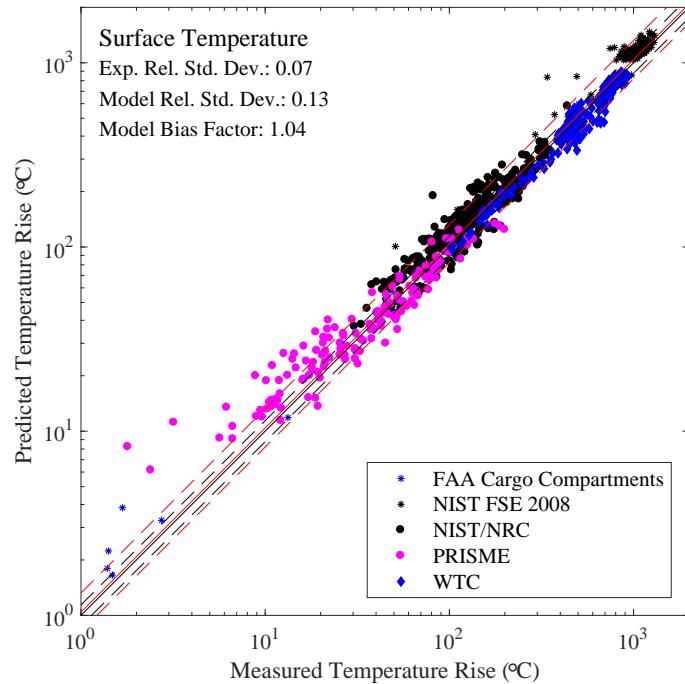


Figure 11.40: Summary of compartment surface temperature predictions.

## **11.2 Target Temperature**

A “target” refers to any object that is not a wall, ceiling, or floor. In the sections to follow, the targets consist of structural steel members, electrical cables, and various other objects.

### **11.2.1 NIST/NRC Experiments**

Electrical cables of various types (power and control), and configurations (horizontal or vertical; in tray or free-hanging), were installed in the test compartment. For each of the four cable targets considered, measurements of the local gas temperature, surface temperature, radiative heat flux, and total heat flux are available. The following pages display comparisons of surface temperature for Control Cable B, Horizontal Cable Tray D, Power Cable F, and Vertical Cable Tray G. For the bundled cables within horizontal and vertical trays (Targets D and G), FDS assumes them to be rectangular slabs of thickness comparable to the diameter of the individual cables. For the free-hanging cables B and F, FDS assumes them to be cylinders of uniform composition.

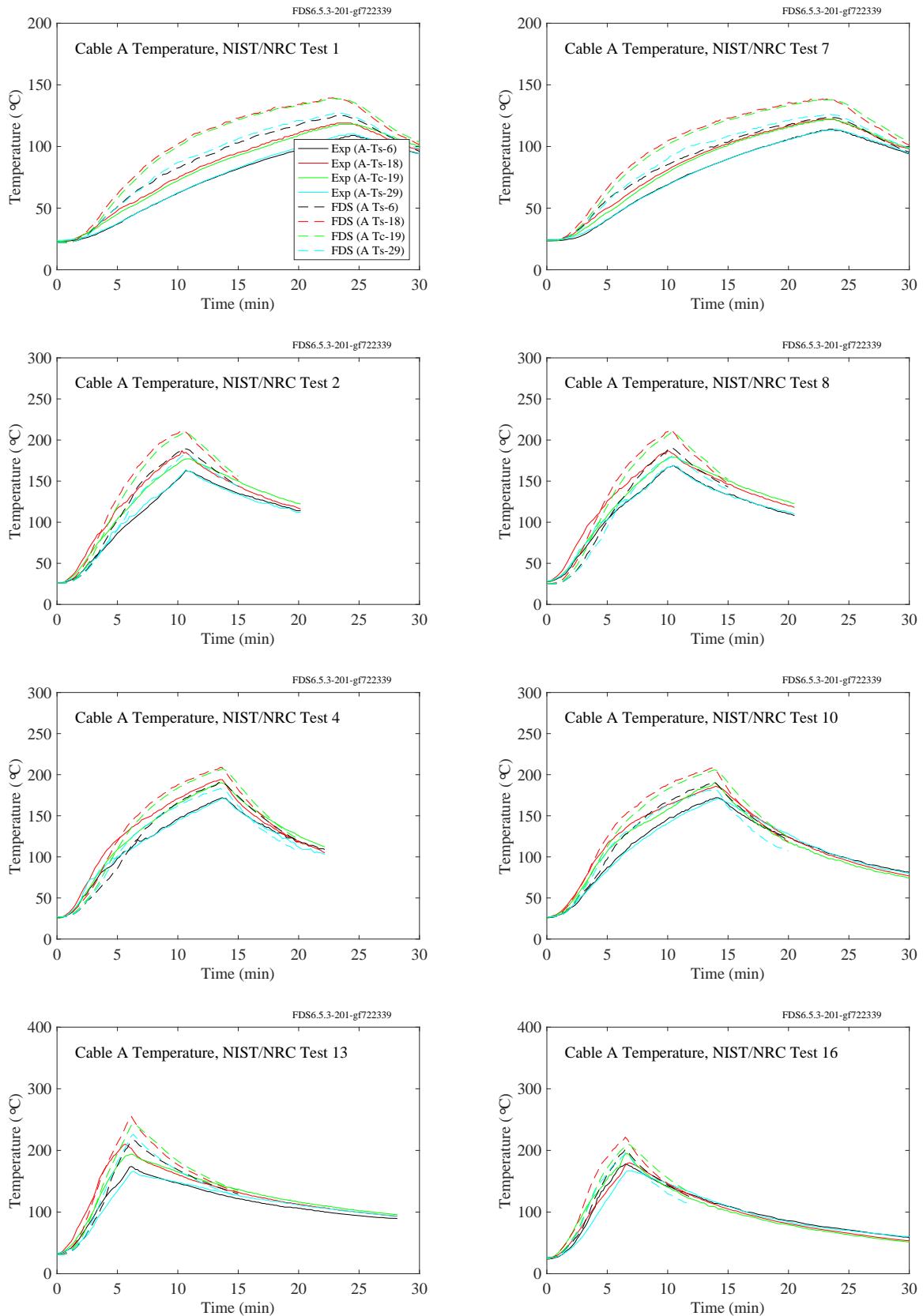


Figure 11.41: NIST/NRC experiments, Cable A temperatures, Tests 1, 2, 4, 7, 8, 10, 13, 16.

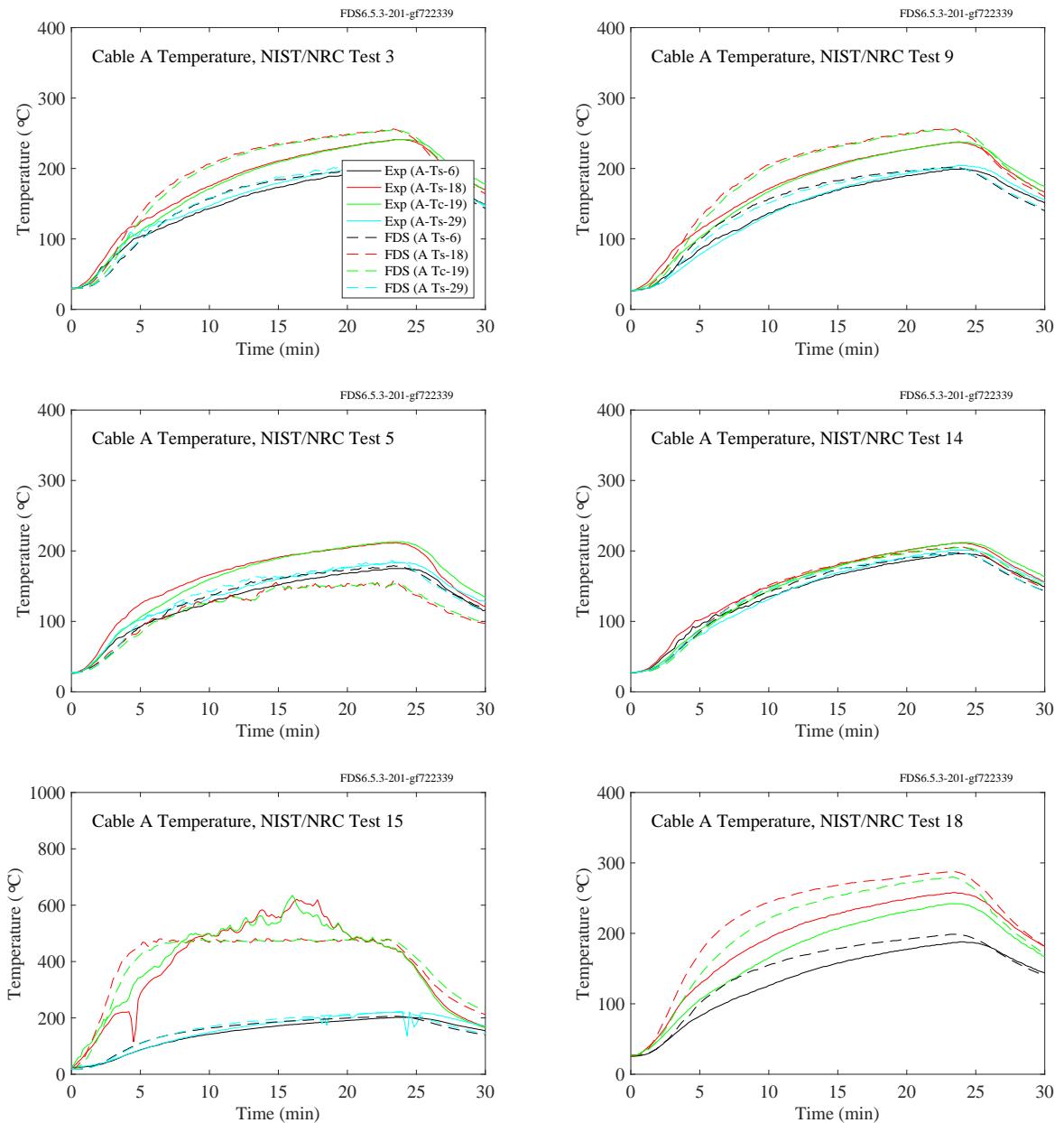


Figure 11.42: NIST/NRC experiments, Cable A temperatures, Tests 3, 5, 9, 14, 15, 18.

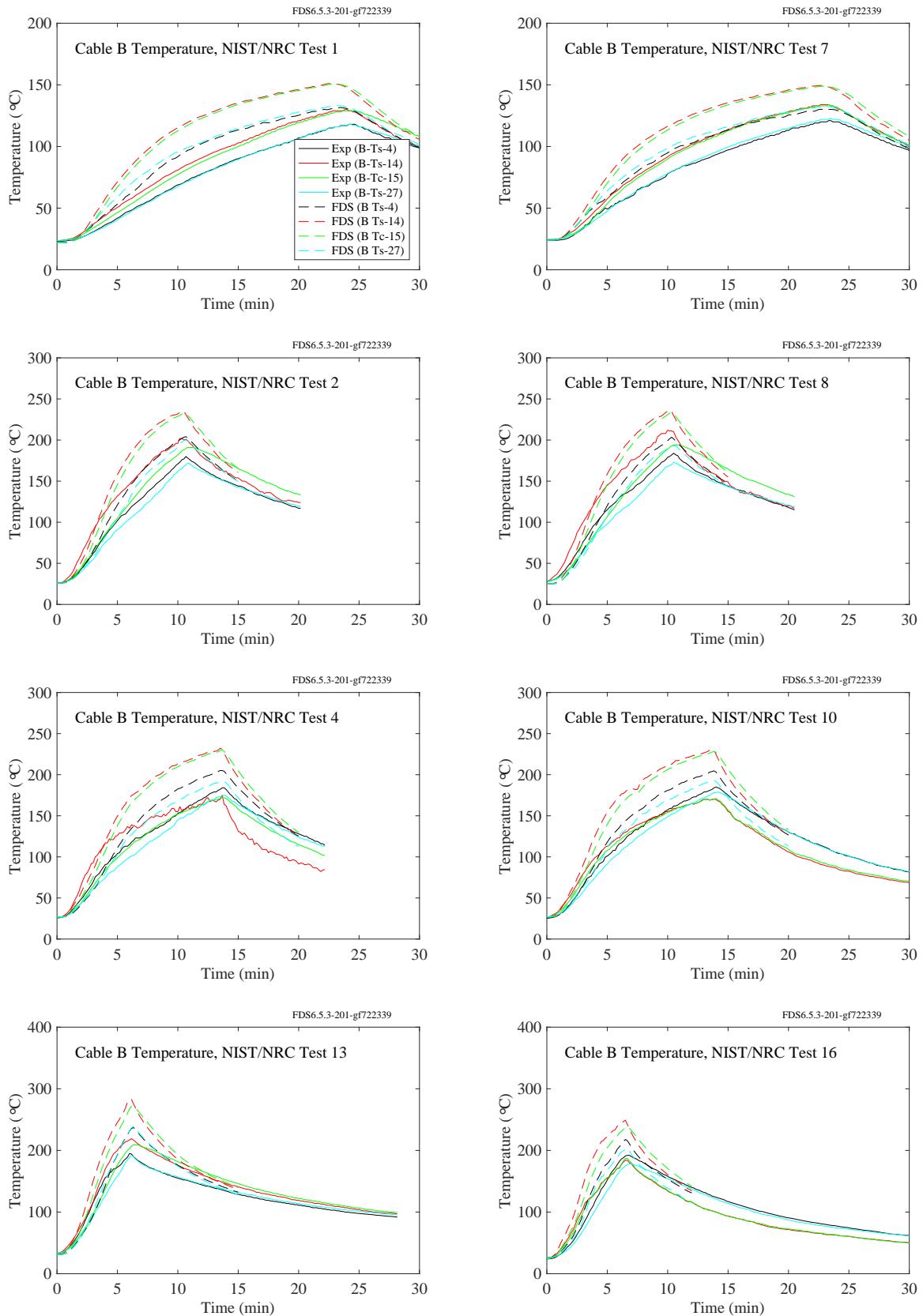


Figure 11.43: NIST/NRC experiments, Cable B temperatures, Tests 1, 2, 4, 7, 8, 10, 13, 16.

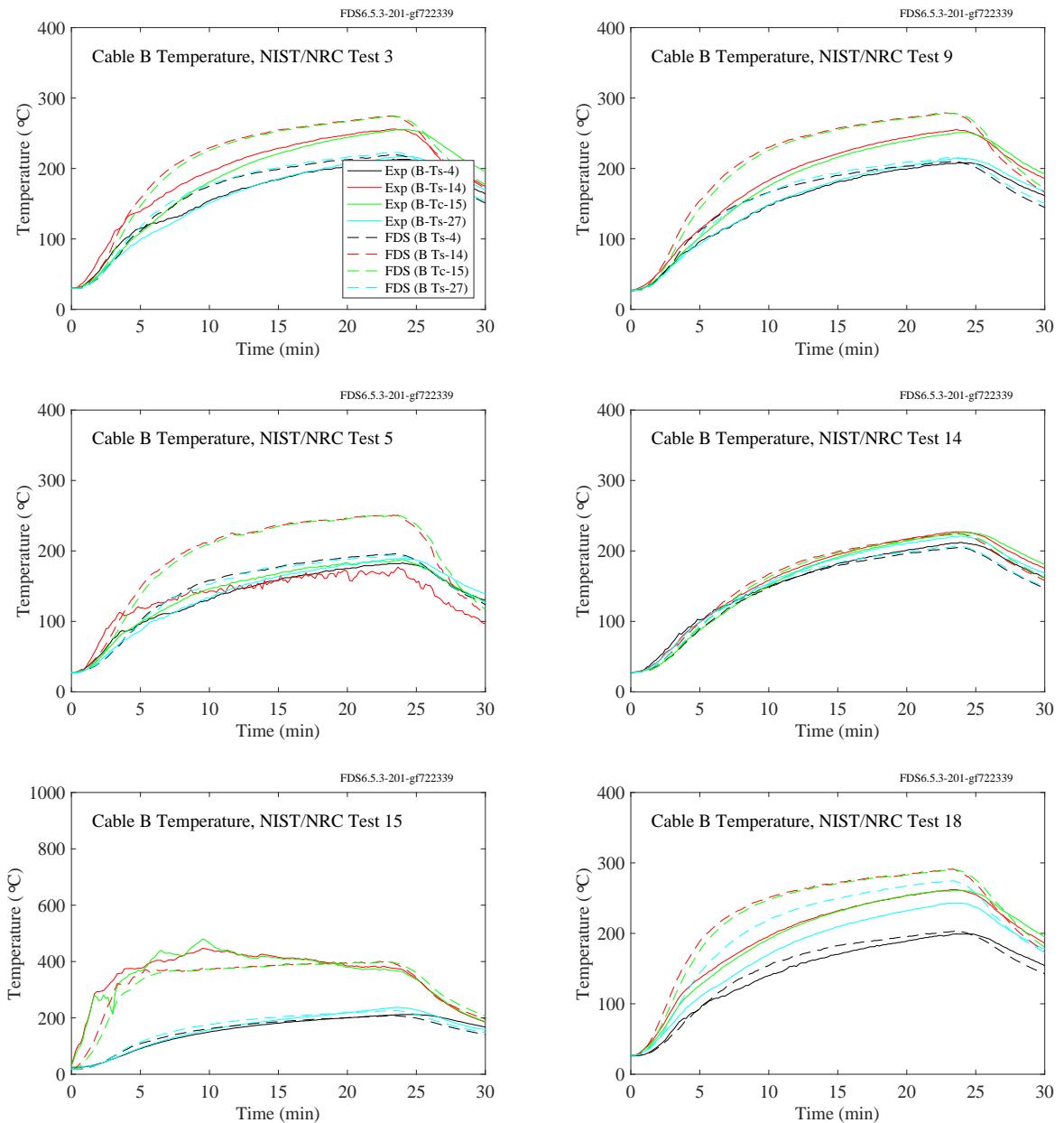


Figure 11.44: NIST/NRC experiments, Cable B temperatures, Tests 3, 5, 9, 14, 15, 18.

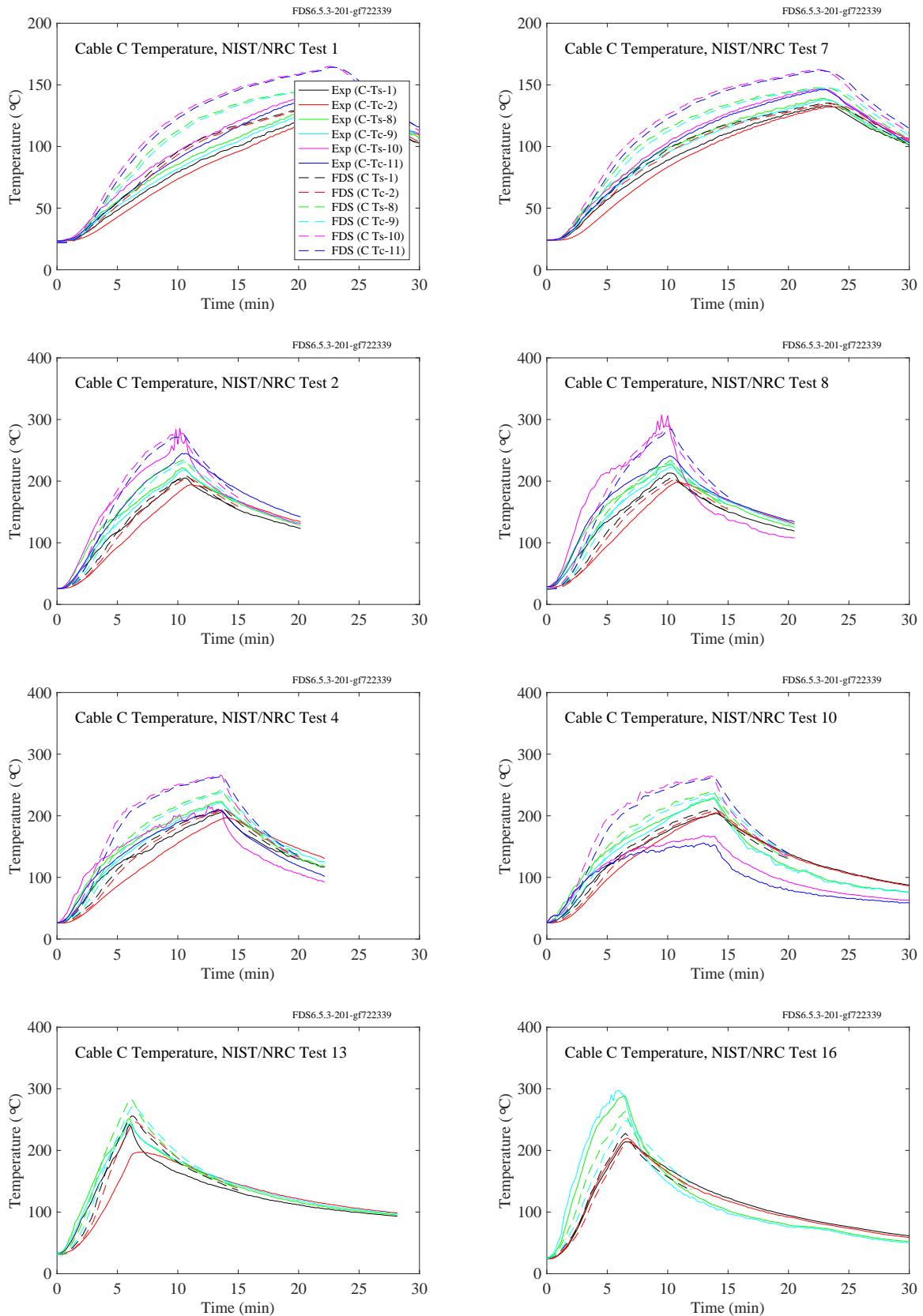


Figure 11.45: NIST/NRC experiments, Cable Ca temperatures, Tests 1, 2, 4, 7, 8, 10, 13, 16.

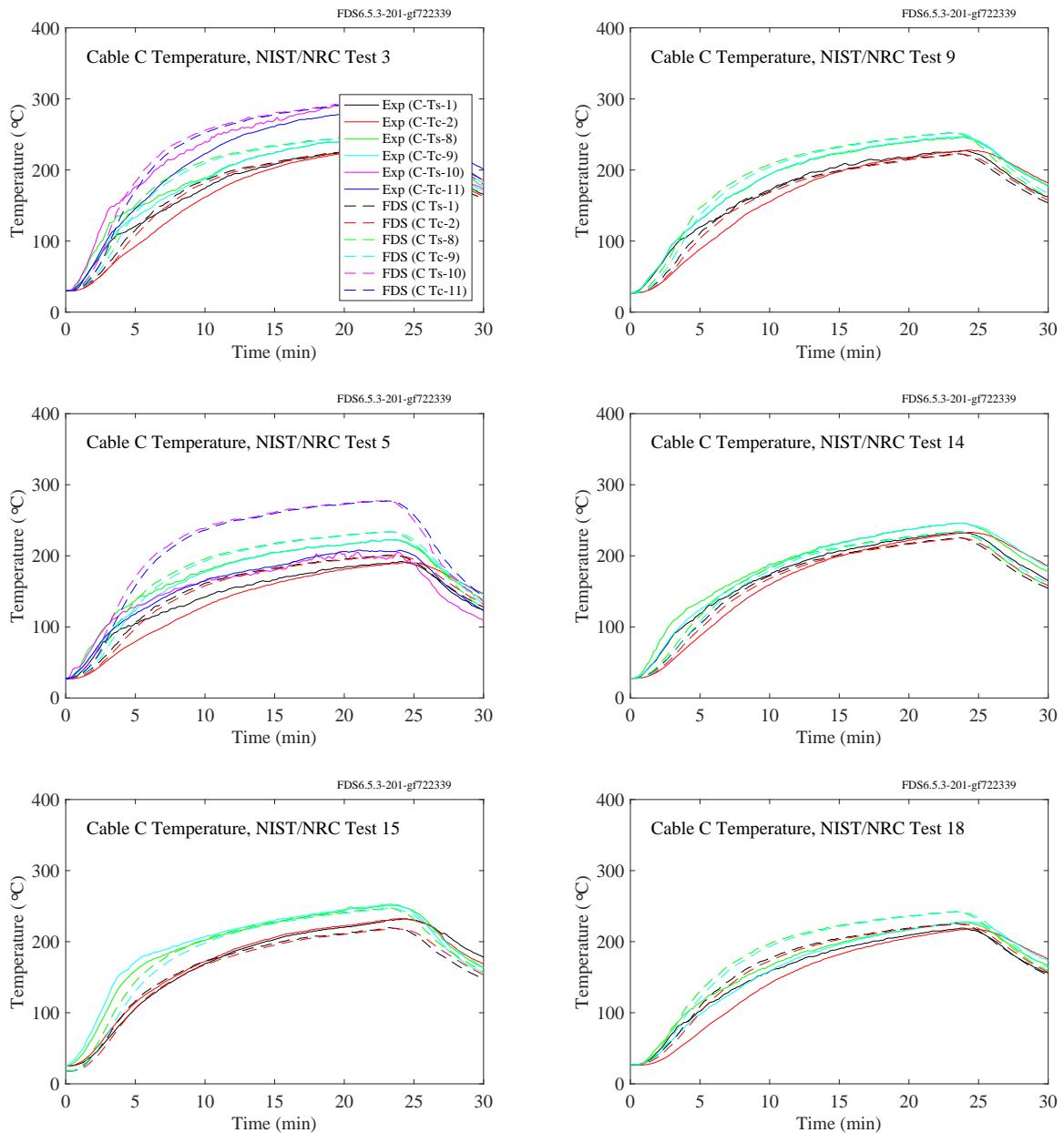


Figure 11.46: NIST/NRC experiments, Cable Ca temperatures, Tests 3, 5, 9, 14, 15, 18.

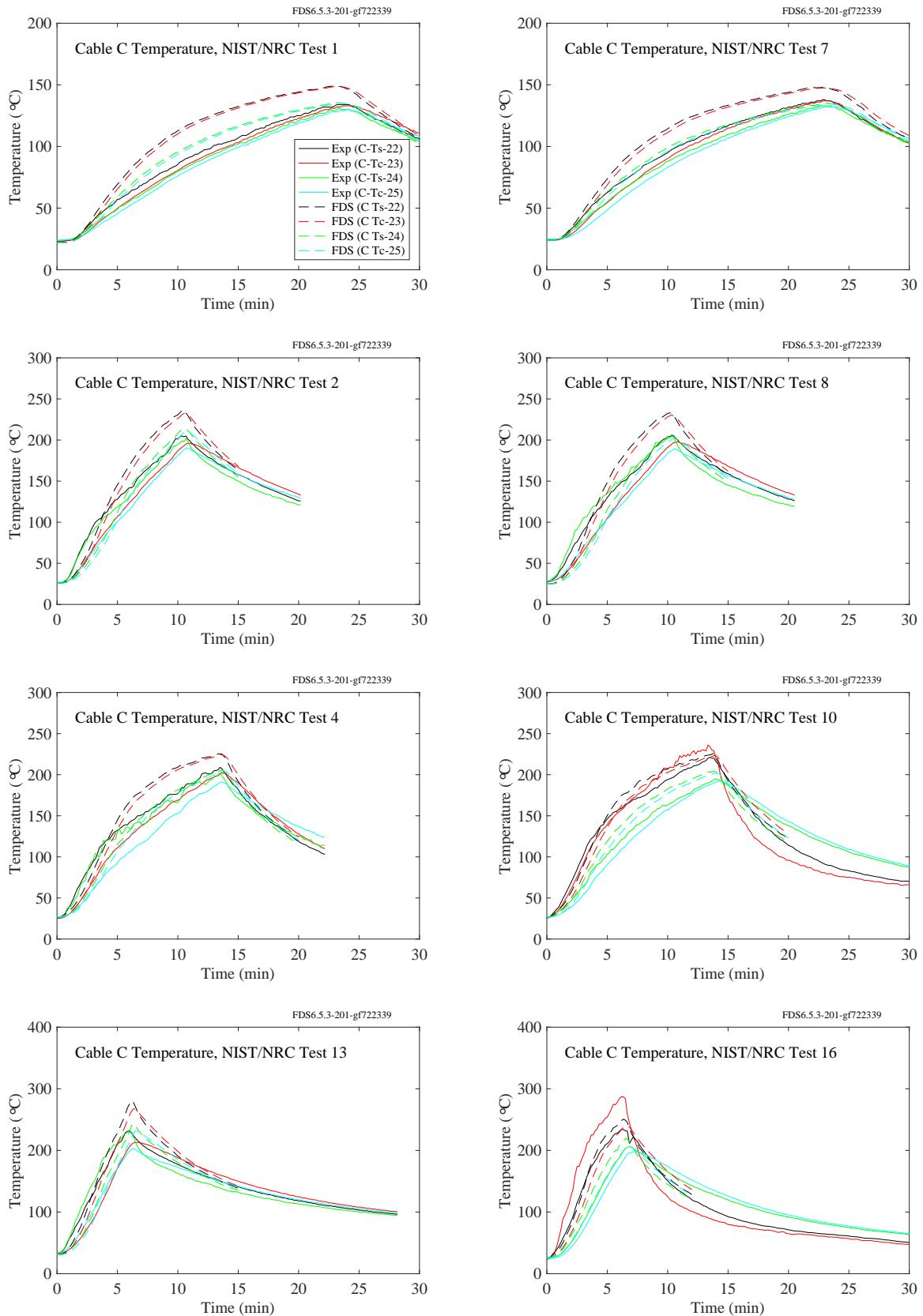


Figure 11.47: NIST/NRC experiments, Cable Cb temperatures, Tests 1, 2, 4, 7, 8, 10, 13, 16.

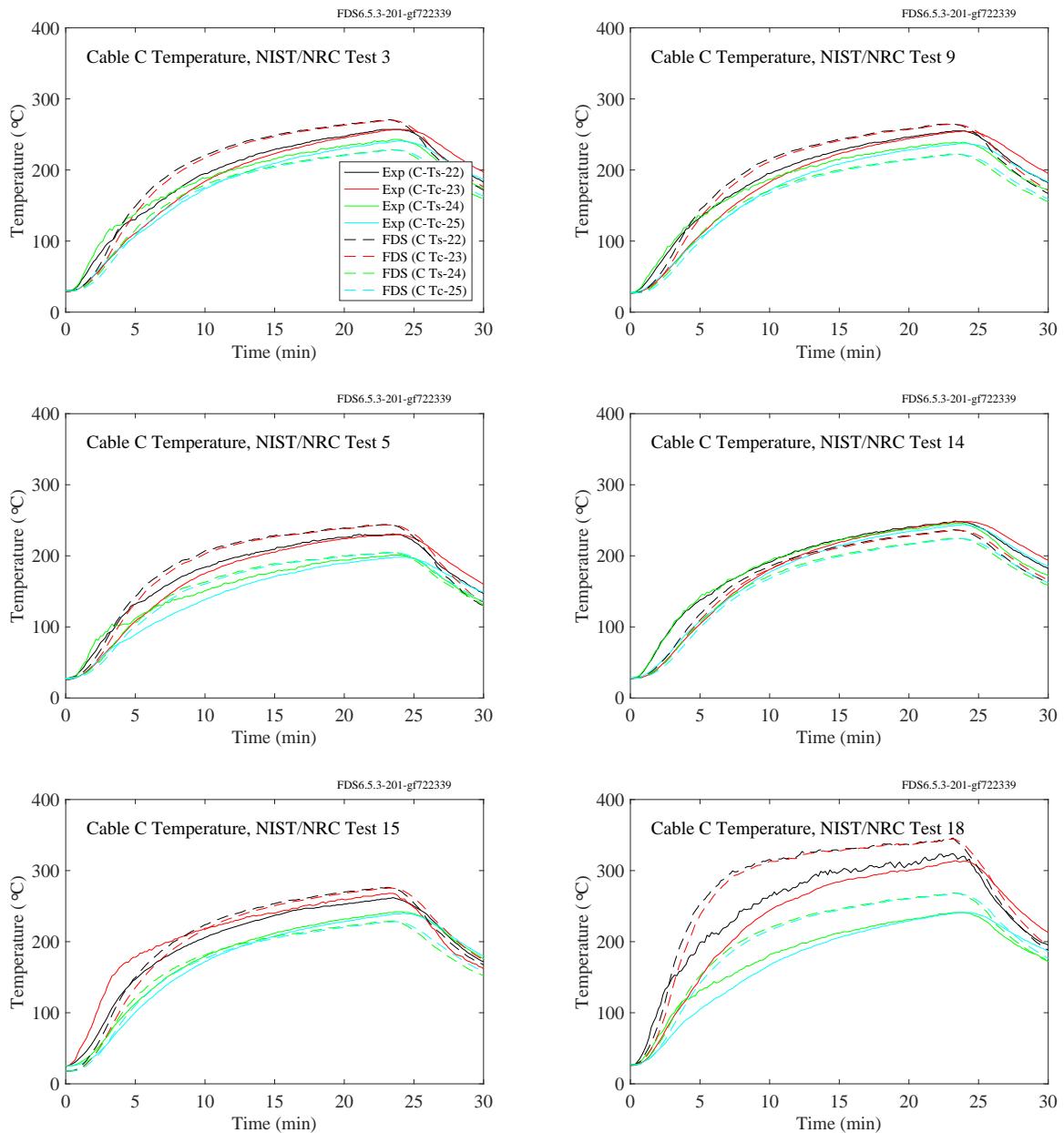


Figure 11.48: NIST/NRC experiments, Cable Cb temperatures, Tests 3, 5, 9, 14, 15, 18.

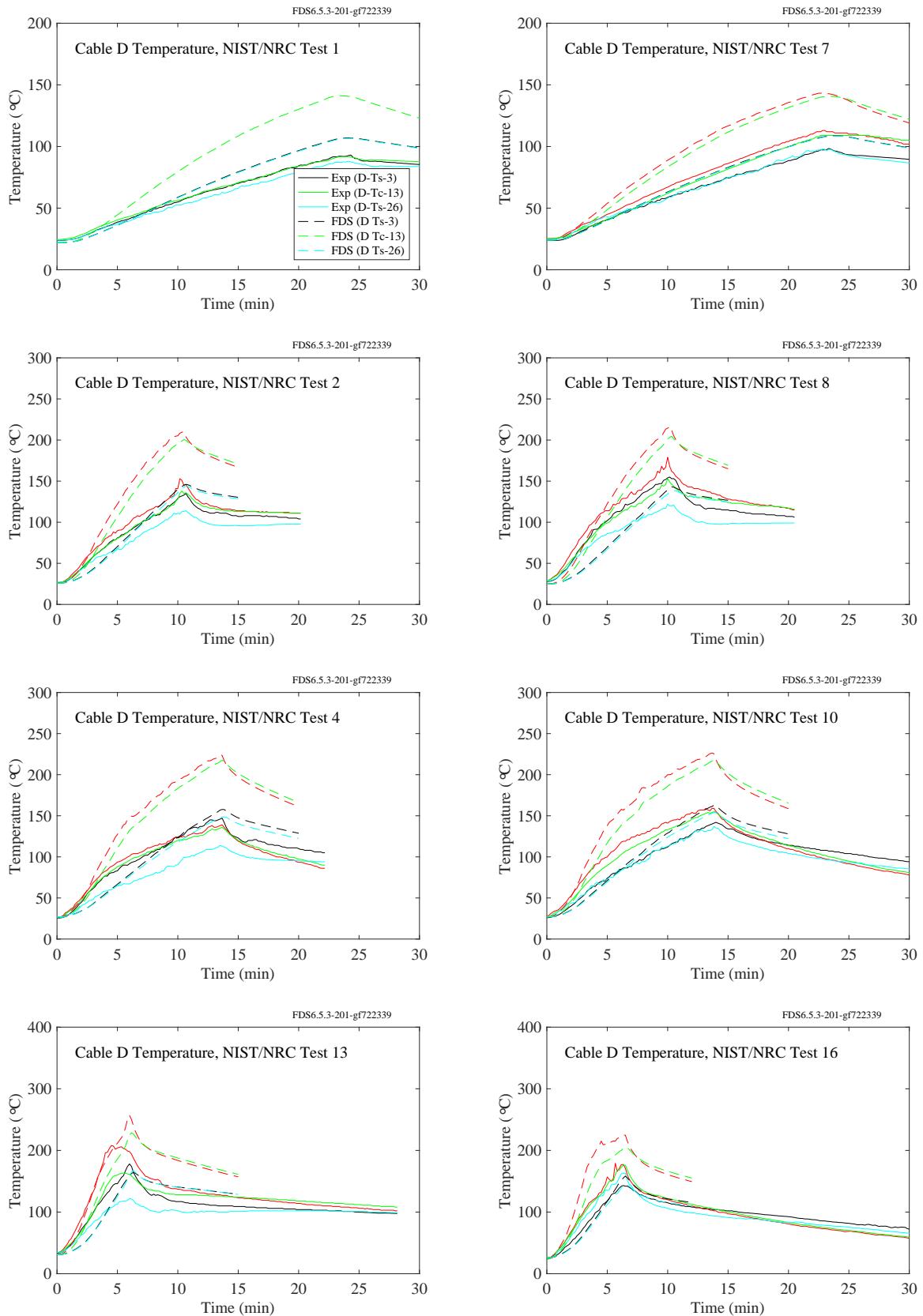


Figure 11.49: NIST/NRC experiments, Cable D temperatures, Tests 1, 2, 4, 7, 8, 10, 13, 16.

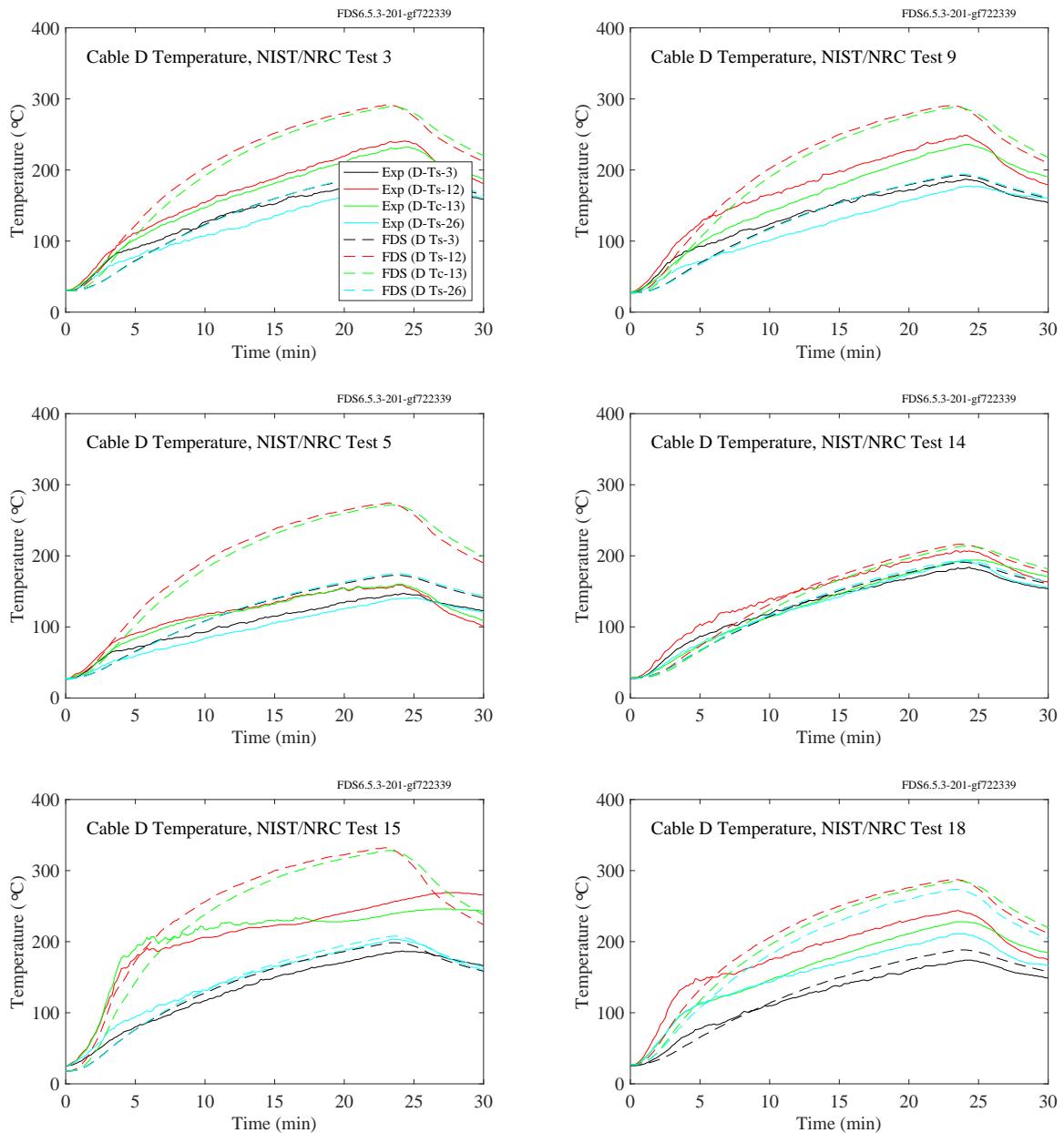


Figure 11.50: NIST/NRC experiments, Cable D temperatures, Tests 3, 5, 9, 14, 15, 18.

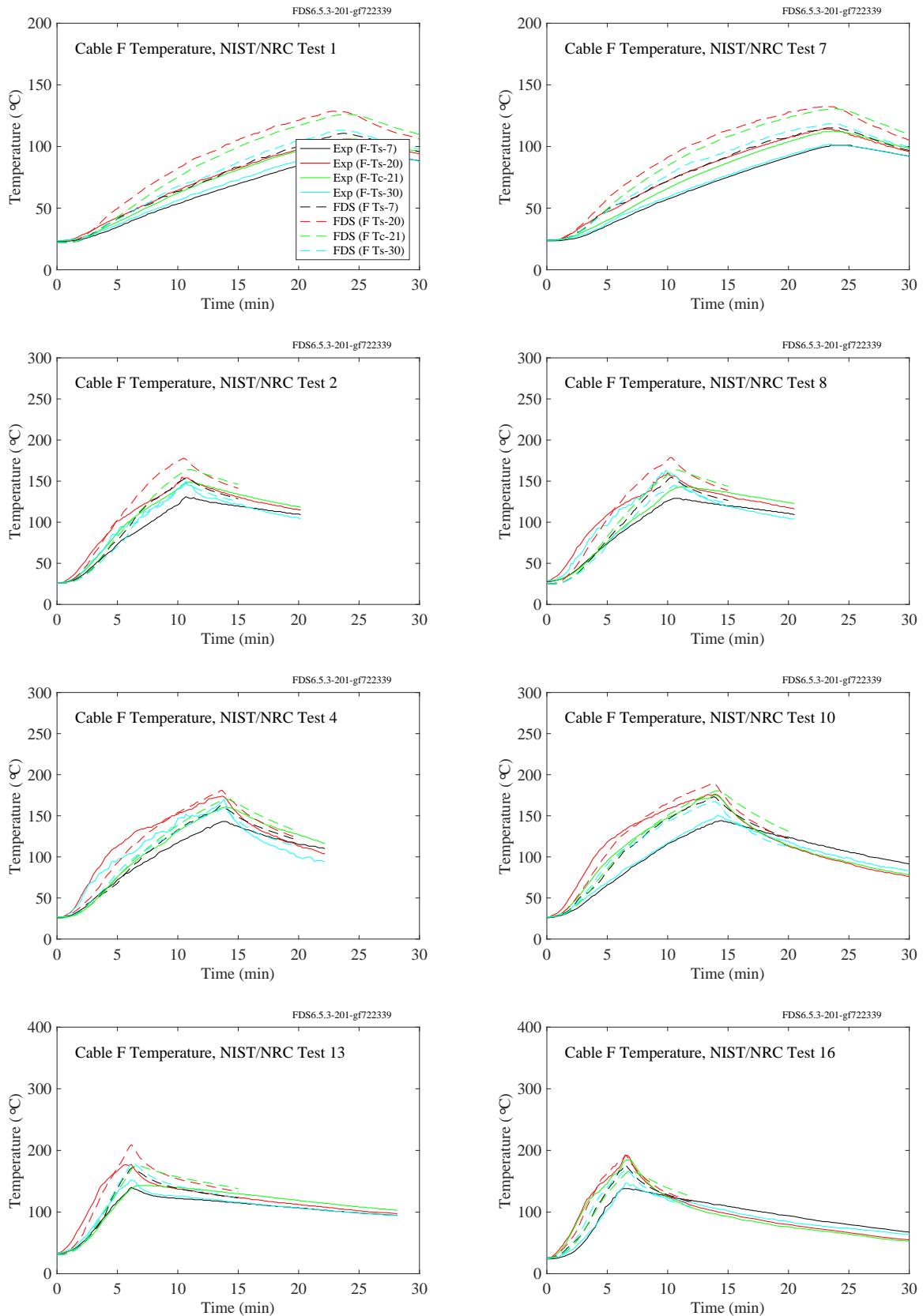


Figure 11.51: NIST/NRC experiments, Cable F temperatures, Tests 1, 2, 4, 7, 8, 10, 13, 16.

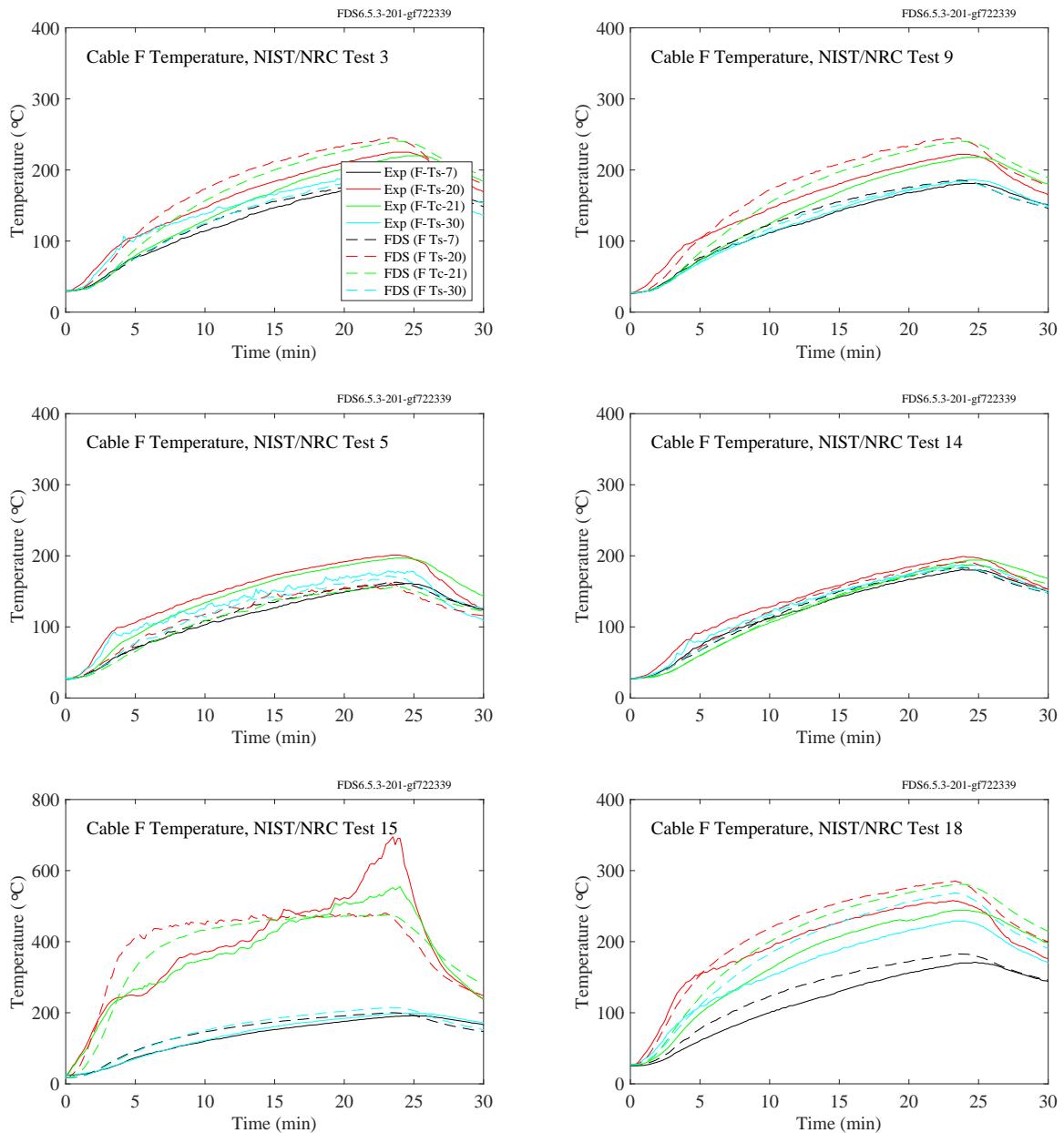


Figure 11.52: NIST/NRC experiments, Cable F temperatures, Tests 3, 5, 9, 14, 15, 18.

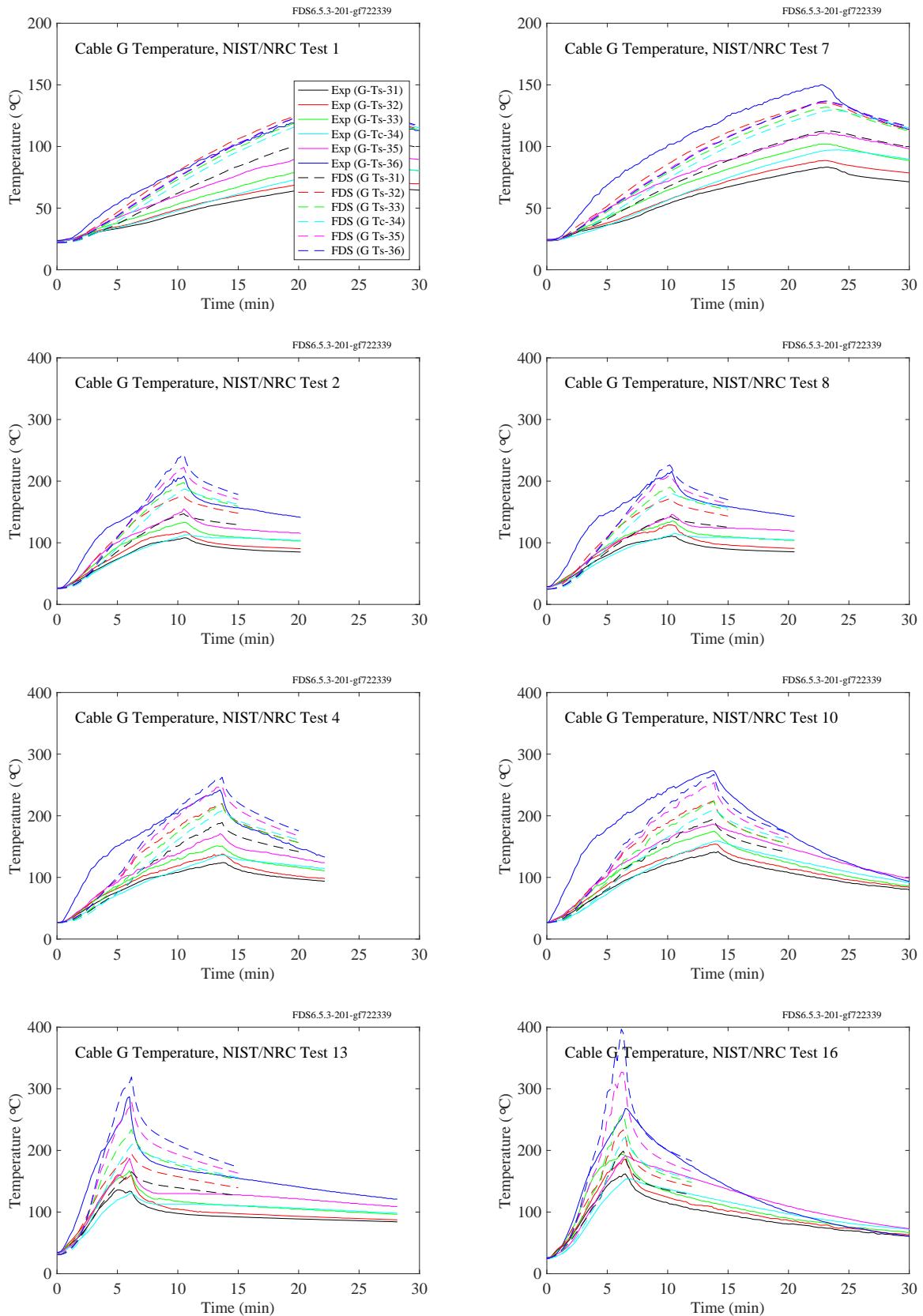


Figure 11.53: NIST/NRC experiments, Cable G temperatures, Tests 1, 2, 4, 7, 8, 10, 13, 16.

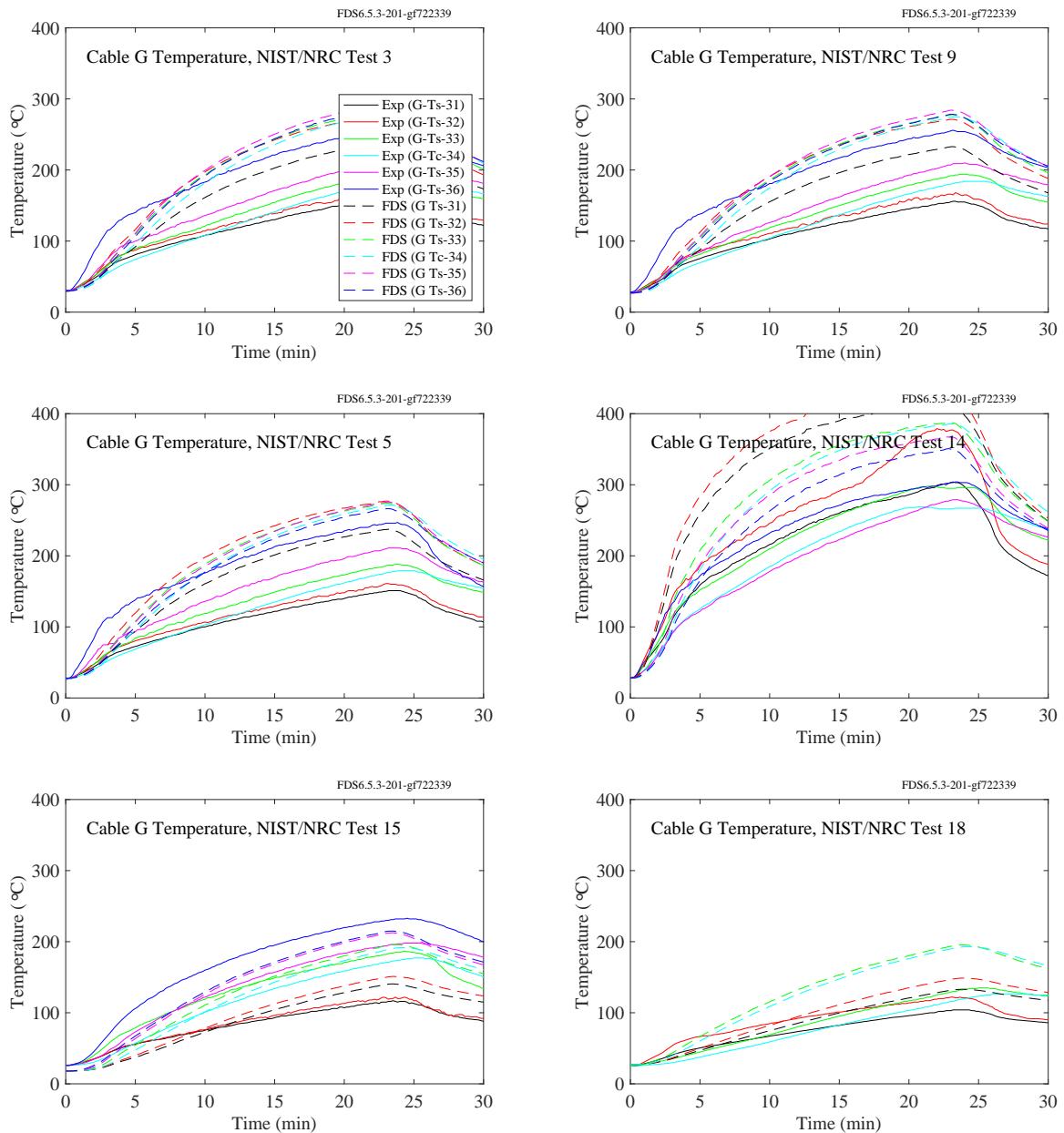


Figure 11.54: NIST/NRC experiments, Cable G temperatures, Tests 3, 5, 9, 14, 15, 18.

## 11.2.2 SP Adiabatic Surface Temperature Experiments

Comparisons of FDS predictions of gas, plate thermometer, and steel temperatures for compartment and pool fire experiments conducted at SP, Sweden, are presented on the following pages.

### Compartment Fire Experiments

Three experiments were conducted in a standard compartment, 3.6 m long by 2.4 m wide by 2.4 m high, with a 0.8 m wide by 2.0 m high door centered on the narrow wall. Each experiment used a constant 450 kW propane burner and a single beam suspended 20 cm below the ceiling along the centerline of the compartment. There were three measurement stations along the beam at lengths of 0.9 m (Position A), 1.8 m (Position B), and 2.7 m (Position C) from the far wall where the fire was either positioned in the corner (Tests 1 and 2), or the center (Test 3). The beam in Test 1 was a rectangular steel tube filled with an insulation material. The beam in Tests 2 and 3 was an I-beam. Details can be found in the test report [198].

Each page to follow contains the results for a single experiment and measuring station. There are nine in all. In addition to predictions plate thermometer and steel temperatures, there are predictions of the adiabatic surface temperature (AST) for the locations and orientations of the plate thermometers. The AST is a useful quantity that serves as a boundary condition for thermal resistance calculations of structures. The basic idea is as follows. The *net* heat flux to the solid surface is given as the sum of radiative and convective components:

$$\dot{q}_r'' + \dot{q}_c'' = \epsilon (\dot{q}_{r,inc}'' - \sigma T_s^4) + h(T_g - T_s) \quad (11.1)$$

where  $\dot{q}_{r,inc}''$  is the incident radiative flux,  $T_s$  the surface temperature,  $T_g$  the gas temperature near the surface, and  $h$  the convective heat transfer coefficient. Following the idea proposed by Wickström [241], the AST is defined as the surface temperature of a perfectly insulated solid. This is equivalent to saying that the net heat flux to this (hypothetical) surface is zero:

$$0 = \epsilon (\dot{q}_{r,inc}'' - \sigma T_{AST}^4) + h(T_g - T_{AST}) \quad (11.2)$$

This definition of the AST forms the theory behind the plate thermometer, a 10 cm by 10 cm thin metal plate with an insulated backing that is designed to measure the AST, albeit with a slight time lag due to the fact that it is not a perfect insulator.

FDS calculates the AST by solving the following equation implicitly for  $T_{AST}$ :

$$\dot{q}_r'' + \dot{q}_c'' = \epsilon (\sigma T_{AST}^4 - \sigma T_s^4) + h(T_{AST} - T_s) \quad (11.3)$$

Equation (11.3) is simply Eq. (11.1) minus Eq. (11.2). As such, it shows that the AST can be regarded as an *effective* gas temperature for the purpose of providing boundary conditions for a detailed heat conduction calculation within the solid.

FDS calculates the AST using Eq. (11.3) and the plate thermometer temperature via its standard one-dimensional heat conduction calculation for a two layer solid of metal and insulating material. In the experiments, the plate thermometer temperature was obtained from a thermocouple attached to the back side of the thin metal plate, and the AST was derived from the measured plate thermometer temperature by a back calculation involving only the thermal lag due to the plate, not the insulation material.

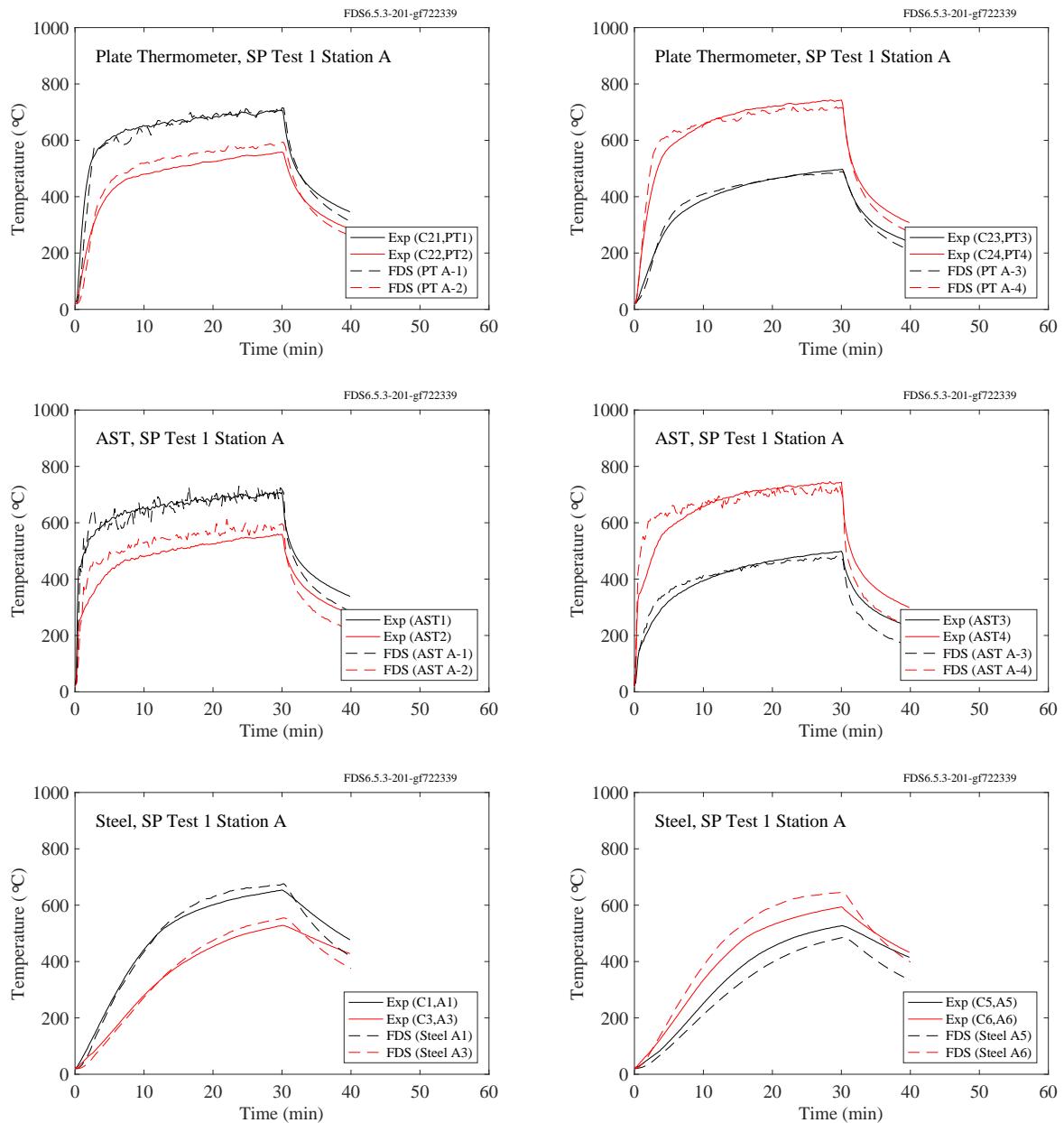


Figure 11.55: SP AST experiments, Station A plate, adiabatic surface, and steel temperatures, Test 1.

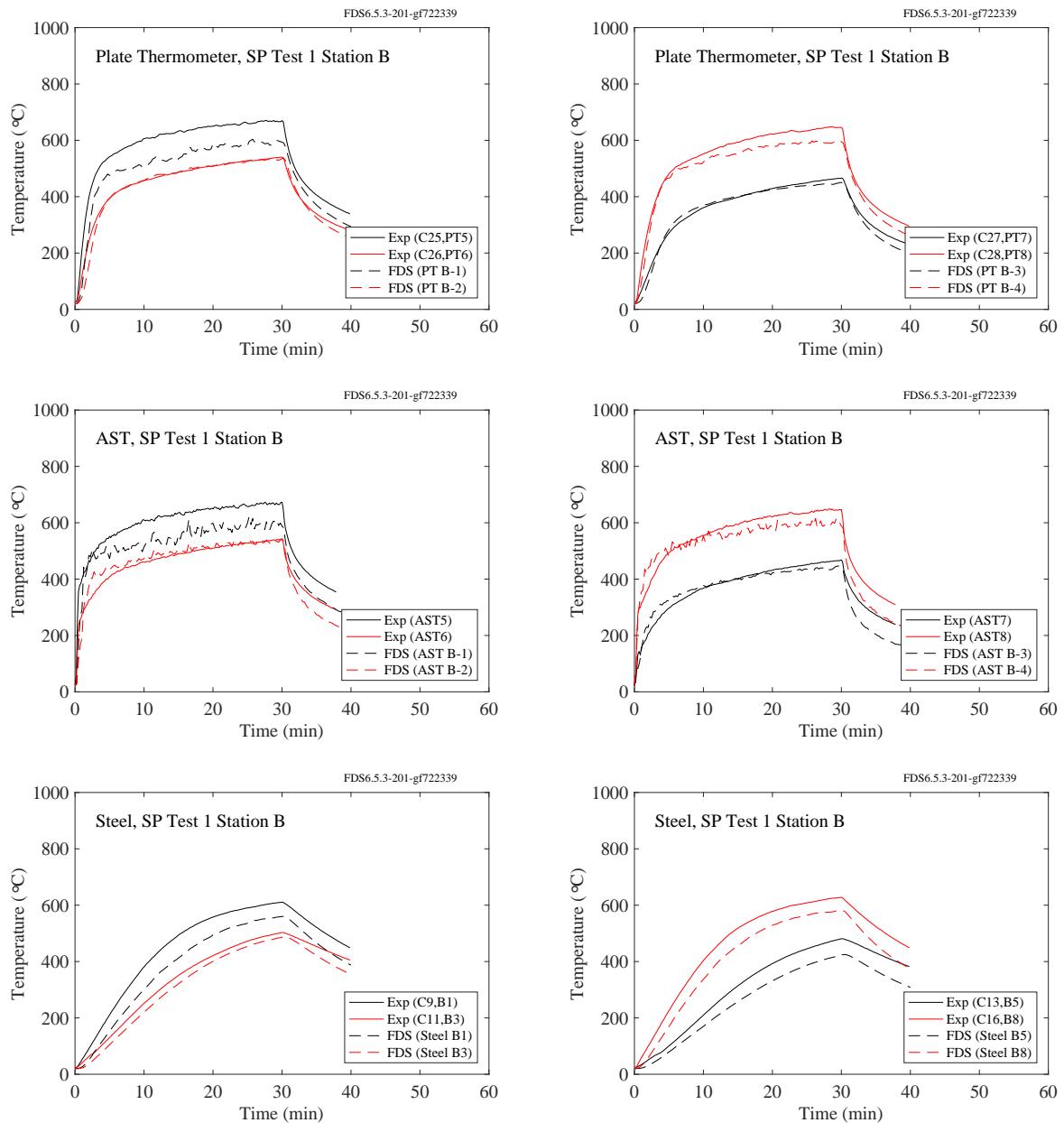


Figure 11.56: SP AST experiments, Station B plate, adiabatic surface, and steel temperatures, Test 1.

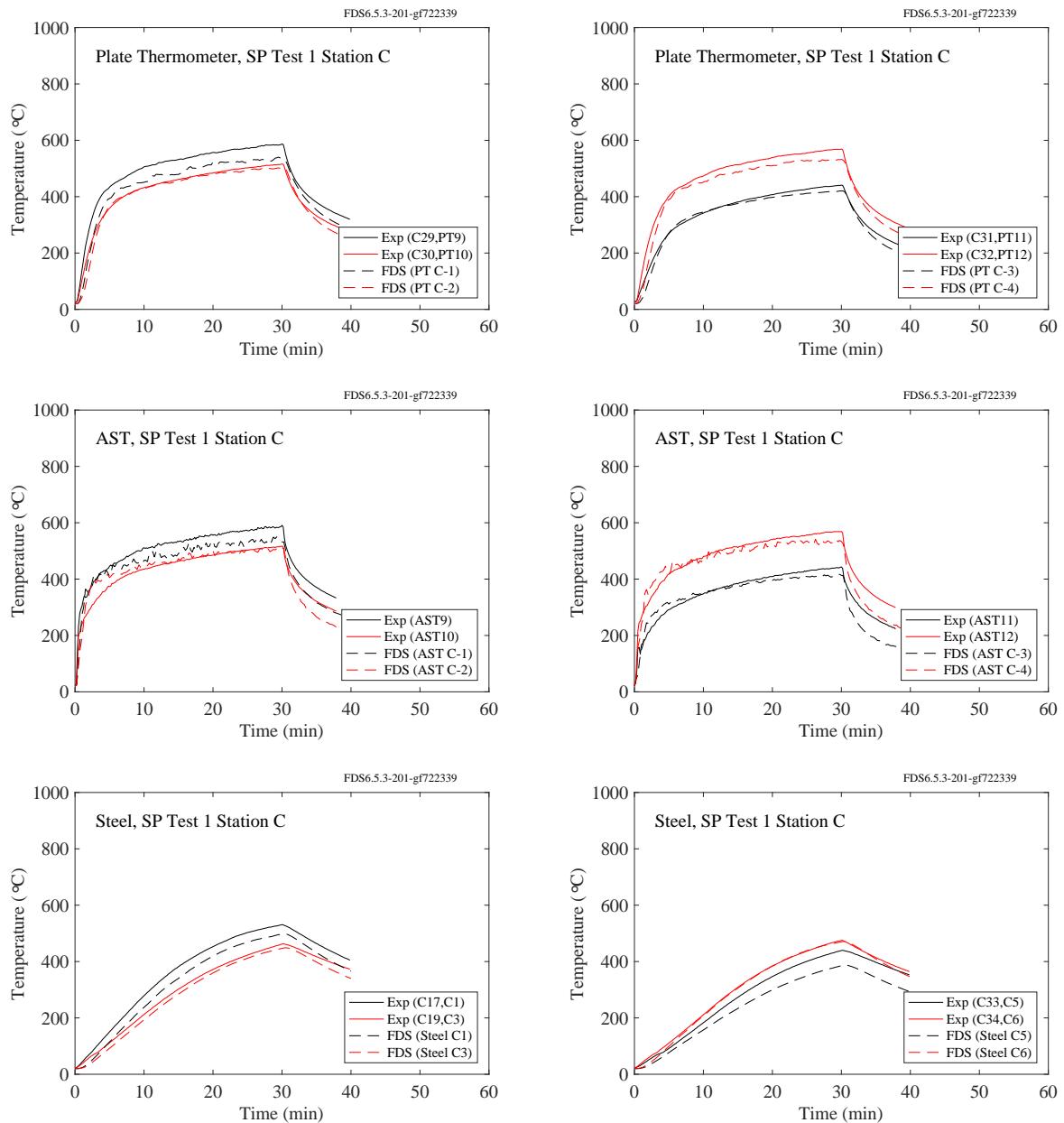


Figure 11.57: SP AST experiments, Station C plate, adiabatic surface, and steel temperatures, Test 1.

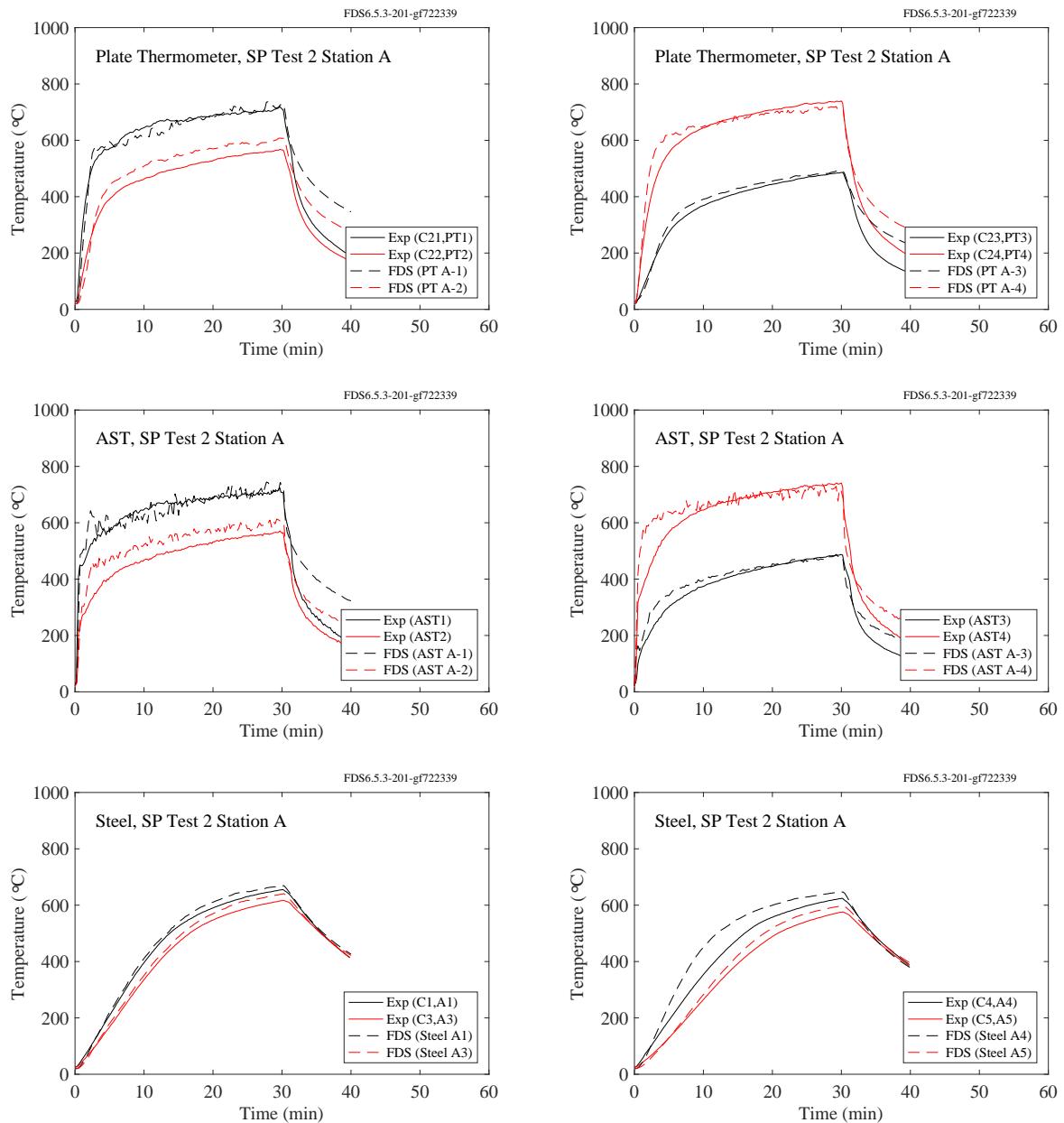


Figure 11.58: SP AST experiments, Station A plate, adiabatic surface, and steel temperatures, Test 2.

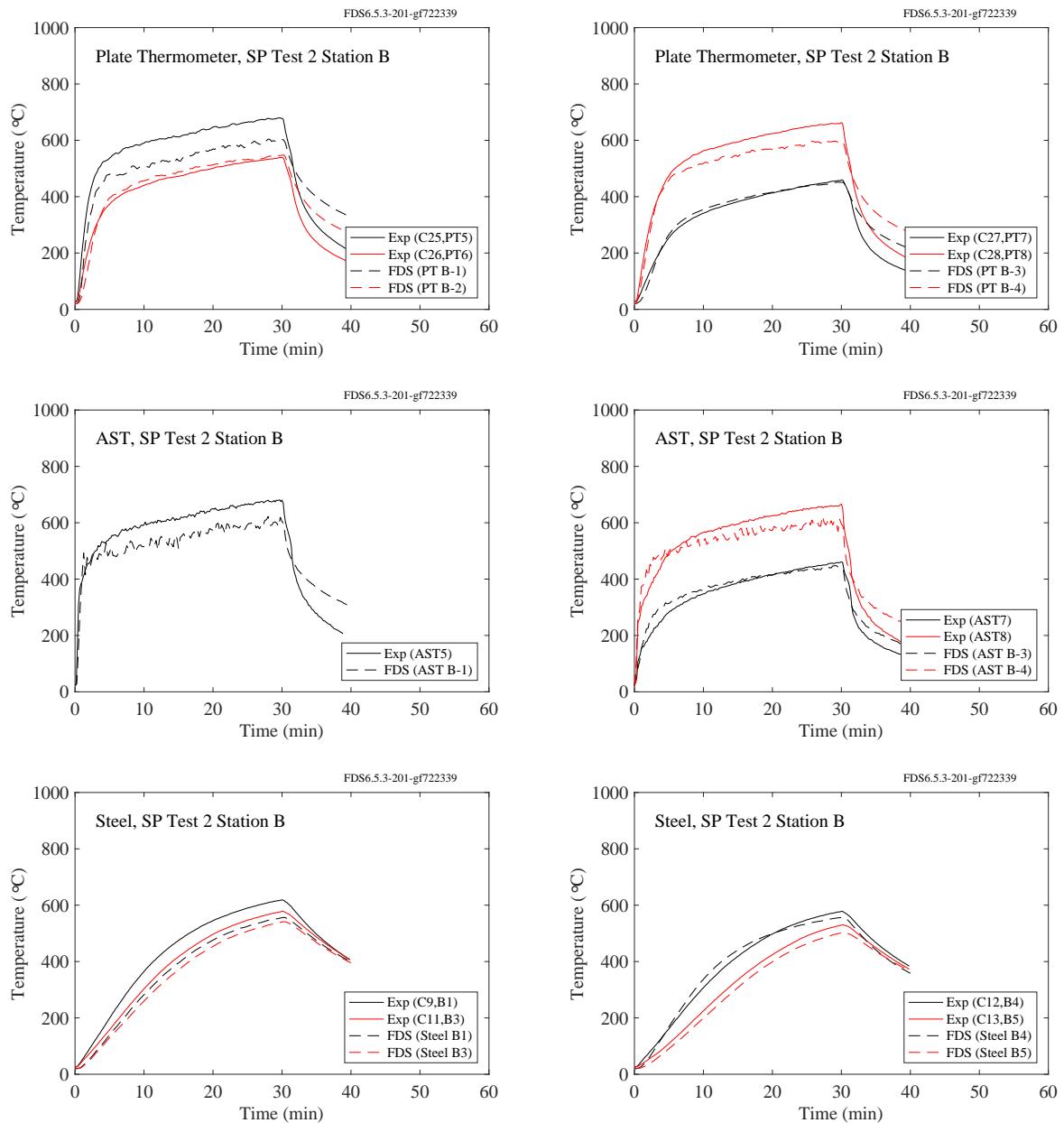


Figure 11.59: SP AST experiments, Station B plate, adiabatic surface, and steel temperatures, Test 2.

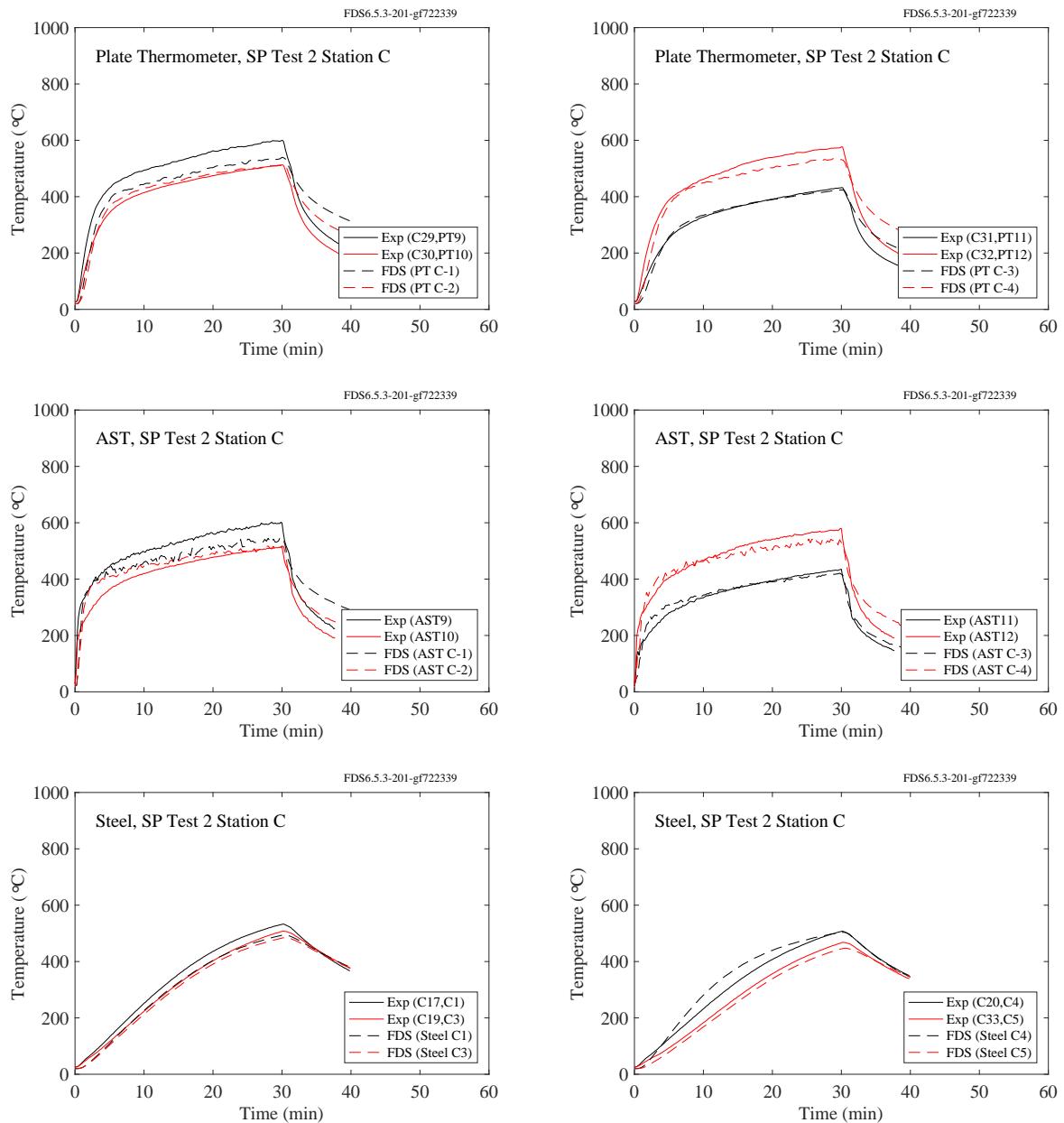


Figure 11.60: SP AST experiments, Station C plate, adiabatic surface, and steel temperatures, Test 2.

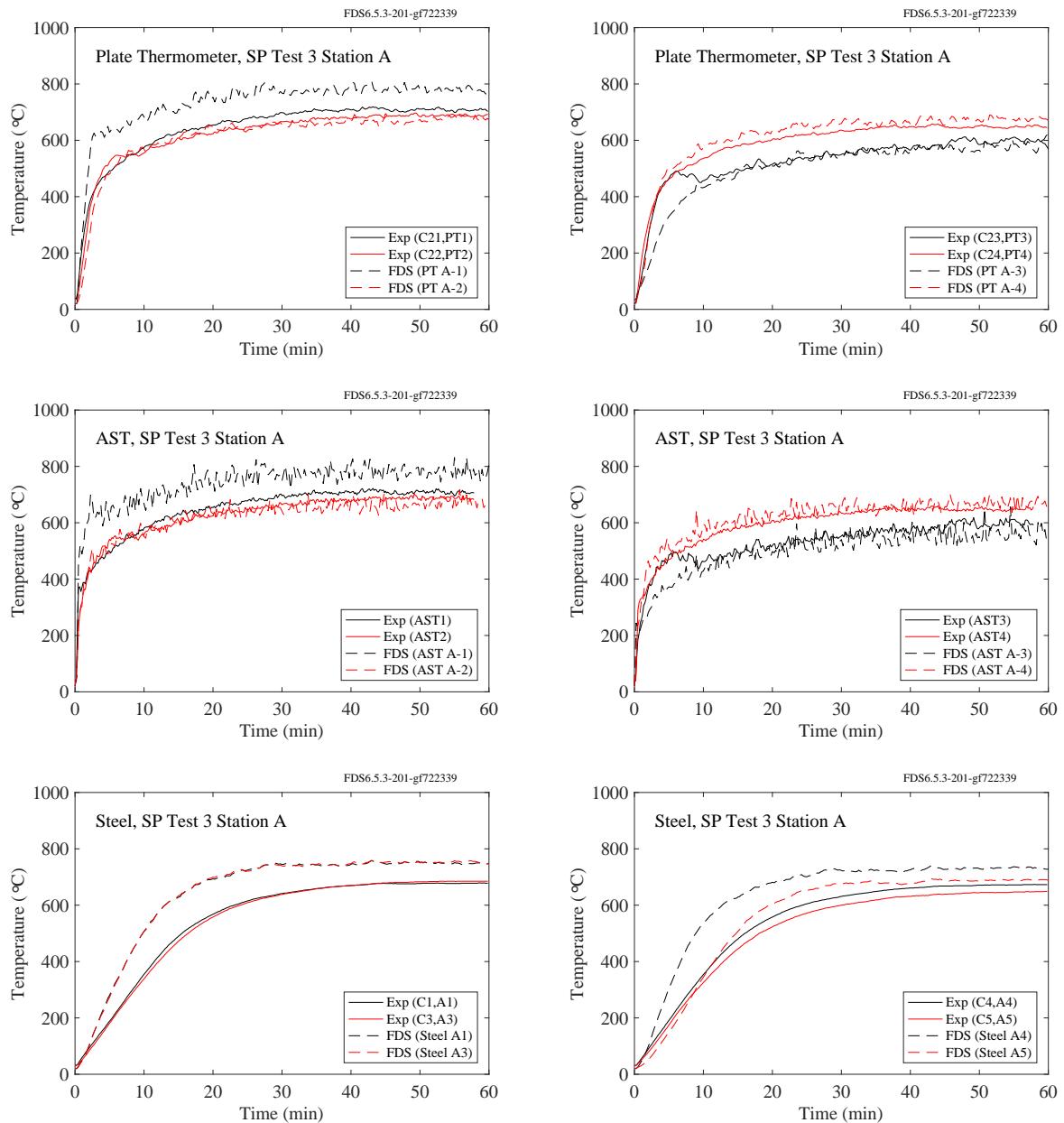


Figure 11.61: SP AST experiments, Station A plate, adiabatic surface, and steel temperatures, Test 3.

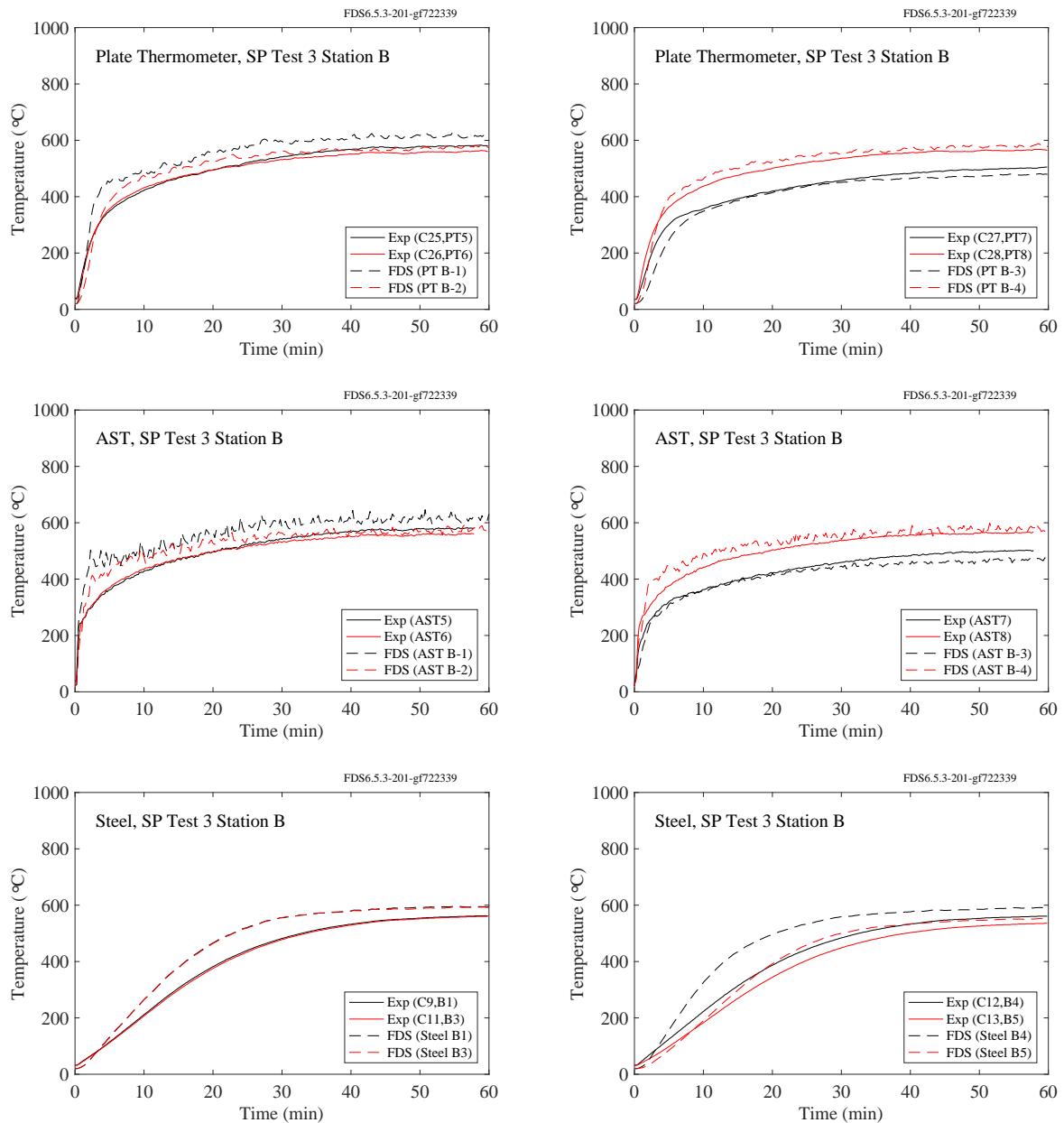


Figure 11.62: SP AST experiments, Station B plate, adiabatic surface, and steel temperatures, Test 3.

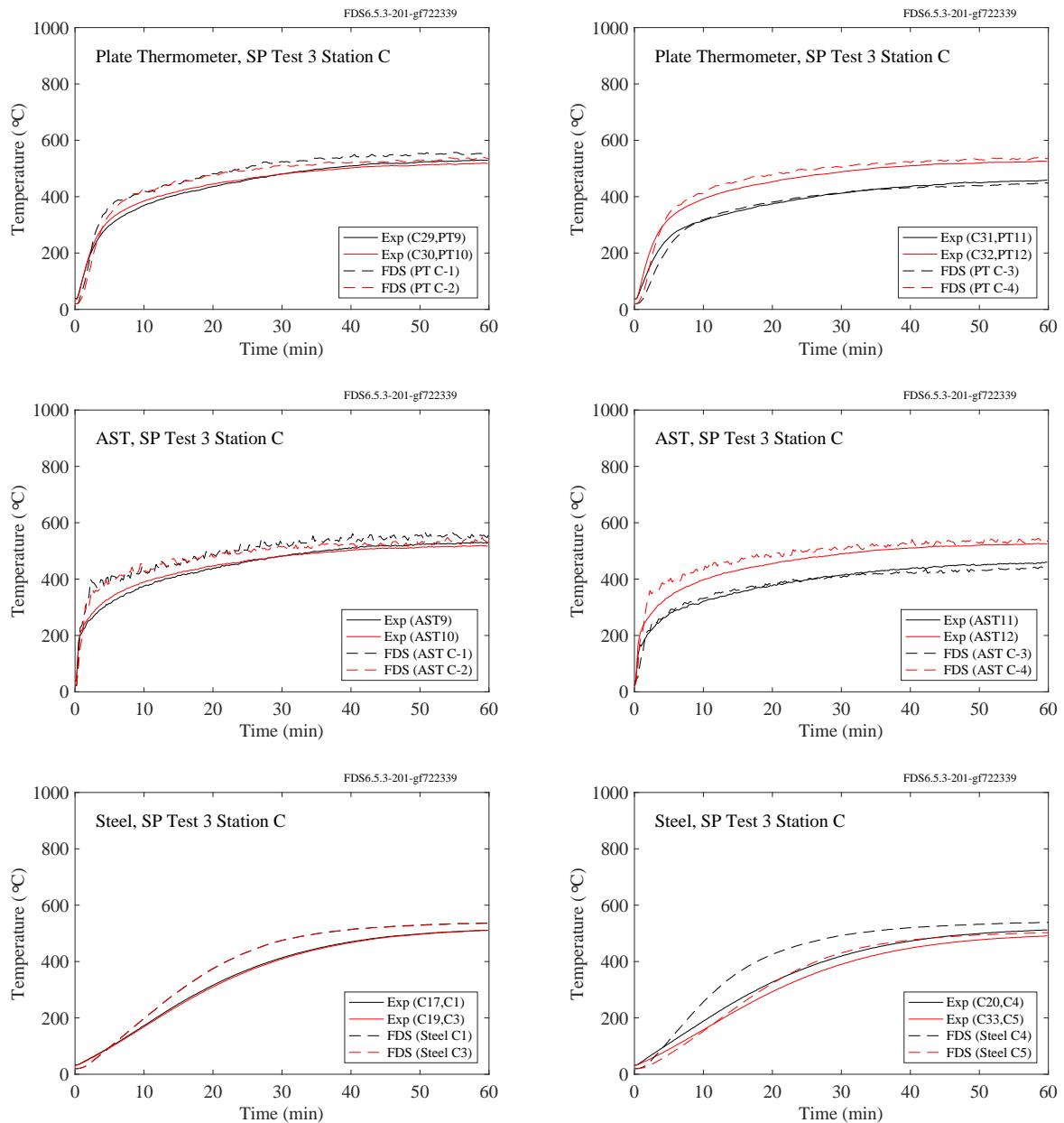


Figure 11.63: SP AST experiments, Station C plate, adiabatic surface, and steel temperatures, Test 3.

## **Pool Fire Experiments**

Three experiments were conducted at SP, Sweden, in 2011, in which a 6 m long, 20 cm diameter vertical column was positioned in the middle of 1.1 m and 1.9 m diesel and 1.1 m heptane pool fires [199]. Gas, plate, and steel surface temperature measurements were made at heights of 1 m, 2 m, 3 m, 4 m, and 5 m above the pool surface. At heights of 1 m, 3 m, and 5 m, these measurements were made at only one angular position. However, at 2 m and 4 m, the measurements were made at four positions. At these heights, two conventional plates thermometers were positioned approximately 10 cm from the column surface, along with two special plate thermometers (SPT) that were installed flush with the column surface. At each height, comparable predictions were made with FDS, but at only one angular position because there is no predominant direction of leaning in the simulation. In the experiments, the fire was reported to lean in the direction of Position 1. The lean was significant for the 1.9 m diesel fuel fires, in which case only data from 1 m and 2 m above the pool are used. Also, FDS assumes the column to be square in cross section (20 cm by 20 cm), rather than circular. The grid spacing is 10 cm.

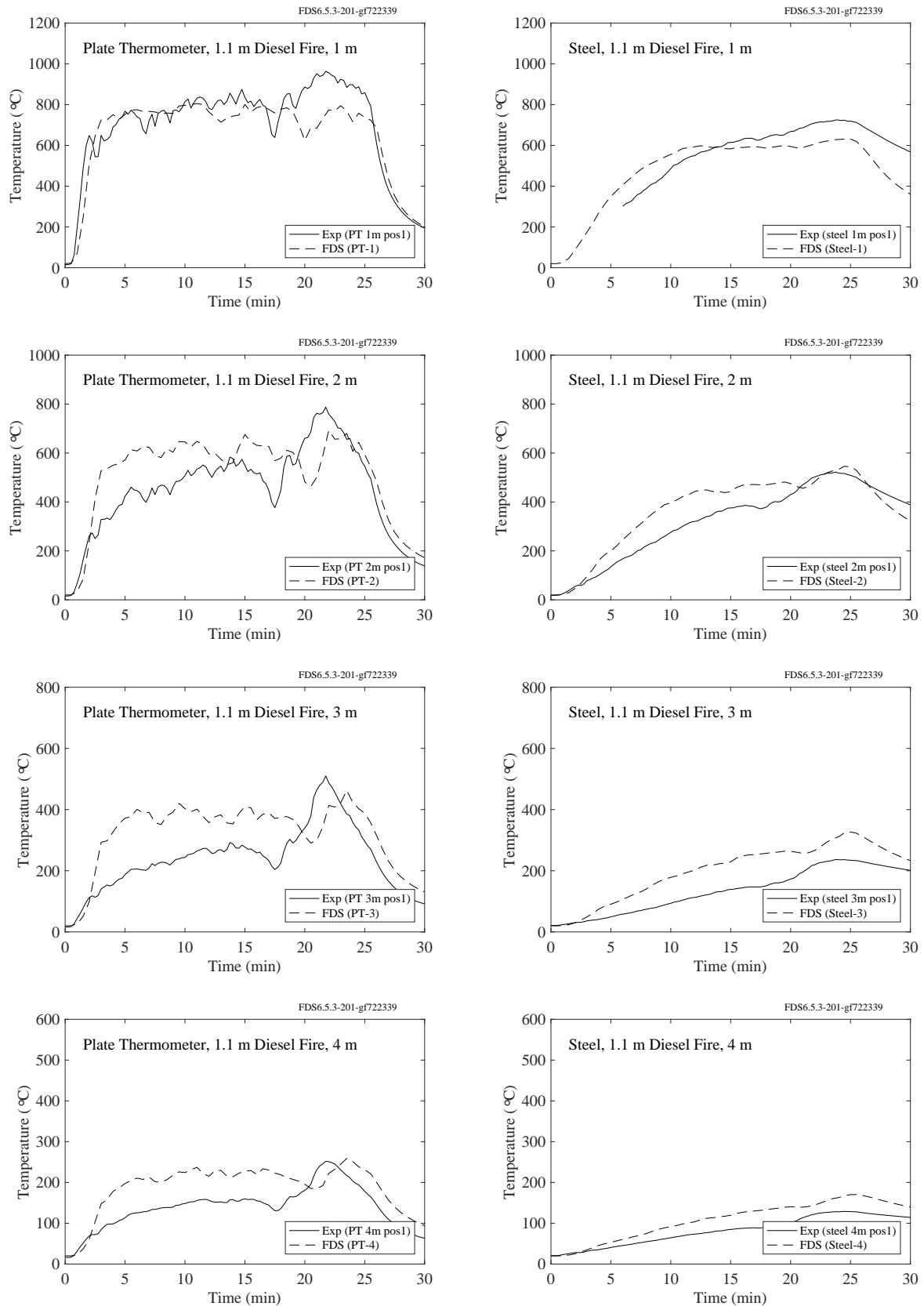


Figure 11.64: SP AST experiments, steel temperatures, 1.1 m diesel fire.

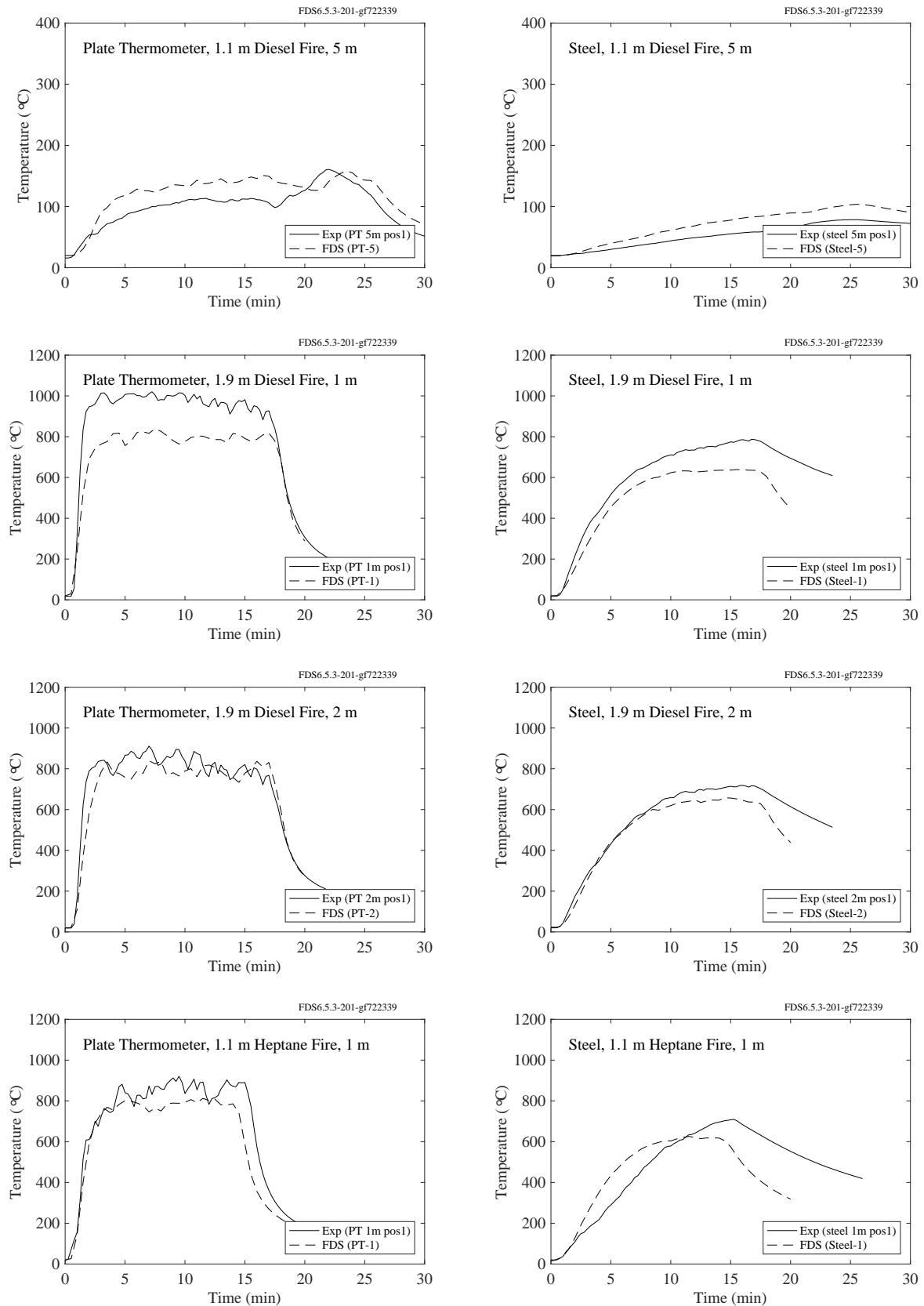


Figure 11.65: SP AST experiments, steel temperatures, 1.1 m and 1.9 m diesel, 1.1 m heptane fires.

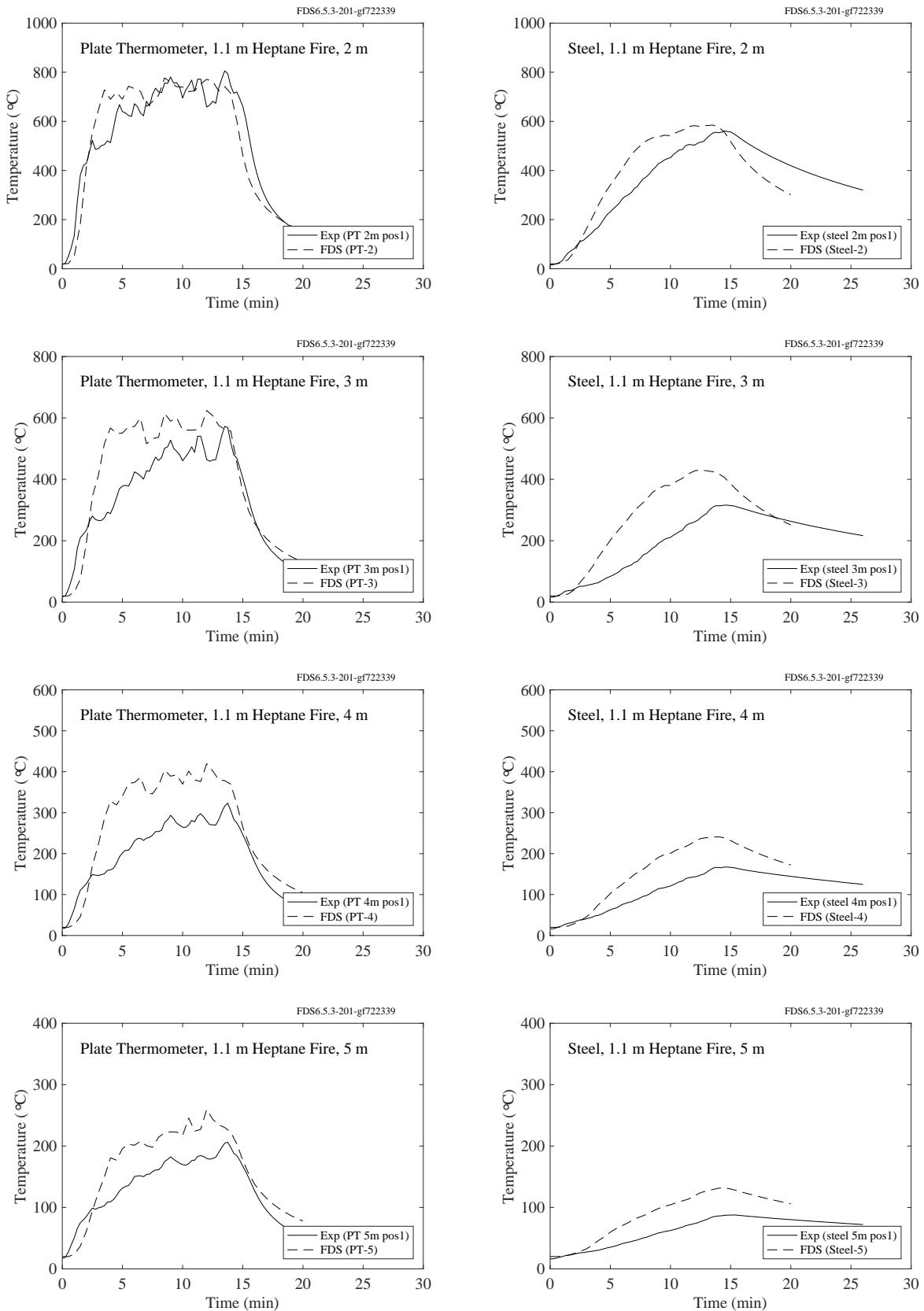


Figure 11.66: SP AST experiments, steel temperatures, 1.1 m heptane fire.

## **Insulated Room Experiments**

The plots on the following pages display measured and predicted plate thermometer (PT) temperatures for a series of single compartment experiments conducted by SP, Sweden [200]. The compartment was 2.7 m long, 1.8 m wide, and 1.8 m tall, with a 0.6 m by 1.5 m door centered on one of the short walls. The PTs were affixed to the walls. The designations of right and left wall are from the perspective of a person looking into the room. The back wall is the short wall without the door; the front wall is opposite. When referring to a given PT, the terms left/right, upper/lower, front/back refer to the quadrant where the PT is located. The PTs are centered within each quadrant, and are thus located at one-fourth or three-fourths of the wall's length, width or height. The term "center" refers to the center point of the entire wall. The designation "back wall upper" refers to the upper left quadrant of the back wall, and "back wall lower" refers to the lower right quadrant of the back wall.

The 12 experiments were conducted with four different wall linings. In Series A, the compartment was lined with a 10 cm thick light concrete block. In Series B, the compartment was lined with a 5 cm thick layer of insulation backed by a 3 mm thick plate of steel. In Series C, the compartment was lined with an uninsulated 3 mm thick steel plate. In Series D, the compartment was lined with a 3 mm thick steel plate backed by a 5 cm thick layer of insulation (the opposite of Series B).

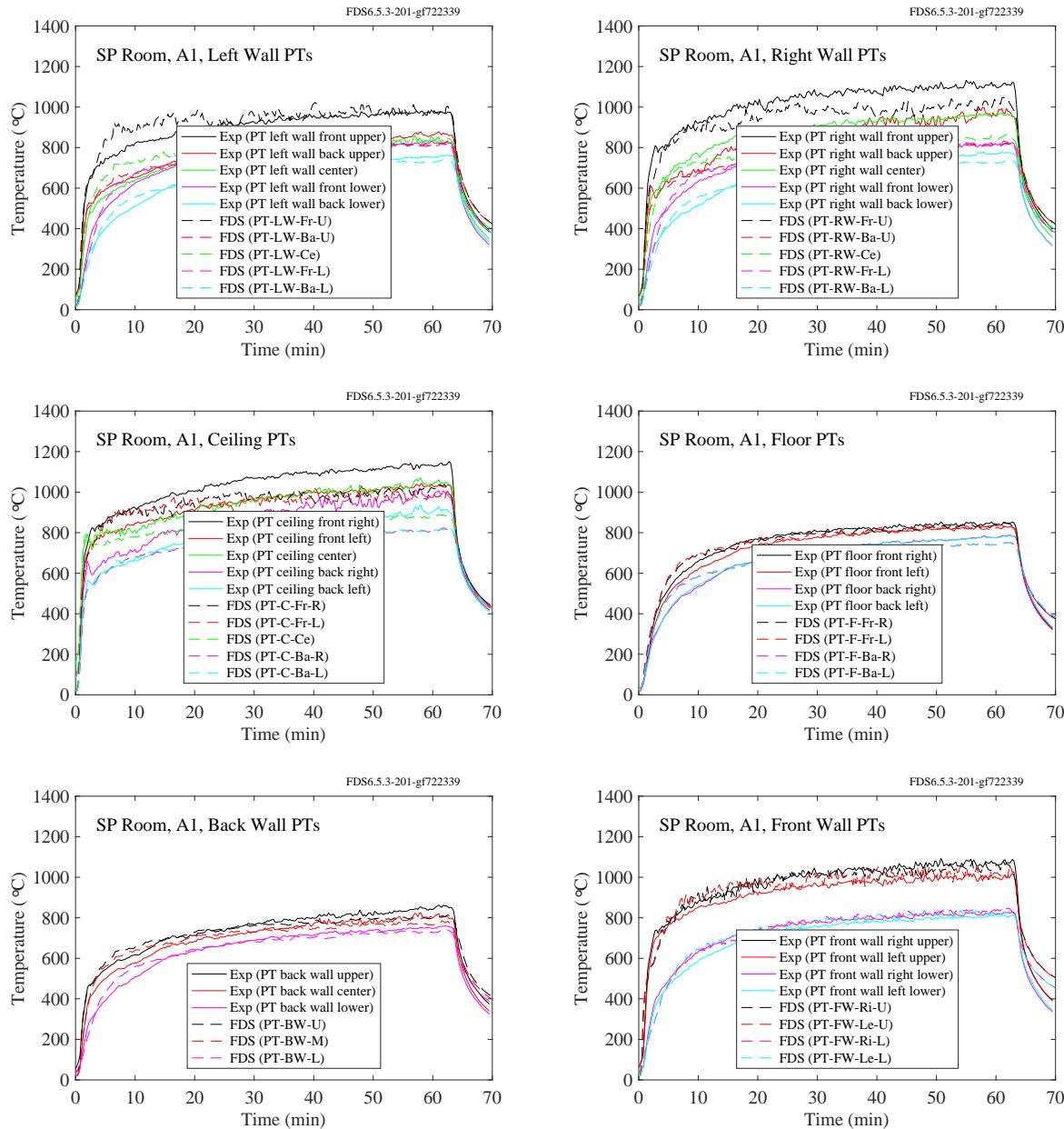


Figure 11.67: SP AST experiments, Insulated Room, Test A1.

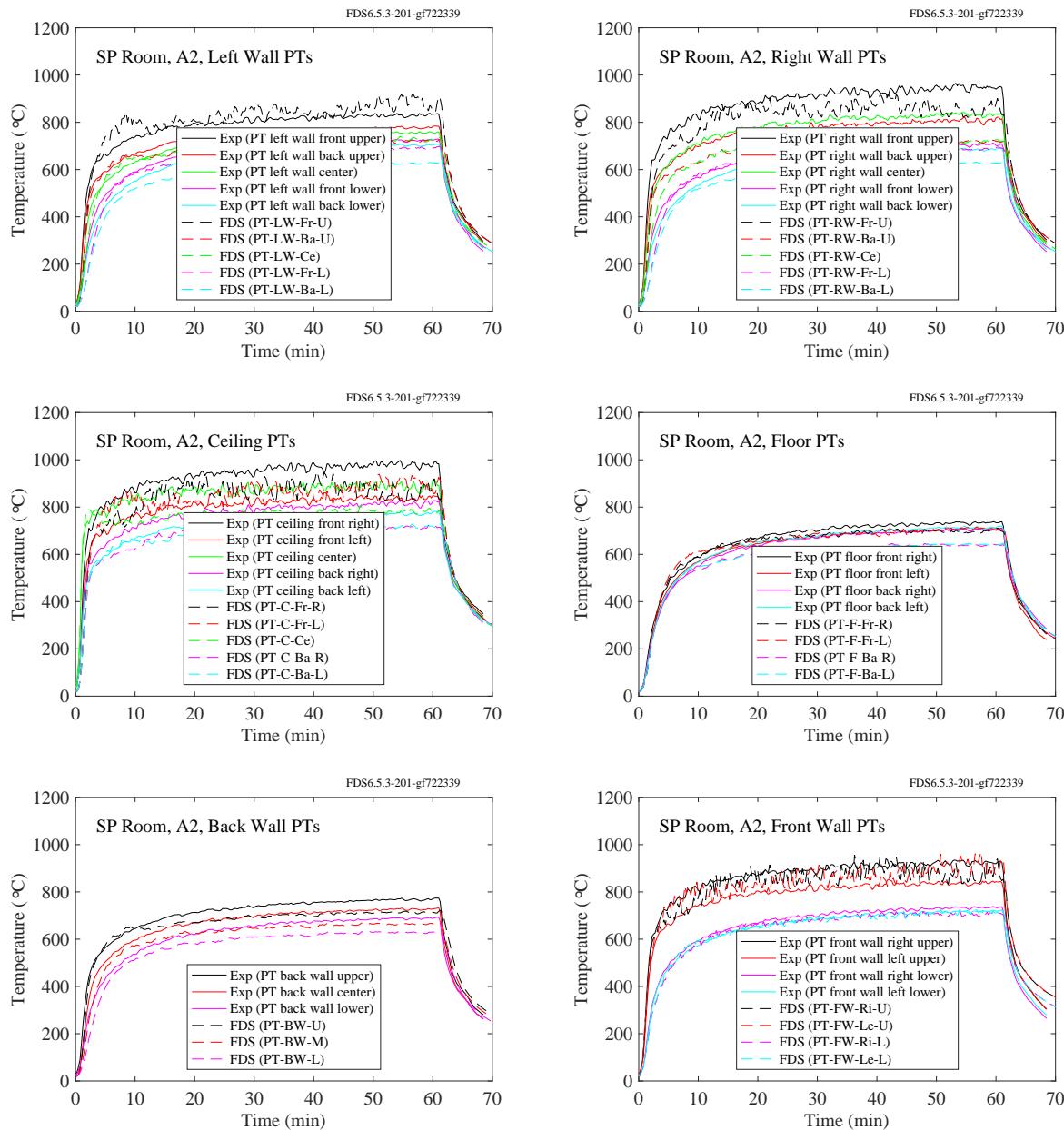


Figure 11.68: SP AST experiments, Insulated Room, Test A2.

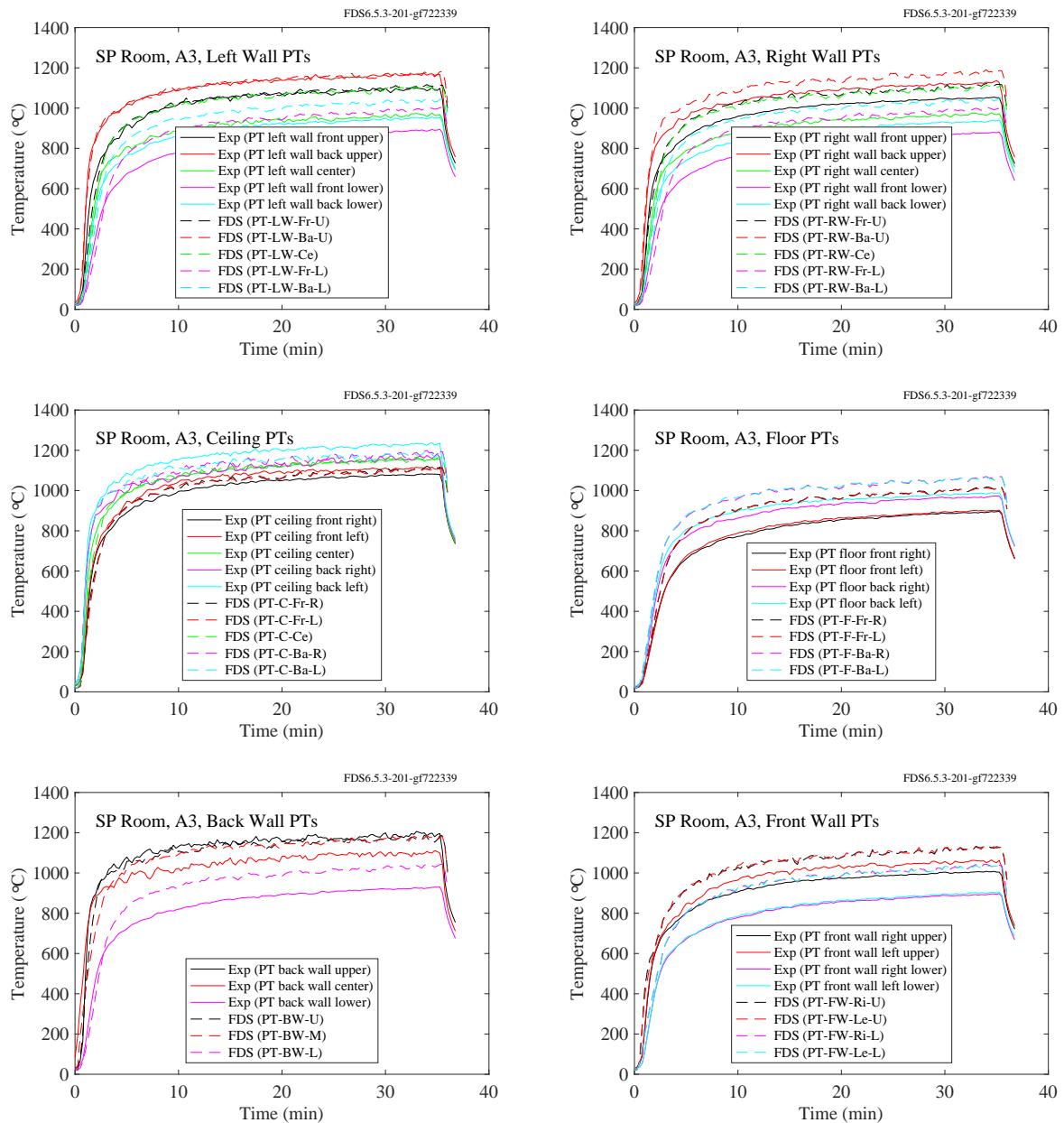


Figure 11.69: SP AST experiments, Insulated Room, Test A3.

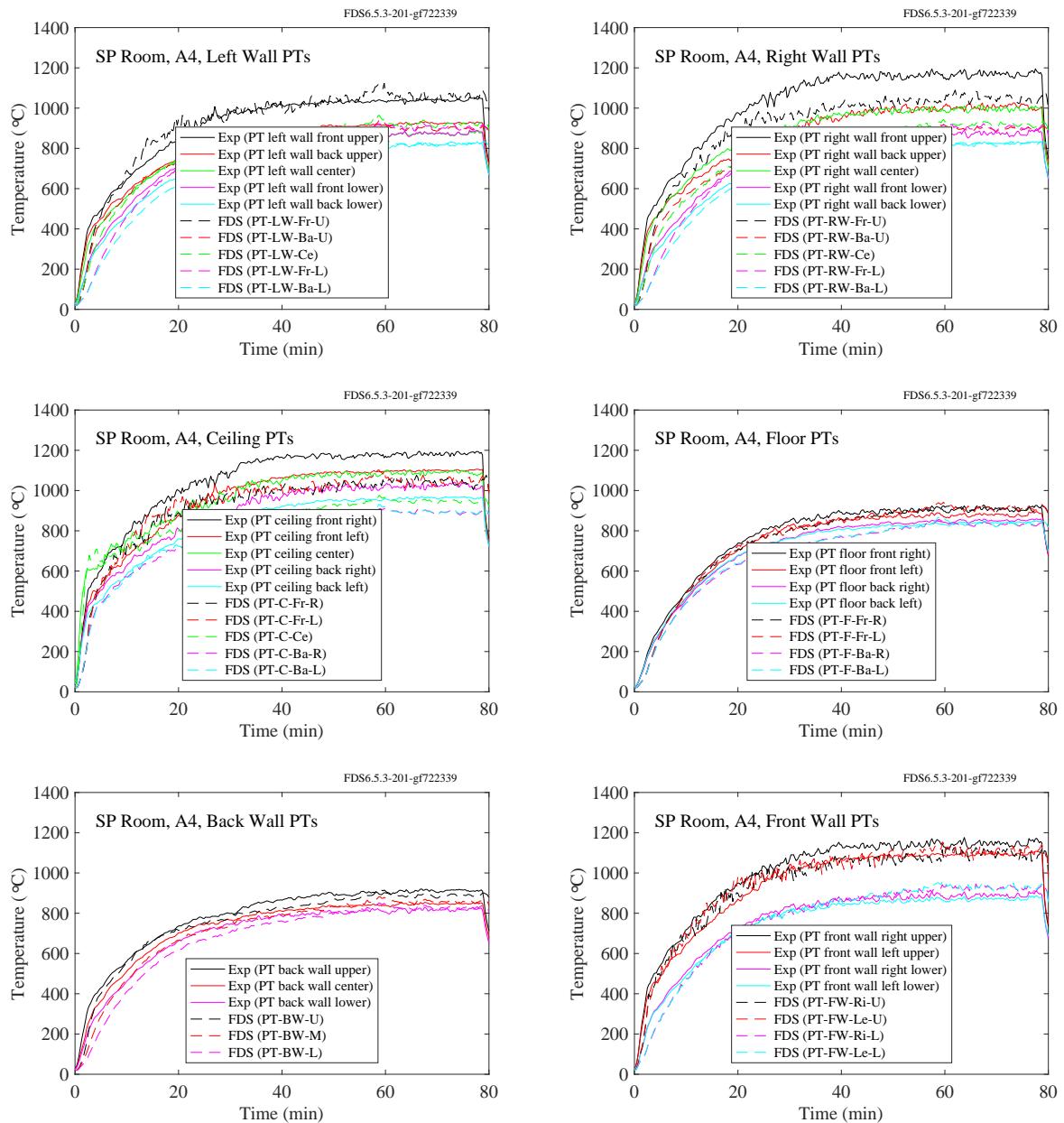


Figure 11.70: SP AST experiments, Insulated Room, Test A4.

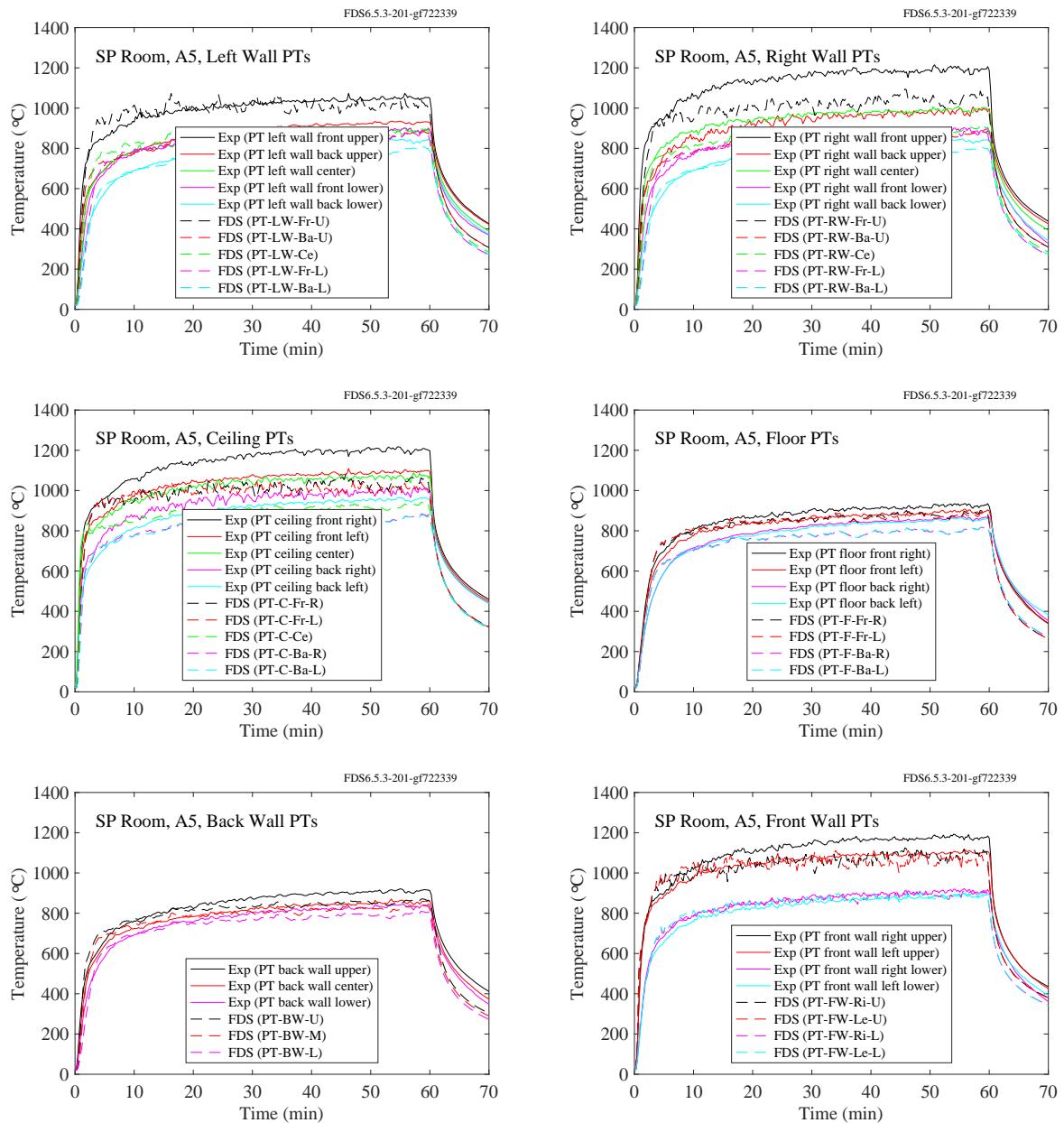


Figure 11.71: SP AST experiments, Insulated Room, Test A5.

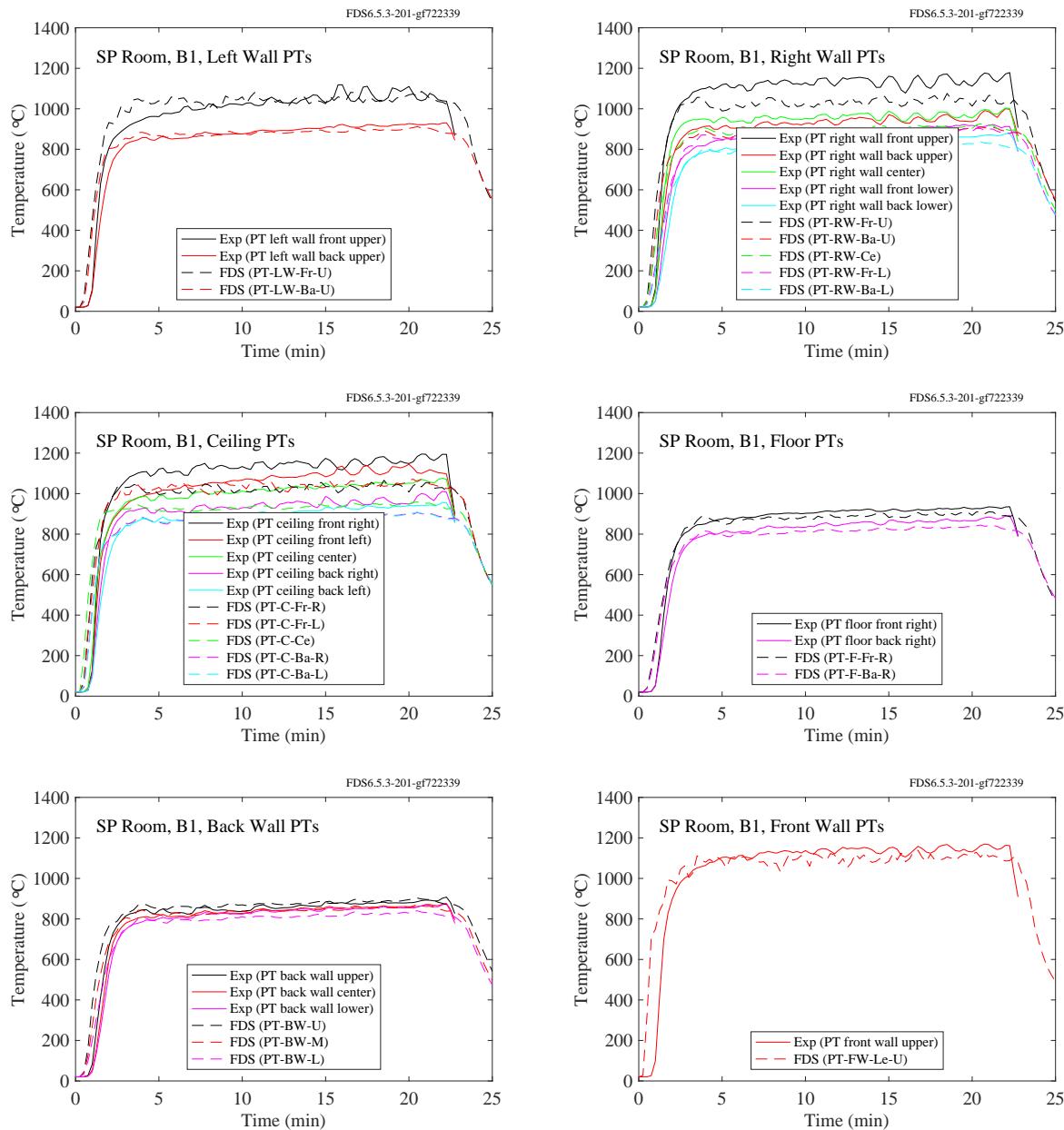


Figure 11.72: SP AST experiments, Insulated Room, Test B1.

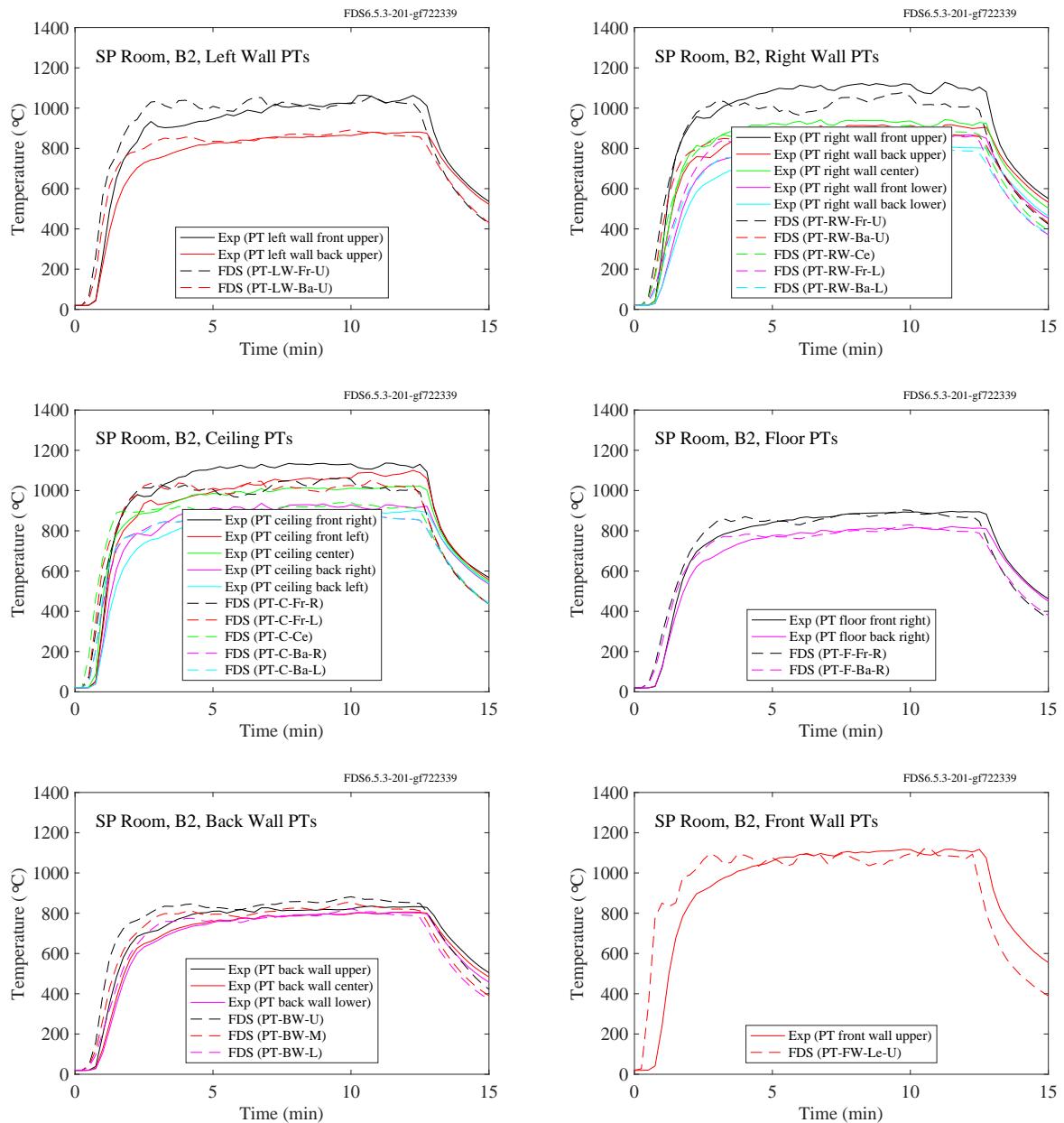


Figure 11.73: SP AST experiments, Insulated Room, Test B2.

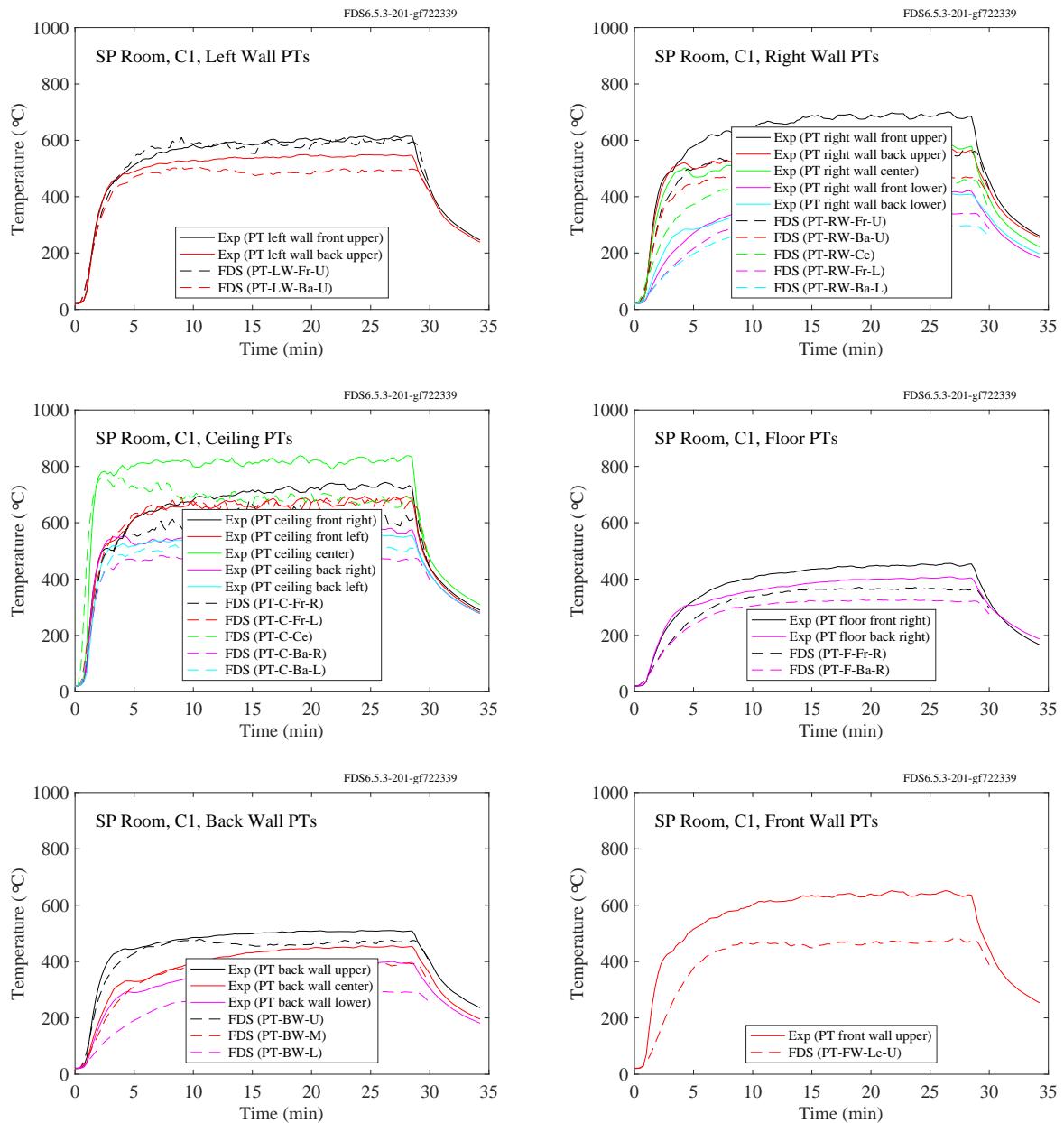


Figure 11.74: SP AST experiments, Insulated Room, Test C1.

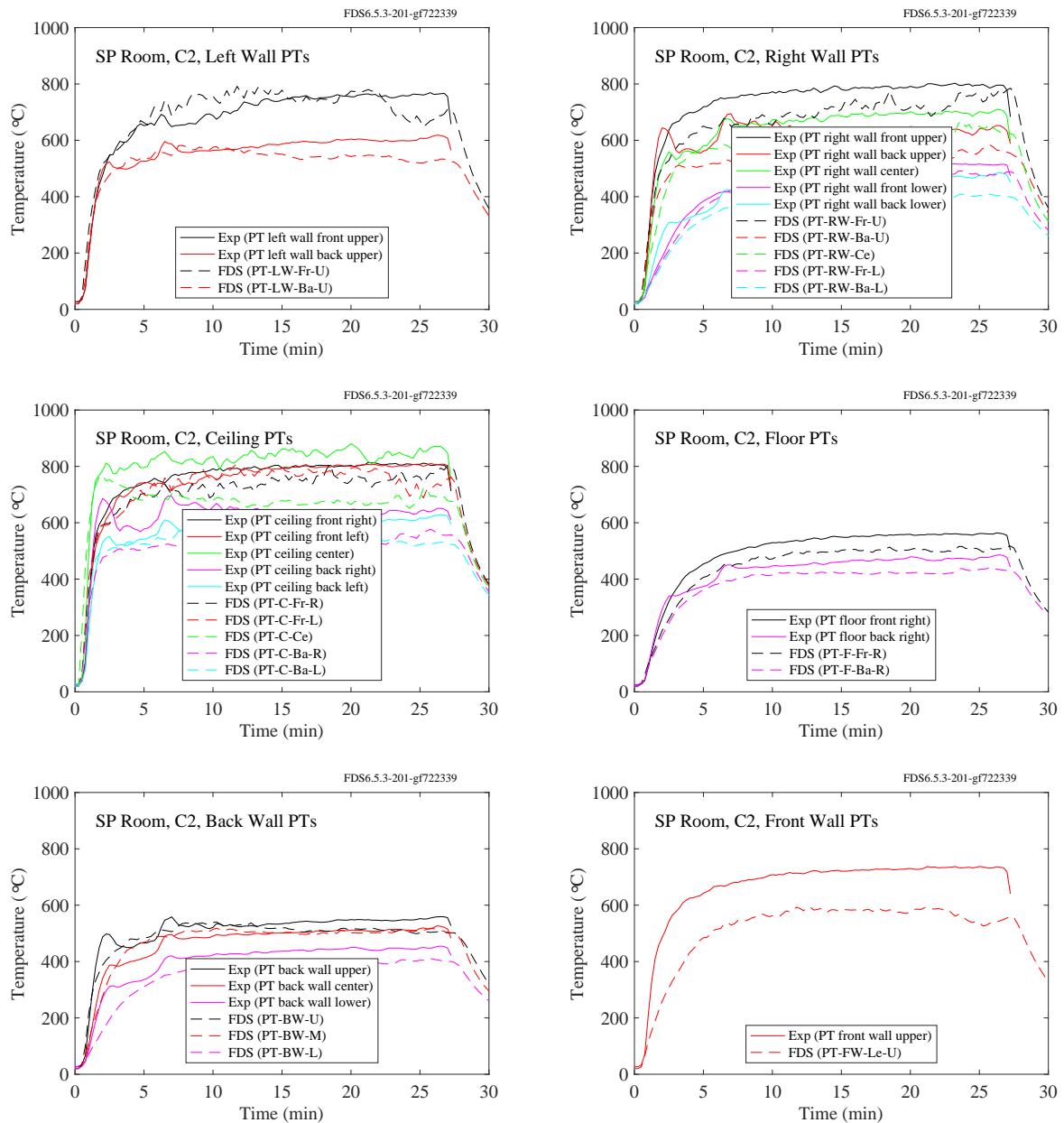


Figure 11.75: SP AST experiments, Insulated Room, Test C2.

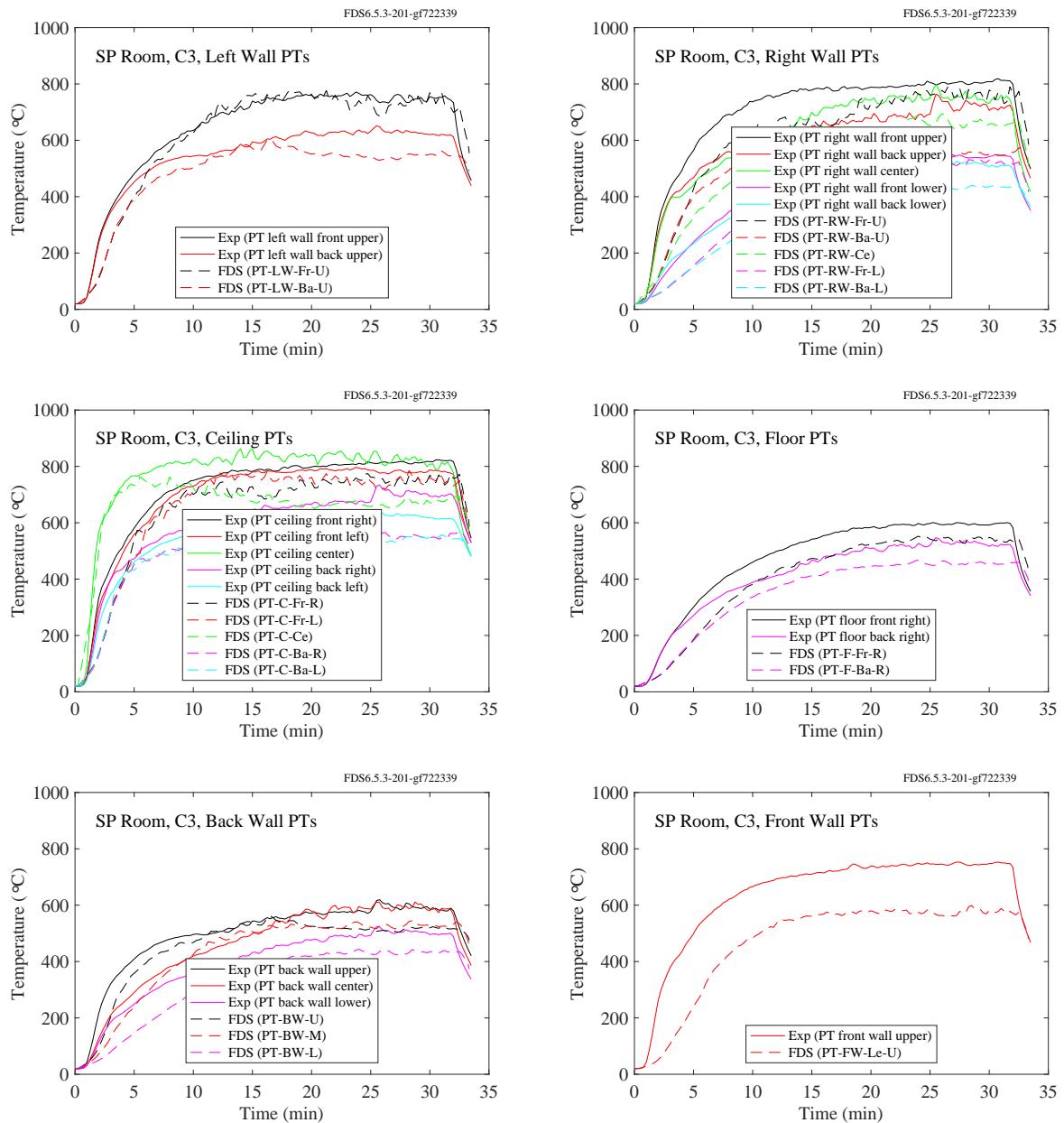


Figure 11.76: SP AST experiments, Insulated Room, Test C3.

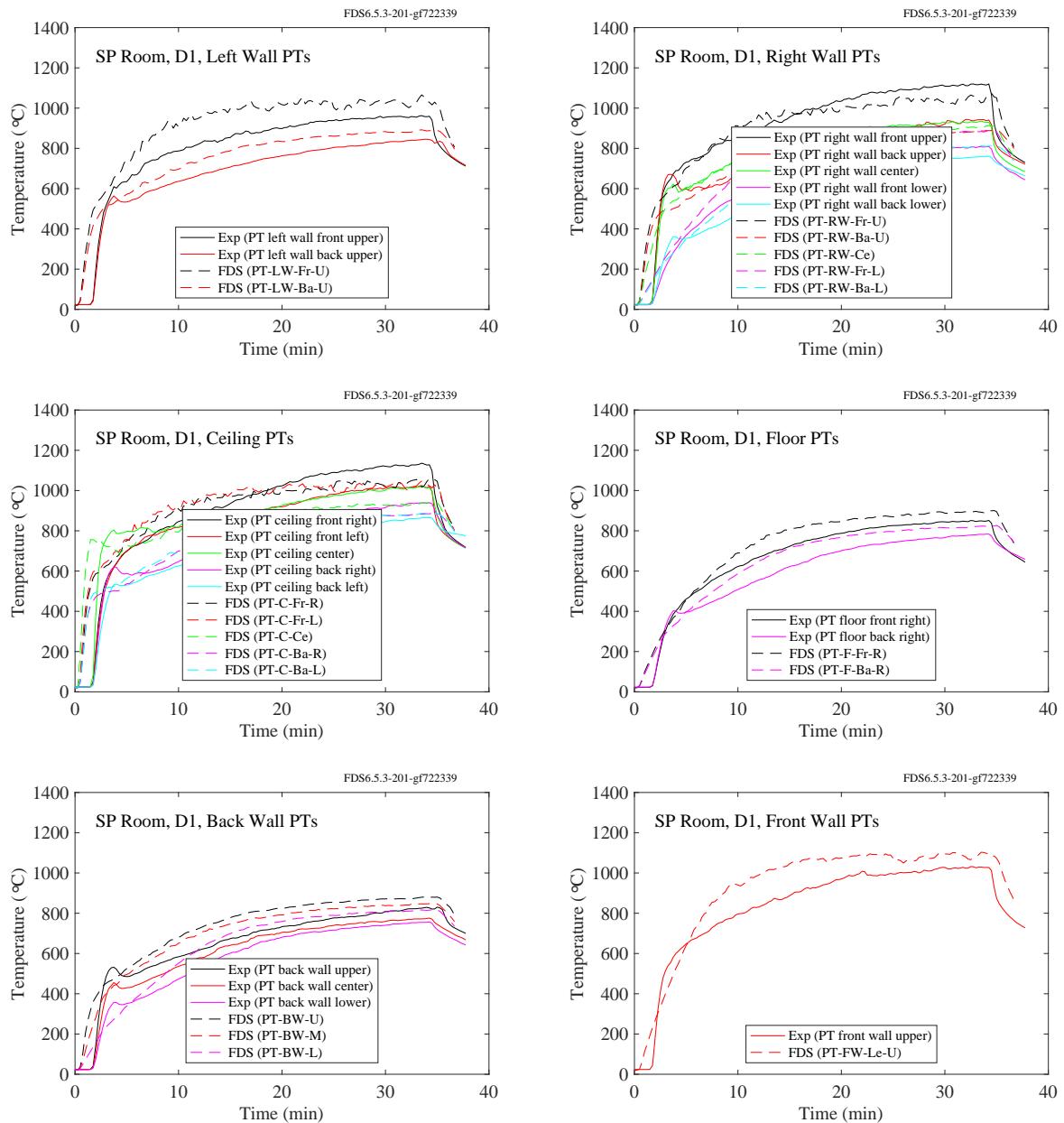


Figure 11.77: SP AST experiments, Insulated Room, Test D1.

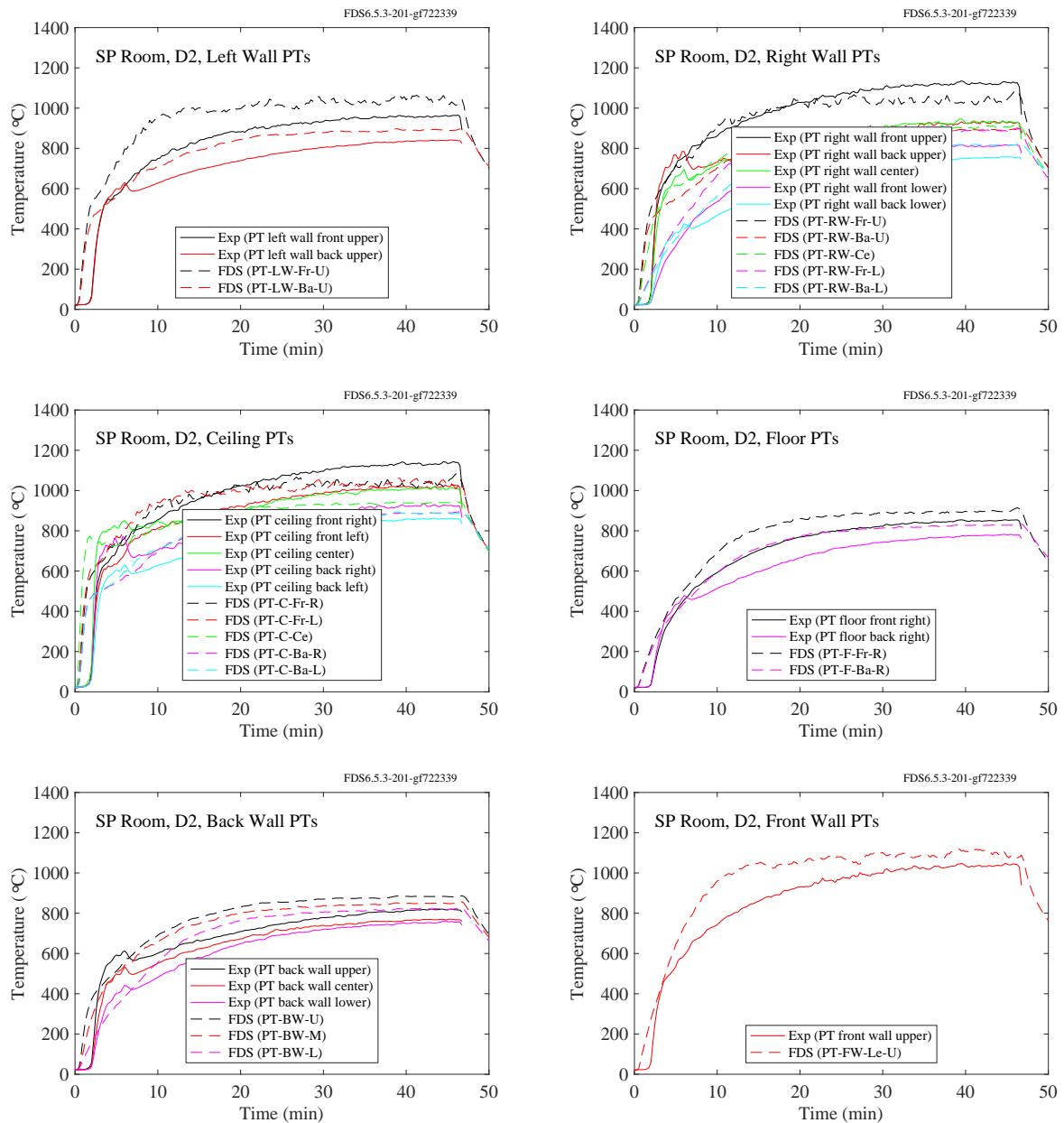


Figure 11.78: SP AST experiments, Insulated Room, Test D2.

## Plate Thermometer Validation

The simulations of the SP Adiabatic Surface Temperature experiments include a 1-D model of a plate thermometer (PT). A PT is constructed of a thin, 10 cm square sheet of Inconel backed by a layer of insulation material. A single thermocouple is attached to the back side of the Inconel plate. To test the FDS PT model, a real PT was placed in a cone calorimeter at NIST and exposed to nominal heat fluxes of  $25 \text{ kW/m}^2$  and  $75 \text{ kW/m}^2$ . The results are shown in Fig. 11.79.

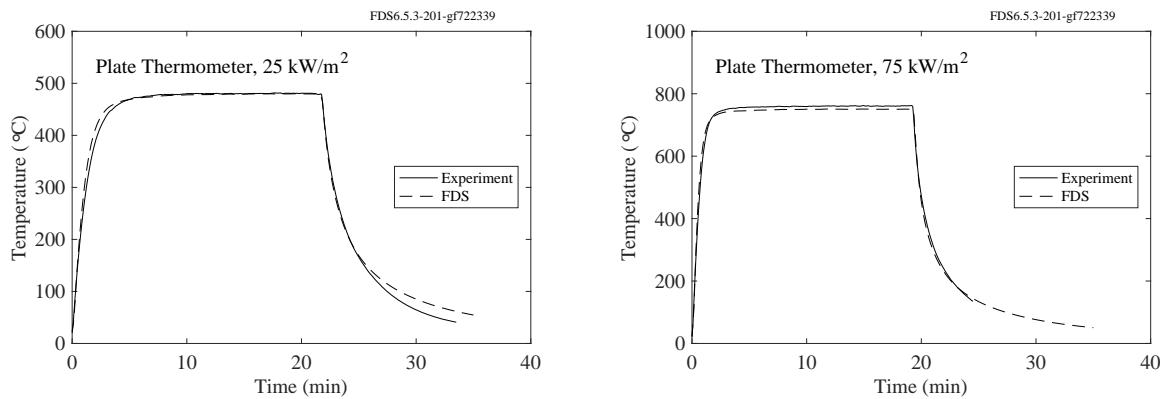


Figure 11.79: Predictions of plate thermometer temperatures in a cone calorimeter.

### **11.2.3 WTC Experiments**

The compartment for the WTC experiments contained a hollow box column roughly 0.5 m from the fire pan, two trusses over the top of the pan, and one or two steel bars resting on the lower truss flanges. In Tests 1, 2 and 3, the steel was bare, and in Tests 4, 5 and 6, the steel was coated with various thicknesses of sprayed fire-resistive materials. The column was instrumented near its base (about 0.5 m from the floor, middle (1.5 m), and upper (2.5 m). Four measurements of steel (and insulation) temperatures were made at each location, for each of its four sides. These elements were modeled using thin sheet obstructions with a resolution of 10 cm.

In addition to the steel structural elments, five cylinders (“slugs”) of nickel 200 ( $\geq 99\%$  nickel), 25.4 cm long and 10.2 cm in diameter, were positioned 50 cm north of the centerline in the WTC experiments. Slugs 1 through 5 were 2.92 m, 1.82 m, 0.57 m, 0.05 m, and 1.56 m, respectively, from the longitudinal axis of the fire pan. All the slugs were 50 cm north of the lateral axis. The fire pan measured 2 m by 1 m. Four thermocouples were inserted into each slug at various locations. All four temperatures for each slug were virtually indistinguishable. Rectangular obstructions were used to model the slugs, but the one-dimensional heat conduction calculation was performed using cylindrical coordinates.

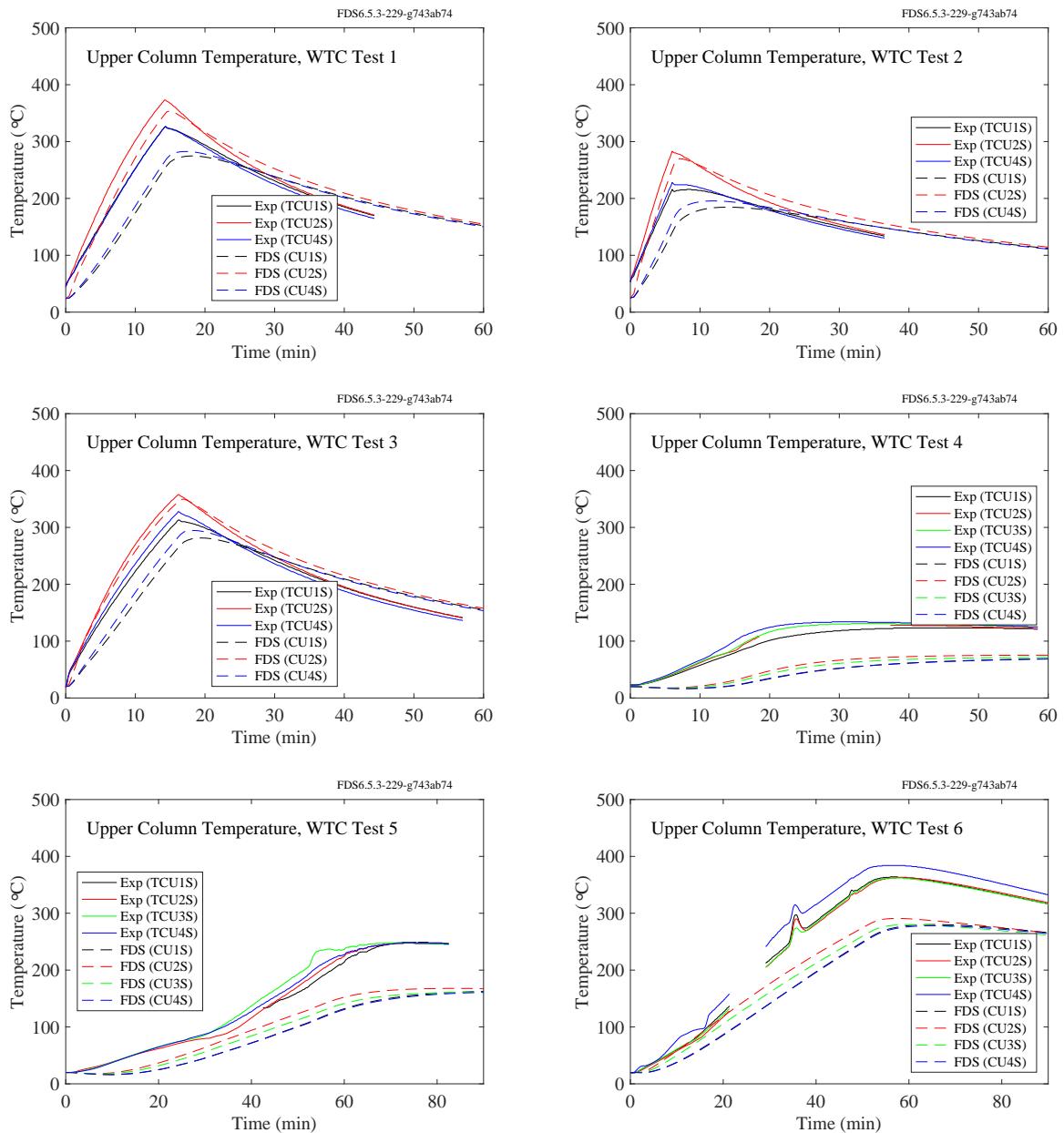


Figure 11.80: WTC experiments, steel temperatures, upper column.

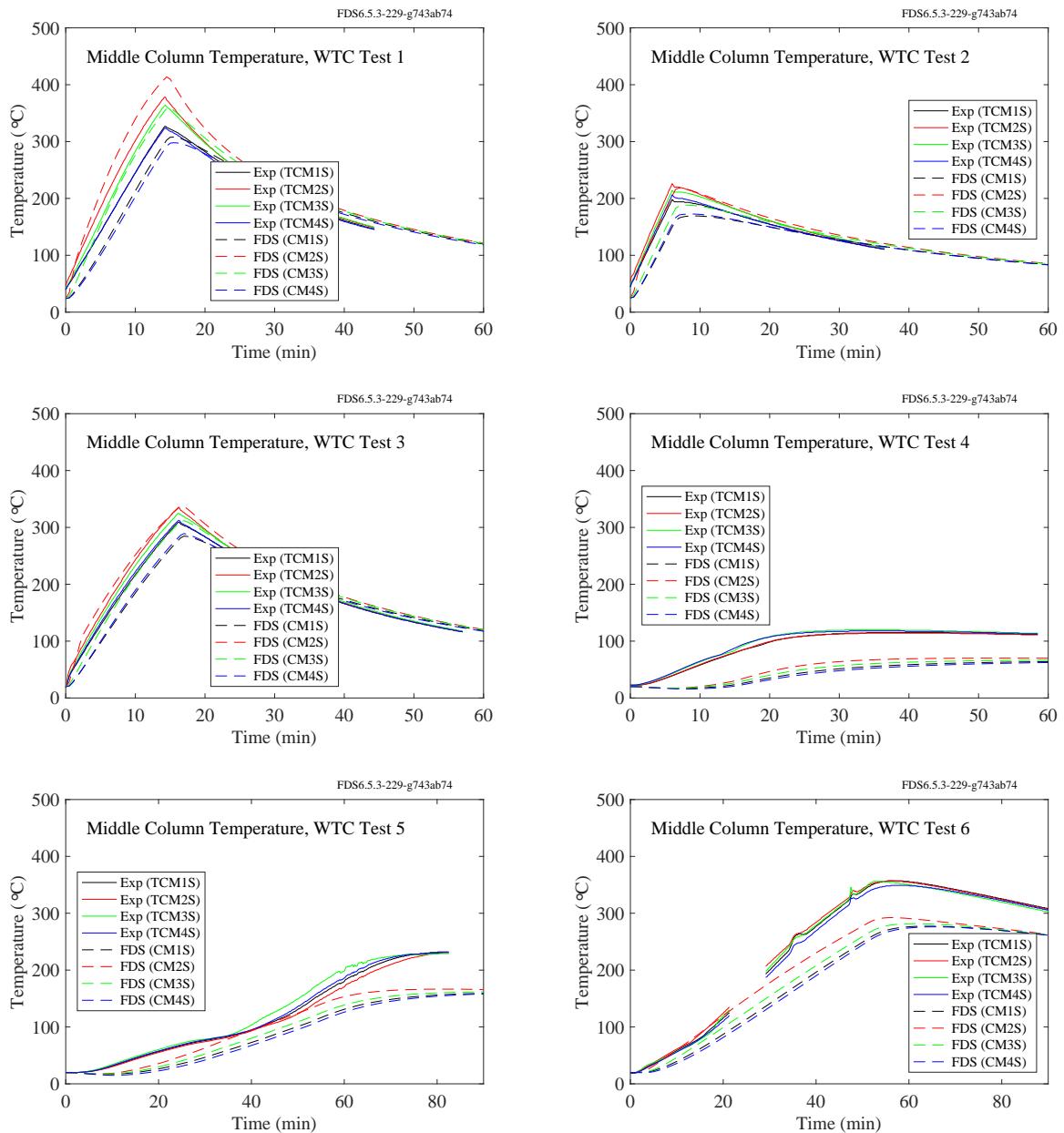


Figure 11.81: WTC experiments, steel temperatures, middle column.

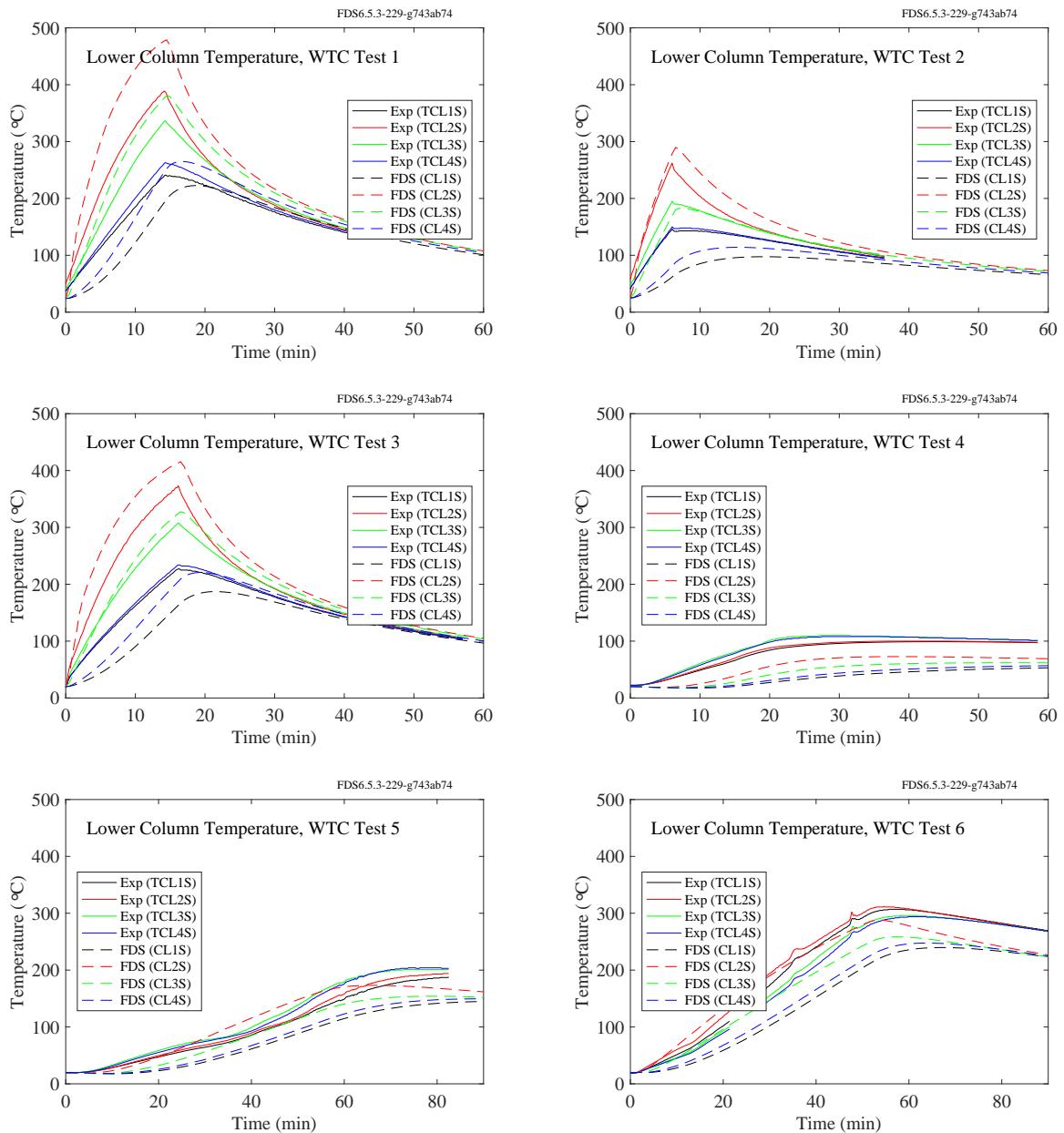


Figure 11.82: WTC experiments, steel temperatures, lower column.

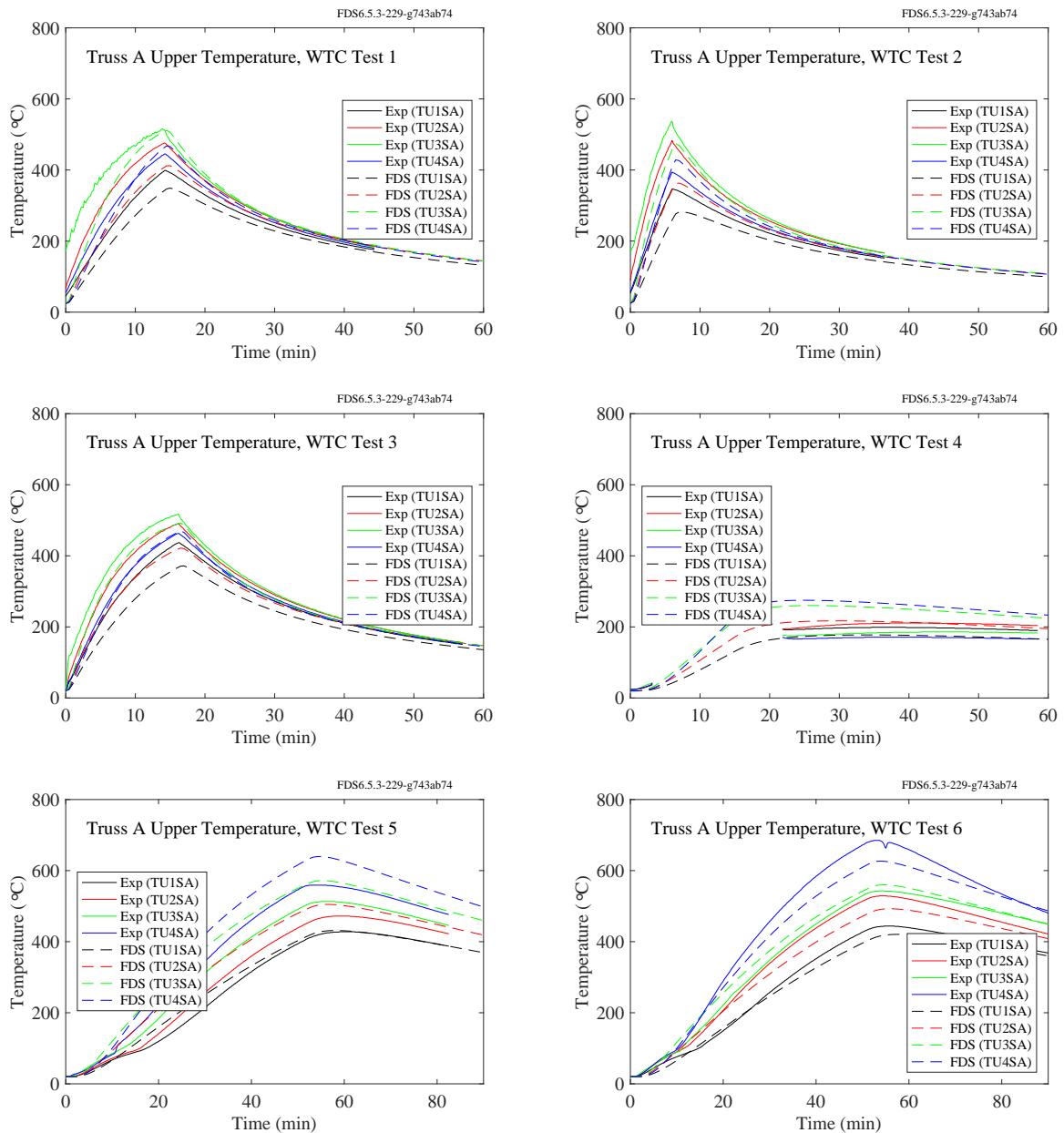


Figure 11.83: WTC experiments, steel temperatures, upper Truss A.

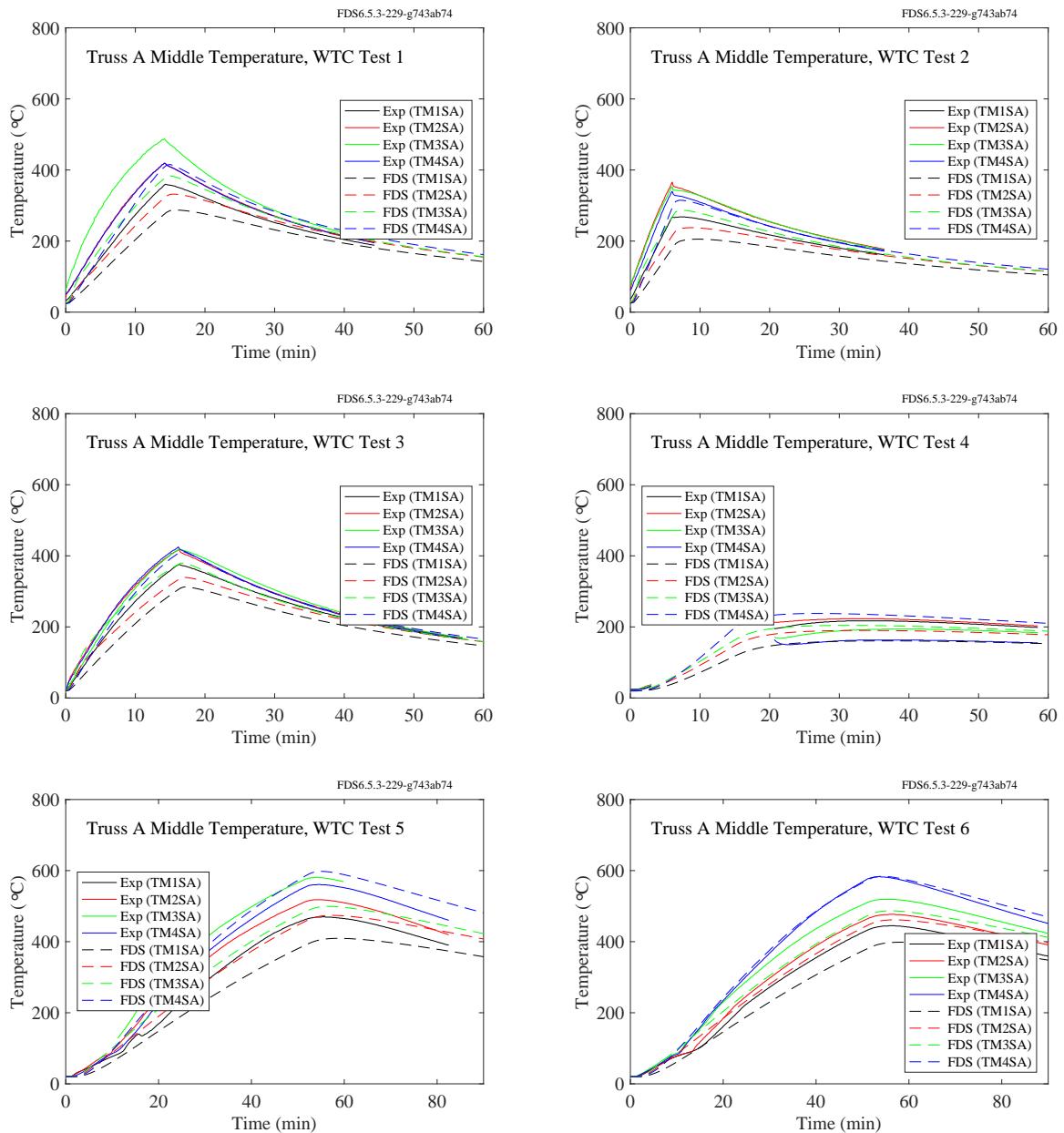


Figure 11.84: WTC experiments, steel temperatures, middle Truss A.

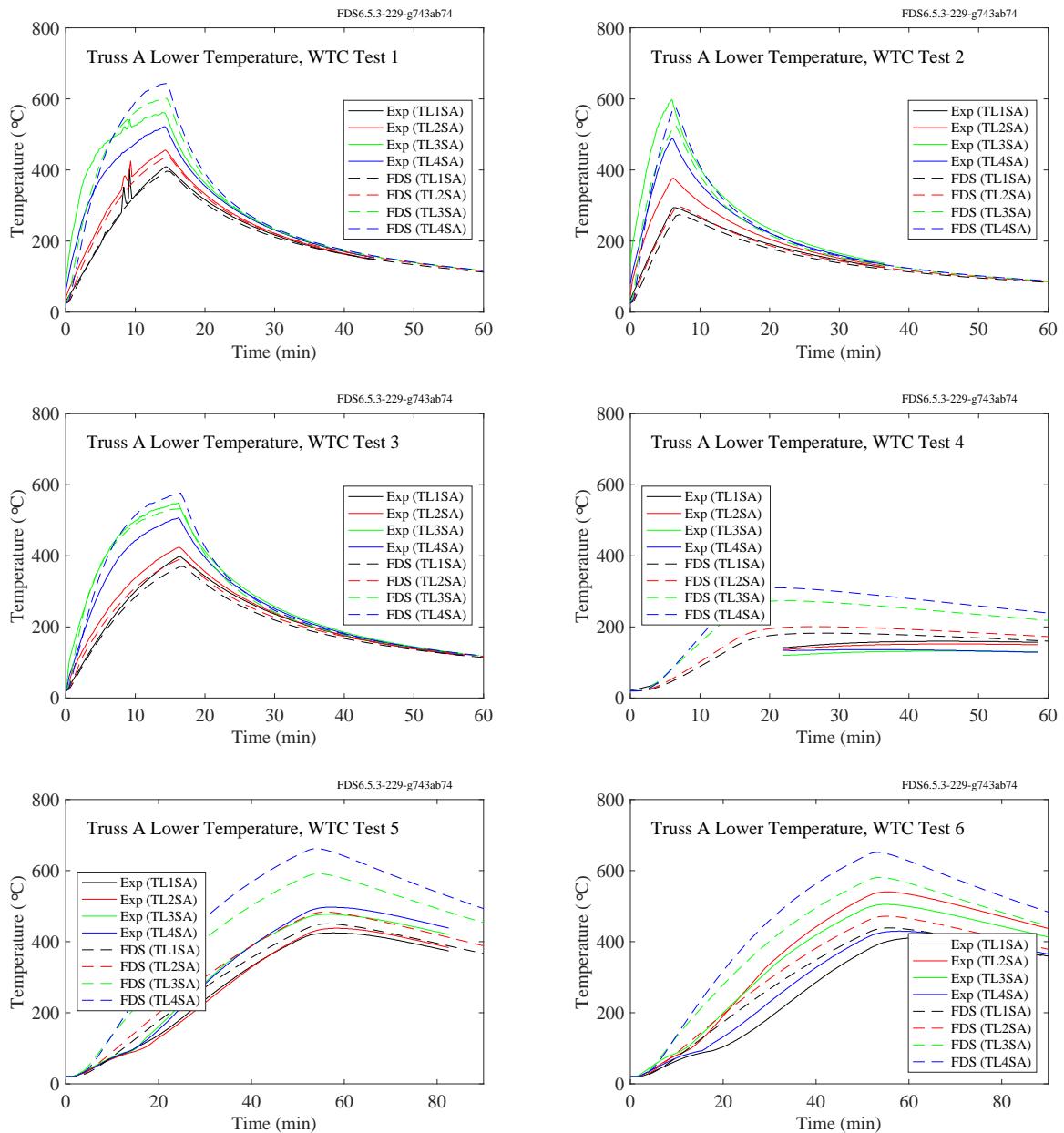


Figure 11.85: WTC experiments, steel temperatures, lower Truss A.

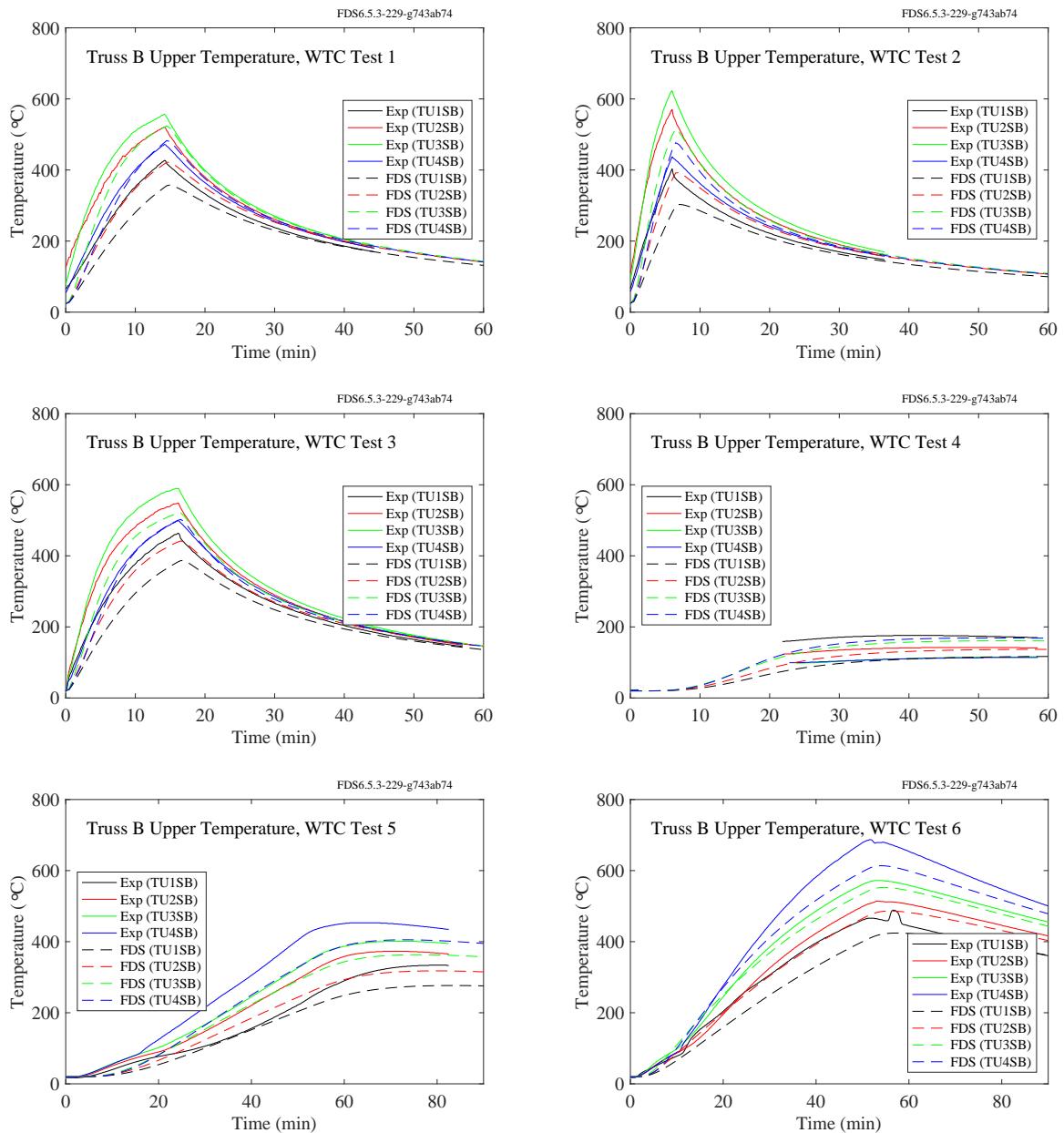


Figure 11.86: WTC experiments, steel temperatures, upper Truss B.

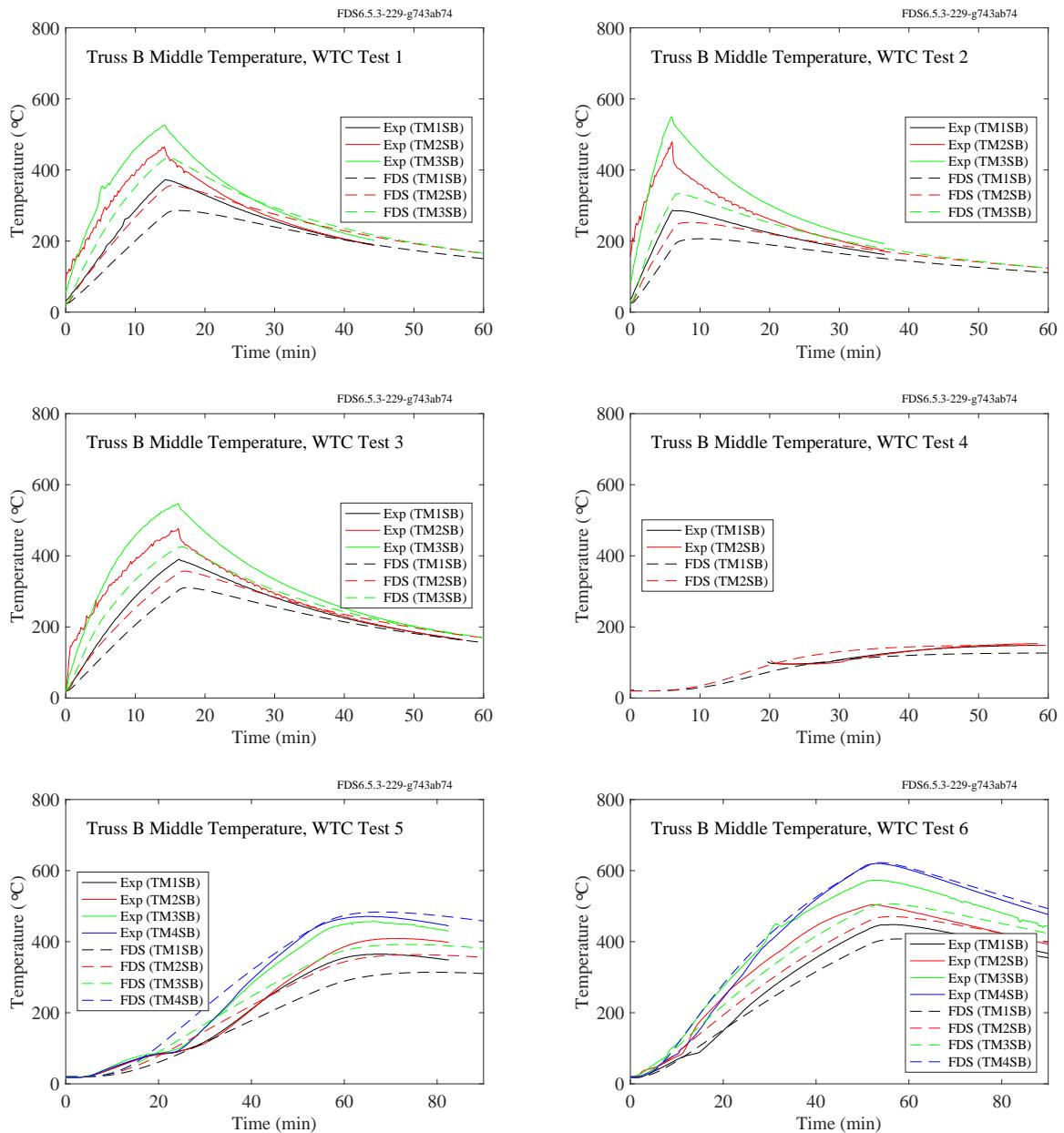


Figure 11.87: WTC experiments, steel temperatures, middle Truss B.

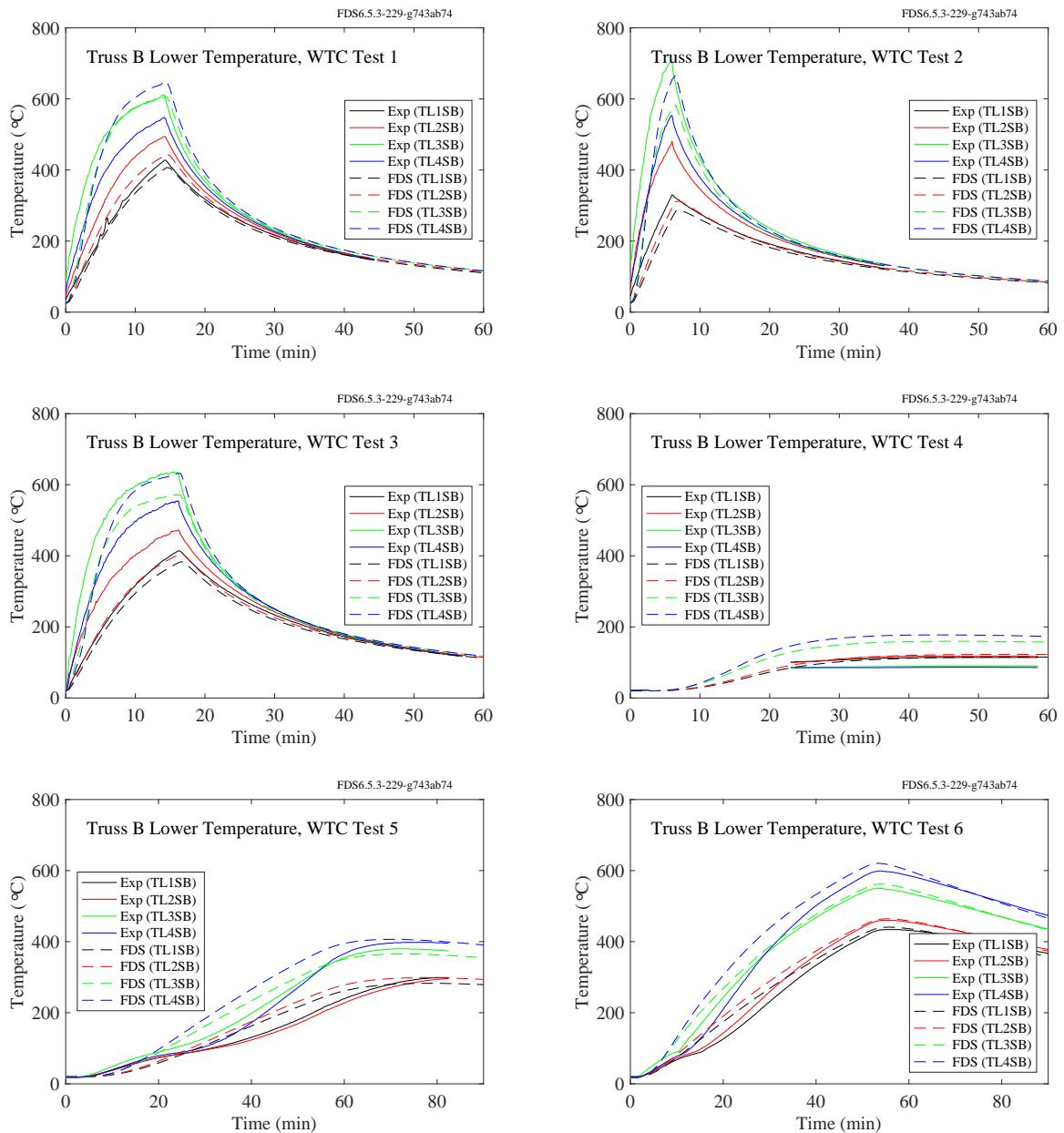


Figure 11.88: WTC experiments, steel temperatures, lower Truss B.

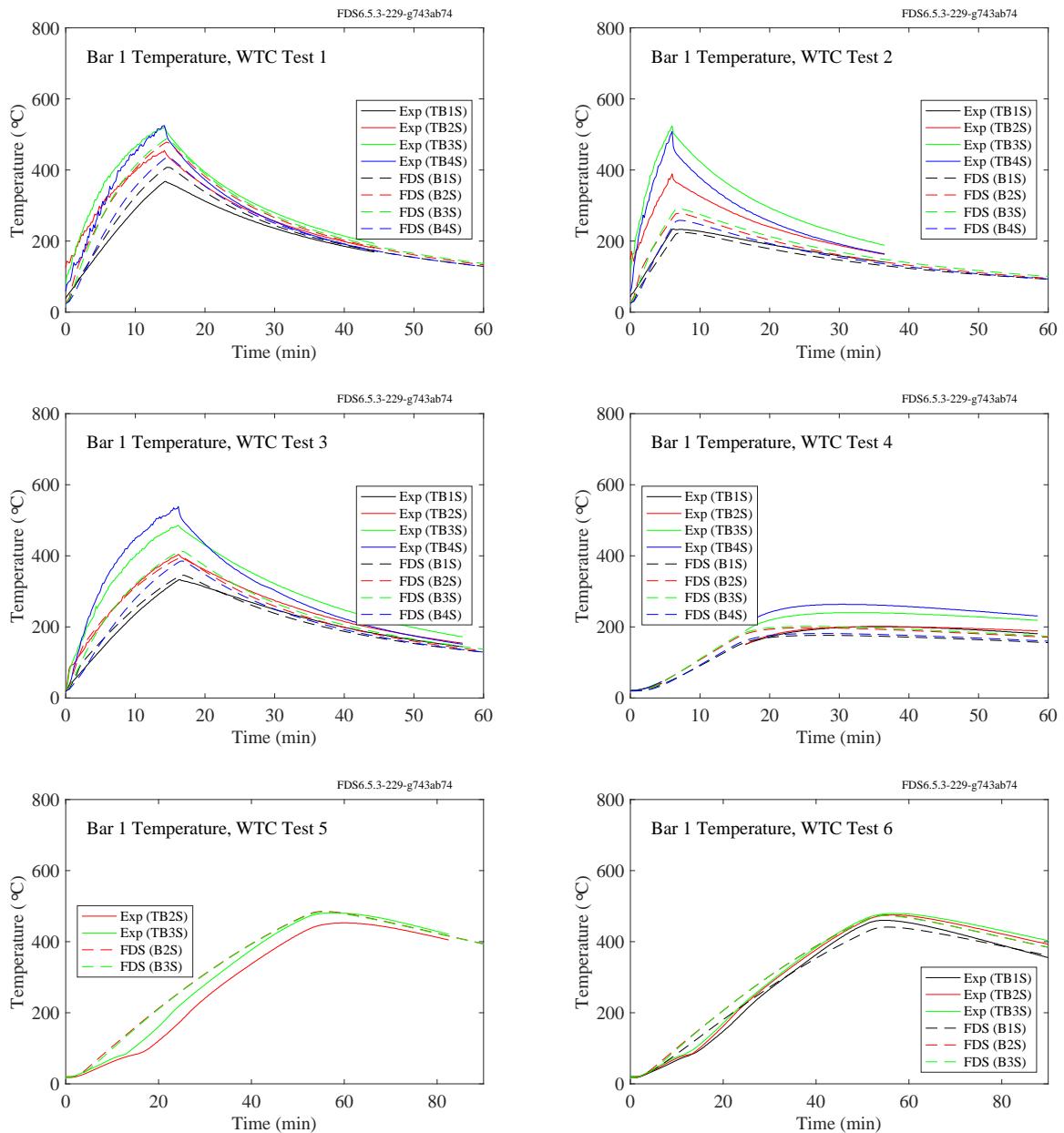


Figure 11.89: WTC experiments, steel temperatures, Bar 1.

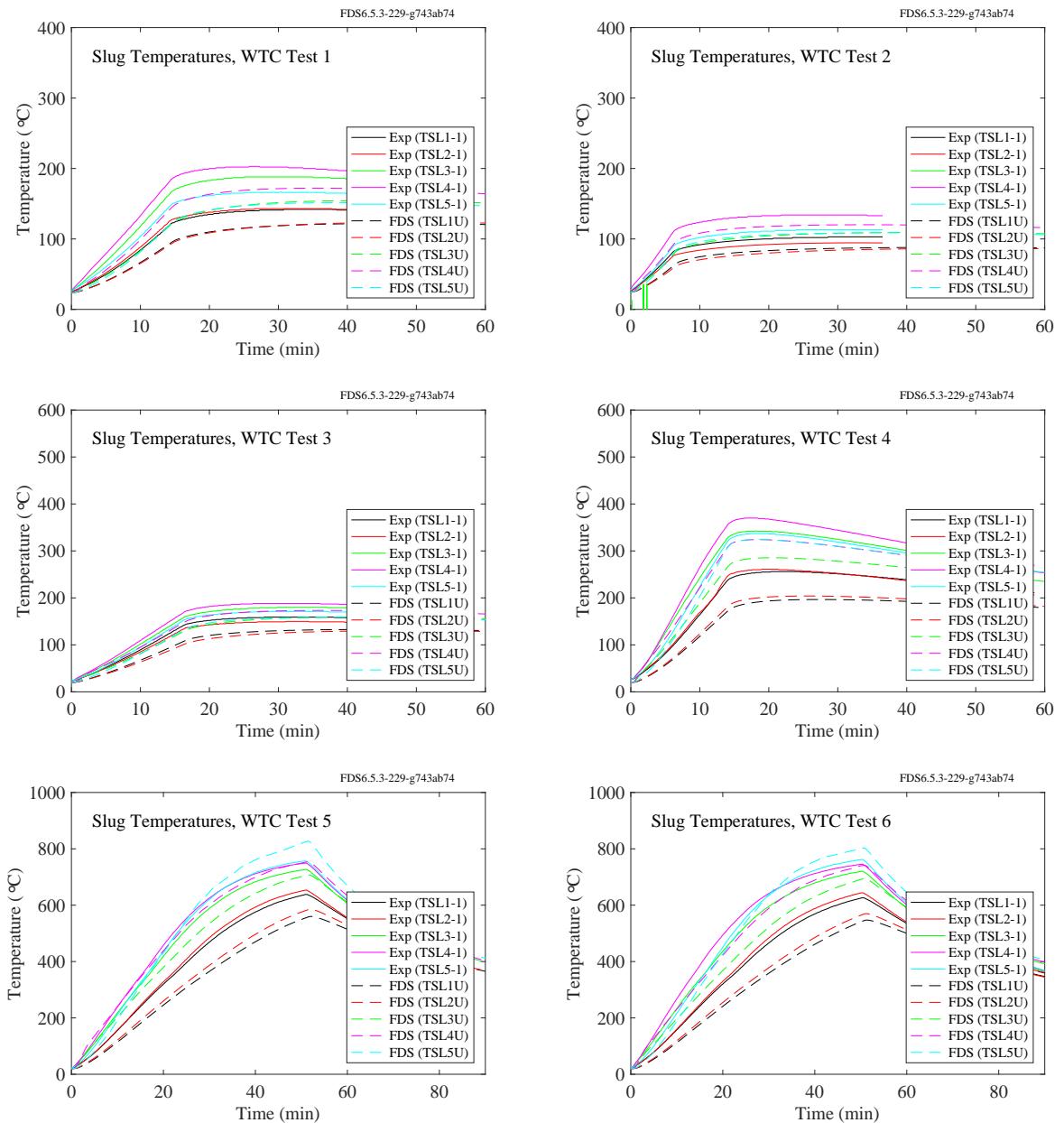


Figure 11.90: WTC experiments, slug temperatures.

#### 11.2.4 CAROLFIRE Experiments

On the following pages are predictions of the THIEF (thermally-induced electrical failure) model compared to 35 experiments conducted at Sandia National Laboratory [139]. In these experiments, an instrumented electrical cable was run through a heated cylindrical “shroud.” The shroud temperature is an input for the model, and the cable temperature (and in some cases that of the steel conduit enclosing the cable) is predicted. Note that the cables generally fall into two categories – thermoset and thermoplastic. Thermoset cables form a char layer when burned and typically fail electrically at temperatures near 400 °C. Thermoplastic cables typically melt and then burn, leaving little residue behind except the conductors. These cables typically fail between 200 °C and 250 °C. Some cables, as in Tests 18 and 31, do not fall into either category. The thermoset cables were exposed to temperatures in the neighborhood of 480 °C, and the thermoplastics were exposed to temperatures near 300 °C.

Note in the plots to follow that the objective of the calculation is to predict the cable temperature just inside of the jacket until the cable fails electrically. In some experiments, the short-circuiting of the cable led to ignition of the pyrolyzates. This behavior is not captured in the model, which is why some of the experimental data shows a rapid rise in temperature at a certain point in the test. In many cases, electrical failure occurred very shortly, or at about the same time, as ignition.

Figure 11.104 compares the measured versus predicted time to a “threshold” temperature. The threshold temperature is 400 °C for thermoset cables and 200 °C for thermoplastics.

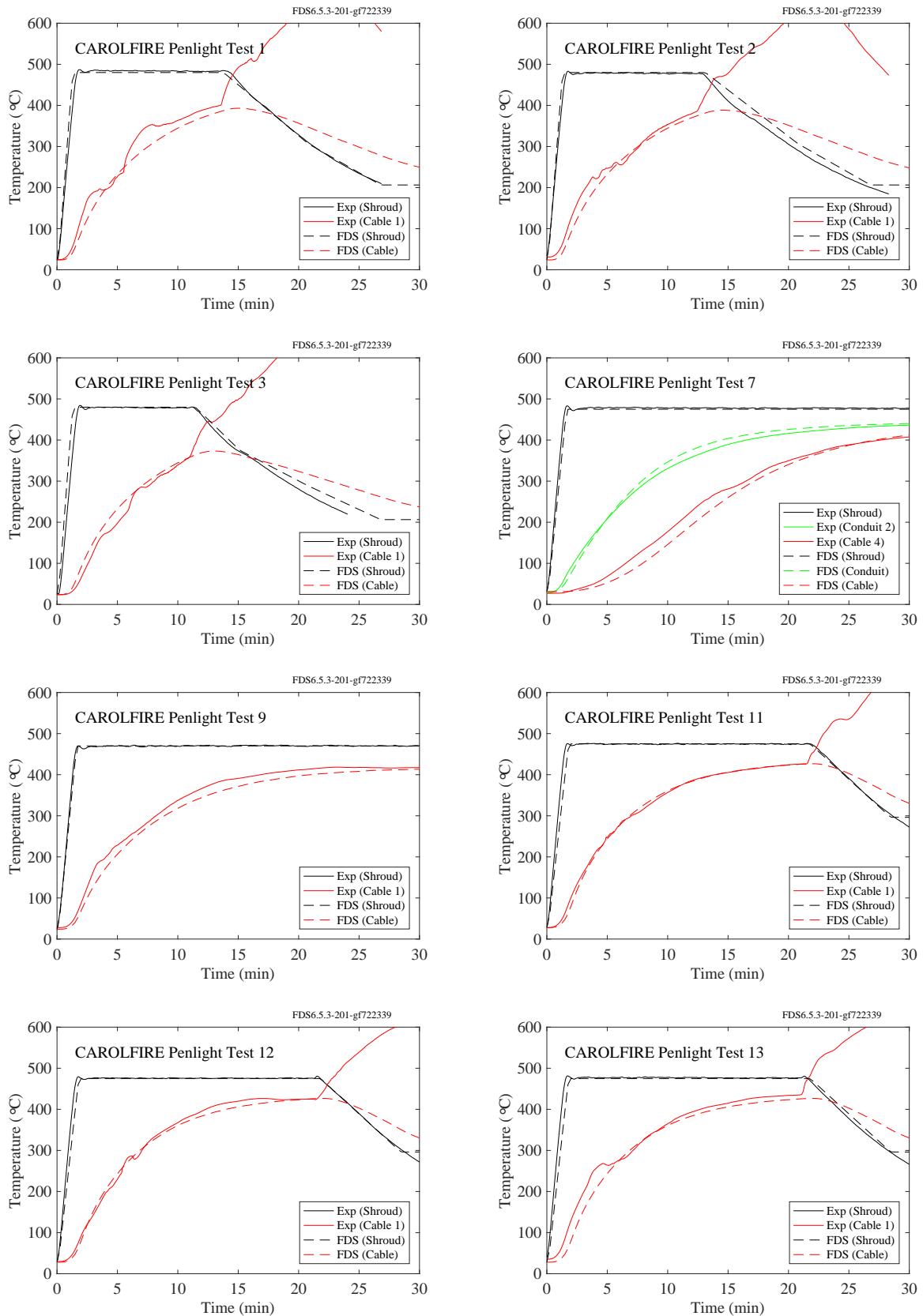


Figure 11.91: CAROLFIRE, electrical cable temperatures, Penlight Tests 1, 2, 3, 7, 9, 11-13.

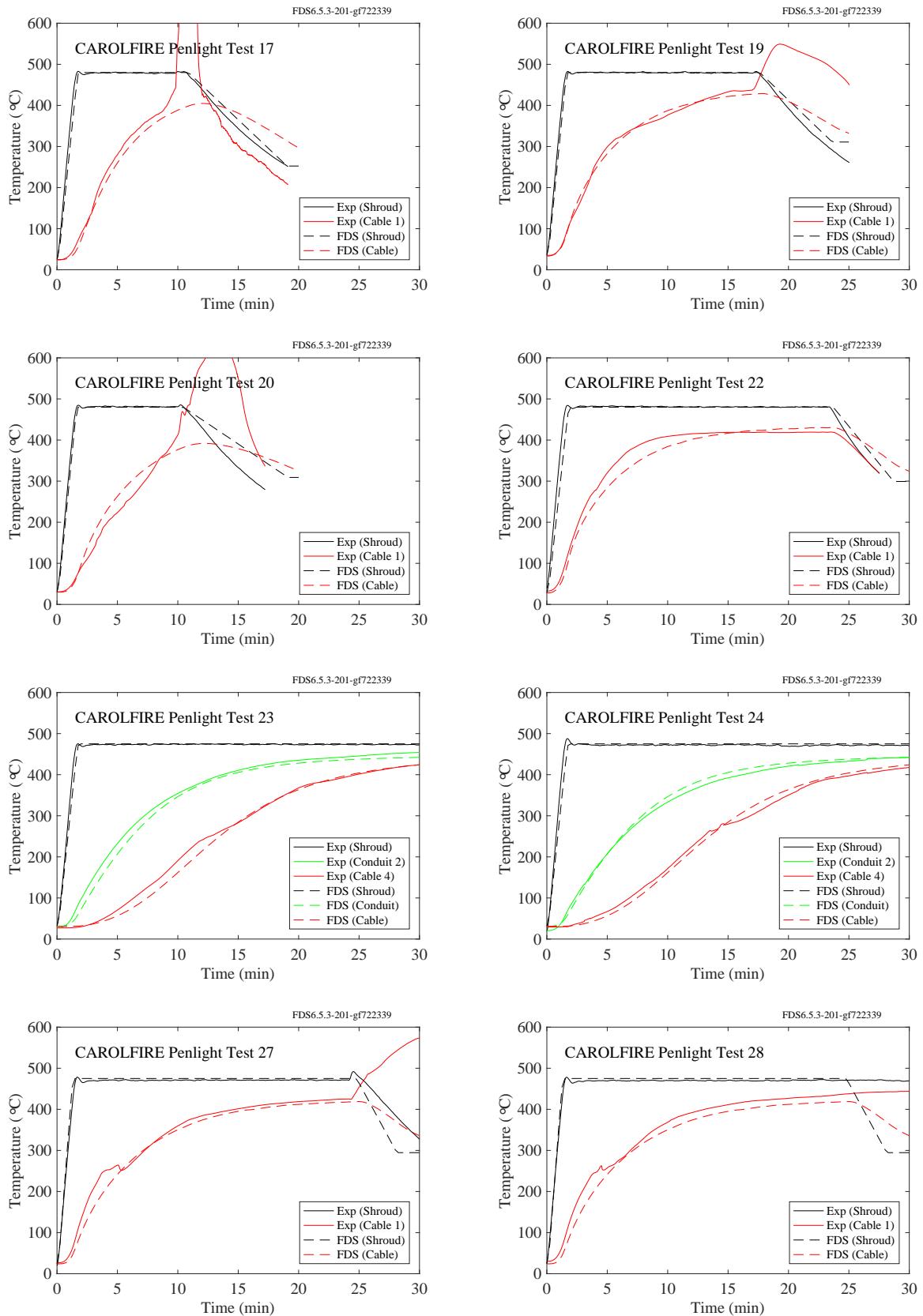


Figure 11.92: CAROLFIRE, electrical cable temperatures, Penlight Tests 17, 19-20, 22-24, 27-28.

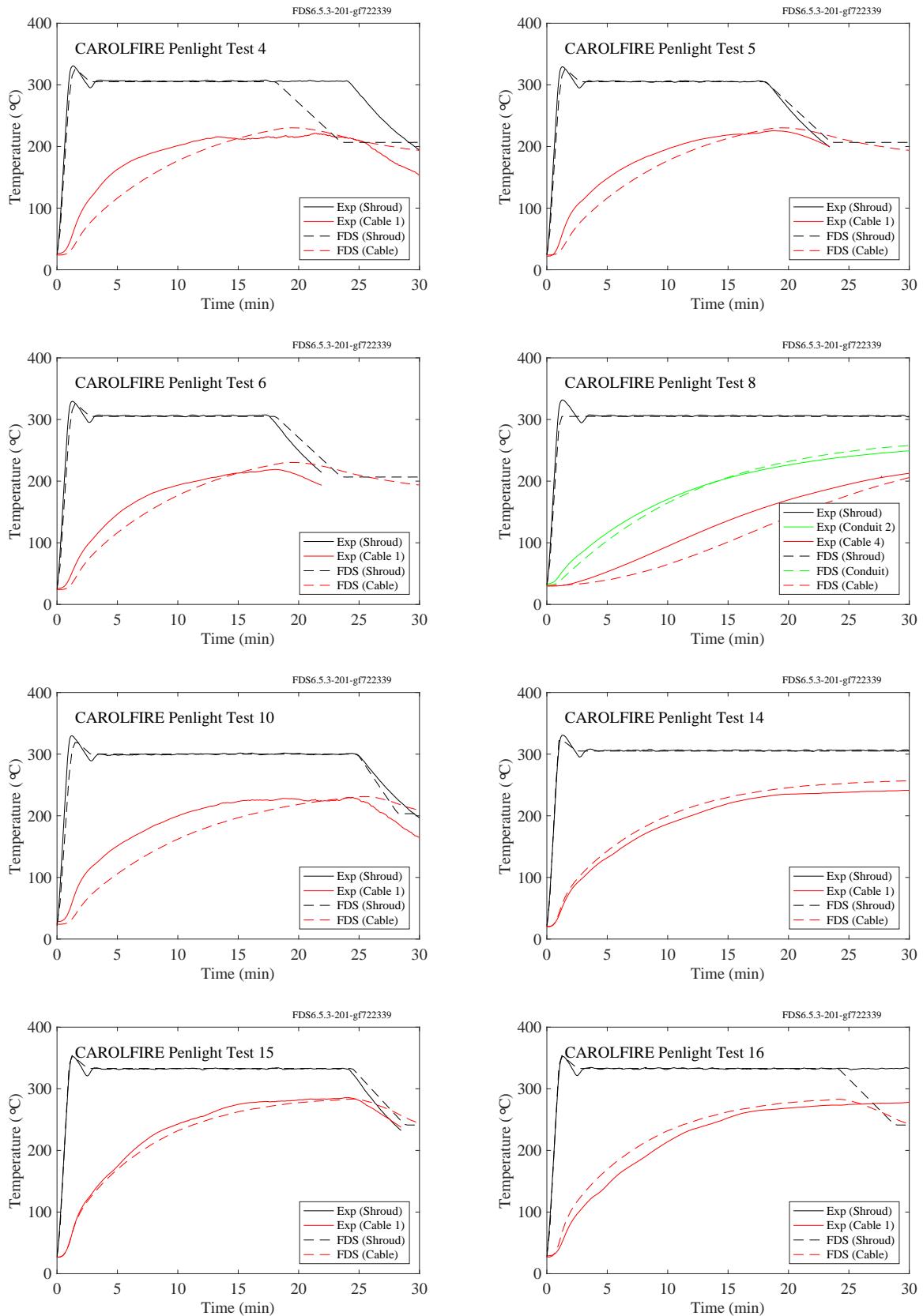


Figure 11.93: CAROLFIRE, electrical cable temperatures, Penlight Tests 4-6, 8, 10, 14-16.

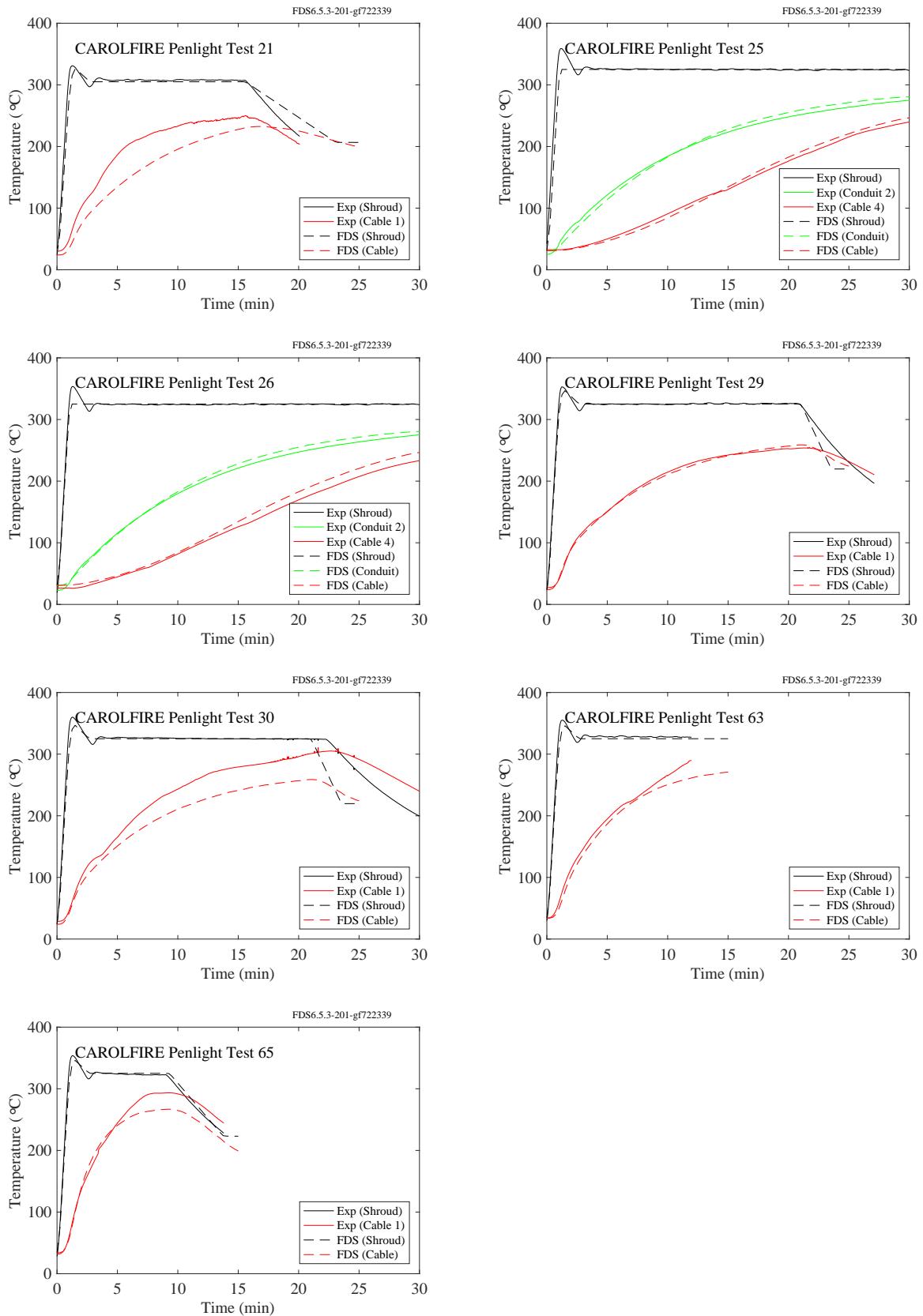


Figure 11.94: CAROLFIRE, electrical cable temperatures, Penlight Tests 21, 25-26, 29-30, 63, 65.

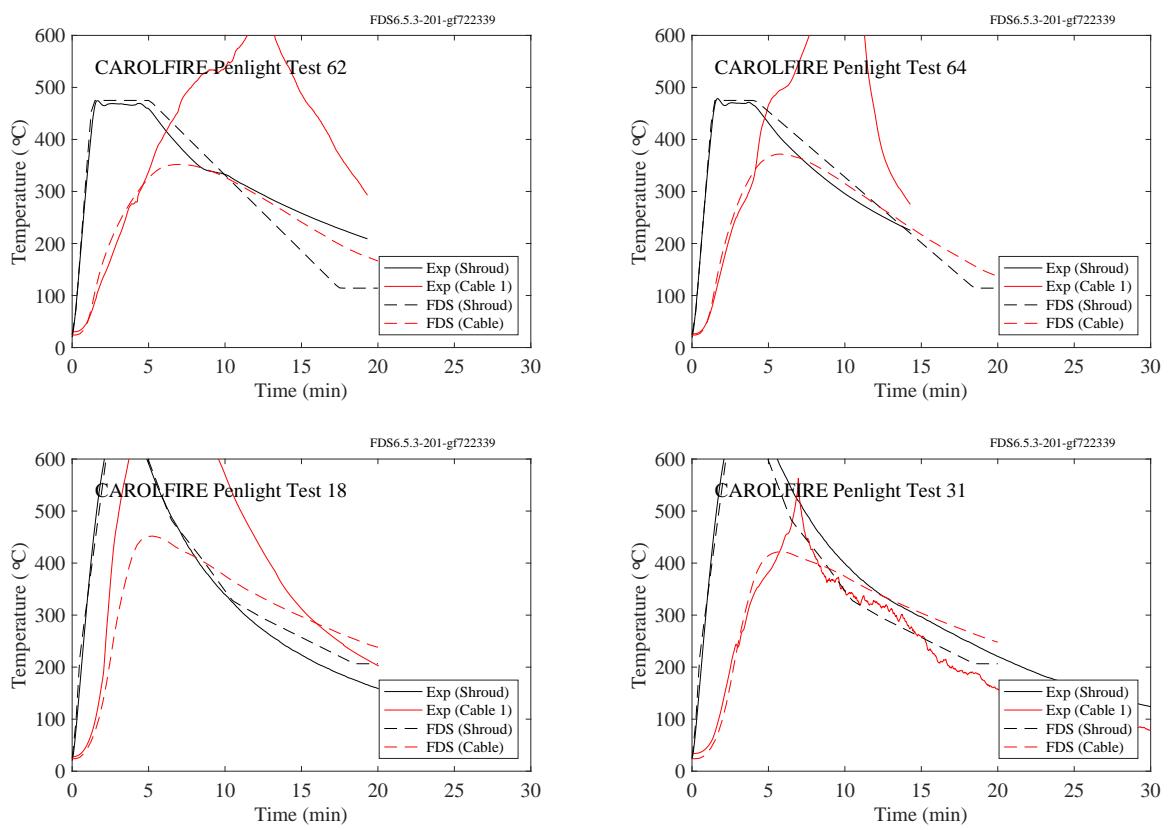


Figure 11.95: CAROLFIRE, electrical cable temperatures, Penlight Tests 18, 31, 62, 64.

### 11.2.5 PRISME Experiments

In most of the PRISME experiments, instrumented electrical cables were laid within trays at various heights in the test compartment. For the PRISME LEAK series of experiments (Figs. 11.96 and 11.97), the gas temperature in the vicinity of the cables was measured and served as the exposing heat source for calculations using the THIEF (Thermally-Induced Electrical Failure) model [185].

For the PRISME Door experiments, the temperatures of surrogate cables were predicted directly from the predicted thermal environment of the entire compartment. The measurement points in these experiments were labelled, for example, TCA\_L2\_HE\_SURF, meaning thermocouple of the “analytical” cable, compartment 2, *haut* (high), east, surface. BW means *bas* (low) west, for example. Thermocouples were positioned on the cable surface (SURF), halfway towards center (INTER), and center (CENTRE).

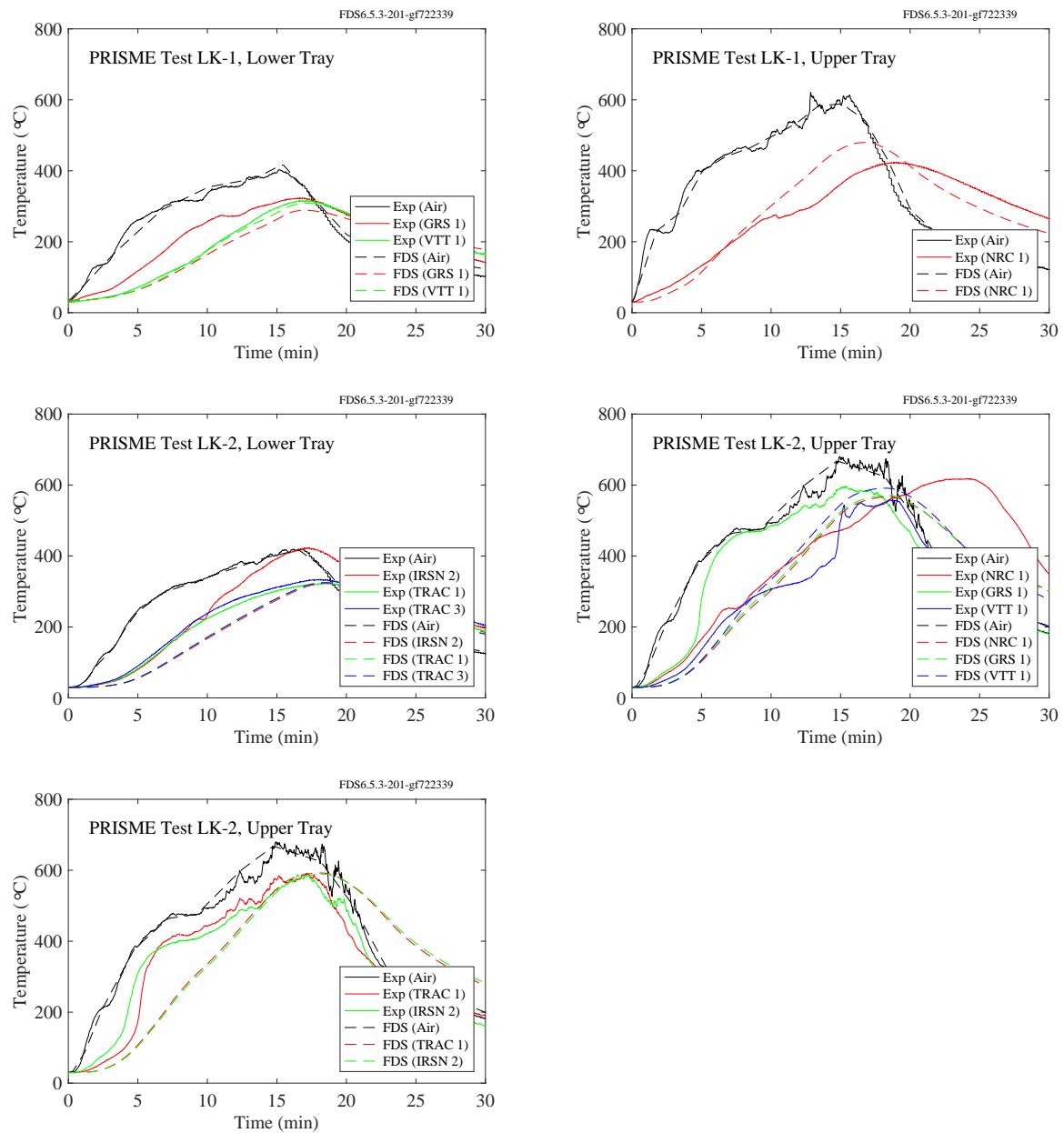


Figure 11.96: PRISME LEAK experiments, cable temperature, Tests 1 and 2.

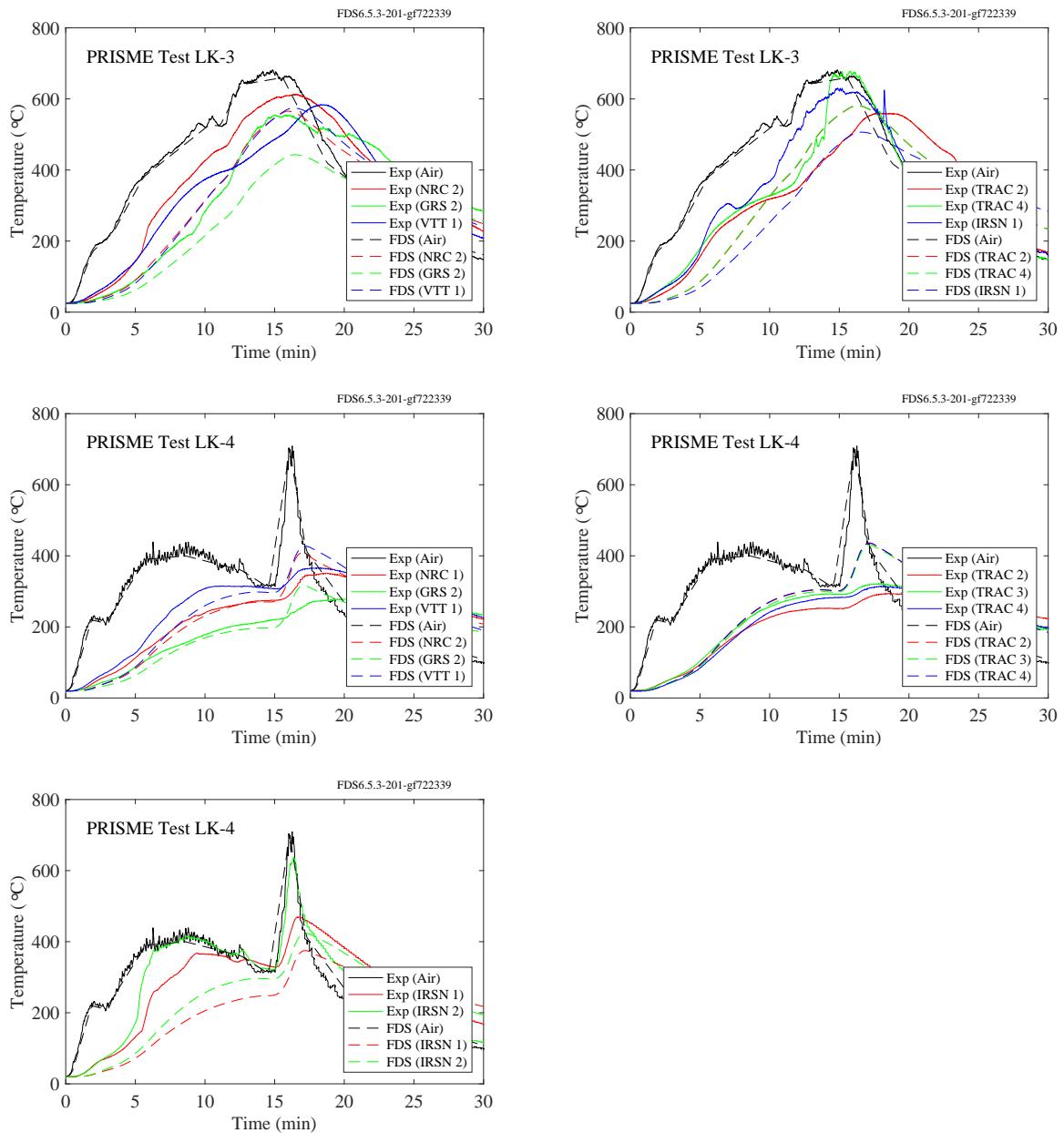


Figure 11.97: PRISME LEAK experiments, cable temperature, Tests 3 and 4.

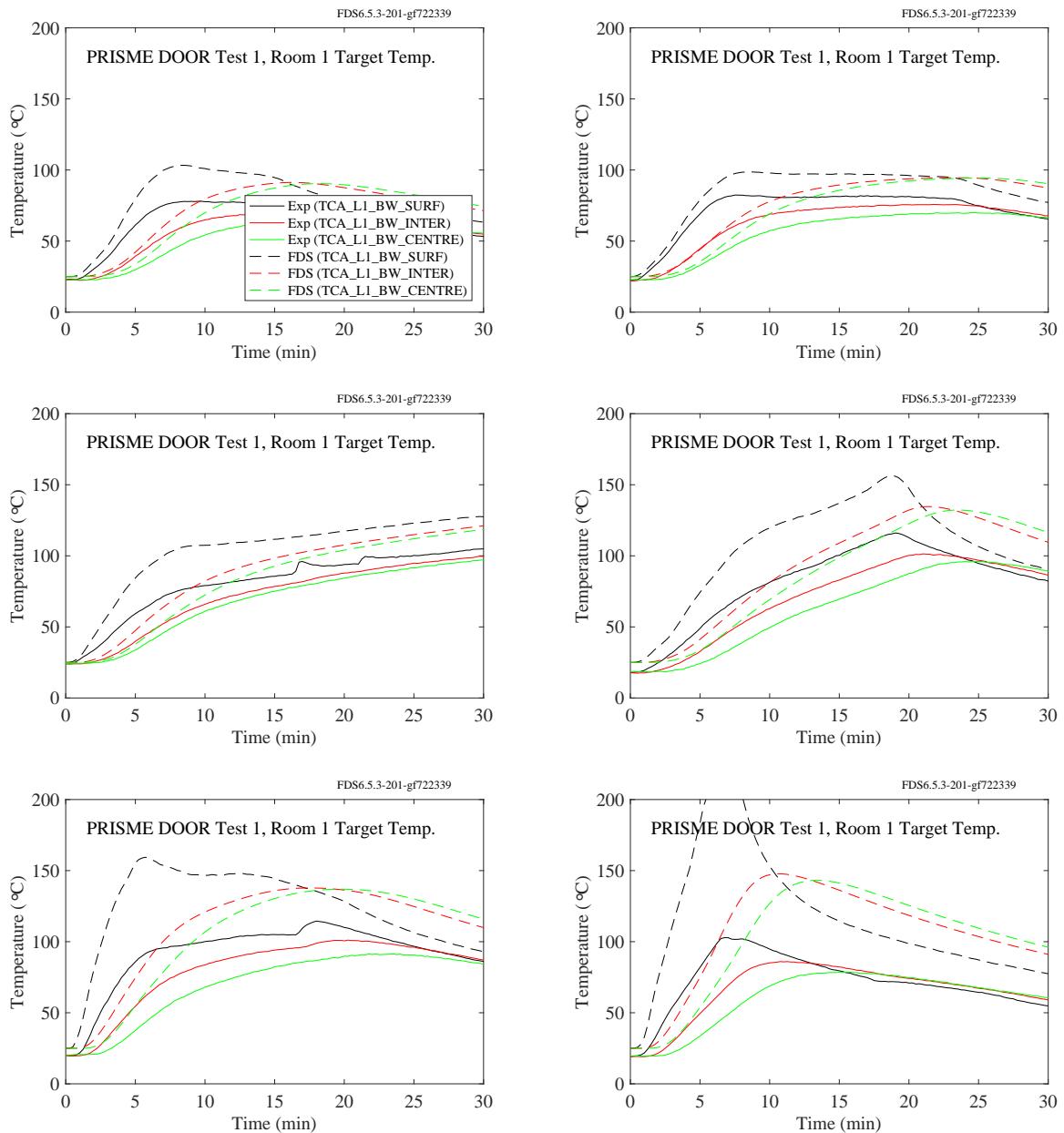


Figure 11.98: PRISME DOOR experiments, cable temperature, Room 1, Cable BW.

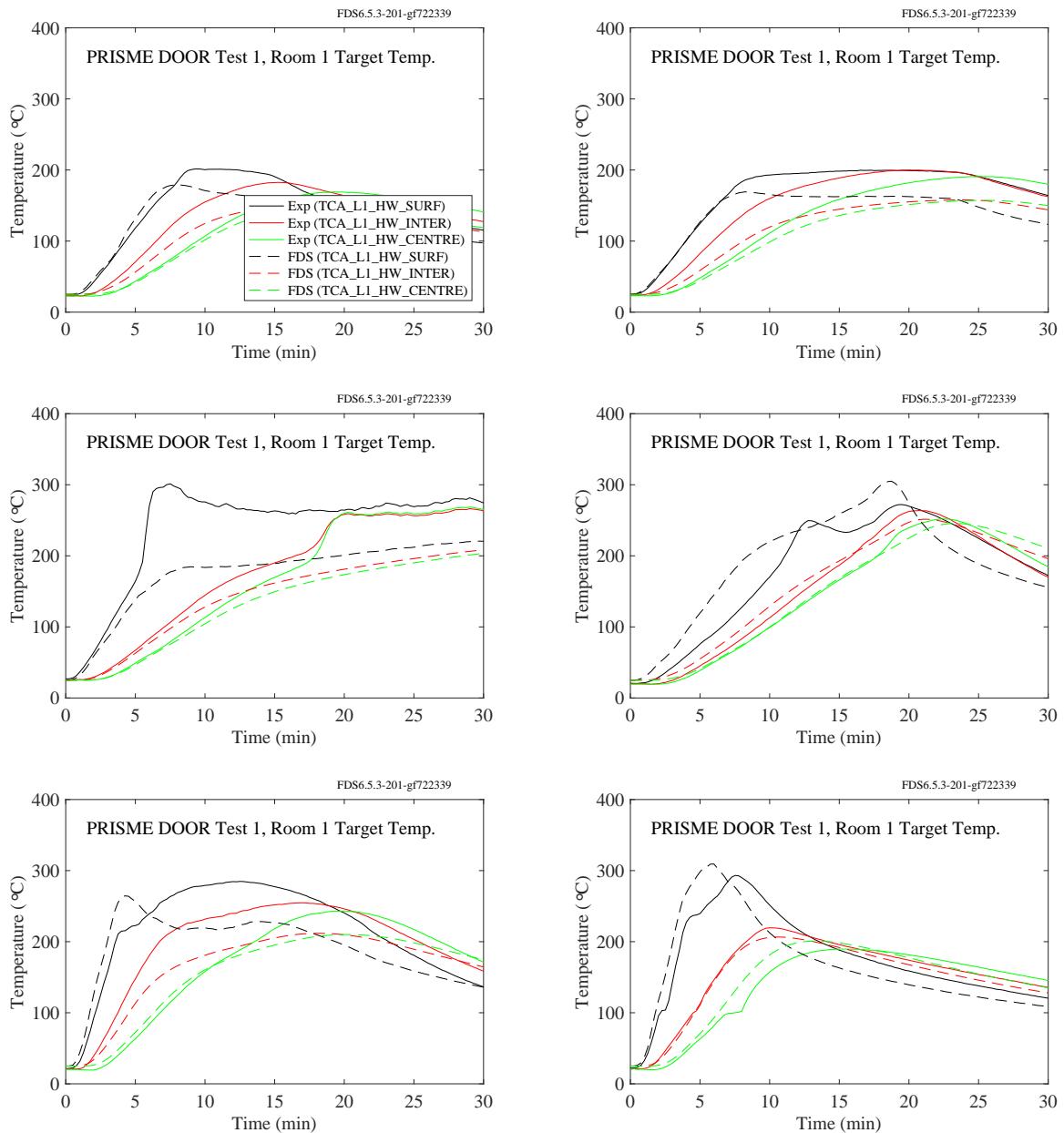


Figure 11.99: PRISME DOOR experiments, cable temperature, Room 1, Cable HW.

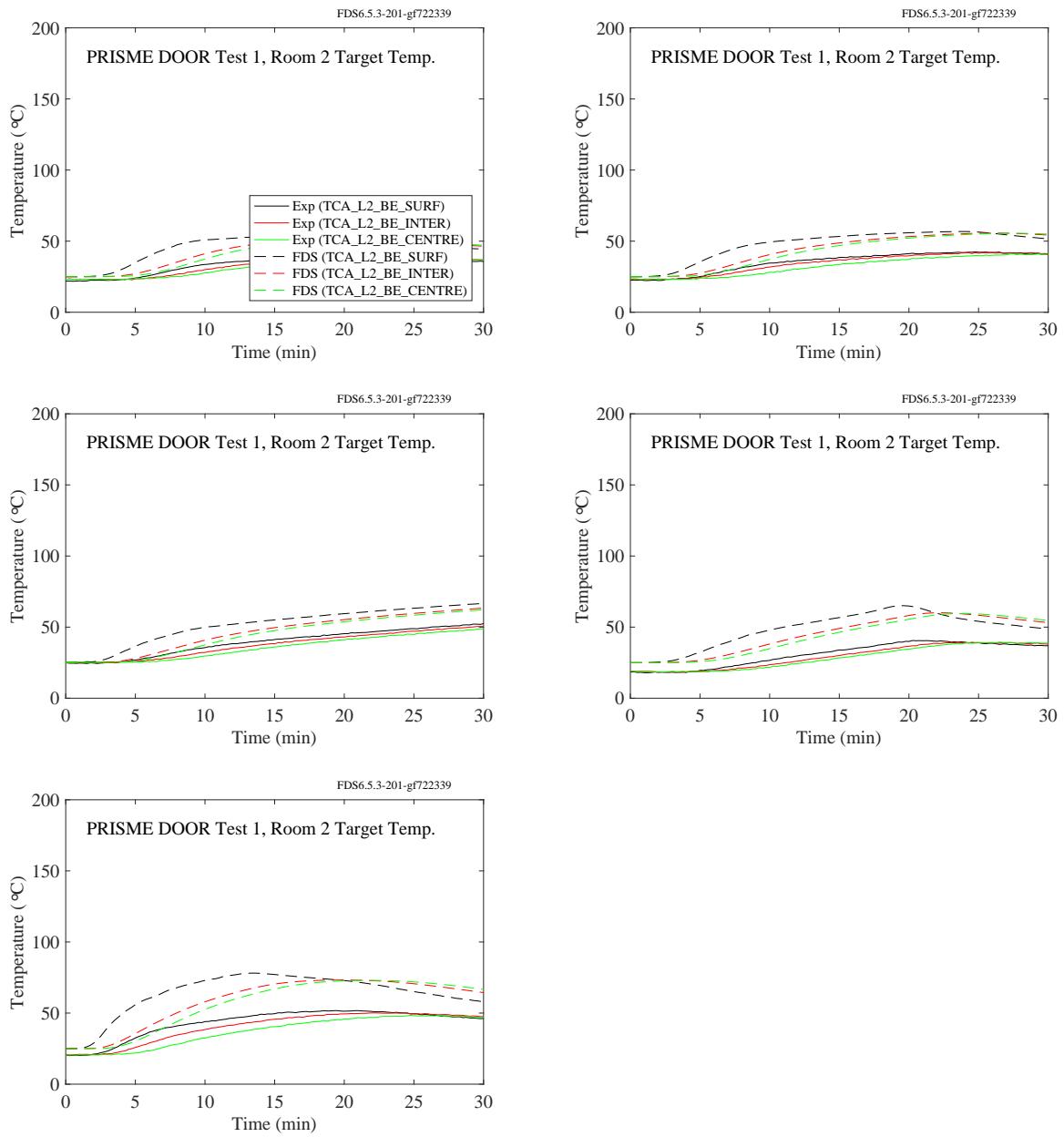


Figure 11.100: PRISME DOOR experiments, cable temperature, Room 2, Cable BE.

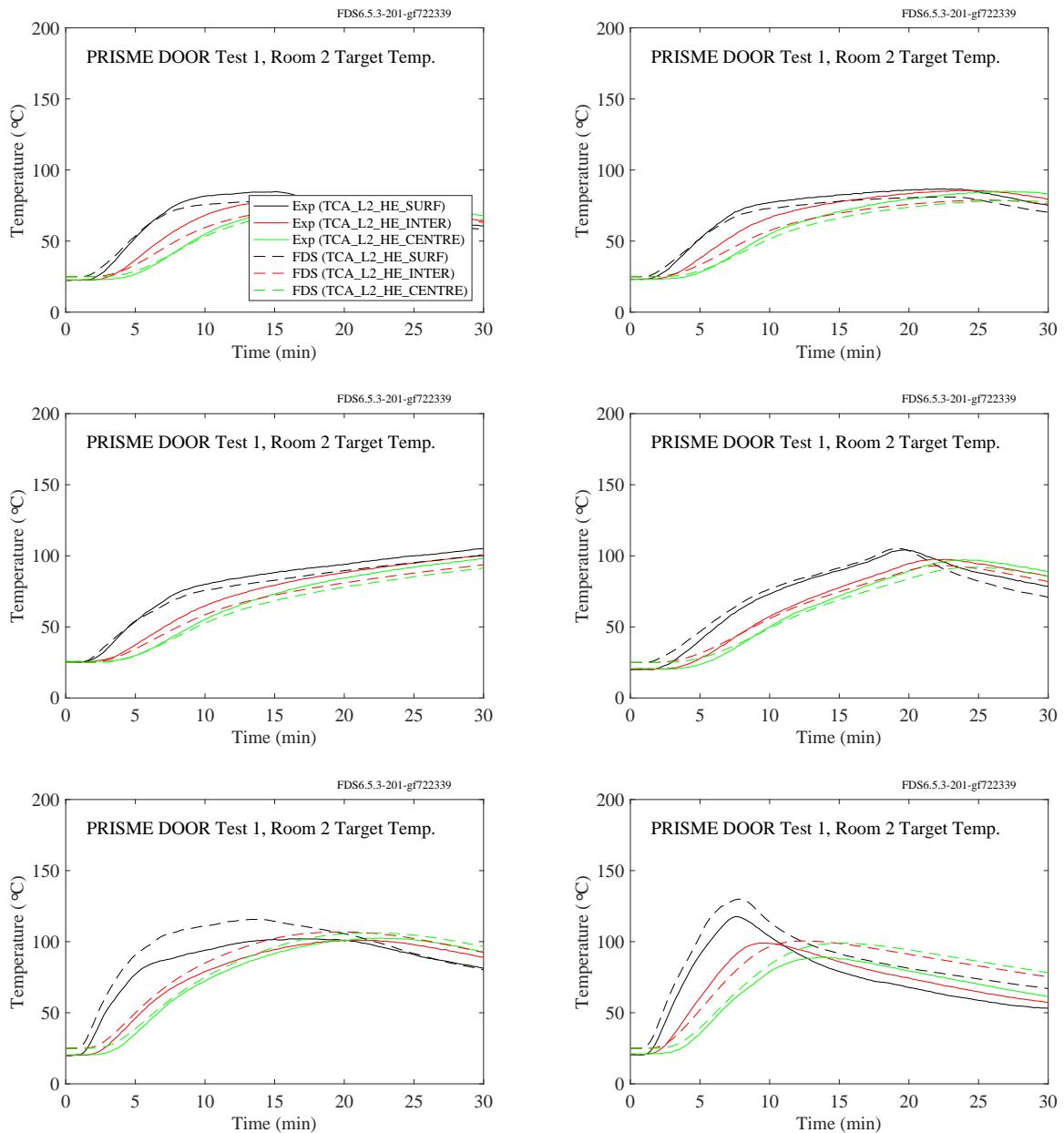


Figure 11.101: PRISME DOOR experiments, cable temperature, Room 2, Cable HE.

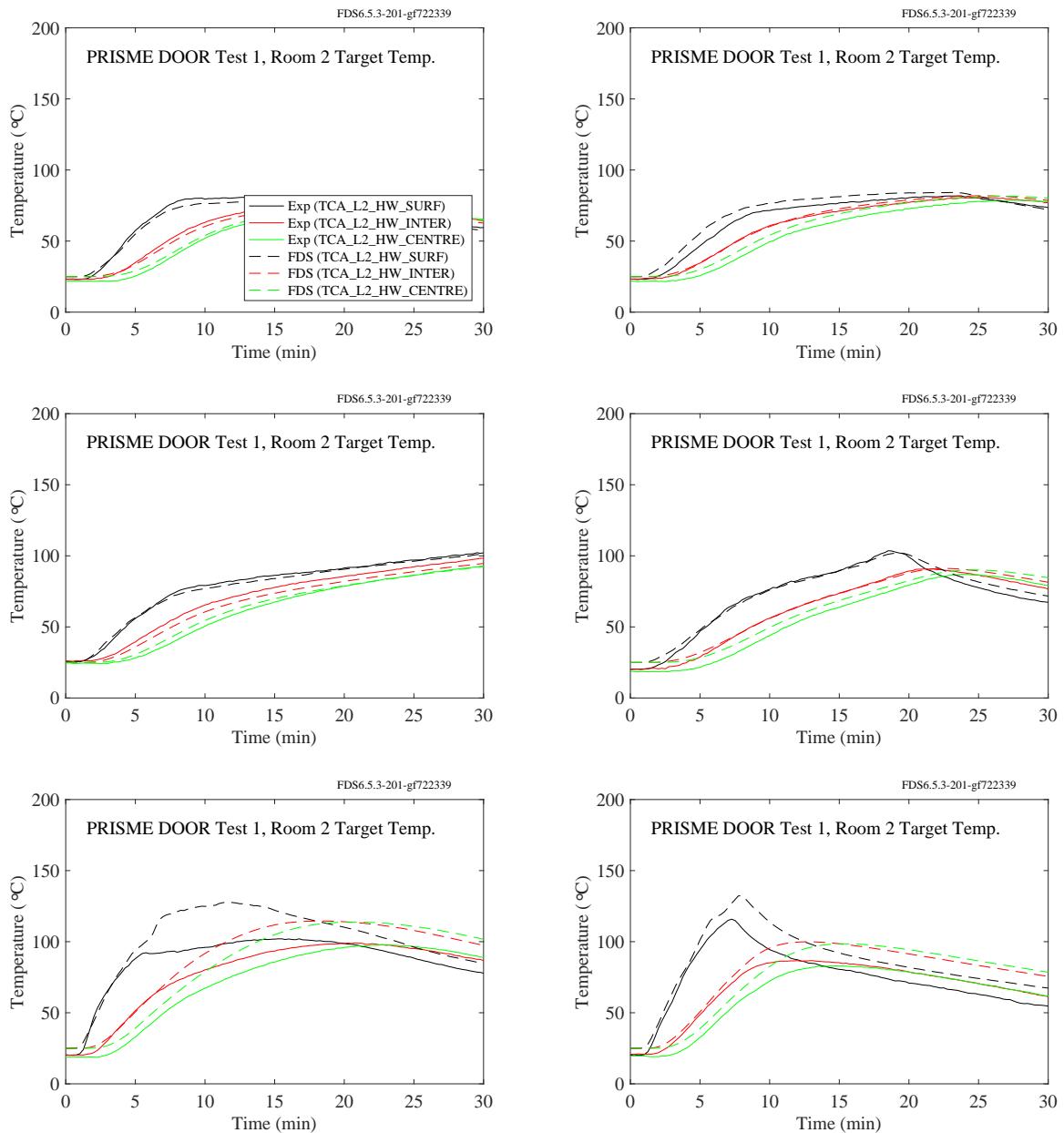


Figure 11.102: PRISME DOOR experiments, cable temperature, Room 2, Cable HW.

### 11.2.6 Summary of Target Temperature Predictions

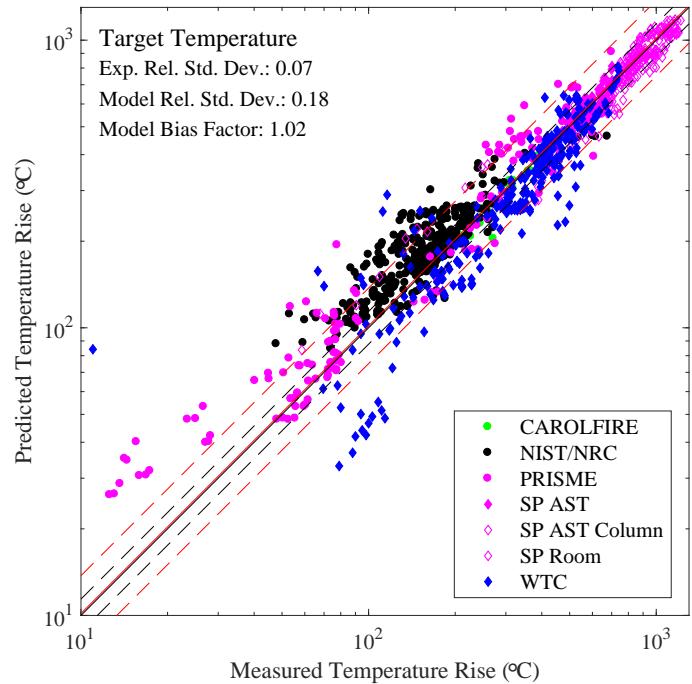


Figure 11.103: Summary of target temperature predictions.

### 11.2.7 Time to Failure

In addition to comparing the peak temperature predictions and measurements for electrical cables, it is also useful to consider the uncertainty in predicting the time to cable failure. Obviously, the two quantities are related, but from a practical standpoint, it is the time to failure that is of interest in these types of analyses. Figure 11.104 displays results for the CAROLFIRE experiments.

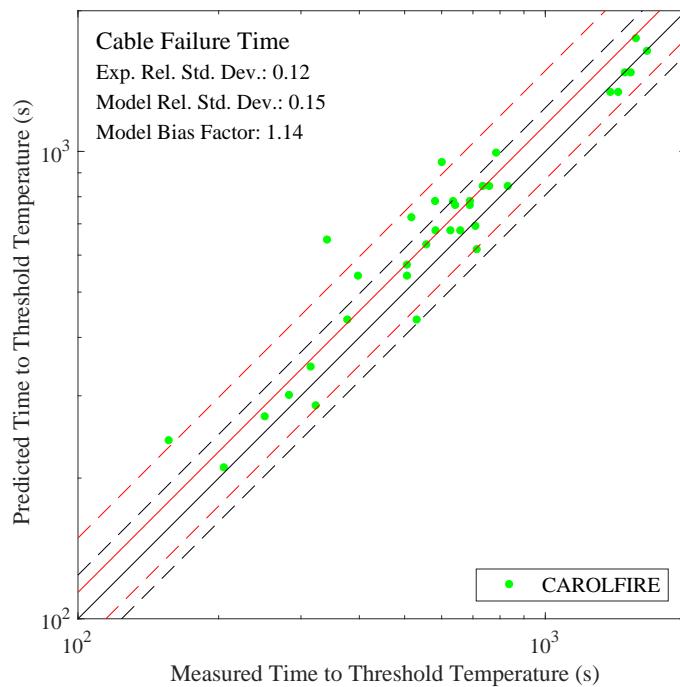


Figure 11.104: Summary of time to failure predictions for electrical cables.

## **Chapter 12**

# **Heat Flux**

Radiative heat transfer is included in FDS via the solution of the radiation transport equation for a gray gas, and in some limited cases using a wide band model. The equation is solved using a technique similar to finite volume methods for convective transport, thus the name given to it is the Finite Volume Method (FVM). Using approximately 100 discrete angles, the finite volume solver requires about 20 % of the total CPU time of a calculation, a modest cost given the complexity of radiation heat transfer. The absorption coefficients of the gas-soot mixtures are computed using the RadCal narrow-band model. Liquid droplets can absorb and scatter thermal radiation. This is important in cases involving mist sprinklers, but also plays a role in all sprinkler cases. The absorption and scattering coefficients are based on Mie theory.

This chapter contains a wide variety of heat flux measurements, ranging from less than a  $\text{kW/m}^2$  from very small methane gas burners up to about  $150 \text{ kW/m}^2$  in full-scale compartment fires.

## 12.1 Heat Flux to Walls, Ceiling, and Floor

### 12.1.1 FAA Cargo Compartments

Measurements of heat flux and surface temperature were made at two ceiling locations (denoted A and B in Fig. 7.10). The heat flux measurements are shown below.

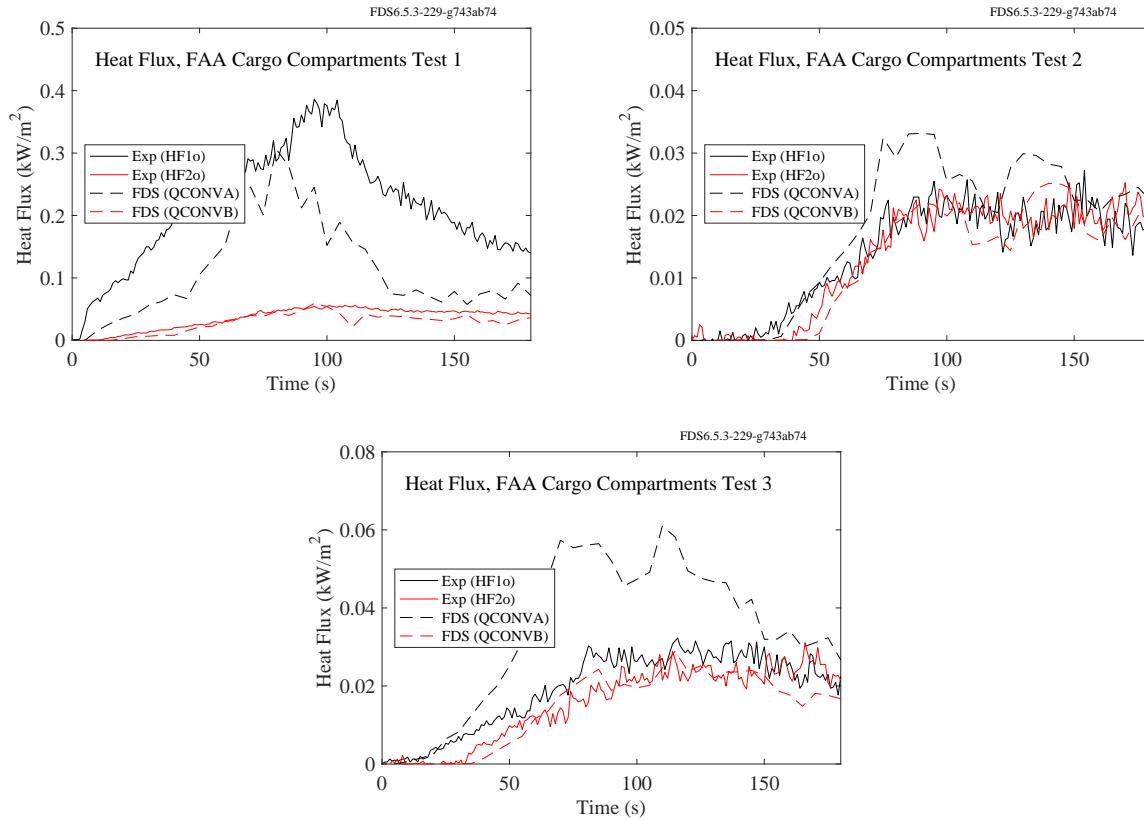


Figure 12.1: FAA Cargo Compartment experiments, heat flux to ceiling.

### 12.1.2 FM Parallel Panel Experiments

Predicted and measured vertical heat flux profiles for three propane and three propylene fires (30 kW, 60 kW, and 100 kW) sandwiched between two 2.4 m high, 0.6 m wide panels are presented below.

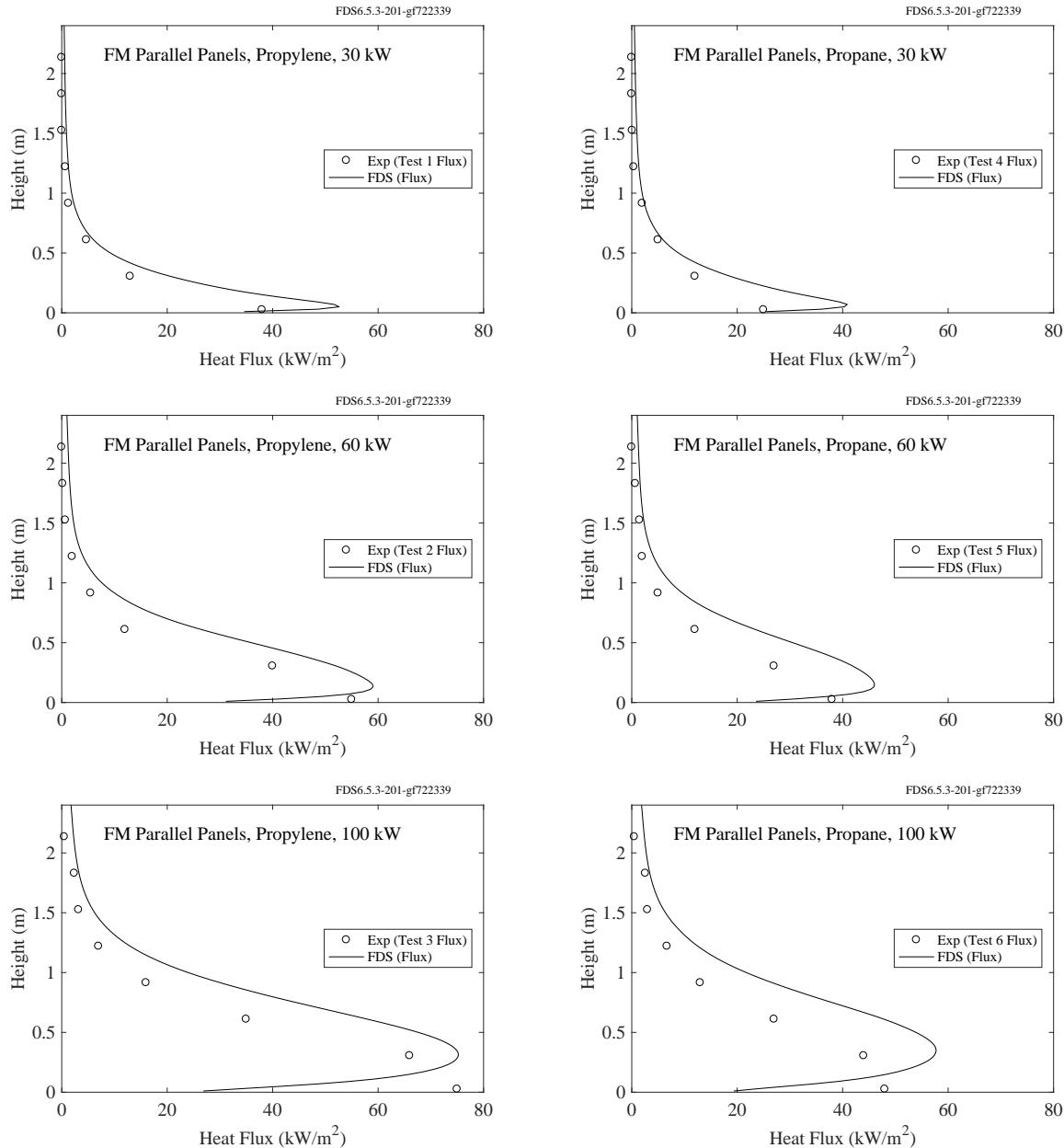


Figure 12.2: FM Parallel Panel experiments, side wall heat flux.

### 12.1.3 NIST/NRC Experiments

Heat flux gauges and thermocouples were positioned at various locations on the walls, floor, and ceiling of the compartment. The locations are given in Table 11.1. The heat flux gauges were not water cooled; thus, they measured the *net* rather than the *gauge* heat flux. However, the net heat flux is a function of the temperature of the heat flux gauge itself, which is not something that is modeled. To better compare model and measurement, the measured net heat flux is converted into a gauge heat flux using the following formula:

$$\dot{q}_{\text{gauge}}'' = \dot{q}_{\text{net}}'' + \sigma \left( T_{\text{gauge}}^4 - T_{\infty}^4 \right) + h (T_{\text{gauge}} - T_{\infty}) \quad \text{kW/m}^2 \quad (12.1)$$

where  $\sigma = 5.67 \times 10^{-11} \text{ kW/m}^2/\text{K}^4$  and  $h = 0.005 \text{ kW/m}^2/\text{K}$ .

Also, over the course of 15 experiments, numerous heat flux gauges failed, most often due to loss of contact with the wall or faulty thermocouples. All of the measurements from Test 13 and 16 were found to be flawed.

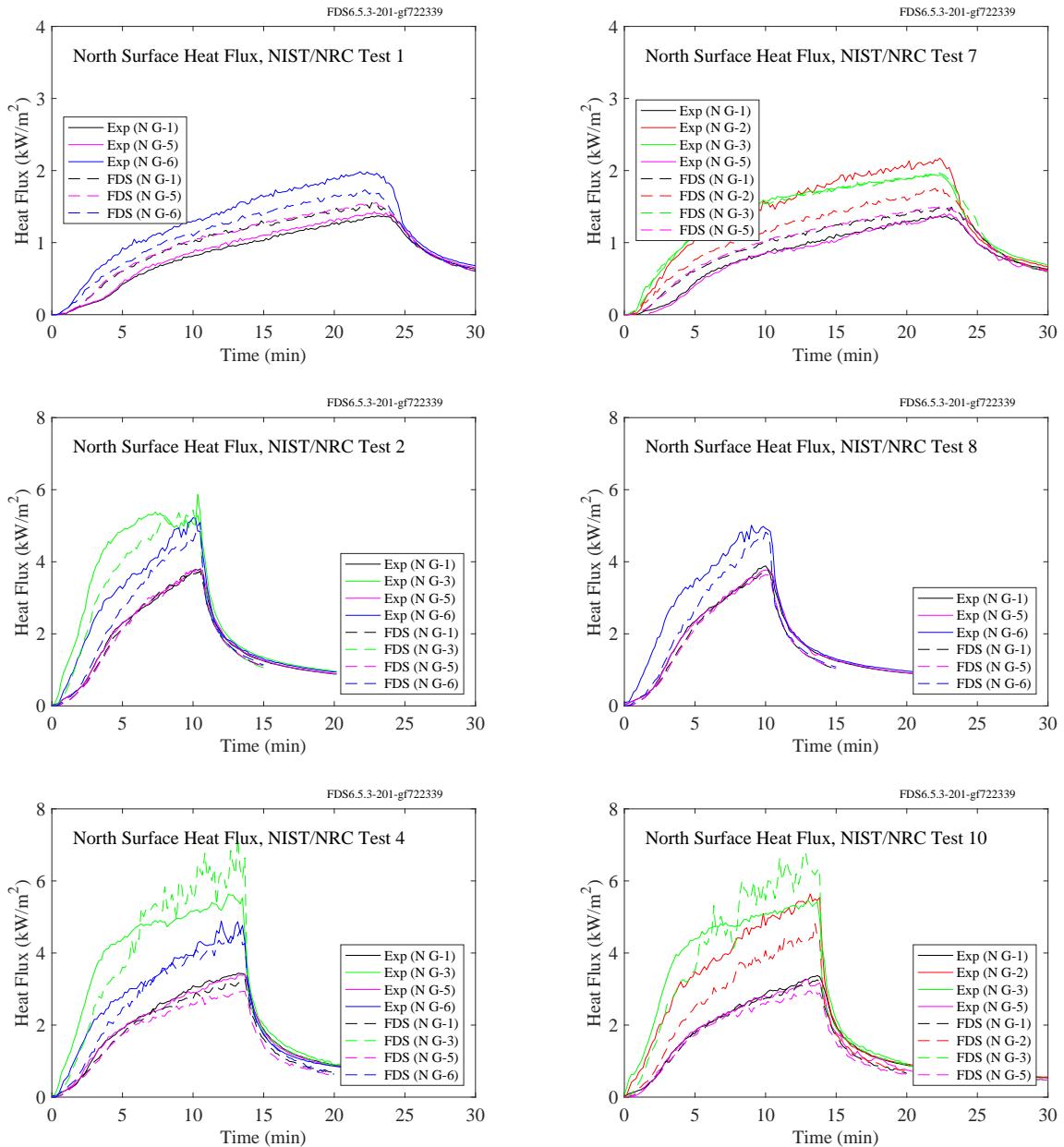


Figure 12.3: NIST/NRC experiments, heat flux to north wall, Tests 1, 2, 4, 7, 8, 10.

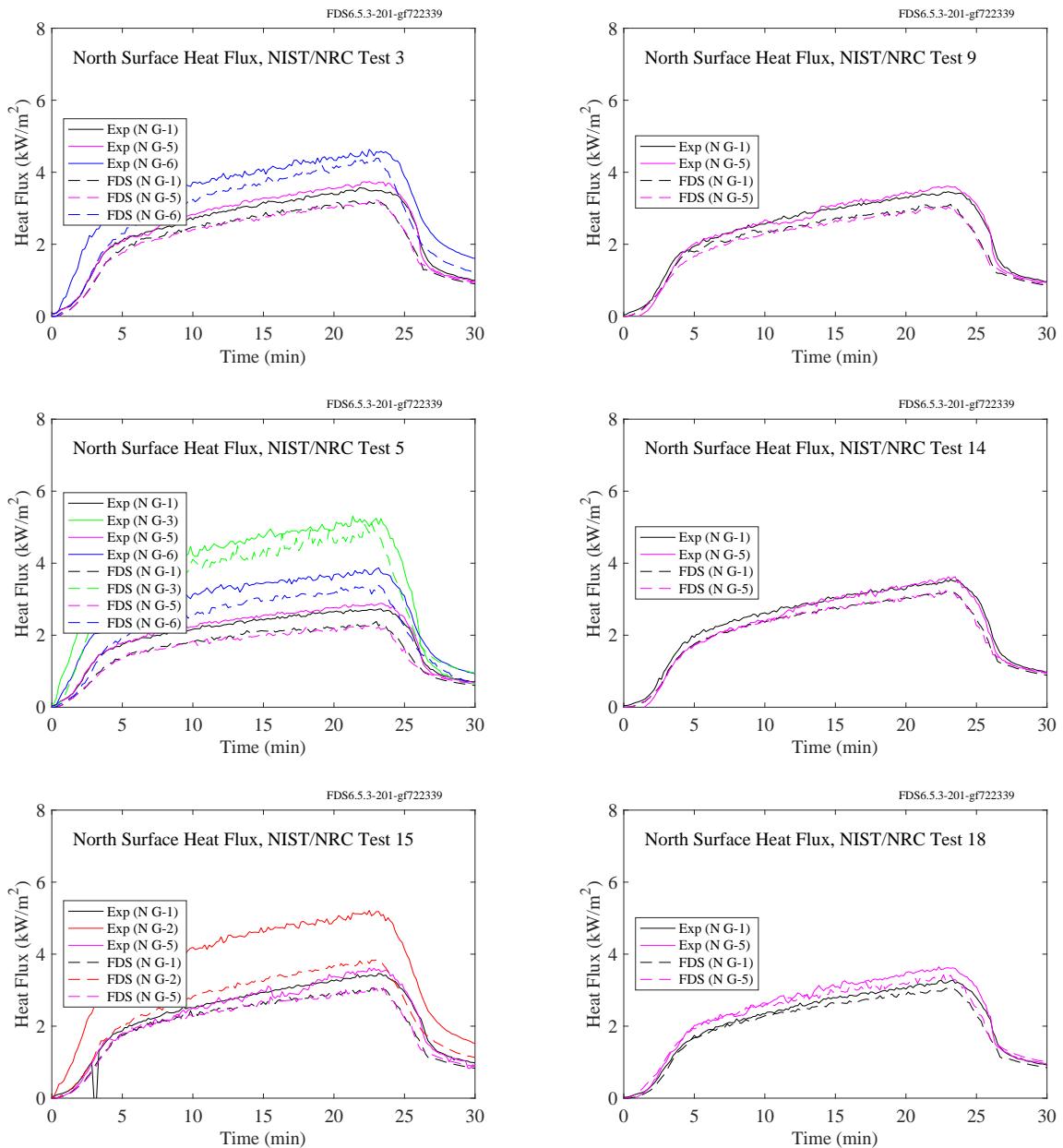


Figure 12.4: NIST/NRC experiments, heat flux to north wall, Tests 3, 5, 9, 14, 15, 18.

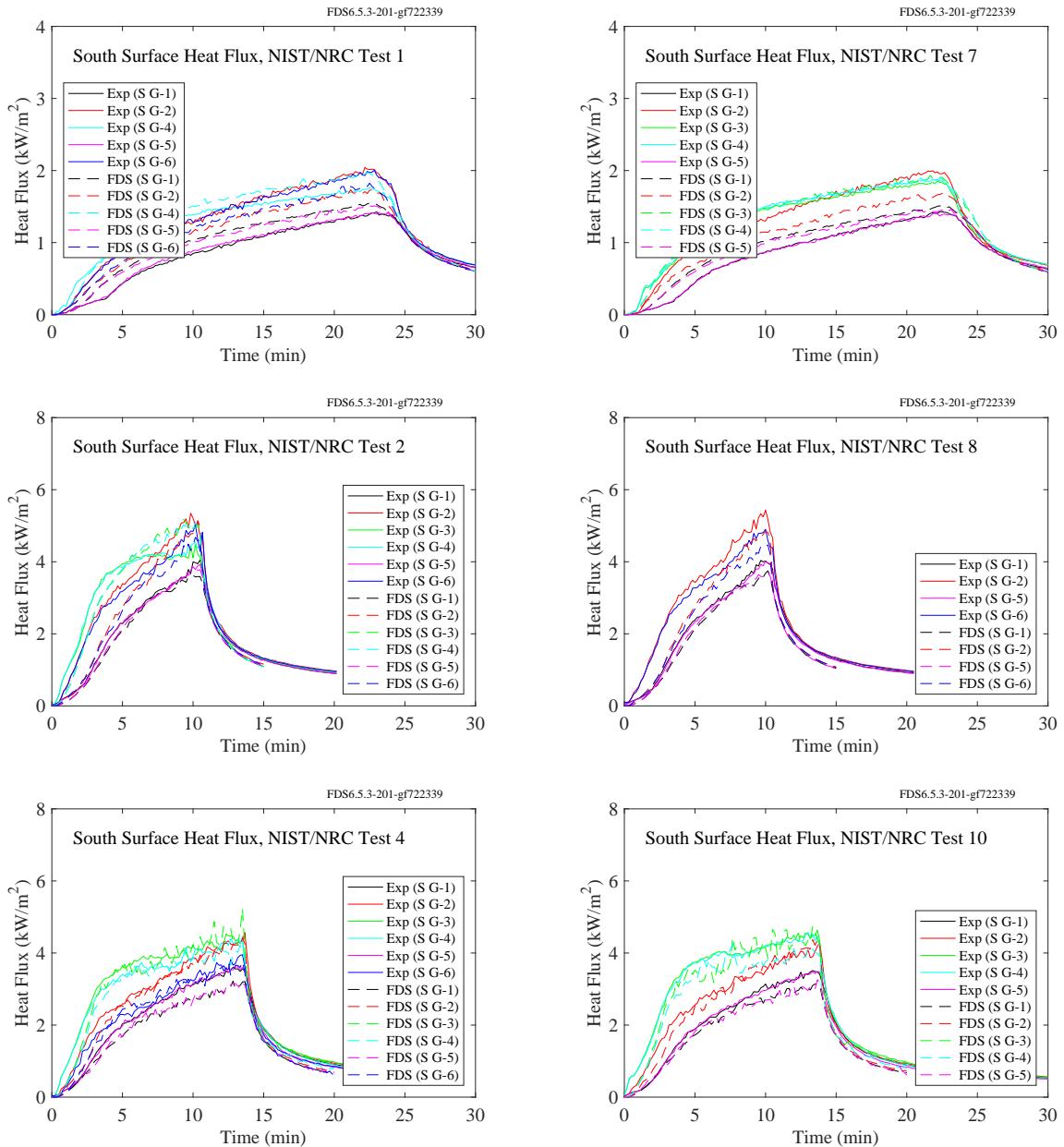


Figure 12.5: NIST/NRC experiments, heat flux to south wall, Tests 1, 2, 4, 7, 8, 10.

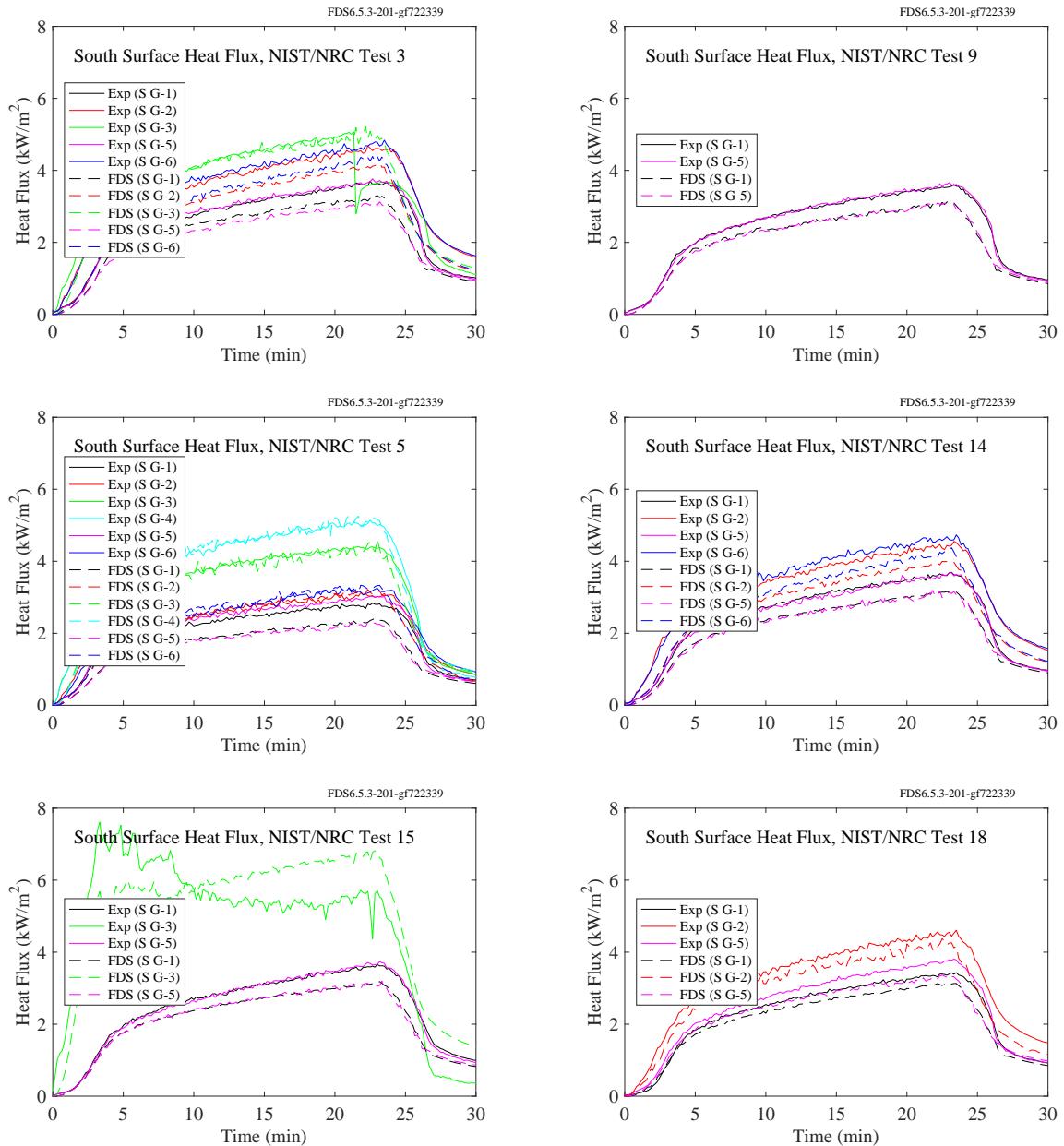


Figure 12.6: NIST/NRC experiments, heat flux to south wall, Tests 3, 5, 9, 14, 15, 18.

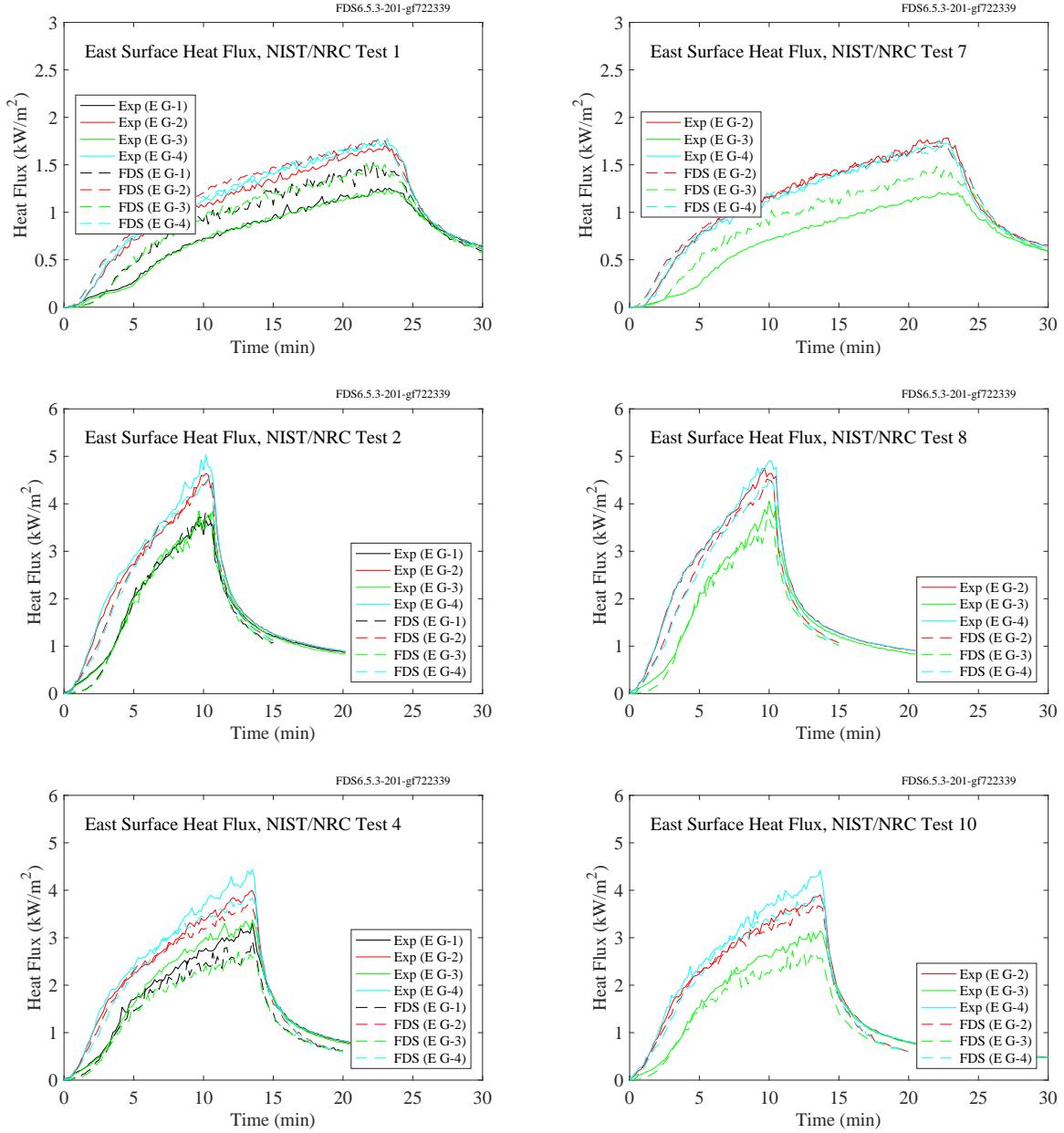


Figure 12.7: NIST/NRC experiments, heat flux to east wall, Tests 1, 2, 4, 7, 8, 10.

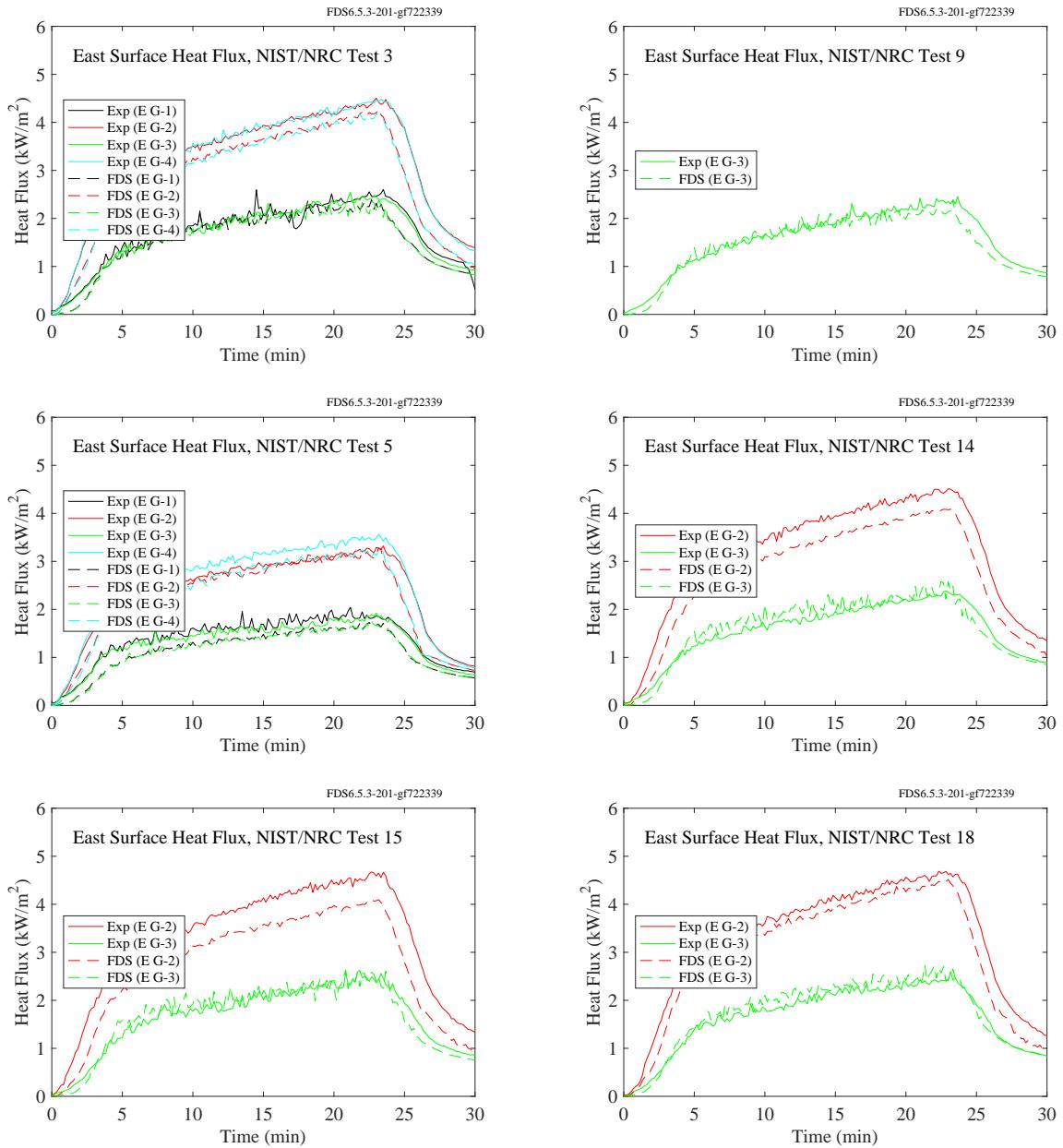


Figure 12.8: NIST/NRC experiments, heat flux to east wall, Tests 3, 5, 9, 14, 15, 18.

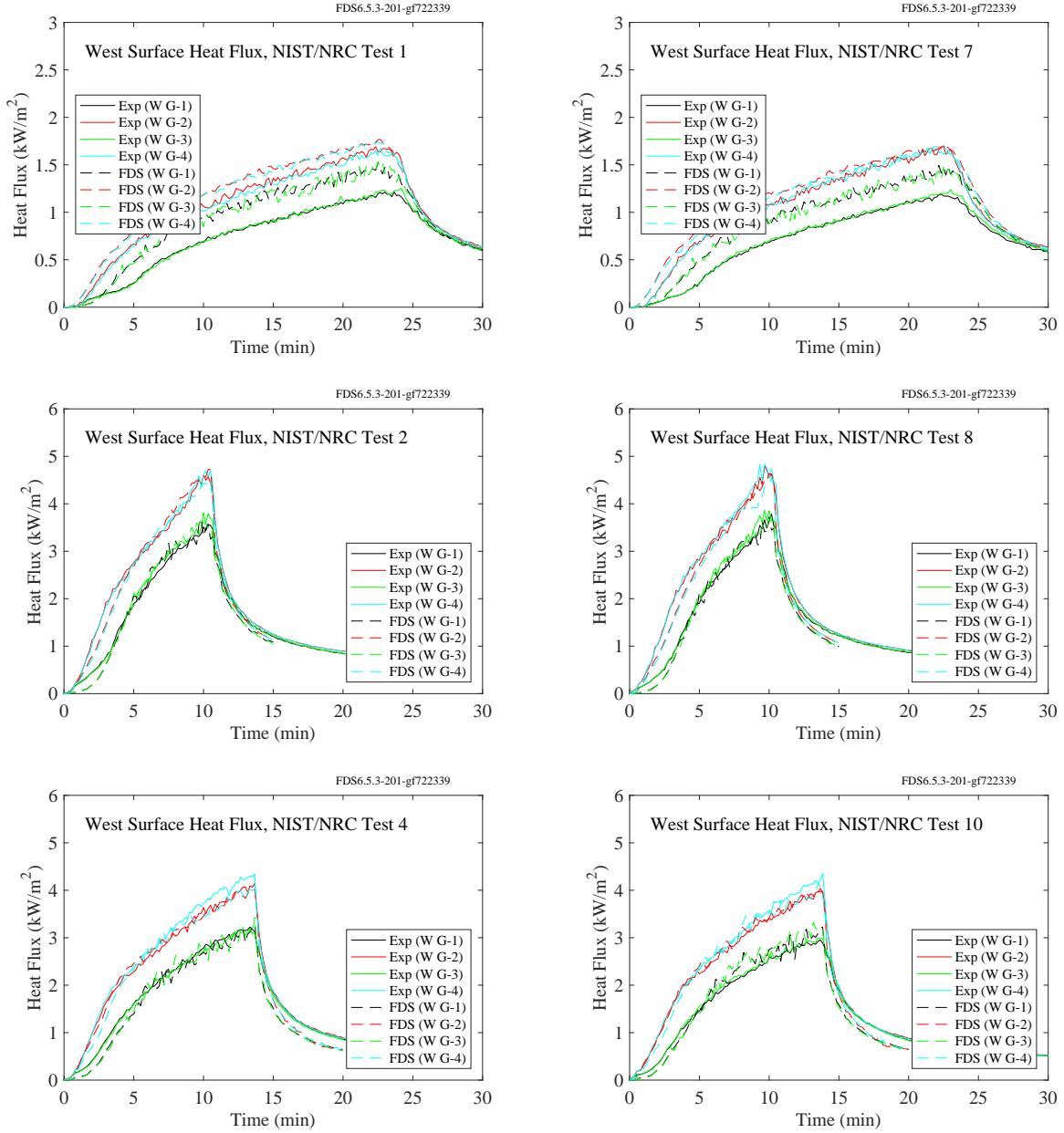


Figure 12.9: NIST/NRC experiments, heat flux to west wall, Tests 1, 2, 4, 7, 8, 10.

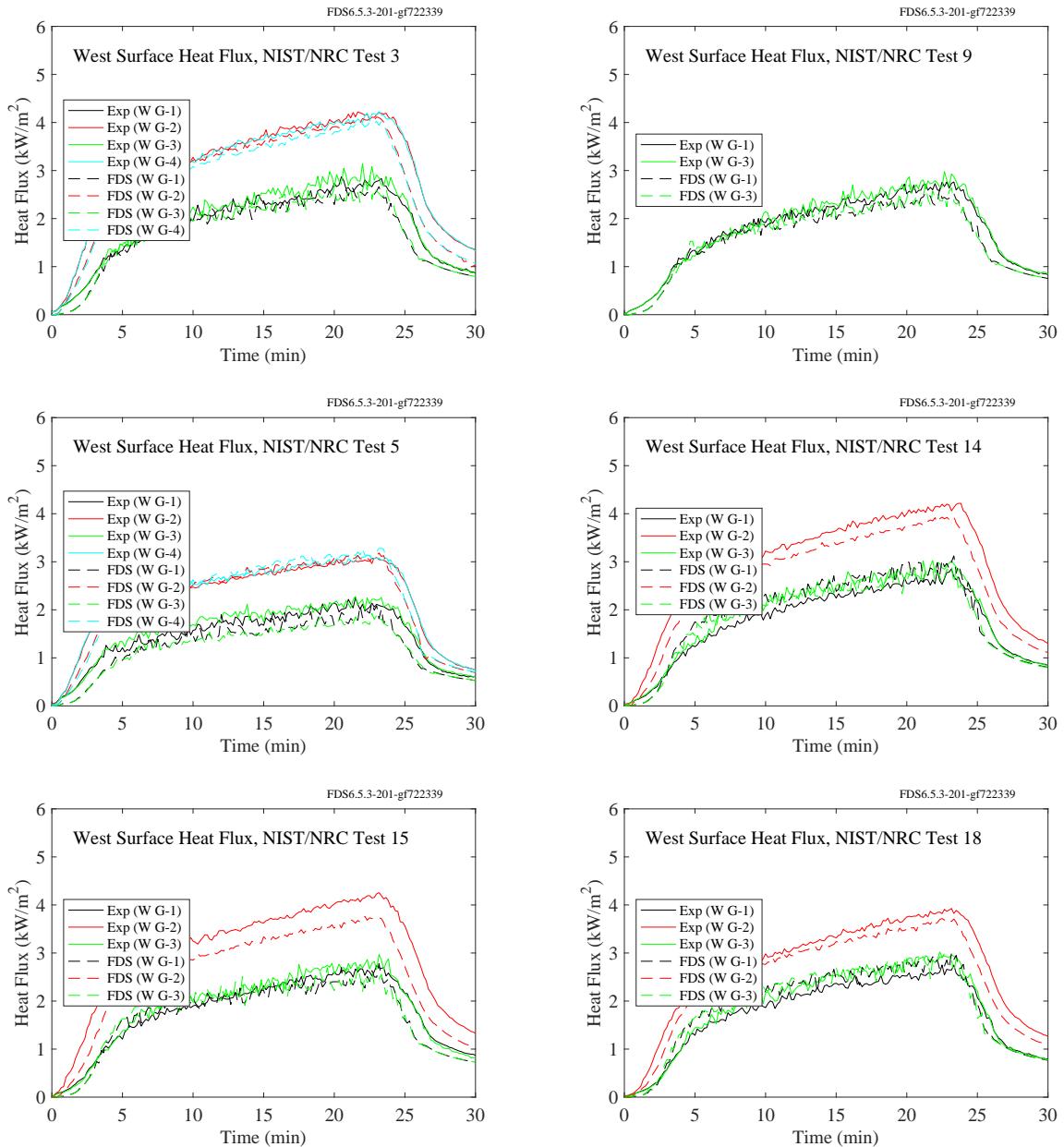


Figure 12.10: NIST/NRC experiments, heat flux to west wall, Tests 3, 5, 9, 14, 15, 18.

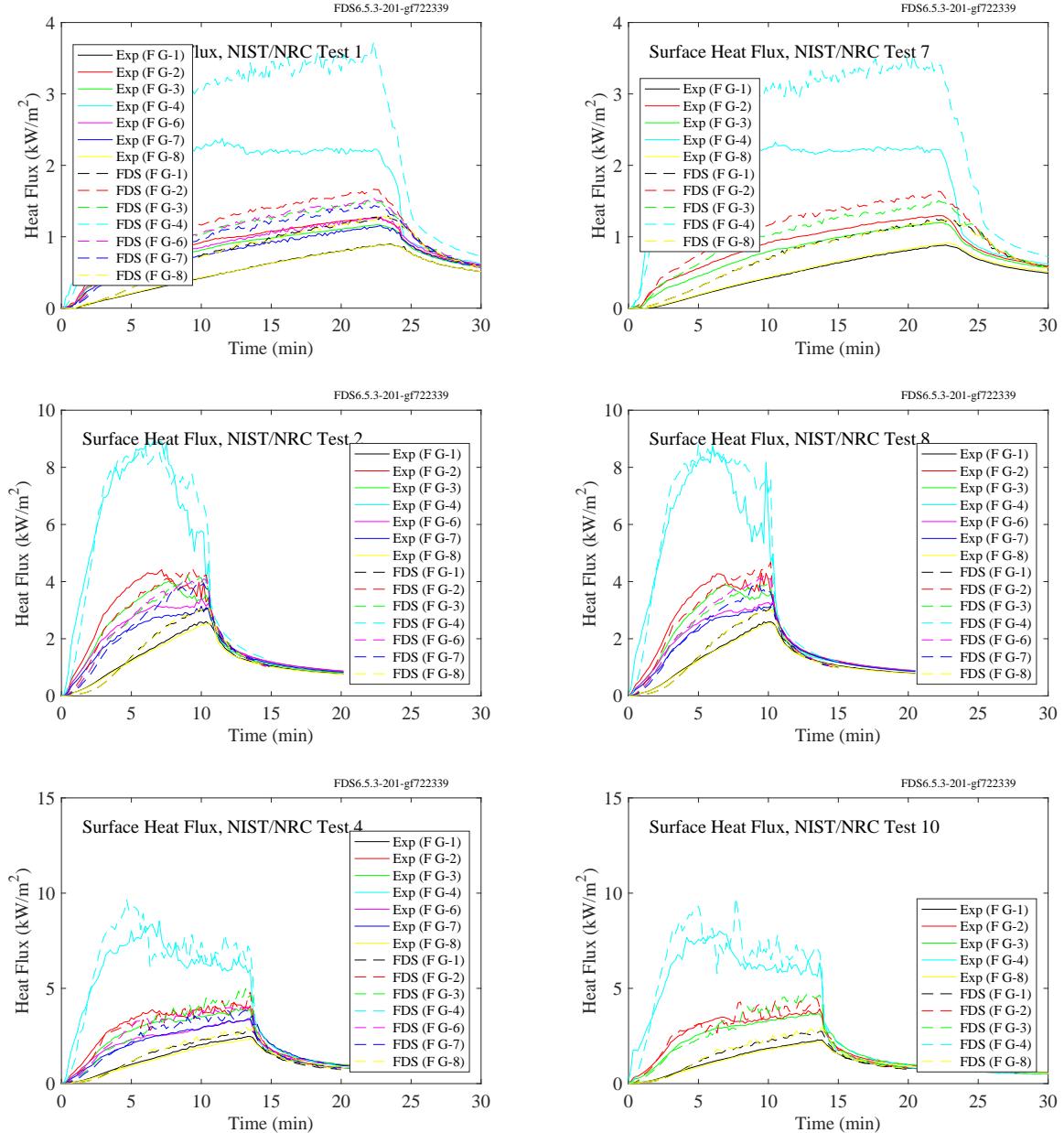


Figure 12.11: NIST/NRC experiments, heat flux to the floor, Tests 1, 2, 4, 7, 8, 10.

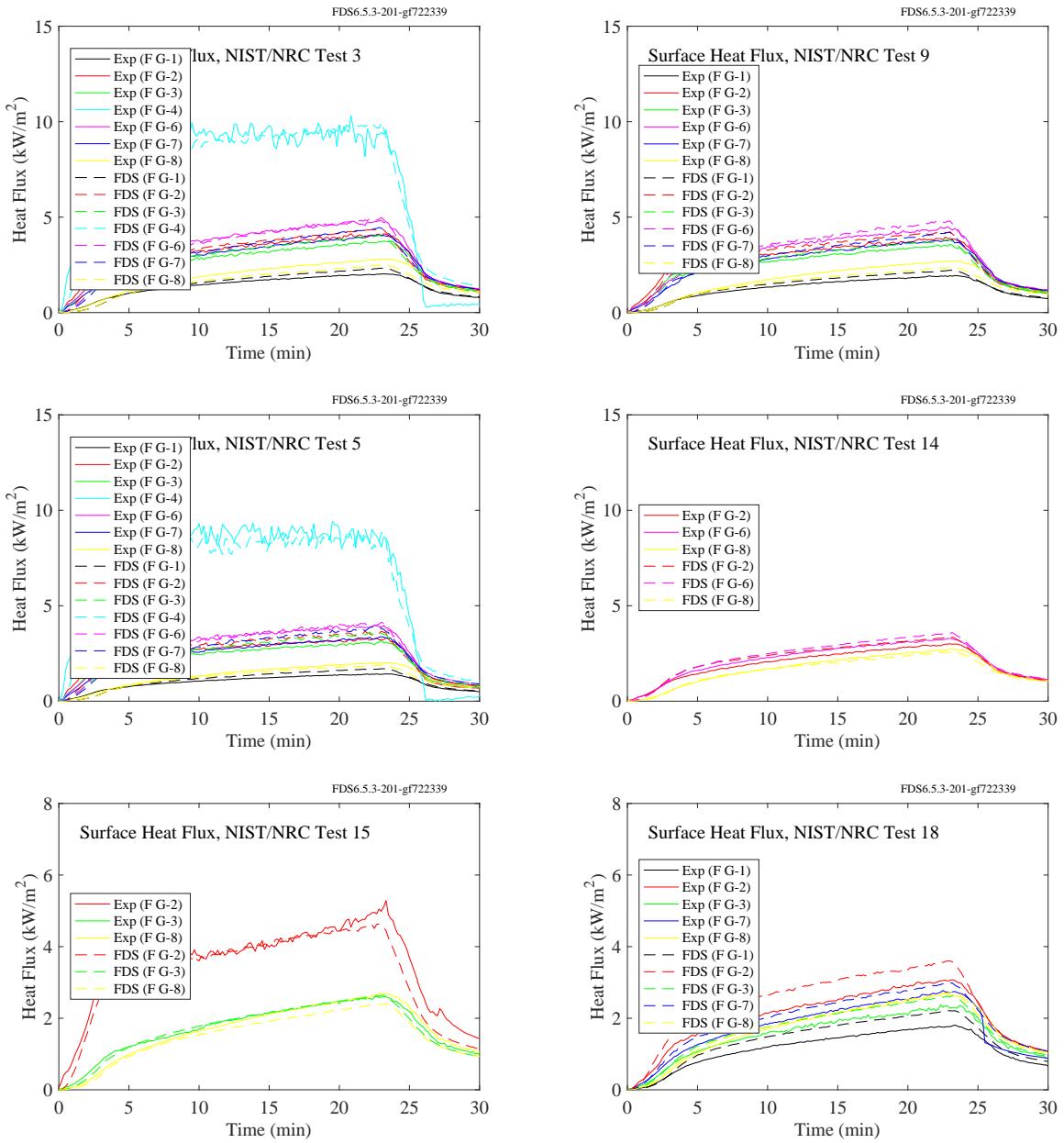


Figure 12.12: NIST/NRC experiments, heat flux to the floor, Tests 3, 5, 9, 14, 15, 18.

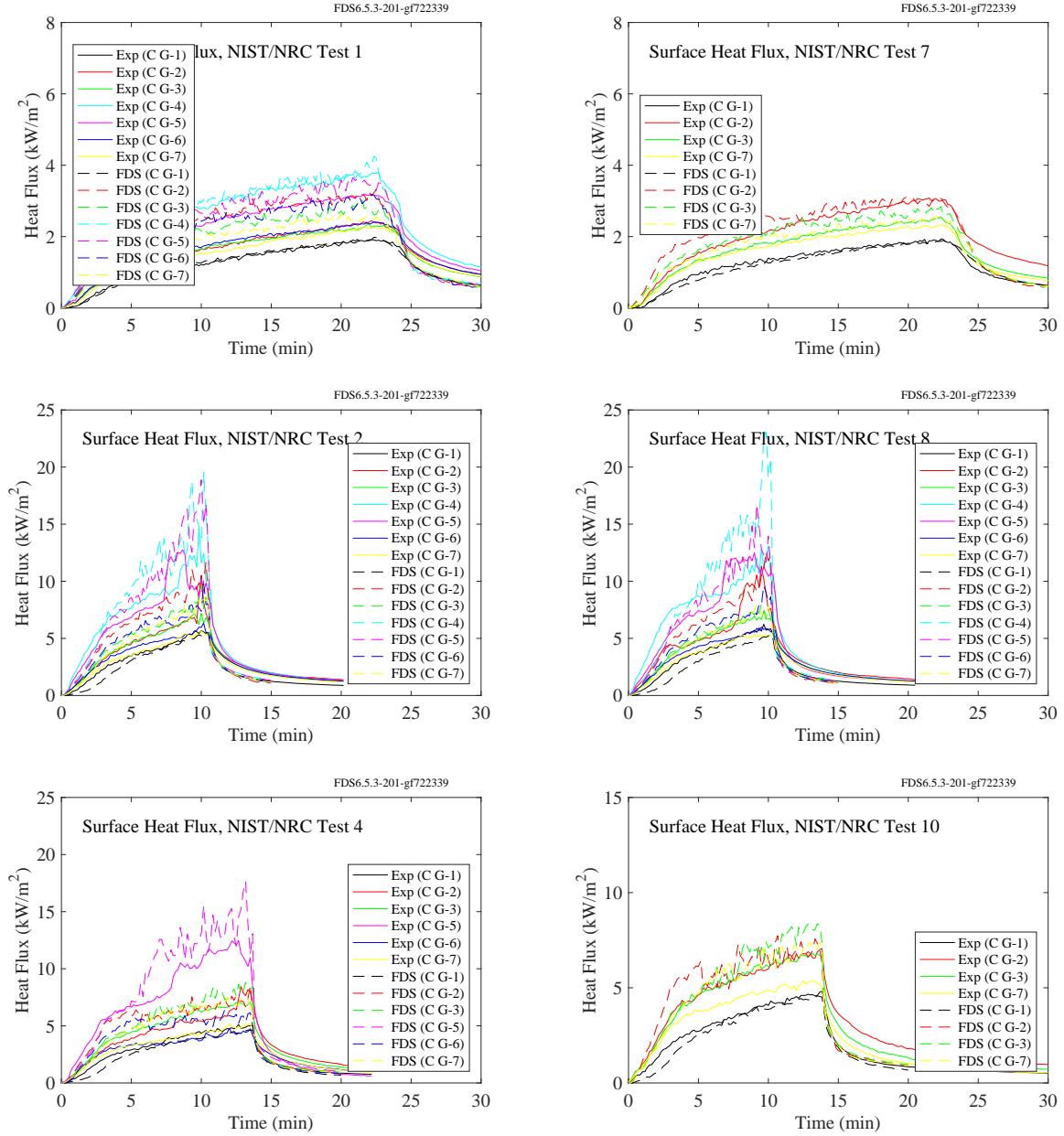


Figure 12.13: NIST/NRC experiments, heat flux to the ceiling, Tests 1, 2, 4, 7, 8, 10.

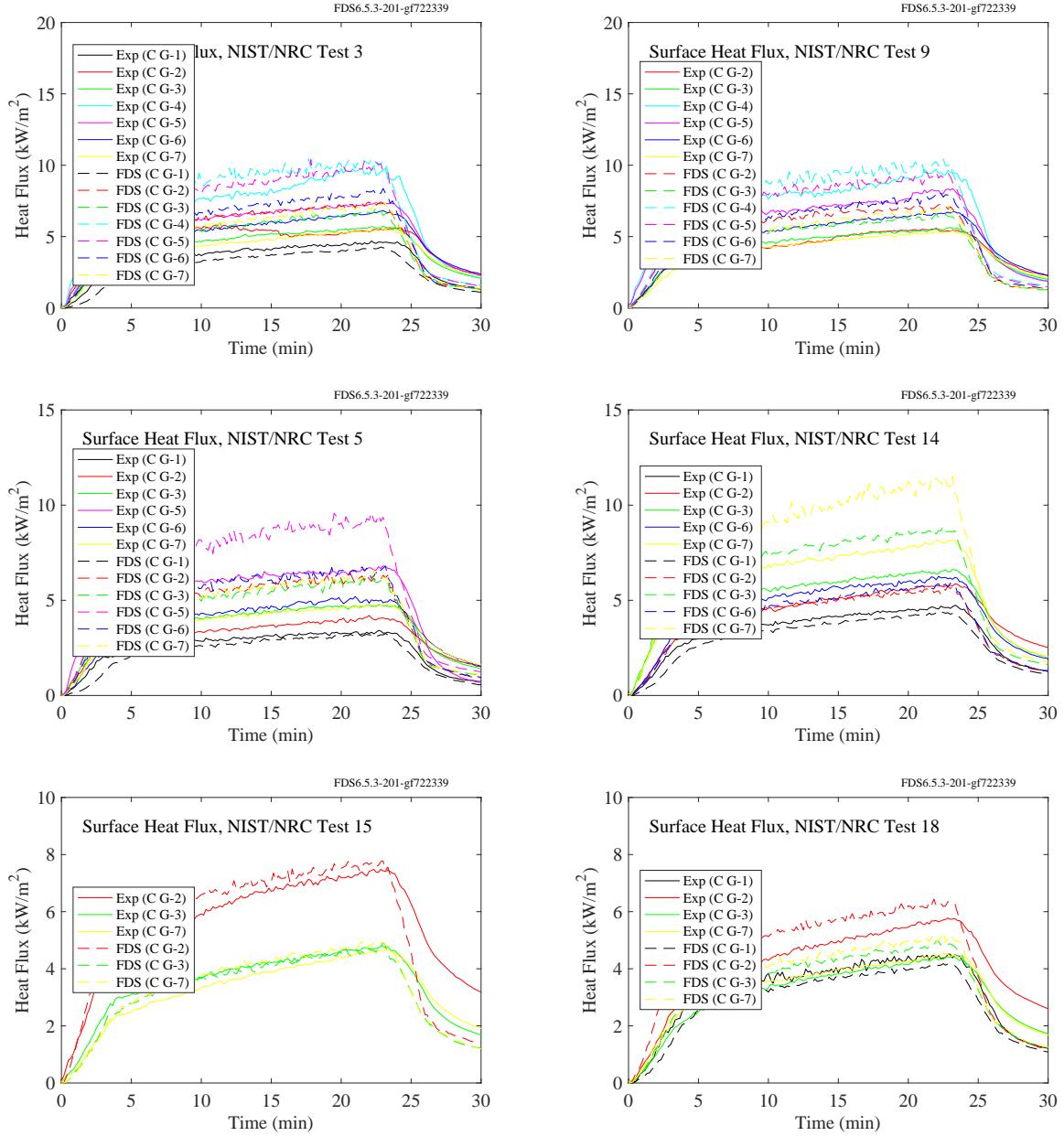


Figure 12.14: NIST/NRC experiments, heat flux to the ceiling, Tests 3, 5, 9, 14, 15, 18.

#### 12.1.4 NRCC Facade Experiments

Figure 12.15 displays the simulation of a 10.3 MW fire inside and outside of a small enclosure. The purpose of the experiment was to measure the heat flux to the exterior facade. The FDS heat flux predictions are made at the location of the green points.

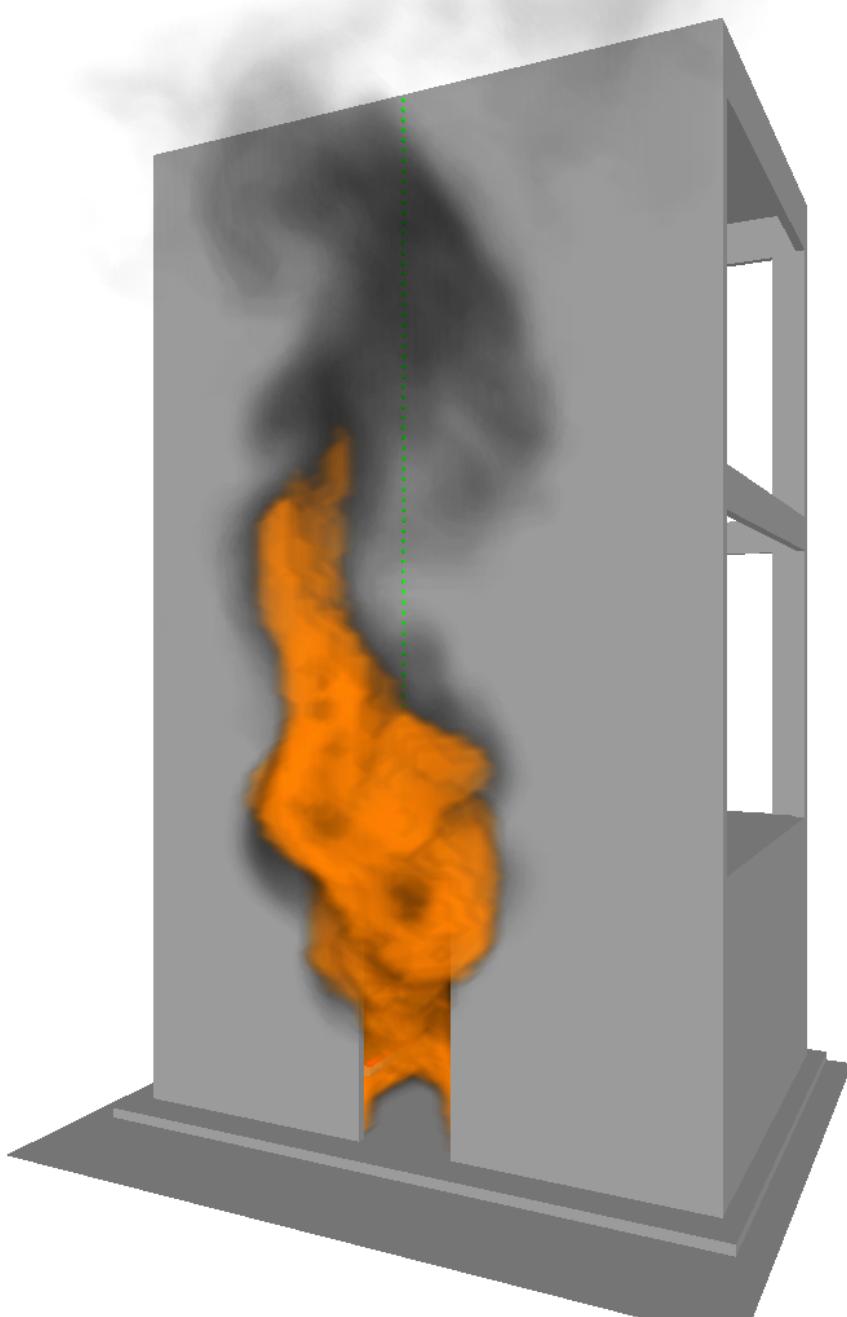


Figure 12.15: Smokeview rendering of one of the NRCC Facade experiments. The door is 0.94 m by 2.70 m tall (referred to as “Window 2” in the comparison plots). The fire is 10.3 MW.

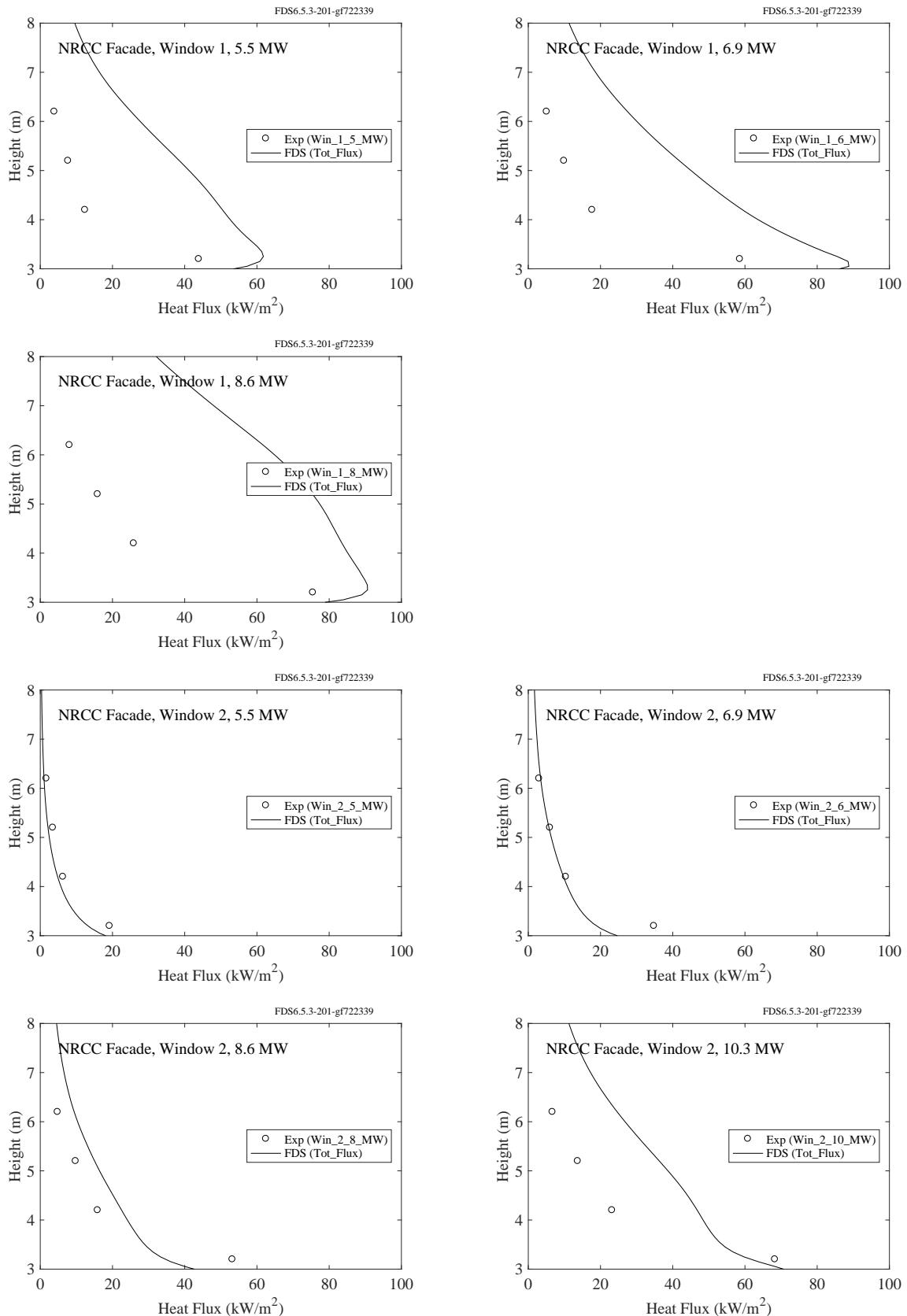


Figure 12.16: NRCC Facade experiments, heat flux, window configuration 1 and 2.

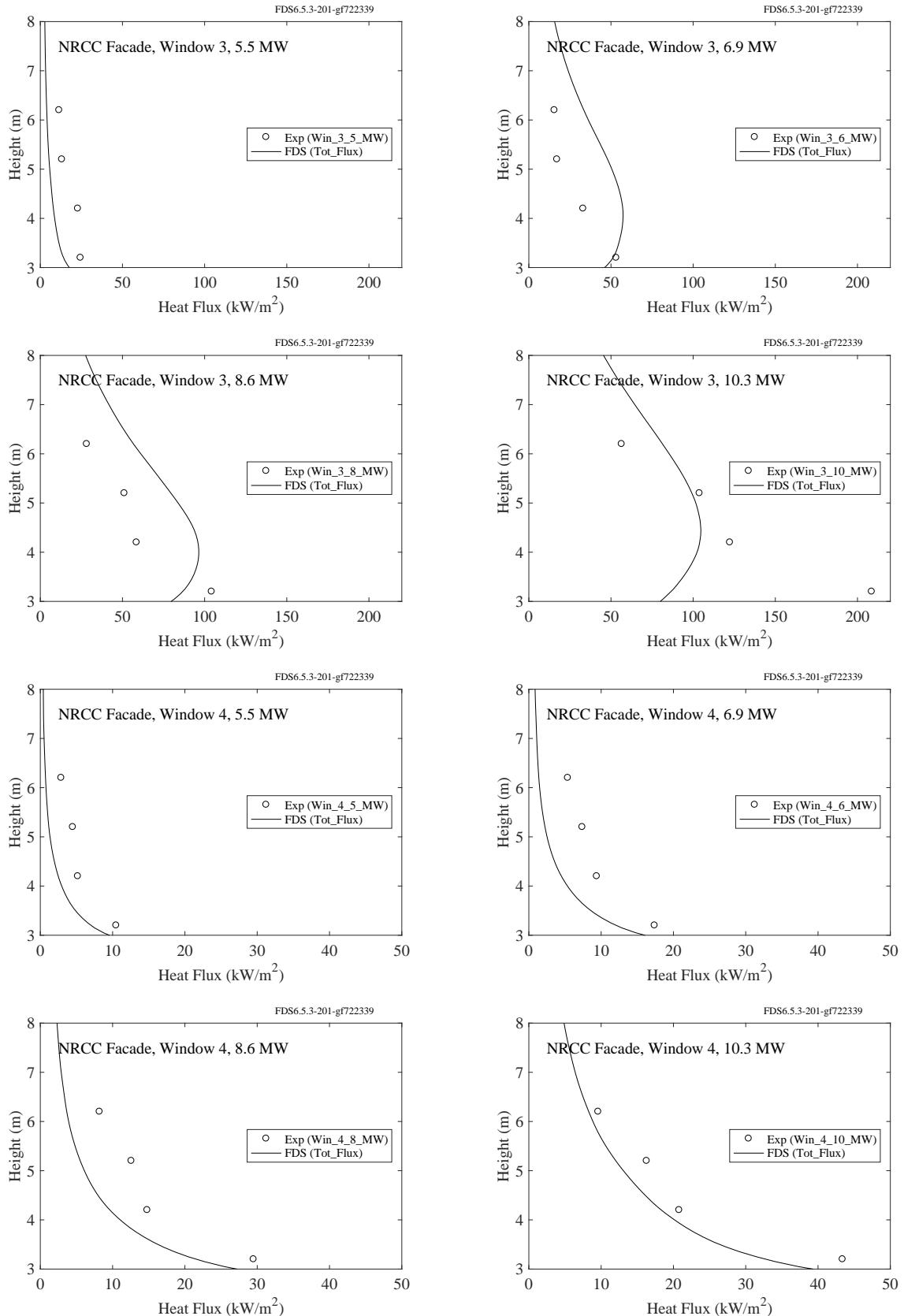


Figure 12.17: NRCC Facade experiments, heat flux, window configuration 3 and 4.

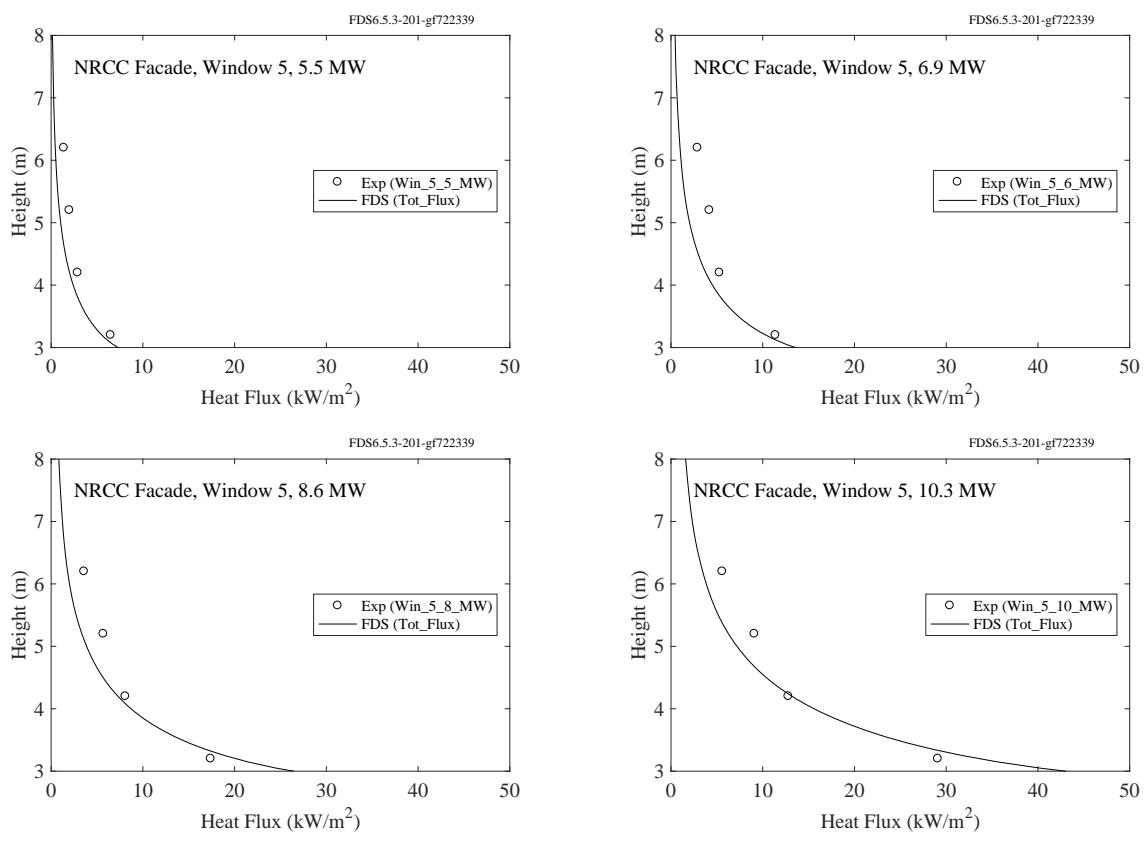


Figure 12.18: NRCC Facade experiments, heat flux, window configuration 5.

### 12.1.5 NRL/HAI Experiments

Predicted and measured vertical heat flux profiles from 9 propane sand burner fires are shown on the following pages. The parameters for each experiment are listed in Table 12.1 below. Note that all the FDS simulations were performed with a grid resolution such that  $D^*/\delta x = 10$ .

Table 12.1: Summary of the NRL/HAI Wall Heat Flux Measurements.

Test Number	$D$ (m)	$D^*$ (m)	$\dot{Q}$ (kW)	$Q^*$	Observed Flame Height (m)
1	0.28	0.30	53	0.85	0.79
2	0.70	0.30	56	0.09	0.36
3	0.48	0.33	68	0.28	0.60
4	0.37	0.39	106	0.84	1.00
5	0.48	0.43	136	0.57	0.87
6	0.48	0.51	204	0.85	1.45
7	0.70	0.52	220	0.36	1.20
8	0.57	0.60	313	0.85	2.20
9	0.70	0.74	523	0.85	2.9 (based on 500 °C)

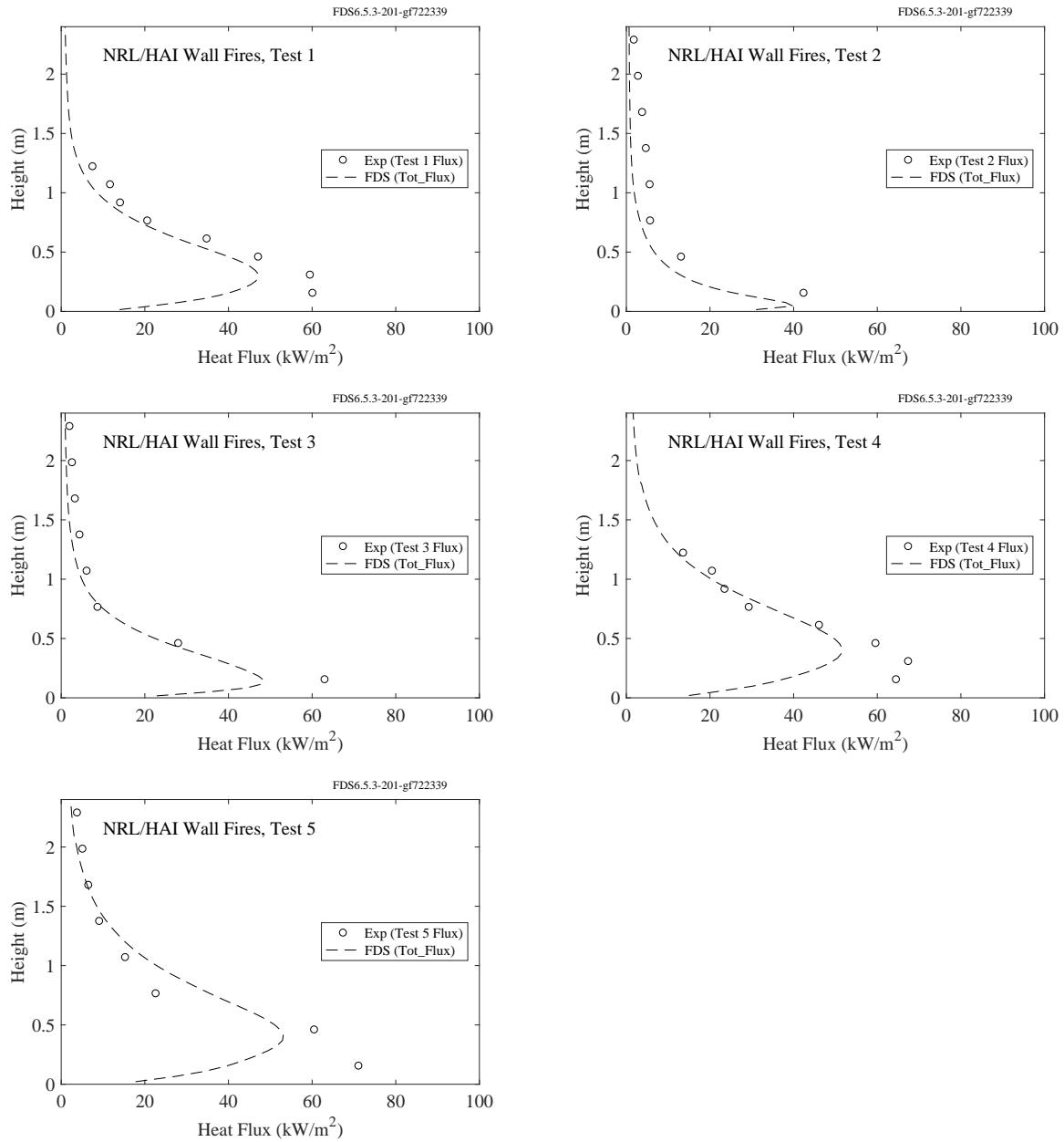


Figure 12.19: NRL/HAI experiments, heat flux to the wall, Tests 1-5.

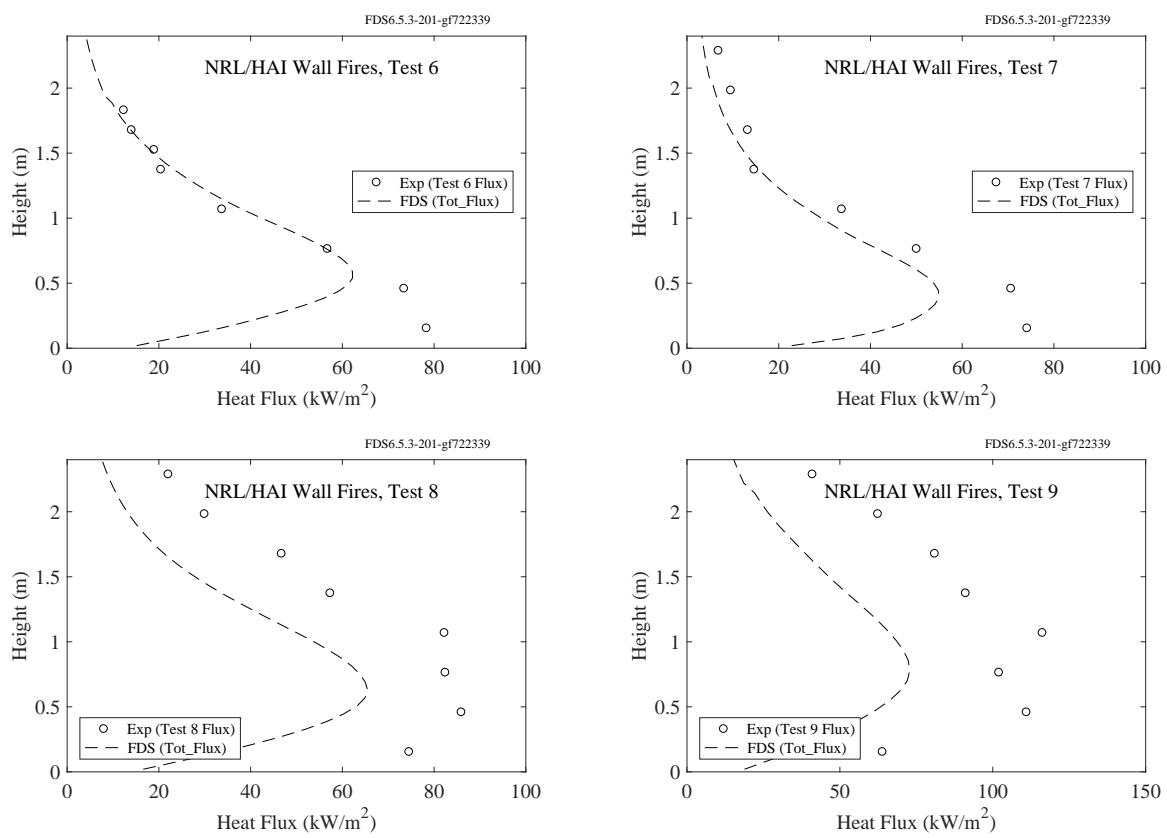


Figure 12.20: NRL/HAI experiments, heat flux to the wall, Tests 6-9.

### 12.1.6 PRISME DOOR Experiments

Total and radiative heat flux gauges were positioned at various points on the walls. Each room contained a vertical array labelled, for example, FLT\_L1\_NC265. The FLT indicates a surface total heat flux measurement, L1 indicates compartment 1, which is where the fire was located, NC indicates north wall center, and 265 indicates the number of centimeters above the floor. In addition, each room contained four measurement points centered on each wall at a height of approximately 260 cm. These points are labelled, for example, FLT\_L2\_SC265, compartment 2, center of south wall, 265 cm high.

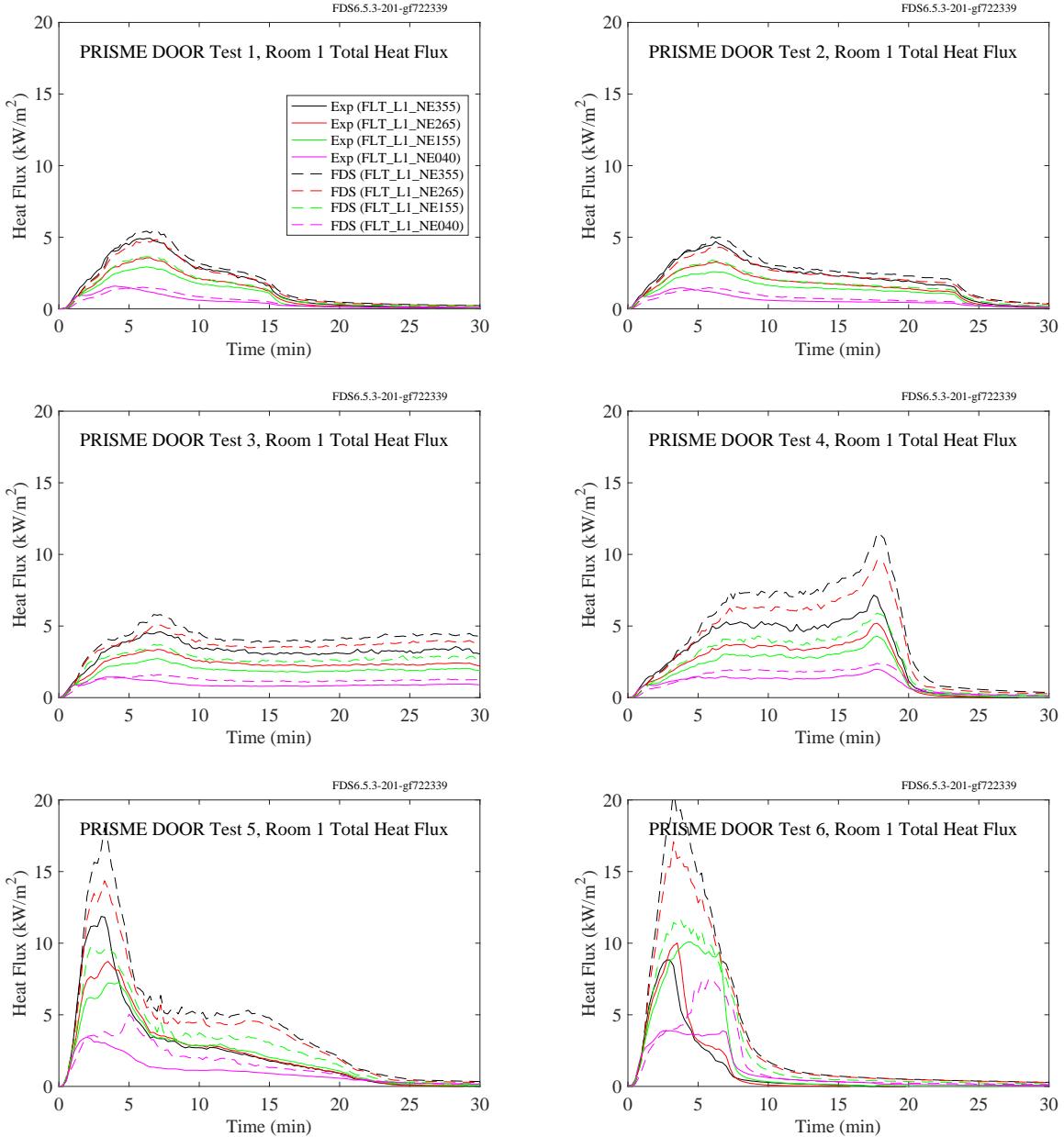


Figure 12.21: PRISME DOOR experiments, total heat flux, vertical array, Room 1.

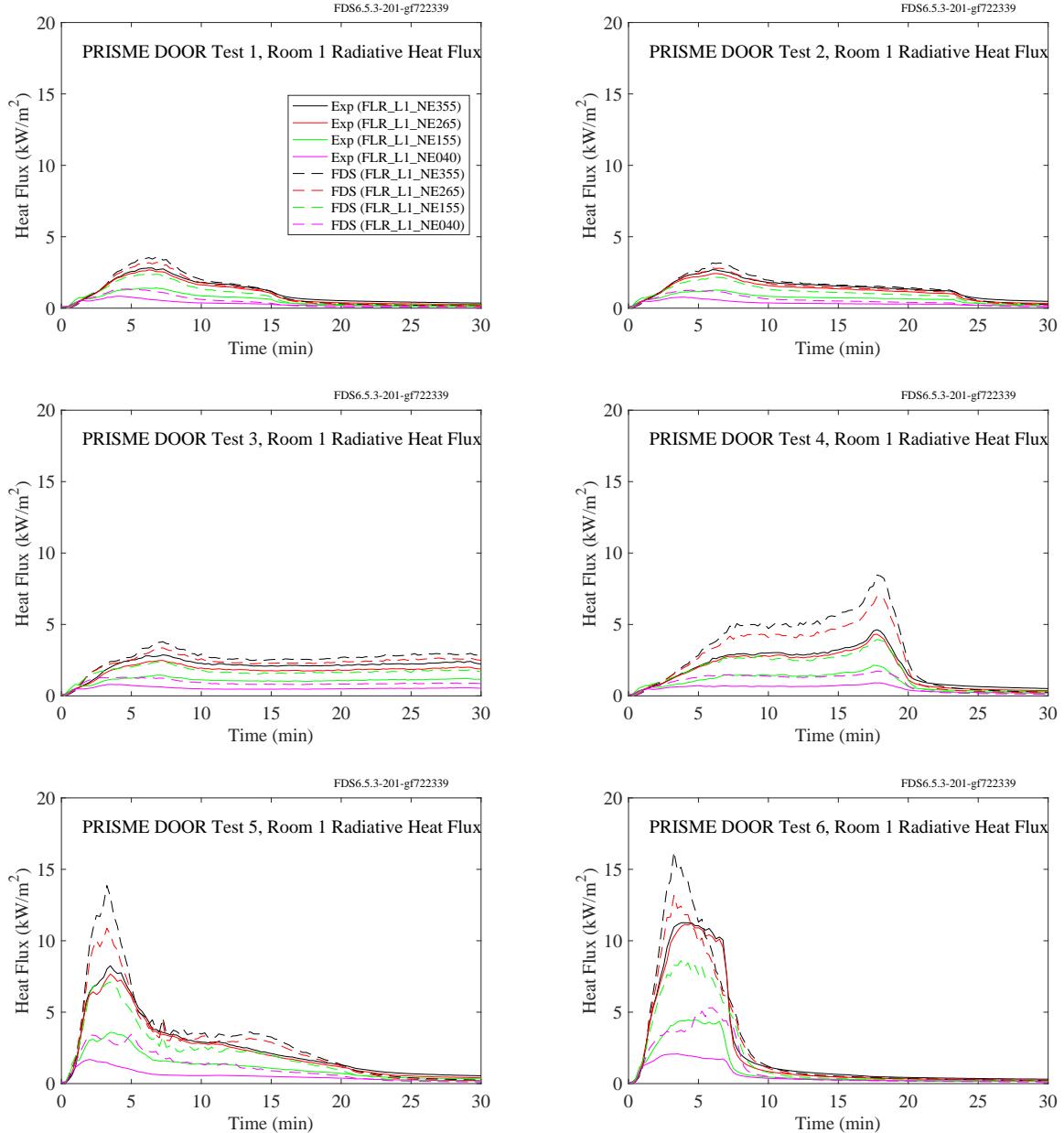


Figure 12.22: PRISME DOOR experiments, radiative heat flux, vertical array, Room 1.

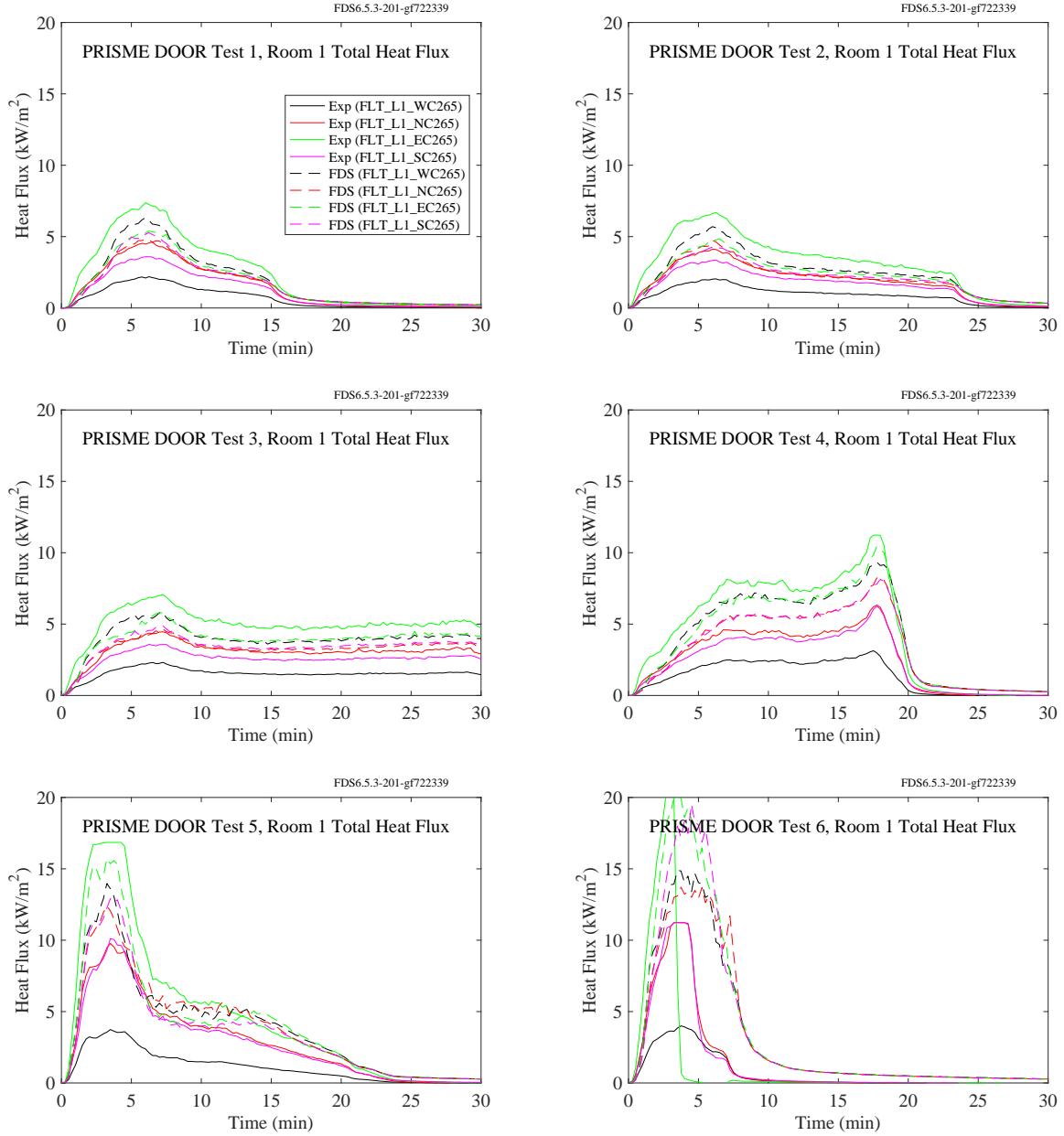


Figure 12.23: PRISME DOOR experiments, total heat flux, four walls, Room 1.

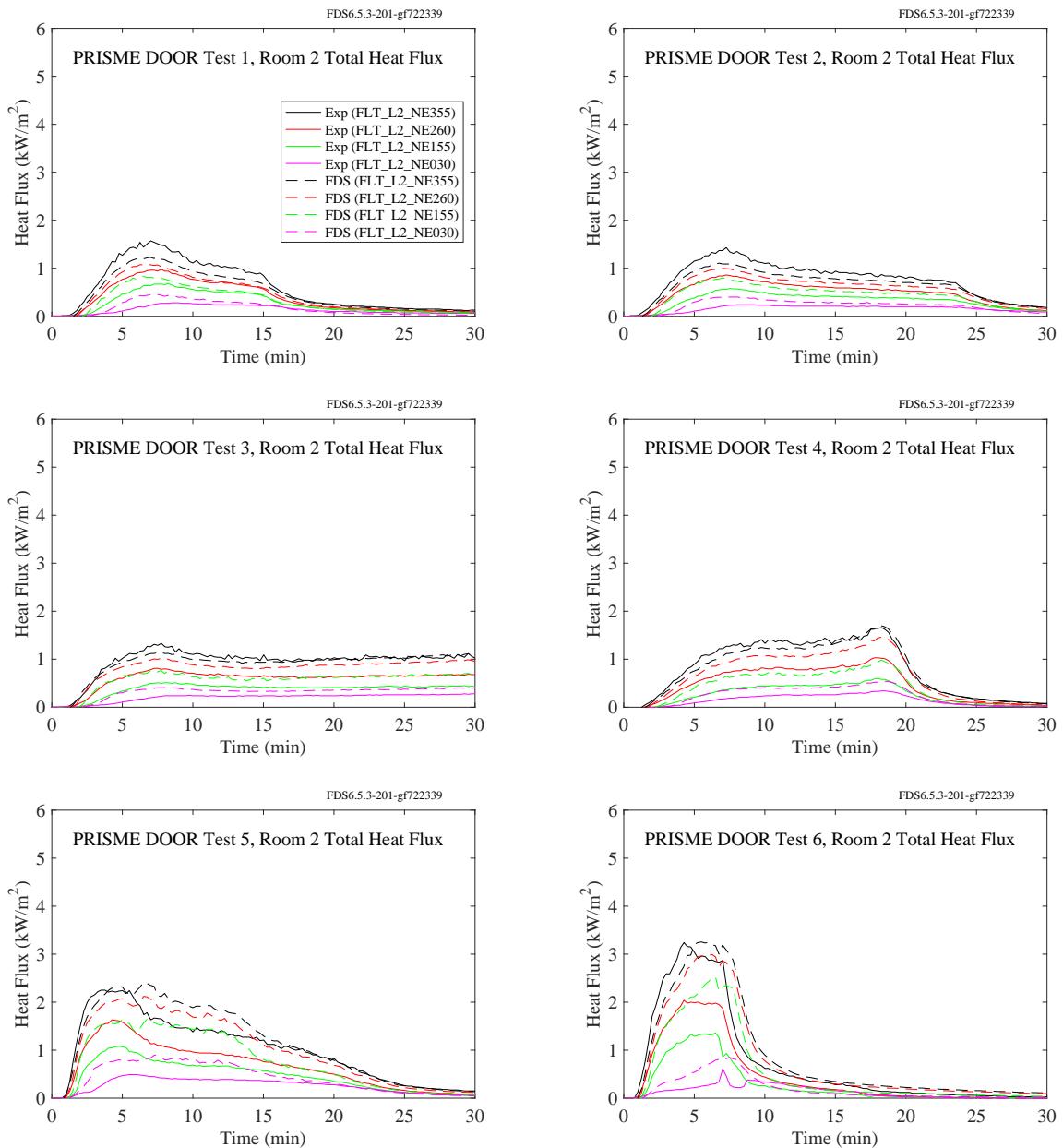


Figure 12.24: PRISME DOOR experiments, total heat flux, vertical array, Room 2.

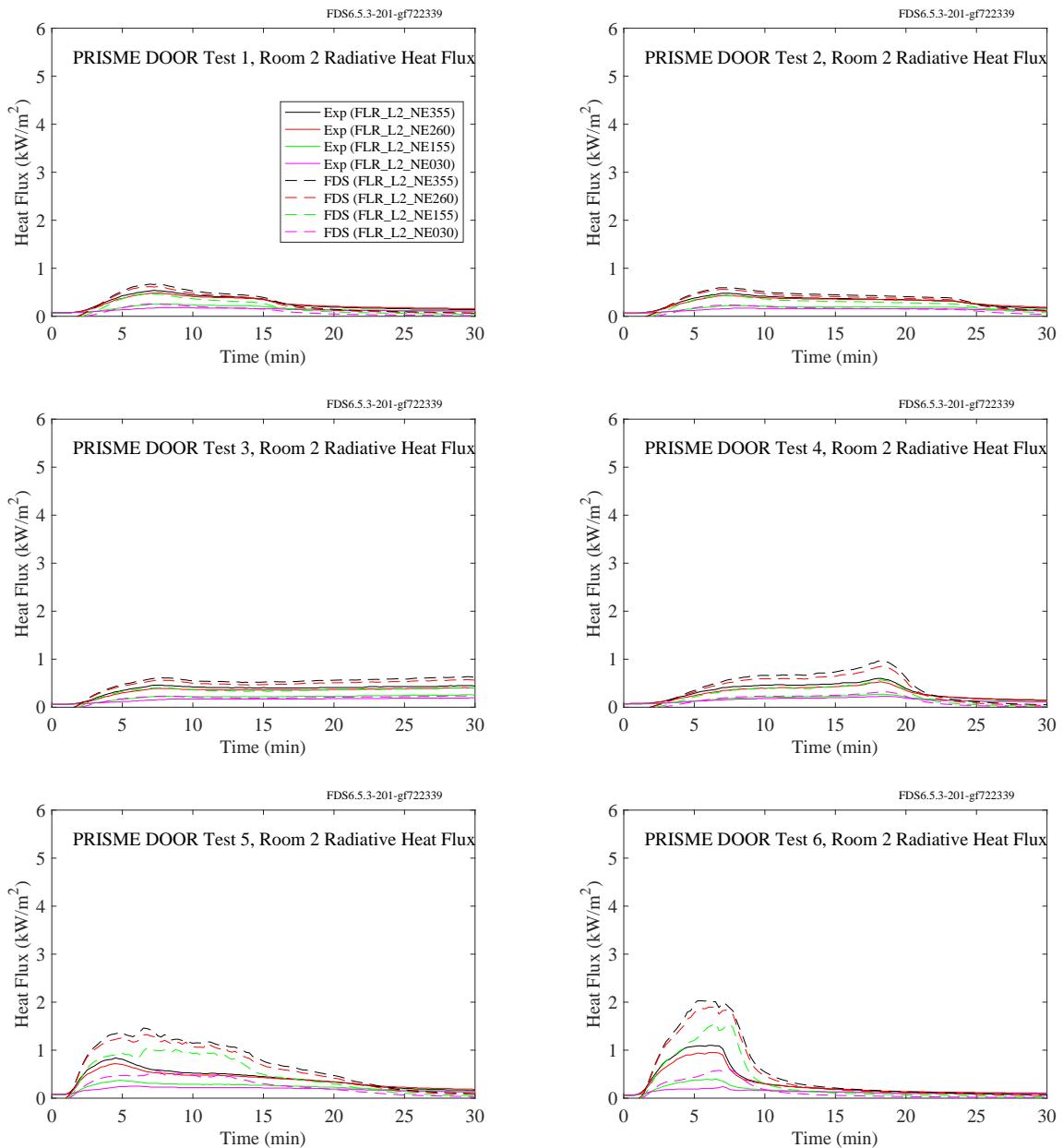


Figure 12.25: PRISME DOOR experiments, radiative heat flux, vertical array, Room 2.

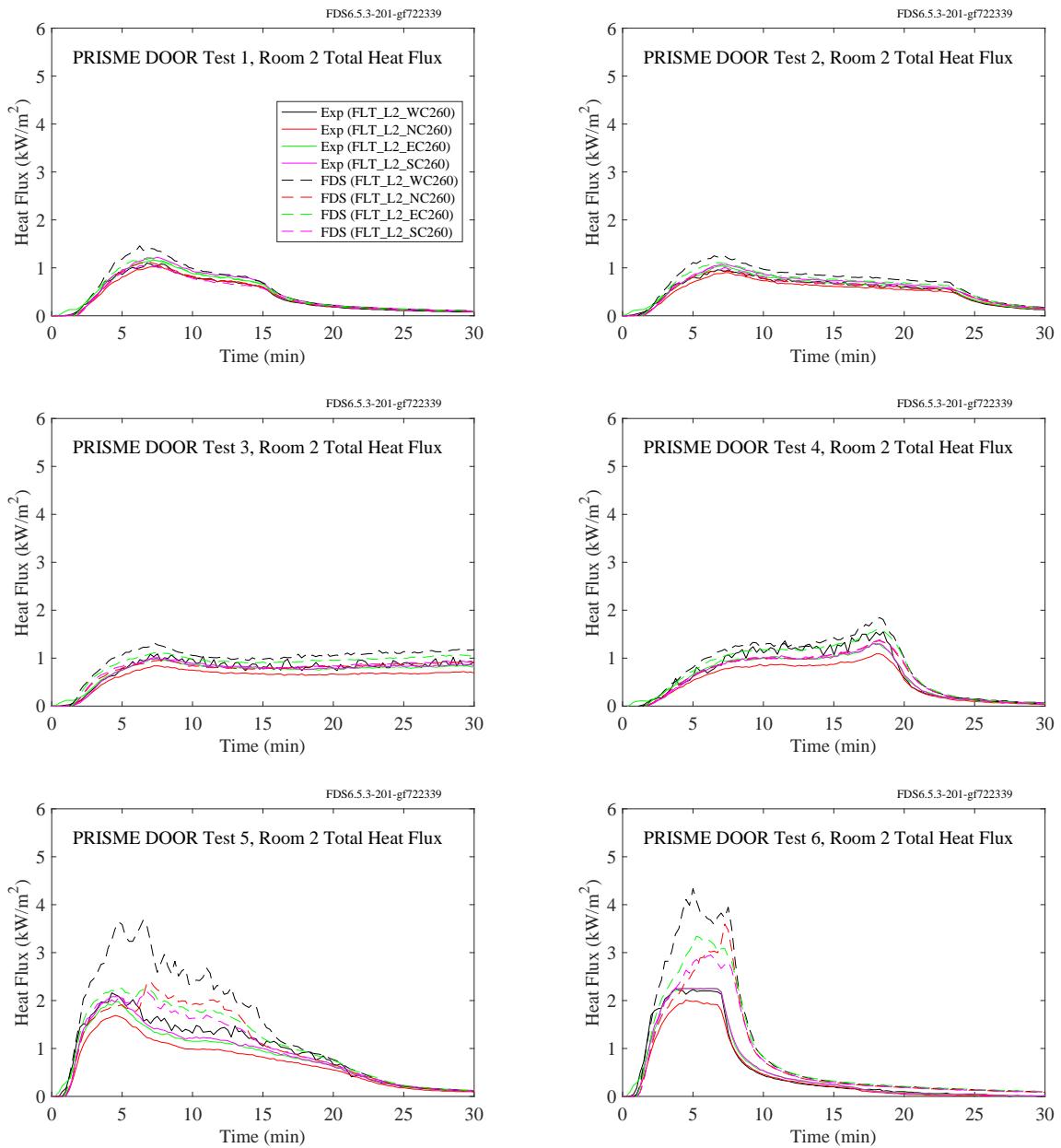


Figure 12.26: PRISME DOOR experiments, total heat flux, four walls, Room 2.

### **12.1.7 PRISME SOURCE Experiments**

Total and radiative heat flux gauges were positioned at various points on the walls. Each room contained a vertical array labelled, for example, FLT\_L1\_NC265. The FLT indicates a surface total heat flux measurement, L1 indicates compartment 1, which is where the fire was located, NC indicates north wall center, and 265 indicates the number of centimeters above the floor. In addition, each room contained four measurement points centered on each wall at a height of approximately 260 cm. These points are labelled, for example, FLT\_L2\_SC265, compartment 2, center of south wall, 265 cm high.

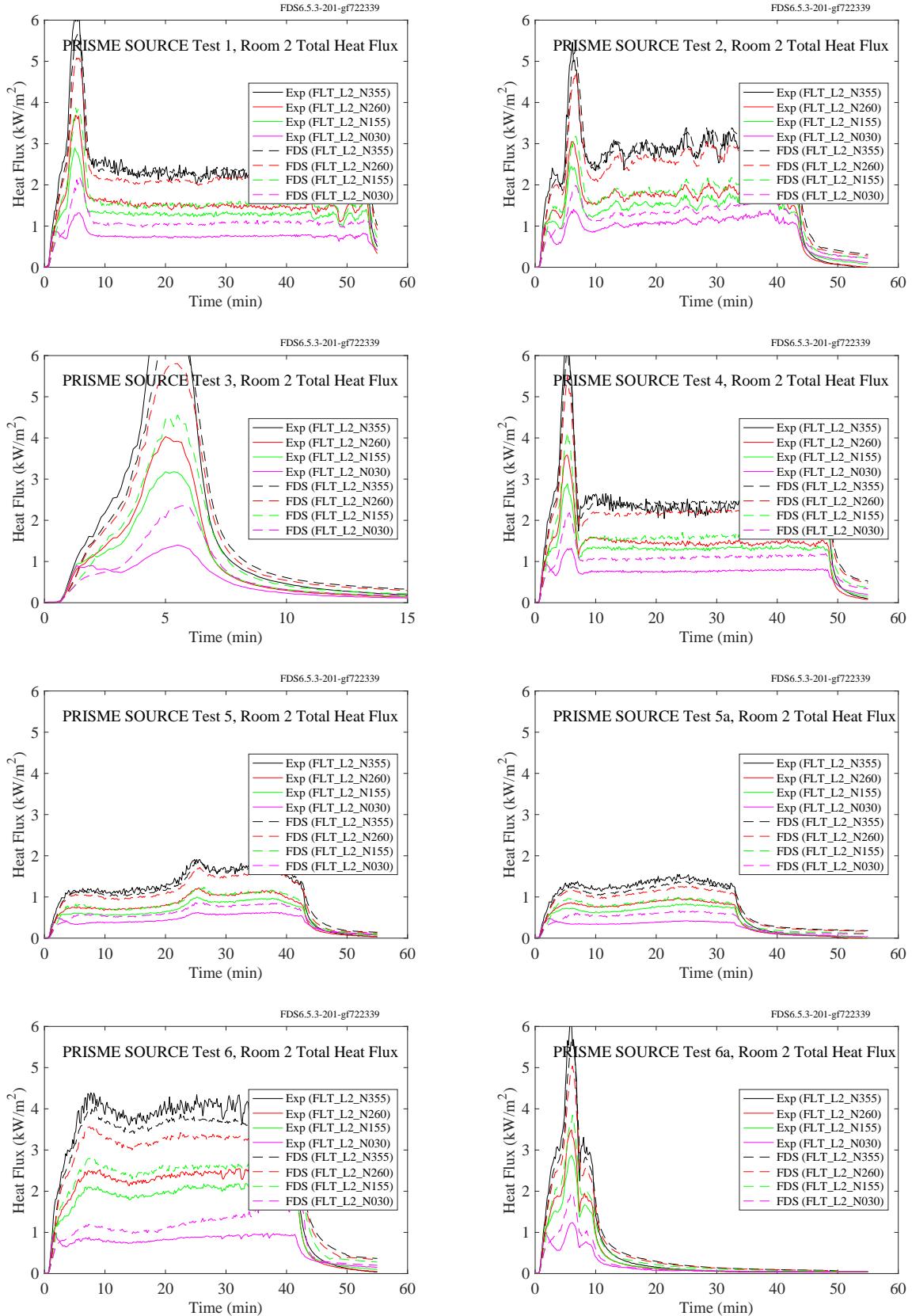


Figure 12.27: PRISME SOURCE experiments, total heat flux, vertical array, Room 2.

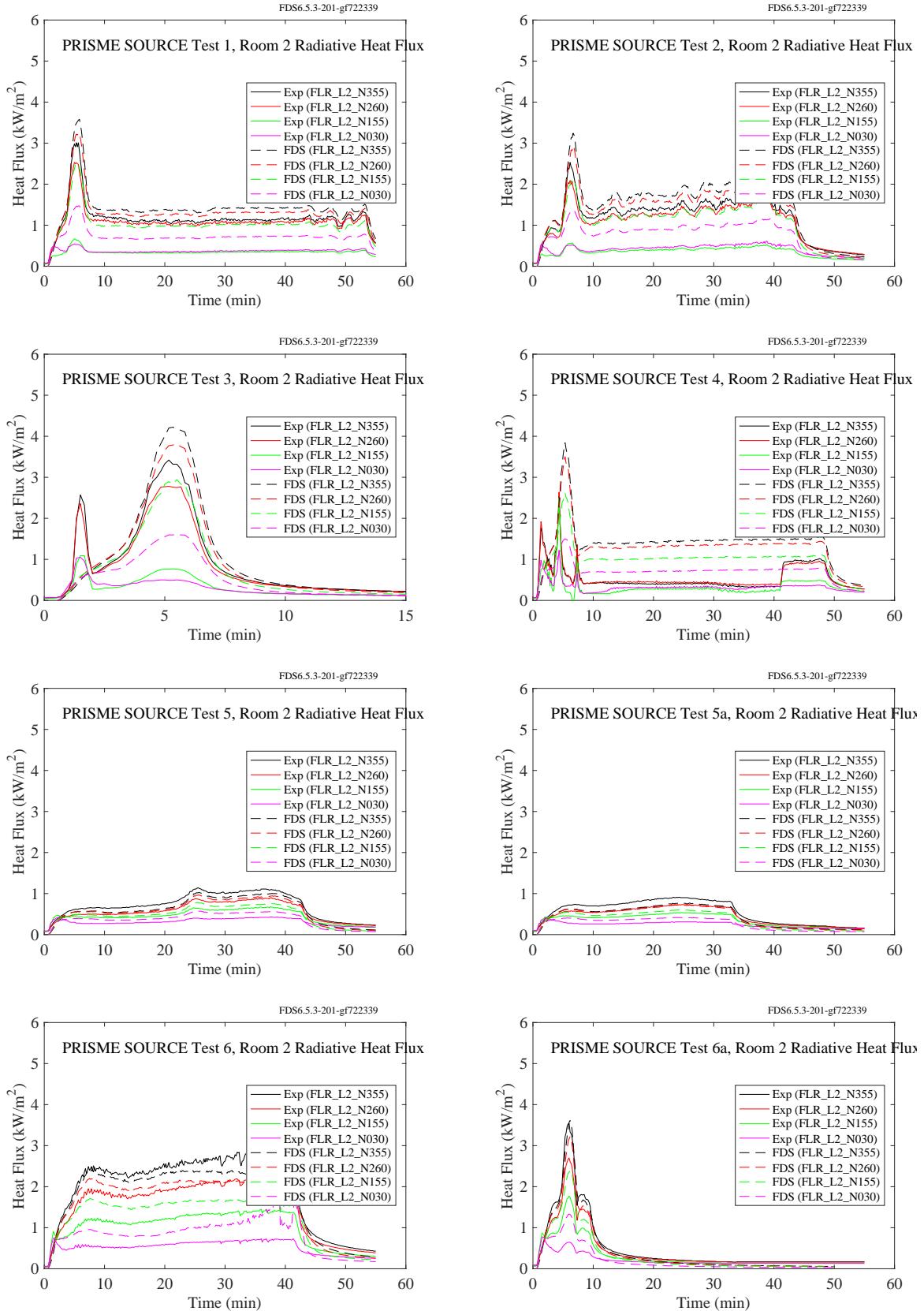


Figure 12.28: PRISME SOURCE experiments, radiative heat flux, vertical array, Room 2.

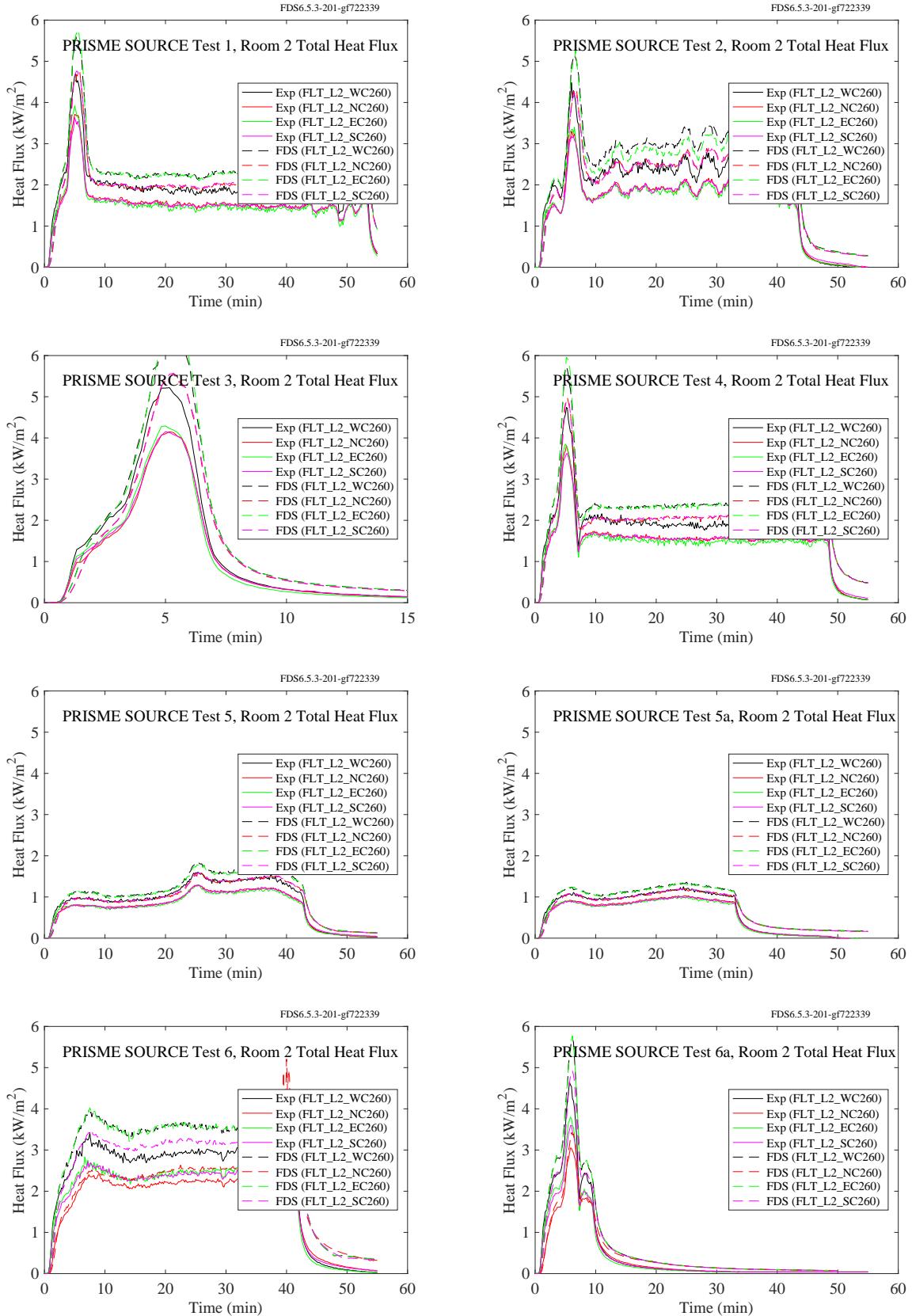


Figure 12.29: PRISME SOURCE experiments, total heat flux, four walls, Room 2.

### 12.1.8 Ulster SBI Experiments

Predicted and measured vertical heat flux profiles for three propane fire sizes in the single burning item (SBI) enclosure at the University of Ulster are shown on the following page. Measurements were made on two vertical panels that form a corner, at the base of which was a triangular-shaped burner with sides of length 25 cm. Three vertical profiles were measured on each panel at distances of 3.25 cm, 16.5 cm, and 29 cm from the corner.

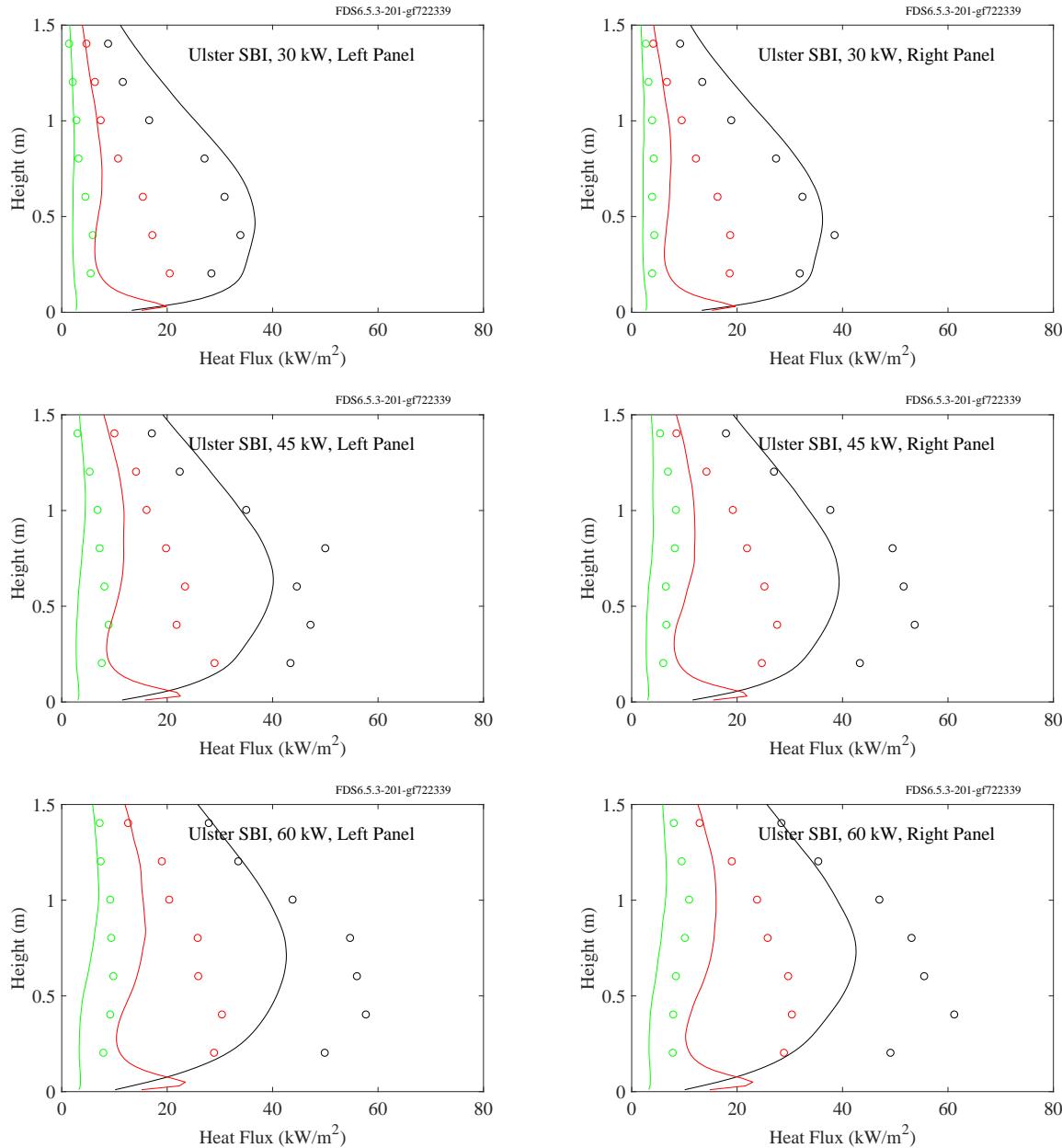


Figure 12.30: Comparison of predicted (lines) and measured (circles) heat fluxes to adjacent panels forming a corner in the single burning item (SBI) apparatus at the University of Ulster.

### 12.1.9 WTC Experiments

There were a variety of heat flux gauges installed in the test compartment. Most were within 2 m of the fire. Their locations and orientations are listed in Table 12.2. This section contains the measurements at the floor and ceiling.

Table 12.2: Heat flux gauge positions relative to the center of the fire pan in the WTC series.

Name	$x$ (m)	$y$ (m)	$z$ (m)	Orientation	Location
H2FU	0.64	0.63	3.30	$+z$	Truss Support
H2RU	0.64	0.51	3.30	$+z$	Truss Support
H2FD	0.64	0.30	3.15	$-z$	Truss Support
H2RD	0.64	0.42	3.15	$-z$	Truss Support
HCoHF	-0.90	0.84	3.46	$+x$	Column, facing fire
HCoHW	-0.97	0.92	3.27	$+y$	Column, facing north
HCoLF	-0.90	0.84	0.92	$+x$	Column, facing fire
HCoLW	-0.97	0.92	1.02	$+y$	Column, facing north
HF1	1.06	0.13	0.13	$+z$	Floor
HF2	1.56	0.10	0.13	$+z$	Floor
HCe1	-0.45	0.35	3.82	$-z$	Ceiling
HCe2	0.05	0.35	3.82	$-z$	Ceiling
HCe3	0.80	0.35	3.82	$-z$	Ceiling
HCe4	2.56	0.35	3.82	$-z$	Ceiling

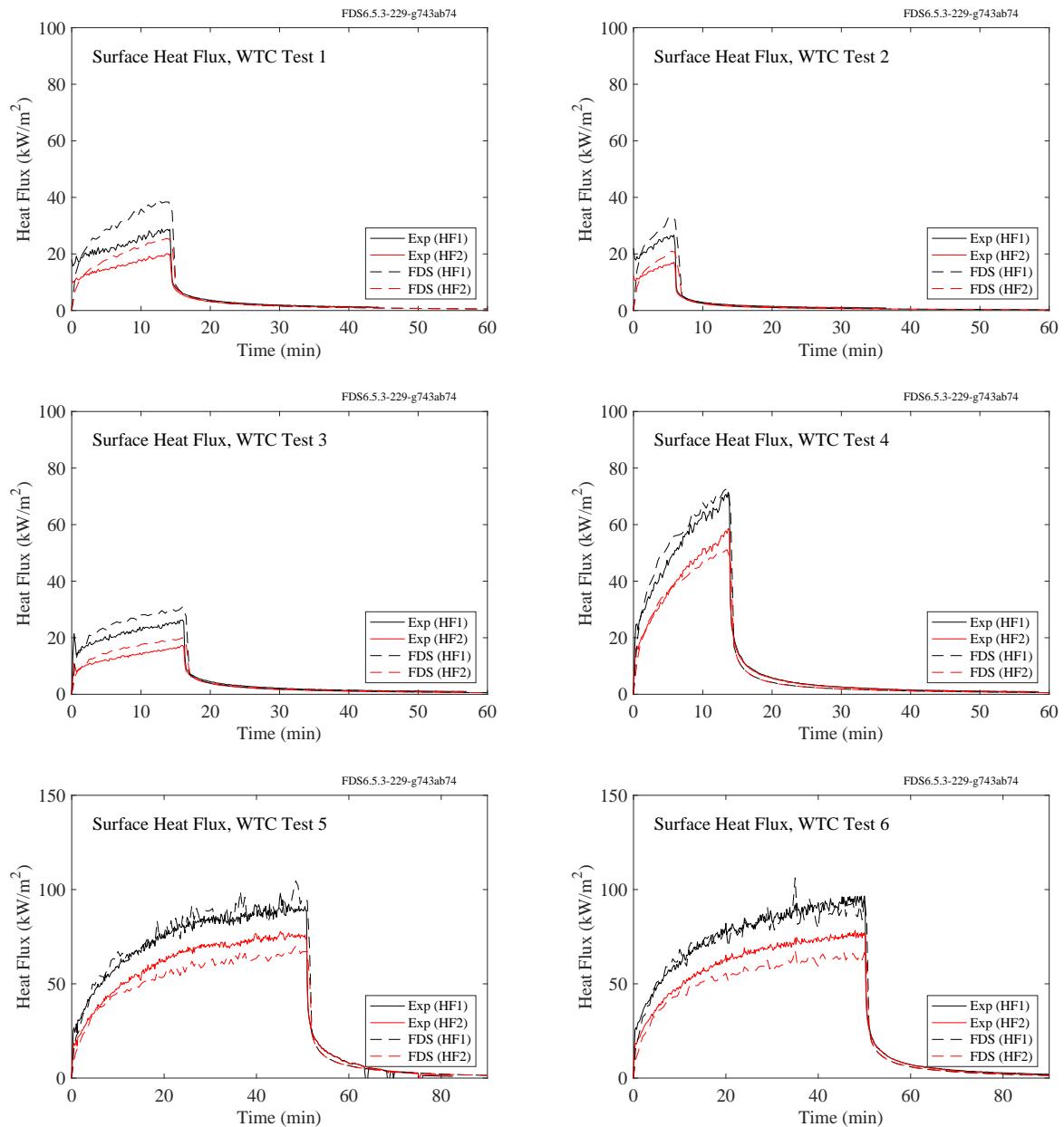


Figure 12.31: WTC experiments, heat flux to the floor.

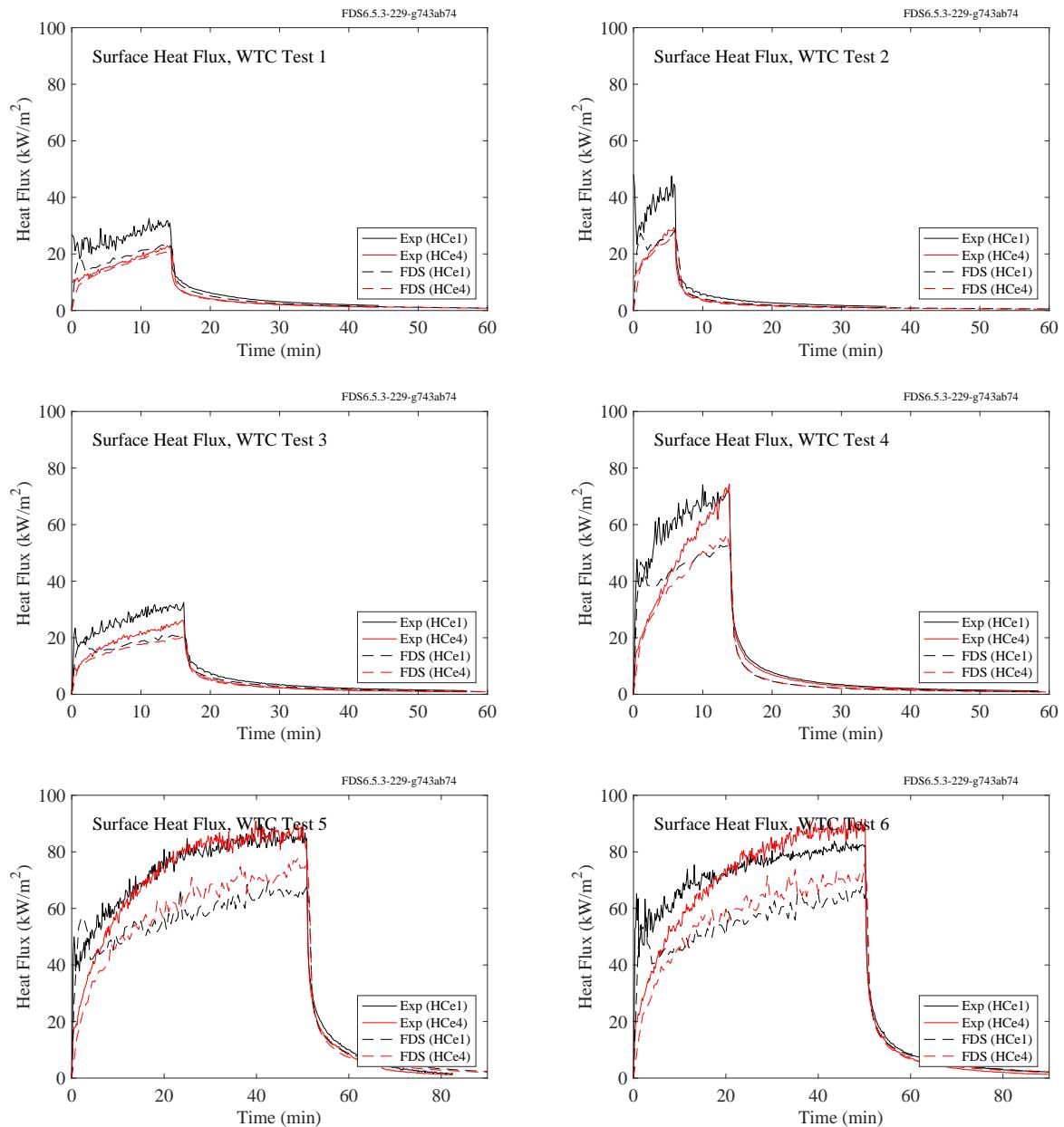


Figure 12.32: WTC experiments, heat flux to the ceiling.

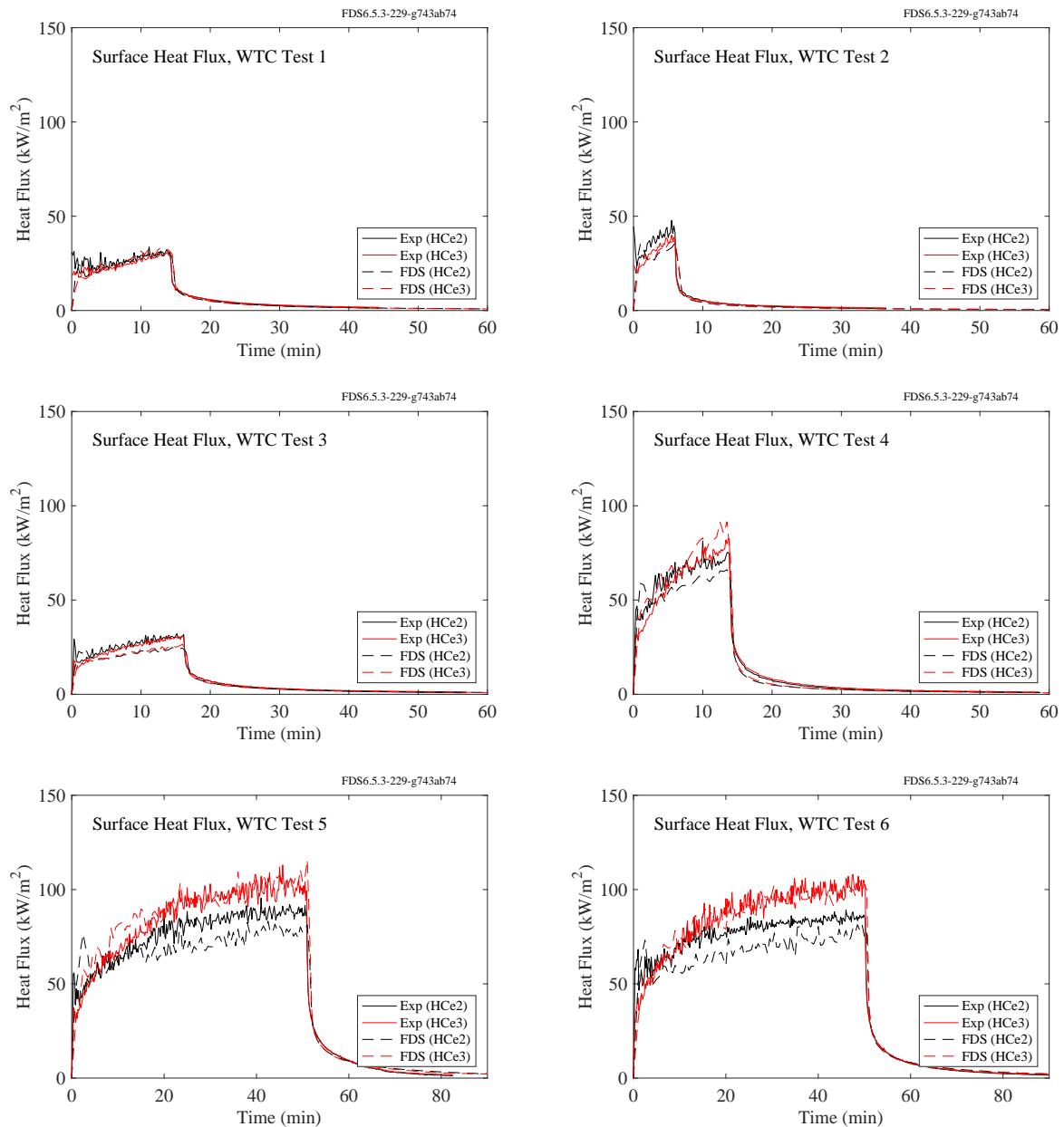


Figure 12.33: WTC experiments, heat flux to the ceiling.

### 12.1.10 Summary of Wall, Ceiling and Floor Heat Flux Predictions

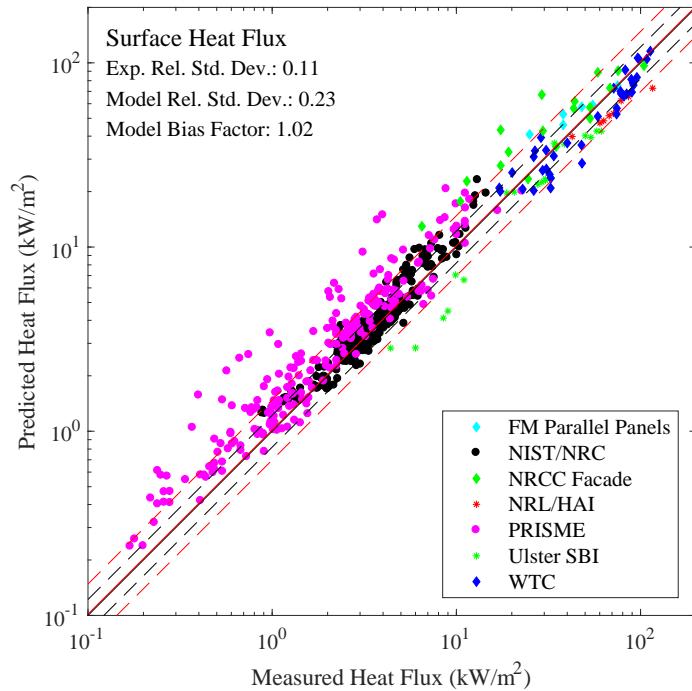


Figure 12.34: Summary of surface heat flux predictions.

## **12.2 Heat Flux to Targets**

### **12.2.1 Fleury Experiments**

The plots on the following pages contain comparisons of predicted and measured heat fluxes from a series of propane burner fires. Heat flux gauges were mounted on moveable dollies that were placed in front of, and to the side of, burners with dimensions of 0.3 m by 0.3 m (1:1 burner), 0.6 m by 0.3 m (2:1 burner), and 0.9 m by 0.3 m (3:1 burner). The heat release rates were set to 100 kW, 150 kW, 200 kW, 250 kW, and 300 kW. The gauges were mounted at heights of 0 m, 0.5 m, 1.0 m, and 1.5 m relative to the top edge of the burner. Each page contains the results for a given HRR.

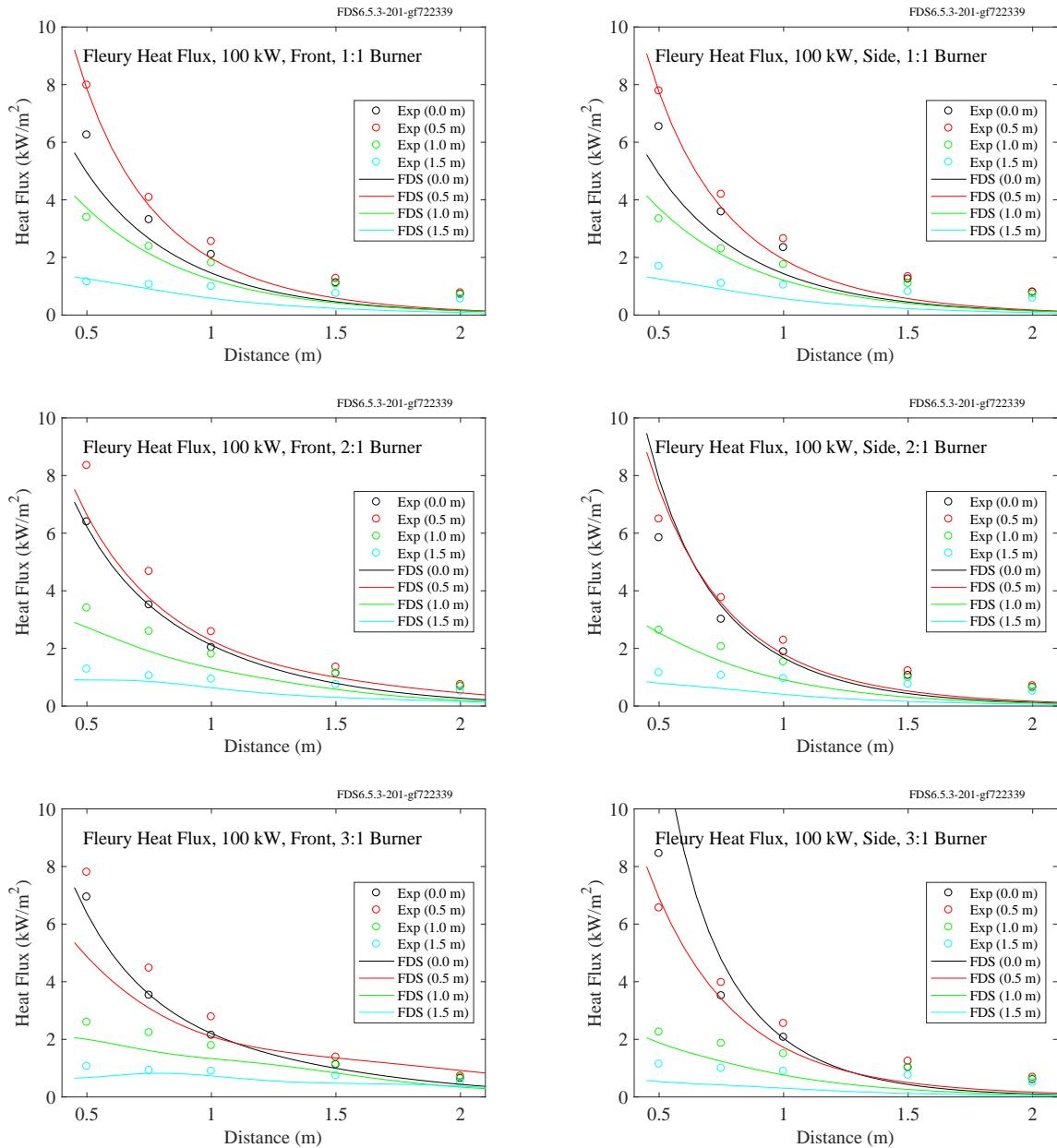


Figure 12.35: Comparison of predicted (lines) and measured (circles) heat flux for the 100 kW Fleury fires.

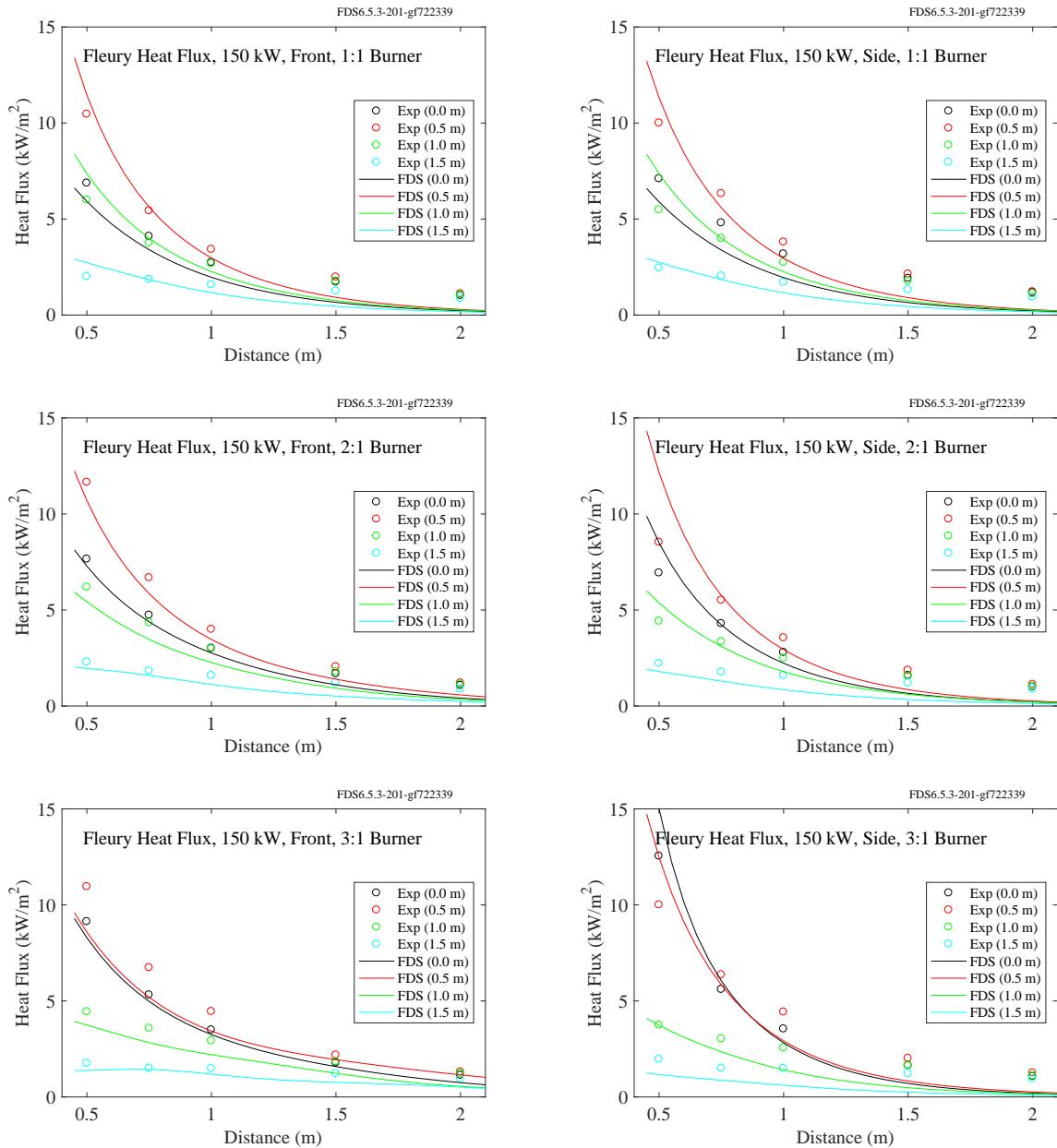


Figure 12.36: Comparison of predicted (lines) and measured (circles) heat flux for the 150 kW Fleury fires.

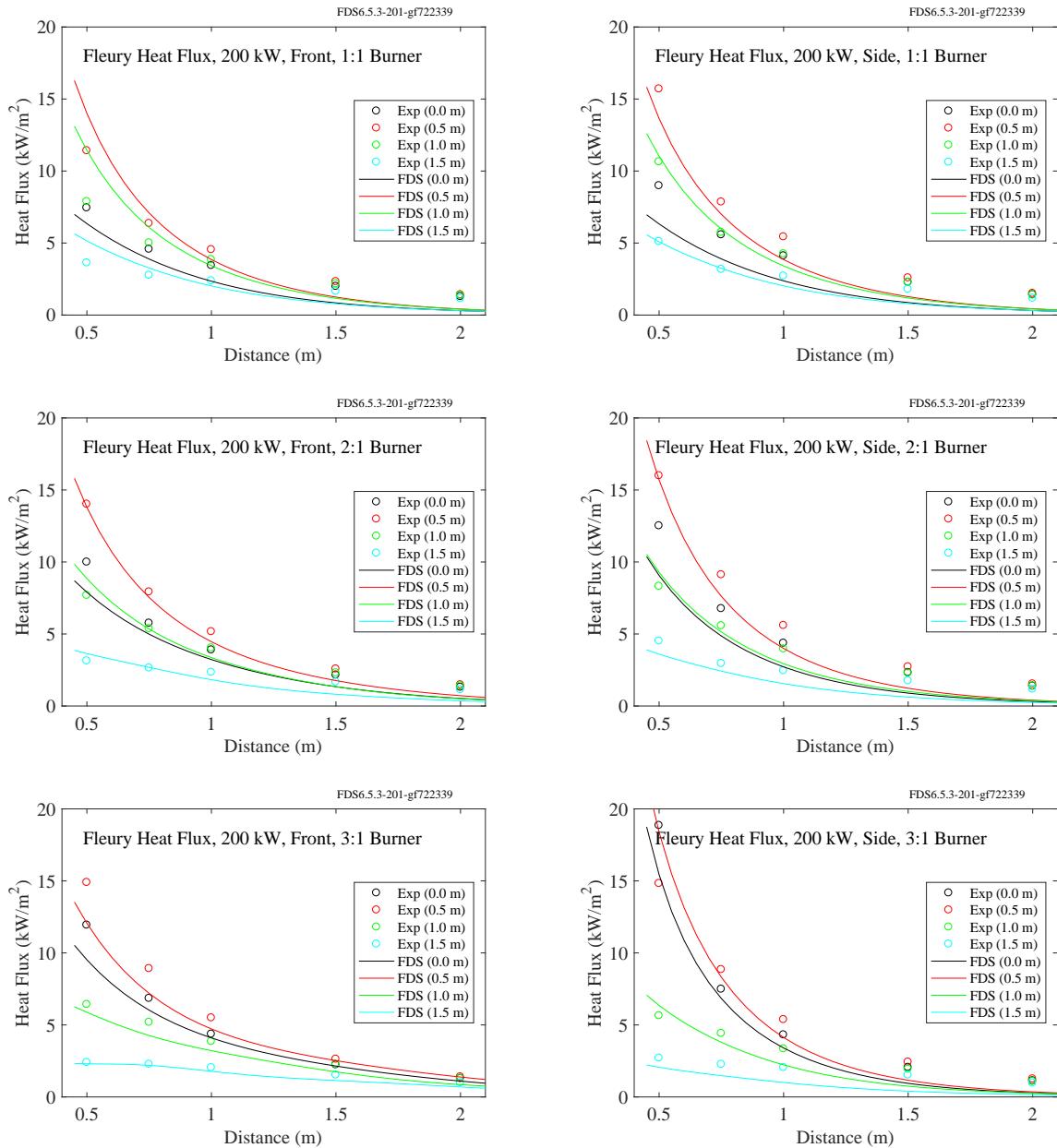


Figure 12.37: Comparison of predicted (lines) and measured (circles) heat flux for the 200 kW Fleury fires.

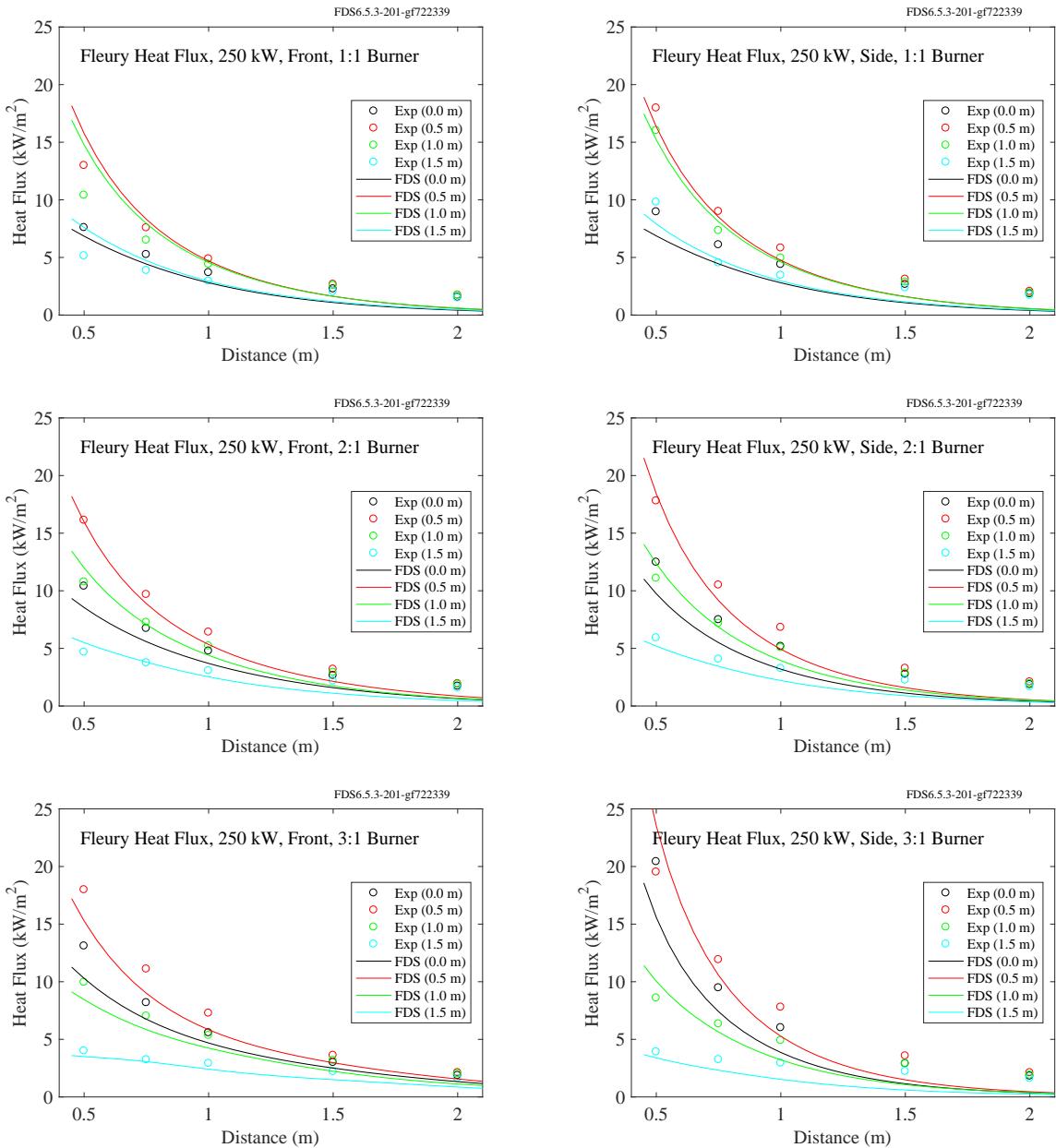


Figure 12.38: Comparison of predicted (lines) and measured (circles) heat flux for the 250 kW Fleury fires.

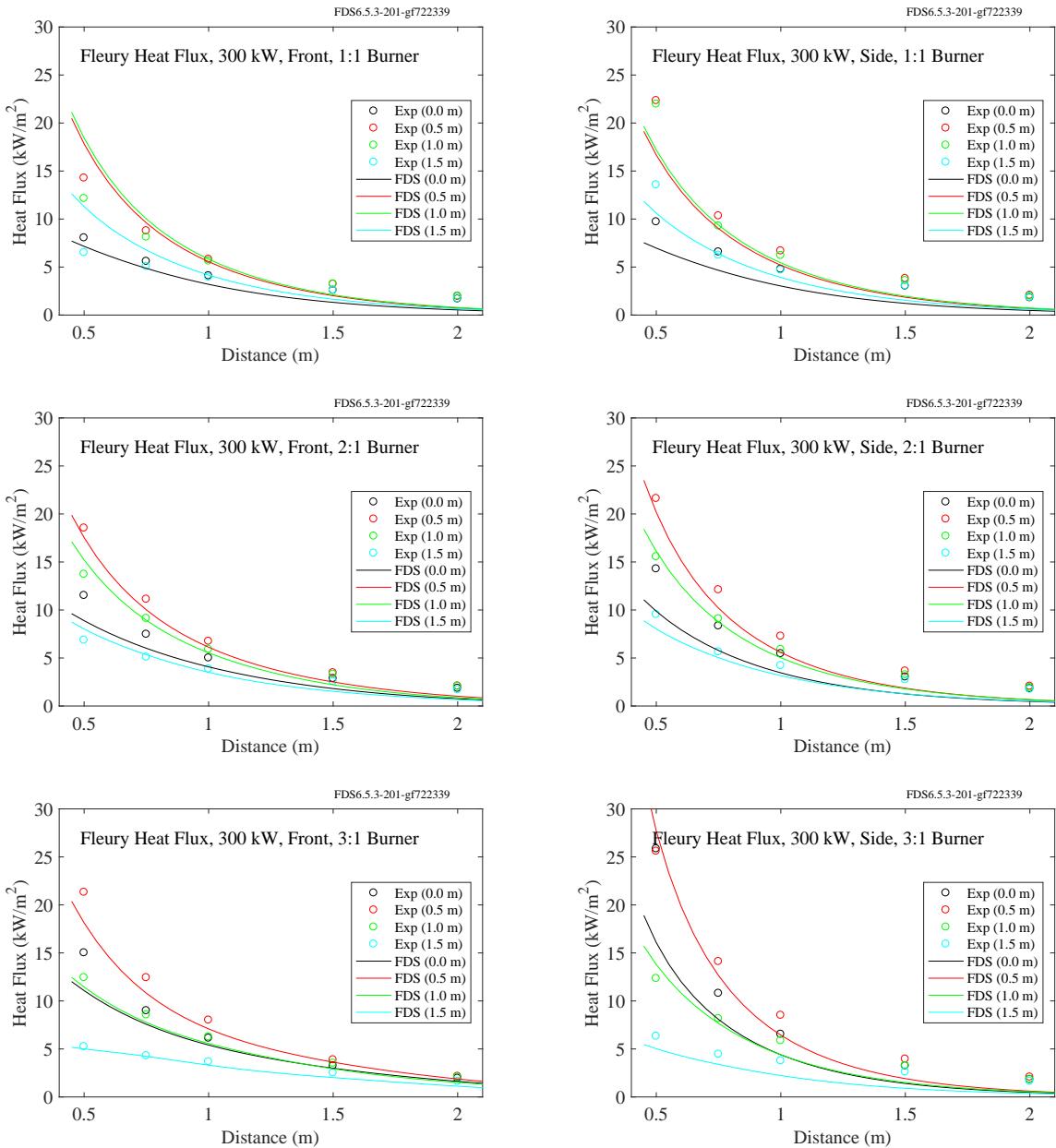


Figure 12.39: Comparison of predicted (lines) and measured (circles) heat flux for the 300 kW Fleury fires.

### 12.2.2 Hamins Gas Burner Experiments

Predicted and measured radial and vertical heat flux profiles from 30 methane, 34 propane, and 16 acetylene gas burner fire experiments conducted by Anthony Hamins [242] are displayed in this section. The relevant information about the fires is included in Tables 12.3, 12.4, and 12.5. In each table,  $D$  is the diameter of the burner and  $R_0$  is the radial distance from the burner centerline to the position of the vertical heat flux measurements.  $\dot{Q}$  is the product of the mass loss rate,  $\dot{m}$ , and the heat of combustion. The heat of combustion of acetylene is 48.2 kJ/g; and for propane, 46.4 kJ/g. For the methane experiments, either methane (50.03 kJ/g) or natural gas (49.4 kJ/g) was used.  $\dot{Q}''$  is the heat release rate per unit area, and

$$\dot{Q}^* = \frac{\dot{Q}}{\rho_\infty T_\infty c_p \sqrt{g D D^2}} \quad ; \quad D^* = \left( \frac{\dot{Q}}{\rho_\infty T_\infty c_p \sqrt{g}} \right)^{2/5} \quad (12.2)$$

Note that in the test matrices, the values to the right of the double lines indicate parameters used in the simulations. The values for radiative fraction,  $\chi_{\text{rad}}$ , are suggested by Hamins [242]. The quantity  $D^*/\delta x$  is an indicator of grid resolution, where  $D^*$  is the characteristic burner dimension and  $\delta x$  is the grid cell size.

## Methane Experiments

Table 12.3: Parameters of the Hamins methane burner experiments. The asterisk after the Test No. indicates that natural gas was used as fuel. The soot and CO yields were assumed to be zero.

Test No.	$D$ (m)	$R_0$ (m)	$\dot{Q}$ (kW)	$\dot{m}$ (g/s)	$\dot{Q}''$ (kW/m <sup>2</sup> )	$\dot{Q}^*$	$\chi_{\text{rad}}$	$D^*/\delta x$
1	0.1	0.13	0.42	0.0085	53.5	0.12	0.13	8.6
2	0.1	0.13	0.61	0.0122	77.7	0.18	0.13	10.0
3	0.1	0.13	0.78	0.0155	99.3	0.22	0.13	11.0
4	0.1	0.13	1.11	0.0222	141.3	0.32	0.16	12.7
5	0.1	0.13	1.89	0.0378	240.6	0.54	0.16	15.7
6*	0.35	0.40	11.2	0.226	115.9	0.14	0.08	6.4
7*	0.35	0.40	15.3	0.310	159.0	0.19	0.10	7.2
8*	0.35	0.40	10.5	0.212	109.0	0.13	0.08	6.2
9*	0.35	0.40	6.67	0.135	69.3	0.08	0.07	5.2
10*	0.35	0.64	19.3	0.391	200.7	0.24	0.12	7.9
11*	0.35	0.63	27.0	0.546	280.3	0.34	0.15	9.1
12*	0.35	0.81	40.6	0.822	422.2	0.51	0.18	10.7
13*	0.35	0.92	63.5	1.285	659.9	0.80	0.21	12.8
14*	0.35	0.92	90.3	1.828	938.7	1.13	0.22	14.7
15	0.35	0.92	178	3.567	1854.6	2.24	0.20	19.3
16	0.35	0.92	210	4.194	2180.8	2.63	0.20	20.6
17	0.35	0.92	34.0	0.679	353.2	0.43	0.16	9.9
18	0.35	0.90	145	2.904	1510.0	1.82	0.28	17.8
19	0.35	0.90	125	2.495	1297.7	1.56	0.23	16.7
20*	1.0	1.00	49.0	0.997	62.4	0.04	0.14	5.8
21*	1.0	1.00	81.0	1.648	103.1	0.07	0.15	7.0
22*	1.0	1.00	112	2.282	142.8	0.10	0.17	8.0
23*	1.0	1.00	129	2.635	164.8	0.12	0.18	8.5
24*	1.0	0.79	52.7	1.069	67.1	0.05	0.12	5.9
25*	1.0	0.79	69.7	1.414	88.8	0.06	0.12	6.6
26*	1.0	0.79	87.3	1.771	111.2	0.08	0.13	7.3
27*	1.0	0.79	102	2.081	130.6	0.09	0.13	7.7
28*	1.0	0.79	121	2.462	154.5	0.11	0.14	8.3
29*	1.0	0.79	138	2.793	175.3	0.12	0.16	8.7
30*	1.0	0.79	172	3.482	218.5	0.16	0.18	9.5

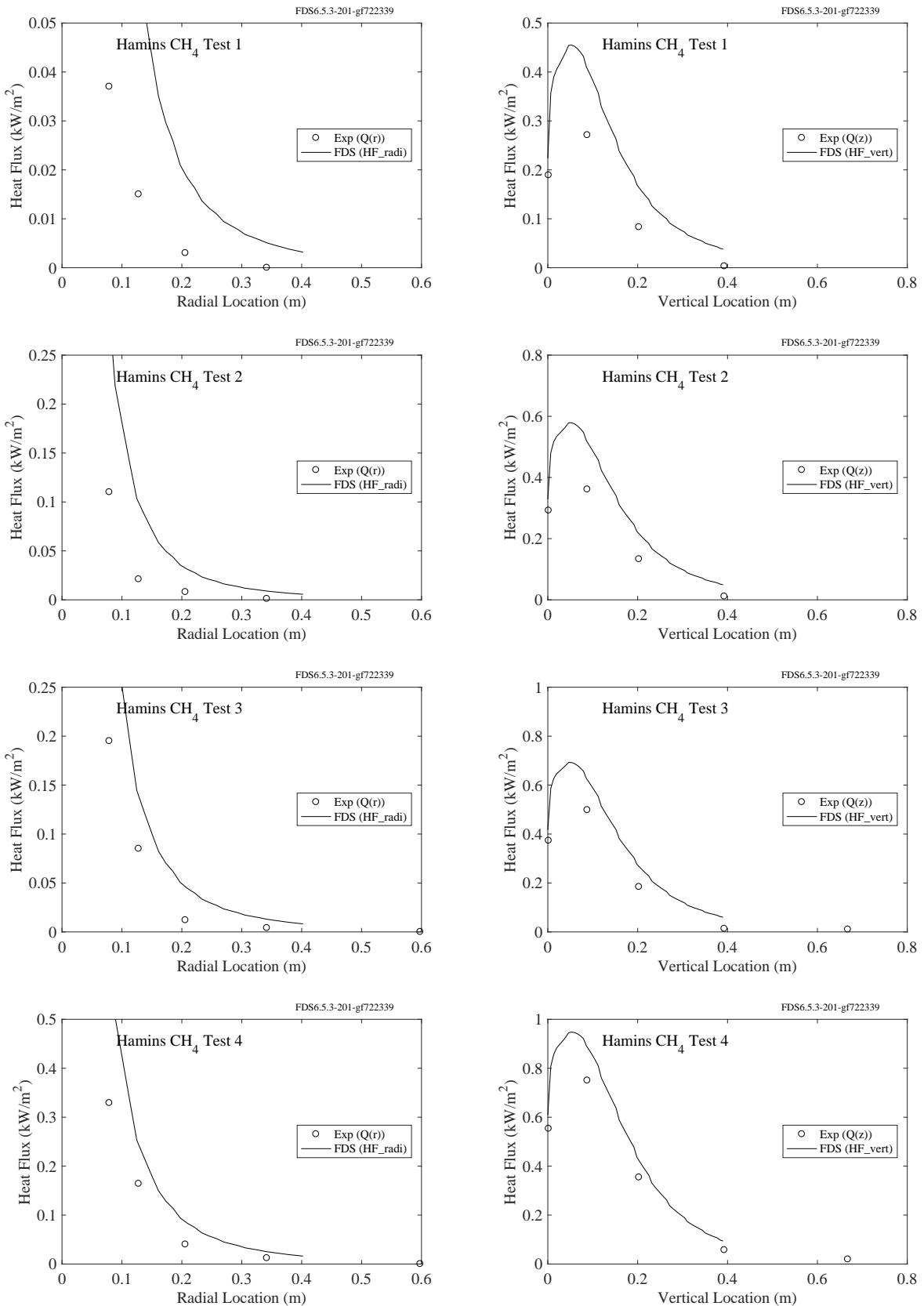


Figure 12.40: Comparison of predicted and measured heat fluxes, Hamins Methane Tests 1-4.

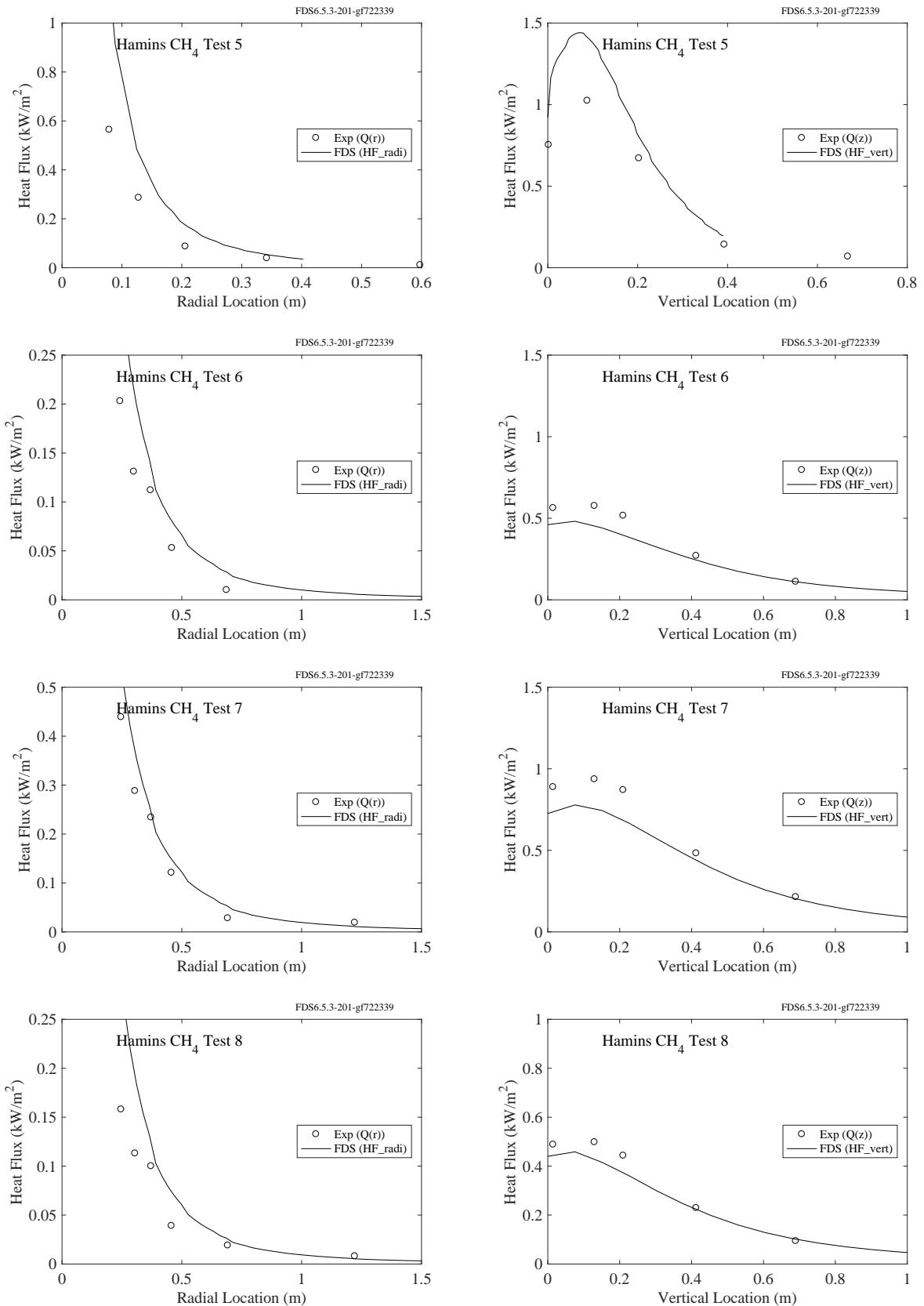


Figure 12.41: Comparison of predicted and measured heat fluxes, Hamins Methane Tests 5-8.

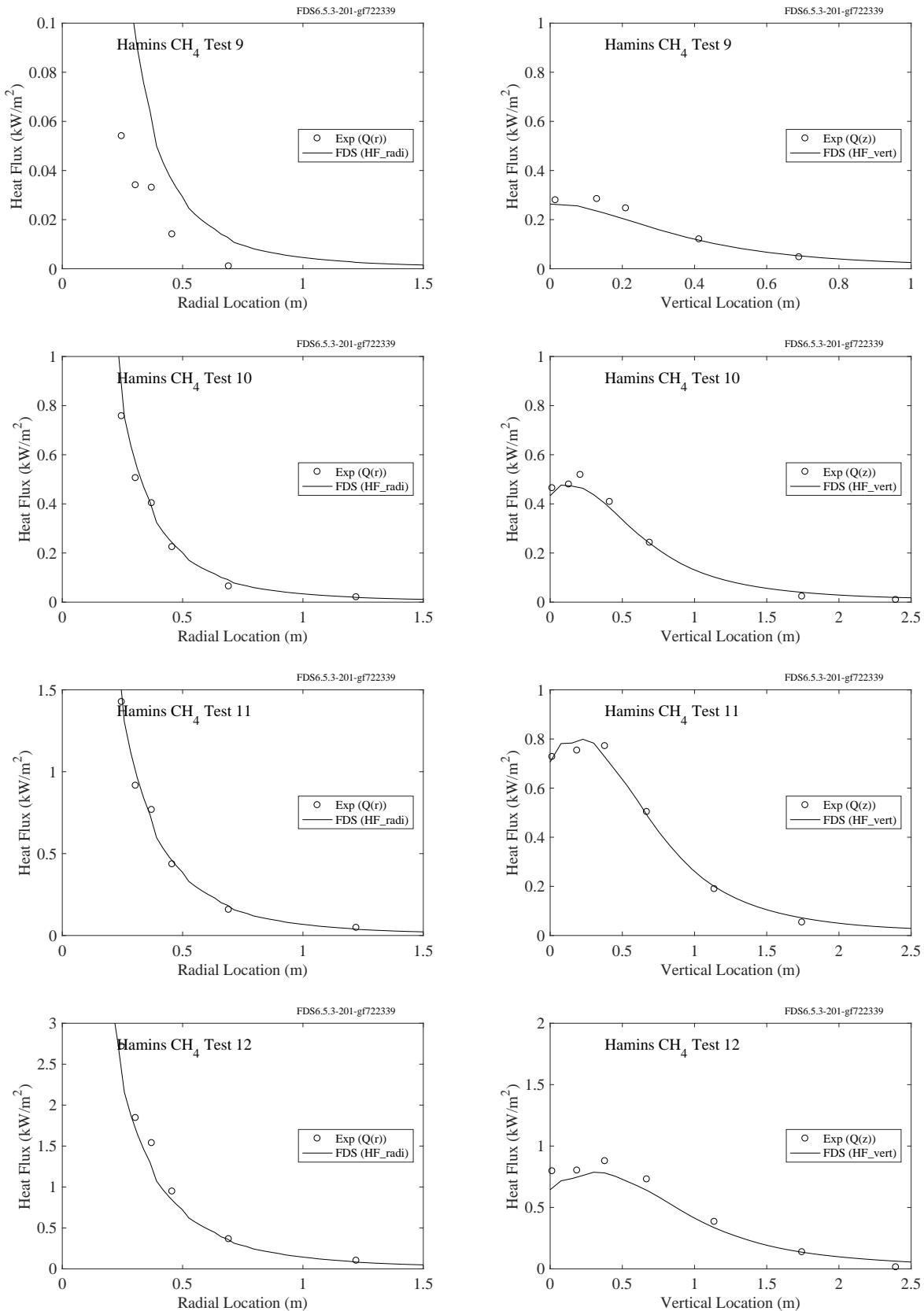


Figure 12.42: Comparison of predicted and measured heat fluxes, Hamins Methane Tests 9-12.

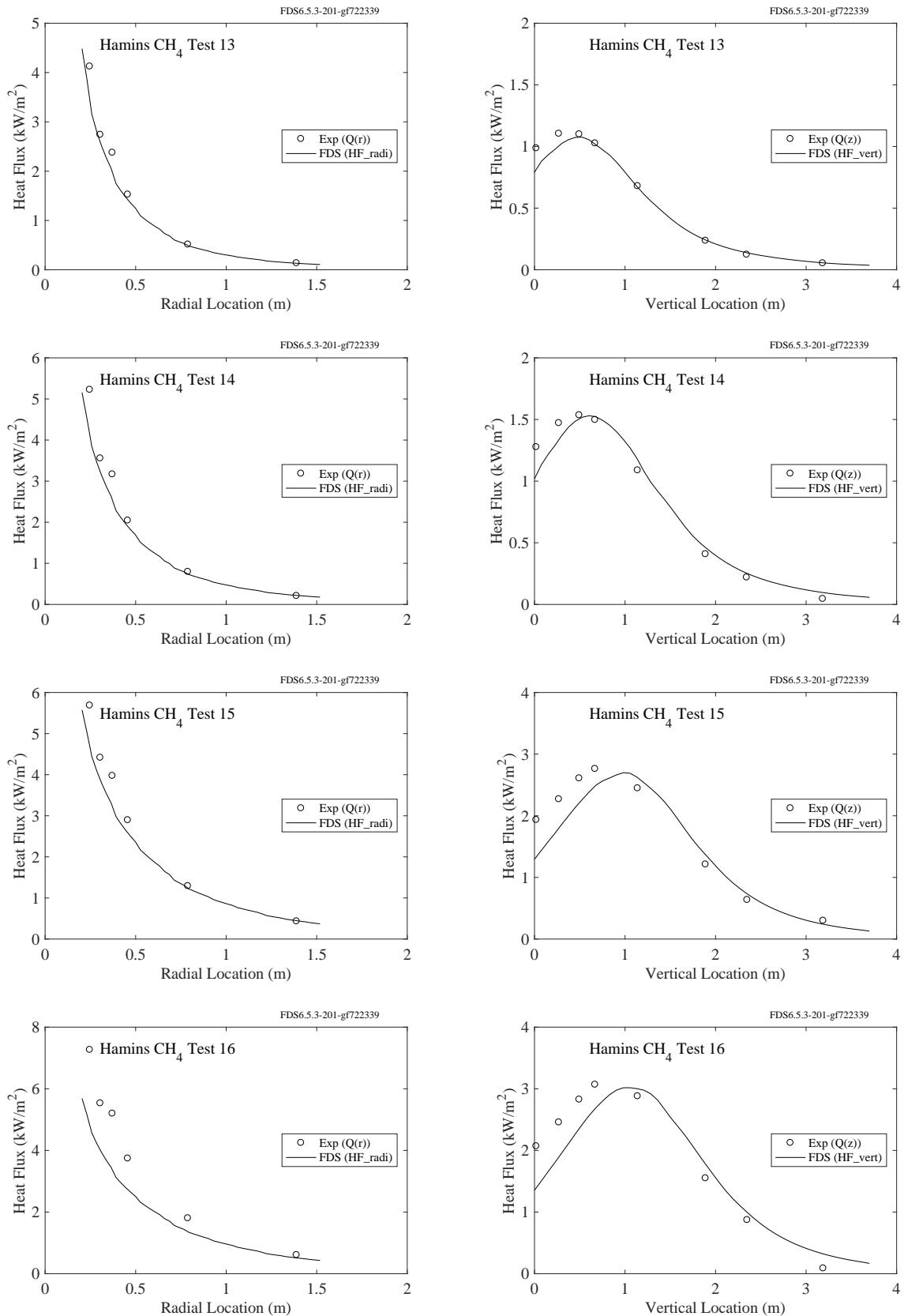


Figure 12.43: Comparison of predicted and measured heat fluxes, Hamins Methane Tests 13-16.

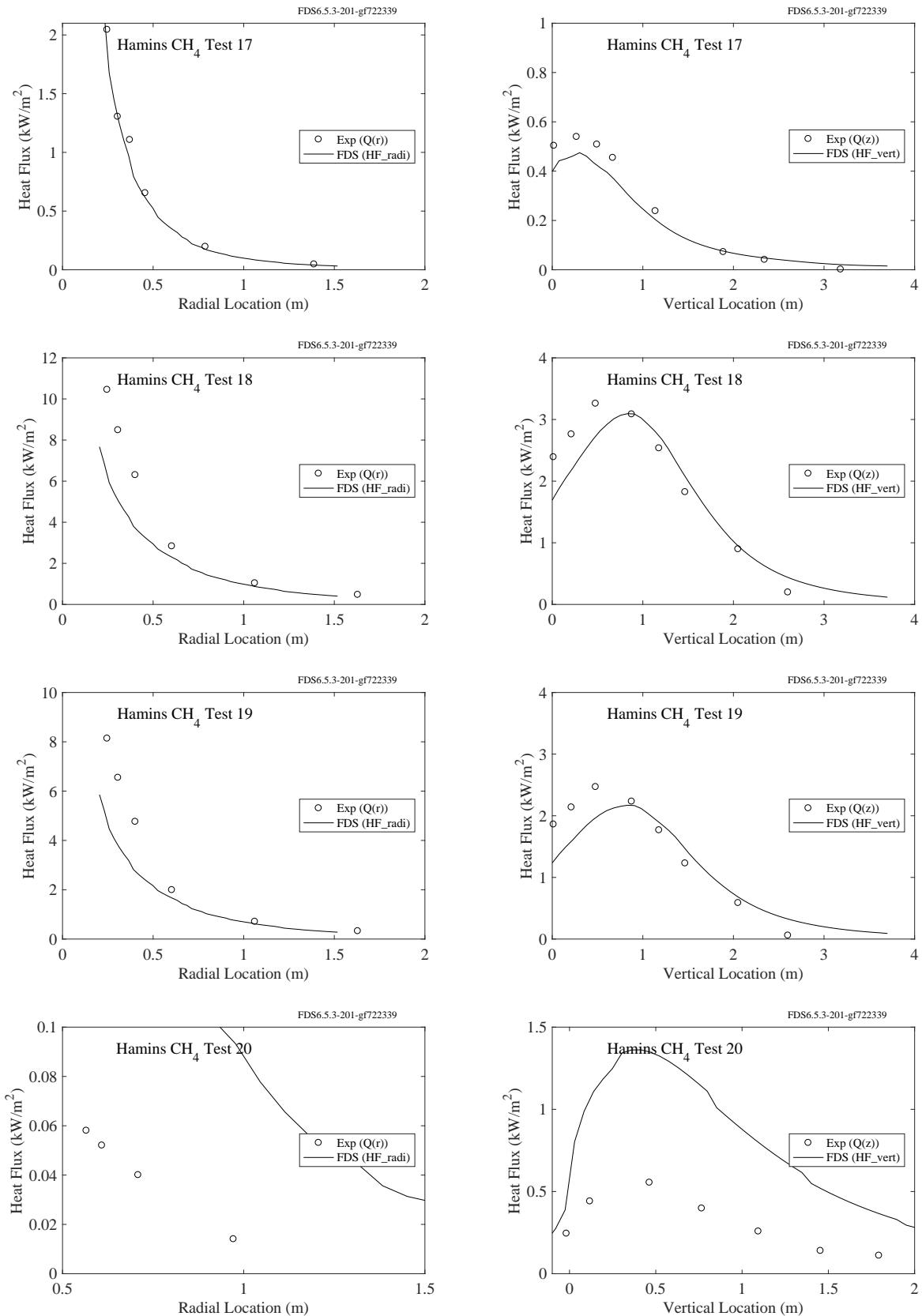


Figure 12.44: Comparison of predicted and measured heat fluxes, Hamins Methane Tests 17-20.

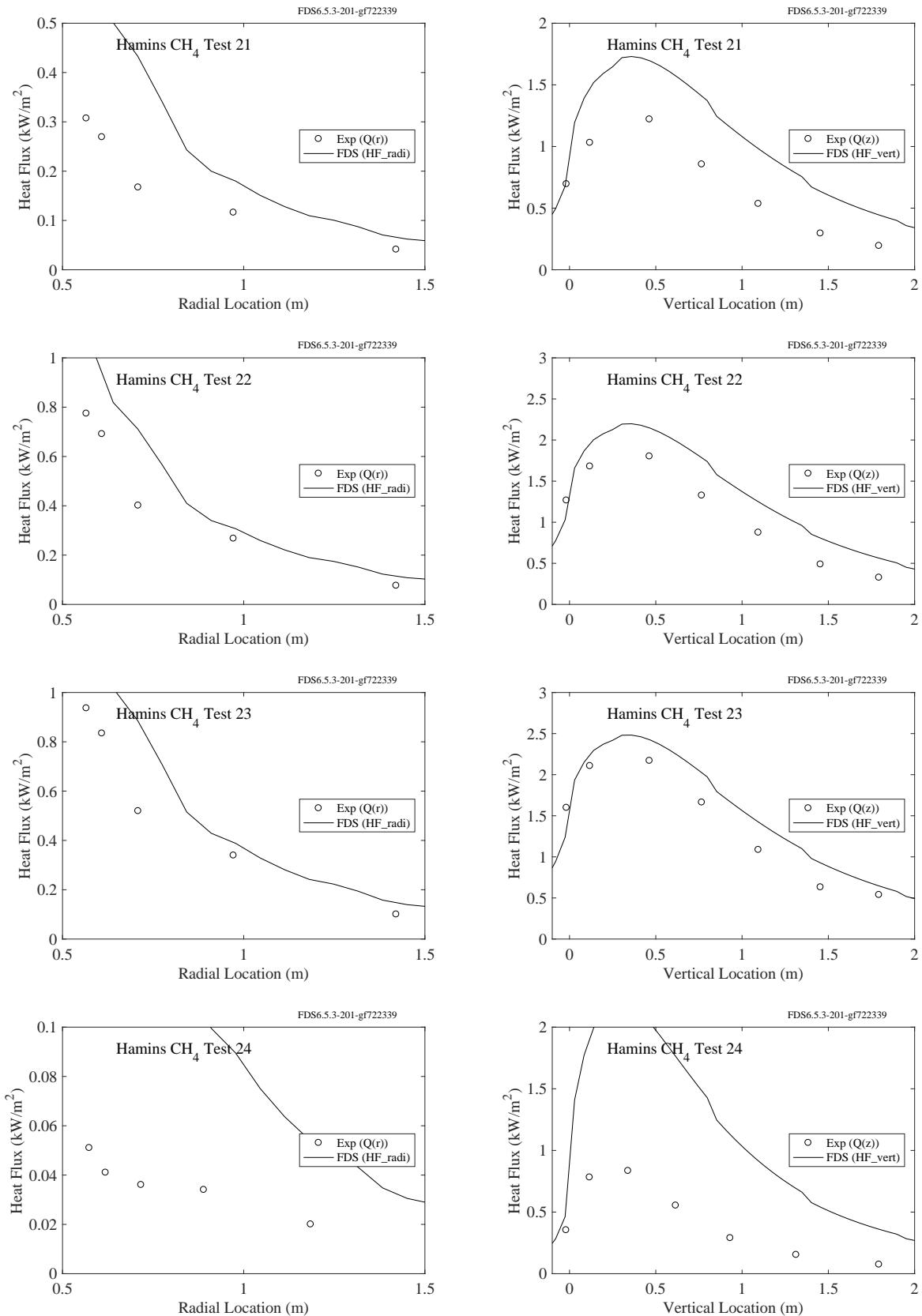


Figure 12.45: Comparison of predicted and measured heat fluxes, Hamins Methane Tests 21-24.

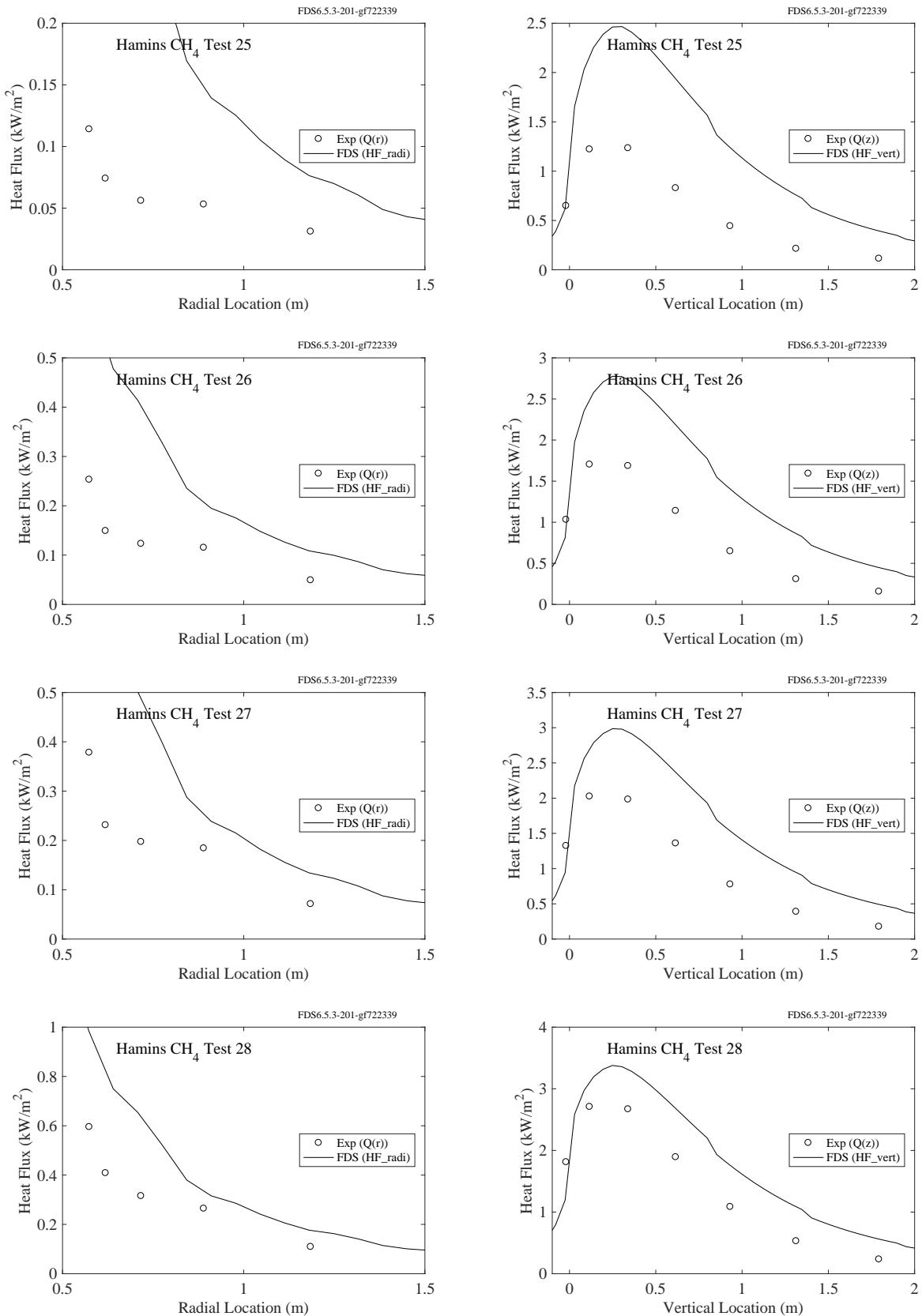


Figure 12.46: Comparison of predicted and measured heat fluxes, Hamins Methane Tests 25-28.

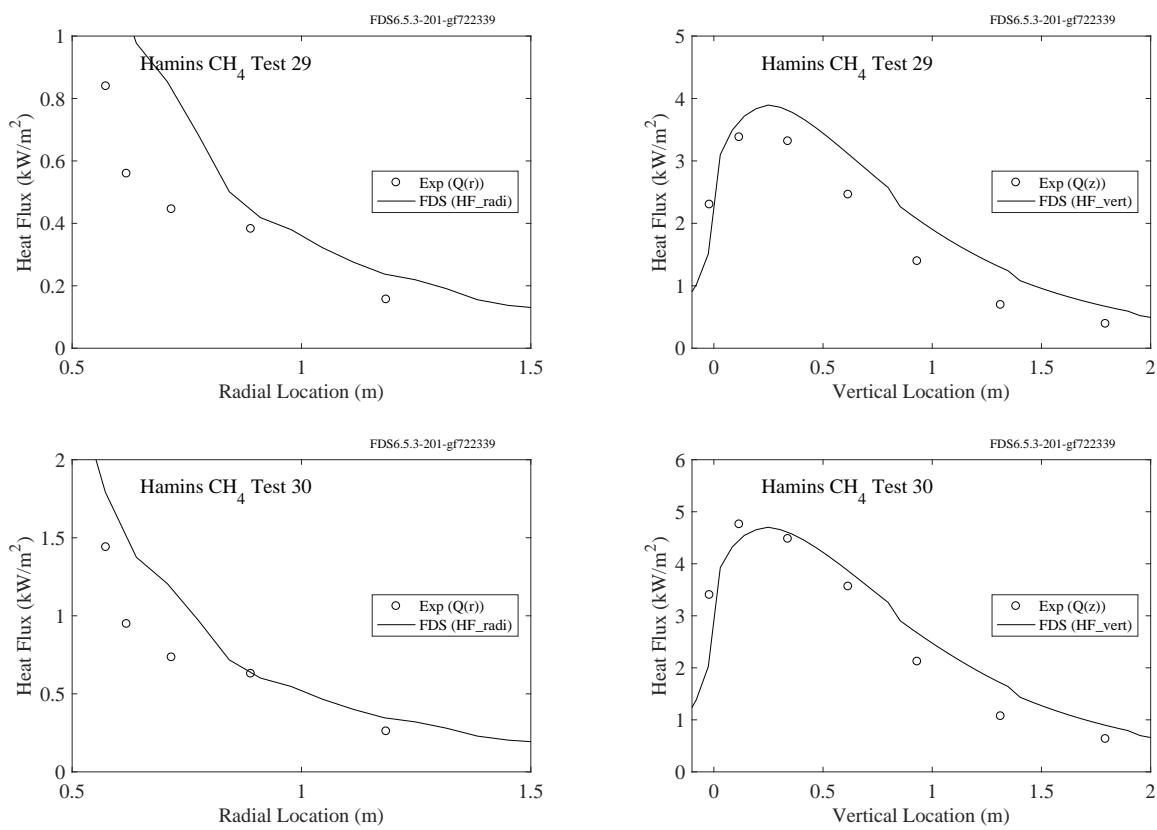


Figure 12.47: Comparison of predicted and measured heat fluxes, Hamins Methane Tests 29-30.

## Propane Experiments

Table 12.4: Parameters of the Hamins propane burner experiments. Note that in all cases, the soot and CO yields were taken to be 0.024 and 0.005, respectively, based on the measurements of Tewarson [214].

Test No.	$D$ (m)	$R_0$ (m)	$\dot{Q}$ (kW)	$\dot{m}$ (kg/s)	$\dot{Q}''$ (kW/m <sup>2</sup> )	$\dot{Q}^*$	$\chi_{\text{rad}}$	$D^*/\delta x$
1	0.1	0.26	2.7	0.058	343.8	0.78	0.22	9.0
2	0.1	0.26	6.8	0.148	870.9	1.96	0.27	13.1
3	0.1	0.26	11.8	0.254	1499.9	3.38	0.29	16.3
4	0.1	0.37	17.9	0.386	2277.8	5.14	0.29	19.2
5	0.1	0.37	25.2	0.543	3203.5	7.22	0.30	22.1
6	0.1	0.49	36.9	0.796	4698.3	10.6	0.30	25.7
7	0.1	0.13	0.4	0.010	56.0	0.13	0.12	4.4
8	0.1	0.13	0.8	0.017	99.3	0.22	0.12	5.5
9	0.1	0.13	0.6	0.013	76.4	0.17	0.12	4.9
10	0.1	0.13	1.0	0.021	123.5	0.28	0.15	6.0
11	0.1	0.13	1.4	0.031	183.3	0.41	0.18	7.0
12	0.1	0.13	2.2	0.046	273.7	0.62	0.23	8.2
13	0.1	0.19	3.4	0.074	434.2	0.98	0.24	9.9
14	0.1	0.19	5.6	0.122	718.1	1.62	0.26	12.1
15	0.1	0.28	11.9	0.257	1513.9	3.41	0.26	16.3
16	0.1	0.28	24.8	0.535	3156.4	7.12	0.29	21.9
17	0.35	0.92	33.9	0.732	352.8	0.43	0.25	9.9
18	0.35	0.92	124.9	2.694	1298.1	1.56	0.30	16.7
19	0.35	0.57	20.0	0.431	207.9	0.25	0.18	8.0
20	0.35	0.57	15.6	0.336	162.0	0.20	0.14	7.3
21	0.35	0.39	19.0	0.409	197.3	0.24	0.13	7.9
22	0.35	0.39	14.6	0.316	152.2	0.18	0.10	7.1
23	0.35	0.68	108.2	2.334	1124.5	1.36	0.29	15.8
24	0.35	0.68	102.3	2.207	1063.7	1.28	0.31	15.5
25	0.35	0.68	79.7	1.719	828.4	1.00	0.28	14.0
26	0.35	0.51	12.0	0.258	124.5	0.15	0.08	6.6
27	1.0	0.81	55.2	1.190	70.2	0.05	0.11	6.0
28	1.0	0.81	81.7	1.761	104.0	0.07	0.15	7.1
29	1.0	0.81	107.3	2.315	136.7	0.10	0.18	7.9
30	1.0	1.00	136.4	2.943	173.7	0.12	0.22	8.7
31	1.0	0.97	55.6	1.199	70.8	0.05	0.12	6.1
32	1.0	0.97	82.5	1.779	105.0	0.07	0.14	7.1
33	1.0	0.97	107.9	2.326	137.3	0.10	0.17	7.9
34	1.0	0.97	137.3	2.963	174.9	0.12	0.23	8.7

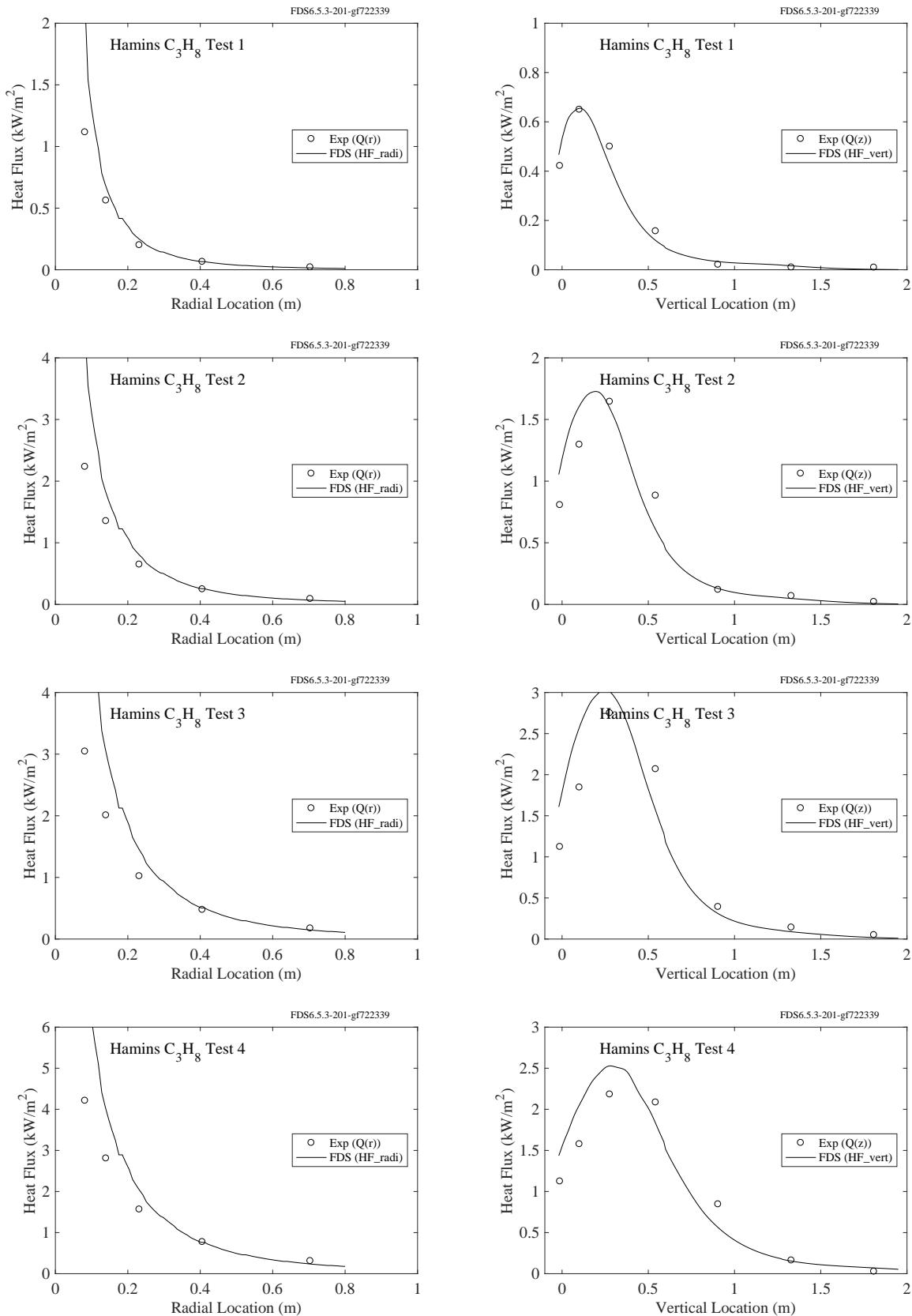


Figure 12.48: Comparison of predicted and measured heat fluxes, Hamins Propane Tests 1-4.

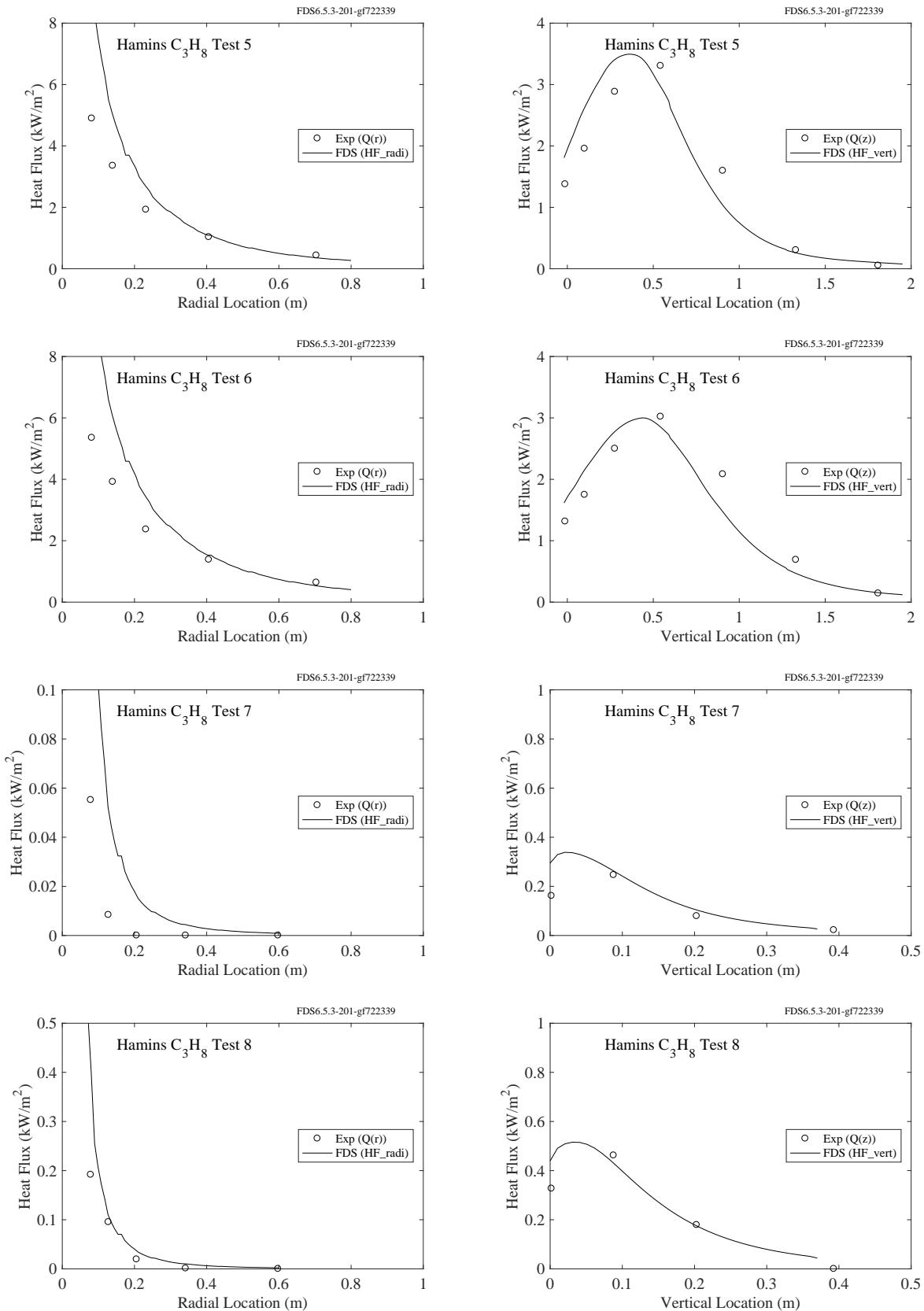


Figure 12.49: Comparison of predicted and measured heat fluxes, Hamins Propane Tests 5-8.

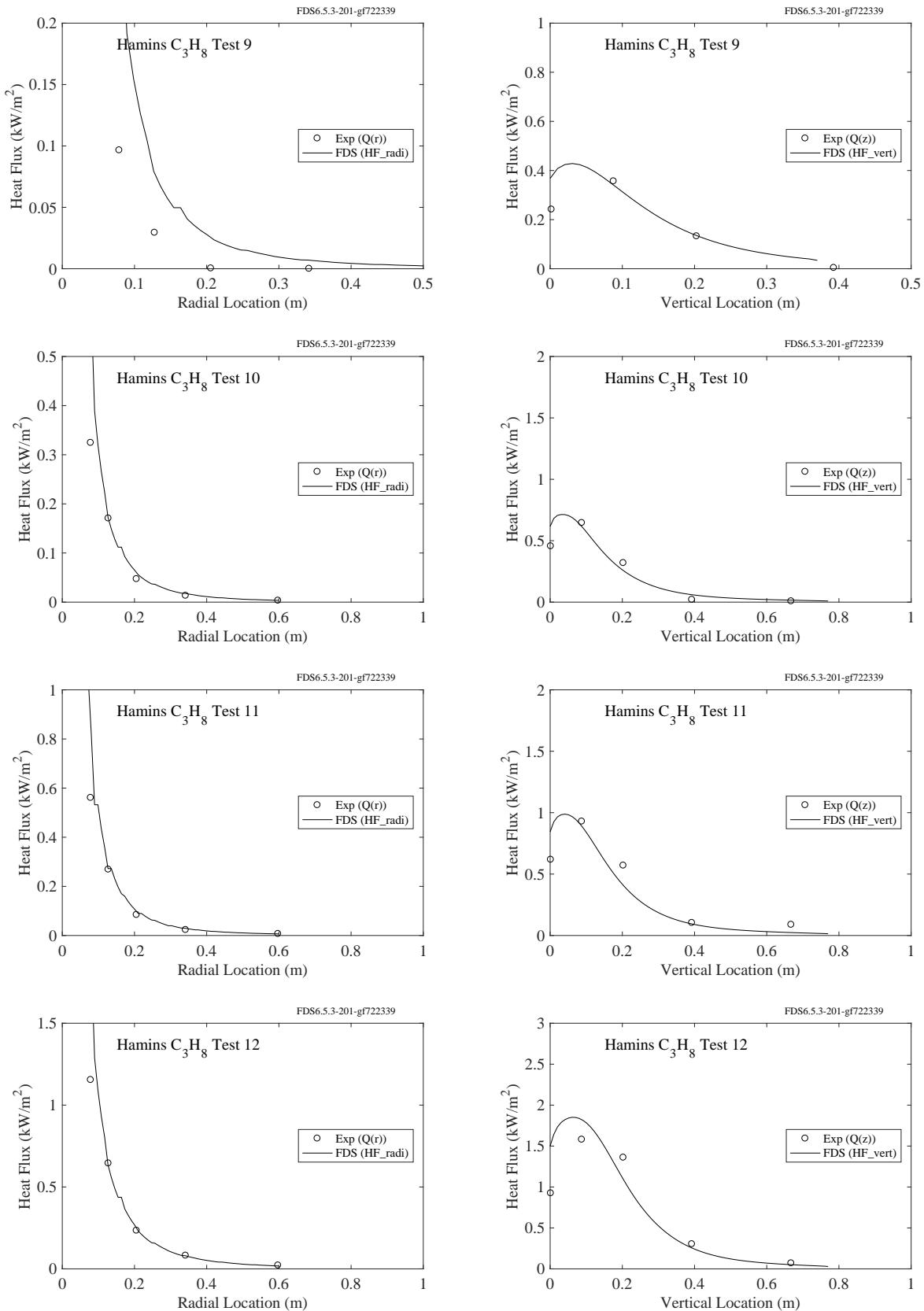


Figure 12.50: Comparison of predicted and measured heat fluxes, Hamins Propane Tests 9-12.

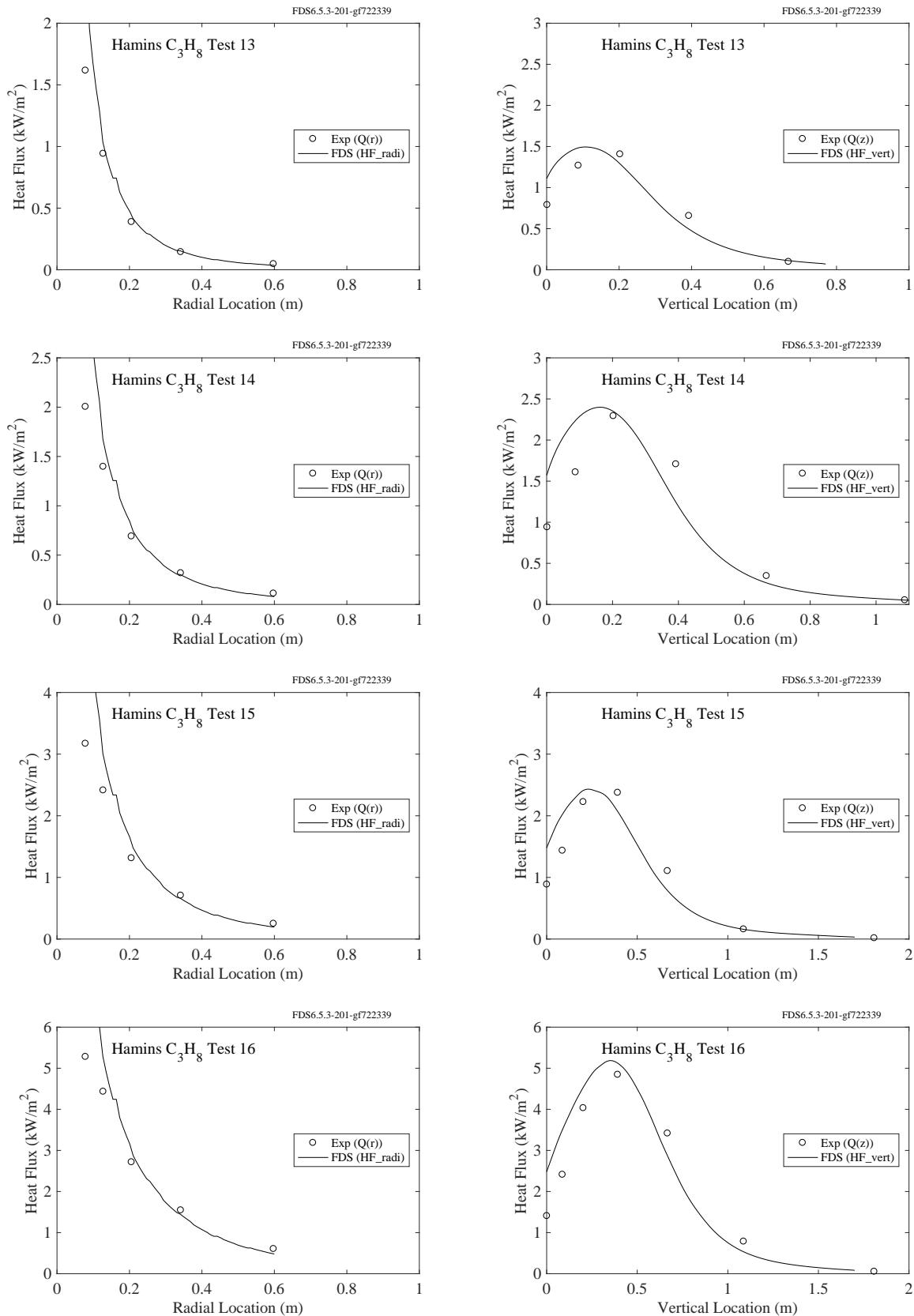


Figure 12.51: Comparison of predicted and measured heat fluxes, Hamins Propane Tests 13-16.

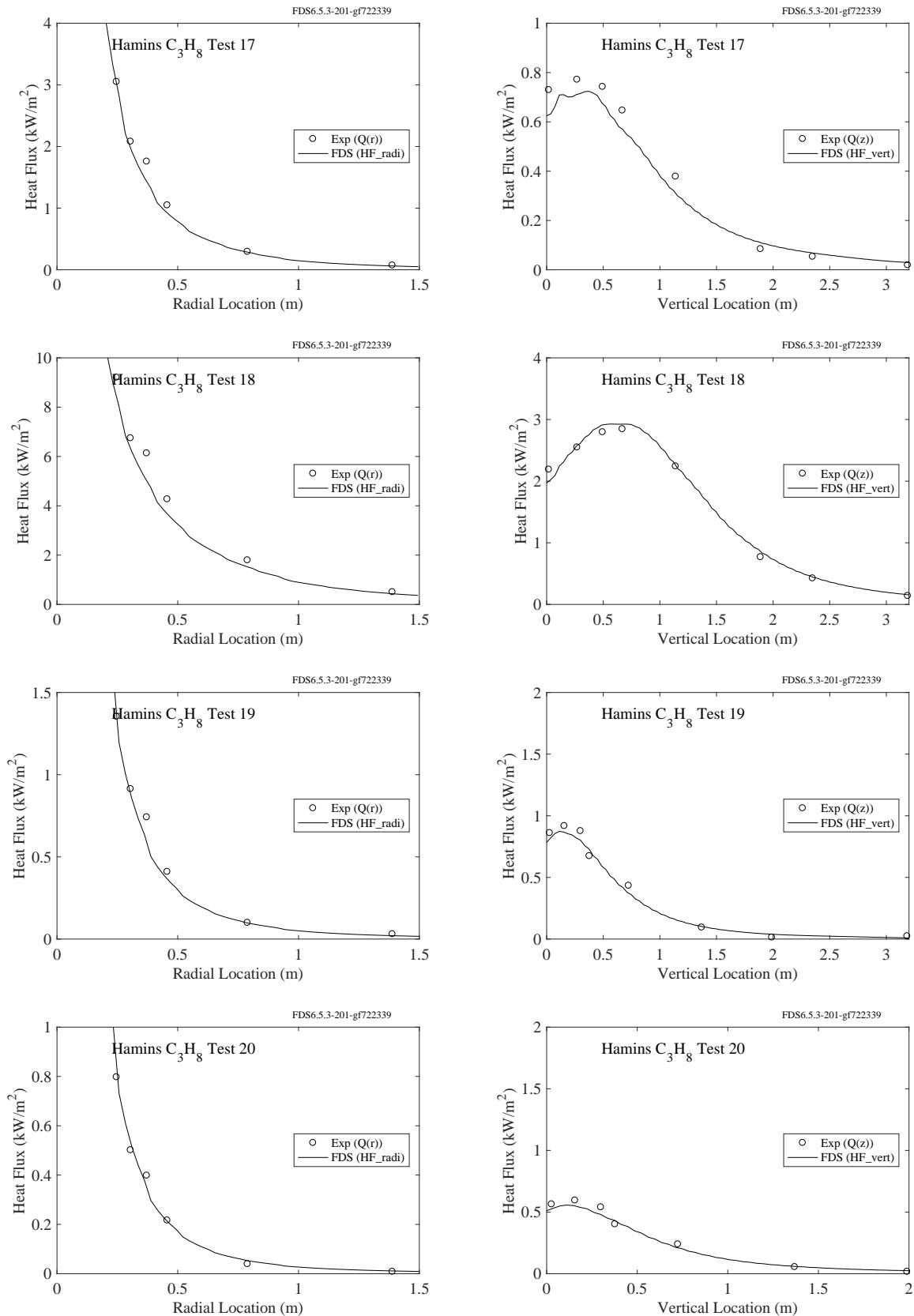


Figure 12.52: Comparison of predicted and measured heat fluxes, Hamins Propane Tests 17-20.

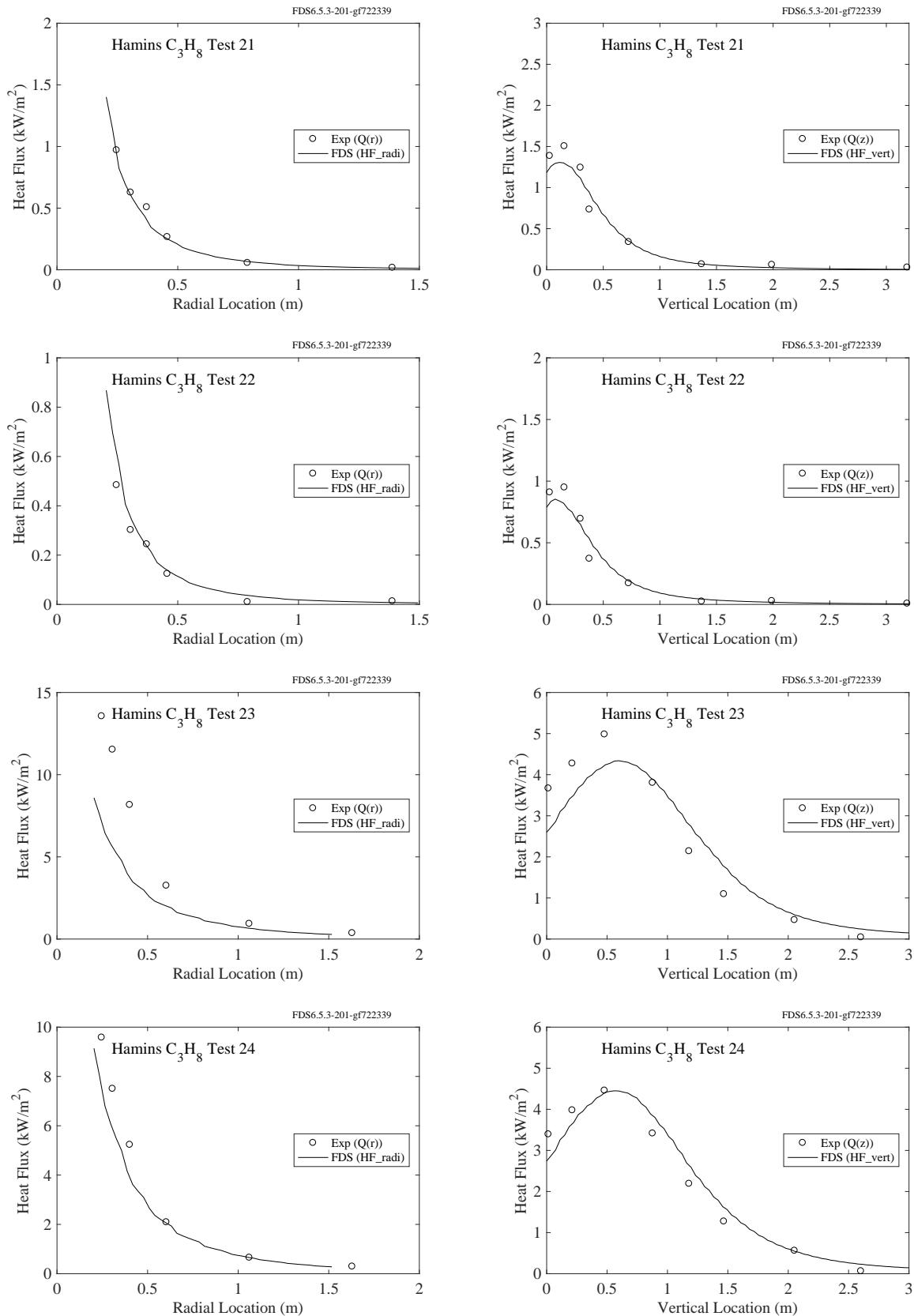


Figure 12.53: Comparison of predicted and measured heat fluxes, Hamins Propane Tests 21-24.

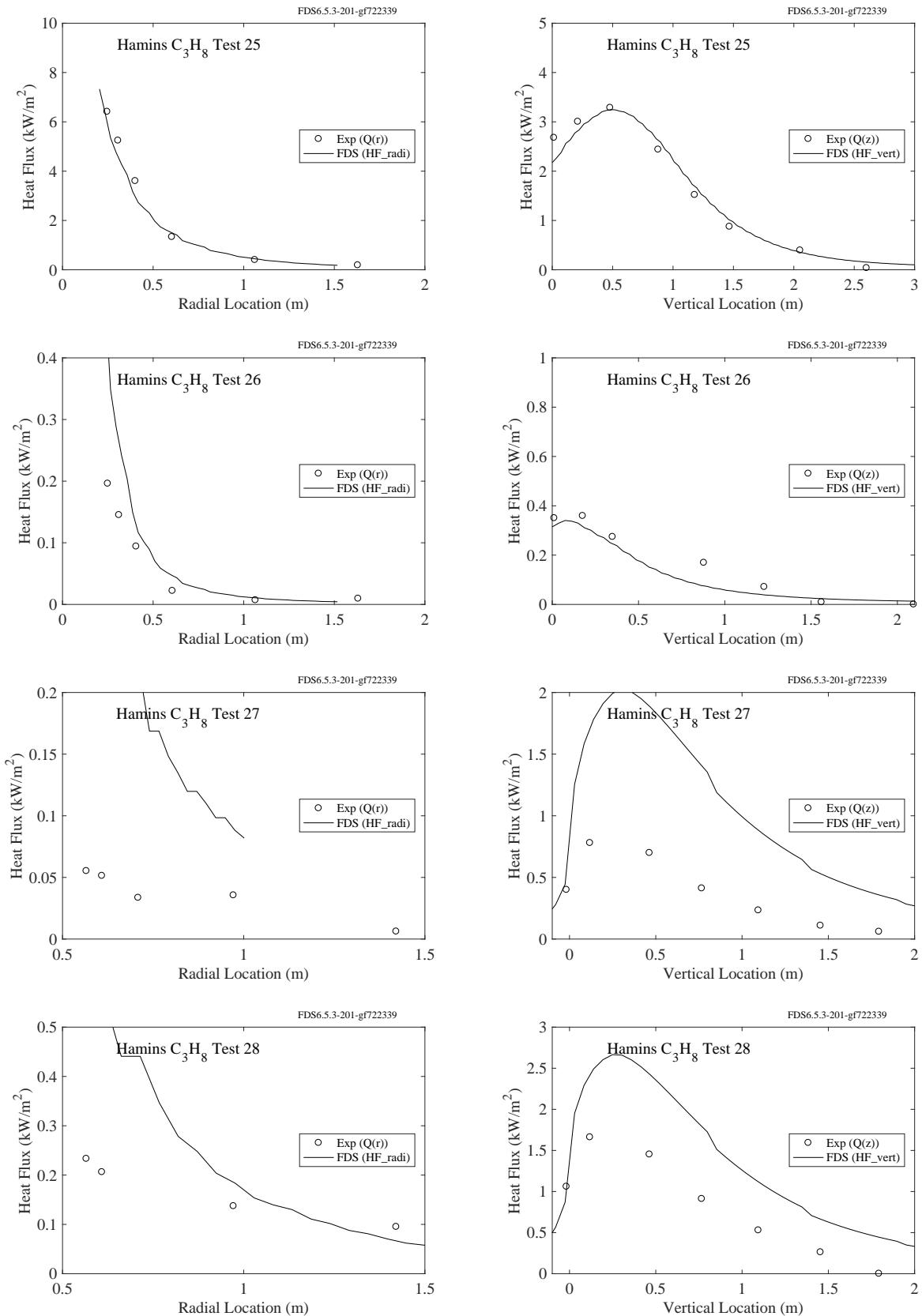


Figure 12.54: Comparison of predicted and measured heat fluxes, Hamins Propane Tests 25-28.

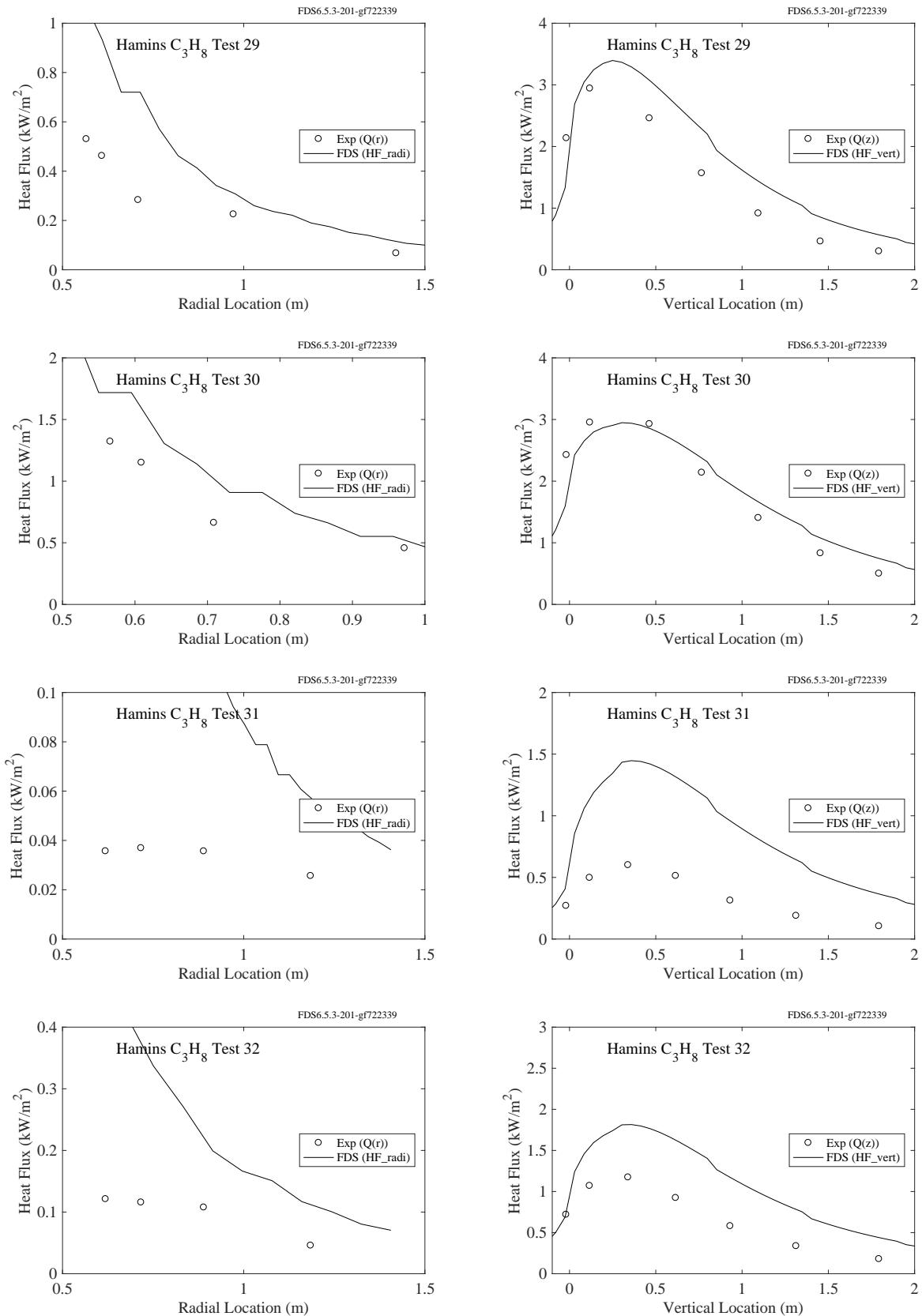


Figure 12.55: Comparison of predicted and measured heat fluxes, Hamins Propane Tests 29-32.

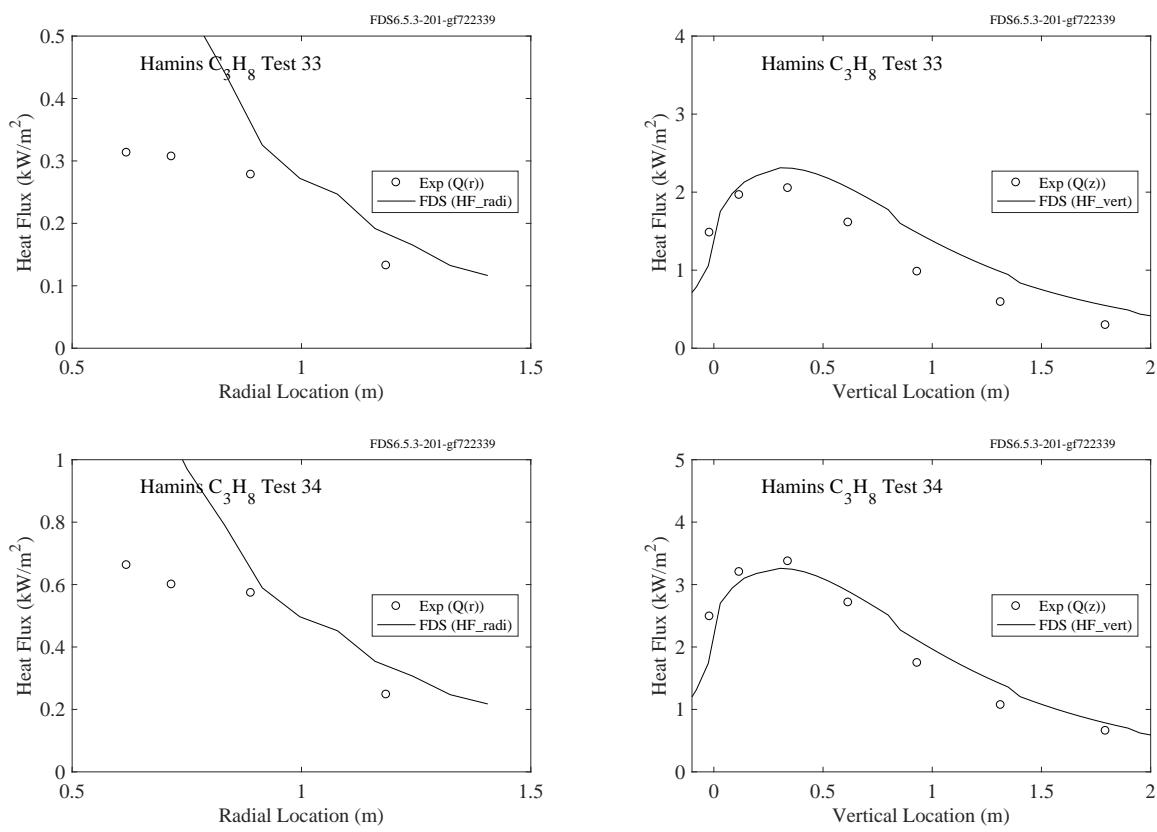


Figure 12.56: Comparison of predicted and measured heat fluxes, Hamins Propane Tests 33-34.

## Acetylene Experiments

Table 12.5: Parameters of the Hamins acetylene burner experiments. Note that in all cases, the soot and CO yields were taken to be 0.096 and 0.042, respectively, based on the measurements of Tewarson [214].

Test No.	$D$ (m)	$R_0$ (m)	$\dot{Q}$ (kW)	$\dot{m}$ (kg/s)	$\dot{Q}''$ (kW/m <sup>2</sup> )	$\dot{Q}^*$	$\chi_{\text{rad}}$	$D^*/\delta x$
1	0.10	0.13	0.45	0.009	57.3	0.13	0.12	4.4
2	0.10	0.13	0.56	0.012	71.3	0.16	0.15	4.8
3	0.10	0.13	0.90	0.019	114.6	0.26	0.18	5.8
4	0.10	0.13	1.29	0.027	164.2	0.37	0.27	6.7
5	0.10	0.13	1.54	0.032	196.1	0.44	0.31	7.2
6	0.35	0.39	12.5	0.259	129.9	0.16	0.13	6.7
7	0.35	0.51	11.0	0.229	114.3	0.14	0.09	6.3
8	0.35	0.51	20.4	0.424	212.0	0.26	0.22	8.1
9	0.35	0.51	31.3	0.648	325.3	0.39	0.33	9.6
10	0.35	0.69	38.2	0.793	397.0	0.48	0.38	10.4
11	0.35	0.69	48.0	1.000	498.9	0.60	0.41	11.4
12	0.35	0.69	62.4	1.290	648.6	0.78	0.42	12.7
13	0.35	0.69	76.3	1.580	793.0	0.96	0.43	13.8
14	0.35	0.69	109.2	2.270	1135.0	1.37	0.44	15.9
15	0.35	0.69	117.2	2.430	1218.2	1.47	0.43	16.3
16	0.35	0.69	134.7	2.790	1400.0	1.69	0.46	17.3

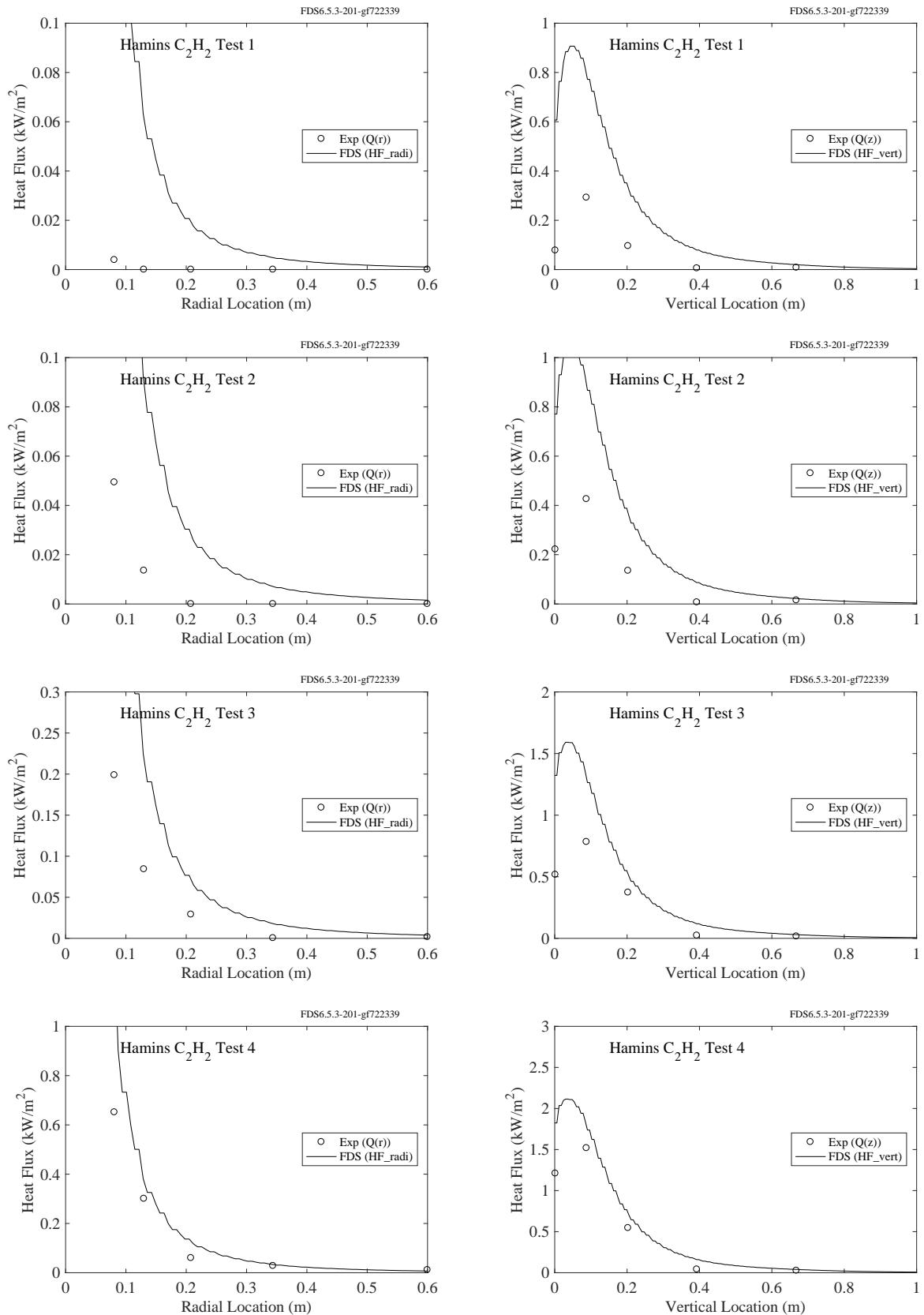


Figure 12.57: Comparison of predicted and measured heat fluxes, Hamins Acetylene Tests 1-4.

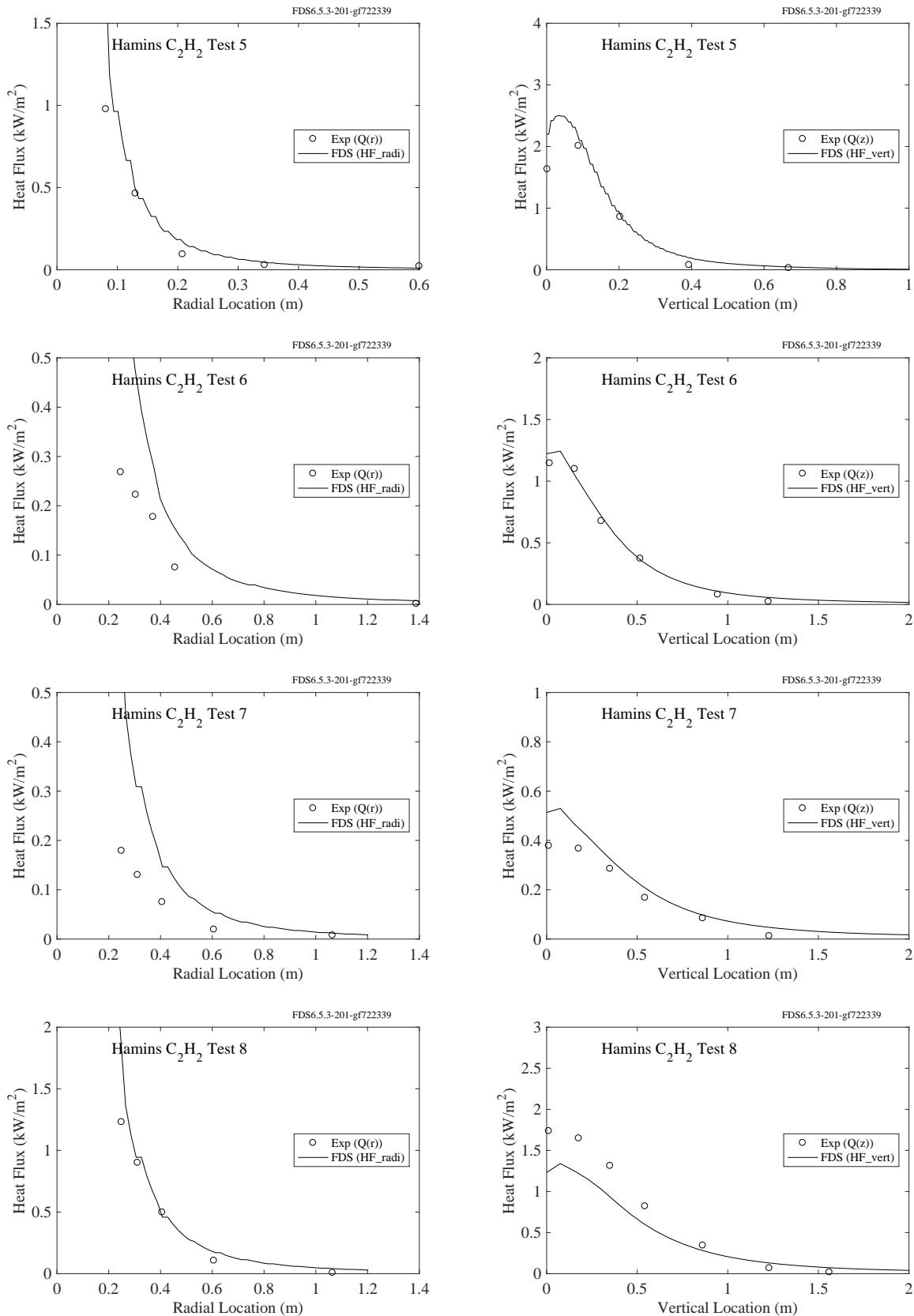


Figure 12.58: Comparison of predicted and measured heat fluxes, Hamins Acetylene Tests 5-8.

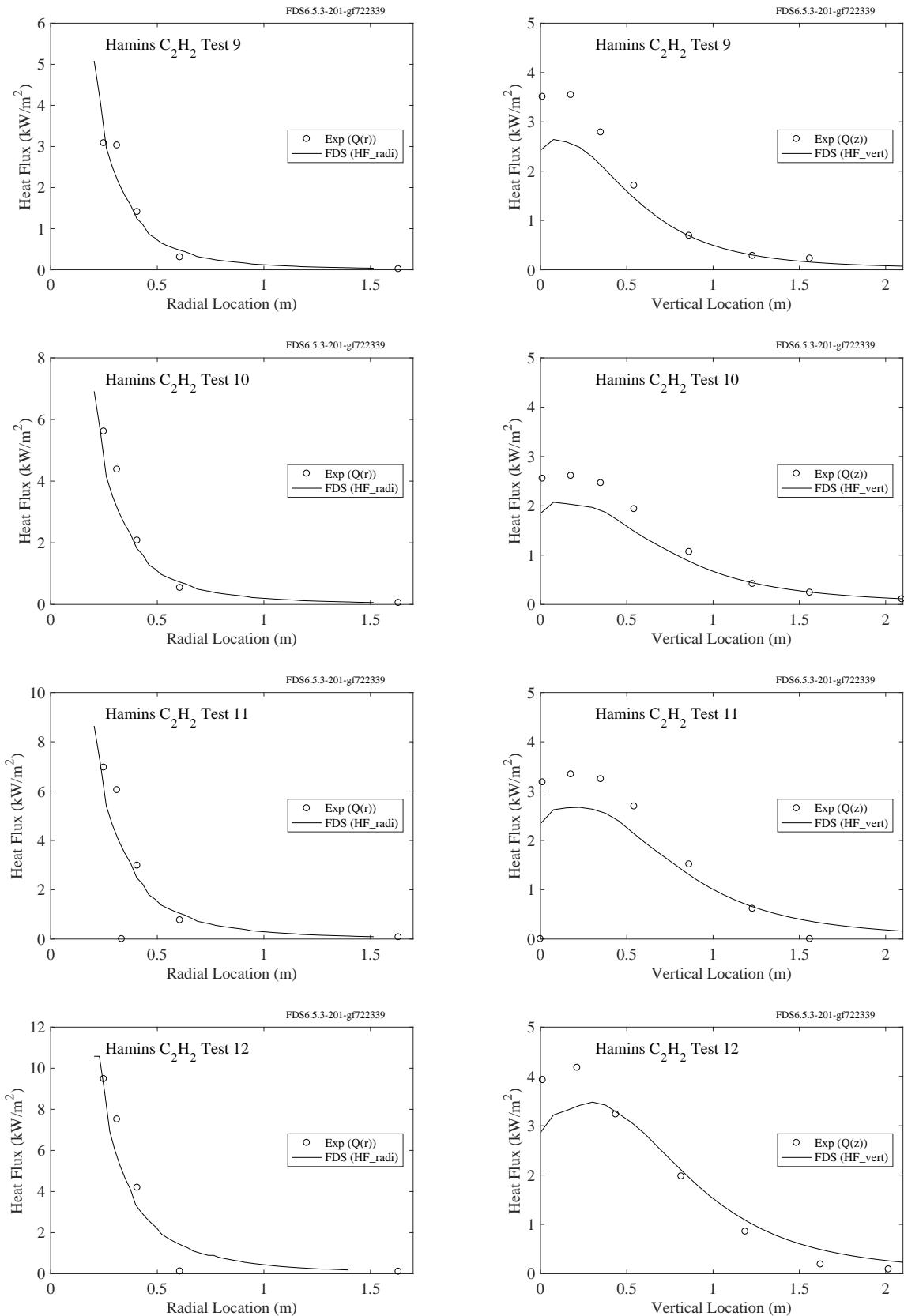


Figure 12.59: Comparison of predicted and measured heat fluxes, Hamins Acetylene Tests 9-12.

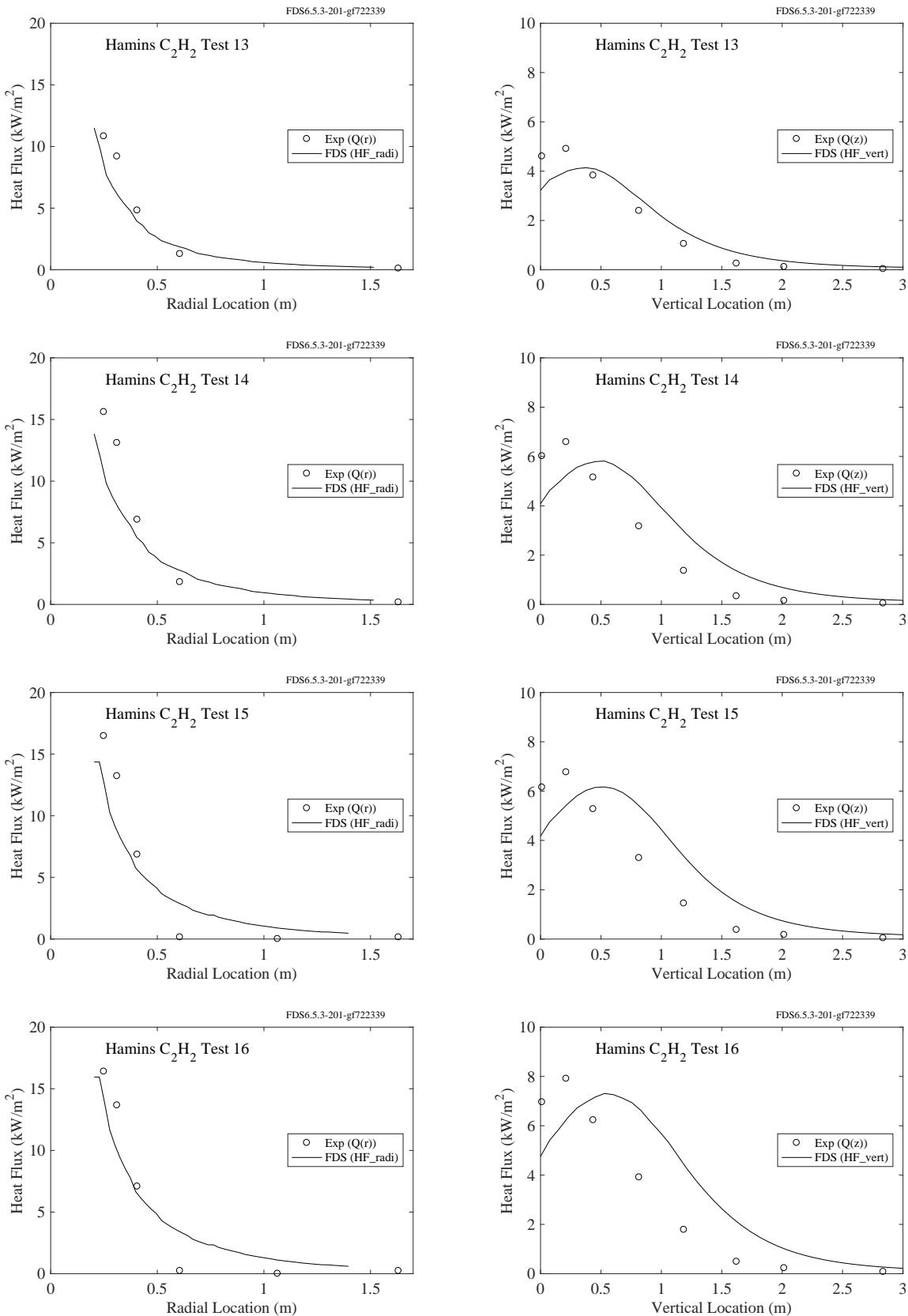


Figure 12.60: Comparison of predicted and measured heat fluxes, Hamins Acetylene Tests 13-16.

### **12.2.3 NIST/NRC Experiments**

Cables in various types (power and control), and configurations (horizontal, vertical, in trays or free-hanging), were installed in the test compartment. For each of the four cable targets considered, measurements of the radiative and total heat flux were made with gauges positioned near the cables themselves. The following pages display comparisons of these heat flux predictions and measurements for Control Cable B, Horizontal Cable Tray D, Power Cable F and Vertical Cable Tray G.

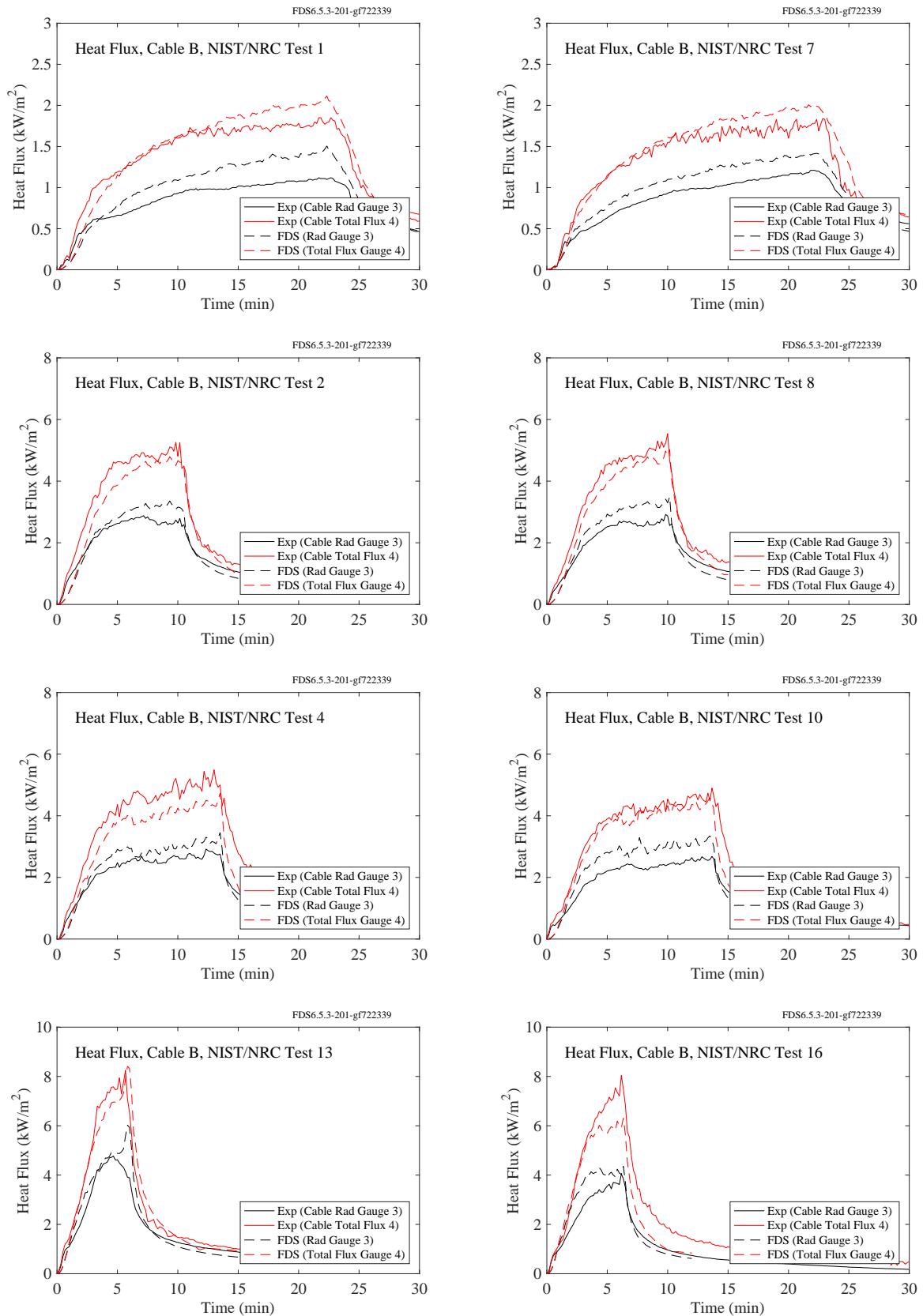


Figure 12.61: NIST/NRC experiments, heat flux to Cable B, Tests 1, 2, 4, 7, 8, 10, 13, 16.

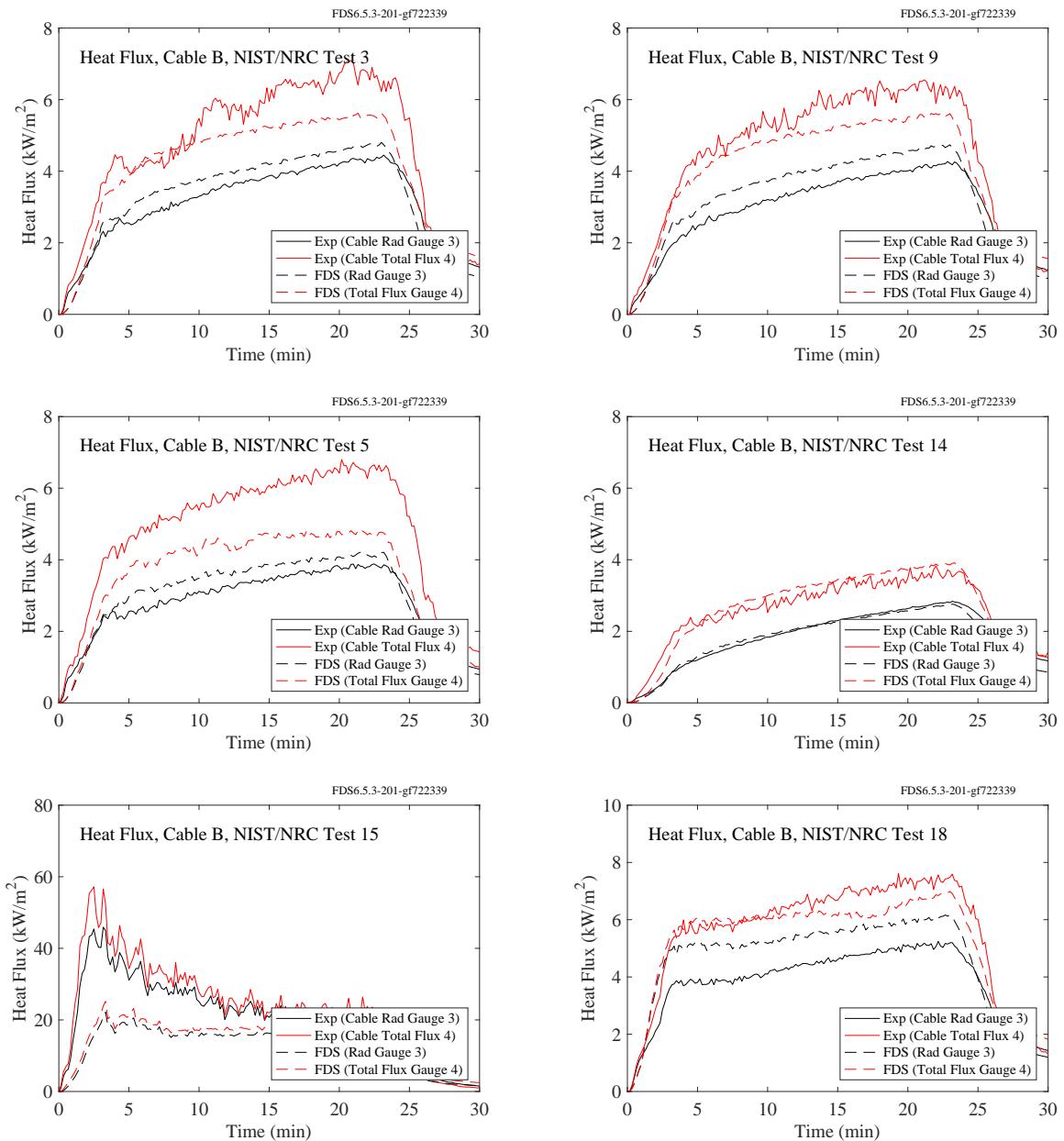


Figure 12.62: NIST/NRC experiments, heat flux to Cable B, Tests 3, 5, 9, 14, 15, 18.

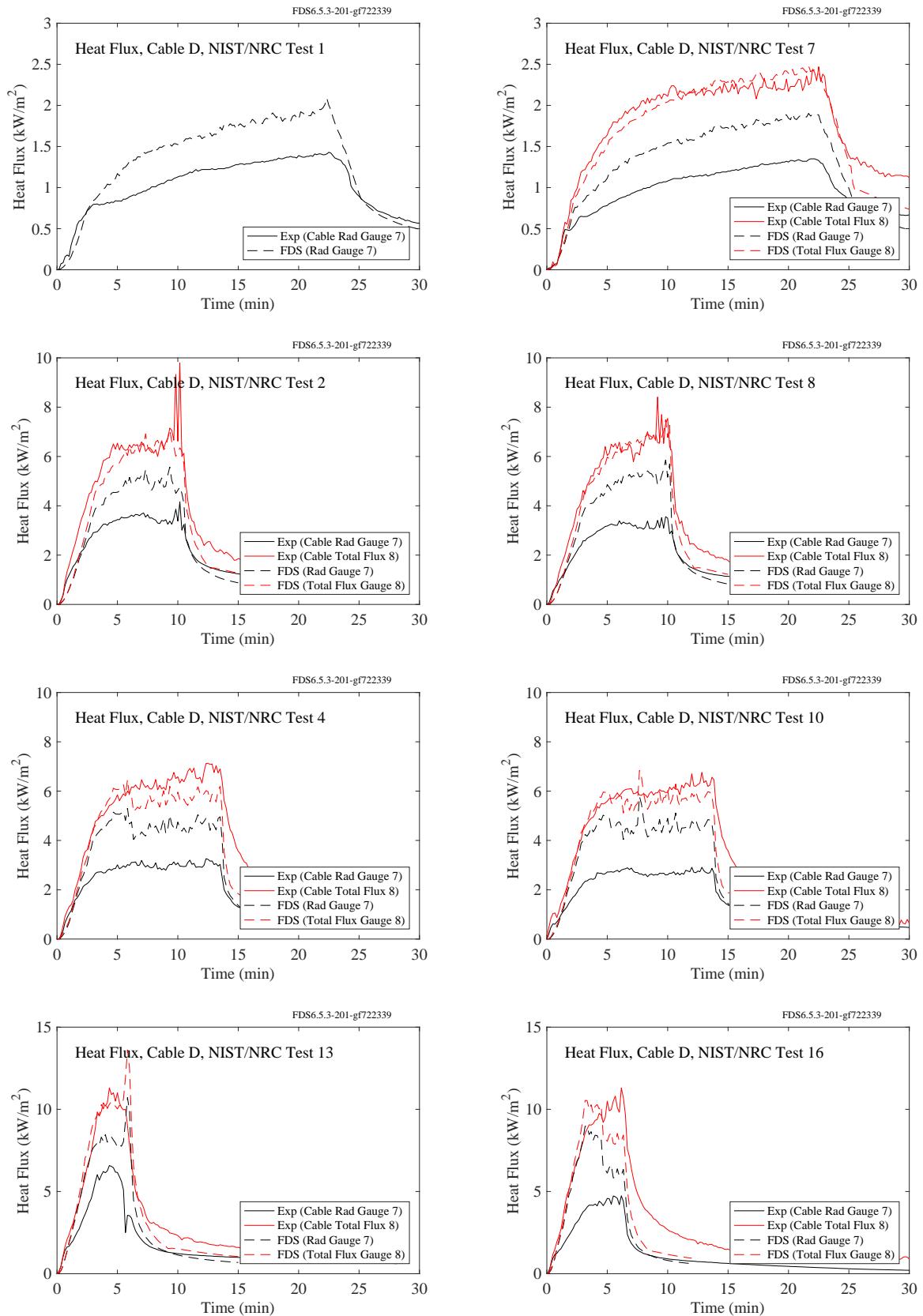


Figure 12.63: NIST/NRC experiments, heat flux to Cable D, Tests 1, 2, 4, 7, 8, 10, 13, 16.

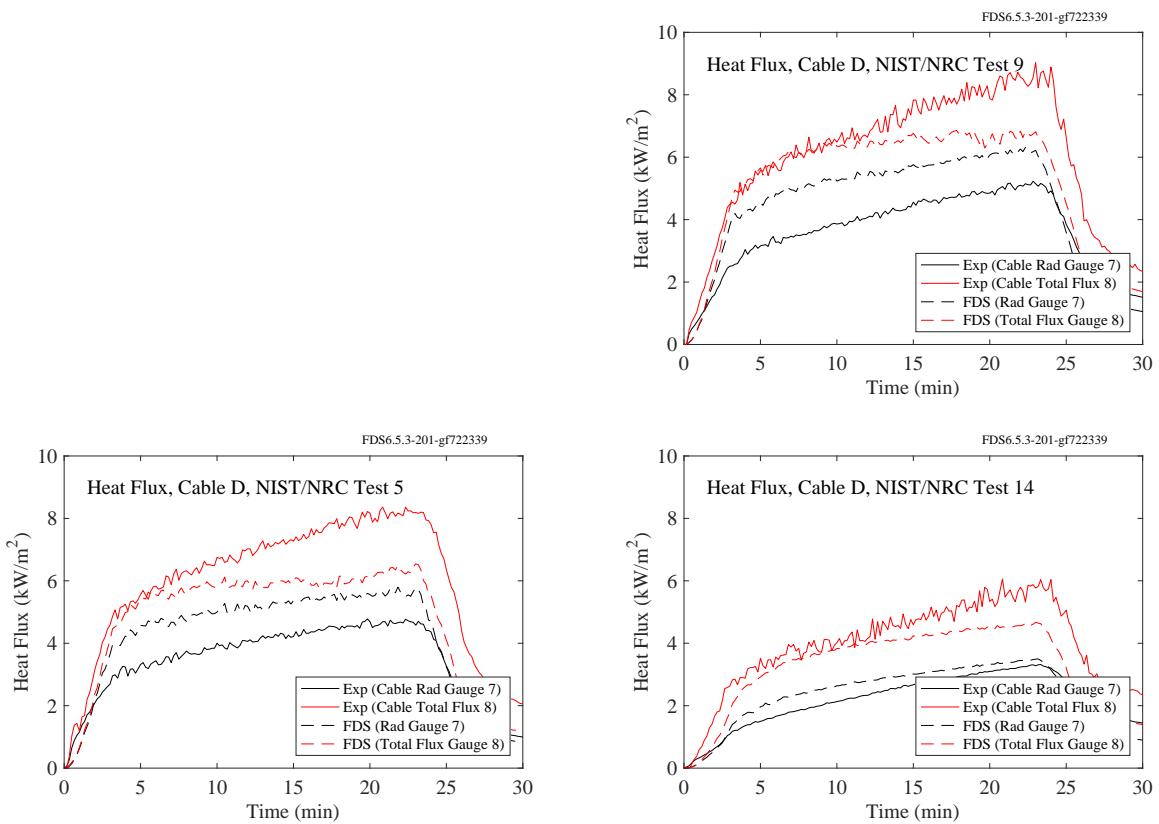


Figure 12.64: NIST/NRC experiments, heat flux to Cable D, Tests 5, 9, 14.

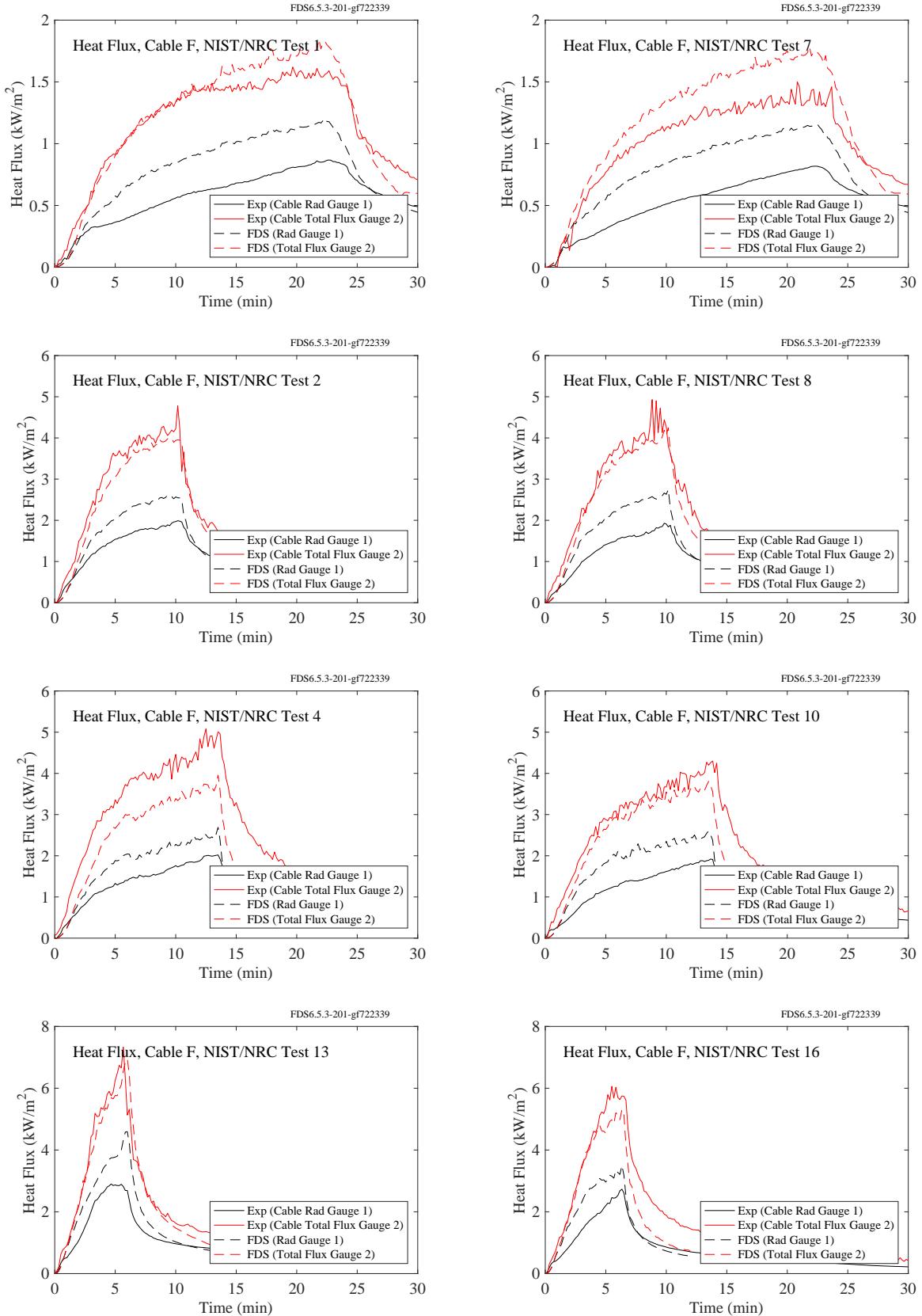


Figure 12.65: NIST/NRC experiments, heat flux to Cable F, Tests 1, 2, 4, 7, 8, 10, 13, 16.

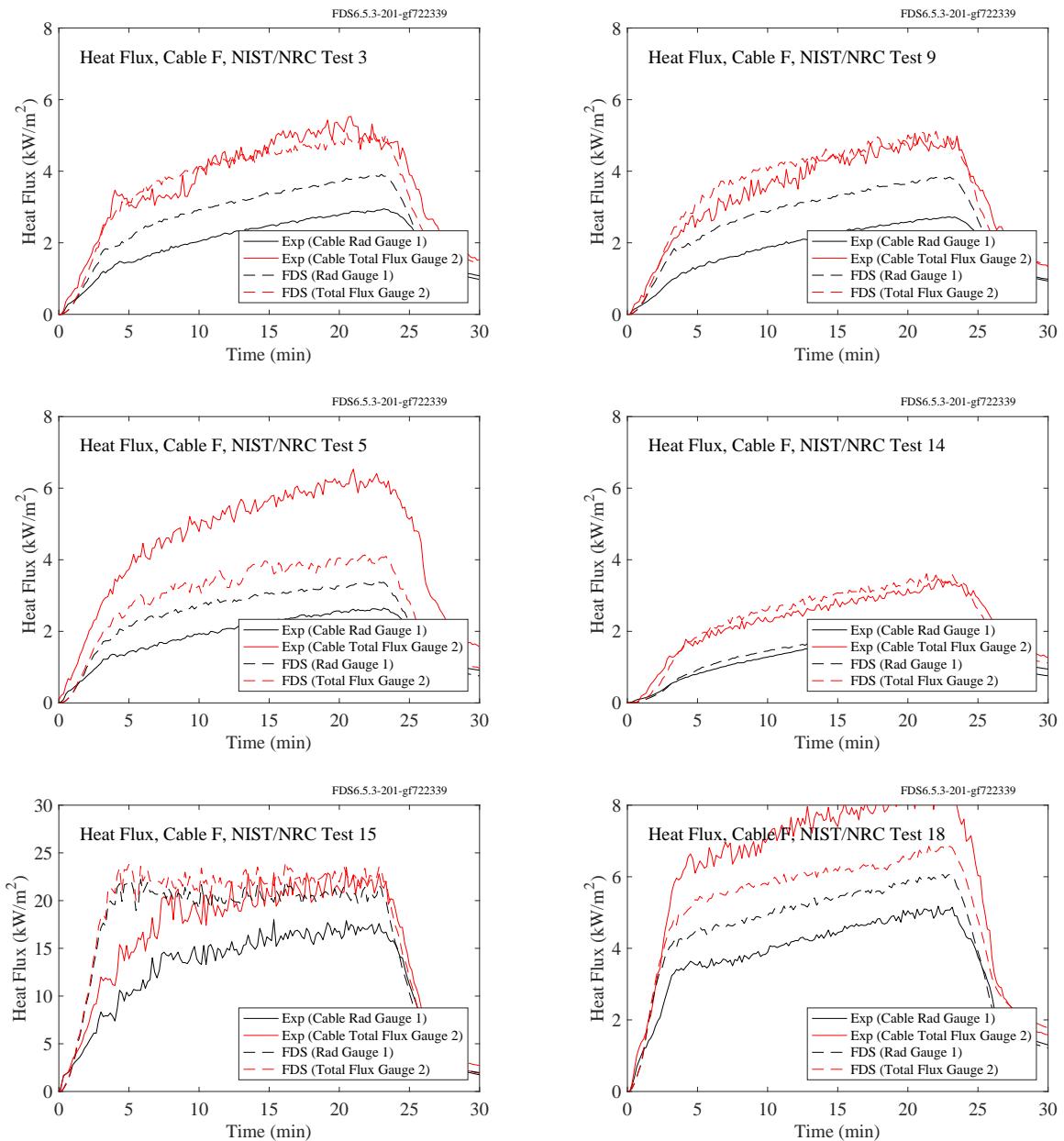


Figure 12.66: NIST/NRC experiments, heat flux to Cable F, Tests 3, 5, 9, 14, 15, 18.

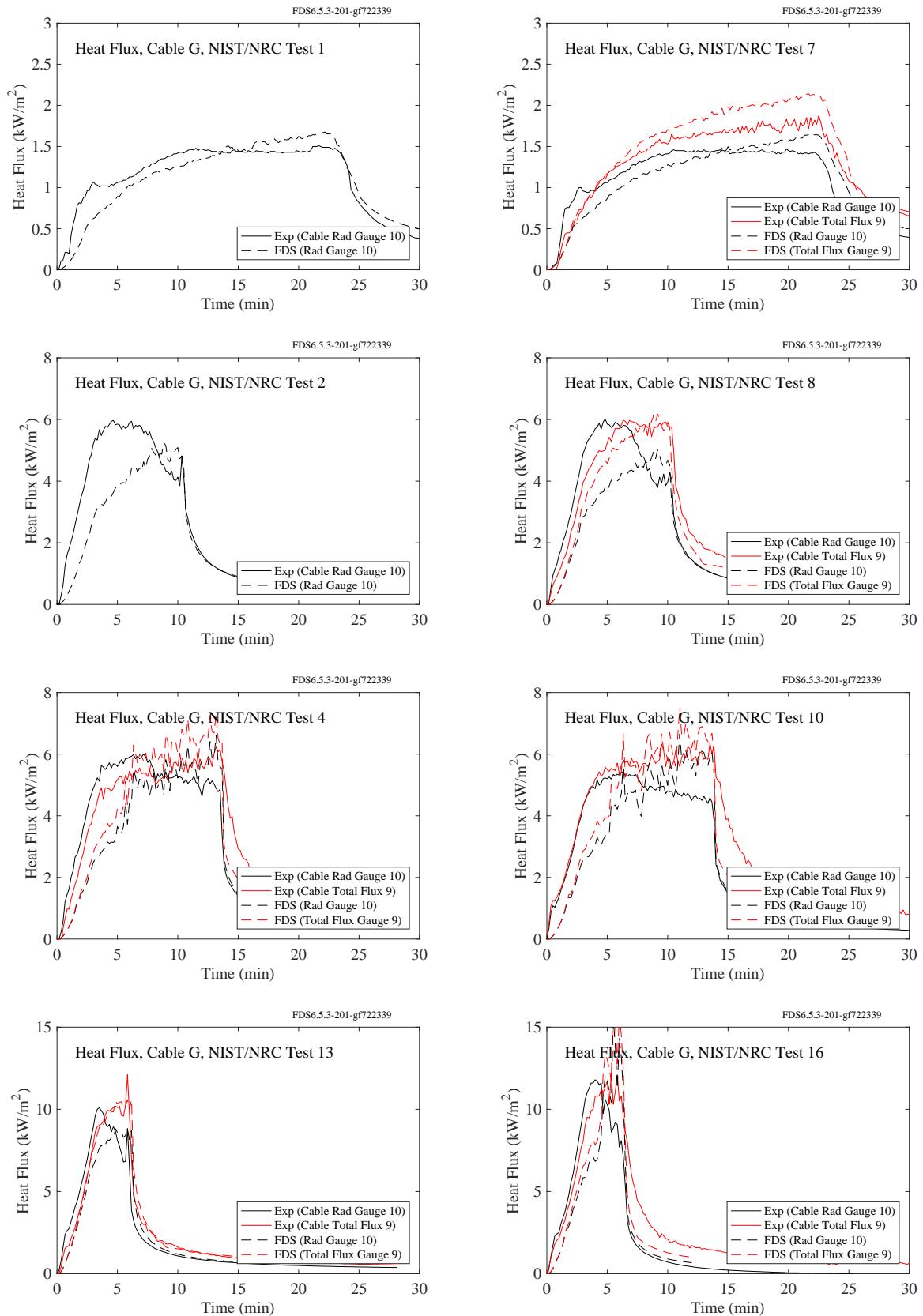


Figure 12.67: NIST/NRC experiments, heat flux to Cable G, Tests 1, 2, 4, 7, 8, 10, 13, 16.

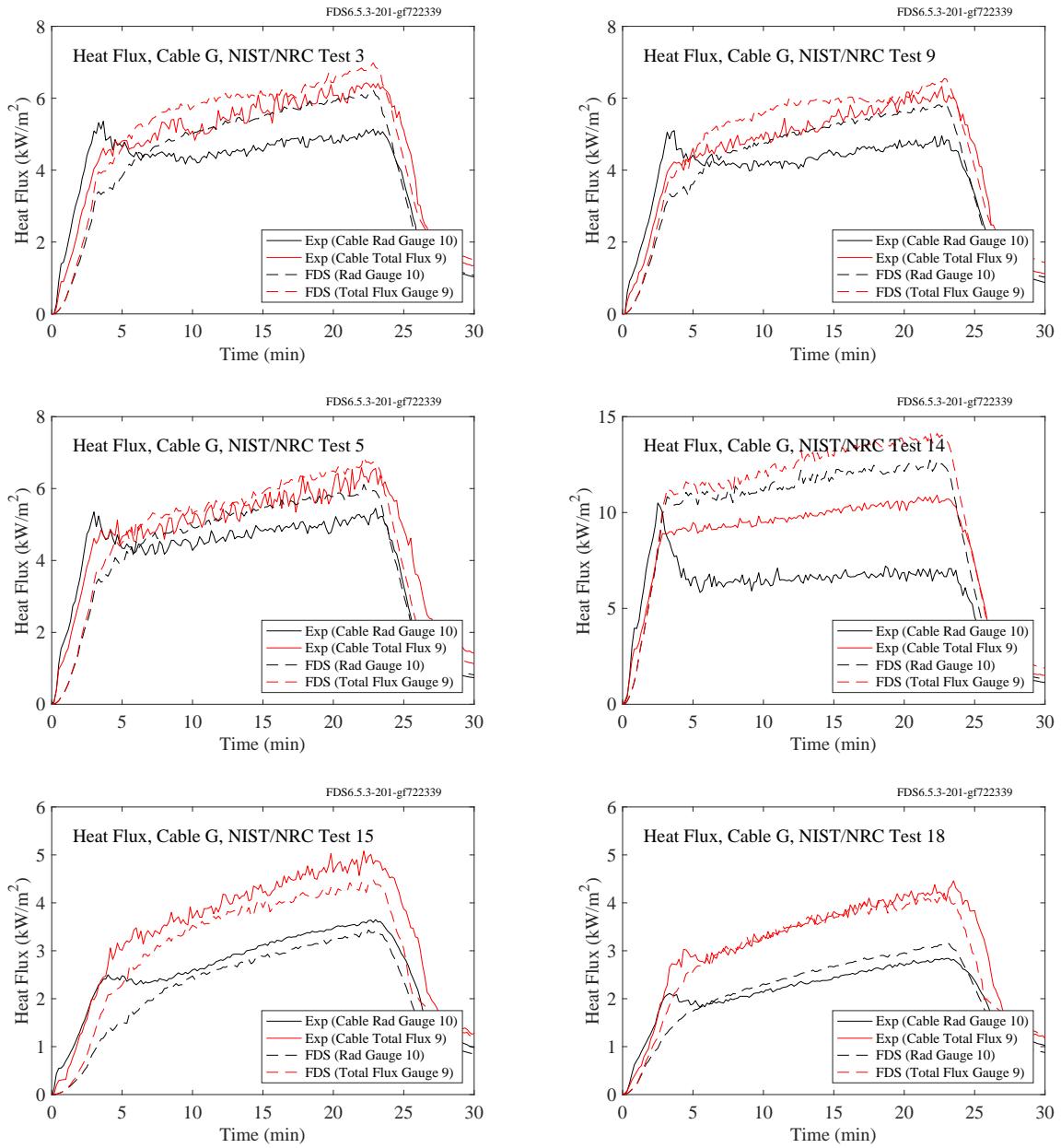


Figure 12.68: NIST/NRC experiments, heat flux to Cable G, Tests 3, 5, 9, 14, 15, 18.

## 12.2.4 WTC Experiments

There were a variety of heat flux gauges installed in the test compartment. Most were within 2 m of the fire. Their locations and orientations are listed in Table 12.2.

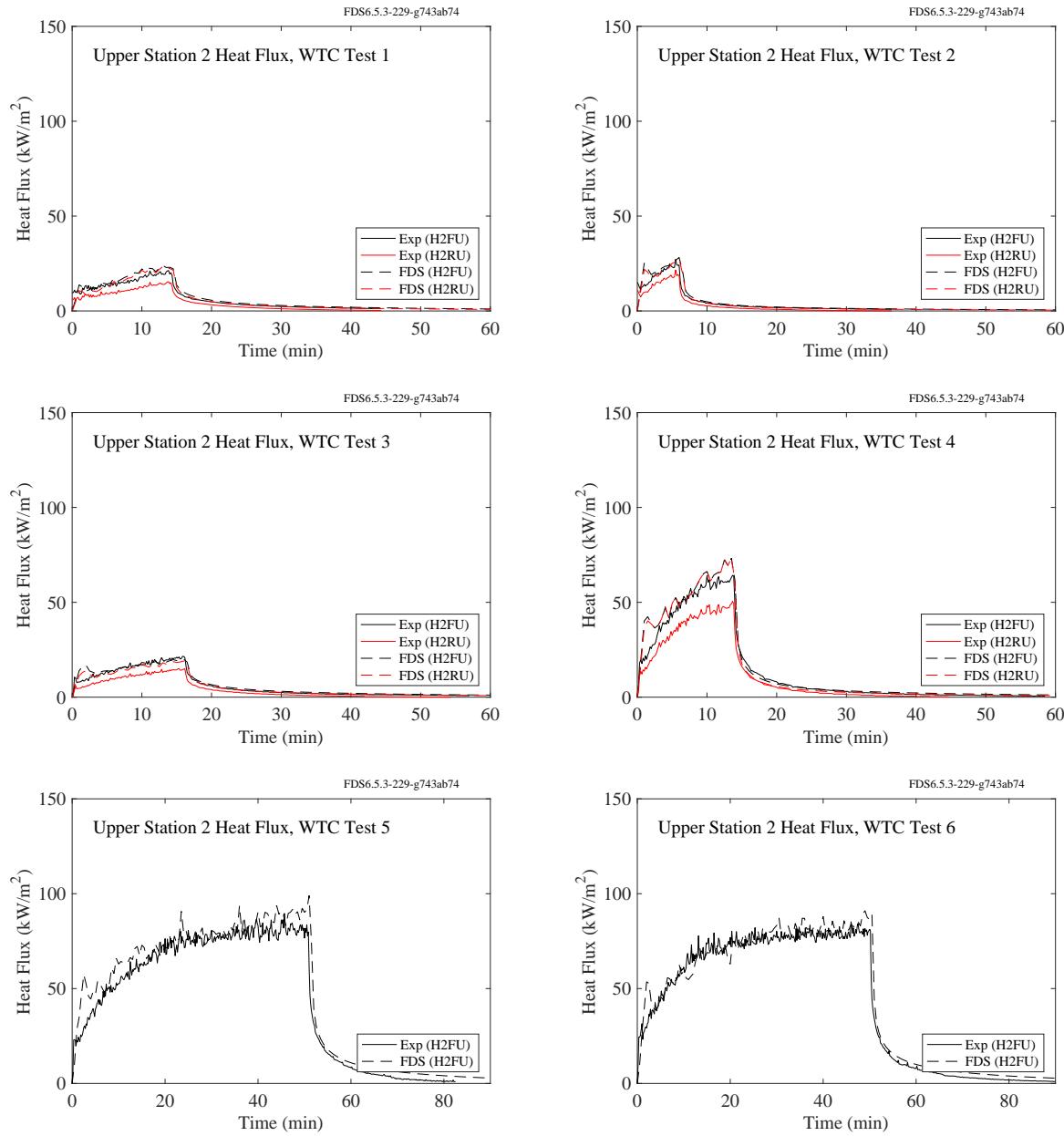


Figure 12.69: WTC experiments, heat flux at Station 2, high position.

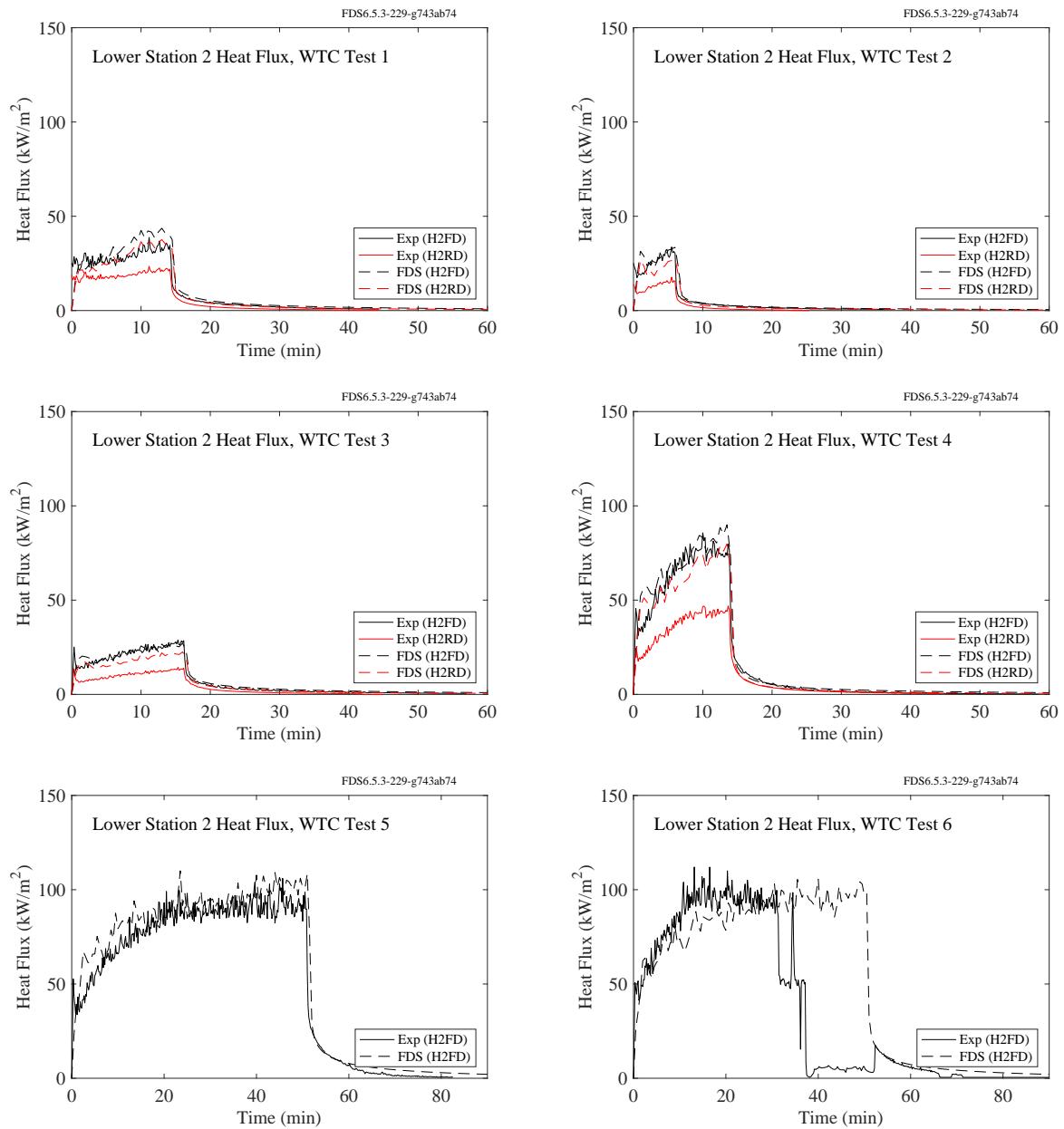


Figure 12.70: WTC experiments, heat flux at Station 2, low position.

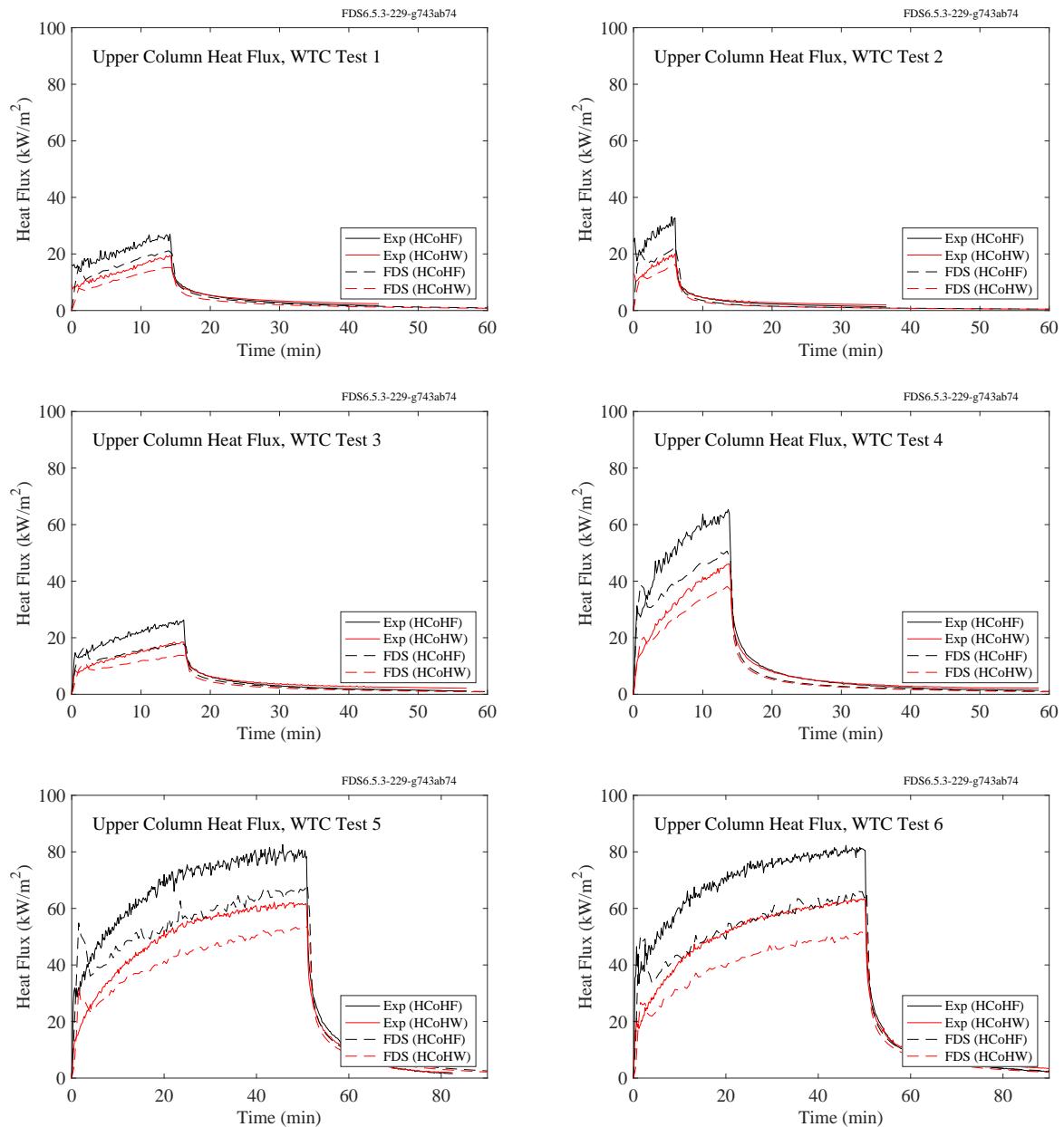


Figure 12.71: WTC experiments, heat flux to upper column.

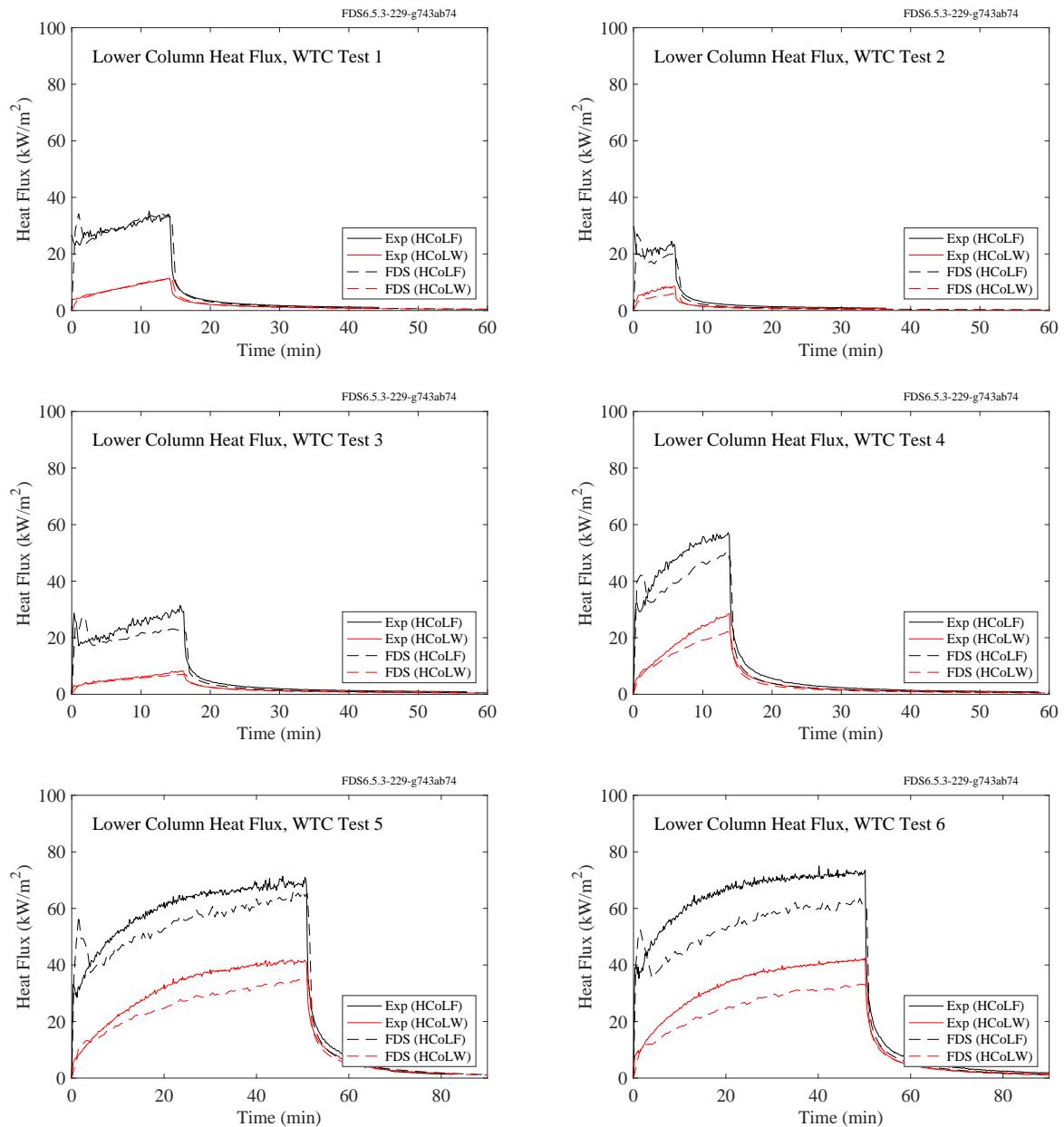


Figure 12.72: WTC experiments, heat flux to lower column.

### 12.2.5 Summary of Target Heat Flux Predictions

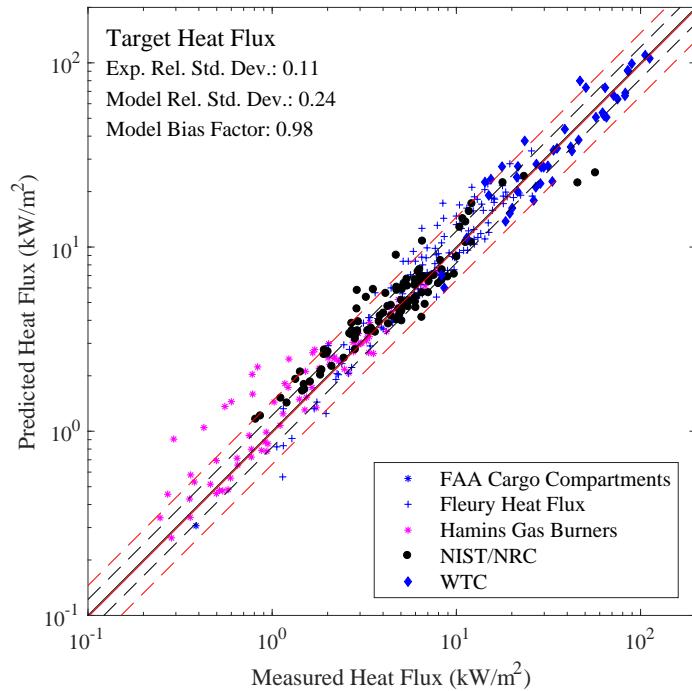


Figure 12.73: Summary of target heat flux predictions.

## 12.3 Attenuation of Thermal Radiation in Water Spray

This section presents the results of simulations of spray experiments where the reduction of thermal radiation by a fine water spray was measured.

### 12.3.1 BRE Spray Experiments

Attenuation of thermal radiation by a water spray was measured using three full-cone type hydraulic nozzles at eight different pressures. The initial droplet speeds were determined using a simple hydraulic relation,  $v = 0.9\sqrt{2P/\rho}$ . The median drop size distributions were determined by assuming  $d_m \propto p^{-1/3}$  and finding the constant of proportionality by fitting to the experimental PDPA measurement 1 m below the nozzles. Measured median diameters,  $d_{v50}$ , are compared against mean diameters,  $d_{43}$ . The arithmetic mean of the droplets is used for vertical velocity. The comparison of predicted and measured attenuation, Fig. 12.75, is made at a distance of 4 m from the heat source.

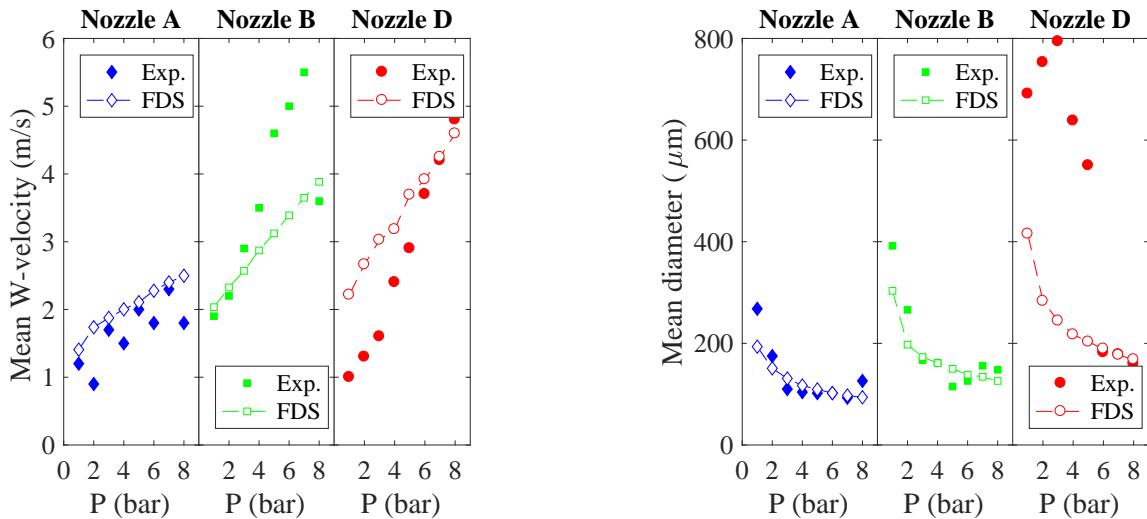


Figure 12.74: Comparison of experimental and predicted droplet speeds and mean diameters for the three nozzles and different pressures.

### 12.3.2 LEMTA Spray Experiments

The attenuation of thermal radiation was measured at five heights in water sprays produced by seven full-elliptic type hydraulic nozzles. The operating pressure was 4 bar. The initial speed was deduced from the water flow rate and the orifice diameter. The droplet size at the injection point was determined by comparing the predicted and measured results at the PDPA measurement location 0.2 m below the nozzles. The comparison of predicted and measured attenuations, Fig. 12.75, is made at five locations.

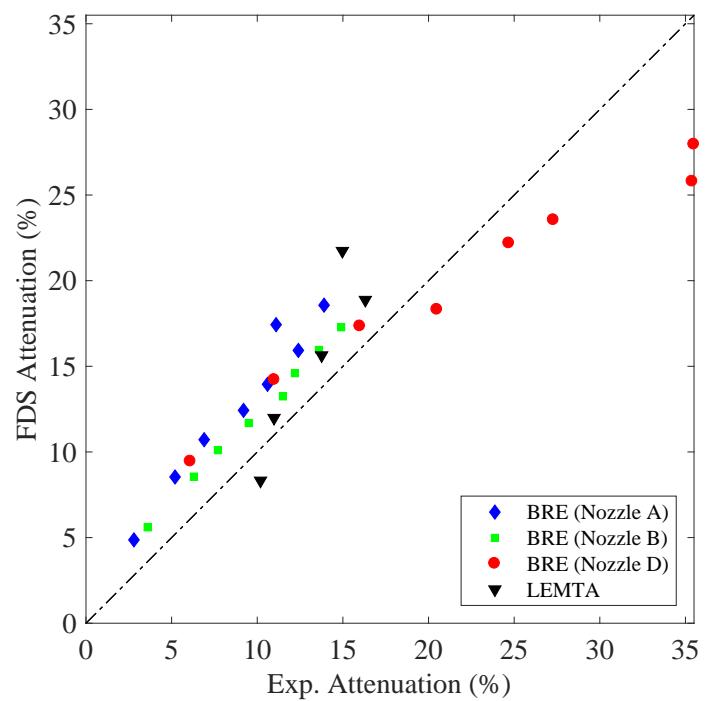


Figure 12.75: Comparison of predicted and measured radiation attenuation in the spray experiments at BRE and at LEMTA.

## 12.4 Convective Heat Flux

This section focuses specifically on experiments that primarily involved convective heat transfer.

### 12.4.1 Bouchair Solar Chimney

The plots on the following pages compare the predicted air mass flow rates through the test apparatus shown in Fig. 3.3. The measurements were made at both the inlet and outlet of the thermal cavity. Note that in Bouchair's thesis [133], the measurements were presented as mass flow rates per unit length of the inlet slot, 1.4 m. In the plots on the following pages, the measurements and simulation results are presented simply as a total mass flux, kg/s.

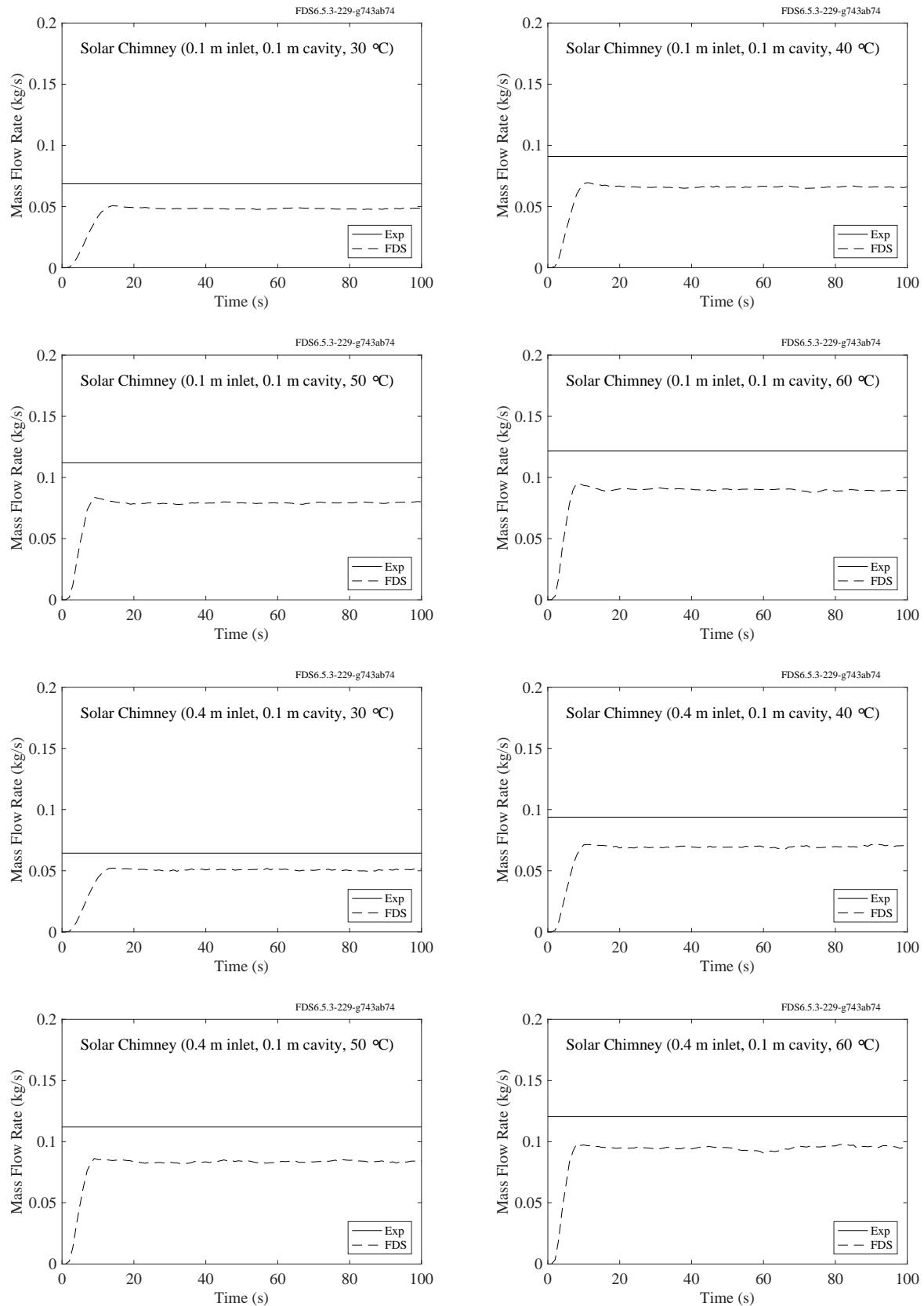


Figure 12.76: Bouchair Solar Chimney, 0.1 m thermal cavity.

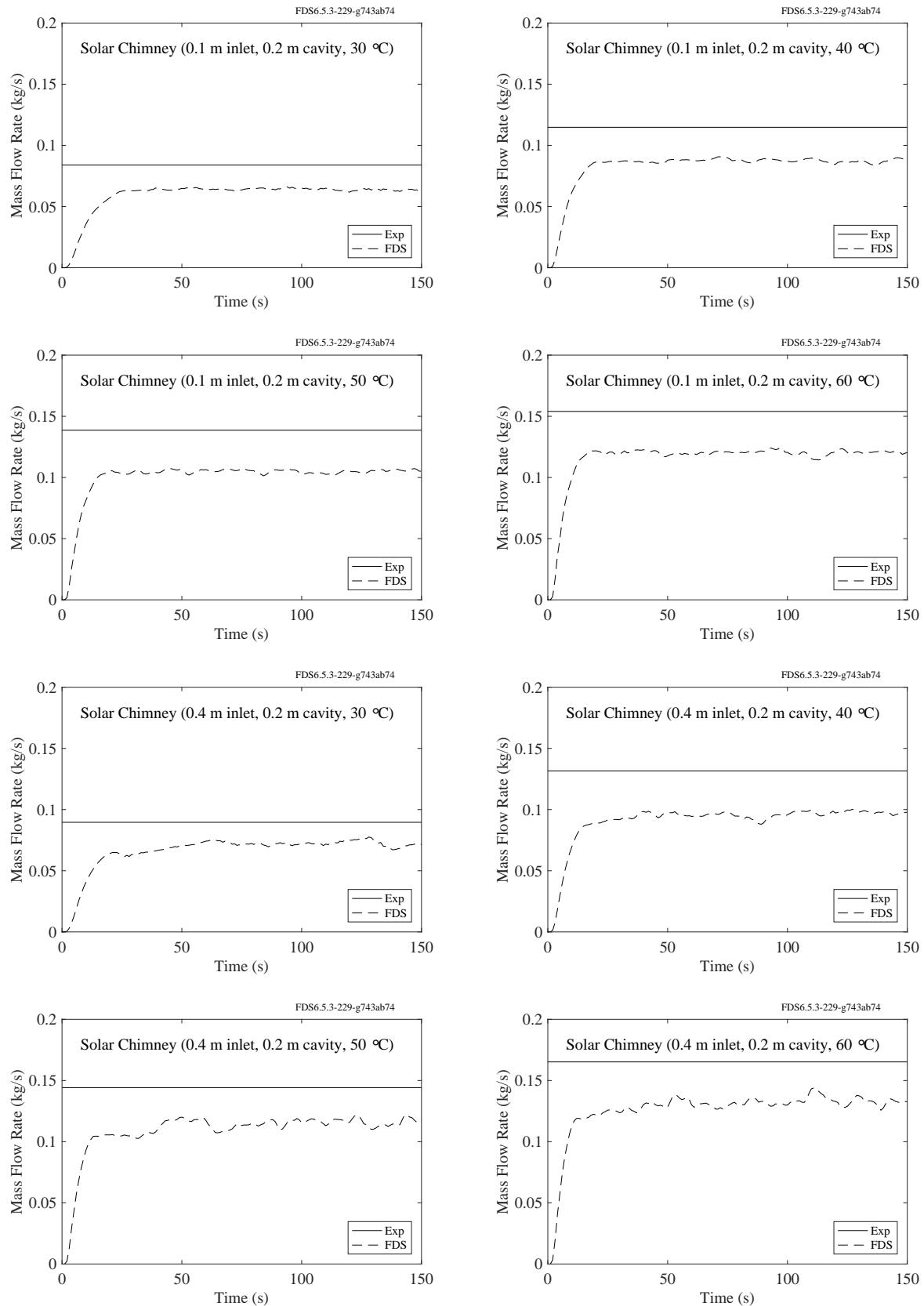


Figure 12.77: Bouchair Solar Chimney, 0.2 m thermal cavity.

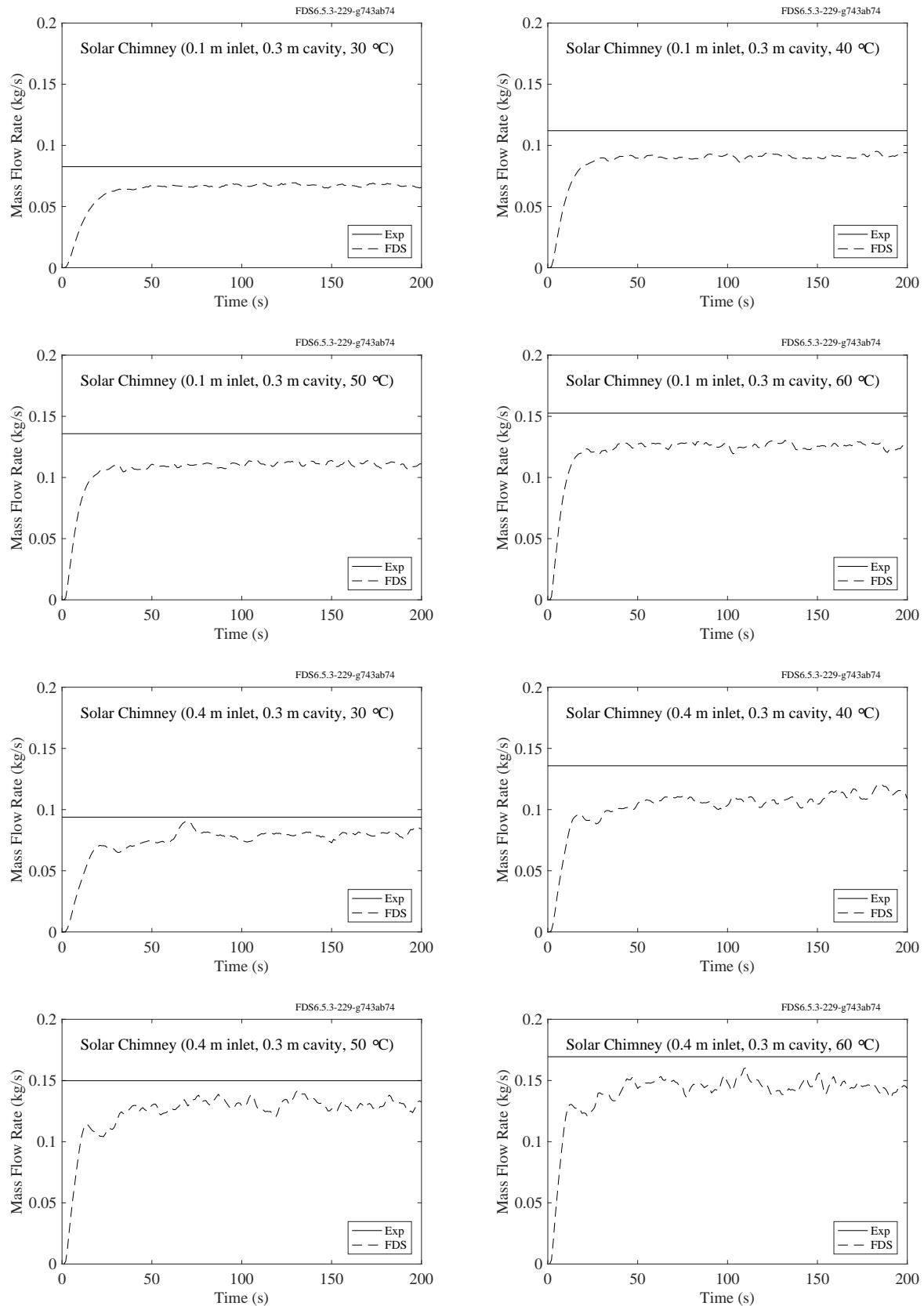


Figure 12.78: Bouchair Solar Chimney, 0.3 m thermal cavity.

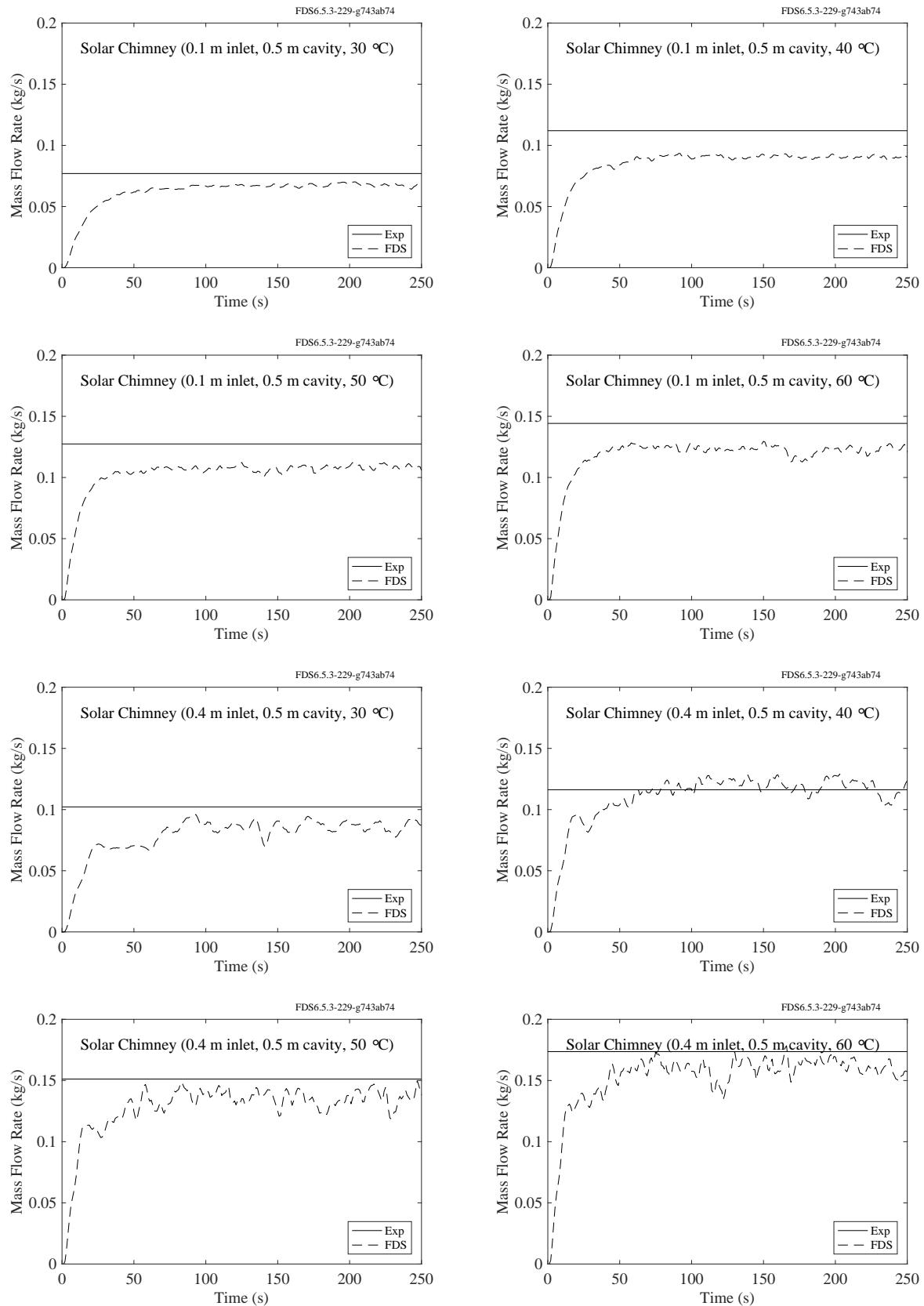


Figure 12.79: Bouchair Solar Chimney, 0.5 m thermal cavity.

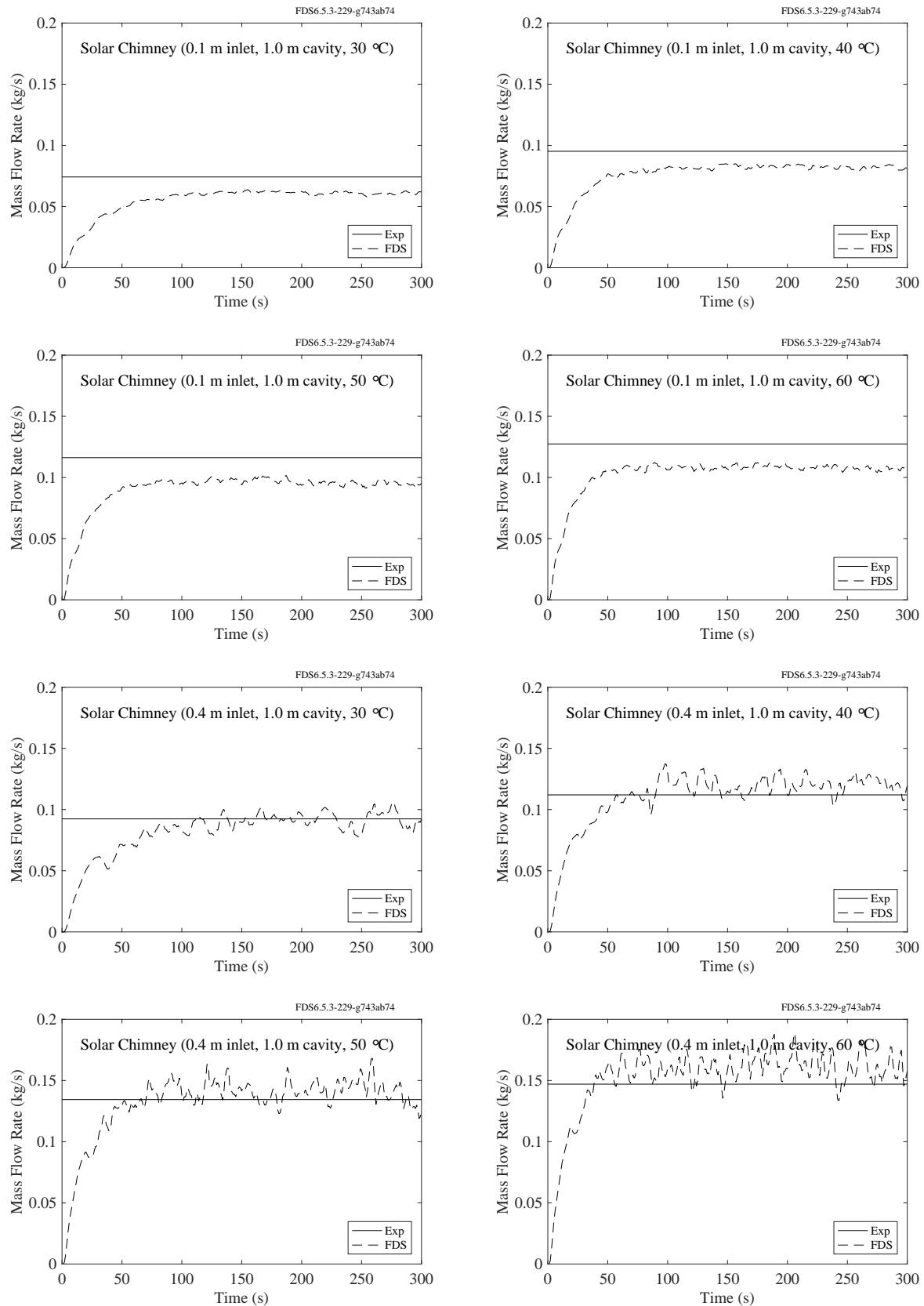


Figure 12.80: Bouchair Solar Chimney, 1.0 m thermal cavity.

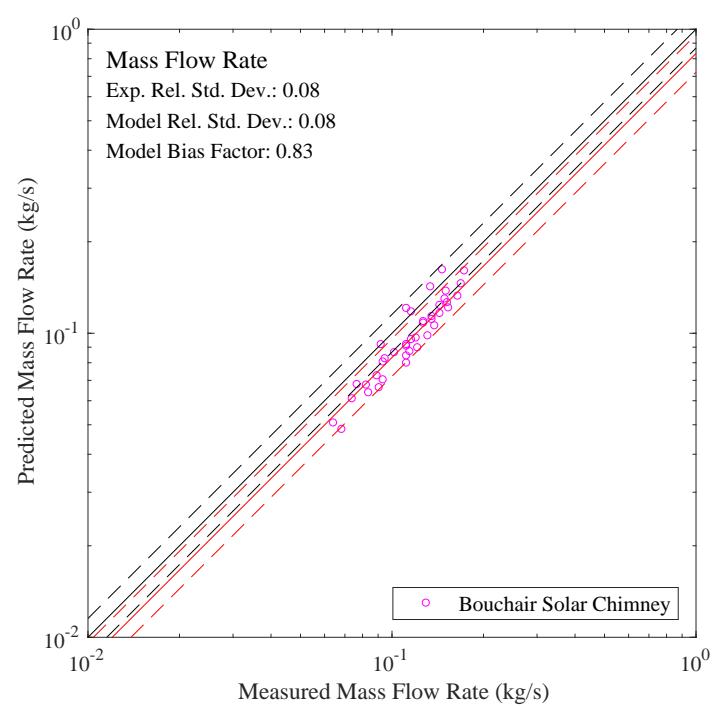


Figure 12.81: Summary of Bouchair Solar Chimney results.



# **Chapter 13**

## **Suppression**

This chapter looks at validation exercises where the aim is to predict the extinguishment of a fire.

### **13.1 Cup Burner Experiments**

The Cup Burner is an apparatus used to determine the minimum extinguishing concentration (MEC) for combinations of fuels and suppression agents. Two fuels (methane and n-heptane) and four suppression agents (argon, carbon dioxide, helium, and nitrogen) are considered. For the simulations, the MEC is found when the post-ignition HRR drops below  $1 \times 10^{-10}$  kW. The critical flame temperatures specified for the fuel reactions are 1630 °C and 1560 °C for methane and n-heptane, respectively. The suppression agent concentration is measured at a height level to the cup rim and 2 mm outside of the outer edge of the cup rim. In Figs. 13.1 and 13.2, methane is indicated by blue symbols and n-heptane is indicated by red symbols. The four suppression agents are identified by unique symbols.

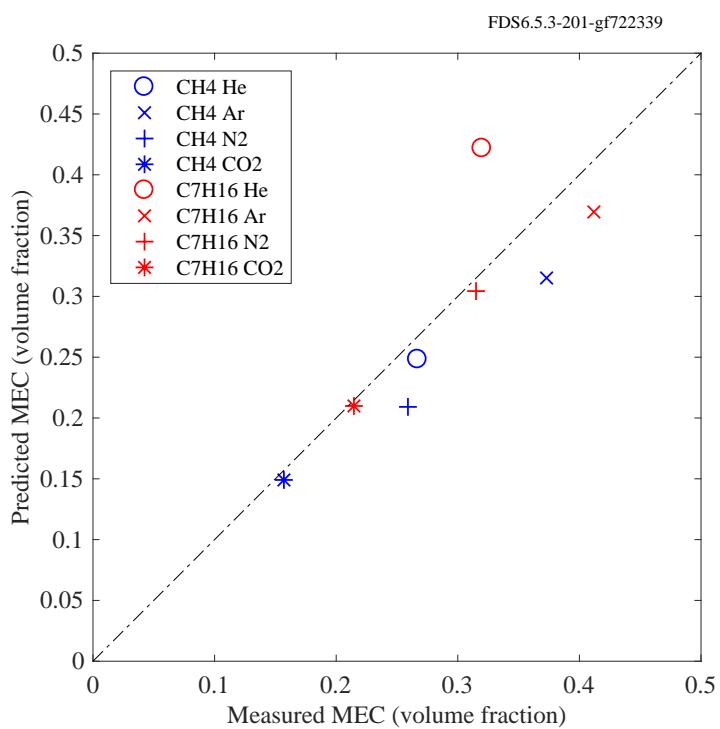


Figure 13.1: Comparison of measured and predicted minimum extinguishing volume fractions for the cup burner tests with methane and heptane.

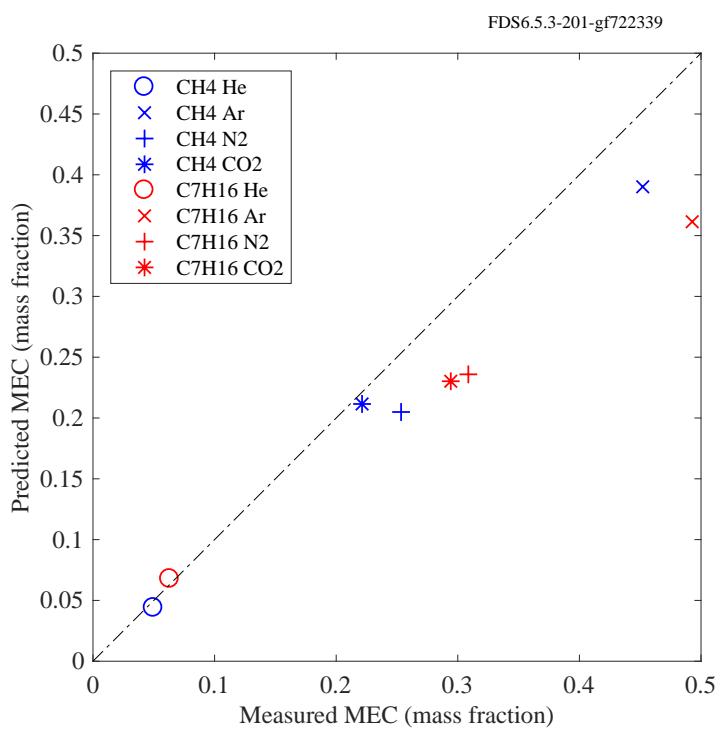


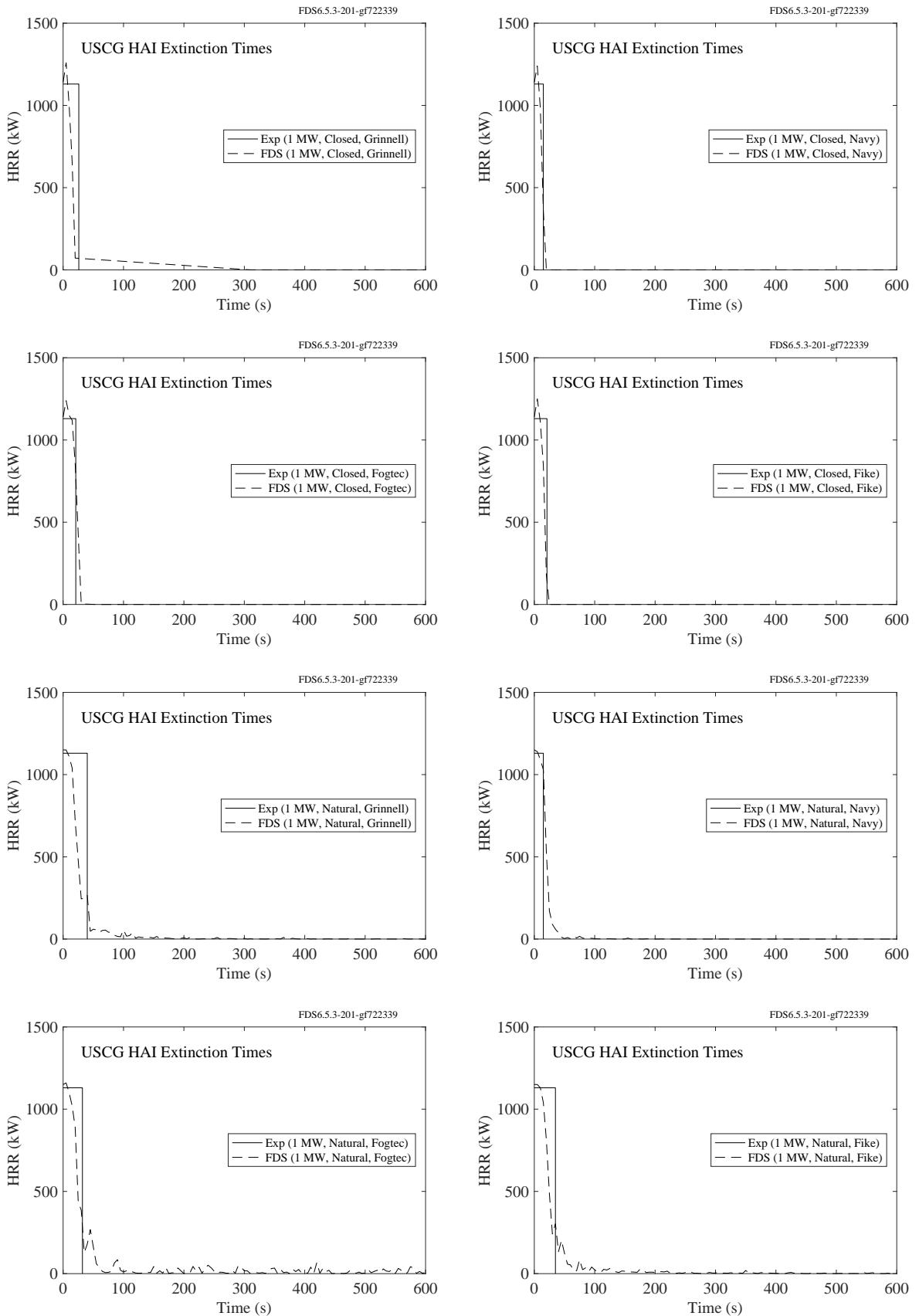
Figure 13.2: Comparison of measured and predicted minimum extinguishing mass fractions for the cup burner tests with methane and heptane.

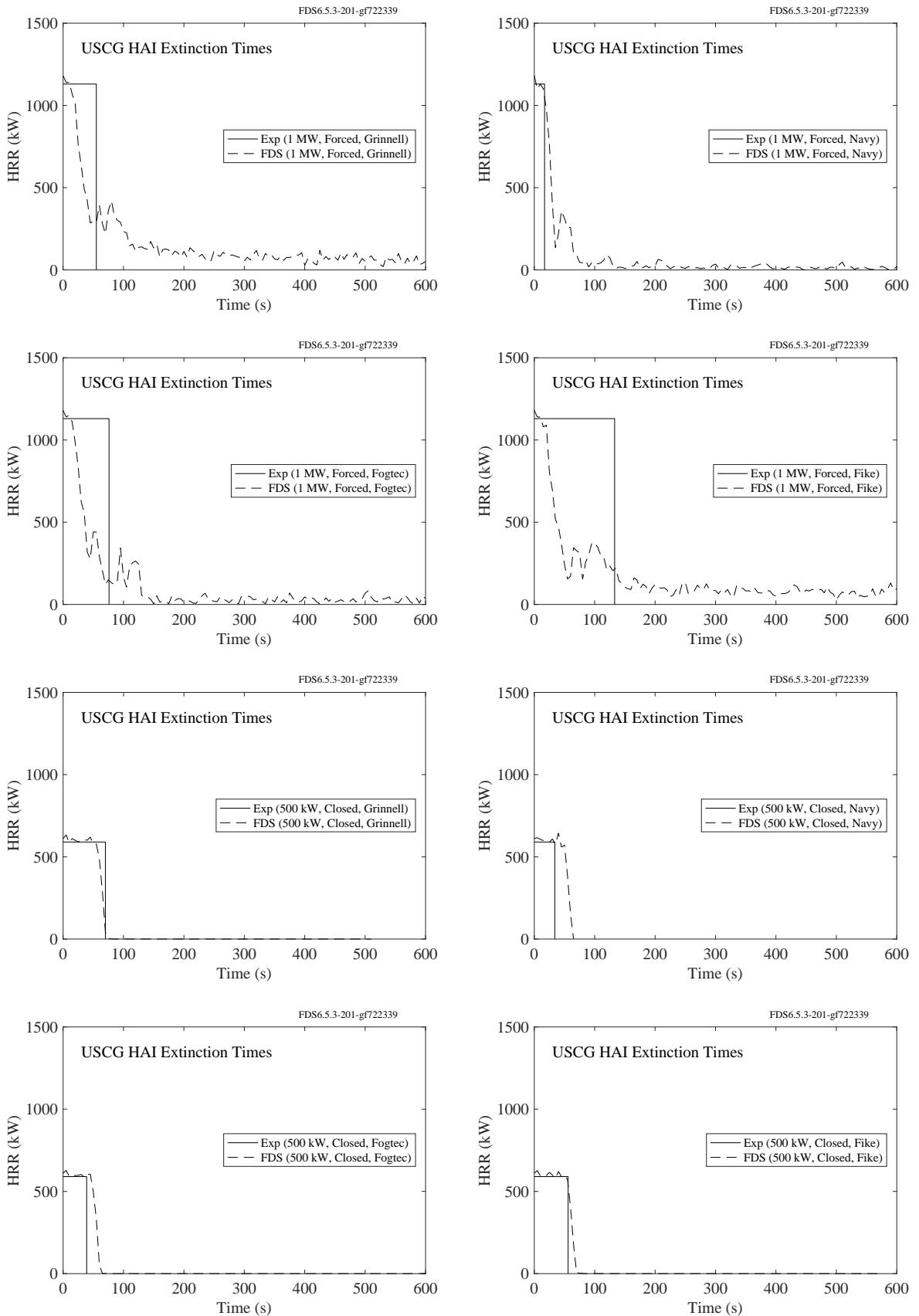
## 13.2 USCG/HAI Water Mist Suppression Tests

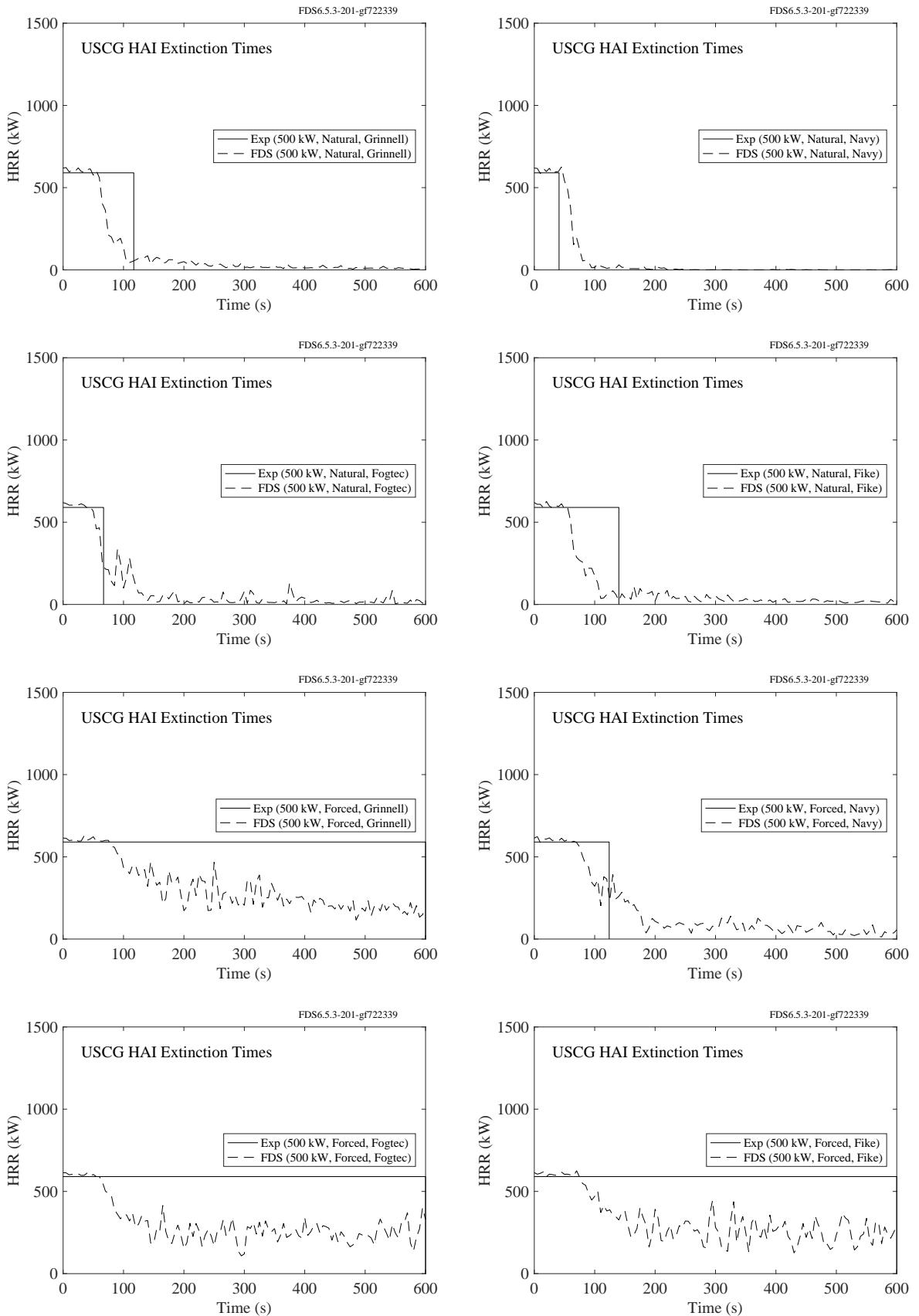
The following pages contain comparisons of the predicted heat release rates for fires that are suppressed with a water mist system. In all cases, the flow rate of liquid fuel is specified in the model, but the decrease in HRR due to the extinguishing system is predicted by the model. Table 13.1 reports the observed extinction times. Figure 13.3 compares the measured versus predicted extinction times. For the simulations, the extinction time is taken to be when the HRR drops to half of its specified value.

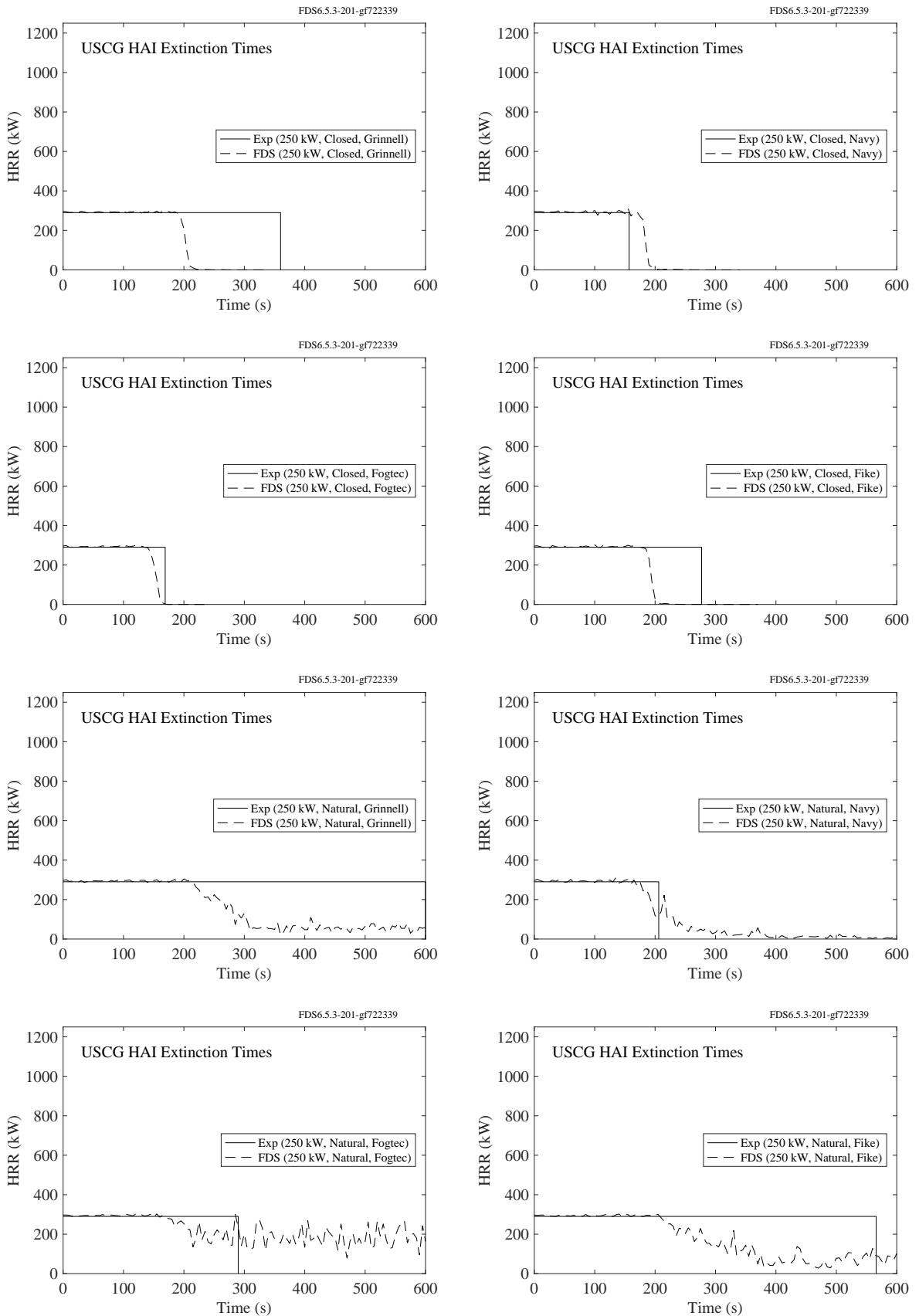
Table 13.1: Recorded extinction times for the USCG/HAI water mist suppression tests in a small shipboard machinery space. “No” means that the fire was not extinguished within 600 s of nozzle activation.

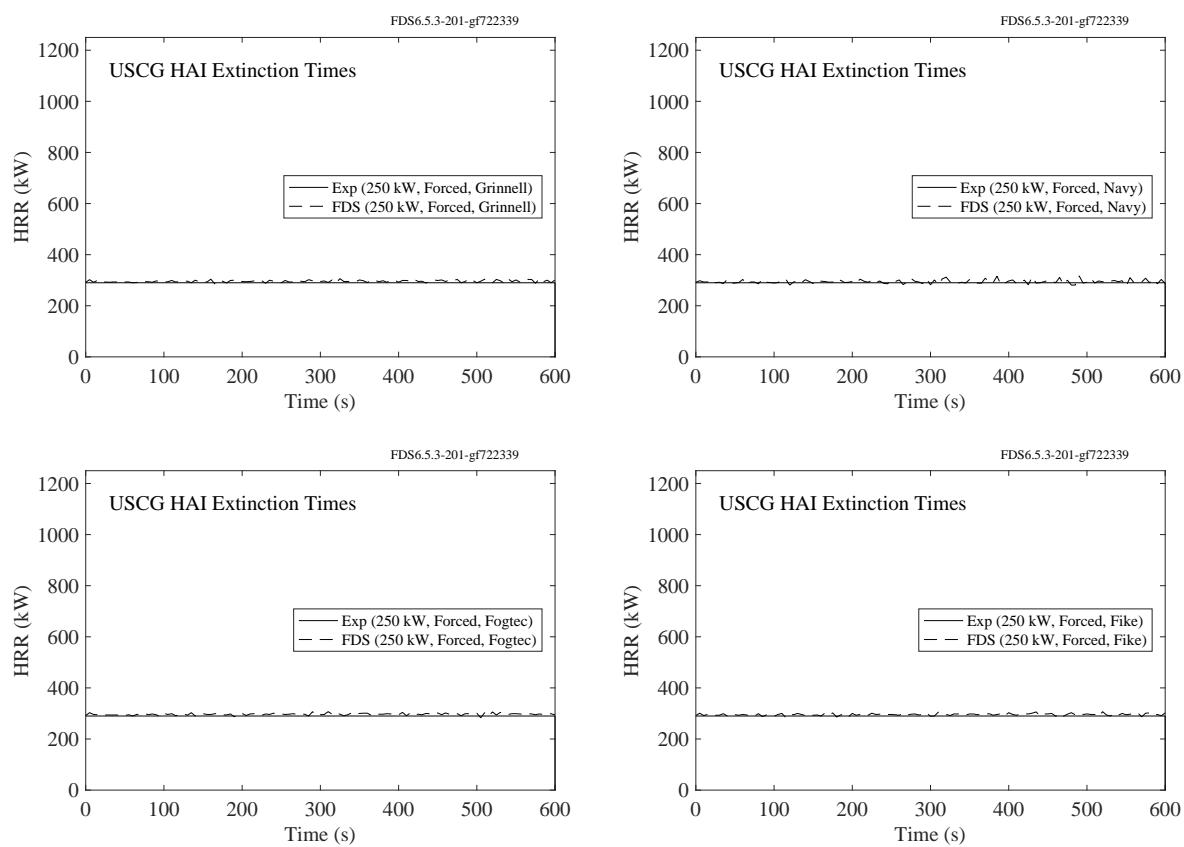
System	Navy	Grinnell	Fogtec	Chemetron	Fike
Number of Nozzles	6	6	6	15	6
Operating Pressure (bar)	70	13	100	12	21
Flow Rate (L/min)	68	75	22	70	48
Assumed Median Drop Size ( $\mu\text{m}$ )	175	225	100		200
Assumed Initial Velocity (m/s)	75	32	90		41
Assumed Spray Angle (deg.)	120	90	120		90
Fire Scenario	Ventilation	Extinguishment Time (s)			
1.0 MW Spray	Closed	15	26	21	27
1.0 MW Spray	Natural	15	40	32	43
1.0 MW Spray	Forced	17	55	76	357
0.5 MW Spray	Closed	34	70	39	53
0.5 MW Spray	Natural	41	117	67	158
0.5 MW Spray	Forced	124	No	No	No
0.25 MW Spray	Closed	157	360	169	314
0.25 MW Spray	Natural	206	No	290	525
0.25 MW Spray	Forced	No	No	No	No











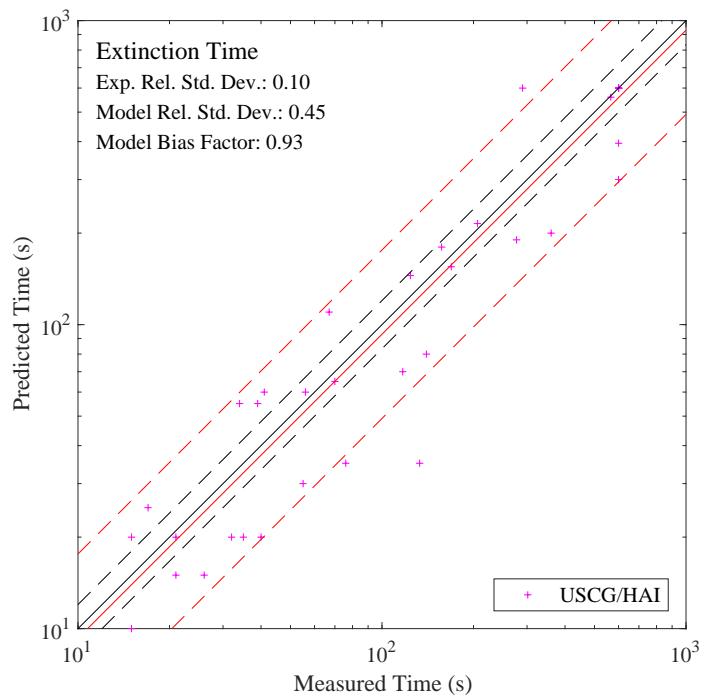


Figure 13.3: Comparison of measured and predicted extinguishment times for the USCG/HAI water mist suppression tests.

### 13.3 VTT Water Spray Experiments

Figure 13.4 presents profiles of mean droplet diameter, mean velocity, and droplet flux below a single 74° hollow-cone water mist nozzle. The pressure behind the nozzle was 2 MPa, and the flow constant was 0.077 L/min/bar<sup>1/2</sup>. The experimental data represents average values at each distance calculated over the four measuring points at that distance (except for the point at the spray axis). A comparison of droplet speed, mist flux and Sauter mean diameter ( $D_{32}$ ) profiles are shown in Fig. 13.4. Comparisons are shown at 40 cm and 62 cm vertical distances from the nozzle. Simulation results are reported for three spatial resolutions: 1 cm, 2 cm, and 4 cm.

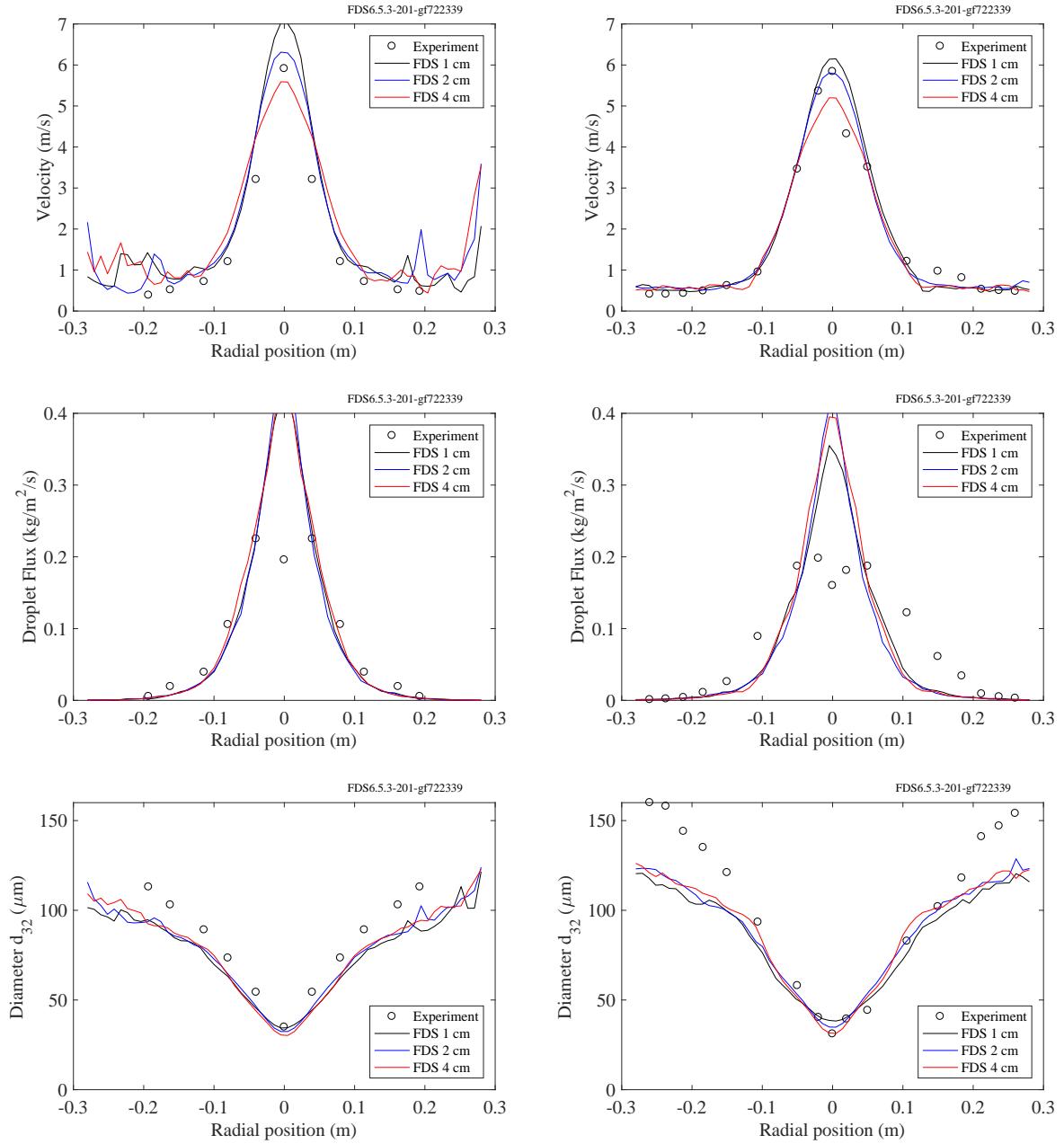


Figure 13.4: Comparison of predicted and experimental droplet speed (top), droplet flux (middle) and mean diameter (bottom) profiles of the LN-2 nozzle. The left column corresponds to measurements made 40 cm from the nozzle, while the right column corresponds to measurements made 62 cm from the nozzle.

# Chapter 14

## Burning Rate and Fire Spread

This chapter contains a series of validation exercises where the aim is to *predict* the burning and spread rate of the fire. Most of the simulations included in the previous chapters involved a *specified* burning or heat release rate. Here, the objective is to apply measured thermophysical properties of the material and predict its burning rate, either with a specified heat flux or as a free burn.

### 14.1 FAA Polymers

The U.S. Federal Aviation Administration (FAA) has studied various plastics that are commonly used aboard commercial aircraft.

This section presents measured properties of various polymers and the numerical predictions of their mass loss and/or burning rates under constant heat heating. Two types of experiments are considered. First, the NIST Gasification Apparatus is used to measure the mass loss rate of non-burning samples in a nitrogen atmosphere. Second, the standard Cone Calorimeter [243] is used to measure the heat release rate of materials in a normal atmosphere. When just the mass loss rate of a non-burning sample has been measured, FDS is run in “solid phase only” mode; that is, a 1-D heat conduction calculation is performed in a single grid cell. The result is the predicted mass loss rate as a function of time. To simulate a cone calorimeter experiment, FDS simulates the burning of a 10 cm by 10 cm sample with a specified heat flux to represent the effect of the cone heater. The cone itself is not included in the simulation. As the sample burns, FDS predicts the additional radiative and convective heating of the sample as a result of the fire.

In general, the burning/gasification rate of a charring polymer is more difficult to predict than a non-charring one because there are more parameters that need to be measured and more complicated behavior, like intumescence, need to be considered.

#### 14.1.1 Glossary of Terms

**Assumption:** Characteristics were assumed from known properties in similar materials.

**Cone Calorimeter** (ASTM E 1354 [243]) The Cone Calorimeter exposes a small sample to a constant external radiant heat flux simulating exposure of the sample to a large scale fire. The device records mass loss data along with heat release data through oxygen consumption calorimetry. From this a variety of heat release related properties can be found including heat of combustion.

**Constant Volume:** The material is assumed to maintain a constant volume during the solid phase reactions.

**Direct:** Direct measurement of densities is performed by measuring the dimensions and mass of the sample.

**DSC:** (ASTM E 2070 [244]) A Differential Scanning Calorimeter precisely raises the temperature of a small sample of material at a constant rate. This coupled with knowledge of heat absorbed by the sample allows for the calculation of the specific heat function of a material as well as heats of reaction and phase change.

**Estimated:** Characteristics were approximated based on known properties in similar materials.

**FTIR:** Fourier Transform Infrared Spectroscopy uses a spectrometer to simultaneously characterize the absorption of all frequencies of infrared light. In testing a sample is exposed to infrared light and a detector records light that has passed through the sample. A Fourier transform of detector measurement is then translated into absorption information.

**Gasification Apparatus:** Similar to the Cone Calorimeter however flaming is prevented. This is done typically through the introduction of inert purge gases.

**Inherited:** The properties of the product or component are assumed to be the same as the original material.

**Inverse Analysis:** Property was established by fitting a model to measured temperatures from the Cone Calorimeter or Gasification Apparatus.

**IS:** (ASTM E 1175 [245]) An Integrating Sphere, or an Ulbricht Sphere, is a hollow cavity whose interior has a high diffuse reflectivity. A sample placed inside the sphere is exposed to incident radiation and reflectivity measured. Emissivity can be determined from this information. The standard above is for measurement of Solar reflectivity, and was not necessarily precisely followed.

**Laser Flash:** (ASTM E1461 [246]) In the Laser Flash Method one surface of a sample is rapidly heated using a single pulse from a laser. Heat sensors on the opposite side of the sample record the arrival of the resulting temperature disturbance. From this thermal diffusivity/thermal conductivity can be calculated.

**Literature:** Results were found within previously published literature.

**MCC:** (ASTM D 7309 [247]) The Microscale Combustion Calorimeter (MCC) rapidly pyrolyzes a milligram size sample in an inert atmosphere. The pyrolyzate is then exposed to an abundance of oxygen. Heat release history is obtained from oxygen consumption. Similar to TGA with heat release recorded rather than mass loss rate.

**Pulsed Current:** Can refer to different types of tests. Generally, a sample is positioned between two electrodes in a sealed chamber with an inert atmosphere. The sample is heated through pulses of current. Measurements of the sample and the chamber can give information regarding specific heat, emissivity, or other material properties.

**TGA:** (ASTM E 1131 [248]) In Thermal Gravimetric Analysis (TGA) a small sample is heated at uniform rate, generally in an Nitrogen ( $N_2$ ) atmosphere. The percentage weight loss of the sample is recorded relative to the sample's temperature. Rate constants can then be fitted to the data. Similar to MCC with mass loss recorded instead of heat release.

**TLS:** (ASTM D 5930 [249]) The Transient Line Source method records temperature of a single point at a fixed distance in a sample over time using a probe. Given knowledge of the heat exposure of the sample the thermal conductivity can be found from the slope of the recorded data.

### 14.1.2 Non-Charring Polymers, HDPE, HIPS, and PMMA

A non-charring polymer is considered one of the easier solids to model because it typically involves only a single, first order reaction that converts solid plastic to fuel vapor. No residue is formed and the plastic is completely pyrolyzed. Table 14.1 lists nine parameters for each polymer studied. These values have been input directly into FDS, and the predicted mass loss rates are compared with measured values from the NIST Gasification Apparatus, a device that pyrolyzes the solid in a nitrogen environment to prevent combustion of fuel gases. The results are shown in Fig. 14.1. The exposing heat flux was  $52 \text{ kW/m}^2$ . A 1 cm layer of insulation was placed under the sample. Its properties are given in Ref. [149].

Table 14.1: Input parameters for FAA Polymers non-charring samples. Courtesy S. Stoliarov, M. McKinnon and J. Li, University of Maryland. See Section 14.1.1 for an explanation of terms.

Property	Units	HDPE	HIPS	PMMA	Unc. (%)	Method	Ref.
Density	$\text{kg/m}^3$	860	950	1100	5	Direct	[149]
Conductivity	$\text{W/m/K}$	0.29	0.22	0.20	15	TLC	[149]
Specific Heat	$\text{kJ/kg/K}$	3.5	2.0	2.2	15	DSC	[250]
Emissivity		0.92	0.86	0.85	20	IS	[251]
Absorption Coef.	$\text{m}^{-1}$	1300	2700	2700	50	FTIR	[252]
Pre-Exp. Factor	$\text{s}^{-1}$	$4.8 \times 10^{22}$	$1.2 \times 10^{16}$	$8.5 \times 10^{12}$	50	TGA	[149]
Activation Energy	$\text{kJ/kmol}$	$3.49 \times 10^5$	$2.47 \times 10^5$	$1.88 \times 10^5$	3	TGA	[149]
Heat of Reaction	$\text{kJ/kg}$	920	1000	870	15	DSC	[250]

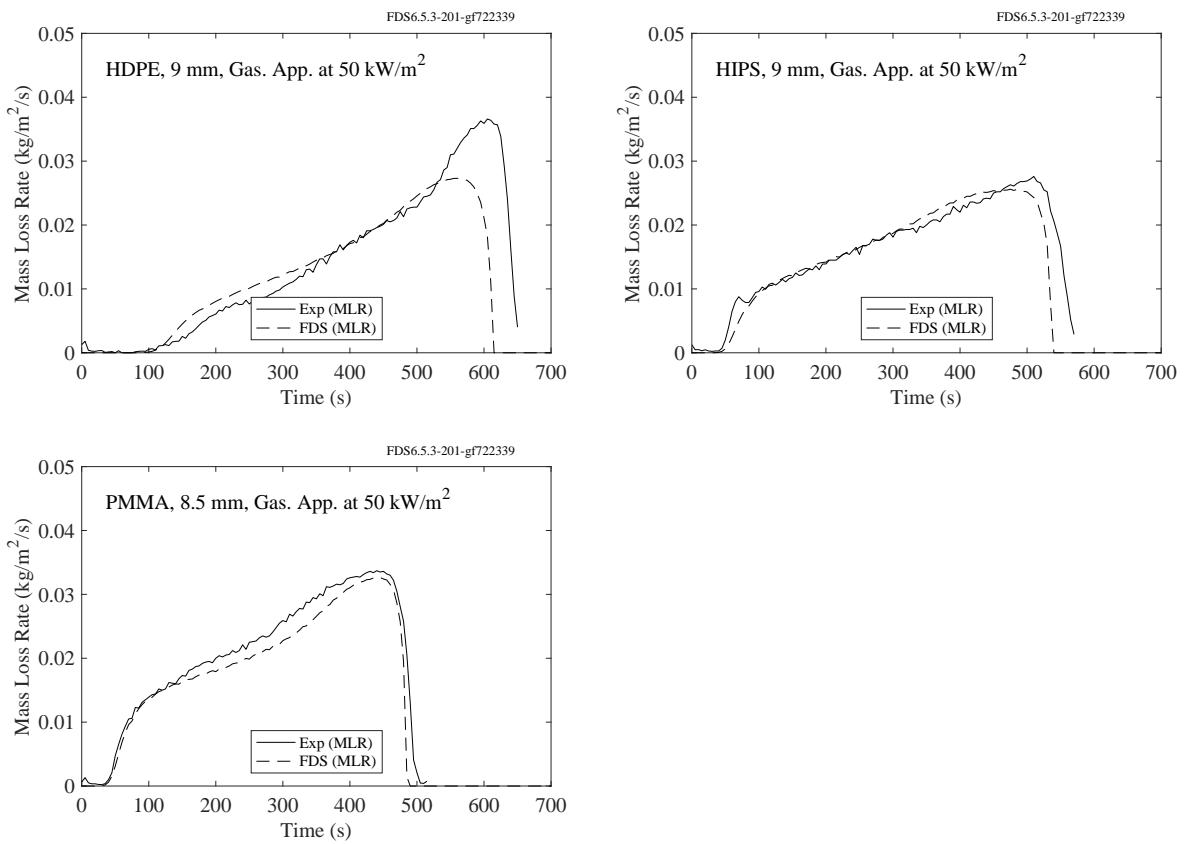


Figure 14.1: Comparison of predicted and measured mass loss rates for three non-charring polymers exposed to a heat flux of  $52 \text{ kW/m}^2$  in a nitrogen environment.

### 14.1.3 Complex Non-Charring Polymers: PP, PA66, POM, and PET

The polymers described in this section exhibit slightly more complex behavior than those in the previous section because they exhibit foaming and bubbling as they degrade. Table 14.2 lists the properties of each polymer. In the model, the polymers melt to form a liquid with identical properties as the solid, and the liquid evaporates. The melting is characterized by a threshold temperature and a heat of reaction equivalent to a heat of melting. These values have been input directly into FDS, and the predicted mass loss rates are compared with measured values from the NIST Gasification Apparatus, a device that pyrolyzes the solid in a nitrogen environment to prevent combustion of fuel gases. The results are shown in Fig. 14.2. The exposing heat flux was  $50 \text{ kW/m}^2$ . A thin sheet of aluminum foil and a 2.5 cm layer of Foamglas insulation was placed under the sample. Its properties are given in Ref. [253].

Table 14.2: Input parameters for FAA Polymers complex non-charring samples [253]. Courtesy S. Stolarov, G. Linteris and R.E. Lyon. See Section 14.1.1 for an explanation of terms.

Property	Units	PP	PA66	POM	PET	Unc. (%)	Method
Density	$\text{kg/m}^3$	910	1150	1425	1380	5	Direct
Conductivity	$\text{W/m/K}$	0.24	0.34	0.28	0.29	15	TLC
Specific Heat	$\text{kJ/kg/K}$	2.68	2.54	1.88	2.01	15	DSC
Emissivity		0.96	0.95	0.95	0.903	20	IS
Absorption Coef.	$\text{m}^{-1}$	966	3920	3550	2937	50	FTIR
Pre-Exp. Factor	$\text{s}^{-1}$	$1.6 \times 10^{23}$	$5.7 \times 10^{17}$	$3.7 \times 10^{10}$	$4.50 \times 10^{18}$	50	TGA
Activation Energy	$\text{kJ/kmol}$	$3.52 \times 10^5$	$2.74 \times 10^5$	$1.57 \times 10^5$	$2.81 \times 10^5$	3	TGA
Heat of Reaction	$\text{kJ/kg}$	1310	1390	1570	1800	15	DSC
Heat of Melting	$\text{kJ/kg}$	80	55	141	37	15	DSC
Melting Temperature	K	158	262	165	253	15	DSC

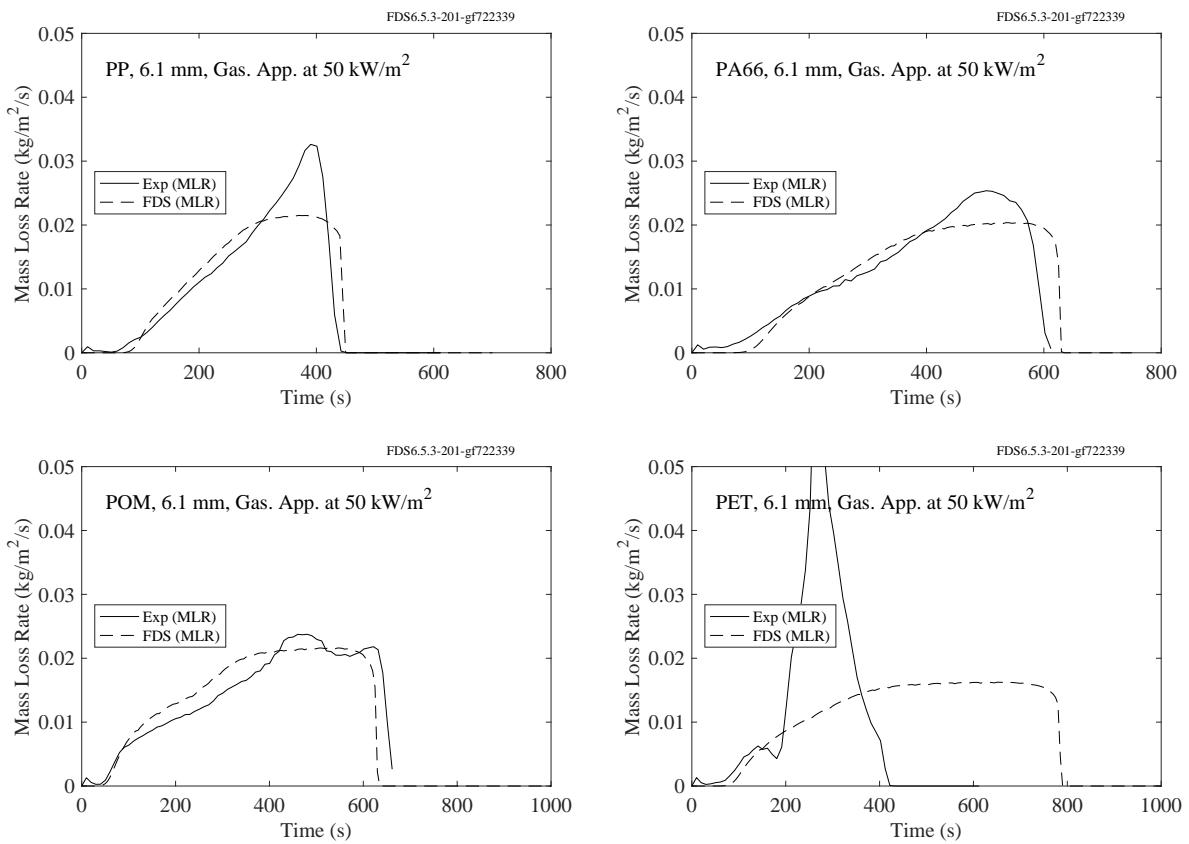


Figure 14.2: Comparison of predicted and measured mass loss rates for four complex non-charring polymers exposed to a heat flux of  $50 \text{ kW/m}^2$  in a nitrogen environment.

#### 14.1.4 Polycarbonate (PC)

Table 14.3 lists the measured properties of polycarbonate. These values have been input directly into FDS, and the predicted heat release rates are compared with measured values from the Cone Calorimeter. The results for samples of various thicknesses and imposed heat fluxes are shown in Fig. 14.3. A 1 cm layer of Kawool insulation was placed under the sample. Its properties are given in Ref. [150]. It is assumed that the polymer undergoes a single step reaction that forms fuel gas and char.

Table 14.3: Properties of polycarbonate (PC). Courtesy S. Stolarov, University of Maryland. See Section 14.1.1 for an explanation of terms.

Property	Units	Value	Method	Reference
Polymer Density	kg/m <sup>3</sup>	1180 ± 60	Direct	[150]
Polymer Conductivity	W/m/K	0.22 ± 0.03	Literature	[150]
Polymer Specific Heat	kJ/kg/K	1.9 ± 0.3	DSC	[250]
Polymer Emissivity		0.90 ± 0.05	IS	[251]
Polymer Absorption Coef.	m <sup>-1</sup>	1770 ± 590	FTIR	[252]
Char Density	kg/m <sup>3</sup>	248	Cone Calorimeter	[150]
Char Conductivity	W/m/K	0.37	Cone Calorimeter	[150]
Char Specific Heat	kJ/kg/K	1.72 ± 0.17	Pulsed Current	[150, 254]
Char Emissivity		0.85 ± 0.05	Pulsed Current	[150, 254]
Char Absorption Coef.	m <sup>-1</sup>	Opaque	Assumption	[150]
Pre-Exp. Factor	s <sup>-1</sup>	(1.9 ± 1.1) × 10 <sup>18</sup>	TGA	[150]
Activation Energy	kJ/kmol	(2.95 ± 0.06) × 10 <sup>5</sup>	TGA	[150]
Heat of Reaction	kJ/kg	830 ± 140	DSC	[250]
Heat of Combustion	kJ/kg	25600 ± 130	MCC	[150]
Combustion Efficiency		0.84 ± 0.03	Cone Calorimeter	[150]

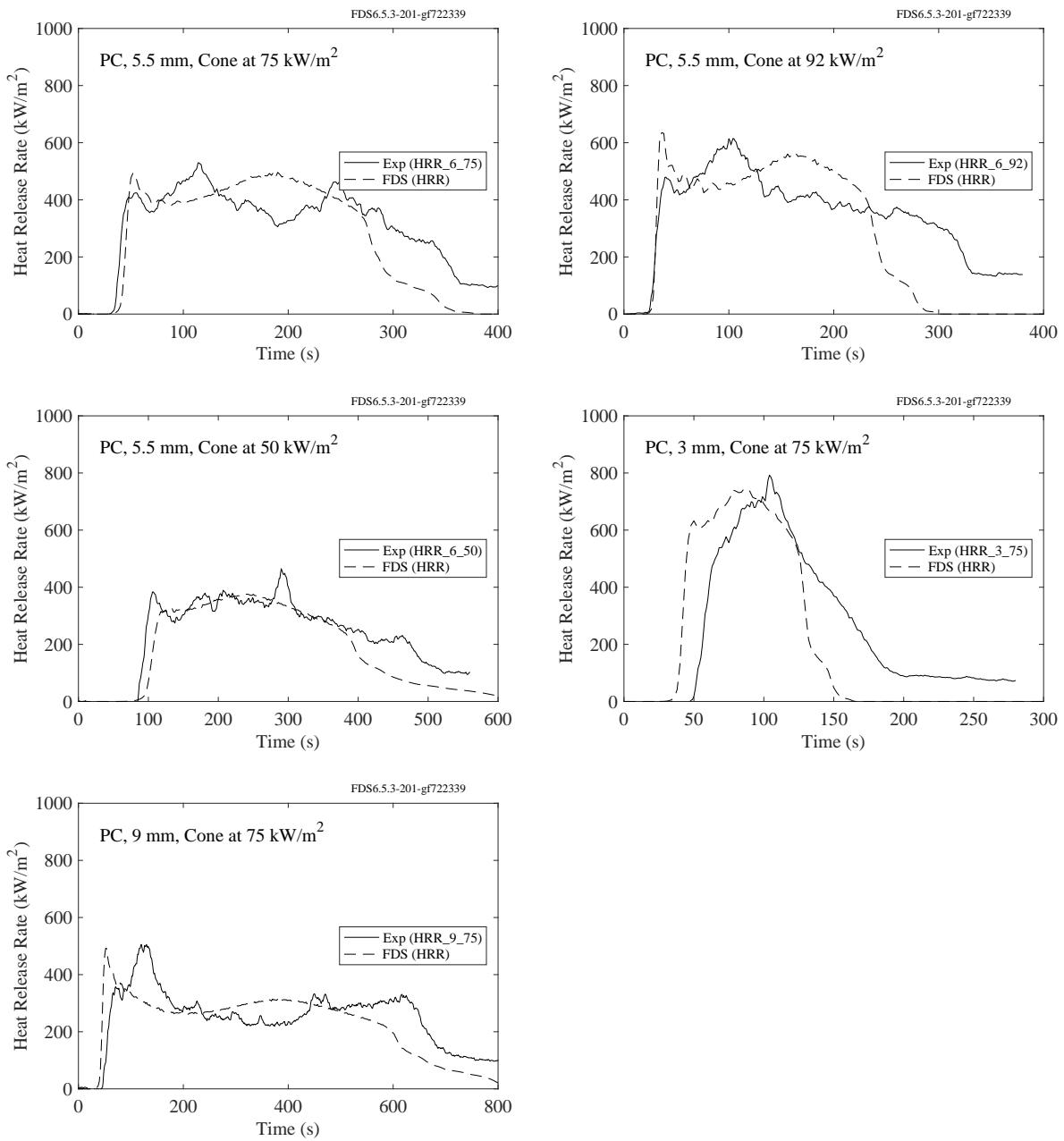


Figure 14.3: Comparison of predicted and measured heat release rates for polycarbonate (PC).

### 14.1.5 Poly(vinyl chloride) (PVC)

Table 14.4 lists the measured properties of poly(vinyl chloride). These values have been input directly into FDS, and the predicted heat release rates are compared with measured values from the Cone Calorimeter. The results for samples of various thicknesses and imposed heat fluxes are shown in Fig. 14.4. A 1 cm layer of Kawool insulation was placed under the sample. Its properties are given in Ref. [150].

It is assumed that the polymer decomposes via a two-step reaction:



Table 14.4: Properties of poly(vinyl chloride) (PVC). Courtesy S. Stolarov, University of Maryland. See Section 14.1.1 for an explanation of terms.

Property	Units	Value	Method	Reference
Polymer Density	kg/m <sup>3</sup>	1430 ± 70	Direct	[150]
Polymer Conductivity	W/m/K	0.17 ± 0.01	Literature	[150]
Polymer Specific Heat	kJ/kg/K	1.55 ± 0.25	DSC	[250]
Polymer Emissivity		0.90 ± 0.05	IS	[251]
Polymer Absorption Coef.	m <sup>-1</sup>	2145 ± 715	FTIR	[252]
Char 1 Density	kg/m <sup>3</sup>	629	Constant Volume	[150]
Char 1 Conductivity	W/m/K	0.17	Inherited	[150]
Char 1 Specific Heat	kJ/kg/K	1.55 ± 0.25	Inherited	[150]
Char 1 Emissivity		0.90 ± 0.05	Inherited	[150]
Char 1 Absorption Coef.	m <sup>-1</sup>	2453	Inverse Analysis	[150]
Char 2 Density	kg/m <sup>3</sup>	296	Constant Volume	[150]
Char 2 Conductivity	W/m/K	0.26	Inverse Analysis	[150]
Char 2 Specific Heat	kJ/kg/K	1.72 ± 0.17	Pulsed Current	[150, 254]
Char 2 Emissivity		0.85 ± 0.05	Pulsed Current	[150, 254]
Char 2 Absorption Coef.	m <sup>-1</sup>	Opaque	Assumption	[150]
Reac 1 Pre-Exp. Factor	s <sup>-1</sup>	(1.4 ± 0.8) × 10 <sup>33</sup>	TGA	[150]
Reac 1 Activation Energy	kJ/kmol	(3.67 ± 0.07) × 10 <sup>5</sup>	TGA	[150]
Reac 1 Char Yield		0.44 ± 0.01	TGA	[150]
Reac 1 Heat of Reaction	kJ/kg	170 ± 17	DSC	[250]
Gas 1 Heat of Combustion	kJ/kg	2700 ± 300	MCC	[150]
Gas 1 Combustion Efficiency		0.75 ± 0.03	Cone Calorimeter	[150]
Reac 2 Pre-Exp. Factor	s <sup>-1</sup>	(3.5 ± 2.1) × 10 <sup>12</sup>	TGA	[150]
Reac 2 Activation Energy	kJ/kmol	(2.07 ± 0.04) × 10 <sup>5</sup>	TGA	[150]
Reac 2 Char Yield		0.47 ± 0.01	TGA	[150]
Reac 2 Heat of Reaction	kJ/kg	1200 ± 900	DSC	[250]
Gas 2 Heat of Combustion	kJ/kg	36500 ± 1800	MCC	[150]
Gas 2 Combustion Efficiency		0.75 ± 0.03	Cone Calorimeter	[150]

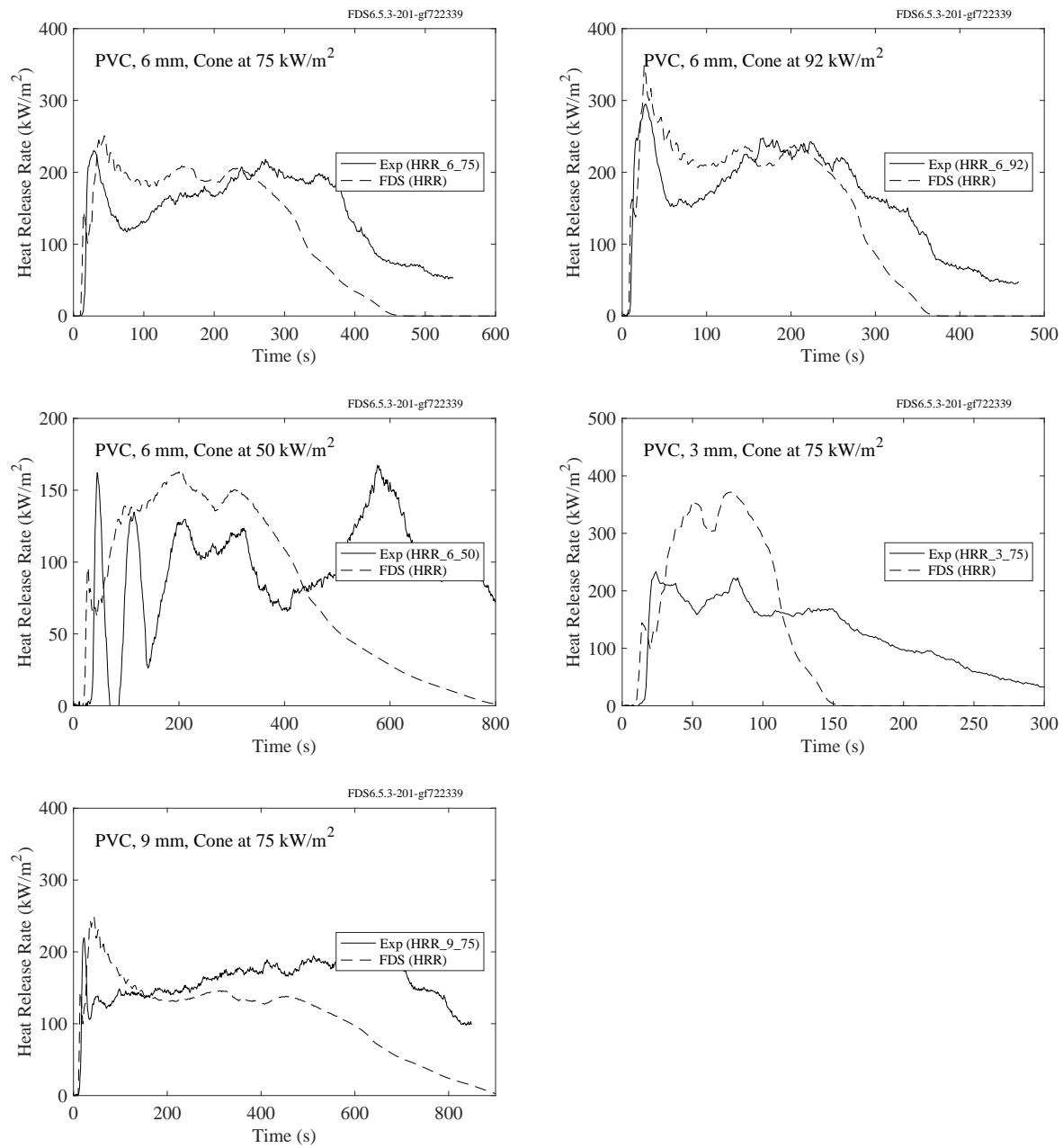


Figure 14.4: Comparison of predicted and measured heat release rates for poly(vinyl chloride) (PVC).

#### 14.1.6 Poly(aryl ether ether ketone)) (PEEK)

Table 14.5 lists the measured properties of poly(aryl ether ether ketone)<sup>1</sup>. Its property values have been input directly into FDS, and the predicted heat release rates are compared with measured values from the Cone Calorimeter. It is assumed that the polymer decomposes via a four-step reaction:



It is also assumed that the gaseous fuel molecule is C<sub>19</sub>H<sub>12</sub>O<sub>3</sub>. A 1 cm layer of Kaowool insulation was placed under the sample. Its properties are given in Ref. [150].

The results for 3.9 mm samples at imposed heat fluxes of 50 kW/m<sup>2</sup>, 70 kW/m<sup>2</sup>, and 90 kW/m<sup>2</sup> are shown in Fig. 14.5. Note that the plots on the left are the results of simulations of the solid phase only, where the heat feedback from the fire is assumed to be 15 kW/m<sup>2</sup> and it is applied at the time of ignition. The plots on the right are from 3-D simulations of the solid sample and the fire. In these cases, the radiative feedback is not specified but rather calculated.

---

<sup>1</sup>Trade name VICTREX PEEK 450G. The sample has been thoroughly dried.

Table 14.5: Properties of poly(aryl ether ether ketone) (PEEK). Courtesy E. Oztekin, U.S. FAA and S. Sto-liarov, University of Maryland. See Section 14.1.1 for an explanation of terms.

Property	Units	Value	Method	Reference
Polymer Density	kg/m <sup>3</sup>	1300	Direct	[255]
Polymer Conductivity	W/m/K	0.28	Inverse Analysis	[255]
Polymer Specific Heat	kJ/kg/K	2.05	Inverse Analysis	[255]
Polymer Emissivity		0.90	Inverse Analysis	[255]
Polymer Absorption Coef.	m <sup>-1</sup>	1690	Inverse Analysis	[255]
Char 1 Density	kg/m <sup>3</sup>	810	Constant Volume	[255]
Char 1 Conductivity	W/m/K	0.37	Inverse Analysis	[255]
Char 1 Specific Heat	kJ/kg/K	0.24	Assumed	[255]
Char 1 Emissivity		1	Assumed	[255]
Char 1 Absorption Coef.	m <sup>-1</sup>	81000	Assumed opaque	[255]
Char 2 Density	kg/m <sup>3</sup>	710	Constant Volume	[255]
Char 2 Conductivity	W/m/K	0.37	Inverse Analysis	[255]
Char 2 Specific Heat	kJ/kg/K	0.27	Assumed	[255]
Char 2 Emissivity		1	Assumed	[255]
Char 2 Absorption Coef.	m <sup>-1</sup>	71000	Assumed opaque	[255]
Reac 1 Pre-Exp. Factor	s <sup>-1</sup>	$1.0 \times 10^{32}$	TGA	[255]
Reac 1 Activation Energy	kJ/kmol	$5.57 \times 10^5$	TGA	[255]
Reac 1 Char Yield		0.62	TGA	[255]
Reac 1 Heat of Reaction	kJ/kg	350	Inverse Analysis	[255]
Gas 1 Heat of Combustion	kJ/kg	16000	Cone calorimetry	[255]
Gas 1 Combustion Efficiency		1	Assumed	[255]
Reac 2 Pre-Exp. Factor	s <sup>-1</sup>	$1.0 \times 10^3$	TGA	[255]
Reac 2 Activation Energy	kJ/kmol	$8.9 \times 10^4$	TGA	[255]
Reac 2 Char Yield		0.88	TGA	[255]
Reac 2 Heat of Reaction	kJ/kg	0	Assumed	[255]
Gas 2 Heat of Combustion	kJ/kg	27000	Cone Calorimetry	[255]
Gas 2 Combustion Efficiency		1	Assumed	[255]
Reac 3 Pre-Exp. Factor	s <sup>-1</sup>	$1.0 \times 10^5$	TGA	[255]
Reac 3 Activation Energy	kJ/kmol	$1.47 \times 10^5$	TGA	[255]
Reac 3 Char Yield		0.88	TGA	[255]
Reac 3 Heat of Reaction	kJ/kg	0	Assumed	[255]
Reac 4 Pre-Exp. Factor	s <sup>-1</sup>	$1.0 \times 10^3$	TGA	[255]
Reac 4 Activation Energy	kJ/kmol	$1.29 \times 10^5$	TGA	[255]
Reac 4 Char Yield		0	TGA	[255]
Reac 4 Heat of Reaction	kJ/kg	0	Assumed	[255]

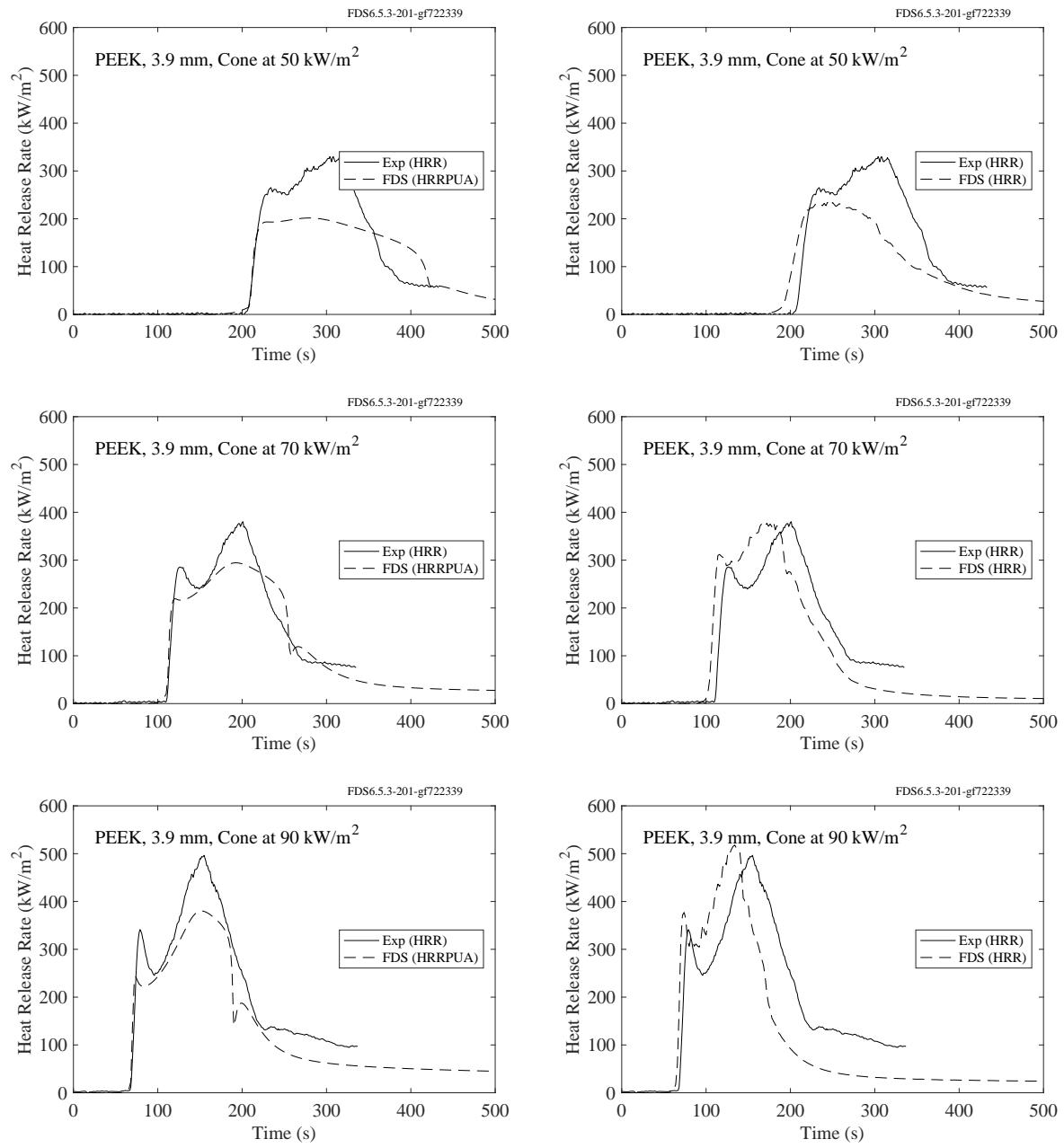


Figure 14.5: Comparison of predicted and measured heat release rates for poly(aryl ether ether ketone) (PEEK). The plots on the left include only a simulation of the solid phase with an added heat flux of  $15 \text{ kW/m}^2$  to account for the radiative feedback from the flame. The plots on the right are 3-D simulations of the solid sample and the fire.

### 14.1.7 Poly(butylene terephthalate) (PBT)

Samples of poly(butylene terephthalate) (PBT)<sup>2</sup> have been burned without oxygen in the Gasification Apparatus and with oxygen in the Cone Calorimeter. The properties of PBT are listed in Table 14.6. It is assumed that the polymer undergoes a single step reaction that forms fuel gas and no char.

The results of the simulations are shown in Fig. 14.6. Note that the effect of the flame radiation heat feedback to the sample surface is accounted for by increasing the imposed heat fluxes of 35 kW/m<sup>2</sup> by 39 %, 50 kW/m<sup>2</sup> by 22 %, and 70 kW/m<sup>2</sup> by 6 % [256].

Table 14.6: Properties of poly(butylene terephthalate) (PBT). Courtesy S. Stolarov, University of Maryland, and Florian Kempel. See Section 14.1.1 for an explanation of terms. Note that the Specific Heat and Conductivity result from averaging the reported temperature dependent properties over the room to decomposition temperature range (300 K – 650 K). The heat capacity value is increased by 0.13 kJ/kg/K to account for the heat of melting (-46 kJ/kg), which takes place at 493 K.

Property	Units	Value	Method	Reference
Density	kg/m <sup>3</sup>	1300 ± 70	Direct	[256]
Specific Heat	kJ/kg/K	2.23 ± 0.34	DSC	[256]
Conductivity	W/m/K	0.29 ± 0.05	TLS	[256]
Emissivity		0.88 ± 0.05	FTIR	[257]
Absorption Coefficient	m <sup>-1</sup>	2561 ± 140	FTIR	[257]
Pre-Exp. Factor	s <sup>-1</sup>	(2.49 ± 0.62) × 10 <sup>14</sup>	TGA	[256]
Activation Energy	kJ/kmol	(2.12 ± 0.53) × 10 <sup>5</sup>	TGA	[256]
Heat of Reaction	kJ/kg	507	DSC, Literature	[256, 258]
Heat of Combustion	kJ/kg	19500	Cone Calorimeter	[256]
Combustion Efficiency		1	Assumption	[256]

<sup>2</sup>Tradename Arnite T06-200, DSM Engineering Plastics

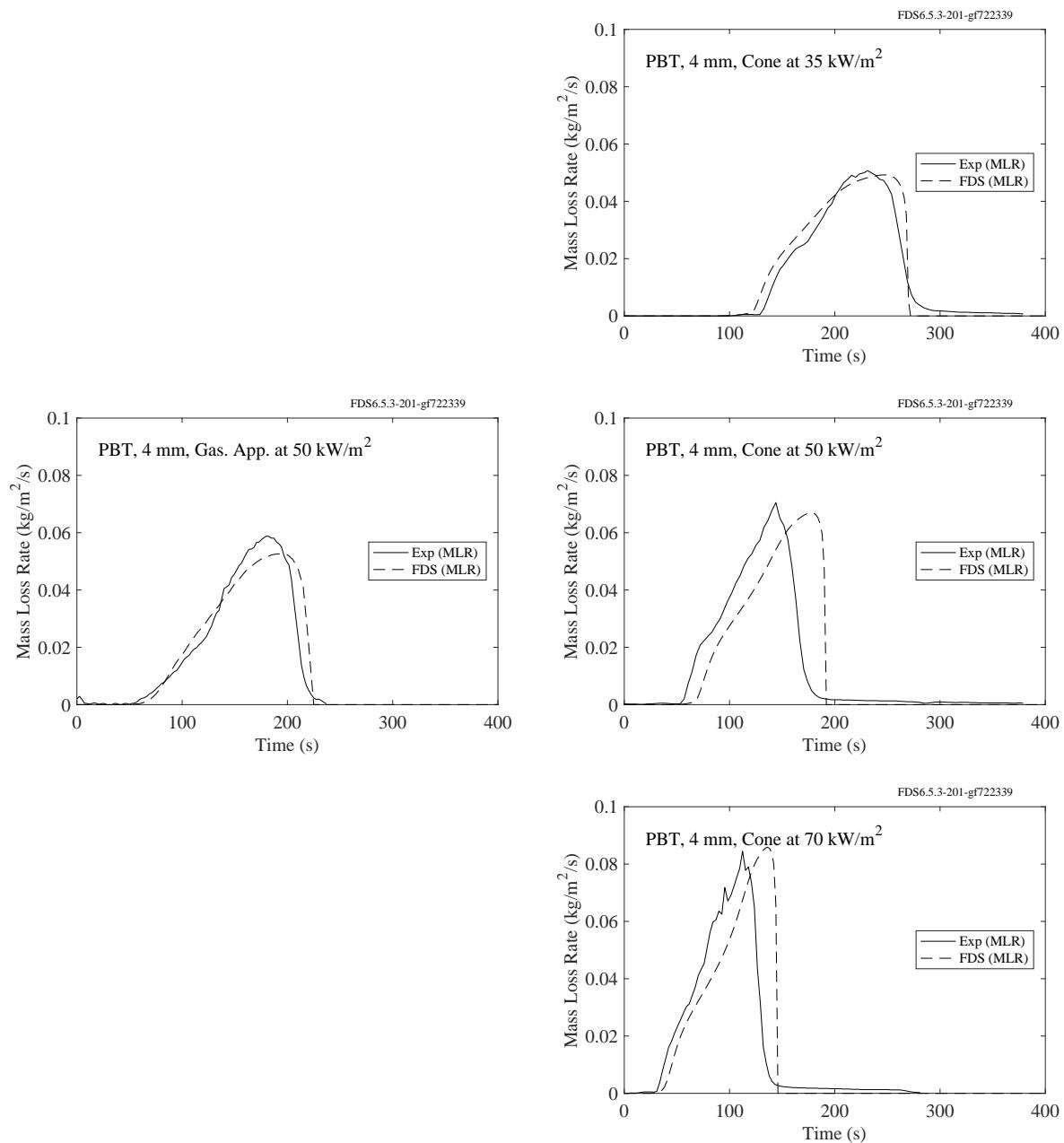


Figure 14.6: Comparison of predicted and measured mass loss rates for poly(butylene terephthalate) (PBT) in both the Gasification Apparatus and Cone Calorimeter.

### 14.1.8 PBT with Glass Fibers (PBT-GF)

Samples of poly(butylene terephthalate) (PBT), blended with 30 % by mass glass fibers<sup>3</sup>, have been burned without oxygen in the Gasification Apparatus and with oxygen in the Cone Calorimeter. The properties of PBT-GF are listed in Table 14.7. It is assumed that the polymer undergoes a single step reaction that forms fuel gas and char.

The results of the simulations are shown in Fig. 14.7. Note that the effect of the flame radiation heat feedback to the sample surface is accounted for by increasing the imposed heat fluxes of 35 kW/m<sup>2</sup> by 33 %, 50 kW/m<sup>2</sup> by 16 %, and 70 kW/m<sup>2</sup> by 5 % [256].

Table 14.7: Properties of poly(butylene terephthalate) with glass fibers (PBT-GF). Courtesy S. Stoliarov, University of Maryland. See Section 14.1.1 for an explanation of terms. Note that the Polymer Specific Heat and Polymer Conductivity are the result of averaging the reported temperature dependent properties over the room to decomposition temperature range (300 K – 650 K). The heat capacity value is increased by 0.09 kJ/kg/K to account for the heat of melting (-32 kJ/kg), which takes place at 493 K.

Property	Units	Value	Method	Reference
Polymer Density	kg/m <sup>3</sup>	1520 ± 80	Direct	[256]
Polymer Specific Heat	kJ/kg/K	1.68 ± 0.26	DSC	[256]
Polymer Conductivity	W/m/K	0.36 ± 0.06	TLS	[256]
Polymer Emissivity		0.87 ± 0.05	FTIR	[257]
Polymer Absorption Coef.	m <sup>-1</sup>	2860 ± 150	FTIR	[257]
Char Density	kg/m <sup>3</sup>	482	Constant Volume	[256]
Char Specific Heat	kJ/kg/K	0.85	Literature	[259]
Char Conductivity	W/m/K	0.07 ± 0.02	Laser Flash	[256]
Char Emissivity		0.85	Literature	[260]
Char Absorption Coef.	m <sup>-1</sup>	10000	Estimated	[256]
Pre-Exp. Factor	s <sup>-1</sup>	(2.49 ± 0.63) × 10 <sup>14</sup>	TGA	[256]
Activation Energy	kJ/kmol	(2.12 ± 0.53) × 10 <sup>5</sup>	TGA	[256]
Heat of Reaction	kJ/kg	355	DSC, Literature	[256, 258]
Heat of Combustion	kJ/kg	19500	Cone Calorimeter	[256]
Char Yield		0.32 ± 0.05	Gasification Device	[256]
Combustion Efficiency		1	Assumption	[256]

<sup>3</sup>Tradename Arnite TV4-261, DSM Engineering Plastics

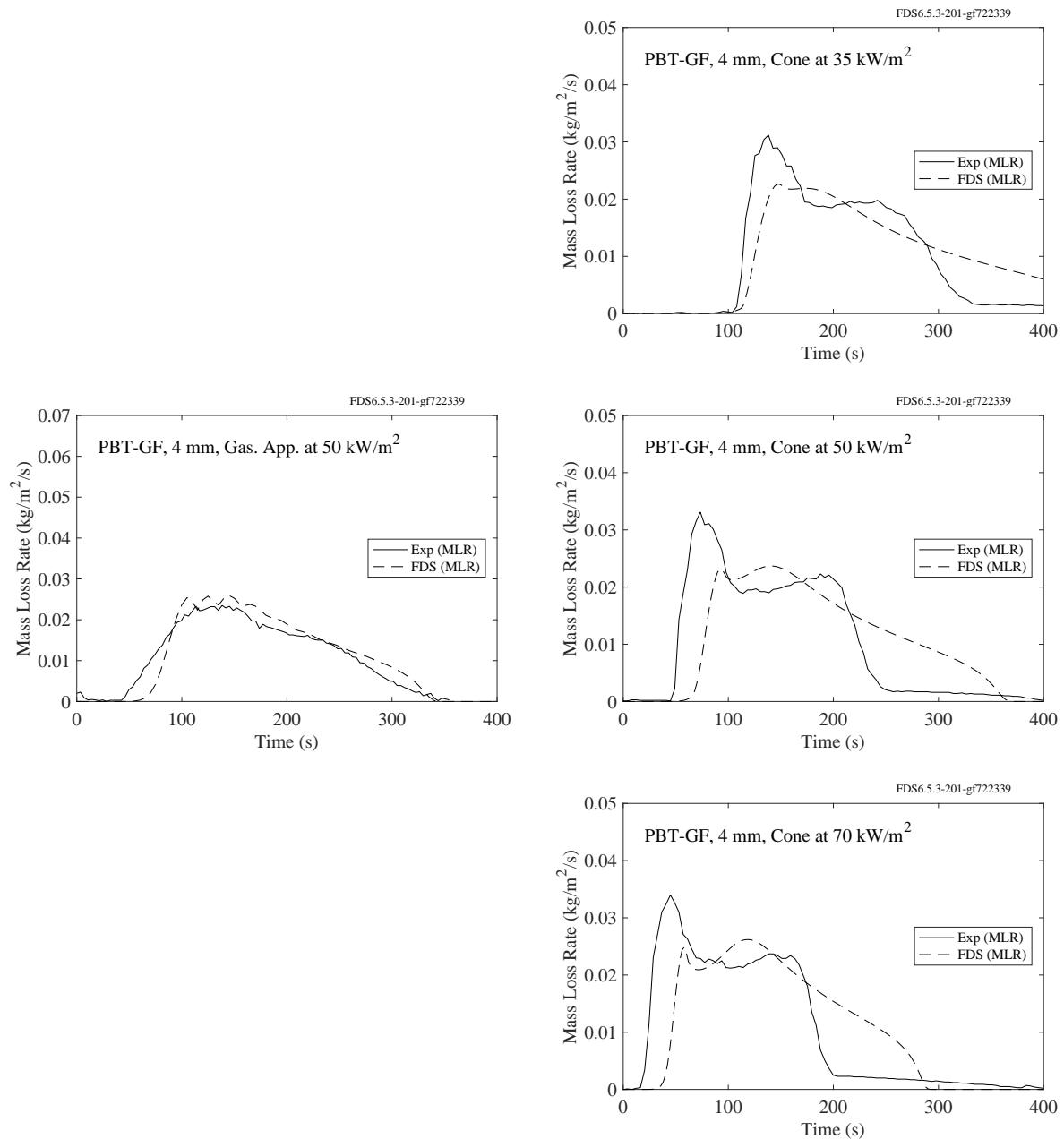


Figure 14.7: Comparison of predicted and measured mass loss rates for poly(butylene terephthalate) with glass fibers (PBT-GF) in both the Gasification Apparatus and Cone Calorimeter.

## 14.2 UMD Polymers

This section contains a description of seven polymers analyzed by J. Li for his doctoral thesis at the University of Maryland [261]. In addition to the thesis itself, details of the measurement techniques can be found in Refs. [206, 207, 257, 208, 209].

In the experiments, samples of seven different polymers were exposed to several different heat flux levels in the controlled atmosphere pyrolysis apparatus (CAPA) developed at the University of Maryland. This apparatus is similar to a cone calorimeter, but with a nitrogen environment. Thus, it is similar in function to the Gasification Apparatus. In each experiment, a roughly 6 mm sample was placed upon a wire mesh with no insulated backing. The top side of the sample was exposed to a specified heat flux, while the bottom remained exposed to ambient conditions. The mass loss rate of the sample was measured, and in the sections to follow the measured values are compared to FDS predictions. The seven polymers are organized into groups with one, two, or three degradation steps.

### 14.2.1 One-Step Degradation: ABS, HIPS, and PMMA

These three polymers are assumed to pyrolyze according to the following single step process:



The properties of the virgin polymer, the char, and the reaction kinetics are listed in Table 14.8.

Table 14.8: Properties of ABS, HIPS, and PMMA. Note that the temperature dependence of the thermal conductivity is assumed to be linear, unlike some of those reported in Ref. [261].

Property	Units	ABS	HIPS	PMMA
Polymer Density	kg/m <sup>3</sup>	1050	1060	1160
Polymer Cond.	W/m/K	$0.30 - 0.00028T$	$0.10 + 0.0001T$	$0.45 - 0.00038T, T < 378\text{ K}$ $0.27 - 0.00024T, T \geq 378\text{ K}$
Polymer Spec. Heat	kJ/kg/K	$1.58 + 0.0013T$	$0.59 + 0.0034T$	$0.60 + 0.0036T$
Polymer Emissivity		0.95	0.95	0.95
Polymer Abs. Coef.	m <sup>-1</sup>	1800	2250	2240
Char Density	kg/m <sup>3</sup>	80	Same as Polymer	Same as Polymer
Char Conductivity	W/m/K	$0.13 - 0.00054T$	Same as Polymer	Same as Polymer
Char Specific Heat	kJ/kg/K	$0.82 + 0.00011T$	Same as Polymer	Same as Polymer
Char Emissivity		0.86	Same as Polymer	Same as Polymer
Char Abs. Coef.	m <sup>-1</sup>	2500	Opaque	Same as Polymer
Pre-Exp. Factor	s <sup>-1</sup>	$1.00 \times 10^{14}$	$1.70 \times 10^{20}$	$8.60 \times 10^{12}$
Activation Energy	kJ/kmol	$2.19 \times 10^5$	$3.01 \times 10^5$	$1.88 \times 10^5$
Heat of Reaction	kJ/kg	460	689	846
Heat of Combustion	kJ/kg	28750	29900	24450
Residue Fraction		0.023	0.043	0.015

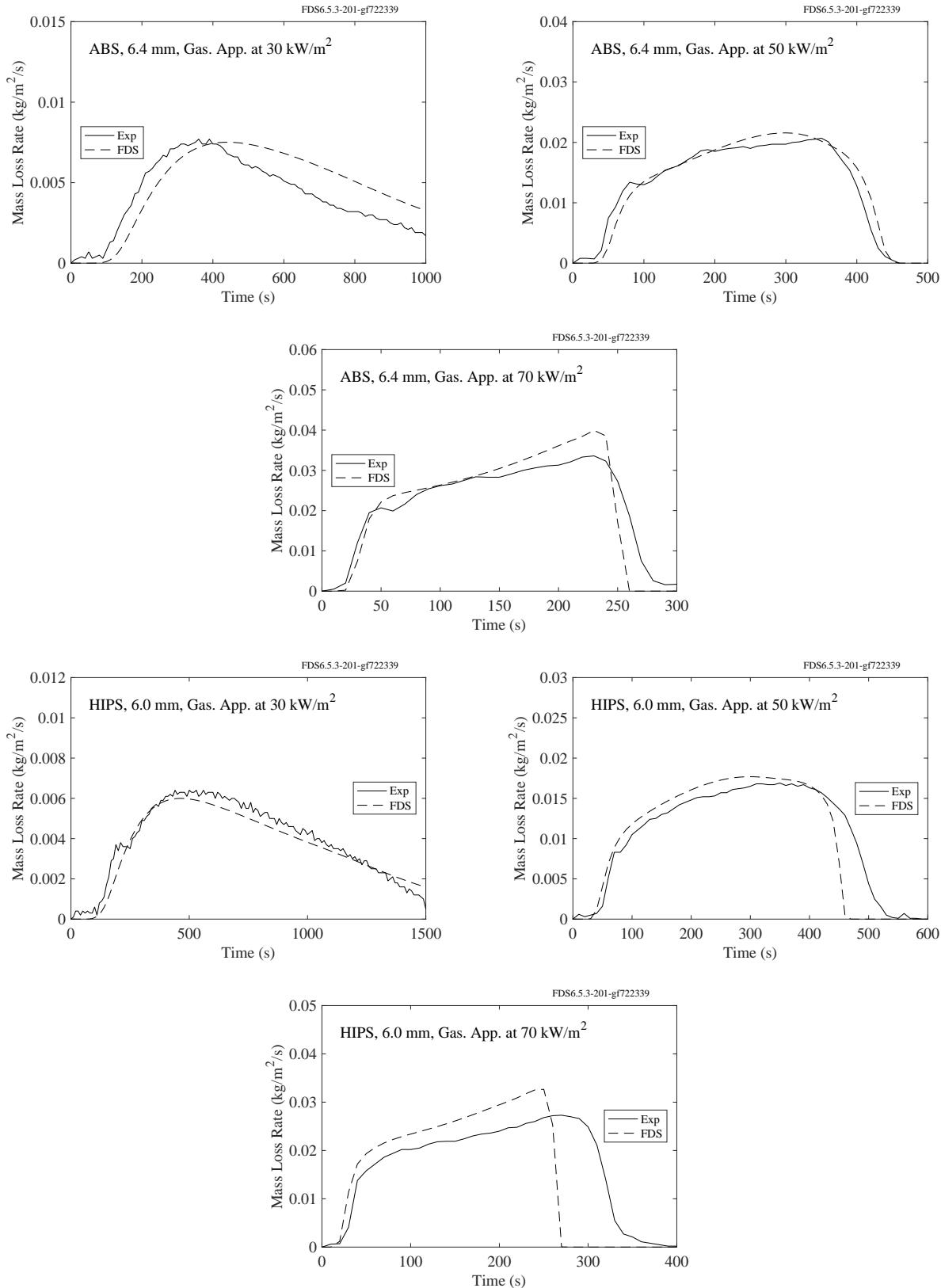


Figure 14.8: Comparison of predicted and measured mass loss rates for ABS and HIPS.

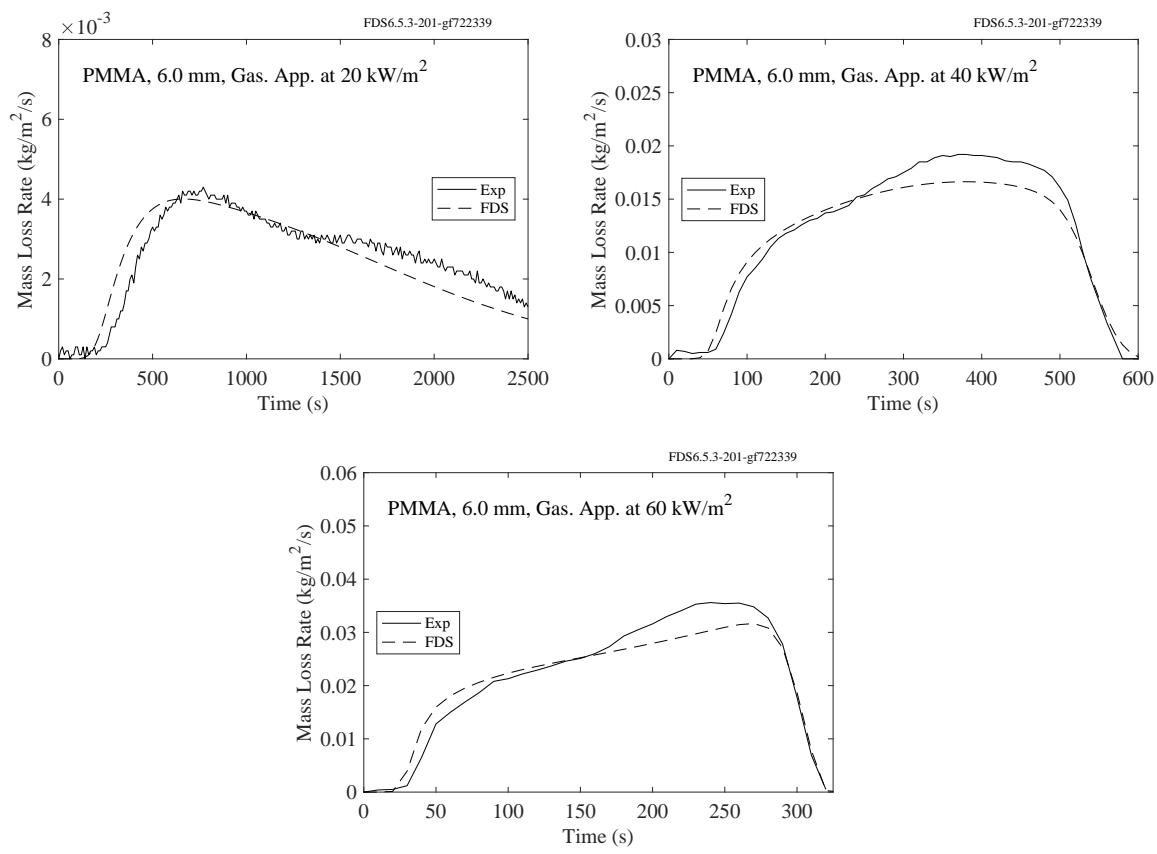
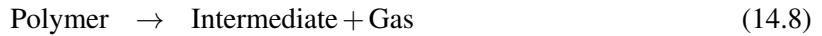


Figure 14.9: Comparison of predicted and measured mass loss rates for PMMA.

### 14.2.2 Two-Step Degradation: Kydex

This polymer is assumed to pyrolyze according to the following two step process:



The properties of the polymer and the reaction kinetics are listed in Table 14.9 and the mass loss rate comparisons are shown on the following page. Note that nominal exposing heat flux values of  $30 \text{ kW/m}^2$ ,  $50 \text{ kW/m}^2$ , and  $70 \text{ kW/m}^2$  were changed slightly in the simulations to account for the fact that the intumescent material surface moved closer to the heater during the course of the experiment [209].

Table 14.9: Properties of Kydex. Note that the temperature dependence of the thermal conductivity is assumed to be linear, unlike some of those reported in Ref. [261].

Property	Units	Kydex
Polymer Density	$\text{kg/m}^3$	1350
Polymer Cond.	$\text{W/m/K}$	$0.28 - 0.00029T$
Polymer Spec. Heat	$\text{kJ/kg/K}$	$-0.62 + 0.00593T$
Polymer, Int. Emissivity		0.95
Polymer Abs. Coef.	$\text{m}^{-1}$	2135
Int. Density	$\text{kg/m}^3$	Same as Char
Int. Cond.	$\text{W/m/K}$	$0.55 + 0.00003T$
Int. Spec. Heat	$\text{kJ/kg/K}$	$0.27 + 0.00301T$
Int. Abs. Coef.	$\text{m}^{-1}$	3000
Char Density	$\text{kg/m}^3$	100
Char Conductivity	$\text{W/m/K}$	$0.21 + 0.00034T$
Char Specific Heat	$\text{kJ/kg/K}$	$1.15 + 0.00010T$
Char Emissivity		0.86
Char Abs. Coef.	$\text{m}^{-1}$	10000
Reac. 14.8 Pre-Exp. Factor	$\text{s}^{-1}$	$6.03 \times 10^{10}$
Reac. 14.8 Act. Energy	$\text{kJ/kmol}$	$1.41 \times 10^5$
Reac. 14.8 Heat of Reac.	$\text{kJ/kg}$	180
Reac. 14.8 Residue Frac.		0.45
Reac. 14.9 Pre-Exp. Factor	$\text{s}^{-1}$	$1.36 \times 10^{10}$
Reac. 14.9 Act. Energy	$\text{kJ/kmol}$	$1.74 \times 10^5$
Reac. 14.9 Heat of Reac.	$\text{kJ/kg}$	125
Reac. 14.9 Residue Frac.		0.31
Gas Heat of Combustion	$\text{kJ/kg}$	12650

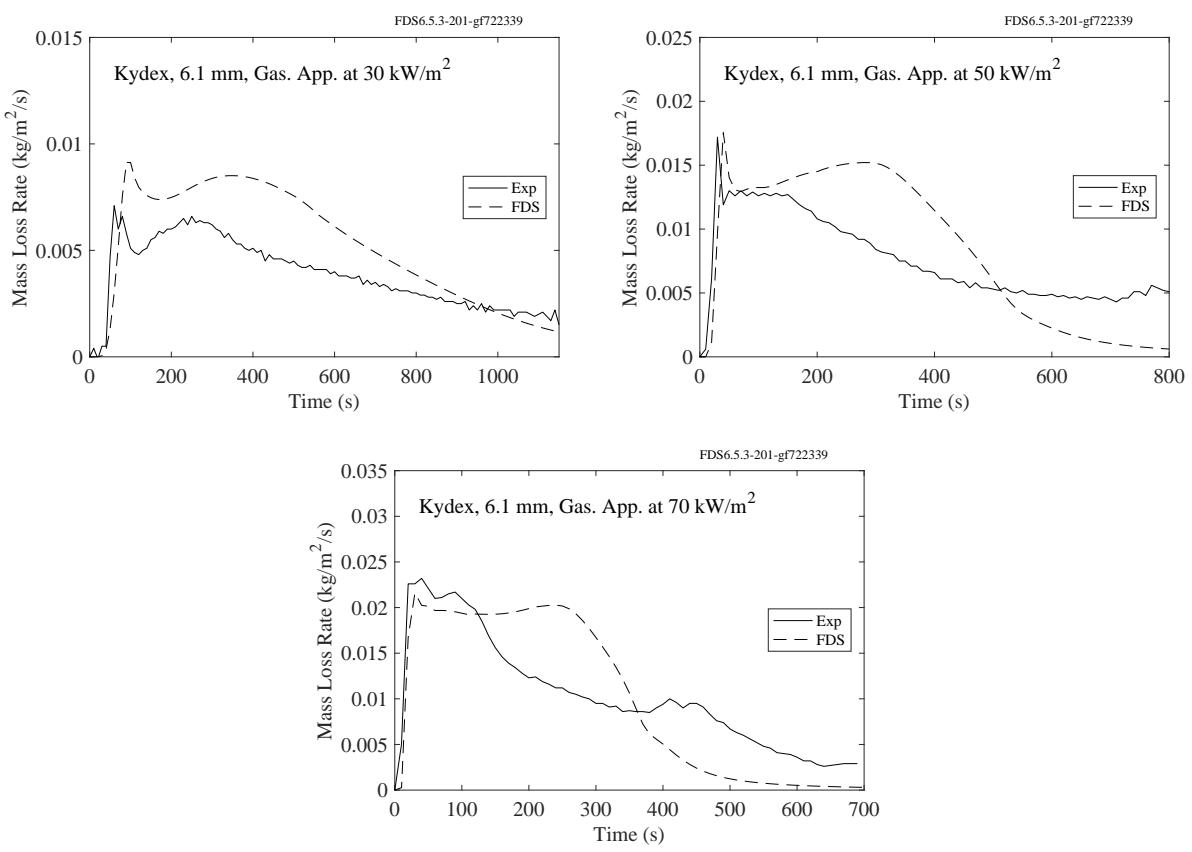
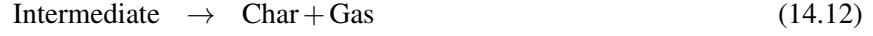


Figure 14.10: Comparison of predicted and measured mass loss rates for Kydex.

### 14.2.3 Three-Step Degradation: PEI, PET, and POM

These three polymers are assumed to pyrolyze following the three-step process:



The property data is listed in Table 14.10 and the mass loss rate comparisons are shown on the subsequent pages.

Table 14.10: Properties of PEI, PET, and POM. Note that the temperature dependence of the thermal conductivity is assumed to be linear, unlike some of those reported in Ref. [261].

Property	Units	PEI	PET	POM
Polymer, Melt Density	kg/m <sup>3</sup>	1285	1385	1424
Polymer Cond.	W/m/K	$0.40 - 0.00040T$	$0.34 - 0.00046T$	$0.25 + 0.00002T$
Polymer Spec. Heat	kJ/kg/K	$-0.04 + 0.00410T$	$-0.27 + 0.00464T$	$-1.86 + 0.0099T$
Polymer, Melt, Int. Emiss.		0.95	0.95	0.95
Polymer Abs. Coef.	m <sup>-1</sup>	1745	1940	3050
Melt Cond.	W/m/K	$0.32 - 0.00033T$	$0.33 - 0.00002T$	$0.21 + 0.00001T$
Melt Spec. Heat	kJ/kg/K	$1.88 + 0.00057T$	$2.05 - 0.00021T$	$1.65 + 0.00120T$
Melt Abs. Coef.	m <sup>-1</sup>	128500	Same as Polymer	Same as Polymer
Int. Density	kg/m <sup>3</sup>	Same as Char	730	Same as Polymer
Int. Cond.	W/m/K	$0.45 + 0.00019T$	$0.45 + 0.00020T$	$0.19 - 0.00006T$
Int. Spec. Heat	kJ/kg/K	$1.59 + 0.00031T$	$1.44 - 0.00005T$	Same as Melt
Int. Abs. Coef.	m <sup>-1</sup>	8000	1025	Same as Polymer
Char Density	kg/m <sup>3</sup>	80	80	Same as Int.
Char Conductivity	W/m/K	$0.45 + 0.00013T$	$0.34 + 0.00046T$	Same as Polymer
Char Specific Heat	kJ/kg/K	$1.30 + 0.00004T$	$0.82 + 0.00011T$	Same as Int.
Char Emissivity		0.86	0.86	Same as Polymer
Char Abs. Coef.	m <sup>-1</sup>	Same as Int.	8000	Same as Polymer
Reac. 14.10 Pre-Exp. Factor	s <sup>-1</sup>	1	$1.50 \times 10^{36}$	$2.69 \times 10^{42}$
Reac. 14.10 Act. Energy	kJ/kmol	0	$3.80 \times 10^5$	$3.82 \times 10^5$
Reac. 14.10 Heat of Reac.	kJ/kg	1	30	192
Reac. 14.10 Residue Frac.		1	1	1
Reac. 14.11 Pre-Exp. Factor	s <sup>-1</sup>	$7.66 \times 10^{27}$	$1.60 \times 10^{15}$	$3.84 \times 10^{14}$
Reac. 14.11 Act. Energy	kJ/kmol	$4.65 \times 10^5$	$2.35 \times 10^5$	$2.00 \times 10^5$
Reac. 14.11 Heat of Reac.	kJ/kg	-80	220	1192
Reac. 14.11 Residue Frac.		0.65	0.18	0.4
Reac. 14.12 Pre-Exp. Factor	s <sup>-1</sup>	$6.50 \times 10^2$	$3.53 \times 10^4$	$4.76 \times 10^{44}$
Reac. 14.12 Act. Energy	kJ/kmol	$0.88 \times 10^5$	$0.96 \times 10^5$	$5.90 \times 10^5$
Reac. 14.12 Heat of Reac.	kJ/kg	-5	250	1352
Reac. 14.12 Residue Frac.		0.77	0.72	0.018
Gas Heat of Combustion	kJ/kg	18050	15950	14350

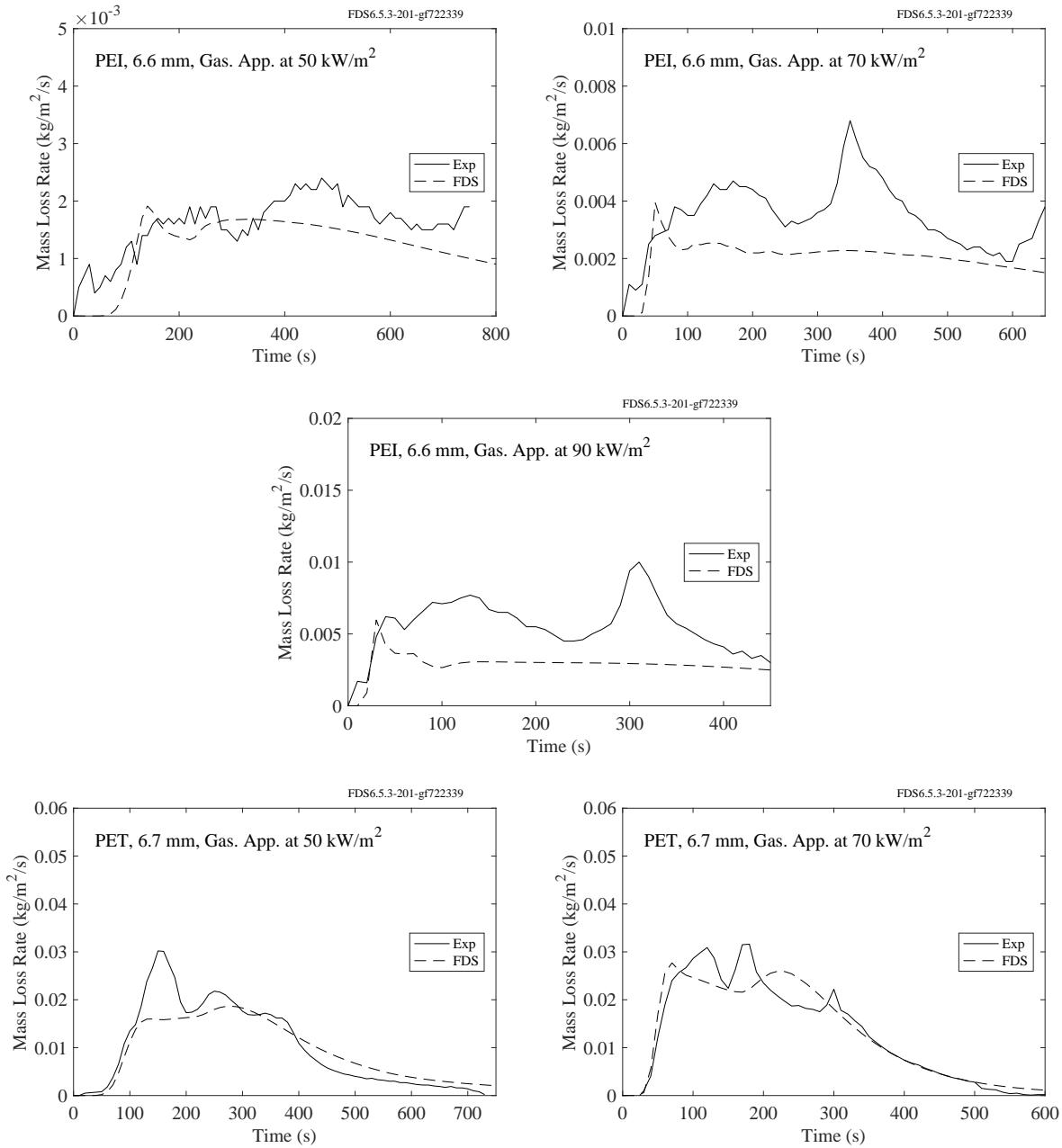


Figure 14.11: Comparison of predicted and measured mass loss rates for PEI and PET.

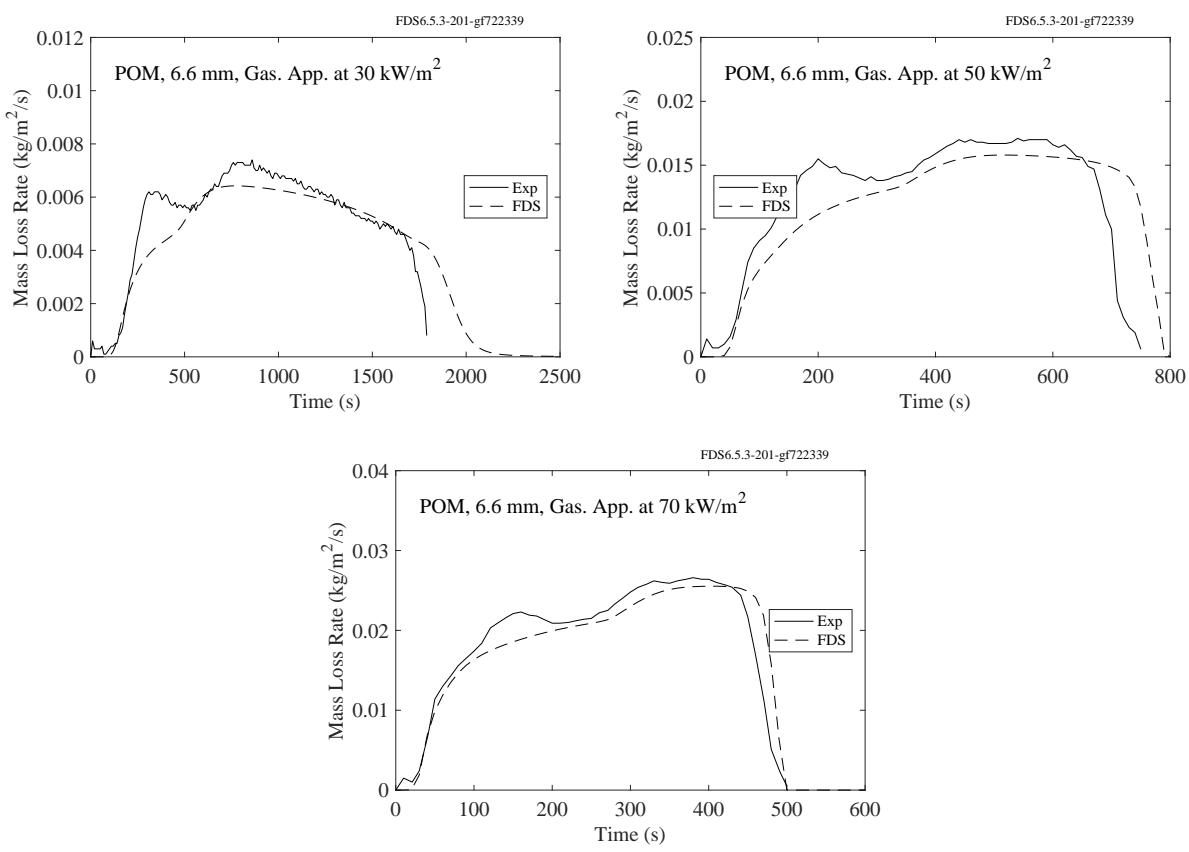


Figure 14.12: Comparison of predicted and measured mass loss rates for POM.

## 14.3 Corrugated Cardboard

Table 14.11 lists the measured properties of a double-wall corrugated cardboard with the conventional U.S. designation 69-23B-69-23C-69. Corrugated cardboard is characterized by alternating layers of homogeneous, planar liner boards and corrugated sections made up of periodic flutes. The numbers in the specification indicate the areal density in lb/(1000 ft<sup>2</sup>) and the letters indicate the flute designation (B indicates a range of 45 to 52 flutes per foot and C indicates a range of 39 to 43 flutes per foot). It is assumed that each layer consists of the same lingo-cellulosic, charring material with the density defined as the mass of the solid material divided by the volume of the layer. This representation requires slightly different definitions for the properties of each unique layer – liner board (LB), C-flute layer (CFL), and B-flute layer (BFL).

The reaction mechanism for the cardboard material includes one reaction to describe the release of residual moisture and three sequential reactions to describe the thermal degradation of the virgin material to a final residual char. Each of the initial solid components (LB, CFL, and BFL) undergoes the same four-step mechanism.



Table 14.11: Properties of corrugated cardboard. Courtesy M. McKinnon, University of Maryland. See Section 14.1.1 for an explanation of terms.

Property	Units	Value	Method	Reference
Moisture Density	kg/m <sup>3</sup>	1000	Direct	[262]
Moisture Conductivity	W/m/K	0.1	Inherited	[262]
Moisture Specific Heat	kJ/kg/K	4.19	Literature	[263]
Moisture Emissivity		0.7	Inherited	[262]
LB Density	kg/m <sup>3</sup>	520	Direct	[262]
LB Conductivity	W/m/K	0.1	Inverse Analysis	[262]
LB Specific Heat	kJ/kg/K	1.8	DSC	[262]
LB Emissivity		0.7	Inverse Analysis	[262]
LB Intermediary Density	kg/m <sup>3</sup>	468	Constant Volume	[262]
LB Intermediary Conductivity	W/m/K	$0.05 + 7.5 \times 10^{-11} \times T^3$	Inverse Analysis	[262]
LB Intermediary Specific Heat	kJ/kg/K	1.55	DSC	[262]
LB Intermediary Emissivity		0.775	Inverse Analysis	[262]
LB Char 1 Density	kg/m <sup>3</sup>	173	Constant Volume	[262]
LB Char 1 Conductivity	W/m/K	$1.5 \times 10^{-10} \times T^3$	Inverse Analysis	[262]
LB Char 1 Specific Heat	kJ/kg/K	1.3	DSC	[262]
LB Char 1 Emissivity		0.85	Literature	[264]
LB Char 2 Density	kg/m <sup>3</sup>	102	Constant Volume	[262]
LB Char 2 Conductivity	W/m/K	$1.5 \times 10^{-10} \times T^3$	Inverse Analysis	[262]
LB Char 2 Specific Heat	kJ/kg/K	1.3	DSC	[262]
LB Char 2 Emissivity		0.85	Literature	[264]
CFL Density	kg/m <sup>3</sup>	49	Constant Volume	[262]
CFL Conductivity	W/m/K	0.1	Inverse Analysis	[262]

Table 14.11: Continued

CFL Specific Heat	kJ/kg/K	1.8	DSC	[262]
CFL Emissivity		0.7	Inverse Analysis	[262]
CFL Intermediary Density	kg/m <sup>3</sup>	44	Constant Volume	[262]
CFL Intermediary Conductivity	W/m/K	$0.05 + 7.5 \times 10^{-10} \times T^3$	Inverse Analysis	[262]
CFL Intermediary Specific Heat	kJ/kg/K	1.55	DSC	[262]
CFL Intermediary Emissivity		0.775	Inverse Analysis	[262]
CFL Char 1 Density	kg/m <sup>3</sup>	16	Constant Volume	[262]
CFL Char 1 Conductivity	W/m/K	$1.5 \times 10^{-9} \times T^3$	Inverse Analysis	[262]
CFL Char 1 Specific Heat	kJ/kg/K	1.3	DSC	[262]
CFL Char 1 Emissivity		0.85	Literature	[264]
CFL Char 2 Density	kg/m <sup>3</sup>	9.4	Constant Volume	[262]
CFL Char 2 Conductivity	W/m/K	$1.5 \times 10^{-9} \times T^3$	Inverse Analysis	[262]
CFL Char 2 Specific Heat	kJ/kg/K	1.3	DSC	[262]
CFL Char 2 Emissivity		0.85	Literature	[264]
BFL Density	kg/m <sup>3</sup>	74	Constant Volume	[262]
BFL Conductivity	W/m/K	0.1	Inverse Analysis	[262]
BFL Specific Heat	kJ/kg/K	1.8	DSC	[262]
BFL Emissivity		0.7	Inverse Analysis	[262]
BFL Intermediary Density	kg/m <sup>3</sup>	67	Constant Volume	[262]
BFL Intermediary Conductivity	W/m/K	$0.05 + 7.5 \times 10^{-10} \times T^3$	Inverse Analysis	[262]
BFL Intermediary Specific Heat	kJ/kg/K	1.55	DSC	[262]
BFL Intermediary Emissivity		0.775	Inverse Analysis	[262]
BFL Char 1 Density	kg/m <sup>3</sup>	25	Constant Volume	[262]
BFL Char 1 Conductivity	W/m/K	$1.5 \times 10^{-9} \times T^3$	Inverse Analysis	[262]
BFL Char 1 Specific Heat	kJ/kg/K	1.3	DSC	[262]
BFL Char 1 Emissivity		0.85	Literature	[264]
BFL Char 2 Density	kg/m <sup>3</sup>	15	Constant Volume	[262]
BFL Char 2 Conductivity	W/m/K	$1.5 \times 10^{-9} \times T^3$	Inverse Analysis	[262]
BFL Char 2 Specific Heat	kJ/kg/K	1.3	DSC	[262]
BFL Char 2 Emissivity		0.85	Literature	[264]
Reaction 1 Pre-Exp. Factor	s <sup>-1</sup>	6.14	TGA	[262]
Reaction 1 Activation Energy	kJ/mol	23500	TGA	[262]
Reaction 1 Heat of Reaction	kJ/kg	2445	Literature	[263]
Reaction 1 Char Yield		0	TGA	[262]
Reaction 2 Pre-Exp. Factor	s <sup>-1</sup>	$7.95 \times 10^9$	TGA	[262]
Reaction 2 Activation Energy	kJ/mol	$1.30 \times 10^5$	TGA	[262]
Reaction 2 Char Yield		0.9	TGA	[262]
Reaction 2 Heat of Reaction	kJ/kg	0	DSC	[262]
Fuel Gas 2 Heat of Combustion	kJ/kg	18500	MCC	[262]
Reaction 3 Pre-Exp. Factor	s <sup>-1</sup>	$2 \times 10^{11}$	TGA	[262]
Reaction 3 Activation Energy	kJ/mol	$1.60 \times 10^5$	TGA	[262]
Reaction 3 Char Yield		0.37	TGA	[262]
Reaction 3 Heat of Reaction	kJ/kg	126	DSC	[262]
Fuel Gas 3 Heat of Combustion	kJ/kg	13600	MCC	[262]

Table 14.11: Continued

Reaction 4 Pre-Exp. Factor	$s^{-1}$	0.0261	TGA	[262]
Reaction 4 Activation Energy	kJ/mol	17000	TGA	[262]
Reaction 4 Char Yield		0.59	TGA	[262]
Reaction 4 Heat of Reaction	kJ/kg	0	DSC	[262]
Fuel Gas 4 Heat of Combustion	kJ/kg	14000	MCC	[262]

Table 14.12 lists the composition and thickness of each of the layers. The sample is insulated with 28 mm of Kaowool PM board, manufactured by ThermalCeramics ([www.thermalceramics.com](http://www.thermalceramics.com)). The gasification

Table 14.12: Cardboard composition and dimensions.

Layer	Composition	Thickness (mm)
1	Liner Board	0.64
2	C Flute Layer	3.2
3	Liner Board	0.64
4	B Flute Layer	2.1
5	Liner Board	0.64
6	Kaowool	28

experiments were conducted in a modified cone calorimeter referred to as the controlled atmosphere pyrolysis apparatus (CAPA) [265], in which the sample is surrounded by nitrogen to prevent ignition. Measured and predicted mass loss rates at imposed heat fluxes of  $20 \text{ kW/m}^2$ ,  $40 \text{ kW/m}^2$ , and  $60 \text{ kW/m}^2$  are shown in Fig. 14.13.

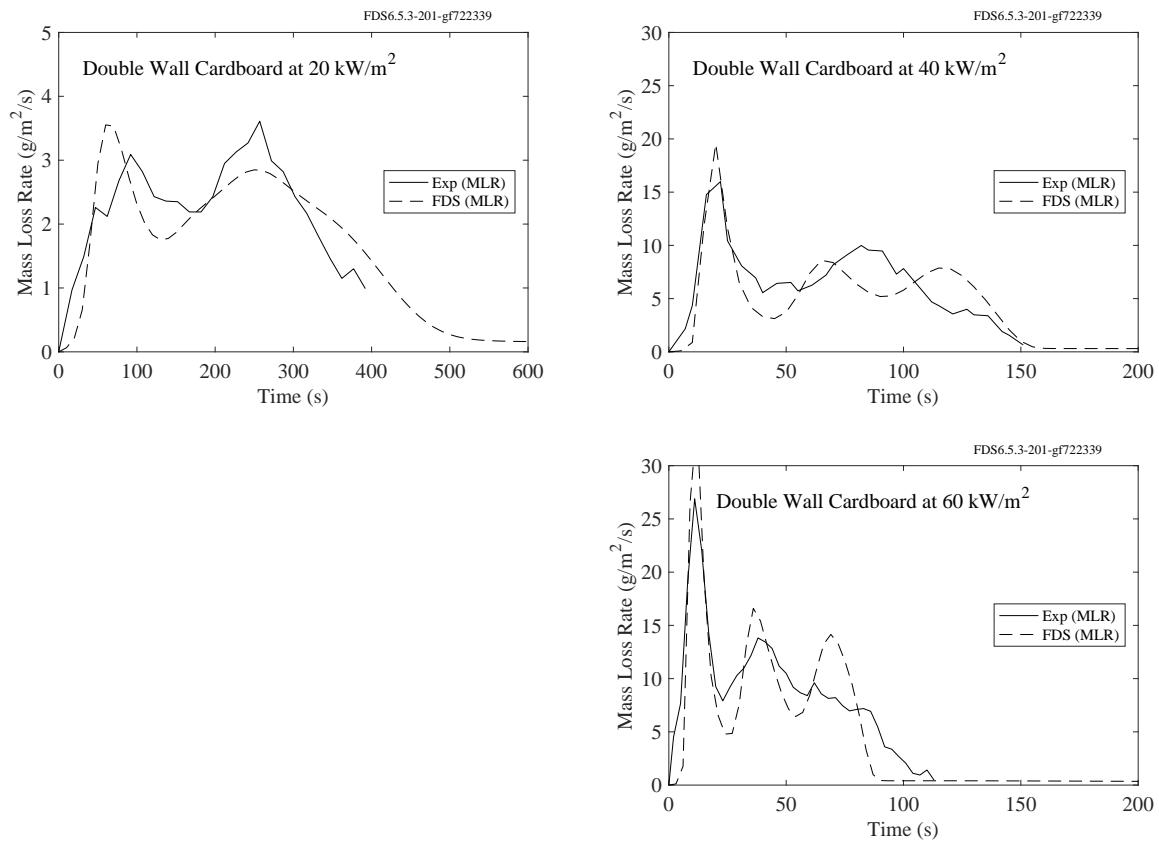


Figure 14.13: Mass loss rate of corrugated cardboard.

## 14.4 Electrical Cables (CHRISTIFIRE)

The U.S. Nuclear Regulatory Commission has sponsored a study of the burning behavior of electrical cables typically found in nuclear power plants [266]. The project has been given the acronym CHRISTIFIRE (Cable Heat Release, Ignition, and Spread in Tray Installations). In this section, the modeling of a particular type of cable is presented. The sample cable (referred to as 701 in the report) has seven conductors and is 14 mm in diameter. The jacket material is polyvinyl chloride (PVC) and the insulation is polyethylene (PE). The mass fractions are 0.24 and 0.18, respectively, and the remaining mass is copper.

Thermo-gravimetric analysis (TGA) with a heating rate of 10 K/min and micro-combustion calorimetry (MCC) with a heating rate of 60 K/min were performed for the jacket and insulation materials separately. Cone calorimeter experiments were performed for sample of seven 10 cm cable segments at exposing heat fluxes of 25 kW/m<sup>2</sup>, 50 kW/m<sup>2</sup>, and 75 kW/m<sup>2</sup>. The experimental methods are explained in Section 14.1.

### 14.4.1 Estimation of Pyrolysis Kinetics

The pyrolysis kinetics were estimated from the TGA results. The kinetic parameters depend on the choice of the reaction path, and for this example two different reaction paths are used. The first one (v1) consists of several parallel, independent reactions that each yield both fuel (combustible) and inert (incombustible) gas. The last reaction also yields residue. The second reaction path (v2) is more complex. For the PVC jacket, the model consists of three components: pure PVC, plasticizer and CaCO<sub>3</sub>. Pure PVC degrades in two steps, first yielding inert gas and small amounts of fuel gas and residue, and second yielding larger amounts of fuel gas and residue. In air, the residual char is also oxidized, which contributes to the greater mass loss and release of fuel at high temperatures. The plasticizer degrades simultaneously with the first reaction of PVC yielding fuel gas. CaCO<sub>3</sub> degrades at high temperatures yielding only inert gas and residue. The initial mass fraction of these three components, the reaction yields and the heats of combustion are determined by comparing the mass loss results of the TGA analysis to the heat release results of the MCC.

The estimated reaction parameters are listed in Tables 14.13 and 14.14. The experimental and FDS results are shown in Fig. 14.14.

Table 14.13: Reaction path, kinetic parameters and heat of combustion for sheath and insulation material of cable 701 v1. The values are provided in the same units as in FDS input file.

	Sheath				Insulation		
	Comp 1	Comp 2	Comp 3	Comp 4	Comp 1	Comp 2	Comp 3
MATL_MASS_FRACTION	0.6	0.13	0.034	0.229	0.57	0.12	0.31
A	$3.6 \cdot 10^{21}$	$1.2 \cdot 10^{29}$	$5.1 \cdot 10^{15}$	$6.0 \cdot 10^{12}$	$1.3 \cdot 10^{25}$	$1.9 \cdot 10^{27}$	$1.6 \cdot 10^{12}$
E	$2.4 \cdot 10^5$	$3.8 \cdot 10^5$	$3.0 \cdot 10^5$	$2.5 \cdot 10^5$	$2.7 \cdot 10^5$	$3.6 \cdot 10^5$	$2.1 \cdot 10^5$
N_S	2.9	4.1	2.7	1.4	3.2	3.7	4.4
N_O2	-	-	-	1.5	-	-	-
NU_SPEC (propane)	0.33	0.77	0.0	0.34	0.31	0.86	0.0
NU_SPEC (water vapor)	0.67	0.23	1.0	0.0	0.69	0.14	0.17
NU_MATL	0.0	0.0	0.0	0.66	0.0	0.0	0.83
MATL_ID	-	-	-	ASH	-	-	CHAR-I
HEAT_OF_COMBUSTION	46450	46450	0	45000	46450	46450	0

Table 14.14: Reaction path, kinetic parameters and heat of combustion for sheath and insulation material of cable 701 v2. The values are provided in the same units as in FDS input file.

	Sheath					Insulation		
	Comp 1 'PVC 1'	Comp 2 'PVC 2'	Comp 3 'Plast.'	Comp 4 'CaCO <sub>3</sub> '	Comp 5 'Char'	Comp 1 'Plast.'	Comp 2 'PE'	Comp 3 CaCO <sub>3</sub>
MATL_MASS_FRACTION	0.514	0.0	0.268	0.218	0.0	0.57	0.12	0.31
A	$2.1 \cdot 10^{26}$	$2.0 \cdot 10^{25}$	$2.1 \cdot 10^{26}$	$9.8 \cdot 10^{24}$	$2.3 \cdot 10^{10}$	$1.3 \cdot 10^{25}$	$1.9 \cdot 10^{27}$	$1.6 \cdot 10^{12}$
E	$2.8 \cdot 10^5$	$3.2 \cdot 10^5$	$2.8 \cdot 10^5$	$2.9 \cdot 10^5$	$2.3 \cdot 10^5$	$2.7 \cdot 10^5$	$3.6 \cdot 10^5$	$2.1 \cdot 10^5$
N_S	3.7	4.9	3.7	0.96	1.2	3.2	3.7	4.4
N_O2	-	-	-	-	1.5	-	-	-
NU_SPEC (propane)	0.043	0.751	1.0	0.0	0.34	1.0	1.0	0.0
NU_SPEC (water vapor)	0.602	0.0	0.0	0.34	0.0	0.0	0.0	0.17
NU_MATL	0.355	0.249	0.0	0.816	0.66	0.0	0.0	0.83
MATL_ID	COMP 2	CHAR-S	-	CHAR-S	ASH	-	-	CHAR-I
HEAT_OF_COMBUSTION	49100	35800	30200	0.0	37000	14445	39734	0.0

#### 14.4.2 Estimation of Thermal Parameters and Validation

The remaining pyrolysis model parameters were estimated by fitting the calculated cone calorimeter results to the experimental ones at 50 kW/m<sup>2</sup> heat flux. The cone calorimeter sample consisting of seven cables is modeled as a rectangular solid. The layer structure of the cable sample is assumed to be symmetrical:

1. sheath (2.1 mm)
2. insulation (2.1 mm)
3. conductor (2.5 mm)
4. insulation (2.1 mm)
5. sheath (2.1 mm)
6. insulating calcium silicate backing board (20 mm)

The layer thicknesses are calculated using the component mass fractions and densities. For fitting the thermal parameters, the experimental heat release rate and mass loss rate curves were used. The results of the fitted models are shown in Fig. 14.15. The remaining parameters for v1 and v2 are listed in the following tables.

Next, the model parameters were fixed and the model is validated by comparing the FDS and experimental results at 25 kW/m<sup>2</sup> and 75 kW/m<sup>2</sup> heat fluxes. The results are shown in Fig. 14.16.

Table 14.15: Thermal parameters for CHRISTIFIRE cable 701 v1.

	DENSITY	CONDUCTIVITY	SPECIFIC_HEAT	HEAT_OFREACTION	EMISSIVITY
Sheath					
Comp 1	1542	0.15	3.22	1607	0.7
Comp 2	1542	0.18	3.45	1425	1.0
Comp 3	1542	0.10	3.50	43	1.0
Comp 4	1542	0.1	3.5	40	1.0
Ash	344	0.12	3.5	-	0.85
Insulation					
Comp 1	1153	0.78	3.36	1408	1.0
Comp 2	1153	1.0	3.40	1516	1.0
Comp 3	1153	0.09	2.74	445	1.0
CHAR-I	297	0.01	1.29	-	1.0

Table 14.16: Thermal parameters for CHRISTIFIRE cable 701 v2.

	DENSITY	CONDUCTIVITY	SPECIFIC_HEAT	HEAT_OFREACTION	EMISSIVITY
Sheath					
Comp 1	1542	0.15	3.4	206	1.0
Comp 2	281	0.20	2.3	1783	1.0
Comp 3	1542	0.19	2.8	1112	1.0
Comp 4	1542	0.48	3.5	1669	1.0
Comp 5	344	0.2	2.5	1500	1.0
Ash	235	0.6	3.0	-	1.0
Insulation					
Comp 1	1153	0.59	3.0	691	1.0
Comp 2	1153	0.25	1.94	1760	1.0
Comp 3	1153	0.28	2.9	353	1.0
CHAR-I	297	0.34	1.3	-	1.0

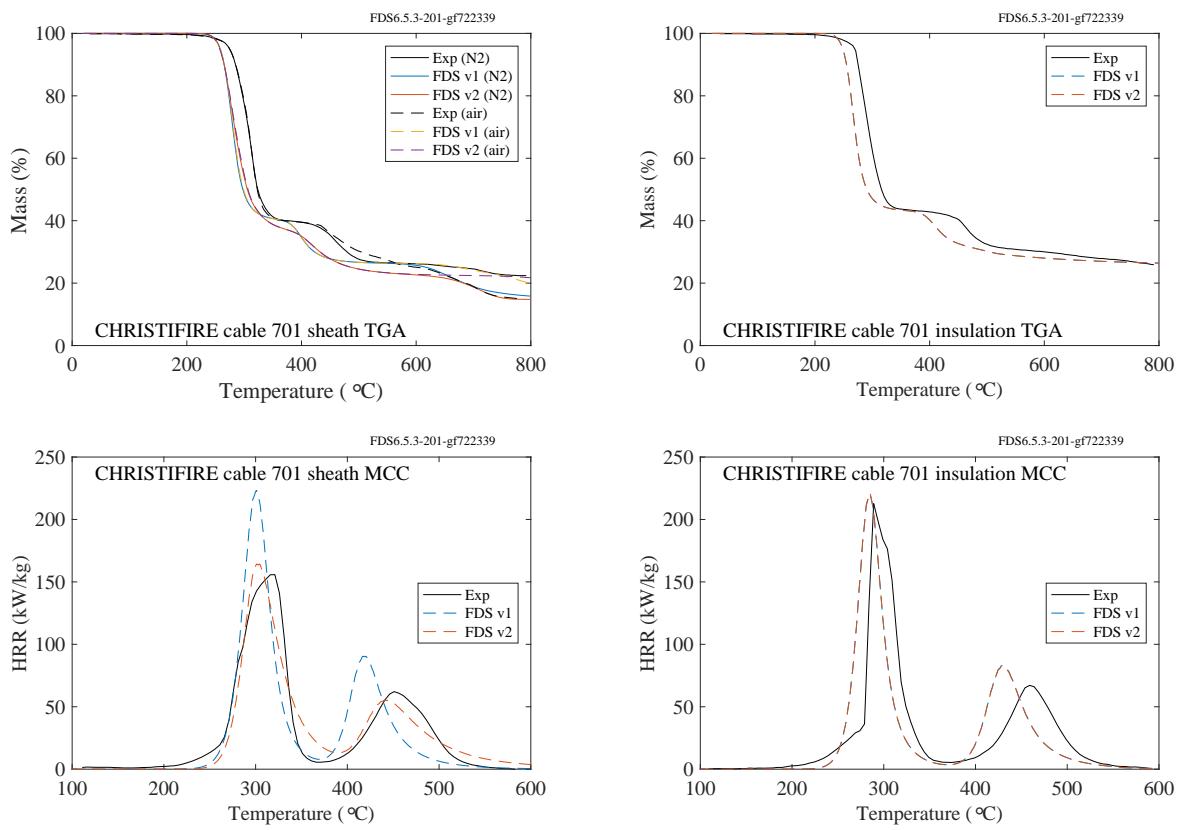


Figure 14.14: Small scale results of the CHRISTIFIRE cable 701 sheath and insulation.

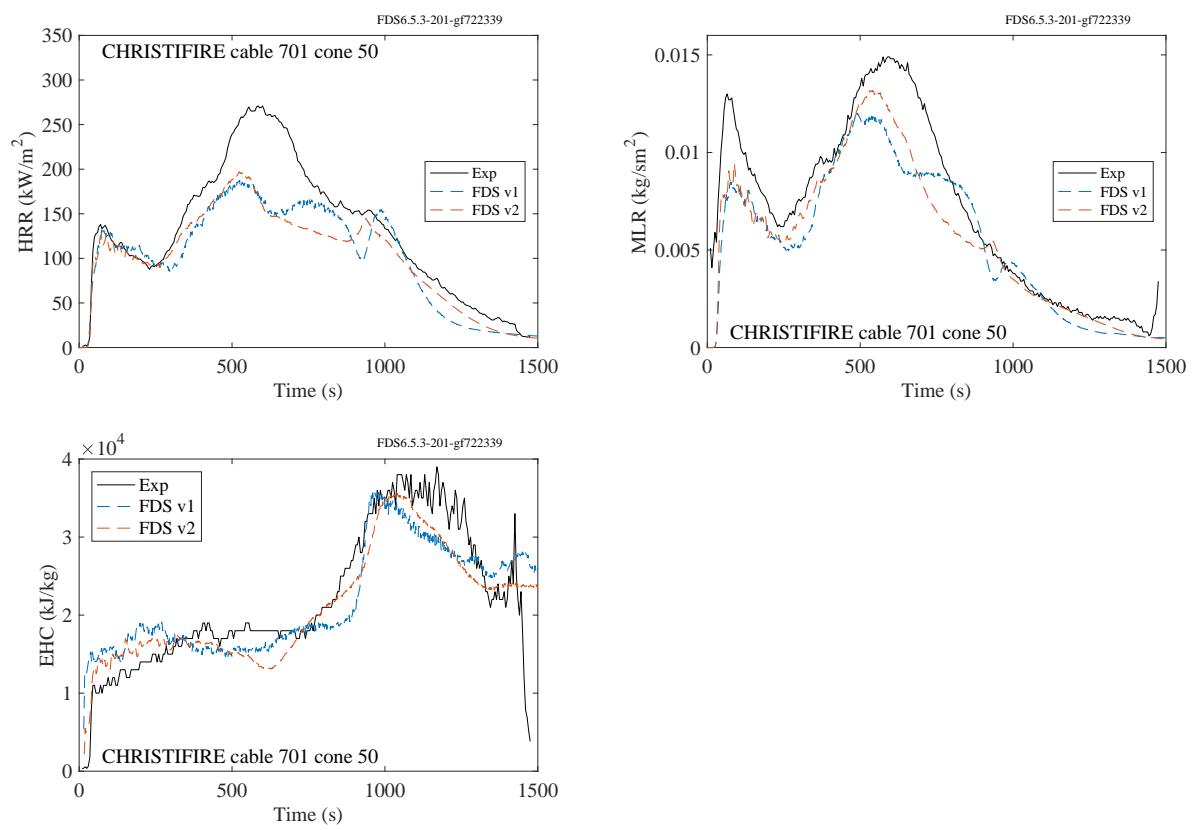


Figure 14.15: Cone calorimeter fitting of CHRISTIFIRE cable 701 at  $50 \text{ kW/m}^2$  heat flux.

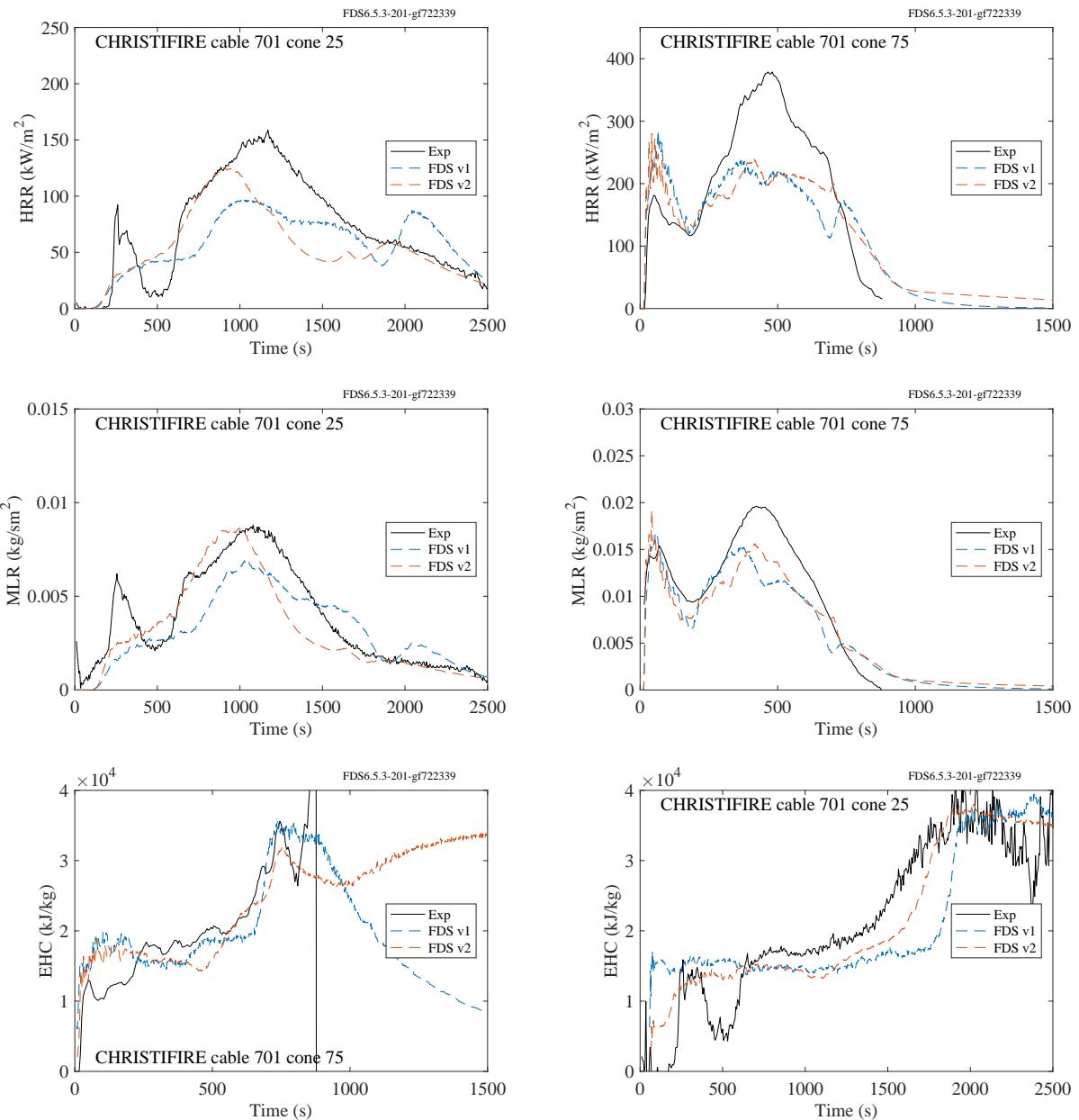


Figure 14.16: Cone calorimeter validation of CHRISTIFIRE cable 701 at 25 and 75  $\text{kW/m}^2$  heat fluxes.

## 14.5 Liquid Pool Fires

In this section, the predicted burning rates of a variety of liquid fuels confined within a 10 cm deep, 1 m square tray are compared with an empirical correlation. The burning rate of liquid hydrocarbon fuels has been found to correlate well [267] with the ratio of the heat of combustion,  $\Delta h_c$ , and the heat of gasification,  $\Delta h_g$ :

$$\dot{m}'' = 0.001 \frac{\Delta h_c}{\Delta h_g} ; \quad \Delta h_g = \Delta h_v + \int_{T_0}^{T_b} c_p dT \quad (14.17)$$

where  $\Delta h_v$  is the latent heat of vaporization,  $T_0$  is the initial temperature,  $T_b$  is the boiling temperature, and  $c_p$  is the specific heat of the liquid fuel. The heat of gasification is the amount of energy required to raise the fuel from its initial temperature to its boiling temperature and evaporate it. Figure 14.17 shows a comparison of predicted burning rates with experimental values listed in Ref. [267] or the correlation, Eq. (14.17).

Table 14.17 lists the liquid fuel properties used in the simulations. Note that the heats of vaporization are evaluated at the liquid boiling points. The thermal conductivities,  $k$ , are found in Ref. [268], except for butane, which is found in Ref. [269]. The heats of combustion,  $\Delta h_c$ , are computed in FDS based on the heats of formation of the reactants and products listed in Ref. [270]. The heats of combustion account for the presence of products of incomplete combustion, like CO and soot.

The effective absorption coefficients,  $\kappa$ , for benzene and ethanol are based on curve fits to experimental data as explained in Appendix K of the FDS Technical Reference Guide. The absorption coefficient for methanol presented in Appendix K is calculated with the assumption that the incoming radiation is approximately blackbody radiation. The absorption coefficient for ethanol is calculated based on experimentally determined spectrum of an ethanol flame. Since both methanol and ethanol flames are low sooting, the blackbody radiation assumption is not correct. Instead it is assumed that the absorption coefficient for methanol should be of similar magnitude as that for ethanol. For heptane, butane and acetone the absorption coefficients are simple order of magnitude estimates.

Table 14.17: Liquid fuel properties.

Fuel	$\rho$ kg/m <sup>3</sup> [271]	$c_p$ kJ/(kg · K) [272]	$k$ W/(m · K) [268]	$\Delta h_v$ kJ/kg [269]	$\Delta h_c$ kJ/kg See text	$\chi_r$ [214]	$y_{CO}$ g/g [214]	$y_s$ g/g [214]	$T_b$ °C [273]	$\kappa$ m <sup>-1</sup> See text
Acetone	791	2.13	0.20	501	28555	0.27	0.003	0.014	56.3	100
Benzene	874	1.74	0.14	393	33823	0.60	0.067	0.181	80.3	123
Butane	573	2.28	0.12	385	44680	0.31	0.007	0.029	0	100
Ethanol	794	2.44	0.17	837	27474	0.25	0.001	0.008	78.5	1534.3
Heptane	675	2.24	0.14	317	43580	0.33	0.010	0.037	98.5	187.5
Methanol	796	2.48	0.20	1099	20934	0.16	0.001	0.001	64.8	1500

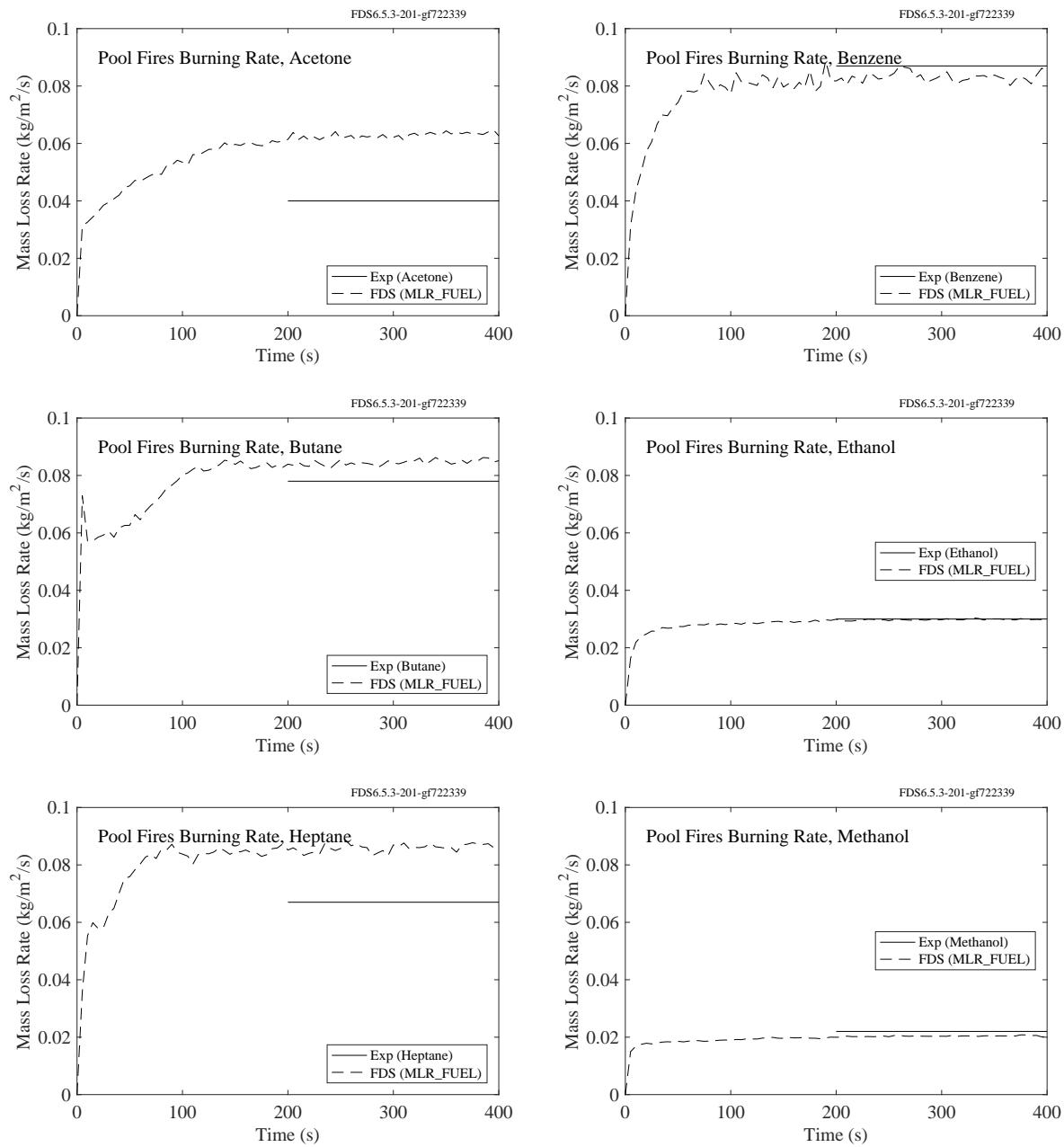


Figure 14.17: Comparison of burning rates for various liquid pool fires.

## 14.6 Wildland Fire Spread (CSIRO Grassland Fires)

This section contains a description and results for simulations of two of the CSIRO Grassland Fire experiments. The first experiment, C064, was conducted on a 100 m by 100 m plot; the second, F19, was conducted on a 200 m by 200 m plot. Measured properties for the specific types of grasses burned in the two experiments are listed in Table 14.18. Properties that were not measured are listed in Table 14.19. These assumed properties are typically for wood or cellulosic fuels. The moisture is modeled as water. The grass is assumed to be composed primarily of cellulose.

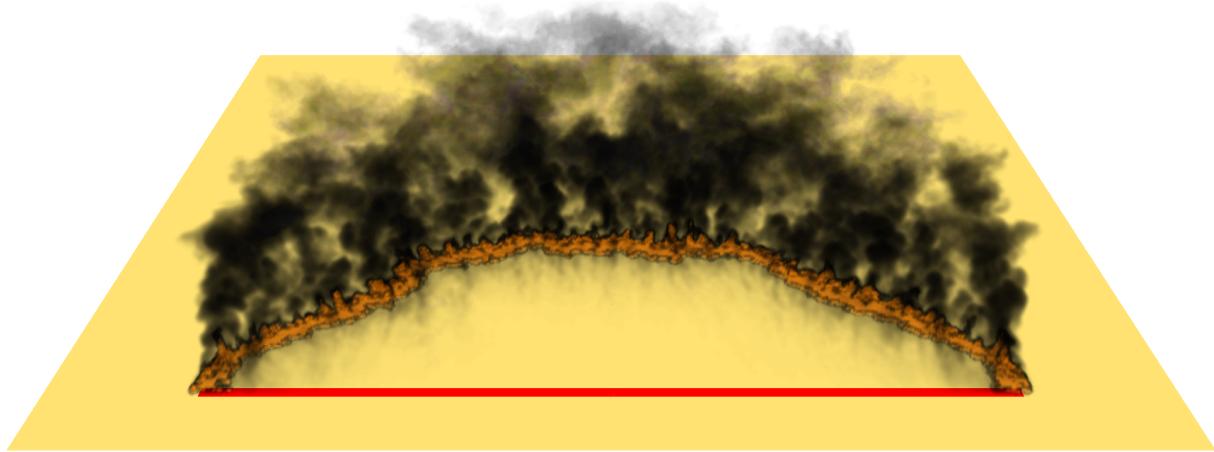


Figure 14.18: Snapshot of the simulation of CSIRO Grassland Fire F19.

A snapshot of the simulation of Experiment F19 is shown in Fig. 14.18. The computational domain in this case is 240 m by 240 m by 20 m. The grid cells are 0.5 m cubes. The domain is subdivided into 36 individual meshes and run in parallel. The grass is represented by 800,000 Lagrangian particles with a cylindrical geometry, or about 5 simulated blades per grid cell. The radius of the cylinder is derived from the measured surface area to volume ratio. Each simulated blade of grass represents many more actual blades of grass. The weighting factor is determined from the measured bulk mass per unit area. The fires in the experiments were ignited by two men carrying drip torches walking in opposite directions along the upwind boundary of the plot (the red strip in Fig. 14.18). In FDS, this action was modeled using a specified spread rate along the strip.

The results of the simulations are shown in Fig. 14.19. The fire front in the FDS simulations is defined as the location of the maximum gas temperature in a 1 m wide, 1 m tall strip along the centerline of the grass field. The experimental points were determined from aerial photography.

Table 14.18: Measured properties for the CSIRO Grassland Fire cases [141].

Property	Units	Case F19	Case C064
Wind Speed	m/s	4.8	4.6
Ambient Temperature	°C	34	32
Surface Area to Volume Ratio	$\text{m}^{-1}$	12240	9770
Grass Height	m	0.51	0.21
Bulk Mass per Unit Area	$\text{kg}/\text{m}^2$	0.313	0.283
Moisture Fraction	%	5.8	6.3

Table 14.19: Assumed properties for various types of dried grass and soil. Note that the Pyrolysis Temperature is taken to be the temperature at which the mass loss rate peaks in the TGA experiments of Morvan and Dupuy [274].

Property	Units	Value	Reference
Chemical Composition	–	$\text{C}_6\text{H}_{10}\text{O}_5$	Assumption
Heat of Combustion	kJ/kg	15600	[275]
Soot Yield	kg/kg	0.015	[214]
Char Yield	kg/kg	0.2	[275]
Specific Heat	kJ/(kg·K)	1.5	Various sources
Conductivity	W/(m·K)	0.1	Assumption
Density	$\text{kg}/\text{m}^3$	512	[276]
Heat of Pyrolysis	kJ/kg	418	[274]
Pyrolysis Temperature	°C	200	[274]
Soil Specific Heat	kJ/(kg·K)	2.0	[277]
Soil Conductivity	W/(m·K)	0.25	[277]
Soil Density	$\text{kg}/\text{m}^3$	1300	[277]

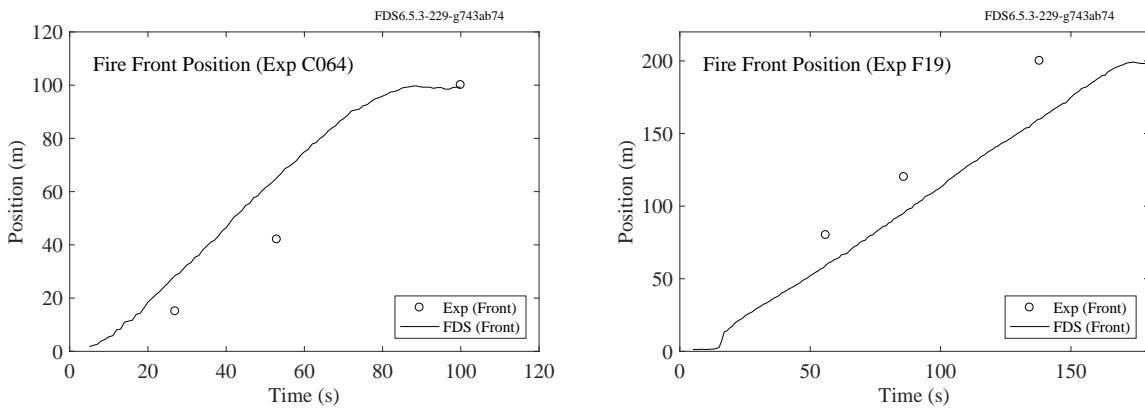


Figure 14.19: Comparison measured and predicted fire front position for the CSIRO Grassland Fires.

## 14.7 Burning Trees (NIST Douglas Firs)

This section contains a description and results of three Douglas fir tree fire simulations. Measured properties of the trees are listed in Table 14.20. Generic vegetation properties are listed in Table 14.21. These assumed properties are typically for wood or cellulosic fuels. The moisture is modeled as water. The vegetation is assumed to be composed primarily of cellulose. Reference [168] provides an estimate of the distribution of mass for the foliage, roundwood less than 3 mm in diameter, roundwood 3 mm to 6 mm, and roundwood 6 mm to 10 mm. For the 2 m trees, the distribution is approximately 64 %, 11 %, 10 %, and 15 %, respectively. For the 5 m trees, it is 60 %, 17 %, 12 %, and 11 %, respectively.

Snapshots of the simulation of the 2 m tall, 14 % moisture tree are shown in Fig. 14.20. The computational domain in this case is 2 m by 2 m by 4 m. The grid cells are 5 cm cubes. The pine needles are represented by 130,000 Lagrangian particles with a cylindrical geometry, or about 25 simulated needles per grid cell. The radius of the cylinder is derived from the measured surface area to volume ratio. Each simulated pine needle or segment of roundwood represents many more actual needles or segments. The weighting factor is determined from the estimated bulk mass per unit volume. The results of the simulations are shown in Fig. 14.21.

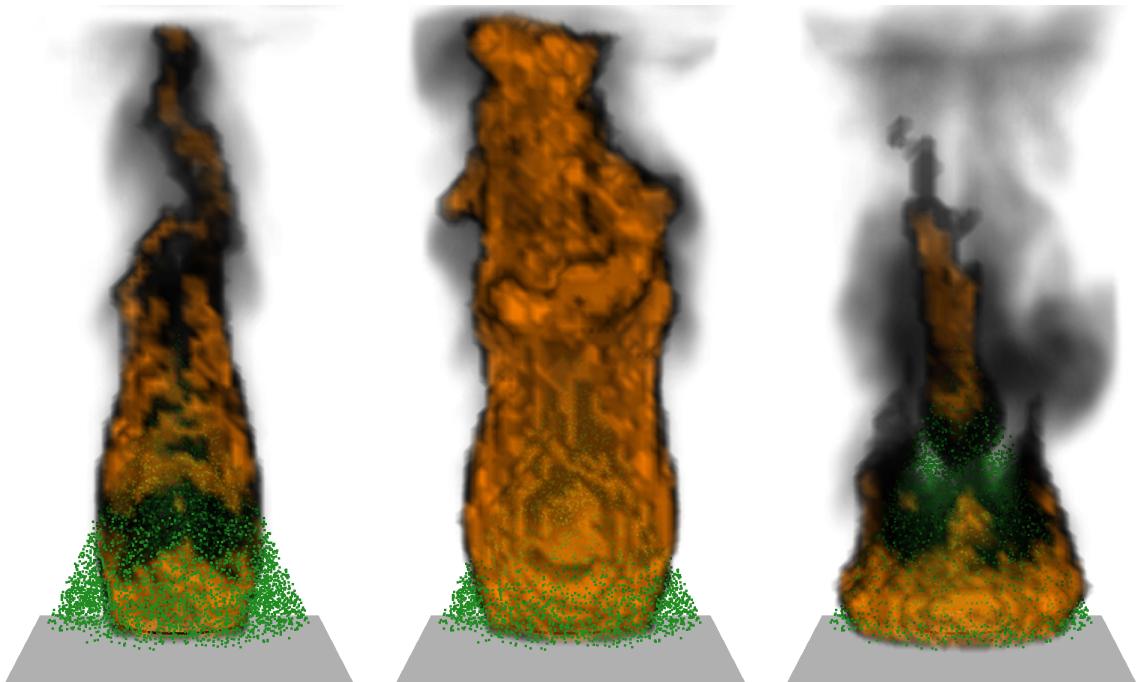


Figure 14.20: Snapshots of the simulation of the 2 m tall Douglas fir tree, 14 % moisture.

Table 14.20: Measured properties for the NIST Douglas fir trees [168].

Property	Units	Case 1	Case 2	Case 3
Replicate Experiments	–	6	3	3
Avg. Crown Height	m	1.9	1.9	4.2
Avg. Base Height	m	0.15	0.15	0.3
Avg. Base Width	m	1.7	1.7	2.9
Foliage Surface Area to Volume Ratio	$\text{m}^{-1}$	3940	3940	3940
Avg. Initial Mass	kg	9.7	13.5	57.9
Avg. Moisture Fraction	%	14	49	26
Assumed Bulk Mass per Unit Volume	$\text{kg}/\text{m}^3$	3.2	4.6	2.7

Table 14.21: Assumed properties for the vegetation. Note that the Pyrolysis Temperature is taken to be the temperature at which the mass loss rate peaks in the TGA experiments of Morvan and Dupuy [274].

Property	Units	Value	Reference
Chemical Composition	–	$\text{C}_6\text{H}_{10}\text{O}_5$	Assumption, Cellulose
Heat of Combustion	kJ/kg	17700	[275]
Soot Yield	kg/kg	0.015	[214]
Char Yield	kg/kg	0.26	[275]
Specific Heat	$\text{kJ}/(\text{kg}\cdot\text{K})$	1.2	Various sources
Conductivity	$\text{W}/(\text{m}\cdot\text{K})$	2	Assumption
Density	$\text{kg}/\text{m}^3$	514	[276]
Heat of Pyrolysis	kJ/kg	418	[274]
Pyrolysis Temperature	°C	200	[274]

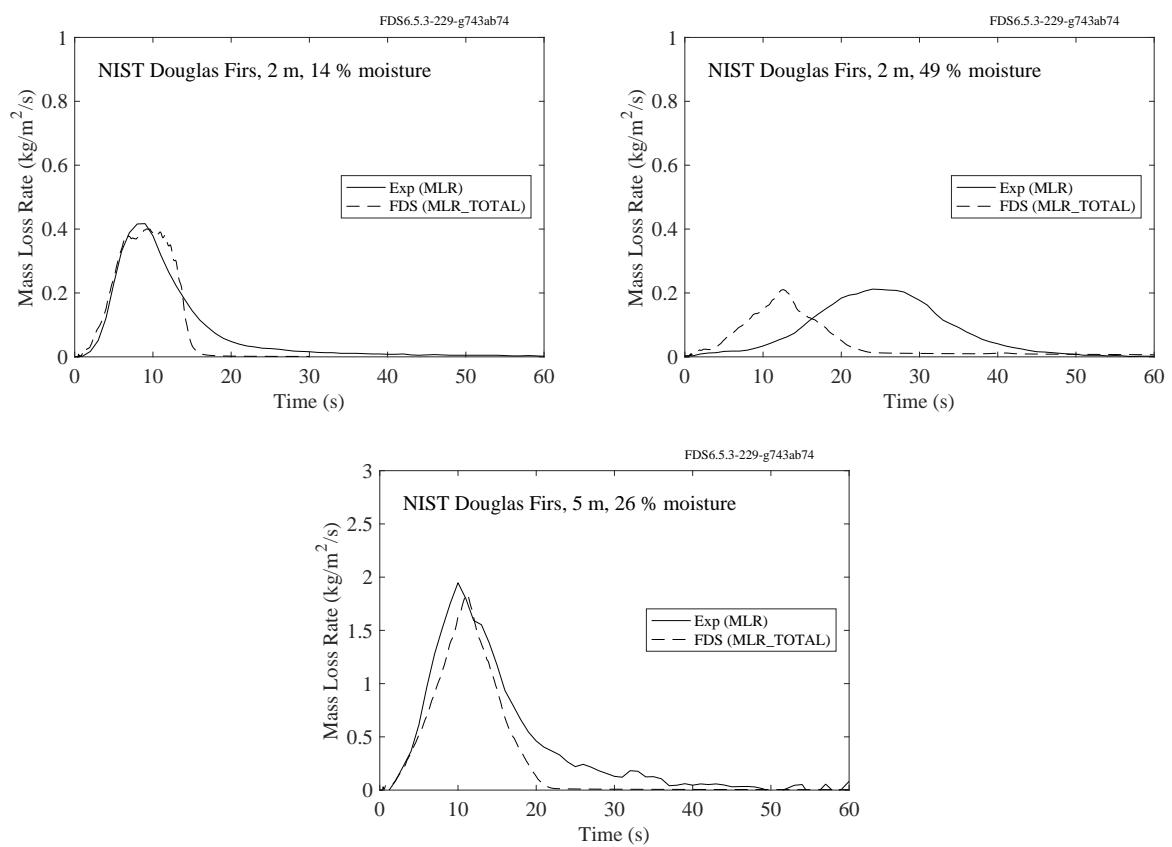


Figure 14.21: Comparison measured and predicted mass loss rate for the Douglas fir tree experiments.

## 14.8 Summary of Burning Rates

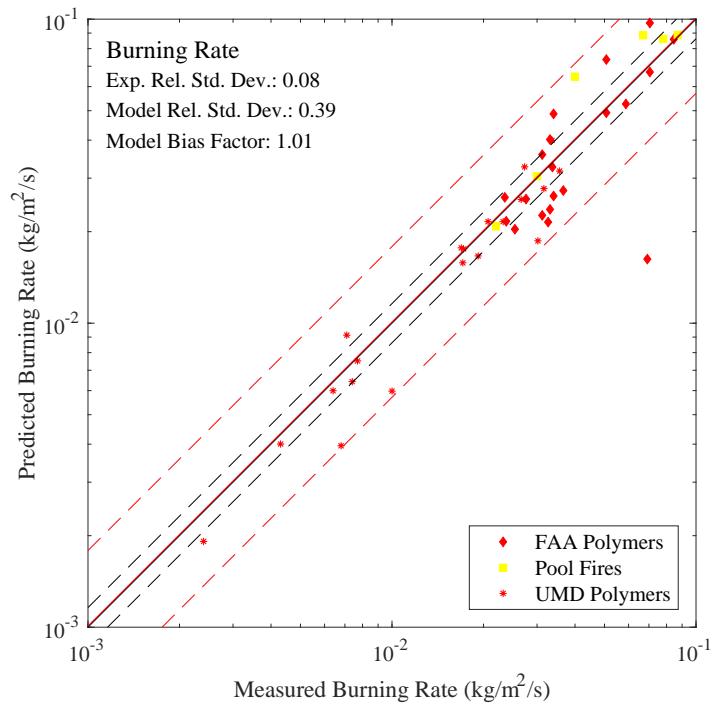


Figure 14.22: Summary of burning rate predictions.



# Chapter 15

# Wind Engineering and Atmospheric Dispersion

This chapter presents results of simulations of wind over structures and atmospheric dispersion, all involving a simplified atmospheric boundary layer model in FDS.

## 15.1 LNG Dispersion Experiments

The simulations of liquified natural gas (LNG) dispersion experiments that are described in this section were originally designed by Jeffrey Engerer and Anay Luketa of Sandia National Laboratories on behalf of the Pipeline and Hazardous Materials Safety Administration of the U.S. Department of Transportation.

### Atmospheric Boundary Layer

The input parameters to FDS allow one to specify an initial velocity and temperature profile for the atmospheric boundary layer. Periodic boundaries at the four sides of the computational domain then allow the flow field to develop naturally. The initial velocity and temperature profiles are modeled using Monin-Obukhov similarity theory. The wind speed,  $u$ , and potential temperature<sup>1</sup>,  $\theta$ , vary with height,  $z$ , according to:

$$u(z) = \frac{u_*}{\kappa} \left[ \ln \left( \frac{z}{z_0} \right) - \psi_m \left( \frac{z}{L} \right) \right] \quad (15.1)$$

$$\theta(z) = \theta_0 + \frac{\theta_*}{\kappa} \left[ \ln \left( \frac{z}{z_0} \right) - \psi_h \left( \frac{z}{L} \right) \right] \quad (15.2)$$

where  $u_*$  is the friction velocity,  $\kappa = 0.41$  is the Von Kármán constant,  $z_0$  is the *aerodynamic* roughness length,  $\theta_*$  is the scaling potential temperature,  $\theta_0$  is the ground level potential temperature,  $L$  is the Monin-Obukhov length, and the similarity functions are those proposed by Dyer [278] and discussed in the report

---

<sup>1</sup>The potential temperature is given by

$$\theta = T \left( \frac{p_0}{p} \right)^{R/(W_{\text{air}} c_p)}$$

where  $p_0$  is typically 1000 mbar and  $R/(W_{\text{air}} c_p) \approx 0.286$ .

of the Falcon field experiments [279]:

$$\psi_m\left(\frac{z}{L}\right) = \begin{cases} -5\frac{z}{L} & : L \geq 0 \\ 2\ln\left[\frac{1+\zeta}{2}\right] + \ln\left[\frac{1+\zeta^2}{2}\right] - 2\tan^{-1}(\zeta) + \frac{\pi}{2} & : L < 0 \end{cases} \quad (15.3)$$

$$\psi_h\left(\frac{z}{L}\right) = \begin{cases} -5\frac{z}{L} & : L \geq 0 \\ 2\ln\left[\frac{1+\zeta^2}{2}\right] & : L < 0 \quad \zeta = \left(1 - \frac{16z}{L}\right)^{1/4} \end{cases} \quad (15.4)$$

The Monin-Obukhov length indicates the thermal stratification of the atmosphere. When the Monin-Obukhov length is negative, the atmosphere is unstably stratified; when positive, the atmosphere is stably stratified. The stabilizing or destabilizing effects of stratification are strongest as the Monin-Obukhov length nears zero. Accordingly, a neutrally stratified atmosphere would have an infinite Monin-Obukhov length. Generally, low stability corresponds to decreasing temperature with height and relatively large fluctuations in wind direction/velocity. Cases with low stability are strongly affected by the buoyancy-generated turbulence, resulting in enhanced mixing. Conversely, highly stable atmospheric conditions suppress turbulent mixing.

Field experiments like those discussed in this section typically characterize the atmospheric conditions via the Monin-Obukhov length,  $L$ , friction velocity,  $u_*$ , and ground level temperature,  $T_0 = \theta_0$ . From these, the scaling potential temperature can be obtained from the relation:

$$L = \frac{u_*^2 \theta_0}{g \kappa \theta_*} \quad (15.5)$$

Parameters for the LNG dispersion experiments are given in Table 15.1. In some cases, values of the Monin-Obukhov parameters are taken directly from the test reports. However, for some of the experiments, these parameters were not derived using the same similarity functions as those presented above, in which case the parameters have been recomputed to best fit the measured velocity and temperature profiles.

Figure 15.1 through Fig. 15.4 display the measured velocity and temperature profiles, the corresponding Monin-Obukhov profiles that serve as initial and boundary conditions for FDS, and the resulting time-averaged profiles from the FDS simulations.

## Surface Roughness

The default rough wall model used in FDS, in the “fully rough” limit, is given by the following log law:

$$\frac{u(z)}{u_*} = \frac{1}{\kappa} \ln\left(\frac{z}{s}\right) + 8.5 \quad (15.6)$$

The *sandgrain* roughness length used here,  $s$ , is not the same as the *aerodynamic* roughness length,  $z_0$ , used in Eq. (15.1). However, for the purpose of implementing the Monin-Obukhov model within FDS, the velocity profiles given by Eq. (15.1) and (15.6) near the ground where  $\psi_m \approx 0$  can be superimposed, leading to the effective translation of roughness factors:

$$s = z_0 e^{8.5 \kappa} = 30 z_0 \quad (15.7)$$

The values of  $z_0$  are given in Table 15.1.

## Sensible Heat Flux

The ground temperature relative to the air temperature is an important consideration in these experiments because the natural gas that readily evaporates from the pool of spilled LNG is cold and remains near the ground as it is swept downwind. In the simulation, one can either specify a ground temperature or equivalent heat flux based on the computed sensible heat flux from the field experiments. According to Monin-Obukhov theory, the sensible heat flux is given by

$$\dot{q}'' = \rho c_p u_* \theta_* \quad (15.8)$$

where a negative value indicates that the ground is warmer than the air above. The values of  $\dot{q}''$  are given in Table 15.1.

## Source Model

In the various experiments, a fixed mass,  $m$ , of LNG was spilled onto water, forming a pool of increasing radius. For modeling purposes, it is assumed that the mass flux of natural gas from the circular pool is fixed at  $\dot{m}_{\max}'' = 0.167 \text{ kg}/(\text{m}^2 \cdot \text{s})$ , and the temperature of the gas is  $-162^\circ\text{C}$ , as suggested in the testing protocols. The diameter of the pool,  $D$ , is calculated using the assumed mass flux per unit area, the reported mass of LNG,  $m$ , and the spill duration,  $\Delta t$ .

$$D = \sqrt{\frac{4m}{\pi \dot{m}_{\max}'' \Delta t}} \quad (15.9)$$

The values of  $D$  are given in Table 15.1.

## Comparison of Measured and Predicted Downwind Gas Concentrations

Figures 15.5–15.6 compare measured and predicted downwind concentrations of natural gas originating from spills of liquified natural gas (LNG) on water. In each case, the measured values are short-time (1 s to 3 s) averages of sensors positioned in arcs at discrete distances downwind of the spill site. For each arc, the maximum value is chosen. The processing of the FDS results follows the same procedure. The sensors were generally located a few meters off the relatively dry, flat terrain.

Table 15.1: Summary of LNG Dispersion Experiments.

Series Number	Burro				Coyote				Falcon				Maplin Sands			
	3	7	8	9	3	5	6	1	3	4	27	34	35			
Parameters supplied by test reports																
Fuel Mass, $m$ (kg)	14712	17289	12453	10730	6532	12676	10139	28074	21435	18984	3714	2094	3658			
Spill Duration, $\Delta t$ (s)	167	174	107	79	65	98	82	131	154	301	160	95	135			
$\rho_0$ (mbar)	948	940	941	940	936	939	942	908.9	900.8	906.3	—	—	—			
$T_0$ (°C)	34.5	33.8	32.9	35.4	39.6	29.3	24.1	32.2	35.0	30.8	14.9	15.2	16.1			
RH (%)	5.2	7.4	4.5	14.4	11.3	22.1	22.8	—	4.0	12.0	53	90	77			
Computed parameters																
$L$ (m)	-9.49	-111	162	-142	-8.56	-33.2	82.5	4.96	-422	69.4	-14.4	-75.5	-81.2			
$u_*$ (m/s)	0.255	0.372	0.074	0.252	0.310	0.480	0.210	0.061	0.305	0.369	0.190	0.280	0.315			
$z_0$ (m)	0.0002	0.0002	0.0002	0.0002	0.0002	0.0002	0.0002	0.0002	0.008	0.008	0.008	0.0003‡	0.0003‡	0.0003‡		
$\theta_*$ (K)	-0.532	-0.097	0.026	-0.035	-0.890	-0.520	0.039	0.058	-0.018	0.152	-0.180	-0.075	-0.088			
$q''$ (W/m <sup>2</sup> )	-154	-41	2	-10	-314	-284	9	4	-5	58	-39	-24	-32			
$D$ (m)	25.9	27.5	29.9	32.2	27.7	31.4	30.6	19.5†	16.0†	10.8†	13.3	12.8	14.4			

‡ The roughness length was changed to 0.00002 m to better match the measured velocity and temperature profiles

† The Falcon experiments involved 4 separated spills

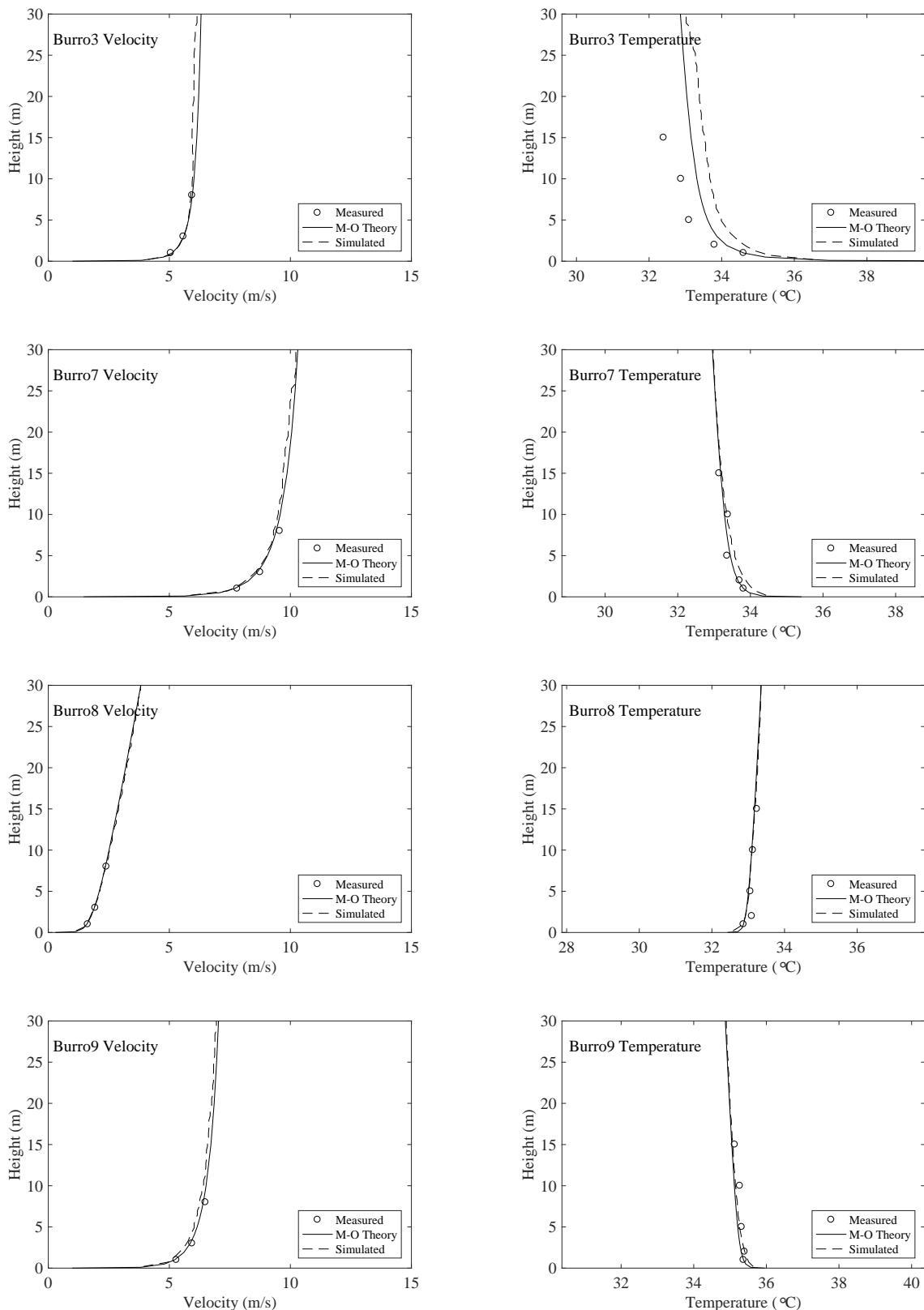


Figure 15.1: LNG Dispersion experiments, Burro velocity and temperature profiles.

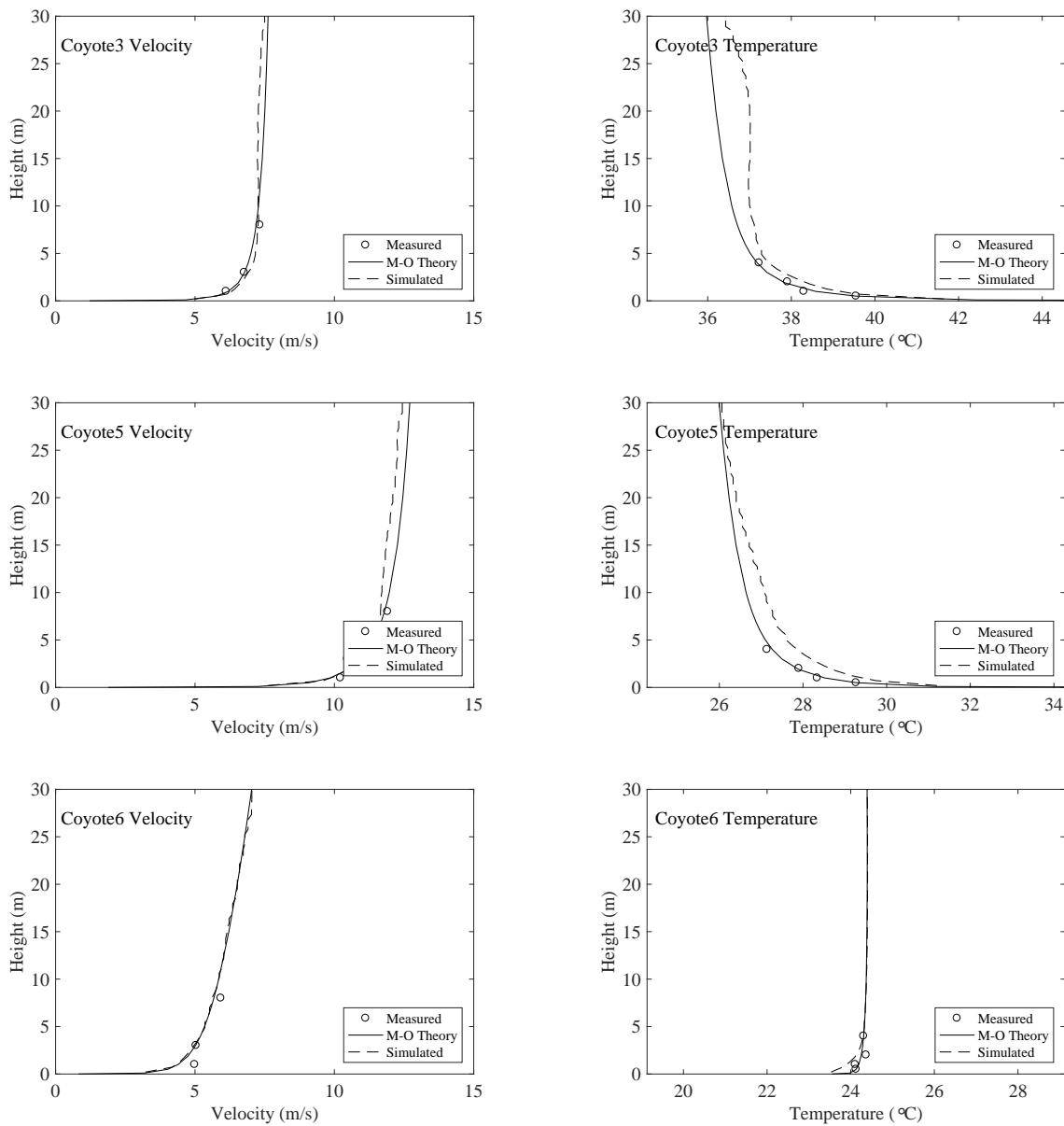


Figure 15.2: LNG Dispersion experiments, Coyote velocity and temperature profiles.

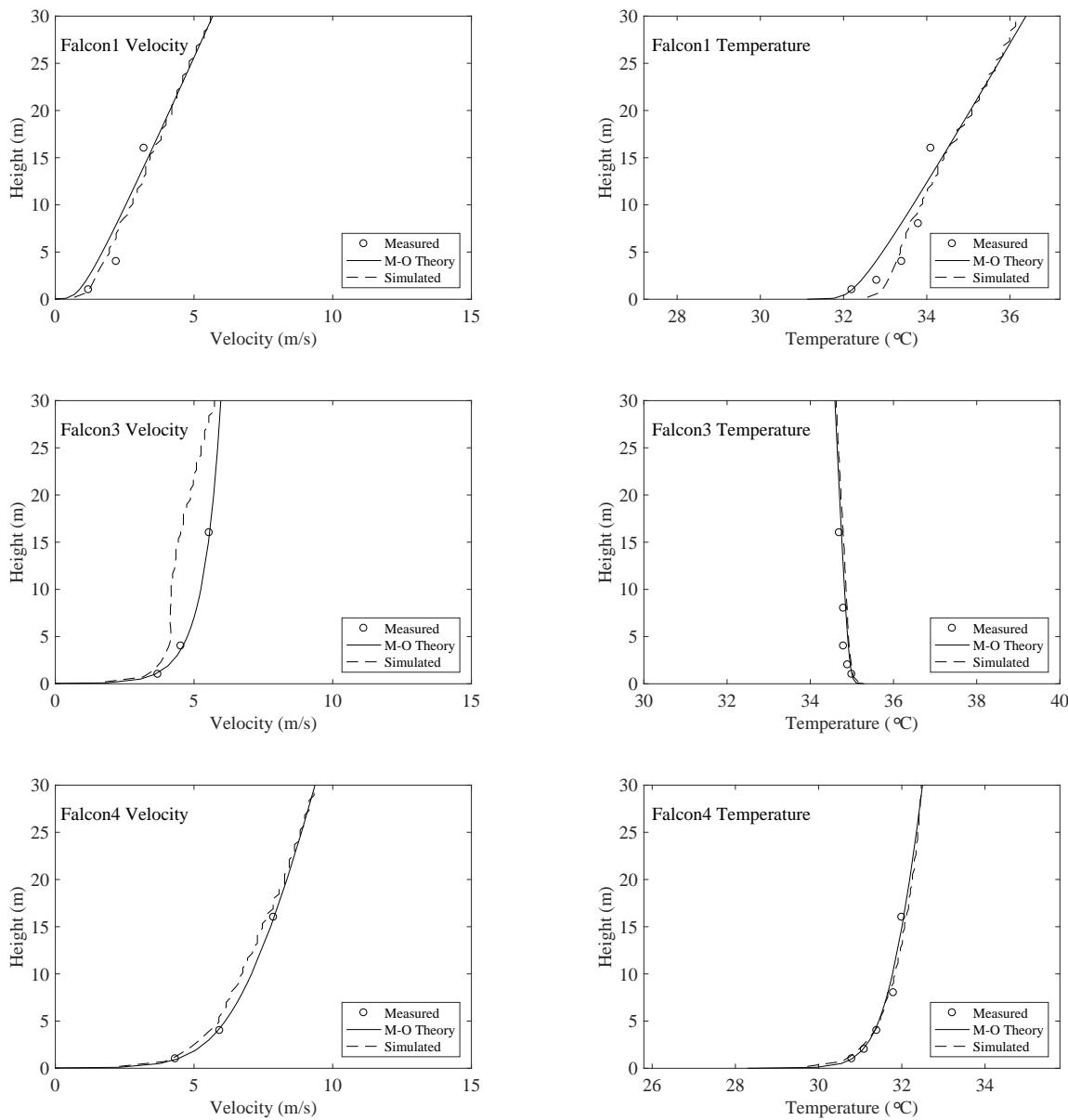


Figure 15.3: LNG Dispersion experiments, Falcon velocity and temperature profiles.

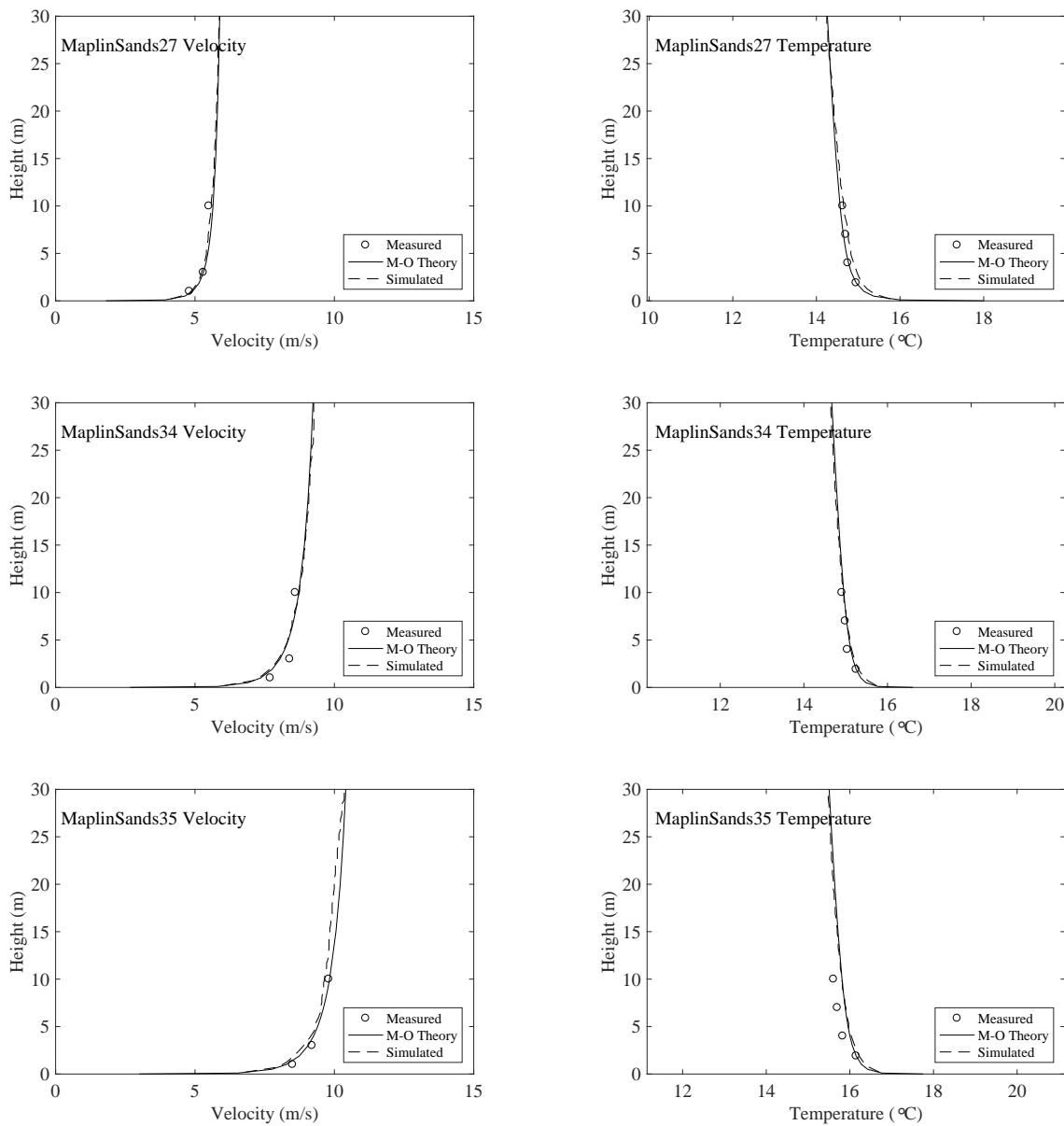


Figure 15.4: LNG Dispersion experiments, Maplin Sands velocity and temperature profiles.

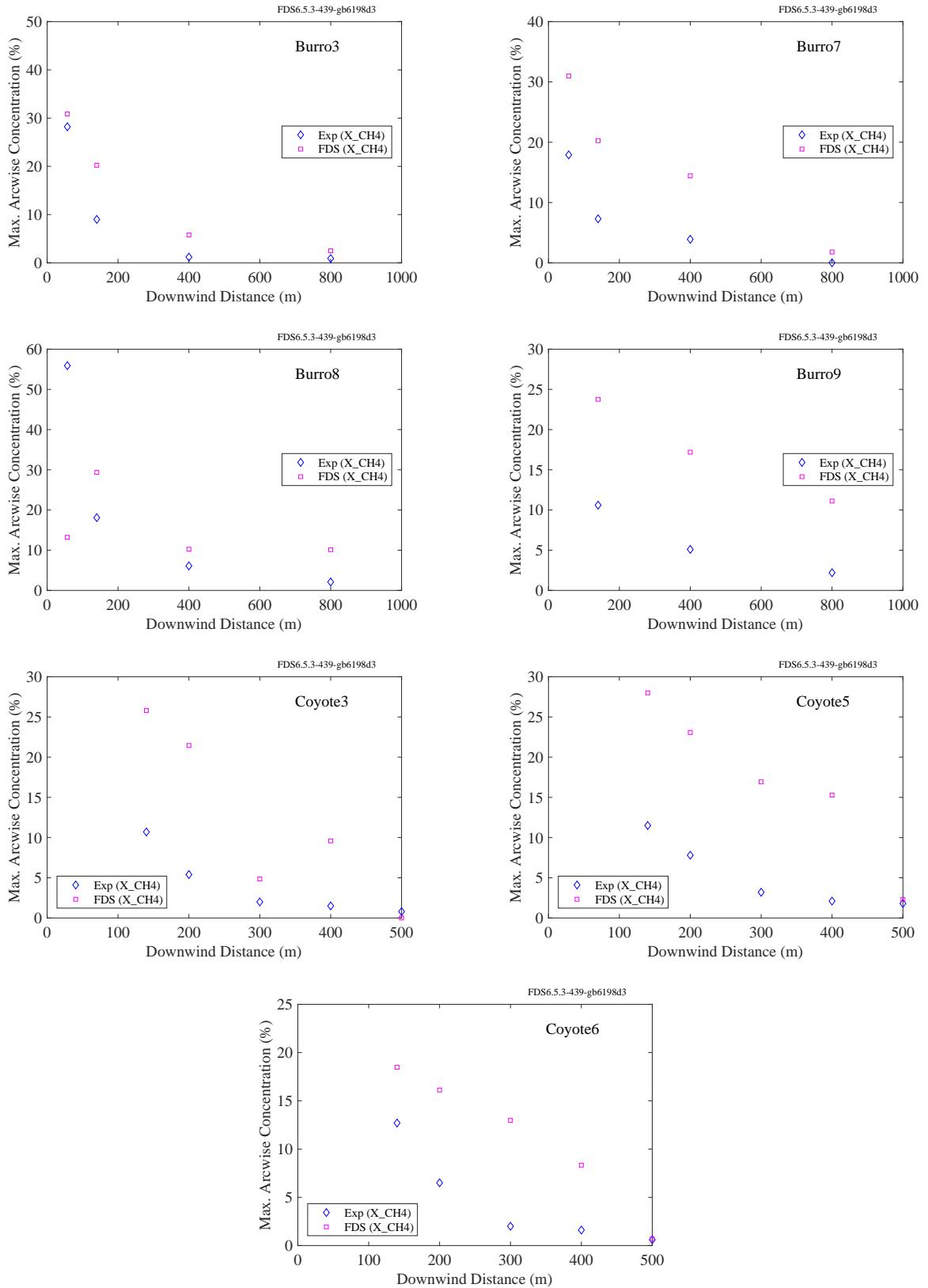


Figure 15.5: LNG Dispersion experiments, Burro and Coyote.

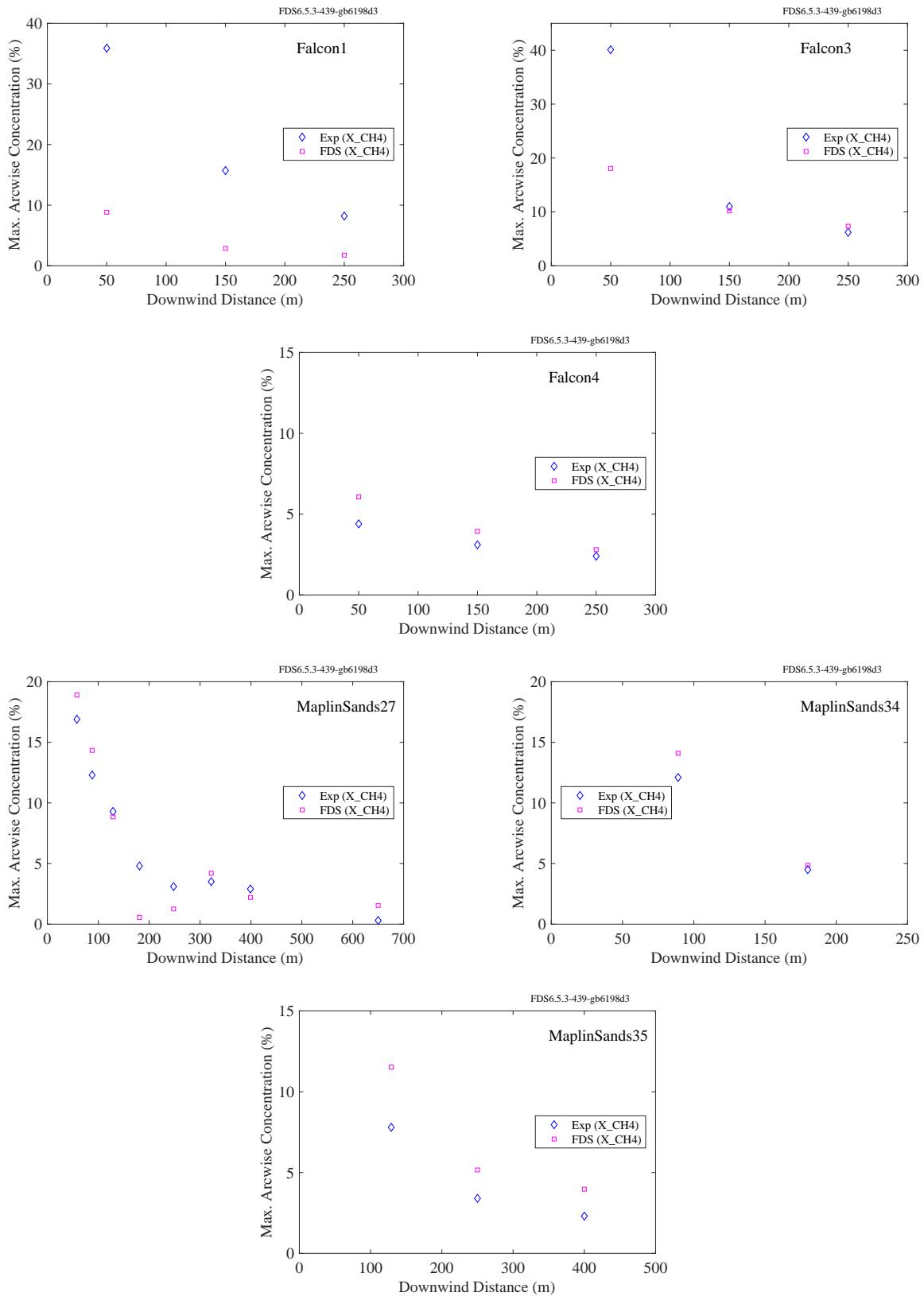


Figure 15.6: LNG Dispersion experiments, Falcon and Maplin Sands.

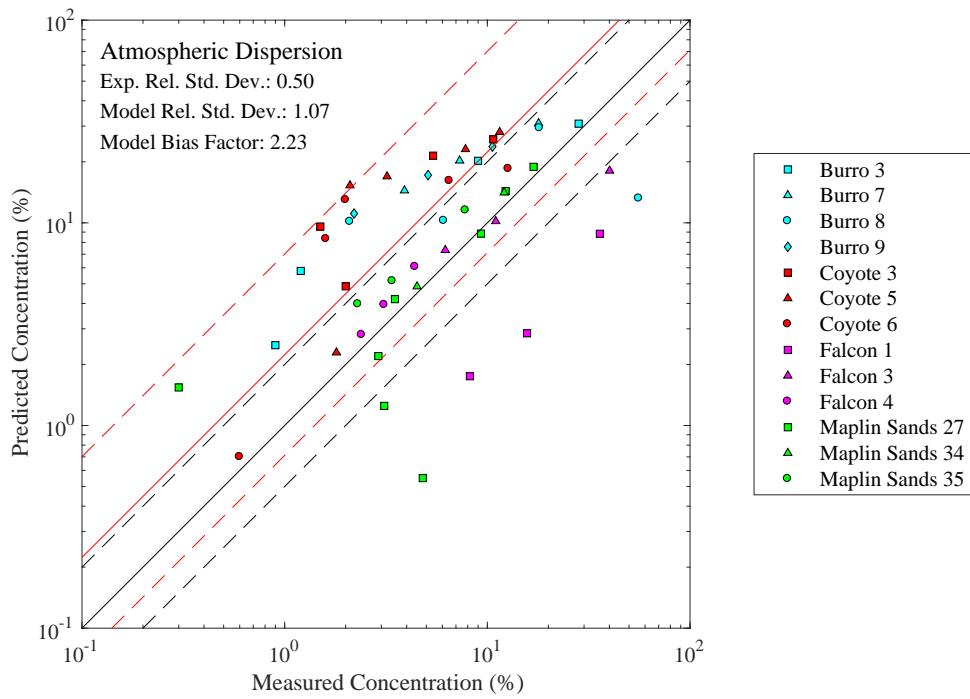


Figure 15.7: Summary of LNG Dispersion predictions. Note that the dashed black lines denote plus/minus a factor of two from the measured values. The red dashed lines represent two relative standard deviations about the solid red line, the model average.



# Chapter 16

## Conclusion

### 16.1 Summary of FDS Model Uncertainty Statistics

Table 16.1 lists the summary statistics for the different quantities examined in this Guide. This is, for each quantity of interest, Table 16.1 lists the bias and relative standard deviation of the predicted values. It also lists the total number of experimental data sets on which these statistics are based, as well as the total number of point to point comparisons. Obviously, the more data sets and the more points, the more reliable the statistics.

For further details about model uncertainty and the meaning of these statistics, see Chapter 4.

Table 16.1: Summary statistics for all quantities of interest

Quantity	Section	Datasets	Points	$\tilde{\sigma}_E$	$\tilde{\sigma}_M$	Bias
HGL Temperature, Forced Ventilation	5.16	5	132	0.07	0.17	1.13
HGL Temperature, Natural Ventilation	5.16	11	191	0.07	0.07	1.04
HGL Temperature, No Ventilation	5.16	3	32	0.07	0.07	1.12
HGL Depth	5.16	10	198	0.05	0.05	1.04
Ceiling Jet Temperature	7.1.17	18	961	0.07	0.13	1.04
Plume Temperature	6.1.7	8	107	0.07	0.15	1.16
Oxygen Concentration	9.1.9	9	184	0.08	0.14	0.99
Carbon Dioxide Concentration	9.1.9	10	181	0.08	0.12	1.00
Smoke Concentration	9.2.2	1	14	0.19	0.59	2.56
Compartment Over-Pressure	10.6	4	75	0.17	0.17	0.89
Target Temperature	11.2.6	7	1258	0.07	0.18	1.02
Surface Temperature	11.1.7	5	1009	0.07	0.13	1.04
Target Heat Flux	12.2.5	5	348	0.11	0.24	0.98
Surface Heat Flux	12.1.10	7	633	0.11	0.23	1.02
Velocity	8.10	7	222	0.08	0.09	0.99
Sprinkler Activation Time	7.2.1	5	232	0.06	0.17	0.95
Smoke Detector Activation Time	7.3	1	142	0.27	0.27	0.58
Smoke Detector Activation Time, Temp. Rise	7.3	1	142	0.33	0.33	1.02
Cable Failure Time	11.2.7	1	35	0.12	0.15	1.14
Sprinkler Actuations	7.2.2	3	38	0.15	0.31	0.89
Burning Rate	14.8	3	47	0.08	0.39	1.01
Carbon Monoxide Concentration	9.3.6	6	93	0.19	1.01	0.96

Quantity	Section	Datasets	Points	$\tilde{\sigma}_E$	$\tilde{\sigma}_M$	Bias
Entrainment	6.3	2	87	0.05	0.05	1.13
Extinction Time	13.2	1	36	0.10	0.45	0.93
Species Concentration	9.4	1	126	0.08	0.15	0.98
Smoke Obscuration	9.2.3	1	18	0.20	0.20	0.98
Mass Flow Rate	12.81	1	40	0.08	0.08	0.83
Atmospheric Dispersion	15.1	13	51	0.50	1.07	2.23

## 16.2 Normality Tests

The histograms on the following pages display the distribution of the quantity  $\ln(M/E)$ , where  $M$  is a random variable representing the Model prediction and  $E$  is a random variable representing the Experimental measurement. Recall from Chapter 4 that  $\ln(M/E)$  is assumed to be normally distributed. To test this assumption for each of the quantities of interest listed in Table 16.1, Spiegelhalter's normality test has been applied [280]. This test examines a set of values,  $x_1, \dots, x_n$  whose mean and standard deviation are computed as follows:

$$\bar{x} = \sum_{i=1}^n x_i \quad ; \quad \sigma^2 = \frac{1}{n-1} \sum_{i=1}^n (x_i - \bar{x})^2 \quad (16.1)$$

Spiegelhalter tests the null hypothesis that the sample  $x_i$  is taken from a normally distributed population. The test statistic,  $S$ , is defined:

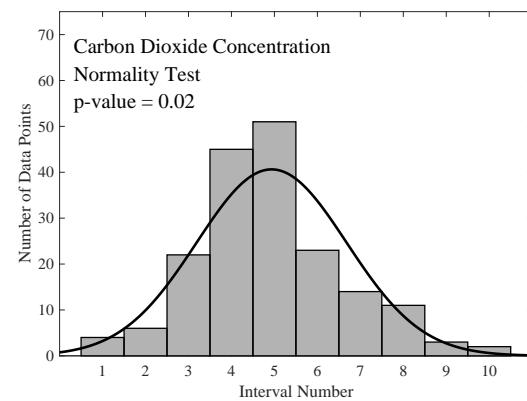
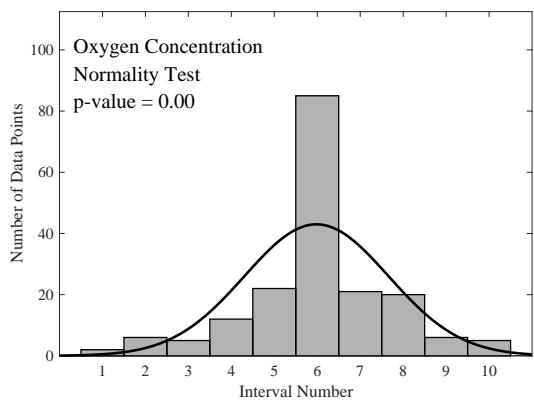
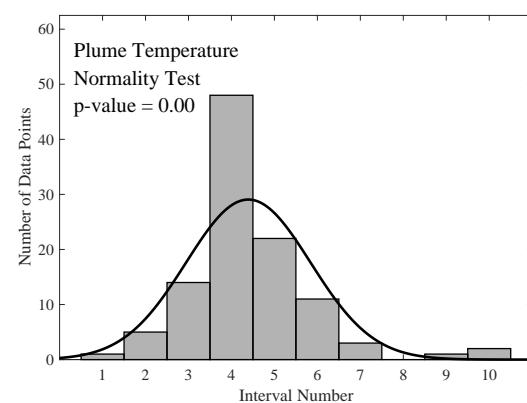
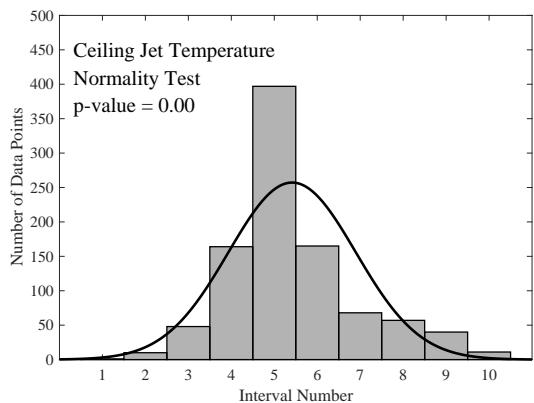
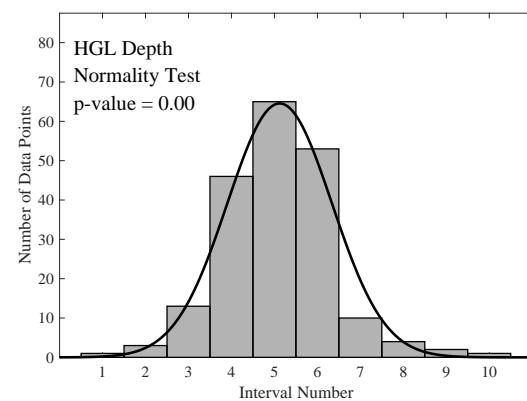
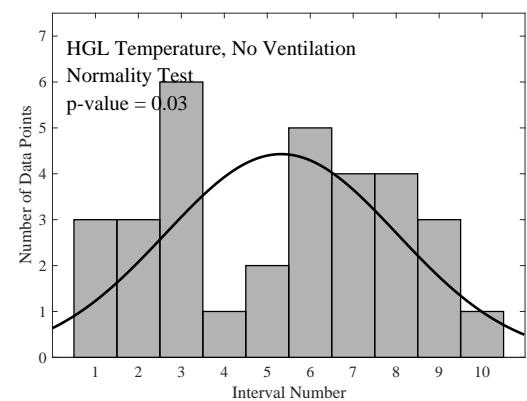
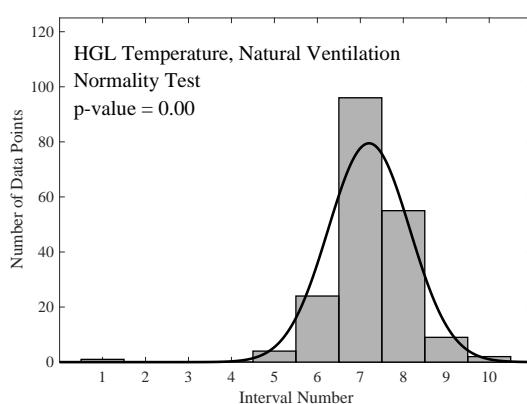
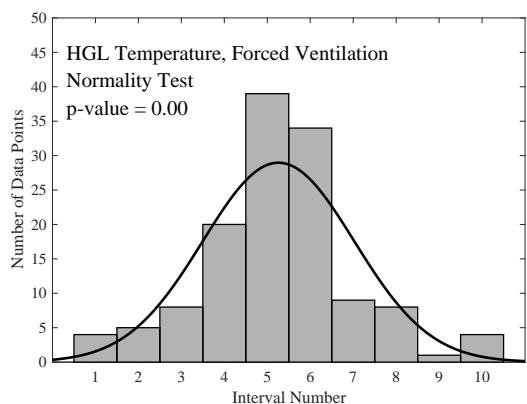
$$S = \frac{N - 0.73n}{0.9\sqrt{n}} \quad ; \quad N = \sum_{i=1}^n Z_i^2 \ln Z_i^2 \quad ; \quad Z_i = \frac{x_i - \bar{x}}{\sigma} \quad (16.2)$$

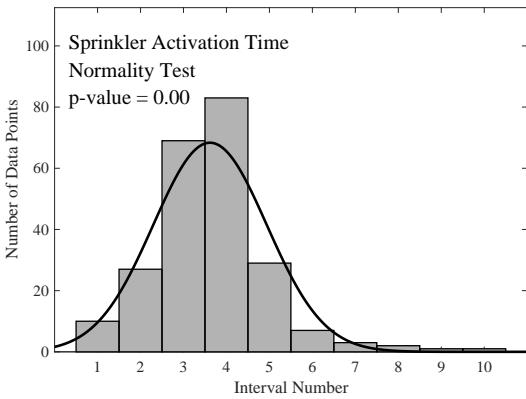
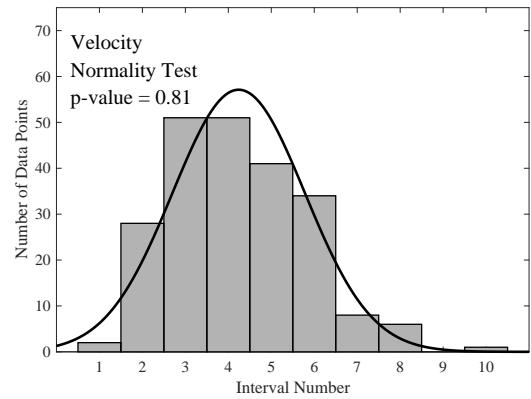
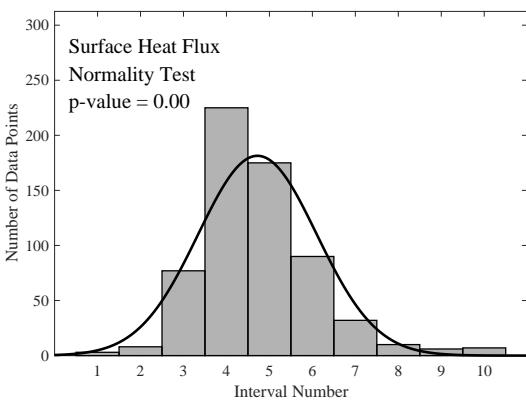
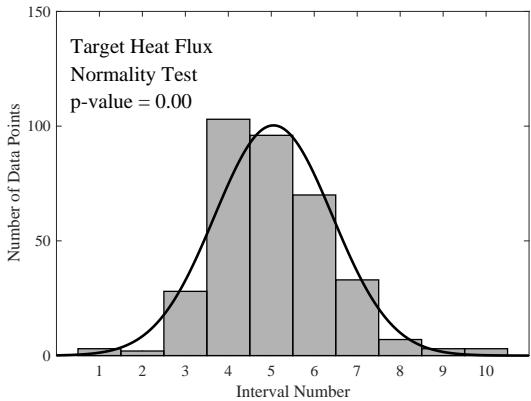
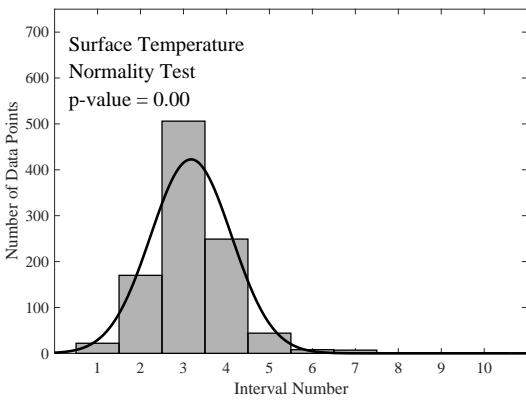
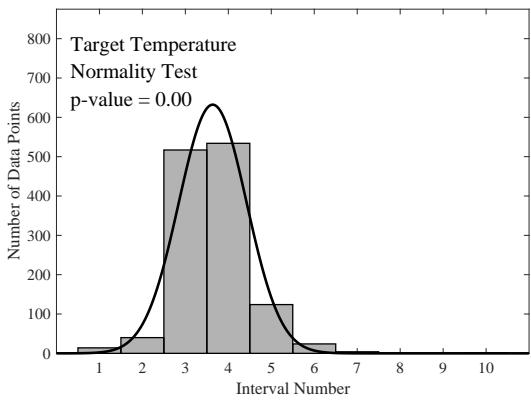
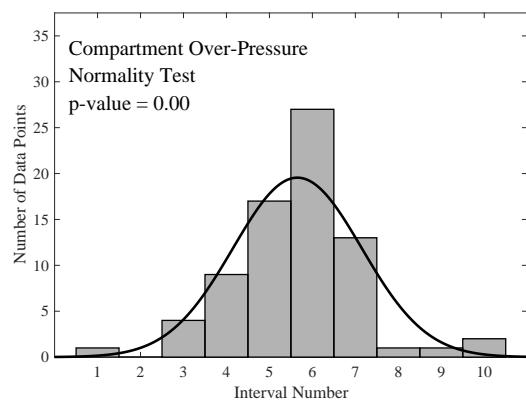
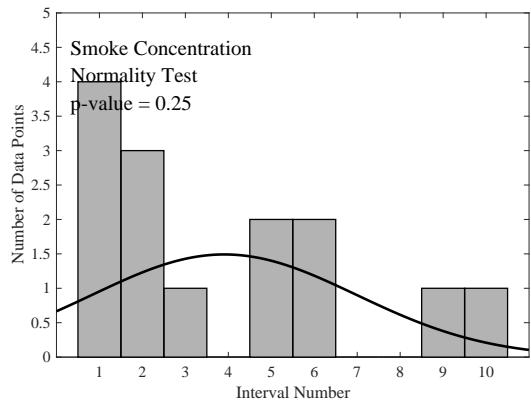
Under the null hypothesis, the test statistic is normally distributed with mean 0 and standard deviation of 1. If the  $p$ -value

$$p = 1 - \left| \operatorname{erf} \left( \frac{S}{\sqrt{2}} \right) \right| \quad (16.3)$$

is less than 0.05, the null hypothesis is rejected.

The flaw in most normality tests is that they tend to reject the assumption of normality when the number of samples is relatively large. As can be seen in some of the histograms on the following pages, some fairly “normal” looking distributions fail while decidedly non-normal distributions pass. For this reason, the  $p$ -value is less important than the qualitative appearance of the histogram. If the histogram exhibits the typical bell-shaped curve, this adds confidence to the statistical treatment of the data. If the histogram is not bell-shaped, this might cast doubt on the statistical treatment for that particular quantity.







## 16.3 Summary of FDS Validation Git Statistics

Table 16.2 shows the Git repository statistics for all of the validation datasets. For each dataset, the corresponding last changed date and Git revision string are shown. This indicates the Git revision string and date for which the most recent validation results for a given dataset were committed to the repository.

Table 16.2: Validation Git statistics for all data sets

Dataset	FDS Revision Date	FDS Revision String
BRE_Spray	Dec 8, 2016	FDS6.5.3-201-gf722339
Bryant_Doorway	Dec 8, 2016	FDS6.5.3-201-gf722339
CAROLFIRE	Dec 8, 2016	FDS6.5.3-201-gf722339
CHRISTIFIRE	Dec 8, 2016	FDS6.5.3-201-gf722339
Cup_Burner	Dec 8, 2016	FDS6.5.3-201-gf722339
FAA_Polymers	Dec 8, 2016	FDS6.5.3-201-gf722339
FM_Parallel_Panels	Dec 8, 2016	FDS6.5.3-201-gf722339
Fleury_Heat_Flux	Dec 8, 2016	FDS6.5.3-201-gf722339
Hamins_Gas_Burners	Dec 8, 2016	FDS6.5.3-201-gf722339
Heskestad_Flame_Height	Dec 8, 2016	FDS6.5.3-201-gf722339
LEMTA_Spray	Dec 8, 2016	FDS6.5.3-201-gf722339
Moody_Chart	Dec 8, 2016	FDS6.5.3-201-gf722339
NIST_He_2009	Dec 8, 2016	FDS6.5.3-201-gf722339
NIST_NRC	Dec 8, 2016	FDS6.5.3-201-gf722339
NIST_RSE_2007	Dec 8, 2016	FDS6.5.3-201-gf722339
NIST_Smoke_Alarms	Dec 8, 2016	FDS6.5.3-201-gf722339
NRCC_Facade	Dec 8, 2016	FDS6.5.3-201-gf722339
NRL_HAI	Dec 8, 2016	FDS6.5.3-201-gf722339
PRISME	Dec 8, 2016	FDS6.5.3-201-gf722339
Pool_Fires	Dec 8, 2016	FDS6.5.3-201-gf722339
Restivo_Experiment	Dec 8, 2016	FDS6.5.3-201-gf722339
SP_AST	Dec 8, 2016	FDS6.5.3-201-gf722339
Sippola_Aerosol_Deposition	Dec 8, 2016	FDS6.5.3-201-gf722339
Steckler_Compartment	Dec 8, 2016	FDS6.5.3-201-gf722339
UL_NIST_Vents	Dec 8, 2016	FDS6.5.3-201-gf722339
UMD_Polymers	Dec 8, 2016	FDS6.5.3-201-gf722339
USCG_HAI	Dec 8, 2016	FDS6.5.3-201-gf722339
Ulster_SBI	Dec 8, 2016	FDS6.5.3-201-gf722339
VTT_Sprays	Dec 8, 2016	FDS6.5.3-201-gf722339
Vettori_Flat_Ceiling	Dec 8, 2016	FDS6.5.3-201-gf722339
Vettori_Sloped_Ceiling	Dec 8, 2016	FDS6.5.3-201-gf722339
ATF_Corridors	Dec 13, 2016	FDS6.5.3-229-g743ab74
Arup_Tunnel	Dec 13, 2016	FDS6.5.3-229-g743ab74
Backward_Facing_Step	Dec 13, 2016	FDS6.5.3-229-g743ab74
Beyler_Hood	Dec 13, 2016	FDS6.5.3-229-g743ab74
Bouchair_Solar_Chimney	Dec 13, 2016	FDS6.5.3-229-g743ab74
CSIRO_Grassland_Fires	Dec 13, 2016	FDS6.5.3-229-g743ab74
DelCo_Trainers	Dec 13, 2016	FDS6.5.3-229-g743ab74

Dataset	FDS Revision Date	FDS Revision String
FAA_Cargo_Compartments	Dec 13, 2016	FDS6.5.3-229-g743ab74
FM_FPRF_Datacenter	Dec 13, 2016	FDS6.5.3-229-g743ab74
FM_SNL	Dec 13, 2016	FDS6.5.3-229-g743ab74
Harrison_Spill_Plumes	Dec 13, 2016	FDS6.5.3-229-g743ab74
LLNL_Enclosure	Dec 13, 2016	FDS6.5.3-229-g743ab74
MPI_Scaling_Tests	Dec 13, 2016	FDS6.5.3-229-g743ab74
McCaffrey_Plume	Dec 13, 2016	FDS6.5.3-229-g743ab74
NBS_Multi-Room	Dec 13, 2016	FDS6.5.3-229-g743ab74
NIST_Douglas_Firs	Dec 13, 2016	FDS6.5.3-229-g743ab74
NIST_RSE_1994	Dec 13, 2016	FDS6.5.3-229-g743ab74
NRCC_Smoke_Tower	Dec 13, 2016	FDS6.5.3-229-g743ab74
Sandia_Plumes	Dec 13, 2016	FDS6.5.3-229-g743ab74
Smyth_Slot_Burner	Dec 13, 2016	FDS6.5.3-229-g743ab74
Turbulent_Jet	Dec 13, 2016	FDS6.5.3-229-g743ab74
UL_NFPRF	Dec 13, 2016	FDS6.5.3-229-g743ab74
UMD_Line_Burner	Dec 13, 2016	FDS6.5.3-229-g743ab74
USN_Hangars	Dec 13, 2016	FDS6.5.3-229-g743ab74
VTT	Dec 13, 2016	FDS6.5.3-229-g743ab74
WTC	Dec 13, 2016	FDS6.5.3-229-g743ab74
Purdue_Flames	Dec 23, 2016	FDS6.5.3-273-g808792a
NIST_FSE_2008	Dec 31, 2016	FDS6.5.3-325-gc9ee16b
LNG_Dispersion	Jan 11, 2017	FDS6.5.3-439-gb6198d3



# Bibliography

- [1] K. McGrattan, S. Hostikka, R. McDermott, J. Floyd, C. Weinschenk, and K. Overholt. *Fire Dynamics Simulator, User's Guide*. National Institute of Standards and Technology, Gaithersburg, Maryland, USA, and VTT Technical Research Centre of Finland, Espoo, Finland, sixth edition, September 2013. [vii, 325](#)
- [2] American Society for Testing and Materials, West Conshohocken, Pennsylvania. *ASTM E1355-12, Standard Guide for Evaluating the Predictive Capabilities of Deterministic Fire Models*, 2012. [vii, 1](#)
- [3] R.G. Rehm and H.R. Baum. The Equations of Motion for Thermally Driven, Buoyant Flows. *Journal of Research of the NBS*, 83:297–308, 1978. [6](#)
- [4] H.R. Baum, R.G. Rehm, P.D. Barnett, and D.M. Corley. Finite Difference Calculations of Buoyant Convection in an Enclosure, Part I: The Basic Algorithm. *SIAM Journal of Scientific and Statistical Computing*, 4(1):117–135, March 1983. [6](#)
- [5] R.G. Rehm, P.D. Barnett, H.R. Baum, and D.M. Corley. Finite Difference Calculations of Buoyant Convection in an Enclosure: Verification of the Nonlinear Algorithm. *Applied Numerical Mathematics*, 1:515–529, 1985. [6](#)
- [6] R.G. Rehm, H.R. Baum, D.W. Lozier, H. Tang, and J. Sims. Buoyant Convection in an Inclined Enclosure. In *Fire Safety Science – Proceedings of the Third International Symposium*, pages 313–323. International Association for Fire Safety Science, 1991. [6](#)
- [7] H.R. Baum, O.A. Ezekoye, K.B. McGrattan, and R.G. Rehm. Mathematical Modeling and Computer Simulation of Fire Phenomenon. *Theoretical and Computational Fluid Dynamics*, 6:125–139, 1994. [6](#)
- [8] K.B. McGrattan, R.G. Rehm, and H.R. Baum. Fire-Driven Flows in Enclosures. *Journal of Computational Physics*, 110(2):285–291, 1994. [6](#)
- [9] R.G. Rehm, K.B. McGrattan, H.R. Baum, and K.W. Cassel. Transport by Gravity Currents in Building Fires. In *Fire Safety Science – Proceedings of the Fifth International Symposium*, pages 391–402. International Association for Fire Safety Science, 1997. [6](#)
- [10] H.R. Baum, K.B. McGrattan, and R.G. Rehm. Three Dimensional Simulations of Fire Plume Dynamics. In *Fire Safety Science – Proceedings of the Fifth International Symposium*, pages 511–522. International Association for Fire Safety Science, 1997. [6](#)
- [11] H.R. Baum, K.B. McGrattan, and R.G. Rehm. Large Eddy Simulations of Smoke Movement in Three Dimensions. In *Proceedings of the Seventh International Interflam Conference*, pages 189–198. Interscience Communications, London, 1996. [6](#)

- [12] H.R. Baum and B.J. McCaffrey. Fire Induced Flow Field – Theory and Experiment. In *Fire Safety Science – Proceedings of the Second International Symposium*, pages 129–148. International Association for Fire Safety Science, 1989. [6](#)
- [13] H.R. Baum, K.B. McGrattan, and R.G. Rehm. Three Dimensional Simulations of Fire Plume Dynamics. *Journal of the Heat Transfer Society of Japan*, 35(139):45–52, 1997. [6](#)
- [14] J.M. Clement and C.M. Fleischmann. Experimental Verification of the Fire Dynamics Simulator Hydrodynamic Model. In *Fire Safety Science – Proceedings of the Seventh International Symposium*, pages 839–862. International Association for Fire Safety Science, 2002. [6](#)
- [15] K.B. McGrattan, H.R. Baum, and R.G. Rehm. Large Eddy Simulations of Smoke Movement. *Fire Safety Journal*, 30:161–178, 1998. [6](#)
- [16] W. Mell, K.B. McGrattan, and H. Baum. Numerical Simulation of Combustion in Fire Plumes. In *Twenty-Sixth Symposium (International) on Combustion*, pages 1523–1530. Combustion Institute, Pittsburgh, Pennsylvania, 1996. [6](#)
- [17] T. Cleary, M. Anderson, J. Averill, and W. Grosshandler. Evaluating Multi-Sensor Fire Detectors in the Fire Emulator/Detector Evaluator. In *Proceedings of the Eighth International Interflam Conference*, pages 453–464. Interscience Communications, June 1999. [6](#)
- [18] W. Davis, K Notarianni, and K. McGrattan. Comparison of Fire Model Predictions with Experiments Conducted in a Hangar with a 15 Meter Ceiling. NISTIR 5927, National Institute of Standards and Technology, Gaithersburg, Maryland, December 1996. [6, 48](#)
- [19] S.J. Emmerich and K.B. McGrattan. Application of a Large Eddy Simulation Model to Study Room Airflow. *ASHRAE Transactions*, 104(1):1–9, 1998. [6, 48](#)
- [20] S.J. Emmerich. Use of Computational Fluid Dynamics to Analyze Indoor Air Quality Issues. NISTIR 5997, National Institute of Standards and Technology, Gaithersburg, Maryland, April 1997. [6, 48](#)
- [21] W.K. Chow and R. Yin. Discussion on Two Plume Formulae with Computational Fluid Dynamics. *Journal of Fire Sciences*, 20:179–201, May 2002. [7](#)
- [22] F. Battaglia, K. McGrattan, R. Rehm, and H. Baum. Simulating Fire Whirls. *Combustion Theory and Modeling*, 4:123–138, 2000. [7](#)
- [23] K.M. Liang, T. Ma, J.G. Quintiere, and D. Rouson. Application of CFD Modeling to Room Fire Growth on Walls. NIST GCR 03-849, National Institute of Standards and Technology, Gaithersburg, Maryland, April 2003. [7, 10](#)
- [24] T. Ma and J. Quintiere. Numerical Simulation of Axi-Symmetric Fire Plumes: Accuracy and Limitations. *Fire Safety Journal*, 38:467–492, 2003. [7, 10](#)
- [25] G. Hesketh. *SFPE Handbook of Fire Protection Engineering*, chapter Fire Plumes, Flame Height and Air Entrainment. National Fire Protection Association, Quincy, Massachusetts, 4th edition, 2008. [7, 30, 172, 174](#)
- [26] C. Gutiérrez-Montes, E. Sanmiguel-Rojas, A. Viedma, and G. Rein. Experimental data and numerical modelling of 1.3 and 2.3 MW fires in a 20 m cubic atrium. *Building and Environment*, 44:1827–1839, 2009. ([Web Link](#)). [7](#)

- [27] M. Hurley and A. Munguia. Analysis of FDS Thermal Detector Response Prediction Capability. NIST GCR 09-921, National Institute of Standards and Technology, Gaithersburg, Maryland, 2009. 7
- [28] M. Hurley and A. Munguia. Analysis of FDS Thermal Detector Response Prediction Capability. *J. Fire Protection Engineering*, 20, 2009. 7
- [29] Y. Xin. Baroclinic Effects on Fire Flow Field. In *Proceedings of the Fourth Joint Meeting of the U.S. Sections of the Combustion Institute*. Combustion Institute, Pittsburgh, Pennsylvania, March 2005. 8
- [30] Y. Xin, J.P. Gore, K.B. McGrattan, R.G. Rehm, and H.R. Baum. Fire dynamics simulation of a turbulent buoyant flame using a mixture-fraction-based combustion model. *Combustion and Flame*, 141:329–335, 2005. 8, 48, 191, 192
- [31] Y. Xin, J.P. Gore, K.B. McGrattan, R.G. Rehm, and H.R. Baum. Large Eddy Simulation of Buoyant Turbulent Pool Fires. In *Twenty-Ninth Symposium (International) on Combustion*, pages 259–266. Combustion Institute, Pittsburgh, Pennsylvania, 2002. 8
- [32] X.C. Zhou and J.P. Gore. Experimental estimation of thermal expansion and vorticity distribution in a buoyant diffusion flame. In *Twenty-Seventh Symposium (International) on Combustion*. Combustion Institute, Pittsburgh, Pennsylvania, 2001. 8, 48, 191, 193
- [33] Y. Xin, J.P. Gore, K.B. McGrattan, R.G. Rehm, and H.R. Baum. Large Eddy Simulation of Buoyant Turbulent Pool Fires. In *Proceedings of the 2002 Spring Technical Meeting, Central States Section*. Combustion Institute, Pittsburgh, Pennsylvania, April 2002. 8
- [34] Y. Xin and J.P. Gore. Two-dimensional soot distributions in buoyant turbulent fires. In *Thirtieth Symposium (International) on Combustion*. Combustion Institute, Pittsburgh, Pennsylvania, 2005. 8
- [35] Y. Biswas, Y. Zheng, C.H. Kim, and J.P. Gore. Stochastic time series analysis of pulsating buoyant pool fires. In *Thirty First Symposium (International) on Combustion*. Combustion Institute, Pittsburgh, Pennsylvania, 2007. 8
- [36] S. Hostikka, K.B. McGrattan, and A. Hamins. Numerical Modeling of Pool Fires using Large Eddy Simulation and Finite Volume Method for Radiation. In *Fire Safety Science – Proceedings of the Seventh International Symposium*, pages 383–394. International Association for Fire Safety Science, 2002. 8, 30
- [37] J. Hietaniemi, S. Hostikka, and J. Vaari. FDS Simulation of Fire Spread – Comparison of Model Results with Experimental Data. VTT Working Papers 4, VTT Building and Transport, Espoo, Finland, 2004. 8, 10
- [38] A. Musser, K. B. McGrattan, and J. Palmer. Evaluation of a Fast, Simplified Computational Fluid Dynamics Model for Solving Room Airflow Problems. NISTIR 6760, National Institute of Standards and Technology, Gaithersburg, Maryland, June 2001. 8, 48, 279
- [39] X. Yuan, Q. Chen, L.R. Glicksman, Y. Hu, and X. Yang. Measurements and Computations of Room Airflow with Displacement Ventilation. Technical Report RP-949, American Society of Heating, Refrigerating, Air-Conditioning Engineers, 1999. 8
- [40] A. Musser and L. Tan. Control of Diesel Exhaust Fumes in Enclosed Locomotive Facilities. Technical Report RP-1191, American Society of Heating, Refrigerating, Air-Conditioning Engineers, 2003. 8

- [41] K. Mniszewski. The Use of FDS for Estimation of Flammable Gas/Vapor Concentrations. In *Proceedings of the 3rd Technical Symposium on Computer Applications in Fire Protection Engineering*, pages 143–155. Society for Fire Protection Engineers, Bethesda, Maryland, September 2001. 8
- [42] S. Kerber and W. Walton. Characterizing Positive Pressure Ventilation using Computational Fluid Dynamics. NISTIR 7065, National Institute of Standards and Technology, Gaithersburg, Maryland, February 2003. 8
- [43] R. Rehm, K. McGrattan, H. Baum, and E. Simiu. An Efficient Large Eddy Simulation Algorithm for Computational Wind Engineering: Application to Surface Pressure Computations on a Single Building. NISTIR 6371, National Institute of Standards and Technology, August 1999. 9
- [44] R.G. Rehm, K.B. McGrattan, and H.R. Baum. Large Eddy Simulation of Flow over a Wooded Building Complex. *Wind & Structures*, 5(2):291–300, 2002. 9
- [45] H.Y. Wang and P. Joulain. Numerical Simulation of Wind-Aided Turbulent Fires in a Ventilated Model Tunnel. In *Fire Safety Science – Proceedings of the Seventh International Symposium*, pages 161–172. International Association for Fire Safety Science, 2002. 9
- [46] B.F. Magnussen and B.H. Hjertager. On Mathematical Modeling of Turbulent Combustion with Special Emphasis on Soot Formation and Combustion. In *Proceedings of the Sixteenth Symposium (International) on Combustion*, pages 719–729. Combustion Institute, Pittsburgh, Pennsylvania, 1977. 9
- [47] C.H. Chang and R.N. Meroney. Concentration and flow distributions in urban street canyons: wind tunnel and computational data. *Journal of Wind Engineering and Industrial Aerodynamics*, 91:1141–1154, 2003. 9
- [48] K. Moon, J. M. Hwang, B. G. Kim, C. Lee, and J. Choi. Large-eddy simulation of turbulent flow and dispersion over a complex urban street canyon. *Environmental Fluid Mechanics (on-line)*, January 2014. 9
- [49] H. Le, P. Moin, and J. Kim. Direct numerical simulation of turbulent flow over a backward-facing step. *Journal of Fluid Mechanics*, 330:349–374, 1997. 9
- [50] S. Jovic and D. M. Driver. Backward-facing step measurements at low Reynolds number,  $Re_h=5000$ . *NASA Technical Memorandum*, 108807, February 1994. 9, 19, 270
- [51] M. Sarwar, K. A. M. Moinuddin, and G. R. Thorpe. Large eddy simulation of flow over a backward facing step using Fire Dynamics Simulator (FDS). *Fourteenth Asian Congress of Fluid Mechanics*, pages 469–474, October 2013. 9
- [52] K.B. McGrattan, H.R. Baum, and R.G. Rehm. Numerical Simulation of Smoke Plumes from Large Oil Fires. *Atmospheric Environment*, 30(24):4125–4136, 1996. 9
- [53] T. Yamada. Smoke Plume Trajectory from In-Situ Burning of Crude Oil in Tomakomai. Technical report, National Research Institute of Fire and Disaster, Japan, November 1998. 9
- [54] Y. Mouilleau and A. Champassith. CFD simulations of atmospheric gas dispersion using the Fire Dynamics Simulator (FDS). *Journal of Loss Prevention in the Process Industries*, 22:316–323, 2009. published by Elsevier. 9

- [55] J. Floyd. Comparison of CFAST and FDS for Fire Simulation with the HDR T51 and T52 Tests. NISTIR 6866, National Institute of Standards and Technology, Gaithersburg, Maryland, March 2002. 10
- [56] J.E. Floyd, K.B. McGrattan, S. Hostikka, and H.R. Baum. CFD Fire Simulation Using Mixture Fraction Combustion and Finite Volume Radiative Heat Transfer. *Journal of Fire Protection Engineering*, 13:11–26, February 2003. 10, 14
- [57] A. Kashef, N. Benichou, G.D. Lougheed, and C. McCartney. A Computational and Experimental Study of Fire Growth and Smoke Movement in Large Spaces. Technical Report NRCC-45201, National Research Council Canada, 2002. 10
- [58] K.B. McGrattan, T. Kashiwagi, H.R. Baum, and S.L. Olson. Effects of Ignition and Wind on the Transition to Flame Spread in a Microgravity Environment. *Combustion and Flame*, 106:377–391, 1996. 10
- [59] T. Kashiwagi, K.B. McGrattan, S.L. Olson, O. Fujita, M. Kikuchi, and K. Ito. Effects of Slow Wind on Localized Radiative Ignition and Transition to Flame Spread in Microgravity. In *Twenty-Sixth Symposium (International) on Combustion*, pages 1345–1352. Combustion Institute, Pittsburgh, Pennsylvania, 1996. 10
- [60] W. Mell and T. Kashiwagi. Dimensional Effects on the Transition from Ignition to Flame Spread in Microgravity. In *Twenty-Seventh Symposium (International) on Combustion*, pages 2635–2641. Combustion Institute, Pittsburgh, Pennsylvania, 1998. 10
- [61] W. Mell, S.L. Olson, and T. Kashiwagi. Flame Spread Along Free Edges of Thermally-Thin Samples in Microgravity. In *Twenty-Eighth Symposium (International) on Combustion*, pages 2843–2849. Combustion Institute, Pittsburgh, Pennsylvania, 2000. 10
- [62] K. Prasad, Y. Nakamura, S.L. Olson, O. Fujita, K. Nishizawa, K. Ito, and T. Kashiwagi. Effect of Wind Velocity on Flame Spread in Microgravity. In *Twenty-Ninth Symposium (International) on Combustion*, pages 2553–2560. Combustion Institute, Pittsburgh, Pennsylvania, 2002. 10
- [63] Y. Nakamura, T. Kashiwagi, K.B. McGrattan, and H.R. Baum. Enclosure Effects on Flame Spread over Solid Fuels in Microgravity. *Combustion and Flame*, 130:307–321, 2002. 10
- [64] W.E. Mell, K.B. McGrattan, and H.R. Baum. g-Jitter Effects on Spherical Diffusion Flames. *Microgravity Science and Technology*, 15(4):12–30, 2004. 10
- [65] S. Hostikka and K.B. McGrattan. Large Eddy Simulations of Wood Combustion. In *Proceedings of the Ninth International Interflam Conference*, pages 755–762. Interscience Communications, London, 2001. 10
- [66] S.J. Ritchie, K.D. Steckler, A. Hamins, T.G. Cleary, J.C. Yang, and T. Kashiwagi. The Effect of Sample Size on the Heat Release Rate of Charring Materials. In *Fire Safety Science - Proceedings of the 5th International Symposium*, pages 177–188. International Association For Fire Safety Science, 1997. 10
- [67] J.W. Kwon, N.A. Dembsey, and C.W. Lautenberger. Evaluation of FDS V.4: Upward Flame Spread. *Fire Technology*, 43:255–284, 2007. 10

- [68] J. Mangs and S. Hostikka. Experiments and Numerical Simulations of Vertical Flame Spread on Charring Materials at Different Ambient Temperatures. In *Fire Safety Science 10 – Proceedings of the 10th International Symposium*, pages 499–512, University of Maryland, College Park, Maryland, USA, 2011. [11](#)
- [69] A. Hamins, A. Maranghides, K.B. McGrattan, E. Johnsson, T. Ohlemiller, M. Donnelly, J. Yang, G. Mulholland, K. Prasad, S. Kukuck, R. Anleitner, and T. McAllister. Federal Building and Fire Safety Investigation of the World Trade Center Disaster: Experiments and Modeling of Structural Steel Elements Exposed to Fire. NIST NCSTAR 1-5B, National Institute of Standards and Technology, Gaithersburg, Maryland, September 2005. [11, 67, 288](#)
- [70] A. Hamins, A. Maranghides, K.B. McGrattan, Ohlemiller, and R. Anletiner. Federal Building and Fire Safety Investigation of the World Trade Center Disaster: Experiments and Modeling of Multiple Workstations Burning in a Compartment. NIST NCSTAR 1-5E, National Institute of Standards and Technology, Gaithersburg, Maryland, September 2005. [11](#)
- [71] K. McGrattan, C. Bouldin, and G. Forney. Federal Building and Fire Safety Investigation of the World Trade Center Disaster: Computer Simulation of the Fires in the WTC Towers. NIST NCSTAR 1-5F, National Institute of Standards and Technology, Gaithersburg, Maryland, September 2005. [11, 15](#)
- [72] G. Rein, C. Abecassis Empis, and R. Carvel, editors. *The Dalmarnock Fire Tests: Experiments and Modelling*. University of Edinburgh, 2007. [11](#)
- [73] G. Rein, J.L. Torero, W. Jahn, J. Stern-Gottfried, N.L. Ryder, S. Desanghere, M. Lázaro, F. Mowrer, A. Coles, D. Joyeux, D. Alvear, J.A. Capote, A. Jowsey, C. Abecassis-Empis, and P. Reszka. Round-Robin Study of a priori Modelling Predictions of The Dalmarnock Fire Test One. *Fire Safety Journal*, 44(4):590–602, 2009. ([Web Link](#)). [11](#)
- [74] W. Jahn, G. Rein, and J.L. Torero. The Effect of Model Parameters on the Simulation of Fire Dynamics. In *Proceedings of the Ninth Symposium on Fire Safety Science*, September 2008. Karlsruhe, Germany ([Web Link](#)). [11](#)
- [75] B.M. Storm and M.R. Pantesjö. The use of simulation in fire investigation. Bachelors thesis, Stord/Haugesund University College, Norway, 2009. [11](#)
- [76] R. Vettori. Effect of an Obstructed Ceiling on the Activation Time of a Residential Sprinkler. NISTIR 6253, National Institute of Standards and Technology, Gaithersburg, Maryland, November 1998. [12, 63, 84](#)
- [77] R. Vettori. Effect of a Beamed, Sloped, and Sloped Beamed Ceilings on the Activation Time of a Residential Sprinkler. NISTIR 7079, National Institute of Standards and Technology, Gaithersburg, Maryland, December 2003. [12, 66](#)
- [78] K.B. McGrattan, A. Hamins, and D. Stroup. Sprinkler, Smoke & Heat Vent, Draft Curtain Interaction — Large Scale Experiments and Model Development. NISTIR 6196-1, National Institute of Standards and Technology, Gaithersburg, Maryland, September 1998. [12, 53](#)
- [79] A. Hamins and K.B. McGrattan. Reduced-Scale Experiments to Characterize the Suppression of Rack Storage Commodity Fires. NISTIR 6439, National Institute of Standards and Technology, Gaithersburg, Maryland, 1999. [12](#)

- [80] A. Hamins and K.B. McGrattan. Reduced-Scale Experiments on the Water Suppression of a Rack-Storage Commodity Fire for Calibration of a CFD Fire Model. In *Fire Safety Science – Proceedings of the Seventh International Symposium*, pages 457–468. International Association for Fire Safety Science, 2002. [12](#)
- [81] S. Olenick, M. Klassen, and R.J. Roby. Validation Study for FDS for a High Rack Storage Fire Involving Pool Chemicals. In *Proceedings of the 3rd Technical Symposium on Computer Applications in Fire Protection Engineering*. Society of Fire Protection Engineers, Bethesda, Maryland, September 2001. [12](#)
- [82] S.C. Kim and H.S. Ryou. An Experimental and Numerical Study on Fire Suppression using a Water Mist in an Enclosure. *Building and Environment*, 38:1309–1316, 2003. [12](#)
- [83] S.C. Kim and H.S. Ryou. The Effects of Water Mist on the Compartment Fire. *International Journal of Air-Conditioning and Refrigeration*, 12(1):30–36, 2004. [12](#)
- [84] B.P. Hume. Water Mist Suppression in Conjunction with Displacement Ventilation. Master's thesis, University of Canterbury, Christchurch, New Zealand, February 2003. Fire Engineering Research Report 03/4. [12](#)
- [85] S. Hostikka and K.B. McGrattan. Numerical modeling of radiative heat transfer in water sprays. *Fire Safety Journal*, 41:76–86, 2006. [12](#)
- [86] N. O'Grady and V. Novozhilov. Large Eddy Simulation of Sprinkler Interaction with a Fire Ceiling Jet. *Combustion Science and Technology*, 181(7):984–1006, 2009. [12](#)
- [87] H. Ingason and S. Olsson. Interaction between Sprinklers and Fire Vents. Technical report, Swedish National Testing and Research Institute (SP), 1992. SP Report 1992:11. [12](#)
- [88] B. Xiao. Comparison of Numerical and Experimental Results of Fire Induced Doorway Flows. *Fire Technology*, 48:595–614, 2012. [12](#)
- [89] P. Friday and F. W. Mowrer. Comparison of FDS Model Predictions with FM/SNL Fire Test Data. NIST GCR 01-810, National Institute of Standards and Technology, Gaithersburg, Maryland, April 2001. [13](#)
- [90] W. Zhang, A. Hamer, M. Klassen, D. Carpenter, and R. Roby. Turbulence Statistics in a Fire Room Model by Large Eddy Simulation. *Fire Safety Journal*, 37:721–752, 2002. [13](#)
- [91] S. Cochard. Validation of Fire Dynamics Simulator (Version 2.0) Freeware. *Tunnel Management International Journal*, 6(4), December 2003. [13](#)
- [92] K. B. McGrattan and A. Hamins. Numerical Simulation of the Howard Street Tunnel Fire, Baltimore, Maryland, July 2001. NISTIR 6902, National Institute of Standards and Technology, Gaithersburg, Maryland, January 2003. Joint Publication of NIST and the US Nuclear Regulatory Commission (NUREG/CR-6793). [13](#)
- [93] A. Piergiorgio, D. Giuseppe, F. Dino, G. Zappellini, and A. Ferrari. CFD Simulations of a Truck Fire in the Underground Gran Sasso National Laboratory. In *Proceedings of the 5th Italian Conference on Chemical and Process Engineering*, volume 5 of *AIDIC Conference Series*. Associazione Italiana Di Ingegneria Chimica (AIDIC), Elsevier, May 2002. Papers presented at ICeAP-5, Florence, Italy, May 20-23, 2001. [13](#)

- [94] J.C. Edwards, R.A. Franks, G.F. Friel, and L. Yuan. Experimental and Modeling Investigation of the Effect of Ventilation on Smoke Rollback in a Mine Entry. In *Proceedings of the SME Annual Meeting*, pages 1–6. Society for Mining, Metallurgy and Exploration, 2005. [13](#)
- [95] C.C. Hwang and J.C. Edwards. The critical ventilation velocity in tunnel fires – a computer simulation. *Fire Safety Journal*, 40:213–244, 2005. [13](#)
- [96] J.C. Edwards and C.C. Hwang. CFD Modeling of Fire Spread Along Combustibles in a Mine Entry. In *Proceedings of the SME Annual Meeting*, pages 1–5. Society for Mining, Metallurgy and Exploration, 2006. [13](#)
- [97] M. Bilson, A. Purchase, and C. Stacey. Deluge System Operating Effectiveness in Road Tunnels and Impacts on Operating Policy. In *Proceedings 13th Australian Tunnelling Conference, Melbourne, Victoria, Australia*, May 2008. The Australasian Institute of Mining and Metallurgy. [13](#)
- [98] K.J. Harris. Water Application Rates for Fixed Fire Fighting Systems in Road Tunnels. In *Proceedings of the Fourth International Symposium on Tunnel Safety and Security*, pages 351–362, 2010. [13](#)
- [99] M. Arvidson. Large-Scale Water Spray and Water Mist Fire Suppression System Tests. In *Proceedings of the Fourth International Symposium on Tunnel Safety and Security*, pages 283–296, 2010. [13](#)
- [100] J. Trelles and J.R. Mawhinney. CFD Investigation of Large Scale Pallet Stack Fires in Tunnels Protected by Water Mist Systems. *Journal of Fire Protection Engineering*, 20(3):149–198, August 2010. [13](#)
- [101] J.R. Mawhinney and J. Trelles. Testing Water Mist Systems Against Large Fires in Tunnels: Integrating Test Data with CFD Simulations. *Fire Technology*, 48:565–594, 2012. [13](#)
- [102] V. D’Souza, J.A. Sutula, S.M. Olenick, W. Zhang, and R.J. Roby. Use of Fire Dynamics Simulator to Predict Smoke Detector Activation. In *Proceedings of the 2001 Fall Technical Meeting, Eastern States Section*, pages 175–178. Combustion Institute, Pittsburgh, Pennsylvania, December 2001. [13](#)
- [103] R.J. Roby, S.J. Olenick, W. Zhang, D.J. Carpenter, M.S. Klassen, and J.L. Torero. A Smoke Detector Algorithm for Large Eddy Simulation Modeling. NIST GCR 07-911, National Institute of Standards and Technology, Gaithersburg, Maryland, 2007. [14](#)
- [104] W. Zhang, S.M. Olenick, M.S. Klassen, D.J. Carpenter, R.J. Roby, and J.L. Torero. A smoke detector activation algorithm for large eddy simulation fire modeling. *Fire Safety Journal*, 43:96–107, 2008. [14](#)
- [105] D.R. Brammer. A Comparison between Predicted and Actual Behaviour of Domestic Smoke Detectors in a Realistic House Fire. Master’s thesis, University of Canterbury, Christchurch, New Zealand, 2002. [14](#)
- [106] T. Cleary, M. Donnelly, G. Mulholland, and B. Farouk. Fire Detector Performance Predictions in a Simulated Multi-Room Configuration. In *Proceedings of the 12th International Conference on Automatic Fire Detection (AUBE ’01)*. National Institute of Standards and Technology, Gaithersburg, Maryland, March 2001. NIST SP 965. [14](#)
- [107] A. Mukhopadhyay and I.K. Puri. An Assessment of Stretch Effects on Flame Tip Using the Thin Flame and Thick Formulations. *Combustion and Flame*, 133:499–502, 2003. [14](#)

- [108] A. Hamins, M. Bundy, I.K. Puri, K.B. McGrattan, and W.C. Park. Suppression of Low Strain Rate Non-Premixed Flames by an Agent. In *Proceedings of the 6th International Microgravity Combustion Workshop, NASA/CP-2001-210826*, pages 101–104. National Aeronautics and Space Administration, Lewis Research Center, Cleveland, Ohio, May 2001. [14](#)
- [109] S. Dillon and A. Hamins. Ignition Propensity and Heat Flux Profiles of Candle Flames for Fire Investigation. In Vytenis Babrauskas, editor, *Fire Science Applications to Fire Investigations*, pages 363–376. Interscience Communications, London, 2003. [14](#)
- [110] A. Hamins, M. Bundy, and S.E. Dillon. Characterization of Candle Flames. *Journal of Fire Protection Engineering*, 15(4):265–285, 2005. [14](#)
- [111] J.E. Floyd, C. Wieczorek, and U. Vandsburger. Simulations of the Virginia Tech Fire Research Laboratory Using Large Eddy Simulation with Mixture Fraction Chemistry and Finite Volume Radiative Heat Transfer. In *Proceedings of the Ninth International Interflam Conference*. Interscience Communications, London, 2001. [14](#)
- [112] Y. Xin and J.P. Gore. Measurements and Calculations of Spectral Radiation Intensities in Buoyant Turbulent Flames. In *Proceedings of the Third Joint Meeting of the U.S. Sections of the Combustion Institute*. Combustion Institute, Pittsburgh, Pennsylvania, 2003. [14](#)
- [113] W. Zhang, N. Ryder, R.J. Roby, and D. Carpenter. Modeling of the Combustion in Compartment Fires Using Large Eddy Simulation Approach. In *Proceedings of the 2001 Fall Technical Meeting, Eastern States Section*. Combustion Institute, Pittsburgh, Pennsylvania, December 2001. [14](#)
- [114] D. Gottuk, C. Mealy, and J. Floyd. Smoke Transport and FDS Validation. In *Fire Safety Science – Proceedings of the Ninth International Symposium*, pages 129–140. International Association for Fire Safety Science, 2008. [14, 15](#)
- [115] A. Hamins, A. Maranghides, R. Johnsson, M. Donnelly, G. Yang, G. Mulholland, and R.L. Anleitner. Report of Experimental Results for the International Fire Model Benchmarking and Validation Exercise 3. NIST Special Publication 1013-1, National Institute of Standards and Technology, Gaithersburg, Maryland, May 2006. Joint Publication of NIST and the US Nuclear Regulatory Commission (NUREG/CR-6905). [14, 15, 40, 79, 80, 82, 83](#)
- [116] J. Floyd and R. McDermott. Modeling Soot Deposition Using Large Eddy Simulation with a Mixture Fraction Based Framework. In *Proceedings of the Twelfth International Interflam Conference*. Interscience Communications, London, 2010. [15](#)
- [117] S. Riahi. *New Tools for Smoke Residue and Deposition Analysis*. PhD thesis, The George Washington University, Washington, DC, 2011. [15](#)
- [118] B.D. Cohan. Verification And Validation Of A Candidate Soot Deposition Model In Fire Dynamics Simulator Version 5.5.1. Master's thesis, University of Maryland, 2010. [15](#)
- [119] K.J. Overholt and O.A. Ezekoye. An Inverse Fire Modeling Methodology for the Determination of Fire Size, Fire Location, and Soot Deposition in a Compartment. In *Proceedings of 2012 ASME International Mechanical Engineering Congress and Exposition*. American Society of Mechanical Engineering, November 2012. IMECE2012-88924. [15](#)
- [120] W.L. Grosshandler, N. Bryner, D. Madrzykowski, and K. Kuntz. Report of the Technical Investigation of The Station Nightclub Fire. NIST NCSTAR 2, National Institute of Standards and Technology, Gaithersburg, MD, June 2005. [15](#)

- [121] D. Madrzykowski and R.L. Vettori. Simulation of the Dynamics of the Fire at 3146 Cherry Road NE Washington D.C., May 30, 1999. NISTIR 6510, National Institute of Standards and Technology, Gaithersburg, Maryland, April 2000. [15](#)
- [122] R.L. Vettori, D. Madrzykowski, and W.D. Walton. Simulation of the Dynamics of a Fire in a One-Story Restaurant – Texas, February 14, 2000. NISTIR 6923, National Institute of Standards and Technology, Gaithersburg, Maryland, October 2002. [15](#)
- [123] D. Madrzykowski, G.P. Forney, and W.D. Walton. Simulation of the Dynamics of a Fire in a Two-Story Duplex, Iowa, December 22, 1999. NISTIR 6854, National Institute of Standards and Technology, Gaithersburg, Maryland, January 2002. [15](#)
- [124] D. Madrzykowski and W.D. Walton. Cook County Administration Building Fire, 69 West Washington, Chicago, Illinois, October 17, 2003: Heat Release Rate Experiments and FDS Simulations. NIST Special Publication SP-1021, National Institute of Standards and Technology, Gaithersburg, Maryland, July 2004. [15](#)
- [125] N. Bryner, S.P. Fuss, B.W. Klein, and A.D. Putorti. Technical Study of the Sofa Super Store Fire, South Carolina, June 18, 2007. NIST Special Publication 1118, National Institute of Standards and Technology, Gaithersburg, MD, March 2011. [15](#)
- [126] P. Camp and N. Townsend. Computer Modelling vs Reality – Can We Predict the Behaviour of Fires? In *Proceedings of the Ninth International Interflam Conference*, pages 195–202. Interscience Communications, London, 2001. [15](#)
- [127] G. Rein, A. Bar-Ilan, N. Alvares, and A.C. Fernandez-Pello. Estimating the Performance of Enclosure Fire Models by Correlating Forensic Evidence of Accidental Fires. In *Proceedings of the Tenth International Interflam Conference*, pages 1183–1194. Interscience Communications, London, 2004. [16](#)
- [128] M. Spearpoint, F.W. Mowrer, and K. McGrattan. Simulation of a Compartment Flashover Fire Using Hand Calculations, Zone Models and a Field Model. In *Proceedings of the Third International Conference on Fire Research and Engineering (ICFRE3)*, pages 3–14. Society of Fire Protection Engineers, Bethesda, Maryland, 1999. [16](#)
- [129] D.J. Carpenter and C.B. Wood, editors. *Proceedings of the 3rd Technical Symposium on Computer Applications in Fire Protection Engineering*. Society for Fire Protection Engineers, Bethesda, Maryland, September 2001. [16](#)
- [130] A.M. Christensen and D.J. Icove. The Application of NIST's Fire Dynamics Simulator to the Investigation of Carbon Monoxide Exposure in the Deaths of Three Pittsburgh Fire Fighters. *Journal of Forensic Sciences*, 49(1):1–4, 2004. [16](#)
- [131] D.T. Sheppard and B.W. Klein. Burn Tests in Two Story Structure with Hallways. Technical report, ATF Laboratories, Ammendale, Maryland, 2009. [17](#)
- [132] C. Belyer. Major Species Production by Diffusion Flames in a Two-Layer Compartment Fire Environment. *Fire Safety Journal*, 10:47–56, 1986. [19](#)
- [133] A. Bouchair. *Solar Induced Ventilation in the Algerian and Similar Climates*. PhD thesis, University of Leeds, Leeds, West Yorkshire, England, 1989. [20](#), [603](#)

- [134] L. Shi and G. Zhang. An empirical model to predict the performance of typical solar chimneys considering both room and cavity configurations. *Building and Environment*, 103:250–261, 2016. [20](#)
- [135] J.V. Murrel, D. Crowhurst, and P. Rock. Experimental Study of The Thermal Radiation Attenuation of Sprays from Selected Hydraulic Nozzles. In *Proceedings of Halon Options Technical Working Conference 1995*, pages 369–378. The University of New Mexico, Albuquerque, 1995. [21](#)
- [136] R.A. Bryant. A comparison of gas velocity measurements in a full-scale enclosure fire. *Fire Safety Journal*, 44:793–800, 2009. [21](#), [80](#), [273](#)
- [137] R.A. Bryant. The application of stereoscopic particle image velocimetry to measure the flow of air into an enclosure containing fire. *Experiments in Fluids*, 47:295–308, 2009. [21](#)
- [138] R.A. Bryant. Evaluating practical measurements of fire-induced vent flows with stereoscopic PIV. In *Proceedings of the Combustion Institute*. Elsevier, 2010. [21](#)
- [139] S.P. Nowlen, F.J. Wyant, and K.B. McGrattan. Cable Response to Live Fire (CAROLFIRE). NUREG/CR 6931, United States Nuclear Regulatory Commission, Washington, DC, April 2008. [21](#), [501](#)
- [140] P. Andersson and P. Van Hees. Performance of Cables Subjected to Elevated Temperatures. In *Fire Safety Science – Proceedings of the Eighth International Symposium*, pages 1121–1132. International Association of Fire Safety Science, 2005. [21](#)
- [141] N.P. Cheney, J.S. Gould, and W.R. Catchpole. The Influence of Fuel, Weather and Fire Shape Variables on Fire-Spread in Grasslands. *International Journal of Wildland Fire*, 3(1):31–44, 1993. [23](#), [661](#)
- [142] W. Mell, M.A. Jenkins, J. Gould, and P. Cheney. A physics-based approach to modelling grassland fires. *International Journal of Wildland Fire*, 16(1):1–22, 2007. [23](#)
- [143] F. Takahashi, G.T. Linteris, and V.R. Katta. Extinguishment Mechanisms of Coflow Diffusion Flames in a Cup-Burner Apparatus. *Proceedings of the Combustion Institute*, 31:2721–2729, 2007. [23](#)
- [144] T.A. Moore, C.A. Weitz, and R.E. Tapscott. An update on NMERI cup-burner test results. In *Halon Options Technical Working Conference*, New Mexico, USA, 1996. [23](#)
- [145] J.M. Willi, C. Weinschenk, and D. Madrzykowski. Propane Gas Fire Experiments in Residential Scale Structures. NIST Technical Note XXXX, National Institute of Standards and Technology, Gaithersburg, Maryland, 2016. [23](#)
- [146] J. Suo-Anttila, W. Gill, C. Gallegos, and J. Nelsen. Computational Fluid Dynamics Code for Smoke Transport During an Aircraft Cargo Compartment Fire: Transport Solver, Graphical User Interface, and Preliminary Baseline Validation. Report DOT/FAA/AR-03/49, Federal Aviation Administration, Office of Aviation Research, Washington, DC 20591, October 2003. [23](#)
- [147] J. Suo-Anttila, W. Gill, A. Luketa-Hanlin, and C. Gallegos. Cargo Compartment Smoke Transport Computational Fluid Dynamics Code Validation. Report DOT/FAA/AR-07/27, Federal Aviation Administration, Office of Aviation Research and Development, Washington, DC 20591, July 2007. [23](#)
- [148] D. Blake. Development of a Standardized Fire Source for Aircraft Cargo Compartment Fire Detection Systems. Report DOT/FAA/AR-06/21, Federal Aviation Administration, Office of Aviation Research and Development, Washington, DC 20591, May 2006. [23](#)

- [149] S.I. Stoliarov, S. Crowley, R.E. Lyon, and G.T. Linteris. Prediction of the burning rates of non-charring polymers. *Combustion and Flame*, 156:1068–1083, 2009. [24](#), [625](#)
- [150] S.I. Stoliarov, S. Crowley, R.N. Walters, and R.E. Lyon. Prediction of the burning rates of charring polymers. *Combustion and Flame*, 157:2024–2034, 2010. [24](#), [629](#), [631](#), [633](#)
- [151] R. Fleury. Evaluation of Thermal Radiation Models for Fire Spread Between Objects. Master's thesis, University of Canterbury, Christchurch, New Zealand, 2010. [24](#)
- [152] S. Thumuluru, B. Ditch, P. Chatterjee, and M. Chaos. Experimental Data for Modeling Validation of Smoke Transport in Data Centers. Technical report, FM Global, Norwood, Massachusetts, 2014. [26](#)
- [153] J. Floyd, H. Boehmer, and D. Gottuk. Validation of Modeling Tools for Detection Design in High Air flow Environments: Phase II – Task 4b and 4c: Full Scale Model Verification and Validation. Technical report, Fire Protection Research Foundation, Quincy, Massachusetts, 2014. [26](#)
- [154] P.A. Beaulieu. Parallel Panel Experiments of FRP Composites. Technical Report 0003024286, FM Global, Norwood, Massachusetts, December 2007. [26](#)
- [155] S.P. Nowlen. Enclosure Environment Characterization Testing for the Baseline Validation of Computer Fire Simulation Codes. NUREG/CR-4681 (SAND86-1296), Sandia National Laboratory, Albuquerque, New Mexico, March 1987. Work performed under contract to the US Nuclear Regulatory Agency, Washington DC. [26](#)
- [156] J.M. Chavez and S.P. Nowlen. An Experimental Investigation of Internally Ignited Fires in Nuclear Power Plant Control Cabinets, Part II: Room Effects Tests. NUREG/CR-4527 (SAND86-0336), Sandia National Laboratory, Albuquerque, New Mexico, November 1988. Work performed under contract to the US Nuclear Regulatory Agency, Washington DC. [26](#)
- [157] R. Harrison. *Entrainment of air into thermal spill plumes*. PhD thesis, University of Canterbury, Christchurch, New Zealand, 2009. [30](#), [176](#)
- [158] R. Harrison and M. Spearpoint. Characterization of Balcony Spill Plume Entrainment using Physical Scale Modeling. In *Fire Safety Science – Proceedings of the Ninth International Symposium*, pages 727–738. International Association for Fire Safety Science, 2008. [30](#)
- [159] R. Harrison and M. Spearpoint. The balcony spill plume: entrainment of air into a flow from a compartment opening to a higher projecting balcony. *Fire Technology*, 43(4):301–317, 2007. [30](#)
- [160] R. Harrison and M. Spearpoint. Physical scale modeling of adhered spill plume entrainment. *Fire Safety Journal*, 45:149–158, 2010. [30](#)
- [161] G. Heskestad. Luminous Heights of Turbulent Diffusion Flames. *Fire Safety Journal*, 5:103–108, 1983. [30](#)
- [162] S. Lechêne. *Étude expérimentale et numérique des rideaux d'eau pour la protection contre le rayonnement thermique*. PhD thesis, Université Henri Poincaré, Nancy, France, 2010. [30](#)
- [163] K.L. Foote. 1986 LLNL Enclosure Fire Tests Data Report. Technical Report UCID-21236, Lawrence Livermore National Laboratory, August 1987. [32](#)
- [164] M.J. Ivings, S.E. Gant, S.F. Jagger, C.J. Lea, J.R. Stewart, and D.M. Webber. Evaluating vapor dispersion models for safety analysis of LNG facilities. Report Number MSU/2016/17, Health and Safety Laboratory, Buxton, Derbyshire, United Kingdom, September 2016. [32](#)

- [165] J.R. Stewart, S. Coldrick, C.J. Lea, S.E. Gant, and M.J. Ivings. Validation Database for Evaluating Vapor Dispersion Models for Safety Analysis of LNG Facilities: Guide to the LNG Model Validation Database Version 12. Report Number MSU/2016/12, Health and Safety Laboratory, Buxton, Derbyshire, United Kingdom, September 2016. [32](#)
- [166] B.J. McCaffrey. Purely Buoyant Diffusion Flames: Some Experimental Results. NBSIR 79-1910, National Bureau of Standards (now NIST), Gaithersburg, Maryland, October 1979. [32](#)
- [167] R.D. Peacock, S. Davis, and W.T. Lee. An Experimental Data Set for the Accuracy Assessment of Room Fire Models. NBSIR 88-3752, National Bureau of Standards (now NIST), Gaithersburg, Maryland, April 1988. [32](#)
- [168] W. Mell, A. Maranghides, R. McDermott, and S. Manzello. Numerical simulation and experiments of burning Douglas fir trees. *Combustion and Flame*, 156:2023–2041, 2009. [35](#), [662](#), [663](#)
- [169] N. Bryner, E. Johnsson, and W. Pitts. Carbon Monoxide Production in Compartment Fires - Reduced-Scale Test Facility. NISTIR 5568, National Institute of Standards and Technology, Gaithersburg, MD, 1994. [35](#), [334](#)
- [170] M. Bundy, A. Hamins, E.L. Johnsson, S.C. Kim, G.H. Ko, and D.B. Lenhert. Measurements of Heat and Combustion Products in Reduced-Scale Ventilation-Limited Compartment Fires. NIST Technical Note 1483, National Institute of Standards and Technology, Gaithersburg, Maryland, 2007. [35](#)
- [171] A. Lock, M. Bundy, E.L. Johnsson, A. Hamins, G.H. Ko, C. Hwang, P. Fuss, and R. Harris. Experimental Study of the Effects of Fuel Type, Fuel Distribution, and Vent Size on Full-Scale Underventilated Compartment Fires in an ISO 9705 Room . NIST Technical Note 1603, National Institute of Standards and Technology, Gaithersburg, Maryland, 2008. [37](#), [349](#)
- [172] W.M. Pitts, J.C. Yang, and M.G. Fernandez. Experimental Characterization of Helium Dispersion in a 1/4-Scale Two-Car Residential Garage. NIST Technical Note 1694, National Institute of Standards and Technology, Gaithersburg, Maryland, March 2011. [37](#)
- [173] R.W. Bukowski, R.D. Peacock, J.D. Averill, T.G. Cleary, N.P. Bryner, W.D. Walton, P.A. Reneke, and E.D. Kuligowski. Performance of Home Smoke Alarms Analysis of the Response of Several Available Technologies in Residential Fire Settings. NIST Technical Note 1455-1, National Institute of Standards and Technology, Gaithersburg, Maryland, February 2008. [42](#), [84](#), [262](#)
- [174] I. Oleszkiewicz. Heat Transfer from a Window Fire Plume to a Building Facade. In *HTD – Collected Papers in Heat Transfer*, volume 123, pages 163–170. American Society of Mechanical Engineers, 1989. Book No. H00526. [44](#)
- [175] I. Oleszkiewicz. Fire Exposure to Exterior Walls and Flame Spread on Combustible Cladding. *Fire Technology*, 26(4):357–375, 1990. [44](#)
- [176] Y. Wang. A Study of Smoke Movement in Multi-storey Buildings Using Experiments and Computer Modelling. Master's thesis, Carleton University, Ottawa, Ontario, Canada, 2008. [44](#)
- [177] Y. Wang, E. Zalok, and G. Hadjisophocleous. An Experimental Study of Smoke Movement in Multi-Storey Buildings. *Fire Technology*, 47:1141–1169, 2011. [44](#)
- [178] G. Hadjisophocleous and Q. Jia. Comparison of FDS Prediction of Smoke Movement in a 10-Storey Building with Experimental Data. *Fire Technology*, 45:163–177, 2009. [44](#)

- [179] P.J. Tyson. Validation of Fire Dynamics Simulator (FDS) v6.2 for Smoke and Heat Transport in Multi-Storey Multi-Compartment Buildings. Master's thesis, Ulster University, Londonderry, Northern Ireland, United Kingdom, 2015. [44](#)
- [180] G.Y. Achakji. NRCC Experimental Fire Tower for Studies on Smoke Movement and Smoke Control in Tall Buildings. Internal Report No. 512, National Research Council Canada, 1987. [47](#)
- [181] National Fire Protection Association, Quincy, Massachusetts. *NFPA 92, Standard for Smoke Control Systems*, 2012. [47](#)
- [182] G. Back, C. Beyler, P. DiNenno, and P. Tatem. Wall Incident Heat Flux Distributions Resulting from an Adjacent Fire. In *Fire Safety Science – Proceedings of the Fourth International Symposium*, pages 241–252. International Association of Fire Safety Science, 1994. [47](#)
- [183] L. Audouin, L. Rigollet, H. Prétrel, W. LeSaux, and M. Röwekamp. OECD PRISME project: Fires in confined and ventilated nuclear-type multi-compartments—Overview and main experimental results. *Fire Safety Journal*, 62:80–101, 2013. [47](#)
- [184] J. Wahlqvist and P. van Hees. Validation of FDS for large-scale well-confined mechanically ventilated fire scenarios with emphasis on predicting ventilation system behavior. *Fire Safety Journal*, 62:102–114, 2013. [47](#)
- [185] J. Dreisbach, S. Nowlen, K. McGrattan, and S. Hostikka. Electrical Cable Failure – Experiments and Simulation. In *Interflam 2010: Proceedings of the Twelfth International Symposium*, pages 1857–1866. Interscience Communications, London, 2010. [47, 507](#)
- [186] Y. Xin. *A theoretical and experimental study of buoyant turbulent flames with emphasis on soot and radiation*. PhD thesis, Purdue University, West Lafayette, USA, 2002. [48](#)
- [187] X.C. Zhou. *An experimental and theoretical investigation of flows induced by buoyant diffusion flames*. PhD thesis, Purdue University, West Lafayette, USA, 1999. [48](#)
- [188] A. Restivo. Turbulent Flow in Ventilated Rooms. Technical report, University of London, Department of Mechanical Engineering, 1979. [48](#)
- [189] T. J. O'Hern, E. J. Weckman, A. L. Gerhart, S. R. Tieszen, and R. W. Schefer. Experimental study of a turbulent buoyant helium plume. *J. Fluid Mech.*, 544:143–171, 2005. [48, 177](#)
- [190] T. K. Blanchat. Characterization of the air source and plume source at FLAME. Technical Report SAND01-2227, Sandia National Laboratory, Albuquerque, New Mexico, 2001. [48, 177](#)
- [191] P. E. DesJardin, T. J. O'Hern, and S. R. Tieszen. Large eddy simulation and experimental measurements of the near-field of a large turbulent helium plume. *Physics of Fluids*, 16(6):1866–1883, 2004. [48, 177](#)
- [192] S. R. Tieszen, T. J. O'Hern, E. J. Weckman, and R. W. Schefer. Experimental study of the effect of fuel mass flux on a 1-m-diameter methane fire and comparison with a hydrogen fire. *Combustion and Flame*, 139:126–141, 2004. [48, 182, 188](#)
- [193] S. R. Tieszen, T. J. O'Hern, R. W. Schefer, E. J. Weckman, and T. K. Blanchat. Experimental study of the flow field in and around a one meter diameter methane fire. *Combustion and Flame*, 129:378–391, 2002. [48, 182, 187](#)

- [194] M. Sippola. *Particle Deposition in Ventilation Ducts*. PhD thesis, University of California, Berkeley, Berkeley, California, 2002. [48](#)
- [195] M. Sippola and W.W. Nazaroff. Experiments Measuring Particle Deposition from Fully Developed Turbulent Flow in Ventilation Ducts. *Aerosol Science and Technology*, 38:914–925, 2010. [48](#)
- [196] T.S. Norton, K.C. Smyth, J.H. Miller, and M.D. Smooke. Comparison of Experimental and Computed Species Concentration and Temperature Profiles in Laminar, Two-Dimensional Methane/Air Diffusion Flames. *Combustion Science and Technology*, 90:1–34, 1993. [49](#)
- [197] K.C. Smyth. NO Production and Destruction in a Methane/Air Diffusion Flame. *Combustion Science and Technology*, 115:151–176, 1996. [49](#)
- [198] U. Wickström, R. Jansson, and H. Tuovinen. Verification fire tests on using the adiabatic surface temperature for predicting heat transfer. Technical Report 2009:19, SP Technical Research Institute of Sweden, Bōras, Sweden, 2009. [49, 461](#)
- [199] J. Sjöström, A. Byström, and U. Wickström. Large scale test on thermal exposure to steel column exposed to pool fires. Technical Report 2012:04, SP Technical Research Institute of Sweden, Bōras, Sweden, 2012. ISBN: 978-91-87017-21-6. [50, 164, 471](#)
- [200] J. Sjöström, U. Wickström, and A. Byström. Validation data for room fire models: Experimental background. Technical Report 2016:54, SP Technical Research Institute of Sweden, Bōras, Sweden, 2016. ISBN: 978-91-88349-56-9. [51, 475](#)
- [201] K.D. Steckler, J.G. Quintiere, and W.J. Rinkinen. Flow Induced By Fire in A Compartment. NBSIR 82-2520, National Bureau of Standards (now NIST), Gaithersburg, Maryland, September 1982. [51, 139, 280](#)
- [202] K.M. Oper. Assessment of Natural Vertical Ventilation for Smoke and Hot Gas Layer Control in a Residential Scale Structure. Master's thesis, University of Maryland, College Park, Maryland, 2012. [51](#)
- [203] D.T. Sheppard and D.R. Steppan. Sprinkler, Heat & Smoke Vent, Draft Curtain Project – Phase 1 Scoping Tests. Technical report, Underwriters Laboratories, Northbrook, Illinois, May 1997. [53, 54](#)
- [204] J.M.A Troup. Large-Scale Fire Tests of Rack Stored Group A Plastics in Retail Operation Scenarios Protected by Extra Large Orifice (ELO) Sprinklers. Technical Report FMRC J.I. 0X1R0.RR, Factory Mutual Research Corporation, Norwood, Massachusetts, November 1994. Prepared for Group A Plastics Committee, Lansdale, Pennsylvania. [59](#)
- [205] J.P. Zhang, M. Delichatsios, M. Colobert, J. Hereid, M. Hagen, and D. Bakirtzis. Experimental and Numerical Investigations of Heat Impact and Flame Heights from Fires in SBI Tests. In *Proceedings of the Ninth Symposium on Fire Safety Science*, September 2008. Karlsruhe, Germany. [60](#)
- [206] J. Li, J. Gong, and S.I. Stoliarov. Gasification Experiments for Pyrolysis Model Parameterization and Validation. *International Journal of Heat and Mass Transfer*, 77:738–744, 2014. [60, 640](#)
- [207] J. Li and S.I. Stoliarov. Measurement of kinetics and thermodynamics of the thermal degradation for non-charring polymers. *Combustion and Flame*, 160:1287–1297, 2013. [60, 640](#)
- [208] J. Li and S.I. Stoliarov. Measurement of kinetics and thermodynamics of the thermal degradation for charring polymers. *Polymer Degradation and Stability*, 106:2–15, 2014. [60, 640](#)

- [209] J. Li, J. Gong, and S.I. Stoliarov. Development of pyrolysis models for charring polymers. *Polymer Degradation and Stability*, 115:138–152, 2015. [60](#), [640](#), [643](#)
- [210] J. P. White, E. D. Link, A. C. Trouvé, P. B. Sunderland, A. W. Marshall, J. A. Sheffel, M. L. Corn, M. B. Colket, M. Chaos, and H.-Z. Yu. Radiative emissions measurements from a buoyant, turbulent line flame under oxidizer-dilution quenching conditions. *Fire Safety Journal*, 76:74–84, 2015. [61](#), [195](#), [315](#)
- [211] G. Back, B. Lattimer, C. Beyler, P. DiNenno, and R. Hansen. Full-Scale Testing of Water Mist Fire Suppression Systems for Small Machinery Spaces and Spaces with Combustible Boundaries, Volume I. Report CG-D-21-99, I, U.S. Coast Guard Research and Development Center, 1082 Shennecossett Road, Groton, Connecticut, 06340, October 1999. [63](#)
- [212] J.E. Gott, D.L. Lowe, K.A. Notarianni, and W.D. Davis. Analysis of High Bay Hangar Facilities for Fire Detector Sensitivity and Placement. NIST Technical Note 1423, National Institute of Standards and Technology, Gaithersburg, Maryland, February 1997. [63](#)
- [213] S. Hostikka, M. Kokkala, and J. Vaari. Experimental Study of the Localized Room Fires. VTT Research Notes 2104, VTT Technical Research Centre of Finland, Espoo, Finland, 2001. [66](#)
- [214] A. Tewarson. *SFPE Handbook of Fire Protection Engineering*, chapter Generation of Heat and Gaseous, Liquid, and Solid Products in Fires. National Fire Protection Association, Quincy, Massachusetts, fourth edition, 2008. [67](#), [336](#), [572](#), [582](#), [658](#), [661](#), [663](#)
- [215] J. Vaari, S. Hostikka, T. Sikanen, and A. Paajanen. Numerical simulations on the performance of water-based fire suppression systems. VTT Technology Report 54, VTT Technical Research Centre of Finland, Espoo, Finland, 2012. [67](#)
- [216] K.A. Notarianni and G.W. Parry. *SFPE Handbook of Fire Protection Engineering*, chapter Uncertainty. National Fire Protection Association, Quincy, Massachusetts, 4th edition, 2008. [75](#)
- [217] N.O. Siu and G.E. Apostolakis. Probabilistic Models for Cable Tray Fires. *Reliability Engineering*, 3:213–227, 1982. [76](#)
- [218] D. Stroup and A. Lindeman. Verification and Validation of Selected Fire Models for Nuclear Power Plant Applications. NUREG-1824, Supplement 1, United States Nuclear Regulatory Commission, Washington, DC, 2013. [77](#), [89](#)
- [219] B.N. Taylor and C.E. Kuyatt. Guidelines for Evaluating and Expressing the Uncertainty of NIST Measurement Results. NIST Technical Note 1297, National Institute of Standards and Technology, Gaithersburg, Maryland, 1994. [79](#)
- [220] G.W. Mulholland and C. Croarkin. Specific Extinction Coefficient of Flame Generated Smoke. *Fire and Materials*, 24:227–230, 2000. [80](#)
- [221] R.L. Alpert. *SFPE Handbook of Fire Protection Engineering*, chapter Ceiling Jet Flows. National Fire Protection Association, Quincy, Massachusetts, 4th edition, 2008. [82](#), [83](#), [84](#)
- [222] R.W. Bukowski and J.D. Averill. Methods for Predicting Smoke Detector Activation. In *Proceedings of the Fire Suppression and Detection Research Application Symposium, Orlando, Florida*. National Fire Protection Association, Quincy, Massachusetts, 1998. [85](#), [262](#)

- [223] K. McGrattan and B. Toman. Quantifying the predictive uncertainty of complex numerical models. *Metrologia*, 48:173–180, 2011. [85](#)
- [224] R.D. Peacock, P.A. Reneke, W.D. Davis, and W.W. Jones. Quantifying fire model evaluation using functional analysis. *Fire Safety Journal*, 33:167–184, 1999. [86](#)
- [225] G. Oehlert. A Note on the Delta Method. *The American Statistician*, 46(1):27–29, 1992. [86](#)
- [226] A. Gelman, J.B. Carlin, H.S. Stein, and D.B. Rubin. *Bayesian Data Analysis*. Chapman and Hall/CRC Press, Boca Raton, Florida, 2nd edition, 2004. [87](#)
- [227] J.W. Tukey. Curves as Parameters, and Touch Estimation. In *Proc. Fourth Berkeley Symp. on Math. Statist. and Prob.*, volume 1, pages 681–694. (Univ. of Calif. Press, 1961. [88](#)
- [228] M.L. Janssens and H.C. Tran. Data Reduction of Room Tests for Zone Model Validation. *Journal of Fire Science*, 10:528–555, 1992. [91](#)
- [229] Y.P. He, A. Fernando, and M.C. Luo. Determination of interface height from measured parameter profile in enclosure fire experiment. *Fire Safety Journal*, 31:19–38, 1998. [91](#)
- [230] F.R. Steward. Prediction of the height of buoyant diffusion flames. *Combustion Science and Technology*, 2(4):203–212, 1970. [172](#), [174](#)
- [231] H. Becker and D. Liang. Visible length of vertical free turbulent diffusion flames. *Combustion and Flame*, 32:115–137, 1978. [172](#), [174](#)
- [232] G. Cox and R. Chitty. Some source-dependent effects of unbounded fires. *Combustion and Flame*, 60:219–232, 1985. [172](#), [174](#)
- [233] Y. Hasemi and T. Tokunaga. Some experimental aspects of turbulent diffusion flames and buoyant plumes from fire sources against a wall and in corners. *Combustion Science and Technology*, 40:1–17, 1984. [172](#), [174](#)
- [234] B.M. Cetegen, E.E. Zukoski, and T. Kubota. Entrainment in the near and far field of fire plumes. *Combustion Science and Technology*, 39(1):305–331, 1984. [172](#), [174](#)
- [235] M.A. Delichatsios. Flame heights in turbulent wall fires with significant flame radiation. *Combustion Science and Technology*, 39:195–214, 1984. [172](#), [174](#)
- [236] F. Tamanini. Direct Measurement of the Longitudinal Variation of Burning Rate and Product Yield in Turbulent Diffusion Flames. *Combustion and Flame*, 51:231–243, 1983. [172](#)
- [237] N. Jarrin. *Synthetic Inflow Boundary Conditions for the Numerical Simulation of Turbulence*. PhD thesis, The University of Manchester, Manchester M60 1QD, United Kingdom, 2008. [270](#)
- [238] K. McGrattan, S. Hostikka, R. McDermott, J. Floyd, C. Weinschenk, and K. Overholt. *Fire Dynamics Simulator, Technical Reference Guide, Volume 1: Mathematical Model*. National Institute of Standards and Technology, Gaithersburg, Maryland, USA, and VTT Technical Research Centre of Finland, Espoo, Finland, sixth edition, September 2013. [325](#)
- [239] J. Andersen, C.L. Rasmussen, T. Giselsson, and P. Glarborg. Global combustion mechanisms for use in cfd modeling under oxy-fuel conditions. *Energy & Fuels*, 23(3):1379–1389, 2009. [328](#)

- [240] C.K. Westbrook and F.L. Dryer. Simplified Reaction Mechanisms for the Oxidation of Hydrocarbon Fuels in Flames. *Combustion Science and Technology*, 27:31–43, 1981. [328](#)
- [241] U. Wickström, D. Duthinh, and K.B. McGrattan. Adiabatic Surface Temperature for Calculating Heat Transfer to Fire Exposed Structures. In *Proceedings of the Eleventh International Interflam Conference*. Interscience Communications, London, 2007. [461](#)
- [242] A. Hamins. Energetics of Small and Moderate-Scale Gaseous Pool Fires. NIST Technical Note 1926, National Institute of Standards and Technology, Gaithersburg, Maryland, 2016. [562](#)
- [243] American Society for Testing and Materials, West Conshohocken, Pennsylvania. *ASTM E 1354-04a, Standard Test Method for Heat and Visible Smoke Release Rates for Materials and Products Using an Oxygen Combustion Calorimeter*, 2007. [623](#)
- [244] American Society for Testing and Materials, West Conshohocken, Pennsylvania. *ASTM E 2070-08, Standard Test Method for Kinetic Parameters by Differential Scanning Calorimetry Using Isothermal Methods*, 2008. [624](#)
- [245] American Society for Testing and Materials, West Conshohocken, Pennsylvania. *ASTM E 1175-87(2009), Standard Test Method for Determining Solar or Photopic Reference, Transmittance, and Absorptance of Materials Using a Large Diameter Integrating Sphere*, 2009. [624](#)
- [246] American Society for Testing and Materials, West Conshohocken, Pennsylvania. *ASTM E 1461-07, Standard Test Method for Thermal Diffusivity by the Flash Method*, 2007. [624](#)
- [247] American Society for Testing and Materials, West Conshohocken, Pennsylvania. *ASTM D 7309-11, Standard Test Method for Determining Flammability Characteristics of Plastics and Other Solid Materials Using Microscale Combustion Calorimetry*, 2011. [624](#)
- [248] American Society for Testing and Materials, West Conshohocken, Pennsylvania. *ASTM E 1131-08, Standard Test Method for Compositional Analysis by Thermogravimetry*, 2008. [624](#)
- [249] American Society for Testing and Materials, West Conshohocken, Pennsylvania. *ASTM D 5930-09, Standard Test Method for Thermal Conductivity of Plastics by Means of a Transient Line-Source Technique*, 2009. [624](#)
- [250] S.I. Stoliarov and R.N. Walters. Determination of the heats of gasification of polymers using differential scanning calorimetry. *Polymer Degradation and Stability*, 93:422–427, 2008. [625](#), [629](#), [631](#)
- [251] J.R. Hallman. Polymer surface reflectance-absorptance characteristics. *Polymer Engineering and Science*, 14:717–723, 1974. [625](#), [629](#), [631](#)
- [252] P.T. Tsilingiris. Comparative evaluation of the infrared transmission of polymer films. *Energy Conversion and Management*, 44:2839–2856, 2003. [625](#), [629](#), [631](#)
- [253] S.I. Stoliarov, R.E. Lyon, and G.T. Linteris. Prediction of the Gasification Rate of POM, PP, PA66 and PET in Fire-Like Environments. *Fire and Materials*, 2012. [627](#)
- [254] T. Matsumoto, A. Ono, Y. Noumaru, and F. Takeda. Measurements of Specific Heat Capacity and Emissivity of Graphite Samples using Pulse Current Heating at High Temperatures (III). In *Proceedings of the Seventeenth Japan Symposium on Thermophysical Properties*, pages 183–186, 1996. [629](#), [631](#)

- [255] E.S. Oztekin, S.B. Crowley S.B., R.E. Lyon, S.I. Stoliarov, P. Patel, and T.R. Hull. Sources of Variability in Fire Test Data: A Case Study on Poly(aryl ether ether ketone) (PEEK). *Combustion and Flame*, 159(4):1720–1731, 2012. [634](#)
- [256] F. Kempel, B. Schartel, G. T. Linteris, S.I. Stoliarov, R.E. Lyon, R.N. Walters, and A. Hofmann. Prediction of the Mass Loss Rate of Polymer Materials: Impact of Residue Formation. *Combustion and Flame*, 159:2974–2984, 2012. [636](#), [638](#)
- [257] G. Linteris, M. Zammarano, B. Wilthan, and L. Hanssen. Absorption and reflection of infrared radiation by polymers in fire-like environments. *Fire and Materials*, 36(7):537–553, 2012. [636](#), [638](#), [640](#)
- [258] R.E. Lyon and M.L. Janssens. *Encyclopedia of Polymer Science & Engineering*, chapter Polymer Flammability. Wiley, New York, 2005. [636](#), [638](#)
- [259] TIE-31: Mechanical and Thermal Properties of Optical Glass. Technical Information, Advanced Optics, SCHOTT AG, July 2004. [638](#)
- [260] G. Braeuer. Large Area Glass Coating. *Surface and Coatings Technology*, 112:358–365, 1999. [638](#)
- [261] J. Li. *A Multi-Scale Approach to Parameterization of Burning Models for Polymeric Materials*. PhD thesis, University of Maryland, College Park, Maryland, 2014. [640](#), [643](#), [645](#)
- [262] M.B. McKinnon, S.I. Stoliarov, and A. Witkowski. Development of a pyrolysis model for corrugated cardboard. *Combustion and Flame*, 160:2595–2607, 2013. [648](#), [649](#), [650](#)
- [263] P.J. Linstrom and W.G. Mallard. Evaluated Infrared Reference Spectra. WebBook. NIST Chemistry WebBook, NIST Standard Reference Database Number 69. [648](#), [649](#)
- [264] T. Matsumoto and A. Ono. Specific Heat Capacity and Emissivity Measurements of Ribbon-Shaped Graphite Using Pulse Current Heating. *International Journal of Thermophysics*, 16:267–275, 1995. [648](#), [649](#)
- [265] M.R. Semmes, X. Liu, M.B. McKinnon, S.I. Stoliarov, and A. Witkowski. A Model for Oxidative Pyrolysis of Corrugated Cardboard. In *Fire Safety Science – Proceedings of the 11th International Symposium*, University of Canterbury, Christchurch, New Zealand, 2014. Accepted. [650](#)
- [266] K. McGrattan, A. Lock, N. Marsh, M. Nyden, S. Bareham, M. Price, A.B. Morgan, M. Galaska, K. Schenck, and D. Stroup. Cable Heat Release, Ignition, and Spread in Tray Installations During Fire (CHRISTIFIRE), Phase 1: Horizontal Trays. NUREG/CR 7010, Vol. 1, United States Nuclear Regulatory Commission, Washington, DC, July 2012. [652](#)
- [267] D.T. Gottuk and D.A. White. *SFPE Handbook of Fire Protection Engineering*, chapter Liquid Fuel Fires. National Fire Protection Association, Quincy, Massachusetts, 4th edition, 2008. [658](#)
- [268] W.M. Haynes, editor. *CRC Handbook of Chemistry and Physics*, chapter Thermal Conductivity of Liquids. CRC Press/Taylor and Francis, Boca Raton, Florida, 95th edition, (Internet Version 2015). [658](#)
- [269] E.W. Lemmon, M.O. McLinden, and D.G. Friend. *NIST Chemistry WebBook, NIST Standard Reference Database Number 69*, chapter Thermophysical Properties of Fluid Systems. National Institute of Standards and Technology. <http://webbook.nist.gov>, (retrieved May 23, 2014). [658](#)

- [270] M.W. Chase. *NIST-JANAF Thermochemical Tables*. Journal of Physical and Chemical Reference Data, Monograph No. 9. American Chemical Society, Woodbury, New York, 4th edition, 1998. [658](#)
- [271] V. Babrauskas. *SFPE Handbook of Fire Protection Engineering*, chapter Heat Release Rates. National Fire Protection Association, Quincy, Massachusetts, 4th edition, 2008. [658](#)
- [272] E.S. Domalski and E.D. Hearing. *NIST Chemistry WebBook, NIST Standard Reference Database Number 69*, chapter Condensed Phase Heat Capacity Data. National Institute of Standards and Technology. <http://webbook.nist.gov>, (retrieved May 23, 2014). [658](#)
- [273] R.L. Brown and S.E. Stein. *NIST Chemistry WebBook, NIST Standard Reference Database Number 69*, chapter Boiling Point Data. National Institute of Standards and Technology. <http://webbook.nist.gov>, (retrieved May 23, 2014). [658](#)
- [274] D. Morvan and J.L. Dupuy. Modeling the propagation of a wildfire through a Mediterranean shrub using a multiphase formulation. *Combustion and Flame*, 138:199–210, 2004. [661](#), [663](#)
- [275] R.A. Susott. Characterization of the thermal properties of forest fuels by combustible gas analysis. *Forest Science*, 2:404–420, 1982. [661](#), [663](#)
- [276] R.C. Rothermel. A Mathematical Model for Predicting Fire Spread in Wildland Fuels. Research Paper INT-115, Intermountain Forest and Range Experiment Station, USDA Forest Service, Ogden, Utah, January 1972. [661](#), [663](#)
- [277] O.T. Farouki. Thermal properties of soils. CRREL Monograph 81-1, U.S. Army Corps of Engineers, Cold Regions Research and Engineering Laboratory, Hanover, New Hampshire, December 1981. [661](#)
- [278] A.J. Dyer. A review of flux profile relationships. *Boundary-Layer Meteorology*, 7:363–372, 1974. [667](#)
- [279] T.C. Brown, R.T. Cederwall, S.T. Chan, D.L. Ermak, R.P. Koopman, K.C. Lamson, J.W. McClure, and L.K. Morris. Falcon Series Data Report: 1987 LNG Vapor Barrier Verification Field Trials. Data Report GRI-89/0138, Lawrence Livermore National Laboratory, June 1990. [668](#)
- [280] D.J. Spiegelhalter. Diagnostic tests of distributional shape. *Biometrika*, 70(2):401–409, 1983. [680](#)